FLUID POWER
FUTURE TECHNOLOGY!

CONFERENCE PROCEEDINGS

12th International Fluid Power Conference (12. IFK)

October 12 – 14, 2020

in Dresden

Volume 1 – Symposium

Group A:	**Materials**
Group B:	**System design & integration**
Group C:	**Novel system solutions**
Group D:	**Additive manufacturing**
Group E:	**Components**
Group F:	**Intelligent control**
Group G:	**Fluids**
Group H | K:	**Pumps**
Group I | L:	**Mobile applications**
Group J:	**Fundamentals**

Publisher:

Dresdner Verein zur Förderung der Fluidtechnik e. V. Dresden
c/o Professur für Fluid-Mechatronische Systemtechnik
Technische Universität Dresden
01062 Dresden

Alle Rechte vorbehalten.
Alle hier veröffentlichten Beiträge sind als Manuskript gedruckt.
Die Autoren sind für ihren Beitrag inhaltlich und redaktionell verantwortlich.
Nachdruck – auch auszugsweise – nur mit Zustimmung des Herausgebers und des Verfassers.

All rights reserved.
All papers are published as manuscript.
The autors are responsible as regards content and edition.
No part of this publication – also in extracts – may be produced without prior permission of the publishers.

Online Publication:

Eine elektronische Version der Tagungsbände wird dauerhaft archiviert und öffentlich zur freien Benutzung bereitgestellt.
Sie finden die Dokumente unter der dauerhaften stabilen URN: urn:nbn:de:bsz:14-qucosa2-386614

An electronic version of these proceedings will be permanently archived and publicly available for free personal use.
It can be found using the persistent identifier URN: urn:nbn:de:bsz:14-qucosa2-386614

https://nbn-resolving.org/urn:nbn:de:bsz:14-qucosa2-386614

WELCOME TO THE 12TH IFK

Dear Sir or Madam,

we are pleased to present the conference proceedings for the 12th edition of the International Fluid Power Conference (IFK). The IFK is one of the world's most significant scientific conferences on fluid power control technology and systems. It offers a common platform for the presentation and discussion of trends and innovations to manufacturers, users and scientists.

The Chair of Fluid-Mechatronic Systems at the TU Dresden is organizing and hosting the IFK for the sixth time. Supporting hosts are the Fluid Power Association of the German Engineering Federation (VDMA), Dresdner Verein zur Förderung der Fluidtechnik e. V. (DVF) and GWT-TUD GmbH. The organization and the conference location alternates every two years between the Chair of Fluid-Mechatronic Systems in Dresden and the Institute for Fluid Power Drives and Systems in Aachen.

The symposium on the first day is dedicated to presentations focused on methodology and fundamental research. The two following conference days offer a wide variety of application and technology orientated papers about the latest state of the art in fluid power. It is this combination that makes the IFK a unique and excellent forum for the exchange of academic research and industrial application experience.

A simultaneously ongoing exhibition offers the possibility to get product information and to have individual talks with manufacturers.

The theme of the 12th IFK is "Fluid Power – Future Technology", covering topics that enable the development of 5G-ready, cost-efficient and demand-driven structures, as well as individual decentralized drives. Another topic is the real-time data exchange that allows the application of numerous predictive maintenance strategies, which will significantly increase the availability of fluid power systems and their elements and ensure their improved lifetime performance.

We create an atmosphere for casual exchange by offering a vast frame and cultural program. This includes a get-together, a conference banquet, laboratory festivities and some physical activities such as jogging in Dresden's old town.

I hope you enjoy reading the conference proceedings.

Prof. Dr.-Ing. Jürgen Weber

PROGRAM COMMITTEE

Achten, P.	Dr. ir., INNAS B.V., Breda NL
Bauer, F.	Dr.-Ing., Hydac Technology GmbH, Sulzbach/Saar
Boes, C.	Dr.-Ing., MOOG GmbH, Böblingen
Fabianek, M.	Dipl.-Ing., Liebherr Machines Bulle S.A., Bulle CH
Faß, U.	Dr.-Ing., Volvo Construction Equipment Germany GmbH, Konz
Fedde, T.	Dr.-Ing., CLAAS Tractor, Paderborn
Fiedler, M.	Dr.-Ing., Norgren GmbH, Fellbach
Fischer, M.	Dr.-Ing., Argo-Hytos Management + Consulting GmbH, Zug CH
Hahmann, W.	Dr.-Ing., Hydac International GmbH, Sulzbach/Saar
Hunger, I.	Lic. oec., Hunger DFE GmbH, Würzburg
Huster, G.	Dipl.-Ing., KraussMaffei Technologies GmbH, München
Igelhorst, W.	Dipl.-Ing., SMS Group, Mülheim an der Ruhr
Jähne, H.	Dr.-Ing., Hydrive Engineering GmbH, Freital
Kempermann, C.	Dr.-Ing., Fluitronics GmbH, Krefeld
Klug, D.	Dr.-Ing., Schuler Pressen GmbH, Waghäusel
Knobloch, M.	Dipl.-Ing., HAWE Hydraulik SE, München
Krallmann, J.	Dr.-Ing., Thomas Magnete GmbH, Herdorf
Krieg, M.	Dr.-Ing., Bosch Rexroth AG, Lohr am Main
Langen, A.	Dr.-Ing., Linde Hydraulics GmbH & Co. KG, Aschaffenburg
Legner, J.	Dipl.-Ing., ZF Friedrichshafen AG, Friedrichshafen
Leonhard, A.	Dr.-Ing., Parker Hannifin Manufacturing Germany GmbH & Co. KG, Chemnitz
Lindemann, L.	Dr., Fuchs Petrolub SE, Mannheim
Luther, R.	Dipl.-Ing., Fuchs Schmierstoffe GmbH, Mannheim
Lüüs, H.	Dipl.-Ing., Bucher Hydraulics GmbH, Klettgau
Martens, O.	Dr.-Ing., KOMATSU Mining Germany GmbH, Düsseldorf
Mundry, S.	Dr.-Ing., Caterpillar Global Mining Europe GmbH, Lünen
Neumeier, R.	Dipl.-Ing., Bürkert Werke GmbH, Ingelfingen
Pfab, H.	Dr.-Ing., Liebherr-Werk Bischofshofen GmbH, Bischofshofen AUT
Post, P.	Prof. Dr.-Ing., Festo AG & Co. KG, Esslingen
Rahmfeld, R.	Dr.-Ing., Danfoss Power Solutions GmbH & Co. OHG, Hamburg
Saffe, P.	Dr.-Ing., Aventics GmbH, Laatzen
Schmitz, K.	Prof. Dr.-Ing., RWTH Aachen
Schultz, A.	Dr.-Ing., Magnet-Schultz GmbH & Co. KG, Memmingen
Tappe, P.	Dr.-Ing., Magnet-Schultz GmbH & Co. KG, Memmingen
Sondermann, G.	Dipl.-Ing., Siempelkamp Maschinen- und Anlagenbau GmbH & Co. KG, Krefeld
Synek, P.	Dipl.-Ing., Fachverband Fluidtechnik im VDMA, Frankfurt am Main
Weber, J.	Prof. Dr.-Ing., TU Dresden

INTERNATIONAL ADVISORY COMMITTEE

Professor Eric Bideaux
INSA de Lyon, France

Professor Kalevi Huhtala
Tampere University of Technology, Finland

Professor Petter Krus
Lingköping University, Sweden

Professor Andrew Plummer
University of Bath, United Kingdom

Professor Kazushi Sanada
Yokohama National University, Japan

Professor Rudolf Scheidl
Johannes Kepler University Linz, Austria

Professor Kim Stelson
University of Minnesota, USA

Professor Huayong Yang
Zhejiang University, China

Professor Andrea Vacca
Purdue University, USA

Professor Takao Nishiumi
Shibaura Institute of Technology, Japan

PEER REVIEW AT THE 12TH IFK

peer reviewed

Many public institutions that support research projects require regular publication of the results. To ensure that the results are of scientific value, peer review is often required. Therefore we offer all authors the opportunity to have their work evaluated in order to be able to prove the scientific value.

A paper that has been chosen by the author to be reviewed will be subjected to an independent examination by a total of three specialized experts among the Program Committee as well as the Institute of Mechatronic Engineering at the TU Dresden, or the Institute for Fluid Power Drives and Systems at RWTH Aachen University. After this initial evaluation, the authors have the opportunity to revise their paper as needed and resubmit it with the necessary changes. If the reviewers accept the changes, the paper will be included in the conference proceedings as peer reviewed.

This extensive assessment process serves the purpose of quality assurance in terms of content and form, and would not have been possible without the expert support of the Program Committee. The organizers of the IFK want to thank all reviewers for their support.

The IFK traditionally is a colloquium where both scientists and representatives of industry come together to exchange their knowledge and experience. Accordingly, a peer review is only meaningful for some of the speakers, with the associated additional effort for both sides. Therefore the peer review is not intended to classify the paper but rather to support the need for it.

GROUP A
Materials

A-1 CHALLENGES FOR NOVEL LEAD-FREE ALLOYS IN HYDRAULICS
Björn Reetz, OTTO FUCHS Dülken GmbH & Co.KG, Germany 17

A-2 RESEARCHES ON WATERHYDRAULIC MOTOR
Franc Majdič, University of Ljubljana, Slovenia 27

A-3 ORIFICES FLOW SATURATION IN OIL HYDRAULIC APPLICATIONS
Pietro Marani, CNR-IMAMOTER, Italy 33

GROUP B
System design & integration

B-1 FREQUENCY BASED EFFICIENCY EVALUATION – FROM PATTERN RECOGNITION VIA BACKWARDS SIMULATION TO PURPOSEFUL DRIVE DESIGN
Martin Starke, Technische Universität Dresden, Germany 43

B-2 OPTIMIZATION OF OPERATION STRATEGY FOR PRIMARY TORQUE BASED HYDROSTATICS DRIVETRAIN USING ARTIFICIAL INTELLIGENCE
Yusheng Xiang, Karlsruhe Institute of Technology, Germany 55

B-3 HARDWARE-IN-THE-LOOP SIMULATION OF HYBRID HYDROMECHANICAL TRANSMISSIONS
Viktor Larsson, Linköping University, Sweden 67

B-4 APPLICATION OF MACHINE LEARNING TO IMPROVE THE PERFORMANCE OF A PRESSURE-CONTROLLED SYSTEM
Fabian Kreutmayr, HAWE Hydraulik SE, Germany 77

GROUP C
Novel system solutions

C-1 A CLOSED CIRCUIT ELECTRO-HYDRAULIC ACTUATOR WITH ENERGY RECUPERATION CAPABILITY
Shaoyang Qu, Purdue University, USA 89

C-2 ANALYSIS OF NOVEL ZONAL TWO-CYLINDER ACTUATION SYSTEM FOR HEAVY LOADS
Tatiana Minav, Tampere University, Finnland 99

C-3 EXPERIMENTAL EVALUATION OF AN ELECTRO-HYDROSTATIC ACTUATOR FOR SUBSEA APPLICATIONS IN A HYPERBARIC CHAMBER
João Pedro Duarte da Silva, Federal University of Santa Catarina (UFSC), Brazil 105

GROUP D
Additive manufacturing

D-1 TRIBOLOGICAL INVESTIGATIONS ON ADDITIVELY MANUFACTURED SURFACES USING EXTREME HIGH-SPEED LASER MATERIAL DEPOSITION (EHLA) AND LASER POWDER BED FUSION (LPBF)
Achill Holzer, RWTH Aachen University, Germany 119

D-2 ASSESSMENT OF FRICTION LOSS TO HORIZONTALLY BUILT FLUID PASSAGES USING ADDITIVE MANUFACTURING
Yi Zhu, Zhejiang University, China 129

D-3 DESIGN AND EXPERIMENTAL INVESTIGATION OF AN ADDITIVE MANUFACTURED COMPACT DRIVE
Gunnar Matthiesen, RWTH Aachen University, Germany 137

D-4 ADDITIVE MANUFACTURING OF HYDRAULIC MANIFOLDS - A HOLISTIC APPROACH ACROSS THE ENTIRE VALUE CHAIN
Bastian Beckmann, Bosch Rexroth AG, Germany 149

D-5 AM-DRIVEN DESIGN OF HYDRAULIC MANIFOLDS: ENHANCING FLUID FLOW AND REDUCING WEIGHT
Yi Zhu, Zhejiang University, China 155

GROUP E
Components

E-1 FUNCTIONAL PROOF OF A FLAT SLIDE VALVE AS A 4/3-WAY PROPORTIONAL VALVE
Stefan Aengenheister, RWTH Aachen University, Germany 163

E-2 CONTROL CONCEPT FOR A GREASE LUBRICATED HYDROSTATIC BEARING
Igor Mass, Hochschule Niederrhein, Germany 171

E-3 FOAM ACCUMULATORS: PACKAGING AND WEIGHT REDUCTION FOR MOBILE APPLICATIONS
Peter F. Pelz, Technische Universität Darmstadt, Germany 181

E-4 ONE DIMENSIONAL UNSTEADY MODEL OF A HYDROPNEUMATIC PISTON ACCUMULATOR BASED ON FINITE VOLUME METHOD
Filipp Kratschun, RWTH Aachen University, Germany 189

E-5 EXPERIMENTAL TESTS OF FLUID EXCHANGE PROCESS IMPROVEMENT IN A NEW DESIGN OF HYDRAULIC CYLINDER WITH A SUPPLY SYSTEM
Tomasz Siwulski, Wrocław University of Science and Technology, Poland 199

GROUP F
Intelligent control

F-1 SIMULATION OF AN INTERLOCKING HYDRAULIC DIRECT-DRIVE SYSTEM FOR A BIPED WALKING ROBOT
Juri Shimizu, Waseda University and Hitachi, Japan ____ 211

F-2 NONLINEAR FORCE TRACKING CONTROL OF ELECTROHYDROSTATIC ACTUATORS SUBMITTED TO MOTION DISTURBANCES
Tahereh Vaezi, Laboratoire Ampère CNRS, France ____ 221

F-3 MULTIDIMENSIONAL FLOW MAPPING FOR PROPORTIONAL VALVES
André Sitte, Technische Universität Dresden, Germany ____ 231

F-4 MULTI-OBJECTIVE CONTROL OF A SELF-LOCKING COMPACT ELECTRO-HYDRAULIC CYLINDER DRIVE
Nikolaj Grønkær, Aalborg University, Denmark ____ 241

F-5 POSITION SIGNAL FILTERING FOR HYDRAULIC ACTIVE HEAVE COMPENSATION SYSTEM
Wojciech Pomierski, National Oilwell Varco Poland, Poland ____ 253

GROUP G
Fluids

G-1 NUMERICAL PREDICTION AND EXPERIMENTAL INVESTIGATION OF CAVITATION EROSION OF HYDRAULIC COMPONENTS USING HFC
Atena Moosavi, Technische Universität Dresden, Germany ____ 263

G-2 BASIC ASPECTS WHEN USING IONIC LIQUIDS AS A HYDRAULIC FLUID
Darko Lovrec, University of Maribor, Slovenia ____ 273

G-3 COMPUTATIONAL APPROACH TO THE EXPERIMENTAL DETERMINATION OF DIFFUSION COEFFICIENTS FOR OXYGEN AND NITROGEN IN HYDRAULIC FLUIDS USING THE PRESSURE-DECAY METHOD
Andris Rambaks, RWTH Aachen University, Germany ____ 283

G-4 OPTIMIZING HYDRAULIC RESERVOIRS USING EULER-EULER-LAGRANGE MULTIPHASE CFD SIMULATION
Lukas Muttenthaler, Johannes Kepler University, Austria ____ 295

GROUP H | K
Pumps

H-1 THE INFLUENCE OF THE SWASH PLATE OSCILLATION ON PRESSURE RIPPLE IN VARIABLE DISPLACEMENT AXIAL PISTON PUMP
Junhui Zhang, Zhejiang University, China 307

H-2 INVESTIGATION OF THE WEAR BEHAVIOR OF THE SLIPPER IN AN AXIAL PISTON PUMP BY MEANS OF SIMULATION AND MEASUREMENT
Roman Ivantysyn, Technische Universität Dresden, Germany 315

H-3 A FAST APPROACH FOR COUPLED FLUID-THERMAL MODELING OF THE LUBRICATING INTERFACES OF AXIAL PISTON MACHINES
Swarnava Mukherjee, Purdue University, USA 327

H-4 A CFD DESIGN OF ENGINEERED SURFACE FOR TRIBOLOGICAL PERFORMANCE IMPROVEMENTS IN HYDRAULIC PUMPS
Paolo Casoli, University of Parma, Italy 341

H-5 A STUDY INTO FORCES AND MOMENTS ACTING ON THE SWASH PLATE OF AN AXIAL PISTON PUMP USING A NOVEL APPROACH TO REDUCE PRESSURE AND FLOW PULSATIONS.
Ram S. Chandran, Kettering University, USA 351

H-6 WEAR PREDICTION OF PISTON/CYLINDER PAIR IN AXIAL PISTON PUMP
Junhui Zhang, Zhejiang University, China 361

H-7 NUMERICAL CALCULATION OF DYNAMIC STIFFNESS AND DAMPING COEFFICIENTS OF OIL LUBRICATION FILM IN INTERNAL GEAR MOTORS AND PUMPS
Pham Trong Hoa, University of Transport and Communications, Vietnam 369

K-1 DAMPING STRATEGIES FOR ENERGY EFFICIENT PRESSURE CONTROLLERS OF VARIABLE DISPLACEMENT PUMPS
Florian Schoemacker, RWTH Aachen University, Germany 379

K-2 OPTIMIZATION OF THE TRIBOLOGICAL CONTACT OF VALVE PLATE AND CYLINDER BLOCK WITHIN AXIAL PISTON MACHINES
Stefan Geffroy, RWTH Aachen University, Germany 389

K-3 NUMERICAL AND EXPERIMENTAL STUDY ON NOVEL HYDRAULIC PUMP CONCEPT
Seong-Ryeol Lee, RWTH Aachen University, Germany 399

K-4 A NUMERICAL MODEL FOR THE EVALUATION OF GEROTOR TORQUE CONSIDERING MULTIPLE CONTACT POINTS AND FLUID-STRUCTURE INTERACTIONS
Zubin Mistry, Purdue University, USA 409

GROUP I | L
Mobile applications

I-1 OPTIMIZATION OF HYDROSTATIC-MECHANICAL TRANSMISSION CONTROL STRATEGY BY MEANS OF TORQUE CONTROL
Yusheng Xiang , Bosch Rexroth AG, Germany ____ 421

I-2 REINFORCEMENT LEARNING: A CONTROL APPROACH FOR REDUCING COMPONENT DAMAGE IN MOBILE MACHINES
Lars Brinkschulte, Karlsruhe Institute of Technology, Germany ____ 433

I-3 INTELLIGENT TWIN STEERING SYSTEM
Biagio Borretti, Dana Motion Systems Italia srl, Italy ____ 445

I-4 AUTONOMOUS CONTROL OF HYDRAULIC MOBILE APPLICATIONS – A 21-TON EXCAVATOR CASE STUDY
Tim Opperwall, Husco International, USA ____ 453

I-5 ELECTRIFICATION OF HYDRAULIC SYSTEMS USING HIGH-EFFICIENCY PERMAMENT MAGNET MOTORS
Pablo Eduardo Castro Palavicino, University of Wisconsin-Madison, USA ____ 461

L-1 CHALLENGES AND POSSIBILITIES OF THE INTEGRATION OF ELECTRIC DRIVES IN MOBILE MACHINERY
Andreas Opgenoorth, RWTH Aachen, Germany ____ 471

L-2 RESEARCH ON EFFICIENT DRIVING METHOD OF HEAVY HYDRAULIC EXCAVATOR BOOM
Long Quan, Taiyuan University of Technology, China ____ 481

L-3 OPTIMAL CONTROL OF THE HYDRAULIC ACTUATED BOOM SYSTEM BASED ON PORT-HAMILTONIAN FORMULATION
Lingchong Gao, Technical University of Munich, Germany ____ 489

L-4 THE USE OF A HOLISTIC MACHINE SIMULATION FOR THE DEVELOPMENT OF HYDRAULIC HYBRID MODULES TO REDUCE TRANSIENT ENGINE-OUT EMISSIONS
Lars Brinkschulte, Karlsruhe Institute of Technology, Germany ____ 499

GROUP J
Fundamentals

J-1 IMPEDANCE MEASUREMENT IN A HYDROSTATIC DRIVE
Benedikt Müller, FLUIDON Gesellschaft für Fluidtechnik mbH, Germany ____ 513

J-2 ON THE THERMODYNAMIC CONSISTENCY OF EXPERIMENTALLY DETERMINED FLUID PROPERTIES
Enrico Pasquini, FLUIDON Gesellschaft für Fluidtechnik mbH, Germany ____ 523

J-3 FLUID-THERMAL CO-SIMULATION FOR A HIGH PERFORMANCE CONCRETE MACHINE FRAME
Christoph Steiert, Technische Universität Dresden, Germany ____ 533

J-4 THE APPLICABILITY OF THE MASS-FLOW-MODEL ACCORDING TO ISO 6358 WITH THE PARAMETER CRITICAL CONDUCTANCEC AND CRITICAL PRESSURE RATIO B FOR GASES IN HIGH-PRESSURE RANGE UP TO 300 BAR
Lucian Pasieka, Eugen Seitz AG, Switzerland ____ 541

GROUP A

Materials

peer reviewed

CHALLENGES FOR NOVEL LEAD-FREE ALLOYS IN HYDRAULICS

Björn Reetz*, Tileman Münch

OTTO FUCHS Dülken GmbH&Co.KG, Heiligenstraße 70, D-41751 Viersen
* Corresponding author: Tel.: +49 2162 9567738; E-mail address: bjoern.reetz@otto-fuchs.com

ABSTRACT

Different special brass (e.g. CuZn37Mn3Al2PbSi) and bronze alloys (e.g. CuPb15Sn) are well known for use in oil-hydraulics having in common to be alloyed with lead. The lead content of special brass alloys in this use ranges from 0.1 to 2.0 mass-%. Some bronze alloys provide even much higher contents of lead of 10 to 15 mass-%. Typically, lead is considered for improvement of machinability or castability. Beyond this purpose lead in brass and bronze alloys affects many more properties of manufacturing and application. During the shaping of the parts by means of hot or cold forming often the materials are strained close to their limits. Thanks to lead cracking is prevented during this process. Lead is also of great importance for the improvement of tribological systems. The surfaces of these systems are exposed to friction and wear. Lead is incorporated in the surface layers and supports the tribological system in their running-in process to achieve a steady state of friction and wear.

Above all lead is unique because it forms no solid solution with copper or brass and forms no compounds with other typical copper alloying elements. The feasibility assessment of elements in order to substitute lead in brass or bronze alloys has to be done for each alloy and application individually. In oil-hydraulic applications as bushings, slippers or distributor plates, lead-free alloys must fulfil different profiles of requirements, depending on the conditions of manufacturing and application. The requirements do not only include mechanical strength, formability and thermal strength, but also fatigue strength, low friction and high wear resistance and lubricant compatibility.

Consequently, the substitution of lead in brass and bronze alloys for application in oil-hydraulics is a challenging task. This does not only apply for the requirements for machining and forming, but particularly for the need of the new alloys to function under wear, friction and corrosion. Examples are given for how these challenges of new lead-free special brass alloys can be met in bushings (machining, friction properties), slippers (forming, strength) and distributor plates (fatigue strength) for axial piston pumps. Further on, new lead-free special brass alloys for contact with environmentally compatible lubricants are presented. All these examples show that there is not the one and only lead-free alloy for applications in oil-hydraulics. In fact, every application requires a different alloy which is composed and processed individually to meet the specific demands.

Keywords: Special brass alloys, lead free, axial piston pump, slipper, bushings, valve plates, challenges

1. INTRODUCTION

Typically, copper alloys for oil-hydraulics are alloyed with more than 0.1 mass-% lead. The content of lead ranges from 0.1 to 2 mass-% in special brass alloys (e.g. CuZn37Mn3Al2Pb Si), up to 3.5 mass-% in brass alloys for machining and even up to 23 mass-% in lead bronze alloys. Special brass is brought into final shape by hot and cold forming.

Since the European Commission has endorsed the decision to classify lead as Toxic to Reproduction, producers and consumers of copper alloys are becoming more and more active to develop and to validate alternative lead-free copper alloys. This is also the case of application in oil-hydraulics where alloys once validated and used for decades are to be replaced.

Reason enough to look on the impact of lead on microstructures and properties of these alloys, before going into any specific examples for the substitution of lead.

2. IMPACT OF LEAD ON MANUFACTURING AND APPLICATION PROPERTIES OF COPPER ALLOYS

The improvement of machinability is regarded as being the primary effect of lead. Chip breaking is supported because lead is insoluble and forms precipitations.

Beyond that, lead affects many other properties of copper alloys [1]:

- In casting copper alloys, lead migrates into micropores increasing the density of the cast product.
- Lead contributes to grain refinement of copper alloys which results in an increase of strength and toughness of these alloys [2].
- Investigations on machining brass indicate that lead also affects relaxation strength of brass alloys positively [3].
- Trials with CuZn42have shown the formation of microcracks. This effect was not encountered with CuZn40Pb2 [3].
- Enhanced use of bio-compatible lubricants provokes dezincification or stress corrosion cracking of parts made of copper alloys. Lead supports the formation and stability of passivation layers and, therefore, enhances the corrosion resistance of copper alloys in bio compatible lubricants [4].
- Surface layers are not only formed due to corrosion but also during friction (so-called “3rd body”). Lead is incorporated into friction layers [5], thereby increasing load capacity and reducing friction.
- When lead is used for alloying for hydraulics it does not diminish thermal conductivity of the alloy [6]. Sufficient thermal conductivity is needed for hydraulic parts and prevents them from overheating.
- As lead alloys provide low material costs and additional cost savings due to improvement of manufacturing properties, the total costs of the finished parts made of lead alloys are also lower compared to lead free alloys.

Some negative aspects of lead should be mentioned also. These include upcoming legal restrictions, but also technical disadvantages. One of the main technical shortcomings is that lead enhances hot shortness in copper alloys.

3. STATE OF THE ART IN OIL-HYDRAULICS

Special brass alloys are specially designed for use in lubricated sliding contacts and they are exposed to specifically high mechanical and thermal loadings. Axial piston pumps and gear pumps and hydraulics in automotive are typical examples for applications.

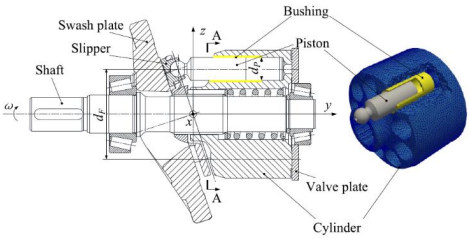

Figure 1: Scheme picture of axial piston pump [7], only main components shown, slipper, bushings and valve plate typically made of special brass

Typically, these special brass alloys contain from 20 to 30 mass-% zinc. Further on, silicon and one or more of the elements aluminium, manganese, nickel and iron are alloyed. The sum of these alloying elements amounts to 10 mass-% or even higher. Finally, the serial special brass alloys for hydraulics are alloyed with lead. Generally, these alloys consist of a matrix of α/β-brass and silicides (also referred to as intermetallics or particles). These silicides are distributed within the matrix uniformly and, therefore, they are embedded both in the interior and on the grain boundaries of the grains of the brass matrix.

4. NEW LEAD-FREE COPPER ALLOYS FOR THE OIL-HYDRAULIC INDUSTRY

4.1. New lead-free Special Brass Alloys for Bushings in axial Piston Pumps

Cylinder bushings are a good example for parts whose final dimensions and surfaces must be generated by machining. Lead has a strong impact on machinability and, consequently, the influence of lead-free chemical compositions on machinability must be considered thoroughly. OTTO FUCHS investigated the machinability of different lead-free special brass alloys systematically and, therefore, regarded chip

breaking, wear of cutting tools, machining force and surface roughness of the machined part (detailed description [8]).

Typically, special brass materials for bushings provide a heterogeneous matrix of α and β-phase (see **Figure 2**). A certain content of β-phase is required for improvement of the wear resistance of the bushings. But a major part of α-phase is also needed, since cold drawing of the pre-material for cylinder bushings is mandatory to achieve suitable tolerances for machining and the α-phase improves cold drawability. Nevertheless, due to the α-phase the material is relatively soft and, therefore, is taking advantage from presence of lead which supports chip breaking. In general, such a material without lead (e.g. see **Figure 2b**) forms long chips (see **Figure 3a**) or a build-up of material on the edge of the cutting device.

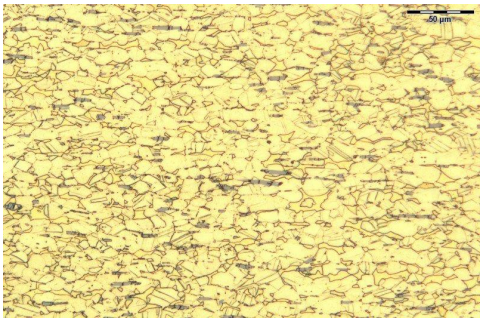

a

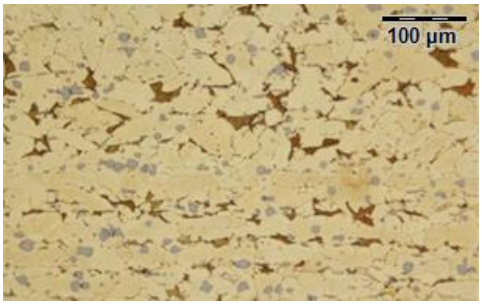

b

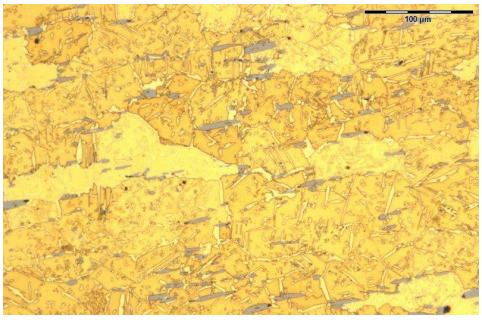

c

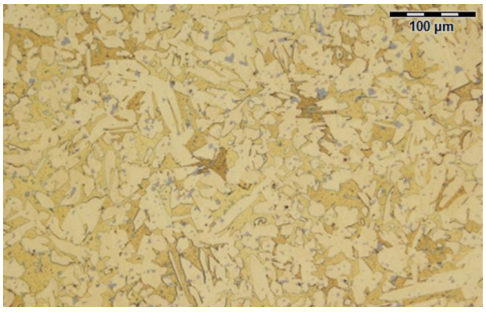

d

Figure 2: Microstructures of different special brass alloys for bushings in oil-hydraulics, light optical micrographs, CuZn37Mn3Al2PbSi (a), lead-alloyed near-α-alloy (OF 2297, b), lead-free near-α-alloy (OF 2295, c), lead-free α/β-alloy (OF 2299, d)

Figure 2d shows the microstructures of the recently developed lead-free special brass alloy OF 2299. Its optimized fine two-phase-microstructures of α/β-phase support discontinuous chip breaking as shown in **Figure 3c**.

a

b

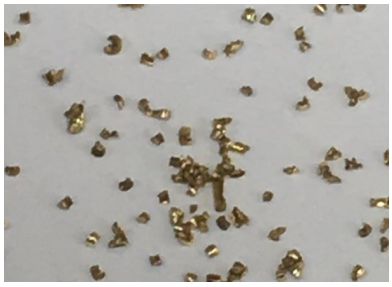

c

Figure 3: Chip breaking of different special brass alloys for use in hydraulics, lead-alloyed near-α-alloy for bushings (a), lead-free near-α-alloy for bushings (b), optimized lead-free α/β-alloy (c)

So far, machinability was considered. But machinability is not the only requirement for alloys which are used in bushings in axial piston pumps. Strong friction forces appear on the bushing due to the forces acting on the piston and tilting the piston against the bushing. These friction forces are not constant but depend on the position and movement of the piston during rotation of the swash plate together with the inclination angle of the swash plate (**Figure 4**).

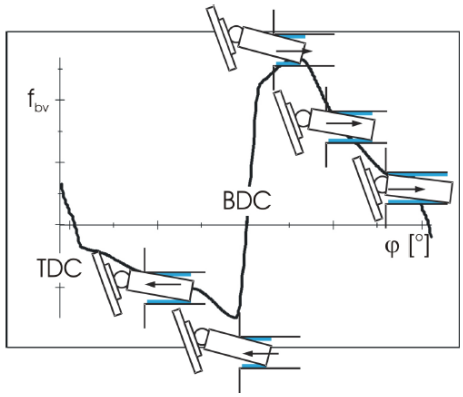

Figure 4: Typical friction progress for a piston-bushing-contact at low turning speed, top (TOD) and bottom dead centre (BDC), angle position φ of swash plate [9]

Under friction, lead functions as a dry lubricant and, hereby, counteracts adhesion in the piston-bushing-contact. Despite all reservations against lead, a solution is yet to be found for avoiding this kind of adhesion in lead-free special brass alloys. Interestingly, investigations with different lead-free alloys show that there is no single material property dominating adhesion resistance. Adhesion resistance can be correlated neither with phase composition nor with hardness.

Under standard conditions the new lead-free alloy OF 2299 copes with the friction conditions in axial piston pumps and motors very well. But in some special cases, customers design their axial piston pumps and motors in such a way that friction in the piston-bushing-contact is particularly challenging. For this special purpose the near-α-alloy OF 2297 has the best characteristics compared with all other lead-free alloys of this study. The good adhesion resistance of this alloy was not to be expected, as there is a relatively soft matrix of α-phase. Although a soft surface functions as a shearing layer to support sliding against the counter surface, it is known to provoke adhesion. This is the more reason, why a combined influence of both phase distribution and chemical composition is considered mandatory for such an outstanding adhesion resistance of the alloy OF 2297. Thus, a lot of questions remain open and further investigations are planned for deeper understanding of the mechanisms which protect the alloy OF 2297 against adhesion.

4.2. New lead-free Special Brass Alloys for Slippers in axial Piston Pumps

Another part of axial piston pumps and motors with particularly complex requirements are slippers (**Figure 5a**). Good hot formability is requested for extrusion and forging of raw parts and good machinability for production of machined parts. The flange of the slipper is joined with the sphere of the piston for achieving a hinged and free-moving assembly. Consequently, a good cold formability is needed for joining. On the one hand, the assembly is exposed to high mechanical loadings during service but on the other hand, the piston must stay free to move well in the calotte of the slipper. Under these conditions, slipper and piston need to stay connected un-detachably. High strength, fatigue strength and wear resistance are further requirements for slippers.

a

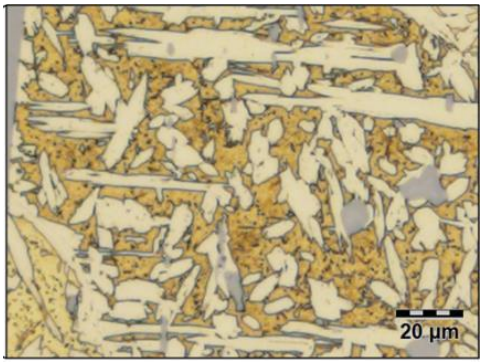

b

Figure 5: Picture of a slipper for axial piston pumps and motors (a) and micrograph, light optical microscopy, lead-free alloy OF 2299 from OTTO FUCHS (b)

Cold deformation during joining is performed close to the formability limit of the alloy. This forming process is already a challenge for lead-alloyed special brass alloys. Even more challenging is this process of joining, when it is applied to lead-free alloys where the positive lubrication effect of lead in cold forming is missing. It is inevitable, that lead-free alloys must be optimized for the requirements of such a cold forming process. Investigations with different lead-free alloys have revealed that the following characteristics are needed to achieve this formability even without lead:

- Fine grained microstructures
- High content of β-phase for hot forming and strength properties
- Certain content of α-phase for cold forming
- Micro alloying which serves for balancing different requirements

According to these requirements the new special brass alloy OF 2299 provides outstanding performance. Its microstructures show a perfect realization of the characteristics which are needed for slippers (illustrated in **Figure 5b**).

4.3. New lead-free high strength alloys for distributor plates

Lead bronze alloys provide very high lead content which ranges from 10 to 23 mass-% and, consequently, they are used when high loadings or poor lubrication is applied (e.g. for certain types of valve plates, **Figure 6**). Lead is insoluble in copper and forms coarse precipitations which are distributed in a matrix of pure α-phase. The diameter of the precipitations of lead amounts to several hundred microns. These precipitations serve as a reservoir for lead as dry lubricant against friction under high loadings or poor external lubrication. During relative movement of both sliding partners lead is set free and distributed over the sliding surface.

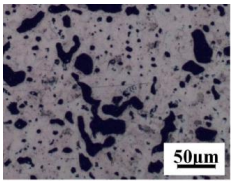

a

b

Figure 6: Example of a bimetal distributor plate ([10], a) and micrograph of a lead bronze typically used for friction layers of bimetal distributor plates (b, [11])

Lead bronze is used either as a bulk material or it is plated on a steel back. The steel back of the bi-metal plates contributes to their high fatigue strength. So far, the use of bronze-plated steel distributor plates for axial piston pumps and

motors with very high loadings was indispensable. Existing leaded brass alloys do not deal with such extreme loadings, properly. But the development of new lead-free special brass alloys opened new opportunities also for heavy conditions. New special-brass alloys (**Table 1**) cover a range of properties from standard applications to high pressure pumps and motors in a way that had not been possible before.

Table 1: Typical mechanical properties of existing and new alloys for distributor plates, room temperature

Properties	Bimetal, lead bronze layer	OF 2212 (leaded brass)	OF 2295 (lead-free, standard applications)	OF 2290 (lead-free, high strength)
Yield Strength [MPa]	430-500	250-350	320-450	500-650
Tensile Strength [MPa]	620-850	510-610	550-650	700-850
Elongation at break [%]	>14	>8	>8	>10
Hardness HBW	270-400	150-180	150-180	210-260
Bending fatigue strength [MPa]	250-280	170-200	170-200	230-250

The new special brass alloys OF 2295 is suitable for standard applications. Its mechanical properties are already superior to reference leaded alloys, but still too low for the use of it in new generations of piston pumps and motors with higher pressures. Under these conditions the new high strength special brass alloy OF 2290 can be applied. OF 2290 combines high strength with acceptable toughness (**Table 1**).

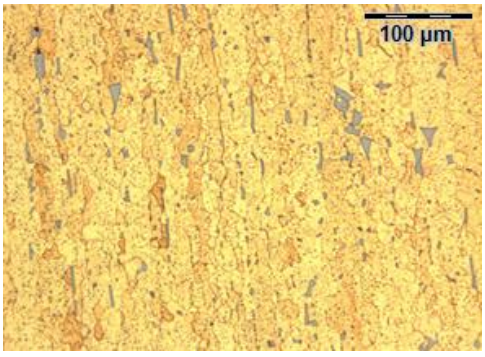

Figure 7: Micrograph of high strength lead-free special brass alloy for high strength valve plates, alloy OF 2290

The outstanding properties of alloy OF 2290 are due to the following measurements (**Figure 7**):

- Chemical composition containing aluminium and nickel
- Matrix of β-phase
- Fine grained microstructures
- Fine precipitations
- Several microalloying elements

4.4. New lead-free special brass alloys for contact with environmentally compatible lubricants

Environmentally compatible lubricants (biolubricants), e.g. esters, PAOs and PAGs are of increasing importance for oil-hydraulics. Biolubricants do have a market share of about 5 to more than 10 % [12, 13]. The reasons for this are manifold and range from environment and health protection to increasing efficiency of components and systems lubricated with biolubricants.

Unfortunately, most copper alloys, e.g. certain special brass alloys, provide poor compatibility with biolubricants. The reason for this is that biolubricants are prone to aging. Aging of PAGs occurs by oxidisation. Esters are decomposed forming acids. The acidity of the biolubricants increases due to aging and, consequently, brass alloys are exposed to corrosion attack. Corrosion may occur in the form of dezincification or stress corrosion cracking when internal or external stresses are present [14, 15, 16]. Under these circumstances, lead contributes to the improvement of corrosion resistance which is achieved by the formation of passivation layers. Accordingly, CuZn37Mn3Al2PbSi is a standard leaded alloy for use against biocorrosion (**Figure 8**).

Consequently, when brass is made lead-free these alloys need to be optimized to get similar corrosion resistance as before. For that reason, different lead bearing and lead-free special brass alloys were tested using the following conditions:

- Test fluid was a mixture of engine oil, sulphuric acid and 20 % of bioethanol E85.
- ph value of test fluid was 2.6.
- Testing temperature was 60°C.

Cylindrical samples were put into the test fluid for different times. After tests, change of weights of the samples was determined and sample surface was characterized with light optical microscopy.

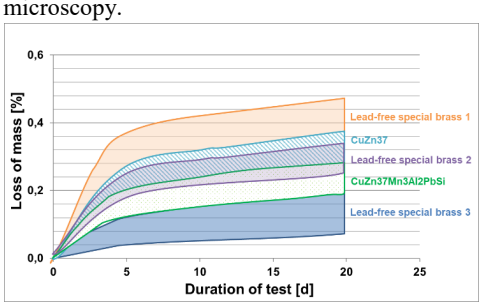

Figure 8: Loss of mass of different brass alloys, exposed to a fluid mixture of engine oil, 20% bioethanol E85 and sulphuric acid, ph-value=2.6, testing temperature=60°C, variation of duration time

In this study, CuZn37 was also tested. CuZn37 provides a matrix of mainly α-phase. Only on the grain boundaries of the α-phase some β-phase might be present and, then, reduces the corrosion resistance of the alloy. No alloying elements are present in CuZn37 which could protect against corrosion. Thus, along the β-phase corrosion can propagate into the depth and (**Figure 10c**) and reduce material strength significantly.

The results with CuZn37 underline that when giving up lead other elements are needed for passivation. For that purpose, new lead-free special brass alloys contain aluminium, manganese and other elements, additionally. **Figure 9** shows the microstructures of these new lead-free special brass alloys. The microstructures range from pure β-phase to a mixture of α– and β-phase.

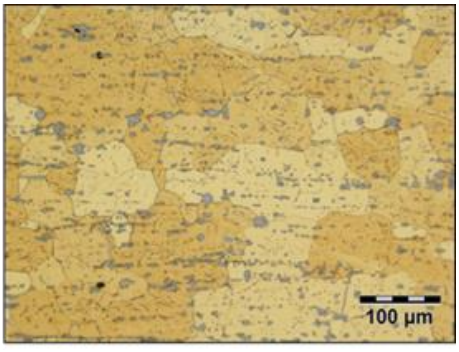

a

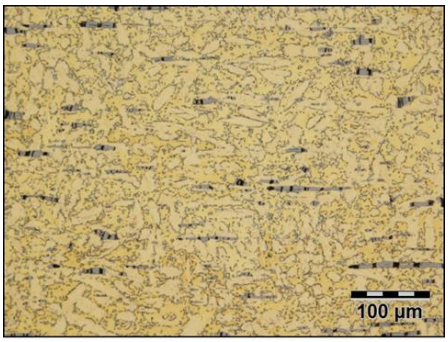

b

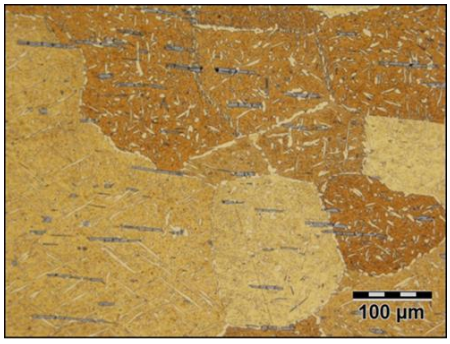

c

Figure 9: Light optical micrographs of new lead-free special brass alloys for contact with environmentally compatible lubricants, lead-free special brass alloy 1 (a), 2 (b) and 3 (c)

The corrosion resistance against biolubricants of all these alloys is similar or even superior to CuZn37Mn3Al2PbSi, which is taken as a reference.

In tribological applications wear superposes corrosion and enhances material damage. Therefore, an optimized alloy for use in friction and wear with environmentally compatible lubricants need to combine both a good corrosion and wear resistance. This perfect combination is given with alloy 1. Corrosion resistance of alloy 1 against biocorrosion is very close to reference alloy CuZn37Mn3Al2PbSi. Alloy 1 has a matrix of β-phase (**figure 9a**) and provides tensile strength values of up to 900 N/mm^2. Corrosion attack on alloy 1 is very homogeneous (**Figure 10d**). Consequently, alloy 1 combines extraordinary strength with remarkable corrosion resistance.

For some other reasons, a mixture of α/β-phase might be requested for application. Generally, the coexistence of α-phase and β-phase in the matrix of brass alloys is disadvantageous for resistance to galvanic corrosion. The more important is to support passivation in these alloys and this aim was attained (**Figure 10e**). Thanks to alloying with additional aluminium and manganese and some further microelements the lead-free α/β-special brass alloys 2 and 3 form passivation layers which are strong and dense enough to protect the surfaces as can be seen in **Figure 8**.

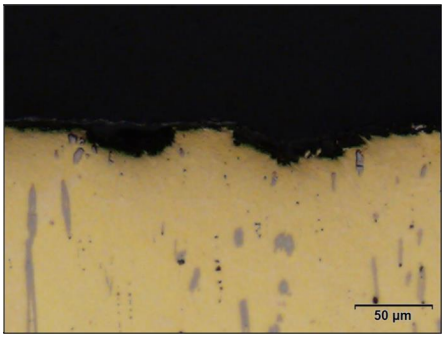

a

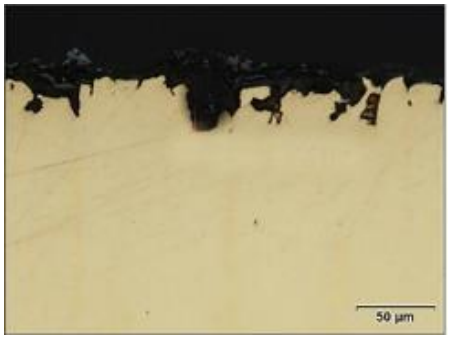

b

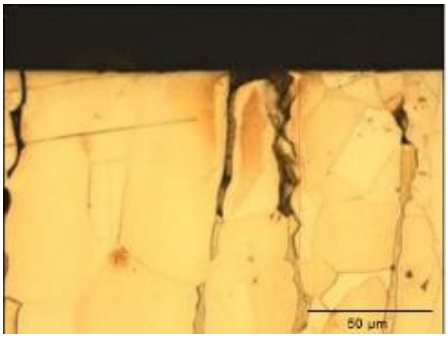

c

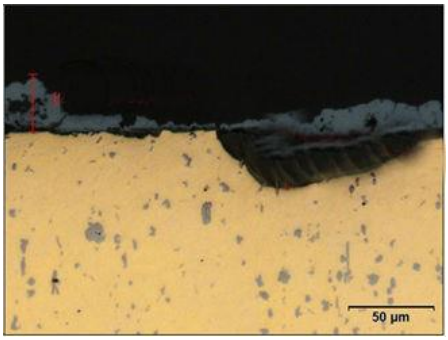

d

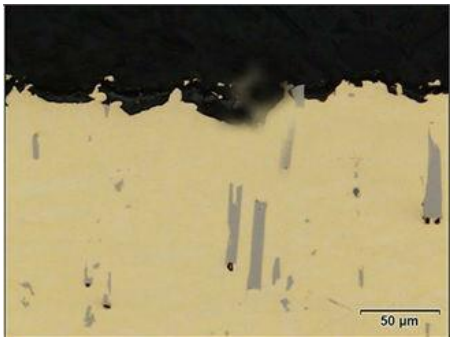

e

Figure 10: Light optical micrograph of different brass alloys after corrosion testing, CuZn37Mn3Al2PbSi (a), CuZn37 (b+c), alloy 1 (d), alloy 2 (e)

4.5. Further lead-free applications for hydraulics and new opportunities

There are many more applications of special brass alloys in oil-hydraulics. Axial piston pumps are not only equipped with slippers, valve plates and cylinder bushings, they also contain holding segments, ball guides and bearing shells. All these parts are made of special brass alloys, too. Not only axial piston pumps, but inner gear pumps are equipped with parts made of special brass, e.g. thrust bearings and crecents.

All these parts open a wide field of further applications for the new lead-free special brass alloys described in this publication.

5. SUMMARY

Due to the banishment of lead from copper alloys lead bearing alloys which have been proven and used for application in hydraulics for decades are to be replaced. Using the examples of cylinder

bushings, slippers and valve plates for axial piston pumps it was demonstrated which challenges need to be tackled in replacing leaded alloys with new lead-free alloys.

Lead as an alloying element is beneficial for a lot of different properties like casting, machining and forming, but also for mechanical properties, low friction, corrosion and wear resistance. All these requirements can be fulfilled with new lead-free brass alloys which was shown in this article. New lead-free alloys especially for requirements from applications in oil-hydraulics have been developed. These new alloys are available on the market and provide a technical performance which is similar or even superior to existing alloys containing lead. The outstanding properties of the new alloys were achieved through a combination of adjustment of chemical composition, heat treatment and the resulting microstructures. Maybe, in the future it will be also possible to conquer new applications with these new alloys where the properties of conventional leaded alloys would not have been sufficient.

REFERENCES

[1] Deutsches Kupferinstitut: https://www.kupferinstitut.de/en/consultation/copper-wiki/details/article/was-bewirkt-das-legierungselement-blei-pb.html [20-08-2019]

[2] Brunhuber E (1959) Schmelz- und Legierungstechnik von Kupferwerkstoffen. Edition, 1. Publisher, Schiele & Schön, 1959

[3] PHOENIX Contact GmbH&Co. KG and HARTING KGaA (2015) Original Application for Exemption Renewal Request, 16.01.2015

[4] URL: https://elv.exemptions.oeko.info/fileadmin/user_upload/Consultation_2014_1/Ex_3/E3__30__supplier_8__corrosion_journal-bearing.pdf [20-08-2019]

[5] Paulus A (2017) Reaktionsschichtbildung auf bleifreien Bronze- und Messingwerkstoffen im Kontakt von Zylinder und Steuerscheibe einer Axialkolbenpumpe. Dissertation, RWTH Aachen

[6] Pawlek A, Reichel K. (1956) Z. Metallkunde 47, pp. 347-56

[7] Jihai J, Kelong W, Zebo W, Yi S (2019) IEEE Access 7, pp. 24971-24977

[8] Nobel C, Klocke F (2013) Entwicklung einer Hochleistungszerspanung für schwer zerspanbare bleifreie Kupferknet- und -gusslegierungen. Schlussbericht des geförderten Vorhabens IGF16867 N

[9] Murrenhoff H, Scharf S (2006) International Journal of Fluid Power 7 No. 3, pp. 13-20

[10] KUGLER BIMETAL: https://www.hannovermesse.de/produkt/bimetal-verteilerplatte/170413/N1374441 [31-10-2019]

[11] Zhang X, Ren X-y, Hong X, Gaoc X-y (2019) RSC Adv., pp. 34972-34985

[12] Luther R (2011) Bioschmierstoffe für den kommunalen Fuhr- und Maschinenpark. Kongress NawaRo-Kommunal Berlin, 22./23.11.2011

[13] Bressling J (2012) Life Cycle Assessment der alterungsbedingten Umweltverträglichkeit biogener Hydraulik- Schmierstoffe. Dissertation, RWTH Aachen

[14] Werner M. (2000) Das Betriebs- und Alterungsverhalten schnell abbaubarer Hydrauliköle. Dissertation, RWTH Aachen

[15] Göhler O.-C., Schmidt M. (2004) Einfluss der Alterung auf das tribologische Verhalten umweltverträglicher Ester. O+P 48, pp. 322-326

[16] Murrenhoff H (2012) Bioschmierstoffe – Ein Überblick zu Vor- und Nachteilen der eingesetzten Produktgruppen. Bioschmierstoff-kongress der FNR, Oberhausen

RESEARCHES ON WATERHYDRAULIC MOTOR

Franc Majdič*

Laboratory for fluid power and controls, Faculty of mechanical engineering, University of Ljubljna, Aškerčeva 6, SI-1000 Ljubljana, Slovenia

* Corresponding author: Tel.: +386 1 4771 411; E-mail address: franc.majdic@fs.uni-lj.si

ABSTRACT

Tribology has been recognized as a very important discipline in different branches of industry because almost every mechanical system has some moving parts. Due to the relative motion between these different mechanical parts, a variety of contacts are formed, and they are very often lubricated with oil. Environmental protection and ecological awareness are becoming increasingly important, which in turn has resulted in the shift to a low-carbon society, making water more interesting as a possible lubricant. On the one hand, water is less environmentally damaging as a lubricant than oil, but on the other hand, water has very poor lubrication properties, as its viscosity is 100 times lower than the viscosity of oil. These limitations might be overcome by appropriate surface engineering (e.g., diamond-like carbon, DLC). Tribological tests were performed in oil and water for two different contacts. Steel/steel and steel/DLC were investigated. DLC was recognized as a very promising solution, which ensures low friction and low wear. DLC was deposited on a real hydraulic part in an orbital hydraulic motor and tested under real industrial conditions. The overall efficiency of the hydraulic motor was measured.

Keywords: water hydraulics, orbital hydraulic motor, tribology, stainless steel, DLC coatings, efficiency

1. INTRODUCTION

Hydraulics is an important way of transferring power. Different fluids are used for the energy transfer from hydraulic pumps, through valves and pipelines to actuators. Nowadays, spilling harmful hydraulic fluids into the environment occurs frequently. Environmentally friendly alternative hydraulic fluids to replace the most commonly used mineral oils are bio-degradable fluids [1], ionic liquids [2] and water [3, 4]. Water hydraulics is still in the development phase [5]. A lot of different water-hydraulics components are missing. One of them is high-torque, slow-speed, gerotor hydraulic motors [6].

Researchers have tested the performance of water in various conditions [6, 7]. Kano et al. [8] found that the coefficient of friction is low when tested for SS/DLC in water due to the favorable energy conditions in the contact. Ohana et al. [9] found that the coefficient of friction in a contact of stainless steel with DLC lubricated with water is lower than 0.1.

2. WATER AS A HYDRAULIC FLUID

The most important properties of water as a hydraulic pressure medium are power transfer, lubrication, sealing, cooling, kinematic viscosity, compressibility, evaporation pressure, and air consumption. [10]. Power transfer is the basic function of a hydraulic fluid. A hydraulic pump transfers the mechanical energy to the hydraulics, which is transferred with the fluid through the hydraulic system to the actuators. Water has no significant difference in terms of power transfer compared to the most frequently used hydraulic mineral oil. Lubrication is an important property of hydraulic fluid as it reduces the friction and wear in the sliding contacts inside the hydraulic components. Water has very poor lubrication properties in the contacts of steel surfaces as it is generally used in oil hydraulics. The sealing connected to the kinematic viscosity of the fluid has an important role in the low-gap sliding contact inside of hydraulic components. Due to the significantly lower kinematics viscosity of water compared to hydraulic mineral oil, gaps in the water hydraulic components should be at least

half the size. The kinematic viscosity of water is 55-times lower than that of mineral oil (ISO VG46 at 50 °C). The cooling properties of water are significantly better than those of hydraulic mineral oil. The compressibility module of water is $2.1 \cdot 10^5$ MPa, this is 46 % lower than for mineral hydraulic oil. Very important advantages of water are its availability in nature and its friendless to the environment (no danger of pollution). The most important properties of water with respect to being a hydraulic fluid are described in **Table 1**. **Figure 1** shows the temperature dependence of the kinematic viscosity of water.

Table 1: Important parameters of water as a hydraulic fluid **[10]**

Water properties	Value
Kinematics viscosity at 3° C	1.6 mm^2/s
Kinematics viscosity at 50° C	0.55 mm^2/s
Density at 50° C	999.15 kg/m^3
Compressibility	$2.4 \cdot 10^9$ N/m^2
Evaporation pressure at 50° C	0,12 bar
Speed of sound at 20° C	1480 m/s
Specific heat at 20° C	4390 J/(kg · °C)
Useful temperature range	3° C to 50 °C

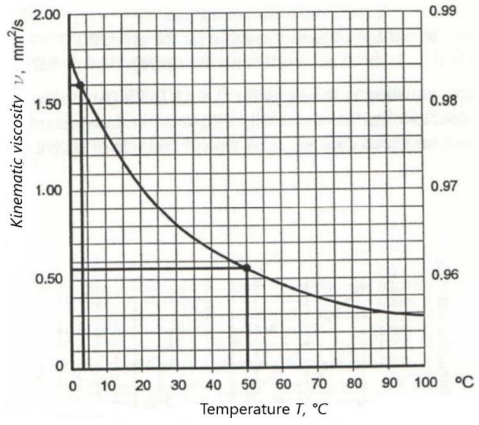

Figure 1: Kinematic viscosity of water as a function of temperature [10]

3. GEROTOR HYDRAULIC MOTOR

A specimen, high-torque, low-speed, hydraulic motor is shown in **Figure 2** and **Figure 3**. The main parts of the motor are: rotor (1), rotor-ring (2), shaft (3), housing (4), valve plate (5), two conical bearings (6), upper (7) and lower (8) housing, static sealing (9) and shaft sealing (10). **Figure 3** shows the three pressure (P) and three return (T) chambers and the rotation direction of the shaft. The rotation of the output shaft of the hydraulic motor is due to the pressure in the three pressure chambers (P). The pressure tends to increase in the pressure chambers and thus the rotor rolls along the rotor ring.

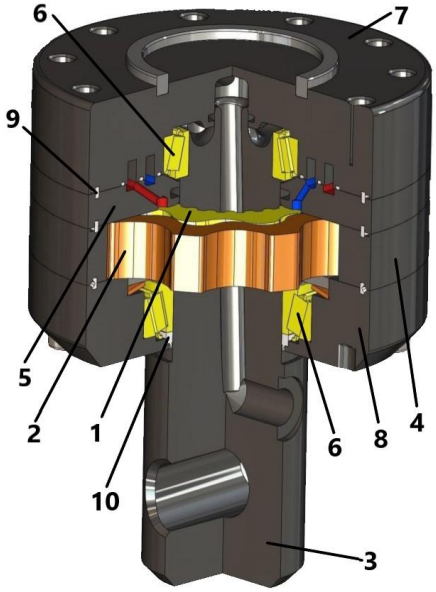

Figure 2: Cross-section of specimen – gerotor hydraulic motor

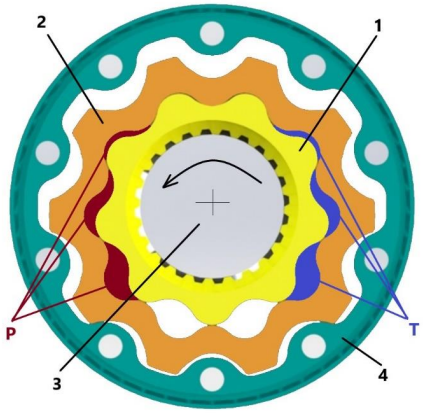

Figure 3: The most important parts of the gerotor

4. EXPERIMENTAL

The gerotor hydraulic motor was developed in two ways: first the basic tribological material tests and then the water hydraulic tests.

4.1. Tribological investigations

Tribological tests of highly loaded surfaces lubricated once with the hydraulic mineral oil ISO VG 46 and second with distilled water were made on a Tribometer Cameron Plint TE 77 (**Figure 4**) with stainless-steel ball bearings (X105CrMo17) oscillatory sliding against a stainless-steel disc (X105CrMo17). The discs were hardened to 60 HRC with a roughness of 0.05 mm. All the tests were made in a period of 3 hours with a frequency of 5 Hz at an amplitude of 10 mm and a total sliding distance of 1080 m.

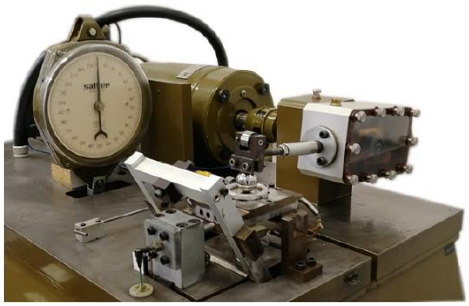

Figure 4: Tribometer Cameron Plint TE 77

4.2. Hydraulic investigations

After the selection of a proper material pair from the tribological tests, a new configuration of the sliding material pair in the hydraulic motor was prepared, mounted and investigated on a special hydraulic test rig, shown in **Figure 5**. The tested hydraulic motor (1) is mechanically connected through a shaft on a precise angular measuring device (3), then on a torque sensor (4) and on the end of the shaft on a hydraulic brake (6). On the hydraulic input and output port are the pressure and temperature sensors (2). The inlet flow was measured with gear-type flow meter (5).

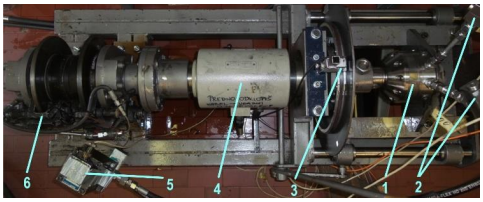

Figure 5: Special hydraulic test rig for hydraulic motor investigations

Figure 6 shows the hydraulic test rig circuit. It contains two different circuits. The main circuit is water hydraulics and is connected to the tested hydraulic motor (3), the second is the mineral oil hydraulics and is connected to an independent hydraulic brake (4, 5). The in-line piston water hydraulic pump (1) is driven with a 16-kW electric motor (2). The hydraulic pump (1) sucks the water from the tank (11) and pumps it into a pressure pipe through the pressure-compensated flow-control valve (10) and the flow meter (12). The water is than directed into the 4/3 directional control valve (17) and then into the tested hydraulic motor (3). The rotation direction of the hydraulic motor can be switched forwards and backwards and it is possible to switch off the motor with the directional control valve (17). On the tested hydraulic motor (3) the input and output ports are two pressure sensors (15) and two temperature sensors (16). The return hydraulic line of water is from the hydraulic motor (3) directed through the 4/3 directional control valve (17) and through the return-line hydraulic filter with the $ß_3$ valve higher than 100 back to the water tank (11). The pressure level is protected by the pressure-relief valve (8) at 350 bar. The tested hydraulic motor shaft (3) is mechanically connected to the hydraulic brake (4, 5) through an angular measuring sensor (14) and torque sensor (13). The second hydraulic circuit is designed to control the load – the hydraulic brake (4, 5) of the tested hydraulic motor (3). It is totally independent of the water-hydraulics test rig. It uses hydraulic mineral oil (23) to transfer the power from hydraulic oil variable-displacement axial piston pump (21) powered by the 22-kW electric motor (22) and pumped into the pressure line through the pressure-reducing valve (27) and the 4/3 directional control valve (26) to the cylinder on the hydraulic brake (5). The highest pressure is limited b the pressure-relief valve (24).

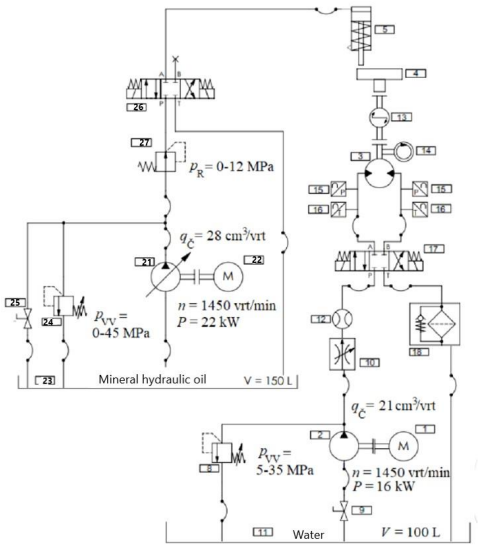

Figure 6: Water-hydraulics test rig for a hydraulic motor

5. RESULTS

First we will present the results of the tribological investigations on two different surfaces for three different forces lubricated first with oil and then with water. The results of a real hydraulic test on a hydraulic motor follow.

5.1. Tribological investigations

Figure 7 shows the first results of the tribological investigations made on the contact of a stainless-steel ball against a stainless-steel disc with a hardness of 60 HRC and a surface roughness of 0.05 µm. The highest coefficient of friction (COF), 0.44 was found with water at a force of 115 N, the lowest COF with water was found at a force of 40 N. The contact of the stainless-steel/stainless-steel lubricated with mineral hydraulic oil ISO VG 46 gives a more than 6-times lower COF than with water under the same conditions (normal force, velocity, material). The highest COF with oil, 0.095 was at a normal force 15 N, the lowest COF, 0.075, was found at a normal force of 115 N.

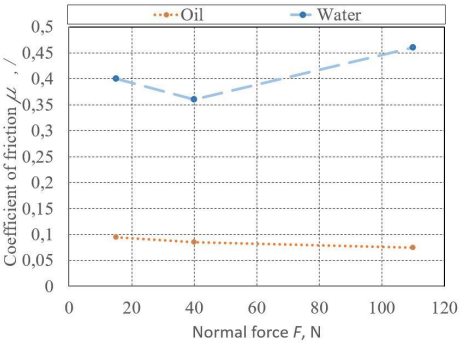

Figure 7: Measured coefficient of friction for stainless-steel ball and disc, 60 HRC and 0.05 µm (Ra)

Figure 8 shows the results of the tribological investigations made on the contact of a stainless-steel ball against a DLC-coated stainless-steel disc with a hardness of 60 HRC and a surface roughness of 0.05 µm. The highest coefficient of friction (COF), 0.081, was found with oil at a force of 115 N, the lowest COF with oil was found at a force of 15 N. The contact of the stainless-steel-ball/DLC-coated stainless-steel disc lubricated with water gives between 3 % and 37 % lower COF than with hydraulic mineral oil under the same conditions (normal force, velocity, material). The highest COF with water, 0.069, was observed at a normal force 15 N, the lowest COF, 0.059, was found out at normal force of 115 N.

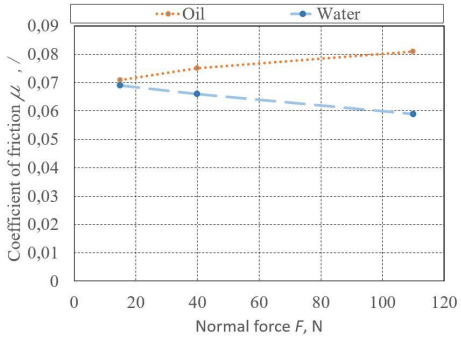

Figure 8: Measured coefficient of friction for stainless-steel ball and disc with DLC coating, 60 HRC and 0.05 µm (Ra)

5.2. Hydraulic

Figure 9 shows the results for the hydraulic motor with hardened steel contacts lubricated

with hydraulic mineral oil. The common results show the total efficiency of the hydraulic motor under different working parameters. The best overall efficiency, 0.45, was observed for pressures higher than 10 MPa and a rotational speed higher than 3 rpm. The lowest overall efficiency, 0.15, was found at pressures lower than 10 MPa and rotational speeds higher than 8 rpm.

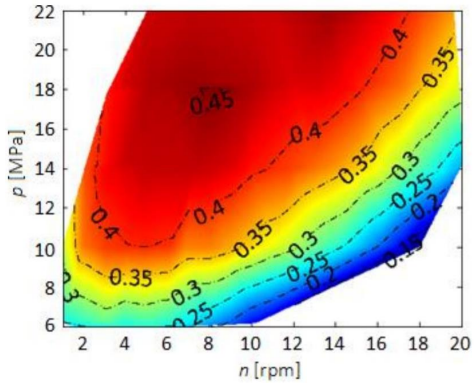

Figure 9: Overall efficiency of gerotor hydraulic motor with hydraulic mineral oil and steel/steel contacts

Figure 10 shows the main results of the real tests on the hydraulic motor tested with hydraulic mineral oil and water. In connection with the tribological tests, real hydraulic test with water also showed a very high COF for the sliding contact of hardened steel against hardened steel. In this case the hydraulic motor did not rotate on the shaft.

After the DLC was applied to the middle element of the gerotor hydraulic motor, the rotor-ring, its shaft start to rotate and the overall efficiency was 12 %. It should probably be higher, but the geometric irregularity did not allow it.

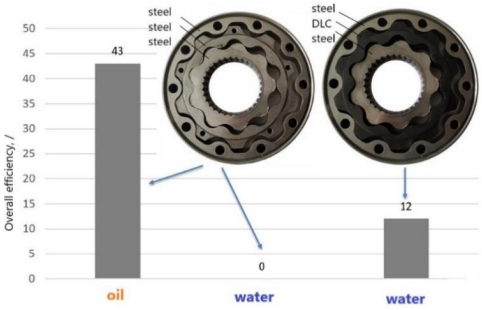

Figure 10: Overall efficiency of gerotor motor with oil (steel/steel), water (steel/steel), water (DLC/steel)

6. CONCLUSION AND OUTLOOK

Water hydraulics is one of the possible solutions to prevent environment pollution with harmful hydraulic fluids. An important reason for its non-frequent use is the leaking of water-hydraulic components. This paper shows the research and development phase of a low-speed and high-torque water gerotor hydraulic motor.

The common conclusions about the water-hydraulics motor are:

- For classic hardened steel materials the coefficient of friction (COF) for water lubrication is up to 6-times higher than the COF in the same contacts lubricated with mineral hydraulic oil.
- The lowest COF, 0.059, in the tribological investigations was for water in the case of a contact with hardened steel against a DLC-coated surface.
- The COFs in water were for DLC from 3 % up to 37 % lower in water in comparison to oil under the same conditions.
- Steel/steel contacts during lubrication with water do not allow the hydraulic motor shaft to rotate due to a too high COF.
- The tribological contacts of DLC/steel are a promising solution to give a chance for the poorer lubrication of water under higher surface loads. In this case the water-hydraulics motor work with an overall efficiency of 12 %.

NOMENCLATURE

DLC	Diamond-like carbon
SS	Stainless steel
COF	Coefficient of friction, /
T	Temperature, °C , K
p_{vv}	Pressure setting of relief valve, MPa
p_R	Pressure setting of reducing valve, MPa
$q_č$	Displacement of hydraulic pump, cm^3/rot.
n	Rotational speed, rpm
P	Power, W
V	Volume, L

ACKNOWLEDGEMENTS

For the full support of this research the author is sincerely grateful to Prof. Dr. Mitjan Kalin, Head of TINT. For technical support the author is grateful to Ervin Strmčnik and Rok Jelovčan.

REFERENCES

[1] Kalin M, Vizintin J (2006) A comparison of the tribological behaviour of steel/steel, steel/DLC and DLC/DLC contacts when lubricated with mineral and biodegradable oils. Wear 261:1, 22–31.

[2] Kambič M, Kalb R, Tič V, Lovrec D (2018) Compatibility of ionic liquids with hydraulic system components. Advances in production engineering & management, ISSN 1854-6250, vol. 13, no. 4, 492-503,

[3] Trostmann E (1996) Water Hydraulics Control Technology, Lyngby, 1996, Technical University of Denmark, ISBN: 0-8247-9680-2.

[4] Majdic F (2010) Voda kot kapljevina v pogonsko-krmilni hidravliki (doctoral disertation), Water as a hydraulic pressure medium, Faculty of mechanical engineering, University of Ljubljana, Slovenia.

[5] Koskinen K, Leino T, Riipinen H (2008) Sustainable development with water hydraulics – possibilities and challenges," Proceedings of the 7th JFPS Interantional Symposium in Fluid Power, 2008, Toyama, Japonska, Vol. 1, pp. 11 – 18.

[6] Gamez-Montero P J, Codina E, Castilla R (2019) A Review of Gerotor Technology in Hydraulic Machines, *Energies*, 12 (12), 1–44.

[7] Strmcnik E, Majdic F, Kalin M (2019) Water-lubricated behaviour of AISI 440C stainless steel and a DLC coating for an orbital hydraulic motor application. Tribology International 131 pp. 128–136.

[8] Kano M (2015) Overview of DLC-Coated Engine Components. V: S. Cha, A. Erdemir (ur.): Coating Technology for Vehicle Applications. Springer, Cham, 2015, pp. 37–62.

[9] Ohana T, Suzuki M, Nakamura T, Tanaka A, Koga Y (2004) Tribological properties of DLC films deposited on steel substrate with various surface roughness. Diamond and Related Materials 13:11 pp. 2211–2215.

[10] Trostmann E, Frolund B, Elesen B H, Hilbrecht B (2001) Tap Water As A Hydraulic Pressure Medium, Marcel Dekker, New York, 2001.

peer reviewed

ORIFICES FLOW SATURATION IN OIL HYDRAULIC APPLICATIONS

Pietro Marani[1]*, Massimo Martelli[1], Silvia Gessi[1], Cesare Dolcin[2]

[1]*CNR-IMAMOTER, Via Canal Bianco, 28, 44124, Italy*
[2]*WALVOIL SpA, Via Adige, 13/D, 42124, Reggio Emilia, Italy*
*Corresponding author: Tel.: +39 0532 735 611, E-mail address: p.marani@imamoter.cnr.it

ABSTRACT

Even though the orifice is the simplest and most common control component in fluid power systems and cavitation is an already well-established topic in the scientific literature, the flow choking or saturation effect is largely overlooked in the common engineering practice. Most of the times the phenomenon is completely ignored, unless the peculiar hissing noise is observed at the test rig, giving a hint that something wrong is happening in the hydraulic system. Even then, the focus is just on the possible component damage induced by strong cavitation, while the functional implications – in terms of flow characteristic – are neglected.

The objective of the paper is to study the phenomenon of flow saturation in hydraulic orifices to assess the formulation of the different critical cavitation numbers and cavitation indexes available from literature. For this reason, a full factorial design of experiments (DOE) is performed to determine the influence of three factors: orifice size, fluid temperature and upstream pressure. The testing is carried out on 5 orifice sizes at 3 different temperatures and 5 different upstream pressure levels. In each test, the downstream pressure is changed from 0 to the upstream pressure level, to sweep the available Δp range, both ascending and descending. In the results section an analysis of the experimental results is drawn, proposing a correlation between the critical cavitation index and the factors considered in the DOE.

To the authors' knowledge, no systematic analysis, as the one here proposed, currently exists in literature for mineral oil applications.

Keywords: Cavitation, Flow Saturation

1. INTRODUCTION

Although flow through orifices is the bread and butter of fluid power, the fact that the flow passing through an orifice actually presents an upper limit or a saturation is largely overlooked by the community of technicians and engineers.

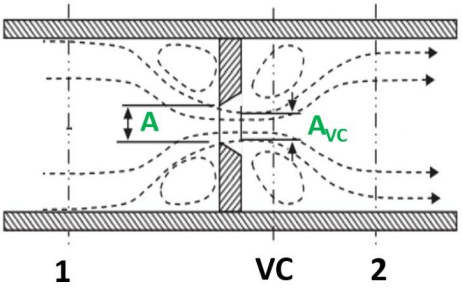

Figure 1: Classical orifice schematic

Looking at the fluid power scientific production, as stated in [1], the literature on this topic appears insufficient in terms of fundamental and applied knowledge of cavitating flow and numerically quite limited compared to the large body of research covering cavitation in flows through orifices, nozzles and Venturi tubes, often targeting real-world applications like piping systems, fuel injectors, cooling systems.

According to the most accepted explanation, the flow characteristic is quadratic until the onset of cavitation, i.e. when pressure at the vena contracta drops below the vaporization pressure (p_v). Below this threshold, and as pressure drop further increases, an increasing fraction of liquid evaporates creating the two-phase mixture. When the liquid sonic speed is reached, the fully choked flow condition is achieved, in this condition the flow rate can't increase any more i.e. flow saturation is reached; a further increase in

pressure differential will intensify the phenomenon, with flow remaining primarily in vapour phase ("flashing" condition) [2].

The release of dissolved gas (air) can also occur near the inception of cavitation, while the vaporization of the fluid, characterized by the typical hiss sound, is the dominant phenomenon during actual cavitation flow choking [1, 2, 3].
In [3] an interesting theoretical framework for the study of cavitating flow in orifices is provided.

Flow rate can be written as:

$$Q = C_d A \sqrt{\frac{2(p_1 - p_2)}{\rho}} \tag{1}$$

or

$$Q = C_c A \sqrt{\frac{2(p_1 - p_{vc})}{\rho}} \tag{2}$$

Cavitation happens when the pressure at vena contracta drops below vapour pressure, i.e. basically when Equation 3 is true:

$$C_d\sqrt{2(p_1 - p_2)} = C_c\sqrt{2(p_1 - p_v)} \tag{3}$$

Knowing the values of the discharge and contraction coefficients it would be theoretically easy to predict cavitation, but unfortunately they show variations from classical formulation due to geometry parameters and fluid properties.

Several cavitation indexes are proposed with the aim of predicting cavitation, the most significant formulae found in literature are C_{I1} [3, 4, 5, 6], C_{I2} [1, 2], C_{I3} [7], C_{I4} [3, 8].

$$C_{I1} = \frac{2(p_2 - p_v)}{\rho v^2} \approx \frac{2p_2}{\rho v^2} \tag{4}$$

$$C_{I2} = \frac{p_1 - p_v}{p_1 - p_2} \approx \frac{p_1}{p_1 - p_2} \tag{5}$$

$$C_{I3} = \frac{2(p_1 - p_2)}{\rho v^2} \tag{6}$$

$$C_{I4} = \frac{p_2 - p_v}{p_1 - p_2} \approx \frac{p_2}{p_1 - p_2} \tag{7}$$

where $v = \frac{Q}{A}$.

As shown in Equations 4, 5, 7, hydraulic fluids have negligible vapour pressures, so that this term can be safely be ignored with respect to upstream and downstream pressures.

We can note that cavitation index 1 is the mathematic representation of the ratio between the static pressure opposing to cavitation and the dynamic pressure tending to produce it, then the lower the index is, the higher the likelihood of cavitation.

Another comment can be done on the fact that the previous equations are not independent, in fact cavitation index 4 can be obtained by subtracting C_{I2} to one, C_{I1} can be obtained by multiplying C_{I2} by the square of the discharge coefficient and finally C_{I3} is the ratio of C_{I1} to C_{I4}.

The geometries of the orifice considered in this paper can be categorized as long orifice since the ratio of length to diameter is greater than 1.5, in this case, as discussed in reference [1], the flow is reattached downstream to the vena contracta region but before the exit from the orifice. From the practical side, it can be noted that most of the commercial available orifices fall into the above category of long orifices.

2. TEST METHODS

A test rig was assembled in the laboratory at Walvoil Test Department according to the ISO 4411 standard [9], in compliance with the recommended distance between the connection ports and the component under test (**Figure 2**).
The pump P supplies the circuit with an ISO VG-46 hydraulic oil. The orifice inlet pressure is kept constant via pressure relief valve V1, while electro-proportional pressure relief valve V2 controls the outlet pressure. Four measurements are acquired during the testing: inlet and outlet pressure (p_1 and p_2), flow rate through the orifice (Q) and fluid temperature (T), see **Table 1** for the details of the sensors used.

Table 1: List of sensors acquired

Design ation	Sensor type	Full Scale	Overall Precision
p_1	Thin film press. transducer	600 bar	±0,3% F. S.
p_2	Thin film press. transducer	600 bar	±0,3% F.S.
T	Semiconductor temp. transducer	-40°C 120°C	±1,5% F.S.
Q	Gear flow meter	40 l/min	±0,3% reading

A specific pipe was built including a seat for a drilled pad (**Figure 3**). The 4 mm long orifices were manufactured taking care to provide an almost square entry, being the chamfers size less than 0.01 mm.

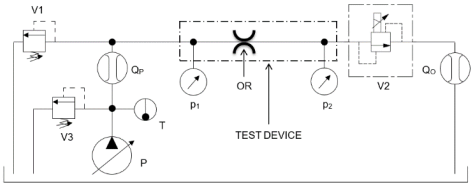

Figure 2: Test circuit

In each test, p_1 was set at a fixed nominal value, while p_2 was slowly varied from the maximum allowed pressure to the minimum and back in order to determine the flow characteristic $Q = Q(\Delta p)$.

A first full factorial design of experiments (DOE) was performed (**Table 2**) to determine the influence of three factors: orifice size (D), fluid temperature (T) and upstream pressure (p_1). The testing was carried out on 5 orifices sizes at 3 different temperatures and 5 different upstream pressure levels. Since the pad length is constant, to have additional insight of the problem additional tests were carried out with reduced orifice depth.

Table 2: Parameters of DOE

Parameter	Values	UoM
D	0.50 - 0.75 - 1.05 - 1.33 - 1.72	mm
p_1	100 – 150 – 200 – 250 - 300	bar
T	30 – 40 – 60 – 80	°C

As mentioned before, 40 additional tests were carried out at reduced orifice length, in particular tests on two additional orifices of ϕ 0.75 x 2.3 mm and of ϕ 0.75 x 2.6 mm were carried out at the 5 considered upstream pressure levels and 4 temperatures.

An important factor is the fluid, whose properties are listed below (**Table 3**).

Table 3: Fluid properties

Property	standard	Value	UoM
Viscosity ISO class	ISO 3448	VG 46	-
Density at 20°C	ASTM D 1298	869	kg/m^3
Kinematic viscosity at 0°C	ASTM D 445	552.5	cSt
Kinematic viscosity at 40°C	ASTM D 445	43.1	cSt
Kinematic viscosity at 100°C	ASTM D 445	6.83	cSt
Viscosity index	ASTM D 2270	112	-
Vapour pressure	-	<0.5	bar

3. EXPERIMENTAL RESULTS

20 tests for each orifice were carried out (5 upstream pressures by 4 temperatures), the result can be clustered by temperature, obtaining five steady flow characteristics, corresponding to five upstream pressure levels. An example of these results is shown in **Figure 4**.

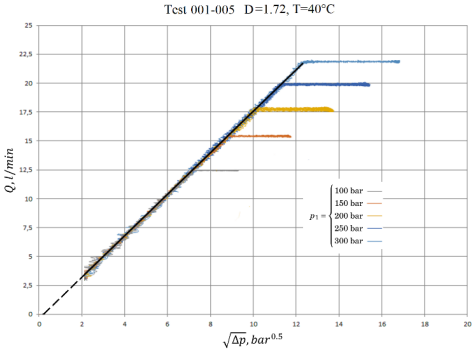

Figure 4: Flow characteristics (D = 1.72 mm, T = 40°C)

The Results, of which **Figure 4** provides a representative sample, highlight interesting properties:

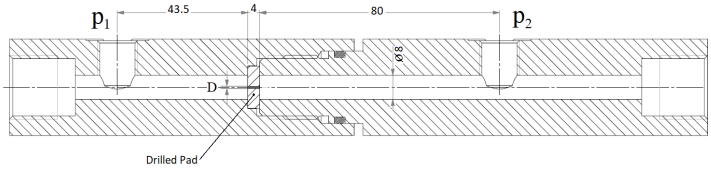

Figure 3: Test pipe with drilled pad and measurement ports

- The non-saturated flow rate characteristics at different upstream pressure overlap almost perfectly and they substantially comply with the quadratic rule.
- The flow rate becomes constant after a specific value of pressure drop is reached, clearly confirming the presence of cavitation and flow saturation.
- The characteristics show almost no hysteresis, thus it is quite easy to identify the incipient flow saturation condition and a critical cavitation index.

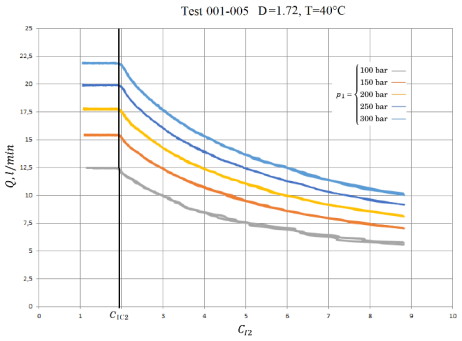

Figure 5: Cavitation index C_{I2} (D = 1.72 mm, T = 40°C)

With regard to the last observation, it is interesting to note as the hysteresis phenomenon is very relevant in particular works [3], while in other it was not observed or considered [1, 2, 4, 5]. This fact is absolutely worth investigating, and the opinion of the authors is that this discrepancy could be caused by the application air content, the type of fluid and the specific component geometry.

Since in a previous paper [1] the authors had used index C_{I2}, this index was the first one to be used.

Plotting the flow rate as a function of C_{I2} calculated from the experimental data gives a pretty clear representation of the transition from no saturation to saturation. A clear threshold separating these two distinct phases can be determined, then is it possible to define the critical cavitation index C_{IC2} as the value of the cavitation index at the boundary between saturation and no saturation flow.

Figure 5 shows a very distinct critical cavitation index that takes approximately the same value in all the tests showed, carried out at different inlet pressures and constant temperature.

4. ANALYSIS OF RESULTS

The great amount of data available from 140 tests were aggregated and sorted for diameter, temperature and upstream pressure.

4.1. DOE Results

The first results presented are referred to the full factorial DOE of the following parameters: diameter, temperature, upstream pressure, for a total 100 tests. In this case the orifices were manufactured by drilling a pad of a constant length of 4 mm.

Table 4: Sample of aggregated data

#	D [mm]	T [°C]	P_1 [bar]	C_{IC2} [-]	C_{IC5} [-]
1	1.72	32.4	98.2	1.889	2.820
2	1.72	32.6	151.0	1.932	2.815
3	1.72	31.6	199.7	1.935	2.785
4	1.72	32.6	250.7	1.929	2.804
5	1.72	32.7	299.6	1.942	2.776
6	1.72	40.7	99.4	1.912	2.846
7	1.72	39.8	150.5	1.943	2.828
8	1.72	40.3	200.9	1.958	2.820
9	1.72	40.3	250.7	1.988	2.832
10	1.72	40.9	301.1	2.000	2.803
11	1.72	60.7	100.1	1.958	2.843
12	1.72	57.6	149.6	1.995	2.822
13	1.72	60.5	201.0	1.943	2.806
14	1.72	60.4	251.4	2.019	2.811
15	1.72	58.8	304.5	1.946	2.784
16	1.72	79.5	99.8	2.008	2.825
17	1.72	80.8	150.7	2.066	2.802
18	1.72	80.9	204.0	2.061	2.785
19	1.72	78.2	250.7	2.046	2.784
20	1.72	77.9	302.2	1.978	2.733
21	1.33	30.7	100.8	1.477	2.169
22	1.33	30.9	151.7	1.526	2.135
23	1.33	32.4	201.7	1.582	2.139
24	1.33	31.6	250.5	1.611	2.125
25	1.33	32.3	302.1	1.631	2.119
26	1.33	39.8	101.9	1.572	2.138
27	1.33	40.4	151.0	1.595	2.137
28	1.33	40.2	203.4	1.619	2.136
29	1.33	41.0	251.3	1.645	2.123
30	1.33	40.6	299.0	1.638	2.108
31	1.33	60.9	100.6	1.624	2.125
32	1.33	61.1	149.9	1.630	2.133
33	1.33	59.8	199.6	1.662	2.124
34	1.33	58.6	249.2	1.691	2.117
35	1.33	61.2	300.3	1.687	2.101

36	1.33	80.3	101.6	1.692	2.122
37	1.33	80.8	149.3	1.704	2.109
38	1.33	81.2	198.9	1.686	2.096
39	1.33	78.9	247.7	1.714	2.086
40	1.33	79.5	300.7	1.705	2.081

Looking at **Table 4** representing a sample of the final table, and considering the calculated values of critical cavitation index 2 it is possible to note a large standard deviation. Aggregating the data by diameter it was found that σ=4.8% for diameter 1.72 and σ=4.8% for diameter 1.33. This can be graphically displayed in **Figure 6** and it basically means that the chosen index has low accuracy in predicting cavitation, in particular if the temperature is varied.

A possible explanation for the dispersion of C_{IC2} might be the fact that the discharge coefficient of a short orifice is almost independent from the temperature, while in case of a long orifice, characterized by reattached flow, it is affected by the viscosity and the temperature.

Considering the full spectrum of C_{IC2} for all orifice diameters (corresponding to the complete version of **Figure 6**, not shown here for simplicity), a clear trend is determined. For any given diameter, as T increases, the vertical offset of the $C_{IC2} = f(\Delta p)$ curve increases, whilst its steepness decreases, in other words the curve moves up and becomes flatter.

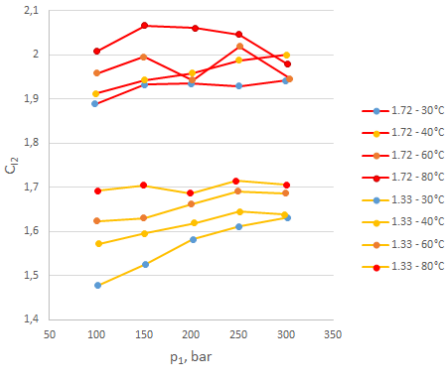

Figure 6: Critical cavitation index C_{IC2} (D = 1.72 mm, D = 1.33 mm)

The observations confirmed that the discharge coefficient calculated from the experiments highlight a sensible variation with respect to temperature. Moreover, considering that the denominator of Equation 5 represents the dynamic pressure generated by the fluid velocity, a new formula is proposed by replacing the pressure drop with a kinetic term depending on the mean velocity of fluid passing through the orifice.

$$C_{I5} = \frac{2(p_1 - p_v)}{\rho v^2} \approx \frac{2p_1}{\rho v^2} \qquad (6)$$

Formula (6) is coherent with the discussion [11] in reference to paper [12] by Cunningham who reported that pressure drop (p_1 - p_2) can be a poor approximation of the jet dynamic pressure. Consequently, he proposed the upstream to vena contracta differential pressure ($p_1 - p_{vc}$) as a more logical choice.

Critical cavitation index 5 has been calculated for each diameter highlighting a better accuracy in predicting the saturation (σ = 2.6% for diameter 1.72 and σ = 2.0% for diameter 1.33). The lower dispersion of the critical cavitation indexes 5 can be appreciated from **Figure 7** which basically is a zoom-in of the complete map of critical cavitation index 5 calculated for all tests, shown in **Figure 8**.

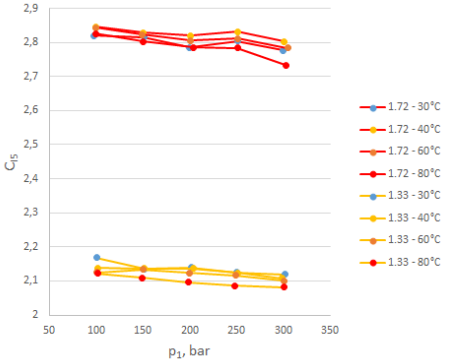

Figure 7: Critical cavitation index C_{IC5} (D = 1.72 mm, D = 1.33 mm)

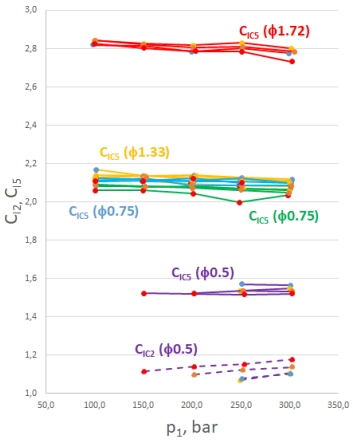

Figure 8: Critical cavitation index C_{IC5} for all the full factorial DOE

Looking at **Figure 8** is it possible to note that some points are missing for diameter 0.5. To explain this remark it is necessary to observe the critical cavitation index 2 at diameter 0.5, which is very near to unity. That is, the orifice will saturate when the pressure drop is near to the inlet pressure or, in other terms, when the downstream pressure is near to zero. Since the test rig has a minimum achievable pressure, because of the characteristics of the control valves at the orifice outlet (V2 on **Figure 2**), it was not possible to reach the saturation for all tests.

Another remark can be done on the fact that the cavitation index 5 show a small variation for each diameter but is quite difficult to find a relationship between diameter and critical cavitation index. In fact, the mean value of the index for the central values of diameter considered (D = 0.75, 1.05, 1.33) are almost overlapped while on the other hand C_{IC5} mean value is considerably lower for 0.5 mm diameter and higher for 1.72 mm.

The distribution of critical cavitation indexes is far from linear with respect to geometry parameters such as diameter or flow area.

An attempt to gain a better insight on the phenomenon has been made by considering the length of the orifice. In fact, since the pad has a constant width, the L/D parameter i.e. the ratio between length and diameter increases at decreasing diameters.

The influence of the L/D ratio on flow is thoroughly investigated in literature [10, 13], and in particular, its influence on the discharge coefficient is known, thus it is reasonable to expect a remarkable effect of L/D on the critical cavitation index.

Speaking of numbers, the L/D parameter is respectively 2.33 for ϕ 1.72, 3.01 for ϕ 1.33, 3.81 for ϕ 1.05, 5.33 for ϕ 0.75, and 8 for ϕ 0.5 mm diameter.

4.2. Additional Tests with reduced Orifice Length

In order to address the doubts which have arisen in the previous paragraph, two additional pads were prepared with reduced width, specifically an orifice of ϕ 0.75 x 2.3 mm (L/D = 3.07) and an orifice of ϕ 0.5 x 2.6 mm (L/D = 5.26).

The new orifices were tested according to the previous methods, at the same inlet pressure and at the same temperature levels.

As for the previous test batch, the critical cavitation indexes 5 show an extremely low variability.

The results of these tests are presented in **Figure 9** including also the previous results of orifice ϕ 0.5 (L/D = 8, purple lines), ϕ 0.75 (L/D = 5.33, light blue lines), ϕ 1.33 (L/D = 3.01, yellow lines).

We can couple the results for L/D matching ϕ 0.75 x 2.3 mm to ϕ 1.33 x 4 mm (blue and yellow) characterized by L/D ≈ 3 recording that the critical cavitation index 5 decreases as the diameter increases, at constant L/D ratio. On the other hand, looking at the couple ϕ 0.5 x 2.3 mm to ϕ 1.33 x 4 mm (L/D ≈ 5) we could come up with the diametrically opposite conclusion.

Observing the effect of L/D at constant diameter [ϕ 0.5 x 2.6 mm, ϕ 0.5 x 4 mm] and [ϕ 0.75 x 2.3 mm, ϕ 0.75 x 4 mm] we get a similar discrepancy. In fact, in the first couple ϕ 0.5) C_{I5} slightly decreases as the L/D ratio decreases, on the other hand, for ϕ 0.75 the index increases.

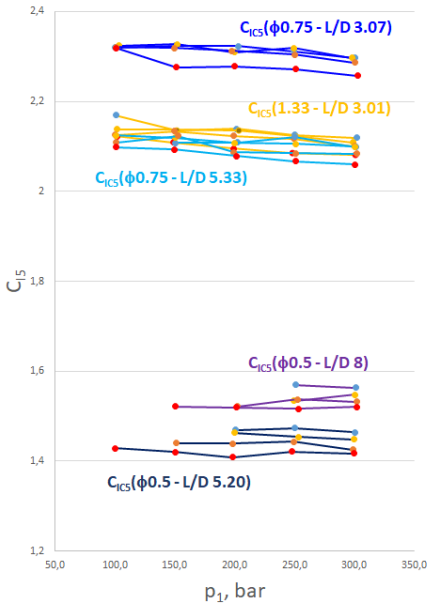

Figure 9: Comparison of critical cavitation indexes C_{I5} for different orifice lengths.

We can then conclude that even if the C_{IC5} values show a good internal consistency, it is not possible to identify a clear trend relating geometry parameters to the critical cavitation index from this set of data.

5. CONCLUSION AND OUTLOOK

A full factorial DOE was performed to study cavitation in hydraulic orifices of constant length taking into account diameter, temperature and upstream pressure. It was observed that:

- The cavitation is reached at a specific value of pressure drop, after this threshold the flow saturates (remains constant), almost no hysteresis was observed in the tests, .
- The cavitation index can be defined in different ways, a definition based on the ratio between the upstream pressure and fluid velocity proved to be an effective marker for the cavitation, dependent only from the geometry.
- The cavitation indexes based on the ratio of pressure drop and upstream/downstream pressure are less effective because they suffer from a strong dependence on temperature.
- An explicit function which relates orifice geometry to cavitation index was not found, nevertheless it was found that both diameter and length/diameter ratio influence the critical cavitation index but unfortunately the function is clearly not linear.

Starting from this study, actions on various fronts can be put in place to increase the knowledge on orifice cavitation:

- Additional testing, with particular attention to the effect of geometry parameters such as L/D.
- CFD methods can be trained with the large amount of data to get a better insight of micro-phenomena and to further explore additional cases.

Finally, cavitation is unanimously recognized as a harmful event to be prevented as much as possible because of the potential damage of components. However, the conditions for flow saturation discussed in this paper are similar to those found in current fluid power circuits, thus many components are potentially exposed to it. The fact that this allegedly may concern not only the orifices but also the valves in general from the point of view of authors represent a good point to put more effort on the topic of cavitating flows.

NOMENCLATURE

A	Orifice area
A_{vc}	Area at vena contracta
C_c	Contraction coefficient
C_d	Discharge coefficient
C_{Ij}	j-th orifice cavitation index
C_{ICj}	j-th orifice critical cavitation index
D	Orifice diameter
L	Orifice length
p_1	Orifice upstream or input pressure
p_2	Orifice downstream or output pressure
p_v	Fluid vapour pressure
p_{vc}	Vena contracta pressure
Q	Volumetric flow rate
T	Fluid temperature (upstream)
v	Orifice average flow velocity
ρ	Fluid density
σ	Standard deviation

REFERENCES

[1] Martelli, M., Gessi, S., Massarotti, G.P., Marani, P., Zarotti, G.L. (2017) On Peculiar Flow Characteristics in Hydraulic Orifices, ASME/BATH Symposium on Fluid Power and Motion Control, Sarasota, USA, 2017 FPMC2017-4313

[2] Ebrahimi, B., He, G., Tang, Y., Franchek, M., Liu, D., Pickett, J., Springett, F., and Franklin, D. (2017) Characterization of High-Pressure Cavitating Flow through a Thick Orifice Plate in a Pipe of Constant Cross Section. Int. J. Thermal Sciences 114, pp. 229-240

[3] Pearce, I.D., Lichtarowicz, A. (1971) Discharge performance of long orifices with cavitating flow, in: Proc. Second Fluid Power Symposium, January 1971, Guildford Paper D2, University of Surrey, 1971, pp. D2-13–D2-35

[4] Yan, Y., Thorpe, R.B. (1990) Flow Regime Transitions Due to Cavitation in the Flow through an Orifice. Int. J. Multiphase Flow, Vol. 16, No. 6, pp. 1023-1045.

[5] Koivula, T. (2000) On Cavitation in Fluid Power. Proc. 1st FPNI-PhD Symposium, Hamburg, Germany, pp. 371-382.

[6] Johnson, R.W. [Edited by] (2000) The Handbook of Fluid Dynamics. CRC Press LLC and Springer-Verlag GmbH, Chapter 20. ISBN 3-540-64612-4

[7] Brinkhorst, S., von Lavante, E., Wendt, G. (2016) Experimental and Numerical Investigation of the Cavitation-Induced Choked Flow in a Herschel Venturi-Tube. Flow Measurement and Instrumentation 54, pp. 56-67

[8] Castillo, M. (1993) An Analysis of Cavitation Activity at Orifices of the FFG-7 Seawater Piping System. MRL Technical Note MRL-TN-637. Department of Defence, Australia

[9] International Standard (2008). ISO 4411:2008. Hydraulic fluid power – Valves – Determination of pressure differential/flow characteristics.

[10] Lichtarowicz, A., Duggins, R. K., Markland, E. (1965) Discharge coefficients for incompressible non-cavitating flow through long orifices, J Mech Eng Sci, 1965, 7, 210–219

[11] Cunningham, R. G., Discussion: “Cavitation Inception in Spool Valves”, 1981, ASME J. Fluids Eng., 103, pp. 575–576

[12] Martin, C. S., Medlarz, H., Wiggert, D. C., and Brennen, C., Cavitation Inception in Spool Valves, 1981, ASME J. Fluids Eng., 103, pp. 564–575

[13] Idelchik, I.E. (1994) Handbook of hydraulic resistance, - 3rd Edition, CRC Press, ISBN: 0-8493-9908-4, p.222.

GROUP B

System design & integration

FREQUENCY BASED EFFICIENCY EVALUATION – FROM PATTERN RECOGNITION VIA BACKWARDS SIMULATION TO PURPOSEFUL DRIVE DESIGN

Martin Starke[1]*, Benjamin Beck[2], Denis Ritz[2], Frank Will[1]*, Jürgen Weber[2]

[1]*Institute of Mechatronic Engineering, Endowed Chair of Construction Machines, Technische Universität Dresden, Münchner Platz 3, 01062 Dresden*
[2]*Institute of Mechatronic Engineering, Chair of Fluid-Mechatronic Systems, Technische Universität Dresden, Helmholtzstraße 7a, 01062 Dresden*
*Corresponding author: Tel.: +49 351 463 39278; E-mail address: martin.starke@tu-dresden.de

ABSTRACT

The efficiency of hydraulic drive systems in mobile machines is influenced by several factors, like the operators' guidance, weather conditions, material respectively loading properties and primarily the working cycle. This leads to varying operation points, which have to be performed by the drive system. Regarding efficiency analysis, the usage of standardized working cycles gained through measurements or synthetically generated is state of the art. Thereby, only a small extract of the real usage profile is taken into account. This contribution deals with process pattern recognition (PPR) and frequency based efficiency evaluation to gain more precise information and conclusion for the drive design of mobile machines. By the example of an 18 t mobile excavator, the recognition system using Hidden – Markov - Models (HMM) and the efficiency evaluation process by means of backwards simulation of measured operation points will be described.

Keywords: process pattern recognition, hidden-markov-model, backward simulation, alternative modelling methods, efficiency evaluation

1. INTRODUCTOIN

Hydraulic drives have operating point-dependent efficiency characteristics, which result in user-specific primary energy requirements. For this reason, in addition to knowing the operation profile of each construction machine, it is important to obtain information on the efficiency of each task performed (pattern) in order to incorporate this data into the development process or into the current operation. The energy efficiency of mobile machinery must therefore be analysed and evaluated using frequency-based operation point distributions, taking into account the range of applications of the machine. To achieve this goal, two major areas of work were carried out:

1. The model-based efficiency evaluation of the drive system using frequency-based operation point data of parallel-operated axes on a common hydraulic supply.
2. The process pattern recognition for the automated recording of the frequency as well as start and end times of the patterns.

2. STATE OF THE ART

Pattern Recognition

Pattern recognition with its various mathematical methods and approaches is defined in its entirety as machine learning [1]. The different methods of pattern recognition always have to solve the same task, which follows the same sequence. This includes the data preprocessing (e.g. frequency filtering) of a data signal in the so-called analyzer with subsequent transfer to the characteristic space. These characteristics are assigned to classes. The classification then represents the different patterns, which have to be detected [2]. There is a large number of algorithms that must be selected according to the requirements of the recognition task. (e.g. template matching procedure, artificial neural networks, support vector machines (SVM), decision trees or the nearest neighbour classification, hidden markov models (HMM)). These algorithms are already successfully used in areas such as speech, gesture and handwriting recognition [3–6]. In the field of

mobile machinery Wünsche showed in [7] the recognition of cycles on a wheel loader. With the help of CAN bus signals, a principal component analysis is carried out using a sliding window. Various activities are identified based on the first principal component. The performed investigations show a high sensitivity of the detection rate to the window size used. It remains open whether the main components are suitable as classification features for the identification of complex motion sequences of several loads operated in parallel.

Keller describes in [8] the possibility to detect a loading cycle of a mini excavator. Due to the simplicity of the algorithm, the method of the decision tree is used. 16 loading cycles are carried out on a test machine and the existing measured variables are recorded. The decision tree algorithm is then trained with this data, which represents the assignment of the activity label. The sub-processes idling, driving, unloading, slewing and digging are labelled. In the subsequent recognition phase, he examines the accuracy of the calculated sequences with 20% of the recorded data and the influence of the available signals on the machine. In the result, the joystick signals are identified as the most influential signals.

In [9] the suitability of the template matching procedure and HMM to define customer usage profiles are shown. Thereby HMM show the best results for the recognition of sequences of various lengths. This and the other listed examples show only the recognition of individual working cycles. Relevant points such as determining the cycle duration, the detection of different cycles, the learning of unknown processes and further the evaluation of the detected processes are not considered yet. This contribution deals with these issues.

Efficiency evaluation

Due to the great heterogeneity of mobile machinery, it is very difficult to define specific methods for evaluating energy efficiency. In addition, the machine operators have a major influence on the energy consumption of the machine (design, selected machine size, age of the machine) [10]. Today, however, there are several methods and guidelines for evaluating fuel consumption for different types of mobile machinery. Three approaches can be distinguished:

1. direct fuel measurements [11–14]
2. subsystem tests [15]
3. model-based system analysis [10, 16–23]

While in one measurements are possible in real life and based on defined cycles, the procedures in two and three are limited to reference cycles.

Mieth shows that it seems most reasonable to use a small, representative number from the set of all measured cycles on the basis of the density distribution function for the efficiency evaluation. In this example, a very good agreement in the load distribution on the stick cylinder could be obtained by using only 10 instead of all 92 measured cycles [10]. This underlines the necessity to use a statistically proven set of operation points for the efficiency evaluation. With regard to the traction drive of a mobile machine, a corresponding methodology has been developed in [24, 25]. Jähne sets up simulation models for different transmission structures and derives efficiency maps by varying the model input variables (v_i, F_i). These maps can easily be calculated with the frequency data of the operation points in order to determine a system input power. In general, this methodology can be applied to all systems with only one active load. As soon as several consumers are operating simultaneously, the dimension of the efficiency maps increases and with it the simulation effort to generate them. For the calculation of the system input power for given operation points of consumers operated in parallel other calculation methods have to be developed, which are part of this paper. The term "efficiency model" will be introduced to describe the resulting models.

3. VALIDATION OBJECT

The validation of the efficiency assessment methodology, including process pattern recognition, was carried out on an A918 mobile excavator from Liebherr. The machine is equipped with a LUDV valve system and a hydraulic-mechanical load-sensing concept for adjusting the pump. Measurement series with 16 cycles for digging with the corresponding flux and potential values at the main loads boom, stick, bucket and swing gear were used. These are shown in extracts in **Figure 1**.

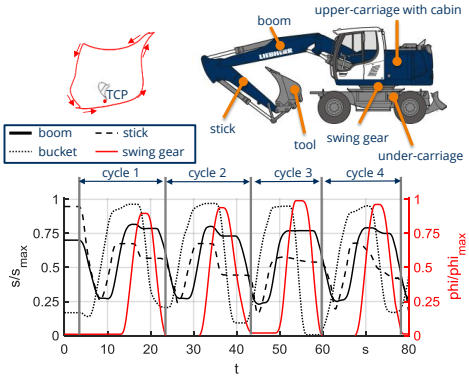

Figure 1: A918 object of examination – digging cycle

This machine and its provided data is used for the development and validation of the shown system in this contribution.

4. PROCESS PATTERN RECOGNITION

The Hidden Markov Models (HMM) used in this publication are particularly well suited for an application in the area of mobile machinery, as they can also cope with widely varying cycle times and, in addition, an increase in detection quality can be achieved through adaptation during operation [9].

HMM are stochastic calculation models, which have the characteristic to assign states to observable parameters (sensor signals). For this purpose, the process pattern (set of similar working cycles) to be determined can be allocated to the order of a time sequence of states, which can assume any number n.

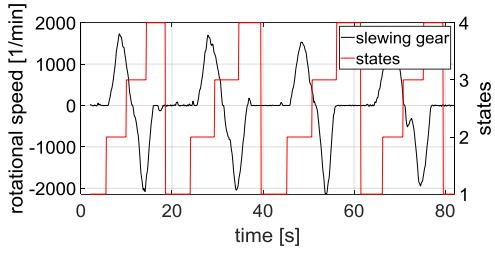

Figure 2: sensor signal and calculated state sequence

Figure 2 shows this context with the calculation of $n = 4$ states to the time sequence of four digging cycles represented in the rotational speed of the slewing gear. If the HMM calculates the sequence of states, a subsequent evaluation algorithm can determine the pattern out of the order of state sequence.

Before this recognition can be performed, the HMM hast to be trained. Therefore, the sequence of states to be calculated must be assigned to the training data, which must be the same sensor signal as in the detection phase. In the training phase the HMM learns the allocation of the predefined state sequence and the sensor signal. A problem with this procedure is that not every sensor signal is suitable for a high calculation quality of the state sequence. It depends on the spread of the measured values between two different states, which has to be significantly greater than the spread yielded by the sensor within a state. This behavior is varying for the different working cycles. It leads to the first problem that unknown patterns, which the HMM does not know, could not be used for a training without an elaborate statement of suitability. Due to this a new method, called quadrant method (QM), of data preprocessing was introduced in [26]. The approach was chosen due to the requirement of the independence of certain sensor signals. The basic idea is the regard of every single load and its working point in the speed-force- respectively speed-torque-diagram (flux and potential values). Not the absolute values are examined, but only the appearance in the quadrant of the particular diagram of the load in every time step is observed. By computing the combination of all loads in every time step a sequence is achieved, which is the substructure both of the training and of the application of the HMM. In **Figure 3**, the combination sequence with 3 loads (boom, stick, bucket cylinder) of the 16 cycles of the A918 is presented.

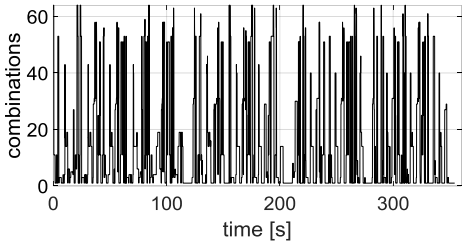

Figure 3: combination sequence of 16 digging cycles

The next step is the state assignment to this sequence before HMM training can be done. As well as the so far described functions, this is realized in Matlab® by an algorithm in the following named *autostate* function. The functionality aims to the possibility of an

automatic state assignment for new patterns, which are unknown. Especially for an online implementation this is necessary. The approach that is chosen is known from handwriting recognition. Here, stair-like state progressions are used for observation sequences of different lengths, which are represented by different symbols, letters and operators. The idea is now to assign a staircase to a process pattern and use it for the training of the HMM. The number of states is freely selectable and influences the configuration of the HMM regarding fluctuating detection rates.

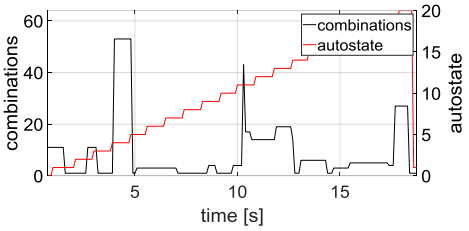

Figure 4: autostate assignment for one cycle

Counting of patterns

The counting of the patterns consists of the determination of start and end times and the calculated duration. This also results in the number of occurring patterns. For this purpose, the state sequence with 20 states shown in **Figure 4** is used (one cycle). The advantage is the possibility of counting the sequences calculated by the HMM afterwards in the recognition phase, which in the best case can be computed exactly as a staircase sequence. **Figure 5** shows this approach exemplarily for four states. The counting event is triggered when all states have been passed through one after the other and the stack is filled. This method makes it very easy to determine the times and thus the durations of each pattern, since both the start time with the beginning of the stack filling and the end time with the filled stack are available.

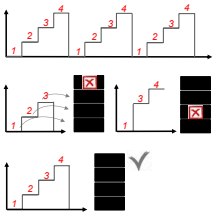

Figure 5: principle of the memory stack

Operation point storage

Since QM already uses the flux and potential values of each load, the operation points are known at the time the pattern occurs. However, due to the storage requirements, the operation point storage has a high significance. For the transfer of the time-based continuous data stream into the frequency distributions required for the efficiency evaluation, the storage of the operation points using multidimensional classification with dynamically growing list is applied. With this method only operation points that actually occur are stored for every pattern. This must be done during online recognition parallel to the actual recognition. The model must detect the beginning of a pattern and fill the dynamic list during recognition. After the recognition and thus the assignment to a pattern, the newly occurring operation point combinations extend the list of this pattern.

Evaluation

The model is designed so that it can be used both online and offline as a data evaluation tool. The current state of development is the possibility of recognizing an automatically trained pattern and the saving of the operation points with their start and end times for the efficiency evaluation. In a reduced offline version, the recognition of different trained and unknown patterns is possible. However, in this model the start and end times can only be determined with insufficient accuracy. For this reason, this publication uses the online model that is implemented in Simulink. **Figure 6** shows the recognition result of 16 digging cycles of the Liebherr A918 with 64 trained states. The recognition rate is 93 % because 15 of the 16 cycles were detected by the HMM. The red line is the calculated state sequence, were the stairway of the trained sequence is identifiable. The last cycle is not detected, because no following cycle let the HMM calculate a state which indicates the end of this sequence and the start of the new one.

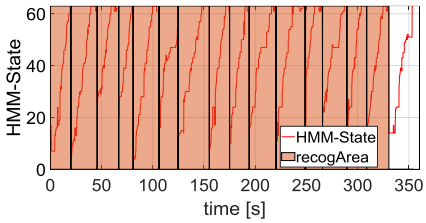

Figure 6: detection result of Liebherr A918 data

The interesting thing is the result shown in **Figure 7**, where the detection result of the excavator CASE WX 185 data is presented. This data contains 8 cycles of digging and 8 cycles of levelling. The HMM which was used for the detection is the same like in the first example. Due to the usage of the QM method, which uses the separate loads of the machine at least 5 of the 8 included cycles are detected (2, 3, 5, 6, 7). Cycle 1 & 4 are detected, but with wrong cycles times. The last cycle detected (8) is a wrong detection. The levelling cycles weren't determined.

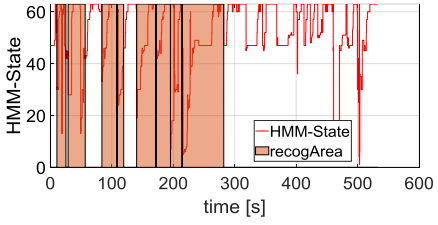

Figure 7: detection result of Case WX 185 data

The stairway is not as well calculated as in **Figure 6** but nevertheless the individual cycles can be identified and detected by the HMM. This is caused by the completely different general conditions, which are a different machine, another operator, a varying time and a differing load.

This model was implemented on a control unit (STW ESX-3XM) and is used in a hardware-in-the-loop test bench and on the excavator. As the excavator A918 was not available for validation purposes, the excavator CASE WX 185 and a corresponding real-time capable model were used. Since QM can be used, as shown before, across all machines, the application can also be carried out on multiple machines. With that online application the shown detection results can be achieved in real time and the operation points and the duration of every single cycle are saved in matrix and are available for the efficiency evaluation described in the following chapter.

5. EFFICIENCY EVALUATION

An important prerequisite for efficiency analysis is the choice of the system boundary. For the investigations in this publication the mechanical power of the actuators (cylinders, motors) represents the one system boundary. A measurement of cylinder or motor pressures can be easily realized in practice. These should be used to calculate the occurring cylinder force / motor torque. Sensors in the course of automation on the machines partly already record the speeds and revolutions of the output drives. If this is technically more difficult, as for example with bucket cylinders on excavators, it is assumed that estimated values from the measured joystick deflection are available. For a practicable efficiency model, the other system boundary should be designed flexibly depending on the available data for modelling or measurement and should be located between fuel consumption at the engine, mechanical shaft power of the engine and hydraulic power of the pump(s). In principle, it is also conceivable to equip the machine with maximum sensor technology and to make simple monitoring possible over the period of use. However, this can only provide information depending on the currently installed system. The following is possible by measuring the mechanical output power and converting it via a model of the drive system (efficiency model) to the required input power and other intermediate variables:

1. calculation of the necessary input power depending on the selected system boundary
2. analysis of the loss points in the system
3. assistance in the engineering process to find the energetically optimal drive structure for certain tasks.

The special feature compared to the classical simulation is the backward calculation of the state variables in the system based on the measured operation points. Whereas in the classical system simulation, for example, the motor speed, pump swivel angle and deflection of the valve spools are pre-set, whereupon the speeds of the axes are adjusted according to the acting loads, these variables must now be calculated based on the pre-set forces and speeds. The principle of the efficiency model is displayed in **Figure 9.**
For practicability, the efficiency model should obtain the static loss behaviour of the system, be easily parameterisable and calculate the solution within seconds.

5.1. System description

The load sensing system with secondary pressure compensators is a widespread hydraulic system for mobile excavators on the European market. The test object mobile excavator used here also contains this drive system. In detail, it contains of a hydraulic-mechanically controlled load-sensing pump connected to a diesel engine, a LUDV valve block, pipe breakage safety valves and hydraulic-mechanically Joysticks. According to the 90°-digging cycle, the main consumers boom, stick, bucket and slew drive, which are all valve-controlled on a single pump are taken into account. Because the backwards calculation of the hydraulic pressure at the pump is the biggest problem, this is the focus in the following. A simplified hydraulic circuit diagram of an exemplary chosen two consumer LUDV-system is displayed in **Figure 8**.

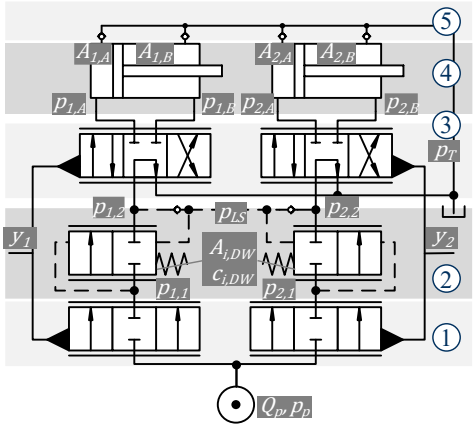

Figure 8: simplified hydraulic circuit diagram of a LUDV system

It can be divided into five sections with the following stationary element equations:

1. Metering orifices (MO)

$$Q_{i,MO} = K_{i,MO} \cdot A_{i,MO}(y_i) \cdot \sqrt{p_p - p_{i,1}} \quad (1)$$

2. Individual pressure compensators (IPC)

$$Q_{i,IPC} = K_{IPC} \cdot A_{IPC}(y_{i,IPC}) \cdot \sqrt{p_{i,1} - p_{i,2}} \quad (2)$$

$$y_{i,IPC} = \frac{A_{i,IPC}}{c_{i,IPC}} \cdot (p_{i,1} - \max(p_{i,2})) \quad (3)$$

3. Direction edges (DE)

$$Q_{i,DE_up} = K_{DE_up} \cdot A_{DE_up}(y_i) \cdot \sqrt{p_{i,2} - p_{i,A/B}} \quad (4)$$

$$Q_{i,DE_down} = K_{DE_down} \cdot A_{DE_down}(y_i) \cdot \sqrt{p_{i,2} - p_{i,A/B}} \quad (5)$$

4. Actuators indexed with ascending alphanumeric numbers

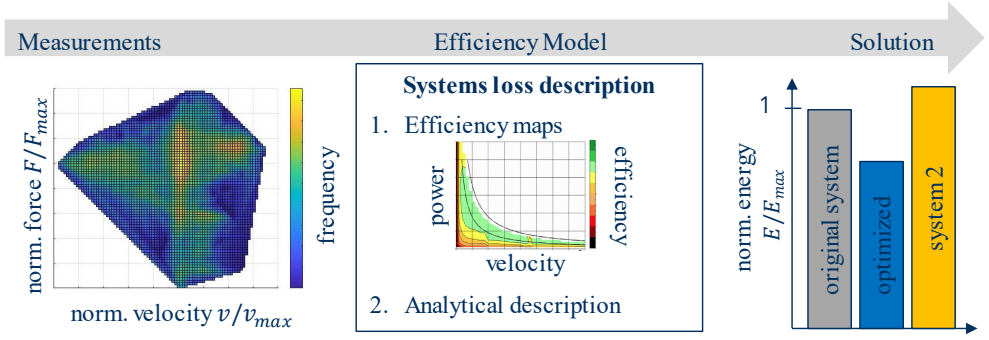

Figure 9: concept of efficiency modelling

$$F_{i,zyl} = p_{i,A} \cdot A_{i,A} - p_{i,B} \cdot A_{i,B} \quad (6)$$

$$v_i = \frac{Q_{i,A}}{A_{i,A}} = \frac{Q_{i,B}}{A_{i,B}} \quad (7)$$

5. Suction valves (SV)

$$Q_{i,SV} = K_{SV} \cdot A_{SV} \cdot \sqrt{p_T - p_{i,A/B}} \quad (8)$$

Besides this, the following balance equations are valid:

6.

$$F_i = F_{i,cyl} \quad (9)$$

$$Q_{i,A/B} = Q_{i,DE_up} + Q_{SV} \quad (10)$$

$$Q_{i,B/A} = Q_{i,DE_down} + Q_{SV} \quad (11)$$

$$Q_{i,DE_up} = Q_{i,IPC} \quad (12)$$

$$Q_{i,IPC} = Q_{i,MO} \quad (13)$$

$$Q_p = \sum Q_{i,MO} \quad (14)$$

$$p_p = max(p_{i,2}) + \Delta p_{LS} \quad (15)$$

Thereby, the cylinder chamber pressure $p_{i,A/B}$, the intermediate pressures $p_{i,1/2}$, the valve stroke y_i, the IPC stroke $y_{i,IPC}$ and the pump pressure p_p are unknwokn.

It becomes obvious that the system of equations is solvable in principle, since determinacy exists (seven equations and seven unknown variables). Due to the discontinuities (opening of suction valves, maximum load pressure in eq. (3)), the non-linearity's (root function in flow equations and $A(y)$ characteristic of the control edges), a direct inversion of the input and output variables is impossible.

To overcome this issue, three different variants of efficiency models were developed, named as:

1. Serial Iteration
2. Parallel Iteration
3. Blackbox Model

The methods one and two belong to the category of light-grey box models, as they are based on the static system equations and contain characteristic curves of the valves. Both methods use the equations described above. The serial iteration uses the bisection method for iterative solutions. With the "parallel iteration" model, the approach is to use existing "classical forward models" and vary the potential quantities until all balance equations are approximately zero. For this purpose, a multidimensional Newton iteration method is applied. The disadvantage of this method is that the solution of the Newton method depends strongly on the starting value of the iteration. This is contrasted by the method of black box modelling. The idea here is to train the relationship between the operating points at the consumers and at the pump based on measured data or an already existing complex system simulation models. This model can then be used to quickly simulate further operation points. However, physical parameterisation is not necessary. The three methods were implemented in Matlab® and then compared with the measured operation points of the pump.

In [27] it could be shown that the black box model requires the least computing time and achieves the highest accuracy. However, the accuracy decreases strongly with measurement data deviating strongly from the training data set and an interpretability due to missing physical correlations is not given. When comparing the two iterative methods with each other, serial iteration is preferable because of its better accuracy and higher speed. However, parallel iteration is much easier to model and thus to apply, as it is possible to derive the efficiency model from existing classical models. However, the computing times are unacceptably high.

Detailed description of serial iteration model

The diagram in **Figure 10** shows the basic procedure of the developed program. In principle, this is divided into two calculation phases. In the first part the pump pressure is calculated. To determine the valve stroke, it is assumed that the set LS pressure, which drops across the pressure compensator and the metering orifice, is constant. The volume flow required for the movement, which must be conveyed by the pump, results from the product of the cylinder area and cylinder speed. From the pressure and the volume flow it is possible to determine the valve stroke. Since the pressure compensator and the main valve are not mechanically coupled, the pressure compensator must be balanced hydraulically as well as mechanically. With the so determined valve stroke it is now possible to calculate all other variables backwards from the tank and to get a statement about the required pump pressure for each consumer. The highest determined pump pressure represents the pump pressure that is set.

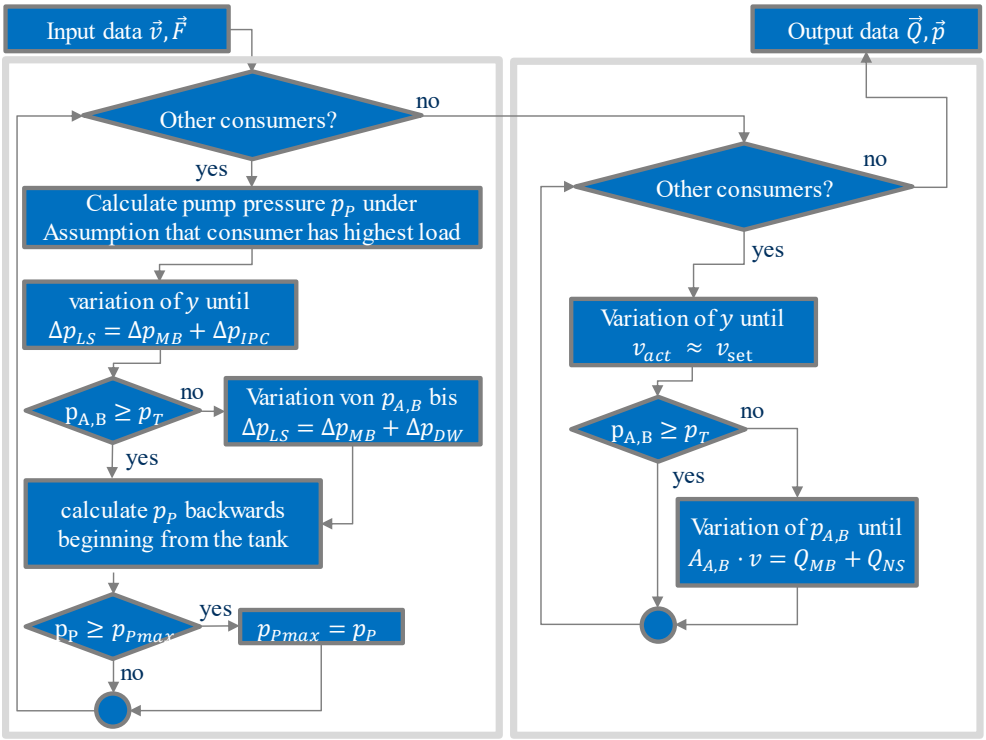

Figure 10: schematic of the developed program for the "serial iteration" efficiency model

$$v_{cyl} = \frac{A_P \cdot p_p - A_T \cdot p_T - F_{cyl}}{{A_P}^3 \cdot \left(\frac{1}{{K_{MO}}^2 \cdot y^2} + \frac{1}{{K_{DE_up}}^2 \cdot y^2} + \frac{1}{{K_{IPC}}^2 \cdot {y_{IPC}}^2} \right) + {A_T}^3 \cdot \left(\frac{1}{{K_{DE_down}}^2 \cdot y^2} \right)} \tag{16}$$

In the second part of the program, the volume flows, pressures and valve strokes of the lower-load consumers are calculated. Here, the valve stroke is varied until the speed of the cylinder at a given pump pressure almost corresponds to the measured value. For this purpose the static control law is used according to the following equation:

5.2. Special Modelling aspects

Control edge geometry

The mapping of the opening cross section as a function of the valve stroke $A(y)$ plays a central role, especially in the field of mobile machinery, since the valves are designed for the operator-guided process and thus include both a fine control range and a range of high speeds in combination with a positive overlap. In addition, the control edges have different characteristics to intercept conditions such as pulling loads. For the modelling it has turned out to be advantageous to ignore the positive overlap range at first, i.e. not to calculate system states. This is realized by simple *IF-THEN-ELSE* queries. Furthermore, it is advantageous to carry out a normalization from zero to one. The volume flow amplification K_i of the individual control edges contains, on the one hand, the flow coefficient α, which is an empirical value to take into account all losses such as fluid friction or turbulence. This factor depends mainly on the Reynolds number and the geometry of the control edges. Realistic values for valves are in the range between 0.6 and 0.8, whereby a good approximate value of 0.7 can be assumed. On the other hand K_i contains the density, which is assumed to be $\rho = 880\ kg\ /\ m3$.

Input pressure compensator

This is relatively simply implemented by an IF-THEN-ELSE query. A fixed volume flow rate value is calculated at the set LS pressure differential if no consumers are moved.

Secondary pressure limitation

The secondary pressure relief valves are coupled to the control signal of the valves. They limit the load pressure p_L when the valve is closed to a fixed set value p_{closed}. When the valve is fully open, the maximum load pressure p_{max} is set. Mathematically, the relationship can be described according to the following equation:

$$p_L = (p_{max} - p_{closed}) \cdot \frac{y}{y_{max}} + p_{closed} \qquad (17)$$

Regeneration position in the main valves

Some of the valve systems installed today already feature section-internal regeneration between the cylinder chambers due to improved energy efficiency of the machine. This is particularly the case with the boom and stick. However, this poses a major challenge for backward calculation with the efficiency model, as there is no longer a direct correlation between cylinder speed and volume flow over the directional edges. The system is therefore under-determined and cannot be calculated. There are two possibilities to solve this problem:

1. assumption of a fixed volume flow distribution
2. measuring another system parameter and feeding it back into the efficiency model

Solution 1 is to be preferred, since measuring another variable within the system does not correspond to the philosophy of the efficiency model as described above. However, in the case under investigation this could only be applied to the boom cylinder. For the stick cylinder, the measurement of the pressure in the node of the volume flow distribution had to be resorted to.

5.3. Results on demonstrator

The results of the efficiency model for the test object are shown in **Figure 11**. The accuracy of 2 % of the overall normalized energy consumption of the duty cycle shows that the efficiency model can be used for further investigations. The computing time of 182 s for 35.761 operation points (=357 s duration) is acceptable and meets the requirement "within a few seconds". A transferability to other systems, especially open-center systems with many volume flow distributions, seems impracticable from the authors' point of view. For this purpose, other methods such as real-time capable, classical

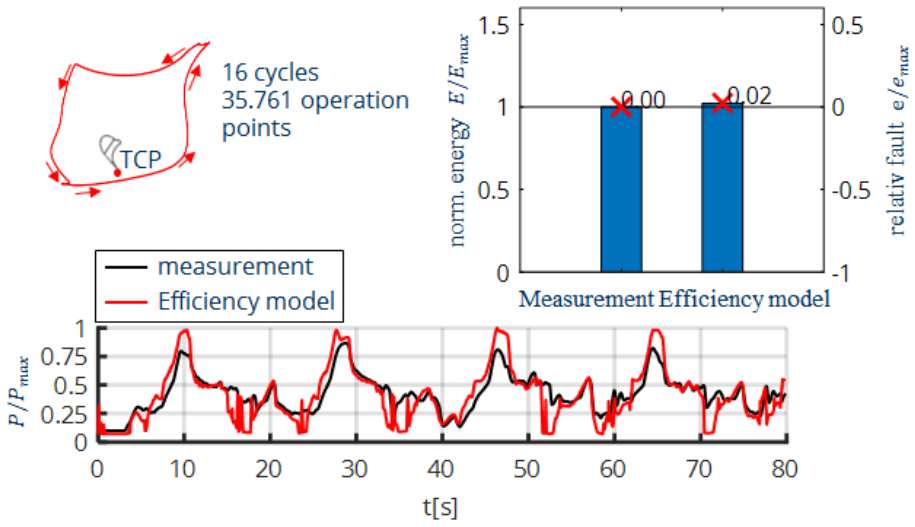

Figure 11: Results of "serial Iteration" efficiency model for typical duty cycles of mobile excavator

forward models or direct energy monitoring with a few model-based components are proposed.

6. CONCLUSION AND OUTLOOK

This paper shows a new method that allows the analysis and evaluation of energy efficiency of mobile machinery by means of frequency-based operation point distributions. First, the occurring duty cycles and the frequency of their occurrence are detected by the process pattern recognition (PPR). The duration of the cycles and the operation points contained therein are stored. These are subsequently used to calculate backwards the input power of the drive system through the efficiency model. The two subsystems PPR and efficiency evaluation are combined in one overall system, which makes it possible to achieve a better understanding of the use of machines and the resulting loads on the drive system with minimal effort. It can be assumed that the automated collection and processing of the application data is a continuous process which will not be limited to a single machine development project. The creation of a statistically secured database with a corresponding scope thus serves to build up the basic knowledge for the conception and design of future machine generations or their components and subsystems.

7. ACKNOWLEDGEMENT

The project Ref. No. AiF 19613 BR/1 was financed and supervised by the Research Association Mechanical Engineering (FKM). In the scope of the Programme to promote Industrial Collective Research it was funded by the German Federation of Industrial Research Associations (AiF) with means of the Federal Ministry of Economic Affairs and Energy (BMWi) on the basis of a decision by the German Bundestag.

REFERENCES

1. Aunkofer B Machine Learning vs Deep Learning – Wo liegt der Unterschied? – Data Science Blog. https://data-science-blog.com/blog/2018/05/14/machine-learning-vs-deep-learning-wo-liegt-der-unterschied/. Accessed 20 Dec 2019
2. Hoffmann R (1998) Signalanalyse und -erkennung: Eine Einführung für Informationstechniker
3. Dahl G, Yu D, Deng L, Acero A (2011) Context-dependent pre-trained deep neural networks for large-vocabulary speech recognition. IEEE Transactions on audio, speech, and language processing 20:30–42
4. Gales M, Young S (2008) The application of hidden Markov models in speech recognition. Foundations and Trends® in Signal Processing 1:195–304
5. Lizhong G Appearance-based hand gesture recognition and study on human-robot interaction [D]. PhD Thesis, Doctoral Dissertation
6. Yun L, Lifeng Z, Shujun Z (2012) A hand gesture recognition method based on multi-feature fusion and template matching. Procedia Engineering 29:1678–1684
7. Wuensche M, Mostaghim S, Schmeck H, et al (2010) Organic computing in off-highway machines. In: Proceedings of the second international workshop on Self-organizing architectures. ACM, pp 51–58
8. Keller NJ, Ivantysynova M, Vacca A, et al (2019) Classification of machine functions: a hydraulic excavator case study. In: Proceedings. Tampere, pp 410–422
9. Mieth S, Weber J (2016) Methode zur Online Prozessmustererkennung für die Ermittlung von Kundenkollektiven an mobilen Arbeitsmaschinen. TU Dresden Professur für Baumaschinen, Dresden
10. Kunze G, Mieth S, Voigt S (2011) BEDIENEREINFLUSS AUF LEISTUNGSZYKLEN MOBILER ARBEITSMASCHINEN. ATZoffhighway 4:70–79
11. Helmus M, Fecke M (2015) Standardisierung definierter Lastzyklen und Messmethoden für die Energieverbrauchsermittlung von Baumaschinen. Bergische Universität Wuppertal, Interdisziplinäres Zentrum III
12. Liebherr Wheel Loaders L550 - L586
13. Pfab H, Altenberger F, Gappmaier R (2017) Flottenmessungen zur Optimierung des Maschineneinsatzes. KIT Scientific Publishing, Karlsruhe, p 19
14. Verein deutscher Ingenieure (2012) VDI 2198 - Type sheets for industrial trucks
15. Berlenz S (2015) Potentialanalyse bedarfsgerecht betriebener Nebenaggregate an

einem Off-Highway-Motor. Logos Verlag, Berlin
16. Deiters H (2009) Standardisierung von Lastzyklen zur Beurteilung der Effizienz mobiler Arbeitsmaschinen. Technische Universität Carolo-Wilhelmina zu Braunschweig
17. Filla R (2005) Operator and machine models for dynamic simulation of construction machinery. Linköpings universitet
18. Finzel R (2011) Elektrohydraulische Steuerungssysteme für mobile Arbeitsmaschinen. TU Dresden
19. Fleczoreck T (2013) Effizienzbewertung von Antrieben mobiler Arbeitsmaschinen am Beispiel eines Mähdreschers. Shaker, Aachen
20. Holländer C (1998) Untersuchungen zur Beurteilung und Optimierung von Baggerhydrauliksystemen. VDI-Verl, Düsseldorf
21. Inderelst M (2013) Efficiency improvements in mobile hydraulic systems. Shaker
22. Sitte A, Uhlmann J, Weber J, et al (2017) MODEL BASED EFFICIENCY ANYLYSIS OF MOBILE HYDRAULIC MACHINERY - On The Example of Mate rial Handling Machines. JFPS, Fukuoka, p 10
23. Sturm C (2015) Bewertung der Energieeffizienz von Antriebssystemen mobiler Arbeitsmaschinen am Beispiel Bagger. KIT Scientific Publ, Karlsruhe, Baden
24. Jähne H (2009) Simulation of Drive Systems for Mobile Machines. Dresden
25. Jähne H (2013) Struktursystematik und Effizienzpotentiale hydraulischer Fahrantriebe unter Einbeziehung der Applikation. Shaker
26. Starke M (2019) Automatic Process Pattern Recognition for mobile machinery. In: Proceedings. Tampere, pp 450–461
27. Beck B, Koch O, Ritz D, et al (2018) Modellbasierte Entwicklung mobiler Maschinensysteme. In: 7. Fachtagung Baumaschinentechnik 2018. Dresden, pp 185–200

peer reviewed

OPTIMIZATION OF OPERATION STRATEGY FOR PRIMARY TORQUE BASED HYDROSTATICS DRIVETRAIN USING ARTIFICIAL INTELLIGENCE

M. Sc. Yusheng Xiang*, Prof. Dr. Marcus Geimer

Institute of Vehicle System Technology, Chair of Mobile Machines, Karlsruhe Institute of Technology, Rintheimer Querallee 2, 76131 Karlsruhe, Germany

* Corresponding author: Tel.: +49 17672361970; E-mail address: yusheng.xiang@partner.kit.edu

ABSTRACT

A new primary torque control concept for hydrostatics mobile machines was introduced in 2018 [1]. The mentioned concept controls the pressure in a closed circuit by changing the angle of the hydraulic pump to achieve the desired pressure based on a feedback system. Thanks to this concept, a series of advantages are expected [2]. However, while working in a Y cycle, the primary torque controlled wheel loader has worse performance in efficiency compared to secondary controlled earthmover due to lack of recuperation ability. Alternatively, we use deep learning algorithms to improve machines' regeneration performance. In this paper, we firstly make a potential analysis to show the benefit by utilizing the regeneration process, followed by proposing a series of CRDNNs, which combine CNN, RNN, and DNN, to precisely detect Y cycles. Compared to existing algorithms, the CRDNN with bi-directional LSTMs has the best accuracy, and the CRDNN with LSTMs has a comparable performance but much fewer training parameters. Based on our dataset including 119 truck loading cycles, our best neural network shows a 98.2 % test accuracy. Therefore, even with a simple regeneration process, our algorithm can improve the holistic efficiency of mobile machines up to 9% during Y cycle processes if primary torque concept is used.

Keywords: Mobile machines, Y cycle detection, Deep learning, Power management, Hydrostatics, Primary torque control

1. INTRODUCTION

A new primary torque control concept for hydrostatics mobile machines was introduced in 2018 [1] and after that, a series of further development has also been made [2]. To date, there are two kinds of mature torque control for hydrostatic drivetrain solution. Unlike the secondary control concept that typically has one or more hydraulic accumulators to build up a constant pressure and controls the output torque by adapting the angle of hydraulic motor, the primary torque control concept controls the pressure in a closed circuit by changing the angle of the hydraulic pump based on a feedback system but without accumulators. Although there are many advantages, primary torque control also has a disadvantage compared to secondary control. While working in Y cycles, which is a typical working process for wheel loaders, secondary control shows an excellent system efficiency even with a simple operation strategy due to its recuperation ability. Without hydraulic accumulators, recuperation is no more possible in a conventional vehicle that has only a combustion engine as its power source, resulting in a lower system efficiency for primary torque controlled mobile machines. Thus, an intelligent operation strategy is needed for primary torque control to improve regeneration performance to compensate for its disadvantage due to the lack of recuperation ability during a Y cycle. Concretely, we use deep learning algorithms to detect Y cycles so that that a current working-process-based operation strategy for primary torque control that can be implemented to improve system efficiency. Apparently, the success of this strategy highly depends on the accuracy of individual working process identification. In this paper, we will focus on the Y cycles detection algorithms. In order to reveal the benefit, we

make a potential analysis of regeneration process during Y cycles.

2. BACKGROUND

2.1. Wheel loader

The wheel loader is a typical mobile machine used for moving earth. A typical working process is the so-called Y cycle. Concretely, the machine digs the heap and transfers the soil to a truck. During this process, the machine is usually driving in a trajectory similar to a letter Y. **Figure 1** illustrates this cycle.

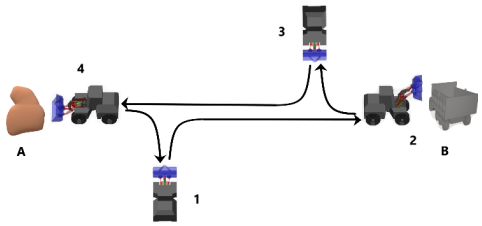

Figure 1: A typical truck loading process (Y cycle)

2.2. Primary torque control

Murrenhoff has drawn a rule in [3] to classify the different kinds of control concepts, and concrete details are shown in **Figure 2**.

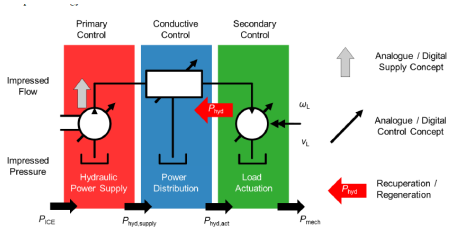

Figure 2: Segment of control concepts [3]

One significant advantage of primary torque control is its high efficiency due to the successful introduction of central power management. The basic idea of central power management derives from the requirement that the power made available to the system should be precisely the same as the power consumed by the system. Besides, in case of power shortage, power management will cut down the power supply to the devices which have a lower priority [1].
To follow this basic idea, every component will compute the energy it requires first, and then the center power manager gathers the information, compares it with the disposable power of power source, and distributes the power to each requester [1].

On hydrostatic mobile machines, there is no restrain condition between engine rotation speed and vehicle speed. Thus, optimization of engine efficiency is possible. Generally, the engine speed is set to as low as possible considering the requested vehicle dynamics.

2.3. Operation strategy

As aforementioned, a primary torque based wheel loader without a hydraulic accumulator cannot recuperate the energy.

In order to increase the efficiency of our system, we use the regeneration method. Instead of using an additional component, we use our implement to regain the energy. Concretely, we transform the kinetic energy of earthmover to potential energy of the material in the shovel. By the time when the machine decelerates in the truck loading cycle, the hydraulic motor is working as a pump and transfers the energy to lift the shovel. As a light of that, instead of losing this energy, our operation strategy uses this energy to accelerate the pump for implements on mobile machines.

2.4. Working process detection algorithms

Many scholars are interested in utilising machine learning to improve mobile machines regarding efficiency, maintenance, and usability. Especially in the field of working process detection, a series of methods have been drawn. Pohlandt has used two simple neural networks to predict and recognize the desired work process separately on electrical mobile machines [4]. According to his publication, he splits the time series of measured power into many small slip windows to train the simple neural networks. In his research, he found out neural networks might work for some simple cases [4]. Another research is from Brinkschulte who points out that the prediction accuracy with bagged trees may dramatically decrease when the drivers have different driving skills [5]. Besides machine learning algorithm, research by Nilsson introduced a method that combined several individually simple techniques including signal processing, state automation techniques, and parameter estimation algorithms. Based on 159 cycles, the accuracy is 93% [6]. In 2019, Keller made a case study for an excavator to classify the

machine functions using decision tree with an accuracy of 99.97% without using slip windows [7]. In addition, Starke shows that Y cycle can be online recognized with hidden Markov Models (HMM) since HMM was widely used within the context of word recognition to deal with the temporal variability of text or speech [8, 9], before 2012 [10]. Also, he pointed out that truck loading is a high variance problem and a simple algorithm should be used owing to the limited of on-board ECU [8].

3. PROBLEM STATEMENT

Based on our dataset and previous studies, we summarize the problems faced in this research.

First of all, the detection of arbitrary Y cycles is a high variance problem. Y cycles are different from site to site. The distance between heap and truck can be quite different. Moreover, drivers are also different. Some drivers have many years of driving experience, and thus have become more aggressive. By contrast, some drivers are still novices who correct themselves during some processes. Last but not least, the materials for transport are different. Therefore, a complicated method is needed to handle the high variance.

Another problem is the limitation of the computing capacity of the ECU on mobile machines. Backpropagation consumes more CPU than forward propagation; thus, online learning usually entails the adoption of a swallow neural networks or an efficiency well-known machine learning algorithm, such as support vector machine (SVM). Consequently, less intelligent learning ability is expected. As a light of that, we dedicate to find an off-line method. Since a simple algorithm might not be really good for dealing with high variance problems, scientists in the fields of Natural language processing (NLP) usually use algorithms that combine many technologies. In the case of HMM, vocal tract length normalization (VTLN) and feature-space maximum likelihood linear regression (fMLLR) are used before HMMs [11]. Neural networks should also be combined together [12].

4. WHY WE USE RNN, LSTM?

The initial idea to use long short-term memory (LSTM) is inspired by analogy. Recurrent neural network has been proven to be a powerful tool in the fields of NLP in the past years [10]. One of the significant progress is the introduction of LSTM [13, 14]. More details about LSTMs can be found in [15]. In western countries, clauses are used extensively in writing, making sentences extremely and differently long. Splitting the sentence into many words and using a simple deep neural network (DNN) with a certain number of input layer units, the translation performance is usually unsatisfied. Intuitively, different lengths of sentences make the selection of numbers of input units difficult. A deeper reason lies in the fact that, the simple neural network does not take the sequence of words appearing in the sentence into consideration. With limited input units, simple neural networks can only detect the current situation based on a specific past period. If the decisive information occurred a long time ago, the artificial intelligence (AI) must make its decision based on somewhat useless information causing no wonder a detection mistake. To overcome this problem, LSTM uses update and forget gates to make a shortcut for the vital information to help with the current decision. Akin to complicated sentences with clause, Y cycles can have very different lengths due to its transport process or workers of different proficiency. As a light of that, LSTM shall solve this principally similar challenge.

Since our goal is using AI algorithm to detect the working process and thus improve the efficiency of mobile machines by regenerating, “future” information can be used to increase the detection accuracy. Generally, earthmover is first be accelerated in reverse direction and then decelerated after digging into a heap. The duration here implies that even though the algorithm does not recognize directly at the time Y cycle begins, it does not harm the regeneration performance as long as it detects the Y cycle slightly before the deceleration process. Therefore, we also use bi-directional LSTM to improve prediction accuracy.

Similar to HMM that may use some additional technologies to improve its performance, LSTMs also have better performance if convolutional neural networks (CNNs) and DNNs are cooperating together [16–18]. The advantages of the combination of CNNs, RNNs, and DNNs, which we call CRDNN in this paper, are shown in the next section.

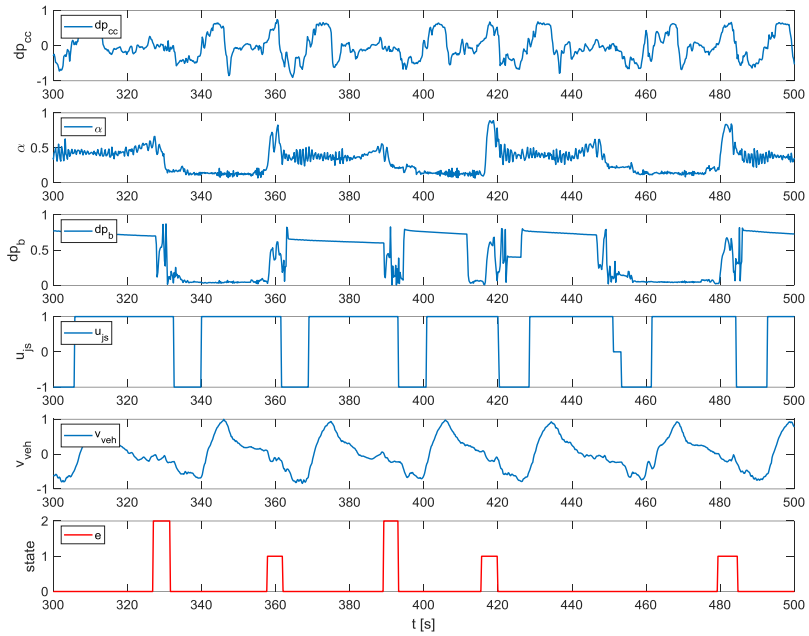

Figure 3: Normalized measurement data with label

5. POTENTIAL ANALYSIS OF REGENERATION PROCESS

In this section, a potential analysis is made to show how much energy we can regenerate from the vehicle under the assumption that our detection algorithm works 100% well, and the regeneration process works perfectly. A study mentioned that vehicle energy is difficult to reuse due to the high rolling friction by mobile machines [19]. However, according to our observation, most of the experienced drivers flatten the pavement using shovel as a warm-up process. With the preliminary process, they reduce the road roughness to have better driver comfort. Obviously, it also reduces the rolling friction and thereby makes the recuperation or regeneration possible.

Concretely, we build a wheel loader in Simscape [20] to simulate Y cycles. The interactions of vehicle mass, vehicle velocity, material mass, and the friction coefficient are studied. Based on our results, the regeneration process can increase system efficiency by about 9% in general. More details will be found in our other paper. In our simulation, we set the parameters based on the real vehicle and environment data, see **Table 1**

Table 1: Parameters of the vehicle and environment

Cylinder parameter	Value [m²]
Vehicle mass	10 t
Materials mass	4 t
Rolling friction coefficient	[0.01 0.05 0.3]
Pump loss coefficient	0.8
Motor loss coefficient	0.8
Mechanical loss coefficient	0.98

6. DEEP LEARNING ALGORITHM

As aforementioned, we use a series of neural networks to recognize Y cycles. For the sake of simplification, we can say that artificial intelligence is a scientific method for recognizing pattern based on the data with which it has been trained. However, truck loading cycles can be quite different from each other regarding traveling length between heap and truck, driver's

skill level, materials, and the dimension of mobile machines. The training of an end-to-end neural network needs a vast dataset, which is still a cost-challenging task today. Instead, we proposed a multi-step approach to detect truck loading cycles. Instead of predicting the Y cycle directly, we firstly predict the loading, the traveling, and the unloading processes since much less data is required for training. Furthermore, after neural networks output its prediction, we might use a modification measure to avoid obvious mistakes. As a light of that, we divide our processes into three sub-processes: vehicle travels, loading, and unloading.

As we mentioned before, we would like to use a more complicated and therefore smarter neural network so that we adopt the off-line learning method to avoid the time-consuming backpropagation.

6.1. Data acquaint and allocation

Data is the heart of deep learning. We split the dataset into training and test data set, 80% and 20%, respectively. Besides, we consciously selected three different drivers and did the measurement in different days. Some measurements were done on a rainy day so that the density of material changes. Moreover, we changed the position of heap and truck to vary the length of the Y cycles. The test drivers were not given the information about what we were going to do so that they would behave the same in their daily operations. In short, we consciously increased the diversity of our dataset and tried to include more challenging cases in our dataset.

The data we fed into the neural networks were selected from the typical sensors on primary torque controlled mobile machines. Concretely, there are pressure difference inside of the bucket, vehicle velocity, vehicle direction signal on joystick, pressure difference inside of closed-circuit drivetrain, and driver drive pedal. The sample rate is 50Hz so that we will not overload ECU.

Totally, we have created a dataset with 119 Y cycles. 40 of them are gathered from an experienced test engineer, 30 of them are from a development engineer who has aggressive drive behavior, 20 of them are collected when the machine was not well tuned, 29 of them are measured by a senior manager who works many decades in the field of mobile machine. None of the data is collected by a complete layman since we do not think it makes sense. Notice that we have allocated the data collected as the machine with insufficient calibration process into training dataset since it can improve the robustness of our algorithm but not affect our test accuracy. The measurement dataset is labeled as shown in **Figure 3**. In the real world, the data is often not perfect. That is, some people may mislabel a tiny portion of data. Therefore, we deliberately labeled some windows as travels through it is actually a loading or unloading process to check the robustness of our algorithms.

Apparently, the variable pressure inside of bucket and vehicle velocity indicates a very strong seasonally. The pressure inside of closed-circuit implies the behaviors of a loading process. Moreover, the signal on joystick demonstrates the state change. Solely based on these variables, an experienced test engineer can tell whether the mobile machine is loading or unloading with almost 100% accuracy. Without a doubt, a deep learning model can take over the job to detect Y cycles. However, in the measurement data we have, the Y cycle is not always so regular. For instance, one Y cycle does not always begin with a loading process, followed by an unloading process. The driver might think he has loaded too small amount of load so he comes back after a small reversing process and digs into the heap again. It happens when the driver is not so skilled or is mistaken. Such a case increases the difficulties of detecting the truck loading process by deep learning.

6.2. Data preparation

The measurement data were not pre-treated by human observation depending on the dataset before fed into neural networks even we agree a pre-processing can surely increase the accuracy of prediction. The reason for that is we are worried about the pre-processing may exaggerate the performance of neural network since some pre-processing are almost impossible in reality. Therefore, we did use the non-adaptive method to prepare the dataset: only a first-order system is used to smooth our data. After that, the dataset will be split into small slip windows. If the size of time windows is 10 sample times, the events in the past 2 seconds are taken into consideration since our sample frequency is 50Hz. Slip

windows are used for avoiding the influence of data too long ago.

The measured data is normalized before training since we want to avoid one single variable that has too much influence on each gradient descent step. As a result of that, the cost function's shape changes into a more spherical one rather than a high curvature ellipse one.

Besides, the labeled date is converted into one hot vector to have the same categorical value, as shown in **equation 1**,

$$Y^{(1)} = [0\ 1\ 0] \tag{1}$$

which demonstrates that the 1st sample is labelled as loading.

In our dataset, 11.62% of all working time is in the loading process, and 7.86% is in the unloading process. Obviously, our dataset for truck loading process is skewed. That means, even if we always predict that we are neither in loading nor unloading process, we have a test accuracy at about 80%. To avoid it, we should use confusion matrices and micro average F1 scores to evaluate the performance of our algorithm. Based on an exploratory training, the training cost without anti overfitting goes down to an extremely low level while the test cost goes firstly down and then explodes up. This indicated that our dataset has well considered the variance of Y cycle in different cases.

7. COMBINED NEURAL NETWORKS

To have a better detection performance, we take the advantages of combined neural networks, CRDNNs. We are going to explore the combination of CNNs, RNNs, and DNNs in this section. They all have limitations so that we believe that combined neural networks can be complementary for the disadvantages of each other. For example, LSTMs are good at temporal modelling while they cannot have a more significant number of hidden layers.

As shown in **Figure 4**, we use one one-dimensional convolutional neural network (conv1D) at the beginning to provide better features for LSTMs. It is followed by two DNNs to reduce the dimension of the output of CNN. Further, we add two LSTMs since it is considered as an excellent tool for many time series

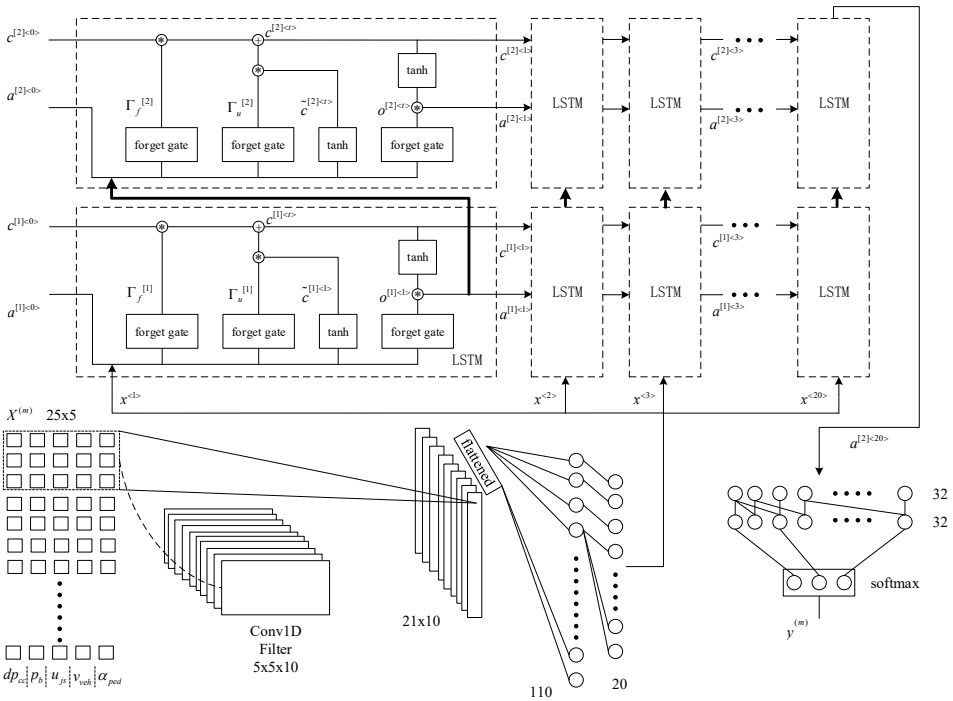

Figure 4: Detailed description of CRDNN with two LSTMs

applications. At the end, two DNNs are used to increase nonlinear hidden layers and thus increase the prediction performance by making a deeper mapping. The core of LSTMs is the update and forget gate to handle the long and short term data. **Equation 4** demonstrates the idea.

$$\begin{cases} \tilde{c}^{\langle t \rangle} = tanh\left(W_c\left[a^{\langle t-1 \rangle}, x^{\langle t \rangle}\right] + b_c\right) \\ \Gamma_u = \sigma\left(W_u\left[a^{\langle t-1 \rangle}, x^{\langle t \rangle}\right] + b_u\right) \\ \Gamma_f = \sigma\left(W_f\left[a^{\langle t-1 \rangle}, x^{\langle t \rangle}\right] + b_f\right) \\ \Gamma_o = \sigma\left(W_o\left[a^{\langle t-1 \rangle}, x^{\langle t \rangle}\right] + b_o\right) \\ c^{\langle t \rangle} = \Gamma_u * \tilde{c}^{\langle t \rangle} + \Gamma_f * c^{\langle t-1 \rangle} \\ a^{\langle t \rangle} = \Gamma_o * tanh\, c^{\langle t \rangle} \end{cases} \quad (2)$$

Generally, the learning ability is increasing as the number of hidden layers increase. However, more hidden layers result in much more training parameters that may be a heavy load for vehicle ECU. In this section, we evaluate the CRDNNs' test accuracy regarding the hidden layer, the units in a hidden layer, and time windows.

Theoretically, LSTMs do not need a slip window. However, we need to avoid the data before a disruptive event, such that the driver stops the vehicle to relax for a while, which affects the prediction performance. Therefore, we also use the slip windows for CRDNN. The window size can affect the performance of neural networks since a larger window size allows the neural

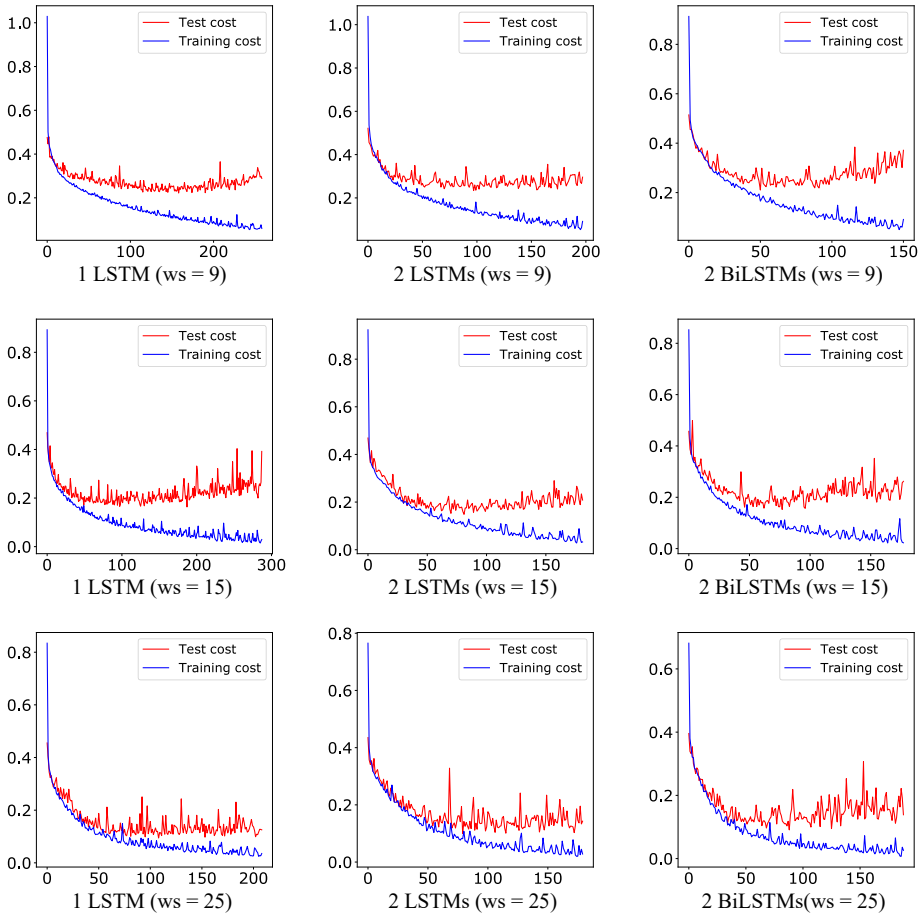

Figure 5: Training- and test costs versus epochs

networks considered a more extended period to make the decision.

Since we want to know which model has the best test accuracy and which one has a good test accuracy but with fewer training parameters, we show the different performances of different architecture with different window sizes. We supervise the training- and test costs over epochs and stop the optimization process when there is a noticeable tendency that test cost increases. The training cost versus iteration of different neural networks is shown in Figure 5. For example, in the case of CRDNN with 2 LSTMs that is fed the data with a window size of 9, we stop the iteration at epoch 60.

To find out the suitable hyper-parameters of neural networks, we analyze the weights of each layers of neural networks. However, while people recognize the working process mainly by watching the pressure inside of bucket, CRDNNs do not pay too much attention to this variable since the absolute value of weight for it is no considerably larger than the others.

As shown in Figure 5, the cost goes down to a certain level and then fluctuates if the regularization and drop-out method are used. Notice that the cost with anti-overfitting methods is higher since we use the regulation method: it does not mean the accuracy is worse than the one without anti-overfitting methods. Also, we add weight to the cost function. The weight can avoid a certain kind of error by recognizing. For instance, if the weight on loading is higher than the weight on the traveling process, the optimization process will take more attention to avoid the errors on loading rather than on the traveling process. Formally, see **equation 2**.

$$J(\theta) = \frac{1}{m}\sum_{i=1}^{m}\sum_{k=1}^{K}\left[-y_k^{(i)}\log\left(\left(h_\theta x^{(i)}\right)_k\right) - \left(1-y_k^{(i)}\right)\log\left(1-\left(h_\theta x^{(i)}\right)_k\right)\right]w_k + \frac{\lambda}{2m}\left[\sum_{j=1}^{32}\sum_{k=1}^{32}\left(\theta_{j,k}^{(1)}\right)^2 + \sum_{j=1}^{3}\sum_{k=1}^{32}\left(\theta_{j,k}^{(2)}\right)^2\right] \quad (3)$$

Obviously, compared to the cost function without regularization, the regularization might increase the total value of cost function. The w_k denotes the weight of k state. In our case, we recommend setting the weight as

$$\widetilde{W} = [1\ 4\ 7]^T \quad (4)$$

Since rectified linear unit (ReLu) has a constant gradient if the X>0, we use ReLu as activation function so that the calculation effort can be reduced and thereby converging or learning much faster.

The Hyper-parameters we used are shown in **Table 2**.

Table 2: Parameters of CRDNN

Hyper-parameters	Value
Window size (ws)	[9, 15, 25]
Batch size	128
Learning rate	1×10^{-4}
Num filter conv1D	10
Kernel size	5
Num units 1st layer (RNN)	32
Num units 2nd layer (RNN)	32
Num units 1st layer (DNN)	32
Num units 2nd layer (DNN)	32

Generally, we shall use the F1 micro average to evaluate and select the best suitable architecture. Nonetheless, since we are going to implement an operation strategy based on the learning algorithm later, the F1 score alone does not indicate whether a result is easy to correct or not, so we also use confusion matrices to evaluate the results, see Figure 6, where the abscissa indicates the predicted value and the ordinate indicates the ground truth label. e_0 , e_1 , e_2 denote the travelling process, the loading process, and the unloading process appropriately. The F1 score is used as a subordinate criterion to select the better overall performance solution. Obviously, the CRDNN with two bidirectional LSTMs has the best performance, which is similar to our assumption, with an overall accuracy at 98.5%. Compared to simple DNNs, CRDNN has an improvement of about 3%. Bidirectional LSTMs make the decision using a relatively more prolonged-time period and can consider the data after the event so with no doubt it has better accuracy. The improvement compared to DNN is because LSTMs are good at dealing with long term problems so that we can use a larger window size to fit into CRDNNs. Another potential architecture is CRDNN with two LSTMs, which is only slightly worse than the one with bidirectional LSTMs but the training parameters are much fewer. An additional advantage of

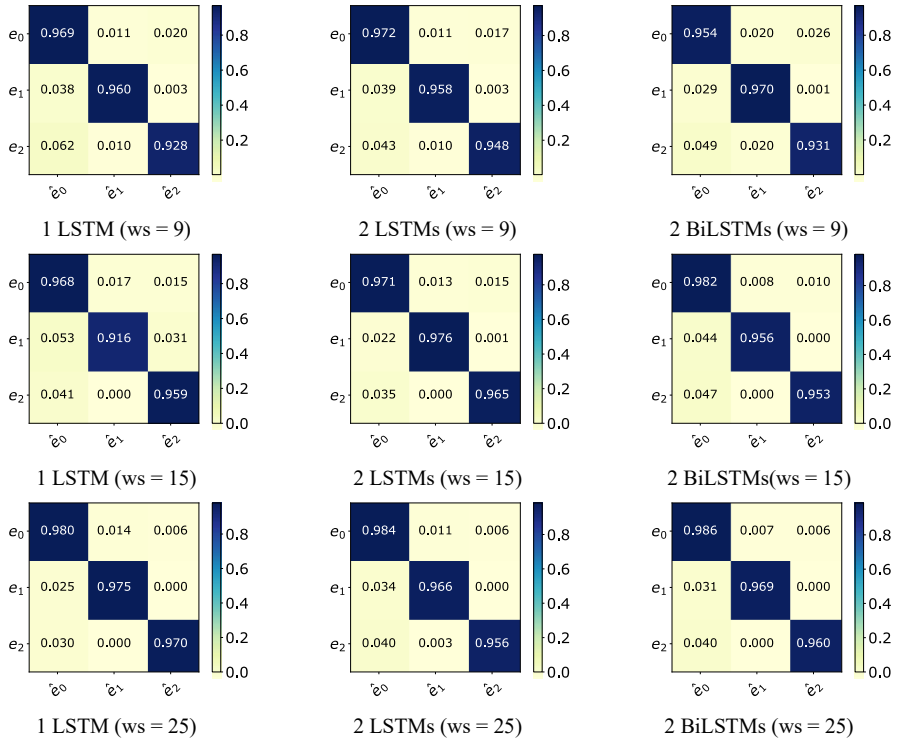

Figure 6: Confusion matrices of CRDNNs

CRDNNs is that it has even fewer training parameters though it has a complicated architecture. Compared to the simple neural networks with two hidden layers and 128 units per layer, CRDNN with two layers of LSTMs has only 16,295 training parameters while the former has more than 30,000 training parameters, resulting in a much faster on-board calculation.

8. EVALUATION OF THE METHODS

As the results are shown in the last section, the improvement of test accuracy is almost stopped at 98.2%. To further improve the prediction accuracy, we draw out the place where our algorithm has made a mistake.

As shown in **Figure 7**, we draw the ground truth and the mistakes made by CRDNN with two bidirectional LSTMs. The blue line denotes the ground truth label and the color points represent the place where CRDNN recognizes a different result as ground truth label and thus we say it makes a mistake. Obviously, the mistakes mainly occur at the time when the machine changes its state from one to another. However, we can say that they are the states which are also controversial for humans to say whether the state should be loading, unloading, or travel since the features are vague in this region. When we further draw all the falsely recognized time windows, we found that almost all of the mistakes occur when the state is really fuzzy.

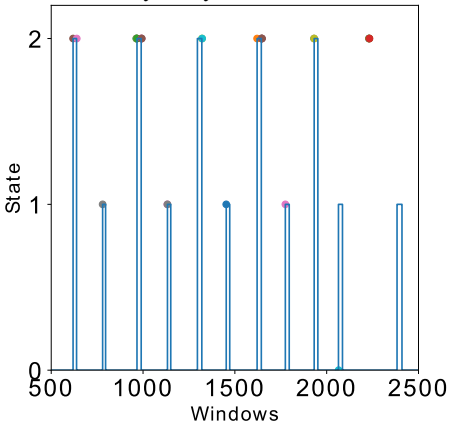

Figure 7: Ground truth and prediction mistakes

One exception is the windows around the 2250th window in **Figure 7**, corresponding to the measurement data at 450 seconds, see **Figure 3**. As mentioned before, the time windows at 450 seconds are the windows that we consciously mislabeled to the travel process. This proves that our CRDNN has a robust performance even if a few data is mislabeled. That is, the CRDNN with two bidirectional LSTMs accurately identified that the process is actually an unloading process rather than a travel process. Therefore, we believe that about 98% is the best number since different engineers define the ground truth differently with their plausible reasons. Moreover, although a tiny number of mislabeling might harm the test accuracy. However, it cannot affect the prediction performance of the CRDNN.

9. CONCLUSION AND OUTLOOK

In this paper, we have shown that CRDNN with bidirectional LSTMs has the best performance to detect the truck loading cycles, and the CRDNN with 2 LSTMs has the best performance-cost ratio if primary torque control concept is used. Because we use an offline learning strategy and the forward propagation is much faster than backward propagation, this method will not take up too much computational effort. By considering a period of 5 seconds, the test accuracy reaches 98.2%, and it never mistakes the loading process with the unloading process or vice versa, which makes the operation strategies easily to be implemented. Also, since we have a large dataset, a tiny mislabel could not harm the real performance of the CRDNNs. It is also worthy to point out that although CRDNN has only increased the test accuracy by 3%, it increases the most challenging 3%. As we mentioned before, we increase the difficulties by adding the data gathered when the drivers did not operate well. As a result of successful detection of truck loading process, our primary torque controlled wheel loader can increase its efficiency up to 9% due to regeneration process.

The dataset and the code in this paper are also published on our Github website. https://github.com/XiangYusheng/IFK2020_TruckLoadingProcessDetection_Xiang.

9.1. Outlook

Although the proposed deep learning algorithm can successfully handle the time series problem so as we can further improve the operation strategy of mobile machines, this method is challenging to predict the next process of mobile machines since truck loading cycles are quite different from the others. However, the Pandora's box has not been fully opened yet. To achieve autonomous working mobile machines or further increasing work efficiency using artificial intelligence, the advantages of image recognition must be taken into account. With a camera, we can not only detect the current working process of mobile machines but also predict its intention. Consequently, power management can make better preparation.

In our next paper, we are going to introduce the two-dimensional image detection method. The method proposed in this paper also provides the relevant information so that we can fuse them to produce even higher accurate classification or prediction results. A regret is that we did not spend much time optimizing the CRDNNs to detect truck loading processes due to the limited time. With further optimization, at least the training parameters can be reduced so that an even faster CRDNN can be expected.

10. REFERENCES

[1] Mutschler S, Norman B, Xiang Y (2018) Torque Control for Mobile Machines. In: Fluid power networks : proceedings : 19th - 21th March 2018 : 11th International Fluid Power Conference, vol 3, pp 186–195

[2] Xiang Y, Mutschler S, Brix N et al. (2020) Optimization of hydrostatic-mechanical transmission control strategy by means of torque control. In: Fluid power networks : proceedings : 12th International Fluid Power Conference

[3] Murrenhoff H (2008) Servohydraulik – Geregelte Hydraulische Antriebe, 3., neu überarbeitete Auflage. Shaker Verlag, Aachen

[4] Pohlandt C (2018) Intelligentes Gesamtmaschinenmanagement für elektrische Antriebssysteme. Karlsruher Schriftebreihe Fahrzeugsystemtrchnik, vol 60. KIT Scientific Publishing, Karlsruhe

[5] Brinkschulte, L.: Daiß, K., Geimer M (2018) Der Nutzen einer Fahr- und Arbeitszustandserkennung am Beispiel eines

Radladers. Land. Technik - Agricultural Engineering - Das Forum für agrartechnische Innovationen, Leinfelden-Echterdingen VDI Bericht 2332: 41–50

[6] Nilsson T, Nyberg P, Sundström C et al. (2014) Robust Driving Pattern Detection and Identification with a Wheel Loader Application. International Journal of Vehicle Systems Modelling and Testing 9(1): 56–76. doi: 10.1504/IJVSMT.2014.059156

[7] Keller NJ, Ivantysynova M, Vacca A et al. (2019) Classification of Machine Functions: A Hydraulic Excavator Case Study. In: Huhtala K, Tikkanen S, Uusi-Heikkilä J (eds) 16th Scandinavian International Conference on Fluid Power. Tampere University, Tampere, pp 410–422

[8] Starke M, Will F (2019) Automatic Process Pattern Recognition for Mobile Machinery. In: Huhtala K, Tikkanen S, Uusi-Heikkilä J (eds) 16th Scandinavian International Conference on Fluid Power. Tampere University, Tampere, pp 450–461

[9] Weber J, Mieth S (2016) Process Assist: Methode zur Online Prozessmustererkennung für die Ermittlung von Kundenkollektiven an mobilen Baumaschinen. Abschlussbericht IGF-Forschungsvorhaben, Dresden

[10] Hinton G, Deng L, Yu D et al. (2012) Deep Neural Networks for Acoustic Modeling in Speech Recognition. IEEE Signal Processing Magazine 29(6): 82–97

[11] Hagen S, George S, Kingsbury B (2010) The IBM Attila Speech Recognition Toolkit. In: Hakkani-Tür D, Ostendorf M (eds) 2010 IEEE Spoken Language Technology Workshop. IEEE, Berkeley, pp 97–102

[12] Sainath TN, Mohamed AR, Kingsbury B et al. (2013) Deep Convolutional Neural Networks for LVCSR. In: IEEE Signal Processing Society (ed) 2013 IEEE International Conference on Acoustics, Piscataway, NJ, IEEE, pp 8614–8618

[13] Bengio Y, Simard P, Frasconi P (1994) Learning Long-term Dependencies with Gradient Descent is Difficult. IEEE Transactions on Neural Networks 5(2): 157–166

[14] Hochreiter S (1991) Untersuchungen zu dynamischen neuronalen Netzen. Dissertation, Technische Universität München

[15] Hochreiter S, Schmidhuber J (1997) Long Short-term Memory. Neural computation 9(8): 1735–1780

[16] Sainath TN, Vinyals O, Senior A et al. (2015) Convolutional, Long Short-term Memory, Fully Connected Deep Neural Networks. In: 2015 IEEE International Conference on Acoustics, Speech and Signal Processing (ICASSP). IEEE, Brisbane, pp 4580–4584

[17] Deng L, Platt JC (2014) Ensemble deep learning for speech recognition. In: Fifteenth Annual Conference of the International Speech Communication Association, Singapore, pp 1915–1919

[18] Razvan Pascanu, Caglar Gulcehre, Kyunghyun Cho et al. (2014) How to Construct Deep Recurrent Neural Networks. arXiv preprint arXiv:1312.6026

[19] Kliffken MG, Mutschler S, Langenbeck B et al. (2008) Systematic of Hydrostatic Drive Trains for Mobile Applications. In: Fluid power networks: 6th international Fluid Power Conference Dresden, Dresden, pp 65–76

[20] MATLAB (2019) Version 9.06.0 (R2010a). The MathWorks Inc, Natick, Massachusetts

HARDWARE-IN-THE-LOOP SIMULATION OF HYBRID HYDROMECHANICAL TRANSMISSIONS

L. Viktor Larsson*, Liselott Ericson, Petter Krus

Division of Fluid and Mechatronic Systems, Linköping University, 581 83 Linköping, Sweden
* Corresponding author: Tel.: +46 13281346; E-mail address: viktor.larsson@liu.se

ABSTRACT

Increased demands on fuel-efficient propulsion motivate the use of complex hybrid hydromechanical transmissions in heavy construction machines. These transmissions offer attractive fuel savings but come with an increased level of complexity and dependency on computer-based control. This trend has increased the use of computer-based simulations as a cost-effective alternative to hardware prototyping when developing and testing control strategies. Hardware-In-the-Loop (HWIL) simulations that combine physical and virtual model representations of a system may be considered an attractive compromise that combine the benefits of these two concepts. This paper explores how HWIL simulations may be used to evaluate powertrain control strategies for hybrid hydromechanical transmissions. Factors such as hardware/software partitioning and causality are discussed and applied to a test rig used for HWIL simulations of an example transmission. The results show the benefit of using HWIL simulations in favour of pure offline simulations and prototyping and stress the importance of accurate control with high bandwidth in the HWIL interface.

Keywords: Hardware-In-the-Loop Simulations, Hydromechanical Transmissions, Hydraulic Hybrids

1. INTRODUCTION

A Hardware-in-the-Loop (HWIL) simulation may be defined as a time-domain simulation of a model that contains both physical (hardware) and virtual (software) representations of a studied system. Within fluid power research in academia, the concept is often used for experimental validation. In an early example (1989), Krus and Palmberg [1] used a servo valve to simulate a load-sensing system connected to a real lorry crane, in a concept referred to as “hybrid simulations”. In the automotive industry, HWIL simulation traditionally refers to Controller Hardware-In-the-Loop (CHIL) simulation, which is the real-time testing of control code in a physical control unit (the hardware) that interacts with software system models [2]. This interaction takes place in the signal domain with low power levels. In this paper, HWIL rather refers to Power Hardware-In-the-Loop (PHIL) simulation, which, in contrast to CHIL simulation, has substantial power amplification present in the hardware/software interface [3]. With this feature, HWIL simulation may then be interpreted as an extension to pure offline simulation, where any model component may be replaced with its hardware equivalent, for instance a hydraulic pump or an electric motor. This interpretation of HWIL simulation is illustrated in **Figure 1**, where the concept is regarded as a middle-way alternative between pure offline simulation and prototype testing of the full system when validating a control strategy.

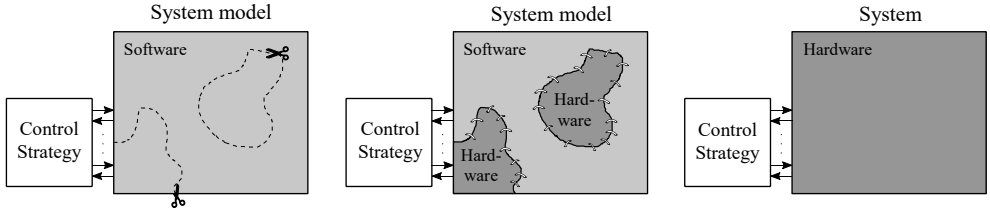

a) Offline simulation **b)** HWIL simulation **c)** Prototype test

Figure 1: Hardware-in-the-loop simulation as a middle way between pure offline simulations and prototype test.

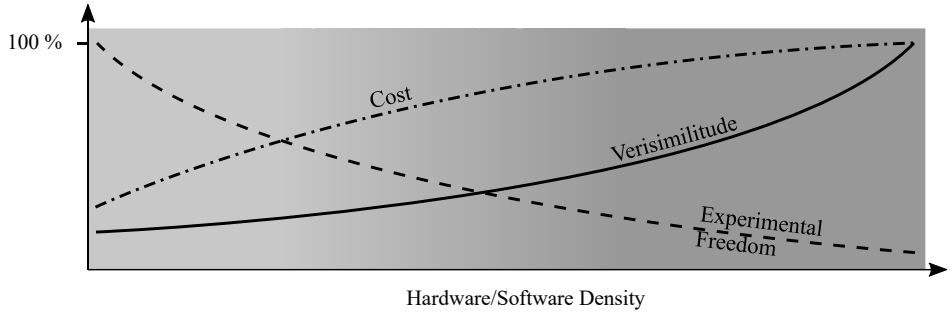

Figure 2: Cost, verisimilitude and experimental freedom.

The choice of HWIL simulation in favour of any of its two extremes may be motivated by comparing their respective pros and cons, as illustrated in **Figure 2**. Offline simulations offer low cost and high experimental freedom, since, for instance, a model is easy to modify and allows for observation of all the system variables [4]. On the other hand, a full system prototype experiment offers high verisimilitude (truthlikeness). That is, the more hardware that is included in the experiment, the closer to reality it is (should be).

1.1. Hybrid Hydromechanical Transmissions

In this paper, a Hydromechanical Trans-mission (HMT) is defined as a transmission that transfers power in both the mechanical and the hydraulic domains, between the engine and the wheels in a vehicle driveline. A *hybrid* HMT also use hydropneumatic accumulators, that enable energy recuperation and reuse. A general hybrid HMT for a construction machine is shown in **Figure 3**, and may be represented as a hydraulic circuit with accumulator and variable displacement units connected to a transmission subsystem. The transmission subsystem may contain spur gears and planetary gears to form different transmission architectures, such as input coupled, output coupled or compound power-split [6], depending on the application. For demanding applications, such as heavy wheel loaders, multiple-mode transmissions with clutches are required to fulfil requirements on operating range and cost. A key challenge in the design of these transmissions is the large design space, where simulation-based optimisation has shown to be an important tool [7].

Complex hybrid HMTs also rely heavily on control. As indicated in **Figure 3**, fast and accurate control of the variable displacement units is required on an actuator level. At a system level, powertrain control manages the engine speed, the system pressure and the operator's

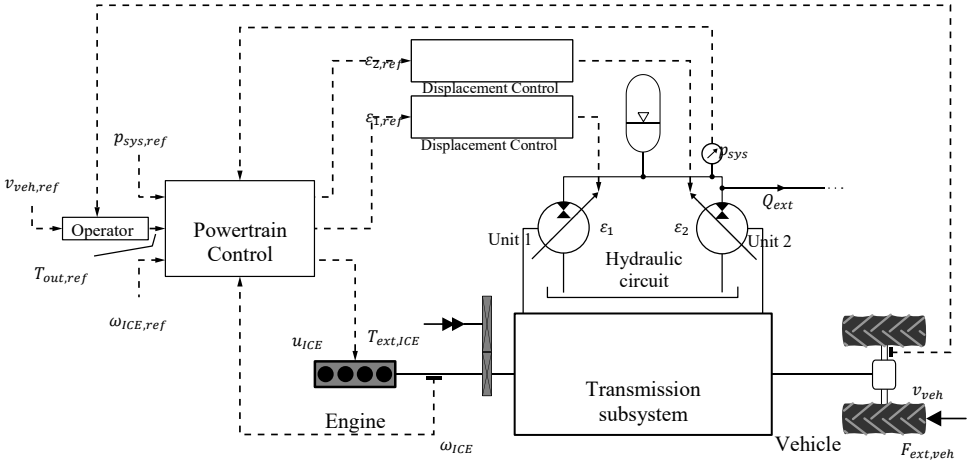

Figure 3: A general hydraulic hybrid drivetrain with its related control aspects and disturbances, from [5].

torque request. For hybrid systems, proper energy management of the accumulator and optimal choice of engine operating point are also required to ensure fuel-efficient operation. These topics are out of the scope of this paper but have, for instance, been studied in [8] for on-road vehicles and in [9] for wheel loaders. In **Figure 3**, it is thus assumed that the system pressure and engine speed reference values are outputs from high- and mid-level strategies that focus on fuel efficiency, while the powertrain control strategy ensures that these values are fulfilled in a stable, accurate manner.

One aspect that distinguishes working machines from e.g. on-road vehicles, is that they have several substantial power consumers in addition to the driveline. These are primarily work functions, such as a loader with boom and bucket, that are actuated with a working hydraulics system. This aspect has big influence on how the machine is designed and controlled [10]. Although the focus in this paper is on the transmission, the presence of additional power consumers is considered as external disturbances in **Figure 3**. $F_{ext,veh}$ in **Figure 3** indicates an external disturbance force, for instance from a gravel pile.

HWIL simulation has frequently been used in the past for validating and testing control strategies for HMTs. In the early 1990s the concept was applied to hydrostatic transmissions by Jansson et. al. [11] and Lennevi and Palmberg [12]. In the late 1990s, Sannelius [13] used HWIL simulations in the testing of control strategies for the two-motor transmission. A more recent example (2014) is the blended hydraulic hybrid investigated by Sprengel and Ivantysynova [14]. As stressed in [14], HWIL simulations are valuable as alternative to full-scale vehicle tests when evaluating control strategies for novel transmission concepts. Since the transmission does not have to be mounted in a real vehicle, HWIL simulations enable a higher degree of control and repeatability and accurate measurements with high-quality instruments that do not need to be carried on-board the vehicle.

1.2. Contributions

This paper explores the application of HWIL simulation as a tool for validation of powertrain control strategies for hybrid HMTs for construction machines. Enablers of HWIL are highlighted and discussed from this perspective, and their implementation in a test rig recently used for this application in [5] is presented. A HWIL simulation is carried out of a reference vehicle for a short cycle and compared to the same cycle in offline simulation.

2. THE HARDWARE-IN-THE-LOOP INTERFACE

The key to successful HWIL simulation lies in the hardware/software interface, illustrated in **Figure 4**. On a conceptual level, the interface may be compared with power ports similar to those used in bond graph modelling [14]. In the HWIL power port, the flow/effort variable is then determined by the software while the effort/flow variable is determined by the hardware. HWIL simulation thus imply a *bidirectional* hardware/software communication, which, at the implementation level, is realised with control [2]:

"...a H(W)IL simulator is in essence a control system whose virtual components command its hardware to "track" a hypothetical reference "system"."

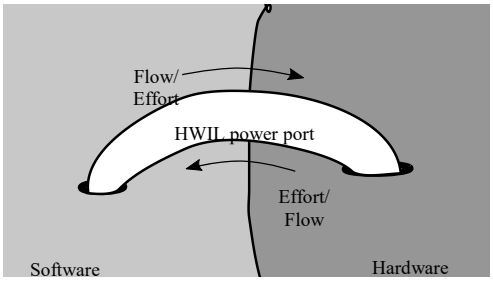

a) Conceptual (modelling) level

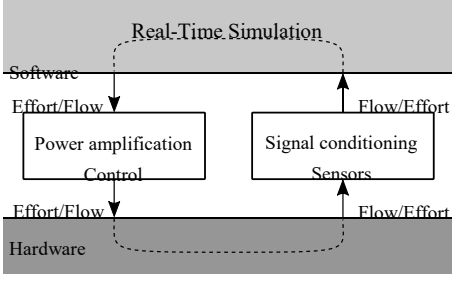

b) Implementation level, adapted from [1, 2].

Figure 4: Different levels of the HWIL interface.

The dependence on real-time control introduces a number of key enablers of HWIL simulation, as listed by Fathy et. al. [2]. For instance, high bandwidth and accuracy of the control is required to maximise the reliability of the results. Consequently, high focus in previous research has been on control aspects of HWIL simulation, e.g. [11,13,15]. Another important enabler is the hardware/software integration, which may be divided into partitioning and connection causality [2].

2.1. Partitioning

Partitioning relates to the question of how much, and which parts of the studied system that should be represented as hardware or software. The answer to this question is usually a result of the combination of the scope of the investigation and what is feasible (recall **Figure 2**). In the context of transmission development, Sannelius [13] distinguishes between component focus, where a system is simulated around a new (hardware) component, and system focus, where the new component is simulated in an existing (hardware) system.

If a specific HMT concept is investigated, it is convenient to represent the engine and vehicle as software and the transmission as hardware [14]. For instance, in [11], where a hydrostatic transmission is in focus, the engine is represented as a servo valve-controlled pump/motor while the vehicle is represented as an equivalent inertia (flywheel) with simulated load torque.

When aspects such as emissions and fuel efficiency are studied, the engine is usually represented as hardware connected to a dynamometer which emulates a vehicle, then referred to as Engine-in-the-Loop [16]. With so called rolling road or chassis dynamometers, the complete vehicle is present as hardware, while its surroundings are emulated [17].

The partitioning also determines in which power domain the HWIL interface is inserted, which in turn affects the control implementation. For fluid power systems and hydromechanical transmissions, hydraulic (pressure/flow) or mechanic rotational (torque/angular velocity) interfaces are most often used [13].

2.2. Connection Causality

Connection causality relates to the question whether the interface's flow variable (flow/speed) should be determined by the hardware, while the effort variable is determined by the software (pressure/torque), or vice versa. The answer to this question is highly influenced by the behaviour of the hardware and the control performance of the HWIL interface. For instance, the slow variation in pressure caused by the accumulators used in hybrid hydrostatic transmissions motivated a switch from torque to speed control of the output shaft during HWIL simulation of the blended hybrid in [14].

Another example of causality-related difficulties is inertia simulation. If the software controls the speed of a transmission output shaft, vehicle inertia simulation can be carried out via integration of the measured shaft torque. On the other hand, if the software controls the shaft torque, inertia simulation is carried out based on angular acceleration, which often needs to be estimated as the speed time derivative [15]. Another alternative is to represent vehicle inertia as a flywheel and add air drag and other losses via torque control. This is often carried out in rolling road dynamometers, where a set of flywheels can be combined to simulate different vehicle sizes [17]. In a combined approach, Jansson et. al. [11] found that the inertia of the flywheel could be increased around 240 % through estimation of the acceleration, and that higher increases were limited by the stability of the control loop.

2.3. Fixed-Step Integration

Fixed-step integration is another key enabler of HWIL simulation. As the interaction between the software and hardware representations of the model takes place in real time, the solver for the software simulation models must be able to finish each integration step within the equivalent step taken by the real-time computer [2]. In this sense, the use of the Transmission Line element Method (TLM) for software system representation is highly motivated. TLM is based on the theory of bilateral delay lines which introduces physically motivated time delays to model physical components [18]. This enables the use of distributed equation solvers without introducing numerical errors and consequently, fast numerically stable simulations with high accuracy may be achieved in real time [19]. In addition, if TLM is used for offline simulation of the full system as well, the same model can be re-used during the HWIL simulation without

making reductions in model fidelity, which facilitates the control strategy development process [7].

In this paper, the Hopsan software is used for all software models. Hopsan is a system simulation tool developed at Linköping University [20]. It uses a fixed-step implementation of TLM and has, for instance, been used for simulation of hydrostatic transmissions and other HMTs in the past, se e.g. [13, 21].

3. TEST RIG

The test rig is shown in **Figure 5** and **Figure 6**. The basic idea of the setup is to enable HWIL simulation of the generic hybrid hydro-mechanical transmission shown in **Figure 3**. In relation to the previously discussed topics, the following implementations are made.

3.1. Partitioning

The hardware part of the simulation is the hydraulic circuit, while engine, transmission subsystem and vehicle are represented as software. This partitioning can be motivated by the complex nature of accumulators and hydrostatic unit losses, which are difficult to model mathematically. In addition, testing of different transmission concepts (series hybrid, input/output coupled power-split, multiple-mode etc.) is facilitated via modification of the software model. The hydraulic circuit contains two Bosch A11VO four-quadrant in-line axial piston units with 110 cm^3/rev displacement. These are equipped with electro-hydraulic displacement actuators that are controlled with external feedback, see [22, 23]. They are connected in open circuit with two 20-L piston accumulators connected in parallel on the high-pressure side. A servo-valve is connected to the high-pressure side to simulate the effect of flow disturbances, for instance from a working hydraulics system.

3.2. Connection causality

The shaft torques of the hydraulic units are measured in the test rig and sent to the software model, which calculates the corresponding shaft speeds. These values are sent to the rig controller, which controls the actual shaft speeds in closed loop with a servo valve-controlled pump/motor connected to each hydrostatic transmission unit. This causality (measure torque → control speed) is motivated by the fact that the hydrostatic units act as torque sources due to the impressed system pressure [14]. No flywheels are used on the shafts, since all vehicle and engine inertial effects are present in the model. This enables fast

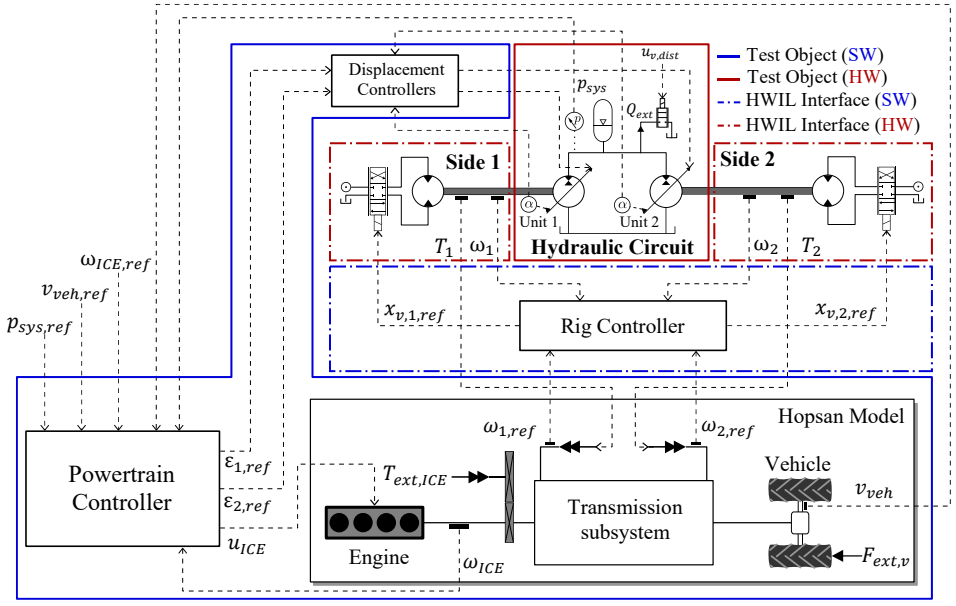

Figure 5: Working principle of the test rig used in the study. SW = Software, HW = Hardware.

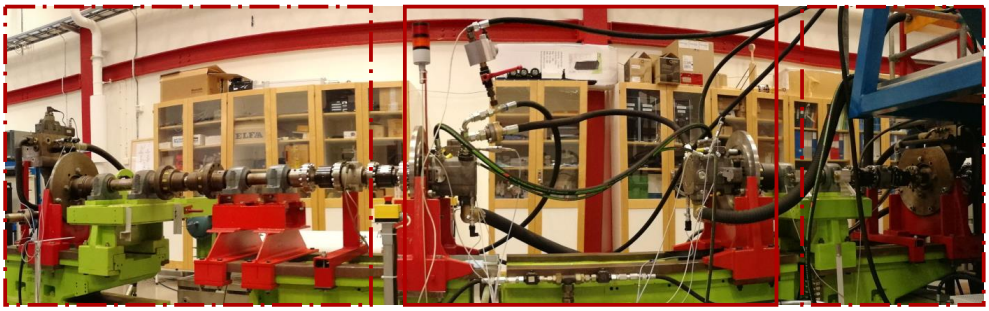

Figure 6: HWIL Simulation test rig main view.

response of the rig shaft speed controllers, although the control becomes sensitive to torque disturbances. The control strategy used in the rig is described in more detail in appendix D in [5], and uses a feedback controller combined with feedforward and disturbance rejection based on estimation of the torque of each transmission pump/motor unit.

3.3. Real-time and fixed-step integration

The software model is implemented as a Hopsan model executed on a National Instruments PXI computer that runs in real time with a sampling frequency of 1 kHz. This computer also handles the control of the HWIL interface. The full Hopsan offline simulation model is re-used by replacing the hydrostatic circuit with torque sources and adding communication ports. Communication with the PXI computer for software model/controller updates and during HWIL simulation in real time is carried out on a LabVIEW-based Graphical User Interface (GUI) called Viking [24]. See [25] for details on the implementation of the real-time Hopsan simulation and [22] for further details on the data acquisition system hardware.

4. VEHICLE SIMULATION EXAMPLE

To illustrate the working principle of the test rig, a reference vehicle equivalent to a compact wheel loader was simulated for a short cycle. The vehicle parameters are provided in Table 1. The vehicle was tested with an input-coupled power-split transmission, which means that the transmission's input shaft is directly connected to the hydraulic circuit, while the output shaft is connected to both the hydraulic circuit and the input shaft via a planetary gear train [6].

Table 1: Parameters of the reference vehicle

Parameter	Value
Vehicle mass	5500 kg
Maximum speed	30 km/h
Maximum tractive force	50 kN
Max engine power	52.7 kW

The reference vehicle was simulated for the same cycle in both HWIL simulation and offline simulation. **Figure 7** shows screen shots of the Hopsan models used for these simulations. The offline model represents the complete transmission with hydraulic circuit, diesel engine and vehicle. For the HWIL simulation, the same model was re-used, but the hydraulic circuit was replaced by torque sources fed with the torques measured in the rig. Derivation of the component models used in the Hopsan system models is provided in appendix A in [5].

The powertrain control strategy tested in the simulations has been developed in previous work by the authors [26, 27] and is based on decoupled control. In short, this means that a decoupling strategy is used to transform the Multiple-Input Multiple-Output (MIMO) control problem to three Single-Input Single-Output (SISO) loops (system pressure, vehicle speed and engine speed), each controlled with a decoupled control signal. The decoupled control signal for the pressure is the desired net accumulator flow, for the vehicle speed the net transmission output torque and for the engine speed the net engine torque. In the simulations shown, proportional SISO controllers were used, and the tests were carried out by varying of the reference signals (pressure, vehicle speed and engine speed).

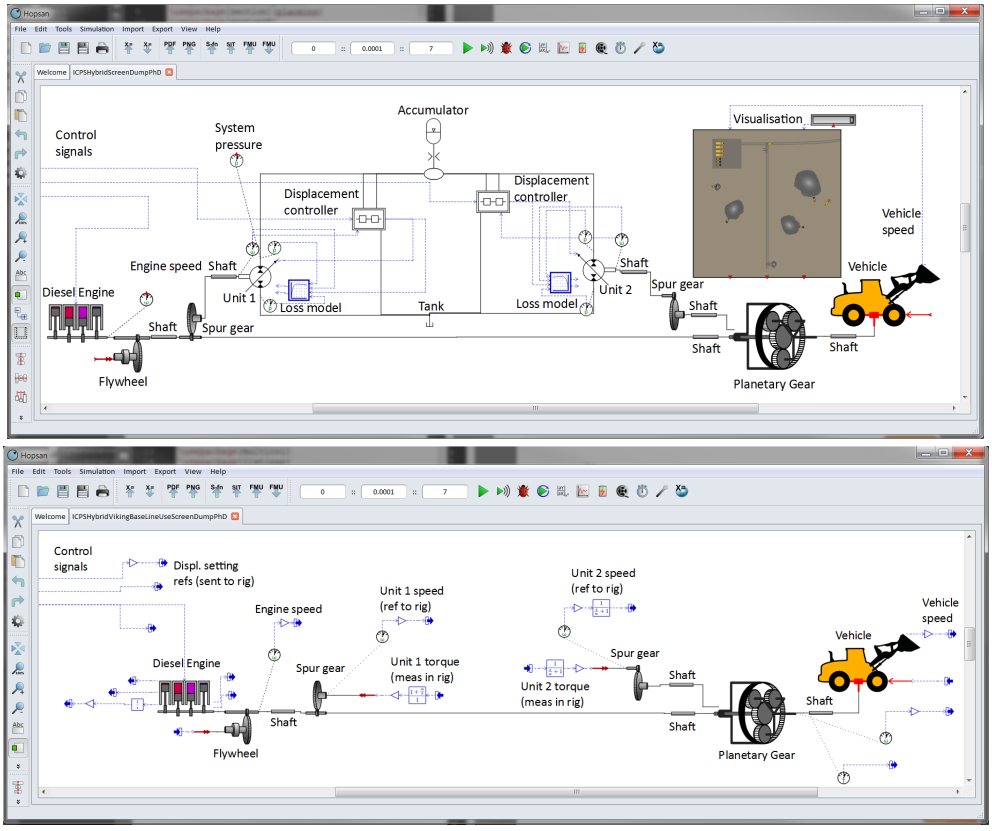

Figure 7: Hopsan models used for the offline (top) and HWIL simulations (bottom). For the HWIL model, the offline model was reused by replacing the hydraulic circuit with torque sources that read filtered signals from the measured rig torques.

4.1. Results and Discussion

The simulated cycle for HWIL and offline simulation of the reference vehicle is shown in **Figure 8**. The cycle aims at simulating a case in which all required vehicle power is provided by the accumulator. As the vehicle is accelerated (1-3 seconds), the accumulator pressure is lowered, and when it brakes (5-6 seconds), the pressure is increased. The engine speed is controlled at a constant 1800 rpm and is not shown here. The injected engine fuel (u_{ICE}) is maintained at low levels to overcome engine losses while the accumulator is used to power the vehicle.

The red curves in the two upper graphs indicate the decoupled control signals. For the pressure, the controller demands positive accumulator flow ($Q_{acc,ref}$) to increase the pressure and negative flow to decrease it. Similarly, the output speed controller may be interpreted as an operator who demands positive output torque ($T_{out,ref}$) to accelerate and negative torque do decelerate. At the lowest control signal level, however, the hydraulic unit displacement settings ($\varepsilon_1, \varepsilon_2$) and the injected engine fuel vary depending on the kinematic relationships of the transmission subsystem.

In the bottom graph in **Figure 8**, the power flows of the different components during the HWIL simulation are plotted. These have been calculated by multiplying the torque and shaft speeds at the different transmission shafts. P_1 and P_2 marks the hydrostatic unit powers, where $P_1, P_2 > 0$ indicates pumping mode. The accumulator power has been calculated as $P_{acc} = P_1 + P_2$. The same graph also includes the consumed fuel of the engine. It may be observed

that the consumption is lowered when the vehicle energy is recuperated at 5.5 seconds. It should be noted though, that the shown simulation is primarily an example of a cycle, and any estimations in terms of fuel efficiency improvements require comparisons with state-of-the-art systems and more appropriate energy management strategies.

Benefits with HWIL simulation may be illustrated via a comparison with the offline simulation results. The difference between the two simulations is small in large portions of the cycle. Given that the strategy was developed and validated in offline simulations, the small difference indicates that the strategy would work appropriately in a final implementation.

Between 5 and 6 seconds, however, a significant difference between the offline and HWIL simulated values of $T_{out,ref}$ may be observed. The reason for this difference is that the friction loss model for the hydraulic units used in the offline simulation is insufficiently accurate in the given operating point. For an input-coupled power-split transmission, the output torque is proportional to the torque of unit 2, which in turn is controlled by ε_2 due to the slowly varying system pressure. The difference in friction losses in the HWIL simulations therefore causes a saturation in ε_2 which is not present in the offline simulation. Consequently, output torque is also limited which results in a significant increase in desired output torque at this point (the operator floors the brake pedal). In a real vehicle, this phenomenon is non-desirable, and could be avoided via manipulation of the reference signals (e.g. higher pressure), application of friction brakes or a different transmission design. Particularly the latter action may be taken with relatively low cost compared to if this problem had been discovered in a prototype transmission.

Although the HWIL simulation indeed increases the system knowledge, it is important to note that its fidelity relies heavily on accurate control in the HWIL interface. **Figure 9** shows the rig control performance during the simulated cycle. During transients, the rig speed control is sensitive to torque disturbances due to the low inertia of the shafts. For instance, at 5-6 seconds, at which significant differences between offline and HWIL simulations were discovered, the rig control error is around 12 %. The previously drawn conclusion concerning the friction loss models could therefore be questioned, and

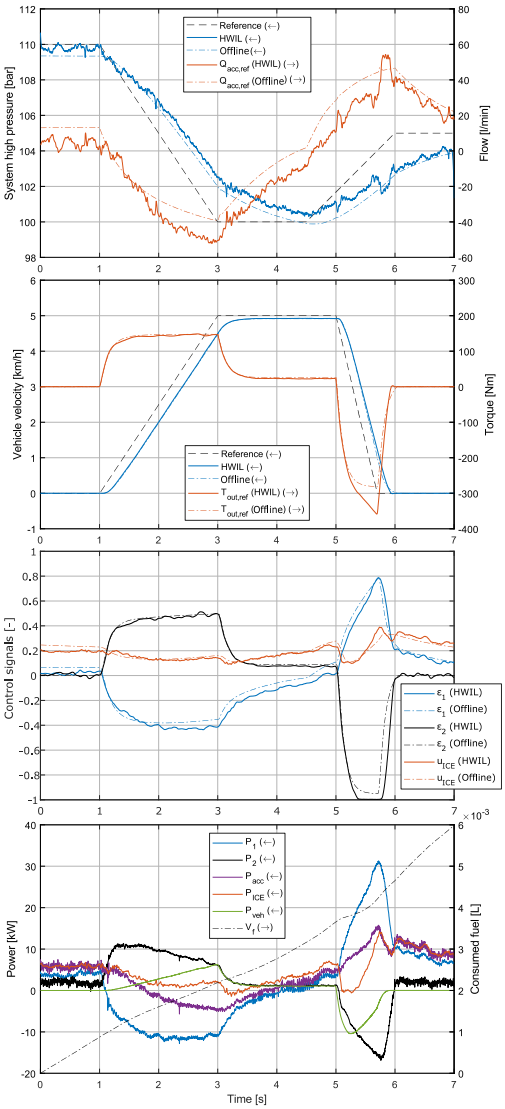

Figure 8: HWIL simulation of the reference vehicle for a short drive cycle. A time step of 0.1 ms was used in the Hopsan models. *Offline* denotes results from the offline simulation of the full system.

improvements of the HWIL interface are motivated. The difference in unit shaft torques between the offline and HWIL simulation (**Figure 9**) at 5-6 seconds does, however, indicate improper loss modelling as a cause of the difference between the offline and HWIL simulations.

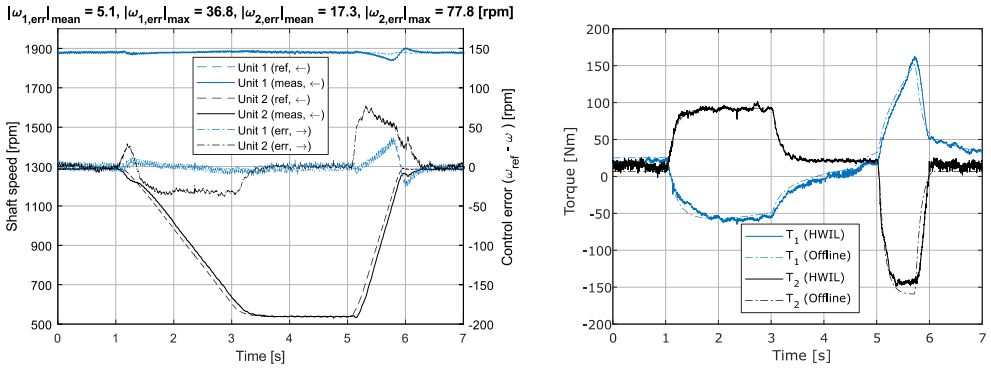

Figure 9: Rig reference tracking (left) and hydraulic unit shaft torques (right) for the drive cycle.

5. CONCLUSION AND OUTLOOK

Hardware-in-the-loop simulation is an attractive alternative to offline simulations and prototype testing when evaluating powertrain control strategies for hybrid hydromechanical transmissions in construction machines. By introducing the hydraulic circuit as hardware, the verisimilitude of the simulation increases, while different transmission architectures may be evaluated in a simple manner by changing the software model. This increase in verisimilitude does, however, rely on fast, accurate control in the hardware-in-the-loop simulation interface, and the rig control error should always be considered in model validity assessments. For the presented setup, enhanced control strategies and update of the rig hardware could therefore be reasonable topics for future work. Studies may also be extended to include hardware or software representations of working hydraulics and focus on energy management strategies for construction machines.

NOMENCLATURE

$\varepsilon_{1/2}$	Relative displacement of unit 1/2
$F_{ext,veh}$	External vehicle disturbance force
$\omega_{1/2}$	Shaft speed of unit 1/2
ω_{ICE}	Engine shaft speed
p_{sys}	Transmission high pressure
Q_{ext}	External disturbance flow
$Q_{acc,ref}$	Desired accumulator net flow
$T_{1/2}$	Shaft torque of unit 1/2
$T_{ext,ICE}$	External engine disturbance torque
$T_{out,ref}$	Desired transmission output torque
u_{ICE}	Normalised engine injected fuel
$u_{v,dist}$	Disturbance valve signal
v_{veh}	Vehicle velocity
$x_{v1/2}$	Servo valve displacement of rig side 1/2
CHIL	Controller-Hardware-In-the-Loop
GUI	Graphical User Interface
HMT	Hydromechanical Transmission
HWIL	Hardware-In-the-Loop
ICE	Internal Combustion Engine
PHIL	Power-Hardware-In-the-Loop
ref	Reference value
TLM	the Transmission Line element Method

REFERENCES

[1] Krus P, Palmberg J-O (1989) Integration of Simulation and Measurement in Time and Frequency Domains. The 2nd Int Conf on Fluid Power and Control 512-519

[2] Fathy H, Filipi Z, Hagena J, Stein J (2006) Review of Hardware-in-the-Loop Simulation and Its Prospects in the Automotive Area. Modeling and Simulation for Military Applications 6228

[3] Steurer M, Edrington C, Sloderbeck M, Ren W, Langston J (2010) A Megawatt-Scale Power Hardware-in-the-Loop Simulation Setup for Motor Drives. IEEE Transactions on Industrial Electronics 57.4 1254 – 1260

[4] Fritzson P (2003) Principles of Object Oriented Modeling and Simulation with Modelica 3.3: a cyber-physical approach. Wiley-IEEE Press

[5] Larsson L V (2019) Control of Hybrid Hydromechanical Transmissions. PhD thesis, Linköping University, Linköping, Sweden

[6] Kress J H (1984) Hydrostatic Power-Splitting Transmissions for Wheeled Vehicles –

Classification and Theory of Operation. SAE Technical Paper 680549

[7] Uebel K (2017) Conceptual Design of Complex Hydromechanical Transmissions. PhD thesis, Linköping University, Linköping, Sweden

[8] Karbaschian M A, Söffker Dirk (1996) Review and Comparisons of Power Management Approaches for Hybrid Vehicles with Focus on Hydraulic Drives. Energies 7.6 3512-3536

[9] Wang F, Mohd Zulkefli M A, Sun Z, Stelson K A (2015) Energy management strategy for a for a power-split hydraulic hybrid wheel loader. Proceedings of the Institution of Mechanical Engineers, Part D: Journal of Automobile Engineering

[10] Uebel K, Raduenz H, Krus P, De Negri V J (2018) Design Optimisation Strategies for a Hydraulic Hybrid Wheel Loader. ASME/Bath 2018 Symposium on Fluid Power and Motion Control

[11] Jansson A, Lennevi J, Palmberg J-O (1993) Modelling, simulation and control of a load simulator for hydrostatic transmissions. 3rd Int Scandinavian Conf on Fluid Power

[12] Lennevi J, Palmberg J-O (1995) Application and Implementation of LQ Design Method for the Velocity Control of Hydrostatic Transmissions. Proceedings of the Institution of Mechanical Engineers, Part I

[13] Sannelius M (1999) On Complex Hydrostatic Transmissions, Design of a Two-Motor Concept using Computer Aided Development Tools. PhD thesis, Linköping University, Linköping, Sweden

[14] Sprengel M, Ivantysynova, M (2014) Hardware-in-the-Loop testing of a Novel Blended Hydraulic Hybrid Transmission. 8th FPNI PhD Symposium on Fluid Power

[15] Du Z, Li P, Cheong K L, Chase T R (2014) Design and Experimental Validation of a Virtual Vehicle Control Concept for Testing Hybrid Vehicles using a Hydrostatic Dynamometer. The ASME 2014 Dynamic Systems and Control Conf

[16] Filipi Z, Fathy H, Hagena J, Knafl A, Ahlawat R, Liu J, Jung D, Assanis D, Peng H, Stein J (2006) Engine-in-the-Loop Testing for Evaluating Hybrid Propulsion Concepts and Transient Emissions – HMMWV Case Study. SAE 2006 World Congress & Exhibition

[17] Martyr A J, Plint M A (2007) Engine Testing: Theory and Practice. Elsevier Ltd.

[18] Auslander D M (1968) Distributed System Simulation With Bilateral Delay Models. Journal of Basic Engineering 195-200

[19] Krus P (2009) Robust Modelling using Bi-Lateral Delay Lines for Real Time and Faster Than Real Time System Simulation. ASME 2009 International Design Engineering Technical Conferences & Computers and Information in Engineering Conference

[20] Linköping University, Division of Fluid and Mechatronic Systems. Hopsan https://liu.se/en/research/hopsan. Last visited: 2020-01-23

[21] Lennevi J (1995) Hydrostatic Transmission Control. PhD thesis, Linköping University, Linköping, Sweden

[22] Larsson L V, Krus P (2016) Modelling of the Swash Plate Control Actuator in an In-Line Axial-Piston Unit for a Hardware-in-the-Loop Simulation Test Rig. The 9th FPNI PhD Symposium on Fluid Power

[23] Larsson L V, Krus P (2017) Displacement Control Strategies of an In-Line Axial-Piston Unit. The 15th Scandinavian International Conference on Fluid Power (SICFP'17)

[24] Prevas (2010) Viking GUI – User Manual

[25] Braun R, Krus P (2012) Multi-threaded real-time simulations of fluid power systems using transmission line elements. The 8th International Fluid Power Conference

[26] Larsson L V, Krus P (2018) A General Approach to Low-Level Control of Heavy Complex Hybrid Hydromechanical Transmissions. ASME/Bath 2018 Symposium on Fluid Power and Motion Control

[27] Larsson L V, Ericson L, Uebel K, Krus P (2019) Low-Level Control of Hybrid Hydromechanical Transmissions for Heavy Mobile Working Machines. Energies 12.9

peer reviewed

APPLICATION OF MACHINE LEARNING TO IMPROVE THE PERFORMANCE OF A PRESSURE-CONTROLLED SYSTEM

Fabian Kreutmayr*, Markus Imlauer

HAWE Hydraulik SE, Einsteinring 17, 85609 Aschheim / München
* Corresponding author: Tel.: +49 (89) 379100 - 1149; E-mail address: f.kreutmayr@hawe.de

ABSTRACT

Due to the robustness and flexibility of hydraulic components, hydraulic control systems are used in a wide range of applications under various environmental conditions. However, the coverage of this broad field of applications often comes with a loss of performance. Especially when conditions and working points change often, hydraulic control systems cannot work at their optimum. Flexible electronic controllers in combination with techniques from the field of machine learning have the potential to overcome these issues. By applying a reinforcement learning algorithm, this paper examines whether learned controllers can compete with an expert-tuned solution. Thereby, the method is thoroughly validated by using simulations and experiments as well.

Keywords: Hydraulic control systems, Machine learning, Reinforcement learning

1. INTRODUCTION

Since hydraulic control systems are used in various fields with a wide range of different operating conditions, e.g. range of oil temperature, range of pressure, and type of fluid, the design of these systems is a challenging procedure. Hereby, the availability of hydraulic components that can deal with this variety of requirements is crucial. For this purpose, a major design criterion for hydraulic components is that they remain flexible. This flexibility is conventionally achieved at the expense of performance, which influences the whole hydraulic control system.

Moreover, fixed inflexible mechanic controllers are still used for many applications. Whilst these are self-sufficient and robust against influences like temperature changes or heavy vibrations, adaptability to different working points is not given. Additionally, these controllers suffer from abrasion.

By using electronic instead of mechanic controllers, these drawbacks can be compensated, because their parameters can be changed easily. Though, since the system dynamics are often partially or completely unknown, tuning these control parameters is time consuming and may result in non-optimal solutions. So, the application of methods from the field of artificial intelligence, i.e. machine learning, can help to reduce the effort of complex parameter tuning. Especially reinforcement learning (RL) algorithms have already shown promising results for solving various control tasks [1, 2, 3].

This work examines the applicability of such RL algorithms to control hydraulic systems. For this purpose, a mathematical model of an example system is derived and implemented in simulation. Afterwards, the deep deterministic policy gradient (DDPG) [4] algorithm is applied to tune the parameters of a PID controller.

In order to validate this method, simulations and measurements are done. By performing the same control task on a test rig, the method's applicability to a real hydraulic system is evaluated.

2. SYSTEM

In the following, the system that is used to evaluate the previously introduced approach is described.

2.1. Description

The control system used in this work contains of a hydro motor surrounded by two proportional valves. The first valve is on its a-side connected to a pump that delivers a constant pressure. On its b-side, the valve is connected to the a-side of the

hydro motor. On the b-side of the motor follows the a-side of the second valve, while the b-side of this valve is connected to a tank. A representation of this system can be seen in **Figure 1**.

The goal of the control task is to achieve a certain pressure $p_{V,1,b} \in \mathbb{R}_+$ between the first valve and the motor. Hereby, the first valve controls the volumetric flow rate via a predefined lookup-table. The second valve is expected to control the pressure $p_{V,1,b}$. Moreover, the hydro motor simulates unknown disturbances that may influence the system performance.

2.2. Mathematical Model

In this chapter, a mathematical description of the proposed system is introduced. Hereby, formulas for each component are used to derive a complete state-space model of the system.

Hydraulic motor

The hydraulic motor can be described by the following differential equation:

$$\ddot{\varphi} = \frac{1}{I}\left(\frac{V_d}{2\pi}(p_a - p_b) - d\dot{\varphi} - M\right). \quad (1)$$

With $\dot{\varphi} \in \mathbb{R}$ as angular velocity, $\ddot{\varphi} \in \mathbb{R}$ as angular acceleration, $I \in \mathbb{R}$ as the moment of inertia, $V_d \in \mathbb{R}$ as reference volume, $p_a, p_b \in \mathbb{R}_+$ as the pressure on a- and b-side, $d \in \mathbb{R}$ as the damping factor, and $M \in \mathbb{R}$ as an external torque. Moreover, the volumetric flow rate $Q_M \in \mathbb{R}$ inside the motor is defined as

$$Q_M = \dot{\varphi}\frac{V_d}{2\pi}. \quad (2)$$

Proportional valve

Since both proportional valves are of the same type, also their dynamics are similar. Thus, they can be described as follows:

$$Q_{V,i} = \alpha A_i(I_{V,i})\sqrt{2\frac{\Delta p_{V,i}}{\rho}}. \quad (3)$$

Here, $Q_{V,i} \in \mathbb{R}$ is the volumetric flow through the valve, $\alpha \in \mathbb{R}$ is the discharge coefficient, $A_i(I_{V,i}) \in \mathbb{R}_+$ is the valve opening, $I_{V,i} \in \mathbb{R}$ is the control current that is applied on the valve, $\Delta p_{V,i} \in \mathbb{R}_+$ is the difference between the pressures $p_{V,i,a} \in \mathbb{R}_+$ and $p_{V,i,b} \in \mathbb{R}_+$, and $\rho \in \mathbb{R}_+$ is the fluid density. Furthermore, the index $i = \{1,2\}$ refers to one of the two valves.

As written above, the opening of the proportional valve depends on the control current $I_{V,i}$ that is applied. However, the correlation between A_i and $I_{V,i}$ is nonlinear. Additionally, the derivation of a mathematical connection is difficult, since different effects, e.g. magnetization hysteresis, friction, and spring properties, need to be considered.

Thus, $A_i(I_{V,i})$ is approximated by the hysteresis in **Figure 2**. In the simulation, those values are stored in a look-up table. While this might not cover the detailed physical behavior of the valve, experiments have shown that this simplification is sufficient for the purpose of this paper.

Hydraulic pipes

Another significant influence in the system comes from the hydraulic pipes that connect the motor and the valves. Moreover, the pressure sensors, which are necessary to achieve the control objective, are located in these pipes. As proposed in literature [5], the rate of change of the pressure $p_{V,1,b}$ is defined as

$$\dot{p}_{V,1,b} = \frac{1}{c_1}(Q_{V,1} - Q_M). \quad (4)$$

With $c_1 \in \mathbb{R}_+$ as constant for the combination of bulk modulus and fluid volume. Analogously, the rate of change of $p_{\mathrm{V,2,a}}$ can be written as

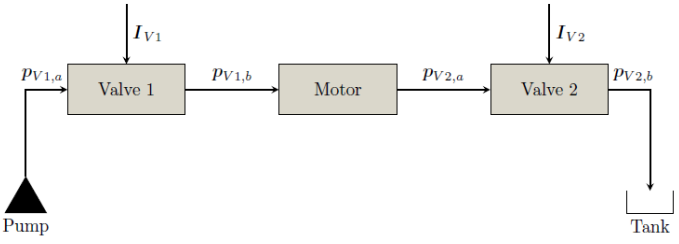

Figure 1: Simplified visualization of the hydraulic system that is used in this work.

$$\dot{p}_{V,2,a} = \frac{1}{c_2}\left(Q_M - Q_{V,2}\right). \quad (5)$$

Hence, both pressures $p_{V,1,b}$ and $p_{V,2,a}$ can be calculated from the integral of Equation 4 and 5, respectively. This results in

$$p_{V,1,b} = \frac{1}{c_1}\int\left(Q_{V,1} - Q_M\right)dt \quad (6)$$

for $p_{V,1,b}$ and

$$p_{V,2,a} = \frac{1}{c_2}\int\left(Q_M - Q_{V,2}\right)dt \quad (7)$$

for $p_{V,2,a}$.

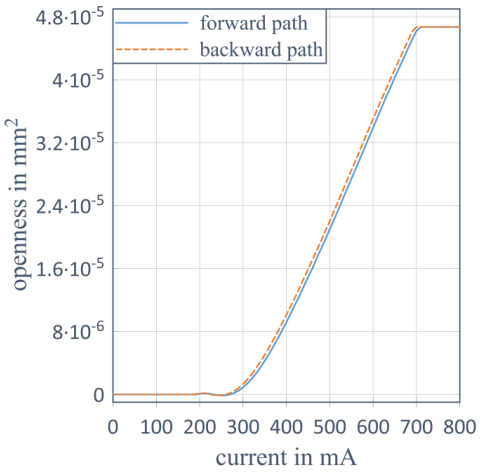

Figure 2: Hysteresis of the valve opening A. The width of the hysteresis is 10 mA.

2.3. State-Space Model

As already mentioned in the previous section, the presented formulas are used for a state-space representation. Because of the nonlinear and time-variant behavior of the system, e.g. through the hysteresis caused by the proportional magnet, the system is formulated in the form of a nonlinear dynamical system, which is:

$$\dot{x} = f\left(x(t), u(t)\right). \quad (8)$$

Here, $\dot{x}$ is the derivative of the state vector x, which is defined as follows:

$$x = \begin{bmatrix} \varphi \\ \dot{\varphi} \\ p_{V,1,b} \\ p_{V,2,a} \end{bmatrix}. \quad (9)$$

Thus, $\dot{x}$ is defined as

$$\dot{x} = \begin{bmatrix} \dot{\varphi} \\ \ddot{\varphi} \\ \dot{p}_{V,1,b} \\ \dot{p}_{V,2,a} \end{bmatrix}. \quad (10)$$

In order to achieve a concise state-space description, it is necessary to transform the formulas from the previous section into a consistent form. Since $p_a = p_{V,1,b}$ and $p_b = p_{V,2,a}$, Equation 1 can be reformulated as

$$\ddot{\varphi} = \frac{1}{I}\left(\frac{V_d}{2\pi}\left(p_{V,1,b} - p_{V,2,a}\right) - d\dot{\varphi} - M\right). \quad (11)$$

Moreover, Equation 2 and Equation 3 can be inserted in Equation 4, which results in

$$\dot{p}_{V,1,b} = \frac{1}{c_1}\left(\alpha A_1\left(I_{V,1}\right)\sqrt{2\frac{\Delta p_{V,1}}{\rho}} - \dot{\varphi}\frac{V_d}{2\pi}\right). \quad (12)$$

Analogously, Equation 2 and Equation 3 can be inserted in Equation 5, which leads to

$$\dot{p}_{V,2,a} = \frac{1}{c_2}\left(\dot{\varphi}\frac{V_d}{2\pi} - \alpha A_2\left(I_{V,2}\right)\sqrt{2\frac{\Delta p_{V,2}}{\rho}}\right). \quad (13)$$

Finally, the state-space description of the valve-motor-valve system is:

$$\dot{x} = \begin{bmatrix} \dot{\varphi} \\ \frac{1}{I}\left(\frac{V_d}{2\pi}\left(p_{V,1,b} - p_{V,2,a}\right) - d\dot{\varphi} - M\right) \\ \frac{1}{c_1}\left(\alpha A_1\left(I_{V,1}\right)\sqrt{2\frac{\Delta p_{V,1}}{\rho}} - \dot{\varphi}\frac{V_d}{2\pi}\right) \\ \frac{1}{c_2}\left(\dot{\varphi}\frac{V_d}{2\pi} - \alpha A_2\left(I_{V,2}\right)\sqrt{2\frac{\Delta p_{V,2}}{\rho}}\right) \end{bmatrix}. \quad (14)$$

2.4. Controller

As described in the previous sections, the valve opening is controlled by the electric current $I_{V,i}$.

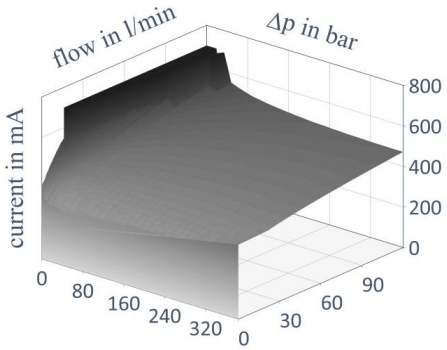

Figure 3: 3D-plot of the look-up table for the open-loop control of valve 1.

Valve 1: Open-loop control

The first valve is controlled by using a static look-up table. Hereby, the pressure difference $\Delta p_{V,1}$ and the desired flow Q is used as an input for the table. The combination of these values results in an electric current $I_{V,1}$, which leads to an opening A_1 that leads to the desired flow. Since this is a simple open-loop control approach, there is no guarantee that the resulting flow corresponds with the desired flow.

Though, since the look-up table was created experimentally and, thus, is fitted to the used valve type, it shows a reasonable performance. A visualization of the look-up table used for open-loop control is shown in **Figure 3**.

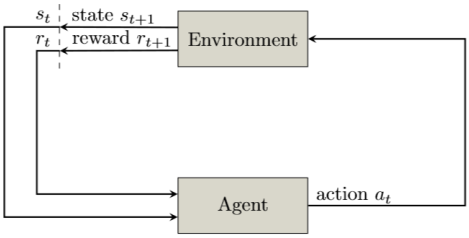

Figure 4: Basic reinforcement learning structure.

Valve 2: Closed-loop control

For the second valve, which controls the pressure $p_{V,1,b}$, a closed-loop control strategy is used. Since the PID controller is a standard in industrial applications and in hydraulics, it is also used in this work. Moreover, the usage of a state-of-the-art control structure gives a reasonable benchmark for the evaluation of the approach introduced in this paper.

While there are various forms of the PID controller available, this work uses the standard form, given by the following mathematical expression:

$$u = K_p e + K_i \int e \, d\tau + K_d \dot{e} \tag{15}$$

Here, $u \in R$ is the controller output, $K_p \in \mathbb{R}$ is the proportional gain, $K_i \in \mathbb{R}$ is the integral gain, $K_d \in \mathbb{R}$ is the differential gain, $e \in \mathbb{R}$ is the control error, and $\dot{e} \in \mathbb{R}$ is the derivative of the control error. Moreover, the control error is defined as:

$$e = p_{V,1,b,ref} - p_{V,1,b} \tag{16}$$

with $p_{V,1,b,ref} \in \mathbb{R}_+$ as the reference signal.

3. DEEP DETERMINISTIC POLICY GRADIENT

This section provides both a short introduction into the basics of reinforcement learning [6] and the information about the deep deterministic policy gradient algorithm, which is used in this work.

3.1. Reinforcement learning

The aim of reinforcement learning (RL) is that an agent learns through interaction with an environment (see **Figure 4**). This environment can be modeled as a Markov decision process (MDP), which is defined as a quadruple (S, A, f, J). Thereby, $S \in \mathbb{R}^n$ is the state space vector, $A \in \mathbb{R}^m$ is the action space vector, $f: S \times A \to S$ is the transition function, and $f: S \times A \to \mathbb{R}$ is the reward function. Furthermore, $n, m \in \mathbb{N}$ denote as the number of states and actions, respectively.

In each timestep t, the agent receives information about the state $s_t \in S$ from the environment and the agent chooses an appropriate action $a_t \in A$. Consequently, the environment moves into the next state $s_{t+1} \in S$, which is described by the transition function:

$$s_{t+1} = f(s_t, a_t). \tag{17}$$

Moreover, the agent receives a feedback in form of a reward, which gets calculated by the reward function:

$$r_{t+1} = J(s_t, a_t). \tag{18}$$

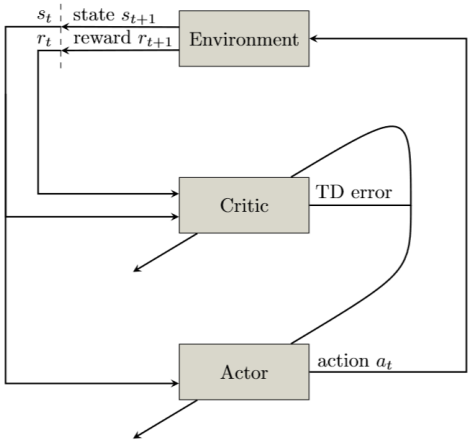

Figure 5: Visualization of the actor-critic structure.

Summing up these rewards results in the discounted overall expected return:

$$R_{t+1} = \sum_{t=0}^{\infty} \gamma^t r_{t+1}, \quad (19)$$

with $R_{t+1} \in \mathbb{R}$ as the discounted return and $\gamma \in [0,1]$ as a discount factor. This overall expected reward assumes that the agent performs an action in a certain state s_t and then continues to follow the policy π. Throughout this paper, it is assumed that the policy is deterministic. To stay concise with already existing literature, μ refers to deterministic policies, while π can represent both deterministic and stochastic policies.

In order to characterize such policies, state-action value functions, namely Q-functions, are widely used by many RL algorithms. In a Q-function, the overall expected reward for any state-action pair is stored. This correlation is defined as:

$$Q(s_t, a_t) = \mathbb{E}[\sum_{t=0}^{\infty} \gamma^t r_{t+1}]. \quad (20)$$

Since an RL agent is expected to pick the best action in the current state, the policy is given as follows:

$$\mu(s_t) = arg\max_{\mu} Q(s_t, a_t). \quad (21)$$

So, it is ensured that the policy returns always the action that maximizes the expected reward for a certain state.

Since the Q-function is usually unknown, the aim of RL is to iteratively calculate it. For this purpose, a wide range of approaches make use of the Bellman equation [7]:

$$Q(s_t, a_t) = r(s_t, a_t) + \gamma \max_a Q(s_{t+1}, a_{t+1}). \quad (22)$$

This theory lays the foundation for all kinds of different RL algorithms, e.g. Q-learning [8], SARSA [9] or PoWeR [10].

Though, as it can be seen from the definitions the action and state spaces need to be finite and discrete. Since most real-world applications are continuous, those conditions are usually harmed and classic RL methods cannot be applied. This issue is often referred to as the "curse of dimensionality" [11]. To avoid this, function approximators are required to apply RL in continuous spaces.

3.2. Deep deterministic policy gradient

With the deep deterministic policy gradient (DDPG), Lillicrap et al. [4] introduced an algorithm that is able to solve continuous problems.

Background

Unlike standard RL algorithms, DDPG uses an actor-critic structure and neural networks as function approximators.

In the actor-critic setting, the agent is split into two models, namely the actor and the critic. The actor takes the state s_t as input and computes an appropriate action a_t. The critic judges the action by calculating a Q-value from the input state s_t. This Q-value is compared to the actual reward r_t and based on the resulting temporal difference

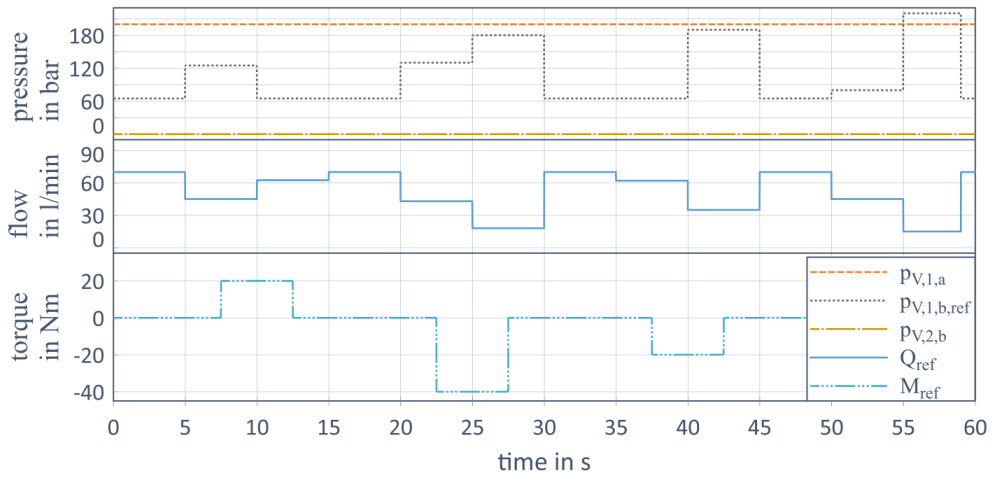

Figure 6: The test case used for training the agent.

error, both actor and critic are optimized. So, it can be said that both parts of the agents are learning from each other's predictions.

In order to overcome the restriction of RL to discrete problems, both actor and critic are modeled as neural networks. Thus, continuous problems can be solved by the DDPG.

To ensure a more stable learning behavior, the algorithm uses soft target updates. This means that copies of both the critic and the actor network are created. These target networks are updated slower than the networks on which the learning is performed.

Additionally, a replay buffer is added to the algorithm in order to make it more data-efficient. This means that each tuple (s_t, a_t, r_t, s_{t+1}) is saved for a given time. In each learning step, a batch with a predefined size is randomly sampled from the replay buffer. Hence, the algorithm learns not only from current observations, but also from experience.

Algorithm

To optimize the critic network, the loss $L \in \mathbb{R}$ needs to be minimized:

$$L(\theta^Q) = \frac{1}{N}\sum_{j=1}^{N}\left(y_j - Q(s_j, a_j|\theta^Q)\right)^2. \qquad (23)$$

Here, $N \in \mathbb{N}$ is the number of samples that are taken from the replay buffer, $\theta^Q \in \mathbb{R}^w$ is the set of parameters that defines the critic network, and $w \in \mathbb{N}$ is the number of parameters of the critic network. Moreover, $y_j \in \mathbb{R}$ is the updated Q-value, which is expressed by:

$$y_j = r_j + \gamma Q'(s_{j+1}, \mu'(s_{j+1}|\theta^{\mu'})|\theta^{Q'}), \qquad (24)$$

with μ' as the policy that is defined by the target actor network, $\theta^{\mu'} \in \mathbb{R}^{o'}$ as the set of parameters that defines the target actor network, $o' \in \mathbb{N}$ as the number of parameters of the target actor network, Q' as the Q-function that is formulated by the target critic network, $\theta^{Q'} \in \mathbb{R}^{w'}$ as the set of parameters that defines the target critic network, and $w' \in \mathbb{N}$ as the number of parameters of the target critic network. By comparing

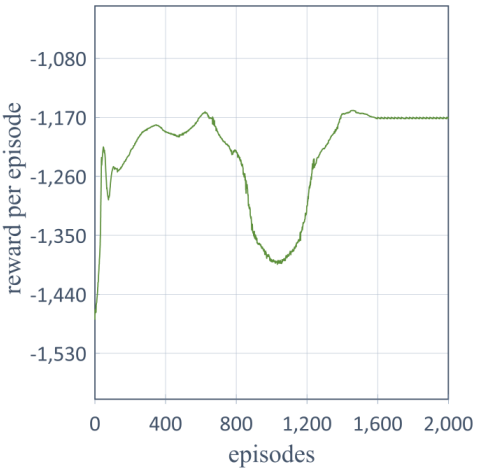

Figure 7: Visualization of the episodic reward.

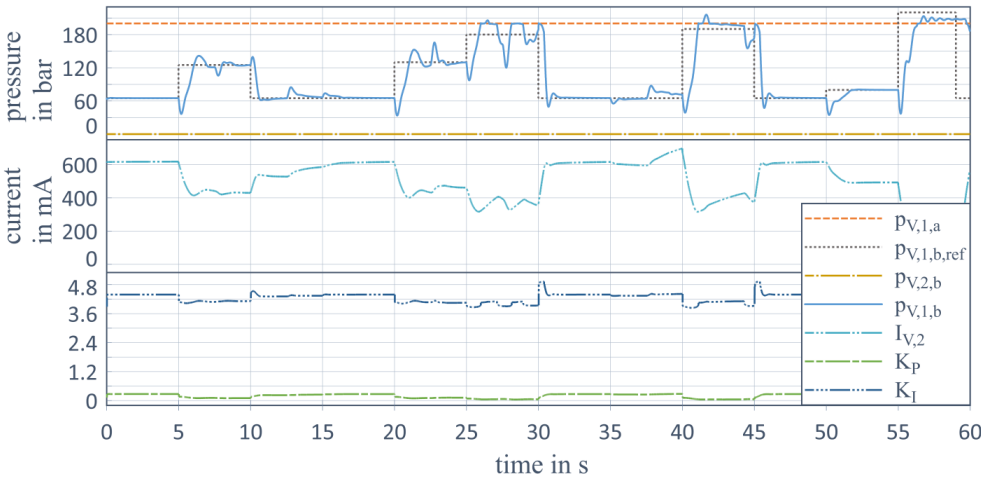

Figure 8: Performance of the learned agent in the simulative environment.

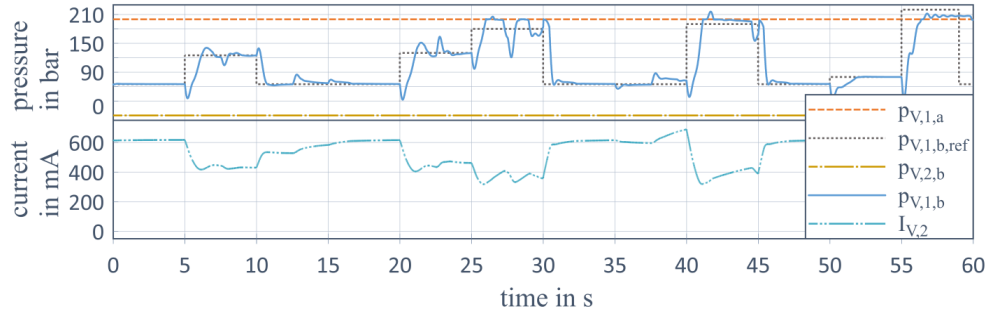

Figure 9: Performance of an expert tuned controller in the simulative environment.

Equation (22) with Equation (24), it can be seen that the update law is based on the Bellman equation.

The policy network is optimized by maximizing the expected return $J(\theta^\mu) \in \mathbb{R}$, which is defined as:

$$J(\theta^\mu) = \mathbb{E}\left[Q(s,a)|_{s=s_t,a=\mu(s_t)}\right]. \quad (25)$$

Now, the policy gradient can be calculated via

$$\nabla_{\theta^\mu} J(\theta^\mu) \approx \nabla_a Q(s,a)|_{s=s_t,a=\mu(s_t)} \nabla_{\theta^\mu}\mu(s|\theta^\mu)|_{s=s_t}. \quad (26)$$

Here, $\theta^\mu \in \mathbb{R}^o$ denotes the set of parameters that defines the actor network and $o \in \mathbb{N}$ the number of parameters of the actor network. Because the DDPG always takes a batch of samples for optimization from the replay buffer, the mean of the gradients in Equation (25) is used:

$$\nabla_{\theta^\mu} J(\theta^\mu) \approx \frac{1}{N}\sum_{j=1}^{N}\left[\nabla_a Q(s,a)|_{s=s_j,a=\mu(s_j)} \nabla_{\theta^\mu}\mu(s|\theta^\mu)|_{s=s_j}\right]. \quad (27)$$

Moreover, the target networks are updated as follows:

$$\theta^{Q'} \leftarrow \tau\theta^Q + (1-\tau)\theta^{Q'}, \quad (28)$$

$$\theta^{\mu'} \leftarrow \tau\theta^\mu + (1-\tau)\theta^{\mu'}, \quad (29)$$

with $\tau \in [0,1]$ as the update rate.

A block diagram of the actor-critic structure is displayed in **Figure 5**.

4. EXPERIMENTAL SETTING

This section explains, the experimental setting of system and agent.

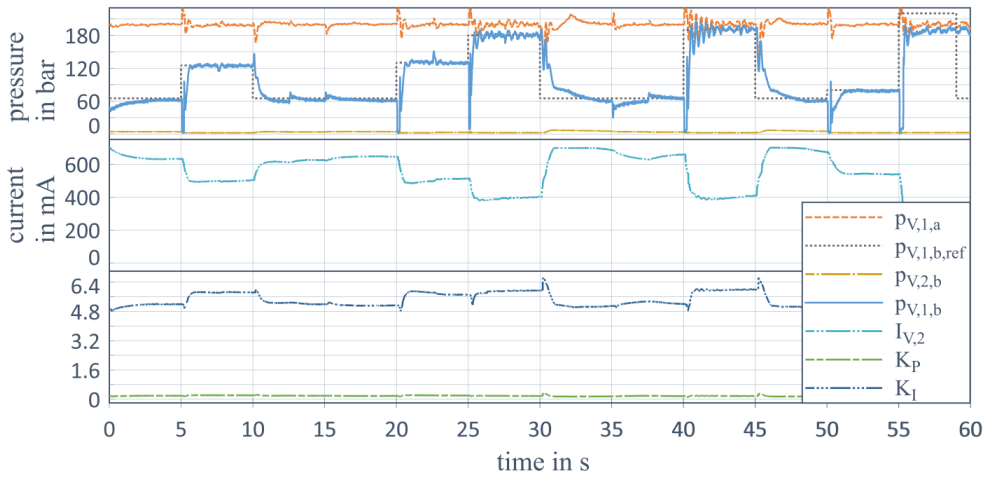

Figure 10: Performance of the learned agent on the test rig.

4.1. System setting

In order to evaluate the proposed method, a simulative experiment is conducted. For this purpose, the algorithm is expected to track the pressure profile that can be seen in **Figure 6**. In the same figure, there can be seen a corresponding volumetric flow profile and a disturbance caused by the motor.

As previous experiments have shown, the proposed system reacts highly sensitive to the usage of the differential gain. Thus, K_d remains 0 for all the experiments. This results in a PI-controller, which means that the agent needs to set a proportional gain K_p and an integral gain K_i.

While the system receives the values of those two gains from the agent, it is required to send back its resulting state.

The system's sample time is set to 5 ms. Moreover, each 5th sample is evaluated by the reward function and stored into the replay buffer. Throughout the experiments, this setting has shown the best balance between the saving of computational power and accuracy.

In order to evaluate the performance of the system, the reward function is set as follows:

$$r_t = -exp\left(\frac{-1}{1+1.5*10^{-3}e^2+0.5*10^{-4}\left(\dot{p}_{V,1,b}\right)^2}\right). \quad (30)$$

As it can be seen in Equation 30, the reward in each step is bounded in the interval $r_t \in [-1, -exp(-1)]$. Moreover, the reward depends on the control error e and the pressure's rate of change $\dot{p}_{V,1,b}$.

4.2. Agent setting

As explained in Chapter 3, the agent is designed in an actor-critic structure. The neural network (NN), which describes the actor, has 18 neurons in the input layer. Each of the following two hidden layers contains 256 neurons with rectified non-linearity [12] as activation. Moreover, there are 2 neurons in the sigmoid-activated output layer.

The critic NN consists of an input layer with 18 neurons. Both hidden layers consist of 256 neurons with rectified non-linearity as activation. The second hidden layer additionally includes the actions as input. The output layer consists of a neuron with linear activation.

In addition, it is to mention that the layers of all networks are fully connected. As input states, the agent receives the pressures $p_{V,1,a}, p_{V,1,b}, p_{V,2,a}, p_{V,2,b}$ the reference pressure $p_{V,1,b,ref}$, the control error e, the currents $I_{V,1}$ and $I_{V,2}$, the reference volumetric flow Q_{ref}, and the gradients of these values.

While the system state is sampled every 5 ms, the agent is allowed to adapt the parameters every 50 samples, i.e. every 250 ms. This restriction is based on the fact that the valve needs enough time to react to the changes. Faster changes would not be recognized by the hardware and, thus, not lead to any performance improvement. Thus, also policy updates are performed each 250 ms during the learning phase.

The complete parameter settings for the training of the agent are listed in **Table 1**.

Table 1: Parameters of the DDPG agent

DDPG parameter	Value
Actor learning rate	0.000015
Critic learning rate	0.00015
Replay buffer size	100000
Batch size	32
γ	0.0
τ	0.001
K_P bound	[0, 10]
K_I bound	[0, 20]

5. EXPERIMENTAL EVALUATION

The upcoming section starts with an evaluation of the simulative experiments. Afterwards, results from hardware tests are presented.

5.1. Simulative experiment

The simulative experiment is set up as explained in the previous section and starts with the training of the DDPG agent. The test case from **Figure 6** is simulated for 2000 epochs. While a single epoch equals 60 seconds (real-time) of interaction, the agent gets 2000 minutes of interaction time with the system the learn an appropriate control law.

As **Figure 7** shows, the learning process converges to a reward of about -1170 after about 1600 epochs. So, it can be assumed that the agent is able to find an optimal solution for the control problem.

In order to evaluate the learned result, the agent is evaluated on the test case and compared to an expert-tuned controller. **Figure 8** shows the

performance of the agent's policy. By comparing this result with that of the expert-tuned controller, which can be seen in **Figure 9**, the behavior is nearly identical. This is also supported by the overall achieved rewards, which is -1165.02 for the agent and -1166.84 for the expert.

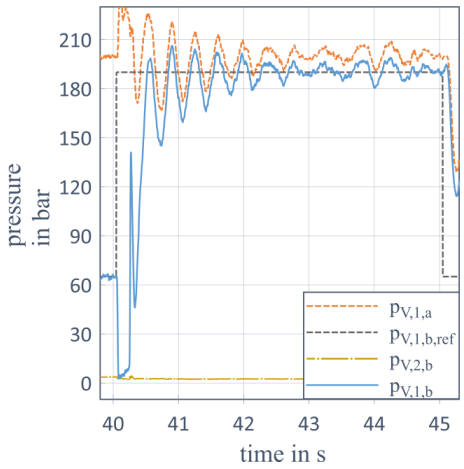

Figure 11: Visualization of a descending oscillation.

5.2. Hardware experiment

Since the method shows promising results in the simulation environment, it is also evaluated on real hardware. The same system as described in **Chapter 2** is build up as a test-rig.

In the hardware setting, a training phase cannot be conducted, because that would mean to run the test rig nonstop for more than 30 hours. Moreover, the hardware could be damaged, if the agent tries to set PI-values that destabilize the system. To overcome these issues, the learned agent from the simulative experiment is directly applied to the test rig.

The result of the experiment can be seen in **Figure 10**. Here, the agent accurately follows the desired pressure profile $p_{V,1,b,ref}$. By comparing this with the result from **Figure 8**, it can be even said that the overall performance is comparable to that in the simulative environment.

This is remarkable as there are several differences between the simulation and the test rig. The major one might be the pressure $p_{V,1,a}$. In the simulation, this value is assumed as constant, since there is no implementation of the pump model. Though, in the test rig $p_{V,1,a}$ might change or even oscillate in some situations. As a result, also $p_{V,1,b}$ starts to oscillate, e.g. between 40 s and 45 s (see **Figure 11**). However, the oscillation decays over time, which is acceptable in this test scenario.

Moreover, also $p_{V,2,b}$ is not as ideal as in simulation, where this value is simply set to 0 bar. Though, also this causes no trouble for the agent.

In addition, the motor torque M is much smoother in the test rig than in the simulation. This comes from the fact that the real motor cannot perform jumps as the motor model from the simulation. So, the disturbance caused by the motor is applied smoother, but for a longer time interval.

6. CONCLUSION AND OUTLOOK

This paper shows that PID-controllers for hydraulic systems can be autonomously learned by RL algorithms. The used DDPG algorithm achieves a performance that is comparable to an expert-tuned controller within an acceptable simulation time.

Additionally, the evaluation on a test rig shows that a simplified system model is sufficient to transfer knowledge gained in simulation to a real hardware application without a considerable drop in performance. The algorithm is even robust against previously unknown system behavior and disturbances. This implies that the agent is somehow able to generalize its experience.

For future work, it will be necessary to further explore this generalization behavior, e.g. to a wider range of test cases or even different hardware components inside the test rig. Moreover, a strategy for fine-tuning or learning on the hardware is required to enable RL to a wider range of applications in hydraulic control systems. In this context, a thorough stability analysis of the method and the learned controller might be required.

Finally, it can be said that reinforcement learning methods have a great potential for making hydraulic control systems more efficient and flexible.

NOMENCLATURE

Throughout the work, it can be assumed that derivations and gradients are performed with respect to time. Any exceptions are explicitly specified.

DDPG	Deep Deterministic Policy Gradients
RL	Reinforcement Learning
MDP	Markov Decision Process
NN	Neural Network
φ	Rotation angle in rad
$\dot{\varphi}$	Angular velocity in rad/s
$\ddot{\varphi}$	Angular acceleration in rad/s^2
$I_{V,i}$	Control current in mA
M	Torque in Nm
c_i	Bulk modulus and fluid volume in kg/(m^{4}s^2)
d	Damping factor in Nm s/rad
V_d	Reference volume in l
I	Moment of inertia in kg m^2
Q	Volumetric flow in l/min
$A_i(.)$	Valve opening in mm^2
ρ	Fluid density in kg/m^3
i	Index denoting valve number
j	Counter variable
α	Discharge coefficient
t	Time in s
x	State vector of the dynamic system
$\dot{x}$	Derivative of the state vector
S, s_t	Set of states and state at time t
A, a_t	Set of actions and action at time t
u	PID control output in mA
K_P	Proportional control gain
K_I	Integral control gain
K_D	Derivative control gain
e	Control error in bar
R, r_t	Overall expected reward and reward at time t
J	Reward function
γ	Discount factor
$Q(.)$	Q-function
$\mu(.)$	Policy function
$L(.)$	Loss function
$\theta(.)$	Critic function
$p_{V,i,a}$	Pressure on valve's a-side in bar
$p_{V,i,b}$	Pressure on valve's b-side in bar
$\theta^{\mu}, \theta^{\mu\prime}$	Set of parameters of target network
$\theta^{Q}, \theta^{Q\prime}$	Set of parameters of actor network
o, o'	Number of parameters in actor network
w, w'	Number of parameters in critic network
y_j	Updated Q-value
τ	Update rate

REFERENCES

[1] Bischoff B, Nguyen-Tuong D, Koller T, Markert H, Knoll A (2013) Learning Throttle Valve Control Using Policy Search. In: Blockeel H, Kersting K, Nijssen S, Železný F (eds) Machine Learning and Knowledge Discovery in Databases. ECML PKDD 2013. Lecture Notes in Computer Science, vol 8188. Springer, Berlin, Heidelberg

[2] Kim J, Jeon J, Heo H (2011) Design of adaptive PID for pitch control of large wind turbine generator. 10th International Conference on Environment and Electrical Engineering, Rome, Italy

[3] Deisenroth M, Rasmussen CE (2011) PILCO: A model-based and data-efficient approach to policy search. In: Lise G, Scheffer T (eds) Proceedings of the 28th International Conference on Machine Learning, Bellevue, July 2011, Omnipress Publishing, Madison

[4] Lillicrap T, Hunt J, Pritzel A, Heess N, Erez T, Tassa Y, Silver D, Wierstra D (2016) 4th International Conference on Learning Representations. San Juan, Puerto Rico, May 2-4, 2016

[5] Akkaya AV (2006) Effect of Bulk Modulus on Performance of a Hydrostatic Transmission Control system. Sadhana 543 - 556

[6] Sutton RS, Barto AG (1998) Reinforcement Learning – An Introduction. MIT Press, Cambridge, USA

[7] Bellman RE (1957) Dynamic Programming. Princeton University Press, Princeton, USA

[8] Rummery GA, Niranjan M (1994) On-Line Q-Learning Using Connectionist Systems. University of Cambridge, Department of Engineering Cambridge, England

[9] Watkins CJCH (1989), Learning from Delayed Rewards. King's College, Cambridge, England.

[10] Kober J, Peters JR (2008) Policy Search for Motor Primitives in Robotics. In: Advances in Neural Information Processing Systems 21. 22nd Annual Conference on Neural Information Processing Systems, British Columbia, Canada, December 8-11, 2008, p 849

[11] Bellman RE (1961) Adaptive Control Processes. Princeton University Press, Princeton USA

[12] Glorot X, Bordes A, Bengio Y (2011) Deep sparse rectifier neural networks. In. Proceedings of the Fourteenth International Conference on Artificial Intelligence and Statistics, Fort Lauderdale, USA, April 11-13, 2011, p 315

GROUP C

Novel system solutions

peer reviewed

A CLOSED CIRCUIT ELECTRO-HYDRAULIC ACTUATOR WITH ENERGY RECUPERATION CAPABILITY

Shaoyang Qu[1]*, David Fassbender[1], Andrea Vacca[1], Busquets Enrique[2], Uwe Neumann[2]

[1] *Maha Fluid Power Research Center, Purdue University, Indiana, USA*
[2] *Bosch Rexroth, South Carolina, USA*
* Corresponding author: Tel.: +1 765 409 3503; E-mail address: qu82@purdue.edu

ABSTRACT

The recent electrification trend in the off-road market has incentivized research towards the proposal of compact, cost-effective and energy-efficient solutions for hydraulic actuators. As a result, increased attention has been given to electro-hydraulic actuator (EHA) architectures. The paper offers a study performed on a novel closed-circuit EHA architecture with the goal to maximize the overall system efficiency while meeting or exceeding traditional off-road applications performance, thereby enabling further electrification of off-road applications. Both numerical and experimental approaches are utilized to validate the functionality of the proposed EHA circuital configuration in four quadrants. Moreover, the actuator functionality at both high and low velocities are considered, which has never been explored in the past due to the limitations on the hydraulic machine driving speed. The good match between the experimental data and the simulation results confirms the potential of the simulation model for sizing such EHA architecture for different actuator sizes, duty cycles, and performance levels.

Keywords: Electro-Hydraulic Actuator, Closed Circuit, 4-Quadrant Functionality

1. INTRODUCTION

Nowadays, an increasing interest in replacing classical hydraulic architectures with energy-efficient, compact and plug-and-play system configurations brings electro-hydraulic actuator (EHA) concepts to the center of the court. Hence, efforts aiming at the optimal solution for mobile applications never stop. However, apart from a few aerospace cases [1][2], EHAs have failed to penetrate the markets, especially construction and off-road vehicle markets, which contribute much to industrial energy consumption.

In terms of energy efficiency, an optimal hydraulic system should avoid metering losses and restore energy from the assistive load as much as possible. The core concept of EHA—Individualized actuator—makes the optimization achievable. The individualization levels of fluid power systems were scientifically investigated by Weber et al. [3], which clearly demonstrated the trade-off between cost and flexibility. In terms of solutions for variable EH units, a classification of different electro-hydraulic drive (EH) types has been studied [4][5], which comprises two options for EH units: one uses a variable electric motor and the other a variable pump. Studies on the fixed motor and variable pump (FMVP) configurations have shown good controllability [6]. Research on hydraulic transmission control based FMVP has also been conducted [7]. However, architectures with a variable motor and fixed pump (VMFP) receive more spotlight due to the better energy efficiency and cost consideration.

Based on VMFP, a compact EHA design has been obtained and proposed for its use in a 'more electric aircraft' [8], where the peak power of the unit is a constraint. A self-contained EHA with peak power scalable up to 80 kW has also been studied including a dynamic analysis [9]. Energy efficiency and performance analysis were conducted for a linear double drive EHA with self-locking function and scalable power up to 50 kW [10]. As for energy regeneration and recuperation, relating to applications on hydraulic excavators, studies have demonstrated large regenerative power sections for a boom actuator and presented a possible solution including an accumulator-motor-generator [11].

A novel driving system with an EHA concept for hydraulic excavators has been proposed using an asymmetric pump, which is able to regenerate more than 80% of potential energy [12].

One of the most significant technical challenges impeding the introduction of industrialized EHAs is the pump speed limitation constraint, which hinders the functionality of closed-circuit EHAs for low-speed actuation. This paper addresses this challenge and proposes a solution. The study presented in this paper is structured in the following order: system configuration of proposed EHA, accumulator sizing for the self-contained system, development of simulation model and results, experimental setup and test results, conclusion and outlook.

2. SYSTEM CONFIGURATION

2.1. Hydraulic architecture

The proposed system configuration is shown in **Figure 2**. A fixed-displacement hydraulic pump (HP) and a variable speed electric motor (EM) constitute the individual EH drive unit. The actuator is a single-rod double-acting cylinder (CYL). The differential flow required by the difference between the bore side and rod side area is compensated by the low-pressure accumulator (ACC), together with two pilot check valves (PCV) controlling its charging or discharging. Two directional on/off valves (DV) allow for load holding at rest condition and the flow direction that realizes the cylinder motion is dictated by the four-quadrant EH unit. Pressure relief valves (RV) are installed on both sides of the pump in order to avoid over-pressurizations in either extension or retraction. A proportional 2/2 directional valve is used as a bypass (BP) parallel to the cylinder, which allows for slow or fast actuation when exceeding the speed range of the gear pump. This will be further explained in the following sections. A filter (FL) and two check valves (CV) are necessary for a self-contained implementation. An external pump drain line needs to be connected to the accumulator to maintain the overall amount of fluid within the system constant for all possible CYL positions.

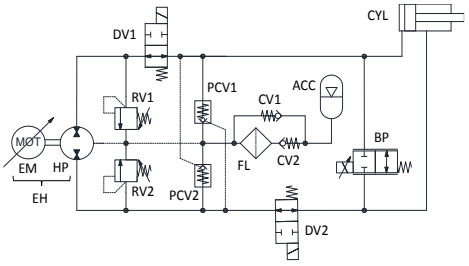

Figure 2: Proposed system configuration

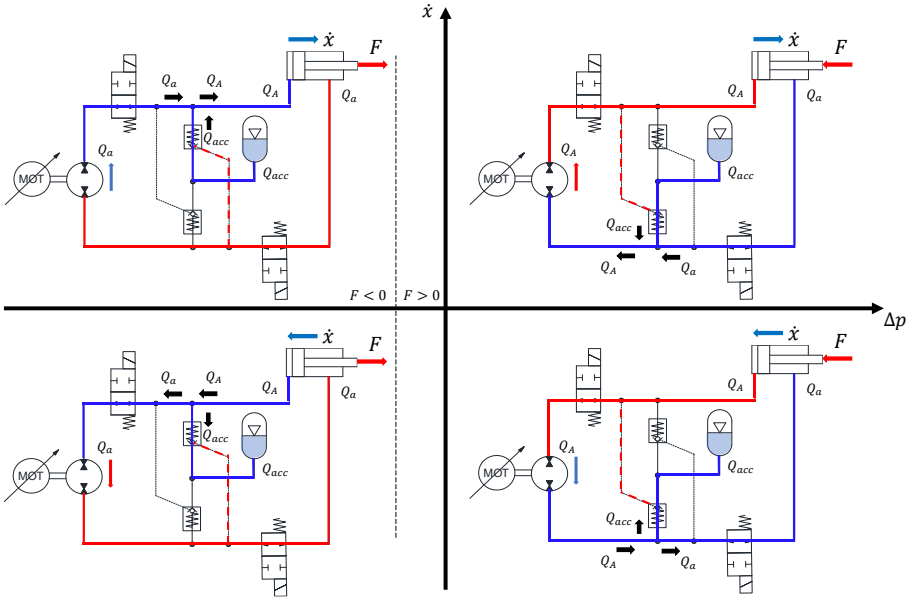

Figure 1: Functionality in four quadrants illustrated by simplified schematic

2.2. Four-quadrant functionality

The functionality of the proposed architecture can be summarized with the representation of **Figure 1**, where the schematic is simplified for a clear representation of the operating conditions in 4 quadrants. The x-axis shows the pressure difference between the cylinder chambers, which is positive for higher pressure on the piston side. The y-axis shows the actuator velocity. A positive velocity means the extension of the cylinder. High/low pressures are highlighted by red/blue color. Because of the cylinder differential area, the corresponding port flow rates are different, which are denoted as Q_A and Q_a. On the contrary, the pump inlet and outlet are ideally constant. Therefore, the differential flow needs to be compensated by the flow from/to accumulator, as $Q_{acc} = Q_A - Q_a$. It follows that the accumulator must always discharge in the extension phase and charge in the retraction phase. In summary, the first and third quadrants outline the pumping modes of the EH unit. The motoring modes on the other hand are given in the second and fourth quadrants, where the overrunning load makes it possible to recuperate energy by accumulator and electronic subsystems for storing energy. Since the accumulator defines the lowest pressure in the circuit, the DVs are located outside of the discharging path of ACC, in order to decrease the possibility of cavitation.

It should be noted that in the four-quadrant map, the origin represents an equal pressure in both chambers of the cylinder and no motion, but not a zero load F due to the differential cylinder areas. A line representing zero load is noted across the second and third quadrant in **Figure 1**. It is also important to note that a switch between modes may pose challenges on the stable motion of the actuator [13].

2.3. Modes beyond speed range of EH

Even though the functionality shown in **Figure 1** may cover most hydraulic applications, the operating conditions beyond the speed limitation of the EH unit are not considered. Slow cylinder speeds are challenging as common fixed displacement pumps typically cannot be operated below a certain minimum shaft speed. The idea of the proposed solution consists of dividing the flow into the circuit by using BP. Focusing on the fourth quadrant in **Figure 1** for the retraction phase with overrunning load, an illustration with more details is given in **Figure 3**, which highlights the function of BP.

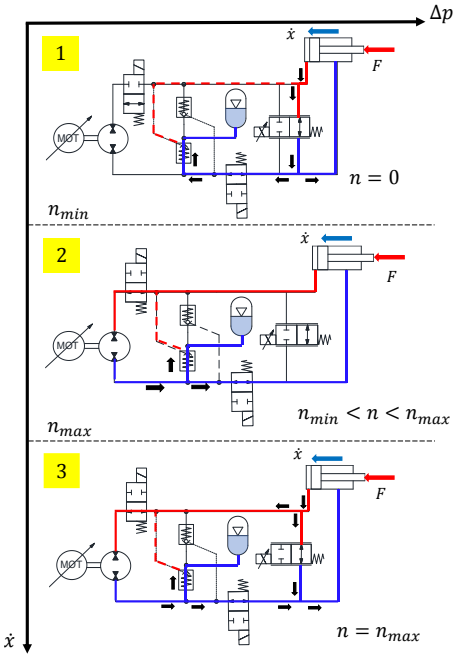

Figure 3: Working modes in the retraction phase with overrunning load

The y-axis shows the actuation speed, which is in normal mode proportional to the speed of the EH unit $(n_{min} < n < n_{max})$. This condition is given in the middle—case 2. However, the EH unit cannot handle the low speed under n_{min}. As illustrated in case 1, the bypass valve controls the low-speed retraction without the pump. The BP works as a metering orifice, and the differential flow still comes from the low-pressure accumulator. Although an overrunning load is applied, different from case 2, the EH unit will not recuperate energy for case 1. Furthermore, a high-speed mode may be required in certain applications where the flow demand is higher than the maximum limit of the EH unit. Case 3 represents this high-speed condition. Both EH and BP are activated and determine the retracting speed. Ideally, a maximum speed is set at the EH unit, as given in case 3, to avoid an excess of flow going though BP resulting in metering losses. The solution for covering low/high speeds works not only in the second quadrant as described in this paper, but also for all others quadrants.

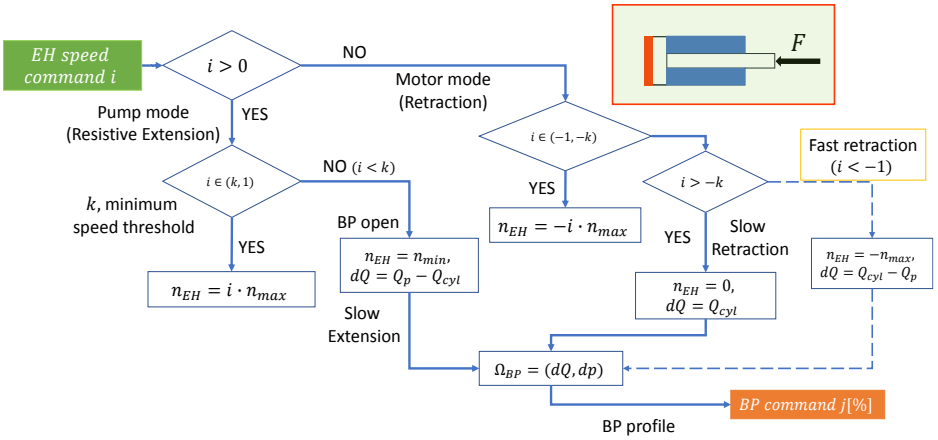

Figure 4: Conceptual flow chart for logic of switching modes

Details are omitted for brevity. Essentially, the first and third quadrants are symmetric and have the same modes, while the second and fourth share the same modes of **Figure 3**.

2.4. Logic for switching modes

In order to control the actuation velocity, two inputs are applied to the system: the speed command to the EH unit and the command to control the opening of BP. A third signal to open the DVs is always given, when any speed is demanded. The logic for determining these commands is summarized in **Figure 4**, covering all cases where the load on the cylinder is positive (first and fourth quadrants in **Figure 1**). A typical case for this working mode can be represented by a gravitational load, such as the boom implement of a construction machine, or the hitch of an agricultural tractor.

The operator gives a certain speed command i which is converted to the pump speed and control current of BP. Then, i can be easily defined as a normalized number with a range between -1 and 1. Two modes are distinguished first—pumping mode (resistive, quadrant 1) and motoring mode (assistive, quadrant 4)—by the sign of the given command. The command compared to a threshold k defines the next sub-model in order to keep the pump speed above the minimum limit. If the magnitude of i is greater than k, BP does not need to be opened, and the pump can control the actuation speed itself. Slow modes including extension and retraction are activated if the magnitude of i is less than k. For slow extension, the desired actuator flow rate Q_{cyl} is obtained by the difference between pump flow Q_p and the flow rate of BP (dQ). On the other hand, under the slow retraction case the pump speed is set to zero, and the actuator flow is only controlled by BP. To control the opening of BP, the flow rate dQ as well as the pressure difference dp are needed, resulting in a requirement of pressure sensors(as listed in the experimental section, Table 2). An exception-mode i less than -1 is denoted with a dotted line in the flow chart. While the pump already operates at maximum speed, an extra flow from the actuator circulates through BP. At the end, by knowing the (Q, dp) characteristics of BP, it is possible to determine the command j for the desired opening area.

3. SIZING OF ACCUMULATOR

The ACC has two essential roles in the self-contained EHA system: 1) as a flow source and 2) as a reservoir, allowing the CYL differential flow requirement to be compensated. The drain line of the pump is also connected to the ACC in order to avoid losing flow during operation. Moreover, the ACC energy can be recuperated during overrunning phases and introduced back into the system during resistive phases of the CYL motion. These aspects have to be taken into account when sizing ACC.

In general, a hydro-pneumatic accumulator utilizes the compressibility of gas to store energy and adjust flow in a hydraulic circuit. According

to the ideal-gas law (assuming nitrogen as an ideal gas) the relationship between gas or oil volume and pressure of the accumulator can be generalized as a polytropic process:

$$pV^n = p_0V_0^n = \mathrm{C} \quad (1)$$

For an adiabatic process, n is equal to 1.4. According to the equation, **Figure 5** represents the relationship between volume and pressure of the gas inside the ACC. The pre-charge status is (p_0, V_0), where V_0 is the ACC total volume. Two states (p_1, V_1) and (p_2, V_2) correspond to both ends of the cylinder stroke.

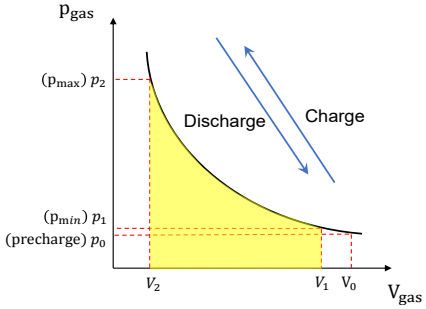

Figure 5: Polytropic process of gas in the accumulator

The condition $p_0/p_1 = 90\%$ ensures that a minimum amount of oil always remains in the ACC which can compensate losses due to leakage across the cylinder rod seal. The volume to compensate the differential flow is given by:

$$\Delta V = V_1 - V_2 = V_{rod} = \frac{\pi d^2 L}{4} \quad (2)$$

With respect to the pump drain line restrictions $p_2 < p_{drain}$ is a further restriction, which leads to:

$$p_2 = p_0 \left(\frac{V_0}{\sqrt[n]{0.9}V_0 - V_{rod}}\right)^n < p_{drain} \quad (3)$$

For a maximum drain line pressure of 10 bar and the consideration of compactness, the size of ACC is chosen as 4L with a pre-charge pressure of 4.5bar.

4. SIMULATION MODEL

4.1. Parameters

Based on the configuration proposed in **Figure 2**, a lumped parameter simulation model of the proposed EHA was built in Simcenter Amesim (Simens PLM Software). For the purpose of conducting an initial validation of the system functionality, the hydraulic components are developed with basic equations, as outlined in Table 1. To extend the accuracy of the model, actual performance data for the individual components is included in the model.

Table 1: Development of the simulation model

Components	Equation
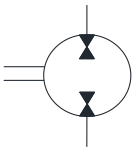	Pumping mode $Q_e = \eta_v n V_D$ $T = \Delta p V_D = \eta_{hm} P_t/\omega$ Motoring mode $Q_e = nV_D/\eta_v$ $T = \frac{P_t}{\omega} = \eta_{hm}\Delta p V_D$
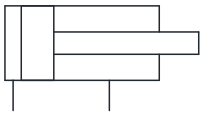	$p_1 A - p_2 a = F$ $\frac{\partial p}{\partial t} = \frac{K}{V}\left(\sum Q - \frac{\partial V}{\partial t}\right)$
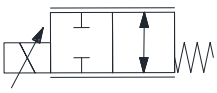	$Q = c_f \Omega_o \sqrt{\frac{2\Delta p}{\rho}}$ $= c_f \Omega_o \sqrt{\frac{2\lvert p_1 - p_2\rvert}{\rho}}\alpha$ $\alpha = sign(p_1 - p_2)$
	$pV^n = p_0V_0^n = \mathrm{C}$ $n = 1.4$ (adiabatic) $V_0 > V_1 - V_2 = V_{rod}$

The parameter setting of the simulation model considers the components chosen and utilized in the experimental setup, which will be described in Chapter 5. The main parameters of the model are summarized in Table 2.

Table 2: Main parameters in the simulation model

Parameter	Value[unit]
Length of stroke L	0.8865[m]
Diameter of piston D	69.9[mm]
Diameter of rod d	44.2[mm]
Pump displacement V_p	14.53[cc/rec]

Volume of Accumulator V_0	4 [L]
Pre-charge pressure p_0	4.5[bar]
Pump maximum speed n_{max}	4000[rpm]
Pump minimum speed n_{min}	600[rpm]
Relief pressure p_r	210[bar]

4.2. Simulation results

Based on the given parameters and the proposed system architecture, simulations are conducted to validate the different modes' functionality in steady-state. To do so, an input command is given to the system each time. This results in an actuation velocity and pump speed as outputs. All working conditions in the four-quadrant map are covered, including extension and retraction with overrunning or resistive loads.

A force pushing the cylinder is defined as positive (first and fourth quadrants in **Figure 1**), while negative force is pulling (second and third quadrants in **Figure 1**). The direction of extension is defined as positive for the velocity. For positive forces up to 70kN, the functionality is represented in **Figure 6**. The volumetric efficiency of pump is simplified as 100% ideally, and HP speed only depends on the command. Moreover, the CYL velocity must be robust with respect to different load conditions. This is reasonable as the behavior of the EHA should be independent of the load. The area ratio of the single-rod cylinder results in the different velocities for extension and retraction, as the same flow rate is going into the actuator. During fast assistive retraction, the pump is set to maximum speed, and BP is opened at a certain rate to achieve the same velocity as under the resistive retraction. During slow CYL motions, the pump speed is set at the minimum speed in the resistive phase, while with assistive loads the EH needs to be set to zero speed. A mismatch can be noticed for a negative full command. The reason is that the simplified control does not implement the exact valve characteristics of BP for all possible pressure drops.

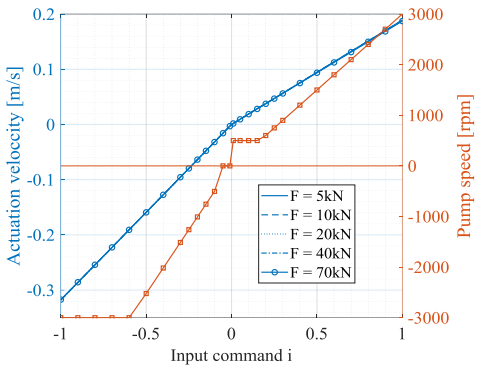

Figure 6: Simulated working modes in the first & fourth quadrants

For negative loads, the results look different, as shown in **Figure 7**. Because of the specifications of the EHA, at the same actuation velocity, the pump speed is different from the actuation at a positive load. For instance, in assistive extension modes, pump flow is determined by the CYL rod side, noted as Q_a in the second quadrant in **Figure 1**. In this case, the maximum pump speed is not required for the maximum demanded actuator velocity. On the other hand, retraction becomes resistive, so that the maximum retraction speed leads to the saturation given in **Figure 6**, where BP is opend as explained. Another important fact caused by the area ratio is that the origin of zero force on the cylinder interface does not match zero pressure difference between both sides of the pump. For the 0 kN loading case, the pressures in the cylinder chambers are different. Though not significant, the pressure in the CYL rod side is higher than the piston side. As a result, the EH unit operates in a resistive pumping mode with cylinder extension, while it operates as a motor when retracting the cylinder. When it comes to the EH unit, the 0 kN case is similar to a negative loading cases. This case is denoted in the second and third quadrants in **Figure 1**. **Figure 7** shows the results of negative and zero loading conditions.

It can be seen that the curve in the slow velocity mode area is not linear. According to the logic represented in **Figure 4**, if the load is resistive, the pump is set to minimum speed, otherwise to zero, and the activated BP controls the actuation.

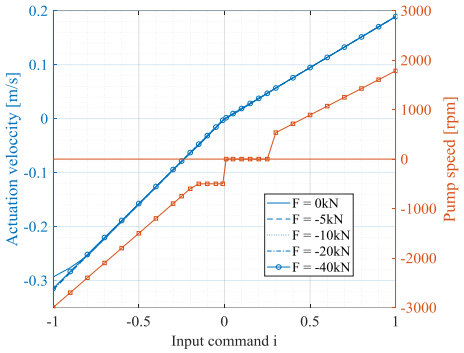

Figure 7: Working modes in second & third quadrants

For a better understanding of the low-speed modes, **Figure 8** represents a comparison between two typical conditions, based on normalized actuation velocity and EH speed. 20 kN force is applied to the cylinder, in both directions. In theory, the actuation velocity should closely follow the command, (10% command meaning 10% of the maximum speed). The maximum command ($i = 1$) should result in the maximum speed in resistive modes. As explained before, the pump works in different modes and does not follow the input command in all modes, which can be also observed in **Figure 8**. Two factors dominate the pump speed in the EHA. Firstly, the same extension/retraction speed may require different flow rates from the pump, according to the loading condition, which can be assistive or resistive. The impact can be well seen for input commands higher than 0.3 in **Figure 8**. Secondly, BP is opened under slow modes (zoomed-in part in **Figure 8**) and fast retraction modes (command $i < -0.5$), so that the pump flow can be divided and re-circulated in the circuit. During slow motions, the pump speed is set to minimum speed in resistive phase, while under assistive loads it is zero. As given in the zoomed-in part of **Figure 8**, the slow modes for positive and negative loads are symmetric around origin, while the actuation velocity remains linear with the input command.

5. EXPERIMENTS

5.1. Test rig setup

A test rig is built at Maha Fluid Power Research Center, Purdue University, Lafayette, USA to validate the functionality of the proposed system. The conceptual structure of the test rig is shown in **Figure 9**.

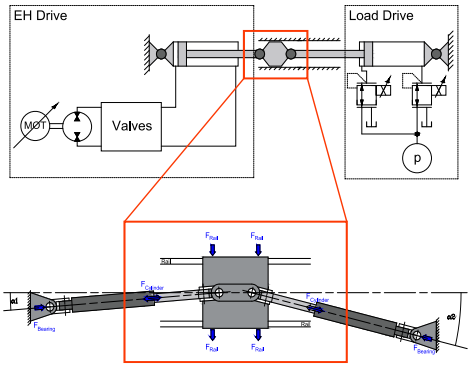

Figure 9: Conceptual structure of the test rig

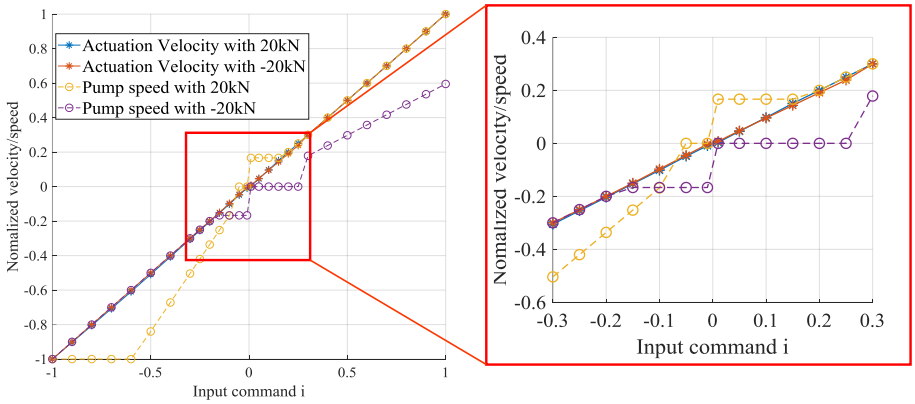

Figure 8: Actuation velocity/pump speed vs input command i from simulation

The designed test rig consists of two coupled cylinders. One cylinder is operated as part of the proposed EHA system while the other cylinder is pressure controlled and can be used to apply a defined load force to the EH drive. The cylinders are on both sides connected by dual-axis joints which prevent bending forces on the cylinder in case of misalignment. Side forces resulting from misalignment are compensated by linear ball rail guides.

The electric hardware needed for control and data acquisition on the test rig is listed in Table 3, including electronical control units, sensors, valves, and a servomotor.

Table 3: Hardware list for test rig

Hardware	Product number
Controller	NI cRio-9024
Analog modules	NI9264 NI9205 NI9472
Digital modules	NI9403 NI6421 NI9472
Pressure sensor 600bar	Rexroth R917A10105
Position sensor 1000mm	ASM WS42
On/off valves	Rexroth OD150536A000000
Prop. 2/2 directional valve	Rexroth KKDSR1NB/HCG24N 0K4V
Gear pump/motor	Rexroth AZMF - 12 -016 URR 12 ML
HDP servomotor	ABB VM47A00202001B00
Inverter	ABB ACS800-U11

The platform for control and data acquisition was established between hardware (sensors, NI cRio) and software (Simulink, Veristand).
The experimental setup located in the Maha Lab can be seen in the picture in **Figure 10**.

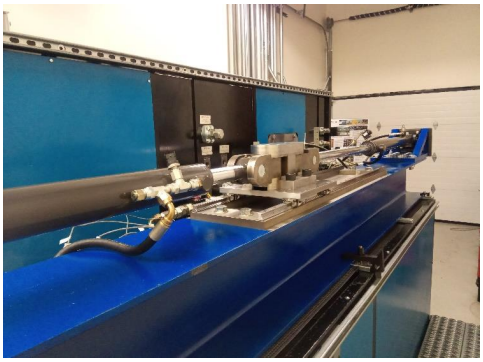

Figure 10: Experiment set up of the proposed EHA

5.2. Measurements

Measurements are conducted in order to show the functionality of the proposed circuit and to validate the results from the simulation. Input commands are the same for the experiments as for the simulation. Differently to the simulation, actuation velocities do not stay exactly the same at different loading conditions. **Figure 11** represents an example of that.

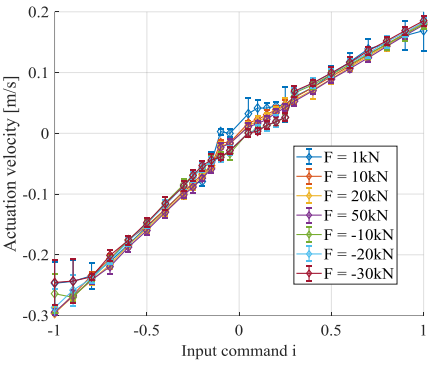

Figure 11: Measured actuation velocity from the test

One reason is that the actual pump has an efficiency map, meaning the volumetric efficiency may vary with different loading conditions. In addition, the low-speed mode works but the behavior is not as linear as desired for low speeds close to zero due to the nonlinear characteristics of BP under this range. More tuning of the parameters of BP may help to improve the performance. Moreover, fast retraction in resistive phases (minus force) may cause cavitation due to DV1 given in **Figure 2**.
For validation, a comparison between simulation and measurements is made based on normalized

velocity/speed. **Figure 12** shows the results at a 20kN load, which represents the baseline in **Figure 6** from the simulation.

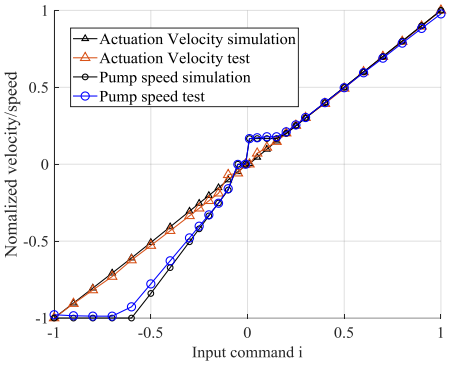

Figure 12: Comparison between measurements and simulation, F = 20kN

The results match well as given in the figure, though a minor difference is noticeable between the actuation velocity in the test and the simulation. Since the EH unit developed in the simulation model is always assumed ideally 100% efficient, it is reasonable that in the test extension can be slightly slower, while retracting slightly faster.

As for the cases given in **Figure 7**, a negative 20kN load is applied as well. The results are shown in **Figure 13**. The slow mode works as expected, and the linear performance can be improved by further control strategies on BP. As all measured points in the figure are actually the average of a certain time-period measurement, the noticeable discrepancies can be caused by measuring errors and noise.

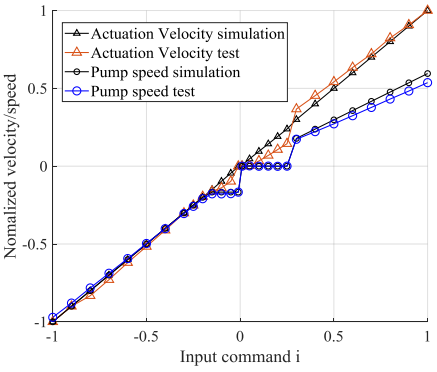

Figure 13: Comparison between measurements and simulation, F = -20kN

In summary, all working modes in all four-quadrants are reflected in the test, and the functionality of the proposed novel EHA system was proved. An optimized control structure and efficiency map of EH may help improve the accuracy and to match the results between simulation and measurements.

6. CONCLUSION AND OUTLOOK

This paper presented a novel closed-loop EHA system, with the capability to cover a broad range of velocities and to recuperate energy. Following both numerical and experimental approaches, the performance verification, as well as the validation of its functionality in four quadrants was conducted for the proposed EHA. The method of sizing the accumulator was described, as a design guideline for different actuator sizes, duty cycles, and power levels.With the utilization of a bypass valve in the closed circuit, slow actuation speeds can be achieved by means of proper control logic for switching between high and low-speed control modes. Based on an experimental set up developed at Maha Fluid Power Research Center, all possible modes to operate the EHA were tested. The performance of experiments at a steady-state was compared with the simulation results obtained from the Amesim model. The good match between experiments and simulation confirms the potential for further applications for such kind of EHA architecture.
With the basis of solid functionality, more research can be conducted in the future on the dynamic parts, such as an optimized control strategy for EHA systems. In addition, the energy-saving capability of the proposed EHA can be focused on more details. Especially a comparison with classical hydraulics is needed to study potential energy benefits and efficiency improvements. Moreover, long-term tests to validate the self-contained performance will be done. Ongoing studies also focus on the thermal behavior of closed-loop EHAs. Finally, solutions for cooling and filtration must be investigated in order to enable the technical realization of EHAs in commercial high-power applications.

NOMENCLATURE

EHA	Electro-Hydraulic Actuator
EH	Electro-Hydraulic Drive
FMVP	Fixed-Motor-Variable-Pump

VMFP	Variable-Motor-Fixed-Pump
HP	Hydraulic Pump
EM	Electric Motor
ACC	Accumulator
CYL	Hydraulic Cylinder
PCV	Pilot Check Valve
DV	Directional Valve
BP	Bypass Valve
FL	Filter
CV	Check Valve
p_0	Pre-charge pressure of Accumulator
V_0	Volume of Accumulator
V_1, V_2	Maximum/minimum Gas Volume in ACC
p_1, p_2	Minimum /Maximum Gas Pressure in ACC
V_{rod}	The volume of the Cylinder Rod
p_{drain}	Drain Line Pressure of Pump
i	Input Command
F	Force Applied on the Load Interface
Q_p	Flow Rate from Pump
Q_{cyl}	Flow Rate required from the actuator
dQ	Flow Rate through Bypass Valve
n_{EH}	Operating Speed of EH unit
n_{min}	Minimum Speed of EH unit
n_{max}	Maximum Speed of EH unit
Ω_{BP}	The open area of the Bypass valve

REFERENCES

[1] Navarro R (1997) Performance of an electro-hydrostatic actuator on the F-18 systems research aircraft. NASA Tech Memo

[2] Frischemeier S (1997) Electrohydrostatic actuators for aircraft primary flight control-types, modelling and evaluation. Proc Fifth Scand …1–16. https://doi.org/10.15480/882.236

[3] Beck DB, Fischer DE, Kolks DG, et al (2016) Novel System Architectures by Individual Drives. 10th Int Fluid Power Conf 29–62

[4] Mattos W, Brazil BR (2016) 4EE – High Performance Energy Efficiency for Hydraulic Machine Drive 4EE Energy Efficiency

[5] Ketelsen S, Padovani D, Andersen TO, et al (2019) Classification and review of pump-controlled differential cylinder drives. Energies 12:1–26. https://doi.org/10.3390/en12071293

[6] Habibi S, Goldenberg A (1999) Design of a New High Performance. Int Conf Adv Intell Mechattronics 227–232

[7] Pastrakuljic V (1995) Design and Modeling of a New Eleciro Hydraulic Actuator. 137

[8] Altare G, Vacca A (2015) A Design Solution for Efficient and Compact Electro-hydraulic Actuators. Procedia Eng 106:8–16. https://doi.org/10.1016/j.proeng.2015.06.003

[9] Padovani D, Ketelsen S, Hagen D, Schmidt L (2019) A self-contained electro-hydraulic cylinder with passive load-holding capability. Energies 12:1–19. https://doi.org/10.3390/en12020292

[10] Schmidt L, Ketelsen S, Brask MH, Mortensen KA (2019) A class of energy efficient self-contained electro-hydraulic drives with self-locking capability. Energies 12:1–27. https://doi.org/10.3390/en12101866

[11] Lin T, Wang Q (2012) Hydraulic accumulator-motor-generator energy regeneration system for a hybrid hydraulic excavator. Chinese J Mech Eng (English Ed 25:1121–1129. https://doi.org/10.3901/CJME.2012.06.1121

[12] Ge L, Quan L, Li Y, et al (2018) A novel hydraulic excavator boom driving system with high efficiency and potential energy regeneration capability. Energy Convers Manag 166:308–317. https://doi.org/10.1016/j.enconman.2018.04.046

[13] Williamson C, Ivantysynova M (2010) Stability and Motion Control of Inertial Loads with Displacement Controlled Hydraulic Actuators. 6th FPNI - PhD Symp 499–514

ANALYSIS OF NOVEL ZONAL TWO-CYLINDER ACTUATION SYSTEM FOR HEAVY LOADS

Tatiana Minav[1]*, Jani Heikkinen[2], Soumadipta Pyne[2], Sami Haikio[3], Juha Nykanen[4], Matti Pietola[2]

[1]*IHA Innovative Hydraulics and Automation, Tampere University, Korkeakoulunkatu 6, 33720 Tampere, Finland*
[2]*Department of Mechanical Engineering, Aalto University, Sahkomiehentie 4, Espoo, Finland*
[3]*Sandvik Mining and Rock Technology, Turku, Finland*
[4]*Parker, Vantaa, Finland*

* Corresponding author: Tel.: +358505940496; E-mail address: tatiana.minav@tuni.fi

ABSTRACT

Climate change and economic opportunities motivate investigating electric distributed power for working hydraulics in non-road mobile machinery (NRMM) instead of conventional hydraulics. This recent method allows significant energy savings in hydraulic systems, which was demonstrated previously by many independent studies. In this study, zonal hydraulics (as electrically distributed) are realized with direct driven hydraulics drive (DDH) units. Unlike conventional hydraulic drives the DDH units are disconnected from the engine (main prime mover) and distributed throughout the system. In a DDH unit, a single fixed displacement pump/motor with a speed-controlled electric servomotor directly controls the flow. The aim of this paper is to determine functionality of this new two-cylinder DDH-system in a lifting work cycle (or a swerve motion of the work machine). For this purpose, a model was created to investigate performance of the new test rig Dolores. The results of the simulation model will be utilized in future research to discover and compare other alternatives for working hydraulics architectures.

Keywords: direct driven hydraulics, zonal hydraulics

1. GENERAL INSTRUCTIONS

Many factors such as climate change and economic opportunities motivate investigating the electrification of heavy-duty non-road mobile machinery (NRMM). NRMM has been a field of extensive research due to various environmental concerns and enforced upcoming Tier V regulations for non-road engines [1].

According to [2], electric powertrains for NRMM are commercially viable in all power classes. However, according to [3] because of the heavy-load, low-speed and periodically operation mode, the authors stated that electric technology cannot be applied directly in construction machinery. This is why in order to decrease the fuel consumption in construction machinery, the usage of hybrid powertrain technology has increased. Manufacturers have made significant progress in recent years, examples of commercially available electrified excavators are Kobe Steel series-parallel hybrid excavator [4], Doosan [5] and Komatsu [6] series-parallel hybrid excavator, Hitachi [7] and New Holland [8] parallel hybrid excavator and Kobelco [9] parallel hybrid excavator.

Low powered electric vehicles (under 10kW) are most technologically feasible for electrification, as this category has the largest variety of products in the market. The electromechanical solutions perform better at higher power and higher speeds as compared to hydraulic solutions. However, reliability in these systems requires detailed investigation. Despite the shortcomings, prototype actuators with electromechanical solutions were recently released. For more details refer to Volvo [10] and Yanwar [11].

Electric powertrains are seen as a local emission-free solution that can increase overall system work efficiency but as it was demonstrated, developments are mostly concentrated on drivetrains. One solution that brings further improved efficiency is based on electric distributed power for working hydraulics

in NRMM instead of conventional hydraulic ones. This concept is known as zonal or decentralized hydraulics.

This recent concept allows significant energy saving in hydraulic systems, which has been demonstrated by many studies previously. In [12, 13] the results manifested high energy efficiency for both stationary and mobile applications.

In this study, zonal hydraulics (as electrically distributed) are realized with a direct driven hydraulics drive (DDH) units. Compared to conventional systems the DDH units are disconnected from the engine (main prime mover) and distributed throughout the system. In a DDH unit, single fixed displacement pump/motors with a speed-controlled electric servomotor directly control the flow.

The aim of this paper is to determine functionality of this new two-cylinder DDH-system under in a lifting work cycle (or a swerve motion of the work machine). For this purpose, a model is created and initial investigations are performed in this study on new test rig Dolores.

2. DOLORES TEST RIG

Figure 1 illustrates the test rig Dolores. Dolores is a new full-scale test rig for zonal hydraulics in Aalto University for simulating high power applications.

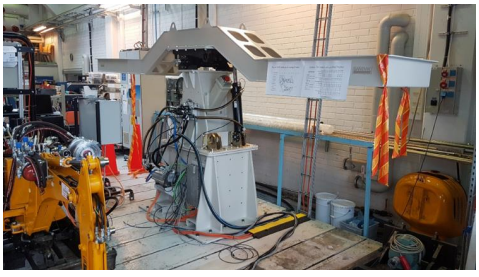

Figure 1: Test rig Dolores

The current setup is a two-cylinder DDH-solution, which represents one working hydraulic zone in a work machine, illustrated in **Figure 2**. This proposed architecture is new, but based on existing on market components (servomotor 80 kW, pump, and cylinders are manufactured by Parker).

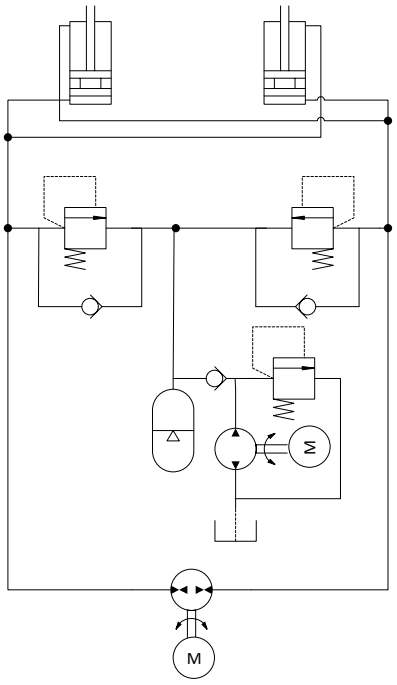

Figure 2: Simplified hydraulic schematics

Table 1 summarized utilized components in current version of Dolores test rig.

Table 1: Dolores Test rig components

Component	Manufacturer	Model
pump	Parker	PVD 3668_GB
Controller	Parker	IQAN-MC43FS
Display	Parker	IQAN-MD4
Electric Drive	Sevcon	Gen4 S10

The current version of the test rig is designed for testing of steering applications. Two cylinders steer the angle of the middle joint. The hydraulic cylinders are powered by a single fixed-displacement pump, which is run by an electric motor. The electric motor is controlled and powered by a SEVCON Gen4 Size 10 AC motor controller, which gets the DC power input from HVDC power supply. **Figure 3** demonstrates Dolores electrical circuit.

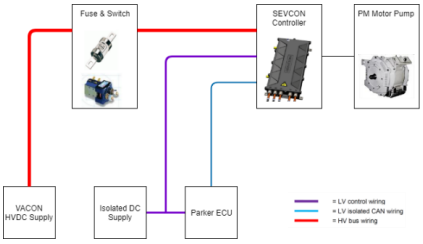

Figure 3: Electrical circuit of Dolores test rig

The test rig is currently controlled by a Parker ECU (Figure 3). It consists of a MC43 controller, MD4 display, wiring terminal, joystick, emergency switch, and fuses F2-F6. The Parker ECU communicates with the SEVCON controller via CANopen bus and with control valves using an analog signal.

There is a pre-charge system included in the test rig, which charges oil back to the system, provides cooling for SEVCON and electric motor, and also produces flushing flow for the pump casing.

3. MODELING

In order to investigate functionality of the new two-cylinder DDH-system, this study constructed a model in Matlab/Simulink, which integrated with hydraulic and electric systems of the test rig. The mathematical models of cylinder, pump/motors, pipes, and electric motor of DDH are built in the Matlab/Simulink environment utilizing Simscape blocks. A permanent Magnet Synchronous motor drive implemented with classic vector control with autotuning was utilized. The drive is powered from a three-phase voltage source with phase to phase voltage equal to 460 V.

Table 2 summarized parameters of cylinders.

Table 2: Parameters of the cylinder

Cylinder parameter	Value [unit]
Cap end area A_A	7.85×10^{-3} [m²]
Rod end area A_B	5.89×10^{-3} [m²]
length	0.45 [m]

Table 3 summarized parameters of system utilized during modeling.

Table 3: Parameters of the system

Parameter	Value [unit]
electric motor speed	2000 [rpm]
resistance	0.0315[ohm]
inductance	0.571×10^{-3} [H]
hydraulic motor displacement	19 [cm^3/rev]

The following section presents simulation results of the proposed model based on simplified hydraulic schematics and includes initial analysis of them.

4. SIMULATION

The results of the simulation are presented in the figures in this section. For each simulation case, results are shown in terms of quality of the produced motion, as well as the cylinder chamber flows.

Figure 4 demonstrates the electric motor speed profile as a response to the step input reference.

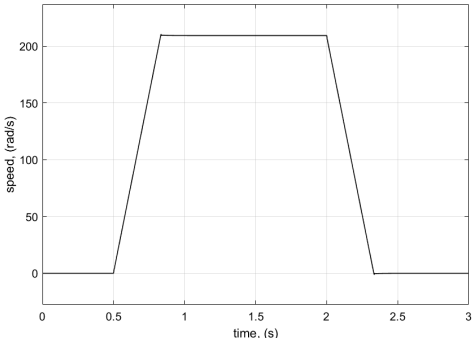

Figure 4: Utilized electric motor speed profile

Figure 5 illustrates electric motor torque requested by the hydraulic load.

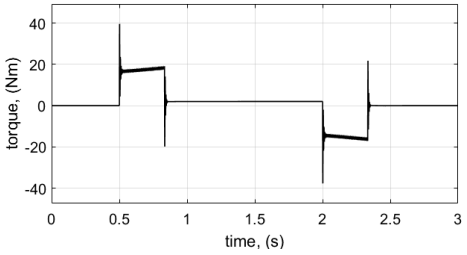

Figure 5: Electric motor torque

Figure 6 illustrates hydraulic motor out- and incoming flow, this demonstrates that models work as expected.

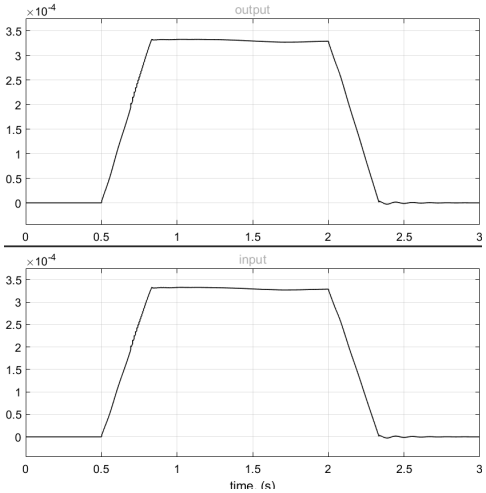

Figure 6: Pump outlet and inlet flows

Figure 7 shows the two cylinder positions as a response to the single utilized speed profile (see **Figure 4**). There is no motion until the electric motor starts; after 2.5 seconds, both cylinders are stopped.

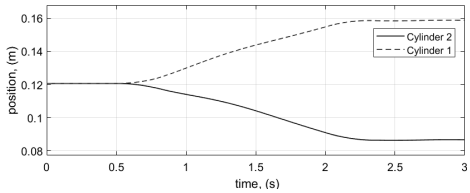

Figure 7: Cylinder positions

Figure 8 illustrates the flow variation during the performed cycle for the piston (A-side) and the rod (B-side) sides for cylinder 1 and 2, respectively. It can be seen in Figure 8 that the A-side in-flow cylinder 1 is equal to out-flow of A-side cylinder 2. Small difference in magnitude could be corrected with rigid cylinder connections to the joints and adjusting of pressure setting in valves.

5. DISCUSSION

Simulation demonstrated that effects of in- and out- coming flow to the system functionality is significant. Also, model functionality was sensitive to the tuning of electric motor control due to nature of direct control of the flow with speed-controlled electric servomotor.

This study is an initial investigation of a new two-cylinder DDH-system in a selected cycle with zonal hydraulics as a part of the EZE project. This paper evaluates functionality of the zonal hydraulics based on the simulation results from a Matlab/Simscape model as a function of parameters such as flow, position torque, and speed.

Coupling with multibody dynamics of the test rig was omitted in this stage of research. The developed electro-hydraulic model was tested a single cycle.

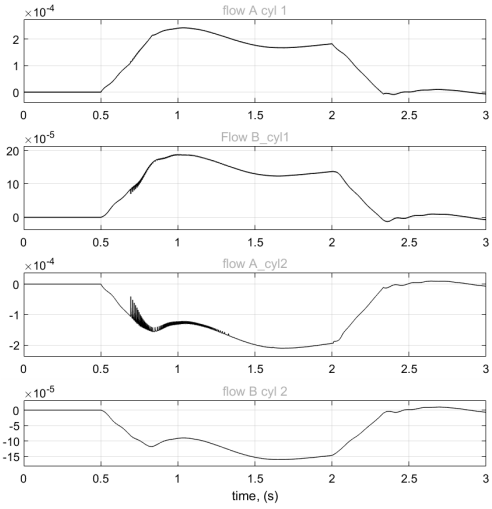

Figure 8: In- and out- flow from cylinders

The developed Matlab/Simscape model of the DDH will be validated against measurements under typical cycles. In future studies, empirical investigation with detailed energy balance is also needed as the generation mode (motoring mode for hydraulic motor) and near-zero speed operation was not investigated by the developed model.

Therefore, the aim of this work was to demonstrate functionality of the simulated architecture.

6. CONCLUSION AND OUTLOOK

The emissions of heavy-duty non-road mobile machinery are pushing towards more efficient solutions, hence fully electric powertrains are

becoming a viable alternative to conventional diesel and valve-controlled systems. This paper analyses the functionality of a new two-cylinder DDH-system in a typical lifting-lowering work cycle. In this study, a model and initial simulation investigation was performed on the new test rig Dolores. The results of the simulation model demonstrated ability of the system to respond to the direct motor control.

Future research will discover and compare other alternatives for working hydraulic architectures with use of this new test rig Dolores.

ACKNOWLEDGEMENTS

The research was enabled by the financial support of the EZE (Easy zonal hydraulics) project, and internal funding at the Department of Mechanical Engineering at Aalto University, and IHA group at Tampere University, Finland.

NOMENCLATURE

DDH Direct driven hydraulics
NRMM Non-road mobile machinery

REFERENCES

[1] Dieselnet, (2016) EU: Non-road Engines. Retrieved: 2018.10.24 https://www.dieselnet.com/standards/eu/nonroad.php

[2] Paraszczak, J. et al., (2014) Electrification of Loaders and Trucks – A Step towards More Sustainable Underground Mining. International conference on renewable energies and power quality, April 8-10, 2014, pp.81-86

[3] Wang J, Yang Z, Liu S, et al (2016) A comprehensive overview of hybrid construction machinery. Adv Mech Eng 8:1–15. https://doi.org/10.1177/1687814016636809

[4] M. Kagoshima, (2012), The development of an 8 tonne class hybrid hydraulic excavator SK80H, R&D Kobe Steel Engineering Reports, 0373-8868, 62 (1) (2012), pp. 14-18

[5] Doosan series-parallel hybrid excavator, https://www.khl.com/construction-europe/electric-and-hybrid-sparking-a-new-era/139690.article

[6] Inoue H. (2009), Introduction of PC200-8 hybrid hydraulic excavators. Technical report, vol. 54, no. 161, pp.1–6, Komatsu, Japan, 27 March 2009.

[7] Hitachi construction machinery, https://www.hitachicm.eu/hybrid/, Retrieved: 20.01.2020

[8] D. Geske, Newholland“ex”-ercises hybrid option, http://ptmedia.isuzuengines.com/downloads/News/DPI424_LR.pdf

[9] Yamazaki Y, Saiki S, Koga N, Tsutsui A, Sekiyam A K, Maeda K. (2019), Development of 20-tonne Class Hybrid Excavator, SK200H-10, kobelco technology review NO. 37 APR. 2019 https://www.kobelco.co.jp/english/ktr/pdf/ktr_37/025-030.pdf

[10] Volvo CE unveils 100% electric compact excavator prototype, (2017), press release, https://www.volvoce.com/global/en/news-and-events/press-releases/2017/volvo-ce-unveils-100-percent-electric-compact-excavator-prototype/

[11] Yanwar, eFuzion Concept, https://www.yanmar.com/global/construction/news/2019/04/10/53748.html

[12] Koitto T., Kauranne H., Calonius O., Minav T., Pietola M., (2019) Experimental Study on Fast and Energy-Efficient Direct Driven Hydraulic Actuator Unit, Energies 2019, 12(8), 1538; https://doi.org/10.3390/en12081538

[13] Zhang S., Minav T., Pietola M., Kauranne H., Kajaste J., (2019) The effects of control methods on an electro-hydraulic excavator equipped with zonal hydraulics, Automation in Construction, Volume 100, April 2019, Pages 129-144

EXPERIMENTAL EVALUATION OF AN ELECTRO-HYDROSTATIC ACTUATOR FOR SUBSEA APPLICATIONS IN A HYPERBARIC CHAMBER

João Pedro Duarte da Silva[1*], Amadeu Plácido Neto[2], Victor Juliano De Negri[1], Alexandre Orth[2]

[1]*Federal University of Santa Catarina (UFSC), Laboratory of Hydraulic and Pneumatic Systems (LASHIP), Florianópolis, Santa Catarina, Brazil.*
[2]*Bosch Rexroth AG, Lohr am Main, Germany.*
* Corresponding author: Tel.: +55 48 996841944; E-mail address: joao.pedro.d.silva@posgrad.ufsc.br

ABSTRACT

A novel Electro-Hydrostatic Actuator (EHA) prototype – designed to operate on subsea gate valves in deep and ultra-deep water – is analysed and qualified in terms of functionality under design and normative constraints. The prototype is assembled in a test bench for load control in a hyperbaric chamber where the high subsea environmental pressure can be emulated. The process variables under evaluation are monitored through a set of pressure and position sensors, which are part of the prototype design. The experimental results demonstrate a robust behaviour of the actuator concerning the imposed external pressure and load forces even with a forced limitation in its power input. Moreover, the prototype performs consistently throughout the entire endurance trial, asserting high reliability. With the results obtained, the subsea EHA concept is effectually eligible to a technology readiness level 4, according to the API 17N.

Keywords: Electro-hydrostatic actuator, Subsea production systems, Hyperbaric test, Ultra-deep water, Verification and validation

1. INTRODUCTION

In the context of subsea oil & gas production systems, there is an ongoing transition to All-Electric Systems (AES). Particularly for subsea actuators, this trend has surged due to their several advantages in comparison with the conventional hydraulic and electrohydraulic counterparts, such as installation and operational costs reduction, fast system response, reduction of umbilical diameter, high level of operational flexibility and environment-friendly design [1] [2]. Yet, many AES actuator solutions rely on electromechanical principle, which brings along substantial drawbacks. Namely, low power-density, cumbersome fail-safe mechanisms – if any – and higher system complexity, compromising reliability.

The application of an electro-hydrostatic actuator (EHA) in subsea production systems is a solution that can be seamlessly implemented in AESs preserving all of its good attributes aforementioned and adding the inherent advantages of conventional electro-hydraulic systems, such as reliability, compactness, robustness, high power density, high load capacity, low maintenance, simple and effective overload protection and uncomplicated commissioning [3]. All the while, it prevents the drawbacks found in the current electromechanical actuators.

In the oil and gas industry EHAs are already utilized on topsides and onshore systems, however, the adaptation of this concept for subsea application is entirely novel, which highlights the importance of its validation in hyperbaric environment. This actuator principle is already a mature technology meeting the most rigorous safety requirements in aircraft applications, where these systems are referred as 'power-by-wire' type of actuation systems [4].

All oil and gas equipment intended to be applied in the bathypelagic zone – located in depths between 1830 to 3000 meters – must be designed accounting the harsh environmental conditions, such as the high external pressures

due to the water column and the difficulty to perform maintenance in such places. Beyond these considerations, in order to reduce operating costs, the equipment must operate with high availability and minimum maintenance during the entire service life of a field, which can be 25 years or more [5] [6]. To ensure this suitability, a series of international standards and norms have been issued, containing extensive qualification tests targeting all subsea-rated equipment.

In this paper, a novel EHA for subsea valves – henceforth designated as subsea valve actuator (SVA) – is evaluated according to these qualification requirements, particularly in respect to the hyperbaric conditions. The precise standards applicable for subsea actuators that are considered in this evaluation are the ISO 10423, ISO 13628-4 and the API 17F. To achieve this objective, first the test subject is briefly described. Then, a test methodology is presented and, finally, the results obtained are discussed in respect to the qualification requirements present in the standards.

2. ELECTRO-HYDROSTATIC ACTUATOR PROTOTYPE DESCRIPTION

The subsea valve actuator prototype studied in this research is an electro-hydrostatic actuator (EHA) devised to operate with 2 inches gauge gate valves at depths of up to 3000 meters. Its simplified composition, disregarding most of the redundancies and auxiliary features, is illustrated in **Figure 1** and described next.

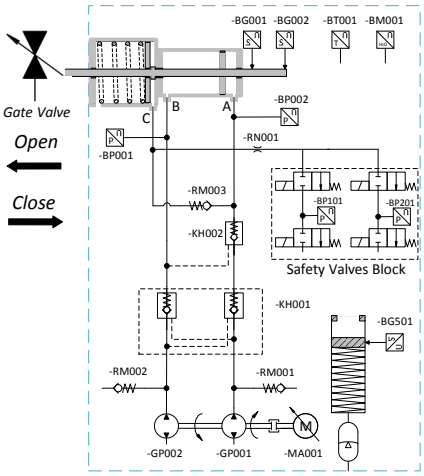

Figure 1: Schematic diagram of the SVA prototype

The components illustrated within the blue dashed rectangle in **Figure 1** are all submerged in hydraulic fluid – contained inside the hull of the actuator that serves as the hydraulic reservoir as well. The electric servomotor, designated MA001 in the schematic, is coupled to two hydraulic pumps (GP001 and GP002) by a gear transmission. This drive system is responsible for the *regular actuation function*, moving the four-chamber hydraulic cylinder by controlling the flow rate through its chambers (A, B and C).

The four-chamber hydraulic cylinder can be divided as a spring cylinder and the work cylinder. The spring cylinder, which houses the spring, has a piston unattached to its rod, which enables it to move freely in the forward direction. For the returning direction, there is a mechanical contact between piston and rod, which does not allow the spring cylinder piston to move freely in the closing direction once it reaches this contact. The spring release occurs once the ON-OFF solenoids of the safety valves are de-energized, allowing the flow rate from chamber C to the reservoir. The flow restrictor (RN001) guarantees a smooth and controlled return. This mechanism constitutes the *fail-safe close function* of the SVA. During the regular actuation function, the spring cylinder is clamped and the ON-OFF safety valves are closed, while the gate valve movement is driven solely by the work cylinder.

The system also contains check valves (RM001 and RM002) to prevent low pressure in the hydraulic lines, pilot operated check valves (KH001 and KH002) to latch the position of the work cylinder when the drive system is at rest, another check valve (RM003) which allows the flow rate to fill the cylinder chamber C, locking the spring compressed. Finally, the pressure inside of the SVA hull is compensated and pressurized to be constantly higher – from about 0.5 to 2 bar – than the environmental pressure by action of several pressure compensation units in parallel. The additional pressure is generated by the preloaded springs, which compresses the piston of each compensator, as illustrated in **Figure 2**. The purpose is to avoid any ingress contamination from the environment such as seawater, sand, or organic materials in case of an external leakage. This constitutes the *external pressure compensation function*.

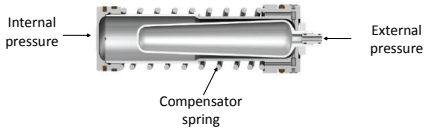

Figure 2: Pressure compensator system.

The SVA is also instrumented with a series of sensors to monitor and assess the state of its subsystems. Namely, the work cylinder is equipped with two position encoders (BG001 and BG002) and two absolute pressure sensors (BP001 and BP002). There are two additional pressure sensors between the safety valves (BP101 and BP201), one position encoder in one of the pressure compensation units (BG501) to assess approximately the available volume for compensation, and, in contact with the hydraulic medium, there are a temperature sensor and a water contamination sensor (BT001 and BM001 respectively). In addition, the motor can have its velocity, electric current consumption and winding voltages externally monitored.

The SVA control interface is solely comprised of an electrical connector, which enables an external controller unit to read its instruments, and control both the servomotor and solenoid valves.

By means of these subsystems, the scope of the functional validation of the SVA can be delineated by the following three main functions:

- Regular actuation function;
- Fail-safe close function;
- External pressure compensation function;

3. EXPERIMENTAL METHODOLOGY

The methodology used to evaluate the SVA is based off in the systematic approach by Kleppmann [7]. This approach consists of initially describing the test subject – as has been done in the previous section – followed by the definition of the test objectives, the test procedure description, the test bench description and finally the results interpretation.

3.1. Test objective

Within this approach, the test objective is to fulfil the qualification requirements regarding hyperbaric environment of the relevant standards. In addition, design requirements of the prototype relevant in hyperbaric environment that are not required by the standards are also listed for evaluation. All of the considered standards required that for the design validation of subsea actuation systems, hydraulic actuators shall be submitted to a functional test in a hyperbaric environment. ISO 10423 [8] particularly specifies the load to be either a valve/choke or a fixture that emulates the opening/closing dynamic force profile of a valve/choke with a specific well pressure differential. API 17F [9] specifies minimum rates of pressurization and depressurization of the hyperbaric chamber. The number of functional cycles is divergent in each standard, thus the harshest requirement is adopted as objective.

A summary of the test requirements is given as follows:

- Submit the equipment in a hyperbaric condition of 110% of the maximum rated depth for at least 6 hours, without compromising its functionality;
- 200 regular actuation cycles at hyperbaric condition of 110% of the maximum rated depth, with 10000 psi differential pressure in the valve fixture;
- 400 regular actuation cycles at atmospheric pressure, without load;
- 3 fail-safe cycles at hyperbaric condition of 110% of the maximum rated depth, with 10000 psi differential pressure in the valve fixture;
- 3 fail safe cycles at hyperbaric condition of 110% of the maximum rated depth, without load;
- 3 fail safe cycles at atmospheric pressure, with 10000 psi differential pressure in the valve fixture;
- 3 fail safe cycles at atmospheric pressure, without load;
- 3 pressurization-depressurization cycles from atmospheric to 110% of the maximum rated depth with minimum pressurization rate of 24 bar/min and depressurization of 36 bar/min;

The required pressure differential in the valve fixture disregards the downstream pressure, which is caused by the weight from the column of fluid. In practice, the pressure differential should be considerably lower, giving the load in this test condition a substantial safety factor. Furthermore, the well pressure in a field tends to decrease as the production advances, which would render a decreasing load force through the

cycles. This is not considered, constituting, in this sense as well, a test condition more severe than the real application.

To comply additional design constraints, all cycles must be performed with a power input limitation of 250 W in the SVA drive. This affects the system, as the actuation velocity is controlled to perform a full stroke in 60 seconds (disregarding the time to latch the spring cylinder). Moreover, the fail-safe cycles must finish the closing motion in less than 30 seconds.

3.2. Test procedure

The test shall consist of devising a device to produce a controllable force that can be mechanically coupled to the SVA stem, serving as the valve fixture. The force in such a fixture shall have to emulate the same forces involved in a real subsea actuator and gate valve interaction. The main forces involved in such assembly are delineated in **Figure 3**.

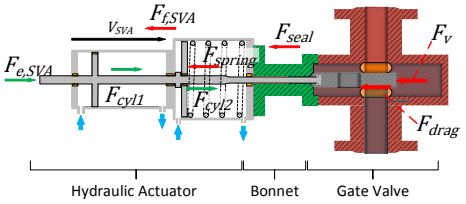

Figure 3: Force diagram in a subsea gate valve/actuator assembly.

Forces present on the actuator:

- $F_{e,SVA}$: Enclosure force, caused by the reservoir pressure;
- F_{cyl1} : Work cylinder hydraulic force;
- F_{cyl2} : Spring cylinder hydraulic force;
- F_{spring} : Fail-safe spring force;
- $F_{f,SVA}$: SVA friction forces.

Forces present on the gate valve and bonnet:

- F_v : Force acting on the stem due to the valve internal pressure;
- F_{drag} : Friction force between the gate and seats of the valve;
- F_{seal} : Friction force due to the contact between the seals and the stem in the bonnet.

The resultant force is then the sum of the three mentioned forces present on the gate valve and bonnet. This force profile is a function of the valve position, as the normal force in the gate valve changes dramatically once the gate valve starts to open. The normal force influences the friction force between the gate and seats of the valve [6] [10]. The load force profile applied to the SVA during the tests is illustrated in **Figure 4**. The steepness in which the drag force changes depends on the valve geometry and discharge factor.

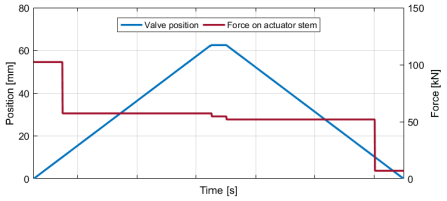

Figure 4: Force profile acting on the actuator stem as a position function, according to standard test conditions.

The load force profile of **Figure 4** emulates a 2 inches gate valve with wellbore pressure of 10000 psi (690 bar) in test condition where the pressure differential through the gate decreases abruptly once the valve starts to open [6] [11]. It can be noticed that the maximum required force to move the gate valve occurs at the beginning of the movement while the valve is still closed and its pressure differential is maximum. This force is equal to 102.3 kN considering the parameters of the gate valve taken. The minimum force occurs after closing the valve when its pressure differential is maximum again. The position where the valve starts to open is referred as crack-open position, and can be better visualized in **Figure 5**.

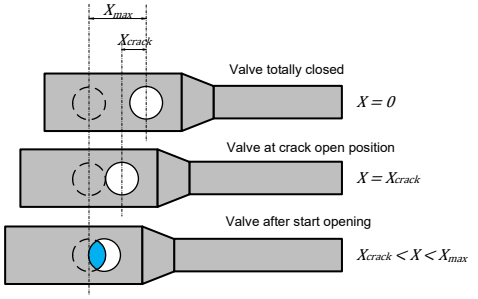

Figure 5: Representation of the opening area in a gate valve according to its position.

Finally, the assembled SVA and valve fixture shall be mounted in controllable hyperbaric environment, where the tests shall be carried out. A control module shall simultaneously control the force in the valve fixture and the function

cycle in the SVA while records the data from the instruments.

3.3. Test bench

The hyperbaric chamber available at the Bremen University in Bremen, Germany, was employed to emulate the hyperbaric environment due to the column of water.

The valve fixture was realized with a mechanically coupled load hydraulic cylinder (MM201. The force profile is then applied by controlling its pressure differential with a proportional valve (QM101) powered by its own hydraulic power unit. This separated hydraulic circuit is partly embedded in the pressure chamber using pressure-sealed components. This prevents the pressure in the hyperbaric chamber disturbing the load control. A schematic of the test bench design is illustrated in **Figure 6**.

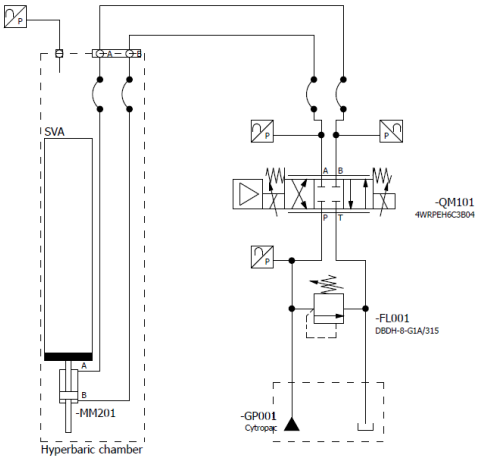

Figure 6: Schematic diagram of the test bench.

The test bench controller consists of an industrial PLC connected to both the instruments and the proportional valve of the load cylinder, and the electrical interface of the SVA running through a pressure-tight fitting located in the hyperbaric chamber lid.

The control architecture implemented to execute the test is shown in **Figure 7**. The SVA position controller is implemented as a finite-state machine. It receives the test configurations from the user and, according to its state, generates the reference for the SVA velocity controller, which, in turn, is implemented and tuned as a proportional-integral controller. The velocity controller drives the servomotor in the SVA to maintain the work cylinder velocity equal to the reference velocity. Simultaneously, the load force model calculates the differential pressure reference in the load cylinder according to the SVA position. This feeds yet another proportional-integral controller, whose action modulates the opening in the proportional valve, regulating the pressure in the load cylinder. Finally, to mitigate the disturbance of the SVA movement in the load force due to pressure imbalance in the load cylinder – a phenomenon that would not happen with a purely mechanical force in a real application – the SVA velocity is supplied to a feed-forward controller, which compensates the control effort in the proportional valve.

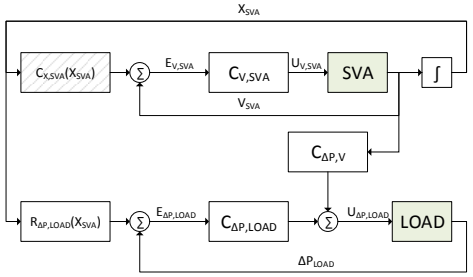

Figure 7: Test bench control architecture.

Because of the test bench layout, another three additional forces were included in the load force model. This is to compensate the friction force of the load cylinder ($F_{f,load}$), the force caused by the hydrostatic pressure acting on the load cylinder rod ($F_{e,load}$), and the weight force (F_W) of the moveable parts, which are now vertically positioned with the valve fixture underneath the actuator. All friction forces, drag forces and the weight force depend on the movement direction. The pressure differential reference for the load cylinder ($R_{\Delta p,load}$) is then given by the sum of the mentioned forces divided by the load cylinder effective area (A_{load}), as shown in Equation 1.

$$R_{\Delta p,load} = \frac{F_v \pm F_{seal} \pm F_{drag} \pm F_{f,load} - F_{e,load} \pm F_W}{A_{load}} \quad (1)$$

In **Figure 8**, there is a depiction of the SVA coupled with the load cylinder during commissioning in the pressure chamber.

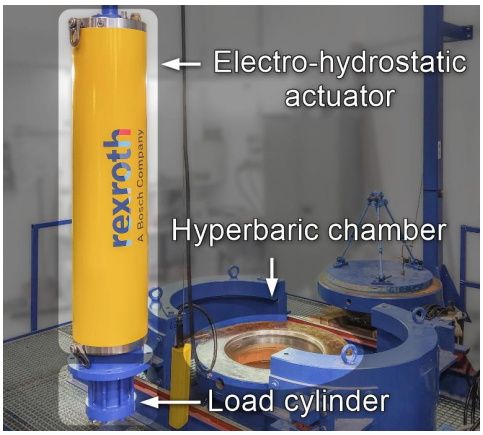

Figure 8: Test bench during commissioning.

A software was programmed to execute the regular actuation function and the fail-safe close function cycles.

The regular actuation function cycle consists of enabling the load controller, regulating the force on the fixture until within a tolerance of the reference. Then the SVA safety valves are closed and the velocity controller is enabled, driving the valve until the open position. There, the velocity controller stops the drive and waits 2 seconds to avoid dynamic distortions on the process variables, after which the velocity controller begins to drive the valve back to the closed position. The load controller continually regulates the load force to maintain the model reference force. When the actuator is back on the closed position, a completed cycle is accounted. After all cycles are completed, the safety valves are open and the spring chamber is released.

The fail-safe close function cycle is similar to the regular actuation up until the valve is open. Then, the velocity controller shuts down and the safety valves turned off, releasing the spring chamber. The load controller keeps regulating the force while the spring force passively brings the valve to the closed position. Once the closed position is reached, the cycle is counted as complete.

The hyperbaric chamber controls cannot be automated, thus the pressurization-depressurization cycles have to be executed manually. The pressure in the chamber can be finely controlled via the user interface, the pressurization rate, however, cannot. In spite of that, the chamber is instrumented, so the cycles can be repeated on different conditions to achieve the qualification requirement.

4. RESULT ANALYSIS

The trials in hyperbaric chamber were executed over the course of six non-continuous days, in which the actuator and valve fixture were continuously immersed in the chamber filled with sink water for fourteen days. During the experiment sessions, the actuator was submitted to the equivalent pressure of the maximal rated depth for extended lengths of time, the longest lasting 8 hours and 36 minutes. This corresponds to 143.6% the time required by norm. During all trials, there was no loss of functionality observed. The internal pressure was steadily kept above the environment pressure, which asserts the structural integrity of the equipment.

4.1. Regular actuation function

Cycles in hyperbaric environment

To achieve the qualification conditions for the regular actuation function in hyperbaric environment, as previously declared in the test objectives, the hyperbaric chamber was kept at an average pressure of 332.3 bar (σ = 15.0 bar) throughout all cycles, or 110.7% the pressure at maximum rated depth. The average force (disregarding $F_{e,load}$ for comparison) throughout the cycles in the valve fixture before crack open – where the load is at its peak – was 101.2 kN (σ = 0.1 kN). This deviation of the average of less than 2% from the reference value is deemed acceptable and demonstrates the controller overall effectiveness, asserting the validity of the test conditions as well. In these circumstances, 300 cycles were executed in total, 150% of the amount required for qualification.

In **Figure 9** (time axis deliberately omitted), two full cycles are exhibited. It can be noticed a delay before the actuator starts moving after the test initialization. This corresponds to the spring chamber being latched. The compression can be seen indirectly as the SVA force rises linearly. Once latched, the actuator can move back and forth without having to push the spring chamber every cycle. Although the abrupt changes in the load force, the system position derivative does not see to change at all, which highlights a robust behavior towards load variations. The difference

between the SVA force and the load force during the opening is caused by the friction between the hydraulic cylinder piston and rod and its seals. During the close motion, the valve force actually helps the movement. However, to prevent any uncontrollable outcome, the SVA dissipates the additional force in the piloted valves.

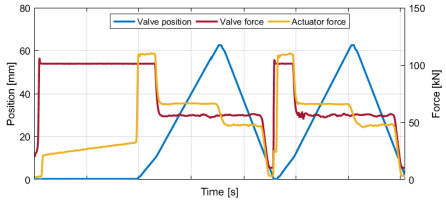

Figure 9: Actuator and load force and position in hyperbaric environment.

The system endurance is evaluated by averaging the load force as well as the SVA velocity and force were in their steady states before and after the crack-open during the opening motion for all cycles. These operational ranges were selected because correspond to the most demanding parts of the functional cycles. **Figure 10** shows these values through the cycles.

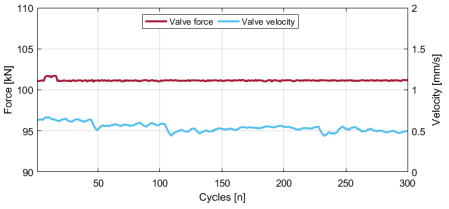

Figure 10: Average SVA velocity and load force during opening motion before crack open throughout all cycles in the hyperbaric environment.

Cycles in atmospheric pressure environment

The cycles in atmospheric pressure were executed after the tests in the hyperbaric chamber. In total, 610 cycles were executed, 152.2% of the required for qualification. Instead of executing these cycles without load as required, the same load condition equivalent to 10000 psi through the valve fixture was applied in all of the cycles as well. Considering all cycles in atmospheric pressure, the average force applied by the valve fixture during opening before crack open was equal to 103.9 kN (σ = 0.03 kN), again, less than 2% deviation from the reference value. In **Figure 11**, it is depicted two full cycles under the aforementioned conditions.

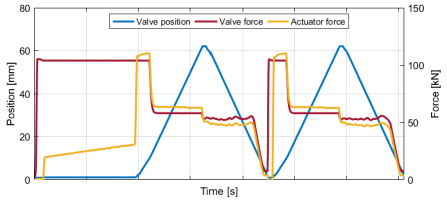

Figure 11: Actuator and load force and position in atmospheric pressure environment.

In comparison with the cycles executed in hyperbaric condition, the internal friction in the actuator observed in atmospheric pressure was 41.1% lower. This phenomenon is described by Suisse [12], where it is stated that, as the applied pressure increases, the friction forces between the dynamic seals and the cylinder piston and rod increases symmetrically, due to a higher normal force.

The SVA endurance was evaluated in atmospheric pressure in the same manner as it was in hyperbaric environment. **Figure 12** depicts the averaged load force and SVA velocity during opening before crack open throughout all cycles.

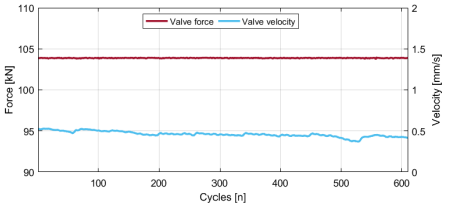

Figure 12: Average SVA velocity and load force during opening motion before crack open throughout all cycles in atmospheric pressure environment.

The steady decrease in the average velocity suggests a degradation of the volumetric efficiency, since the velocity is controlled but the input power is limited. This decrease was expected, most likely because the internal seals – particularly in the hydraulic pump – degrade with time due to the compression set of the work pressure [13]. Nonetheless, this does not compromise the opening time, as the controller can be configured to compensate the setback after the crack open, where the load is significantly lower with sufficient power available to drive the valve faster.

4.2. Fail-safe close function

Cycles in hyperbaric environment

In total, 30 cycles of the fail-safe close function were executed in hyperbaric environment. Half of the cycles were executed without load and the other half with the load equivalent of 10000 psi pressure differential in the valve fixture. When executing the cycles without load, during the amount required by norm, the average pressure in the hyperbaric chamber was 333.0 bar (σ = 0.7 bar). This corresponds to 111% the pressure at maximum rated depth. On the cycles with load, during the cycles required by norm, the average pressure was 341.8 bar (σ = 1.1 bar), or 113.9% the pressure at maximum rated depth. Counting the additional cycles executed for internal qualification, this amounts to 500% the number of required cycles for each condition.

The valve position and load force during the fail-safe close from one of the cycles with load is depicted in **Figure 13**. It can be seen that, during the closing motion, the resultant load force acts in the same direction, pushing the movement at a faster rate than the spring piston. At the crack open position, the friction force increases sharply, to which the resulting force from the load alone cannot finish the remaining stroke. The spring piston catches up after a few seconds, finishing the close movement. Considering all cycles, the average time for complete close with the load was 16.9 seconds (σ = 0.1 seconds), 43.60% less than the maximum tolerable time according to design requirements. The fastest cycle closed in 16.6 seconds, while the slowest finished in 17.1 seconds.

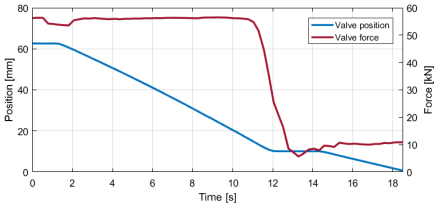

Figure 13: SVA and load actuator force and position through time in hyperbaric environment.

In the cycles without load, the closing movement is pushed entirely by the spring piston. This can be seen from the valve position during the closing of one of the cycles in **Figure 14**, which indirectly shows as the spring force decreases while relaxing. Considering all cycles, the average time for complete close without load was 24.5 seconds (σ = 0.4 seconds), 18.2% less than the maximum tolerable time. The fastest of these cycles closed in 23.9 seconds, the slowest in 25.6 seconds.

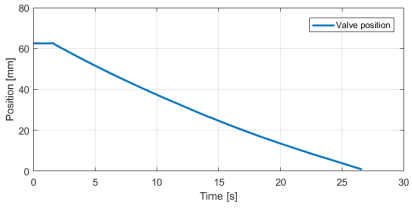

Figure 14: Valve position during fail-safe close without load in hyperbaric environment.

Cycles in atmospheric pressure environment

Another 30 cycles were correspondingly executed at an atmospheric pressure environment, again half of those with the prescribed load and half without it. The fail-safe close function did not present significant dynamic divergences from the tests ran in the hyperbaric chamber. However, due to the reduced internal friction, the average time to close was slightly smaller on both conditions.

The average time to close with load was 15.3 seconds (σ = 0.1 seconds), 49.1% less than the maximum tolerable time and 9.5% faster than the average obtained under hyperbaric environment. The fastest cycle closed in 15.1 seconds and the slowest in 15.5 seconds. Without load, the average time to close was 20.5 seconds (σ = 0.1 seconds), 31.7% under the threshold and 16.3% lower than the same indicator obtained in the hyperbaric condition. The fastest cycle finished in 20.3 seconds, the slowest in 20.7 seconds.

4.3. Pressure compensation function

The actuator has been submitted to twice the amount of required cycles of pressurization and depressurization. Due to facility limitations, as aforementioned, the intensity of the pressurization and depressurization rates could be only marginally controlled. Therefore, the measurements have relatively higher standard deviations. Half of the cycles were executed with a relatively moderate rate and the other half with a more aggressive rate.

The most moderate pressurization cycle had already on average a pressurization rate of 55.6

bar/min (σ = 12.4 bar/min) – 231.7% of the required by norm – and a depressurization rate of 71.0 bar/min (σ = 33.6 bar/min), 197.2% of the required by norm. The average pressurization rate inside the EHA was 55.2 bar/min (σ = 12.6 bar/min) only 0.8% slower than the hyperbaric chamber, whereas its depressurization rate of 70.6 bar/min was 0.6% slower. This negligible delay is mostly caused by the dynamic response of the mechanical components of the pressure compensator. In **Figure 15** it is depicted the internal pressure and the position of one of the pressure compensator units in respect to the external pressure during this particular cycle.

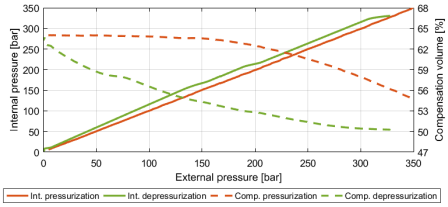

Figure 15: Compensator volume and internal pressure during a moderate pressurization-depressurization cycle.

In the most aggressive pressurization cycle, the average pressurization rate was 103.7 bar/min (σ = 5.1 bar/min), 432.1% of the required by norm. The average depressurization rate was 327.6 bar/min with a brief maximum rate of 2647.2 bar/min and minimum rate of 38.4 bar/min towards the end, the average being equivalent to 910% of the required by norm. In **Figure 16** the internal pressure and the position of one of the pressure compensator units in respect to the external pressure during this cycle is plotted. In this case, the actuator presented on average a pressurization rate of 103.4 bar/min (σ = 4.2 bar/min), 0.3% slower than the chamber and a rate of 309.5 bar/min (σ = 99.7 bar/min) during depressurization, 5.5% slower than the chamber. This shows as a hysteresis behavior, when the compensator begins to saturate its dynamic response to abrupt variations in the environmental pressure. Nonetheless, such extreme conditions are not realistically feasible in a real application and serves mostly to demonstrate the robustness of the system.

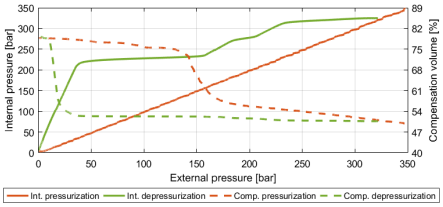

Figure 16: Compensator volume and internal pressure during an aggressive pressurization-depressurization cycle.

5. CONCLUSION AND OUTLOOK

A novel concept of an electro-hydrostatic actuator (EHA) for subsea gate valves was presented, highlighting its several advantages over current technologies in this branch. The introduction of such systems in the market has the potential to drive considerably down the overall costs in oil and gas production, for instance. However, due to the stern reliability requirements of this industry, a series of experiments have to be executed in order to qualify this equipment before introducing it in the market. Part of these experiments require functionality validation under hyperbaric conditions.

In this paper, the qualification requirements, mostly relevant for hyperbaric conditions, were assessed and summarized as test objectives. Then a test procedure was devised and realized in a test bench, which was proven suitable to reproduce the required test conditions accurately. Yet, a remark to improve the reproducibility in future hyperbaric tests is to employ a hyperbaric chamber with an autonomous control of its pressurization-depressurization rates.

The prototype underwent a series of trials to achieve all qualification requirements. To meet the quality standards at Bosch Rexroth, these requirements were increased in all relevant aspects: actuator load, external pressure and amount of cycles. The results were then treated to guarantee proper statistical significance. In respect to all of its functions, the test subject exhibited a consistent robust performance even under the most unrealistic conditions. It has been noticed, as expected, a mild degradation on the volumetric efficiency throughout the endurance cycles and a variation of the friction forces in the hyperbaric environment. These factors, however, did not disturb the functional performance of the device.

With these results, this actuator prototype already meets nearly all the criteria for technology readiness level 4, according to API 17N [14]. To complete its qualification process, additional functional validation tests are currently being executed in a temperature-controlled environment. Thereafter, the concept shall be considered sufficiently mature to be commissioned in the field.

ACKNOWLEDGMENTS

We would like to acknowledge and express our gratitude to the Laboratory of Hydraulic and Pneumatic Systems (LASHIP) at the Federal University of Santa Catarina, Brasil; to Bosch Rexroth AG, Germany; to the Center for Marine Environmental Sciences (MARUM) at Bremen University, Germany; to DNV-GL auditors and to all partners directly or indirectly involved. This study was made possible only through the collaboration of all these parties.

LIST OF SYMBOLS

A_{load}	Effective area of the load cylinder
F_{cyl1}	Hydraulic force in the work cylinder
F_{cyl2}	Hydraulic force in the spring cylinder
F_{drag}	Friction force between gate and valve seats
$F_{e,SVA}$	Enclosure force
$F_{e,load}$	Hydrostatic force caused by pressure acting on the load cylinder rod
$F_{f,load}$	Friction force of the load cylinder
$F_{f,SVA}$	Friction forces in the SVA
F_W	Weight force of the SVA and load cylinder piston and rods
σ	Standard deviation
F_{seal}	Friction force between the bonnet seals and the stem
F_{spring}	Fail-safe spring force
F_v	Stem expulsion force due to the valve internal pressure
$C_{X,SVA}$	Position controller of the SVA
$C_{V,SVA}$	Velocity controller of the SVA
$C_{\Delta p,load}$	Pressure controller of the load cylinder
$C_{\Delta p,V}$	Feed-forward controller to compensate SVA velocity disturbance in the load force
$R_{\Delta p,load}$	Reference of pressure of the load cylinder
X_{SVA}	SVA position signal
V_{SVA}	SVA velocity signal
Δp_{load}	Load cylinder pressure differential signal
$U_{X,SVA}$	SVA motor control signal
$U_{\Delta p,load}$	Load proportional valve control signal

REFERENCES

[1] Berven, J (2013) Subsea production control systems for all-electric Xmas trees. Master thesis, Universitetet i Stavanger, Norway.

[2] Abicht, D.; Halvorsen, G.; Ramberg, R. M. (2017) Subsea all-electric. Paper presented at Offshore Technology Conference 2017, Houston, 1 – 4 May 2017.

[3] Weber, J. et al. (2016) Novel system architectures by individual drives. Paper presented at 10th International Fluid Power Conference, Dresden, 8 – 10 March 2016.

[4] Alle, N. et. al. (2016) Review on Electro Hydrostatic Actuator for Flight Control. In: International Journal of Fluid Power, Issue 17(2): 125 – 145.

[5] Orth, A.; Hendrix, G. (2018) An electro-mechanical actuator with hydrostatic drive for subsea trees to reduce CAPEX and OPEX with higher reliability and safety levels. Paper presented at Offshore Technology Conference 2018, Houston, 30 April – 3 May 2018.

[6] Mashiba, M. H. D. S. (2011) A influência dos parâmetros de operação e projeto no desempenho de atuação hidráulica de válvulas submarinas do tipo gaveta. Master thesis, Universidade Federal do Rio de Janeiro, Brasil.

[7] Kleppmann, W. (8th) (2013) Versuchsplanung: Produkte und Prozesse optimieren. Hanser, Munich.

[8] European Committee for Standardization (2009) EN ISO 10423 Petroleum and natural gas industries – Drilling and production equipment – Wellhead and Christmas tree equipment. Belgium.

[9] American Petroleum Institute (2017) API Standard 17F Standard for subsea control systems. USA.

[10] Goularte, R. M.; Silva, J. P. D.; De Negri, V. J.; Orth, A. (2018) Static and dynamic performance analysis of an electro-hydrostatic system for ultra-deep water. Paper presented at Rio Oil & Gas 2018, Rio de Janeiro, 24 – 27 September 2018.

[11] European Committee for Standardization (2011) EN ISO 13628-4 Petroleum and natural gas industries – Design and operation of subsea production systems – Part 4: Subsea wellhead and tree equipment. Belgium.

[12] Suisse, B. (2005) Research for dynamic seal friction modeling in linear motion hydraulic

piston applications. Master thesis, The University of Texas at Arlington, Texas, USA.

[13] Plácido Neto, A. (2018) Failure distribution analysis of a novel subsea valve actuator concept based on reliability database. Paper presented at 10th IFAC Symposium on Fault Detection, Supervision and Safety for Technical Processes, Warsaw, 29 – 31 August 2018.

[14] American Petroleum Institute (2017) API Recommended practice 17N Recommended practice on subsea production system reliability, risk and integrity management. USA.

GROUP D

Additive manufacturing

peer reviewed

TRIBOLOGICAL INVESTIGATIONS ON ADDITIVELY MANUFACTURED SURFACES USING EXTREME HIGH-SPEED LASER MATERIAL DEPOSITION (EHLA) AND LASER POWDER BED FUSION (LPBF)

Achill Holzer[1]*, Stephan Koß[2], Gunnar Matthiesen[1], Daniel Merget[2], Stephan Ziegler[2], Johannes Henrich Schleifenbaum[2,3], Katharina Schmitz[1]

[1]*Institute for Fluid Power Drives and Systems, RWTH Aachen University, Germany*
[2]*Digital Additive Production, RWTH Aachen University, Germany*
[3]*Fraunhofer Institute for Laser Technology ILT, Germany*
* Corresponding author: Tel.: +49 241 8047731, E-mail address: achill.holzer@ifas.rwth-aachen.de

ABSTRACT

Today's economic and ecological directives demand for highly sustainable machine parts by low production cost and energy consumption. Consequently, it is crucial to guarantee a long service life by protecting all components against wear and corrosion. However, hydraulic components always include stressed surfaces, which suffer from heavy loads at high relative speeds. To prevent fretting, coating processes like thermal spraying or hard chrome have a long history in the field of hydraulics. New additive laser-based processes like EHLA and LPBF offer the potential to apply new coatings without environmentally hazardous substances such as chromium or to manufacture complex parts with new functionalities. So far, additively manufactured surfaces with relative movements are post-processed to obtain surface qualities similar to subtractive methods, as the tribological properties of additive surfaces have not been investigated to date. Therefore, this paper investigates the frictional behavior of 316L surfaces produced by laser-based EHLA and LPBF processes using a disc-disc tribometer.

Keywords: Tribology, Additive Manufacturing, Hydraulic components, 316L, Wear, Corrosion, LPBF, EHLA

1. INTRODUCTION

Additive Manufacturing (AM) processes are increasingly being used in industrial production. They offers a good opportunity for the production of customer-specific solutions. Since the 1980s, AM was mainly used as a technology for the production of prototypes. Since then, the technology has developed strongly. Manufacturing quality such as density, surface quality and geometric accuracy and also the process speed and reliability have improved. Today, hydraulic components are still produced mostly using subtractive manufacturing technologies. Hydraulic components are often exposed to the environment such as sun, rain, salt water, dust, etc. and should have the longest possible service life. In addition, the friction contacts and supply lines should have the lowest possible resistance so that the losses that occur are small. For these requirements, AM offers new possibilities for the various challenges of applications and components. In the field of fluid drive systems, most components can be divided into two main component geometries, cylindrical and complex 3D geometries. By using Extreme High-Speed Laser Material Deposition (EHLA), surfaces of cylindrical components can be protected against wear and corrosion with new materials and with dense metallurgically bonded coatings. 3D geometries with integrated functions such as cooling and hydraulic fluid lines can be generated using Laser Powder Bed Fusion (LPBF). By using LPBF, the number of individual parts can be reduced, the complexity of the respective components can be increased, and concepts that could not be realized using conventional methods can be implemented. An example of an additively manufactured PowerPack is shown in **Figure 1**.

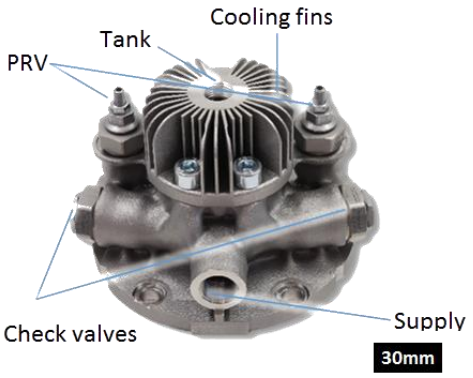

Figure 1: Additively manufactured PowerPack [9]

The central housing accommodates all valves and the gear set of the pump, and all peripheral channels are also integrated into the topology-optimized structure. This design allows for a weight reduction by a factor of four compared to the conventional design with individual blocks connected by pipes. Due to the integrated pump with its rotating components, the challenge arises that tribological contacts with additive surfaces occur here. While the structural or flow-optimal design of such components has been extensively researched, there is a large research gap in the behaviour of tribologically highly stressed additive surfaces. In order to unleash the full potential of additive manufacturing in fluid power, this gap must therefore be closed in order to efficiently produce surfaces in contact with, for example, valve spools, hydraulic cylinders or pistons of a pump. In this work, additively manufactured surfaces without post-processing are to be investigated and characterized with respect to their tribological behaviour.

2. EXTREME HIGH-SPEED LASER MATERIAL DEPOSITION (EHLA)

Extreme High-Speed Laser Material Deposition (EHLA) is a new development based on the Laser Material Deposition (LMD) process. In the LMD process, a molten pool is generated on a metallic substrate by means of laser radiation into which a filler material is added. In this way, components can be coated and 3D geometries can be generated. In the EHLA process, the laser beam energy is absorbed primarily in the filler material and not in the substrate. In this way, the heat-affected zone on the substrate is significantly reduced and unconventional material pairings can be realized. Due to these characteristics, process speeds of up to 500 m/min and layer thicknesses of 20 to 350 µm can be achieved. The coatings are dense and metallurgically bonded to the substrate. **Figure 2** shows the EHLA process principle. The high process speeds are achieved by a rotation of the component. The powder focus is located above the substrate. Due to the increased interaction time between the laser beam and the powder particles, the powder is melted before it reaches the substrate. The energy of the laser beam that is not absorbed in the powder generates a small melt pool with a small heat-affected zone on the substrate. The characteristics of the EHLA process make it well suited as a coating process for wear and corrosion protection coatings, it can serve as one of the substitute processes for the chromium VI process. One area of application for this process is the coating of hydraulic cylinders. So far, EHLA coatings have not been tribologically examined in detail. [1]

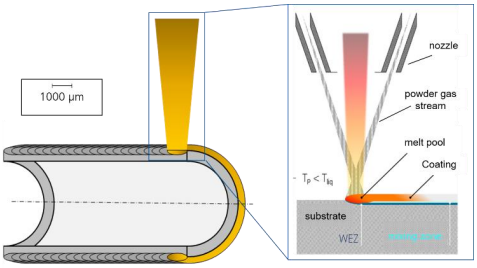

Figure 2: Schematic picture of the EHLA process [1]

For the process development and the coating of the tribo discs, a 4-axis machining system (**Figure 3**) from Hornet is used. In the first step of the process development, 316L coatings consisting of one layer are produced on the base material (42CrMoV4 / 1.7225) and examined metallographically.

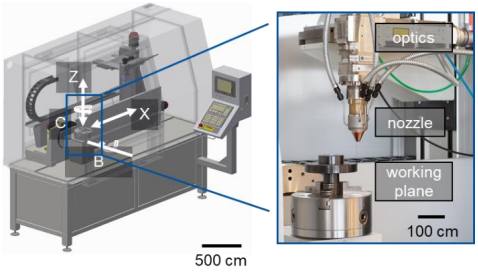

Figure 3: Schematic picture of the EHLA machine

The aim of the process development is to create a pore- and crack-free layer without bonding defects. This includes a variation of the process parameters, e.g. process speed, track displacement, laser power and powder mass flow. For the tribological investigations, coatings with a layer thickness of 1200 ± 100 µm are produced. **Figure 4** depicts a metallographic cross section of the 316L coating as an example of the reflected light microscopic analysis.

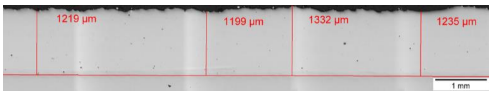

Figure 4: Metallographic cross section of an EHLA coated disc

In a hydraulic application, a much thinner layer would be used to save material and time during the coating process. The coated disc prior to the tribological tests is shown in **Figure 5**. Due to the high process temperatures in the EHLA process, a dense oxide layer has grown.

Figure 5: Surface of the EHLA coated disc

Microscopic investigations (**Figure 6**) using the focus variation method shows a coarse surface with parallel welding beads with a spacing of about 200 µm. Temper colors are also visible. Welding splatters can be observed in a uniform distribution.

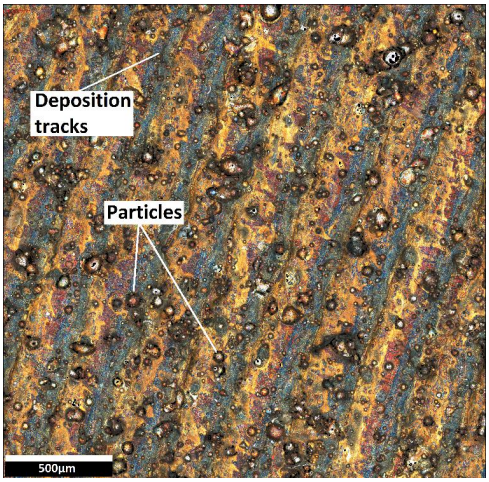

Figure 6: Microscopic view of the EHLA coated disc (magnification 100x)

Generally, a surface like this cannot be considered a suitable tribological contact partner. Because of the high roughness, the real contact area is much smaller than the theoretical area. This leads to extremely high contact pressures.
Roughness measurements of the top layer (**Figure 7**) showed a wavy surface with a wavelength of 40 µm.

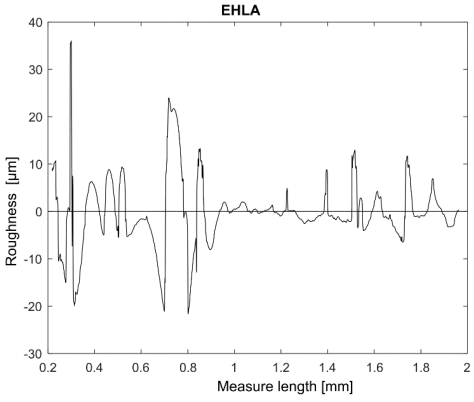

Figure 7: Roughness plot of the EHLA coated disc

For a more accurate layer characterization, the layers were etched with V2A etching solution to analyze the microstructure. The etched cross section of the sample with magnifications of 25x, 200x and 500x is shown in **Figure 8**. The individual layers are visible in the 25x magnification. The material has a dendritic

structure with a growth of grains epitaxial vertically to the surface.

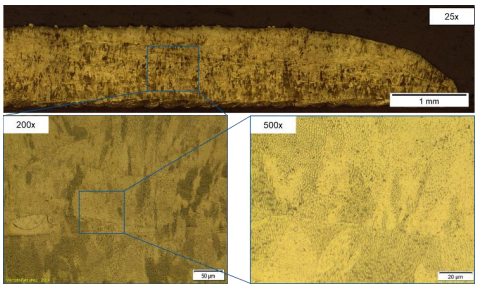

Figure 8: Cross section etched with V2A etching solution

The hardness of the deposited layer was determined using the Vickers method with a test load of 3 N. The mean value of the 6 hardness measurements is approximately 205 HV0,3.

3. LASER POWDER BED FUSION (LPBF)

Laser Powder Bed Fusion (LPBF) is the most common additive manufacturing process for the production of dense metal parts [4]. A part is manufactured by selectively melting consecutive thin layers (approx. 30 µm) of metal powder by a laser beam according to a digital slice model of the part. The process principle is shown in **Figure 9**. A detailed description of the process can be found in [5].

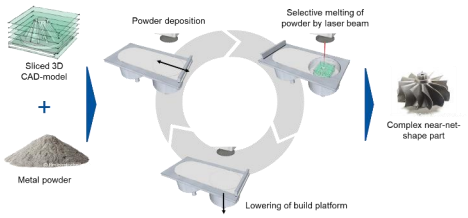

Figure 9: The LPBF process steps [6]

The powder is fully melted in the process, resulting in a relative density usually exceeding 99.5 %. The high cooling rate of up to 7 x 10^6 K/s of the molten material generally leads to a fine and homogeneous microstructure and high strength of the material [7]. Standard mechanical properties of the materials can usually be reached or exceeded. The range of applicable and commercially available materials includes aluminium alloys, stainless and tool steels, nickel-based alloys as well as titanium alloys. The material efficiency of the process is high, as the unmelted powder can be fully reused.

3.1. LPBF Process Parameters

The main process parameters affecting the stability of the build process and the material properties are laser power (P_L), layer thickness (D_S), scan speed (v_S) and hatch distance, the distance between neighboring laser scan vectors (Δy_S), all shown in **Figure 10**.

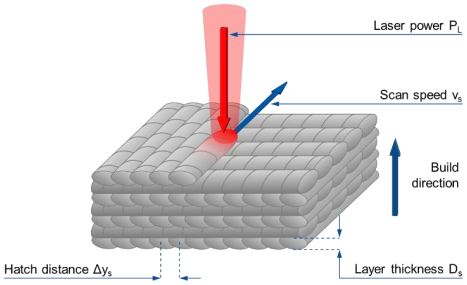

Figure 10: The main LPBF process parameters

The LPBF specimens used in this work were manufactured on an EOS M290 LPBF machine. A fixture was manufactured and mounted on the substrate plate to ensure the correct alignment of the tribo disc preforms to the machine coordinate system and to ensure a sufficient thermal contact to the substrate plate. The preforms were then inserted into the fixtures and the 316L test sections with a thickness of 1 mm were manufactured on the preforms using a layer thickness of D_S = 30 µm.
The LPBF sections were manufactured using an upskin parameter set (different parameters for improved surface roughness) for the surfaces that later act as the tribo surfaces. A coated disc prior to the tribological tests is shown in **Figure 11**.

Figure 11: Surface of the LPBF coated disc

Microscopic investigations (**Figure 12**) using the focus variation method showed a coarse surface with parallel welding beads with a spacing of about 100 µm. Welding splatters can be observed uniformly distributed.

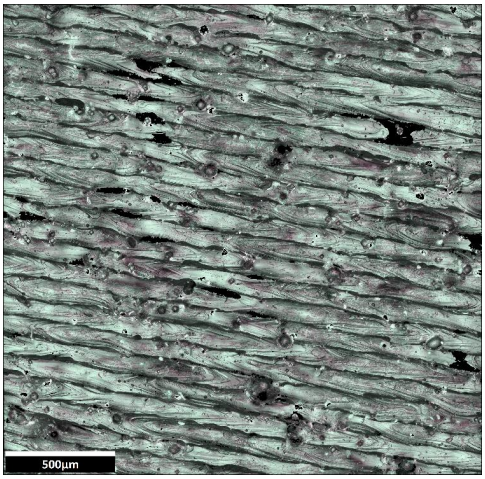

Figure 12: Microscopic view on the LPBF coated disc (magnification 100x)

Roughness measurements of the surface showed a waviness with a periodicity of about 200 µm (see **Figure 13**). Contrary to prior expectations, there is no clear orientation dependence regarding the welding beads.

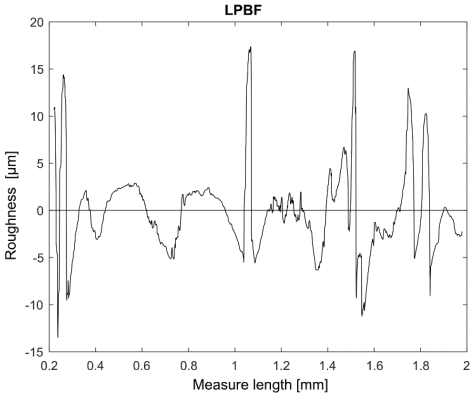

Figure 13: Roughness of the LPBF coated disc

The hardness of the deposited layer was determined using the Vickers method with a test load of 3 N. The mean value of the 6 hardness measurements is approximately 242 HV0,3.
For a more accurate layer characterization, the layers were etched with V2A etching solution and oxalic acid to analyze the microstructure. The etched cross section of the sample with magnifications of 25x, 200x and 500x is shown in **Figure 14**.

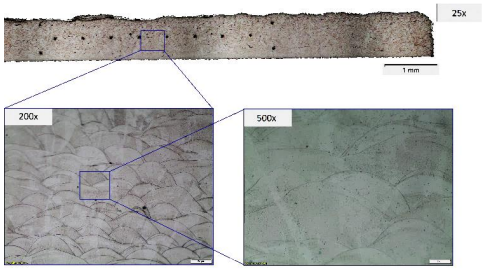

Figure 14: Cross section etched with V2A etching solution and oxalic acid

4. MATERIAL

The 316L-powder used in the EHLA- and LPBF-process consists of spherical particles with a particle diameter in the range of 15 µm – 45 µm. A SEM image showing the typical particle morphology of this type of powder is given in **Figure 15**, a typical particle size distribution in **Figure 16**:

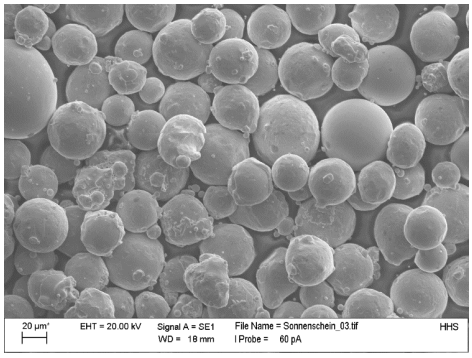

Figure 15: SEM image of typical 316L LPBF powder

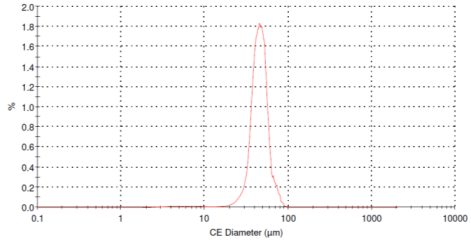

Figure 16: Volume-weighted particle size distribution of typical 316L LPBF powder

316L is an austenitic stainless steel with a very high corrosion resistance. The chemical composition is given in **Table 1**:

Table 1: Chemical composition of 316L [10]

C	Si	Mn	P	S	Cr	Mo	Ni	Fe
≤ %	≤ %	≤ %	≤ %	≤ %	%	%	%	%
0.03	1.0	2.0	0.045	0.015	16.5 - 18.5	2.0 - 2.5	10.0 - 13.0	Bal.

316L was chosen for this work as it is one of the most widely used alloys in AM, especially for the LPBF-process.

5. TRIBOLOGIC SYSTEM WITH A FOCUS ON HYDRAULIC SYSTEMS

Due to varying pressures and rotational speed levels, all states of friction can occur in tribological contacts in hydraulic units. Starting with boundary lubrication in the very first moment after the speed-up, followed by a phase of mixed lubrication, a purely hydrodynamic lubrication is aimed for in the steady-state of operating. A high pressure oil supply often allows for the use of hydrostatic bearings or pockets. Nevertheless the use of lead-free materials leads to new challenges in choosing materials. According to Czichos, planar contact pressures can be between $1 \cdot 10^{-3}$ and $4 \cdot 10^{3}$ MPa [2].

5.1. Tribological investigations

Wear measurements can be made by different approaches. Wear can be defined as material loss per sliding distance as shown in **Equation 1**:

$$w = \frac{dm}{dx}\frac{1}{\rho} \tag{1}$$

Whereas the wear over time can be seen as

$$\dot{w} = \frac{d\dot{m}}{dx}\frac{1}{\rho} \tag{2}$$

The test bench currently does not allow for the measurement of the material loss online. Therefore the tribo discs have to be dismounted periodically and weighed externally. Alternatively, wear can be defined as loss of thickness per sliding distance.

$$w = \frac{ds}{dx} \tag{3}$$

The loss of thickness is measured by comparing the primary surface profile inside and outside the tribologically active area.

5.2. Disc – Disc Tribometer

A wide range of tribological contacts in hydraulic systems can be simplified as planar contacts, which can be investigated using a disc - disc tribometer as it is used at ifas (see [3]), turning two discs with a speed up to 15 m/s and contact pressure up to 40 MPa.

The disc – disc tribometer consists of a stator and a rotor, which are pressed together using a hydraulic cylinder. For geometrical details see **Table 2.** The applied normal force is constantly regulated by a normal force sensor. The rotor is driven by a hydraulic motor and transmits its torque to the stator which is connected to a force sensor using a lever. Both discs are completely covered with a specific test fluid which is temperature regulated and constantly filtered (see **Figure 17**).

Table 2: Parameters of the tribo discs

Geometric parameter	Value
Contact area A_c	946 mm²
Outer diameter d_a	70 mm
Inner diameter d_i	59 mm
Roughness R_a (reference disc)	0.4 µm

Knowing the frictional force and the normal force, a dimensionless friction coefficient can be calculated:

$$f = \frac{F_R}{F_N} \tag{5}$$

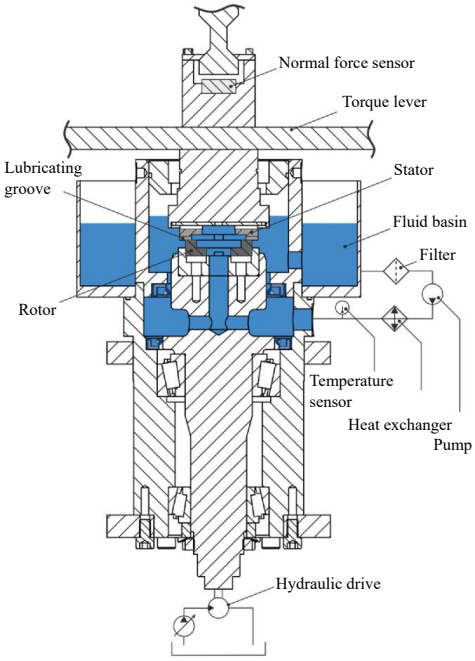

Figure 17: Cross section of the disc - disc tribometer [3]

5.3. Reference measurements

For generating reference measurements, a standard quenched and tempered steel, 42CrMoV4 (1.7225) is used, which is shown in **Figure 18**. The tribologically active surfaces have been lapped to a surface roughness of R_a 0.4. This surface can be considered a standard tribological contact partner in hydraulic applications. By now it is not possible to use hard-hard pairings under extreme pressure for longer times. All measurements have been carried out using a Shell standard mineral hydraulic oil HLP with a viscosity of 32 according to DIN 51524-2. Over the different tests the temperature was kept at 40° Celsius.

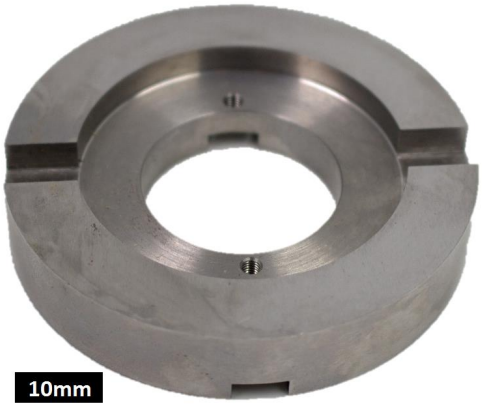

Figure 18: Surface of the reference disc

The status of the surface prior to the test runs is shown in **Figure 19** and **Figure 20**.

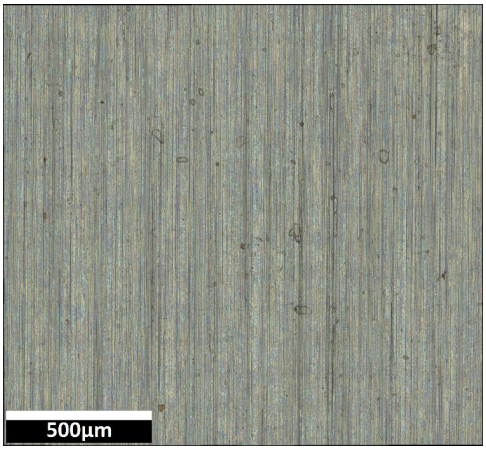

Figure 19: Microscopic view of the reference disc (magnification 100x)

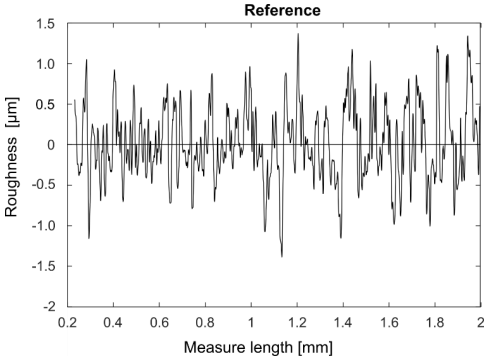

Figure 20: Roughness of the reference disc

6. MEASUREMENT RESULTS EHLA

After a run-in of 30 minutes at 100 rpm with a very low load of 100 N, equivalent to a contact pressure of 0.1 MPa, a visual check of the tribo disc surface revealed severe wear between the EHLA and EHLA surfaces. Between the EHLA and the reference surface, the wear is very low.

Figure 21: Wear track on the EHLA disc against the reference disc

6.1. EHLA against Reference

Testing the EHLA coated tribo disc against the reference disc shows a very good result. The wear for this pairing is very low, although the rather low contact pressure and the very slow sliding speed have to be considered. Tests with more realistic speeds and loads are planned in the future. The material loss is 0,097 g for a sliding distance of 1 km. The profile is shown in **Figure 22**.

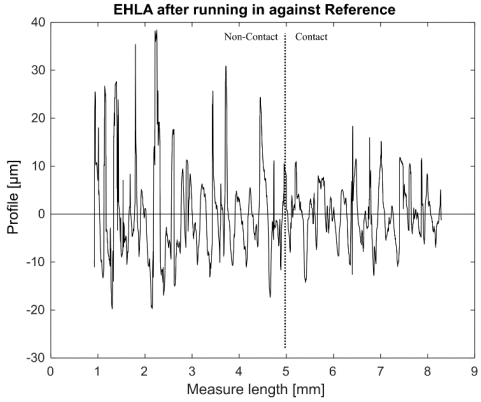

Figure 22: Profile of the EHLA disc after the run-in

The profile shows a very small loss of material. Basically the welding beads have been flattened during the process.

6.2. EHLA against EHLA

The measured results of the EHLA against EHLA surface are definitely not as good as the results against the reference material. This can be explained with the used material itself. Generally, a tribological pairing should not consist of pairing partners consisting of the same material, as there is always a potential for welding. 316L steel in particular is known to have a tendency for welding. **Figure 23** shows the profile of the EHLA disc after the run-in.

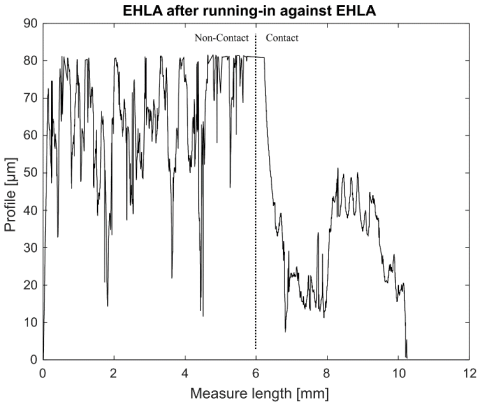

Figure 23: Profile of the EHLA disc after the run-in

The material loss is 0,387 g for a sliding distance of 1 km.

7. MEASUREMENT RESULTS LPBF

After a run-in of 30 minutes at 100 rpm with a very low load of 100 N, equivalent to a contact pressure of 0.1 MPa, a visual check of the tribo surface revealed severe wear on both pairings (LPBF-LPBF and LPBF-reference). One wear track is shown in **Figure 24**.

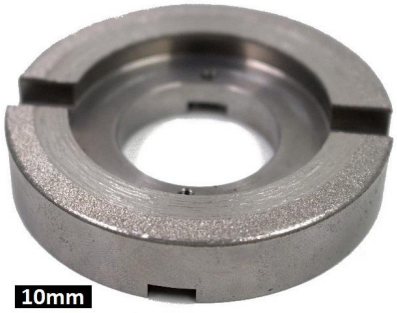

Figure 24: Wear track on the LPBF disc

7.1. LPBF against Reference

A visual check of the tribo surface revealed definitely more than a flattening of the welding beads. Measurements of the profile of the surface (**Figure 25**) show a material loss of around 80 µm for a sliding distance of 1 km.

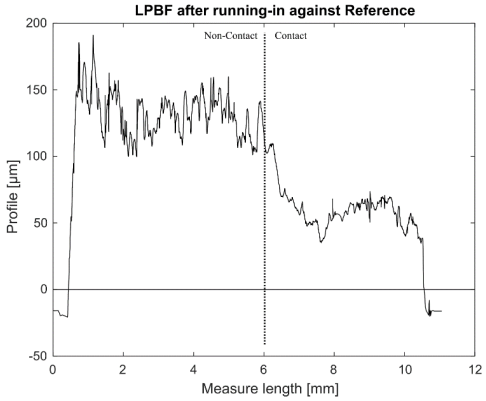

Figure 25: Profile of the SLM disc after run-in

The material loss was 0,297 g for a sliding distance of 1 km.

7.2. LPBF against LPBF

Compared to the reference disc, LPBF against LPBF is also prone to welding. Measuring the profile of the surface (**Figure 26**) shows a material loss of around 70 µm.

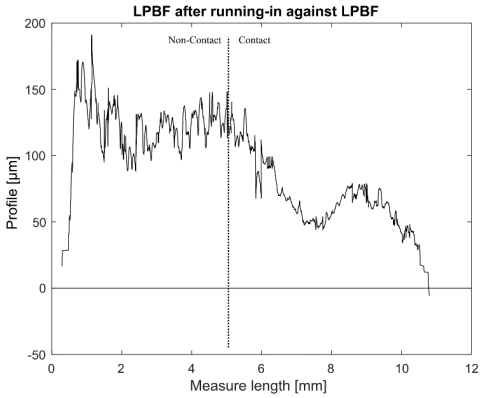

Figure 26: Profile of the LPBF disc after run-in

The material loss was 0,346 g for a sliding distance of 1 km.

8. CONCLUSION AND OUTLOOK

First investigations on the tribological properties of 316L stainless steel surfaces manufactured additively by EHLA and LPBF showed several problems.

By now it is not possible to use said materials “as printed” for tribological contacts. A good indicator for the endurance of tribological systems is the diagram of Vogelpohl [8], which compares different standard pairings by their wear rate measured in µm per km sliding distance. To have an overview, the results of the measured samples in this work have been added to the diagram (**Figure 27**).

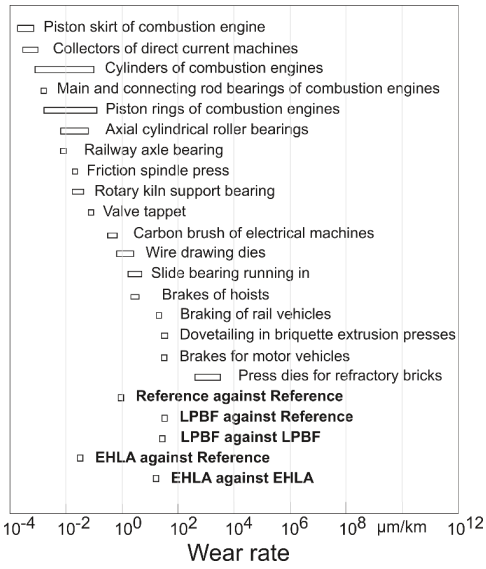

Figure 27: Typical wear rates according to Vogelpohl [8] compared with the tested samples

Nevertheless, the ability of printing complete pump assemblies in one single 3d-print job without any post-treatment would enable a fully automatic and cost optimized production process for hydraulic units.
Further investigations with several post-treatments like laser remelting and grinding are ongoing.

NOMENCLATURE

A	Area [mm^2]
AM	Additive Manufacturing
D_S	Layer Thickness [µm]
Δy_S	Hatch Distance [µm]
EHLA	High-Speed Laser Material Deposition
f	Coefficient of Friction [-]
Fn	Normal Force [N]
Fr	Friction Force [N]
HV	Vickers Hardness
LPBF	Laser Powder Bed Fusion
Mr	Friction Torque [Nm]
P_L	Laser Power [W]
v	Average Sliding Speed [m/s]
v_S	Scan Speed [m/s]
w	Total Wear [mg]
σ	Contact Pressure [N/mm^2]

REFERENCES

[1] Schopphoven, T., Gasser, A., Wissenbach,K., Poprawe, R. (2016): "Investigations on ultra-high-speed laser material deposition as alternative for hard chrome plating and thermal spraying", Journal of Laser Applications, Vol. 28 no 2.

[2] Czichos, H.; Habig, K-H. (Hg.) (2015): "Tribologie-Handbuch. Tribometrie, Tribomaterialien, Tribotechnik". 4., vollst. überarb. und erw. Aufl. Wiesbaden: Springer Vieweg.

[3] Otto, N (2018) "Experimental Analysis of Sustainable Ester- and Water-Based Hydraulic Fluids", PhD thesis, RWTH Aachen University, Germany.

[4] Wohlers Associates. Wohlers Report 2017-"3D Printing and Additive Manufacturing State of the Industry - Annual Worldwide Progress Repor"t. Fort Collins, Colorado, USA, 2017.

[5] Meiners, W. "Direktes Selektives Laser Sintern einkomponentiger metallischer Werkstoffe" Dissertation, Aachen, Germany, Shaker Verlag, 1999.

[6] Schleifenbaum, H., Meiners, W., Wissenbach, K. and Hinke,C. „Individualized production by means of high power Selective Laser Melting." CIRP Journal of manufacturing science and technology, Bd. 2, Nr. 3, 2010.

[7] Buchbinder, D. „Generative Fertigung von Aluminiumbauteilen für die Serienproduktion - AluGenerativ". Final project report, Aachen, 2010.

[8] Vogelpohl, G.: "Verschleißmaß und Verschleißspektrum. Forschungsergebnissen". Forsch. Ing.-Wes. 35 (1969) 1, S. 1 – 6.

[9] Matthiesen, G., Merget, D., Pietrzyk, T., Schleifenbaum, J.H., Schmitz, K. (2020), „Design and experimental investigation of an additive manufactured", 12th International Fluid Power Conference, Dresden, March 9-11, 2020, Dresden, Germany

[10] http://www.m-woite.de/de/werkstoffe/14404.shtml, Accessed 15 November 2019

peer reviewed

ASSESSMENT OF FRICTION LOSS TO HORIZONTALLY BUILT FLUID PASSAGES USING ADDITIVE MANUFACTURING

Yi Zhu*, Lei Zhou, Lei Zhang, Cong Zhao, Zimu Wang, Huayong Yang

State key laboratory of fluid power and mechatronic systems, Zhejiang University, 38 Zheda Road, 310027 Hangzhou, China

* Corresponding author: Tel.: +86 18694580181; E-mail address: yiz@zju.edu.cn

ABSTRACT

Selective laser melting (SLM), is a type of additive manufacturing, which selectively melts a pre-spread layer of metal powders and produce a part by a layer-on-layer manner. SLM has demonstrated a great potential to reduce size and weight in hydraulic manifolds. However, a theoretical base is lacking since friction loss is unclear in a SLMed fluid passage. In this study, various fluid passages without supports, from diameters from 4 mm to 16 mm, were produced horizontally using SLM. The profile was measured using a 3D scanner and surface roughness was measured using a confocal laser scanning microscope. Friction factor was studied using simulation, experiments, and classical theory. The hydraulic diameter of the SLMed passages is smaller than the design diameter. Surface roughness is extremely high on the top part of the inner wall while the rest part is around 10 μm. Such trends are irrelevant of passage diameters. Friction factors in SLMed passage is much larger than those predicted using Moody theory, particularly in laminar flow. The transition from laminar flow to turbulent flow appears at a smaller Reynolds number with increased passage diameter. The influence of the profile overweighs that of the surface roughness on friction factor.

Keywords: hydraulic manifold; fluid passage; selective laser melting; friction factor

1. INTRODUCTION

Selective laser melting (SLM), as one type of metal additive manufacturing (AM), has drawn interests from hydraulic industries as it could make hydraulic components small and light, which is important to the power-to-mass ratio of hydraulic systems [1–3]. One advantage of AM technology lies in the great design freedom of flow paths compared to conventional machining. However, internal supports in the overhang regions of fluid passages are necessary to avoid fabricating defects and failures in SLM according to the residue stress-induced deformation [4,5]. In SLM design, fluid passages are often curved in order to reduce size and weight. Therefore, those support structures are impossible to be removed by post-processing due to lack of accessibility [6]. SLM passages should be processed without any internal support structures. On the other hand, fluid passages in a hydraulic manifold are often multi-directional which cannot be all built vertically (i.e. when the passage axis is parallel to the building direction) to avoid internal support structures.

Horizontal fluid passages have the largest overhang regions thus are the most difficult to process. Both large shape deviations and high surface roughness are observed [6,7]. Schmelzle et al. [8] proposed non-circular passages (e.g. diamond, teardrop shapes) in a SLM hydraulic manifold which great reduce the overhang regions. However, ideal circular passages have the highest flow capacity and the least stress concentration on the wall compared to any non-circular passages. The influence of a horizontal SLM fluid passage (without supports) on the friction loss becomes critical in designing SLM hydraulic manifolds.

Some work was performed focusing on SLM cooling channels which do not only consider heat transfer effects but also friction loss [7,9–11]. Snyder et al. [7,9] studied the influence of the building directions on the geometric tolerance and surface roughness, and experimentally measured the resultant friction factor of air flow. The authors found that the building direction greatly influence the dimensional tolerance and

surface roughness which further affects transition between flow regimes. The horizontal cylindrical channels have the highest friction factor while the vertical channels have the lowest. Stimpson et al. [10,11] studied the characterization of SLM rectangular channels built diagonally using Inconel 718 and CoCr. They analyzed that influence of materials, upskin and downskin surface on the dimensional tolerance and surface roughness. Friction factor was also measured. Results indicated that the friction factor of the SLM channels is higher than that of laminar flow theory in the low Reynolds number while in the turbulent region the difference in the SLM channels is large. A corrected relation between the friction factor and R_a/D_h was also developed. However, all the work was based on a few types of mini channels (diameter or equivalent diameter < 2 mm). Fluid passages used in most hydraulic industries have much larger diameters which are more difficult to build horizontally using SLM. Kamat et al. [6] studied the horizontal built circular, diamond, and teardrop channels with 12 mm diameter. The shape deviation, particularly on the top of the channels, was found to be critical due to residual stress-induced curling and dross formation in the large overhang regimes. The authors developed an analytical tool to compensate the deformation. However, the high surface roughness and resultant fluid flow were not discussed.

This study presents the friction factor characterization of horizontal SLM hydraulic passages with various diameters. Profile deviation and surface roughness were measured. Friction factor was investigated using computational fluid dynamics simulation and experiments. The work helps to develop design criteria for novel hydraulic components using SLM.

2. METHODS

2.1. Horizontal fluid passage fabrication

The fluid passage samples with various diameters (4, 6, 8, 10, 12, 14, 16 mm) were fabricated using SLM. Those diameters were selected since they are commonly used in industrial hydraulic systems. The length of each passage is 130 mm. The wall thickness of each passage is 2 mm. The building orientation is shown in **Fig. 1**. All fluid passages were built using the same height and design of external support structures on the bottom. No internal support structures were added to any fluid passages. Some samples were also fabricated using the same design and procedure with a short length of 10 mm for surface and profile measurements. The SLM fabrication was performed using a Renishaw (UK) AM250 laser melting unit comprised of an SPI redPOWER 200 W ytterbium fiber laser, an automatic powder layering system, an argon gas protection system, and a process control system. The laser operated with a 70 mm focused beam diameter at a 1071 nm wavelength. A schematic of the SLM system is shown in **Fig. 2**. It is noted that the roller recoats the powder layer from back to forth (where the observation window is) in the Renishaw system which differs from other systems. 316L stainless steel was used in the work. The powder characterization was introduced in our previous work [12–14]. The process parameters used in the study was listed in **Table 1**.

Figure 1: Building orientation of the fluid passages

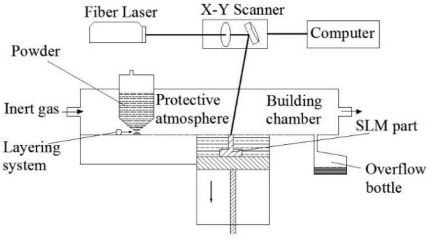

Figure 2: A schematic of SLM system used in the work [13].

Table 1: Process parameters used in the work

Laser power	Layer thickness	Point distance	Exposure time	Hatch space	Scan strategy
200 W	50 µm	65 µm	80 µs	80 µm	Stripes

2.2. Measurements of profile and surface topography of fluid passages

Though all the fluid passage samples were designed with a circular-shape cross section, the as-built samples have geometry errors caused by curling and dross formation on the overhang regimes. Moreover, the inner wall surface of the passage is very rough, particularly on the top part. The profile of each fluid passage sample was measured using an optical 3D scanner (OKIO-3M, Shining 3D Ltd, China) as shown in **Fig. 3**. The 3D scanner has measuring accuracy of 0.005 mm and a scanning distance of 0.04 mm. A commercial software Geomagic Control X was used to analyze the measured profiles of all fluid passages. Hydraulic diameter, which is commonly used to evaluate the flow capacity of non-circular passages, was calculated using profile data. Thus, an optical 3D scanner is used in the work which is not only efficient in measuring profiles of many samples but also low cost compared to the commonly used industrial CT scanner for evaluating the quality of SLM parts. The surface roughness measurements were performed using a confocal laser scanning microscopy (VK150, Keyence, Japan) on four spots of each sample: top, bottom, left, and right, which are shown in Fig. 4. It is noted that those extra samples were produced under the same conditions as the fluid passages. Each measurement was performed by scanning a 1 mm × 1.39 mm area. Such measurement was repeated three times on each spot of the sample along the axial direction. S_a, a 3D surface roughness parameter represents arithmetical mean height, was calculated while the S filter was set to 5μm and the L filter was set to 2 mm. It is noted that S_a is the extension of R_a (arithmetical mean height of a line, 2D) to a 3D surface.

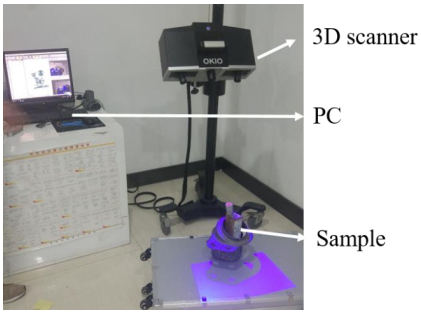

Figure 3: Scanning the sample profile using a 3D scanner (photo taken by L. Zhang).

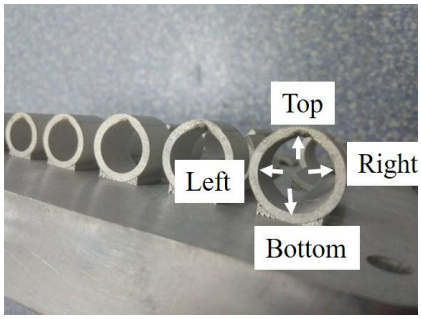

Figure 4: The location of surface roughness measurements by white arrows.

2.3. Simulation

The subject of simulation is to formulate a full map between friction factor, passage diameter, and Reynold number. However, the accuracy of the simulation in terms of friction factor greatly depends on the mesh generation which may cause extremely long computational time. Moreover, the input to the simulation, e.g., the profile data and surface roughness, has simplified compared to the real situation. Therefore, the simulation in the study is mainly used to give a reference and calculate the local loss in the rig in addition to the friction loss in the passage.

The simulation was performed using CFX in ANSYS. Taken the 10 mm (design diameter) SLMed fluid passage for example, unstructured mesh was designed to obtain a ratio between the element size and the minimum passage diameter to be 0.04. The boundary layer was meshed near the internal walls where the friction loss is mainly generated. The parameters in inflation were set to 0.01 mm as the first layer thickness, 26 as the maximum layers, and 1.05 as the growth rate. **Table 2** shows the number of nodes and elements used in the simulation. Simulation of fluid passages with other diameters was run on similar conditions.

Table 2: Mesh characteristics for the CFD analysis with a "mesh ratio" of 0.04

Mesh Ratio: Element Size/Minimum Channel Diameter	0.04
Number of nodes	3,476,468
Number of elements	15,149,160

The fluid used in the simulation is 46# hydraulic oil, which has a kinematic viscosity at 40° of 46 cSt and a density of 860 kg/m3. The imposed boundary conditions were the flow rate used in

the experiments at the inlet and 1 MPa pressure at the outlet. The measured passage profile and surface roughness were given as inputs to the model in the simulation. In addition, k-ω model was used as the turbulence model because it is a model for small Reynolds number, which performs well for hydraulic systems [15].

In the numerical analyze, a fully developed flow was assumed in the measuring length. A finer mesh was also used to generate meshes and run the simulation. Results indicated that the pressure difference between using current mesh (with mesh ratio 0.04) and a finer mesh (with mesh ratio < 0.04) is below the accuracy of the sensors used for measuring pressure loss in the experiments (0.012 MPa). This has confirmed that the current mesh generated does not decrease the simulation accuracy with a reasonable computational time.

2.4. Experimental details

The pressure loss of the fluid passages with various diameters was measured using a customized test rig as shown in Fig. 5. It can be found that the measured pressure loss P_s includes the actually pressure loss along the SLM passage P_0 and the local loss in the measuring equipment. The local loss is calculated in the above-mentioned simulation.

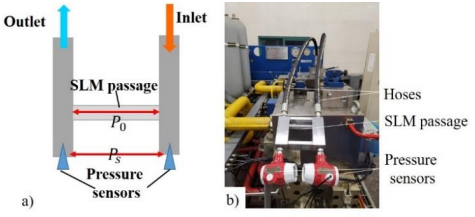

Figure 5: a) Schematic of the test rig; b) a photo showing the test rig.

The friction factor l can be calculated using Equation 1:

$$\lambda = \frac{2dP_0}{l\rho v^2} \quad (1)$$

where d is the hydraulic diameter; l is the passage length; ρ is the density of the fluid; v is the average velocity of the fluid.

3. RESULTS

3.1. Measuring results

The hydraulic diameter results are shown in **Fig. 6**. The relative discrepancy between the design diameter and hydraulic diameter is also illustrated. The results clearly indicate that the geometry errors decrease with increased passage diameters. The diameter difference between the design and the fabricated passages does not vary much.

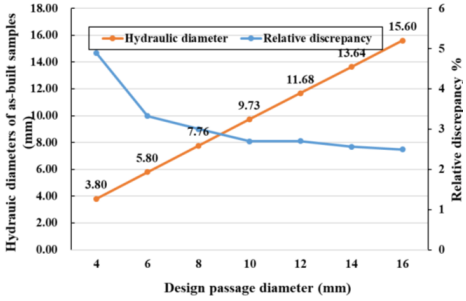

Figure 6: Results of hydraulic diameters

Surface roughness of the four location, top, right, left, and bottom, in each fluid passage are shown in **Fig. 7**. The roughness on the top part is extremely high, from approximately 60 to 80 µm. The surface roughness of the rest, right, left, and bottom, are approximately 10 µm with slight variations, which does not show dependency on the passage diameters. From empirical friction loss calculation of laminar flow, the surface roughness is considered to be below 20 µm using conventional machining for any metal fluid passages in hydraulic systems. Therefore, the surface roughness of the top part creates large difference compared to the conventionally machined fluid passages.

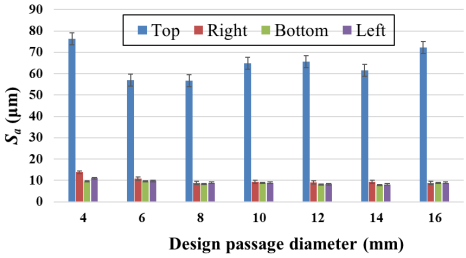

Figure 7: Results of surface roughness

3.2. Friction factor results

Due to the manufacturing discrepancy, the dimensional accuracy of the passage profile varies which is also observed in [7]. Therefore, the passage diameter (or hydraulic diameter) *d* used in Reynolds number is not a constant for

SLMed fluid passages. The variation is related to some manufacturing factors, e.g., building directions, passage structures, and process parameters. Since the influence of the passage diameter cannot be fully represented in the Reynolds number, the friction factor curve of each fluid passage is plotted. A 3D map of the friction factor versus passage diameter and Reynold number is shown in **Fig. 8**. The trends, in general, is similar to the classical Moody diagram. However, it can be seen that the transition from laminar flow to turbulent flow appears at a smaller Reynold number with increased passage diameter. The transition is highlighted using a red dot in **Fig. 8**. The friction factor seems to increase with increased passage diameter which conflicts the classical theory. It may due to the fact that with increased diameter, the friction loss greatly reduces, while the local loss becomes a dominating factor in the total pressure loss measurements. A future work needs to be performed to modify the test rig.

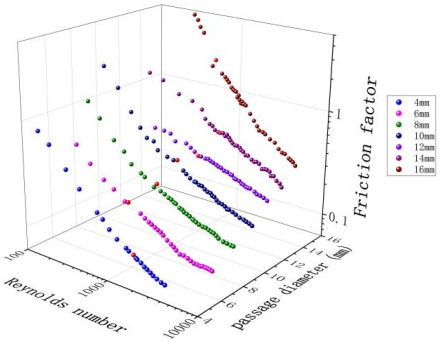

Figure 8: 3D map of friction factor.

Figs. 9-11 show the friction factors obtained from experimental results (blue dots), simulation results (red dots), and classical theory (black solid line for laminar flow and black dashed line for turbulent flow) in three SLMed fluid passages with diameters of 6, 8, and 10 mm. In the classical theory, 75/Re (empirical equation) is used to calculate the friction factor in laminar flow and Blasius equation is used to calculate the friction factor in turbulent flow inside a smooth passage. Compared the experimental results with classical theory of smooth passages, the friction factor of the SLMed passages is much higher. The transition from laminar to turbulent flow of SLMed passages appears at Re~900 which is much smaller than the classical theory. The friction factors obtained from simulations are between the experimental results and the classical theory. With increased passage diameter, the difference between simulation and experimental results decreases.

The experimental results are also plotted with corrected empirical equation (green solid line) and Colebrook equation (green dashed line). The Colebrook equation can be written as:

$$\frac{1}{\sqrt{\lambda}} = -2\lg\left(\frac{\Delta}{3.7d} + \frac{2.51}{\mathrm{Re}\sqrt{\lambda}}\right) \quad (2)$$

where Δ is the roughness parameter. In the laminar flow, the corrected empirical equation indicates a large slope, which becomes even steeper with increased fluid diameters. It is noted that a constant hydraulic diameter in Reynolds number does not fully reflect the actual diameter in a SLMed passage due to manufacturing discrepancy. Thus, fluid passages with different diameters have different equations in the laminar flow. In the turbulent flow, Sa value of the top surface has been selected as the roughness parameter Δ. However, quite large discrepancy can be found between experimental results and Colebrook equations. It is noted the difference between the two becomes even greater with a reduced roughness parameter.

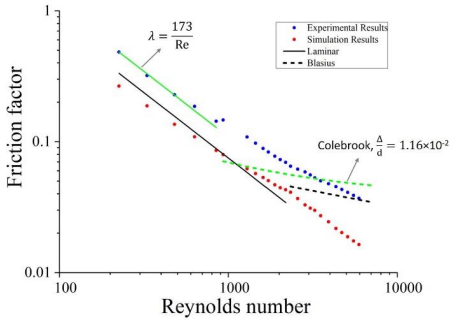

Figure 9: Friction factor comparison of a 6 mm SLMed fluid passage.

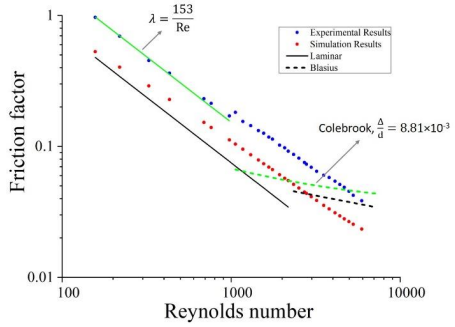

Figure 10: Friction factor comparison of a 8 mm SLMed fluid passage.

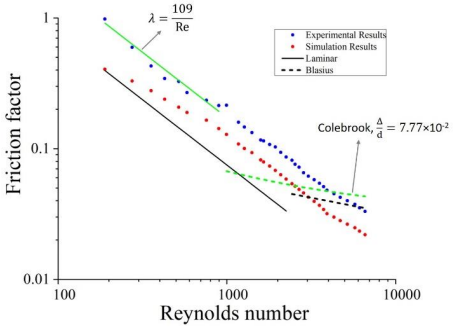

Figure 11: Friction factor comparison of a 10 mm SLMed fluid passage.

4. DISCUSSION

As already pointed out by many researchers [16–18], a large overhang region is subjected to dross formation and curling on the downskin part using SLM technology. As a guideline which is widely used in many SLM systems, manufacturing failure may appear for overhang regions larger than 5 mm. Horizontal fluid passage without supports is one type of overhang structures. According to the produced sample, fluid passage with 16 mm diameter can be fabricated without supports. A 20 mm diameter passage can also be fabricated which is not mentioned in this study. Therefore, the manufacturability of horizontal fluid passages without supports is much beyond the expectation of common design guidelines. On the other hand, dimensional error in the profile seems to be irrelevant to the passage diameter. Moreover, surface roughness shows very similar characteristics among all SLMed fluid passages. Surface roughness on the downskin part is extremely high compared to the other parts, and the roughness value is irrelevant to the passage diameter. Thus, the influence of profile and surface roughness on the fluid flow is more critical for small-diameter passages.

Figs. 9-11 indicate that the SLMed fluid passages do not behave like normal rough channels. Classical theory does not give acceptable results compared to the experiments. The influence of the profile on the friction factor can be clearly seen in the laminar flow. The hydraulic diameter in Reynolds number cannot fully reflect the manufacturing discrepancy. Therefore, each fluid passage has different empirical equation in laminar flow. A more accurate method is required to assess the influence of the profile. Both profile and surface roughness affect the friction factor in turbulent flow. However, large discrepancy still exists even a downskin roughness is used in the Colebrook equation. Therefore, the influence of the profile on the friction factor in turbulent flow is great which also needs a further study.

5. CONCLUSIONS

Various fluid passages from 4 mm to 16 mm without supports were produced horizontally using SLM. Friction factor in the fluid passages is studied using simulation, experiments, and classical theory. The effect of profile and surface roughness is discussed. The study allows the following conclusions to be drawn:

- Curling was observed for on the top part of all SLMed passages. The hydraulic diameter is smaller than the design diameter.
- Surface roughness is extremely high on the top part, which is at least four times higher than the rest part of the inner wall.
- Friction factors in SLMed passage is much larger than those predicted using Moody theory, particularly in laminar flow.
- The transition from laminar flow to turbulent flow appears at a smaller Reynolds number compared to the classical theory. For SLMed fluid passages, the transition appears at a smaller Reynolds number with increased passage diameters.
- The influence of the profile overweighs that of the surface roughness on friction factor.

Many future works are required: 1 to improve manufacturing quality by optimizing process

parameters and to study the friction factor of improved ones; 2 to upgrade the test rig; 3 to study the manufacturing and friction factor of curved fluid passages in different building directions. A design tool of SLMed fluid passage is the final subject which cannot achieved without a friction factor model.

REFERENCES

[1] Https://www.moog.com/3dmetal/index.html, Moog additive overview, (n.d.).

[2] Https://www.renishaw.com/en/hydraulic-block-manifold-redesign-for-additive-manufacturing--38949, Hydraulic block manifold redesign for additive manufacturing, (n.d.).

[3] Https://www.aidro.it/3d-metal-printing.html, Aidro hydraulics and 3D printing, (n.d.).

[4] B. Vandenbroucke, J. Kruth, Selective laser melting of biocompatible metals for rapid manufacturing of medical parts, Rapid Prototyping Journal. 13 (2007) 196–203. doi:10.1108/13552540710776142.

[5] P. Mercelis, J.P. Kruth, Residual stresses in selective laser sintering and selective laser melting, Rapid Prototyping Journal. 12 (2006) 254–265. doi:10.1108/13552540610707013.

[6] A.M. Kamat, Y. Pei, An analytical method to predict and compensate for residual stress-induced deformation in overhanging regions of internal channels fabricated using powder bed fusion, Additive Manufacturing. 29 (2019) 100796. doi:10.1016/j.addma.2019.100796.

[7] J.C. Snyder, C.K. Stimpson, K.A. Thole, D.J. Mongillo, Build Direction Effects on Microchannel Tolerance and Surface Roughness, Journal of Mechanical Design. 137 (2015) 111411. doi:10.1115/1.4031071.

[8] J. Schmelzle, E. V Kline, C.J. Dickman, E.W. Reutzel, G. Jones, T.W. Simpson, (Re)Designing for Part Consolidation: Understanding the Challenges of Metal Additive Manufacturing, Journal of Mechanical Design. 137 (2015) 111404. doi:10.1115/1.4031156.

[9] J.C. Snyder, C.K. Stimpson, K.A. Thole, D. Mongillo, Build Direction Effects on Additively Manufactured Channels, Journal of Turbomachinery. 138 (2016) 051006. doi:10.1115/1.4032168.

[10] C.K. Stimpson, J.C. Snyder, K.A. Thole, D. Mongillo, Scaling Roughness Effects on Pressure Loss and Heat Transfer of Additively Manufactured Channels, Journal of Turbomachinery. 139 (2016) 021003. doi:10.1115/1.4034555.

[11] C.K. Stimpson, J.C. Snyder, K.A. Thole, D. Mongillo, Roughness Effects on Flow and Heat Transfer for Additively Manufactured Channels, Journal of Turbomachinery. 138 (2016) 051008. doi:10.1115/1.4032167.

[12] Y. Zhu, T. Peng, G. Jia, H. Zhang, S. Xu, H. Yang, Electrical energy consumption and mechanical properties of selective-laser-melting-produced 316L stainless steel samples using various processing parameters, Journal of Cleaner Production. 208 (2019) 77–85. doi:10.1016/j.jclepro.2018.10.109.

[13] Y. Yang, Y. Zhu, M.M. Khonsari, H. Yang, Wear anisotropy of selective laser melted 316L stainless steel, Wear. 428–429 (2019) 376–386. doi:10.1016/j.wear.2019.04.001.

[14] Y. Zhu, Y. Yang, X. Mu, W. Wang, Z. Yao, H. Yang, Study on wear and RCF performance of repaired damage railway wheels: Assessing laser cladding to repair local defects on wheels, Wear. 430–431 (2019) 126–136. doi:10.1016/j.wear.2019.04.028.

[15] B. Zardin, G. Cillo, M. Borghi, A. D'Adamo, S. Fontanesi, Pressure losses in multiple-elbow paths and in V-bends of hydraulic manifolds, Energies. 10 (2017). doi:10.3390/en10060788.

[16] J. Kranz, D. Herzog, C. Emmelmann, Design guidelines for laser additive manufacturing of lightweight structures in TiAl6V4, Journal of Laser Applications. 27 (2015) S14001. doi:10.2351/1.4885235.

[17] D. Wang, Y. Yang, Z. Yi, X. Su, Research on the fabricating quality optimization of the overhanging surface in SLM process, International Journal of Advanced Manufacturing Technology. 65 (2013) 1471–1484. doi:10.1007/s00170-012-4271-4.

[18] D. Thomas, The Development of Design Rules for Selective Laser Melting, University of Wales Institute, Cardiff, 2009.

peer reviewed

DESIGN AND EXPERIMENTAL INVESTIGATION OF AN ADDITIVE MANUFACTURED COMPACT DRIVE

Gunnar Matthiesen[1]*; Daniel Merget[2]; Tobias Pietrzyk[1]; Stephan Ziegler[2]; Johannes Henrich Schleifenbaum[2,3]; Katharina Schmitz[1]

[1] *Institute for Fluid Power Drives and Systems, RWTH Aachen University, Germany*
[2] *Digital Additive Production, RWTH Aachen University, Germany*
[3] *Fraunhofer Institute for Laser Technology ILT, Germany*
* Corresponding author: Tel.: +49 241 8047730, E-mail address: gunnar.matthiesen@ifas.rwth-aachen.de

ABSTRACT

In recent years, additive manufacturing (AM) has become one of the most revolutionary and promising technologies in manufacturing. The process of making a product layer by layer is also often referred to as 3D printing. Once employed purely for prototyping, AM is now increasingly used for small series production, for example in aerospace applications. The paper starts with a motivation for AM in hydraulic applications and the development of an AM internal gear pump. For a better understanding of the manufacturing process, a brief introduction to AM highlighting the advantages and challenges is given. The AM internal gear pump is part of an electrohydraulic power pack, which is used to power an electrohydraulic actuator (EHA). The power pack contains all necessary peripherals to realise the hydraulic system of the EHA. The AM process allows for new design possibilities, but the process differs strongly compared to subtractive manufacturing processes and therefore is outlined here. The paper concludes by presenting measurement results of the AM internal gear pump.

Keywords: Additive Manufacturing, LPBF, Internal gear pump, Electrohydraulic power pack, Design for Additive Manufacturing

1. MOTIVATION

Hydraulic components are still mostly produced using traditional manufacturing processes, for example with milling machines, lathes, electric discharge machining, laser cutting or casting. These are mainly CNC-supported manufacturing processes which, with well-coordinated process control, enable high economies of scale in series production. On the downside, there are high ramp-up times for setting up the machines in production lines for series production of new parts. This makes it difficult to implement small batches quickly and economically. In addition, the design freedom of a component is severely restricted by these traditional manufacturing processes, since each process has its own requirements for accessibility to the component, such as lathing which is only possible orthogonally or coaxially to the lathing axis.

Since fluid technology has paid little attention to AM and the research in this field is still focused on increasing efficiency, this paper aims to highlight the opportunities for fluid power arising through AM.

Currently, AM's market penetration is still hindered by lack of design knowledge, high production costs and limited productivity. But as the AM industry is currently growing exponentially, it is essential for each technical domain to evaluate the potential benefits from AM and leverage those.

This paper shows the potential of AM in hydraulic applications. For this purpose, the drive train of the ifas gimmick is used to demonstrate possibilities of AM by redesigning the drivetrain and integration pump and valves into a single light weight housing. The ifas gimmick is a hydraulic driven labyrinth presented at the 11. ifk in Aachen (see **Figure 1**). Two electrohydraulic direct drives are used in the ifas gimmick to realise the rotation around the x-axis and y-axis. Direct drive here means that there are no valves used for controlling the movement of the hydraulic cylinder. The movement is controlled by the rotational speed of the hydraulic pumps.

Each hydraulic pump is driven by a 24 V DC electrical motor, typically used for the electrohydraulic steering in trucks.

Figure 1: The ifas gimmick presented at the 11th ifk

2. ADDITIVE MANUFACTURING

2.1. AM Introduction

So far, adoption of AM has been highest in industries where the higher production costs of AM processes are outweighed by the additional value AM can generate through improved product functionality, higher production efficiency, bigger customization and shorter time to market.

According to ASTM, an AM process is a "process of joining materials to make parts from 3D model data, usually layer upon layer" [1], as opposed to subtractive (e.g. milling) or formative (e.g. bending) manufacturing [2]. Many different manufacturing processes are listed under the label AM, often sharing similarities as well as advantages and disadvantages due to the common layered manufacturing principle. The most important advantage is the high possible part complexity. Most AM processes make it possible to produce undercuts, internal and highly complex structures as well as fluid channels with freeform cross section geometry and placement. This can lead to an improved part functionality or a better function-to-weight-ratio.

One important disadvantage is that AM materials often exhibit anisotropies, with material properties such as tensile strength, elongation at break or heat transfer coefficient in the z-direction (build direction) being different from the properties in the x-y-plane [3]. Also, the layered manufacturing usually leads to a stair-stepping effect on slanted surfaces, resulting in a higher surface roughness compared to machined samples.

Another critical disadvantage affecting the manufacturing of slanted surfaces (also called overhangs) is shared by many AM processes: The build process is only stable when the angle between the overhang and the substrate exceeds a critical value (**Figure 2**). For angles smaller than the critical angle, the build process becomes unstable and huge part deformations occur, often leading to a process failure. The reason is that material can't be placed "in thin air". These areas need support structures to be manufacturable, which can take significant amounts of time and work to be removed after the build process.

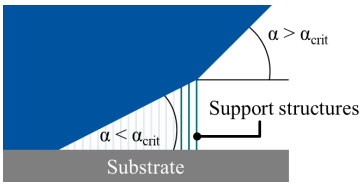

Figure 2: Critical overhang angle

2.2. LPBF

Laser Powder Bed Fusion (LPBF) is the most common additive manufacturing process for the production of dense metal parts [4]. A part is manufactured by selectively melting consecutive thin layers (approx. 30 µm) of metal powder by a laser beam according to a digital slice model of the part. The process principle is shown in **Figure 3**. A detailed description of the process can be found in [5].

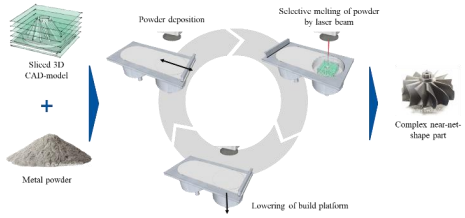

Figure 3: The LPBF process steps [3]

A wide range of materials can be processed by LPBF. Standard materials commercially available from many suppliers include, among others, Aluminum alloys (AlSi10Mg, AlSi12), stainless and tool steels (1.4404, 1.4542, 1.2709), Nickel-based alloys (Inconel 718 and 625) as well as pure Titanium (Titanium Grade 2) and Ti6AlV4 [7,8]. The typical powder used in the process consists of spherical particles with a particle diameter in the range of 15 µm – 45 µm.

The powder is fully melted in the process, resulting in a relative density usually exceeding 99.5 %. The rapid solidification rate of up to $7 \cdot 10^6$ K/s of the molten material generally leads to a fine and homogeneous microstructure and high strength of the material [6], albeit often with anisotropies in the material properties. Heat treatments are available for the reduction of anisotropies or internal stresses. The material efficiency of the process is high, as the unmelted powder can be fully reused.

The cooldown and shrinkage of the bonded consecutive layers leads to a build-up of residual stresses in the material, as shown in **Figure 4**. When overhangs are produced, the residual stresses result in deformation and, when the overhang angle is below the critical angle, in failed builds. Support structures are therefore needed to counteract the stresses. The support structures and the typically rough surfaces of LPBF parts covered with partly melted powder particles (R_a = 10 – 20 µm) generally require post-processing of the parts, consisting at least of (manual) removal of the support structures, abrasive blasting and, in case of functional surfaces with high quality requirements, machining. The need for support structures and thus for post-processing can be greatly reduced by a part design taking into account the process restrictions. [9, 19]

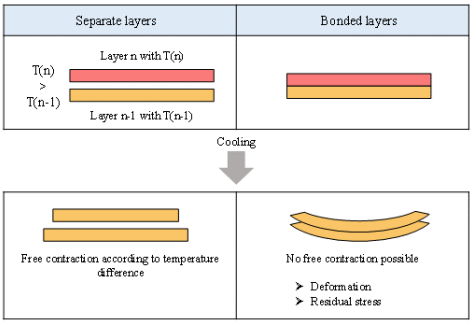

Figure 4: Build-up of residual stresses

For hydraulic applications, it is crucial that no powder particles or remains of support structures remain in part areas that later contain the hydraulic fluid, as this could damage critical parts of the hydraulic system. For this reason, it must be ensured that fluid channels and cavities are either designed in a way that doesn't require support structures, or that the support structures are mechanically removable, e.g. by designing without undercuts.

The geometric changes to achieve a design without the need for support structures can be comparably small, as shown for the cross-section of a fluid channel in **Figure 5**:

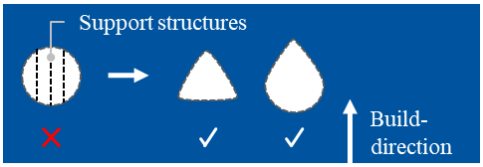

Figure 5: Altered cross-section of a fluid channel

2.3. Additive Manufacturing and Hydraulic Systems

AM has so far been limited to small components and is still primarily considered for prototyping. The possibilities for flow optimization are obvious, but at the same time also stresses introduced into the material at the points of flow deflection [10] can be reduced significantly. Within the same part volume, a higher volume flow with lower energy loss can be achieved with less material input due to reduced flow deflections [11]. Semini et al. also investigated the influence of the surface roughness for components that were treated by shot peening prior to the flow-through test to remove production residues from the surface. No significant effects of the surface on the flow were reported even after longer treatment time [12]. Weight savings of 30 % and more can be achieved for fluid power components especially designed for AM. For complex hydraulic drive components, Guerrier et al. consider the achievement of a shorter development cycle, reduced storage costs for material, better and new repair possibilities promising [13]. A substitution of existing components by a new design for the exploitation of the advantages of additive manufacturing so far hardly has taken place. However, this process is especially interesting for fluid power technology because it offers great potential for flow-optimised design and an enormous lightweight construction potential through functional integration that conventional processes cannot enable. The potential compared to existing components results from the fact, that today's hydraulic components are manufactured mostly with subtractive processes, at the cost of limiting the design freedom of a component.

Especially accessibility is an issue here. For example, valve blocks are hydraulic components with shapes largely determined by the production process. Except by means of primary shaping processes, which are frequently used in standardized valve blocks for mobile machines, it is not possible to manufacture internal connecting lines, so each channel must be led out of the component at least at one point. All channels must be placed in such a way that no unwanted connections occur and sufficient compressive strength is guaranteed. The aforementioned goals are contrary to the goals of lightweight construction, which is why a compromise in design must always be made. The special lightweight construction potential by means of AM arises in particular when the idea of function integration is consistently implemented and individual components or assemblies are fused to form a single component, for example when several housings are combined to accommodate components such as cartridge valves or pump gear sets in a single housing. The exploitation of this potential serves as motivation for the development of the powerpack presented below, which integrates the internal gear pump and valve blocks for the peripherals in one component. The additive manufacturing in combination with modern CAE tools speeds up and simplifies the production of a first prototype with sophisticated geometry.

3. INTERNAL GEAR PUMPS

The most common gear pumps in hydraulic applications are external and internal gear pumps. Both types of pumps are displacement pumps. An internal gear pump is used in this work due to the advantage of lower noise emission [14, 15]. The components and the displacement process of an internal gear pump are shown in **Figure 6**. The external gear, the internal gear and the crescent are the main components of an internal gear pump. The external gear is typically used to drive the pump. In an internal gear pump, the fluid is displaced by decreasing the volume of the displacement chamber, similar to axial piston pumps. For gear pumps, the displacement chamber is formed by the tooth space volume (the volume between the teeth). The volume is decreased (and thus the fluid is displaced) by the meshing of the teeth, which leads to a reduction of the tooth space. At the low pressure port, the teeth move away from each other. The tooth space volume increases and is filled by the fluid. The low pressure side is separated from the high pressure side by the crescent and by the meshing teeth. Due to a small gap between the crescent and the tooth tips, leakage occurs and the pressure increases in this area. The pressure build-up can also be specifically influenced by pressure build-up grooves. If a gearing with a transverse contact ratio > 1 is used, there are areas of tooth meshing where two tooth contacts are present. Due to the two tooth contacts, a small amount of fluid is trapped in between the contacts. The volume of the trapped fluid changes during the rotation. If the volume decreases, the fluid will be compressed and the pressure will increase. As a result, higher load forces as well as vibrations occur and can lead to higher noise emissions [16].

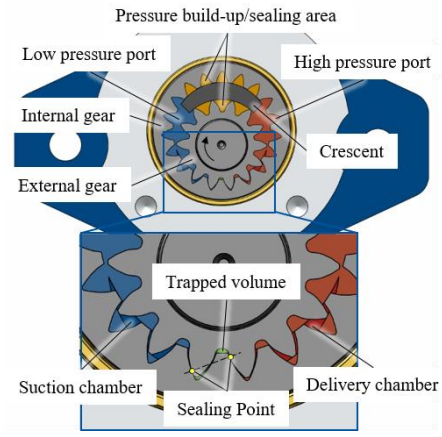

Figure 6: Components and displacement process of an internal gear pump

There are different designs of internal gear pumps. The most common designs available on the market are shown in **Figure 7**. At the top, an internal gear pump with axial inlet and outlet is shown. The fluid is sucked axially into the increasing tooth space volume and is displaced axially at the high pressure port. At the bottom of **Figure 7**, a pump design with radial inlet and outlet is shown. The fluid is displaced and flows through radial bores into the internal gear. This type of pump is often used in combination with gap compensation. The pump design with axial inlet and outlet also allows for a gap compensation. One example for the radial design with gap compensation is the prototype of a high

speed internal gear pump developed at ifas [17]. For the AM power pack presented in this paper

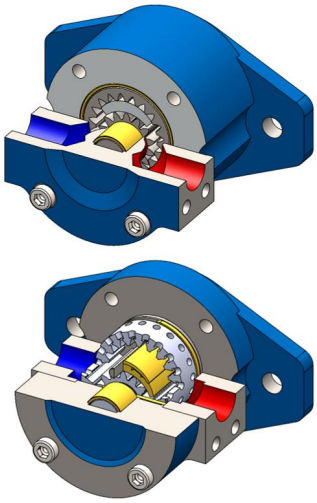

Figure 7: Different designs of internal gear pumps. Top: Axial inlet and outlet pump design. Bottom: Radial inlet and outlet pump design with gap compensation

an internal gear pump design with axial inlet and outlet without gap compensation is chosen. This allows for a compact pump design with very low noise emission as well as low flow pulsation [15]. Due to the application as an electro hydraulic direct drive in a hydraulic driven labyrinth at ifas, the low flow pulsation is a big advantage for the control strategy. The labyrinth serves as a highlight exhibit at the ifas booth during exhibitions and conferences. Therefore, a low noise emission is required. The pump design without gap compensation reduces the complexity of the pump as well as the total number of necessary components. Without the gap compensation, the manufacturing process and the tolerances become more important. The pump is able to work in four quadrant operation.

4. DESIGN PROCESS

For the design of the power pack, the redesign process proposed in [18] (see **Figure 8**) was carried out, which serves as a guideline for the redesign of conventionally manufactured components for additive manufacturing processes. According to the circuit diagram in **Figure 9**, an internal gear pump, two check valves and two pressure relief valves had to be integrated. In the beginning, external design restrictions were identified. The main restriction

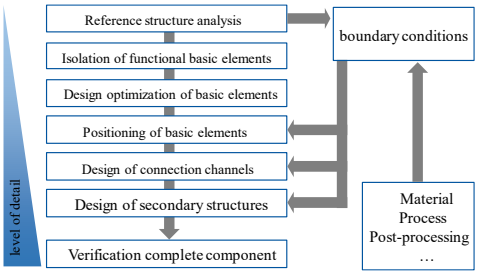

Figure 8: Design process for the redesign of additive hydraulic components [18]

found was the flange geometry, as the generous installation space in the gimmick allows for a great freedom in positioning the hydraulic ports and valves. Due to the coaxiality of shaft and gear set, further requirements for the installation space were derived from this, which had to be adhered to. Since the gear set was taken from a series pump, the ports in the gear chamber were designed identically in order to have comparability later with a variance only in the production process. The gear set originates from a pump with hydrodynamic bearing and thus features a leakage oil port. Since the EHA is operated in a closed circuit and preloaded (see **Figure 9**), a supply port had to be provided for preloading by an external filling pump. In order to minimize the number of hydraulic ports, the pressure relief valves were connected to the leakage port. Thus, at this point all connections between the components were fixed and only the arrangement and positioning of the valves remained. In order to determine the position of the valves, various configurations were determined and evaluated iteratively with regard to the required installation space, line length, flow control and the support structures required

in the production process. In particular, the latter is a major problem as curved channels

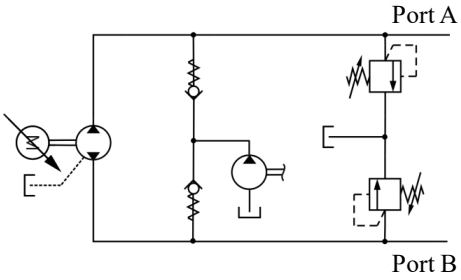

Figure 9: Hydraulic circuit diagram of the compact drive

are difficult to reach with tools such as chisels to remove the support structures without causing unwanted damage to the rest of the structure.
The selected final configuration is shown in **Figure 10**. In this configuration, all connections are easily accessible except the connections of the pressure relief valves (PRVs) and the tank port. These lines were designed small and with a geometrical shape to be printable without a support structure.
The final arrangement of the components is as follows: The port for the leakage (light blue) is provided at the top with a diameter of 5 mm and both PRVs are connected to that port via lines. The lines (not visible here) connecting the supply (purple) and main flow lines (dark blue) via check valves were chosen with a diameter of 6 mm as a compromise between good manufacturability and sufficiently large pipe diameters. The main flow line (dark blue) has a diameter of 10 mm adopted from the series pump from which the gear set was taken. The connection port for the supply (purple) can be seen at the front and a diameter 15 mm was chosen here. The bearing seat (red) is also indicated aswell as the gears (yellow).

4.1. Design Optimization using CAE-Tools

The next step was to design the structure of the housing. Whereas the geometry of a component manufactured subtractively is usually determined by the raw material used and is only reduced to a barely fatigue-resistant geometry in lightweight construction, the situation is different for AM. Here it makes little sense to strive for a geometry similar to well-known, conventionally manufactured components, as this leads to

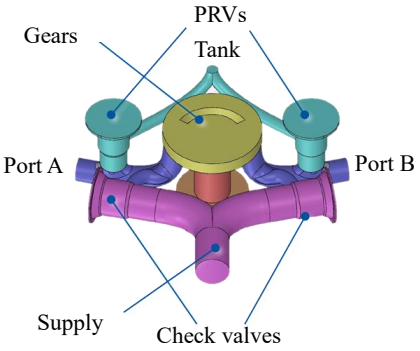

Figure 10: Positioning of all components

unnecessary structures that result in more material, production time, costs and weight. For complex structures, an iterative procedure of designing in a CAD program and subsequent verification using FEM is also conceivable in principle. If, however, one strives to minimize the part volume, this procedure is too inefficient. In order to solve this problem efficiently, various topology optimization algorithms are available. In this work, the software package ABAQUS was used. The 'Condition-based optimization'-algorithm was used to obtain a rough solution quickly and to verify the boundary conditions. Due to the significantly higher computing time, the ‘Sensitivity-based optimization'-algorithm was used to obtain the final solution only in a second step.

The optimization works as follows: A basic geometry (**Figure 11**, top) is transferred to the program. This geometry is segmented into individual volumes, each defining areas that may or may not be removed during the optimization. An FEM simulation is then set up including all boundary conditions and forces relevant for the component.
Also, objectives and constraints are set up for the optimization algorithm. In an iterative process, the part is then simulated and subsequently

altered by the optimization algorithm. These two

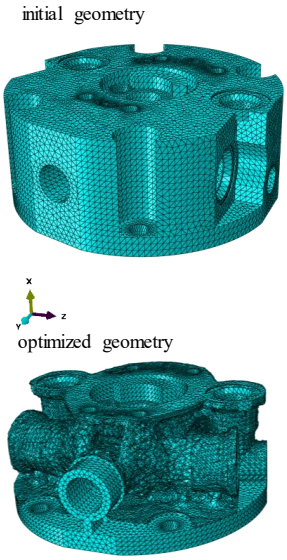

Figure 11: Initial and optimized geometry

steps are repeated until the optimization goals and constrains are reached. The optimization goal is usually given as a volume reduction. The whole optimization process was carried out iteratively in several variants in which different target volumes were defined. After an evaluation of the performance of each solution, the best solution was selected. In this case, the volume was reduced to 48.5% of the initial volume. The selected geometry is shown in **Figure 11** (bottom). The resulting part exported from the program consists only of a triangulated mesh, which has to be translated back into a geometry that can be processed in the AM process chain. As the optimized geometry was created by deleting elements from the initial volume mesh, the surface of the exported part can have very uneven geometry that does not make sense as a technical surface. Therefore, the surface is smoothed in a post-processing step with different automatic and manual methods. The resulting part after smoothing is shown in **Figure 12**. As it is not yet possible to maintain high tolerances during additive manufacturing, additional material must be applied in the areas where high accuracy is required for a subsequent machining step. An additional material layer of 2 mm was applied to all relevant areas. The holes for the positioning pins and screws were completely closed, as these have to be machined anyway and the risk of deflecting the drills is thus avoided.

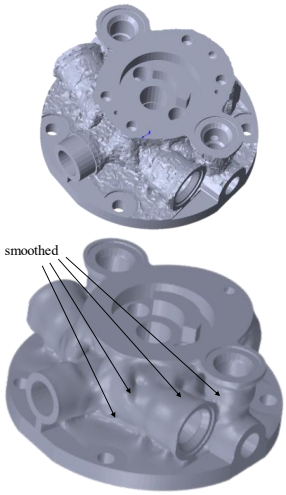

Figure 12: Pump housing before (top) and after (bottom) smoothing

5. PRODUCTION AND POST-PROCESSING

The pump housing and the housing cap were manufactured from 316L on an EOS M290 LPBF machine. The material was chosen because it has a similar thermal expansion coefficient compared to the material of the housing from which the gear set was taken. In this way, jamming between gear teeth and housing due to non-uniform thermal expansion should be avoided. The parts were then removed from the substrate plate by wire erosion. In principle, wire erosion is a process suitable for the production of highly flat surfaces. Unfortunately, the build-up of residual stresses during the LPBF process led to a deformation of the substrate plate. As this led to difficulties in referencing the part in the wire erosion process, the housing had to be re-aligned for further machining. Originally the flange was chosen as the reference and clamping surface for the following processing steps of the power pack. Due to the difficulties with wire erosion, a new reference surface had to be chosen. For the purpose of re-alignment, the shaft tunnel was first redrilled and then the component was clamped with the shaft tunnel as reference. Thus, everything was aligned relative to the shaft tunnel instead of the flange as originally planned. As a

result, the shaft tunnel and gear chamber were slightly oblique to the CAD geometry. However, since the gear chamber and crescent were manufactured after the shaft tunnel, these critical geometries could be aligned precisely with each other. The final result is shown in Figure 13. At the top the raw bodies are shown after the manual support structure removal and the sandblasting process. In the middle, all relevant surfaces and threads are manufactured and the bearings are mounted. At the bottom, valves and gears are added.

6. EXPERIMENTAL RESULTS

6.1. Test rig and experimental validation of the AM prototype pump

For the evaluation of the performance of the AM internal gear pump a test rig for electro hydraulic drives at ifas was used. The hydraulic layout of the test rig is shown in **Figure 14**. One delivery port of the AM pump was used as the low pressure port and connected with the boost port

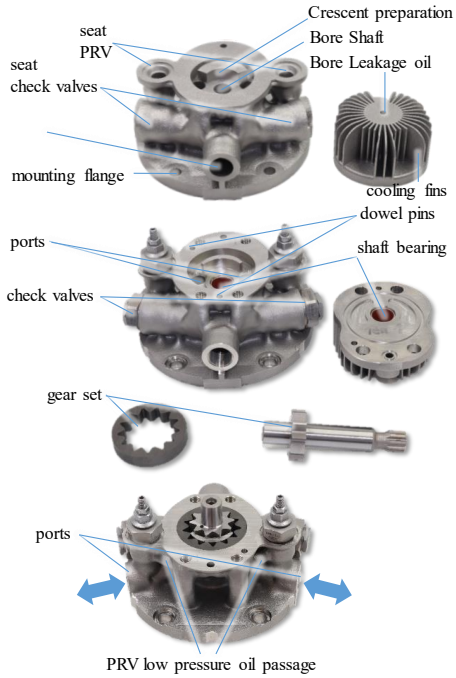

Figure 13: Power pack as-build (top), post-processed (middle) and assembled (bottom)

"B" of the test rig. Therefore, a boost pump in combination with a mechanical PRV was used to pressurize the suction side. The other delivery port was connected with the load port "L". The flow rate sensor measured the delivered volume flow of the AM pump. An electric PRV was used to control the delivery pressure of the AM pump. The leakage port of the AM pump was connected with the reservoir port "R". The suction port "S" of the test rig was not used. For the experiments, both PRVs inside the AM pump were adjusted to a pressure above the load pressure and therefore remained inactive. The test rig for electro hydraulic drives at the ifas lab is shown in **Figure 15**. The AM pump was mounted on the machine bed and connected to the ports according to **Figure 14**. The geometrical displacement of the AM pump was measured in the first step. For this purpose, the boost pressure was adjusted to be equal to the load pressure, resulting in a pressure difference between the low pressure port and the high pressure port close to 0 bar. The delivered volume flow was measured. The measured geometrical displacement was 2.57 cm³.

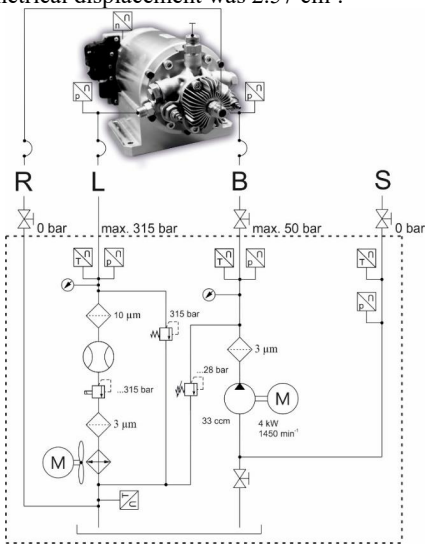

Figure 14: Hydraulic layout of the test rig for the AM pump

In the next step, the pump efficiency was measured. The rotational speed was set to a constant value and the load pressure was increased stepwise

When the maximum load pressure was reached, the load pressure was decreased and the rotational speed was set to a higher level. The temperature

at the boost port was nearly constant at 40°C +1°C/-2°C for the presented measurements. HLP46 was used as the hydraulic fluid. Equation (1) – (3) is used for the efficiency calculation.

Figure 15: Test rig for experimental evaluation of the AM internal gear pump

$$\eta_{vol}^{P} = \frac{Q_{eff}}{Q_{th}} = \frac{Q_{eff}}{n\,V_g} \tag{1}$$

$$\eta_{hyd-mech}^{P} = \frac{\eta_{total}^{P}}{\eta_{vol}^{P}} \tag{2}$$

$$\eta_{total}^{P} = \frac{P_{hydr}}{P_{mech}} \tag{3}$$

The measured volumetric efficiency of the AM pump is shown in **Figure 16**. Due to higher leakage, the volumetric efficiency decreases at increasing delivery pressure. As expected, the volumetric efficiency increases with increasing rotational speed. Due to the hydraulic resonance frequency of the test rig some data points between 45 bar and 65 bar and low rotational speed are not shown in the presented efficiency maps. Due to a power limitation of the electrical motor, it was not always possible to achieve the maximum pressure at higher rotational speed. **Figure 17** shows the hydromechanical efficiency of the AM pump. As expected, the hydromechanical efficiency increases with at higher load pressure. Due to increasing friction at higher rotational speed, the hydromechanical efficiency is lower at high rotational speed. **Figure 18** shows the total efficiency of the AM pump. The maximum total efficiency is about 70 %. Due to the fact, that this is the first iteration in design and manufacturing process of an AM pump, the presented measurements proof the function of the AM pump. However, there is still potential for efficiency improvements.

6.2. Summary

AM is a comparatively new process that allows for greater freedom of design than conventional manufacturing processes. For fluid power technology, this opens up new possibilities in the flow-optimized design of components as well as for more compact and lighter components by eliminating interfaces and sealing surfaces. In this paper, the possibilities offered by AM and the necessary process chain were demonstrated using the example of the presented power pack. Compared to the conventional design, consisting of a series pump and a valve block connected with pipes, the installation space and weight could be reduced by a factor of four with the same nominal operating data. The powerpack was then tested on the test bench and its function verified. However, all functional surfaces were reworked in this design as their tribological properties are still unknown. This research gap must be closed in order to further reduce the necessary reworking and thus accelerate the immediate production of a component that is almost ready for use.

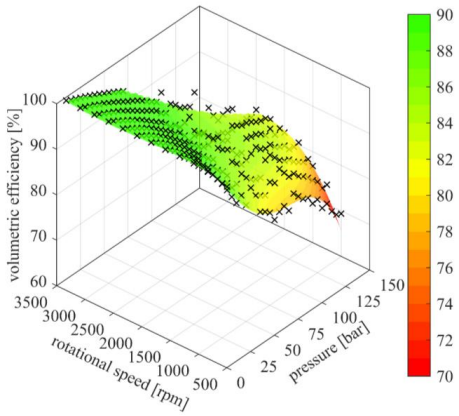

Figure 16: Volumetric efficiency

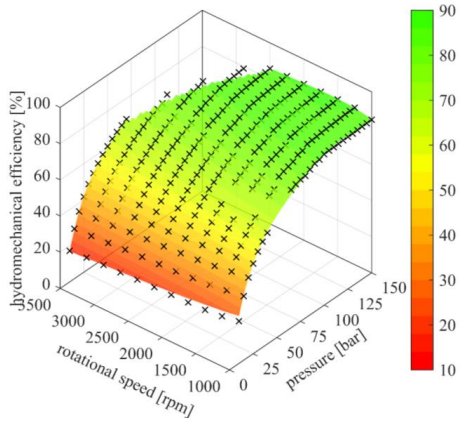

Figure 17: Hydromechanical efficiency

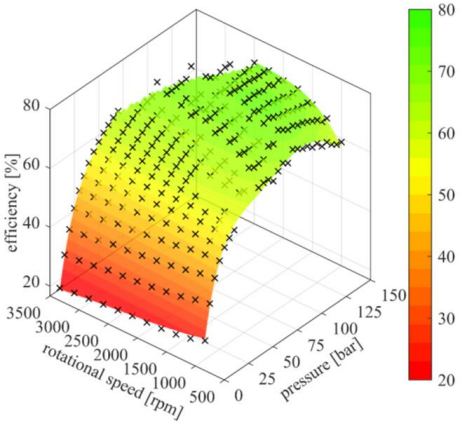

Figure 18: Overall efficiency

ACKNOWLEDGEMENT

The authors would like to thank Bucher Hydraulics GmbH for the extraordinarily extensive technical support in the implementation of this project and the open-mindedness towards this new technology and idea.

REFERENCES

[1] ISO / ASTM52900-15, Standard Terminology for Additive Manufacturing – General Principles – Terminology, ASTM International, West Conshohocken, PA, 2015.

[2] Burns, Marshall. “Automated fabrication: improving productivity in manufacturing”, PTR Prentice Hall, Englewood Cliffs, New Jersey, 1993.

[3] Gebhardt, Andreas: “Generative Fertigungs-verfahren. Additive Manufacturing und 3D Drucken für Prototyping - Tooling – Produktion”, 4. Auflage. Carl Hanser Fachbuchverlag, München, 2013

[4] Wohlers Associates, “Wohlers Report 2017-3D Printing and Additive Manufacturing State of the Industry - Annual Worldwide Progress Repor”,. Fort Collins, Colorado, USA, 2017.

[5] Meiners, Wilhelm. “Direktes Selektives Laser Sintern einkomponentiger metallischer Werkstoffe” Dissertation, Aachen, Germany, Shaker Verlag, 1999.

[6] Buchbinder, Damien. „Generative Fertigung von Aluminiumbauteilen für die Serienproduktion - AluGenerativ“. Final project report, Aachen, 2010

[7] EOS GmbH. "Materials for Metal Additive Manufacturing", accessed October 16, 2018, https://www.eos.info/material-m.

[8] Concept Laser GmbH, "Materials", accessed October 16, 2018, https://www.concept-laser.de/en/products/materials.html.

[9] Matthiesen, Gunnar: “Additive Manufacturing Processes in Fluid Power – Properties and Opportunities Demonstrated at a Flow-Optimized Fitting”, Proceedings of 2018 International Conference on Hydraulics and Pneumatics – HERVEX, 2018, Băile Govora, Romania

[10] Plummer, Andrew. “Additive Manufacture of Hydraulic Components” Paper presented at the The 9th International Conference on Fluid Power Transmission and Control, Zhejiang, China, April 11-13, 2017

[11] Cooper, David, Stanford, Mark, Kibble, Kevin a., Gibbons, Gregory j. “Additive Manufacturing for product improvement at Red Bull Technology”, Material and Design 41, May 2012: 226-300.

[12] Semini, Claudio, Goldsmith Jake, Manfredi, Diego, Calignano, Flaviana, Ambrosio Elisa Paola, Pakkanen Jukka, Caldwell, Darwin G. “Additive manufacturing for agile legged robots with hydraulic actuation”, Paper presented at 2015 International Conference on Advanced Robotics (ICAR), Istanbul, Turkey, July 27-31, 2015

[13] Guerrier, P., Zazynski, T., Gilson, E., Bowen. „Additive Manufacturing for Next Generation Actuation”, Paper presented at 7th International Conference on Recent Advances in Aerospace Actuation Systems and Components, Toulouse, France, 16-18 March, 2016

[14] A. Breuer-Stercken, „Strukturanalyse als Werkzeug zur Geräuschminderung

an hydraulischen Komponenten“, 10. Aachener Fluidtechnisches Kolloquium, 1992

[15] J. Ivantysyn, M. Ivantysynova, “Hydrostatic pumps and motors”, Akademia Books International, New Delhi, India, ISBN-81-85522-16-2, 2001

[16] W. Fiebig, K. Hell, “The New Way of Noise Reduction in External Gear Pumps”, 7th International Fluid Power Conference, Aachen 2010

[17] T. Pietrzyk, et al. Design of a High Speed Internal Gear Pump to Increase the Power Density of Electro Hydraulic Actuators (EHA) in Mobile Applications, International Mechanical Engineering Congress and Exposition, IMECE2019, November 11-14, 2019, Salt Lake City, UT, USA, 2019

[18] Hummel, Gerhard, Konrad, Tim, Harten, Oliver, Altmann, Alexander, Schubert, Frank, Kroll, Lothar. „Additive manufacturing for high pressure hydraulic valve manifold of Airbus A380 spoiler actuator“, Paper presented at 7th International Conference on Recent Advances in Aerospace Actuation Systems and Components, Toulouse, France, 16-18 March, 2016

[19] VDI 3405 Part 3:2015-12; “Additive manufacturing processes, rapid manufacturing - Design rules for part production using laser sintering and laser beam melting”

ADDITIVE MANUFACTURING OF HYDRAULIC MANIFOLDS - A HOLISTIC APPROACH ACROSS THE ENTIRE VALUE CHAIN

Dr.-Ing. Bastian Beckmann

Bosch Rexroth AG, Zum Eisengiesser 1, 97816 Lohr am Main
Tel.: +49(09352)18-4618; E-Mail address: Bastian.Beckmann@boschrexroth.de

ABSTRACT

Manifolds usually consist of metallic, rectangular base bodies into which lines are inserted by means of drilling, thus logically linking the built-on or built-in valves according to the hydraulic circuit diagram. Using additive manufacturing methods, additional degrees of freedom can be used in the design of manifolds, resulting in further benefit in hydraulic drives and their controls. The challenge is not only to understand and apply additive manufacturing technology, but also to align the entire value chain with it.

Keywords: Manifolds, Additive Manufacturing, 3D sand core printing

1. STATE OF THE ART

1.1. Manifold

A hydraulic control block (=manifold) can be described as the link between the drive unit and the consumption of a hydrostatic drive. It thus serves to control the hydraulic energy provided by the hydraulic power unit and required by the actuator to fulfil its function. The engineering of a hydraulic control system can be divided into the steps of project planning, design and manufacturing. In the project planning phase, the essential task is to design a hydraulic control system for the desired load and motion profiles of the hydraulic drives with the corresponding control elements (valves). The result is a device list that gives an overview of the required control elements and a circuit diagram that visualizes them graphically with their logical interconnection.

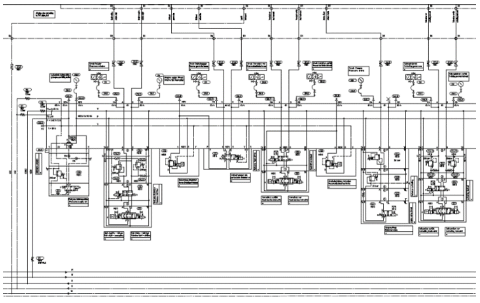

Figure 1: Exemplary hydraulic circuit diagram [1]

In addition, further customer requirements are taken into account, as well as the location of the connections, desired coating, etc. The requirements are implemented in the following design phase**.** Using 3D CAD software, for example, the desired external geometry of the manifold is created virtually and the installation geometry of the valves is applied. After the valves and connections have been loaded from the device list into or onto the installation geometry, they can be connected according to the logical connection on the hydraulic circuit diagram with straight cylindrical geometries resulting from the common manufacturing process of drilling.

In the context of the overall design, dependencies and constraints arise, for example, that the distance between the holes must not fall below a certain value. For reasons of the available installation space, the minimum wall distances and the desired direction of the hole to be drilled, auxiliary holes are often required which in turn must be provided with sealing elements.

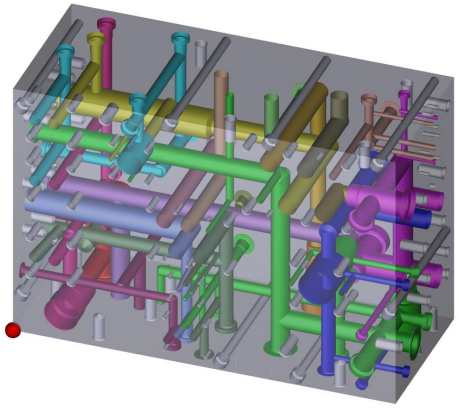

Figure 2: Conventional design of a manifold [1]

For the basic body, which in industrial stationary hydraulics applications usually consists of a simple rectangular geometry, a metallic material such as cast iron, steel or aluminium is generally used to meet the requirements (Operating pressure, Load cycle, Installation space, Costs, ...). In the subsequent manufacturing phase, these rectangular raw materials are appropriately clamped in the cutting machines and provided with straight cylindrical bores according to the production drawing.

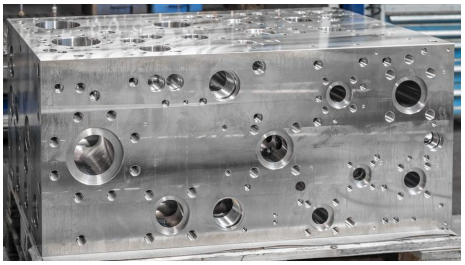

Figure 3: Unassembled manifold [1]

1.2. Additive Manufacturing in the context of manifolds

DIN 8580 [2] classifies additive manufacturing, which refers to the layered or elemental structure of a work piece [3], into the primary forming manufacturing processes.

Bosch Rexroth essentially uses two of the additive manufacturing processes described in [4] and [5]. In the "Selective laser melting" (SLM) process, a thin layer of a powdery metal material is applied to a base plate and locally melted by means of a laser beam, after which a solid material layer is formed by solidification. By lowering the base plate and subsequently applying a new thin layer of metal powder, this process can be repeated as often as necessary to create the desired contours and volumes of the metallic material. Depending on the application, the SLM process is suitable for smaller, more complex components with filigree structures (bore diameter 1-2mm) in the range up to 5kg. According to the current state of the art, the optimum mass of the component is approx. 0.5kg. Initial research projects in which this production technology for manifolds has been investigated indicate an application rate of up to 60 cm^3/h [6].

As hydraulic control blocks, which have a complex internal structure, are usually much heavier than 5 kg and more voluminous, this production technology is only suitable for this purpose to a limited extent.

Therefore, the method of 3D sand core printing is used. First, a sand core is created by additive manufacturing, which reproduces the inner structure of the component. The sand is mixed with an activator and also applied in layers from bottom to top. The print head applies additional binder per layer in the areas relevant to the geometry. This technique allows geometries to be produced that cannot be achieved in traditional core production or only by combining several cores which then have to be laboriously installed together. Depending on the binder system used, various strengths of up to 550 N/cm^2 can be achieved, with which even more filigree structures can be realized [7].

The component is then finally manufactured using the common and established sand core casting process.

Figure 4: Sand core with filigree and rounded structures [1]

2. INNOVATION AND USER BENEFIT

The methods of additive manufacturing open up completely new opportunities for manifolds, as can be seen in the following picture.

Customized products

- Flexible production from lot size 1
- Short TTM from Month to Weeks

Energy efficiency

- Optimized oil flow
- Reduced pressure loss (*delta p*)
- Reduction of screw plugs / Leakage

Weight and design optimization

- Grid structures
- Reduced part weight
- Flexible internal and external geometry (e.g. oval lines)

Functional integration

- New or optimized functionality
- Better control of mechanical properties
- Improved sustainability

Figure 5: Advantages of the additive manufacturing

Due to the free design of the line cross-sections (round, oval, square, diamond-shaped, ...) and the avoidance of abrupt changes in direction of the oil flow through curved lines, the pressure losses and noise emissions can be reduced in a targeted manner. For illustration purposes, the following figure shows the pressure loss due to a flow-optimized line routing.

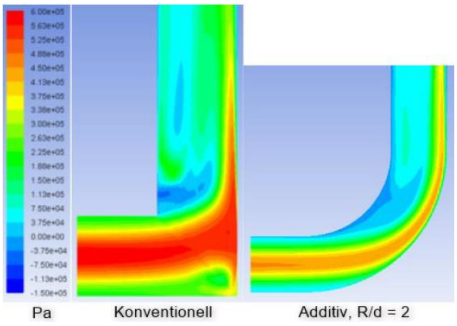

Figure 6: Optimized oil flow due to curved lines. [1]

Due to the flexible internal and external geometry, manifolds can be designed more compact and lighter and almost any outer contour can be realized, thus enabling a precise application in complex installation geometries. The more flexible channel routing also makes it easier to avoid auxiliary drilling.

Basically different design and manufacturing principles have to be applied when designing a manifold which is manufactured by means of 3D sand core printing.

For example, the pressurized surfaces of the lines are no longer a metallic structure that was machined out of the solid base material, but a surface that results from the casting process. This so-called "raw cast skin" has different mechanical properties compared to the surface of the lines, which was worked from the solid material. In the case of external cast skins of cast iron components with nodular graphite (GJS), various post-treatment processes such as blasting or surface hardening are used to increase the fatigue strength or lifetime of components subjected to cyclical loads.

In most cases, these processes cannot be used for internal cast skins due to the lack of accessibility of the areas, which is why there are challenges in the lifetime assessment of such components in this context [8]. In a first approximation, however, a reduction of the life time of cyclically stressed components of approx. 20-30% can be expected. In the design of the manifold, this reduction must at least be compensated by minimizing tension gradients using the degrees of freedom through additive manufacturing of a suitable channel layout.

When designing the sand core, not only the logical connection of the valves, flow-optimized channel routing or other oil-hydraulic aspects play a role, but also technical aspects of the casting process, for example to avoid core breakage or floating of the sand core during casting or to ensure thermal stability. In the design phase of the control block, therefore, the later implementation in the subsequent casting process must always be taken into account in order to enable efficient production or to realize it at all.

The technical documentation is also different. In the past, it was common practice to purchase a rectangular raw material for which the external dimensions were sufficient. In the future, a foundry must be requested to produce a casting with a defined internal structure, for which a corresponding drawing is required in order to forecast the costs if possible.

Bearing in mind that components such as valves, filters, flanges, etc. are mounted on the surface at the outlets of the casted lines, it is clear that the manufacturing tolerances of the casting process must be compatible with the machining of the final product which must also be taken into account in the design phase.

During the final machining operation, in which the mounting surfaces or installation bores of the valves are finished, the components to be manufactured must be clamped in the working area of the processing machine. This fixes the component in a defined position in the machining area and allows the tool to reach it precisely.

The aim here is to realize the machining process with one or only a few setups, since a change of position and layer of the workpiece in the machining area causes valuable time and thus costs. In this context, the flexible external geometries of the additively manufactured manifolds represent an essential challenge for automated production. The added value and opportunities offered by additively manufactured manifolds are matched by the great challenge in the project planning phase of combining them with the customer's problem in the best possible way.This requires a detailed understanding of the customer's hydraulic problem and expert knowledge of the possibilities of additive manufacturing of manifolds.

In the preceding description of the challenges to be met in the various phases of the development of a manifold, it becomes clear that not only the optimization and the development of competence in the individual phases is essential, but rather an interconnection of the individual process steps.

The goal must be a standardized handling process analogous to the conventional manifolds in order to provide a competitive problem solution on the market.

3. MATURITY LEVEL AND RESULT

Bosch Rexroth has pursued this goal as part of a holistic approach. The 3D sand core printing has been applied since 2012, which means that the development of competence in the application of this manufacturing technology is very advanced.

Thus the design of the sand core for the casting process could be optimized and the process times until the ready-to-use casting product could be reduced by several weeks compared to the conventional process sequence [7]. On the basis of various concept studies and further investigations, a design guideline was derived for manifolds manufactured using the 3D sand core printing process. By building up a deeper understanding of the process, an industrial application with a suitable repeatability, machine capability and quality assurance in the process is possible.

For the design phase, specifications are made which maximize the lifetime of the manifold and lead to the best possible manufacturability, for example by taking potential clamping concepts in the processing machines directly into account or necessary reference points to enable precise finishing.

These design guidelines include detailed technical specifications for screw-in holes, duct junctions and transitions, minimum wall thicknesses and specifications for the technical documentation to be prepared. This new type of manifold design thus extends the requirement profile of a design engineer.

In the project planning phase, selected sales staff is trained to ensure that, in addition to their high level of specialist knowledge of hydraulic drive technology, they are also able to provide reasonable solutions to problems using additive manufactured manifolds.

REFERENCES

[1] Bosch Rexroth AG

[2] DIN 8580 (2003); Manufacturing processes – Terms and definitions, division
[3] Andersen O. et. al (2018): Neue Entwicklungen auf dem Gebiet der nicht-strahlbasierten additiven Fertigungsverfahren, in Pulvermetallurgie in Wissenschaft und Praxis, Band 34, Pulvermetallurgie - Neue Herausforderungen und neue Wege, Heimdall Verlag Hagen, pp.255-280
[4] VDI Richtlinie (2014) Addtitive manufacturing processes, rapid manufacturing – Basics, definitions, processes
[5] DIN EN ISO / ASTM 52900 (2018); Additive manufacturing – General principles – Terminology
[6] Schöpf Georg (2019): Hydraulische Steuerblöcke additiv denken, in X-Technik: Additive Fertigung – Fachmagazin für Rapid Prototyping, -tooling – Manufacturing
[7] Spiess O. (2015), Giesserei Heft 04/2015, 3D-Druckverfahren – Die Zukunft der Gießereitechnik;
[8] Bleicher C. et. al. (2019): Einfluss von Gusshautrandzonen auf die Schwingfestigkeit von Gusseisen mit Kugelgrafit, in: Giesserei Heft 11/2019

AM-DRIVEN DESIGN OF HYDRAULIC MANIFOLDS: ENHANCING FLUID FLOW AND REDUCING WEIGHT

Yi Zhu*, Shuai Wang, Chao Zhang, Huayong Yang

State key laboratory of fluid power and mechatronic systems, Zhejiang University, 38 Zheda Road, 310027 Hangzhou, China

*Corresponding author: Tel.: +86 18694580181; E-mail address: yiz@zju.edu.cn

ABSTRACT

Selective laser melting (SLM), one type of metal additive manufacturing (AM) technology, uses a high-intensity laser to selectively melt pre-spread metal powders by a layer-on-layer manner. The technology does not only provide a new way of manufacturing but also innovates product design methodology. In this study, a hydraulic block manifold is designed and manufactured using SLM. In this paper, we present an AM-driven design approach of hydraulic manifolds based on a case study. The target is not only to reduce weight but also to enhance fluid flow by optimizing fluid path to reduce pressure drop. The novelty of the research includes developing a design approach of hydraulic manifolds using SLM with a particular focus on fluid flow. Compared to the traditional hydraulic manifold, the weight of the new SLMed hydraulic manifold was reduced by more than 80%, size by half. Pressure loss of the main functional oil circuit was reduced by 31%, illustrating that the new hydraulic manifold design simultaneously achieves lightweight and high performance. This study contributes to providing theoretical guidance to the design of additively manufactured hydraulic components with high performance.

Keywords: hydraulic manifold; lightweight; selective laser melting; pressure loss

1. INTRODUCTION

Selective laser melting (SLM), one type of metal additive manufacturing (AM) technology, uses a high-intensity laser to selectively melt pre-spread metal powders by a layer-on-layer manner. The technology does not only provide a new way of manufacturing but also innovates product design methodology. Typical examples include AMed fuel nozzles used in GE LEAP engine, heat exchangers, and injection molds with conformal cooling channels. By using AM, hydraulic components can also be compact, lightweight, and high performance, particularly for hydraulic manifolds with complicated fluid passages. However, AM-driven design approach for hydraulic manifolds is lacking which needs to consider supporting structures, building orientation, fluid flow, and wall thickness. Some industrial companies, such as Renishaw, Moog, Aidro, Liebherr, demonstrated their hydraulic manifolds or even integrated components using SLM. Weight and size were considerably reduced. However, detailed data were not published. Schmelzle et al. [1] designed a hydraulic manifold using SLM. 17 parts were combined into a single component and the weight was significantly reduced. In addition, they also proposed a general design approach based on metal AM and the quality inspection was also presented. The main focus is the manufacturability and mechanical properties of the component.

In this paper, we present an AM-driven design approach of hydraulic manifolds based on a case study. The target is not only to reduce weight but also to enhance fluid flow by optimizing fluid path. The novelty of the research includes developing a design approach of hydraulic manifolds using SLM with a particular focus on fluid flows.

2. DESIGN

2.1. Prototype hydraulic manifold

Fig. 1 shows a prototype hydraulic manifold that weighs 33 kg in a missile launch vehicle, the material of which is 316L steel and the size of which is 250 mm × 180 mm × 95 mm. There are many ports in the prototype hydraulic manifold, including one oil inlet (red port), one oil outlet (blue port), four control ports (green ports) and seven auxiliary holes (yellow ports). Nine mounting holes that connect with five solenoid directional valves (S1-S5), one check valve, one three-way flow regulator, one pressure relief valve and one pressure sensor guarantee the high controllability of this hydraulic manifold. The rated flow rate of the hydraulic manifold is 15 L/min and the rated pressure is 21 MPa.

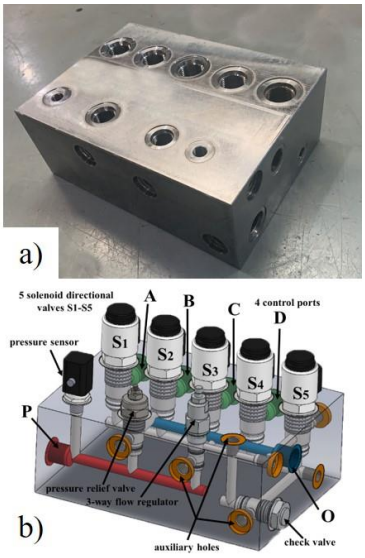

Figure 1: (a) Photograph and (b) schematic diagram of the prototype hydraulic manifold.

2.2. Design of hydraulic manifold based on AM

A schematic diagram of the fluid passage logic block extracted from the prototype hydraulic manifold is shown in Fig. 2. It is apparent that the abrupt right-angle turns and regular layout of the fluid passages in the prototype hydraulic manifold are prepared for the convenience of conventional processing, resulting in the bulk shape. The emergence of SLM provides a new advanced technology to fabricate hydraulic manifolds with complex structures without the limitations of traditional processing methods. Thus, the fluid passages could be redesigned to improve the flow performance and reduce the weight. In this work, the local structures and the layout of fluid passages are redesigned.

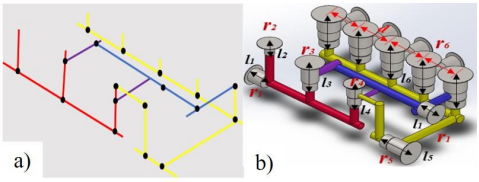

Figure 2: Fluid passage extracted from the prototype hydraulic manifold.

Owing to the limitations of conventional processing, the auxiliary holes are retained in the cross-flow of fluid passages, increasing the risk of leakage and the loss of flow efficiency. Based on the high flexibility of SLM technology, the auxiliary holes can be first removed from the SLMed hydraulic manifold. When hydraulic oils flow in the fluid passages, the abrupt right-angle turns may increase local fluid loss. Replacing these abrupt right-angle turns with gradually curved turns could significantly decrease the loss of flow efficiency. To evaluate the flow efficiency of these three fluid passages with different local designs, a simulation analysis is conducted using computational fluid dynamic software (CFD) software. The accuracy of the CFD analysis results is verified by Zardin et al. [2] using a hydraulic manifold with single passages and theoretical calculations.

The radius of the curved turns R also has significant effect on the flow efficiency of fluid passages with a diameter d. In this simulation, the diameter of all these fluid passages is chosen as 10 mm, which is in accordance with that of the fluid passages in the prototype hydraulic manifold, as shown in Fig. 3(a). Fig. 3(b) shows the effect of the ratio of R to d on the pressure drop between inlet and outlet of a curved fluid passage. It is apparent that the pressure loss decreases as the ratio of R to d increases. However, the space is usually limited in the actual layout of fluid passages, and excessive radius of the curved turns will cause interference with adjacent fluid passages. Therefore, the

design criterion is that the radius of the curved turn should be as large as possible to reduce the pressure loss as much as space permits.

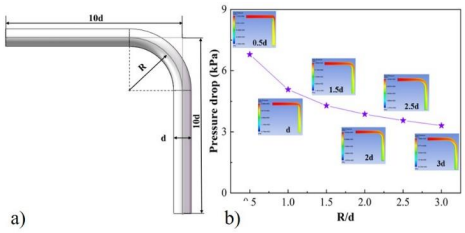

Figure 3: (a) The radius of the curved turns R and (b) the pressure drop of curved junctions with different radii.

In addition to the local design of fluid passages, a reasonable layout of fluid passages is also a necessary and effective way to design a hydraulic manifold while reducing its weight and improving its flow efficiency. Mitsukiyo et al. [22] indicated that a turn in the flow direction readily causes vortices and flow separation, resulting in greater energy consumption and lower flow efficiency. To obtain a manifold having better performance, many researchers mainly focus on only the arrangement of fluid passages and volume reduction. A design aimed at obtaining the minimum size often implies a rather complicated set of drillings to bring about fluid circulation between external ports of the hydraulic components with higher efficiency loss. Thus, in the rearrangement of fluid passages, the turn numbers of the fluid passages should be minimized as much as possible. Fig. 4 shows the fluid passages from the 3-way flow regulator valve outlet to the solenoid directional valve inlet, and there are six turns in the redesigned hydraulic manifold (as indicated by Model I). In contrast to Model I, Model II replaces two right-angle turns with two obtuse-angle turns, and the simulation result of pressure loss for Model II relative to Model I indicates a 13% reduction. In contrast to the two obtuse-angle turns in Model II, the turn number in Model III is further reduced down to two. As a result, compared to that of Model I, the pressure drop of Model III was significantly reduced by 50%. These results indicate that a decrease in the turn numbers of fluid passages can significantly improve the flow efficiency.

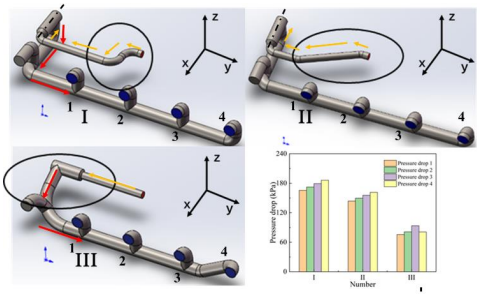

Figure 4: The effect of turn numbers on the pressure drop of fluid passages.

Based on the three aforementioned design criteria, an improved version of a hydraulic manifold with a 3 mm wall thickness is shown in Fig. 5. It is apparent that compared wo the previous hydraulic manifold, the improved hydraulic manifold has a smaller size of 246 mm × 140 mm × 66.5 mm without a bulky shell while retaining the original functionality. The layout of the fluid passages is more compact with fewer turns, and the original right-angle turns are replaced by curved turns. Compared with the prototype hydraulic manifold, the new hydraulic manifold had the seven auxiliary holes removed, and the locations of mounting holes that connect with the three-way flow regulator, pressure relief valve and solenoid directional valve S5 were changed to reduce the volume without destroying the function.

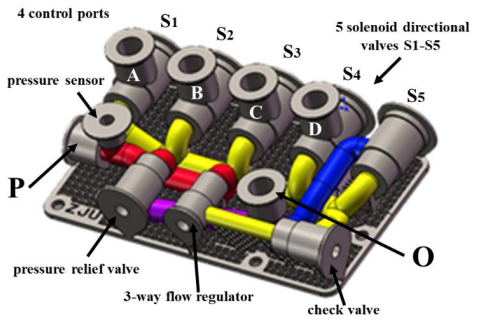

Figure 5: The improved version of the hydraulic manifold

3. PROCESS

The SLM process was conducted in a Renishaw AM 250 machine with an argon atmosphere, which is schematically shown in Fig. 6. The detailed process parameters are indicated in Table 1. After manufacturing, the excess metal powder was removed, and the SLMed hydraulic manifold was obtained from the substrate by a wire electrical discharge machining procedure. The cartridge valve holes and all threaded surfaces were finally improved by machining. A photograph of the finished SLMed hydraulic manifold is shown in Fig. 7.

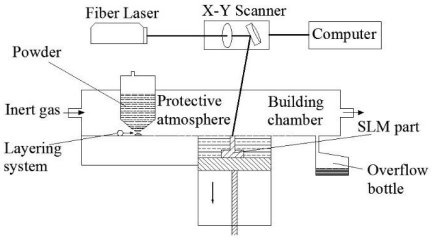

Figure 6: A schematic of SLM system used in the work [3].

Table 1: Process parameters used in the work

Laser power	Layer thickness	Point distance	Exposure time	Hatch space	Scan strategy
200 W	50 µm	65 µm	80 µs	80 µm	Stripes

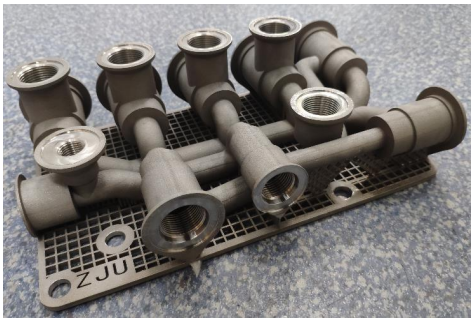

Figure 7: A photograph of the SLMed hydraulic manifold.

4. INSPECTION AND TESTS

The forming quality of the SLMed hydraulic manifold, especially the internal structure of the fluid passages, has a significant effect on its working performance. Therefore, it is very important to detect the forming quality of the fluid passages, which cannot be directly observed intuitively without damage. In this study, a 450 kV industrial CT with micro-and sub-microfocus-capable X-ray sources (IPT04013D manufactured by Beijing Granpect Company) was used to inpect the SLMed hydraulic manifold. Fig. 8 shows three-dimensionally visualized maps and local cross-sections of the SLMed hydraulic manifold. It can be found that the structure of the fluid passages is almostly completely in a good shape, indicating the remarkable forming quality. After industrial CT inspection, dynamic cyclical impact tests were used to evaluate the reliability of the SLMed hydraulic manifold. The test result showed that the SLMed hydraulic manifold can continuously work under 21 MPa at 40℃ for 48 h without leakage or damage, illustrating that the SLMed hydraulic manifold can satisfy the working requirements achieved by the prototype manifold.

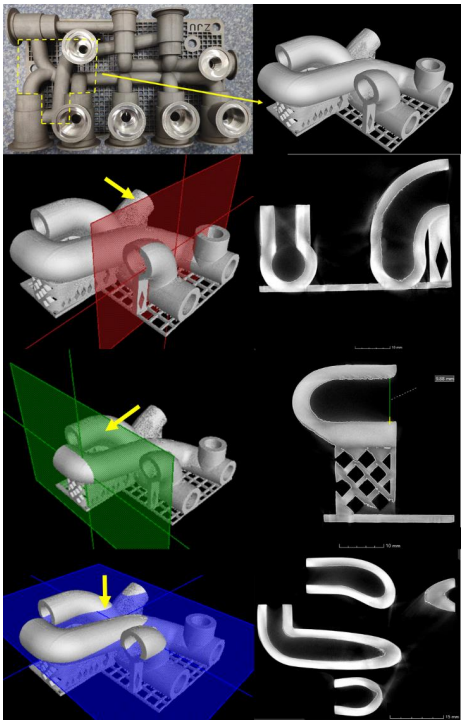

Figure 8: Cross-section of the manifold model and scanning image obtained by industrial CT.

Compared with the 14 kg prototype hydraulic manifold with a large space size, the SLMed

hydraulic manifold that weighs 2.6 kg, corresponding to a great weight reduction of up to 80%, and the space size has also been reduced by 46%. In addition to its lightweight, the flow performance of the SLMed hydraulic manifold is also measured and compared to that of the prototype manifold. In this case, experiments and simulations of the flow performance of the main functional oil circuit, i.e., oil circuit 2, in the prototype and SLMed hydraulic manifolds are conducted. Fig. 9 demonstrates the flow performance tests, while Fig. 10 shows the experimental and simulation results of the flow performance tests for the prototype and SLMed hydraulic manifolds. It is apparent that the experimental results of pressure loss are in good accordance with the simulation results for both the prototype and SLMed hydraulic manifolds. Compared with the prototype hydraulic manifold, the SLMed hydraulic manifold achieved pressure loss reductions of 33%, 31%, 23% and 37% for the port 1, port 2, port 3, and port 4, respectively, and the average pressure loss reduction of the four ports is 31%. These results indicate that compared to the prototype hydraulic manifold, the SLMed hydraulic manifold achieved better flow performance.

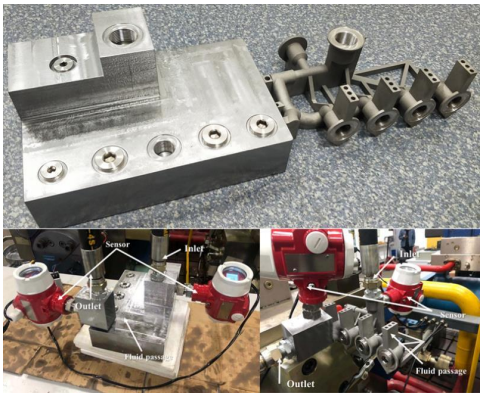

Figure 9: (a) Main functional oil circuit of the prototype (left) and SLMed (right) hydraulic manifolds prepared for flow performance tests; and the flow performance test of (b) prototype and (c) SLMed hydraulic manifolds.

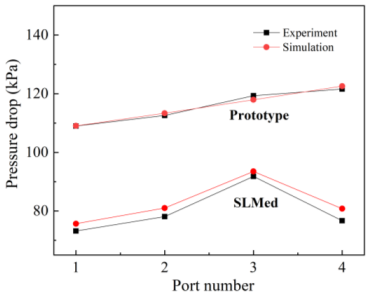

Figure 10: Experimental and simulation results of the flow performance test for both prototype and SLMed hydraulic manifolds.

REFERENCES

[1] J. Schmelzle, E. V Kline, C.J. Dickman, E.W. Reutzel, G. Jones, T.W. Simpson, (Re)Designing for Part Consolidation: Understanding the Challenges of Metal Additive Manufacturing, Journal of Mechanical Design. 137 (2015) 111404. doi:10.1115/1.4031156.

[2] B. Zardin, G. Cillo, M. Borghi, A. D'Adamo, S. Fontanesi, Pressure losses in multiple-elbow paths and in V-bends of hydraulic manifolds, Energies. 10 (2017). doi:10.3390/en10060788.

[3] Y. Yang, Y. Zhu, M.M. Khonsari, H. Yang, Wear anisotropy of selective laser melted 316L stainless steel, Wear. 428–429 (2019) 376–386. doi:10.1016/j.wear.2019.04.001.

GROUP E

Components

peer reviewed

FUNCTIONAL PROOF OF A FLAT SLIDE VALVE AS A 4/3-WAY PROPORTIONAL VALVE

Stefan Aengenheister[1]*; Chao Liu[2]; Christoph Broeckmann[2]; Katharina Schmitz[1]

[1]*Institute for Fluid Power Drives and Systems, RWTH Aachen University, Germany*
[2] *Institute for Material Applications in Mechanical Engineering, RWTH Aachen University, Germany*
* Corresponding author: Tel.: +49 241 8047733, E-mail address: stefan.aengenheister@ifas.rwth-aachen.de

ABSTRACT

With a flat slide valve concept, when compared to conventional piston spool valves, reduced leakage and increased service life could be achieved. In order to achieve a reduction of leakage flows and guarantee the adjustability of the valves at the same time, a correct design of the pressure compensation is essential. The magnitude of force depends on both the operating point of the valve and the position of the slider. Due to the design of the flat slide valve, it is possible to use ceramic semi-finished products for the main stage, which consist of control plates and a slide plate. The geometries are simple enough to be inexpensively manufactured with sufficient accuracy, using a ceramic pre-product using laser cutting technology. This article introduces the concept of the flat slide valve for a proportional 4/3-way valve. The design of the valve, including the design of the metallic main stage is presented. This includes the design of the flow channels, which have to be suitable for ceramic materials. Furthermore the design of the actuator and hydraulic circuit for testing is presented. With the shown design, the function of a 4/3-way valve, known from piston spool valves, can be implemented with a linear behavior between slide plate deflection and opening flow cross section.

Keywords: Flat Slide Valve, High-tech ceramics, Pressure Compensation, Reduction of Wear, Reduction of Leakage, Linear Control Behavior, Innovative Valve Design

1. INTRODUCTION

In hydraulic systems, directional control valves are often used to control fluid flows. In particular, piston spool valves consisting of cylindrical components are employed. In the case of piston spool valves, a rotationally symmetrical spool moves in axial direction within a housing or a sleeve [1]. In most cases, sleeve/housing and slider are made of a metallic material. Thereby, two weak points occur, the first weakness is erosion at the control edges as shown in **Figure 1** and leads to wear of the control edges [3]. This wear has a negative effect on the controllability of the valves and thus limits their service lifetime. The second weakness is the function-related gap between sleeve/housing and spool, which is necessary to be able to adjust the spool, as can be seen in **Figure 2**.

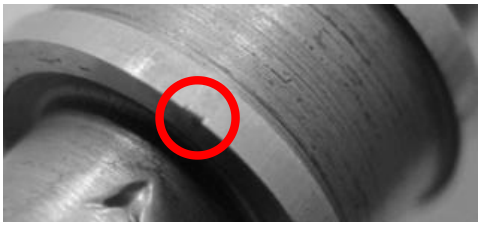

Figure 1: Wear (erosion) at the control edges [2]

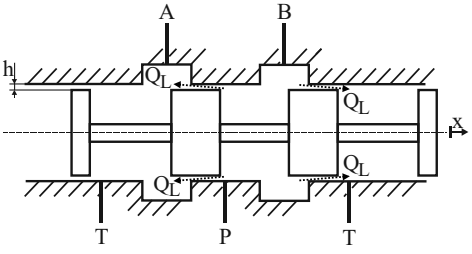

Figure 2: Function-related gap between sleeve/housing and spool

Through the application of a pressure difference, an unavoidable leakage occurs through the gap, leading to a reduced efficiency.
Ideas for a friction- or leakage-minimized design of flat slide valves have already been suggested in [4] and [5]. The patent mentioned in [4]

describes a valve disk package for sanitary applications. The pressures used in sanitary applications are very low compared to the pressures commonly used in standard hydraulics. In the patent applied for in [5], a sleeve is used as a spacer between the cover plate and the base plate. This is to ensure that the sliding plate is movable and no normal force is applied to it. The use of this sleeve however results in a gap between the individual plates, which also leads to leakage as with conventional piston spool valves.

In contrast to the work presented in [4] and [5], the concept of a flat slide valve described compresses plate-shaped components in such a way that theoretically there is no sealing gap between the individual plates. This minimizes the resulting leakage and improves the efficiency of the valves. In addition, this design enables cost-effective integration of ceramics. Ceramics have a higher abrasion resistance, which can contribute to an increase in the service life of the control edges. The investigation of some ceramics which could be used in the flat slide valve has already been investigated in [7]. However, pressing the plates together and hereby reducing the gap, increases friction between the plates, which counteracts an adjustment of the valve and thus must be overcome. The functionality of a ceramic flat slide valve has not yet been proven in hydraulics.

The use of a new, innovative flat slide valve, which is the subject of a multidisciplinary research project at ifas (Institute for Fluid Power Drives and Systems) and IWM (Institute for Material Applications in Mechanical Engineering), is intended to improve upon the weakness of conventional valves and to demonstrate the functionality of a ceramic flat slide valve for hydraulic applications. In a first step, a valve with a main stage made of a metallic material is designed and tested. This first demonstrator is presented in this paper.

2. PRINCIPLE OF THE FLAT SLIDE VALVE

To prove the functionality of the ceramic flat slide valve, a functional model of a flat slide valve is constructed, which is designed as a 4/3-way valve. **Figure 3** shows the basic conceptual design of a flat slide valve.

The main stage of the valve is formed by three plates, which sit on top of one another. Together these plates form the flow channels of the valve.

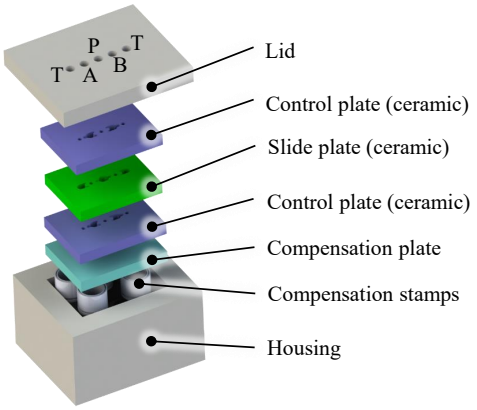

Figure 3: Basic conceptual design of a flat slide valve

The two outer plates are the so-called control plates. The control plates are geometrically identical and fixed in position. The plate between the control plates is the slide plate, which is linearly movable. Depending on the position of the slide plate, the individual connections can be connected to each other, disconnected or partially connected.

Below the main stage is the pressure compensation, which is an elementary part of the concept. In order to prevent a gap between the plates of the main stage, five pressurized stamps are used. The force generated by these stamps is transferred to the main stage by a compensation plate and counteracts a gap formation.
The valve is sealed against the environment with a cover and a housing. In the concept shown, the locations of the hydraulic main connections of the valve are also indicated. These consist of the pump port, the two working ports A and B and the tank ports.

Figure 4 shows the main stage, the compensation plate and the compensation stamps. The compensation stamps press the main stage against the housing so that a normal force acts on the slider plate. On one hand, this normal force prevents a gap widening between the plates, on the other, the necessary actuator force also rises with increasing normal force. The necessary actuator force can be calculated using:

$$F_{\mathrm{Fric}} = \mu \cdot (F_{\mathrm{mech,t}} + F_{\mathrm{mech,b}}) \qquad (1)$$

In addition to the forces applied by the stamps, other forces also act on the main stage, such as the hydraulic pressures, which are present in the valve. In [6] the acting forces and correlations have been explained.

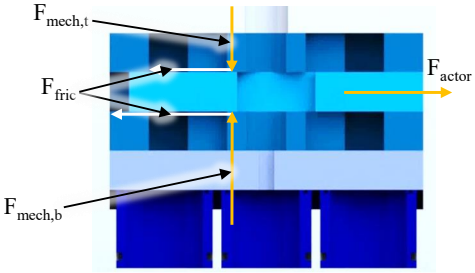

Figure 4: Forces acting on the slider

If the mechanical force is greater than zero, a gap is formed between the plates and the leakage increases. If the normal force is too high, large actuator forces are necessary to change the valve position. An exact calculation and design of the pressure compensation is therefore necessary.

3. THE METALLIC MAIN STAGE

The main stage, which will be made of metal for the first demonstrator, is shown in **Figure 5**.

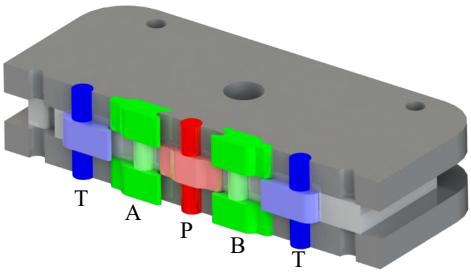

Figure 5: Implemented steel main stage of flat slide valve

The design of this main stage was first presented in [6]. The design criterion for the flow behavior of the main stage was derived from valves of nominal size 6. In concrete terms, this means that at a flow rate of 30 l/min with HLP 46 (40°C) the valve should have a pressure drop of 10 bar at full deflection. In addition, the main stage should be able to withstand hydraulic pressures of up to 300 bar. The individual channels are arranged on one line, so that the compensation only has to balance the forces arising in the valve along this line. In the center of the main stage, the channel connected to the pump port P is drawn in red. To the right and left of the pump port, the two working ports A and B are marked green. The two channels, which are connected to the tank are blue.

The maximum deflection of the main stage is ± 3 mm. Additionally, the main stage has a positive overlap of 1 mm in both directions. This can also be seen in **Figure 6**, which shows the main stage in neutral position (0 mm). In this position all ports are separated and there is no flow between each port. For the first test of the valve, aforementioned positive overlap was chosen in order to be able to investigate the behavior of the valve, in particular the leakage at low flow rates, and to be largely independent of manufacturing tolerances.

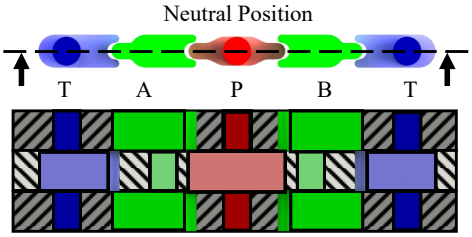

Figure 6: Neutral position of flat slider

Figure 7 shows the main stage at a maximum deflection to the left of -3 mm. This permits a flow from pump port P to working port A and a flow from working port B to tank port T.

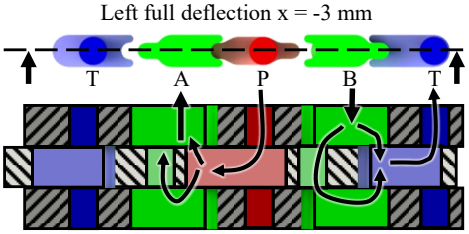

Figure 7: Full deflection of flat slider to the left

When designing the main stage, it was possible to achieve a linear ratio between the valve stroke and the opening flow cross section in the simulations. The relationship between slider deflection and opening flow cross section for pump port P to working port A and pump port P and working port B can be seen in **Figure 8**.

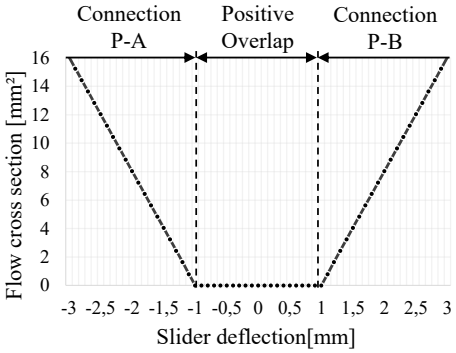

Figure 8: Relationship between slider deflection and flow cross section for P-A and P-B

4. REALIZATION OF THE DEMONSTRATOR

In order not to have to manufacture a new demonstrator for each development stage of the valve, a demonstrator was developed which is able to measure different main stages. The plates of the main stage can have variable thicknesses and can be made of different materials. The special properties of ceramics, such as the comparatively high sensitivity to notch fracture, have also been considered. In addition, different channel geometries can be realized with relatively little effort.

Figure 9 shows the housing, which consists of three parts and the inner parts of the valve.

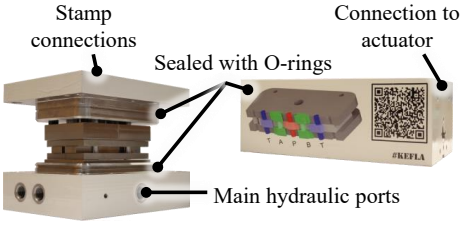

Figure 9: Demonstrator flat slide valve

The housing consists of a lid, a base and an intermediate housing. The lid and the base are aligned with each other via the intermediate housing using dowel pins. O-rings are used to seal the individual housing parts to the outside.
The individual connections for supplying the stamps are located within the cover. In the final application, the flat slide valve should be supplied with the same pressures that are applied to the individual ports. The magnitude of the necessary force is then defined by the size of the pressurized area. However, during function testing this would mean that for each new geometry of the main stage or for each pressure compensation to be tested; a new cover and stamps would have to be manufactured. For this reason, the individual stamps are supplied by pressure reducing valves for functional testing. Thereby a quick adjustment of the pressure compensation is possible.

The individual hydraulic ports (P, A, B, T), which supply the main stage of the valve, are located in the base of the housing. In addition to the hydraulic ports, there is also a leakage port. With this port, the leakage flow that would occur if a gap was formed can flow off to the tank. In addition, the connection can be used to detect the remaining leakage between the plates after finishing the testing of the pressure compensation and thus evaluate the concept.

A pressure sensor, which monitors the housing pressure, is also located in the base of the housing. This can be used to determine the force applied by the pressure to the inner parts of the valve and also allows the implementation of an emergency shutdown in case the housing pressure exceeds a critical level.
The actuator of the valve is attached to the intermediate housing. It is possible to connect actuators on both sides of the intermediate housing. For example, the main stage can be operated tensioned. Currently, one actuator is used to adjust the flat slide valve and the second side is sealed to the outside using a plug and an O-ring.
Figure 10 shows the inner parts of the valve.

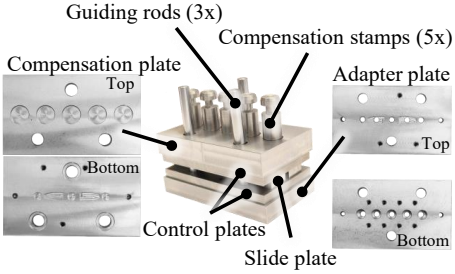

Figure 10: Inner part of the flat slide valve

The pressure compensation is realized by the five compensation stamps and the compensation plate. The pressure compensation is guided by three guiding rods and slide bearings. The upper control plate is aligned with the compensation

plate via dowel pins and is fixed to it with screws. The slider plate is located between the two control plates and can be moved linearly, guided by the three guiding rods shown. The lower control plate is connected to the adapter plate by dowel pins and screws. This adapter plate supplies the main stage with fluid.

Figure 11 shows a sectional view of the inner parts of the valve from Figure 10 and the base of the body.

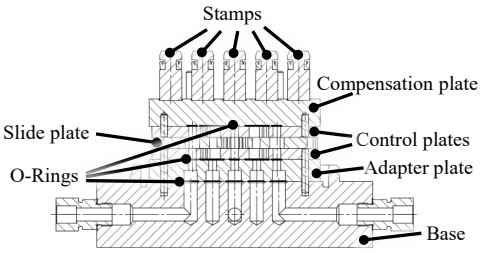

Figure 11: Sectional view of inner parts and base

The dowel pins for alignment of the control plates and the supply of the control plates through the adapter plate and the bottom are shown above. The seals between compensation plate and control plate, and between control plate and adapter plate, ensure that leakage can only occur between slider and control plates.

Figure 12 shows the metallic main stage, consisting of two control plates and a slide plate. Besides the parts shown in Figure 12, another slide plate is made of a special brass (CW713R), which is currently installed in the valve.

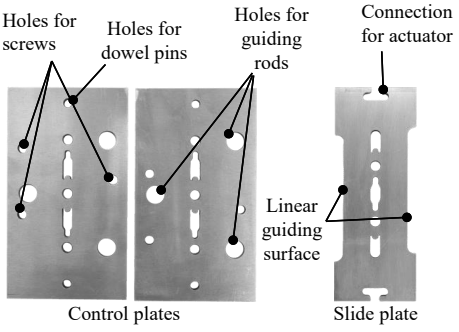

Figure 12: Metal main stage

Additional to the holes for the dowel pins and screw connections, the through-holes for the guiding rods are also shown in the figure. This guide rods are used to guide the compensation plate, and the slide plate linearly using the guide surfaces shown. The flow channels correspond to the geometry shown in Figure 5. On both sides of the intermediate housing a connection geometry is located to attach an actuator.

In order to allow backlash-free adjustment of the slide, the design shown in **Figure 13** was implemented.

The connecting rod connects the actuator with the slider plate through the sleeve, which is shown on the left. The sleeve contains two guide bands, a dynamic seal and a wiper. After testing the pressure compensation, these can be removed in order to be able to measure the force required for adjustment without influencing it. The sleeve is sealed to the outside using an O-Ring by a static seal. The dovetail is secured with help of a notched pin in the connecting rod and can be tightened by the nut. The two pins serve as spacers so that the slide can move without collision.

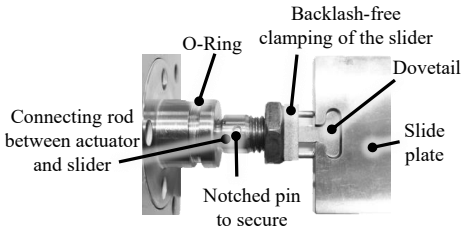

Figure 13: Connection between slide plate and actuator

5. ACTUATION

A stepper motor of size Nema 23 is used to adjust the valve. The motor has a resolution of 200 steps per revolution (1.8°) and the installed encoder can be used to evaluate the steps that have been carried out. **Figure 14** show the assembled actuator unit.

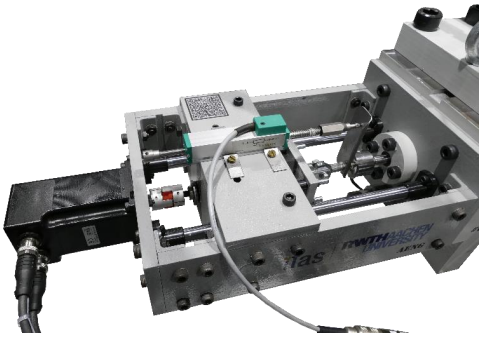

Figure 14: Actuator of flat slide valve

The rotary motion is converted into translatory motion by using a trapezoidal threaded rod and trapezoidal threaded nut. The trapezoidal rod has a pitch of 2 mm. A 64-fold microstepping can be realized with the used the stepper motor clamp. This results in a theoretical adjustability of the unit of:

$$\Delta x = \frac{\text{Pitch of trapezoidal rod}}{\text{Motor steps x Micro stepping}} = 0.00016\ mm \quad (2)$$

Axial needle roller bearings protect the stepper motor from axial overload. To measure the forces, which are required for an adjustment of the slide plate, a force sensor is mounted to the actuator, which can handle forces up to 1000 N. The maximum load capacity of the force sensor also represents the force limitation of the actuator. A combination of clevis joint and head joint has been installed in the actuator to ensure that the force measurement is almost completely free of transverse forces. A distance sensor measures the deflection directly before entering the valve. The actuator is guided by guiding rods and linear ball bearings. **Figure 15** shows the flat slide valve with attached actuator.

Figure 15: Valve with attached actuator

6. HYDRAULIC CIRCUIT FOR LOAD SIMULATION

In order to simulate a load, the hydraulic circuit shown in **Figure 16** is used for testing and measuring of the flat slide valve.

In addition to the pressure sensor shown, each hydraulic connection of the flat slide valve also has a temperature sensor to measure the fluid temperature. This allows a determination of the pressure drop between the individual valve ports and a determination of the viscosity of the fluid. Before the fluid enters pump port P and after the fluid leaves tank port T, a volumetric flow sensor is installed. A leakage or a gap widening between the plates of the main stage can be detected by

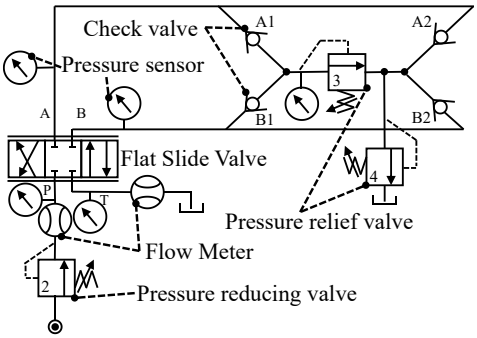

Figure 16: Hydraulic circuit for load simulation

determining the difference between the two measuring signals of the volume flow sensors. For a more precise evaluation of the leakage, the leakage port of the housing can also be used. Thereby the fluid outlet flow can be determined with the use of a scale and time recording. The leakage port is not shown in Figure 16.

With the help of the pressure relief valve (3) and the check valves (A1, A2, B1, B2), a load can be simulated between the working ports A and B. If the flat slide valve connects ports P and A and ports B and T, the pressure at working port A is higher than the pressure at working port B. Thereby check valve A1 is open and due to the lower pressure at working port B, the check valve B1 remains closed. The fluid exiting the pressure relief valve has a lower pressure than the fluid at working port A and a higher pressure than the fluid at working port B. As a result, the check valve B2 and A2 remain closed. The check valves are acting reverse for a connection from P to B and from A to T.

To simplify the control effort, a pressure sensor is located directly in front of the pressure relief valve (3).

The pressure relief valve (4) serves as a safety valve, since the used pressure relief valve (3) is limited to a pressure of 100 bar on the tank side.

Due to manufacturing tolerances, it may happen that one side of the control edges engages before the other. In this case, the high-pressure side would already be connected, and the low-pressure side would still be disconnected from the tank. The resulting overpressure can then flow via the pressure relief valve (4) to the tank and the pressure relief valve (3) is not getting damaged. With the pressure reducing valve (2) it is possible to use only one supplier to supply the flat slide valve and the stamps.

7. VOLUMETRIC MEASUREMENT

To compare the CFD simulations with reality, a measurement of the main stage was carried out. Figure 16 shows the results of this volumetric measurement for a flow from P to A. The volume flow was recorded for multiple positions. As fluid a HLP 46 was used, which had a temperature of 40 °C. The pressure difference between P and A was set to a constant level of 10 bar during the entire duration of the measurement. This also corresponds with the boundary conditions, which were used during the CFD simulations. The individual measuring points are shown as blue asterisks in the diagram. The black dotted line shows an ideal linear flow characteristic.

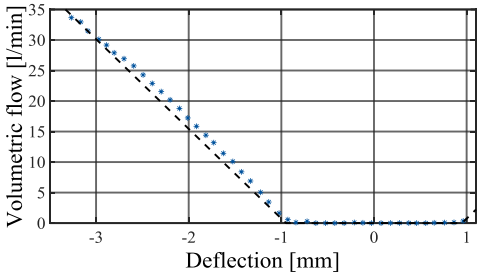

Figure 16: Volumetric flow measurement of main stage

As can be seen in Figure 16, an almost linear flow characteristic can be achieved with the presented channel geometry. The results show good correlation with the CFD simulations shown in [6]. Furthermore, the set target of a flow rate of 30 l/min; at a position of ± 3 mm and a pressure difference of 10 bar; could be achieved.

8. CONCLUSION AND OUTLOOK

In this paper, the advantages of flat slide valves in comparison to the currently used piston valves were presented. By using flat slide valves, a reduction of leakage could be achieved. Furthermore, the use of ceramic plates in the main stage can increase the service life of the valves, due to their better resistance to erosion.

The main stage of the valve consists of two fixed control plates and a linear moving sliding plate. These three plates form the flow channels of the valve. Depending on the position of the sliding plate, the individual ports are connected or disconnected.

In order to counteract the gap formation between the individual plates, a force is applied to the main stage by compensation stamps. However, this applied force must be limited, otherwise movement of the sliding plate is not possible.

A metallic main stage was presented which has a pressure difference of 10 bar at 30 l/min at full deflection, as can be discerned from valves of nominal size 6. A positive overlap was initially provided for further investigation of the leakage behavior. The function of a 4/3-way valve known from piston spool valves can be realized with the shown geometry. During the design of the flow channels a linear behavior between sliding plate deflection and opening flow cross section was achieved. In addition to the metallic main stage, the detailed design of the valve and the actuators used to adjust the position of the main stage were also presented. The circuit diagram shown in Figure 15 allows the valve to be tested with values close to reality.

The valve is currently being tested at ifas. The volumetric measurement of the valve stage shows a good correlation with the CFD simulations presented in [6]. Also an almost linear flow behavior could be achieved. The testing of the pressure compensation will be published and carried out hereafter. After testing the metallic main stage, a second demonstrator will be set up in cooperation with the IWM, which will include a main stage made of ceramic plates. This demonstrator will be used to prove the function of the ceramic flat slide valve. In addition to the functional test of the flat slide valve, the general usability of ceramic materials in hydraulics will be tested with this test setup.

9. ACKNOWLEDGEMENTS

The IGF research project 19576 N / 1 of the research association Forschungskuratorium Maschinenbau e. V. – FKM, Lyoner Straße 18, 60528 Frankfurt am Main was supported from the budget of the Federal Ministry of Economic Affairs through the AiF within the scope of a program to support industrial community research and development (IGF) based on a decision of the German Bundestag.

NOMENCLATURE

A	Hydraulic working port A
B	Hydraulic working port B
P	Hydraulic pump port P
T	Hydraulic tank port T
h	Gap height
x	Deflection of slide plate
F_{actor}	Required actuator force
F_{fric}	Resulting friction force
$F_{mech,t}$	Mechanical force on top side of plate
$F_{mech,b}$	Mechanical force on bottom side of plate
Q_L	Leakage between ports
μ	Friction coefficient

REFERENCES

[1] Schmitz, K., Murrenhoff, H. (2018): Fundamentals of Fluid Power - Part 1 Hydraulics (Translation of the completely reworked German edition of 2018), ISBN: 978-3-8440-6306-6, Shaker Verlag, Aachen, Germany, 2018

[2] Schumacher, J. (2013) Alterungs- und Verschleißverhalten von Druckübertragungsmedien und hydraulischen Ventilen, Doctoral Thesis, RWTH Aachen University, 2013

[3] Weber, P., Reinertz, O., Matthiesen, G., Murrenhoff, H. (2014) Short time ageing test for hydraulic valves, Dutch Fluid Power Conference: Het Hydrauliek Symposium; November 13th, 2014, Ede (NL)

[4] Bergmann, L.(1995) Ventil oder Sanitärarmatur, mit einem Ventilscheibenpaket, DE19526110 C1, Patent, 1995

[5] Kiesbauer, J. et al.(2013) Flat slide valve, EP 2 708 781 A2, European Patent, 2013

[6] Aengenheister, S., Liu, C. Broeckmann, C., Schmitz, K. (2019) A Ceramic Flat Slide Valve for Hydraulic Applications. Symposium on Fluid Power and Motion Control FPMC2019, Sarasota, USA

[7] Liu, C., Aengenheister, S., Herzog, S., Deng, Y., Kaletsch, A., Bezold, A., Schmitz, K., Broeckmann, C. (2019) Tribological Qualification and Prediction of Fracture Probability of High-Performance Ceramics for Applications in Flat Sliding Valves, Ceramic Applications 7 (2019) – ISSN: 2196-2413; Pages 56-62

peer reviewed

CONTROL CONCEPT FOR A GREASE LUBRICATED HYDROSTATIC BEARING

Igor Mass[1]*, Andreas Hoppermann[1], Hubertus Murrenhoff[2]

[1]*Hochschule Niederrhein, Faculty of Mechanical and Process Engineering, Germany*
[2]*RWTH Aachen University, Institute for Fluid Power Drives and Systems (IFAS), Aachen, Germany*
* Corresponding author: Tel.: +49 2151 822 5071; E-mail address: igor.mass@hs-niederrrhein.de

ABSTRACT

In industrial practice greases are mainly used as lubricants in hydrodynamic plain bearings and roller bearings. The use in hydrostatic bearings is avoided due to the difficult controllability. One reason is the complex non-Newtonian flow behavior of greases. The motivation for this paper is the use of greases to increase the efficiency of hydrostatic bearings. The assumption is that the so-called yield stress of consistent greases can lead to self-sealing behavior in the bearing under stationary operation conditions. Assuming a volume-flow-free operation of the bearing, a concept for the active control of the sealing gap height and thus the bearing stiffness was developed. The concept idea is the use of a second medium with Newtonian characteristic for pressure transfer. The grease and the pressure control fluid are structurally separated. The grease is induced in the shortest possible way into the bearing pocket to keep the pressure losses as low as possible. The results of test bench investigations indicate the feasibility of a gap height control with very high bearing stiffness under use of highly consistent greases and initiate further investigation on non-stationary operation.

Keywords: Hydrostatic bearing, Bingham Fluid, Grease rheology

1. INTRODUCTION

Hydrostatic bearings typically operate under fluid friction in the entire movement process of machine elements. This is conditioned due to the application of a hydrostatic pressure inside so-called bearing pockets by an external pump. Conventional hydrostatic bearing designs include the bearing pocket geometry, the sealing gap ring and the lubricant. The design of such a bearing type is usually carried out by an optimization approach in which the necessary pump power is compared with the friction power for continuous movements [1].

Hydrostatic bearings have a number of advantages compared to other bearing variants because of their operation principle. This includes a wear-free operation (this only affects the actual bearing and not the entire periphery which is necessary for operation), a very low coefficient of friction, no static friction and thus no stick-slip effect, high stiffness and good damping properties [2].

A major disadvantage of this type of bearing is the complex periphery, which is necessary for the operation of the bearing. At least one pump needs to run constantly during operation in order to build up a defined volume flow and pressure.

1.1. Field of application

The main function of the bearing in applications, which are characterized by very high bearing loads with few and relatively slow movements (e.g. cranes or nacelles of wind turbines), is the reduction of the starting torque. An external pressurized bearing is able to achieve this requirement. In order to establish fluid friction state the required pump power increases quadratically with increasing bearing load. This can lead to the conflict that the needed pump energy is higher than the energy savings caused in the reduction of friction torque. The investigated approach is to reduce the volume flow of this kind of bearings by use of greases instead of oils.

1.2. Rheology of greases

Greases are characterized by non-Newtonian flow behavior due to their composition. The non-Newtonian flow behavior manifests itself as a presence of a certain yield stress as well as pseudoplastic flow behavior. In addition, they behave thixotropic. This means that their viscosity decreases with increasing shear time. The grease is therefore exposed to continuous wear during operation of the bearing. Due to the examined field of the thixotropy is neglected in the first instance. The two models in Fig. 1 are most commonly used to describe the flow behavior of greases [3].

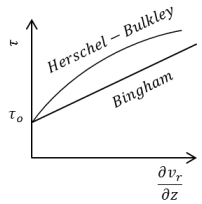

Figure 1: Commonly used flow models for greases

Bingham fluids include a certain yield stress but have constant viscosity after exceeding this yield point:

$$\tau = \tau_o + \eta \frac{\partial v_r}{\partial z} \qquad for\ \tau > \tau_0 \tag{1}$$

$$\frac{\partial v_r}{\partial z} = 0 \qquad for\ \tau \leq \tau_0 \tag{2}$$

The Herschel-Bulkley model incorporates the viscosity change with increasing shear rate. Pseudoplastic flow is determined with the exponent n < 1. For n = 1 we get the Bingham model again, for n > 1 the model behaves dilatant:

$$\tau = \tau_o + k\left(\frac{\partial v_r}{\partial z}\right)^n \qquad for\ \tau > \tau_0 \tag{3}$$

Previous studies by Horowitz and Steidler have already identified a number of advantages and disadvantages in the use of greases instead of Newtonian fluids in hydrostatic bearings coefficients [4]. These include:

- safety at low speeds,
- low side leakage,
- less sensitivity of load and friction to speed changes,
- existence of “cores” of plug flow,
- higher coefficients of friction.

Further investigations from Slibar et al. and Bradford et al. lead to the same conclusions [5], [6]. The occurrence of unsheared cores on the increase of friction in slider bearings is mentioned by Milne [7]. The high age of the mentioned sources is particularly noticeable. The author's assumption is that this approach has not been pursued so far due to the disadvantages in the difficulty of designing and controlling grease-lubricated external pressurized bearings, despite its advantages in lower leakage. The emergence of magnetorheological (MR) fluids, which exhibited Bingham flow behavior when applied by a magnetic field [8], has rekindled interest in the research of non-Newtonian flow behavior in hydrostatic bearings [9].

1.3. Investigations on self-sealing behavior

Considering axial slide bearing with a central pocket a cylindrical coordinate system is defined (Fig. 2):

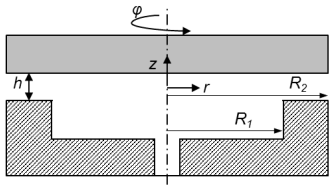

Figure 2: Defined coordinate system

The following assumptions are made for the derivation:

- validity of the Bingham model,
- time independence,
- rotationally symmetric flow,
- laminar flow,
- no rotation of the bearing,
- velocity gradient in the radial direction insignificant in comparison to z-direction.

These simplifications lead to the definition of an infinitesimal element with forces acting only in the radial direction in the sealing gap of the bearing (Fig. 3):

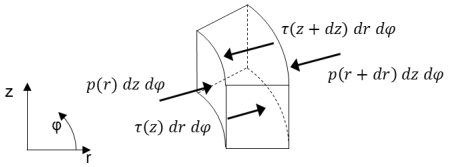

Figure 3: Acting forces in sealing gap

The equilibrium of forces lead to:

$$F_r = 0 = dz\, d\varphi \left(p(r) - p(r+dr)\right) + dr\, d\varphi\, (\tau(z) - \tau(z+dz)) \quad (4)$$

The Taylor series expansion results in:

$$p(r+dr) \approx p(r) + \frac{\partial p}{\partial r}\, dr \quad (5)$$

$$\tau(z+dz) \approx \tau(z) + \frac{\partial \tau}{\partial z}\, dz \quad (6)$$

Applying of Eq. (5) and (6) in (4) forms to:

$$\frac{\partial p}{\partial r} = -\frac{\partial \tau}{\partial z} \quad (7)$$

The used Bingham model from Eq. (1) needs a negative sign due to the definition of the coordinate origin in the middle of the gap:

$$-\tau = \tau_o + \eta\, \frac{\partial v_r}{\partial z} \qquad for\ |\tau| > \tau_0 \quad (8)$$

The derivation of Eq. (8) after the gap height provides:

$$-\frac{\partial \tau}{\partial z} = \eta\, \frac{\partial^2 v_r}{\partial z^2} \quad (9)$$

The insert of Eq. (9) in (7) provides the known differential equation for gap flow in hydrostatic bearings for the defined coordinate system:

$$\frac{\partial p}{\partial r} = \eta\, \frac{\partial^2 v_r}{\partial z^2} \quad (10)$$

Subsequent integration across the gap height reveals the Bingham model:

$$\frac{\partial p}{\partial r} z = \tau_o + \eta\, \frac{\partial v_r}{\partial z} \quad (11)$$

The shear rate takes the value zero if the left term of the equation equals the yield stress τ_0. The gap height variable for this can be defined as z_0. The grease flows as unsheared core through the sealing gap at coordinates below this value. The absolute value bars make sure that this value is positive. Figure 4 illustrates this behavior.

$$\left|\frac{\partial p}{\partial r}\right| z_0 = \tau_o \quad (12)$$

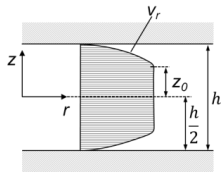

Figure 4: Unsheared core at sealing gap

In an axial sliding bearing with one central circular pocket the pressure drop across the sealing gap follows a logarithmic path. If the ambient pressure at the outlet is set to zero, the pressure can be expressed as:

$$p = p_p \frac{\ln\left(\frac{R_2}{r}\right)}{\ln\left(\frac{R_2}{R_1}\right)} \quad (13)$$

Accordingly, the pressure curve is:

$$\frac{\partial p}{\partial r} = -\frac{p_p}{\ln\left(\frac{R_2}{R_1}\right) r} \quad (14)$$

Insertion of Eq. (14) in (12) provides for each position r the height of the unsheared core:

$$z_0 = \tau_o \frac{r}{p_p} \ln\left(\frac{R_2}{R_1}\right) \quad (15)$$

This equation expresses a linear relationship between z_0 and r. If the height of the core corresponds at least to the sealing gap height h before reaching the outlet, the fluid stops moving. This leads to the following definition for zero flow rate:

$$z_0 \geq \frac{h}{2} \quad (16)$$

The use of this condition in Eq. 15 gives a maximum value for the induced pocket pressure. Fig. 5 illustrates this condition.

$$p_p \leq 2\tau_o \frac{r}{h} \ln\left(\frac{R_2}{R_1}\right) \quad (17)$$

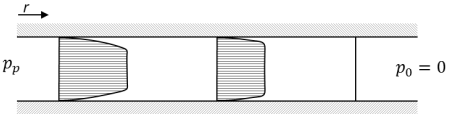

Figure 5: Progress of fluid velocity along the sealing gap at the inflow phase at zero flow rate condition.

Exemplary for the presented hydrostatic thrust bearing (R1 = 50 mm, R2 = 70 mm), operating limits for leakage-free operation can be defined with this equation (17) (Fig. 6). The selected yield stress limits are based on common consistency classes of lubricating greases (NLGI 1 to NLGI 3). Values for the correlation between conus penetration and yield stress values are given by Cameron and Spiegel et al. [10], [11].

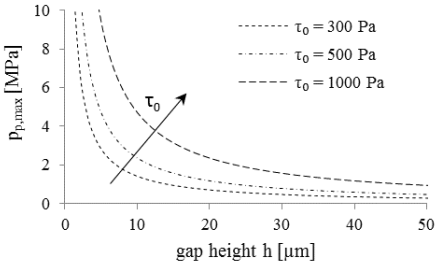

Figure 6: Limits for pocket pressure for leakage-free operation in static condition for exemplary thrust bearing

According to this diagram, NLGI grade 3 grease can be operated at a gap height of 10 µm with a maximum of approx. 4 MPa. The manufacturing quality of the surfaces in the contact area requires high efforts to reach a fluid friction state at this kind of value. For more common gap heights of around 50 µm the maximum pocket pressure drops to 1 MPa.

The presence of a stopping flow front could be determined for selected greases. Fig. 7 displays the flow front of a NLGI class 3 grease at the same pocket pressure and different sealing gap heights. Simulations by the use of a CFD model were also able to prove self-sealing behavior [12].

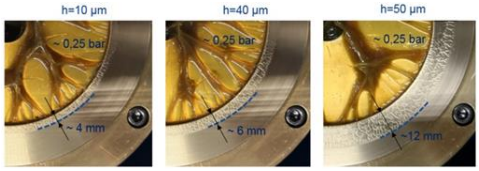

Figure 7: Proven self-sealing effect in a hydrostatic bearing for different gap heights

1.4. Common lubrication gap control

In classic hydrostatic bearings the lubrication gap height is controlled by the volume flow of the pump. An overview can be found in [13]. A distinction is made between three different control systems: one pump per bearing pocket, one pump and fixed restrictors for each pocket or one pump and adjustable restrictors. In all these systems the sealing gap height is regulated by the volume flow. Differences are found between the systems in the bearing stiffness. The stiffness of the hydrostatic bearing K is defined as a quotient of force increase and bearing gap height change.

$$K = -\frac{\Delta F}{\Delta h} \tag{18}$$

The fixed restrictor system is characterized by the lowest stiffness due to a reducing flow rate with increased bearing. In contrast the configuration of the adjustable restrictors is theoretically able to gain a stiffness of infinity by an increasing volume flow. This is usually achieved with membrane restrictors. The system with one pump per bearing pocket lies between both systems, since the flow rate is kept almost constant. Because of the desired absence of volume flow in the described grease lubricated bearing configuration these control mechanisms cannot be used.

These control mechanisms can be referred to as passive controllers. In addition, there are concepts for active controllers that directly determine the lubrication gap height and then react with control signals in order to keep this value as constant as possible. Rehman et al. implement an active control of the lubrication gap of a hydrostatic journal bearing by servo valves [14]. Other researches focus on the use of magnetorheological fluids for an active gap control [9]. A constant lubrication gap is here achieved by the changes of the rheological properties of the magnetic fluids (viscosity and yield point) at constant flow rate by the insertion of a magnetic field.

1.5. Research issue

The mentioned control mechanisms cannot be used because of the intent to operate the grease-lubricated bearings without a volume flow. The pressure transfer in greases behaves transient and is therefore difficult to control [15].

The aim of this investigation is the development of a new control system for grease lubricated hydrostatic bearings that allows the adjustment of different gap heights and reacts actively to changing bearing loads. The target is a bearing with an infinite stiffness.

2. RESEARCHED CONCEPT

The presented solution bases on a separation into two functional areas by a flexible membrane (Fig. 8). The pressure transfer in order to control the hydrostatic compensation and a sealing gap height is ensured by an easy to regulate Newtonian fluid. The Newtonian fluid is led as close as possible to the bearing pocket. The actual lubricant in the bearing pocket is consistent grease. The grease is filled via an additional feed directly into the pocket. The chosen membrane is a rolling diaphragm with high stroke and diameter in order to have a large reservoir of lubricant.

Figure 8: Used rolling diaphragm [16]

The operation steps of the bearing control can be explained accordingly to Fig. 9:

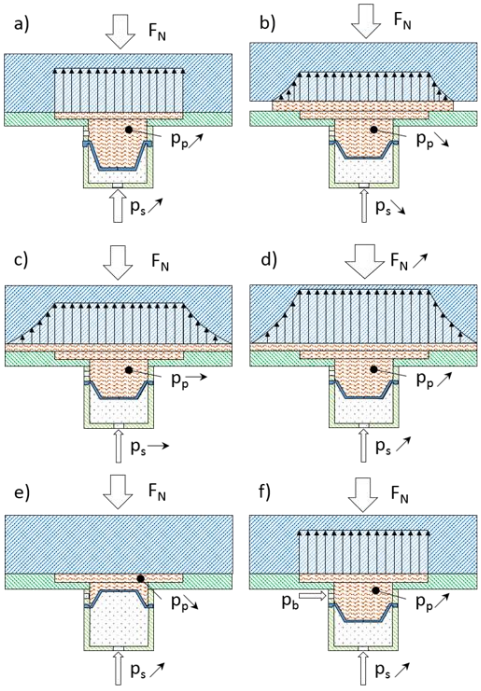

Figure 9: Functional steps of the bearing operation

a) The bearing is loaded by a normal force F_N. The pressure in the pocket p_P is increased by the supply pressure p_S until the resulting force in the pocket is just above the load force.
b) The upper bearing body lifts off after exceeding the balance of forces. As a result, the grease flows into the sealing gap. At constant pocket pressure, the resulting force would directly increase. Therefore, the supply pressure and with it the pocket pressure need to be reduced.
c) At reaching the desired gap height, the pressure must be kept constant. The resulting pressure force must be in the exact balance of forces with the load.
d) In case of a bearing load increase, the supply pressure must ideally be increased at the same time in order to ensure a constant sealing gap height. Likewise, when the load is reduced, the pressure must drop simultaneously.
e) If the gap height cannot be reduced in sufficient time, the maximum leakage is limited by the rolling diaphragm capacity. In the case of a complete exploitation of the diaphragms reservoir, its elastic resistance limits further pressure transfer. The pocket pressure drops in contrast to the supply pressure and the upper bearing element settles down.
f) An additional feed introduces new grease into the pocket (with pressure p_b) until the diaphragm is completely refilled.

2.1. Control of the gap height

For an active control of the sealing gap height the value of the height needs to be measured and the supply pressure must be actively controlled. The used concept can be explained by the schemata of the test bench in Fig. 10 and the control loop in Fig. 11.

The sealing gap height is measured with an inductive sensor directly in the sealing gap. The deviation Δh_e from the desired setpoint value h_i is transferred to a programmable software controller. The controller output is the supply pressure p_s. This supply pressure is adjusted with an electronically controlled pressure reducing valve. The maximum load capacity of the bearing results from the maximum available pressure provided by the pump.

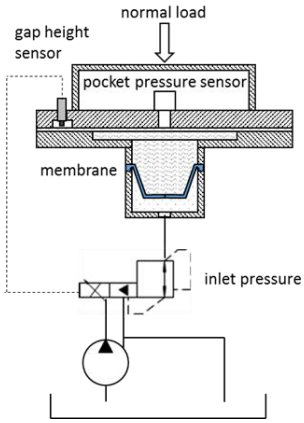

Figure 10: Configuration of the test bench

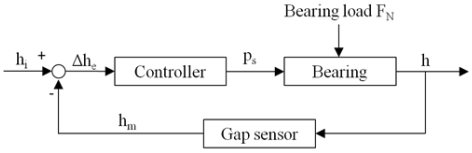

Figure 11: Control loop of the test bench

3. EXPERIMENTAL INVESTIGATION

At the test bench shown in Fig. 10 the control behavior for different lubricants under varying bearing loads was tested. Compressed air was used as pressure transfer medium. This means that the system was pneumatically controlled. The programmed software controller was a proportional plus integral type (PI controller). The decision was driven by a simple implementation. The main purpose of this study was initially a feasibility study of the sealing gap height control with this concept. Furthermore, the transfer on industrial applications in future becomes easier. The control parameters for each fluid were determined empirically due to a complex transfer function of this system.

3.1. Tested fluids

Two NLGI grade 2 non-Newtonian greases and one Newtonian oil were tested. Lubricating grease A is calcium soaped low-temperature grease with a thickener content of approx. 10-12 %. Grease B is a high-temperature grease based on bentonite with a thickener content of approx. 6-8 %. The used Newtonian fluid is a commercially available CLP320 gear oil.
The values for yield stress and dynamic viscosity of the lubricating greases were determined at 20 °C in flow curve measurements by extrapolation. The value for the oil was calculated from the kinematic viscosity and the density. The determined values are summarized in Table 1.

Table 1: Tested fluids

Fluid	NLGI	ν [mm²/s]	τ_0 [Pa]	η [Pas]
Grease A	2	14	205	0.053
Grease B	2	500	710	3.26
CLP320	-	320	-	0.74

3.2. Test procedure

In the first step the control parameters were determined empirically for each fluid by considering the step response to a defined sealing gap height. After the controller adjustment the behavior of the bearing for different sealing gap heights and increasing loads was tested. The dimensions of the tested axial thrust bearing and the selected control variables are diagramed below (Table 2 and 3).

Table 2: Bearing configuration

Parameter	Value	Unit
Inner diameter	100	mm
Outside diameter	140	mm
Pocket depth	5	mm

Table 3: Experimental setup

Parameter	Unit	Min.	Max.	Step
Gap height	µm	10	50	10
Bearing load	N	1000	3500	500

3.3. Results

Gap height adjustment

Example curves in Fig. 12 express the adjustment behavior of the three fluids for a bearing load of 2000 N and a sealing gap height of 20 µm. Comparable behavior could be registered for other combinations of loads and sealing gap heights.

As explained in the functional description Fig. 12 indicate that an overpressure must first be

generated in order to generate a lift of the upper bearing partner. In the greased bearing variants a much higher pressure is required than in the oil lubricated bearing. The most inert behavior can be registered for grease B. The sealing gap initially continues to rise even when the pocket pressure is already reduced significantly. For this reason, the bearing tends to slightly overshoot.

The lubricating oil can be set the fastest to the required gap height, but at the same time it is the most sensitive towards disturbances.

In addition, the test reveals, that, despite of the same bearing load, the resulting pocket pressure differs for all three fluids.

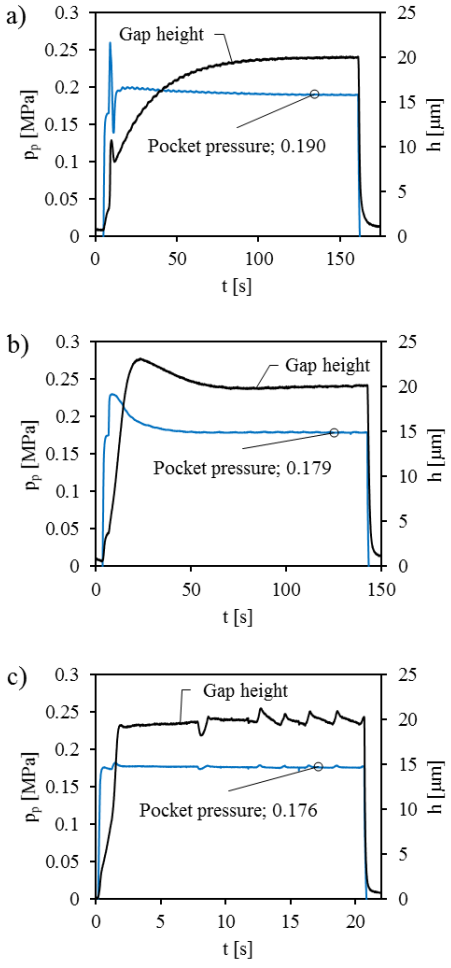

Figure 12: Time course of the adjustment of 20 µm gap height at 2000 N load for Grease A (a), Grease B (b) and CLP320 (c)

The mean values from the resulting pocket pressures for different sealing gap heights (10, 20 and 30 µm) and bearing load levels are plotted in Fig. 13. The calculated lines show the theoretically derived pocket pressures for Newtonian fluids for the used bearing geometry.

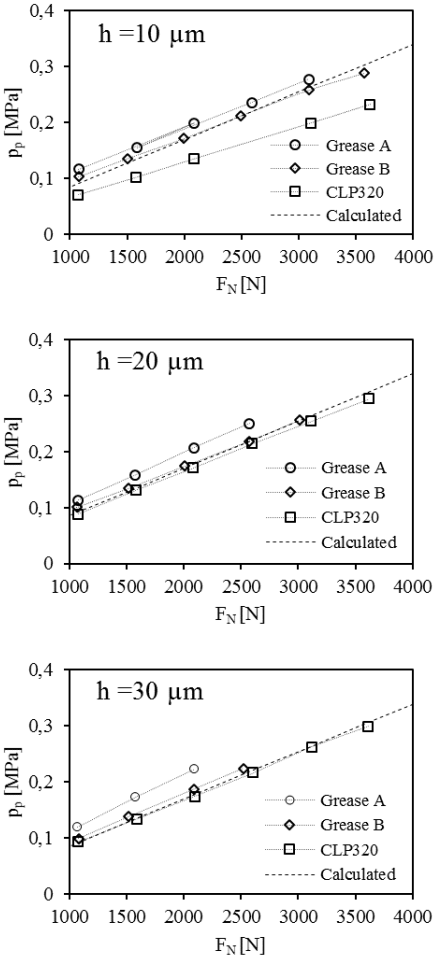

Figure 13: Steady state pocket pressures for different bearing load levels

At sealing gap heights of 20 µm and 30 µm the values determined for the oil correspond to the calculation. Higher values are registered for all loads for the grease-lubricated bearing. From this observation the following assumption can be settled: because of a higher decline of the pressure in the sealing gap with the use of grease, a higher pocket pressure must be applied to get

the same resulting counterforce. At a sealing gap height of 10 µm, the values of Grease B and CLP320 oil are much lower than expected.

Gap height stiffness

When increasing the bearing loads F_N for constant sealing gap heights h a similar behavior is observed as in the previous investigation. Grease B tends again to the most inert reaction (Fig. 14).

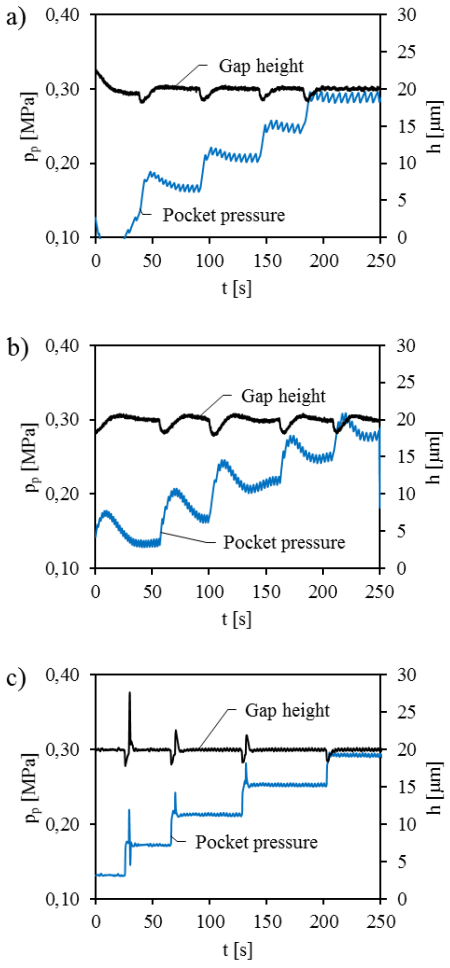

Figure 14: Control of a constant sealing gap height with increasing bearing load F_N from 1500-3500 N for Grease A (a), Grease B (b) and CLP320 (c)

The system becomes increasingly sensitive for increasing gap heights. The performance for Grease B at 40 µm is shown in Fig. 15. The gap height drops down with a greater value by increasing the bearing load and the system requires more time to rebuild the desired lubrication gap to the inertia of the grease.

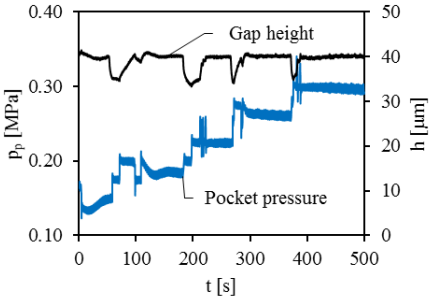

Figure 15: Control of a constant sealing gap height with increasing bearing load from 1500-3500 N for Grease B at 40 µm gap height

4. CONCLUSION AND OUTLOOK

The results indicate that a pressure control via the rolling diaphragm in order to generate desired sealing gap heights at defined operating points is basically possible. For Newtonian oil sealing gaps could be reproduced with an accuracy of ± 0.25 µm, grease A with an accuracy around ± 0.35 µm and the more inert grease B around ± 0.5 µm.

In a stationary view, an infinite stiffness for all three fluids can be proven with this control concept until the maximum supply pressure is reached. At a time perspective, collapses are noticeable in the event of a load change. Depending on the used fluid and the sealing gap height, the collapses vary in magnitude and are compensated at different speeds. This behavior strongly depends on the selected controller and the control parameters.

In addition to the bearing geometry, the rheology of the bearing fluid has a major impact on the controlled system. Due to its linearity, the Bingham model can reproduce the flow behavior with sufficient accuracy only in a defined operating point. The thixotropy and pseudoplasticity behavior are not considered within this model but can have an important impact on the gap control. Advanced models such

as the Herschel-Bulkley or Sisko model include pseudoplasticity, but do not allow analytical solutions [3] .

Another influence on the control behavior could be the occurrence of wall slip [17]. This wall-slip effect can be responsible for the fact that, despite falling below the pressure gradient in the sealing gap and thus the assumption of self-sealing it comes to a flow of an unsheared cores at the wall boundaries.

Nonlinear controllers, such as adaptive controllers or optimal controllers [18], could be able to hold the grease-operated bearings stable at desired working heights even at different operating points. The presented test bench allows the use of different types of controller for closer examination in the future.

Grease A indicates the best performance in terms of tendency to leakage, regulation of the gap height and friction reduction. In previous investigations of the friction torque Grease A achieved comparable friction coefficients as the CLP320 oil, shown in Fig. 16.

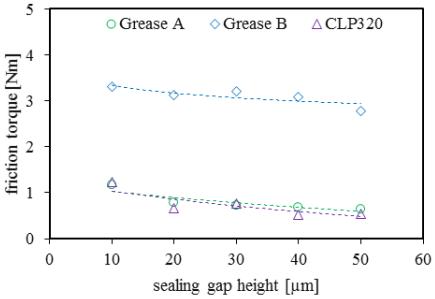

Figure 16: Tested sliding frictions for different gap heights at a bearing load of 1500 N

NOMENCLATURE

F_N	Normal force, bearing load
h	Sealing gap height
p_p	Pocket pressure
p_s	Supply pressure
p_b	Bypass pressure
η	Dynamic viscosity
τ	Shear stress
τ_0	Yield stress

REFERENCES

[1] O'Donoghue J, Rowe W (1969) Optimization of Hydrostatic Bearings for Minimum Power and Low Temperature Rise. Industrial Lubrication and Tribology, Vol. 21, 101 -108

[2] Hamrock B.J, Schmid S.R, Jacobson B.O (2004) Fundamentals of Fluid Film Lubrication. 2nd ed., New York, Dekker

[3] Kuhn E (2017) Zur Tribologie der Schmierfette, Renningen, Expert Verlag

[4] Horowitz H.H, Steidler F.E (1963) Calculated Performance of Greases in Journal Bearings. ASLE Transactions, 239-248

[5] Slibar A, Pasley P.R. (1957) On the Theory of Grease Lubrication Studies in Plain Journal Bearings. ASME Trans. 79, 1229-1234

[6] Bradford L.J, Barber E.M, Muenger P.J (1961) Grease Lubrication Studies in Plain Journal Bearings. J. Basic Eng. ASME Trans. 81, 153-161

[7] Milne A.A (1964) A theory of Grease Lubrication of a Slider Bearing. Proceedings of the Second International Congress on Rheology, New York, Academic Press, 427-436

[8] Butz T, von Stryk O (2002) Modelling and Simulation of Electro- and Magnetorheological Fluid Dampers. ZAMM Vol. 82, No. 1, 3-20

[9] Abel-Keilhack C, Hesselbach J (2003) Active hydrostatic bearing with magnetorheological fluid. Journal of applied physics, 8441-8443

[10] Cameron A (1966) The Principles of Lubrication. London, Longmans Green and Co. Ltd.

[11] Spiegel K, Fricke J, Meis K.R (2000) Das Fließverhalten von Schmierfetten. Schmierfette: Zusammensetzung, Eigenschaften, Prüfung und Anwendung. Renningen, Expert Verlag, 228-265

[12] Mass I, Hoppermann A, Murrenhoff H (2018) Pressure distribution of greases in hydrostatic bearings under static conditions. Fluid power networks : proceedings : 19th - 21th March 2018 : 11th International Fluid Power Conference, Vol. 3, 68-77

[13] Weck M, Brecher C (2019) Werkzeugmaschinen - Fertigungssysteme 1. Berlin, Springer Vieweg

[14] Rehman W.U, Yuanxin L, Guiyun J, Yongqin W, Yun X, Iqbal M.N, et al (2017) Control of an oil film thickness in a hydrostatic journal bearing under different dynamic conditions. Proceedings of the 29th Chinese control and

decision conference (CCDC), Chongqing, China, 28-30 May 2017, 5072–5076

[15] Oliveira G.M, Negrão C.O, Franco A.T (2011) Pressure transmission in Bingham fluids compressed within a closed pipe. Journal of Non-Newtonian Fluid Mechanics, 121-125

[16] Freudenberg Sealing Technologies, [Online]. Available: https://www.fst.com/products/special-sealing-products/diaphragms. [Access on 11 Nov 2019].

[17] Westerberg L, Lundström T.S, Höglund E, Lugt P.M (2010) Investigation of Grease Flow in a Rectangular Channel Including Wall Slip Effects Using Microparticle Image Velocimetry. Tribology Transactions, 53:4, 600-609

[18] Iqbal J, Ullah M, Khan S.G, Khelifa B, Ćuković S (2017) Nonlinear control systems – A brief overview of historical and recent advances. Nonlinear Engineering 6(4)

peer reviewed

FOAM ACCUMULATORS: PACKAGING AND WEIGHT REDUCTION FOR MOBILE APPLICATIONS

Manuel Rexer[1], Peter Kloft[2], Frank Bauer[2], Jakob Hartig[1], Peter F. Pelz[1]*

[1] *Institut für Fluidsystemtechnik, Technische Universität Darmstadt, Otto-Berndt-Straße 2, 64287 Darmstadt*
[2] *HYDAC TECHNOLOGY GmbH, Justus-von-Liebig Straße, Werk 2, 66280 Sulzbach/Saar*
* Corresponding author: Tel.: +49 6151 1627100; E-mail: peter.pelz@fst.tu-darmstadt.de

ABSTRACT

Standardized parts like hydraulic accumulators are used in nearly every hydraulic system, in many cases even several. Therefore, even small changes in size and weight of accumulators can save considerable material costs. In mobile applications, hydraulic accumulators are used among others in hydro-pneumatic suspension systems. There is a strong focus on miniaturization and weight reduction, as the components always have to be transported with the vehicle. Energy density and energy content of conventional hydraulic accumulators cannot be maximized at the same time. This limitation can be overcome by adding a heat capacity with large surface into the gas volume of the accumulator. The heat capacity enlarges the isothermal frequency range and therefore enlarges the energy density of the accumulator at the given frequency and the given size.

In this paper an experimental comparison of conventional hydraulic accumulators and accumulators with foam inserts shows, that at a specific frequency band, the stiffness of foam filled accumulators is significantly lower than of conventional accumulators. The energy density is about 11 % higher than in conventional accumulators. Consequently, a space reduction of about 18 % is possible.

Keywords: foam, hydraulic accumulator, heat sink, hydropneumatic spring,

1. INTRODUCTION

In mobile hydraulics there is a trend to miniaturization and integration of functions to reduce package and external complexity. But not all vehicles are built in sufficient quantities to justify custom built highly integrated hydraulic components. Therefore, standardized parts like hydraulic accumulators should not be overlooked in miniaturization efforts.

Hydraulic accumulators are used to store energy in nearly every fluid system, e.g. for dynamic energy demand. In mobile applications hydraulic accumulators are used among others in hydro-pneumatic suspension systems (see **Fig. 1**) to store potential energy. For these applications space and weight reduction by smaller components is inevitable due to material costs and energy demand.

In this paper hydraulic accumulators with foam in the compressible gas volume are investigated for their space saving potential in mobile applications. Since hydro-pneumatic suspension systems are vibrating systems the stiffness transfer behavior over frequency has to be considered.

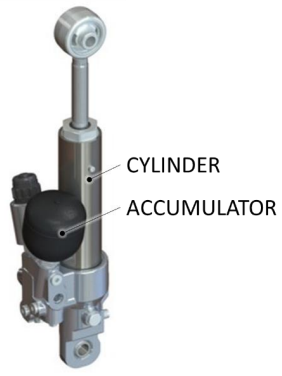

Figure 1: Example for a hydro-pneumatic suspension.

2. METHOD

2.1. Accumulators in hydropneumatic suspension systems

Suspension systems such as those used in vehicles are meant to "carry loads", "store energy" and "damp". Hydro-pneumatic suspension struts consist of at least one hydraulic cylinder and one hydraulic accumulator connected by a throttle. **Fig. 2** shows the basic structure of the hydro-pneumatic strut with level control.

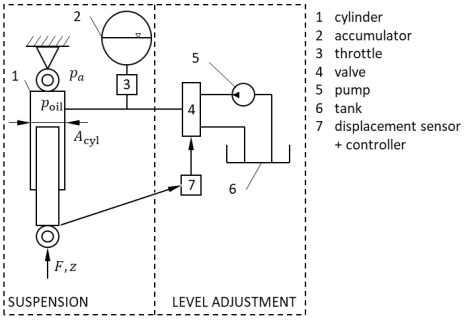

Figure 2: Principle of a hydro-pneumatic suspension. (in accordance with [1])

The hydraulic accumulator thereby fulfills the function of carrying load and storing energy. In the following damping is left out of the equation but can be taken into account using simple models. The force of the hydro-pneumatic strut can be expressed as

$$F = A_{\mathrm{cyl}}(p_{\mathrm{oil}} - p_{\mathrm{a}}). \tag{1}$$

Since the area of the cylinder A_{cyl} and ambient pressure p_{a} are constant and the throttle is neglected the force is only determined by the pressure in the oil p_{oil}. A stiffness K for the hydraulic accumulator can be specified independently of the cylinder surface [1, 2]

$$K = \frac{1}{A_{\mathrm{cyl}}^2}\frac{dF}{dz}\Big|_{z=0} = \frac{dp}{dV}\Big|_{z=0} = n\frac{p_1^2}{p_0 V_0}. \tag{2}$$

The stiffness thus depends on the load pressure p_1, the precharge pressure p_0 and the initial gas volume V_0. For comparison purposes the stiffness is de-dimensioned with

$$K^+ = K\frac{p_0 V_0}{p_1^2}. \tag{3}$$

Therefore, fluctuations in the precharge- and load pressure in the measurement vanish. A polytropic state change with the polytropic exponent n is assumed

$$\left(\frac{p_1}{p_2}\right) = \left(\frac{T_1}{T_2}\right)^{\frac{n}{n-1}} = \left(\frac{V_2}{V_1}\right)^n. \tag{4}$$

The polytropic exponent can be specified for the limiting cases of isothermal and adiabatic state changes as

$$n = \begin{cases} 1: f \to 0 \\ \gamma: f \to \infty \end{cases}. \tag{5}$$

For nitrogen the isentropic exponent γ is about 1.4.

The load pressure p_1 and the precharge pressure p_0 of the accumulator are given by the design and can only be changed to a limited extent [1]. In order to change size or weight while keeping stiffness constant, the polytropic exponent n must be adapted.

The transition between isothermal and adiabatic state change is characterized by a thermal relaxation time, i.e. the ratio of thermal conductivity to thermal capacity. The heat capacity $V_0 c_{\mathrm{v}} \varrho_0$ is that of the gas in the accumulator and the conductivity kA is given by the transition of heat through the wall [3]. The relaxation time yields

$$\tau = \frac{V_0 c_{\mathrm{v}} \varrho_0}{kA}. \tag{6}$$

The transition frequency f_τ between isothermal and adiabatic behavior of the accumulator can be read in the frequency response of the dimensionless stiffness at the point of the largest slope (see **Fig. 3**).

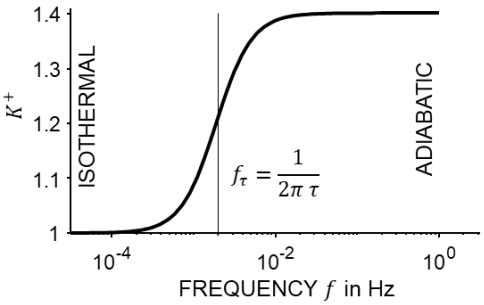

Figure 3: Frequency response of dimensionless stiffness.

As previous studies show foam is assumed to change heat transfer properties of accumulators by being a large heat capacity with large surface

area and thus moving the transition from isothermal to adiabatic behavior [4]. Investigations also show that foam can increase the efficiency of accumulators [5].

2.2. Hydraulic accumulators with foam inserts

Foams are porous media that can be described with two characteristic quantities, porosity and specific surface area. A detailed picture of the polyurethane foam structure filled in the gas volume of the accumulator can be seen in **Fig. 4**. The cells of the foam are open and the pores have a diameter in the order of 0.1 mm.

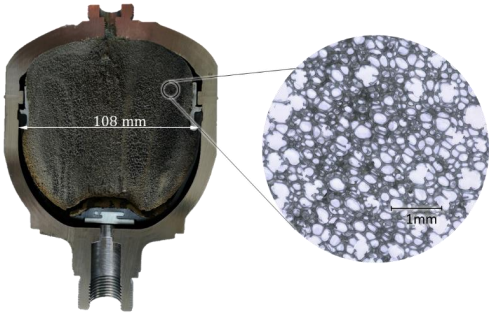

Figure 4: Section through a foamed hydraulic accumulator and detailed structure of the filled foam.

The porosity φ indicates a volume ratio between the gas V_s and the total volume of the accumulator $V_s + V_g$ and is defined as

$$\varphi := \frac{V_g}{V_g + V_s}. \tag{7}$$

Since the stiffness of the accumulator depends on the gas volume (cf. Eq (2)), the porosity can be used to characterize the influence of the foam.

The specific surface area is a measure of the size of the individual foam cells. It indicates the ratio between surface area A_s and volume of the solid V_s

$$s_s := \frac{A_s}{V_s}. \tag{8}$$

For a sphere with the diameter d the specific surface area is given by $s_s = 6/d$.

The larger the specific surface of the foam, i.e. the smaller the pores, the faster a heat exchange between gas and foam takes place. The thermal relaxation time can therefore be shortened.

2.3. Test rig

In order to investigate the dynamic properties of hydraulic accumulators a test rig was developed. The principle of the test rig is shown in **Fig. 5**. The basic design is similar to a hydro-pneumatic suspension strut.

A single-acting hydraulic cylinder is displaced in a path-controlled manner. The oil is moved into the accumulator to be tested. The resulting pressures in oil and gas are measured. The stiffness of the accumulator can thus be determined during harmonious excitation.

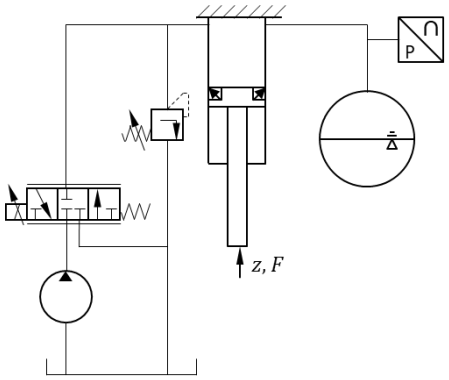

Figure 5: Schematic diagram of the develop test rig.

In addition, a level control system is integrated in the test rig. With a pump and a 3-3-way valve, the working point of the accumulator can be adjusted. In order not to overload the test bench, safety devices are integrated.

The real structure can be seen in **Fig. 6**. The displacement of the cylinder is controlled by a single-axis servo-hydraulic testing.

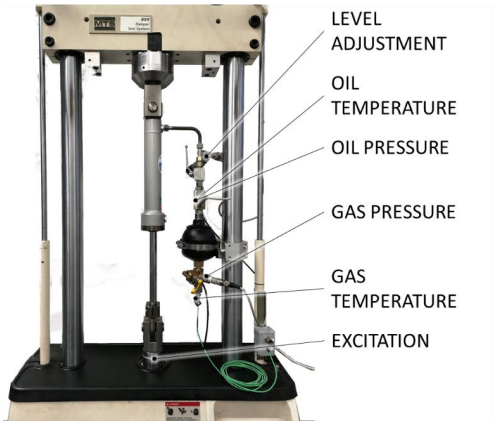

Figure 6: Test rig with level adjustment.

Test rig properties

The features of the test bench are shown in **Table 1**. The values given are the maximum values.

Table 1: Properties of the designed test rig.

Test rig parameter	Value
pressure	250 bar (abs)
oil flow rate	1 l/s
exchange oil volume	± 300 ml

Measured values

The quantities listed in **Table 2** are measured as shown in **Fig. 6**.

Table 2: measured values

symbol	measured value	unit
p_{oil}	oil pressure	bar (abs)
p_{gas}	gas pressure	bar (abs)
T_{oil}	oil temperature	°C
T_{gas}	gas temperature	°C
T_{a}	ambient temperature	°C
ΔV	excitation	ml

2.4. Evaluation Method

The stiffness of an accumulator is defined as the gradient dp/dV of the force-displacement characteristic. Due to the non-linear behavior of an accumulator the stiffness is not constant over the amplitude. Nevertheless, a stiffness characterizing the accumulator should be specified for comparison purposes.
This is possible by defining the stiffness as the diagonal slope of an enclosing rectangle

$$K^{+} := \frac{p_{\max} - p_{\min}}{V_{\max} - V_{\min}}. \tag{10}$$

As long as the accumulator behaves like a linear system the hysteresis curves are elliptical. In this case the slope around the zero position corresponds to the slope of the diagonal (c.f. **Fig. 7**). [6]

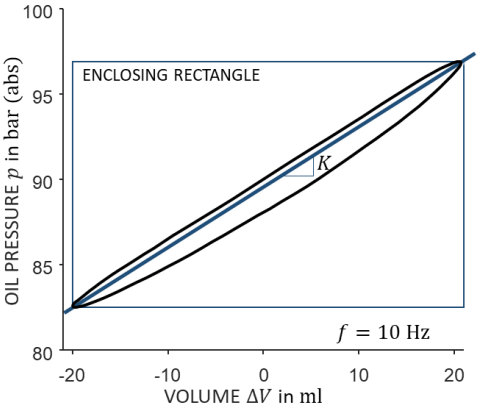

Figure 7: Elliptical hysteresis at 10 Hz with stiffness K.

As the amplitudes increase the accumulator no longer reacts harmoniously. As a result the hysteresis curves lose their elliptic shape and show a progressive course. In order to be able to calculate a characteristic stiffness in this case, evaluation windows are useful. Details can be found in [6]. For this paper only nearly elliptical hysteresis curves have been considered and therefore the enclosing rectangle method was chosen.

To determine the stiffness the accumulators have been excited with several oscillation periods and only the last full period was considered in the evaluation. This assures that the transient response of the accumulator has decayed.

3. RESULTS

The dimensionless stiffness determined at different frequencies as shown in chapter 2.4 can be displayed in a stiffness-frequency diagram.

In **Fig. 8** the dimensionless stiffness (eq. 3) of conventional and foamed accumulators is shown as a function of frequency. In the isothermal frequency range foamed accumulators have a larger stiffness than conventional accumulators. In the adiabatic frequency range the stiffness of the foam accumulators is lower than the stiffness of the conventional hydraulic accumulator for all load pressures. For the frequencies between 1 and 10 Hz an increase in stiffness can be seen in both accumulators. This is due to the different measurements being taken one after another which leads to a temperature increase.

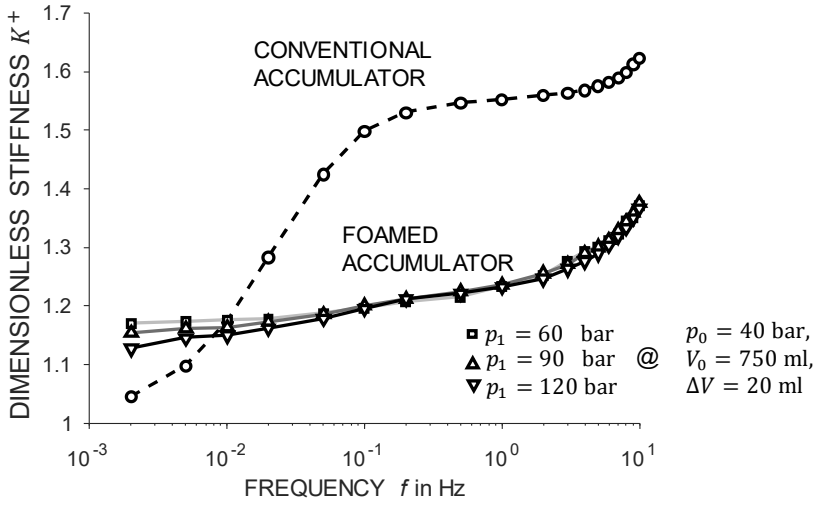

The foam in the accumulator has three effects on its function: (i) reduction of gas volume, (ii) foam mechanics and (iii) added heat capacity.

(i) The porosity of the foam is about 94 % at atmospheric pressure. Thus the volume of the foamed accumulator is 6 % lower than in the conventional accumulator. This leads to a stiffer accumulator recognizable in the isothermal frequency range.

(ii) The foam mechanics add to the stiffness of the accumulator. With a foam accumulator connected to the ambient air the stiffness was measured to be in the realm of 10^{-2} bar/ml. This however is one magnitude lower than the stiffness of the gas.

(iii) The added heat capacity is a heat sink with a large surface. In the isothermal range this heat capacity has no effect since the accumulator is isothermal. In the adiabatic range the temperature rise with compression is lower with the foam since heat can be stored in the foam.

It can be concluded that there is a lower stiffness in foamed hydraulic accumulators even though the foam reduces the gas volume and mechanically adds to the stiffness. The reason for this is the heat capacity. However, impacts of the foam on the mechanics of the moving membrane have not been considered.

With these results an approximate polytropic exponent (c.f. eq. 3) for foamed accumulators can be calculated to be $n = 1.15$. This exponent can be used for design calculations for hydro-pneumatic suspensions systems with foamed accumulators.

3.1. Energy density

In order to be able to classify the accumulators among themselves and in comparison to alternative energy storage options, the energy density is suitable as a benchmark. The energy density w is the ratio of the storable energy W_{acc} to the volume of the accumulator V_{acc}

$$w = \frac{W_{\mathrm{acc}}}{V_{\mathrm{acc}}}. \text{ [7]} \tag{11}$$

The specific energy ϱ_{W} is the storable energy W_{acc} in relation to the mass of the accumulator m_{acc}

$$\varrho_{\mathrm{W}} = \frac{W_{\mathrm{acc}}}{m_{\mathrm{acc}}}. \text{ [7]} \tag{12}$$

To estimate these quantities a spherical accumulator with the specifications in **Table 3** is assumed. The mass of the accumulator was determined from the minimum required wall thickness of a steel sphere that can resist the required pressure according to the Barlow's formula.

Table 3: specifications of the accumulator.

symbol	parameter	value
m_{acc}	mass	76.4 g
d_{acc}	diameter	124 mm
V_{acc}	volume	1 l
p_{max}	maximum pressure	300 bar (abs)

The energy stored in a hydraulic accumulator during a charging process from precharge pressure p_1 to pressure p_2 as can be seen in **Fig. 9** is given by

$$|W| = \int_1^2 p\mathrm{d}V. \tag{13}$$

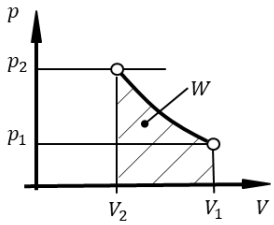

Figure 9: Stored energy of a hydraulic accumulator diagram when charging from p_1 to p_2.

For polytropic state changes (see equations (3) and (4)) with the polytropic exponent n, the maximum storable energy can be specified as

$$W_{\mathrm{poly}} = \frac{p_1 V_1}{n-1}\left(1 - \left(\frac{p_1}{p_2}\right)^{\frac{1-n}{n}}\right). \tag{14}$$

Analogously for isothermal state changes this applies to the stored energy

$$W_{\mathrm{iso}} = p_1 V_1 \ln\left(\frac{p_2}{p_1}\right). \tag{15}$$

For a constant given volume $V_1 = V_{\mathrm{acc}}$ and pressure $p_2 = p_{\mathrm{max}}$, there is an optimum precharge pressure p_1 at which the most energy can be stored in the accumulator. This optimum precharge pressure can be determined by deriving and setting to zero the energy in the accumulator as shown in [3] and was used to calculate the energy here.

In **Fig. 10** the energy density is given as a function of the specific energy. The higher the values for energy density and specific energy, the more efficient the accumulator. A foam accumulator of the same size can therefore store 11 % more energy than an adiabatic accumulator.

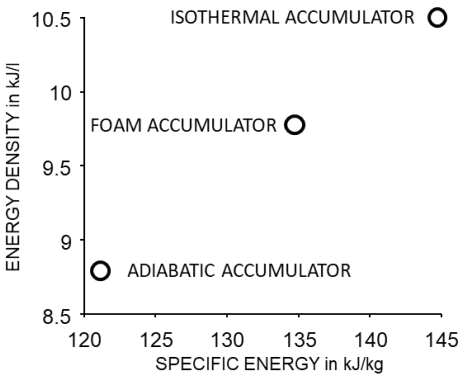

Figure 10: Energy density diagram for conventional and foam hydraulic accumulators.

In **Fig. 10**, the accumulators are each examined at their optimum frequency. For the application in the vertical dynamics of vehicles, frequencies in the range between 0.1 Hz and 25 Hz mainly occur [8]. A conventional accumulator therefore does not operate isothermal in this frequency range. In **Fig. 11**, the energy density is plotted over the frequency at which the accumulator can operate.

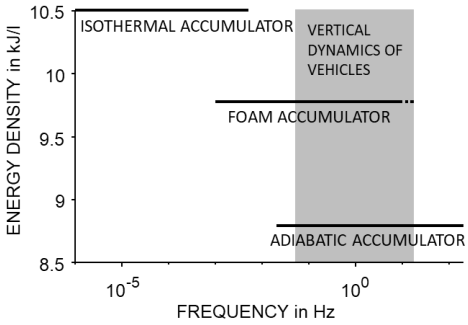

Figure 11: Energy density of foam and conventional accumulators at their operate frequencies.

It is shown that a foam accumulator is suitable for applications in vehicle suspensions and has a higher energy density than a conventional accumulator which operates adiabatically in this frequency range.

A one-mass oscillator is used to investigate the influence of the foam on a hydro-pneumatic suspension in a vehicle application. This simple vibrating system, is considered to be a model for a chassis.

According to equation (2) the volume of the accumulator can be calculated as a function of the natural frequency for foamed and conventional

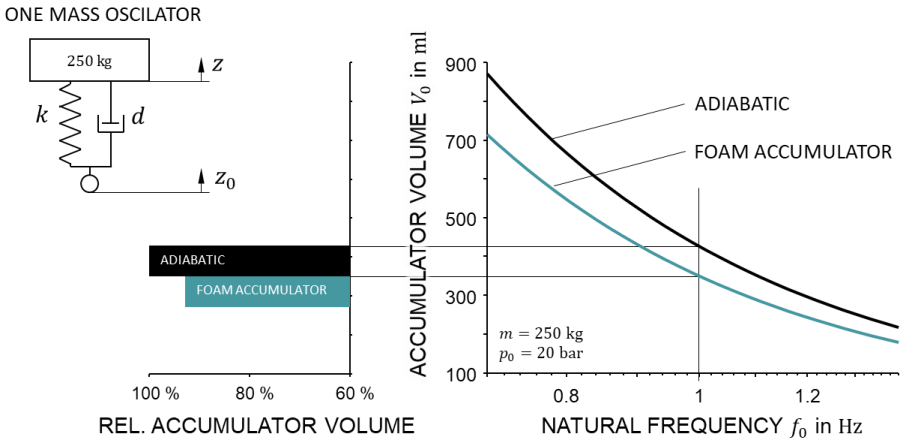

Figure 12: Accumulator volume of foam and conventional accumulators in one mass oscillators.

accumulators (cf. **Fig. 12**). The load pressure p_1 is calculated from the mass m and the gravity g to yield

$$p_1 = \frac{mg}{A_{\mathrm{cyl}}}. \tag{16}$$

At a natural frequency of 1 Hz, which is typical for vehicles, 18 % volume can be saved with a foam accumulator. A small accumulator not only has a smaller package, but also lower weight and lower material consumption.

4. CONCLUSION

It can be concluded that foamed hydraulic accumulators have a lower stiffness and consequently a higher energy density for vibrational applications. This is important for applications in hydro-pneumatic suspension systems. The reason for this behavior is the foam acting as a transient heat sink.

ACKNOWLEDGMENTS

Funded by the Deutsche Forschungsgemeinschaft (DFG, German Research Foundation) – Projektnummer 57157498 – SFB805.

NOMENCLATURE

A	accumulator surface area
A_{cyl}	area of the hydraulic cylinder
A_{s}	foam surface area
γ	isentropic exponent
c_{v}	isochoric Exponent of the gas
d	diameter of a sphere
d	damping constant
d_{acc}	diameter of the accumulator
f	function
f	frequency
f_0	natural frequency
g	gravity
F	force of the hydro-pneumatic strut
k	conductivity for transition through the wall
K	stiffness
K^+	dedimensioned stiffness
m	mass
m_{acc}	mass of the accumulator
n	polytropic exponent
p	pressure
p_{a}	ambient pressure
p_{max}	maximum pressure
p_{min}	minimum pressure
p_{gas}	gas pressure
p_{oil}	oil pressure
p_0	precharge pressure
p_1	load pressure
p_1	inlet pressure of state change
p_2	outlet pressure of state change
φ	porosity
ϱ_0	density of the gas
ϱ_{W}	specific energy
s_{s}	specific surface area
T_{a}	ambient temperature
T_{gas}	gas temperature
T_{oil}	oil temperature
T_1	inlet temperature of state change
T_2	outlet temperature of state change

τ	thermal relaxation time
V	volume
ΔV	displacing volume of the cylinder
V_{acc}	volume of the accumulator
V_g	volume of the gas
V_s	volume of the solid
V_{max}	maximum volume
V_{min}	minimum volume
V_0	accumulator volume
V_1	inlet volume of state change
V_2	outlet volume of state change
W	energy
w	energy density
W_{acc}	storable energy of the accumulator
W_{iso}	maximum storable energy for isothermal state changes
W_{poly}	maximum storable energy for polytropic state changes
z	deviation of the cylinder
Δz	excitation
z_0	initial position

REFERENCES

[1] Bauer W (2008) Hydropneumatische Federungssysteme. VDI-Buch, Berlin, Heidelberg

[2] Pelz PF, Buttenbender J (2004) The dynamic stiffness of an air-spring International Conference on Noise and Vibration Engineering. Katholieke Universiteit Leuven - Departement Werktuigkunde, S 1727–1736

[3] Korkmaz F (1982) Hydrospeicher als Energiespeicher. Springer Berlin Heidelberg, Berlin, Heidelberg

[4] Stroganov A, Sheshin L (Hrsg) (2011) Improvement of Heat-Regenerative Hydraulic accumulators, Bd 11

[5] Geimer M, Synek P-M (2015) Hybride und energieeffiziente Antriebe für mobile Arbeitsmaschinen Arbeitsmaschinen. 5. Fachtagung, 25. Februar 2015, Karlsruhe. Karlsruher Schriftenreihe Fahrzeugsystemtechnik, Bd 30. KIT Scientific Publishing; Technische Informationsbibliothek u. Universitätsbibliothek, Hannover, Karlsruhe

[6] Puff M, Pelz PF (2009) Entwicklung einer Prüfspezifikation zur Charakterisierung von Luftfedern. FAT-Schriftenreihe. Verband der Automobilindustrie (VDA), Berlin

[7] Demirel Y (2012) Energy. Production, conversion, storage, conservation, and coupling. Green energy and technology. Springer, London

[8] Mitschke M, Wallentowitz H (2014) Dynamik der Kraftfahrzeuge, 5. Aufl. Springer Vieweg, Wiesbaden

peer reviewed

ONE DIMENSIONAL UNSTEADY MODEL OF A HYDROPNEUMATIC PISTON ACCUMULATOR BASED ON FINITE VOLUME METHOD

Filipp Kratschun*[1], Jens Köhne[2], Peter Kloft[2], Heiko Baum[3], Katharina Schmitz[1]

1: Institute for Fluid Power Drives and Systems ,RWTH Aachen University, Campus-Boulevard 30, 52074 Aachen
2: HYDAC Technology GmbH, 66280 Sulzbach/Saar
3: FLUIDON GmbH, Jülicher Straße 338a, 52070 Aachen
* Corresponding author: Tel.: +49 241 8047738; E-mail address: filipp.kratschun@ifas.rwth-aachen.de

ABSTRACT

Hydraulic piston accumulators play a major role especially within the field of stationary hydraulics. The calculation of the amount of hydraulic energy which can be stored in such an accumulator is crucial when it comes to a precise system design. The knowledge of the temperature and pressure within the accumulator is required in order to calculate the amount of energy to be stored. The state of the art solution to estimate the state of change of such an accumulator is the implementation of a costly measurement system within the accumulator which tracks the position of the piston.

The goal of this paper is to develop and to analyse a time efficient simulation approach for the gaseous phase within a piston accumulator depending on the accumulator's load cycle. Temperature, pressure, density and velocity profiles inside of the gaseous phase are calculated transiently in order to achieve that goal. The simulation model is derived in one dimensional environment to save computational effort. Having derived a valid model of the gaseous phase it will be possible in future works to replace the expensive position measurement system by pressure and temperature transducers and then use the model to calculate the position of the piston and therefore estimate the state of change.

Keywords: Hydraulic Accumulator, Gas Spring, Change of State, Finite Volume, Gas Dynamics

1. INTRODUCTION

In many fields of engineering hydraulic accumulators play a crucial role. Their possibility to absorb and deliver high peak loads within a very short period of time and the robust design make them indispensable in the field of aircraft engineering, renewable energies, mobile and stationary machinery. A hydro-pneumatic piston accumulator consists of a gaseous volume filled with nitrogen and separated from the hydraulic fluid by a piston.

A dynamic pressure increase within the system resulting from an instant peak load leads to a compression of the nitrogen's volume. In other words the energy of the dynamic load is stored in form of compression energy within the accumulator. The amount of stored energy in the accumulator depends on the change of state during the compression of the nitrogen. For high pressure gradients the change of state is assumed to be isentropic whereas for low gradients the change of state is assumed to be isothermal.

In real applications the change of state is in between of isothermal and isentropic and therefore unknown. This makes it impossible to calculate the exact amount of energy which can be stored or released by the accumulator for a given system for arbitrary dynamic processes. Consequently, the design of a system including a hydraulic accumulator is always connected with inaccuracy. Commonly used methods to estimate the change of state in a hydraulic accumulator make use of the polytropic exponent [1] or the eigen frequency [2], [3]. Both methods rely on measurements of the given geometry and have to be carried out close to the operating conditions of the given device to be designed. This implies tremendous costs and time for the design of the perfect fitting accumulator for a given system. Another method presented by [4] calculates the temperature directly but only for small changes in pressure.

In order to overcome these difficulties this paper presents a simulation modeling approach of a hydraulic accumulator in order to calculate the

temperature and, therefore, the change of state inside of it without measurements for arbitrary operating conditions. The developed model implies the heat transfer between the gaseous phase and the surrounding boundaries.

The working principle of a hydro-pneumatic piston accumulator is depicted in **Figure 1.** The hydraulic oil delivered by the system compresses the nitrogen stored inside the accumulator. The compression energy W_P leads to an increase in the nitrogen's temperature.

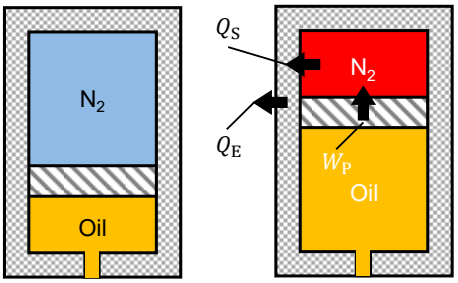

Figure 1: Working principle and energy balance for pistion accumulator

The temperature increase leads to a heat flux from the nitrogen into the surrounding body Q_S which therefore increases its temperature leading to a further heat flux Q_E between the surrounding body and the environment. The amount of the stored energy strongly depends on the temperature inside the nitrogen phase.

The possible scenarios are depicted in **Figure 2.** It is assumed that for a very slow compression the the temperature remains unchanged, whereas for a very quick compression the temperature is calculated using the isentropic phase change. All the changes in between are described by a polytropic exponent. Using the compression ratio ϵ given by (1) the pressure can be calculated using (2).

$$\epsilon = \frac{v_1}{v_2} \tag{1}$$

$$p_2 = p_1 \epsilon^n \tag{2}$$

Two problems arise if this method is used to predict the pressure and therefore the amount of energy to be stored in the given accumulator.

1. The polytropic exponent is dependent on the geometry and the compression velocities, but there is no way yet to quantify it depending on these values.
2. This paper reveals that the upper threshold of $n = \kappa$ is not valid. The polytropic exponent for a compression within a hydraulic accumulator can reach arbitrary values above κ.

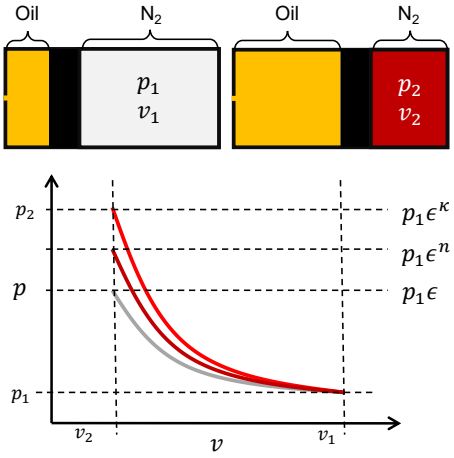

Figure 2: Change of state within a hydraulic piston accumulator

To overcome both problems pressure, temperature, and velocities have to be resolved within the nitrogen phase during the compression. The heat fluxes between the nitrogen and the boundaries have to be calculated depending on the position inside the gaseous phase.

The paper is structured as follows: In the second section the pressure, temperature, density and velocity profiles are calculated adiabatically and without dissipation. In the third part heat transfer and dissipation are added to the calculation. In the fourth section the developed model is validated using a test rig. A brief conclusion is given in the final section.

2. ADIABATIC CALCULATION OF THE GAS

In order to calculate the temperature, pressure, density and velocity profiles in the gaseous phase during a compression or an expansion Eulerian equations given in (3) have to be solved along the gaseous phase length. The vector form of (3) is depicted given by (4), see [5].

$$\begin{pmatrix} \rho \\ \rho u \\ E \end{pmatrix}_t + \begin{pmatrix} \rho u \\ \rho u^2 + p \\ u(E+p) \end{pmatrix}_x = \begin{pmatrix} 0 \\ 0 \\ 0 \end{pmatrix} \tag{3}$$

$$U_t + F(U)_x = 0 \tag{4}$$

Since the compression or expansion process is arbitrary dynamic and there is no exact solution for (4) a finite volume approach is chosen which is presented in **Figure 3**.

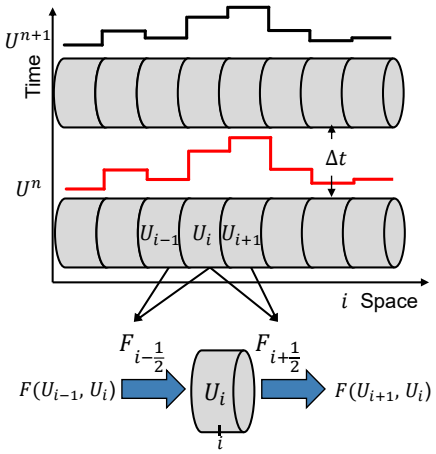

Figure 3: Finite volume method for the inner part of the accumulator

The gaseous phase is discretized in x-direction. In order to calculate the change of mass, momentum or energy within the volume Δx during a time step Δt, it is necessary to construct numerical fluxes $F_{i\pm\frac{1}{2}}$ at the volume's borders. This is done here applying the flux vector splitting solver presented by Steger and Warming [6] given by (5), (6) and (7). This approach calculates positive and negative parts of an inter cell flux with respect to the eigen velocities λ_i of the system. These velocities represent the speed of information propagation inside each cell and are given by (8).

$$F_{i+\frac{1}{2}} = F_i^+ + F_{i+1}^- \tag{5}$$

$$F_i^\pm = \frac{\rho}{2\kappa}\begin{pmatrix} \lambda_1^\pm + 2(\kappa-1)\lambda_2^\pm + \lambda_3^\pm \\ (u-a)\lambda_1^\pm + 2(\kappa-1)u\lambda_2^\pm + (u+a)\lambda_3^\pm \\ (V-ua)\lambda_1^\pm + 2(\kappa-1)u^2\lambda_2^\pm + (V+ua)\lambda_3^\pm \end{pmatrix} \tag{6}$$

$$V = \frac{1}{2}u^2 + \frac{a^2}{\kappa-1} \tag{7}$$

$$\lambda_1 = u-a,\ \lambda_2 = u,\ \lambda_3 = u+a \tag{8}$$

Herein, u is the flow velocity and a the speed of sound which is given by (10), wherein R is the specific gas constant. The sign of the eigenvalues $\lambda_{1,2,3}^\pm$ can be determined using (9) and therefore, the flux given by (6) can be determined for each cell.

$$\lambda_{1,2,3}^\pm = \lambda_{1,2,3} \pm |\lambda_{1,2,3}| \tag{9}$$

$$a_i = \sqrt{\kappa R T_i} \tag{10}$$

The calculation of the flux is estimated and the numerical scheme for each cell of the gaseous phase is finally given by (11).

$$U_i^{n+1} = U_i^n + \frac{\Delta t}{\Delta x}\left(F_{i-\frac{1}{2}} - F_{i+\frac{1}{2}}\right) \tag{11}$$

Thus, calculation of the inner part of the discretized gaseous domain is known now. To enable a compression the boundaries of the numerical domain have to be treated in a different way compared to (5) to find a correct flux formulation.

Fortunately, it is possible to solve the Eulerian equations analytically at the border of a moving wall and one cell exactly. If the wall moves with a lower velocity than the velocity of the first cell ($u_\mathrm{w} < u_1$), an expansion wave is formed whose pressure p_w at the wall can be calculated by (12).

$$p_\mathrm{w} = p_1\left(1 - \frac{\kappa-1}{2}\frac{u_1 - u_\mathrm{w}}{a}\right)^{\frac{2\kappa}{\kappa-1}} \tag{12}$$

For the case of the wall velocity being greater than the velocity of the first cell ($u_\mathrm{w} > u_1$), a shock wave is formed, and the pressure at the wall p can be expressed via (13) [7].

$$p_w = p_1\left(1 + \left(\frac{u_1+u_w}{2C^2}\right)^2 + \frac{u_1+u_w}{2C^2}\sqrt{\frac{8\kappa}{\kappa-1}C^2 + (u_1+u_w)^2}\right) \qquad C = \frac{2p_1}{(\kappa+1)\rho_1} \tag{13}$$

Since pressure and velocity at the wall are calculated analytically, the flux of the moving wall is fully defined and is presented in (14).

$$F_\mathrm{w} = \begin{pmatrix} 0 \\ p_\mathrm{w} \\ u_\mathrm{w} p_\mathrm{w} \end{pmatrix} \tag{14}$$

In front of the moving piston the first cell's volume can be arbitrary small immediately resulting in solver instabilities. To solve this problem the cut cell approach presented by [7] is applied. It is sketched in **Figure 4**.

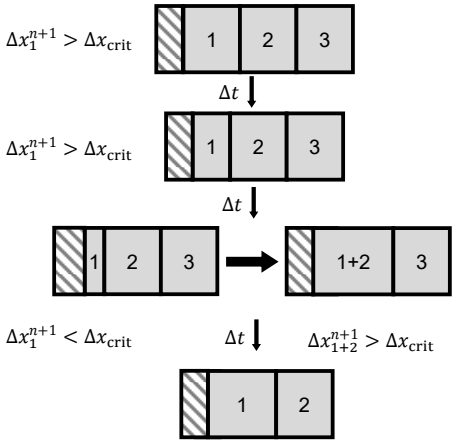

Figure 4: Cut cell approach

The basic idea behind this approach is to merge the first cell in front of the piston with the second cell when the first cell undercuts a critical volume Δx_{crit}. To understand the merging approach, first of all one has to clarify, that the volume of the first cell is not constant and varies in time, see (15).

$$\Delta x_1^{n+1} = \Delta x_1^n - u_{\mathrm{w}}^n \Delta t \qquad (15)$$

Bearing in mind that the entire calculation is carried out using conservative variables, conversion of mass, momentum and energy lead to the trivial equation for the first cell, when its volume is changed (16).

$$U_1^{n+1} = U_1^n \frac{\Delta x_1^n}{\Delta x_1^{n+1}} \qquad (16)$$

It simply states, that the change of volume of a cell does not result in a change of the conservative quantity, for instance, if the volume is reduced due to a compression, the ratio $\frac{\Delta x_1^n}{\Delta x_1^{n+1}}$ becomes greater than unity and the density would increase.

When merging is applied the new cell's volume Δx_1^{n+1} is simply the sum of the first and second cell $\Delta x_1^n + \Delta x$ before merging is executed. The new conservative values of the new first cell are then simply given by (17) to maintain mass, momentum and energy annihilation.

$$\Delta x^n = \Delta x + \Delta x^n, \qquad U_1^n = \frac{U_1^n \Delta x_1^n + U_2^n \Delta x}{\Delta x_1^n + \Delta x} \qquad (17)$$

Due to the merging the volume of the first cell is now much greater compared to the critical volume and (17) can be used in order to calculate the first cell's value. If the first cell is expanded, it has to be divided once its value exceeds the threshold of $\Delta x^n = \Delta x + \Delta x_{\mathrm{crit}}$. The values of the two new cells are simply the value of the cell before division and won't be threated here. The resulting numerical scheme for the first cell is then given by (18).

$$U_1^{n+1} = U_1^n \frac{\Delta x_1^n}{\Delta x_1^{n+1}} + \frac{\Delta t}{\Delta x_1^{n+1}} \left(F_{\frac{3}{2}} - F_{\mathrm{w}} \right) \qquad (18)$$

The embodiment of this approach enables the calculation of compression and expansion within a finite volume approach using conservative variables. In other words, the pressure, temperature, density and temperature profile in the gaseous phase can be calculated during a compression or expansion without heat exchange and dissipative effects. The simulation routine was implemented in DSHplus® software.

To validate the derived method modal acoustic theory is applied [8] [9]. Invoking a pipe with closed endings filled with air and one ending being excited i.e. moving back and forth with a low amplitude one can calculate the frequencies which induce resonance patterns using (19).

$$f_n = \frac{k}{2} \frac{a}{L} \qquad (19)$$

Herein, k is the resonance order, a the speed of sound and L the total length of the pipe.
Figure 5 depicts the pattern for the first and second resonance frequencies.

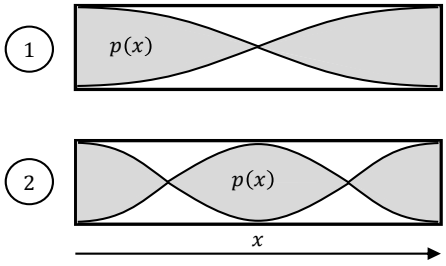

Figure 5: Closed endings resonance pattern

The pressure distribution for the resonance case always consists of one more antinodes than nodes and the antinodes are always at the borders of the pipe. To validate the procedure presented above a pipe of the length $L = 1\,m$, an initial temperature of $T = 290\,K$ resulting in a speed of sound of $a = 341 \frac{m}{s}$ is excited with small amplitude $\hat{x} = 0.1\,mm$ and a frequency of 50 Hz

to 750 Hz. The initial pressure of the pipe is 10 bar. Applying (19) the first four resonance frequencies given by **Table 1** lie within this range and if the simulation routine is correct the resonance patterns described above should occur at exactly these frequencies.

Table 1: Closed ending resonance frequencies

Order	1	2	3	4
Frequency[Hz]	171	342	513	684

Figure 6 presents the frequency dependent pressure deviation distribution $\bar{p} = \frac{p}{p_{\text{initial}}}$ by applying the simulation routine described above.

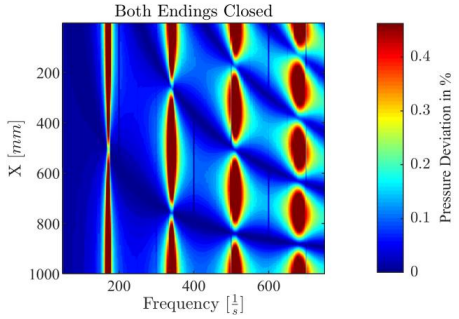

Figure 6: Resonance pattern for both endings closed

One can clearly see that the resonance patterns occur exactly at the frequencies predicted by the theory. Moreover, the sequence of nodes and antinodes is also exact.

For further validation of the presented approach the polytropic exponent for a simulated compression is sought (20). Herein, p_2 is the mean dynamic pressure within the nitrogen phase at the end of the compression (21) and p_1 is the pressure in the nitrogen phase at the beginning of the compression and L the length of the gas phase.

$$n = \frac{\ln\left(\frac{p_2}{p_1}\right)}{\ln(\epsilon)} \tag{20}$$

$$p_2 = \frac{1}{L}\sum_{i=1}^{M}\left(\frac{\Delta x_i p_i}{\kappa - 1} + \frac{\rho_i}{2}\left(u_i^2\right)\right)(\kappa - 1) \tag{21}$$

The results for an adiabatic compression ratio of $\epsilon = 1.25$ depending on the piston's velocity are presented in the **Figure 7**.

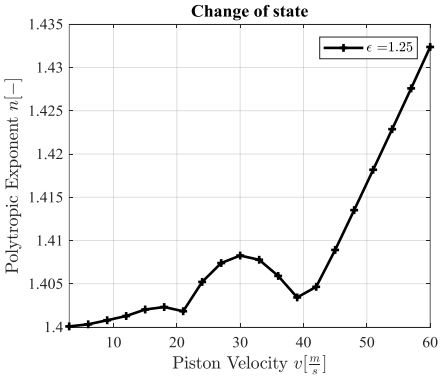

Figure 7: Change of state for a compression

It is remarkable that in contradiction to the theory the polytropic exponent exceeds the value of κ which is in this case 1.4. An increasing piston velocity or in other words a higher compression speed leads to increasing values of n. Furthermore, there is a local maximum at $30\frac{m}{s}$. To seek for the answer to the possible contradiction to theory one has to invoke the very derivation of mechanical work done to the system in conjunction with the theory of a polytropic phase change [10]. **Figure 8** shows an incremental compression of a gas spring and its mathematical formulation given by (22).

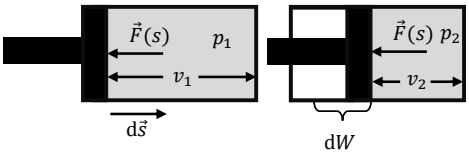

Figure 8: Work delivered to a gas spring

The gas pressure applies a force on the piston which is proportional to the piston's area. So, the incremental compression $d\vec{s}$ and the force $\vec{F}(s)$ can be expressed using volume and pressure instead of force and distance resulting in the integrated form (23).

$$dW = \vec{F}(s) \cdot d\vec{s} = -pA\frac{dV}{A} \tag{22}$$

$$W_{1,2} = -\int_{v_1}^{v_2} p(v)\, dv \tag{23}$$

For the function $p(v)$ a polytropic approach is chosen which leads to (24) or (25) for $n = 1$.

$$W_{1,2} = \frac{v_1 p_1}{n-1}(\epsilon^{n-1} - 1) \quad (24)$$

$$W_{1,2} = v_1 p_1 \ln(\epsilon) \quad (25)$$

The polytropic approach implies that the pressure within the gas is uniform during compression. This means that the pressure before the piston is the same as the pressure in the rest of the vessel. In fact, the pressure in front of the piston cannot be the same as the pressure far away from it, because the speed of sound of the medium has a finite value. A closer look inside the gas phase of the accumulator during compression for different piston velocities shows this behaviour, see **Figure 8** - **Figure 11** [10]. In these graphs the pressure distribution of the normalised pressure $\frac{p}{p_{\text{initial}}}$ are plotted against the vessel's length for 25%, 50% 75% and 100% of the compression time elapsed.

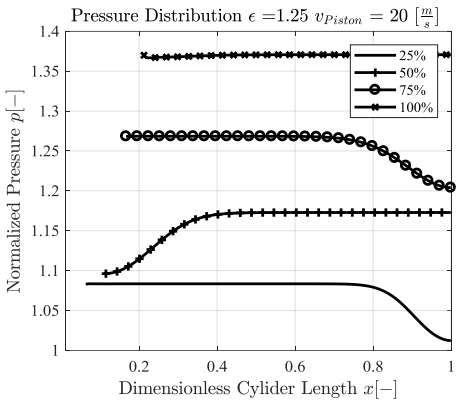

Figure 8: Pressure distribution for different stages of the compression at $v_{Piston} = 20\frac{m}{s}$

The initiation of the compression creates a pressure wave that travels from left to right and is reflected by the rigid wall on the right side and the moving piston on the left side. The amplitude and speed of the compression wave depend on the speed of the piston and the temperature of the gas. A higher pressure compared to the average pressure at the piston and a higher speed inevitably lead to a higher energy demand to fulfil the compression, resolving the above mentioned contradiction. Therefore the polytropic exponent must increase with increasing piston speed..

At a piston speed of 20 m/s, the pressure wave passes through the vessel exactly four times. Each time the pressure wave travels from left to right, the piston must work against a relatively high pressure, while the piston must work against a relatively low pressure compared to the medium pressure when the wave is reflected at the wall. For the case of 30 m/s, the pressure wave has run back and forth once and has been reflected once by the piston. This means that the piston has to work against a relatively high pressure more often than against a relatively low pressure. This leads to a higher amount of energy required for compression and explains the relative maximum of the polytropic exponent at 30 m/s.

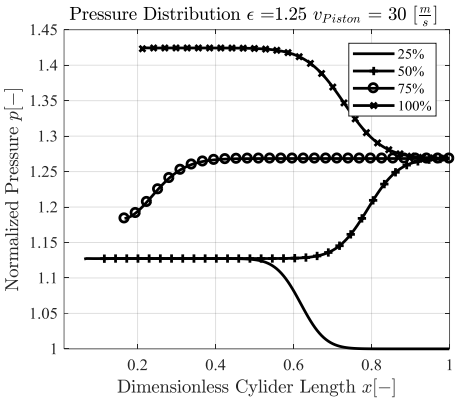

Figure 9: Pressure distribution for different stages of the compression at $v_{Piston} = 30\frac{m}{s}$

At a piston speed of 40 m/s, the pressure wave runs back and forth exactly once, resulting in a relatively low compression energy compared to 30 m/s.

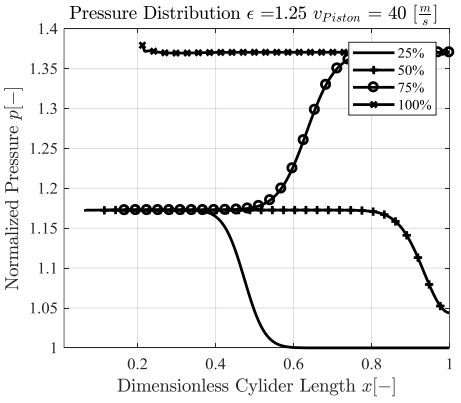

Figure 10: Pressure distribution for different stages of the compression at $v_{Piston} = 40\frac{m}{s}$

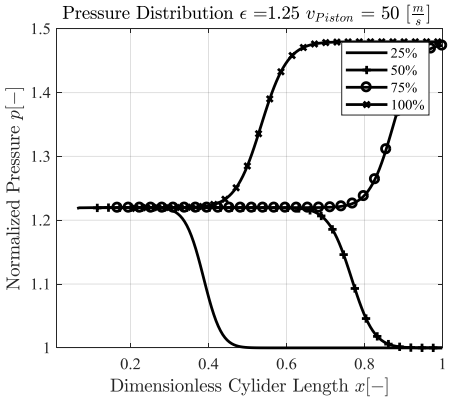

Figure 11: pressure distribution for different stages of the compression at $v_{Piston} = 50\frac{m}{s}$

For a piston velocity of $50\frac{m}{s}$ 65% of the compression takes place at a relatively high pressure resulting in a higher amount of compression work compared to $40\frac{m}{s}$. For increasing piston velocities above $50\frac{m}{s}$ the compression takes place at relatively high pressures only. This results in a higher amount of compression energy needed. **Figure 12** depicts the mean pressure of the first cell at the piston during the compression in relation to the mean pressure of the entire vessel. The shape of the graph is exactly the same as of the polytropic exponent given in figure 5, which proves the validity of the explanations given above.

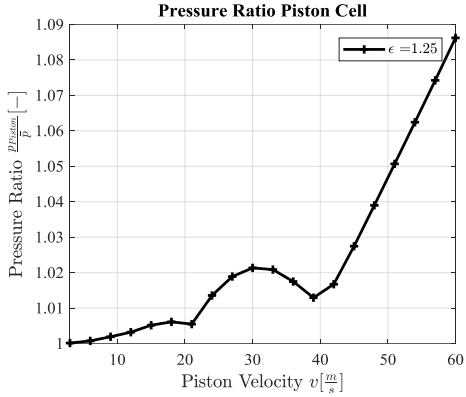

Figure 12: Pressure ratio of the first cell to the mean pressure

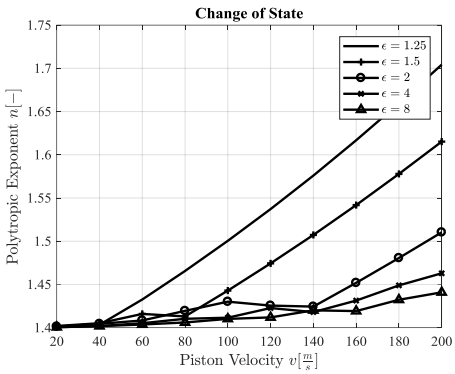

Figure 13: Change of state for different compression ratios

Finally, the polytropic exponents depending on the piston velocity and the compression ratio are calculated and presented in **Figure 13**. The results reveal that for a higher compression ratio the change of state becomes more and more isentropic. The reason for this is that for higher compressions the mean pressure during the compression is higher. Therefore, the amplitude of the pressure waves compared to the mean pressure is smaller. This results in a smaller deviation from the theory of a uniform pressure distribution and consequently in a smaller deviation from the theory which states that the change in state of an adiabatic vessel has to be isentropic, i.e. $n = 1.4$. Moreover, it proves that the implemented simulation represents the physics correctly.

3. DIABATIC CALCULATION OF THE GAS PHASE

The previous results were based upon the assumption of an ideal flow neglecting heat transfer and dissipation. In order to incorporate these effects into the simulation the Eulerian equations have to be updated from (3) to (26).

$$\begin{pmatrix} \rho \\ \rho u \\ E \end{pmatrix}_t + \begin{pmatrix} \rho v \\ \rho u^2 + p \\ u(E+p) \end{pmatrix}_x = \begin{pmatrix} 0 \\ -\frac{1}{2D}\lambda_f \rho u|u| \\ \frac{1}{2D}\lambda_f \rho u^2|u| - \frac{4\alpha(T-T_a)}{D} \end{pmatrix} \quad (26)$$

The new system of equations includes the shear stress at the vessels wall using the friction coefficient λ_f in the momentum equation and the resulting dissipation in the energy equation of (26). Herein, Re_i is the Reynolds number of each finite volume for either laminar or turbulent flow regime.

$$\lambda_f = \frac{64}{Re_i}, \qquad \lambda_f = \frac{0.3164}{\sqrt[4]{Re_i}} \tag{27}$$

The heat transfer between the fluid and the wall is included using the heat transmission coefficient α. The estimation of the heat coefficient is sought using the Nusselt number given by (28), wherein λ_h is the heat conductivity of the nitrogen and D the inner diameter of the vessel.

$$Nu_D = \frac{\alpha D}{\lambda_h} \tag{28}$$

The Nusselt number is calculated invoking the Reynolds Analogy [11] given in (29). This assumption is valid for Prandtl Numbers near unity, because for this case the thickness of the temperature boundary layer is of the same order as the thickness of the velocity boundary layer. In other words, the gradient of the temperature i.e. the heat flux can be expressed via the gradient of the velocity, i.e. the shear stress at the wall.

$$Nu_D = \frac{1}{8} Re \lambda_f \tag{29}$$

For diminishing flow velocities Nu_D is assumed to be 3, see [4]. Numerically, the right hand side of (26) is simply added to the scheme resulting in a source term which can for example be treated using a fractioning time step method [5].

Figure 14 depicts the results for a simulated compression including heat transfer and dissipation for a ratio of $L/D = 100$.

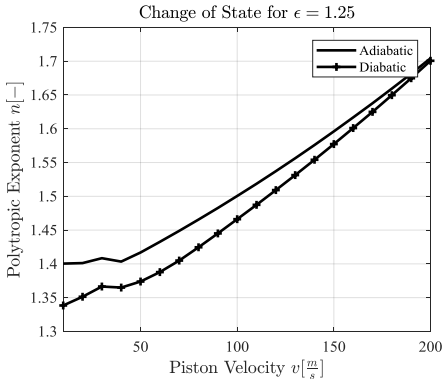

Figure 14: Comparision of diabatic and adiabatic change of state

As expected, the polytropic exponent is reduced by the heat escaping from the accumulator. Nevertheless, the shape of the curve with a local maximum at 30 m/s remains the same as in the adiabatic case, see **Figure 15.** Furthermore, as expected, the polytropic exponent tends towards the values of an adiabatic change of state with increasing piston speeds, since the time for heat transfer decreases with increasing piston speed. This leads to less heat transfer.

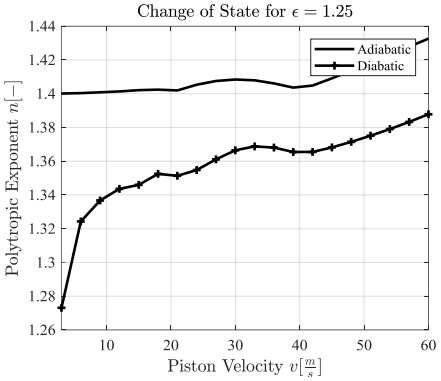

Figure 15: Comparision of diabatic and adiabatic change of state

As there is no analytical case to validate the diabatic results, the validation is carried out with a test rig, which is described in the following chapter.

4. EXPERIMENTAL VALIDATION

In order to validate the simulation method experimentally, a test rig including a piston accumulator with an inner diameter of $D = 0.18\ m$ and a length $L = 1.01\ m$ of the gas phase is set up. The accumulator is equipped with a measurement system of the piston's position inside the gas phase. The pressure within the gas is tracked with a transducer and the initial temperature is measured at the closed ending. The accumulator is filled with nitrogen and to maintain the validity of the ideal gas equation the highest pressure of the experiments does not exceed 25 bar. The set up is depicted in **Figure 16.**

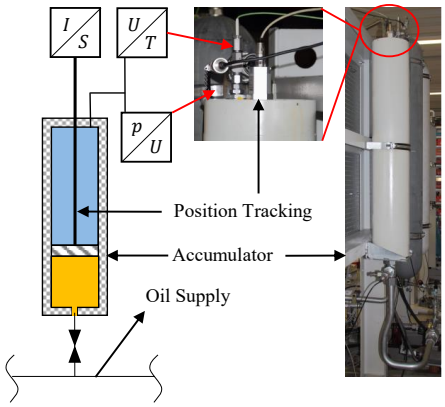

Figure 16: Test rig set up

The experimental procedure is as follows: The accumulator is filled quickly with oil which leads to a fast compression of the nitrogen of up to $\epsilon = 5$. Then the accumulator is discharged slowly. The tracked piston's position is included into the simulation procedure as input leading to a compression or expansion of the gas phase. The pressure is calculated applying the presented model and compared to the measured pressure.

Figure 17 presents the results of the measurement. Especially for the compression the deviation of measurement and simulation is negligible proving the simulation procedure to be valid. Yet, between 8 s and 20 s there is a deviation between the measured and simulated values. The simulated pressure is higher compared to the experimental results. This is closely connected to the temperature of the measured and simulated system. For the simulated case the temperature and therefore, the pressure is higher compared to the measured case for two reasons.

Firstly, within the real system natural convection occurs, especially for the case of diminishing piston velocities this comes into play and explains the deviation starting at approximately 10 s. Secondly, the position measurement system is connected to the piston in the gas phase mechanically. The mechanical construction reaching inside the gas is responsible for direct heat conduction from inside the gas phase to the outer boundaries of the accumulator accelerating the heat transmission outside the gas phase. Both effects described above force a quicker cooling of the gas and therefore a lower pressure.

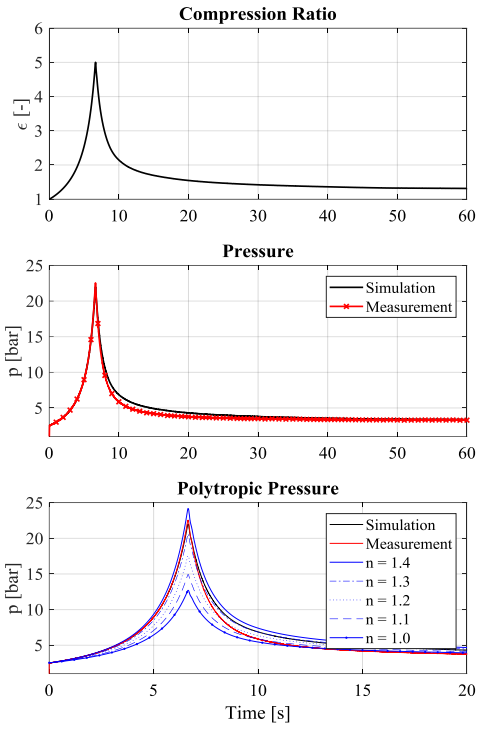

Figure 17: Simulation vs. experimental results

Comparing the simulation results with the polytropic approach (**Figure 17)** between 2.5 s and 12 s the measured pressure crosses all polytropic curves. It reveals the inherent weakness of this approach, since it is impossible to assign "one" polytropic exponent for the process. It displays the advantage of the derived approach including a discretization of the inner part of the accumulator.

5. CONCLUSION AND OUTLOOK

The paper presents a novel approach to calculate the pressure inside a hydro-pneumatic accumulator based on the compression rate. The method is validated analytically and experimentally. The results reveal a very good agreement between simulation and measurement especially taking into account the uncertainties connected to the experimental set up. Yet, there is room for improvement, especially for diminishing piston velocities the model's accuracy has to be increased. The huge advantage of the presented approach is its usability since no parameterization including measured values like

heat transfer coefficients or eigen frequencies [2] are needed. Its gas dynamics computational core allows arbitrary compression ratios and velocities.

NOMENCLATURE

α	heat transfer coefficient
ϵ	compression ratio
λ	eigenvalue
λ_f	coefficient of friction
λ_h	heat conductivity of the gas
κ	isentropic exponent
ρ	density
a	speed of sound
D	diameter
L	length of the gas phase
M	total amount of finite volumes
Nu	Nusselt Number
p	pressure
U	conservative variable
v	particle velocity

REFERENCES

[1] Schmitz,K., Murrenhoff, H. ”Fundamentals of Fluid Power. Part 1: Hydraulics”, Shaker Verlag, 2018

[2] Rupprecht, K., R. “Hydrospeicher – experimentelle und analytische Untersuchung zur Energiespeicherung”, Ph.D. Thesis, Aachen, 1988

[3] Rotthäuser, S., “Verfahren zur Berechnung und Untersuchung hydropneumatischer Speicher”, Ph.D. Thesis, Aachen, 1993

[4] Pelz, P., Buttenbender, J., “The dynamic stiffness of an air-spring”, ISMA2004, Leuven, 2004

[5] Toro, E. F., ”Riemann Solvers and Numerical Methods for Fluid Dynamics”, Springer Verlag, 2009

[6] Steger, J. L., Warming, F. R., “Flux Vector Splitting of the Inviscid Gasdynamic Equations with Application to Finite-Difference Methods”, Journal of Computational Physics 40 (263-293), 1981

[7] G. Yang et al., “A cartesian cut cell method for compressible flows Part B: moving body problems”, The Aeronautical Journal, 1997

[8] Nieter, J.J., Singh, R., “Acoustic modal analysis experiment”, Journal of the Acoustical Society of America, Vol. 72, 1982

[9] Sinambari, Gh., R., Sentpali, S., “Ingenieurakustik” , Springer Verlag, 5. Auflage, 2014

[10] Kratschun, F., Rambaks, A., Schmitz, K.: ”Fully Transient Model of a Hydraulic Accumulator”, Conference Proceedings, International Mechanical Engineering Congress and Exposition, Salt Lake City, Utah, United States of America, 2019

[11] Schlichting, H., Gersten, K., “Grenzschichttheorie”, Springer Verlag, 10. Auflage, 2006

peer reviewed

EXPERIMENTAL TESTS OF FLUID EXCHANGE PROCESS IMPROVEMENT IN A NEW DESIGN OF HYDRAULIC CYLINDER WITH A SUPPLY SYSTEM

Tomasz Siwulski[1]*, Urszula Warzyńska[1], Marcin Rys[2], Maciej Skrzypczak[2]

[1]*Wrocław University of Science and Technology, Faculty of Mechanical Engineering, Łukasiewicza 5, 50-371 Wrocław, Poland*
[2]*HYDROMAR, Powstańców Wlkp. 57a, 64-500 Szamotuły, Poland*
* Corresponding author: Tel.: +48 713202892; E-mail address: tomasz.siwulski@pwr.edu.pl

ABSTRACT

The article presents the results of experimental tests of the liquid exchange level in a new design of a hydraulic cylinder in comparison with the classic one. Comparative results are presented, as well as the influence of the stroke range on the degree of liquid exchange. The results allow the empirical determination of the degree of real improvement of the process of liquid exchange in the cylinder during operation, and thus allow the initial determination of the reliability level increase in hydraulic cylinders. It should be emphasized that the presented results are a part of a research and implementation project carried out in cooperation between a university and an industrial partner. In addition, the presented test method of hydraulic cylinders is, in the opinion of the authors, an interesting proposition, which can be used by manufacturers of this type of components in the world.

Keywords: hydraulic cylinder, fluid exchange process, experimental tests

1. INTRODUCTION

Hydraulic systems for working machines have been developed by Wroclaw University of Science and Technology in cooperation with industrial partners in three main areas. The first research area covers issues related to the influence of static and dynamic forces which are generated during the operation of working systems and which act on hydraulic power systems, with particular emphasis being placed on the phenomena observed in machine boom systems. The second research area is the analysis of pressure pulsations generated when working systems are operated, with primary focus on variable external loads. In the third research area, the aim is to improve the reliability and life of the individual elements of hydraulic systems operated under high ambient temperature conditions. This article presents the results of work performed within the third research area. The article also describes all of the works performed as part of the research and development project, which started from identifying the technical problem and ended with the introduction to the market of a new solution comprising an integrated hydraulic cylinder with a redesigned power supply system.

2. BACKGROUND

The analysis of maintenance reports on self-propelled mining machines operated in Polish deep underground copper mines in the Legnica-Głogów Copper Belt showed that the most failure-prone element of the hydraulic systems are their cylinders [1]. Defects of hydraulic cylinders typically caused the machine to be out of service for the period required to replace the damaged elements with new parts. The damage of hydraulic cylinders typically occurred in their sealing elements (**Figure 1**). The result was a significant increase in internal and external leakages, followed by a substantial drop in their efficiency. Visual inspection of the damaged cylinders revealed that they regularly suffered from thermal degradation of the sealing materials. In effect, the material lost its elastic properties and no longer allowed proper functioning of the cylinder sealings. The loss of tightness in turn allowed external impurities to collect inside the cylinder and entailed

mechanical degradation of the moving surfaces of the piston, the piston rod and the cylinder. At this degradation stage, the cylinders were typically replaced.

Figure 1: Sealing of the hydraulic cylinder, whose material became brittle due to high temperature

3. PROBLEM ANALYSIS

3.1. Liquid exchange model

Both in the literature and in actual engineering calculations of hydrostatic systems, an assumption is made that liquid temperature in the whole system is constant [2, 3]. This assumption is safe in the case when the liquid circulation in the system is complete. However, in a situation when during the operation of the system some liquid volume moves in a certain area of the system and does not return to the tank, this assumption is not entirely valid. An example of such a case is a hydraulic cylinder in which the piston serves as a barrier preventing liquid flow between the chambers. During the operation of the cylinder, the liquid from the chambers is first removed into supply lines, and is further pumped to valves which regulate the flow. The liquid volume which is transferred beyond the control valve returns to the main liquid circulation line in the system and is typically removed to the tank. However, the liquid which does not flow through the control valve when the chamber is emptied will be redirected back when the chamber is filled again. Therefore, it seems justified to conclude that some part of the liquid in the classic solution is never returned to the tank and instead remains in the cylinder and hydraulic power supply lines. In effect, this phenomenon may lead to a significant liquid temperature variation, as observed for example in mining machines. In this case, the temperature values measured on hydraulic cylinders were higher than the temperature values of the liquid circulating in the system and measured with the use of a temperature transducer located in the hydraulic oil tank. For further analysis of this phenomena, in **Figure 2** the schematic of a hydraulic cylinder is shown with the description of parameters, to which will refer equations and plots in the article.

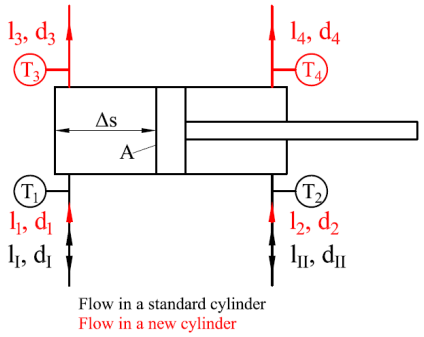

Figure 2: Schematic representation of the system comprising a cylinder and hydraulic power supply lines in the classic and the new solution

The following relationship describes the volume of liquid present in the cylinder chamber at a time of initiating a movement during which the liquid is removed from the chamber and outside of the cylinder – supply lines system V_o:

$$V_o = \begin{cases} 0 \text{ for } V_l \geq V_c \\ V_c - V_l \text{ for } V_l < V_c \end{cases} \quad (1)$$

The equation includes the volume of the cylinder chamber supply line V_l and the initial volume of the cylinder chamber V_c. As can be seen, in the case when, as a result of the piston movement, the volume of liquid removed from the cylinder chamber is smaller than the volume of the power supply line, no part of this volume is removed outside the system. If, however, the volume of liquid removed is greater than the volume of the power supply line, only the part of liquid originally present in the cylinder chamber will be removed outside the system, while the remaining part not leave the supply line. The volumes of the presented cylinder chamber and of the power supply lines may be calculated from basic relationships:

$$V_c = \Delta s \cdot A \quad (2)$$

$$V_l = l \cdot \frac{\pi d^2}{4} \quad (3)$$

The analysis of the above relationships proved that when the cylinder is operated some liquid volume is not exchanged and never leaves the cylinder – supply lines system. As a result, it may have a significantly different temperature than the liquid which flows through the system and is returned to the tank. Moreover, this liquid does not undergo the purification process in filters, and the impurities in it are not removed from the system and continuously affect the cylinder sealings.

3.2. New design of the hydraulic power supply system

Initial identification of the problem enabled works on a modified cylinder supply system. Based on the above relationships, it may be concluded that in order to reduce the volume of liquid remaining in the cylinder – supply lines system, the lines should be of possibly limited length and diameter. However, such limitations are not always desired from the perspective of efficiency and machine construction. They additionally do not ensure full liquid exchange, as some liquid volume never leaves the system. Therefore, a new system was designed in which each of the cylinder chambers has two nozzles with a specified flow direction. (**Figure 3**).

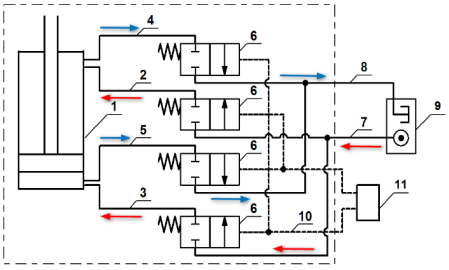

Figure 3: Schematic diagram of a new cylinder design together with a system for liquid exchange in the chambers [4, 5]

Each of the two cylinder working chambers (1) is connected with two hydraulic lines having a defined and unchangeable flow direction. In the described system, the cylinder power supply lines (2 and 3) are only able to supply liquid to the chambers, while the return lines (4 and 5) allow liquid removal. The flow is regulated by valves (6), actuated in pairs by control signals (10) received from the control system (11). The system was designed so that only two hydraulic lines with a specified and unchangeable flow direction are connected with the hydraulic power supply unit (9), i.e. one line is the supply line (7) and the other is the return line (8). It is advantageous to provide the valve system in a block mounted directly on the hydraulic cylinder, as the system is thus connected to the power supply with only two hydraulic lines, in a manner analogical to that in a classic double-acting cylinder. Additionally, the hydraulic lines between the cylinder chambers and the control valves have minimized length and are made in the valve block, which makes them practically resistant to damage during operation. This solution was implemented in a prototype cylinder (**Figure 4**) which was then subjected to a series of tests in a specially designed test stand.

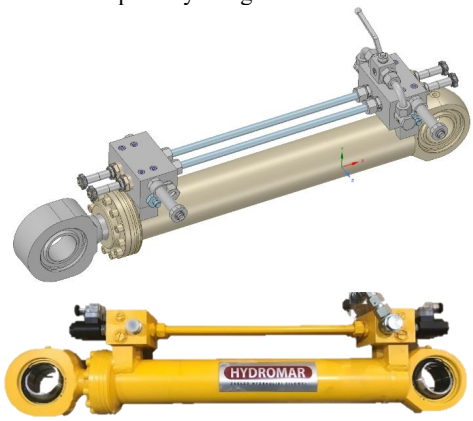

Figure 4: The 3D geometrical model and the prototype version of the new hydraulic cylinder

It should be emphasized that in the application the valves mounted on the cylinder will perform the control functions. In connection with the above, it will become superfluous to install an additional directional valve controlling the operation of the cylinder. In the newly created architecture of the system, it is foreseen to mount only the valve enabling cutting off the liquid supply to the cylinder, whose function will be related to the safety of use of the system. As a result, the preliminary assumption was made that the efficiency of the systems with classic cylinder power supply architecture and with the new

architecture, which is the result of using the solution and its advantages, is comparable. As a result of the application of the described solution, it was possible to supply each chamber of the cylinder independently and in any configuration without the need to expand the system with an additional directional valve responsible for e.g. fast movement of the cylinder or enabling its free movement under the influence of external forces.

3.3. Test stand and test procedure

The test stand, developed as part of the presented research and development works, allows both durability tests and investigations into thermal and dynamic phenomena involved in the operation of hydraulic cylinders **(Figure 5**). It is equipped with a complete set of sensors for measuring pressure, temperature, axial forces on the piston rod and piston extension in real time. At the same time, its design enables simulations of a broad spectrum of loads on the tested cylinders, in both dynamic and static conditions.

Figure 5: Test stand for testing hydraulic cylinders

Additionally, the implemented system is capable of providing any number of repeated piston extension and retraction cycles, based on the preset limit positions. This article presents the results of comparative tests performed for cylinders equipped with the new and the classic fluid supply systems. The tests were performed for several preset cylinder displacements, while the presented results are for a test series in which the piston stroke cycle was between positions located at an equal distance from the middle of the cylinder's total stroke length. (**Figure 6**).

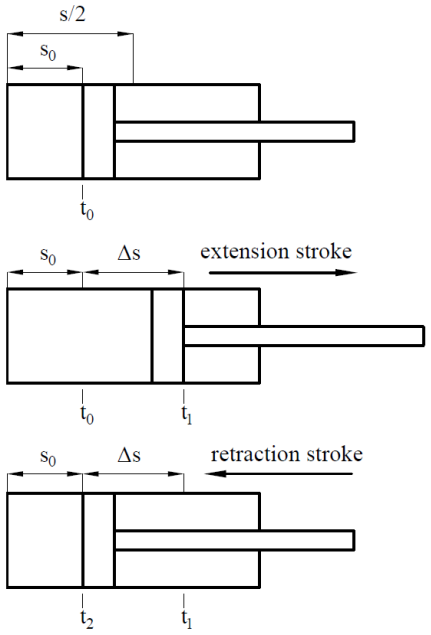

Figure 6: Schematic of a piston movement during the testes with indication of the important parameters

The test stand is operated on the hydraulic oil Renolin HV46. The parameters of the cylinder and of the power supply lines used in the tests are presented in **Table 1**.

Table 1: Parameters of the cylinder

Cylinder parameter	Value [mm]
Piston diameter, D	80
Piston rod diameter, d	50
Piston stroke, s	495
Supply line length, l_I	4930
Supply line length, l_{II}	4370
Supply line length, $l_1=l_2=l_3=l_4$	70
Hose internal diameter, $d_1=d_2=d_3=d_4=d_I=d_{II}$	12.7

In order to obtain two liquid domains having considerably different temperatures both in the hydraulic system of the test stand and in the actual cylinder equipped with the new power supply system, hydraulic bypass lines were designed (**Figures 7 and 8**). It should be emphasized that the four-way, three-position directional valve (4) visible in the diagrams is

used for controlling only in the case of testing the classic solution. In the case of tests of the new solution, its position is unchanged and provides only power supply to the cylinder. Motion control is carried out by means of two-way two-position valves (6) mounted on the cylinder, controlled in pairs. The spool valve in the system was left deliberately in order not to introduce geometric changes in the compared systems. As a result, it was possible to use a throttle valve to heat the liquid in the bypass without the need for piston movement. After the liquid had been heated, valve settings were modified and the tests were started. The heated liquid was in the hydraulic power supply lines, while the liquid present in the cylinder and in the supply system directly linked to this cylinder had a considerably lower temperature. A test of such design allowed observations of the liquid mixing phenomenon during cylinder movement, as well as comparative tests for cylinders with the classic and with the new power supply system. During the tests here described, the liquid in the parallel circuits was always heated to the same initial temperature equal to 55°C. This was followed by closing the parallel circuits and initiating the process of supplying the investigated cylinder with heated liquid. Importantly, during the tests of the cylinder supply according to the new design, the temperature of liquid circulating in the system, as measured with a temperature transducer located on the return line (T5), stabilized at 48°C, while in the case of the classic solution, this temperature was approximately 45°C. This difference was due to different oil volumes originally present in the system of cylinder chambers and power supply lines. The initial temperature of this oil was always 21°C. The constant initial temperature of the cool oil was set when the power lines and the cylinder were subjected to preliminary flushing. As part of test preparations, the piston was also set to its initial position, as predefined for each individual test. The tests allowed plotting curves of time versus temperature, as recorded on the nozzles (T_1, T_2, T_3, T_4) during the cyclical movements of the piston. In this article, the analysis was performed for the first five work cycles of the cylinder.

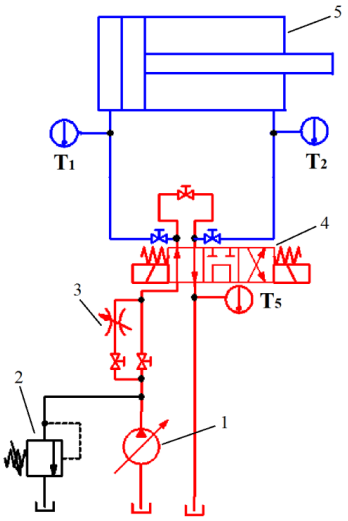

Figure 7: Hydraulic circuit schematic for the standard cylinder test setup: 1 - pump, 2 - pressure relief valve, 3 – choke valve, 4 – directional spool valve, 5 – standard cylinder

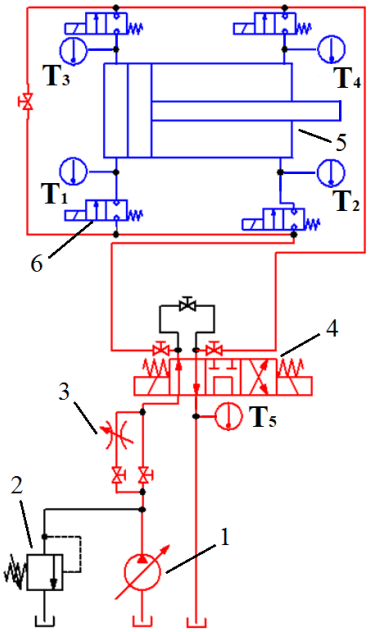

Figure 8: Hydraulic circuit schematic for the new cylinder test setup: 1 - pump, 2 - pressure relief valve, 3 – choke valve, 4 – directional spool valve, 5 – a new cylinder, 6 – control valves

Comparative tests were performed for the classic and the new cylinder power supply systems with allowance for the change of piston strokes (**Table 2**).

Table 2: Experimental tests parameters

Cylinder	s_0 [mm]	Δs [%]	Δs [mm]
Standard	198.0	20	99.0
Standard	148.5	40	198.0
Standard	99.0	60	297.0
Standard	49.5	80	396.0
Standard	0.0	100	495.0
New	198.0	20	99.0
New	148.5	40	198.0
New	99.0	60	297.0
New	49.5	80	396.0
New	0.0	100	495.0

4. TEST RESULTS AND DISCUSSION

The experimental test results are depicted in **Figures 9 – 12** in the form of curves representing changes of liquid temperature measured in measurement points located on the cylinder (T_1, T_2, T_3, T_4) during the tests of the classic and the new power supply solution. Each plot represents five cycles of piston movement with specified strokes, starting from an extension stroke. The grey vertical lines on the plots show a beginning and an end of each stroke.

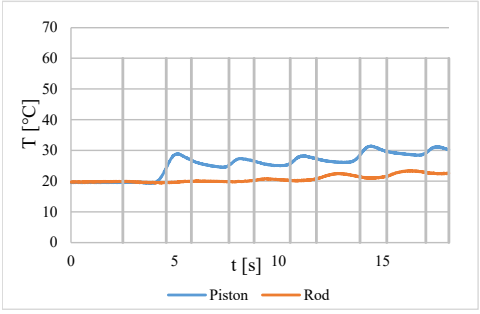

Figure 9: Temperatures measured at the outlets T_1, T_2 in the standard cylinder, Δs=20%

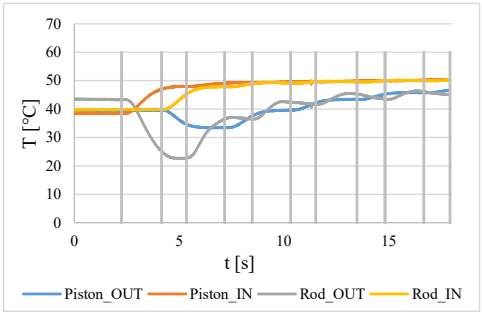

Figure 10: Temperatures measured at the outlets T_1, T_2, T_3, T_4 in the new cylinder, Δs=20%

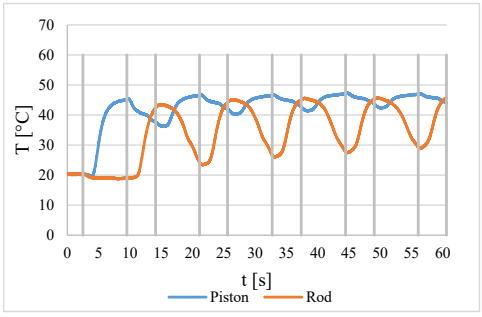

Figure 11: Temperatures measured at the outlets T_1, T_2 in the standard cylinder, Δs=100%

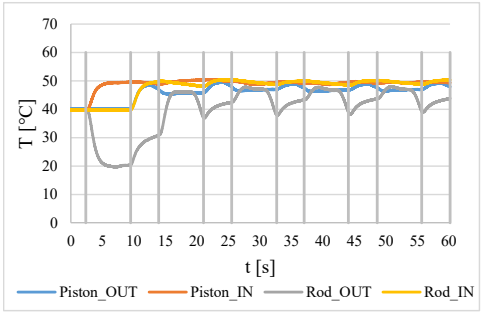

Figure 12: Temperatures measured at the outlets T_1, T_2, T_3, T_4 in the new cylinder, Δs=100%

As the tests were planned in such a manner that the hot oil was supplying cold cylinder system, the presented on the graphs results should be interpreted as: the faster the oil temperature reach stabilized highest value, the better heat dissipation and cylinder chamber flushing. Comparing the tests results for classic and new cylinder design for a small stroke of 20%, it may be seen that in classic design, the temperature of oil does not reach the reference temperature value of about 45°C and is not even close, which means

that the fluid flows between closed volume of lines and cylinder limiting heat dissipation. While in the new solution, even for the small stroke of 20%, the visible fluid circulation may be seen, as the oil temperature reaches the reference value of 48°C after only five cycles, both in the piston and piston-rod chamber. Better fluid circulation may be seen in a classic solution for the full stroke in comparison to the smaller strokes, but for the new cylinder design, the heat energy removal is much faster.

In order to analyze the balance of thermal energy during the investigated piston strokes, the amount of thermal energy introduced into the system was assumed to be:

$$H_{in} = \mathrm{c} \cdot T_{in} \cdot m_{in} \tag{4}$$

The amount of thermal energy discharged from the cylinder may be described with a simplified relationship with allowance for mean value error:

$$H_{out} = \mathrm{c} \cdot T_{av} \cdot m_{out} \tag{5}$$

As the simulated work cycle of the cylinder consists of the extension and retraction strokes, and as the final position of the piston was identical with its initial position (**Figure 6**), an assumption may be made that the mass of liquid introduced to the system equals the mass of liquid removed from the system:

$$m_{in} = m_{out} \tag{6}$$

Therefore, the amount of thermal energy removed from the system (ΔH) during one work cycle is described with the following relationship:

$$\Delta H = H_{out} - H_{in} = C \cdot (T_{av} - T_{in}) \tag{7}$$

where:

$$C = c \cdot m_{in} = \mathrm{c} \cdot m_{out} \tag{8}$$

and C is constant.

The above relationships indicate that mean liquid temperatures measured on the liquid removal lines should be the basic parameter for the comparison of individual solutions aimed at improving the process of removing liquid from the system and exchanging it with new liquid fed from supply lines. The reference temperature was the value of temperature measured at the outlet of the system, after the process of heat exchange has stabilized. **Figures 13 - 16** show graphs of mean temperature values as a function of the number of work cycles.

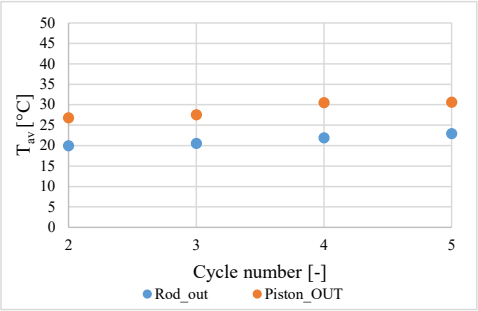

Figure 13: Average temperature values of liquid flowing out from the standard cylinder during each cycle, Δs=20%

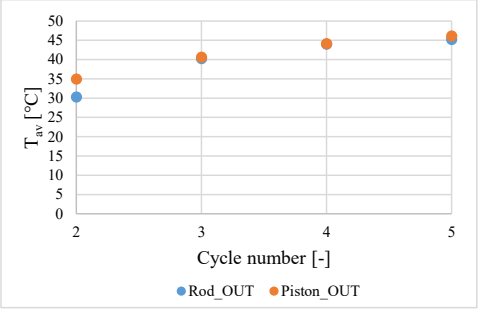

Figure 14: Average temperature values of liquid flowing out from the new cylinder during each cycle, Δs=20%

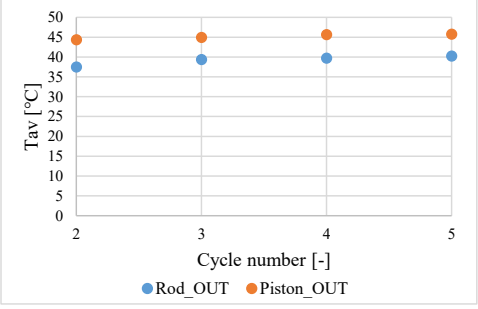

Figure 15: Average temperature values of liquid flowing out from the standard cylinder during each cycle, Δs=100%

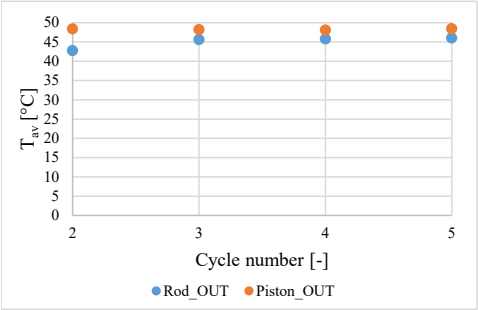

Figure 16: Average temperature values of liquid flowing out from the new cylinder during each cycle, Δs=100%

An interesting observation of such a comparison of the experimental tests results is that for the smallest analyzed stroke, the satisfying heat removal in the new cylinder design may be seen even after only three cycles, and a complete chamber flushing may be obtained after five cycles. During the full stroke of a piston, the complete circulation of oil flow may be seen in the piston chamber after the second cycle. In the piston-rod chamber, the flow circulation is slightly lower because of a piston rod. In the classic cylinder, the high difference of average temperatures may be seen between the piston and piston-rod chambers, which means that in the piston-rod chamber the flow circulation is much lower.

In order to precisely represent the character of the obtained liquid exchange degree for each of the cases, the graphs in **Figures 17 - 20** include compared curves of mean temperature changes, as recorded at the outlet for various piston strokes.

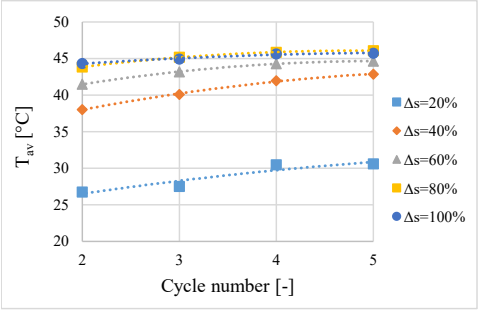

Figure 17: Comparison of average temperature values of liquid flowing out from the piston chamber of the standard cylinder during each cycle for all test cases

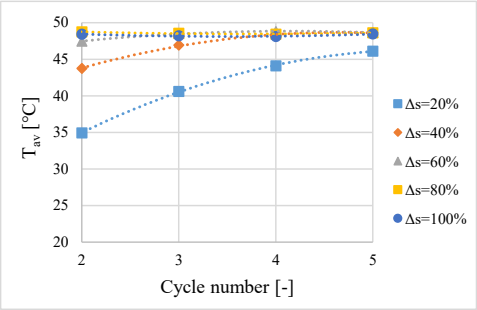

Figure 18: Comparison of average temperature values of liquid flowing out from the piston chamber of the new cylinder during each cycle for all test cases

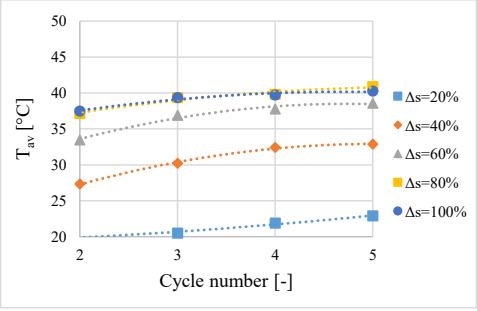

Figure 19: Comparison of average temperature values of liquid flowing out from the piston rod chamber of the standard cylinder during each cycle for all test cases

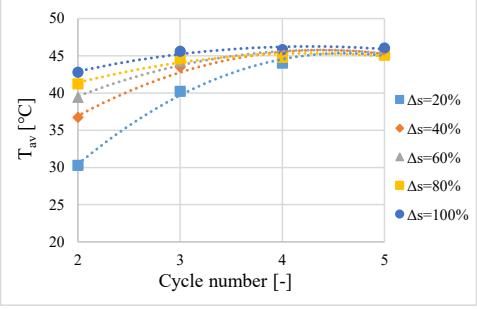

Figure 20: Comparison of average temperature values of liquid flowing out from the piston rod chamber of the new cylinder during each cycle for all test cases

The results clearly indicate that a change in the cylinder power supply method has a significant influence on the liquid exchange degree during different piston strokes.

Analyzing the fluid exchange process in a piston chamber of a new cylinder design it may be seen that for a 20% stroke a full circulation of fluid may be obtained after almost 5 cycles, for the 40% of stroke after almost three cycles, and for the strokes equal or higher than 60% - after two cycles. For the piston-rod chamber of a new cylinder, the fluid circulation more difficult, but the full fluid exchange is possible for all range of strokes after only five cycles.

5. CONCLUSION AND OUTLOOK

Comparative tests of the classic and the new hydraulic cylinder power supply systems provide results which support the theoretical assumptions that the implementation of a new power supply system significantly improves the process of exchanging the liquid supplied to the cylinder with the liquid already present in the cylinder chambers. A particular improvement was achieved in the case when the piston stroke was other than full. The results demonstrate that the new solution allows significantly enhanced thermal energy removal from the chambers of the operating cylinder. Deployment of the new solution especially in machines operated under difficult conditions will provide data on how the modifications influence the actual life of cylinders, and how they will translate into the economic effect. Importantly, the application potential of the test stand developed as part of this project is considerably broader and not limited to the analysis of thermal phenomena. The use of the new solution together with the adapted power supply system, in which the flow resistance will have values comparable to those of the classic architecture system, as shown in the presented test results, will allow the elimination of local thermal energy compensation in the cylinder chambers. Ensuring a significantly higher exchange of liquid in the chambers directly reduces the value of temperatures affecting the seals during operation of heavily operated cylinders and operating at high ambient temperatures. The tests showed the effect of the analyzed phenomenon on the temperatures recorded in the chambers. The results can be used to analyze phenomena occurring in cylinders operated at high ambient temperatures, where the oil temperature values in the cylinders significantly exceed the allowable temperatures for seals, while the oil temperature limit in the tank is not exceeded. In the future it is possible to perform research into the influence of the new solution on the accuracy of piston positioning during the start-up and the braking action. Plans also include comparative tests of the cylinder stiffness parameter in the new and in the classic solutions. Another interesting research area is how the process of liquid mixing is influenced by the shape and the position of the nozzles for supplying liquid to the cylinder chambers.

NOMENCLATURE

A	Piston surface area [mm^2]
c	Specific heat of oil [kJ/kg·K]
$d_{1,\ 2,\ldots}$	Inner diameter of the supply line [mm]
d	Piston rod diameter [mm]
D	Piston diameter [mm]
$H_{in,\ out}$	Thermal energy supplied to/removed from the system [J]
ΔH	Thermal energy removed from the system during one cycle [J]
$l_{1,\ 2,\ldots}$	Length of the supply line [m]
$m_{in,\ out}$	Mass of the liquid supplied to/removed from the system during one working cycle of the cylinder [kg]
s	Piston full stroke [mm]
s_0	Initial position of the piston [mm]
Δs	Piston stroke [mm]
$t_{0,\ 1,\ldots}$	Time of start and stop a piston movement [s]
$T_{1,\ 2,\ldots}$	Temperature of oil measured during tests [°C]
T_{av}	Mean temperature of the liquid flowing from the cylinder chamber between time t_1 and t_2, and further cycles [°C]
T_{in}	Temperature of the liquid flowing into the cylinder [°C]
V_0	Volume of liquid present in the cylinder chamber at a time of initiating a movement [dm^3]
V_c	Initial volume of the cylinder chamber [dm^3]
V_l	Volume of the cylinder chamber power supply line [dm^3]

REFERENCES

[1] Król R, Zimroz R, Stolarczyk Ł. (2009) Failure analysis of hydraulic systems used in mining machines operating in copper ore mine KGHM Polska Miedz S.A. (in Polish). Min Sci; 128:127–39

[2] Stryczek S. (2014) Hydrostatic drive (in Polish) Vol. 1 and 2. Warsaw: WNT

[3] Watton J. (2009) Fundamentals of Fluid Power Control. Cambridge University Press

[4] Siwulski T, Warzyńska U. (2017) The advantages of a new hydraulic cylinder design

with a control system. In: Vladimír Fuis, editor. Eng. Mech. 2017, Brno University of Technology, Institute of Solid Mechanics, Mechatronics and Biomechanics, Brno; 2017, p. 874–877

[5] Siwulski T, Warzyńska U. (2017) Method of filling and emptying the working chamber of the hydraulic cylinder and a hydraulic cylinder together with a control system and a hydraulic cylinder for performing the method according to the invention. PCT/PL2016/000146

GROUP F

Intelligent control

peer reviewed

SIMULATION OF AN INTERLOCKING HYDRAULIC DIRECT-DRIVE SYSTEM FOR A BIPED WALKING ROBOT

Juri Shimizu*, Takuya Otani, Kenji Hashimoto, Atsuo Takanishi

Waseda University and Hitachi, Ltd./#41-304, 17 Kikui-cho 162-0044, Shinjuku-ku, Tokyo, JAPAN
* Corresponding author: Tel.: +81 3 3203 4394; E-mail address: juri-shimizu1112@asagi.waseda.jp

ABSTRACT

Biped robots with serial links driven by an electric motor experience problems because the motor and transmission are installed in each joint, causing the legs to become very heavy. Previous solutions involved robots using servo valves, a type of highly responsive proportional valve. However, high supply pressure is necessary to realize high responsiveness and the resulting energy losses are large. To address this problem, we proposed a hydraulic direct-drive system in which the pump controls the cylinder meter-in flow, while a proportional valve controls the meter-out flow. Furthermore, our hydraulic interlocking drive system connects two hydraulic direct-drive systems for biped humanoid robots and concentrates the pump output on one side cylinder. The meter-in flow rate of the other side cylinder is controlled by the meter-out flow rate of the cylinder on which the pump is concentrated. A comparison of the walking simulation performance with that of the conventional independent system shows that our proposed system reduces the motor output power by 24.3%. These results prove the feasibility of constructing a two-legged robot without having to incorporate highly responsive servo valves.

Keywords: Hydraulics, Bipedal locomotion, Humanoid robot, Flow-based control

1. INTRODUCTION

It is important to conduct safe quantitative assessments of the products people use. The main method currently in use for this purpose is user rating. However, this approach provides qualitative results only. Thus, our research group proposes using a biped humanoid robot instead of humans to evaluate products. Our developed Robot WABIAN-2R (WAseda BIpedal humANoid-No. 2 Refined) can walk with its knees extended by implementing a pelvic mechanism [1]. **Figure 1** shows our biped humanoid robot. In recent years, we have developed robots that can evaluate various products. They run as well as walk. To run, a robot requires a high-power actuator. However, it is difficult to implement high-power electric motors because of the size limitations of robots. To solve this problem, we proposed a method to generate a large torque via pelvic vibration and leg elasticity [2, 3].

To increase the output of electric motors, Urata et al. developed a technology that improves continuous output torque with a liquid cooling system [4]. Other robots have two or three motors on the drive shaft [5–7]. These approaches have led to the development of high-speed, high-torque, and highly mobile joints for humanoid legs. However, these conventional methods require that the shafts of the motor be directly connected by mechanical transmission. It is difficult to place the equipment to have the same weight distribution as in the case of a human. However, the equipment layout can be improved by using a hydraulic system.

The hydraulic system can realize a robot of the same size as a human. For example, Boston Dynamics developed ATLAS [8]. Hyon et al. developed a hydraulic humanoid robot called TaeMu [9], which has the same leg link ratio and weight distribution as humans. This robot can directly control the torque of each joint by adjusting the actuator pressure by using a servo valve. However, for our intended use, we need to reproduce a predetermined motion pattern in order to evaluate a product. This requires a system that can directly control the joint angle.
The displacement control system is flow-based and can directly control the actuator stroke with

the pump discharge flow [10, 11]. Kaminaga et al.'s Electric Hydrostatic Actuator (EHA) is an example of such a system being applied to a robot [12]. However, since EHA uses a through rod cylinder, the output is lower than that of a single rod cylinder, making it difficult to install because of rod moving space.

Previously, we proposed a Hydraulic Direct-Drive system (HDD) based on a displacement control system that uses a single rod cylinder for a biped humanoid robot [13]. In the HDD system, the meter-in flow rate of a single rod cylinder is controlled by the pump discharge flow rate, and the cylinder meter-out flow rate is controlled by a proportional valve. The proposed system showed excellent energy transfer efficiency and excellent speed tracking capability in the evaluation bench system. Furthermore, the results showed that biped walking can be realized by an HDD system using a hydraulic–mechanical co-simulation model [14].

However, the HDD is implemented independently at each joint. This resulted in a problem in that the output of each pump increased to satisfy the required maximum output of each joint. In order to solve this problem, an interlocking circuit that focuses on the symmetry structure of the biped mechanism and the symmetry of motion was proposed [15]. It was shown that the proposed system reduced the maximum output of the motor by 27.3% in the evaluation bench device that simulated the load during walking compared to the case without the system.

In this study, a HDD with an interlocking circuit is applied to a biped humanoid robot to check whether walking can be realized. The results of the performance comparison without application of the interlock circuit verify the effectiveness of the proposed system.

The remainder of this paper is organized as follows: Section 2 introduces the design of the interlock circuit and its theoretical model for the HDD system. Section 3 describes the experimental setup, procedures, and results. Section 4 discusses future prospects and concludes the paper.

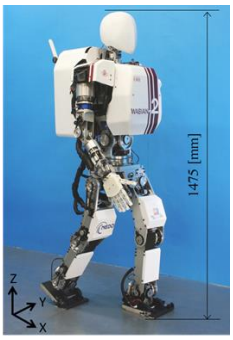

Figure 1: Example of our developed biped robot (WABIAN-2R)

2. CONSTRUCTION OF INTERLOCKING CIRCUIT FOR HYDRAULIC DIRECT-DRIVE SYSTEM

This section describes the configuration and control method of the proposed interlocking circuit for the HDD system. Section 2.1 presents the proposed interlock design, and Section 2.2 establishes the proposed control method.

2.1. Hydraulic Circuit

In a previous work, we proposed a hydraulic interlocking drive system that interlocks two joints [15]. The hydraulic circuit for our proposed system is shown in **Figure 2.** The pump units and cylinders are connected in a closed circuit. Valves 1a, 1b, 2a, and 2b are installed on the flow pass between the pump and cylinder. We use Takako's pump unit [16] for our test rig. An axial piston pump, two relief valves to protect the pump, and a special check valve are included in the unit. The special check valve has two normal check valves, which are connected to each other by a rod. Therefore, this special check valve connects the lower pressure side of the pump port to the tank. The pump unit has two ports and can discharge from both ports. Port A of the pump is connected to the cap side of the cylinder, and Port B is connected to the rod side. Proportional solenoid valves are used for valves 1a, 1b, 2a, and 2b. Four variable relief valves are installed to adjust the relief pressure in order to protect the circuit.
Valve 3a connects Port A of Pump Unit 1 and Port B of Pump Unit 2, and Port B of Pump Unit 1 and Port A of Pump Unit 2. The rod sides of

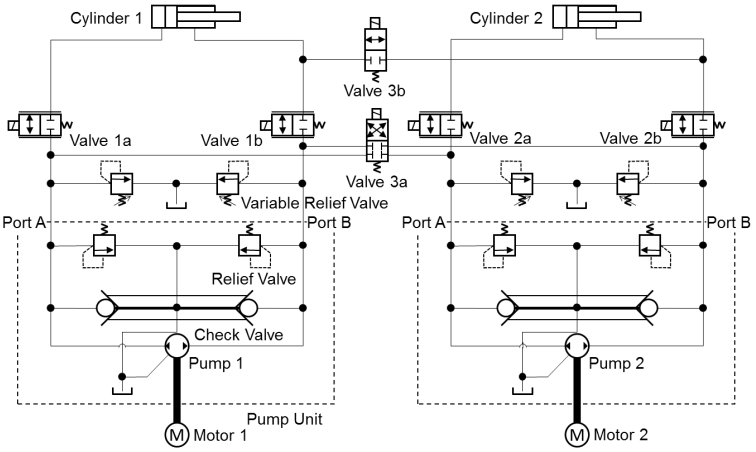

Figure 2: Hydraulic interlocking drive circuit

Cylinders 1 and 2 are connected through Valve 3b. Valves 3a and 3b are solenoid on–off valves. There are two drive modes in the circuit in **Figure 2.** The first drive mode is an independent drive mode. In this mode, it operates as the proposed single HDD system [13]. Pump 1 controls the meter-in flow of Cylinder 1, and Valve 1b or 1a controls its meter-out flow. The meter-in flow and meter-out flow of Cylinder 2 are also controlled by Pump 2 and Valve 2a or 2b. The effects of this mode are demonstrated in our previous work [13, 14].

The second drive mode is an interlocking drive mode. An example of this mode is shown in **Figure 3.** In this drive mode, Valves 3a and 3b are open. An interlocking flow pass is formed by opening Valve 3b. The meter-in flow of Cylinder 1 can be decided by the combined flow of Pumps 1 and 2. The meter-out flow of Cylinder 1 becomes the meter-in flow of Cylinder 2. Valve 2a can control the meter-out flow of Cylinder 2.

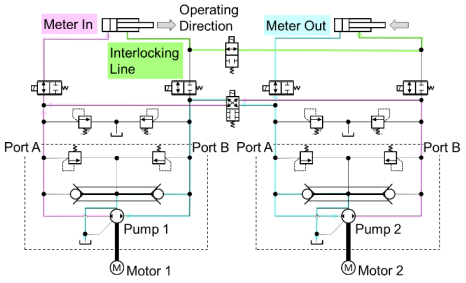

Figure 3: Interlocking drive mode

2.2. Control Method

The control methods of the independent and interlocking drive modes proposed in the previous research [13, 15] are described here.

In the first drive mode, the demand meter-in flow of Cylinder 1 (2), $Q_{dCyl1\,(2)\,in}$, is controlled by the flow delivered by Pump 1 (2). In an HDD system, the flow rate delivered by Pump 1 can be controlled by rotational speed ω_1. The demand meter-out flow of Cylinder 1, $Q_{dCyl1\,out}$, is controlled by the opening area of Valve 1a or 1b (2a or 2b), A_{dV1a} or A_{dV1b} [13]. For $Q_{dCyl1\,in}$, the demand rotational speed of Pump 1, ω_{dPump1}, is given by

$$\omega_{dPump1} = \frac{Q_{dCyl1\,in}}{D_{P1}\,\eta_{pv}}, \tag{1}$$

where D_{P1} is the displacement of Pump 1, and η_{p1v} is its volumetric efficiency. A_{dV1a} is defined as

$$A_{dV1a} = \frac{Q_{dCyl1\,out}}{C_d}\sqrt{\frac{\rho}{2\,(P_{V1a\,in}-P_{V1a\,out})}}, \tag{2}$$

where C_d is the flow coefficient, $P_{V1a\,in}$ and $P_{V1a\,out}$ are the pressures at the input port and output port of Valve 1a, respectively, and ρ is the density of the fluid. $P_{V1a\,out}$ is almost the same as the tank pressure (zero). $P_{V1a\,in}$ is almost the same as the cap pressure of Cylinder 1 in the cylinder stroke drive.

In the simplest pattern in the second drive mode, the velocities of the two cylinders are the same and the operation directions are opposite, as seen in **Figure 3.** In such a pattern, $Q_{dCyl1\,out}$ and the demand meter-in flow of Cylinder 2,

$Q_{dCyl2\ in}$, are equal. $Q_{dCyl1\ in}$ is decided by the flows delivered by Pumps 1 and 2. These flows are controlled by the rotational speeds of Pumps 1 and 2, ω_{dPump1} and ω_{dPump2}, respectively, which are expressed as follows:

$$\omega_{dPump1} = \beta \frac{Q_{dCyl1\ in}}{D_{P1}\,\eta_{p1v}}, \tag{3}$$

$$\omega_{dPump2} = (1-\beta) \frac{Q_{dCyl1\ in}}{D_{P2}\,\eta_{p2v}}, \tag{4}$$

where β is the flow rate ratio delivered by the pump. β is adjusted to compensate for the pressure loss in Valve 3a and make the output of the two pumps uniform. The meter-out flow of Cylinder 2 is controlled by the demand opening area of Valve 2a, A_{dV2a}, based on (2).

In actual patterns such as walking or running, the patterns of actuators are more complicated, and the velocities of the two cylinders are different. Therefore, $Q_{dCyl1\ out}$ and $Q_{dCyl2\ in}$ are different. For such a situation, we proposed flow rate compensation to control $Q_{dCyl2\ in}$. The compensation flow, Q_{Comp}, is given by

$$Q_{Comp} = Q_{dCyl1\ out} - Q_{dCyl2\ in}. \tag{5}$$

There are two modes for Q_{Comp}. In the first mode, Q_{Comp} is positive, and extra flow exists in the interlocking line. This flow must be discharged to the tank. Valve 1b can be used for the discharge, and its demand flow rate, Q_{dV1b}, is given by

$$Q_{dV1b} = \begin{cases} Q_{Comp} & (Q_{Comp} > 0) \\ 0 & (Q_{Comp} < 0) \end{cases}. \tag{6}$$

In the second mode, Q_{Comp} is negative. In this mode, in order to rectify the flow rate deficiency, it is necessary to increase the flow rate from the outside to the interlocking line. Valve 2b and Pump 2 can be used to obtain the required flow rate. The demand flow rate of Valve 2b, Q_{dV2b}, is given by

$$Q_{dV2b} = \begin{cases} 0 & (Q_{Comp} > 0) \\ -Q_{Comp} & (Q_{Comp} < 0) \end{cases}. \tag{7}$$

The delivery flow rate of Pump 2 must also be increased to the delivery demand flow rate of Valve 2b, Q_{dV2b}. Therefore, the demand pump rotational speed, ω_{dPump2}, is determined using (4) and (7).

$$\omega_{dPump2} = \frac{(1-\beta)Q_{dCyl1\ in} + Q_{dV2b}}{D_{P2}\,\eta_{p2v}} \tag{8}$$

When Q_{dV2b} is required, in order to maintain the ratio of $Q_{Cyl1\ in}$ and Q_{dV2b}, it is necessary to control the opening area of Valve 1a based on (2). When Valve 2b is not used, the opening area of Valve 1a is set at the maximum in order to suppress energy loss.

The block diagram of the proposed system is shown **Figure 4.**

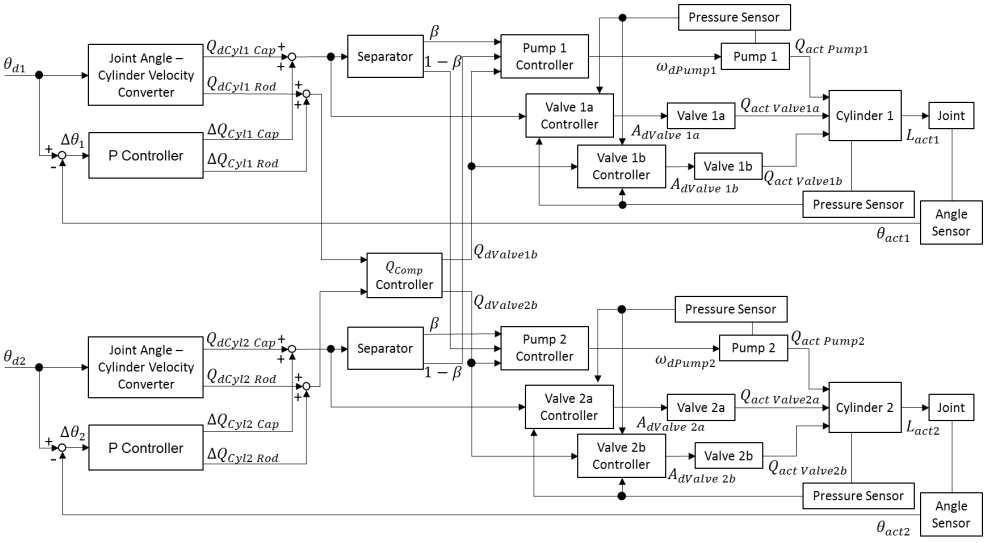

Figure 4: Block diagram of interlocking drive mode

2.3. Evaluation

The energy-saving performance of the proposed interlocking mode was evaluated experimentally. The mechanical hydraulic co-simulation model was used to confirm whether the maximum output of the two pump drive motors can be reduced by the walking pattern. The maximum output of the motor during walking when the HDD was used independently was compared with the situation when the interlocking drive mode was applied. The details are presented in Section III.

3. EXPERIMENTS

The walking simulations for the proposed interlocking circuit are examined, and the simulation setup and results are discussed in Sections 3.1 and 3.2, respectively. We used the physical modeling tool LMS Imagine.Lab Amesim™ (Siemens K.K.) to evaluate the interlocking circuit.

3.1. Experimental setup

We developed the bench test equipment to evaluate the proposed system. The hydraulic circuit of the bench is shown in Fig. 3.

To evaluate the proposed interlocking drive system, we developed a mechanical hydraulic co-simulation model of a biped humanoid robot. The construction of the mechanical model was based on the link mechanism and mass arrangement of our biped humanoid robot WABIAN-2R [1]. The proposed interlocking drive system served as the hydraulic model. Our proposed hydraulic system was applied to the hip pitch joints. The hip joints require high torque and joint density, and mounting the drive system poses difficulties because of space limitations. The other joints in the model used the conventional electrical motor and mechanical transmission system. The hydraulic and mechanical co-simulation models are shown in **Figures 5** and **6,** respectively. The hydraulic model is based on the HDD system constructed in the previous research, and reflects the pump efficiency and responsiveness of the valves and motors based on experiments. The corresponding parameters are listed in **Table 1. Figure 6** shows the link mechanism of the hip joint. The four-bar linkage mechanism was employed to secure a wide joint drive range. The parameters of the link mechanism are listed in **Table 2.**

Table 1: Hydraulic circuit model parameters

Pump displacement [cc/rev]		1.6
Pump relief pressure [MPa]		21.0
Cylinder stroke [mm]		132.0
Cylinder piston diameter [mm]		25.0
Cylinder rod diameter [mm]		16.0
Variable relief valve set pressure [MPa]		4.0
Hose inner diameter [mm]		6.4
Hose length [mm]	Pump to Valves 1a, 1b, 2a, and 2b	1000.0
	Pump to Valve 3a	300.0
	Valves 1a, 1b, 2a, and 2b to Cylinder 1 ,2	2000.0
	Valves 3b to Cylinder 1, 2	300.0
Valves 1a, 1b, 2a, and 2b: Nominal flow rate [L/min/(MPa)]		5.0
Valves 1a, 1b, 2a, and 2b: Valve Natural Frequency [Hz]		20.0
Valves 3a and 3b: Nominal flow rate [L/min/(MPa)]		10.0
Valves 3a and 3b: Valve Natural Frequency [Hz]		20.0
Oil kinematic viscosity [mm^2/s]	40 [deg C]	14.7
	100 [deg C]	3.7
Experimental oil temperature [deg C]		25.0

Table 2: Parameters of the four-bar linkage mechanism (see also Figure 6)

$Link_1$ [mm]	119.0
$Link_2$ [mm]	113.0
X_A [mm]	59.0
X_B [mm]	100.0
Z_A [mm]	34.0
Z_B [mm]	300.0
Z_c [mm]	57.0
Weight of Thigh [kg]	4.2
Weight of cylinder [kg]	2.0
Weight of $Link_1$ [kg]	0.6
Weight of $Link_2$ [kg]	0.4

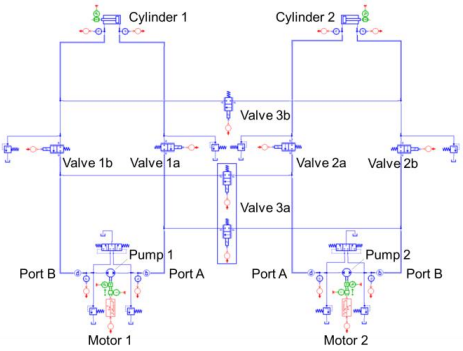

Figure 5: Hydraulic system of the co-simulation model

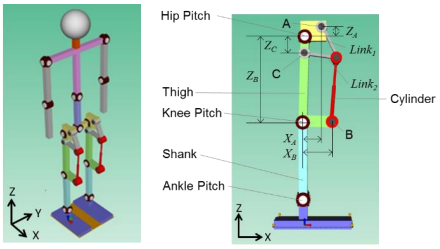

(a) Full mechanical model (b) Link parameters

Figure 6: Mechanical system of the co-simulation model

3.2. Experimental procedure

First, we used simulation experiments to confirm whether walking can be realized with the proposed interlocking system. Previous research suggests that the follow-up to the target trajectory deteriorates when the interlocking system is applied to the bench device [15]. It has been reported that when two pumps are joined to Cylinder 1, the follow-up performance of Cylinder 2 on the drive side worsens depending on the meter-out flow rate of Cylinder 1. In the interlock system, the pump output is concentrated on the cylinder that experiences the increased load. Therefore, when walking, the pump output is combined with the cylinder on the stance side when standing on one side. At this time, since the cylinder on the free leg side is controlled based on the meter-out flow rate of the cylinder on the standing side, there is a concern that the followability to the target trajectory may deteriorate. Even if the followability when the legs are swinging deteriorates, the trajectory is corrected before landing, and the simulation confirms whether walking can be realized.

In addition, using the results of the walking simulation, we evaluate the motor output reduction effect of the proposed interlocking system. In order to verify the effectiveness of the proposed system, we compare it with the results of the walking simulation of an HDD system reported in a previous study [14].

The motor size can be reduced by decreasing the motor output. The motor is selected based on the output required, the goal being to achieve the required maximum output for each axis. If the peak output of each motor is reduced by the interlocking system, a smaller motor can be selected, which contributes to weight reduction of the robot. This means that when a motor with the same output as the conventional one is installed, higher performance than before can be achieved. Therefore, the peak output of the motor during the walking motion is evaluated in the comparative experiment.

The walking pattern of the simulation experiment was generated using the offline pattern generation method proposed by our research group. The group has a proven track record of walking with WABIAN-2R [1], the basis of the mechanism model. In this study, we applied the eight-step walking pattern with the knee extended, which is a feature of WABIAN-2R. The interlocking system was applied in single-stance phases from the second step to the seventh step.

3.3. Experimental results

The results of the walking simulations are shown in **Figures 7** and **8. Figure 7** shows the walking motion of the biped humanoid robot model with the proposed interlocking drive system, and **Figure 8** shows the position responses of the right and left joints during walking. These results show that the proposed interlocking drive system can follow the demand trajectory under the walking motion load, thereby realizing biped walking.

Figure 9 shows the power of Motor 1 without the interlocking drive system. As shown in **Figure 9**, when the joint angle of the right link increases, such as at 2.7–3.4 s, the side with the right link reproduces the single stance phase. In this section, reflection force from ground is added to the cylinder on the right (Cylinder 1). Thus, the output of Motor 1 increases, as shown in

Figure 9. The maximum power in the independent drive mode is 351.6 W.

Figure 10 shows the power of Motor 1 when the interlocking drive mode is applied. This mode is applied during the single stance phase. As shown in **Figure 10,** the peak power of Motor 1 can be reduced to 266.2 W by applying the interlocking drive mode when the single stance on the right side is reproduced. Therefore, the maximum motor power can be reduced by 24.3% with the proposed interlocking drive system.

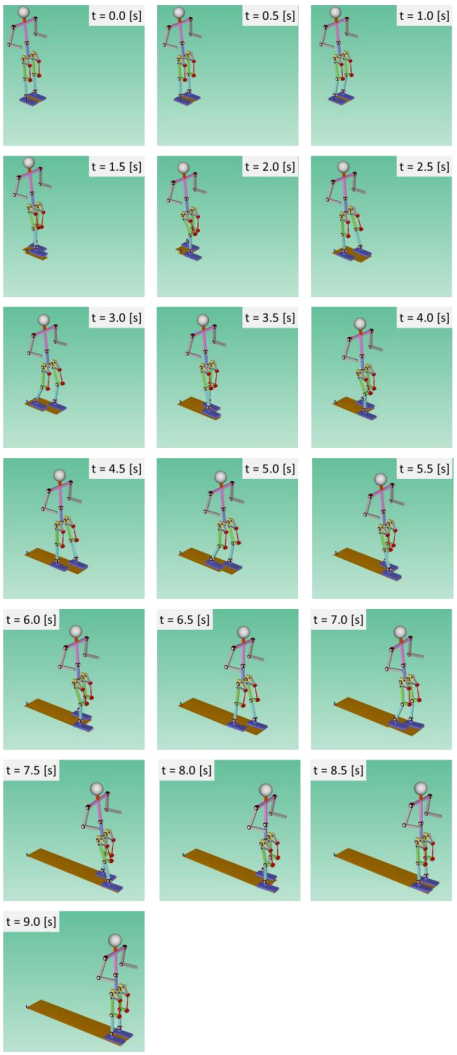

Figure 7: Walking motion of the co-simulation model

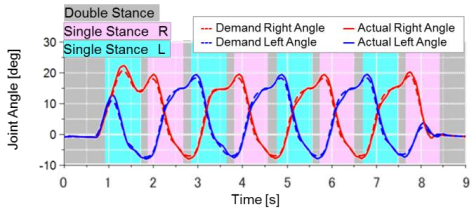

Figure 8: Position time response with proposed interlocking drive system

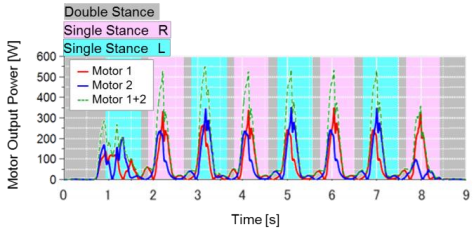

Figure 9: Motor output power without the proposed interlocking drive system

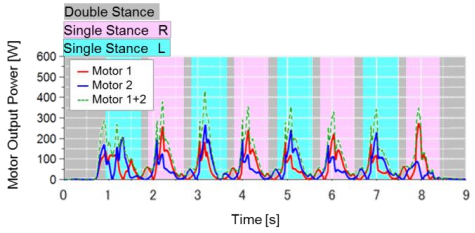

Figure 10: Motor output power with the proposed interlocking drive system

3.4. Discussion

It was confirmed that the peak output of the motors in a single stance can be reduced by applying the proposed interlocking drive system. However, as shown in **Figure 10,** the output of Motor 2 increased in the right stance phase at approximately 8 s. This can be attributed to the fact that the posture of the robot was disturbed at the end of walking. **Figure 7** confirms that the upper body was tilted at approximately 7.5 s due to an error in the joint angle on the swing leg side. **Figure 11** shows the results without the use of the interlock drive system reported in the previous study [14]. As shown in **Figure 11,** when the interlocking system is not used, the error with respect to the target trajectory does not increase during the swinging of the legs. In the interlock system, flow compensation control was proposed

to control the flow rate of the cylinder on the swing leg side. However, it is surmised that the proposed system could not secure the same accuracy as that of a single HDD system, which directly controls the pump-delivered flow rate due to the valve response and flow control accuracy. This problem can be effectively solved by using a highly responsive valve or improving the flow rate control with a proportional valve.
Thus, it was shown that the proposed interlocking drive system is effective when a high output and a low output are repeated periodically and symmetrically, such as when walking. **Figure 12** shows a comparison between the Pump 1 Port A pressures with and without the proposed system in the second step. **Figure 13** shows a comparison between the Pump 1 rotation speeds with and without the proposed system in the second step. As shown in **Figure 12**, the Pump 1 Port A pressure increased from 3.3 MPa to 5.1 MPa by applying the interlocking system. However, as shown in **Figure 13**, the Pump 1 rotation speed decreased from -2826 rev/min to -1564 rev/min. Therefore, the Motor 1 output power can be reduced. The pressure increased because the Cylinder 1 rod side was connected to the Cylinder 2 rod side by opening Valve 3b in the proposed system. As shown in **Figure 14**, when the system was switched to the interlocking system after 2.0 s in the right-stance phase, the cap pressure increased with the rod pressure. As a result, the pump discharge pressure also increased.

In the applied walking pattern, it was necessary for the actuator to actively control the speed, even on the swing leg side. Therefore, for Cylinder 1 without the interlocking system in **Figure 14**, the Cylinder 1 rod pressure increased during the left-stance phase, which is the swing phase. Applying a walking pattern in which the leg in the swing phase moves passively, as in human walking, is considered to reduce the rod pressure of the cylinder during the swing phase. In such a walking pattern, by reducing the rod pressure of the swing-phase cylinder, the motor-output reduction effect of the proposed interlocking system will be even higher.

4. CONCLUSION AND FUTURE WORK

In this study, performance comparison of a hydraulic interlocking drive system with a conventional HDD was conducted to verify the energy reduction effect. A hydraulic and mechanical co-simulation model was used for the evaluation. The results of the simulations confirmed that walking along a predetermined path was possible with the proposed system, and the simulation model was thus tuned based on the experimental results. The results also showed that the motor output could be reduced by 24.3% for walking motion and that the proposed system contributes to size reduction of the installed motors for biped humanoid robots.

In the future, it will be necessary to improve flow control accuracy for flow compensation of the interlock drive system. The proposed system will be applied to a biped humanoid robot to conduct a walking experiment.

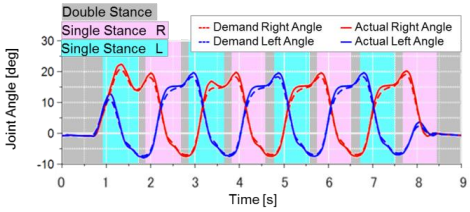

Figure 11: Position time response without the proposed interlocking drive system

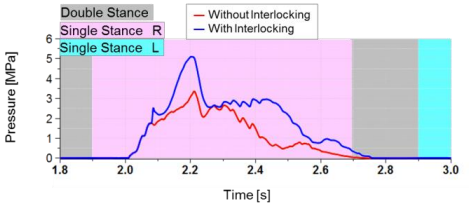

Figure 12: Pressure of Pump 1 Port A

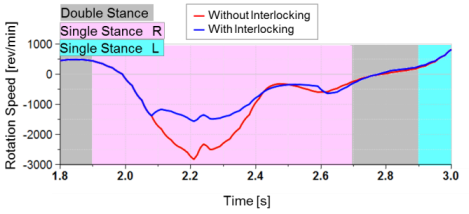

Figure 13: Rotation speed of Pump 1

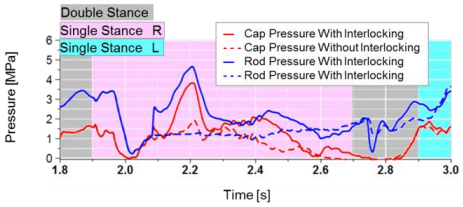

Figure 14: Pressure of Cylinder 1

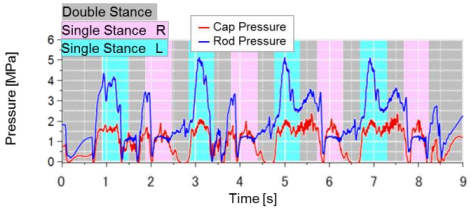

Figure 15: Pressure of Cylinder 1 without the proposed interlocking drive system

5. ACKNOWLEDGMENT

This study was conducted with the support of the Research Institute for Science and Engineering of Waseda University and the Future Robotics Organization of Waseda University. This study was part of the humanoid project at the Humanoid Robotics Institute of Waseda University. We would like to thank Editage (www.editage.jp) for English language editing.

NOMENCLATURE

HDD	Hydraulic direct-drive system
Q	Flow rate
A	Area
ω	Rotational speed
D	Displacement
η	Efficiency
P	Pressure
ρ	Density

REFERENCES

[1] Ogura Y, Shimomura K, Kondo H, Morishima A, Okubo T, Momoki S, Lim HO, Takanishi A (2006) Human-like Walking with Knee Stretched, Heel-Contact and Toe-Off Motion by a Humanoid Robot in the 2006 IEEE/RSJ Int Conf on Intelligent Robots and Systems 3976–3981

[2] Otani T, Hashimoto K, Hamamoto S, Miyamae S, Sakaguchi M, Kawakami Y, Lim HO, Takanishi A (2015) Knee Joint Mechanism that Mimics Elastic Characteristics and Bending in Human Running in the 2015 IEEE/RSJ Int Conf on Intelligent Robots and Systems 5156–5161

[3] Otani T, Hashimoto K, Miyamae S, Ueta H, Sakaguchi M, Kawakami Y, Lim HO, Takanishi A (2017) Angular Momentum Compensation in Yaw Direction Using Upper Body Based on Human Running in the 2017 IEEE Int Conf on Robotics and Automation 4768–4775

[4] Urata J, Nakanishi Y, Okuda K, Inaba M (2010) Design of High Torque and High Speed Leg Module for High Power Humanoid in the 2010 IEEE/RSJ Int Conf on Intelligent Robots and Systems 4497–4502.

[5] Ito Y, Nozawa S, Urata J, Nkaoka T, Kobayashi K, Nakanishi Y, Okada K, Inaba M (2014) Development and Verification of Life-Size Humanoid with High-Output Actuation System in the 2014 IEEE Int Conf on Robotics and Automation 3433–3438.

[6] Park I, Kim J, Lee J, Oh J (2007) Mechanical Design of the Humanoid Robot Platform, HUBO. Advanced Robotics 21(11) 1305–1322

[7] Kaneko K, Kaminaga H, Sakaguchi T, Kajita S, Morisawa M, Kumagai I, Kanehiro F (2019) Humanoid Robot HRP-5P: An Electrically Actuated Humanoid Robot with High Power and Wide Range Joints. IEEE Robotics and Automation Letters 4(2) 1431–1438

[8] Atlas Boston Dynamics, https://www.bostondynamics.com/atlas, accessed 2019/11/12.

[9] Hyon S, Suewaka D, Torii Y, Oku N (2017) Design and Experimental Evaluation of a Fast Torque-Controlled Hydraulic Humanoid Robot. IEEE/ASME Transactions on Mechatronics 22(2) 623–634

[10] Rahmfeld R, Ivantysynova M (1998) Energy Saving Hydraulic Actuators for Mobile Machines in the First Bratislavian Fluid Power Symp 47–57.

[11] Zimmerman J, Busquets R, Ivantysynova M (2011) 40% Fuel Savings by Displacement Control Leads to Lower Working Temperatures – A Simulation Study and Measurements in the Fifty-Second Nat Conf on Fluid Power 693–701.

[12] Kaminaga H, Ono J, Nakashima Y, Nakamura Y (2009) Development of Backdrivable Hydraulic Joint Mechanism for Knee Joint of

Humanoid Robots in the 2009 IEEE Int Conf on Robotics and Automation 1577–1582.

[13] Shimizu J, Otani T, Mizukami H, Hashimoto K, Takanishi A (2019) Experimental Validation of High-Efficiency Hydraulic Direct-Drive System for a Biped Humanoid Robot in the 2019 IEEE Int Conf. on Robotics and Automation 9453–9458.

[14] Shimizu J, Otani T, Hashimoto K, Takanishi A (2019) Simulation of a Hydraulic Direct-Drive System for a Biped Walking Robot in the 16th Scandinavian Int Conf on Fluid Power B6.1.

[15] Shimizu J, Otani T, Mizukami H, Hashimoto K, Takanishi A (2019) Experimental Validation of Hydraulic Interlocking Drive System for Biped Humanoid Robot in the 2019 IEEE/RSJ Int Conf on Intelligent Robots and Systems 7163–7169.

[16] Takako Industries, INC., http://www.takako-inc.com/, accessed 2019/11/12.

peer reviewed

NONLINEAR FORCE TRACKING CONTROL OF ELECTROHYDROSTATIC ACTUATORS SUBMITTED TO MOTION DISTURBANCES

Tahereh Vaezi*, Mohamed Smaoui, Paolo Massioni, Xavier Brun, Eric Bideaux

Laboratoire Ampère CNRS, INSA Lyon, université de Lyon,France
* Corresponding author: E-mail address: Tahereh.vaezi@insa-lyon.fr

ABSTRACT

In some industrial fields, such as aerospace, electro-hydrostatic actuators (EHAs) are increasingly used to replace conventional standard hydraulic actuators due to their better energy performance. Moreover, implementing different type or technology of actuators in redundant actuation systems working on the same moving part introduced some new challenges. This paper presents a force-tracking controller for an asymmetric electro-hydrostatic actuator that is submitted to an external motion generated by an external source. In this case, the rod displacement is considered as an external disturbance for the hydraulic cylinder, but it is assumed that this disturbance can be easily measured using sensors. The theoretical motivation of this work is discussed along and a variable gain state feedback control based on Linear Parameter Varying control (LPV) theory is proposed to achieve stability, disturbance rejection and tracking performance. The Linear Matrix Inequalities (LMI) framework is used to determine a control law including an augmented state feedback with an integral action that reduces trajectory-tracking errors. Simulation results of the control law are finally given to verify the global performance of this control design.

Keywords: electro hydrostatic actuator, force control, Linear parameter variant.

1. INTRODUCTION

Moving towards more electrical systems is generating significant efforts to develop electric powered actuators, especially in aeronautics and automotive industries. For such applications, it may be advantageous to combine a conventional hydraulic actuator and an electric power source. Nowadays, electro-hydrostatic actuators (EHA) have been considered in modern industries due to their reliability, durability, high energetic efficiency and less losses of energy. However, EHAs are highly nonlinear and complex systems. Nonlinearities are mainly related to hydraulic phenomena during the pushing and pulling stroke of the asymmetric cylinder such as variations of the fluid volume under compression, flow characteristics of orifices and pipes, and seal friction. Besides the nonlinearities, some uncertainties originate from fluctuation in supplied pump flow or variation of some parameters such as the bulk modulus and the fluid viscosity. All these considerations make the design of efficient controllers for EHAs really challenging.

Most of the previous research works on force control in the case of hydraulic actuators consider that the rod is fixed or that its displacement is negligible. With this assumption, the volumes of the chambers are generally constant and the flow rate corresponds to the compressibility flow. The control synthesis is consequently simplified.

The literature review brings out different control techniques to solve the force control problem, especially for servo controlled hydraulic actuators (SHA). Among these, PID, lead-lag controllers [1, 2], quantitative feedback theory (QFT) method [3, 4], self-tuning QFT control [5], feed-forward inverse model control [6], fractional order controller [7], hybrid fuzzy-neural technique [8], nonlinear control algorithms [9, 10, 11] and robust H_∞ control [12] have been applied. In these researches, some do not consider the inherent nonlinearities, friction, etc., and some are not practical. Predominantly, in most of these papers, first the effect of the rod

displacement is not taken into account or neglected, and second the stability of the inner states is not discussed. Beside, hydraulic architecture based on independent inputs have been proposed [13, 14, 15], this enables to simultaneously control the effort and the displacement. In this case, thanks to the two inputs the system stability is insured in the whole range of operating points.

Therefore, the objective of this work is to analyze and design of a proper controller for the force trajectory tracking when the EHA is submitted to an external motion. The novelty is here to use a single pump in order to achieve force trajectory tracking. Consequently, difficulties arise since only one input is available and the motion (disturbance) can be antagonist to the force trajectory. Moreover, due to the fact that movement is considered as a disturbance, the EHA is just modeled by its hydraulic equations, which can be considered as a linear parameter varying (LPV) model as it will be shown in section 3.

The study of LPV systems is motivated by the gain scheduling control design methodology. LPV control theory is advantageous because it provides a generic control synthesis method, which insures stability and performance over a wide range of parameter variation. In general, the solution to the LPV control analysis and synthesis problems is formulated as a parameter-dependent linear matrix inequalities (LMIs) problem, which corresponds to a special type of convex optimization problem. The LMI approach provides the design framework to determine feedback laws aiming at asymptotic stabilization including H_∞ and robustness features [16, 17].

In this research, we will apply this method to solve numerically parameter-dependent LMIs associated with LPV analysis and synthesis in the case of the EHA force control. A state feedback control will be deduced by a direct application of Sum Of Squares (SOS) decompositions to the Lyapunov stability analysis for the LPV model.

The remaining sections are organized as follows: first, in Section 2, we will start with basic background of LMI control theory and the formulation needed to solve the SOS problem. In Section 3, we will introduce the model of the system. Then, the LPV control model of the EHA submitted to an external motion will be formulated. In Section 4, we will design the integral state feedback controller based on introduced design procedure for an augmented model of the EHA. In section 5, before concluding, simulation results of closed loop system will be carried out to demonstrate the proposed control method and investigate the effectiveness and robustness of the proposed controller. The capability of the proposed controller will be compared with a controller with parameter-independent gains for the force tracking trajectory.

2. LMI CONTROL THEORY

This section presents the key concept of the control method proposed in this paper. First, we will introduce the basic of Lyapunov stability with the LMI framework. Next, we will formulate the LMI, in the form of Sum Of Squares (SOS). These concepts will be applied in Section 4 to derive a state feedback controller for an EHA submitted to an external motion.

First, let us consider a representation of a LPV system as:

$$\begin{cases} \dot{x}(t) = A\big(\rho(t)\big)x(t) + B_u\big(\rho(t)\big)u(t) + \cdots \\ \qquad\qquad\qquad \ldots + B_w(\rho(t)\,)w(t) \\ y(t) = C\big(\rho(t)\big)x(t) \end{cases} \tag{1}$$

where $x(t)$ is the state vector, $u(t)$ is the control input, $w(t)$ is the exogenous inputs such as perturbation and $y(t)$ is the output of the system.

Assumption1. The state vector $x(t)$ is measurable or can be estimated online.

Assumption2. $\rho(t)$ and $\dot{\rho}(t)$ are continuous and bounded functions of t (hereafter ρ will be used instead of $\rho(t)$).

Lyapunov theory states that the existence of a matrix $P(\rho)$ such that the quadratic Lyapunov function $V(x)$

$$V(x) = x^T P(\rho)x > 0 \text{ for all } x \neq 0 \tag{2}$$

satisfies:

$$\dot{V}(x) = \dot{x}^T P(\rho)x + x^T P(\rho)\dot{x} + x^T \dot{P}(\rho)x < 0 \tag{3}$$

is a necessary and sufficient condition to ensure stability of the system. Equation (2) is a LMI and $P(\rho)$ can be found by solving these inequalities.

Consider system (1) in closed loop with a state feedback controller, $u = K(\rho)x$. From (1), the closed loop model becomes:

$$\begin{cases} \dot{x} = \big(A(\rho) + B_u(\rho)K(\rho)\big)x + B_w(\rho)w \\ y = C(\rho(t))x \end{cases} \quad (4)$$

Furthermore, if a $\mathcal{L}_2$ gain γ constraint for disturbance rejection (5) is added to the previous stability objective, the problem can be expressed similarly on finding a feedback $K(\rho)$ that satisfies the LMIs (2), (3) and (5).

$$\frac{\|y\|_2}{\|w\|_2} \leq \gamma, \quad \gamma > 0 \quad (5)$$

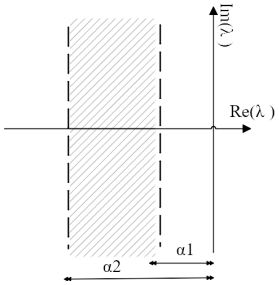

Figure 1: Acceptable pole placement area

However, high controller gains can lead system to instability, due to the discrete-time implementation of the control law. In order to avoid this problem, an upper bound for the module of poles, α_2, should be chosen for pole placement. Therefore, to guarantee prescribed performance requirements, the closed-loop pole locations must be restricted into a specific region (**Figure 1**). Equations (6) then define equivalent Lyapunov conditions.

$$\begin{cases} V(x) > 0 \\ \dot{V}(x) < -\alpha_1 V(x) \\ \dot{V}(x) > -\alpha_2 V(x) \end{cases} \quad (6)$$

The following theorem [19] presents the gain controller design using regional pole location constraints.

Theorem 1: Consider the LPV system in closed-loop with a state feedback controller ($u = K(\rho)x = L(\rho)X^{-1}(\rho)x$), as given in (4). The closed-loop system is stable with an L_2 gain less than $\gamma > 0$, with its closed-loop poles in the specified area if there exists a positive definite matrix $X(\rho) \in \Re^{n\times n}$ and a rectangular matrix $L(\rho) \in \Re^{m\times n}$ subject to (7-9), where $X(\rho) = P^{-1}(\rho)$ and $L(\rho) = K(\rho)X(\rho)$.
If such problem is feasible, a suitable controller gain is:

$$K(\rho) = L(\rho)X^{-1}(\rho). \quad (10)$$

Notice that theorem 1 features parameter dependent LMIs, as explained in [20]. These can be solved efficiently (convex optimisation) by the so-called SOS technique [21].

$$\begin{bmatrix} \left\{ \begin{matrix} A(\rho)X(\rho) + X(\rho)A^T(\rho) + B_u(\rho)L(\rho) + \\ L^T(\rho)B_u^T(\rho) - \sum \frac{\partial X(\rho)}{\partial \rho}\dot{\rho} \end{matrix} \right\} & B_w(\rho) & X(\rho)C^T(\rho) \\ B_w^T(\rho) & -I & 0 \\ C(\rho)X(\rho) & 0 & -\gamma^2 I \end{bmatrix} < 0 \quad (7)$$

$$A(\rho)X(\rho) + X(\rho)A^T(\rho) + B_u(\rho)L(\rho) + L^T(\rho)B_u^T(\rho) - \sum \frac{\partial X(\rho)}{\partial \rho}\dot{\rho} < -2\alpha_1 X(\rho) \quad (8)$$

$$A(\rho)X(\rho) + X(\rho)A^T(\rho) + B_u(\rho)L(\rho) + L^T(\rho)B_u^T(\rho) - \sum \frac{\partial X(\rho)}{\partial \rho}\dot{\rho} > -2\alpha_2 X(\rho) \quad (9)$$

Definition of SOS: X is positive if $X(\rho) > 0$ for all $\in \mathcal{R}^{n\times n}$. A way of establishing whether a function is positive consists of establishing whether it can be written as a Sum Of Squares (SOS) of polynomials.

$$X(\rho) = \sum X_i^2(\rho) \qquad (11)$$

Implementing SOS decomposition is interested because establishing whether a polynomial is SOS, leads to solving a convex optimization problem. Being stricter, the condition that $X(\rho)$ is SOS is computationally much more tractable than positivity; therefore, positivity condition of Lyapunov function can be replaced by the SOS condition.

Theorem 2: [22] Consider system (1). Suppose that there exist a symmetric polynomial matrix X and, a polynomial matrix L, a parameter $\varepsilon_1 > 0$ and an SOS polynomial $\varepsilon_2 : \mathcal{R}^n \to \Re$ such that

- $X(\rho) - \varepsilon_1 I > 0$ is SOS
- $-\Big(A^T(\rho)X(\rho) + X(\rho)A(\rho) + L^T(\rho)B^T(\rho) + B(\rho)L(\rho) - \sum \frac{\partial X}{\partial \rho}\dot{\rho} + \varepsilon_2 I\Big) > 0$ is SOS

Then, the origin of (1) is asymptotically stabilized by a state feedback given by (10).

This technique is originally proposed for polynomial systems, but thanks to some new researches [23], it has been extended to non-polynomial systems.

3. MODELLING

The test rig at which this study is applied is shown in Figure 2. It is a redundant system composed of an EHA connected directly to an electromechanical actuator (EMA). The EMA is position controlled, that is why it will be considered here as the external source generating motion trajectory. On the EHA side, several components are implemented, such as safety valves, electrical motor, hydraulic pump, sensors, etc. Beside the effect of the main components, the performance of the EHA is also affected by pressure losses in transmission lines, parameter changes during the working time, due to temperature change for example.

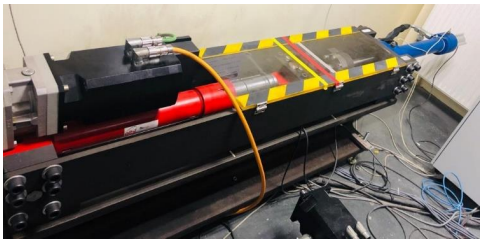

Figure 2: EHA-EMA test rig

There are three different possible configurations of an EHA: Fixed Pump displacement and Variable Motor speed (FPVM), Variable Pump displacement and Fixed Motor speed (VPFM) and Variable Pump displacement and Variable Motor speed (VPVM). Our test rig is equipped with a VPVM configuration and enables therefore to consider the different ways of generating flow

3.1. Simulation Model of EHA

The simulation model has been defined to cross over the gap between control model and reality. It takes into account all the main components of the hydraulic parts and mostly based on physical characteristics provided by datasheets or direct measurements on the test rig. However, some hypothesis have been considered to avoid useless complexity:

- The hydraulic transmission lines are short with reasonably large diameter to keep fluid flow velocities to a low value. In these situations, it is usually reasonable to ignore line resistance, relative line capacitance and fluid inertia, control valve resistance and the inertia of the actuator and load.
- The inlet/outlet port pressures of the hydraulic pump are regarded equal to the pressures inside the chambers of the cylinder.
- The behaviour of the system is supposed to be isothermal.
- The pump/motor unit is an ideal flow rate unit.

The simulation model has been developed in the Simcenter Amesim software from Siemens as shown in **Figure 3**.

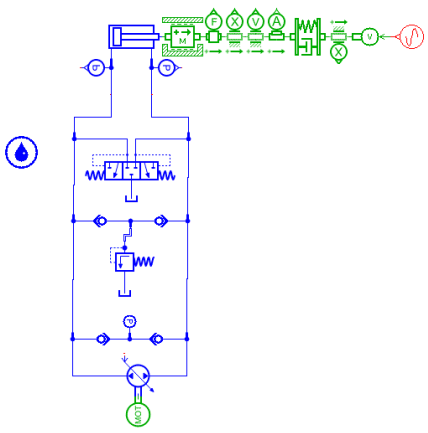

Figure 3: Simulation model in Simcenter Amesim

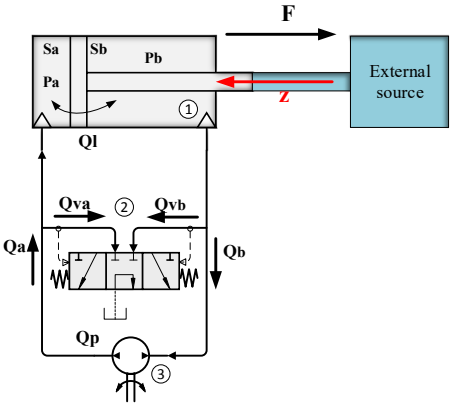

Figure 4: Scheme of the control model

3.2. Control Model of EHA

A control model of the EHA (**Figure 4**) is deduced in this section with the following additional assumptions:

- Dynamic of the pump is neglected. (**Figure 4-3**)
- The recirculation valve is considered to have a linear characteristic and its dynamic is neglected. (**Figure 4-2**)
- Safety and bypass valves are not modelled.
- Minimum pressure of the tank is consider to be zero.

As it is emphasized in **Figure 4**, the cylinder position, z, is negative when the cylinder extends, and positive otherwise, and the force, F, is positive if it is oriented against the velocity.

The flow rate equations of the chambers can be obtained as the following expressions:

$$Q_a = S_a\dot{z} + \frac{V_a}{\beta}\dot{P}_a + Q_l + Q_{va} \tag{12}$$

$$Q_b = S_b\dot{z} - \frac{V_b}{\beta}\dot{P}_b + Q_l - Q_{vb} \tag{13}$$

where, P_a, P_b are respectively the pressures in the cap side and rod side, and:

$$\begin{aligned} V_a &= V_{0a} + S_a z \\ V_b &= V_{0b} - S_b z \end{aligned} \tag{14}$$

V_a, V_b are volumes in each side of the actuator, V_{0a}, V_{0b} are dead volumes and Q_{va} and Q_{vb} represent the flow rates due to the recirculation valve that can be expressed with:

$$\begin{aligned} &Q_{vi} = K_{vi}P_i \ , i = a, b \\ &\begin{cases} K_{vb} = 0 & if \ \ P_b > P_a \\ K_{va} = 0 & if \ \ P_a > P_b \end{cases} \end{aligned} \tag{15}$$

Finally, Q_l is the linear flow leakage between the chambers:

$$Q_l = K_f(P_a - P_b) \tag{16}$$

The output, here the force applied by the hydraulic actuator on the moving mass, is a combination of the hydraulic force and mechanical, inertia and friction forces which are considered negligible compared to the hydraulic force, thus the output is expressed as:

$$F = S_aP_a - S_bP_b \tag{17}$$

The effect of the transmission lines are neglected. So, the flows Q_P, Q_a and Q_b are equal and a function of pump displacement and motor speed (18). Moreover, the VPVM configuration enables the flow rate of the hydraulic pump then to be expressed by the following equation:

$$Q_P = D_{max}\omega_{max}u = Q_{max}u \tag{18}$$

where ω_{max} is the maximum motor speed, D_{max} is the maximum hydraulic pump displacement and $u \in [-1 \ \ 1]$ is the percentage of the maximum flow rate (Q_{max}) which will be taken as the command input. Let us define yet the following change of variable: $\rho = z, w = \dot{z}, x = [P_a \ \ P_b]^T, y = F$.

The LPV model of the EHA is then expressed as:

$$\begin{cases} \dot{x} = A(\rho)x + B_u(\rho)u + B_w(\rho)w \\ y = Cx \end{cases} \tag{19}$$

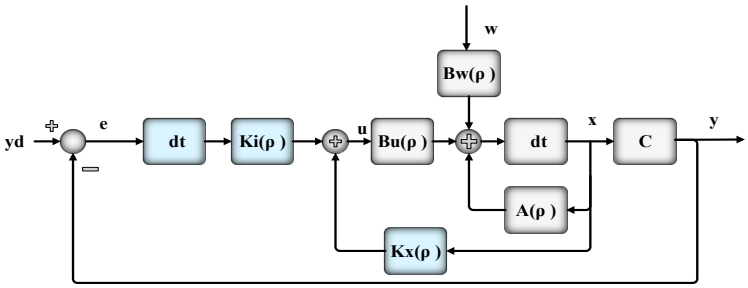

Figure 5: Closed-loop scheme of the system

With:

$$\begin{cases} A = \begin{bmatrix} \dfrac{-\beta(K_{va}+K_f)}{V_a(\rho)} & \dfrac{\beta K_f}{V_a(\rho)} \\ \dfrac{\beta K_f}{V_b(\rho)} & \dfrac{-\beta(K_{vb}+K_f)}{V_b(\rho)} \end{bmatrix} \\ B_u = \begin{bmatrix} \dfrac{\beta D_{max}\omega_n}{V_a(\rho)} \\ \dfrac{-\beta D_{max}\omega_n}{V_b(\rho)} \end{bmatrix}, B_w = \begin{bmatrix} \dfrac{-\beta S_A}{V_a(\rho)} \\ \dfrac{\beta S_B}{V_b(\rho)} \end{bmatrix} \\ C = [S_a \quad -S_b] \end{cases} \quad (20)$$

Notice that, the control model involves two continuous dynamic models depending on the pressures P_a and P_b (15), which are both controllable and marginally stable for all $\underline{\rho} \leq \rho(t) \leq \bar{\rho}$ but uncontrollable model for $P_a = P_b$.

4. CONTROLLER SYNTHESIS

In this section, a parameter dependent state-feedback controller is designed for the force tracking of the EHA submitted to an important external motion. In order to compensate model uncertainties and achieving zero steady state error, an integral action is added to the state feedback controller. **Figure 5** shows the scheme of the control including the state feedback and the integral action. Therefore, let us add in the state space model (19-20) an extra state, x_i, that is the integral of the output error:

$$x_i = \int (y_d - y)dt = \int (y_d - Cx)dt \quad (21)$$

with $x_a = [x^T \quad x_i]^T$ the augmented state vector, $w_a = [w \quad y_d]^T$ the augmented exogenous vector and $C_a = [C \quad 0]$ the augmented output vector and:

$$A_a(\rho) = \begin{bmatrix} A_{2\times2} & 0_{2\times1} \\ -C_{1\times2} & 0 \end{bmatrix},$$

$$B_{a_u} = \begin{bmatrix} B_{u_{2\times2}} \\ 0 \end{bmatrix}, B_{a_w} = \begin{bmatrix} B_{w_{2\times1}} & 0_{2\times1} \\ 0 & 1 \end{bmatrix}$$

Let us now introduce the augmented model as a linear model with a scalar scheduling parameter:

$$A_a = \Delta^{-1}(\rho)\left(\hat{A}_0 + \hat{A}_1\rho + \hat{A}_2\rho^2\right)$$

$$B_{a_u} = \Delta^{-1}(\rho)\left(\hat{B}_{u_0} + \hat{B}_{u_1}\rho + \hat{B}_{u_2}\rho^2\right)$$

$$B_{a_w} = \Delta^{-1}(\rho)\left(\hat{B}_{w_0} + \hat{B}_{w_1}\rho + \hat{B}_{w_2}\rho^2\right)$$

where $\hat{A}_i$, $\hat{B}_{u_i}$ and $\hat{B}_{w_i}(i = 1,2,3)$ are constant matrices of the appropriate dimension and $\Delta(\rho)$ is a polynomial factor that is always positive:

$$\Delta(\rho) = \frac{V_a(\rho)V_b(\rho)}{V_{a0}V_{b0}}$$

Theorem 1 is applied to find the controller gains. Considering that $X(\rho)$ and $L(\rho)$ are chosen to be respectively a constant matrix and a linear polynomial vector defined by now:

$$X = X_0$$
$$L = L_0 + L_1\rho$$

Therefore, $\partial X/\partial\rho = 0$ and it is eliminated from (7-9). The controller gains, $K(\rho) = [K_x(\rho) \quad K_i(\rho)]$, with the $\mathcal{L}_2$ gain bound $\gamma = 1$ are calculated using the Sedumi solver. The LPV controller gains are then derived thanks to (10)

The earlier discussion explained that recirculation valve would provide different models and each model requests its own controller to overcome disturbances and ensure closed loop performance requirements. Therefore, employing switch between controllers is an essential issue. Moreover, stability of the whole system is guaranteed for $P_a < P_b$ (or $P_a > P_b$). However, switches will happen in pressure equalities (uncontrollable modes) where

establishing stability of whole system is a complicated problem, which is not discussed here.

5. SIMULATION RESULTS

The goal of this section is to demonstrate feasibility of the LMI force controller and to illustrate the capability of the proposed approach for disturbance rejection in tracking force trajectory.

Therefore, the controller is executed on the simulation model with the hypothesis introduced in section 3.1. Simcenter Amesim software from Siemens (see Figure 3) is used to examine the suggested controller. System parameters are given in table 1.

The ability of the controlled system to follow a sine-wave trajectory, $y_d = F_0 \sin(2\pi t) + F_1$, with $F_0 = 7kN$ and $F_1 = 2kN$ is investigated in Figure 7, whereas the rod is submitted to different sinusoidal motions generated by the external source (Figure 6).

Table 1: Parameters of the EHA

Cylinder parameter	Value	unit
Cap end area S_a	0.0032	m^2
Rod end area S_b	0.0019	m^2
bulk modulus β	1700	MPa
Inactive volume V_{a0}	0.649×10^{-3}	m^3
Inactive volume V_{b0}	0.387×10^{-3}	m^3
valve coefficient K_{va}, K_{vb}	0.045	$L/s/bar$

Referring to Figure 7, the supplied force by the hydraulic actuator converged to the desired trajectory and the system showed good tracking performance and disturbance rejection for both imposed displacements.

The simulation results of the pressures in the chambers are shown in Figure 8, which shows that the responses contain oscillations around pressure equalities due to the action of the recirculation valve. In addition, it can be observed that the pressures are bound by the lower value defined by the tank.

However, for the force and displacement trajectories, the recirculation valve is always fully opened on the rod side for positive forces and on the cap side for negative forces. The related pressure of the chamber is therefore equal to the tank pressure, which means that the force is always affected by a single pressure.

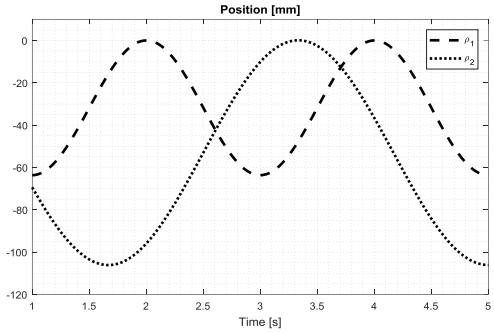

Figure 6: Imposed displacement trajectories

Input saturation may cause oscillatory transient behavior or even instability, and a closer inspection of the control input is shown in Figure 9. Here, as demonstrated, the control input is not saturated and therefore the oscillation of the pressures in Figure 8 can be mainly due to uncontrollability of the system while $P_a = P_b$.

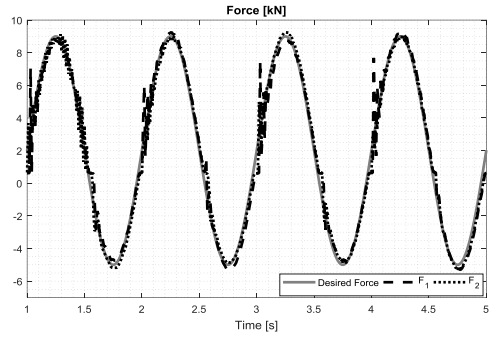

Figure 7: Simulation results for tracking desired force trajectory

Figure 10 shows the results obtained from the controller gains, as shown in the figure switches, which depend on the pressures P_a and P_b. In addition, K_x (bar^{-1}) and K_{xi} $(N^{-1}s^{-1})$ are the polynomial of displacement ($\rho(t)$ or $z(t)$). Although the variation of the gains is small, it is shown that good tracking performance cannot be achieved by constant gains, even for small displacements.

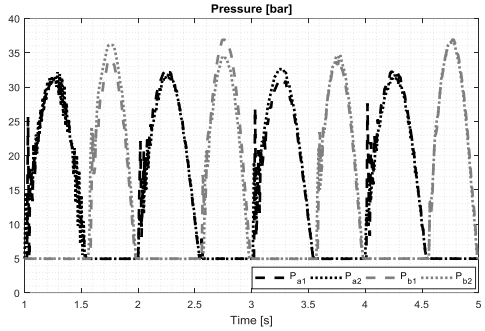

Figure 8: Simulation results for pressures

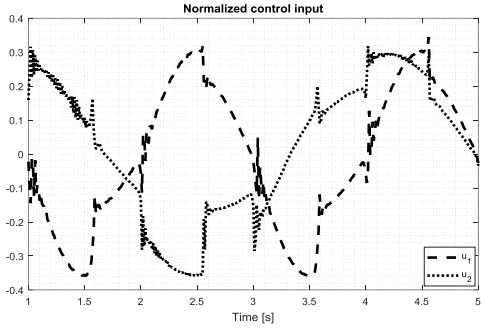

Figure 9: Control inputs

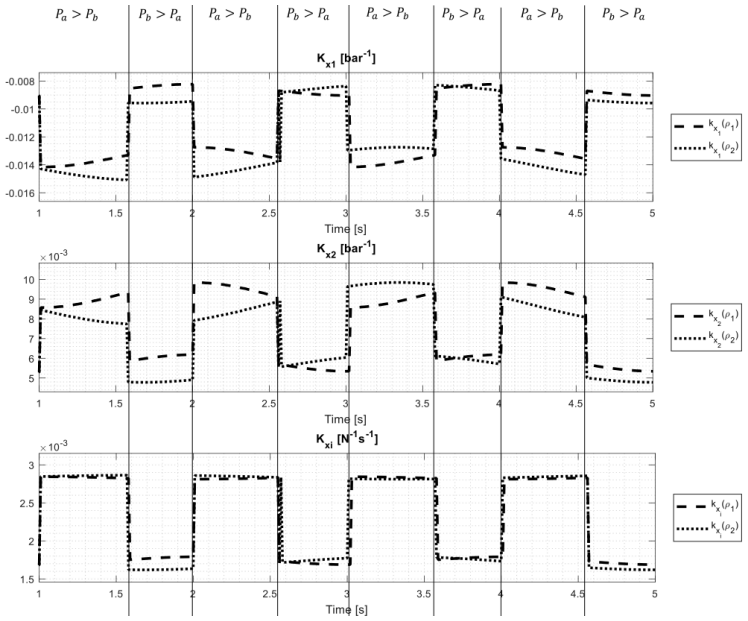

Figure 10: Simulation results for gains: a) k_{x1}, b) k_{x2}, c) k_{xi}

The force tracking performance of the system submitted to a small amplitude sinusoidal motion (16mm) is shown in **Figure 11**. Clearly, the simulation results of the proposed approach (dash curve) presents better tracking performance properties compared to a state feedback controller with constant gains (dots curve).

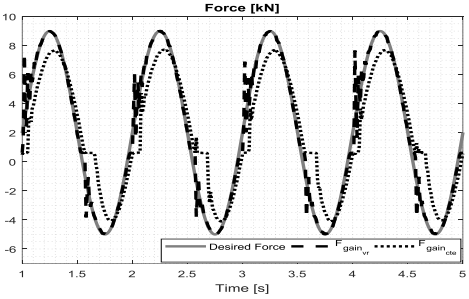

Figure 11: Tracking force trajectory by variable and constant gain controllers

According to the carried out results, it can be concluded that the proposed controller improves the performance of the force control of the EHA when submitted to an external motion compared to state feedback controller with constant gains. In addition, the proposed controller guarantees significant disturbance rejection.

CONCLUSION

Due to the need for improved technology, industries have begun to use heterogeneous redundant actuation systems on their existing machines, leading to new challenges. Even though hydraulic power has always been recognized as being capable of applying high force, today it is necessary to overcome the problems caused by the force-fighting phenomenon that appears on redundant actuation systems.

This paper addressed a new controller for an electro hydrostatic actuator, which had been submitted to an external motion. First, a linear parameter variant model has been deduced. Second, a state-feedback controller with parameter-variant gains such as integral action has been established on the basis of *Linear Matrix Inequalities* framework and the *Sum Of Squares* (SOS) decomposition. The feasible solution of the proposed controller design procedure guarantees the Lyapunov stability and the perturbation rejection. Finally, the ability of the designed controller to follow the desired force trajectory has been verified by the simulation. The designed gains of the controller gains depend only on the position that can be easily measured by the sensors.

NOMENCLATURE

S_a	Cap end Area
S_b	Rod end Area
V_{a0}	Inactive volume cap side
V_{b0}	Inactive volume rod side
β	Bulk modulus
P_a, x_1	Pressure in cap side
P_b, x_2	Pressure in rod side
P_T	Tank pressure
K_f	Inter chamber leakage coefficient
K_{va}, K_{vb}	Recirculation valve coefficient
z, ρ	Displacement of the cylinder
w	Velocity of the cylinder
F, y	Force
y_d	Desired Force
u	Control input
D_{max}	Hydraulic pump displacement
ω_n	Nominal speed of electrical motor
$K(\rho)$	Controller gains
Q_p	Pump flowrate
Q_a	Transmission line flow rate
Q_b	Transmission line flow rate
Q_l	leakage flowrate
Q_{va}, Q_{vb}	Recirculation valve flow rate
EHA	Electro hydrostatic actuator
SHA	servo controlled hydraulic actuators
EMA	Electromechanical actuator
LPV	Linear parameter variant
LMI	Linear matrix inequality
SOS	Sum Of Squares

REFERENCES

[1] Alleyne, A. and Liu, R., (1999). On the limitations of force tracking control for hydraulic servosystems. Journal of dynamic systems, measurement, and control, 121(2), pp.184-190.

[2] Alleyne, A. and Liu, R., (2000). A simplified approach to force control for electro-hydraulic systems. Control Engineering Practice, 8(12), pp.1347-1356

[3] Niksefat, N. and Sepehri, N., (1999). Robust force controller design for an electrohydraulic actuator based on nonlinear model. In Proceedings 1999 IEEE International Conference on Robotics and Automation (Cat. No. 99CH36288C) (Vol. 1, pp. 200-206). IEEE.

[4] Niksefat, N. and Sepehri, N., (2001). Designing robust force control of hydraulic actuators despite system and environmental uncertainties. IEEE Control Systems Magazine, 21(2), pp.66-77.

[5] Ahn, K.K. and Dinh, Q.T., (2009). Self-tuning of quantitative feedback theory for force control of an electro-hydraulic test machine. Control Engineering Practice, 17(11), pp.1291-1306.

[6] Zhao, J., Shen, G., Zhu, W., Yang, C. and Yao, J., (2016). Robust force control with a feed-forward inverse model controller for electro-hydraulic control loading systems of flight simulators. Mechatronics, 38, pp.42-53.

[7] Sangpet, T. and Kuntanapreeda, S., (2013). Force control of an electrohydraulic actuator using a fractional-order controller. Asian Journal of Control, 15(3), pp.764-772.

[8] Liem, D.T., Truong, D.Q., Park, H.G. and Ahn, K.K., (2016). A feedforward neural network fuzzy grey predictor-based controller for force control of an electro-hydraulic actuator. International Journal of Precision Engineering and Manufacturing, 17(3), pp.309-321.

[9] Liu, R. and Alleyne, A., 1999. Nonlinear force/pressure tracking of an electro-hydraulic actuator. IFAC Proceedings Volumes, 32(2), pp.952-957.

[10] Nakkarat, P. and Kuntanapreeda, S., (2009). Observer-based backstepping force control of an electrohydraulic actuator. Control Engineering Practice, 17(8), pp.895-902.

[11] Sun, H. and Chiu, G.C., (1999), June. Nonlinear observer based force control of electro-hydraulic actuators. In Proceedings of the 1999 American Control Conference (Cat. No. 99CH36251) (Vol. 2, pp. 764-768). IEEE.

[12] Baghestan, K., Rezaei, S.M., Talebi, H.A. and Zareinejad, M., (2014). Robust force control in a novel electro-hydraulic structure using polytopic uncertainty representation. ISA transactions, 53(6), pp.1873-1880.

[13] Rehman, W.U., Wang, S., Wang, X., Fan, L. and Shah, K.A., (2016). Motion synchronization in a dual redundant HA/EHA system by using a hybrid integrated intelligent control design. Chinese Journal of Aeronautics, 29(3), pp.789-798

[14] Ferreira, J.A., Sun, P. and Grácio, J.J., (2006). Close loop control of a hydraulic press for springback analysis. Journal of Materials Processing Technology, 177(1-3), pp.377-381

[15] Yao, J., Wang, P., Cao, X.M. and Wang, Z., (2018). Independent volume-in and volume-out control of an open circuit pump-controlled asymmetric cylinder system. Journal of Zhejiang University-SCIENCE A, 19(3), pp.203-210.

[16] Wu, F. and Prajna, S., (2004), June. A new solution approach to polynomial LPV system analysis and synthesis. In Proceedings of the 2004 American Control Conference (Vol. 2, pp. 1362-1367). IEEE.

[17] Hoshino, K., Sonoda, D. and Yoneyama, J., (2016). Design of dynamic output feedback laws based on sums of squares of polynomials. Nonlinear Systems-Design, Analysis, Estimation and Control.

[18] Aktas, A., Yazici, H. and Sever, M., (2019). LMI-based design of an I-PD+ PD type LPV state feedback controller for a gantry crane. Transactions of the Institute of Measurement and Control, 41(6), pp.1640-1655.

[19] Scherer, C., Gahinet, P. and Chilali, M., (1996). H∞ design with pole placement constraints: An LMI approach. IEEE Transactions on Automatic Control, 41(3), pp.358-367.

[20] Wu, F. and Prajna, S., (2005). SOS-based solution approach to polynomial LPV system analysis and synthesis problems. International Journal of Control, 78(8), pp.600-611.

[21] Chesi, G., (2010). LMI techniques for optimization over polynomials in control: a survey. IEEE Transactions on Automatic Control, 55(11), pp.2500-2510.

[22] Prajna, S., Papachristodoulou, A. and Wu, F., 2004, July. Nonlinear control synthesis by sum of squares optimization: A Lyapunov-based approach. In 2004 5th Asian Control Conference (IEEE Cat. No. 04EX904) (Vol. 1, pp. 157-165). IEEE.

[23] Henrion, D. and Garulli, A. eds., 2005. Positive polynomials in control (Vol. 312). Springer Science & Business Media

peer reviewed

MULTIDIMENSIONAL FLOW MAPPING FOR PROPORTIONAL VALVES

André Sitte*, Oliver Koch, Jianbin Liu, Ralf Tautenhahn, Jürgen Weber

Institut für Mechatronischen Maschinenbau, Technische Universität Dresden, Helmholtzstrasse 7a, 01069 Dresden
* Corresponding author: Tel.: +49 351 46333707; E-mail address: andre.sitte@tu-dresden.de

ABSTRACT

Inverse, multidimensional input-output flow mapping is very important for use of valves in precision motion control applications. Due to the highly nonlinear characteristic and uncertain model structure of the cartridge valves, it is hard to formulate the modelling of their flow mappings into simple parameter estimation problems. This contribution conducts a comprehensive analysis and validation of three- and four-dimensional input-output-mapping approaches for a proportional pilot operated seat valves. Therefore, a virtual and a physical test-rig setup are utilized for initial measurement, implementation and assessment. After modeling and validating the valve under consideration, as a function of flow, pressure and temperature different mapping methods are investigated. More specifically, state of the art approaches, deep-learning methods and a newly developed approach (*extPoly*) are examined. Especially ANNs and Polynomials show reasonable approximation results even for more than two inputs. However, the results are strongly dependent on the structure and distribution of the input data points. Besides identification effort, the invertibility was investigated.

Keywords: Valve Control, Flow Mapping , Polynomial Fitting, Artificial Neural Networks, Deep Learning

1. INTRODUCTION

Modern electrohydraulic drive and control tasks are subject to high demands in terms of flexibility and complexity. Various fields of application can be named such as energy-efficient operation, high-precision, closed-loop-control-tasks, automation, fault detection, condition monitoring and diagnostics. The majority of today's hydraulic drive systems incorporate valve-operated actuators. Especially independent metering control systems enable energy efficient and high performance operation by decoupling meter-in and meter-out flow, using regeneration flow and enhanced control possibilities of multiple input system structures. The key elements of such systems are individual valves, preferably of seat type due to advantageous dynamic and static properties. Since the mathematical models of cartridge valves flow mapping is complex, it cannot be described by typical analytical nonlinear equations, commonly used.

Main challenges are the complex non-linear characteristics of hydraulic components, which are exposed to a wide range of external environmental and operational effects as well as internal factors like aging. Besides mainly oil-related thermal dependencies, in particular flow-related friction and throttle losses determine the static and dynamic input-output-behavior.

A common strategy to compensate for these nonlinearities is an inverse feedforward controller. Usually nonlinear or unknown physical relations are modelled using empirical coefficients measured at typical operating points. In many cases, the achievable accuracy is insufficient but the experimental and computational effort to raise the mapping-quality increases dramatically with higher number of measuring points. The present paper aims to analyze different approaches for (inverse) input-output mapping of a pilot operated seat valve.

2. STATE OF THE ART

Experimental system identification, in particular the measurement of input-output-signals, has low information content regarding internal processes and parameter dependencies. A distinction between parametric models utilizing explicit parameters within mathematical/physical equations and nonparametric models, using implicit parameters with purely functional relationships of behavior, can be made [1]. In industrial applications, nonparametric models are widespread. Common to all of them is the problem of identifying and implementing three- or higher-dimensional representations as a nonlinear mapping of two (or more) input variables x_{in}, y_{in}, i_{in} to an output variable $z_{out} = f(x_{in}, y_{in}, i_{in})$. Among others, the following methods can be found: 1. grid maps, 2. polynomial approximations, and 3. artificial neural networks.

Nonlinear static relationships with grid maps are widespread because they are easy to implement on Electronic Control Units (ECU). Often, equidistant grids with $(m \cdot n)$ supporting points in combination with surface interpolation methods are applied. Since each grid-point must correspond to a measuring point, the quality of the map significantly depends on the number of nodes and the degree of non-linearity. Due to computational effort, the number of dimensions is limited. The second class of approximation methods are higher order polynomials such as algebraic polynomials, orthogonal polynomials or Chebyshev polynomials. An advantage of this type of models is a compact form of mathematical representation and an efficient calculation mode. The system degree determines shape and order of the polynomial. With the help of regression methods, the unknown polynomial coefficients are identified and parameterized [2]. Second order polynomials are usually easy to invert analytically, whereas functions of higher order require a numerical solution. Application examples for compensating methods can be found in [3], [4]. Artificial neural networks are highly capable of approximating and representing complex nonlinear and high dimensional functions [5]. There are different classes of neural networks and corresponding training algorithms, each suitable for different approximation problems. Typical examples are Multi-Layer-Perceptrons (MLP) or Radial Base Functions (RBF) [6], [7], [8].

3. IDENTIFICATION METHODS

3.1. General aspects

Experimental modelling (identification) of measurement data enables the determination of characteristic maps. **Figure 1** shows the proposed workflow.

Figure 1: Characteristic map identification workflow

The first step is to acquire a set of measurement data representing all dependencies of interest. It is crucial to collect this data under varying operating conditions and measuring regimes.

If the measurement data is limited or insufficient, simulation data may be used instead or as supplement. This data is referred to as synthetic data. A combination of synthetic and sensor data may be a reasonable compromise.

The next step of the workflow is pre-processing of the raw data. Typically missing or faulty values, noise and outliers are processed and set up for further steps. In some cases a scaling is beneficial, since big values generate great residuals. This is equivalent to weighting in advance.

The following task is finding and training (fitting) the model that captures the relationship between the input and output. Starting point of the experimental modeling is the determination of a suitable model structure. The corresponding model parameters are adapted using optimization procedures, to match input/output behavior of model and measured data. The selected model structure must allow mapping for all physical effects of interest. Basically linear and non-linear as well as static and dynamic models may be distinguished. This contribution deals with static, nonlinear models. In general, nonlinear mapping f of two input variables x_{in} and y_{in} is formulated by:

$$z_{out} = f(x_{in}, y_{in}) \tag{1}$$

To optimize the model parameters usually the sum square error between the measured output z and estimated output $\hat{z}$ is minimized [9].

$$R(\theta) = \sum_{i=1}^{n} \big(z(i) - \hat{z}(i)\big)^2 \qquad (2)$$

The final step is the integration (deployment) of the model into the control platform. Memory requirements as well as cycle time of the device may potentially affect the quality of the model results.

According to [9] the generation of grid maps from measurement data can be performed in three ways. The approaches are adoptable and valid for many identification procedures.

Method 1: The definition of the grid lines/points is either equidistant or it can be chosen individually (optimal distribution) considering process knowledge. The intersections of the grid lines provide direct estimates or training points. The procedure does not require any optimization.

Method 2: As in method 1, an a-priori definition of a grid points takes place. Using optimization techniques the optimal position of a grid point from arbitrarily distributed measurement data is performed in a post-processing step. A necessary condition is the availability of a sufficient number of data points.

Method 3: [10] proposes a method for optimization of grid point positions and heights at the same time. Here nonlinear optimization methods are necessary.

3.2. Grid based look up tables - *gridLUT*

Grid-based look-up tables are the most common type of nonlinear static models used in practice [9], [2]. A nonlinear relationship is modelled by storing input-data-tuples [x_i, y_i] in a grid.

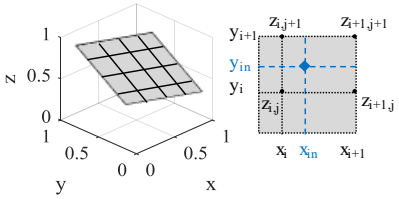

Figure 2: Areas and grid points used for surface interpolation (*gridLUT*)

Typically, they are limited to one or two-dimensional implementations, because measuring approaches mostly consider one effect at a time for a corresponding output. Interpretation and manipulation of 1D-data is very easy and user-friendly.

The model output z for an input vector [x, y] is calculated by local interpolation between the surrounding nodes. In 1D-case, linear interpolation methods may be used. For 2D-case, bilinear interpolation between four surrounding points (vertex points) is necessary. At grid-point positions, the model output is equal to the measured data. Intermediate values that lie within the grid are calculated with aforementioned surface interpolation method [6].

$$\begin{aligned} z = &\big[z_{i,j}(x_{i+1} - x)(y_{i+1} - y) + \\ &z_{i+1,j}(x - x_i)(y_{i+1} - y) + z_{i,j+1}(x_{i+1} - \\ &x)(y - y_j) + z_{i+1,j}(x - x_i)(y - y_j)\big] / \\ &\big[(x_{i+1} - x_i)(y_{j+1} - y_j)\big] \end{aligned} \qquad (3)$$

To determine a desired point [x_{in}, y_{in}] in the input space, all the heights z of the four surrounding grid-points must be explicitly known. The heights of the four vertices are multiplied by the opposing areas and then divided by the total area value.

The number of grid-points in each dimension are chosen according to the accuracy demanded. However, the number of data point's n_P grows exponentially with the number of input dimensions k:

$$n_p = \prod_{i=1}^{k} n_i \qquad (4)$$

If measurement data points are incomplete or do not correspond to the desired positions of the grid, estimation techniques or extra measuring activities have to considered to derive additional grid points. Additional efforts and costs are to be expected. An arbitrary and optimal positioning of grid points represents a nonlinear optimization problem, which potentially increases the resulting quality of the method.

3.3. Polynomials

I Algebraic polynomials - algPoly

Polynomials are typical approximators, characterized in particular by a high calculation and evaluation speeds [1]. The choice of the maximum degree depends on approximation accuracy and other factors. With the help of an algebraic polynomial z a function f is approximated as follows:

$$z(x,y) = a_{0,0} + a_{1,0}x + a_{0,1}y + a_{2,0}x^2 + a_{0,2}y^2 + a_{1,1}xy + a_{m,0}x^m + a_{m-1,1}x^{m-1} + a_{1,m-1}y^{m-1} + a_{0,m}y^m \quad (5)$$

Polynomial terms (x,y) are multiplied by the coefficients $a_{i,j}$, which represent the free parameters of the model approach. With the maximum degree k of the polynomial, the number n_C of unknown coefficients $a_{i,j}$ is:

$$n_C = \frac{1}{2}(k+1)(k+2) \quad (6)$$

There is an uncertainty regarding the order of the polynomials. It should not exceed $(n_p - 1)$, where n_p is the number of data points per input. High order polynomials show an increased oscillation behaviour. For practical use 3rd to 6th order, including interaction-terms, are suitable. Generally speaking, polynomials are characterized by a very good smoothness, simple parameter determination but limited extrapolation capabilities [9].

II Semi empirical flow mapping - twoLine

In [4] Huhtala proposed a mapping description as a function of system variables. The method incorporates the variation of one parameter while the other remains constant. This results in two curves, which are obtained by polynomial fitting. The measurement data needs to cover the whole range of the operating field. The flow rate through a valve can be described as a function of pressure drop and input signal. The basis of the so-called "two-line-models" are measured data of the test valve near the operating boundaries. First, the input voltage is kept constant and the pressure drop is varied from min to max. Next, the input voltage is kept constant at max and the pressure drop dependency is measured. With help of these two data sets, the flow rate as a function of pressure drop can be obtained by using polynomial fitting:

$$z_i(y) = a_{i,1}e^{a_{i,2}y} - a_{i,3}e^{-a_{i,4}y} \quad (7)$$

Next step is a min-max normalization:

$$\hat{z}_i(y) = \frac{z_i(y) - z_i(y_{min})}{z_i(y_{max}) - z_i(y_{min})} \quad (8)$$

The curves for output z (flow rate) as a function of input x (voltage) are identified in the previous mentioned way. First the input y (pressure drop) is kept constant at min (resp. max) and the input voltage is varied from min to max. With help of the polynomial fitting, the flow rate as a function of input voltage can be obtained. The flow rate as a function of pressure drop and input voltage is:

$$z(x,y) = \left\{[\hat{z}_2(y) - \hat{z}_1(y)]\left(\frac{x - x_{min}}{x_{max} - x_{min}}\right) + \hat{z}_1(y)\right\} \cdot [z_4(x) - z_3(x)] + z_3(x) \quad (9)$$

Figure 3 depicts the working principle of the two-line-method (*twoLine*).

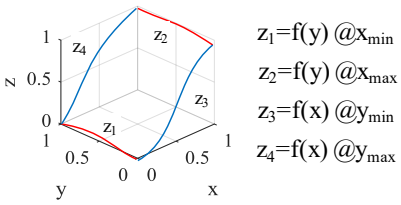

Figure 3: Principle of operation of two-line-method

III Extended algebraic polynomials - extPoly

The proposed polynomial approximation uses the following general approach:

$$Y = \sum_{i_0=0}^{m_0}\sum_{i_1=0}^{m_1}\cdots\sum_{i_n=0}^{m_n} a_{i_0 i_1 \cdots i_n} Y_0^{i_0} Y_1^{i_1} \ldots Y_n^{i_n} \quad (10)$$

The n-dimensional output Y is a result of a polynomial combination of 1-dimensional functional approximation Y_n for each dimension. For this paper, Y_k represents a char curve with its sampling point tuples $(\hat{x}_k, \hat{y}_k)$:

$$Y_k = f_c(\hat{x}_k, \hat{y}_k, x_k) \quad (11)$$

The char curve uses the linear interpolation:

$$Y_k = \frac{\hat{y}_{i+1} - \hat{y}_i}{\hat{x}_{i+1} - \hat{x}_i}(x_k - \hat{x}_i) \quad (12)$$

For instance, a simple three-dimensional relationship has the specific approach:

$$Y = a_{00} + a_{10}Y_0 + a_{01}Y_1 + a_{11}Y_0Y_1 \quad (13)$$

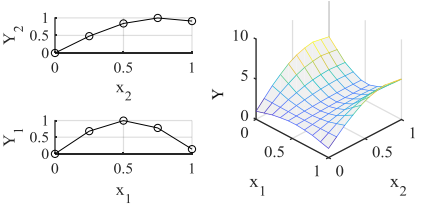

Figure 4: Polynomial approximation example (*extPoly*)

Figure 4 exemplarily illustrates a result for a surface based on 24 parameters (10 for each dimension and the four polynomial factors a_{ik}). This approach is advantageous in the software development for embedded systems to integrate multi-dimensional dependencies with a reduced set of parameters. Using a gradient-based optimization finds the parameters for each approximation.

3.4. Artificial neural networks - *ANN*

Artificial neural networks became very popular in the context of Machine Learning and Big-Data during the last years. Nevertheless, their foundation was laid up back in the 1940s already [11]. Since then a broad variety of different network architectures was developed. However, they all share a common working principle:

The main idea is to connect the outputs and inputs of some information processing units (called nodes or neurons) and to modify their sensitivity to each other by weighting and biasing these connections. Since the nodes and their links among each other are quite similar to the nerve cells (called neurons) and their connections by axons and dendrites the name “artificial neural networks” (ANN) was given.

According to [12] different switching functions inside the information processing units (e.g. binary, linear or sigmoid), different mechanisms for the parametrization of the weights (e.g. supervised, unsupervised and reinforcement learning) and different network architectures (e.g. feed forward, Kohonen or Hopfield networks) for the connections between the units may be used depending on the application. Typical applications are classification, function approximation, image processing or speech recognition. For function approximation multilayer perceptrons (MLPs) or radial basis function networks are advised in literature.

The weights and biases of MPLs are usually parametrised from known data (inputs and associated outputs) in a specialised optimization process, which is called backpropagation training. Afterwards the resulting network will produce similar outputs according to the inputs it was “trained” for. Nevertheless, this concept also provides some generalization. To a certain extent even previously unknown inputs will result in an appropriate output if the network represents the underlying correlations correctly [13].

In the following investigation Bayesian Regularization backpropagation [14] was used for networks with two hidden layers (each holding between two and eight neurons). In this case the output of a single neuron of the nth layer is

$$\sigma_{nj} = \varphi\left(\boldsymbol{w}_{nj}^{T} \cdot \boldsymbol{x}_j + \theta_{nj}\right). \quad (14)$$

Using following expression for the weight factor matrix $\boldsymbol{W}_n = \left[\boldsymbol{w}_{n_1} \dots \boldsymbol{w}_{n_{k_n}}\right]^T$ the output of the whole network results from the matrix equation

$$y = \varphi(\boldsymbol{W}_n \cdot \varphi(\boldsymbol{W}_{n-1} \cdot \varphi + \boldsymbol{\theta}_{n-1}) + \boldsymbol{\theta}_n) \quad (15)$$

with the bias vector $\boldsymbol{\theta_n} = \left[\theta_{n_1} \dots \theta_{n_{k_n}}\right]^{\boldsymbol{T}}$ for each layer number n. The number of neurons in layer l is n_n and the switching function

$$\varphi(\boldsymbol{x}) = 2 \,/\, (1 + exp(-2 \cdot \boldsymbol{x})) - 1 \quad (16)$$

is applied element wise and could be substituted by any another sigmoid function.

4. APLLICATION AND MODELLING

4.1. Proportional flow control valve

One example for a seat type proportional flow control valve is depicted in Figure 5. The operating principle of the so-called *Valvistor* (type A - proportional flow from p_1 to p_2) is based on flow feedback for displacement control of the main poppet (MP- (3)).

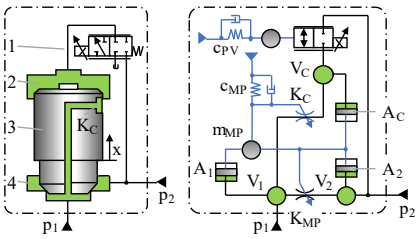

Figure 5: Seat type proportional valve schematic (left) / Simulation model structure (right)

Due to a negative overlap of the control orifice, the pressure p_C in the control chamber V_C is equal to the pressure p_1 at the valve inlet V_1. Area A_C is greater than area A_1, ensuring a closing of the main poppet. Opening the pilot valve (1), enables the pilot flow Q_{PV} and reduces the control pressure p_C in the control chamber. The main

poppet starts moving until the equilibrium of forces is established. Neglecting flow- and friction forces and rearranging the force balance equation for the main poppet leads to:

$$p_C = \frac{p_1}{\varphi} + \left(\frac{\varphi-1}{\varphi}\right) p_2, \text{ with } \varphi = \frac{A_1+A_2}{A_1} \qquad (17)$$

If the area ratio $\varphi=2$, the pressure drop $\Delta p_{1C} = p_1 - p_C$ across control-orifice is equivalent to the pressure drop $\Delta p_{C2} = p_C - p_2$ across the pilot valve. The flow rate across control-orifice results in:

$$Q_C = Q_{PV} = K_C(x_0 + x)\sqrt{\Delta p_{1C}} \qquad (18)$$

According to eq. (17) and (18), the following interrelation can be obtained:

$$x = \left(\frac{Q_{PV}}{K_C}\sqrt{\frac{(\varphi-1)}{\varphi(p_1-p_2)}}\right) - x_0 \qquad (19)$$

The flow rate across main poppet is denoted as:

$$Q_{MP} = K_{MP} x \sqrt{\Delta p_{12}} \qquad (20)$$

Neglecting the negative overlap x_0 in eq. (19) and substituting eq. (19) for eq. (20), results in following equation:

$$Q_{MP} = \left(\frac{K_{MP}}{K_C}\sqrt{\frac{\varphi-1}{\varphi}}\right) Q_{PV} \qquad (21)$$

The total flow rate is:

$$Q_T = Q_{MP} + Q_{PV} \qquad (22)$$

The "Valvistor" is similar to a transistor, which amplifies a small current through the pilot circuit. Amongst others, more information can be obtained in [15] or [16].

4.2. Experimental setup and results

To evaluate the static and dynamic characteristics of the proportional seat-type valve, a test bench has been set up. **Figure 6** briefly illustrates the experimental setup, including pump, sensors and the loading valve controlling the pressure drop across the test valve. A displacement sensor is installed on the main poppet as well as on the pilot spool. The test rig setup is restricted to Q_{max}=200 l/min and p_{max}=200 bar. The test valve is set to discrete opening values. Varying the outlet pressure, the oil flow through the system increases and decreases in a quasi-static manner.

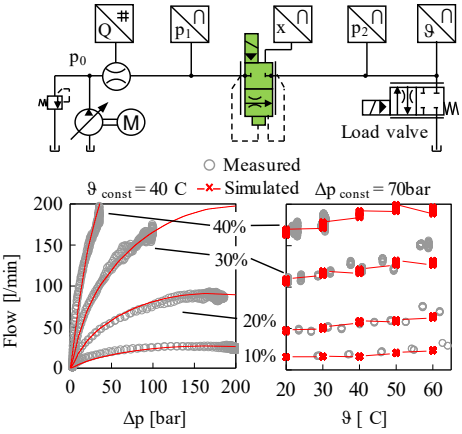

Figure 6: Experimental setup (top) / simulated and measured steady state flow behaviour for discrete input-signals U_{rel} (bottom)

Figure 6 (bottom) shows a comparison of measurement data and simulation results for constant and varying temperatures. The results show a very good correlation.

5. FLOW MAPPING OF TEST DATA

5.1. Training data sets

To test the effectiveness of the approximation methods, different simulated and experimental data-sets are used, as shown in **Figure 7**.

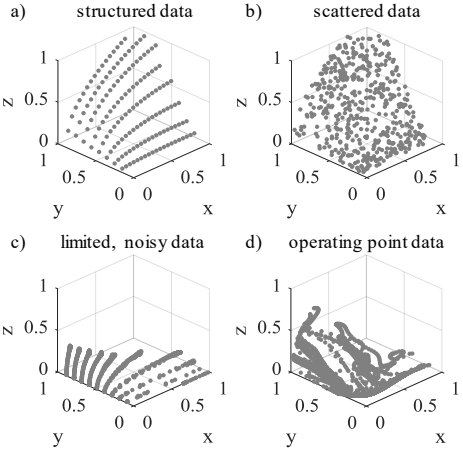

Figure 7: Test source data-types a) structured data / b) scattered data / c) noisy data / d) operating point data

Usually, structured $(\Delta p, Q)$ curves (**Figure 7 a**)) characterize the flow behaviour of throttle valves. These curves are determined at discrete input signals, representing the operating range. There is a high resolution along the x-axis, whereas only a few data point exist along the y-axis. The data-gap increases the requirements for the training procedures (optimization) and eventually creates great deviations between model and estimation. A comprehensive scatter data-set (**Figure 7 b**)) appears to be advantageous in terms of coverage. However, arbitrary data is difficult to interpret and to evaluate, which is why the use of such data is not very widespread. Limited and noisy flow curves like in **Figure 7** c) are more common. The restrictions mostly result from limited capacities of the test rig or system setup. Noise is inherent to measurement data, which requires filtering of data or smoothing capabilities of the approximation procedures.

Figure 7 d) contains operating point data resulting from a typical loading cycle of a material handling excavator. The working cycle is divided in several phases, **Figure 8**. After picking up the bulk material (1), the operator lifts the working equipment (2) from the pile. In addition, the attachment's centre of gravity is moving closer to the rotational axis. It decreases the inertia before starting to swing of the upper carriage (3). Following the rotating phase, the working tools are positioned directly above the silo's opening (4).

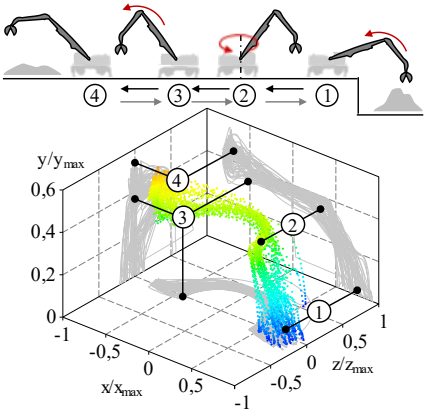

Figure 8: Loading cycle of a material handling excavator [17]

The data-point distribution represents a combination of different of upstream and downstream flow paths.

5.2. Results and Discussion

To investigate the quality and limitations of input-output mapping of the pilot operated seat valve, the methods proposed in ch. 3 are applied to the different training- and test-data sets (ch. 5.1) and the results are analysed. One prerequisite mentioned in the introduction was to use the flow-mapping information for control purposes. To do so, the characteristic interrelation $Q = f(\Delta p, y)$ needs to be inverted to $y = f(\Delta p, Q)$. All procedures are rechecked taking into account this premises.

In order to compare the goodness of fit for the different training-data and mapping approaches the results of the models are plotted against the data source' output values for each set of input variables. With an ideal approximation, all points would lie exactly on the 45° diagonal curve. The unavoidable deviations are characterised in a box plot with regard to their dispersion. This diagram shows the median (centerline), the 25th and 75th percentiles (upper and lower edges of the box) as well as two extreme values, which are determined by $w_{max} = Q_{75} + 1.5 \cdot IQR$ and $w_{min} = Q_{25} - 1.5 \cdot IQR$ respectively. The range between these two extreme values covers approximately $\pm 2.7 \cdot \sigma$ for a normally distributed random quantity and covers thus 99.3 % of the realizations. All points outside these extreme values are called outliers marked separately by a "+" symbol. Additionally the relative error of the fits are plotted against the flow rate to identify critical areas. Each plot contains two different data sets. One was used to parametrize the models while the other holds previously unknown uniformly distributed data over the whole range of input values to assess the generalization capability of the different mapping approaches.

The common methods *([10x10]-gridLUT, twoLine*) show a good approximation quality. However, reasonable results can only be assured for comprehensive scatter data. An extension to even more input variables requires massive additional computing effort. Furthermore, they are not designed for analytical inversion. Here recursive search algorithms of the feedforward maps have to be used.

Regarding approximation quality algebraic polynomials (*x^2y^5-algPoly* with second order for input signal dependency of x and fifth order for pressure dependency of y) show similar results. They prove to be beneficial with limited and

noisy data, though accuracy is decreasing. Using an inverse input-output-relationship for approximation also results in major deviations between model and training data. Limiting the polynomial degree to $k_y = 2$, an analytical inversion is possible without using numerical approaches.

The extended polynomial method (*[10×10]-extPoly*) is able to deal with all kinds of input data and theoretically any number of input dimensions. Regardless of the input data distribution, all results are quite close to each other, illustrating the reasonable modelling accuracy of the proposed method. Since the approach utilizes grid-point-position optimization, a weighting of different regions may be used to considerably increase local accuracy. Because the base function eq.(13) is linear, it may be rearranged in any desired way for inverse input-output-relationship, without any adverse effects.

Using artificial neural networks (*MLP-ANN*) the best fitting results regarding accuracy can be obtained. The fitting quality is highly dependent on the coverage of the training-data. Again, comprehensive scattered data points appear to be most beneficial. Just like all other polynomial-based approaches, ANN show very poor extrapolating behavior. To determine the inverse I/O-relationship the input and output simply have to be interchanged before training. Surprisingly, the results differ from natural I/O-assignment. Obviously, the missing distinction in the inverse pressure-flow-relationship results in major deviations between model and training data. An implementation of ANN-functions in embedded systems could be challenging, since massive floating point matrix operations are necessary.

Table 1 shows the number of parameters (coefficients) for the different methods analysed.

Table 1: Number of parameters

Method	No of parameters	
	3D	4D
[10×10]-gridLUT	120	>1200
twoLine	27	-
x^2y^5*-algPoly*	15	>35
[10×10]-extPoly	44	74
MLP-ANN	38	81

6. CONCLUSION AND OUTLOOK

Inverse, multidimensional input-output flow mapping is very important for use of valves in precision motion control applications. Due to the highly nonlinear characteristic and uncertain model structure of the cartridge valves, it is hard to formulate the modelling of their flow mappings into simple parameter estimation problems. This paper presented an analysis and comparison of different identification methods and training data sets for 3D- and 4D-flow mapping. More specifically, state of the art approaches, deep-learning methods and a newly developed approach (*extPoly*) had been examined. Especially ANNs and Polynomials show reasonable approximation results even for more than two inputs. However, the results are strongly dependent on the structure and distribution of the input data. Besides identification effort, the invertibility was investigated.

The next investigation steps are concerned with the further development of the proposed methods with respect to online identification.

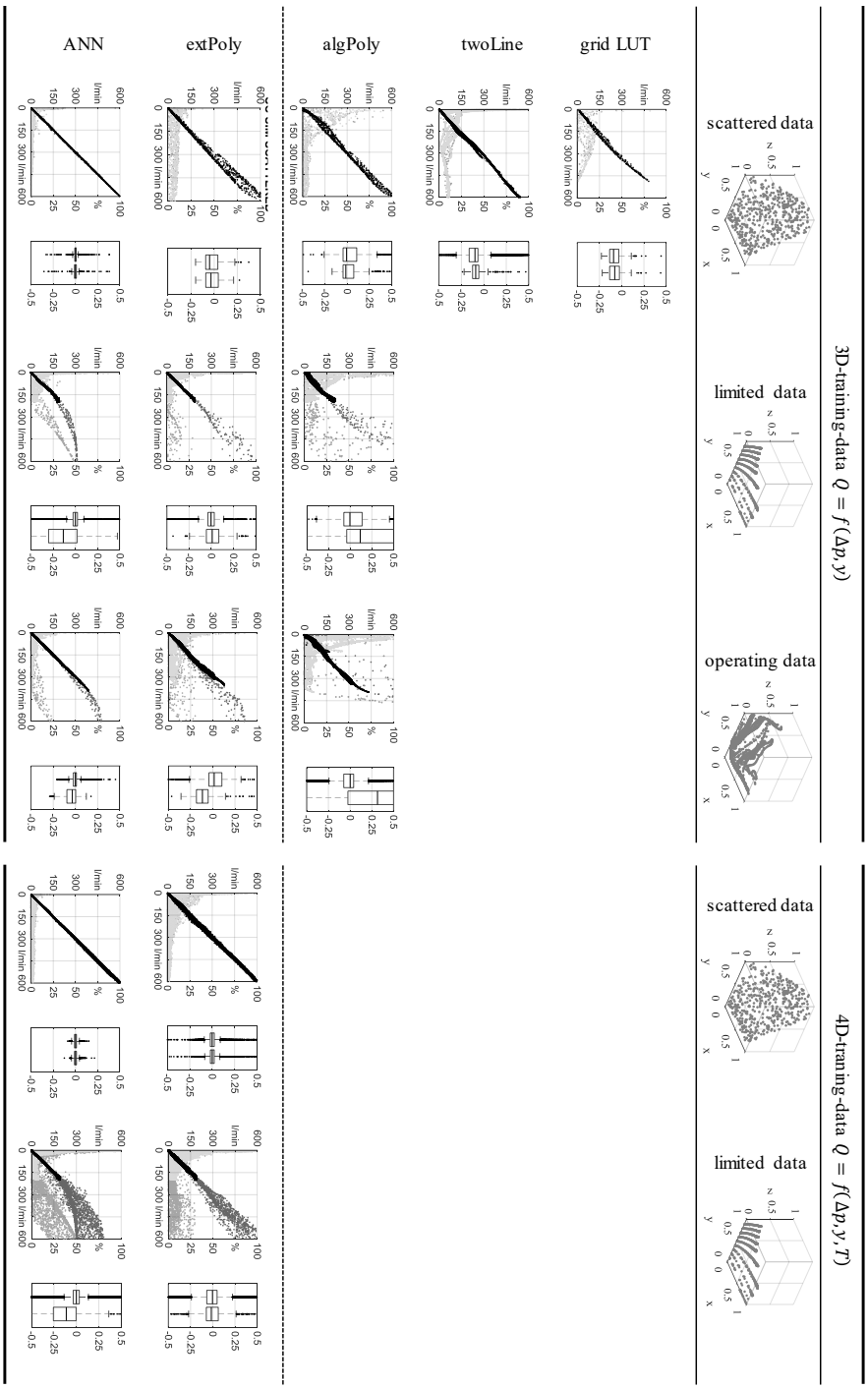

Figure 9: Overall result plots of proposed approximation methods for 3D- and 4D-case

NOMENCLATURE

A	Area
ANN	Artificial Neural Network
ECU	Electronic Control Unit
i	Variable
I/O	Input / Output
IQR	Interquartile Range
MLP	Multi-Layer-Perceptron
MSE	Mean Square Error
n	Number
p	Pressure
Q	Flow Rate
RMSE	Root Mean Square Error
T	Temperature
V	Volume
x	Input Variable
y	Input Variable
z	Output Variable
ϑ	Temperature

REFERENCES

[1] C. Bohn und H. Unbehauen, *Identifikation dynamischer Systeme*. Wiesbaden: Springer Fachmedien Wiesbaden, 2016.

[2] M. Vogt, N. Müller, und R. Isermann, „On-Line Adaptation of Grid-Based Look-up Tables Using a Fast Linear Regression Technique“, *Journal of Dynamic Systems, Measurement, and Control*, Bd. 126, Nr. 4, S. 732, 2004, doi: 10.1115/1.1849241.

[3] S. Chun, B.-R. Yoon, D.-K. Lee, und H.-M. Choi, „Correction of flow metering coefficients using two-dimensional curve fitting“, in *ASME-JSME-KSME 2011 Joint Fluids Engineering Conference*, 2011, S. 17–25.

[4] K. Huhtala, J. K. Karen, und M. J. Vilenius, „Semi-empirical modelling of losses in components of hydrostatic transmission systems“, in *Design and Performance, Eigth Bath International Fluid Power Workshop, 20-22.9.1995*, 1996, S. 236–251.

[5] M. Gori, F. Scarselli, und Ah Chung Tsoi, „Which classes of functions can a given multilayer perceptron approximate?“, in *Proceedings of International Conference on Neural Networks (ICNN'96)*, Washington, DC, USA, 1996, Bd. 4, S. 2226–2231, doi: 10.1109/ICNN.1996.549247.

[6] C. Halfmann und H. Holzmann, *Adaptive Modelle für die Kraftfahrzeugdynamik*. Berlin, Heidelberg: Springer Berlin Heidelberg, 2003.

[7] P. Opdenbosch, „Auto-Calibration and Control Applied to Electro-Hydraulic Poppet Valves“, 2007.

[8] S. Liu und B. Yao, „Automated onboard modeling of cartridge valve flow mapping“, *IEEE/ASME Transactions on Mechatronics*, Bd. 11, Nr. 4, S. 381–388, Aug. 2006, doi: 10.1109/TMECH.2006.878552.

[9] R. Isermann, Hrsg., *Modellgestützte Steuerung, Regelung und Diagnose von Verbrennungsmotoren*. Berlin, Heidelberg: Springer Berlin Heidelberg, 2003.

[10] O. Nelles und A. Fink, „Grid-Based Look-Up Table Optimization Toolbox“, *IFAC Proceedings Volumes*, Bd. 33, Nr. 15, S. 839–844, Juni 2000, doi: 10.1016/S1474-6670(17)39857-9.

[11] W. S. McCulloch und W. Pitts, „A logical calculus of the ideas immanent in nervous activity“, *Bulletin of Mathematical Biophysics*, Bd. 5, Nr. 4, S. 115–133, Dez. 1943, doi: 10.1007/BF02478259.

[12] R. Kruse, C. Borgelt, F. Klawonn, C. Möwes, G. Ruß, und M. Steinbrecher, *Computational Intelligence: Eine methodische Einführung in Künstliche Neuronale Netze, Evolutionäre Algorithmen, Fuzzy-Systeme und Bayes-Netze*. Wiesbaden: Vieweg+Teubner Verlag / Springer Fachmedien Wiesbaden GmbH, Wiesbaden, 2012.

[13] R. Rojas, *Theorie der neuronalen Netze*. Berlin, Heidelberg: Springer Berlin Heidelberg, 1993.

[14] D. J. C. MacKay, „A Practical Bayesian Framework for Backpropagation Networks“, *Neural Computation*, Bd. 4, Nr. 3, S. 448–472, Mai 1992, doi: 10.1162/neco.1992.4.3.448.

[15] B. Andersson, „On the valvistor a proprtional controlled seat valve“, Department of Mechanical Engineering, Linköping University, 1984.

[16] E. Prasetiawan, R. Zhang, und A. Alleyne, „Fundamental performance limitations for a class of electronic two-stage proportional flow valves“, in *American Control Conference, 2001. Proceedings of the 2001*, 2001, Bd. 5, S. 3955–3960.

[17] A. Sitte, J. Weber, Uhlmann, Jonas, B. Meitinger, und Weidner, Yannick, „MODEL BASED EFFICIENCY ANYLYSIS OF MOBILE HYDRAULIC MACHINERY (On The Example of Material Handling Machines)“, in *Proceedings of the JFPS International Symposium on Fluid Power*, Fukuoka, 2017.

peer reviewed

MULTI-OBJECTIVE CONTROL OF A SELF-LOCKING COMPACT ELECTRO-HYDRAULIC CYLINDER DRIVE

Nikolaj Grønkær*, Lasse Nørby Nielsen, Frederik Ødum Nielsen, Søren Ketelsen and Lasse Schmidt

Aalborg University, Department of Energy Technology, Pontoppidanstræde 111, 9220 Aalborg East, Denmark
* Corresponding author: Tel.: +45 2966 7310; E-mail address: ngr@et.aau.dk

ABSTRACT

The field of self-contained linear hydraulic drives based on variable-speed electrical motors and fixed displacement pumps is gaining interest from both industry and academia. Some of the main reasons for this is the possibility to improve the energy efficiency of such drives compared to conventional valve controlled drives, and the possibility for electrical regeneration allowing power sharing between multiple drives [1]. The main drawback for such types of drive concepts is a low pressure in the non-load carrying cylinder chamber. This induces a low drive stiffness limiting the achievable drive bandwidth and hence the application range. However, a so-called self-locking compact drive architecture recently proposed allows maintaining a proper drive stiffness by virtue of separate forward and return flow paths, combining the advantages of efficient flow control into the cylinder and a throttle driven flow out of the cylinder. The multiple inputs available in this architecture allow the control to target several objectives concurrently, for example piston motion, drive stiffness and fluid temperature. The purpose of the study presented is to analyse the dynamic couplings between the control objectives via relative gain array (RGA) methods, and the realization of input- and output transformations effectively decoupling relevant dynamic interactions. These transformations allow the usage of simple SISO-controllers for each control objective, and a method for controlling motion and fluid temperature concurrently, is proposed and experimentally verified.

Keywords: Input- and output transformations, self-contained hydraulic drives, speed-variable drives, multi-objective control, temperature control.

1. INTRODUCTION

The field of pump controlled electro-hydraulic differential cylinder drives is gaining increasing interest both in industry as well as in academia. Especially, actuation by variable-speed electrical drives combined with fixed displacement pumps has been a focus in the last decade [1]. The works on these electro-hydraulic drives have mainly been concerned with single pump closed circuit architectures or dual pump "open circuit" architectures [1-10]. Such electro-hydraulic drives have often been designed with on-board flexible reservoirs in terms of accumulators, making these drives hydraulically self-contained [1,6-10]. Furthermore, such drives feature a high degree of compactness compared to conventional valve drives supplied by hydraulic power units, and fast pump actuation dynamics dependent on the electrical motor and drive configuration. However, some main challenges with self-contained electro-hydraulic drives are low drive stiffness due low pressure in the non-load carrying chamber and temperature control in the presence of a rather small fluid volume. As losses of such drives are generally low, both oil heating

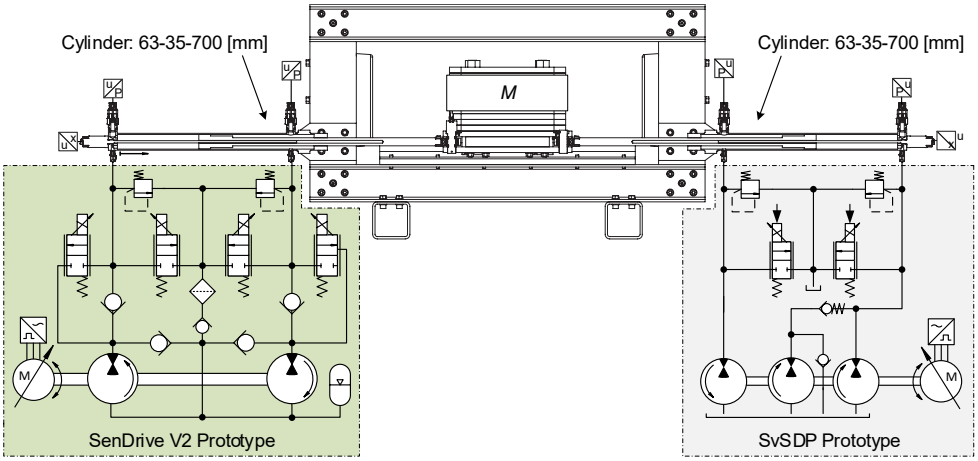

Figure 1*:* Test setup at Aalborg University, Denmark.

and cooling may be required to maintain the fluid temperature at some desired level.

The problem of low fluid stiffness has been addressed in several contributions, e.g. this was sought overcome by the so-called Speed-variable Switched Differential Pump (SvSDP) which is the three pump drive architecture [11-13], depicted in **Fig**. 1. Here the pump and cylinder volume flows are deliberately mismatched, causing the chamber pressures to increase when the pump leakage is overcome. The pressures may then be controlled to an acceptable level by means of throttling of the excess flow, hence drive stiffness is achieved on the cost of energy efficiency. A main drawback of this drive (and other pump controlled drives) is the necessity to compensate pump leakage when the cylinder piston is stationary since this induces power consumption of the electric motor.

An initiative to limit this problem was introduced with a "self-locking" electro-hydraulic drive [14,15], the so-called SenDrive also depicted in **Fig**. 1. This drive separates the flow paths into and out of the cylinder, such that pump flow is passed to the cylinder via rectifying valves and extracted from the cylinder via proportional throttle valves. The drive features a common return flow path allowing for filtering and potentially also cooling of the return flow fluid, or the return flows may bypass the rectifying valves allowing to regenerate energy in load aiding quadrants. Furthermore, as for the SvSDP drive, the pressure level, hence the drive stiffness, may be controlled to a desired level on the cost of energy efficiency. This is the case since the throttling is used to maintain a certain pressure level. However, this induces losses, which elevates the temperature with a certain rate dependent on the pressure level and the velocity/flow, which induces a coupling between the temperature, the drive stiffness and motion.

The five inputs of the drive allow reaching multiple control objectives concurrently, e.g. control of the pressure level and piston position or force. However, as the throttle losses are controllable, the temperature may also be increased to a desired level when heating is needed, while controlling motion or force.

This paper is concerned with a model based control design for the SenDrive architecture discussed above, encompassing decoupling of the main dynamic couplings between the cylinder pressure level and the piston motion, combined with control loops allowing to control the piston position as well as heating of the fluid concurrently. The latter is realized by controlling the pressure level and hence the throttling losses, where the pressure level reference is realized by a temperature control loop, effectively realizing a cascade control structure. The control design is experimentally verified, and results demonstrate that accurate control of the motion and fluid heating is achieved.

1.1. Application for study

All the experimental tests have been conducted on the test bench depicted in **Fig. 1**, and the main components of the SenDrive prototype are listed in **Tab. 1**, which is located at Aalborg University, Aalborg Denmark. The main focus of the paper is the SenDrive prototype, whereas the SvSDP prototype is operating as a load. In the model this load is seen as a constant force as seen in **Fig. 2**. The model parameters used in the following, are verified with experimental data and given in the nomenclature shown in **Tab. 2**.

Table 1: Main components of SenDrive prototype drive. [a]Bosch Rexroth AG, [b]Fjero A/S, [c]Balluf GmbH

Component	Description
[a]MOT-FC-ET2	Induction motor
[a]IndraDrive HCS03-70A	Converter
[a]CSH02.1B	Control unit
[a]AZPFFF-12-016/011	Pump rack
[a]KKDSR1NB	2/2 prop. Valves
[a]HM 20-2X/250	Pres. sensor(s)
[b]Cylinder 63-35-700	Hyd. cylinder
[c]BTL7 - S 5 0	Position sensor

2. MODEL

The model of the SenDrive prototype used in the study is constituted by a hydraulic/mechanical model, which is extended with a thermal model representing the average temperature dynamics.

2.1. Hydraulic model

The hydraulic model of the SenDrive prototype takes offset in the schematic depicted in **Fig**. 2, and is given by **Eqs**. (1)-(13), where j = *vA, vB, vAT, vBT* and i = *AT, BT, TA, TB, R* and k = *A, B, AT, BT, R, T* and $\Delta x_{vA} = x_{vA} - x_d$, $\Delta x_{vB} = x_{vB} - x_d$, $\Delta x_{vAT} = x_{vAT} - x_d$, $\Delta x_{vBT} = x_{vBT} - x_d$.

$$\ddot{x}_p = \frac{1}{M}\left(A_A P_L - B_v \dot{x}_p - F_{ext}\right),\ P_L = P_A - \alpha P_B \quad (1)$$

$$\dot{P}_A = \frac{\beta_A}{V_A}\left(Q_{AT} - Q_{vAT} - Q_{vA} - \dot{x}_p A_A\right) \quad (2)$$

$$\dot{P}_B = \frac{\beta_B}{V_B}\left(Q_{BT} - Q_{vBT} - Q_{vB} + \dot{x}_p A_B\right) \quad (3)$$

$$\dot{P}_{AT} = \frac{\beta_{AT}}{V_{AT}}\left(Q_{TA} + Q_{pA} + Q_{vAT} - Q_{AT}\right) \quad (4)$$

$$\dot{P}_{BT} = \frac{\beta_{BT}}{V_{BT}}\left(Q_{TB} - Q_{pB} + Q_{vBT} - Q_{BT}\right) \quad (5)$$

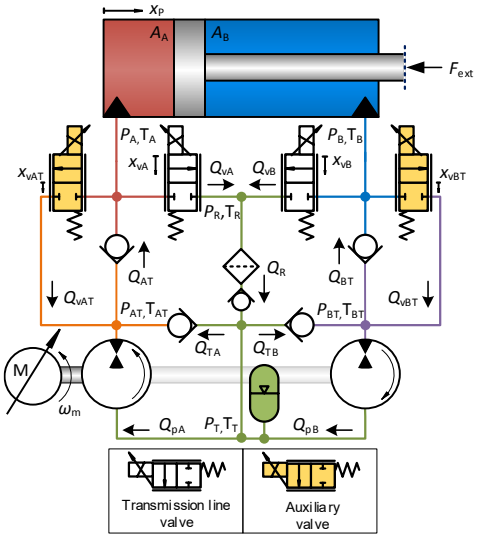

Figure 2: Schematic of Self-locking compact electro-hydraulic cylinder drive with model nomenclature.

$$\dot{P}_R = \frac{\beta_R}{V_R}(Q_{vA} + Q_{vB} - Q_R) \quad (6)$$

$$\dot{P}_T = \frac{\beta_T}{V_T + \frac{\beta_T V_g}{\kappa P_T}}\left(Q_R - Q_{pA} + Q_{pB} - Q_{TA} - Q_{TB}\right) \quad (7)$$

$$\ddot{x}_j = \omega_v^2\left(u_j - x_j\right) - 2\zeta_v\omega_v\dot{x}_j \quad (8)$$

$$\ddot{\omega}_m = \omega_e^2(u_m - \omega_m) - 2\zeta_e\omega_e\dot{\omega}_m \quad (9)$$

$$Q_{pA} = D_A\omega_m - C_{LA}(P_{AT} - P_T) \quad (10)$$

$$Q_{pB} = D_B\omega_m + C_{LB}(P_{BT} - P_T) \quad (11)$$

$$Q_{vA} = \begin{cases} \Delta x_{vA} k_{vA} \tanh\left((P_A - P_R)k_p\right) & , \Delta x_{vA} \geq 0 \\ 0 & , \Delta x_{vA} < 0 \end{cases} \quad (12)$$

$$Q_{vB} = \begin{cases} \Delta x_{vB} k_{vB} \tanh\left((P_B - P_R)k_p\right) & , \Delta x_{vB} \geq 0 \\ 0 & , \Delta x_{vB} < 0 \end{cases} \quad (13)$$

$$Q_{vAT} = \begin{cases} \Delta x_{vAT} k_{vAT} \tanh\left((P_A - P_{AT})k_p\right) & , \Delta x_{vAT} \geq 0 \\ 0 & , \Delta x_{vAT} < 0 \end{cases} \quad (14)$$

$$Q_{vBT} = \begin{cases} \Delta x_{vBT} k_{vBT} \tanh\left((P_B - P_{BT})k_p\right) & , \Delta x_{vBT} \geq 0 \\ 0 & , \Delta x_{vBT} < 0 \end{cases} \quad (15)$$

$$V_A = V_{A0} + x_p A_A,\ V_B = V_{B0} + \left(L_x - x_p\right)A_B \quad (16)$$

$$V_T = V_{ACC} + V_{T0} - V_g, V_g = \begin{cases} V_{ACC} & , P_0 \geq P_T \\ V_{ACC}\left(\frac{P_0}{P_T}\right)^{\frac{1}{\kappa}} & , P_0 < P_T \end{cases} \quad (17)$$

$$Q_{AT} = \begin{cases} K_{AT} x_{AT}\sqrt{P_{AT} - P_A} & , P_{AT} \geq P_A \\ 0 & , P_{AT} < P_A \end{cases} \quad (18)$$

$$Q_{BT} = \begin{cases} K_{BT} x_{BT}\sqrt{P_{BT} - P_B} & , P_{BT} \geq P_B \\ 0 & , P_{BT} < P_B \end{cases} \quad (19)$$

$$Q_{TA} = \begin{cases} K_{TA} x_{TA}\sqrt{P_T - P_{AT}} & , P_T \geq P_{AT} \\ 0 & , P_T < P_{AT} \end{cases} \quad (20)$$

$$Q_{TB} = \begin{cases} K_{TB} x_{TB} \sqrt{P_T - P_{BT}} & , P_T \geq P_{BT} \\ 0 & , P_T < P_{BT} \end{cases} \quad (21)$$

$$Q_R = \begin{cases} K_R x_R \sqrt{P_R - P_T} & , P_R \geq P_T \\ 0 & , P_R < P_T \end{cases} \quad (22)$$

$$x_i = \begin{cases} 0 & , \quad \Delta P_{cv} < P_{cv,cr} \\ \frac{\Delta P_{cv} - P_{cv,cr}}{P_{cv,end} - P_{cv,cr}} & , P_{cv,cr} \leq \Delta P_{cv} < P_{cv,end} \\ 1 & , \quad P_{cv,end} \leq \Delta P_{cv} \end{cases} \quad (23)$$

$$\beta_k = \frac{1}{\frac{1}{\beta_F} + \frac{1}{\left(\frac{\left(\frac{P_{atm}}{P_k + P_{atm}}\right)^{-\frac{1}{\kappa}} - 1}{(1-\eta_{air})\eta_{air}} + 1 \right) \kappa (P_k + P_{atm})}} \quad (24)$$

2.2. Thermal model extension

The thermal model extension is constructed as an average model of the temperature dynamics, as the drive level temperature time constant may be considered strictly larger than the remaining time constants of the drive. The internal temperature variations are uncontrollable due to the internal restrictions and flow paths, but will fluctuate about the average temperature. Assuming a constant ambient temperature, the average temperature dynamics is governed by the hydraulic losses, natural convection, forced convection and radiation. Forced convection is induced by the electric motor cooling fan, also blowing air across the manifold and pumps besides the motor (see **Fig. 3**. (B)). Hence, an average temperature model for drive may be established as Eqs. (25), (26).

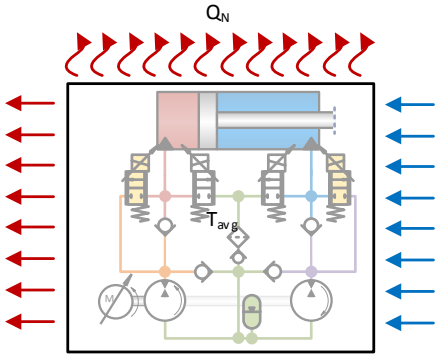

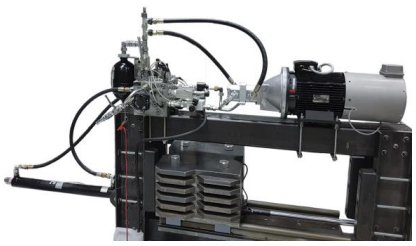
(B)

Figure 3: Thermal model principal for the thermal extension and photo of test setup.

$$\dot{T}_{avg} = \frac{\dot{W}_{loss} - h_t (T_{avg} - T_\infty)}{c_{eq} m_{eq}}, \; h_t = h_n + h_f \quad (25)$$

$$\dot{W}_{loss} = P_{in} - P_{out} = \omega_m \tau_t - P_L A_A \dot{x}_p \quad (26)$$

Note that the thermal model is highly simplified compared to a full model of the thermal behaviour of such a drive (see e.g. [7]). However, in terms of usage of the model for temperature level control design, and the large time constant of the temperature dynamics, the model is considered sufficiently accurate for the purpose of this study.

3. COUPLING ANALYSIS

In the coupling analysis presented in the following, only the case of piston extension is considered for brevity. Furthermore, all check valves are assumed ideal, which is reasonable since the pressure drops across the valves at maximum flow are less than 1 [bar].

Considering **Fig. 2**. under the above mentioned assumption and piston extension, then $\dot{P}_{AT} = \dot{P}_A \rightarrow \beta_A = \beta_{AT}$. Combining **Eqs**. (2), (4) under these considerations, Eq. (27) is obtained.

$$\dot{P}_A = \frac{\beta_A}{V_A + V_{AT}} \left(Q_{PA} - Q_{vA} - \dot{x}_p A_A \right) \quad (27)$$

Furthermore, the following study is restricted to the usage of the "transmission line" valves, hence, under the assumption of ideal check valves, **Eq**. (28) is valid.

$$P_{BT} = P_T, P_R = P_T, Q_{vBT} = Q_{vAT} = 0 \quad (28)$$

Finally, to avoid unnecessary power loss, then under piston extension $Q_{vA} = 0$ is maintained. With these considerations, the drive dynamics under piston extension may be simplified to **Eqs**. (29)-(32).

$$\ddot{x}_p = \frac{1}{M} \left(A_A P_L - B_v \dot{x}_p \right), \; P_L = P_A - \alpha P_B \quad (29)$$

$$\dot{P}_A = \frac{\beta_A}{V_A + V_{AT}} \left(Q_{pA} - \dot{x}_p A_A \right) \quad (30)$$

$$\dot{P}_B = \frac{\beta_B}{V_B} \left(-Q_{vB} + \dot{x}_p A_B \right) \quad (31)$$

$$\dot{T}_{avg} = \frac{\dot{W}_{loss} - h_t(T_{avg} - T_\infty)}{c_{eq} m_{eq}} \quad (32)$$

Linearizing the model **Eqs**. (29)-(32) and **Eqs**. (9)-(11), a combined linear model for the case of piston extension may be established similar to [11], as the transfer function matrix **Eq**. (33). Compared to [11] this model extended with the temperature and the ratio between the cylinder chamber bulk modulii.

$$\begin{bmatrix} \dot{x}_p(s) \\ p_A(s) \\ p_B(s) \\ T_{avg}(s) \end{bmatrix} = \boldsymbol{G}(s) \begin{bmatrix} u_m(s) \\ u_{vB}(s) \end{bmatrix} \quad (33)$$

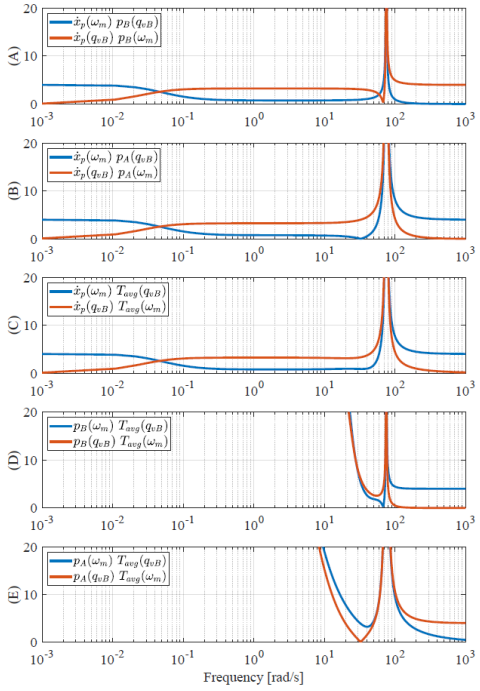

Figure. 4: Relative gain array for system with actuator dynamics.

Using linearization points $x_{p0} = 350\ [mm]$, $P_{A0} = 35\ [bar]$, $P_{B0} = 5\ [bar]$, $\dot{x}_{p0} = 125\ [mm/s]$, $\omega_{m0} = 100\ [rad/s]$, i.e. $F = 10.7\ [kN]$, the RGA numbers depicted in **Fig. 4** may be established. Bearing in mind that in the event of ideally decoupled dynamics, the RGA numbers will be 0 and 4, it is evident that heavy couplings are present, as may be expected. These couplings may complicate control design significantly when targeting the control of both the motion and pressure level concurrently. Hence, in the following a decoupling strategy is proposed, allowing the usage of decentralized control. RGA numbers for different piston positions are depicted in the Appendix.

4. DECOUPLING

The decoupling approach of the drive follows the idea presented in [11]. The utilised control structure is seen in **Fig**. 5, where the input and output transformations are based on the load pressure P_L and a "level pressure" P_H used as the outputs with the corresponding load and level "flows", Q_L and Q_H, used as inputs.

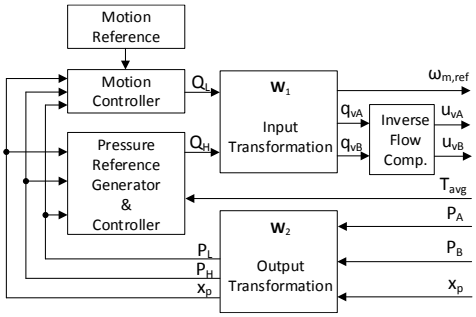

Figure 5: General control structure.

4.1. Output Transformation

The load and level pressures are defined as Eq. (34) with the corresponding dynamics given by Eq. (35).

$$P_L = P_A - \alpha P_B, \quad P_H = P_A + H P_B \quad (34)$$
$$\dot{P}_L = \dot{P}_A - \alpha \dot{P}_B, \quad \dot{P}_H = \dot{P}_A + H\dot{P}_B + \dot{H} P_B \quad (35)$$

With the definitions in **Eq**. (34), the cylinder chamber pressures may be expressed as **Eq**. (36).

$$P_A = \frac{H P_L + \alpha P_H}{H + \alpha}, \quad P_B = \frac{P_H - P_L}{H + \alpha} \quad (36)$$

In [11] it is assumed that $\beta_A = \beta_B$, which is sensible if P_A , P_B > 20 bar. However, the temperature control and efficiency depend on a possibility to control the non-load carrying pressure to lower levels, hence one may assert relation **Eq**. (37), where ϵ is the pressure dependent bulk modulus ratio.

$$\beta_B = \epsilon(P_A, P_B)\beta_A \quad (37)$$

Using this ratio, the pressure dynamics **Eq.** (35) may be expressed with **Eqs**. (30), (31) as **Eqs**. (38), (39), noting **Eq**. (40).

$$\dot{P}_L = \frac{\beta_A(\rho V_A(Q_{pA} - A_A\dot{x}_p) - (A_A\alpha\dot{x}_p - Q_{vB})V_{AP}\alpha\epsilon)}{V_{AP}\rho V_A} \quad (38)$$

$$\dot{P}_H = \frac{\beta_A(A_A(H\alpha\epsilon V_{AP} - \rho V_A)\dot{x}_p - Q_{vB}V_{AP}H\epsilon - \rho V_A Q_{PA})}{\rho V_A V_{AP}} \quad (39)$$

$$+ \frac{(P_H - P_L)\dot{H}}{H+\alpha}$$

$$V_{AP} = V_A + V_{AT},\ \rho = \frac{V_B}{V_A} \quad (40)$$

From the level pressure dynamics **Eq.** (39), it is notable that H influences the volume flow. Hereby, it is found sensible to choose $H = \frac{\rho V_A}{\mu\alpha V_{AP}}$ where μ approximates ϵ. This approximation is made by a simplified version of the bulk modulus ratio model (**Eqs.** (24), (37)) and is given by **Eq.** (41).

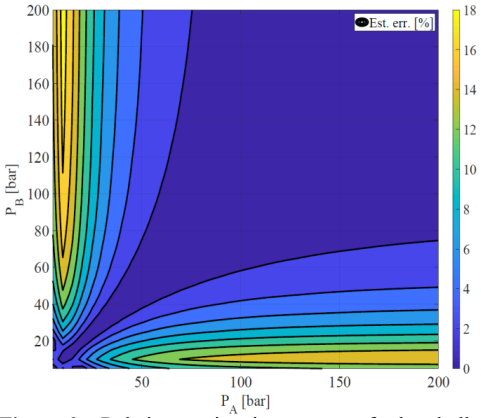

Figure 6: Relative estimation error of the bulk modulus ratio (μ).

$$\mu = \frac{(P_B+P_{atm})^2\left((\eta_{air}+1)P_{atm}^2 + ((P_A+\beta_F)\eta_{air}+2P_A)P_{atm}+P_A^2\right)}{(P_A+P_{atm})^2\left((\eta_{air}+1)P_{atm}^2 + ((P_B+\beta_F)\eta_{air}+2P_A)P_{atm}+P_B^2\right)} \quad (41)$$

With this estimation a maximal estimation error for μ is 20 % in the operational range for the system $P_A, P_B \leq 200$ [bar], as depicted in **Fig**. 6. Furthermore, **Fig**. 6 shows that the estimation error increases if one of the pressures is rather low and a large difference between the pressures is present. From this it is found that the estimation error has the largest magnitude when the load pressure is high and when the non-load carrying pressure is low.

Since the air percentage in the oil is a sensitive parameter, the sensitivity of air in the fluid is investigated. The same map as in **Fig.** 6 is depicted in **Fig**. 7 with the air percentage in the oil doubled ($\eta_{\text{air}} = 2\eta_{\text{air}}$). It is seen that the maximum error increases to 25 %, which indicates that the estimation is fairly insensitive to a parameter error on the air content in the oil. Furthermore, it is seen that the error is largest when the load pressure is negative.

If an ideal approximation of the bulk modulus ratio ($\mu = \epsilon$) is assumed and it is assumed that the ratio is slow varying ($\dot{\epsilon} \approx 0$), the level and load pressure dynamics are simplified to **Eqs**. (42), (43), (44), with $V_{Amax} = A_A L + V_{A0}$.

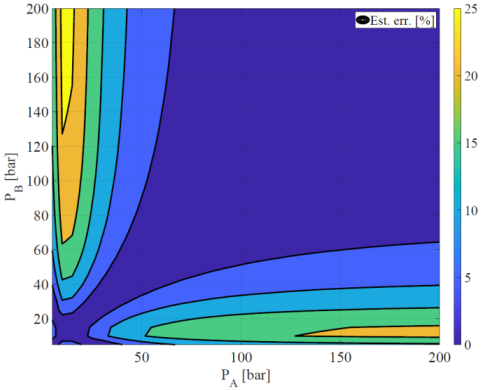

Figure 7: Relative estimation error of the bulk modulus ratio (μ) with twice the amount of air ($\eta_{air} = 2\eta_{air}$).

$$\dot{P}_L = \frac{\beta_A(\rho V_A(Q_{pA} - A_A\dot{x}_p) - (A_A\alpha\dot{x}_p - Q_{vB})V_{AP}\alpha\epsilon)}{V_{AP}\rho V_A} \quad (42)$$

$$\dot{P}_H = \frac{\beta_A(\alpha Q_{PA} - Q_{vB})}{\alpha V_{AP}} + \frac{(P_H - P_L)\dot{H}}{H+\alpha} \quad (43)$$

$$\dot{H} = -\frac{((V_{Amax} + V_{AT})\alpha + V_{B0})}{V_{AP}^2\mu\alpha}\dot{x}_p \quad (44)$$

4.2. Input Transformation

A steady state decoupling may be established, considering the inputs $\omega_m = \frac{A_A}{D_A}\bar{\omega}_m$ and Q_{vB}, and defining a "load flow" **Eq**. 45 and "level flow" **Eq**. (46), constructed from the actuation flows, then the load and level pressures may be described as **Eqs**. (47),(48), such that the coupled input effects are "hidden" from the pressure dynamics.

$$Q_L = \frac{\alpha\epsilon V_{AP}(A_A\alpha\bar{\omega}_m + Q_{vB}) + A_A V_A\rho\bar{\omega}_m}{\alpha^2\epsilon V_{AP} + \rho V_A} \quad (45)$$

$$Q_H = -Q_{vB} \quad (46)$$

$$\dot{P}_L = \frac{\beta_A(\alpha^2\epsilon V_{AP} + \rho V_A)(Q_L - A_A\dot{x}_p)}{V_{AP}\rho V_A} - \frac{\beta_A C_{LA}(\alpha^2\epsilon V_{AP}P_H + P_L\rho V_A)}{V_{AP}(\alpha^2\epsilon V_{AP} + \rho V_A)} \quad (47)$$

$$\dot{P}_H = \frac{\beta_A Q_H}{V_{AP}\alpha} - \frac{\beta_A C_{LA}(\alpha^2\epsilon P_H V_{AP} + P_L V_A\rho)}{(\alpha^2\epsilon V_{AP} + \rho V_A)V_{AP}} + \frac{(P_H - P_L)\dot{H}}{H+\alpha} \quad (48)$$

The control designs may now be conducted in the load and level pressure domain, i.e. for Q_L and Q_H, and then transformed to the physical inputs by **Eq**. (49).

$$Q_{vB} = -Q_H \qquad \bar{\omega}_m = \frac{Q_L}{A_A} + \frac{Q_H}{A_A(H+\alpha)} \quad (49)$$

4.3. Decoupling analysis

In order to verify the impact of the decoupling approach, an additional RGA analysis is carried out for the transformed system with the actuator dynamics, i.e. the system described by **Eqs**. (1), (9), (10), (47), (48). Similar to Section 3, this system is linearized (at the same linearization point), and a transfer function matrix $\widetilde{\boldsymbol{G}}(s)$ may be established, satisfying **Eq**. (50), where p_L, p_H, q_L, q_H denote the change variables of P_L, P_H, Q_L, Q_H.

$$\begin{bmatrix} \dot{x}_p(s) \\ p_L(s) \\ p_H(s) \\ T_{avg}(s) \end{bmatrix} = \widetilde{\boldsymbol{G}}(s) \begin{bmatrix} q_L(s) \\ q_H(s) \end{bmatrix} \quad (50)$$

The results of the analysis are depicted in **Fig**. 8, noting that $\mu \neq \epsilon$ and **Eq**. (41) is used in the transformations. From this it is found that the motion and level pressure are nearly completely decoupled throughout the entire frequency range. However, it seen that coupled effects still are present between the level pressure, motion and the temperature. Especially the level pressure and temperature have a large coupling during the lower frequency range. In a physical sense, this is also expected since the throttle losses increase with the level pressure and hereby the amount of energy dissipated to the oil/system. Furthermore, it is seen that the motion/flow also couples with the temperature in the higher frequency range, which is sensible since the power loss produced by throttling depends on both pressure drop and flow/velocity and hereby motion. Further working points with a varying piston position are depicted in the Appendix for the decoupled system.

From these results, it is found that decentralized (SISO) control designs may be applied for motion and level pressure control, and

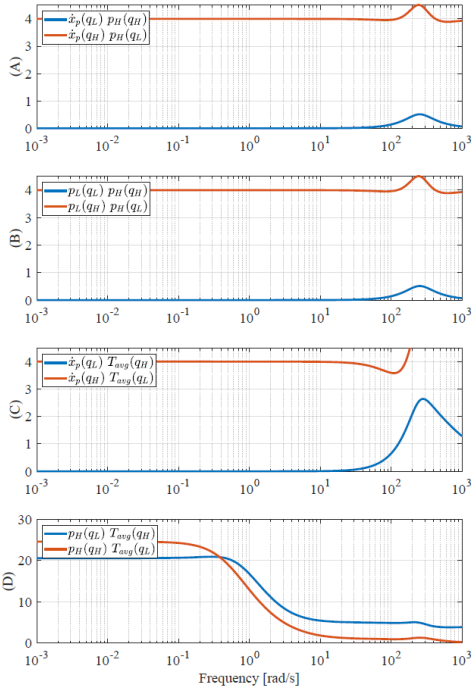

Figure 8. Relative gain array for system with input- and output transformations.

that the level pressure reference may be established as a function of the desired temperature, since the level pressure is highly linked to the losses. In the application of this approach, the pressure level will be dictated by the desired temperature and not e.g. desired stiffness, which also would be possible [14].

5. CONTROL DESIGN

Besides the decoupling methodology, simple proportional control is used for the motion, level pressure and temperature controllers in the decoupled domain. The level pressure and temperature controllers are constructed as a cascade structure, as the output of the temperature controller is the reference to the level pressure controller. The motion controller is a combination of proportional control, velocity feed forward and active damping.

5.1. Level pressure control

The idea behind the level pressure control was originally to control the drive stiffness by controlling the non-load carrying chamber pressure to a certain pressure setting, i.e. such that $\min\{P_A, P_B\} = P_{set}$. From this definition, a switch condition is defined as **Eq**. (51).

$$P_A = P_B = P_{set} \rightarrow P_{L,sw} = P_{set}(1-\alpha)$$
$$P_L \geq P_{L,sw} \rightarrow P_A = P_L + \alpha P_{set}, P_B = P_{set} \quad (51)$$
$$P_L < P_{L,sw} \rightarrow P_A = P_{set},\ P_B = \frac{P_{set}-P_L}{\alpha}$$

The level pressure reference is then generated from the definition of the level pressure **Eq**. (34), given by **Eq**. (52).

$$P_{H,ref} = \begin{cases} P_L + (H+\alpha)P_{set} & P_L \geq P_{L,sw} \\ -\frac{H}{\alpha}P_L + \frac{\alpha+H}{\alpha}P_{set} & P_L < P_{L,sw} \end{cases} \quad (52)$$

From this, the level pressure control error is defined as Eq. (53).

$$e_H = \begin{cases} (H+\alpha)(P_{set}-P_B) & P_L \geq P_{L,sw} \\ \frac{\alpha+H}{\alpha}(P_{set}-P_A) & P_L < P_{L,sw} \end{cases} \quad (53)$$

The proportional level pressure controller is given by **Eq**. (54).

$$Q_H = k_{pp} e_H \quad (54)$$

Note that the switch of the reference **Eq**. (53) is bump-less, since $e_H = 0$ when the switch occurs.

5.2. Motion Control

The position control is realized via the load flow. The position controller is constituted by a proportional position control term, a velocity feed forward and an active damping term since the drive is under damped. The latter is realized by **Eqs**. (55), (56).

$$Q_L = \dot{x}_{p,ref} A_A + k_{px} e_x - k_{ad} P_L^* \quad (55)$$
$$P_L^* = P_L \frac{s}{(s+\omega_c)(s+\omega_f)} \quad (56)$$

In **Eq**. (56) the filter frequencies are chosen such that $\omega_c <$ drive eigenfrequency $< \omega_f <$ measurement noise frequency. This allow pressure transients to pass the filter while attenuating the load pressure level and noise.

5.3. Temperature control

The idea behind the temperature control is that the losses can be controlled directly via the level pressure setting P_{set}, and through this control the temperature, which is justified by **Fig** 8 (D). From the RGA in **Fig** 7 (C) it is found that the temperature and motion dynamics are decoupled, indicating that temperature control is possible without compromising the motion control. Note that the temperature controlled is the average temperature hence variation in the temperature may be present internally in the drive. However, it is assumed that these variations are of less importance. The proportional controller **Eq**. (57) is used to generate the pressure set point.

$$P_{set}^* = \left(T_{set} - T_{avg}\right) k_{pt} \quad (57)$$

To ensure that the pressure is maintained within a reasonable range, a saturation is made on the pressure set point as **Eq**. (58).

$$P_{set} = \begin{cases} P_{set,max}, & P_{set}^* \geq P_{set,max} \\ P_{set}^*, & P_{\text{set,min}} \leq P_{\text{set}}^* \leq P_{\text{set,max}} \\ P_{set,min}, & P_{set}^* \leq P_{set,min} \end{cases} \quad (58)$$

Note that **Eq**. (58) limits the temperature range, especially if the ambient temperature is high such that the natural cooling is low. Hence, the system is forced to be more efficient (lower P_{set}) to maintain the temperature low.

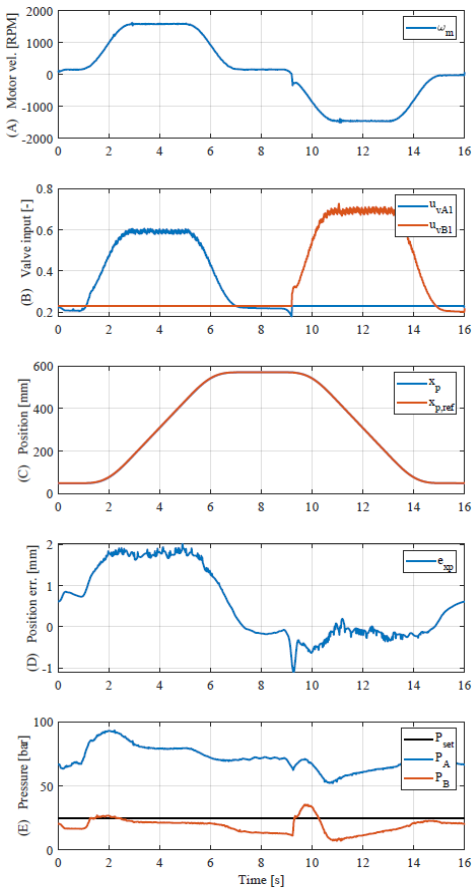

Figure 9: Experimental results from test of position and pressure controller with an external force $F_{ext} = 20$ kN and a maximal piston velocity of 125 mm/s.

6. EXPERIMENTAL VERIFICATION

The experimental results are shown in **Fig**. 9, for a test with an external force of 20 [kN] and a maximal piston velocity of 125 [mm/s]. It is seen that the simple controllers maintain a rather accurate position control with a maximal position error of 2 [mm]. Furthermore, a steady state error is present, which also indicates that a proportional controller may be insufficient for high performance control demands. However, the decoupling allows the usage of two simple decentralised controllers as intended.

In **Fig**. 10 the results of the temperature control are shown. This test is a repeating sequence of the test used in **Fig** 9. A steady state error is expected due to the choice of controller, which also is seen in the figure. However, it is seen in **Fig**. 10 (A) that all the temperatures of the drive lies with a maximum deviation of $\pm 2\,^{\circ}C$, which is an acceptable variation of the temperature throughout the system (Bosch Rexroth Denmark). Furthermore, it is seen in **Fig.** 10 (B) that the pressure is lowered as intended when the temperature is rising. Note that this temperature control has the limitations:

- Upper pressure limit restricts the maximal loss and hereby sets an upper bound on the temperature depending on free and forced convection.
- Lower pressure limit restricts the minimum loss and hereby sets a lower bound on the temperature depending on free and forced convection.
- A high drive stiffness requirement restricts the lower pressure bound even further and hereby the lower bound for the temperature.
- The force and piston velocity limits the temperature range since the throttling depends on these and hereby the amount of power dissipated.

From the latter, it is concluded that the temperature control works as intended, but if the compromise between the temperature control and the drive stiffness should be eliminated, an

additional control input is needed in form of an active cooler

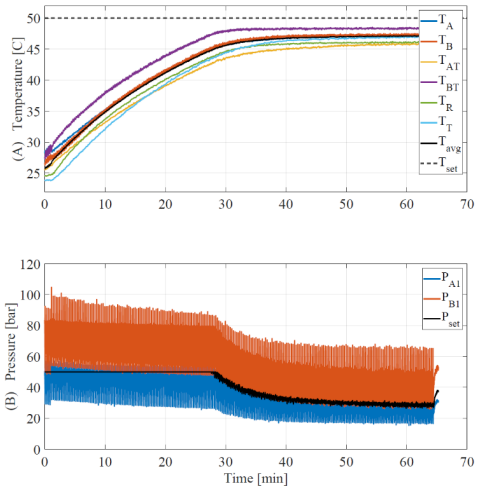

Figure 10. Test results from test of temperature control with an external force of $F_{ext} = 0$ kN and a maximal piston velocity of 125 mm/s.

CONCLUSION

This paper is addressing how a multi-objective control strategy can be developed to obtain multiple independent control variables on a recently introduced self-locking drive concept where simple controllers can act as decentralized controllers. The control variables of interest are the position, the non-load carrying pressure and the drive temperature. Through a decoupling using the load- and level pressures a decoupled system is obtained where it is shown experimentally that a simple proportional controller maintain a maximal position error at 2 [mm]. However, it concluded that the pressure control has spikes when the piston is changing direction. This problem might be due to a too simple pressure controller or disturbances induced by the pressure compensated valves. Regarding the temperature, it is seen that the temperature control works with some steady state error. However, this steady state error may be reduced with another choice of controller. Furthermore, it is concluded that a compromise between the drive stiffness and the temperature is required due to the lack of active cooling. Therefore, if an active cooler in form of a heat exchanger or a fan were mounted on the drive, a more independent temperature control would be achievable since the pressure can be kept high, and thereby the drive stiffness kept high, without compromising the temperature level.

ACKNOWLEDGEMENT

This research was partially funded by the Danish Energy Agency; the Energy Technology Development and Demonstration Programme (EUDP), project: Energy Efficient and Self-contained Hydraulic Drive Concept (SenDrive), project number 64018-0094.

NOMENCLATURE

Variable	Description	Value
A_A	Piston side area	31.17 [cm^2]
A_B	Rod side area	21.55 [cm^2]
B_v	Viscous damping	1053 [Ns/m]
C_{LA}	Pump A leakage coefficient	3.3e-3 [L/min/bar]
C_{LB}	Pump B leakage coefficient	1.0e-3 [L/min/bar]
D_A	Displacement pump A	16.5e-3 [L/rev]
D_B	Displacement pump B	11.3e-3 [L/rev]
L_x	Piston length	700 [mm]
M	Mass	700 [kg]
P_{atm}	Atmospherically press.	1.017 [bar]
V_{A0}	Dead volume piston side	0.33 [L]
V_{B0}	Dead volume rod side	0.12 [L]
V_{AT}	AT chamber volume	0.16 [L]
V_{BT}	BT chamber volume	0.11 [L]
ω_e	Motor eigenfrequency	80π [rad/s]
ω_v	Valve eigenfrequency	42π [rad/s]
ζ_e	Motor damping	0.5 [-]
ζ_v	Valve damping	1 [-]
$K_{\{vA,vB\}}$	Flow gain, valve vA and vB.	8.5 $\left[\frac{L}{\min\sqrt{bar}}\right]$
$K_{\{vAT,vBT\}}$	Flow gain, valve vAT and vBT	8.5 $\left[\frac{L}{\min\sqrt{bar}}\right]$
V_{acc}	Accumulator volume	3.5 [L]
V_{T0}	Accumulator dead volume	0.91 [L]
c_{eq}	Equivalent specific heat capacity for manifold	1500 [J/kg/K]
m_{eq}	Equivalent manifold mass	19.5 [kg]

h_n	Heat transfer coeff., natural convection and radiation part	7.1 [W/K]
h_f	Heat transfer coeff., forced convection part	2.52 [W/K]

REFERENCES

[1] Ketelsen, S., Padovani, D., Andersen, T., Ebbesen, M., and Schmidt, L. (2019). "Classification and Review of Pump-Controlled Differential Cylinder Drives". Energies.

[2] Minav, T., Bonato, C., Sainio, P., and Pietola, M. (2014). "Direct Driven Hydraulic Drive". In Proceedings of the 9th International Fluid Power Conference.

[3] Järf, A., Minav, T., and Pietola, M. (2016) "Nonsymmetrical Flow Compensation Using Hydraulic Accumulator". In Proceedings of the 9th FPNI Ph.D. Symposium on Fluid Power.

[4] C. Pedersen, H. C., Schmidt, L., Andersen, T. O., and Brask, M. H. (2014) "Investigation of New Servo Drive Concept Utilizing Two Fixed Displacement Units". JFPS International Journal of Fluid Power System.

[5] Gøytil, P., Padovani, D., and Hansen, M. R. (2019) "On the Energy Efficiency of Dual Prime Mover Pump-Controlled Hydraulic Cylinders". In Proceedings of the ASME/BATH 2019 Symposium on Fluid Power and Motion Control.

[6] Padovani, D., Ketelsen, S., Hagen, D., and Schmidt, L. (2019) "A Self-Contained Electro-Hydraulic Cylinder with Passive Load-Holding Capability", Energies.

[7] Michel, S., and Weber, J. (2012). "Electrohydraulic Compact-drives for Low Power Applications considering Energy-efficiency and High Inertial Loads". In Proceedings of the 7th FPNI PhD Symposium on Fluid Power.

[8] Michel, S., and Weber, J. (2012). "Energy-efficient electrohydraulic compact drives for low power applications". In Proceedings of the 2012 Bath/ASME Symposium on Fluid Power and Motion Control.

[9] Caliskan, H., Balkan, T., and Platin, B. E., (2016) "A Complete Analysis for Pump Controlled Single Rod Actuators". In Proceedings 10th International Fluid Power Conference.

[10] Brahmer, B. (2012) "CLDP - Hybrid Drive using Servo Pump in Closed Loop". In Proceedings of 8th International Fluid Power Conference.

[11] Schmidt, L, Groenkjaer, M, Pedersen, H, Andersen, T (2017) "Position Control of an Over-Actuated Direct Hydraulic Cylinder Drive". Control Engineering Practice.

[12] Schmidt, L., Roemer, D. B., Pedersen, H. C., and Andersen, T. O. (2015) "Speed-Variable Switched Differential Pump System for Direct Operation of Hydraulic Cylinders". In Proceedings of the ASME/BATH 2015 Symposium on Fluid Power and Motion Control.

[13] Ketelsen, S., Schmidt, L., Donkov, V. H., and Andersen, T. O. (2018) "Energy Saving Potential in Knuckle Boom Cranes using a Novel Pump Controlled Cylinder Drive". Modeling, Identification and Control: A Norwegian Research Bulletin.

[14] Schmidt, L., Ketelsen, S., Brask, M. H., and Mortensen, K. A. (2019) "A Class of Energy Efficient Self-Contained Electro-Hydraulic Drives with Self-Locking Capability". Energies.

[15] Schmidt, L, Ketelsen, S., Padovani, D., and Mortensen K. (2019) "Improving the Efficiency and Dynamic Properties of a Flow Unit in a Self-locking Compact Electro-Hydraulic Cylinder Drive". In proceedings of ASME/Bath 2019 Symposium on Fluid Power & Motion Control.

APPENDIX

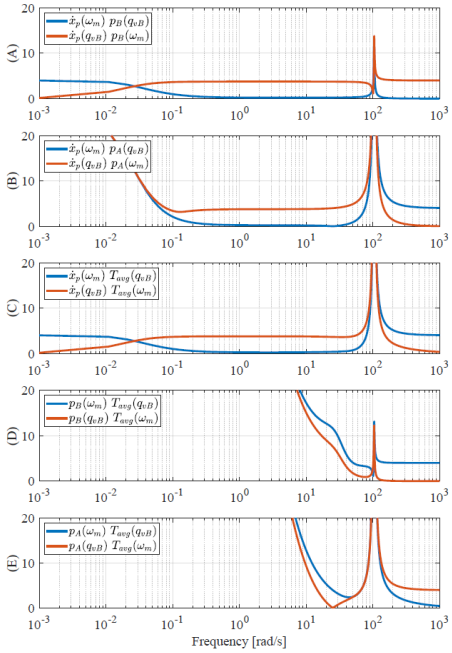

Figure. A1. Relative gain array for system with actuator dynamics and with $x_{p0} = 5[mm]$.

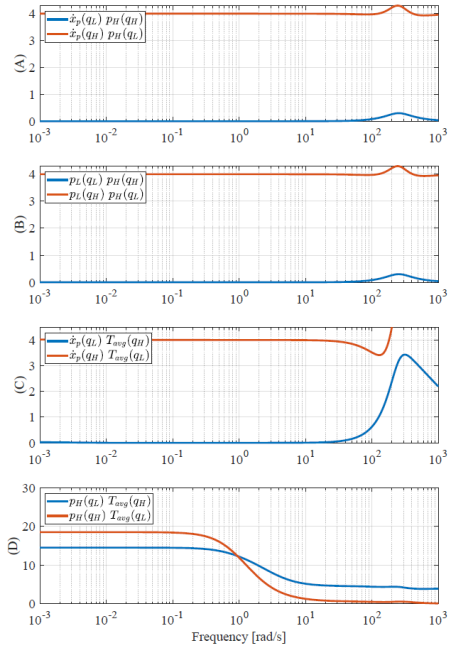

Figure A2. Relative gain array for system with input- and output transformations and with $x_{p0} = 5[mm]$.

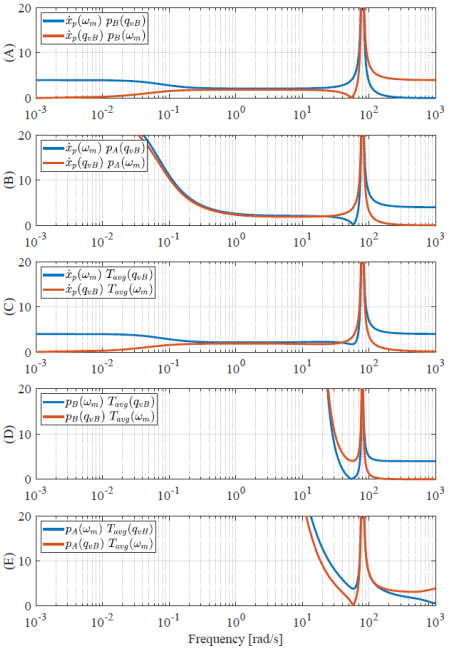

Figure. A3. Relative gain array for system with actuator dynamics and with $x_{p0} = 665[mm]$.

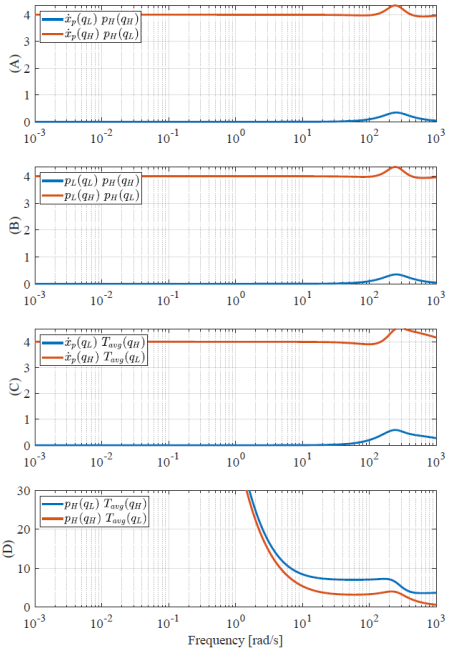

Figure A4. Relative gain array for system with input- and output transformations and with $x_{p0} = 665[mm]$.

POSITION SIGNAL FILTERING FOR HYDRAULIC ACTIVE HEAVE COMPENSATION SYSTEM

Wojciech Pomierski

National Oilwell Varco Poland Sp.z o.o., Aleja Grunwaldzka 411, 80-309 Gdańsk
Tel.: +48 58 5220140; E-mail address: wojciech.pomierski@nov.com

ABSTRACT

In the paper a new position signal filtering method with position prediction is presented along with test results using a simulation tool. The complete active heave compensation system performance with input signal filtering is also shown. The control system uses an input acceleration signal taken from the motion reference unit, which usually contains noise that is not acceptable for the position controller. Currently, a Kalman filter is used which is okay to use for certain conditions. The filter works similarly to how it is used for autonomous applications where two input positions are necessary, one from position sensors and another one taken from the model. The challenge is that there is no physical wave model available for the Kalman filter used for offshore position control and the waves are not predictable. It was found that a Kalman filter with a special signal prediction instead of the model input can be used. This position prediction helps to avoid system delays and the potential of missing the signal for a short period of the time.

Keywords: Signal Filtering, Position Control, Hydraulic Active Heave Compensation System

1. GENERAL ASSUMPTIONS

The idea is to make a new motion reference unit signal filtering algorithm and rig velocity forecast used as "physical model" for Kalman filter. The aim is to protect the system during a short period of the time when the signal is missed and to avoid signal peaks for a good accuracy controlling of active heave compensation systems by using:

- Acceleration special filtering with values forecasting.
- Velocity forecasting and filtering with Kalman filter**.**
- Continuous velocity offset calculation used for acceleration integration**.**
- Continuous position offset calculation used for velocity integration.

2. SIGNAL FLOW

The signal flow from Motion Reference Unit (MRU) to the hydraulic pump or proportional valve is shown in **Figure 1**. The FILTER forecasts acceleration values by using measured acceleration from Motion Reference Unit. The programmable logic controller (PLC) samples the acceleration input data with constant sampling period. INTEGRATOR calculates velocity which is forecasted and filtered. It also calculates movement. Velocity is the most important parameter for the controller so that special attention must be paid here. Controller calculates the signal to the hydraulic device to make the hanging load still. Relative movement measurement of the load to the ship position is used by position controller to avoid load drift.

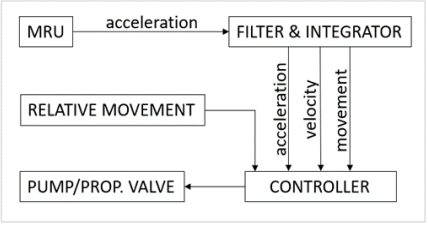

Figure 1: Simplified signal flow scheme

3. FILTER BLOCK DIAGRAMS

3.1. Acceleration forecasting

The diagram shown in **Figure 2** presents the acceleration forecasting algorithm. Deviation value of measurements at_n is calculated first from a_n value. In case of nonacceptable at_n value, the arithmetic string is used for forecasting the proper

output acceleration value af_n. Average value of at_n is calculated to get as_n. The arithmetic string with values difference ks_n for forecasting as_n is chosen here, then output af_n is computed. For acceptable acceleration deviation value, the measurement a_n is taken as final.

3.2. Velocity filtering and forecasting

The diagram is shown in **Figure 3**. On the base of acceleration value af_n the velocity v_n is integrated and offset velocity $v0_n$ for certain period of the time for integration calculation is computed. Average vs_n value of velocity deviation vt_n is calculated. In case of nonacceptable vs_n deviation defined as dvs_n, the arithmetic string with previous dvs_{n-1} value is used for forecasting the proper velocity value ve_n. If dvs_n is acceptable the current dvs_n value is used for forecasting. The ve_n value and v_n value from measurement are used than in Kalman filter to calculate vf_n velocity.

3.3. Position calculation

The diagram is shown in **Figure 4**. On the base of velocity value vf_n the position sf_n is integrated with offset s0 implemented. Offset s0 is calculated for certain period of the time.

4. FILTERS SIMULATION TEST RESULTS

MRU acceleration values from real measurement for the simulation have been taken. The measurements quality is degraded manually then and presented together with results from the filter in **Figure 5**. Velocity results are shown in **Figure 6** and zoomed out in **Figure 7**. For the situation with bad acceleration signal input the results are promising. The filter doesn't cause the signal delay or significate errors.

5. MODULE HENDLING COMPENSATOR SIMULATION

The module handling compensator (MHC), shown in **Figure 8**, is usually used on the board of the ship or platform when the load should smoothly land on the seabed during the ship movements. It contains passive and active cylinders. Active cylinders are controlled by closed circuit pumps when passive cylinders support the load with almost constant pressure, provided by high volume gas accumulators. Theoretically the load should be kept still but the whole signal measurement way and hydraulic control errors cause the load position deviation. For the simulation 1000 [mT] compensator is used with 1000 [mT] load. The "Real" acceleration input is taken from Jonswap model (no errors in such a case for comparison). The vertical ship acceleration "Real" quality is degraded manually for the filter input first to get a_n values. The inputs for the controller are taken from the filters described in chapter 3. The acceleration measured a_n, acceleration filtered af_n and real acceleration "Real" are shown in **Figure 9**. The "Real" acceleration is used for the ship movements when acceleration af_n, velocity vf_n and position sf_n values are used for the controller. The simulation model of MHC contains all important mechanic, hydraulic and controller parts. Simulation load position error (without rope elasticity influence) is shown in **Figure 10**.

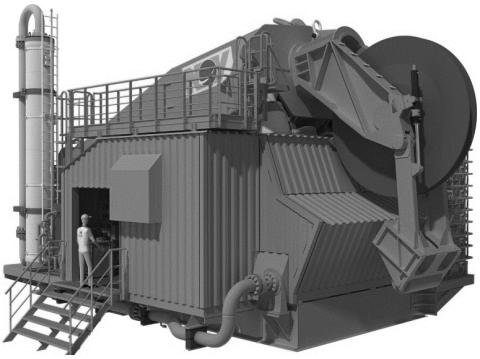

Figure 8: Module handling compensator 3D model

6. CONCLUSION AND OUTLOOK

The simulation results show the usefulness of the filter algorithm. The value forecasting together with the measured values and Kalman filter allow to avoid big controller input errors by avoiding filtered signal delay and big signal deviation caused by unexpected signal noise. Filter needs additional work for checking its correctness in different situation before implementation. During the simulation period of 1 [s] the lack of signal was checked. It must be decided the emergency procedure when the lack of the signal period is longer then assumed. This assumed maximum period shouldn't be so long. Depends on PLC sampling period of the time the value numbers for

calculation average values must be carefully defined. This should be work out by further simulation work and tests on real object.

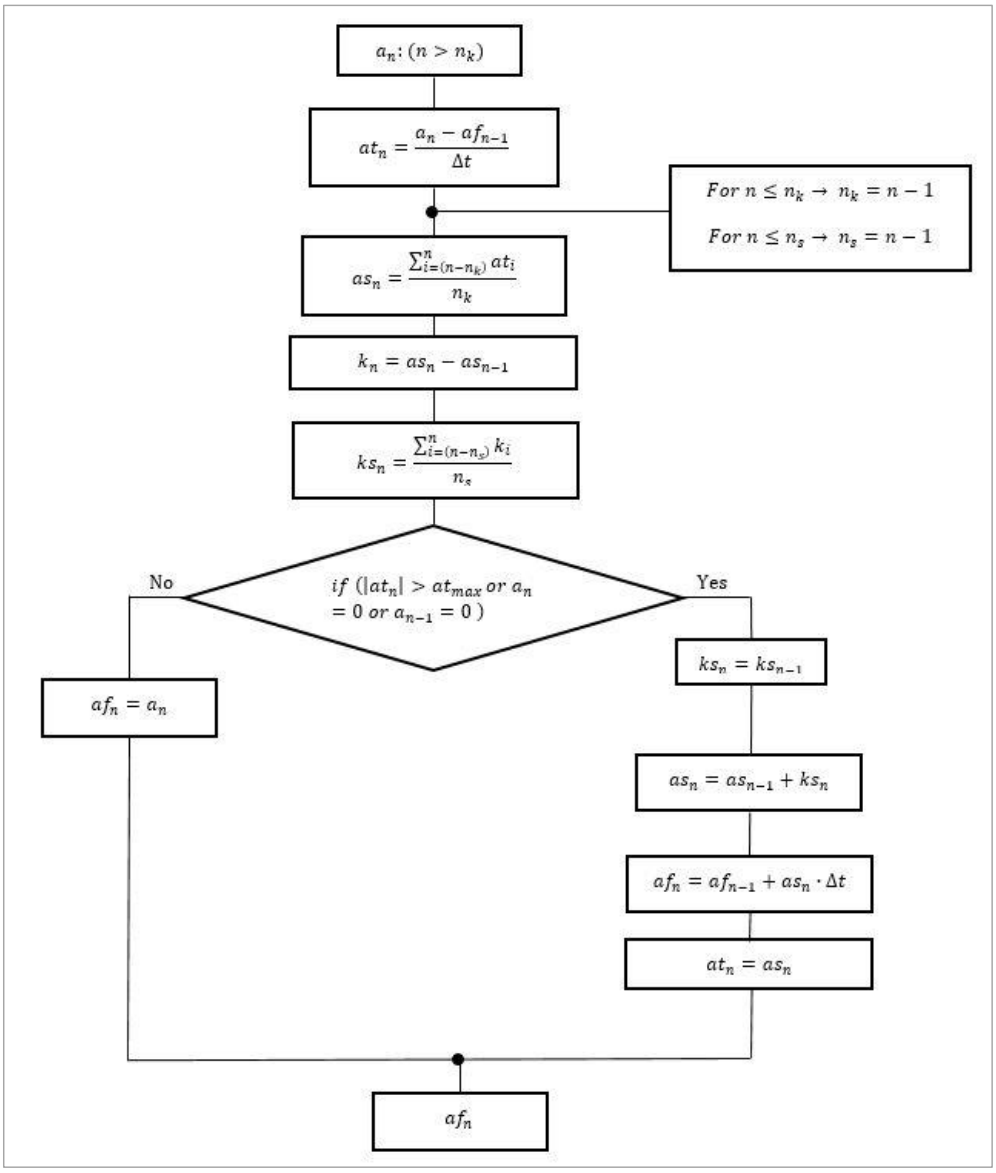

Figure 2: Simplified acceleration filter block diagram with forecasting function

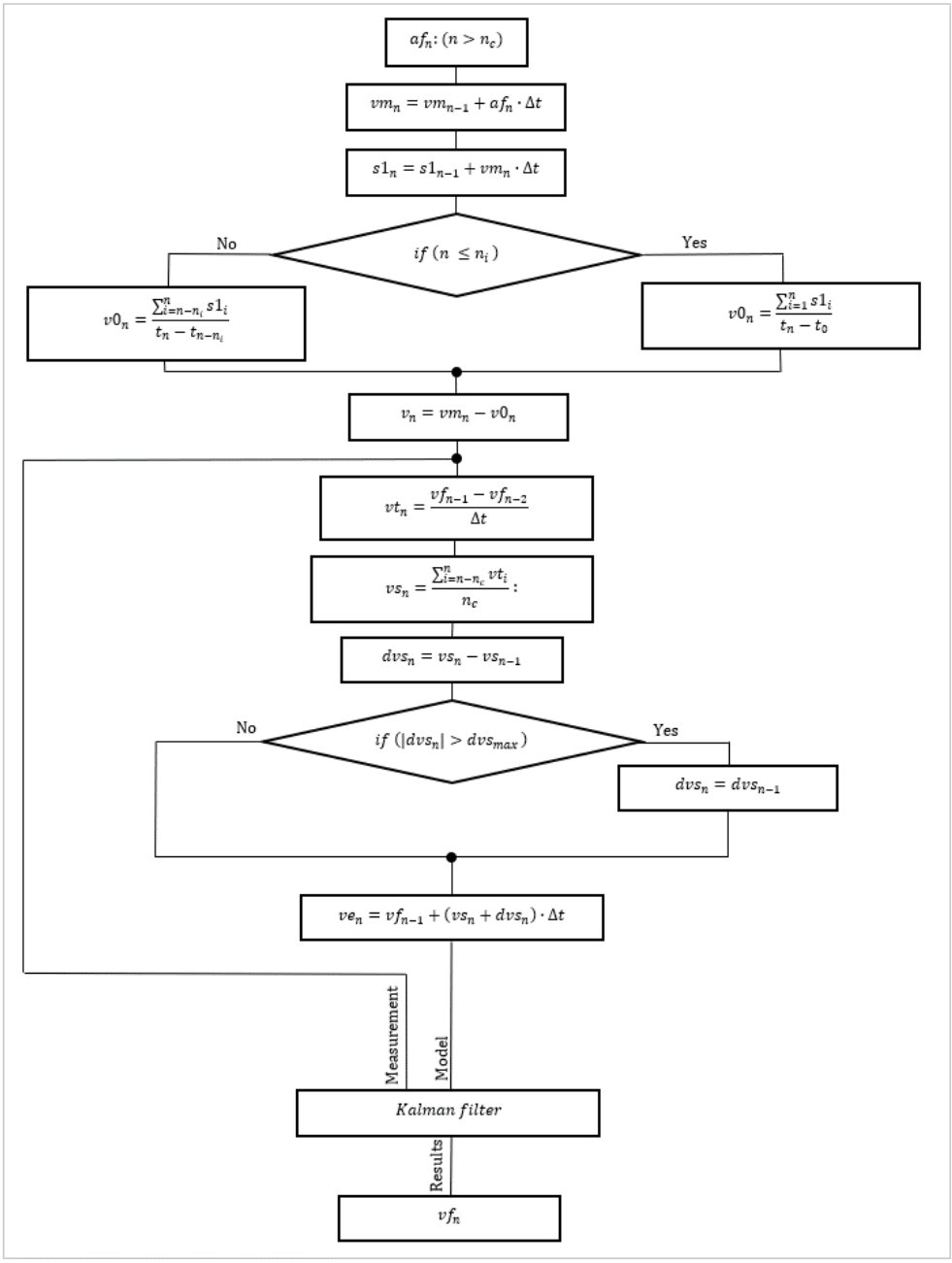

Figure 3: Simplified velocity filter block diagram with forecasting function

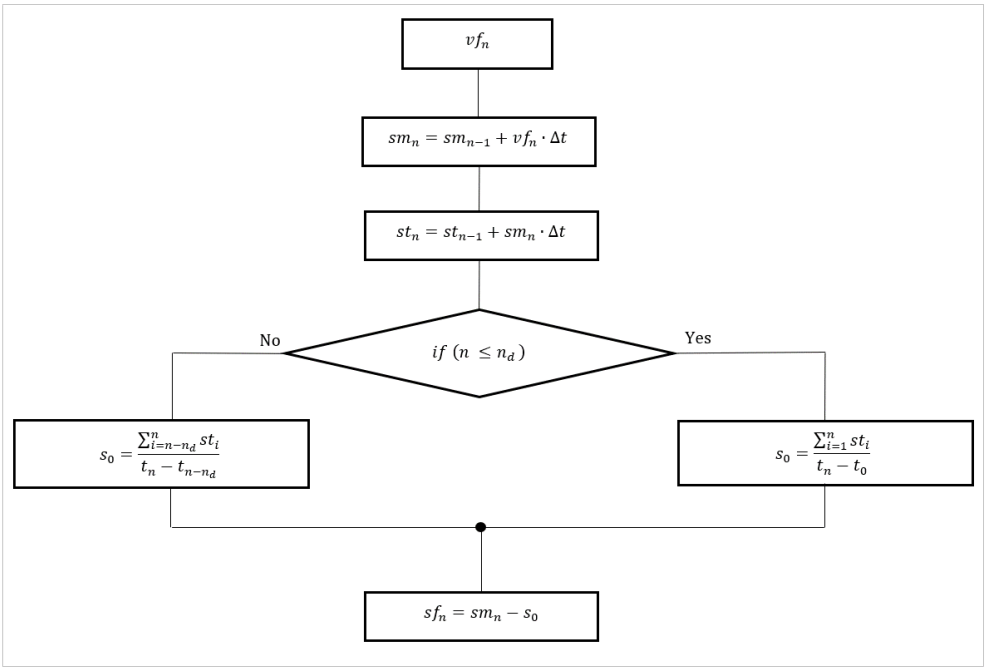

Figure 4: Simplified position calculation block diagram

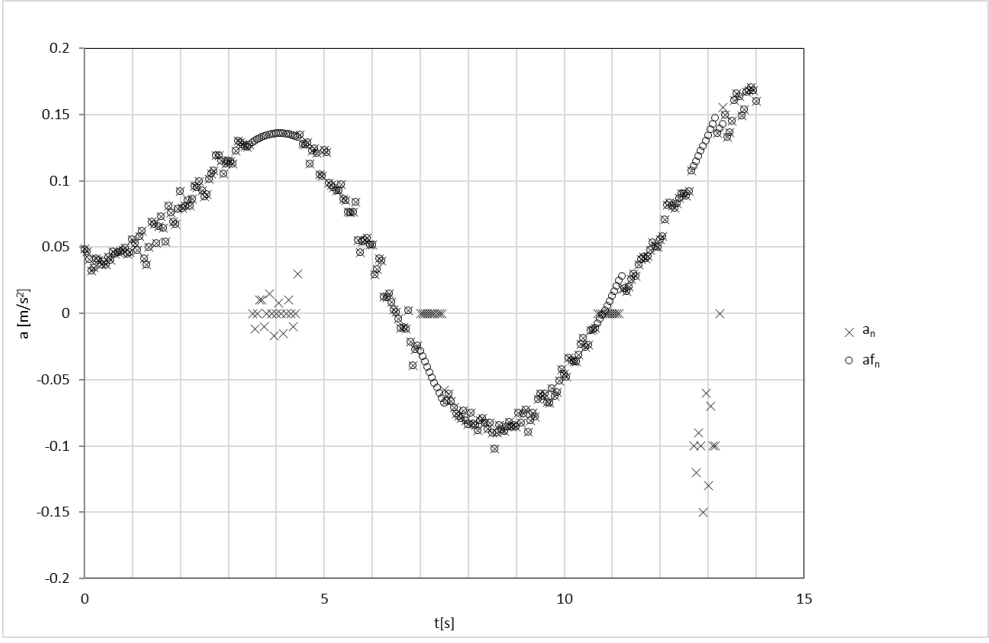

Figure 5: Input acceleration values a_n and after filter forecasting af_n

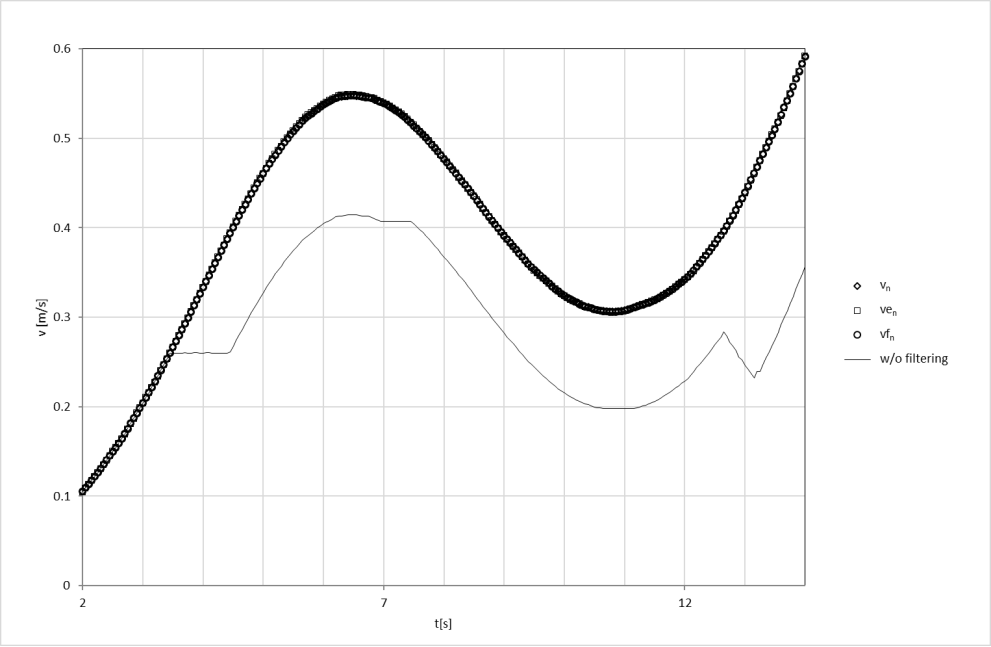

Figure 6: Calculated input velocity v_n, forecasted velocity ve_n, filtered velocity vf_n and without treatment "w/o filtering" comparison

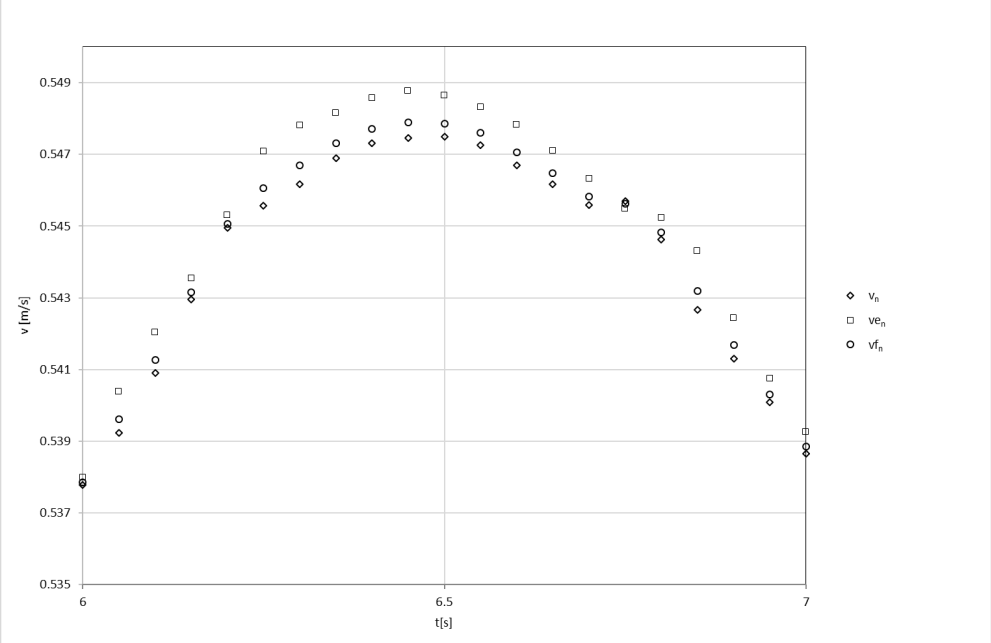

Figure 7: Zooming of the **Figure 6**

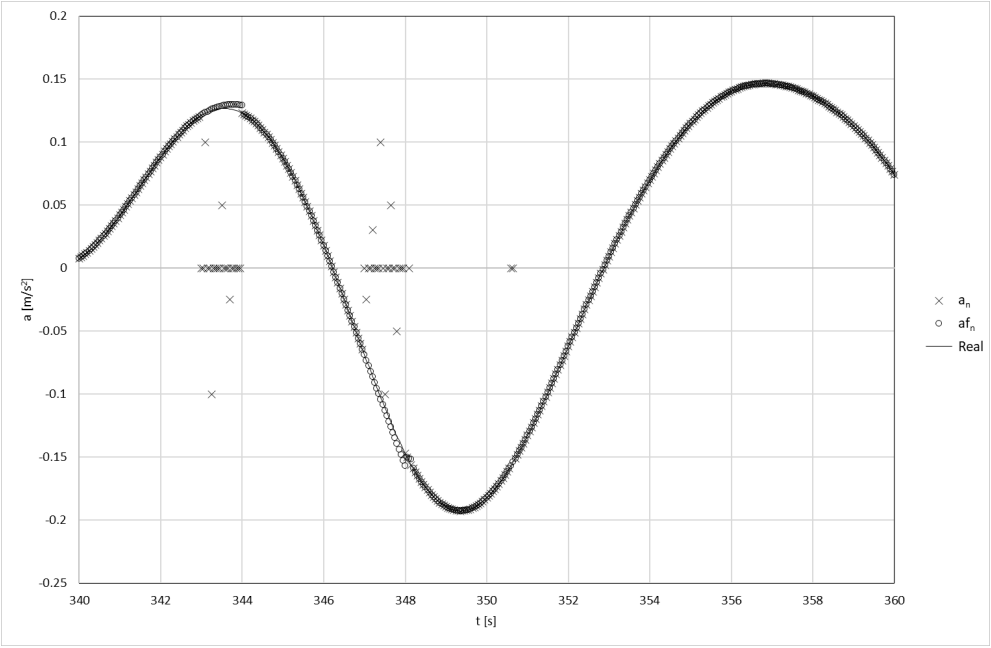

Figure 9: Input acceleration values a_n, after filter forecasting af_n and real acceleration "Real" comparison – values used for MHC simulation

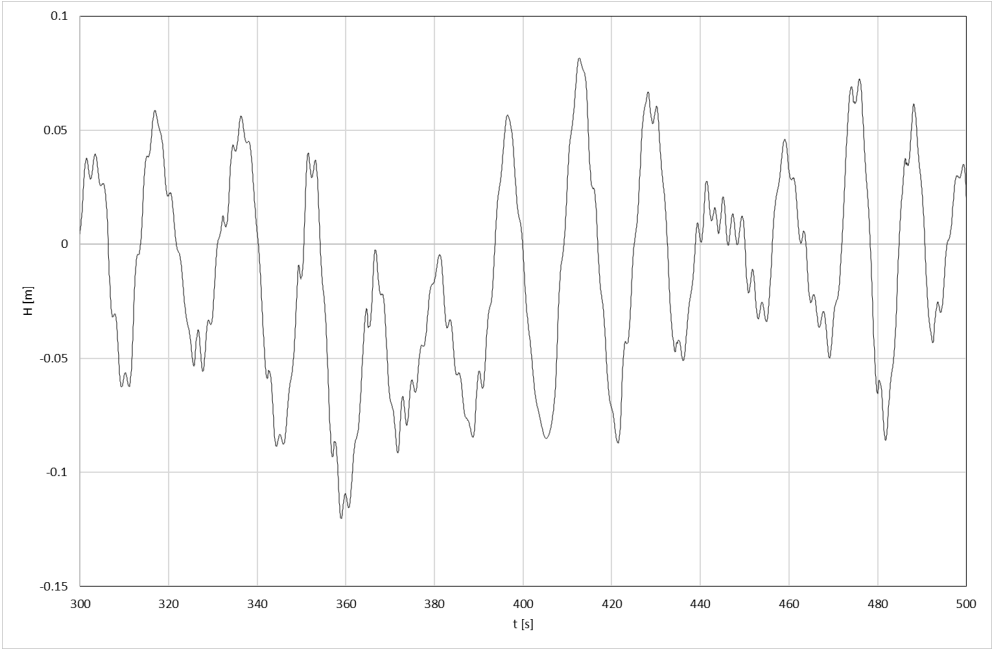

Figure 10: Load position error MHC simulation results with 1000 [mT] load hanging

GROUP G

Fluids

peer reviewed

NUMERICAL PREDICTION AND EXPERIMENTAL INVESTIGATION OF CAVITATION EROSION OF HYDRAULIC COMPONENTS USING HFC

Atena Moosavi*, Sven Osterland, Dominik Krahl, Lutz Müller, Jürgen Weber

Institut für Mechatronischen Maschinenbau, Technische Universität Dresden, Helmholtzstrasse 7a, 01069 Dresden
* Corresponding author: Tel.: +49 351 46334109; E-mail address: atena.moosavi@tu-dresden.de

ABSTRACT

Hydraulic devices play an essential role in mechanical engineering due to their high-power density, good controllability, flexible application and high robustness, which expose innovative methods of energy transmission. However, in applications where there is an increased risk of fire or explosion, the commonly used combustible mineral oils represent an unacceptable safety hazard. In such cases, fire-resistant, water-based hydraulic fluids are in demand. A special feature of these liquids is their high cavitation tendency and the associated strong erosion wear. The aim of this research is to predict the cavitation behaviour of HFC and the subsequent erosion phenomena using numerical methods and to validate the results with experiments. Additionally, experimental results for HFC were compared with HLP. The findings help to implement further developments to decrease the erosive effect of cavitation in high-pressure differences in hydraulic components. For this purpose, flow geometries of typical hydraulic components, e.g. valve and pump, are used for experimental and numerical investigation. The large-eddy simulation (LES) turbulent modelling is used with Zwart-Gerber cavitation model. The cavitation aggressiveness is quantified by cavitation erosion indices according to Nohmi.

Keywords: HFC, Cavitation, Erosion, CFD, Experiment

1. INTRODUCTION

Due to their high-power density, good controllability, flexible energy transmission and high robustness, hydraulic drives are of essential importance for machines and systems engineering. However, in applications where there is an increased risk of fire or explosion, the commonly used flammable mineral oils (HLP) represents an unacceptable safety risk. In applications such as mining, foundry and steel rolling mills, but also for power generation or offshore applications, hydraulic fire-resistant fluids should be selected according to the necessary properties to minimize potential risks. Therefore, low-flammable water-based HF fluids have been developed.

Figure 1: Ignition tendency comparison for HFC and conventional hydraulic oils

One of the most widely used fire-resistant hydraulic fluids, which are nested within the ISO 6743-4:2015 standard is the group of HFC fluids. HFC liquids with a water content between 35% and 50% have established themselves as the most common and economical solution, since with the contact of the liquid with a source of ignition, the water evaporates and a spreading of the fire prevents [1] [4]. **Figure 1** shows comparison of ignition inclination for HFC, HLP and HFDU.

However, due to the low boiling point of water, the liquid evaporates at a relatively low temperature [3], which significantly changes the fluid property of the remained mixture and impairs the function of the hydraulic components, especially in difficult to access hydraulic systems, e.g. in offshore areas. The high vapour pressure of the water leads to cavitation even at moderate pressure differences in the hydraulic devices. Cavitation reduces efficiency, causes noise and accelerates component wear [6] [17]. Therefore, the use of HFC is severely restricted because of its high cavitation tendency and the consequent erosion damage to the components. The accelerated erosion wear when using HFC

fluids due to hydrodynamic cavitation phenomenon widely exists in hydraulic machinery such as valves, pumps, turbines and venturi tubes. This results in a limited operating range and potentially costly downtime, which reduces HFC acceptance. This shows that the consideration of cavitation processes is a priority in the development of HFC components.

In this research, a simplified geometry of a hydraulic valve and a control edge of an axial piston pump have been implemented to carry out experiments, and by this way the cavity prone areas characteristics have been identified.

After comprehend experimental survey, the operating points were simulated by ANSYS CFX, using Nohmi cavity related indices to compare numerical results with those of experiment. Then finding a compatible relationship between the intensity of eroded area and Nohmi indices were necessary. Finally, collect data on the causes and effects of cavitation in different operating points are of interest.

2. FLUID PROPERTIES DETERMINATION

In order to map the specific fluid properties of HFC in numerical flow simulation and choose the correct cavitation type, it is necessary to parameterize the fluid model based on literature references and experiments. The experimental work focuses on the characteristics of the flow field as a function of fluid temperature. Further investigations are carried out by varying the dissolved air content.

The dimensionless cavitation number σ defines the cavitation inclination of liquids. The lower the cavitation number, the more likely the flow is to cavitate, and the greater the number and size of bubbles. As it can be seen in equation (1), σ is proportional to the vapour pressure of the liquid and anti-proportional to its density.

$$\sigma = \frac{p - p_d}{\frac{1}{2}\rho U^2} \tag{1}$$

Therefore, in further investigations special attention should be paid to the thermodynamic properties and their parameterization in the model.

2.1. Density

As part of the parameterization, the dependency of density on temperature and pressure is important. For this Herschel [5] considered two functions $\rho(T)$ and $\rho(p)$. However, the influence of pressure changes on the density for both HLP and HFC is much less than the influence of temperature and $\rho(p)$ is therefore neglected for all subsequent considerations to simplify the modelling.

$$\rho(T) = \frac{\rho_0}{1+\beta_T \cdot (T - T_0)} \tag{2}$$

Equation (2) gives the temperature dependency of density, where ρ_0 is density at ambient pressure at a temperature of 20°C, and β_T is the thermal expansion coefficient according to the manufacturer's specifications in the data sheet of the liquid.

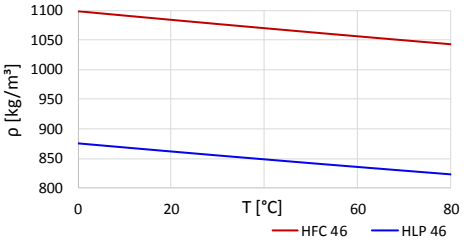

Figure 2: Density-Temperature dependency of HFC and HLP, $\rho_{0,HFC} = 1084\ Kg/m^3$, $\rho_{0,HLP} = 862\ Kg/m^3$, $\beta_{T,HFC} = 0.00065\frac{1}{k}$, $\beta_{T,HLP} = 0.00065\frac{1}{k}$

It can be seen in **Figure 2** that HFC has a higher density than HLP. According to equation (1), the cavitation number for HFC is therefore lower than for HLP at the same pressure ratios and volume flows, indicating that HFC is more susceptible to cavitation than conventional mineral oils.

2.2. Vapour pressure

In industrial applications, keeping the temperature constant is a normal attempt while operating a hydraulic system. Nonetheless, in narrow spaces such as control notches in valves and pumps, the static pressure can locally fall below a certain level and the hydraulic fluid can cavitate.

The Clausius-Clapeyron relation was implemented, which describes the vapour pressure p_D of the liquid at the temperature of T_2 according to the following equation:

$$p_{d1} = p_{d1} \cdot e^{C_d \cdot \left(\frac{1}{273\,°C + T_1} - \frac{1}{273°C + T_2}\right)} \tag{3}$$

Where C_d is a constant, dependent on the specific latent heat of the liquid and specific gas constant. p_D is the vapour pressure at T_1. The respective values from the data sheets [19] [20] at a temperature of T_1=100 °C are applied.

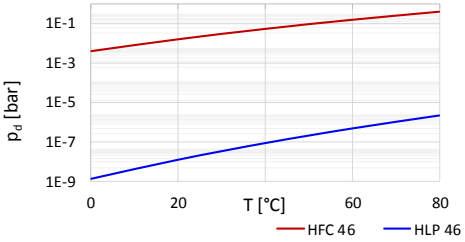

Figure 3: Vapour pressure for HLP and HFC with respect to temperature, According to eq. (2) $p_{d1,\mathrm{HFC}} = 95 \cdot 10^{-3} bar$, $p_{d1,\mathrm{HLP}} = 87 \cdot 10^{-9} bar$, $C_{d,HFC} = 5514$, $C_{d,HLP} = 8687$

Vapour pressure is an indicator of the evaporation rate of a liquid. **Figure 3** shows the vapour pressure-temperature behaviour for HFC and HLP in comparison. It can be seen that at the same temperature, the vapour pressure of HFC is higher than that of HLP, and consequently water-based hydraulic fluids evaporate earlier than conventional mineral oils.

2.3. Viscosity

The viscosity describes the internal friction in moving liquids. It has a decisive influence on the operating behaviour, in particular on wear and performance losses (internal leakage and pressure losses) [5]. Viscosity is strongly temperature-dependent. This dependency can be determined with the Vogel-Cameron relation, equation (4), according to DIN 53017.

$$\eta(T) = A \cdot e^{\frac{B}{T+C}} \tag{4}$$

Figure 4 illustrates viscosity of HFC and HLP according to equation (4) with the help of listed coefficients in Table 1.

Table 1: Vogel-Cameron's coefficients for HLP and HFC

	HLP	HFC
A $[\boldsymbol{Pa \cdot s}]$	$3.9 \cdot 10^{-5}$	$9.2 \cdot 10^{-5}$
B $[\boldsymbol{°C}]$	1019	1113.4
C $[\boldsymbol{°C}]$	107.5	136.7

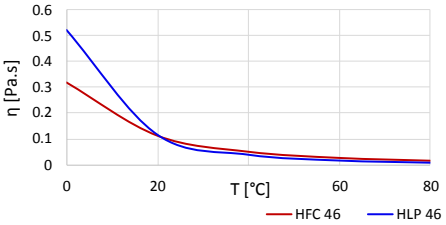

Figure 4: Viscosity-Temperature for HLP and HFC

2.4. Dissolved air

An essential part of the parameterization is the analysis of the cavitation behaviour. The amount of gas that can be dissolved in oil is referred to its solubility [16]. In a study of gas evolution in liquids and cavitation, an expression for predicting the volume of dissolved air as a time dependent function was derived [13]. In derived formulation "half-life" term was defined which was experimentally found to be related to solubility constant according to Hennry's law [13] [7]. In literature, a specific search on the air dissolving capacity of HFC, which produces a clear result, does not exist. This makes an experimental determination of this quantity within the study necessary.

Bunsen coefficient indicates how much volume of a gas V_G is absorbed in the volume of another substance V_L at a partial pressure corresponding to the standard pressure in the physical standard state. A specific test bench, the hydraulic tensile test, which generates a defined pressure drop via volume expansion within a closed cylinder, is used [12]. The Bunsen coefficient of HFC and HLP could be measured using the trend line in the volume ratio-pressure diagram from different operating points, **Figure 5**.

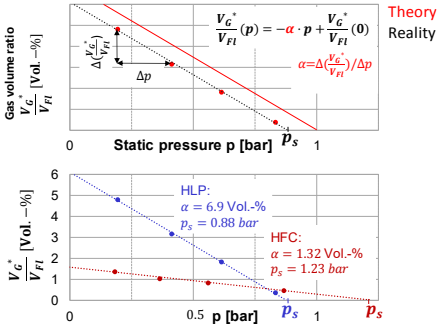

Figure 5: Experimental investigation of the air dissolving capacity for HFC and HLP

Experimental investigations on Bunsen coefficient of HLP and HFC show that the gas solubility of HLP is 6.9% vol.%, while HFC can dissolve up to 1.32% vol.% of free air, which is 5.2 times less than HLP. According to Totten [16] water can dissolve 1.8% vol.% of free air. Meanwhile, water vapour pressure changes strongly with increasing temperature. This illustrates the vapour cavitation sensitivity of water compared to mineral oil. In previous studies, gas cavitation is often neglected for water due to the dominant vapour cavitation [2] [14]. Since HFC is a water-based liquid and the product used in experimental part of this study contains 45% water [19], its cavitation behaviour is approximately equal to that of water. In this research work, gas cavitation of HFC is negligible and only vapour cavitation is considered as the dominant cavitation type. In reverse, HLP has a significant greater capacity of dissolving air, so that gas cavitation cannot be neglected for HLP.

3. EXPERIMENTAL SETUP AND PROCEDURE

An experimental investigation was undertaken to study cavitation damage in a simplified, flat diaphragm geometry of spool valve and axial piston pump, as they are most relevant devices to control hydraulic systems. **Figure 6** illustrates scheme of these experimental geometries.

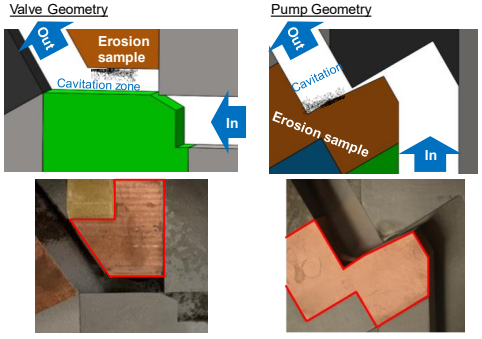

Figure 6: Simplified flat diaphragm geometry of spool valve and axial piston pump

The test facility designed by Mueller [10] was implemented in experimental attempts. It can deliver the required pressure difference, temperature and volume flow rate for the measurement of cavitation erosion. For continuous data recording, temperature and pressure sensors have been mounted at both inlet and outlet of the test geometry. Additionally, a high-speed camera, including lighting and optical components, as in **Figure 7**, have been implemented to record fluid dynamic process with shadowgraphy [15]. Shadowgraph is a density sensitive technique, based on a back illumination and an appropriate defocusing [8]. This method as an optical diagnostic technique is sensitive to density gradients in fluid flow [9].

The experimental analysis of cavitation wear on the valve and pump model was done with both HLP 46 and HFC 46 hydraulic fluids. The exchangeable copper samples, exposed to the erosion area, were tested at different operating points for both HLP and HFC. Each operating point was recorded and analyzed in an ongoing test with a measurement time of 5 hours each.

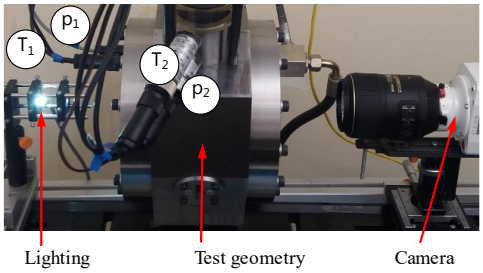

Figure 7: Visual recording of experiment by high-speed camera

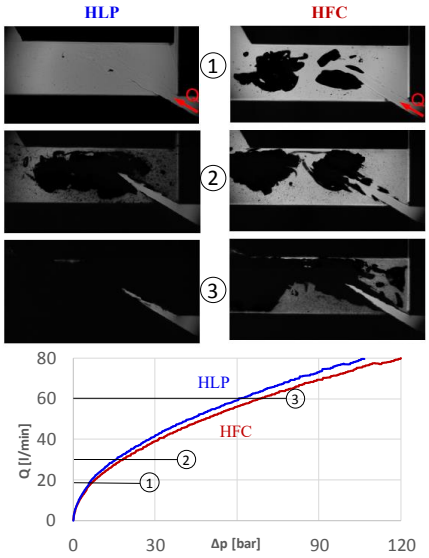

Figure 8: Cavitation intensity comparison for HFC and HLP at 25°C for valve

Figure 8 shows high-speed images, which captured the intensity of cavitation with shadowgraphy method at constant temperature of 25°C but several pressure differences, for both hydraulic fluids HLP and HFC. In HFC, cavitation already starts at lower pressure differences or volume flows than in HLP due to the different saturation vapour pressures, state (1). As the volume flow increases, the proportion of cavity bubbles increases in both, HLP and HFC. As the volume flow increases, the proportion of gas-filled cavities increases in both, but more strongly for HLP than for HFC. This is caused by the release of larger amounts of dissolved air in HLP, while the amount of free air can be assumed to be zero in HFC according to section 2.4.

Before and after each erosion test, the surface of the erosion sample was photographed then it was scanned and analyzed using a 3D profilometer, **Figure 9**. The available 3D surface topography was used to determine both the depth of erosion and the volume removal of the entire sample compared to the non-eroded initial state.

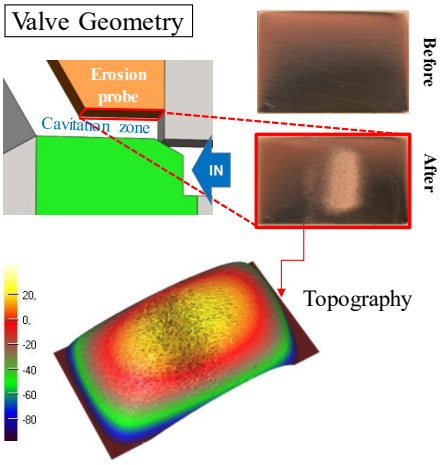

Figure 9: Comparison of erosion probe, before and after test and 3D surface topography after completed erosion test with HFC for Valve

The data in Table 2 gives an overview of the volume removal determined for HLP and HFC at two operating points.

Figure 10 clearly shows that under comparable flow conditions, cavitation at HFC 46 is considerably more aggressive than at HLP 46 and thus leads to significantly greater material removal. The higher the temperature and pressure difference, the higher the removal of material by cavitation erosion.

Table 2: Comparison of the erosion material removal for HFC and HLP in a selected operating point at $\boldsymbol{T = 60°C}$

	Q_{ave} [l/min]	Δp [bar]	Removed volume [mm3]	Maximum depth [µm]
HLP	81.3	93.6	1.8	409
HFC	80.1	117.9	15.71	1651

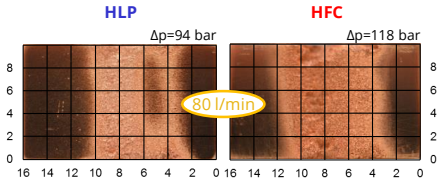

Figure 10: Comparison of the erosion intensity for HFC and HLP at constant volume flow rate of 80 l/min at $T = 60°C$ for valve

4. NUMERICAL METHOD

The aim of the numerical investigation is to identify the zones which are at risk of cavitation and to predict the intensity of erosion using simulation-based methods. In the first step towards numerical flow simulation and analysis, the exact dimensions of the test geometries, used in the test stand, were carefully measured so that the models could be created and meshed in Ansys ICEM. The substantial fluid zones e.g. flow entrance and areas near to the walls, were finely and carefully meshed by blocking method due to the importance effect of the erosion in these parts. The mesh network of valve and pump geometries have 1601280 and 1989844 hexahedral elements, respectively. Boundary zone type specifications, such as WALL, INLET or OUTLET, defined the characteristics of the model at its external or internal boundaries. Consequently, the geometry was imported to Ansys CFX for further calculation.

4.1. Turbulent model

Vapour cavitation refers to the process by which vapour forms in a low-pressure region of a liquid flow. Here a turbulent model that can reproduce low-pressure regions in the flow spatially and temporally, and corresponds almost exactly to the experiment is essential. Initially, independent of the cavitation model, SST and LES turbulent

models were examined to see which approach can depict the necessary pressure drop at the selected operating points from experiments. As the simulations were conducted with cavitation free turbulent modelling, the data from experiment were also compared in the cavitation free area. According to **Figure 11**, both SST and LES show a good consistency for pressure drop with experimental results.

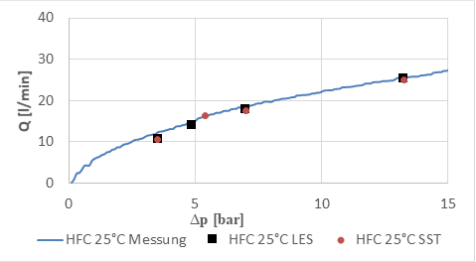

Figure 11: Simulation and experiment comparison of Q-Δp in Cavitation free area

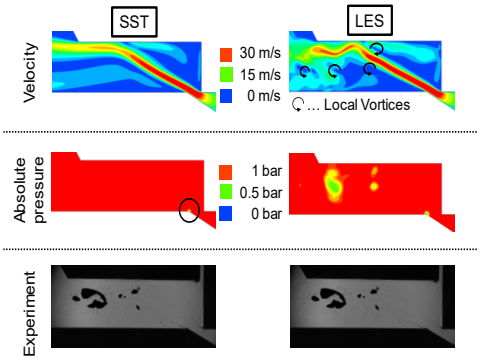

Figure 12: Comparison of Velocity and Pressure simulated by SST and LES models with visual high-speed photos for Valve

Figure 12 shows a glance of velocity field simulated by SST and LES model approaches, as well as a comparison of the absolute pressure in both models with an experimentally recorded cavitation high-speed image. The result shows that the modeling of large-scale vortices is a prerequisite for a correct mapping of the cavitation-relevant pressure drops where RANS modeling, like the SST model e.g. is not able to predict that. RANS models cannot calculate potential cavitation areas in the form of low local pressures at the points, where they occur in the experiment, although the flow characteristics are well reproduced by SST.

4.2. Cavitation model

In CFX, cavitation models are implemented in the multiphase framework as an interphase mass transfer model to simulate the growth of bubbles in a liquid, which user-defined coefficient quantities can be used. In this research HFC and ideal gas water vapour were considered the participant phases. As the vapour volume fraction increases, the nucleation site density must decrease accordingly. With this mind, here the Zwart-Gerber-Belmari [18] cavitation model parametrized for water which is compatible for vaporization with all the turbulence models available in ANSYS, was used as cavitation model for the HFC. Assuming that all the bubbles in a system have the same size, Zwart-Gerber-Belamri proposed that the total interphase mass transfer rate per unit volume (R) is calculated using the bubble radius (R_b), nucleation site volume fraction (α_{nuc}) and evaporation coefficient (F_{evp}), Equation (5).

$$R = F_{evp/cond} \cdot \frac{3\alpha_{nuc}\rho_d}{R_b} \cdot \left(\sqrt{\frac{2}{3} \cdot \frac{|p_d - p|}{\rho_l}}\right) \quad (5)$$

Where bubble radius is $R_b = 10^{-3}\,mm$, nucleation site volume fraction is $\alpha_{nuc} = 5 \cdot 10^{-4}$, evaporation coefficient is $F_{evp} = 50$ and condensation coefficient is $F_{cond} = 0.001$.

4.3. Cavitation index

Nohmi [11] introduced four different indices with which the aggressiveness of vapour cavitation on solid surfaces can be numerically calculated as a function of the local vapour volume fraction and pressure. Nohmi indices are given in equation (6), (7), (8) and (9).

$$Noh1 = \int_0^{T_{sim}} \alpha_d \cdot \max\left(\frac{\delta p}{\delta t}, 0\right) dt \quad (6)$$

$$Noh2 = \int_0^{T_{sim}} \alpha_d \cdot \max[(p - p_d), 0]\, dt \quad (7)$$

$$Noh3 = \int_0^{T_{sim}} \max[(p - p_d), 0] \cdot \max\left[-\frac{\delta \alpha_d}{\delta t}, 0\right] dt \quad (8)$$

$$Noh4 = \int_0^{T_{sim}} \max\left[-\frac{\delta \alpha_d}{\delta t}, 0\right] dt \quad (9)$$

To select the best index with the most accurate prediction of erosion, the numerical data for the four Nohmi indices and the experimental results were compared in two operating points with low and high intensity of cavitation erosion. Numerical investigation shows that Nohmi3,

given by equation (8), is more compatible with experimental results and calculates cavitation erosion more accurate than the other Nohmi indices. **Figure 13** shows a good consistency between experiment and simulation using Nohmi3. For both operating points, both the local prediction of erosion and its intensity agree well with the experimental damage on the erosion samples.

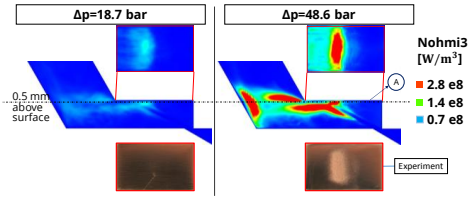

Figure 13: Comparison of Nohmi3 erosion prediction with experimental results of Valve at low and high cavitation intensity

Finally, all simulations were carried out isothermally with LES turbulent model, using Zwart-Gerber-Blamari as cavitation model for the flow at the selected operating points. Nohmi3 was used as the most reliable prediction index of cavitation areas and used for all further simulations.

5. RESULTS AND DISCUSSION

After conducting experimental and numerical investigations, results were compared. Table 3 shows valve's operating points from experiments which were simulated in Ansys CFX.

Table 3 Valve geometry experimental operating points

VOP	T [^{0} C]	p_1 [bar]	p_2 [bar]	Q_{ave} [l/min]
1	25	10.5	1.24	21.8
2	25	15	1.0	26.5
3	25	20	1.3	31
4	25	50	1.4	51
5	40	50	1.4	54
6	40	123	1.55	80
7	60	50	1.4	51.5
8	60	119	0.99	80

At operating point VOP1, water vapour bubbles started to appear and occupied approx. 20 % of the flow space. According to Bernoulli if the static pressure falls locally below the saturation vapour pressure, cavitation begins. In order to cover the entire operating range, in accordance with the experimental investigations, the pressure difference between inlet and outlet was gradually increased with regard to the cavitation tendency. It was found that with rising temperature and rising pressure drop/volume flow rate, the cavitation tendency in the flow increases. This is shown by the simulation results based on experimental operating points and the surface analysis of the experimental erosion samples from 3D scanner. **Figure 14** and **Figure 15** show examples of this correlation for low and high intensity of erosion, VOP3 and VOP4, at 25°C. Pressure difference between inlet and outlet (consequently also the volume flow) at constant fluid temperature was increased from 18.7 bar at VOP3 to 48.6 bar at VOP4. It can be seen that by increasing the pressure difference, Nohmi3 index increased and more erosion was predicted in the operating point with higher pressure drop.

The erosion prediction in higher pressure difference is also interesting. For VOP6, **Figure 16** and for VOP8, **Figure 17** show a comparison between simulation and experiment results. Numerically predicted cavitation erosion through Nohmi3 index was compared with the 3D surface scan of the experiment erosion sample. In VOP6 a maximum water vapour content of 88.7% and in VOP8 85.4% was determined numerically.

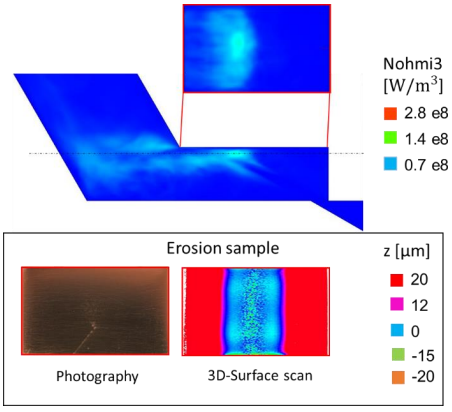

Figure 14: Comparison between simulated cavitation aggressiveness determined using Nohmi3 and experimental 3D surface scan of erosion sample for VOP3 in valve

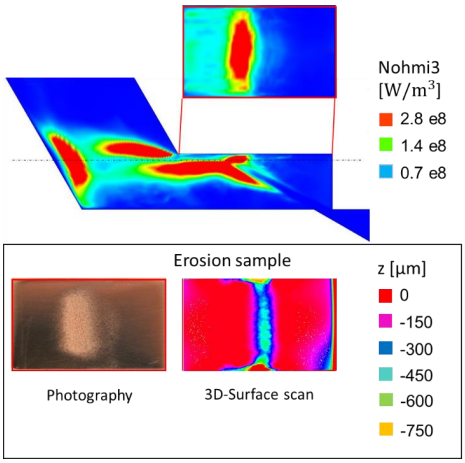

Figure 15: Comparison between simulated cavitation aggressiveness determined using Nohmi3 and experimental 3D surface scan of erosion sample for VOP4 in valve

After comparing the simulation results with the experimental results, obtained from 3D surface scan of the erosion samples, it was determined that the Nohmi3 index can reliably predict the degree of cavitation aggressiveness in the valve geometry. The investigations over valve geometry have shown that with increasing pressure difference and fluid temperature the effects of erosion become more intense, which is also predictable in the numerical simulation model.

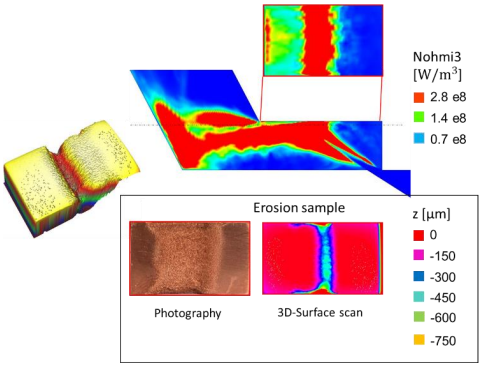

Figure 16: Comparison between simulated cavitation aggressiveness determined using Nohmi3 and experimental 3D surface scan of erosion sample for VOP6 in valve

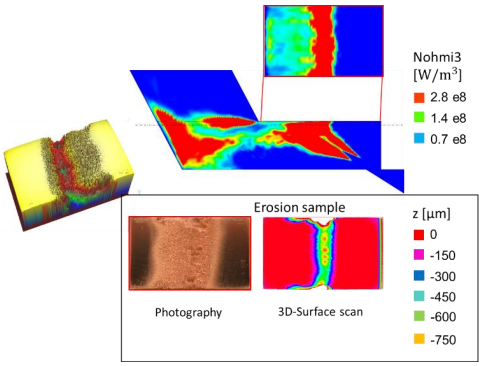

Figure 17: Comparison between simulated cavitation aggressiveness determined using Nohmi3 and experimental 3D surface scan of erosion sample for VOP8 in valve

Table 4: Pump geometry experimental operating points

POP	T [^{0} C]	p_1 [bar]	p_2 [bar]	Q_{ave} [l/min]
1	40	20.1	2.3	17.4
2	40	25	2.2	20.2
3	40	30	1.3	22.4
4	40	99	1.9	42
5	40	150.5	1.26	51

For further investigation, the numerical methods were developed to determine cavitation intensity and erosion wear for another typical hydraulic component. Here the same numerical procedure was taken for the control edge of an axial piston pump, which were under investigation experimentally. Table 4 gives the experimental operating points for the pump geometry that were simulated numerically in the same way as the valve geometry.

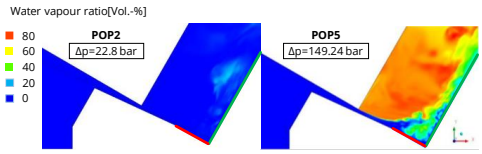

Figure 18: Water vapour ratio comparison in low and high intensity of cavitation for pump geometry at $T = 40°C$

HFC flow was simulated in CFX with POP1 condition through pump geometry, as the starting point of the numerical simulation. At this point there is no erosion and the produced water

vapour, is negligible. By increasing the pressure difference between inlet and outlet, the vapour bubbles started to shown up in the fluid flow, **Figure 18**.

Nohmi3 index was evaluated not only on mid-plane but also on the sidewalls where the erosion damage might be expected. The results from two most intensive erosion at 40°C on the pump geometry are shown in **Figure 19** and **Figure 20**.

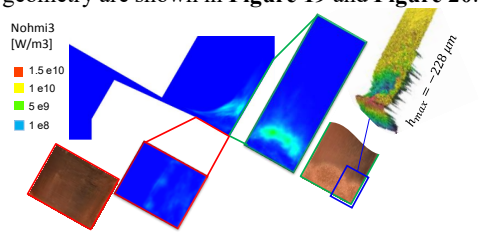

Figure 19: Comparison between simulated cavitation aggressiveness determined using Nohmi3 and experimental 3D surface scan of erosion sample for POP4 in pump

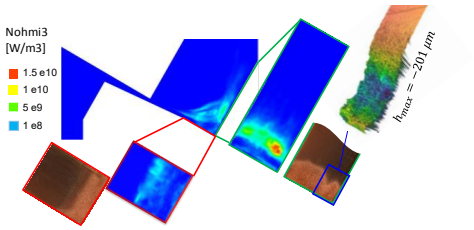

Figure 20: Comparison between simulated cavitation aggressiveness determined using Nohmi3 and experimental 3D surface scan of erosion sample for POP5 in pump

Figure 19 and **Figure 20** indicate that Nohmi3 can predict the erosion also over pump geometry correctly in the terms of spatial and temporal and it can be developed for erosion prediction of other hydraulic geometries.

6. CONCLUSION AND OUTLOOK

Fire-resistant HF fluids, mainly HFC fluids, are legally required in branches of industry with ignition risk. However due to the low boiling point of water, the operating range of HFC components is severely limited compared to conventional mineral oil. The cavitation phenomena when using HFC fluids and the associated cavitation erosion when the permissible operating limits are exceeded are particularly critical. For an economic development of HFC components, however, a systematic processing of the HFC-specific cavitation properties as well as an efficient possibility as a simulation-based prediction of cavitation erosion is missing.

In order to enable a simulation-supported mapping of the flow processes, the material value of the cavitation-relevant fluid parameters was first determined. The experimental investigations showed a significantly lower air dissolving capacity of HFC compared to conventional mineral oil, HLP.

In the further course of the work, the cavitation behaviour was analysed on a typical valve geometry and on the control edge of an axial piston pump experimentally to validate the fluid and cavitation model numerically. All experiments were carried out with HFC and HLP for comparison purposes. The subsequent study on the suitability and validation of different simulation model approaches showed that for the correct mapping of the cavitation-relevant pressure drop the calculation of the large-scale vortices by means of LES simulation is necessary.

With the experimental cavitation erosion analysis, a simulation-based erosion model was developed and comprehensively validated. Corresponding erosion tests were completed with HLP and HFC on two typical hydraulic geometries. Additionally, the damage area and the volume removal of the respective erosion samples were scanned with a 3D profilometer.

The results of the numerical prediction of the cavitation erosion showed that the cavitation index Nohmi3 could predict the damage intensity and its spatial distribution well for both geometries. Based on numerical and experimental analysis on the valve and pump geometry, it was found that, the degree of local erosion risk over the solid surface could be well predicted qualitatively with the cavitation index Nohmi3.

The documentation of the methods and used tools, with results obtained from this research should enable manufacturers to apply them to their own products in order to make their hydraulic equipment more efficient and robust.

NOMENCLATURE

α_{nuc}	-	Nucleation site volume fraction
F_{cond}	-	Condensation coefficient
F_{evp}	-	Evaporation coefficient
h	μm	Depth
m	kg	Mass
p	bar	Pressure
Q	$\frac{l}{min}$	Volume flow rate
R	$\frac{kg}{s \cdot m^3}$	Total interphase mass transfer rate per unit volume
R_b	mm	Bubble radius
R_g	$\frac{J}{kg \cdot K}$	Specific gas constant
t	s	Time
U	$\frac{m}{s}$	Velocity
η	$\frac{kg \cdot m}{s}$	Dynamic Viscosity
ϱ	$Kg/m3$	Density
T	$°C$	Temperature

REFERENCES

[1] Bock W (2009) Hydraulic Fluids – a Liquid Machine Element. VFMZ, Mainz, 2009

[2] Bakir F., Rey R. (2004) Numerical and Experimental Investigations of the Cavitating Behavior of an Inducer. Int. J. Rotating Mach., 10(1), pp. 15–25, 2004

[3] Bosch Rexroth (2015) Schwerentflammbare Hydraulikflüssigkeiten–wasserhaltig, Anwendungshinweise und Anwendungsanforderungen. RD 90223, 2015

[4] Fuchs Petrolub (2002) Im Brennpunkt: Optimaler Brandschutz mit schwer entflammbaren Hydraulikflüssigkeiten. FuchsInfo, Mai 2002

[5] Herschel D (2014) Druckflüssigkeiten für Hydraulikanlagen. Springer, 2014

[6] Hodges P (1996) Hydraulic Fluids, Elservier Ltd., Oxford, 1996

[7] Kim S, Murrenhoff H (2012) Measurement of Effective Bulk Modulus for Hydraulic Oil at Low Pressure. Journal of Fluids Engineering, 134 (2):021201, 2012

[8] Mauger C (2012) Shadowgraph, Schlieren and interferometry in a 2D cavitating channel flow. pringer-Verlag, 2012

[9] Merzkirch W (1981) Density sensitive flow visualization, in: Fluid Dynamics, Ed. R. J. Emrich, Methods of Experimental Physics, Vol. 18, Academic Press, New York, 1981

[10] Mueller L (2013) Messverfahren und numerische Modellierung von Kavitation in einem ölhydraulischen Ventil. O+P 2, 2013

[11] Nohmi M, Ikohagi T, Iga Y (2008) Numerical Prediction Method of Cavitation Erosion. Proceedings of FEDSM, 2008

[12] Petzold M (2016) Dosiergenauigkeit, Wirkungsgrad und Geräusch von elektromagnetisch angetriebenen Kolbenpumpen, Dissertation, TU Dresden, 2016

[13] Schweitzer P. H., Szebehely V.G. (1950) Gas Evolution in Liquids and Cavitation. Journal of Applied Physics, Vol.21, pp. 1218-1224, 1950

[14] Seo J. H. (2008) Prediction of Cavitating Flow Noise by Direct Numerical Simulation. J. Comput. Phys., 227(13), pp. 6511–6531, 2008

[15] Settles G (2001) Schlieren and Shadowgraph Techniques. Springer-Verlag, ISBN 3-540-66155-7, 2001

[16] Totten G. (2000) Handbook of Hydraulic Fluid Technology. United States of America, Marcel Dekker, 2000

[17] Totten G, Wills D, Feldmann D (2001) Hydraulic Failure Analysis – Fluids, Components, and System Effects. ASTM special technical publ. 1339, 2001

[18] Zwart P, Gerber A, Belamri T (2004) A Two-Phase Flow Model for Predicting Cavitation Dynamics. ICMF 2004 International Conference on Multiphase Flow. Yokohama, Japan, 2004

[19] Fuchs data sheet (2014) Hydrotherm 46 M type HFC data sheet. Fuchs, 130, 2014

[20] Elaskon data sheet (2017) HLPD 46, mineral oil. Elaskon, 2017

peer reviewed

BASIC ASPECTS WHEN USING IONIC LIQUIDS AS A HYDRAULIC FLUID

Darko Lovrec[1]*, Roland Kalb[2], Vito Tič[1]

[1]*University of Maribor, Faculty of Mechanical Engineering, Smetanova 17, SI-2000 Maribor, Slovenia*
[2]*Proionic GmbH, Parkring 18, A-8074 Grambach, Austria*
* Corresponding author: Tel.: +386 2 220 7611; E-mail address: darko.lovrec@um.si

ABSTRACT

Hydraulic development engineers and tribology specialist still exert substantial effort, time and resources into finding a hydraulic fluid that would be near an ideal fluid. In addition to its basic physico-chemical properties, it must meet a number of other requirements related to its practical use within hydraulic system and the materials used therein. Ionic Liquids, as novel lubricants, offer the solution in this regard.

The paper gives an overview of the basic properties of selected and tested Ionic Liquids suitable for use as hydraulic fluids. The practically obtained data refer to the basic physico-chemical properties of Ionic Liquids and properties important for practical use within hydraulic system, e.g. compatibility with materials. The results are given in a comparison with common mineral oil based hydraulic oil.

Keywords: Hydraulic fluids, Ionic Liquids, Properties, Material compatibility, Evaluation

1. INTRODUCTION

The lubricant used as a hydraulic fluid must fulfil a number of requirements. It would have to be non-flammable, non-poisonous, corrosion resistant, would have excellent lubricating properties, temperature-independent physico-chemical properties and appropriate viscosity, furthermore energy efficient, mechanically resistant, providing a long service life of components wherein it is used. Besides, it should be also compatible with materials used within hydraulic components etc.

Lubricants' manufacturers try to approach these requirements with special additives added to commonly used mineral based oil in order to improve certain property (e.g. lower temperature dependence of viscosity), which can lead to the deterioration of other properties (e.g. foaming tendency). In addition, such additivated mineral based hydraulic oil or synthetic hydraulic fluid is not necessarily environmentally friendly, absolutely bio-degradable and may have negative effects on the environment. A completely new alternative that to reduce the various shortcomings of mineral based oils successfully are Ionic Liquids – ILs, used as novel, high efficiency lubricants.

Ionic Liquids represent a new class of high-tech liquid materials with extraordinary properties that can have nanostructured organisation. A number of research findings have opened up many new areas of application for the use of these liquids, including hydraulics. Based on their unconventional properties ILs allow fundamentally new approaches to technical challenges. They have the potential to open doors to radical innovations. [1]

2. IONIC LIQUIDS SELECTION PROCESS

Ionic Liquids, a combination of cations and anions, a new class of purely ionic, salt-like materials that are liquid at unusually low temperatures, have been recognized as very promising high-performance lubricants and have attracted considerable attention within the field of tribology.

A large number of studies have already been carried out in this area so far, but only few with ILs suitable for use within hydraulic systems. The choice of cation and anion in an IL, as well as the design of ion side chains, determine the fundamental properties of IL, which permits the creation of tailor-made lubricants and lubricant additives. [2]

When specified cation is combined with specified anion a new IL is obtained. While the process is not done by trial and error but rather knowingly, these can be synthesized into a completely new material with entirely new properties. In our case, we are searching for "liquid salts", which would have the characteristics of a perfect hydraulic fluid. The number of possible combinations of anions and cations is extremely high (1.10^{18} combinations) that is why we have the opportunity to adapt each IL for particular usage.

Despite the excellent individual physico-chemical properties, it is very difficult to find an IL that would combine the majority of favourable physico-chemical properties and characteristics of the "green", high performance hydraulic fluid. For well-known and widely used hydraulic oils, numerous of testing procedures have been developed in order to test almost all of their properties, while as in case of ILs, the situation is completely different. One possibility is to use the same methods as for conventional hydraulic fluids, or another possibility is to use your own, non-standard ones.

When isolating ILs appropriate for use as a hydraulic fluid, the procedures are not as uniformly definite as with other lubricants since their unique properties demand the use of special laboratory equipment. The most of laboratory measurements can be carried out by a wide assortment of typical analytical methods, out of which many were also applicable for ILs, e.g. measurements of density, viscosity, VI-index, corrosion resistance, lubricating properties, flammability, foaming tendency etc. These tests can be carried out within general laboratory using the conventional measuring devices and standards:

- Flash/fire point; ASTM D92/ASTM D93,
- Determination of density; ISO 12185,
- Kinematic viscosity; ASTM D445,
- Viscosity index; ASTM D2270,
- Corrosion in humid chamber; DIN EN ISO 6270-2,
- Corrosiveness to copper; ASTM D130,
- Demulsifying properties; ASTM D1401,
- Foaming of lubricating oils; ASTM D892,
- Welding point and wear diameter; IP 239-85,
- Pour-point; ASTM D 97…

Measurement procedures, sample amounts and the equipment used, mainly relate to the conventional lubricants in accordance with the relevant standard. Tests of ILs properties based on procedures intended mainly for mineral based oils can serve us as a starting-point.

In addition to the mentioned standard tests, several specific, targeted measurements of physico-chemical properties were also used for testing the ILs, as well as for comparing the fluids. Some of these tests, e.g. measurement of breakdown voltage, filterability, Stribeck's curve, contact angle, or to check a compatibility with materials used within hydraulic system e.g. compatibility with reservoir paint coats, compatibility with different sealing material, measurement of compressibility and sound propagation… These tests need to be carried out with special measurement equipment, in specialised laboratories and/or under specific conditions, requirements or procedures. Some of these methods are adapted for testing Ionic Liquids and are not standardized.

3. BASIC PROPERTIES TESTS

Corrosion resistance, good lubricating properties, appropriate fluid density and suitable viscosity in the range of operating parameters, are undoubtedly the remarkably important fluid parameters that ensure long-lasting, energy-efficient and cost-effective operation of the hydraulic system.

3.1. Corrosion protection

Good corrosion protection is a very important feature of a hydraulic fluid. Due to the fact that the Ionic Liquids are actually salts, it can be expected that the corrosion protection would be one of the parameters that is most difficult to achieve in comparison to conventional hydraulic fluids, particularly, the mineral-based oils. That was confirmed by laboratory tests, especially by the very harsh corrosion test in a humid chamber, where most of tested ILs resulted worse than the mineral hydraulic oil.

Resistance to corrosion was tested in three different ways:

- Corrosion test in humid chamber according to DIN 51386-1 and DIN EN ISO 6270-2 was conducted at constant conditions [3]. The chamber was closed throughout the test (with

temperature of 40 °C and relative humidity of 100 %), whereby resistance to corrosion is express in cycles (1 cycle = 24 h).
- Standard test method for corrosiveness to copper according ASTM D 130-04.
- Corrosion in open air (practical method, in accordance with the real atmosphere/operating conditions).

Figure 1 shows the first signs of corrosion in a humid chamber for some tested ILs compared to mineral hydraulic oil HLP VG46. Relevant values in time are given in **Table 1**. It is evident that corrosion protection in most cases has not reached 1 cycle. In that case, the time in minutes or hours up to the occurrence of the first signs of corrosion is added in parentheses. According to this test the corrosion protection of tested ILs is worse in comparison to HLP mineral oil.

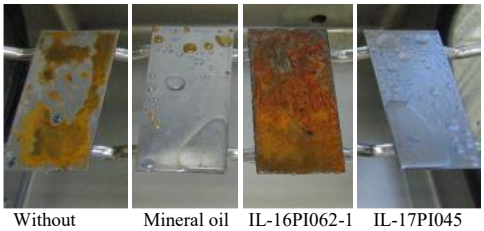

Figure 1: Test plates coated with different lubricants in humid chamber after 24 h

In other cases the corrosion protection is comparable to that of the mineral-based hydraulic oil or even much better, as it can be seen on the last three samples in the Table 1 and respectively from **Figure 1** (IL-17PI045).

Due to the presence of copper-based non-ferrous metals in hydraulic components, it is also necessary to perform a corrosion test of these materials. The corrosiveness to copper was carried out in accordance to ASTM D 130 Standard. Tests have shown that corrosiveness to copper is much lower than that of steel and does not represent any problems. [4]

Also a practical, non-standardised corrosion resistance test, where ILs-coated test plates were exposed to ambient air of average humidity, showed similar interdependencies. Unlike the very harsh test in a humid chamber, the times elapsed when the first signs of corrosion appeared were much longer: mineral oil after 60 days, EMIM-$EtSO_4$ after 2 to 3 days, while as in case of IL-17PI045 the corrosion has not appeared even after 3 months.

More information on corrosion tests, test procedures and conditions and more detailed results are available in the literature, e.g. [4].

When performing durability ILs testing under real operating conditions (changing operating pressure profile 10-210-10 bar, tank contact with ambient air, operating temperature 50°C, load cycle time 2 s, test duration 1 million cycles) after system disassembling and inspection of the vital hydraulic components (pump, tubes, proportional valve, cooler, sensors, tank, filter housing…) no signs of corrosion were observed.

3.2. Lubrication properties and wear

Lubrication properties were first examined using the 4-ball standard test method for lubricants; IP 239/85. With this method we have determined the welding-load and the wear-diameter and was used for the first evaluation of the lubricating properties of ILs. The friction conditions were investigated subsequently on the basis of the obtained results.

The lubricating properties of ILs, which have passed the corrosion test, are in general considerably better than those of conventional mineral based hydraulic oils or other liquid lubricants. **Figure 2** shows the comparison between the welding-loads and wear-diameters` values for different samples of ILs compared to the mineral hydraulic oil HLP 46.

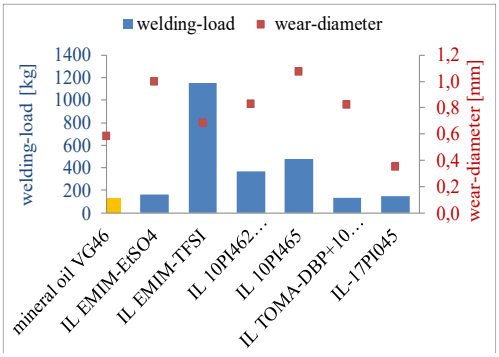

Figure 2: Lubrication properties of tested ILs in comparison with mineral oil

The lubricating properties of some ILs are considerably better than those of HLP VG46 mineral oil. Some samples have an exceptionally high welding-load, for example EMIM-TFSI had as much as 1150 kg, which pointed out exceptional properties at extreme pressures but,

interestingly, the wear-diameter was larger than that of the mineral oil, implying that the anti-wear properties were worse. Because the focus in on better wear properties this IL would be potentially more suitable for use in gearings, maybe even as metalworking fluid during metal machining. In regard to other ILs with high welding-loads values the limitation was, in particular, worse corrosive protection in the presence of moisture or in proper viscosity for the use in hydraulic systems.

The next approach to check the quality of lubrication is to perform Stribeck's test, representing the friction coefficient depending on the Stribeck's parameters, including viscosity, relative surface velocity and load. The measurements of Stribeck's curve for HLP hydraulic oil and some ILs were carried out using a MTM device for measuring friction and lubricating film thickness with ball-disc configurations.

The measured Stribeck's curves for VG46 mineral oil and two ILs at the ambient temperature *T*o and 60 °C are shown in **Figure 3**.

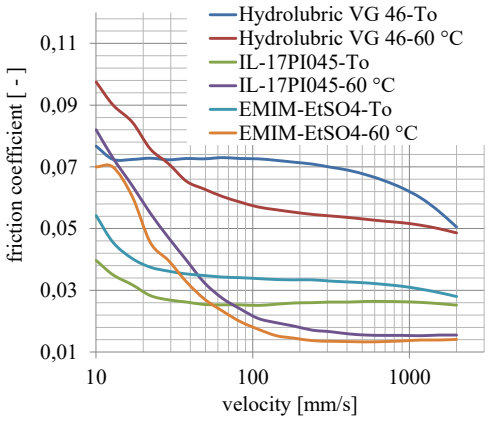

Figure 3: Stribeck's curves of two tested ILs vs. hydraulic mineral oil

It can be seen that the friction coefficient of the mineral oil within the entire range is considerably higher than that of both tested ILs. The two ILs have a very similar friction coefficient within the entire range, the IL-17PI045 having a slightly lower friction coefficient at room temperature, and the EMIM-$EtSO_4$ at 60 °C. All three fluids showed much larger difference between the lowest and highest measured values at 60 °C than at room temperature. Furthermore, at higher temperature the friction coefficient was higher in the range of boundary and mixed lubrication, and lower in the range of elasto-hydrodynamic lubrication. That is probably caused by a smaller lubricating film thickness at higher temperatures, resulting in more direct contacts of the ball and disc surfaces within the range of the boundary and mixed lubrication. More details regarding the lubricating properties, measuring principles and devices used, are given in literature [5] and [6].

3.3. Density, viscosity and VI-Index

One of the most important physico-chemical properties of hydraulic fluids is its kinematic viscosity. Viscosity is an essential property of lubricating oil as it affects its capacity to form a lubricating film or to reduce friction and wear. That is a criterion for resistance to flowing of the fluid under active pressure, except the flow-type, defines the leakage loses and is highly temperature dependent.

Suitable viscosity, with a sufficiently high load capacity of the lubricating film and its low temperature independence, make it possible to ensure the energy-efficient operation of the hydraulic system over a wide operating temperature range.

In case of too high fluid viscosity at low temperature, cavitation, insufficient lubrication and low system dynamic can occur, leading not only to reduced hydraulic-mechanical efficiency, but also to component damage (e.g. at insufficient filling of the pump). Cavitation can also occur when the liquid in a pump turns to a vapour at very low pressures.

On the other hand, too low viscosity at elevated temperatures leads to excessive leakage and, consequently, poor volumetric efficiency, and to insufficient lubrication. Due to the interruption of the lubricant film, this leads to increased friction and wear, which are reflected again in increased leakage.

Apart from the above-mentioned risks in the operation of the device, both too low and too high viscosities are reflected in the volumetric and hydraulic-mechanical efficiency, and, consequently, the overall efficiency.

The resulting requirements must be fulfilled by the lubricant in general: The ability of a lubricant to maintain optimum viscosity under a wide temperature operating window can be achieved with a shear stable fluid, with temperature independent viscosity (with high

viscosity index VI), and with the low friction coefficient at starting and operating temperatures.

Lubricants' manufacturers try to achieve these requirements with special additives that improve certain properties (e.g. lower temperature dependence of viscosity), but, on the other hand, other properties may degrade. In addition, such a fluid is not completely environmentally friendly. Ionic Liquids, as a completely new alternative, solve most of these problems successfully, and can be used as novel high efficiency lubricants.

Kinematic viscosity was measured by capillary viscometers and is given in [mm^2/s]. The measurement is simple, fast and precise, as well as performed at two standard temperatures of measuring, 40 °C and 100 °C. The two kinematic viscosity data at both temperatures are, at the same time, the basis for determining the viscosity index. For the kinematic viscosity measuring, a Cannon-Fenske viscometer with the necessary peripheral equipment (tempered bath, stopwatch) was used and the measurement was performed according the ASTM D445 Standard.

The viscosity index values of higher refined mineral based oils on the market are about 100, while the multi-grade and synthetic oils have a higher viscosity index VI i.e. around 150 and higher. A favourable effect of expanding the temperature operating range can be achieved with a lubricant of the same viscosity class VG along with a higher viscosity index. The Ionic Liquids' viscosity indexes are, in general, higher than those of mineral based oils, wherein the viscosity grade can be adjusted.

The viscosity of most ILs can be deliberately adjusted, which is a significant advantage of these liquids. Another advantage is their high viscosity index, which is commonly much higher than VI of general HLP mineral oils.

Less "preferred property" is the density of ILs suitable for use as a hydraulic fluid, since their densities are usually higher than densities of mineral based hydraulic oils. Density of the ILs range from 944 kg/m^3 up to 1200 kg/m^3 or even higher (measured at 20 °C). This property is negatively reflected in pressure loss, flow rate...

Table 1: Comparison of basic physicochemical properties

Property/Method	Viscosity 40 °C ASTM D 445 [mm^2/s]	Viscosity index ASTM D 2270 [/]	Welding point IP 239-85 [kg]	Wear diameter IP 239-85 [mm]	Corrosion, humid chamber DIN EN ISO 6270-2, cycle
Sample					
Mineral based oil VG 46	47,07	119	140	0,58	0 (3 h)
IL-1 EMIM-$EtSO_4$	39,44	168	180	1,00	0 (15 min)
IL-2 EMIM-TFSI	71,89	132	1120	0,65	0 (1,5 h)
IL-3 10PI462 (EMIM-TFSI)	-	-	-	-	0 (30 min)
IL-4 16PI028-5 (quaternary ammonium dialkylphosphate)	-	-	-	-	0 (30 min)
IL-5 10PI028-3 (quaternary ammonium perfluorocarboxylate)	-	-	-	-	0 (45 min)
IL-6 16PI062-2 (quaternary ammonium dialkylphosphate)	59,14	/	135	0,82	0 (4 h)
IL-7 16PI062-1 (quaternary ammonium perfluorocarboxylate)	61,46	/	-	-	0 (5 min)
IL-8 18PI094 (quaternary ammonium perfluorocarboxylate + 30 % EG)	49,28	109	125	1,04	0 (15 min)
IL-9 17PI064 (quaternary ammonium dialkylphosphate +7 % H_2O)	102,90	105	190	0,49	1
IL-10 18PI163 (quaternary ammonium dialkylphosphate + 40 % NMP)	47,36	155	160	0,38	0 (3,5 h)
IL-11 17PI045	46,59	155	145	0,35	0-1 (>7,5 h)

4. OTHER PROPERTIES TESTS

In addition to the basic physico-chemical properties mentioned in Chapter 3, other properties, such as compressibility (stiffness), foaming tendency, electrical conductivity and filterability, are also important for Ionic Liquids to be used as a hydraulic fluid.

4.1. Compressibility of Ionic Liquids

Bulk modulus of the fluid is crucial for hydraulic systems, particularly for high-pressure hydraulics. It can seriously affect a hydraulic system's performance and its power level, pressure peaks, response time, pulsation and control stability. Water-based hydraulic fluids are considered to be less compressible than conventional mineral oils (low bulk modulus values for oils). Ionic liquids, however, are even less compressible compared to the water. This makes ILs extremely interesting for hydraulic applications.

The compressibility of fluids can be measured in two ways; through changes in pressure and the volume by a known initial volume of the fluid and through the speed of sound that spreads across the fluid. Both mentioned methods were used to determine the compressibility of Ionic Liquids.

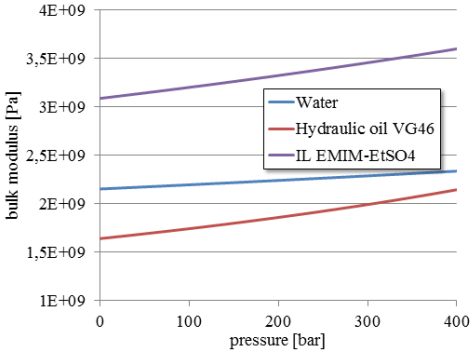

Figure 4: Measured bulk modulus versus pressure for all three considered fluids

More details on the specially designed compressibility testing device, measuring system and measuring procedure are available in the literature [7]. The measured compressibility (respectively bulk modulus) of one discussed IL (EMIM-EtSO4) in comparison to water and standard mineral based oil is shown in **Figure 4**.

The same applies to other types of Ionic Liquids. In regard to the dynamic behaviour of a hydraulic system with built-in IL as hydraulic fluid, special attention should be paid to the compressibility of the used IL.

Low compressibility of a hydraulic fluid leads to a high efficiency factor for a high-pressure machine. In general, all ILs are very incompressible liquids.

As shown in **Figure 4**, the bulk modulus value for EMIM-EtSO4 amounts approx. $3.2 \cdot 10^9$ Pa, and is much higher than that of standard hydraulic mineral oil. This makes ILs extremely interesting for hydraulic applications; however, all the phenomena related to the compressibility of the medium must be taken into consideration: the magnitude of pressure shocks, the precision of positioning of the controlled actuators, the oscillations, the unsteady motion, or the pulsation of the hydraulic pumps [8].

4.2. Foaming tendency

The foaming tendency was analysed for Ionic Liquids with good corrosion protection and lubricating properties, but not in cases when it had been previously discovered that the IL is unsuitable for use as hydraulic fluid because of some other drawbacks. The standard foaming test of the promising samples of ILs e.g. IL-17PI045 were performed according to ASTM D 892 Standard in all 3 sequences. The results are generally positive, except for some samples of ILs e.g. 17PI064 (TOMA-DBP+7 % H_2O) sample, where foaming in sequence I was extremely high. The results are indicated in table 2.

Table 2: Results of the foaming test – ILs vs. oil

Fluid type: Foaming test method ASTM D 892 (ml/ml)	IL-17PI045	TOMA-DBP +7 % H_2O	EMIM-$EtSO_4$	Mineral oil VG 46
Sequence I. (24 ˚C)	70/0	600/20	580/20	0/0
Sequence II. (93,5 ˚C)	0/0	/	/	30/0
Sequence III. (24 ˚C)	80/0	/	/	0/0

When testing sample IL-17PI045 in sequences I and III, after completion of injection a small foam quantity was present. The foams were quickly disappearing and after 10 minutes they were no longer present.

The sample IL-17PI045 e.g., had the more properties in the range of the mineral hydraulic oil, namely viscosity, viscosity index, corrosion properties, lubricating properties (higher welding point and smaller wear diameter than in the case of mineral oil; good foaming properties and compatibility with hydraulic system components. The greatest draw-backs included low boiling and flash points (because of the solvent content) and incompatibility with the usual tank paint coats, which means that during practical use the latter should not be painted.

The foaming problem occurs mainly in the consistent implementation of the standardized foaming test. Foaming was not a problem with the practical use of ionic liquids on a real hydraulic system, under realistic operating conditions. This point to a new aspect: the appropriateness of using the standard testing procedures, normally applicable to mineral oils, for completely new types of fluids, of a completely different composition. The same applies to the filterability test mentioned under point 4.4.

4.3. Electric breakdown voltage

In some cases, the hydraulic fluids are required to have similar properties as transformer oils, i.e. heat capacity, electric insulation and oxidation stability. High heat capacity and oxidation stability are two basic properties hydraulic oils must have, whilst good electric insulation is an additional requirement which must be met for specific systems, for example, when the electric motor is submerged in the hydraulic fluid.

Due to the (currently) higher cost of ILs, applications are targeted at small aggregates where this property may be important. According to the international standard IEC 60296, edition 4, 2012 “liquids for electro-technical applications – non-used mineral insulation oils for transformers and switching the breakdown voltage of the transformer oil denote their resistances to electric voltage in the electrical equipment. The breakdown voltage is measured according to standard IEC 60156.

Two ionic liquids IL-17PI045 and EMIM-EtSO4 were tested and compared to the mineral hydraulic oil VG46. Measurements were performed by the use of the Megger OTS 60 PB apparatus in conformity with the standard. The results are indicated in table 3.

Table 3: Breakdown voltages of ionic liquids and mineral hydraulic oil

Fluid type:	Breakdown voltage (kV)	Dielectric strength (kV/cm)
EMIM-$EtSO_4$	< 1,0	< 4
IL-17PI045	< 1,0	< 4
Mineral oil VG46	60	240

The breakdown voltages of mineral oils are very high and are quite comparable with best transformer oils (usually 40 kV to 60 kV). On the other hand, the breakdown voltages of most ILs (among them e.g. EMIM-$EtSO_4$; and IL-17PI045) are very low.

Therefore, they are not suitable for applications where the electric motor would be submerged in oil. That aspect must be considered when constructing hydraulic systems with small, compact units where, in some configurations, the electric motor without housing is directly submerged in the hydraulic fluid. For conventional hydraulic units design this property is not relevant.

4.4. Filterability

As the fluid in the hydraulic system acts as a lubricant reducing wear of hydraulic elements, elimination of solid particles in the circuit is very important. Especially, where clearances in the hydraulic system are small and a high degree of fluid cleanliness is required for trouble-free operation and reaching the expected useful life time of components. Since contaminants are removed by filters, the next relevant test is hydraulic fluid compatibility with filter cartridge material.

The ability of the hydraulic fluid to flow through fine filter elements without their clogging is called the filterability. The filterability of mineral oils is analysed according to ISO 13357 Standard [9], which imposes the use of a cellulose filter. In parallel with the mentioned filterability test with the cellulose filter material, additional material compatibility tests can be carried out.

As indicated in the ISO 13357 Standard, in addition to mineral oils the method can also be used also for other liquids. However, the latter are

maybe not compatible with cellulose membrane filters, which, in our case, proved to be true. As both ILs (EMIM-$EtSO_4$; and IL-17PI045) deformed the cellulose filter membrane determination of filterability by this method was not possible. The filter element covered with IL-17PI045 started to decompose immediately after the contact with liquid and dissolved rapidly. The sample of EMIM-$EtSO_4$ deformed the filter element into a glassy circle. For more details see [4] and [10].

The above described problem is related to ISO 13357 test, which imposes the use of a cellulose filter. However, in practice there were no significant problems with IL filter compatibility observed, since generally other materials are used for filters.

Nevertheless, it would be necessary to supplement the suitability of this Standard for new types of hydraulic fluids – e.g. ILs.

5. MATERIAL COMPATIBILITY

Compatibility with materials commonly used in hydraulic components must be tested for each new hydraulic fluid. This is especially important in the case of Ionic Liquids. Mentioned filter material compatibility is only one aspect to the otherwise wide-ranging issue of material compatibility.

5.1. Compatibility with paint coat

Most hydraulic tanks are painted inside and outside using different types of paint coats. Therefore, it is very important that the IL used as hydraulic fluid is compatible with the used paint coat. As known, the compatibility the paint coats with mineral based hydraulic oils usually is not a problem.

Concerning protective coatings for hydraulic reservoirs, in particular the compatibility of the protective paint in regard to the type of hydraulic fluid, there is no specific standard which would be related to this issue in detail. There are more or less recommendations or recommended practices (RP), mostly linked to related areas, providing guidance on achieving effective corrosion control in storage tanks. They contain information about suitable lining materials, surface preparation, lining application, curing, and inspection of tank bottom linings for existing and new storage tanks, e.g. API RP652 Standard – Linings of Aboveground Petroleum Storage Tank Bottoms. Thus, manufacturers of lubricants are using simple, practical experiments e.g. testing the continuous contact by immersing painted metal samples in the liquid under test, at constant room temperature: 20 to 25 oC.

The test of paint coat compatibility was performed with two selected ILs, IL-1 (EMIM-EtSO4) and IL-11 (17PI045) – see Table 1. The metal plate samples were painted with two paints typically used for the tank interior and exterior. The interior is painted with epoxy primer coat, while the exterior is additionally coated with epoxy thick-layer finishing coat. Some metal plate samples were painted only with the interior paint while others were additionally painted with exterior finishing coat.

The test compromised about 40 ml of each IL that were poured into glass cups; then single metal plate samples coated with either interior or exterior paint coat were introduced into them. At the beginning of the test the entire metal plates were wetted with the tested liquid; during testing the bottom part of the metal plate was permanently submerged into the liquid, while the top part was above the surface level as shown in **Figure 5**.

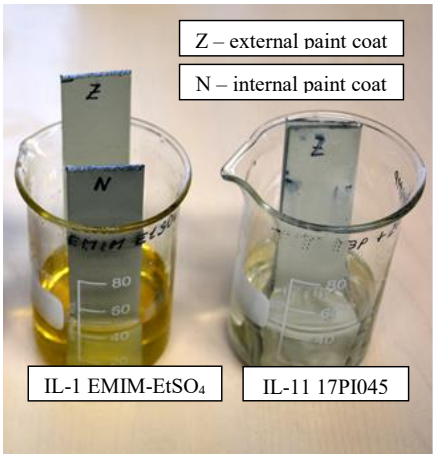

Figure 5: Test of compatibility with paint coats

Already after a few days of testing, it was clear that the IL-11 (17PI045, which in all previous tests proved to be an excellent substitute to mineral oil) was not compatible with internal, neither the external paint. The paint coat started to wrinkle and peeled off where the plate was permanently submerged into the test liquid.

5.2. Compatibility with seal materials

The compatibility of an elastomer with hydraulic fluid is a critical factor in system performance. Although considerable effort has been invested in the attempt to empirically predict seal material compatibility, these efforts have not been successful to date.

One of the main reasons is the inability to accurately model the broad range of environmental conditions and chemical interactions encountered in an actual hydraulic system.

There are numerous elastomer seal materials. However, nitrile (NBR), fluorocarbon (FKM), ethylene propylene (EPR, EPDM), chloroprene (CR), and urethane (AU, EU) are the most commonly used materials for industrial applications and they are still the subject of development.

A seal compatibility test procedure may be performed in accordance with ASTM D1414. Tests that should be performed on the O-rings refer to Hardness change, Volume swell, Shrinkage, as well as mechanical tests like Tensile strength change, Elongation change and Work function change. Detailed test procedure is described in the literature, e.g. [10], [11].

All materials, such as FPM, POM, HPU, NBR, HPU USI, EPDM, MVQ, PTFE I, and for the wear ring, e.g. SCB, PTFE, used for sealing are well compatible with the most commonly used mineral oils, so their material composition is focused to oils. In order to use well-known and established sealing materials with ILs, we need to test compatibility of each sealing material with each IL. Since this can be fairly extensive work, it is reasonable to test only ILs that have proven to be excellent in all the properties mentioned so far.

After conducting compatibility tests of most common sealing materials with certain types of ILs, we came to interesting findings. In some cases, no changes in dimensions, mass and volume of O-Ring were observed, as well as no change in the colour of the seal (e.g. POM, PTFE I with EMIM-EtSO4), or only minor changes occurred (NBR, EPDM, MVQ with EMIM-EtSO4). On the other hand, some sealing materials in combination with certain ILs were completely decomposed in short test time.

In addition, the most suitable sealing material for a given IL (according to the standard test) turns out to be less suitable during the real operation. Conversely, the less appropriate one turns out to be a better solution.

The very briefly mentioned examples do not directly provide useful guidance on the selection of suitable sealing materials with a specific type of IL, but rather present how extremely complex it is to test otherwise well-known materials with new types of fluids.

Furthermore, test results obtained by standardised tests or recommendations may not be directly applicable to real operating systems under real operating conditions. This is especially important when we want to use an IL within a hydraulic system (that was designed for mineral oil) without major modifications.

6. CONCLUSION AND OUTLOOK

The presented results of the research work give the suggestions for the use of Ionic Liquids within hydraulic systems together with some limitations. The first ILs which would be tested were corrosive in the presence of moisture. Consequently, even greater attention must be paid to moisture prevention in the hydraulic system. Alternatively, stainless steel hydraulic components can be used, which, however, results in undesirable structural and price changes.

Some Ionic Liquids, such as e.g. IL-11 (17PI045), show the best proposition for use as a hydraulic fluid, since it has much better properties than mineral oil. But on the other hand is not compatible with conventional paint coats of hydraulic tanks. Therefore, the latter must not be painted, when that liquid is used. Another limitation in the use of this liquid is incompatibility with the cellulose filter elements. As a result, absorption filter elements, usually based on cellulose, could not be utilized, when this liquid is used in the hydraulic system.

At present, one of the greatest limitations for wider technical use of Ionic Liquids, also in hydraulic systems, is considerably higher price in comparison to conventional hydraulic mineral oil (due to the production of small quantities). The target areas of use of Ionic Liquids in hydraulic equipment are currently small-volume hydraulic systems, such as found in wind turbines, mobile hydraulic equipment etc. It follows that each type of IL needs to be tested individually for each important property, although some of its properties have proven to be excellent.

Given information regarding different ILs physico-chemical properties, material compatibilities, testing procedures and Standards etc. can serve users as a guideline for the selection and use of Ionic Liquids as a hydraulic fluid. On the other hand, the information is also valuable to Ionic Liquids developers as first guidelines in which direction these fluids need to be developed in the future.

REFERENCES

[1] Kalb R (2015) Ionic liquids – A New Generation of High-Tech Engineering Liquids, International Conference Fluid Power 2015, Maribor, Slovenia, 49-77

[2] Feng Z, Yongmin L, Weimin L (2009) Ionic liquid lubricants: designed chemistry for engineering applications, Chemical Society Reviews, Vol. 9, No. 38, 2590-2599

[3] ISO 6270-2:2005 (2005) Paints and varnishes – Determination of resistance to humidity – Part 2: Procedure for exposing test specimens in condensation-water atmospheres

[4] Kambič M, Kalb R, Tič V, Lovrec D (2018) Compatibility of ionic liquids with hydraulic system components, Advances in production engineering & management, ISSN 1854-6250, doi: 10.14743/apem2018.4.306,Vol. 13, No. 4, 492-503

[5] Kambič M, Kalb R, Lovrec D (2015) Lubrication properties of ionic liquids suitable for use within hydraulic systems, International Conference Fluid Power 2015, 79-93

[6] Lovrec D, Tič V (2019) Excellent lubricating properties of ionic liquid – myth or trut, 16th International Conference on Tribology, ISSN 2620-2832, Vl. 1, No. 1, 555-562

[7] Kambič M, Kalb R, Tašner T, Lovrec D (2014) High bulk modulus of ionic liquid and effects on performance of hydraulic system, The Scientific World Journal, 1-10, doi: 10.1155/2014/504762

[8] Tič V, Manhartsgruber B, Gubeljak N, Lovrec D (2018) Low compressibility of ionic liquids and its effects on pulsation within hydraulic system. Proceedings, fluid power networks, Vol. 1, 11th International Fluid Power Conference, Aachen, Germany, 486-493

[9] ISO 13357-2:2005 Petroleum products – Determination of the filterability of lubricating oils – Part 2: Procedure for dry oils

[10] Lovrec D (2017) Filterability of ionic liquid used as a hydraulic fluid. The 5th Multidisciplinary Conference QUAESTI, Proceedings, ISSN 2453-7144, Vol. 5, Iss. 1, 160-164

[11] ASTM D 6546, Standard Test Methods for and Suggested Limits for Determining Compatibility of Elastomer Seals for Industrial Hydraulic Fluid Applications

[12] Kalb R, Lovrec D (2019) Seal material compatibility test procedure, International Conference Fluid Power 2019, 1st ed. University of Maribor Press, 133-146

peer reviewed

COMPUTATIONAL APPROACH TO THE EXPERIMENTAL DETERMINATION OF DIFFUSION COEFFICIENTS FOR OXYGEN AND NITROGEN IN HYDRAULIC FLUIDS USING THE PRESSURE-DECAY METHOD

Andris Rambaks*, Filipp Kratschun, Carsten Flake, Maren Messirek, Katharina Schmitz, Hubertus Murrenhoff

Institute for Fluid Power Drives and Systems, RWTH Aachen University, Campus-Boulevard 30, 52074 Aachen
Chair of Technical Thermodynamics, RWTH Aachen University, Schinkelstraße 8, 52062 Aachen
* Corresponding author: Tel.: +49 241 8047723; E-mail address: andris.rambaks@ifas.rwth-aachen.de

ABSTRACT

In the presented paper, the applicability of pressure-decay methods to determine the diffusivities of gases in hydraulic fluids is analysed. First, the method is described in detail and compared to other measurement methods. Secondly, the thermodynamics and the mass transfer process of the system are studied. This results in four different thermodynamic models of the gaseous phase in combination with two diffusion models. Thirdly, the influence of the models on the pressure-decay method is evaluated computationally by examining the diffusion process of air in water as all system parameters are available from literature. It is shown that ordinary pressure-decay methods are not applicable to gas mixtures like air and therefore a new method for calculating the diffusivities is suggested.

Keywords: Diffusivity, Pressure-decay method, Binary and ternary diffusion, Virial equation of state

1. INTRODUCTION

At all times in hydraulic systems a certain amount of air is present. It takes the form of entrained gaseous bubbles as well as dissolved air. Entrained air increases the risk of cavitation damage and reduces the effective bulk modulus of the fluid [1]. Dissolved air normally has no effect on the properties of the fluid but under certain circumstances it can outgas and increase the amount of entrained air in the system [1,2]. Therefore, it is of interest to determine the amount of dissolved air as well as the speed of the diffusion process.

The amount of gas solved in an ideal dilute solution is dependent on Henry's law constant and the partial pressure of the gas [3] given by equation (1):

$$x_i'' \cdot p'' = H_{ik} \cdot x_i' \tag{1}$$

In hydraulics, the Bunsen absorption coefficient is often used instead and is given by equation (2):

$$\alpha_i = \frac{(V_i')_S}{(V_k')_S} \cdot \frac{(p)_S}{p_i''} \tag{2}$$

The speed of the diffusion process depends on the diffusivity of the considered system. For binary system the diffusion process is governed by Fick's 2nd law of diffusion given by equation (3):

$$\frac{\partial C_i'}{\partial t} = D_{ik} \cdot \frac{\partial^2 C_i'}{\partial x^2} \tag{3}$$

Diffusion processes involving more than two solutes can be modelled with the generalized Fick's law or the Maxwell-Stefan equations. Due to their ease of applicability, the Maxwell-Stefan equations are chosen in this research (4):

$$\sum_{\substack{j=1 \\ j\neq i}}^{N} \frac{x_i' \cdot x_j'}{Đ_{ij}} \left(\frac{j_i'}{C_i'} - \frac{j_j'}{C_j'} \right) = -\frac{\partial x_i'}{\partial x} \quad \forall i \tag{4}$$

Currently there is only limited data available for diffusion coefficients of gases in hydraulic fluids. In this paper the authors address the problems involved in estimating the diffusivities for high pressure systems for ideal and non-ideal gases and gas mixtures. The emphasis is placed on the diffusion of nitrogen and oxygen in hydraulic fluids at pressures up to 300 bar. Thus,

the theory of diffusion for binary as well as ternary systems is analysed and their applicability to high pressure conditions is discussed. The three questions to be answered by this paper are:

1. Which method is to be preferred to measure the diffusion coefficients of gases in hydraulic fluids?
2. Is it necessary to regard air as a real gas or can the assumption of an ideal gas be made?
3. Can changes in the molar fractions of the gaseous phase be neglected?
4. How can the diffusivity of oxygen be determined for hydrocarbon-based hydraulic fluids?

2. MEASUREMENT METHODS AND APPARATUS

Several measurement methods for determining the diffusion coefficients of gases in liquids exist, originating from the research of crude oil. The measurement methods are typically categorized into two groups: direct and indirect methods.

Direct methods require measuring concentration profiles of diffusing components in order to directly determine diffusion coefficients. These methods involve either highly error-prone sampling, especially under high pressures [4], or non-invasive analysis techniques, which are usually expensive and demanding, like nuclear magnetic resonance [5], computer-assisted tomography [6,7] or planar laser-induced fluorescence [8,9].

Indirect methods require the observation of phenomena which are influenced by diffusion in order to indirectly determine the diffusivities. Indirect methods include decreasing bubble size methods [10] and constant bubble size methods [11,12]. As the names indicate the volume of a gas bubble inside the liquid phase is observed. The size can be decreasing due to absorption and diffusion of the gas into the liquid phase or the size can be constant if an appropriate gas volume flow into the bubble is provided. Also, indirect methods exist, for which the gas and liquid phase are reversed and the volume [13] or shape [14] of a liquid drop in a gas atmosphere is analysed. Bubble and drop size methods are relatively fast (experimental time within hours) and only need small sample sizes. The drawbacks are the elaborate techniques to isolate and fix the bubbles and drops without deforming them. Similar to drop and bubble size methods are microfluidic approaches in which the change of the interface due to swelling is observed [15].

Most widely used are pressure decay methods [16-22], which is the method of choice in this paper. The advantages of this method are its simplicity and applicability to wide ranges of temperatures and especially pressures. Furthermore, with the same method it is also possible to accurately determine the Bunsen absorption coefficient as shown by Rambaks et al. [23]. A picture of the apparatus is shown in **Figure 1**, the working principles are presented **Figure 2**.

A cylindrical measurement chamber is partially filled with a specified volume of hydraulic fluid and connected to a compressed air bottle. With time nitrogen and oxygen will dissolve into the hydraulic fluid until it is completely saturated. At this point in time thermodynamic equilibrium (State 0) is reached. Subsequently, the piston of the apparatus is used to compress the measurement chamber further to State 1. This is a non-equilibrium state, at which it is assumed that the diffusion process begins and persists until a new thermodynamic equilibrium has been reached in State 2. [23]

During the diffusion process, the amount of gas in the gaseous phase decreases due to the increased solubility of the liquid at higher pressures. Therefore, a drop in pressure over time is measured and used to calculate the diffusion coefficient.

Figure 1: Pressure-decay measurement apparatus

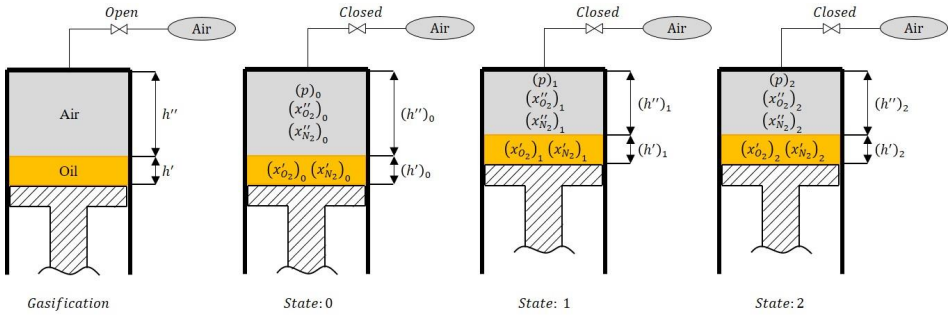

Figure 2: Working principle of the measurement system [23]

3. THERMODYNAMICS AND MASS TRANSFER

The diffusion process is governed either by Fick's 2nd law of diffusion for binary systems (3) or by the Maxwell-Stefan equations (4) if more than two species are involved in the diffusion process.

For binary systems the diffusivity of gases can be determined easily from the measured pressure-decay curves [16-22], however for some systems this approach is not applicable due to safety reasons. The prime example of this is the diffusion of oxygen in hydrocarbon-based hydraulic fluids, which poses ignition risks.

The diffusivity of oxygen in hydraulic fluids could be determined by examining the diffusion of air, but the pressure-decay curve does not provide information about the individual diffusivities of oxygen and nitrogen. To formulate a new method for estimating the diffusivities of individual gas species, different diffusion models are analysed in the following chapters. Prior to that the solubility of gases in liquids is discussed.

3.1. Solubility of gases in liquids

According to Lüdecke et al. [3], thermodynamic equilibrium of a two-phase closed system persists, if it is in mechanical (5), thermal (6) and its components are in chemical equilibrium (7).

$$p' = p'' \tag{5}$$

$$T' = T'' \tag{6}$$

$$\mu_i' = \mu_i'' \quad \forall i \tag{7}$$

In an equilibrium state of the two-phase system, a certain amount of dissolved gas is present in the liquid phase. To calculate the initial values of the concentration of dissolved gas in the liquid phase, the Bunsen absorption coefficient (2) for each species of gas has to be determined.

In Rambaks et al. [23] a method to calculate the Bunsen absorption coefficient for gases at high pressures with the use of measurement data from the equilibrium states was presented. It was found that the Bunsen absorption coefficient (2) can be calculated by evaluating the change in mass of gas in the gaseous phase given by equation (8):

$$\alpha_i = \left(\Delta m_i''\right)_{0\to n} \cdot \frac{\left(R_i\right)_S \cdot \left(T\right)_S}{\left(p_i''\right)_n \cdot \left(V_k'\right)_S} \tag{8}$$

The equation for the change in mass of gas in the gaseous phase is dependent on the pressure and temperature range and if the gas is a single species gas or a gas mixture. The reader is referred to Rambaks et al. [23] for a detailed analysis.

3.2. Binary diffusion model of ideal single species gases

The principle of binary diffusion within the context of the apparatus is depicted in **Figure 3**. The process is governed by Fick's 2nd law of diffusion (3). The initial values for the concentration as well as appropriate boundary conditions must be specified to solve the partial differential equation given by (3).

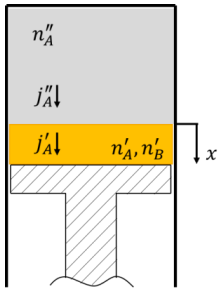

Figure 3: Binary diffusion in measurement apparatus

According to Kratschun et al. [24] and Freudigmann et al. [25] in the timescale of short deviations from a thermodynamic equilibrium of the system the diffusion process in negligible. Consequently, this allows the assumption that during the compression from State 0 to State 1 diffusion is negligible, and that the diffusion process begins only when State 1 has been reached. Therefore, the initial values for species concentration within the liquid phase can be determined based on equation (9):

$$C_i'(x, t = 0) = \alpha_i \cdot \frac{(p'')_0}{\bar{R} \cdot (T)_s} \quad \forall\, x \in (0, L) \tag{9}$$

Because of the diffusion process, the amount of substance and, therefore, the pressure in the measurement chamber decreases. The relationship between pressure, volume, temperature and amount of substance can be described with the equation of state for an ideal single species gas given by equation (10):

$$p_i'' \cdot V'' = n_i'' \cdot \bar{R} \cdot T'' \tag{10}$$

The temporal change in the amount of substance in the gaseous phase can be expressed by taking the derivative of equation (10) with respect to time, resulting in equation (11):

$$\frac{dn_i''}{dt} = \frac{V''}{\bar{R} \cdot T''} \cdot \frac{dp_i''}{dt} \tag{11}$$

By constructing a control volume around the gaseous phase, the molar flux within the gaseous phase can be determined with equation (12):

$$j_i'' = -\frac{4}{\pi \cdot d^2} \cdot \frac{dn_i''}{dt} \tag{12}$$

With the use of a surface mass balance at the interface between the liquid and gaseous phase, the molar flux within the liquid phase is equal to the molar flux within the gaseous phase and can be expressed with expression (13):

$$j_i' = j_i'' \tag{13}$$

From equations (12) and (13) it can be derived, that the molar flux of dissolved gas within the liquid phase is given by equation (14):

$$j_i' = -\frac{4}{\pi \cdot d^2} \cdot \frac{dn_i''}{dt} \tag{14}$$

According to Fick's 1st law of diffusion, the molar flux is directly proportional to the diffusivity and the concentration gradient as given by equation (15):

$$j_i' = -D_{ik} \cdot \frac{\partial C_i'}{\partial x} \tag{15}$$

Equation (15) allows to define Neumann boundary conditions at both ends of the liquid phase. At the gas-liquid interface, no accumulation of substance is possible. Therefore, the concentration gradient at the interface can be expressed with equation (16):

$$\left.\frac{\partial C_i'}{\partial x}\right|_{x=0} = \frac{4}{\pi \cdot d^2 \cdot D_{ik}} \cdot \frac{dn_i''}{dt} \tag{16}$$

Besides the Neumann boundary condition (16), a Dirichlet boundary condition given by equation (17) is specified:

$$C_i'(x = 0, t) = \alpha_i \cdot \frac{p''(t)}{\bar{R} \cdot (T)_s} \tag{17}$$

At the liquid-piston interface, there is no molar flux present and consequently the Neumann boundary condition is given by equation (18):

$$\left.\frac{\partial C_i'}{\partial x}\right|_{x=L} = 0 \tag{18}$$

With equations (9), (16), (17) and (18) the transient diffusion equation (3) is fully defined and can be solved even analytically for certain cases [19].

3.3. Binary diffusion model of real single species gases

According to Lüdecke et al. [3], the ideal gas law is applicable only in small pressure and temperature ranges. To take these limitations into account, a real gas model must be used. For single species gases it is convenient to use the compressibility factor, which is readily available from literature (see Vasserman et al. [28]).

The compressibility factor describes, how much a real gas deviates from the behaviour of an ideal gas. It is given by equation (19):

$$z_i = \frac{p_i'' \cdot V''}{n_i'' \cdot \bar{R} \cdot T} \tag{19}$$

By using equation (19) and the chain rule, an expression for the temporal change in the amount of substance in the gaseous phase is found (20):

$$\frac{dn_i''}{dt} = \frac{V''}{\bar{R} \cdot T'' \cdot z_i^2}\left(z_i - p'' \cdot \frac{dz_i}{dp_i''}\right)\frac{dp_i''}{dt} \tag{20}$$

Because the measurements are taken at high pressures, this approach is necessary due to large deviations from the ideal gas law as can be seen in **Figure 4**.

3.4. Ternary diffusion model of ideal gas mixtures

In the previous sections the theory of binary diffusion was discussed. This theory is applicable if the diffusion process involves the solvent and only one solute from the gaseous phase. It cannot be applied if two or more solutes are involved in the diffusion process at the same time [27].

Air is a multicomponent gas mixture consisting primarily of nitrogen and oxygen. Additionally, other gases like argon, carbon dioxide, neon, helium, water vapour and methane can also be present [3]. As an approximation, air can be treated as a two-component gas mixture consisting of nitrogen and oxygen. This approach is adopted as it significantly simplifies the model.

Because the diffusion process involves three components (ternary diffusion), the Maxwell-Stefan equations (4) must be used. Using relations for the concentration and molar fractions equation (4) is rearranged to give equation (21):

$$\sum_{\substack{j=1 \\ j \neq i}}^{N} \frac{x_j' \cdot j_i' - x_i' \cdot j_j'}{Đ_{ij}} = -C' \cdot \frac{\partial x_i'}{\partial x} \quad \forall i \tag{21}$$

According to Whitaker [27], for ideal dilute solutions the assumptions given by equation (22) can be made for a solvent *k:*

$$\begin{aligned} x_{N_2}' \to 0 \quad &\Longrightarrow \quad C_{N_2}' \to 0 \\ x_{O_2}' \to 0 \quad &\Longrightarrow \quad C_{O_2}' \to 0 \\ x_k' \to 1 \quad &\Longrightarrow \quad C' = C_k' = const. \end{aligned} \tag{22}$$

These assumptions allow to simplify the Maxwell-Stefan equations to obtain expressions (23) and (24):

$$\frac{\partial C_{N_2}'}{\partial x} = -\frac{j_{N_2}'}{Đ_{N_2 k}} \tag{23}$$

$$\frac{\partial C_{O_2}'}{\partial x} = -\frac{j_{O_2}'}{Đ_{O_2 k}} \tag{24}$$

According to Bird et al. [26], the temporal changes of concentration in the liquid phase are governed by equations (25) and (26):

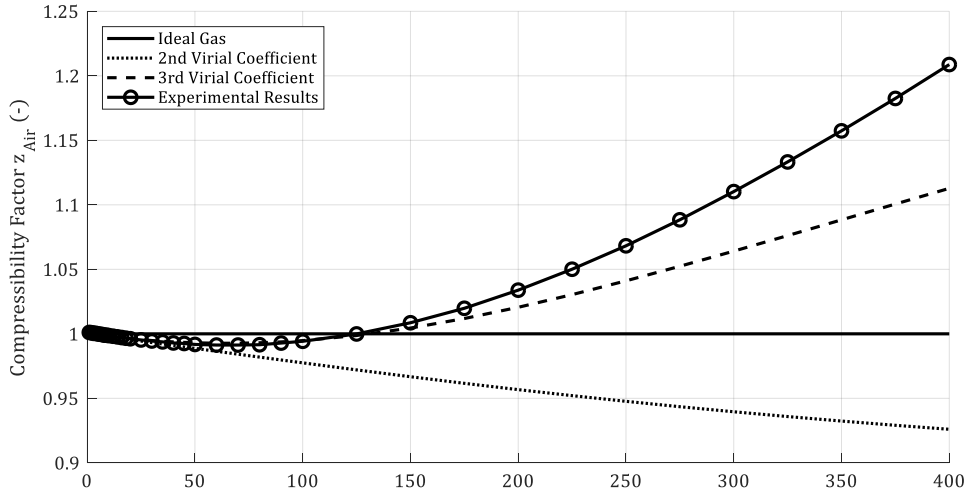

Figure 4: Compressibility factors for air [28]

$$\frac{\partial^2 C'_{N_2}}{\partial x^2} = -\frac{1}{Đ_{N_2 k}} \cdot \frac{\partial j'_{N_2}}{\partial x} \tag{25}$$

$$\frac{\partial^2 C'_{O_2}}{\partial x^2} = -\frac{1}{Đ_{O_2 k}} \cdot \frac{\partial j'_{O_2}}{\partial x} \tag{26}$$

By differentiating (23) and (24) with respect to x and by using equations (25) and (26) expressions for the transient diffusion of nitrogen and oxygen are obtained:

$$\frac{\partial C'_{N_2}}{\partial t} = D_{N_2 k} \cdot \frac{\partial^2 C'_{N_2}}{\partial x^2} \tag{27}$$

$$\frac{\partial C'_{O_2}}{\partial t} = D_{O_2 k} \cdot \frac{\partial^2 C'_{O_2}}{\partial x^2} \tag{28}$$

As can be observed from expressions (27) and (28), the complex Maxwell-Stefan equations reduce to two equations of binary diffusion. The reason for this is the assumption of an ideal dilute solution in which interactions between the solutes do not occur [26]. These assumptions are only possible because the concentration of solvent is almost unity compared to the concentration of the gases to be dissolved. In other words, due to the low solubility of the air's components the Maxwell-Stefan equations converge to Fick's 2nd law but for oxygen and nitrogen separately.

If the diffusivity is to be measured at moderate pressures and temperatures, the ideal gas mixture model can be used. Then, using Dalton's law the temporal changes in the amount of substance of nitrogen and oxygen can be expressed with equations (29) and (30):

$$\frac{dn''_{N_2}}{dt} = \frac{V''}{\bar{R} \cdot T''} \cdot \frac{dp''_{N_2}}{dt} \tag{29}$$

$$\frac{dn''_{O_2}}{dt} = \frac{V''}{\bar{R} \cdot T''} \cdot \frac{dp''_{O_2}}{dt} \tag{30}$$

3.5. Ternary diffusion model of real gas mixtures

When considering the solubility of a real gas mixture, the fugacity coefficient has to be taken into account due to the non-ideal behaviour of the gaseous phase [3]. Hence, equation (1) is rewritten to equation (31):

$$x''_i \cdot \varphi_i \cdot p'' = H_{ik} \cdot x'_i \quad \forall i \tag{31}$$

According to Lüdecke et al. [3], multiple equations of state can be used to calculate the fugacity coefficient of each gas species. In this paper, the virial equation of state with 3 coefficients is chosen and is given by expression (32):

$$p'' \cdot v''_m = \bar{R} \cdot T'' \cdot \left(1 + \frac{B}{v''_m} + \frac{C}{{v''_m}^2}\right) \tag{32}$$

The equation for the fugacity coefficient is given by equation (33):

$$\ln(\varphi_i) = \frac{2}{v''_m} \sum_{j=1}^{N} x''_j B_{ij} - \ln(z) + \frac{3}{2{v''_m}^2} \sum_{j=1}^{N} \sum_{k=1}^{N} x''_j x''_k C_{ijk} \tag{33}$$

Using equation (31) the necessary Dirichlet boundary condition for each species of gas can be calculated with expression (34):

$$x'_i(x = 0, t) = \frac{x''_i \cdot \varphi_i \cdot p''}{H_{i,k}} \tag{34}$$

The pressure-decay method allows to calculate the diffusivity of pure gases, however the diffusivity of oxygen cannot be determined in this way due to ignition risks. Therefore, the authors propose a new approach:

1. Calculate the diffusivity of pure nitrogen;
2. Measure the pressure-decay for air;
3. Determine the diffusivity of oxygen from the pressure-decay curve for air with computational simulations using the ternary diffusion model of real gas mixtures.

4. COMPUTATIONAL ANALYSIS

To demonstrate the discrepancies between the different thermodynamic and diffusion models, simulations were conducted using a finite difference scheme. The liquid domain is discretised and an explicit Euler approach is chosen to calculate the concentration within it over time. The test case considered is the diffusion of nitrogen and oxygen in water, since the values for diffusivities and Henry coefficients are readily available. Also, the thermophysical properties of air are well documented by Vasserman et al. [28].

The single species real gas model was used to calculate the pressure-decay for nitrogen and oxygen separately. The two curves provide an

upper and lower bound for the pressure-decay curves of the ternary diffusion models.

The parameters for the diffusivities, Henry coefficients and virial coefficients are presented in **Table 1**:

Table 1: Diffusivities, Henry and virial coefficients

Diffusivities of system	Value [m²/s]
Diffusivity $D_{N_2H_2O}$	2.000×10^{-9}
Diffusivity $D_{O_2H_2O}$	2.420×10^{-9}
Henry coefficients	Value [Pa]
Henry coefficient $H_{N_2H_2O}$	8.59×10^{9}
Henry coefficient $H_{O_2H_2O}$	4.42×10^{9}
Virial coefficients	Value [m³/mol]
Coefficient $B_{N_2N_2}$	-4.34×10^{-6}
Coefficient $B_{N_2O_2}$	-9.70×10^{-6}
Coefficient $B_{O_2O_2}$	-15.96×10^{-6}
Virial coefficients	Value [m⁶/mol²]
Coefficient $C_{N_2N_2N_2}$	1.90×10^{-9}
Coefficient $C_{N_2N_2O_2}$	1.50×10^{-9}
Coefficient $C_{N_2O_2O_2}$	0.39×10^{-9}
Coefficient $C_{O_2O_2O_2}$	35.00×10^{-12}

The parameters of the measurement chamber are listed in **Table 2**:

Table 2: Dimensions of measurement chamber

Chamber parameters	Value [mm]
Initial gaseous phase height h_0''	10.0
Initial liquid phase height h_0'	150.0
Piston diameter d	65.0

The system is considered isothermal at a temperature of 303.15 K. The initial molar fractions in the gaseous phase are 79.38% nitrogen, 20.62% oxygen for the ternary systems. Because the solvent in this test case is water, water vapour is formed in the gaseous phase and must be considered. The values for the initial pressure (State 0), the intermediate pressure (State 1) and the saturation pressure of water [29] are given in **Table 3**:

Table 3: Values for pressure

Chamber pressures	Value [bar]
Initial pressure p_0''	50.0
Intermediate pressure p_1''	300.0
Saturation pressure of water $p_{H_2O}^S(@303.15\ K)$	42.47×10^{-3}

The molar fraction of water in the gaseous phase can be determined with Raoult's law (35):

$$x_{H_2O}''\left(x_{H_2O}' \to 1\right) = \frac{x_{H_2O}' \cdot p_{H_2O}^S(303.15\ K)}{p_0''} \quad (35)$$

The values of the molar fractions of water in the gaseous phase at 1.0 bar, in State 0 and in State 1 are given in **Table 4**:

Table 4: Values for molar fraction of water in air for system air-water

Molar fractions of water	Value [-]
Molar fraction $x_{H_2O}''(@1\ bar)$	42.47×10^{-3}
Molar fraction $x_{H_2O}''(@50\ bar)$	8.49×10^{-4}
Molar fraction $x_{H_2O}''(@300\ bar)$	1.42×10^{-4}

As can be seen, the water vapour content is significant only at ambient pressure. At higher pressures it is negligible compared to the content of nitrogen and oxygen. Even more interesting is that by considering this test case an upper bound for the molar fraction of water vapour in the gaseous phase is found for all other liquid-air systems.

When considering other fluids, e.g. hydraulic fluids, where the water content in the liquid phase is unknown, the limiting case of Raoult's law (35) for the water-air system is very convenient to use. Applying it to other systems is equivalent to having a relative humidity of 100% of the gaseous phase. Therefore, if in the limiting case given by (35) the molar fraction of water vapour is already negligible, it is also negligible for any other case.

With the given parameters it is possible to simulate the diffusion process and express the pressure in the measurement chamber as a function of time. A comparison between the pressure curves is given in **Figure 5**. As mentioned before the pressure-decay curves of pure nitrogen and pure oxygen provide an upper and lower bound for the ternary model.

As shown, the pressure curves for the ideal and real gas mixture models differ for the given parameters by a maximal value of approximately 10 bar (@190 h). Once thermodynamic equilibrium is reached, the discrepancy is approximately 5 bar. Keeping in mind that the pressure-decay within the measurement chamber is recorded over time, differences in the pressure curves will lead to different values for the diffusivities.

Another observation is depicted in **Figure 6**. Due to the different solubilities of nitrogen and oxygen in water, the molar fraction of nitrogen in the gaseous phase increases while that of oxygen decreases compared to their respective initial values as was already noted by Rambaks et al. [23].

A closer inspection of **Figure 6** reveals that the molar fraction of nitrogen reaches a maximum value and then starts to decrease. The larger diffusion coefficient of oxygen is the most likely explanation for this observation.

The change in gaseous phase composition has a direct effect on the calculation of the diffusivities. This is most notable in equation (33) for the fugacity coefficients and in the expressions for the Dirichlet boundary conditions (34).

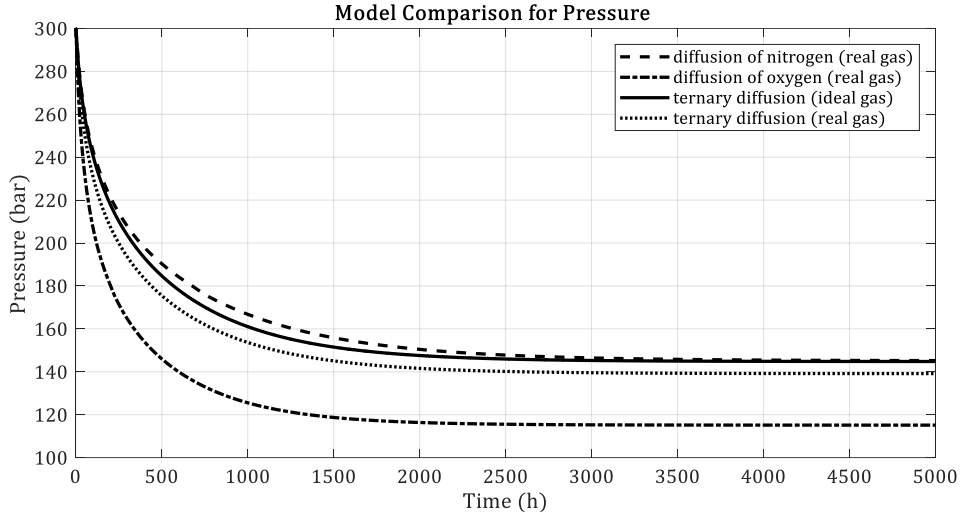

Figure 5: Pressure-decay over time for diffusion in water

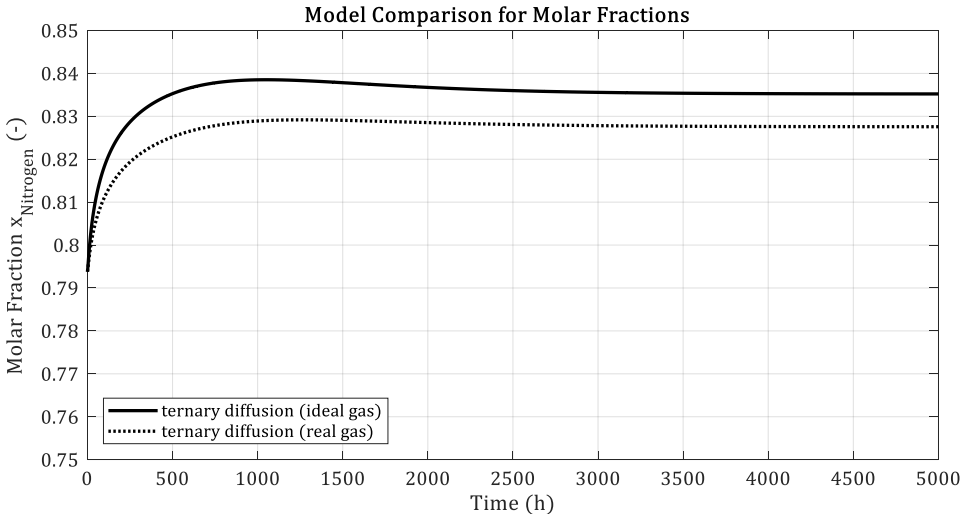

Figure 6: Molar fraction of nitrogen over time for diffusion in water

5. OPERATIONAL TESTING

To test the functionality of the apparatus, a test-run with water and air at low pressure was conducted for a period of 200 hours. The measured pressure-decay curve is shown in **Figure 7**.

The goal of this test was to determine, if the system converges to a state of thermodynamic equilibrium. This would indicate, that the apparatus is leak-proof.

The diffusion process was accelerated with the use of a magnetic stir bar, which was placed in the measurement chamber and activated in the 12th hour of the test. As can be observed, this leads to an immediate decrease in pressure. Following this rapid decrease, it was switched off for 10 hours and activated again within the 22nd hour of the test. Once more, an acceleration of the diffusion process can be noted.

With time the gradient of the pressure-decay curve flattens out as depicted in **Figure 7**. This indicates, that the diffusion process is slowing down and converging to thermodynamic equilibrium. Based on this it can be said, that the measurement apparatus is leak-proof.

From the first 12 hours of testing the resulting preliminary pseudo-diffusivity of air in water is determined to be $D = 1.1 \times 10^{-9}\, m^2/s$. This value is of the same magnitude as the diffusivities of nitrogen and oxygen.

6. CONCLUSION AND OUTLOOK

In the presented paper different methods for determining the diffusivities of nitrogen and oxygen in liquids were discussed. Among these methods the pressure-decay method was chosen as the best suited for hydraulic fluids. A measurement apparatus and its working principles were described along with the design aspects and the operating procedure.

It was shown, that for high pressure diffusion a real gas mixture model has to be used due to the non-ideal behaviour and the changing composition of the gaseous phase. The numerical results reveal that it is necessary to capture these effects when applying the pressure decay method to gas mixtures because otherwise one cannot determine the individual diffusivities and because the non-ideal behaviour introduces severe deviations compared to the ideal gas mixture model, especially if the measurement time is limited to 10 days (240 hours) or less.

The described apparatus has been set up, tested and measurements of the diffusivities are subject to current research at ifas.

ACKNOWLEDGMENTS

This work was funded by the German Research Foundation (DFG) in the scope of the Project „Lösungs- und Entlösungsverhalten von Luft in Hydraulikölen" (MU 1225/41-1). The authors would like to thank the DFG for its support.

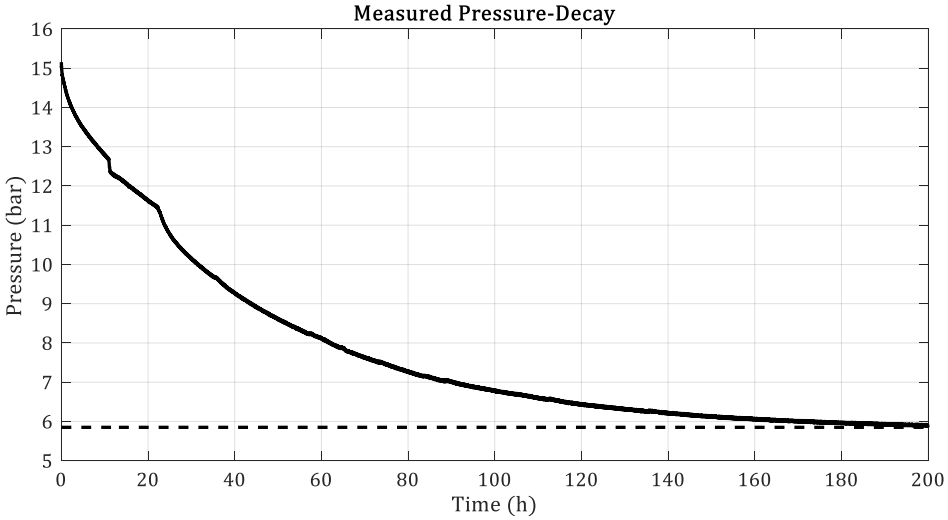

Figure 7: Measured pressure-decay over time for diffusion of nitrogen and oxygen in water

NOMENCLATURE

B	2nd Virial coefficient
C	Concentration / 3rd Virial coefficient
d	Piston diameter
D	Diffusion coefficient
Đ	Maxwell-Stefan-diffusion coefficient
h	Height
H	Henry coefficient
i	Index
j	Index / Molar flux
k	Index
L	Length
m	Mass
n	Index / Amount of substance
N	Index
p	Pressure
R	Specific gas constant
$\bar{R}$	Universal gas constant
S	Standard reference conditions / Saturation
t	Time
T	Temperature
v_m	Molar Volume
V	Volume
x	Coordinate / Molar fraction
z	Compressibility factor
α	Bunsen absorption coefficient
μ	Chemical potential
φ	Fugacity coefficient
$'$	Liquid phase
$''$	Gaseous phase

REFERENCES

[1] Schrank K (2015) Eindimensionale Hydrauliksimulation mehrphasiger Fluide. Dissertation, RWTH Aachen University

[2] Schmitz K, Murrenhoff H (2018) Grundlagen der Fluidtechnik: Hydraulik. Aachen, Germany

[3] Lüdecke C, Lüdecke D (2000) Thermodynamik: Physikalisch-chemische Grundlagen der thermischen Verfahrenstechnik. Berlin, Germany

[4] Peper S, Dohrn R (2012) Sampling from fluid mixtures under high pressure: Review case study and evaluation. The Journal of Supercritical Fluids 66: 2-15. doi: 10.1016/j.supflu.2011.09.021

[5] Wen Y, Bryan J, Kantzas A (2005) Estimation of Diffusion coefficients in bitumen solvent mixtures as derived from low field NMR spectra. Journal of Canadian Petroleum Technology 44: 29-35. doi: 10.2118/05-04-03

[6] Wen YW, Kantzas A (2005) Monitoring bitumen-solvent interactions with low-field nuclear magnetic resonance and X-ray. Energy Fuels 4: 1319-1326. doi: 10.1021/ef049764g

[7] Li X, Song Y, Wu B, Liu Y, Jiang L (2017) Determination of swelling effect in CO_2-brine systems using microfocus X-ray CT. Energy Procedia 142: 3344-3349. doi: 10.1016/j.egypro.2017.12.468

[8] Xu F, Jimenez M, Dietrich N, Hébrard G (2017) Fast determination of gas-liquid Diffusion coefficient by an innovative double approach. Chemical Engineering Science 170: 68-76. doi: 10.1016/j.ces.2017.02.043

[9] Jimenez M, Nicolas D, Cockx A, Hébrard G (2013) Experimental study of O_2 Diffusion coefficient measurement at a planar gas-liquid interface by planar laser-induced fluorescence with inhibition. AIChE J, 59: 325-333. doi: 10.1002/aic.13805

[10] Kireger IM, Mulholland GW, Dickey CS (1967) Diffusion coefficients for gases in liquids from the rates of solution of small gas bubbles. The Journal of Physical Chemistry 71: 1123-1129

[11] De Blok WJ, Fortuin JMH (1981) Method for determining Diffusion coefficients of slightly soluble gases in liquids. Chemical Engineering Science 36 (10): 1687-1694. doi: 10.1016/0009-2509(81)80014-0

[12] Ng WY, Walkley J (2011) Diffusion of gases in liquids: the constant size bubble method. Canadian Journal of Chemistry 47: 1075-1077. doi: 10.1139/v69-170

[13] Yang C, Gu Y (2005) New experimental Method for measuring gas diffusivity in heavy oil by the dynamic pendant drop volume analysis (DPDVA). Industrial & Engineering Chemistry Research 44: 4474-4483. doi: 10.1021/ie0501430

[14] Yang C, Gu Y (2006) A new method for measuring solvent diffusivity in heavy oil by dynamic pendant drop shape analysis (DPDSA). SPE Journal 11: 48-57. doi: 10.2118/84202-PA

[15] Fadaei H, Scarff B, Sinton D (2011) Rapid microfluidics-based measurement of CO_2 diffusivity in bitumen. Energy Fuels 25: 4829-4835. doi: 10.1021/ef2009265

[16] Renner TA (1988) Measurement and correlation of Diffusion coefficients for CO_2 and rich-gas applications. SPE Reservoir Engineering 3: 517-523. doi: 10.2118/15391-PA

[17] Riazi MR, Whitson CH (1993) Estimating Diffusion coefficients of dense fluids. Industrial & Engineering Chemistry Research 32: 3081-3088. doi: 10.1021/ie00024a018

[18] Zhang YP, Hyndmann CL, Maini BB (2000) Measurement of gas diffusivity in heavy oils. Journal of Petroleum Science and Engineering 25: 37-47. doi: 10.1016/S0920-4105(99)00031-5

[19] Sheikha H, Pooladi-Darvish M, Mehrotra AK (2005) Development of graphical methods for estimating the Diffusivity coefficient of gases in bitumen from pressure-decay data. Energy Fuels 19: 2041-2049. doi: 10.1021/ef050057c

[20] Rasmussen ML, Civan F (2009) Parameters of gas dissolution in liquids obtained by isothermal pressure decay. AIChE Journal 55: 9-23. doi: 10.1002/aic.11669

[21] Zheng S, Li HA, Sun H, Yang D (2016) Determination of Diffusion coefficient for alkane solvent-Co_2 mixtures in heavy oil with consideration of swelling effect. Industrial & Engineering Chemistry Research 55: 1533-1549. doi: 10.1021/acs.iecr.5b03929

[22] Yang Z, Bryant S, Dong M, Hassanzadeh (2019) An analytical method of estimation Diffusion coefficients of gases in liquids from pressure decay tests. AIChE Journal 65: 434-445 doi: 10.1002/aic.16408

[23] Rambaks A, Schmitz K (2019) Method for the experimental determination of the Bunsen absorption coefficient of hydraulic fluids. Paper presented at the symposium on fluid power and motion control, Sarasota, 7–9 October 2019

[24] Kratschun F, Schmitz K, Murrenhoff H (2016) Experimental investigation of the Bunsen and the Diffusion coefficients in hydraulic fluids. 10th International Fluid Power Conference 181–192

[25] Freudigmann H-A, Iben U, Pelz PF (2015) Air release measurements of V-oil 1404 downstream of a micro orifice at choked flow conditions. Journal of Physics Conference Series 656. doi: 10.1088/1742-6596/656/1/012113

[26] Bird RB, Stewart WE, Lightfoot EN (2007) Transport Phenomena. New York, USA

[27] Whitaker S (2009) Derivation and application of the Stefan-Maxwell equations. Revista Mexicana de Ingeniería Química 8: 213 – 244.

[28] Vasserman AA, Kazavchinskii YaZ, Rabinovich VA (1966) Thermophysical properties of air and air components. Moscow, Soviet Union

[29] Wagner W, Kruse A (1998) Properties of Water and Steam. Berlin, Germany

peer reviewed

OPTIMIZING HYDRAULIC RESERVOIRS USING EULER-EULER-LAGRANGE MULTIPHASE CFD SIMULATION

Lukas Muttenthaler*, Bernhard Manhartsgruber

Institute of Machine Design and Hydraulic Drives, Johannes Kepler University, Altenbergerstrasse 69, 4040 Linz
* Corresponding author: Tel.: +43 732 2468 6526; E-mail address: lukas.muttenthaler@gmail.com

ABSTRACT

Well working hydraulic systems need clean hydraulic oil. Therefore, the system must ensure the separation of molecular, gaseous, liquid and solid contaminations. The key element of the separation of contaminants is the hydraulic reservoir.
Solid particles are a major source of maintenance costs and machine downtime. Thus, an Euler-Euler-Lagrange multiphase CFD model to predict the transport of solid particles in hydraulic reservoirs was developed. The CFD model identifies and predicts the particle accumulation areas and is used to train port-to-port transfer functions, which can be used in system models to simulate the long-term contamination levels of hydraulic systems. The experimental detection of dynamic particle contamination levels and particle accumulation areas validate and confirm the CFD and the system model.

Both models in combination allow for parameter and design studies to improve the fluid management of hydraulic reservoirs.

Keywords: Hydraulic Reservoir, Particle Contamination, Multiphase CFD Simulation, Optimization

1. INTRODUCTION

Due to the huge impact of hydraulic reservoirs on the fluid properties, the reservoirs must meet certain requirements in modern hydraulic systems. These fluid properties influence the system stiffness, repeatability, components lubrication, wear, noise, machine downtime and fluid degradation.

The hydraulic reservoir is responsible for the separation of solid, liquid, gaseous and molecular contaminations and temperature management directly or indirectly.

The design of the hydraulic reservoir including its inlets and outlets defines the fluid flow. The contaminated and heated hydraulic oil from the system must be cooled and the contaminations must be separated and filtered.

The portion of damages caused by solid contamination is up to 85 % [1]. To halve the number of solid particles in a hydraulic system increases the lifetime of the components by a factor of $1.1 - 1.5$ [2].

Modern approaches use sensor technology and condition monitoring algorithms to observe fluid properties to improve the machine lifetime and reduce machine downtimes and maintenance costs. [3, 4]

Experimental investigations showed the effect of different oil and air flow rates and different reservoir designs on air separation efficiency. [5]

These experiments were the starting point for the development of Euler-Lagrangian CFD codes to simulate and therefore to predict the behavior of air bubbles in hydraulic reservoirs [6, 7]. To avoid expensive and protracted CFD simulations the CFD codes were used to develop a metamodel. [8]

Multiphase CFD simulation enabled the combined investigation of air bubbles and solid particles in hydraulic reservoirs. The influence of the design of the hydraulic reservoir on air and particle separation was demonstrated and different active and passive techniques to improve the separation processes were tested. [9, 10]

Modelling and experimental quantification of particle sources and sinks, e.g. displacement units, cylinder seals, breather filters and oil filters allow for system theory-oriented considerations. [11, 12]

The particle contamination in hydraulic systems can be simulated using lumped-parameter models. In case of simple circuits analytical solutions can be found. More complex systems can be solved by numerical methods. [13, 14]

A systematization and an extensive lumped-parameter modelling of various components of hydraulic systems was done by von Dombrowski [15].

This study determines the particle accumulation areas including the quantification of the probabilities and the inlet-to-outlet transfer functions of particles. The Euler-Euler-Lagrange CFD model, which was developed and tested in [16], shows the particle accumulation areas and is the basis of the fitted system models. Both are compared with experimental results.

The particle accumulation areas and the transfer functions are determined for different particle diameters, reservoir designs and oil flow rates. The lumped-parameter model of the particles in the reservoir is discussed.

2. PROBLEM FORMULATION

The fundamental consideration of the multiphase CFD model is to describe the oil and air phase in the Eulerian and the solid particles in the Lagrangian way.

The Reynolds-averaged Navier-Stokes equations provide the stationary solution of the fluid phases, which are used as flow field to simulate the particle trajectories.

The Lagrangian particle tracking determines the trajectories of each particle and enables a specific view to the transport phenomena.

2.1. Fluid Phase

The volume of fluid method models the oil and air phases including the oil-air-interface. This method solves a single set of momentum equations and a transport equation for each phase. The material properties are represented by the volume fraction weighted average of the property of each phase.

The modelling of the turbulence is done by Menter's Shear Stress Transport model, which ensures good quality of flow results in the whole computational domain using the k-ω approach in wall regions and the k-ε model in free flow regions. Details of the used CFD model are given in [16].

2.2. Particle Phase

Local Particle Sedimentation Probability

Particle sets, or also called dusts, have different numbers of particles in each size class m, which are described by particle size density function $q_n(d_m)$.

Particle size density functions can express the ratio of quantity $q_0(d_m)$, diameter $q_1(d_m)$, cross section/surface $q_2(d_m)$ and volume/mass $q_3(d_m)$ in each size class.

Assuming spherical particles, these particle size density functions can be converted to each other using an integer power law:

$$q_n(d_m) = \frac{d_m^{n-r}\, q_r(d_m)}{\sum_s d_s^{n-r}\, q_r(d_s)\, \Delta d_s} \quad (1)$$

The width of the fraction s is given by Δd_s and n and r characterizes the power law exponents.

Each size class in the CFD simulation is represented by the same number of particles. The local sedimentation probability $f_{n,frac}(x_i, x_j, d_s)$, which is the result of the CFD simulation, can be transformed to get the particle sedimentation probability of a dust $f_{n,t}(x_i, x_j)$ with specific size distribution:

$$f_{n,t}(x_i, x_j) = \sum_s f_{n,frac}(x_i, x_j, d_s)\, q_n(d_s) \quad (2)$$

Dynamic Particle System Model

Lumped-parameter models can describe the transient behaviour of particle sets in a hydraulic system.

To characterize the dynamics of particle sets in a hydraulic reservoir the diameter-dependent mass balance of the change of not-sedimented particles for the reservoir $\dot{m}_{R,d}$ can be written as:

$$\dot{m}_{R,d}(t) = \dot{m}_{In,d}(t) - \dot{m}_{Out,d}(t) - \dot{m}_{S,d}(t) \quad (3)$$

The index d specifies, that the physical quantity is diameter dependent.

The mass flow rate at inlet $\dot{m}_{In,d}(t)$ and outlet $\dot{m}_{Out,d}(t)$ can be expressed by:

$$\dot{m}_{In,d}(t) = c_{In,d}(t)\, Q_{In}(t) \quad (4)$$

$$\dot{m}_{Out,d}(t) = c_{R,d}\,(t)\, Q_{Out}(t) = c_{Out,d}\,(t)\, Q_{Out}(t) \quad (5)$$

The particle mass $\dot{m}_{In,d}$, which enters the reservoir is a function of the particle mass

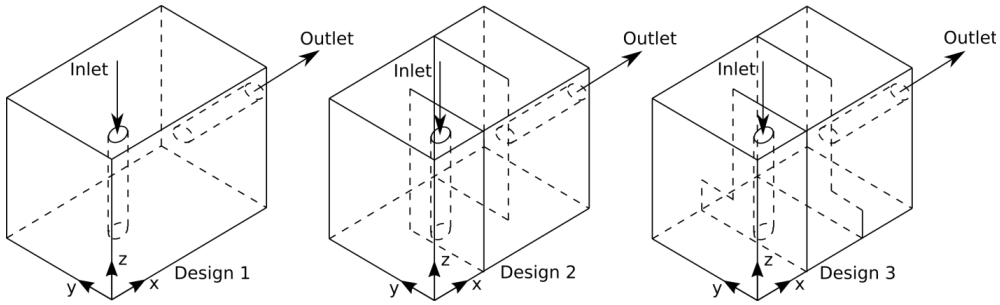

Figure 1: Design of hydraulic reservoirs

$\dot{m}_{Out,d}$, which leaves the reservoir and an additional term $\dot{m}_{Sys,d}$, which represents the net balance of particle sinks and sources in the hydraulic system (except the reservoir):

$$\dot{m}_{In,d}(t) = \dot{m}_{Out,d}(t) + \dot{m}_{Sys,d}(t) \quad (6)$$

Let the inlet and outlet fluid flow be equal and constant. Therefore, filling height h_R and filling volume V_R are constant.

The net mass source referenced to the fluid flow of the system:

$$\dot{m}_{Sys,d}(t) = \mathrm{c_{Sys,d}}(t)\, Q_{Sys} \quad (7)$$

Assume particles entering the reservoir are mixed perfectly along the vertical axis, the sedimentation rate $\dot{m}_S$ is:

$$\dot{m}_{S,d}(t) = \frac{m_{R,d}(t)}{t_{max,d}} = m_{R,d}(t)\ \frac{v_{S,d}}{h_R} \quad (8)$$

The mass sedimentation rate is proportional to the terminal velocity of a falling spherical particle $v_{S,d}$ in a Stokes regime [17]:

$$v_{S,d} = \frac{(\rho_P - \rho)\, g\, d_P^2}{18\, \eta} \quad (9)$$

Inserting Equation 4, 5 and 8 in Equation 3 results in:

$$\dot{m}_{R,d}(t) = \dot{m}_{Sys,d}(t) - m_{R,d}(t)\ \frac{v_{S,d}}{h_R} \quad (10)$$

Expressing Equation 10 in particle state per unit volume and insertion of Equation 7 lead to:

$$\dot{c}_{R,d}(t)\ \mathrm{V_R} = \mathrm{c_{Sys,d}}(t)\, Q_{Sys} - c_{R,d}(t)\ \mathrm{V_R}\ \frac{v_{S,d}}{h_R} \quad (11)$$

Equation 11 is a first order linear differential equation with constant coefficients. Thus, the transfer function with $c_{Sys,d}$ as input and $c_{R,d} = c_{Out,d}$ as output is defined:

$$G_d(s) = \frac{\mathrm{C}_{R,d}(s)}{C_{Sys,d}(s)} = \frac{K_d}{1 + T_{t,d}\ s} \quad (12)$$

The implicit assumption, that particles entering the hydraulic reservoir are mixed immediately in horizontal direction is expressed by Equation 12. Therefore, particles entering the hydraulic reservoir would result in particle fractions, which leave the reservoir without time delay.

Thus, the dead time $T_{d,d}$ is introduced and can be represented by an delay, which means to replace $\dot{c}_{Sys,d}(t)$ by $\dot{c}_{Sys,d}(t - T_{d,d})$:

$$G(s) = \frac{\mathrm{C}_{R,d}(s)}{C_{Sys,d}(s)} = \frac{K_d}{1 + T_{t,d}\ s}\ e^{-T_{d,d}\, t} \quad (13)$$

The introduction of a dead time $T_{d,d}$ is well defined. Because in case of an unknown flow an a priori estimation of the dead time can be done by using the minimum geometric possible way length l_{min} and a representative mean flow velocity $v_{flow,rep}$ in the hydraulic reservoir:

$$T_{d,d} \approx \frac{l_{min}}{v_{flow,rep}} \quad (14)$$

3. SIMULATION AND EXPERIMENTAL SETUP

Figure 1 deals with the designs of the hydraulic reservoirs. The first design does not use baffles, whereas the second one uses two baffles to direct the flow and third one uses baffles with thresholds on the ground.

The hydraulic reservoir with the coordinate axes, the section planes, and the applied sensors, pumps and other hardware are shown in **Figure 2**.

The volume flow, the pressure, the temperature and the particle contamination levels of different particle size classes are measured. The main flow can be varied by a variable-speed motor.

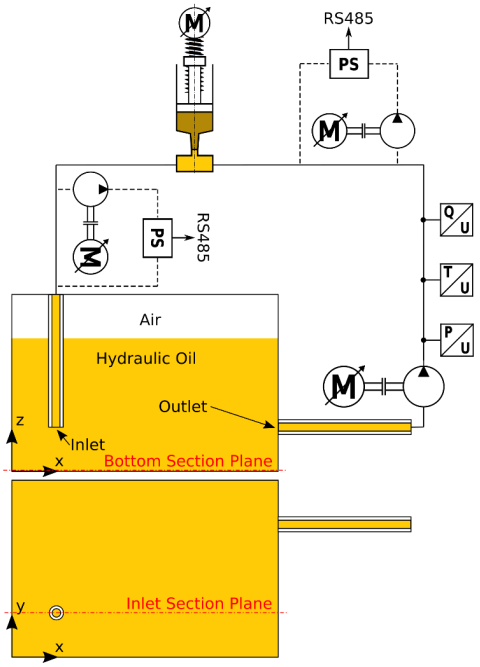

Figure 2: Front and top view of setup

The dimensions of the hydraulic reservoir are listed in **Table 1.** The outer dimensions of the reservoirs are the same for all three considered designs.

Table 1: Geometry of Hydraulic Reservoir

Parameter naming	Value
Basic dimensions $l_x \times l_y \times l_z$	$0.3 \times 0.2 \times 0.2$ m
Inlet/outlet pipe diameter d_{Pipe}	14 mm
Inlet/Outlet pipe length l_I, l_O	150 mm, 140 mm
Inlet pipe axis center x_I, y_I	50 mm, 50 mm
Outlet pipe axis center y_O, z_O	150 mm, 50 mm
Baffle positions x_{B1}, x_{B2}	100 mm, 200 mm
Baffle opening width y_B	35 mm
Baffle threshold height z_B	35 mm

3.1. Simulation Setup

All multiphase CFD simulations are done by ANSYS Fluent 18.2.

The simulation of the fluid flow is done with constant boundary conditions and the simulation aborts after converging to the steady solution.

Then the particle trajectories are calculated, whereby two different sets of particles are considered. One set has their start points on the ground. This set quantifies the particle accumulation areas. The other set starts at the inlet port and is used to determine the transfer function between the ports.

The procedure of the simulation of the fluid flows and the particle trajectories is shown in **Figure 3**.

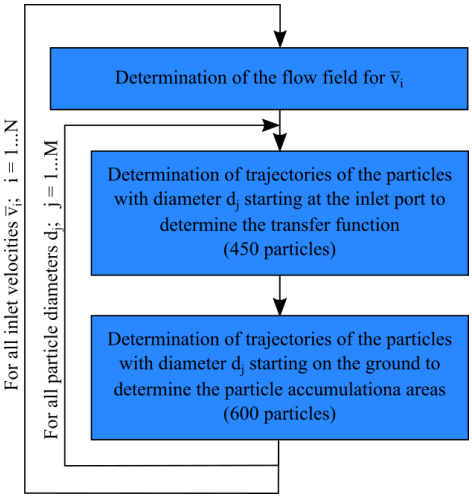

Figure 3: Simulation procedure

Only a short summary of the simulation setup is given in this paper. A detailed description of physical and numerical parameters including explanations of the simulation setup can be found in [16].

Fluid Phase

A parabolic velocity profile is defined as the boundary condition at inlet and outlet ports. The mean velocity is varied in the range of $\bar{v} = 0.05 - 4.0$ m/s.

The top plate was defined as constant pressure boundary condition. All velocity and pressure boundary conditions are set to 4% turbulence.

Due to high density ratio across the oil-air-interface the turbulence damping was enabled, to correct the expected high velocity gradients.

The low-Re correction, the curvature correction and the Kato-Launder limiter are enabled. The surface tension is also considered.

Particle Phase

The particle trajectories were determined in stationary flow fields. Particle sets with diameters in the range $d = 2 - 175$ µm are considered. 450 particles of each diameter starting at the inlet port

and 600 particles starting on the ground represents the particle contamination. Both sets are evenly distributed across the inlet port and on the ground, respectively.

The particles do not interact among each other and have no effect to the fluid flow because of the very low particle volume fraction. Typical particle contaminations in hydraulic systems are several orders of magnitude below 1.

Gravity, virtual mass force, pressure gradient force and a spherical drag law are considered. The collision of particles on the wall is modelled inelastic on the ground and elastic for all other walls.

The mesh consists of about 400 000 cells and is fully structured. To check the mesh convergence simulations with about 1 200 000 cells are done.

3.2. Experimental Setup

The experimental setup is shown in **Figure 4**. The hydraulic reservoir and the inlet and outlet pipes are made of PMMA. A magnetically-coupled centrifugal pump with variable frequency drive is responsible for the fluid flow.

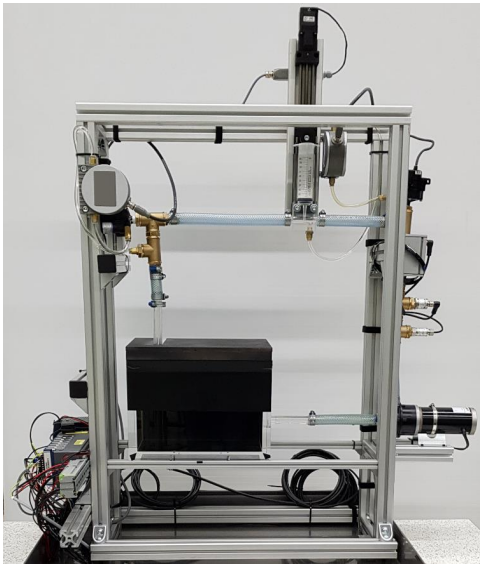

Figure 4: Experimental setup

Two further centrifugal pumps are responsible for the volume flow through particle sensors CS1210 from HYDAC. The sensors measure the cumulative particle quantity for particles with diameters $d_P > 4\ \mu m, 6\ \mu m, 14\ \mu m$ and $21\ \mu m$.

Particles are injected by an automatic dosing system, which consists of a stepper drive, a spindle and a syringe filled with a premixed oil-particle suspension. The particle and oil volumes in the syringe are known. Thus, the injected particle mass and concentration is known.

The hydraulic connections are done with flexible and transparent hoses.

Table 2 lists the material properties of the fluids and particles, which are used in simulations and experiments.

Table 2: Material properties

Parameter naming	Value
Temperature T	$28\ °C$
Oil density ρ_{Oil}	$867\ kg/m^3$
Oil viscosity η_{Oil}	$46.3 * 10^{-3}$ Pa s
Air density ρ_{Air}	$1.149\ kg/m^3$
Air viscosity η_{Air}	$18.69 * 10^{-6}$ Pa s
Particle density ρ_P	$3950\ kg/m^3$

The aluminum oxide test dust particle size distribution is ‘fine’ according to ISO 12103-1:2016-04 A2. [18]

To determine the particle accumulation areas and the transfer functions, two sets of experiments were done.

In the first set of experiments the premixed oil-particle suspension is injected in the constant oil flow with the dosing system. During the experiments an online measurement of the particle quantities was done. The determined transfer functions are compared to the transfer functions determined by CFD simulations.

In the second set of experiments the particles were mixed with the oil in the test bench. A sedimentation time of 120 h enables the particles to sediment. During this period no flow is applied to the testbench.

After this sedimentation time a constant oil flow is applied for $10\ min$ and then the particle accumulation areas are identified.

4. RESULTS AND DISCUSSION

4.1. Fluid Phase

Figure 5 shows that the left side of the hydraulic reservoir is dominated by the downwards jet caused by the inlet flow with a mean flow velocity of $\bar{v} = 1\ m/s$. The not confined vortex affects more than half of the hydraulic reservoir.

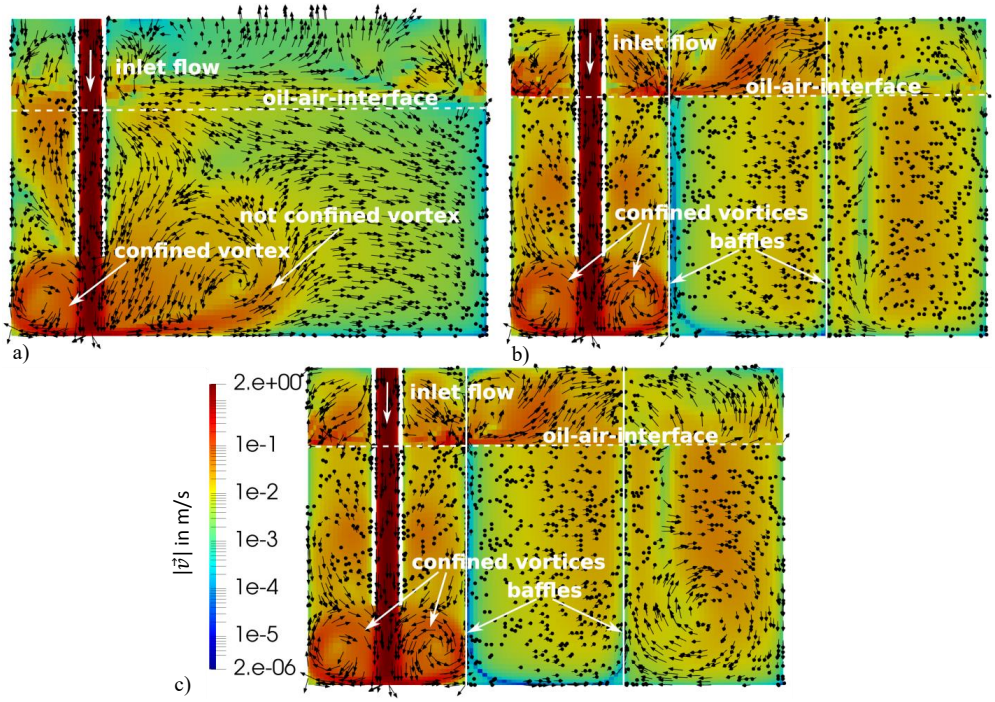

Figure 5: Velocity magnitude $|\vec{v}|$ in m/s on the inlet section plane; $\bar{v} = 1.0$ m/s (a) D1 (b) D2 (c) D3

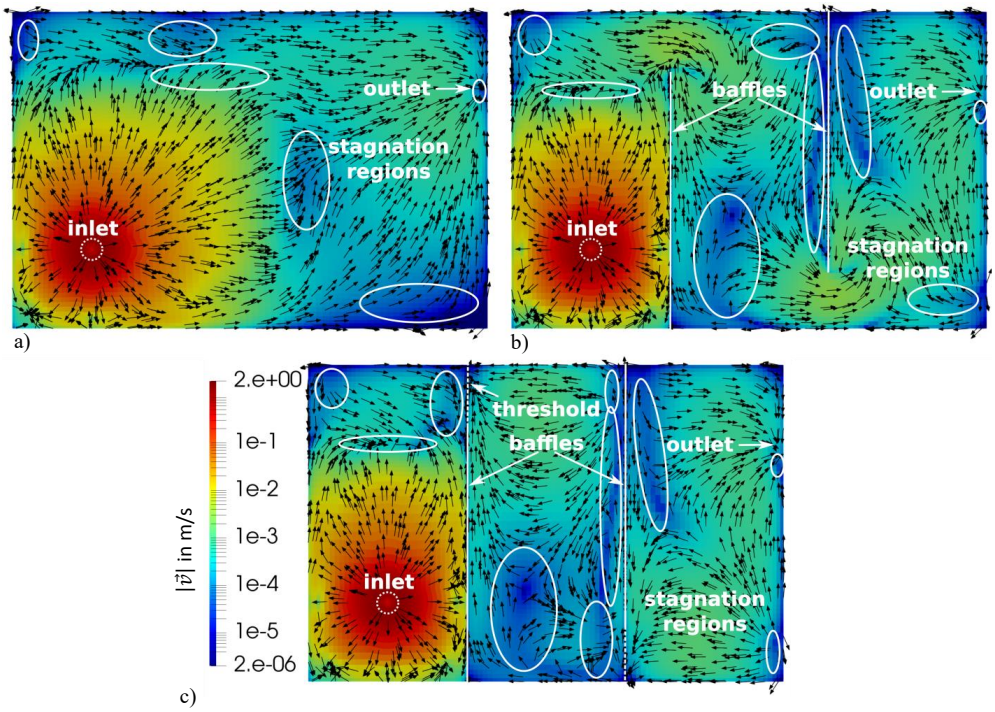

Figure 6: Velocity magnitude on the bottom section plane; $\bar{v} = 1.0$ m/s (a) D1 (b) D2 (c) D3

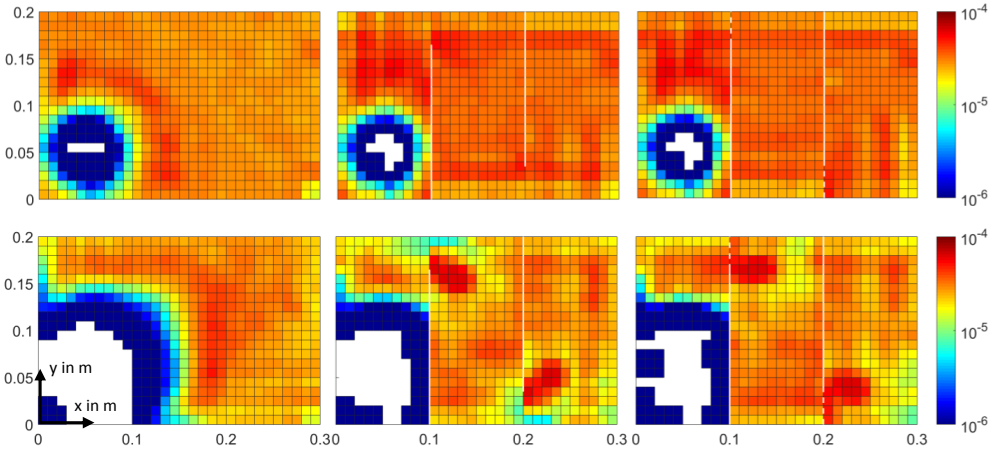

Figure 7: Local cross section-weighted particle sedimentation probability on the bottom; (top) $\bar{v} = 0.25$ m/s (bottom) $\bar{v} = 1.0$ m/s; (left) D1 (middle) D2 (right) D3

The cases with baffles show that the momentum of the inlet jet is contained in the first chamber and confined vortices occur. Sector 2 and 3 are not influenced by the inlet jet, which results in smoother flow.

The velocity magnitude of the air is quite high, due to high density ratio. Therefore, the production of turbulence kinetic energy is high, which leads to high velocity magnitudes.

The influence of the inlet jet to the flow on the ground is shown in **Figure 6** for the same inlet flow characterized by $\bar{v} = 1$ m/s. Without baffles the jet affects half of the ground area.

The jet can affect up to a 2/3 of the ground in case of high flow rates represented by $\bar{v} = 4$ m/s [16].

The baffles reduce the ground area affected by the jet to a quarter of the total area. The thresholds on the ground reduce the ground velocity and are an obstacle for particles creeping on the ground.

4.2. Particle Phase

Local Particle Sedimentation Probability

The ground of the hydraulic reservoirs in **Figure 7** is divided into 10 mm × 10 mm sections, which results in a 30 × 20 grid.
The sedimented particles in each section are counted in the post-processing, which leads to the $q_0(d_m)$-weighted particle sedimentation probability.

To transform the quantity- to the cross section-weighted particle sedimentation probability, shown in **Figure 7**, the transformation from the $q_0(d_m)$ to the $q_2(d_m)$-weighted particle size density function, according to Equation 1, was used. The transformation makes it possible to compare the results with optical experiments.
The upper row of **Figure 7** shows the simulated sedimentation probability in case of $\bar{v} = 0.25$ m/s, whereas the lower row shows the simulation results for $\bar{v} = 1$ m/s. The starting points of the particles are on the ground and are cartesian equally distributed.

All designs and flow velocities show an area beneath the inlet, where the particles are washed away. The size of this area depends on the flow velocity, the design of the reservoir and the particle size.

In cases with baffles the inlet jet is contained by the side walls and the first baffle and thus the area where particles are washed away is also contained.

Resuspended particles accumulate at spots with small velocities. Without baffles a ring around the inlet occurs where the resuspended particles beneath the inlet resediment.

In case of thresholds the velocity on the bottom can be reduced and so more particles resediment.

The comparison of **Figure 6** and **Figure 7** shows that the particle sedimentation regions correspond with the stagnation regions as

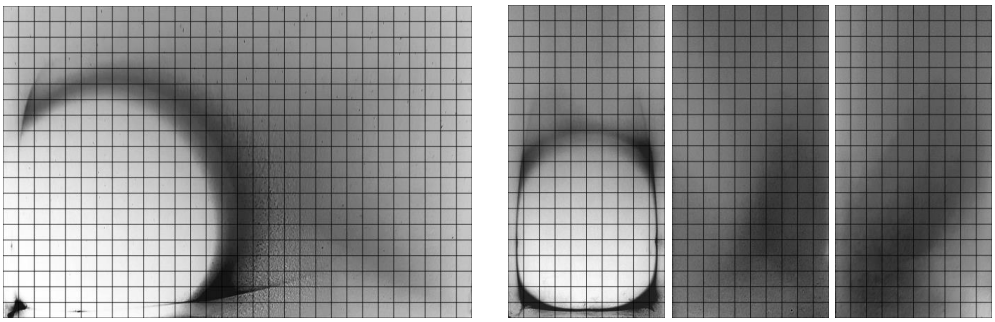

Figure 8: Experimentally determined local cross section-weighted particle sedimentation probability on the bottom; $\bar{v} = 1.0\ \mathrm{m/s}$ (left) D1 (right) D3

described in detail by Muttenthaler and Manhartsgruber [16].

Figure 8 shows postprocessed photos from sedimented particles. The colors of the photos were desaturated, and the contrast was increased.

The same $10\ \mathrm{mm} \times 10\ \mathrm{mm}$ grid for better orientation as in Figure 7 is superimposed.

Figure 8 is divided into two parts. The left side shows the experimentally determined particle sedimentation probability for Design 1. Whereby a circular ring around the inlet occurs. The ring has the same dimension and intensity as in **Figure 7**. The ends of the circular ring are kinked in simulation and experiment. The left bottom corner shows a robust stagnation point where particles are accumulated. The right side shows a homogenous distribution of particles.

The subfigures on the right side show the particle sedimentation probability of the three chambers of Design 3. The left subfigure shows the inlet region where separation lines occur. The effect is dominant in the picture, but the lines become weaker, if the flow is applied longer (like on the left side). Particles accumulate in the corners.

The upper region of the inlet chamber shows few particles and in the middle and right chamber the particle quantity is higher, like **Figure 7**.

Dynamic Particle System Model

Figure 9 shows the comparison of the normalized particle transfer between inlet and outlet determined by CFD simulation, system model and measurements. The particle transfer behaviour between inlet and outlet is determined by CFD simulation and the parameters of $G(s)$ are estimated by least squares fitting. The measurements are plotted to validate the CFD simulation and the estimated transfer functions.

The inlet step is normalized to 1 for each size class and the step starts at $t = 0\ \mathrm{s}$.

The accordance of the models and the measurements is good. The flow rate and the diameter of the particles influences the gains K_d . Increasing flow rates raise the particle output K_d. The faster particles move through the reservoir, the less particles sediment. An increasing particle diameter results in less transferred particles, because the sedimentation velocity increases with the particle size.

The comparison of Design 1 and 3 show that Design 3 has higher separation rates (lower K_d) over all flow rates and particle sizes.

The simulated and measured time constants $T_{t,d}$ are in good agreement. In case of small flow rates, the measured time constant is lower than the simulated one.

The dead times $T_{d,d}$ are higher in Design 3 than in Design 1. Because the minimum geometric length l_{min} of Design 3 is greater. The simulated dead times underestimates the dead time of the measurements in Design 3. A possible reason is a not stationary solution, where particle switch between faster and slower flow paths.

5. SUMMARY AND OUTLOOK

The developed multiphase CFD model can predict particle accumulation areas and port-to-port transfer functions. The trajectories for particles with initial positions on the ground and across the inlet port were calculated correctly for a wide range of particle sizes and oil flow rates.

The actual study compares fluid flow with particle trajectories and identifies the particle

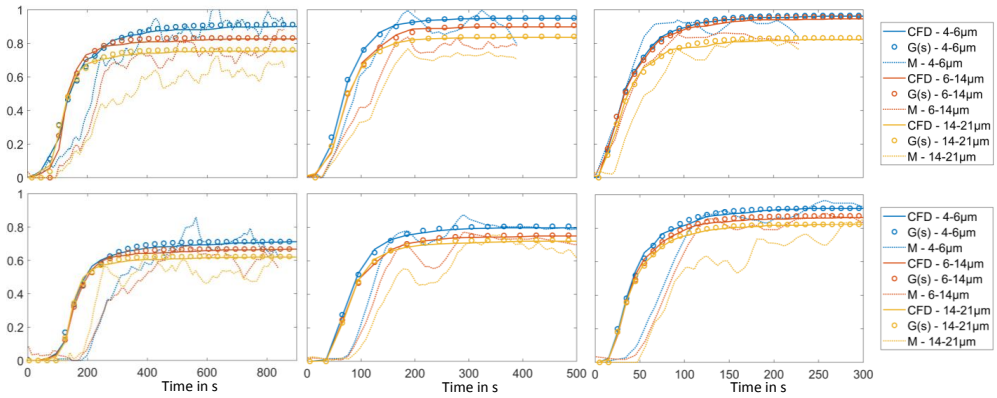

Figure 9: Dimensionless particle step response of hydraulic reservoir; (top) D1 (bottom) D3 (left) $\bar{v} = 0.25$ m/s (middle) $\bar{v} = 0.5$ m/s (right) $\bar{v} = 1.0$ m/s

accumulation areas and the parameters for the lumped-parameter model for different designs of hydraulic reservoirs.

The CFD simulation and the experimental results show a good qualitative accordance of particle accumulation areas and quantitative agreement of dynamic particle contamination levels.

In future, the measurement will be adapted to detect the particle contamination levels for more particle size classes.

The postprocessing of the detection of the accumulation areas will also be improved to make it easier to compare the measured and simulated accumulation areas.

Furthermore, a theory-oriented determination of the parameters of the lumped-parameter model will be done by analytical derivations and flow-based estimations.

Design changes like adding baffles, diffusors and other components to direct the flow can improve the separation behavior significantly.

Therefore, further analyses will apply the lumped-parameter and CFD models to more complex flow situations and geometries.

NOMENCLATURE

$c_{x,d}(t)$	Mass concentration of particles with diameter d at specified place x
d	Particle Diameter
d_{Pipe}	Inner diameter of inlet and outlet pipe
$f_{n,frac}(x_i, x_j, d_s)$	Local sedimentation probability of particle size class s at (x_i, x_j)
$f_{n,t}(x_i, x_j)$	Summed local weighted sedimentation probability of particle class s at (x_i, x_j)
$G_d(s)$	Diameter dependent particle transfer functions
g	Gravity
h_R	Oil filling height in the reservoir
K_d	Gain of PT1 system model
l_{min}	Minimum possible trajectory between inlet and outlet
l_I, l_O	Inlet/Outlet pipe lengths
$l_x \times l_y \times l_z$	Basic dimensions of hydraulic reservoir
$\dot{m}_{x,d}(t)$	Particle mass transport per time of diameter d at specified place x
Q_x	Fluid flow at specified point x
$q_n(d_m)$	Particle size density function of size class m
T	Temperature
$T_{d,d}$	Dead time of system model
$T_{t,d}$	Time constant of PT1 system model
t	Time
$t_{max,d}$	Maximum sedimentation time of particles with diameter d
V_R	Oil volume of the reservoir
$\bar{v}$	Mean flow velocity in the pipe
$\lvert\vec{v}\rvert$	Velocity magnitude of the fluid
$v_{S,d}$	Terminal sedimentation velocity of particles with diameter d
$v_{flow,rep}$	Representative fluid flow velocity
x_I, y_I, y_O, z_O	Inlet/Outlet pipe axis centres
x_i, x_j, x_k	Coordinate in x, y and z direction
η	Dynamic viscosity
ρ, ρ_P	Fluid/Particle density

REFERENCES

[1] Tič V, Lovrec D, Edler J (2012) Operation and accuracy of particle counters for online condition monitoring of hydraulic oils. Annals of Faculty Engineering Hunedoara – International Journal of Engineering, 12(3), 425-428

[2] C.C.Jensen A/S (2017). Clean Oil Guide. 9th edition. Svendborg, Denmark.

[3] Ng F, Harding JA, Glass J (2017) Improving hydraulic excavator performance through in line hydraulic oil contamination monitoring. Mechanical Systems and Signal Processing, 83, 176-193

[4] Dimmler G, Kilian FJ, Bader P, Muttenthaler L, Kapeller P (2018) So that the heart of the machine beats longer. Kunststoffe International, 10, 56-59

[5] Longhitano M, Protase A, Murrenhoff H (2016) Experimental Investigation of the Air Release in Hydraulic Reservoirs. In: Proceedings of the 10th International Fluid Power Conference. Dresden, Germany. March 8-10, 2016. 579-608

[6] Longhitano M, Murrenhoff H (2016) Prediction of Air Release in Hydraulic Reservoirs using Lagrangian Particle Tracking. In: Proceedings of the 9th International Conference on Multiphase Flow. Firenze, Italy. May 22-27, 2016.

[7] Mostafavi R, Tiffin D, Schmitz K (2018) Determination of the dynamic characteristic of a hydraulic reservoir for its air release efficiency using multiphase CFD model. In: Proceedings of the ASME/BATH 2018 Symposium on Fluid Power and Motion Control. Bath, UK. September 12–14, 2019. V001T01A008. ASME. doi.org/10.1115/FPMC2018-8813

[8] Mostafavi R, Schmitz K (2019) Development and Use of a Two-phase CFD Solver for Metamodeling of a Hydraulic Reservoir. Paper presented at the 10th International Conference on Multiphase Flow. Rio de Janeiro, Brazil. September 19–24, 2019. OC.080. ABCM

[9] Tič V, Lovrec D (2013) Air-release and solid particles sedimentation process within hydraulic reservoir. Tehnički vjesnik, 20(3), 407-412.

[10] Beckmann B, Laube M (2018) myCro – Downsizing of hydraulic power units by revolutionizing the design. In: Proceedings of the 11th International Fluid Power Conference. Aachen, Germany. March 19-21, 2018. 579-608

[11] Dahmann P (1992) Untersuchung der Feststoffpartikelkontamination in hydraulischen Systemen, RWTH Aachen University.

[12] Mager M (1999) Untersuchung der Feststoffpartikelkontamination in hydraulischen Systemen, RWTH Aachen University. Verlag Mainz, Aachen, Germany. ISBN 3-89653-266-9

[13] Foord BA (1978) Specifying fluid filtration through computer simulation. In: 34th Proceedings of the National Conference on Fluid Power. Philadelphia, PA, USA. November 7-9, 1978. 197-204

[14] Stecki JS, Chao L (1995) Modelling and Simulation of Contamination in Fluid Power Control Systems. In: Proceedings of the 4th Scandinavian International Conference on Fluid Power. Tampere, Finland. September 26-29, 1995. 356-368

[15] von Dombrowski R (2015) Modellierung der Partikelverteilung in hydraulischen Systemen, RWTH Aachen University. Shaker Verlag, Aachen, Germany. ISBN 978-8440-3744-9

[16] Muttenthaler L, Manhartsgruber B (2019) Prediction of particle resuspension and particle accumulation in hydraulic reservoirs using three-phase CFD simulations. In: Proceedings of the ASME/BATH 2019 Symposium on Fluid Power and Motion Control. Sarasota, Florida, USA. October 07–09, 2019. V001T01A008. ASME. doi.org/10.1115/FPMC2019-1617

[17] Lamb H (1879) Hydrodynamics. Cambridge University Press. Cambridge, UK.

[18] KSL Staubtechnik GmbH (2017) Sicherheitsdatenblatt Prüfstäube mit Korund. 1270-0 Edition. Lauingen, Germany.

GROUP H | K

Pumps

THE INFLUENCE OF THE SWASH PLATE OSCILLATION ON PRESSURE RIPPLE IN VARIABLE DISPLACEMENT AXIAL PISTON PUMP

Xiaochen Huang, Bing Xu, Junhui Zhang*

The State Key Laboratory of Fluid Power and Mechatronic Systems, Zhejiang University, No.38 Zheda Road, 310027 Hangzhou, China

* Corresponding author: Tel.: +86 153 81058508; E-mail address: benzjh@zju.edu.cn

ABSTRACT

The displacement of the variable displacement pumps can be adjusted by changing the swivel angle of the swash plate. In fact, the swivel angle oscillates because of the oscillating torque on the swash plate, which caused by the pressure fluctuation of the piston chamber. The swivel angle is most often considered as a constant value in previous studies. However, the oscillation of the swash plate leads to an additional movement of the piston, which has an impact on the pressure fluctuation and the flow ripple. In this study, an improved model of a self-supplied variable displacement pump is established. The swash plate oscillation under different operating conditions is presented. In order to investigate the effect of the swash plate oscillation on the pressure ripple, a comparison between the case of the fixed swash plate and the oscillated swash plate is conducted. Results show the pressure ripple with an oscillated swash plate shows a smaller pressure ripple. It also shows that the nine pistons and the control mechanism both affect the pressure ripple and flow fluctuation.

Keywords: Variable piston pump, Swash plate, Oscillation, Pressure ripple

1. INTRODUCTION

Variable displacement axial piston pumps take a particularly important place in hydraulic systems due to their high power density, high efficiency, and controllability [1]. The swivel angle of the swash plate is adjusted by the control actuator mechanism. As a result, the outlet flow rate of the pump is altered. As volumetric machines, axial piston pumps discharge an oscillating flow rate, which generates the pressure ripple in hydraulic circuits. It's followed by vibrations in the pump component and pipelines, degrading the reliability and durability of hydraulic system. As a technique of the vibration and noise reduction in axial piston pumps, many previous works have focused on geometric optimization of the valve plate to reduce the amplitude of the pressure ripple [2,3]. Most of the investigations are conducted with a fixed swash plate even if the pump has variable displacement [4,5].

However, the swivel angle oscillates because of the oscillating torque on the swash plate caused by the pressure fluctuation in the piston chamber [6,7]. Especially, the oscillating movements of the swash plate have been measured by Achten [8] and Fang [9] in a variable displacement floating cup pump and a pressure compensated piston pump, respectively.

In recent years, a few researchers investigated the effect of the swash plate oscillation in the design of the valve plate. Ericson [10,11] studied the swash plate oscillations in a pressure-controlled axial piston pump by simulation. Large variations of the flow pulsations were showed between fixed and oscillating swash plates. By the simulation of different valve plate configurations, it conducted that the optimised valve plate design would be changed due to the effect of swash plate oscillation on the flow pulsation.

Schoemacker et al [12] investigated the impact of the valve plate design on the torque load. Comparing the results with three valve plate designs using silencing grooves and bores, the influence of the swash plate oscillation on the pump's output flow strongly depends on the valve plate design. The author summarized that the valve plate should be designed according to

the swash plate control system for a variable displacement pump.

In this study, to investigate the dynamic behavior of the swash plate vibration and the influence of the oscillation on the pressure ripple, an improved model of a self-supplied variable displacement axial piston pump is presented. The oscillation of the swash plate is taken into consideration. The amplitude of the swash plate oscillation at different operating conditions is calculated. To investigate the effect of the swash plate oscillation on the pressure ripple, a comparison between two cases of the fixed swash plate and the oscillated swash plate is conducted. The influence of the oscillation on pumping dynamics and control mechanism dynamics are both discussed.

2. MATHEMATICAL MODELING

2.1. Description of the physical system

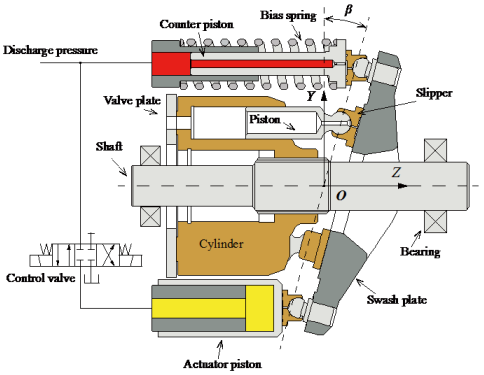

Figure 1: Schematic of the variable displacement pump

Figure 1 shows a schematic of the variable displacement pump. The rotating group rotates with shaft driven by the prime mover. The piston executes the reciprocating motion owing to the inclination of the swash plate. As a consequence, the hydraulic oil flows in and out of the piston chamber. The swash plate swivels with the control flow entering or leaving the actuator piston. And then, the hydraulic displacement of the axial piston pump is changed. In this study, a proportional valve is utilized to control the flow rate of the actuator piston.

2.2. Piston pump dynamics

Since the displacement varies with the swash plate angle, the relationship of the swash plate angle and the motion of the piston must be figured out through the kinematics analysis, which can be expressed as

$$z_i = R\sin\varphi_i \tan\beta \tag{1}$$

$$v = \dot{z}_i = R\omega\cos\varphi_i \tan\beta + \frac{R\sin\varphi_i}{\cos^2\beta}\frac{d\beta}{dt} \tag{2}$$

$$\begin{aligned} a = \ddot{z}_i = {} & \frac{R\sin\varphi_i}{\cos^2\beta}\frac{d^2\beta}{dt^2} + \frac{2R\sin\varphi_i\tan\beta}{\cos^2\beta}\left(\frac{d\beta}{dt}\right)^2 \\ & + \frac{2R\omega\cos\varphi_i}{\cos^2\beta}\frac{d\beta}{dt} - R\omega^2\sin\varphi_i\tan\beta \end{aligned} \tag{3}$$

The motion of the i-th piston is expressed as

$$P_i\frac{\pi}{4}d^2 - f_i - F_{si} = m_{ps}\ddot{z}_i \tag{4}$$

The variation rate of pressure in the piston chamber dP/dt can be derived by applying the continuity equation in integral form as follows

$$\frac{dP_i}{dt} = \frac{K_e}{V_p}(q_{in,i} - q_{out,i} - q_{lk,i} - \frac{dV_p}{dt}) \tag{5}$$

where q_{in} and q_{out} are the flow rate between the piston chamber and the pump port. It can be described as

$$q_{in,i} = CA_{\mathrm{LP}}\sqrt{\frac{2|P_{in} - P_i|}{\rho}}\cdot sgn(P_{in} - P_i) \tag{6}$$

$$q_{out,i} = CA_{\mathrm{HP}}\sqrt{\frac{2|P_{out} - P_i|}{\rho}}\cdot sgn(P_i - P_{out}) \tag{7}$$

The inlet flow rate Q_{in} and the outlet flow rate Q_{out} are the sum of the flow rate from nine pistons.

2.3. Swash plate dynamics

The dynamics of the swash plate are dictated by control moments generated by the pumping piston and control mechanism. These can be described as

$$J_{sw}\frac{d^2\beta}{dt^2} + c_{sw}\frac{d\beta}{dt} = M_p + M_{ap} + M_{cp} \tag{8}$$

where the moment M_p is mainly generated by pumping pistons and can be expressed by

$$M_p = \sum_{i=1}^{N}\frac{R\sin\varphi_i}{\cos^2\beta}F_{si} \tag{9}$$

It's worth mentioning that the moment M_p is the main cause of the swash plate oscillation.
The moment caused by the actuator piston and the counter piston can be respectively described as

$$M_{ap} = F_{ap} L_{ap} \cos\beta \tag{10}$$

$$M_{cp} = F_{cp} L_{cp} \cos\beta \tag{11}$$

2.4. Control mechanism dynamics

The forces on the actuator piston are given by

$$m_{ap}\ddot{x}_{ap} = P_c A_{ap} - f - F_{ap} \tag{12}$$

where the motion of the actuator piston can be written as the function of the swash plate angle as

$$x_{ap} = L_{ap} \sin\beta \tag{13}$$

The pressure within the actuator piston is governed by the continuity equation as

$$\frac{V_{ap}}{K_e}\frac{dP_c}{dt} = Q_{ap} - A_{ap}\dot{x}_{ap} - Q_{apl} \tag{14}$$

Similarly, the dynamic of the counter piston can be expressed as

$$m_{cp}\ddot{x}_{cp} = P_{cp} A_{cp} - f_{cp} - kx_{cp} + F_{sp0} - F_{cpz} \tag{15}$$

$$x_{cp} = L_{ap} \sin\beta \tag{16}$$

$$\frac{V_{cp}}{K_e}\frac{dP_{cp}}{dt} = Q_{cp} - A_{cp}\dot{x}_{cp} - Q_{cpl} \tag{17}$$

2.5. Control valve dynamics

To simplify the analysis, a second-order model is used to compute the dynamics of the proportional valve. It can be written as

$$\frac{x_v}{u} = \frac{k_v\omega^2}{s^2 + 2\xi\omega + \omega^2} \tag{18}$$

Then, the flow rate entering the actuator piston, Q_{ap} is conducted as

$$Q_{ap} = C_q x_v \sqrt{\frac{2\Delta p}{\rho}} \tag{19}$$

3. RESULTS AND DISCUSSION

3.1. Swash plate oscillation analysis

In a variable displacement pump, the pressure ripple in the piston chamber results in variant torque load and therefore the control force is altered to satisfy the balance of the swash plate. That's to say, the fluctuation of the torque acting on the swash plate accounts for the oscillation of the swash plate.

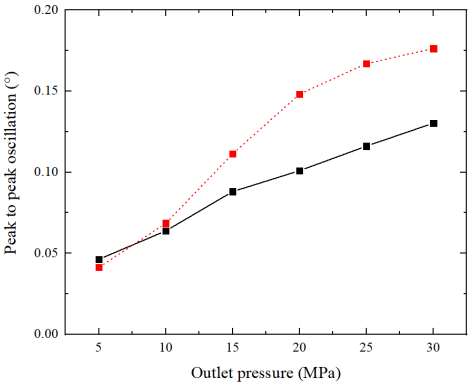

Figure 2: The peak to peak values of swash plate angle under different outlet pressure

Since the oscillation is determined by the torque on the swash plate, it leads us to draw a conclusion that the oscillation has something to do with the outlet pressure. **Figure 2** presents a comparison of the oscillations of the swash plate at different pressure when working conditions are β=12º, n=1000 rpm (solid line) and β=12º, n=1200 rpm (dashed line). From the figure, it can be concluded that the swash plate oscillation is positively correlated with pressure, which can be explained as the increasing torque with the pressure.

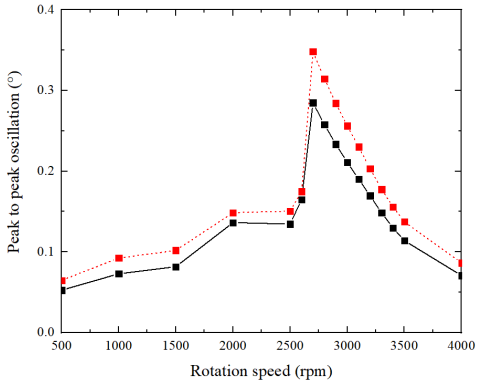

Figure 3: The peak to peak values of swash plate angle under different rotational speed

The peak to peak values of the swash plate angle under different rotational speed are shown in

Figure 3. Simulations are carried out at 12°, 15MPa (solid line) and 12°, 20MPa (dashed line). Especially, the inlet pressure is set to 5 bar in case of cavitation at a high rotational speed. As we can see that the oscillation is speed-dependent but not linear. The highest amplitude, which is about 0.35° at 2700 rpm, may be caused by the resonance frequency of the swash plate control system.

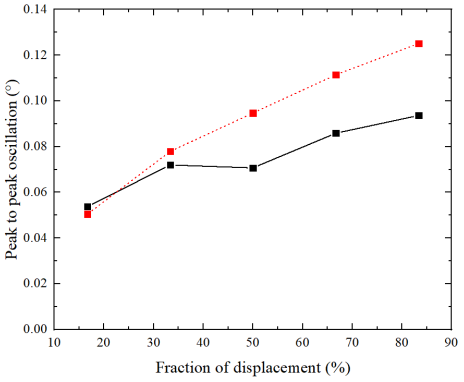

Figure 4: The peak to peak values of swash plate angle under different displacement

The amplitude of the oscillation at the setting angle from 3° to 15°, which equals the fraction of 16.7% to 83.3%, is summarized in **Figure 4**. The solid line and the dashed line represent the swash plate oscillation at n=1000 rpm, P_{out}=15 MPa and n=1200 rpm, P_{out}=15 MPa, respectively. The oscillation increases with the increase in displacement.

From the above results, the oscillation of the swash plate is influenced by outlet pressure, rotational speed, and displacement. However, the amplitude with changing pressure and fraction of displacement is rather smaller than that effected by the rotational speed because of the resonance frequency.

3.2. Effect on pumping dynamics

In order to investigate the influence of the swash plate oscillation on pressure ripple, efforts have been made to simplify the model with an oscillated swash plate. The model with a fixed swash plate set the swash plate angle as a const value. In this case, the control mechanisms including the control actuator and control valve are omitted. The calculated results of the two different models are presented in **Figure 5**. The rotational speed is 1000 rpm and the swash plate angle is 12°. The black line and red line represent the outlet pressure with a fixed and an oscillated swash plate, respectively. As we can see that the fixed swash plate shows a larger pressure ripple, compared with the case of the oscillated swash plate.

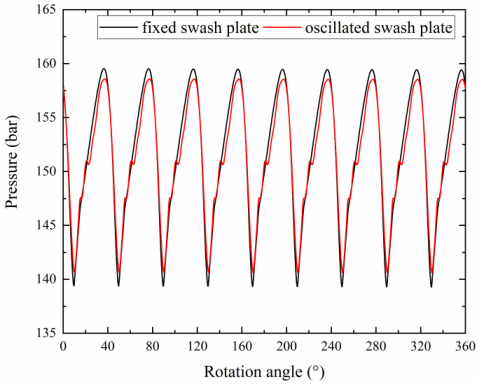

Figure 5: Comparison of pump outlet pressure

Piston motion analysis

More details are required to account for the pressure ripple reduction. **Figure 6** shows the displacement and velocity of one piston for a fixed swash plate and an oscillated swash plate. It's apparent that the oscillated swash plate leads to the vibration of the velocity. And the major difference of the displacement between these can be shown in the enlarged view. At this time, the shaft angle is about 90° and 180°, where the pressure transition of the piston chamber occurs. Therefore, the oscillation is quite important for analyzing the flow fluctuation and the pressure ripple.

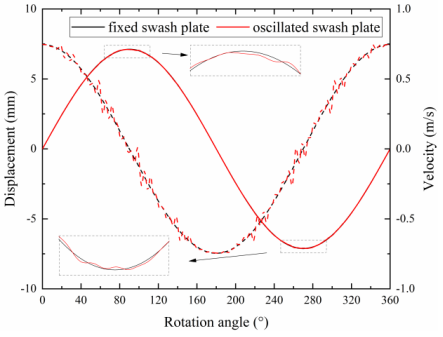

Figure 6: Piston displacement (solid line) and velocity (dashed line) at operation condition: 15MPa, 1000rpm, 12°

Pressure and flow analysis of a single-piston

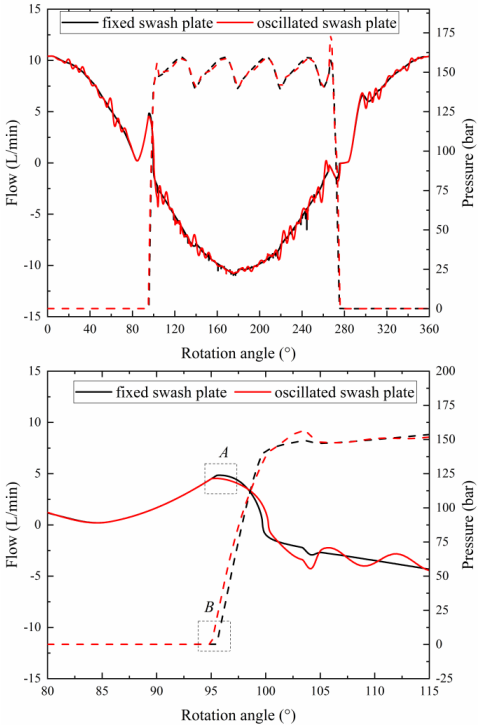

Figure 7: Flow (solid line) and pressure (dashed line) in one piston chamber at operation condition: 15MPa, 1000rpm, 12°

As illustrated in **Figure 7**, the pressure in the piston chamber is closely associated with the flow rate in or out of the piston chamber. The pressure with an oscillated swash plate shows larger pressure overshoot at the end of the increasing pressure transition and at the beginning of the decreasing transition. Unfortunately, the pressure overshoot produces large excitation forces and intensifies the vibration of the pump components. What's worse, the load-bearing and lubrication characteristics might be altered due to the variation of the pressure boundary. Regarding the design of the friction pair, the effect of the swash plate oscillation on the pressure boundary should be taken into consideration, especially in a high pressure variable displacement pump.

It also should be noted that there are many small ripples in the flow curve of the oscillated swash plate, which are caused by the vibration of the velocity in **Figure 6**. Besides, the large backflow in area A is mainly caused by the greater pressure in the discharge port than that in the piston chamber, when the piston starts to connect to the discharge port. It's interesting that the backflow decreases with an oscillated swash plate, which can be explained as an earlier precompression of the piston chamber in area B.

Outlet pressure and flow analysis

The outlet flow rate is shown in **Figure 8**. Compared with the outlet pressure in **Figure 5**, the trend of the flow rate and the pressure is similar. The reduced pressure ripple can be attributed to the decline of the flow fluctuation. The outlet flow rate is the sum of each piston outlet flow. From **Figure 8**, however, the minimum flow rate around the rotation angle of 100° is mainly affected by the backflow.

From the above analysis, we can see that the oscillation of the swash plate plays an important role in the assessment of the performance analysis in an axial piston pump. It can be conducted that the oscillated swash plate angle does help the precompression of the piston chamber. It contributes to the reduction of the backflow of each piston. As a consequence, the amplitude of the flow fluctuation and the pressure ripple can be reduced.

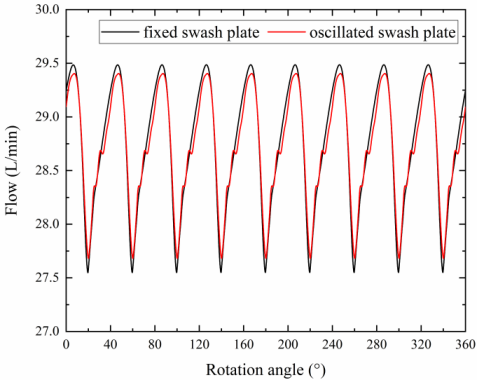

Figure 8: Comparison of pump outlet flow rate

3.3. Effect on control mechanism

Considering the control mechanism, the swash plate oscillation also leads to the motion of the actuator piston and counter piston. The pressure in the actuator piston fluctuates in order to counteract the oscillated torque on the swash plate, while the pressure in the actuator piston

fluctuates almost the same as the outlet pressure. But the variation of flow rate seems to be different from the pressure. **Figure 9** shows the flow rates from different chambers. The black, red, and blue line represent the flow rates from the nine piston chambers, the counter piston chamber, and the actuator piston chamber, respectively. And the mean value of the flow rate from nine piston chambers is subtracted from the instantaneous value. The green line represents the load flow rate. The load flow with a green line is a combination of the flow from different chambers besides compression flow.

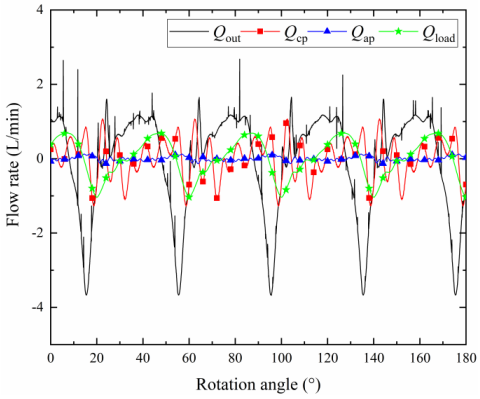

Figure 9: Output flow rate from different chambers at operation condition: 15MPa, 1000rpm, 12°

As we can see, the flow enters in and out of the counter piston chamber with the changing rotation angle. It can be interpreted as the additional movement of the actuator piston, which caused by the swash plate oscillation. The flow from the actuator piston chamber compensates the leakage across the actuator piston and sleeve. Owing to the larger flow ripple of nine pistons, the pressure ripple is generally decided by the flow from nine piston chambers. But for a variable displacement pump, it may also be influenced by the flow rate from the control mechanism. To be specific, the flow from nine piston chambers is less than the average flow (negative value) around 10-20° rotation angle. And the counter piston discharges a certain amount of flow rate which balances out the flow fluctuation caused by the nine-piston pump to some extent.

When large oscillation has been taken into consideration, as demonstrated in **Figure 10**, large flow fluctuation of the counter piston can be found. Especially, the flow from nine piston chamber shows a minimum around 20° rotation angle. At the same time, the hydraulic oil flows out of the counter piston chamber and reaches a peak value. The larger swash plate oscillation, the larger variation of flow rate from the counter piston chamber. As a result, the load flow fluctuation and pressure are changed.

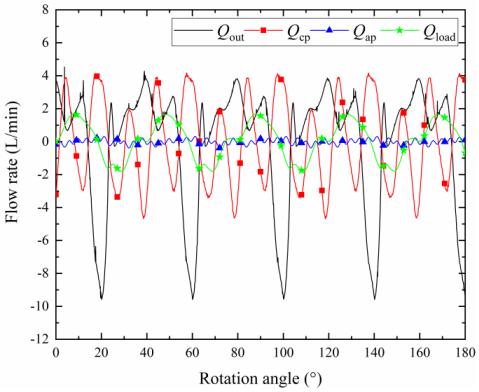

Figure 10: Output flow rate from different chambers at operation condition: 15MPa, 1500rpm, 12°

4. CONCLUSION

In this paper, a mathematical model of a self-supplied variable displacement axial piston pump is established to investigate the dynamic behavior of the swash plate vibration. In the view of the amplitude, the oscillation is more dependent on the rotational speed than pressure and displacement, which may be caused by the resonance frequency of pump dynamic system. However, the amplitude of swash plate oscillation is small in most situations.

Compared to the fixed swash plate, the piston pump with an oscillated swash plate perform a smaller pressure ripple. Analysis has been conducted to figure out the reason for different performance. The swash plate oscillation influences not only the movements of nine pistons, but also the control mechanism. On the one hand, the additional movement of nine pistons around the relief groove often provides a precompression of the pressure in the piston chamber, which sounds attractive to avoid cavitation during pressure transition. And the fluctuated velocity of the piston causes the ripple in flow curve of a single piston.

On the other hand, due to the oscillation of the swash plate, additional movement of the counter piston produces a fluctuated flow. In fact, it does contribute to counteracting the fluctuated flow rate caused by the nine pistons. For the reduction of the pressure ripple in a self-supplied variable displacement pump, the effect of the swash plate oscillation on nine pistons and the control mechanism should be taken into account.

5. ACKNOWLEGEMENTS

The research was supported by the National Key R&D Program of China (Grant Number 2018YFB2001100) and the National Natural Science Foundation of China (Grant Numbers 51890882 and 51835009).

NOMENCLATURE

a	Acceleration of the piston (m/s^2)
A_{ap}	Area of the actuator piston (mm^2)
A_{cp}	Area of the counter piston (mm^2)
A_{HP}	Opening area between the piston chamber and the outlet port (mm^2)
A_{HP}	Opening area between the piston chamber and the inlet port (mm^2)
c_{sw}	The coefficient of viscous friction (N·m/(rad/s))
C	The Flow Coefficient
d	Diameter of the piston (mm)
f	Friction force of the i-th piston (N)
f_{ap}	Friction force of the actuator piston (N)
f_{cp}	Friction force of the counter piston (N)
F	Support force of the i-th piston (N)
F_{ap}	Support force of the actuator piston (N)
F_{cp}	Support force of the counter piston (N)
J_{sw}	Rotary inertia of the swash plate (kg/m^2)
k_v	Gain of the control valve
K_e	Bulk modulus of the fluid (MPa)
L_{ap}	Moment arm of the actuator piston (m)
L_{cp}	Moment arm of the counter piston (m)
M_p	Moment of the piston (N·m)
M_{ap}	Moment of the actuator piston (N·m)
M_{cp}	Moment of the counter piston (N·m)
n	Pump shafe speed (rpm)
N	Piston numbers
P_i	Pressure of the i-th piston chamber (MPa)
P_{in}	Inlet pressure (MPa)
P_{out}	Outlet pressure (MPa)
P_c	Pressure of the actuator piston chamber (MPa)
P_{cp}	Pressure of the counter piston chamber (MPa)
Q_l	Flow rate (m^3/s)
Q_{in}	Inlet flow rate (m^3/s)
Q_{out}	The sum of flow rate from nine piston chambers (m^3/s)
Q_{ap}	Flow rate of actuator piston chamber (m^3/s)
Q_{cp}	Flow rate of actuator piston chamber (m^3/s)
Q_{load}	Load flow rate (m^3/s)
R	Radius of piston around driveshaft (m)
u	Control signal
v	velocity of the piston (m/s)
V_p	the volume of the piston chamber (m^3)
V_{ap}	the volume of the actuator piston chamber (m^3)
V_{cp}	the volume of the counter piston chamber (m^3)
x_{ap}	Displacement of the actuator piston (m)
x_{cp}	Displacement of the counter piston (m)
x_v	Spool displacement of the control valve (m)
z_i	Displacement of the i-th piston (mm)
m_{ps}	Mass of the piston and slipper (kg)
m_{ap}	Mass of the actuator piston (kg)
m_{cp}	Mass of the couter piston and slipper (kg)
β	Swash plate angle (deg)
φ_i	Rotational angle of the i-th piston
ω	Pump shafe speed (rad/s)
ω_v	Frequency of the valve (rad/s)

REFERENCES

[1] Ivantysynova M (2003) Hydrostatic pumps and motors: principles, design, performance, modelling, analysis, control and testing. Tech Books International.

[2] Manring N D. Valve-plate design for an axial piston pump operating at low displacements. Journal of Mechanical Design - Transactions of the ASME[J], 2003, 125(1): 200-205.

[3] Guan C, Jiao Z, He S (2014) Theoretical study of flow ripple for an aviation axial-piston pump with damping holes in the valve plate. Chinese Journal of Aeronautics, 2014, 27(1): 169-181.

[4] Ye S, Zhang J, Xu B, Song W, Chen L, Shi H, Zhu S (2017) Experimental and numerical studies on erosion damage in damping holes on the valve plate of an axial piston pump. Journal of Mechanical Science and Technology, 31(9), 4285-4295.

[5] Kumar Seeniraj G, Ivantysynova M (2011). A multi-parameter multi-objective approach to reduce pump noise generation. International journal of fluid power, 12(1), 7-17.

[6] Zeiger G, Akers A (1985). Torque on the swashplate of an axial piston pump.

[7] Kassem S, Bahr, M K (2000). On the dynamics of swash plate axial piston pumps with conical cylinder blocks. Sixth triennial international symposium on fluid control measurement and visualization.

[8] Achten P (2013). Dynamic high-frequency behaviour of the swash plate in a variable displacement axial piston pump. Proceedings of the Institution of Mechanical Engineers, Part I: Journal of Systems and Control Engineering, 227(6), 529-540.

[9] Fang X, Ouyang X, Yang H (2018). Investigation into the Effects of the Variable Displacement Mechanism on Swash Plate Oscillation in High-Speed Piston Pumps. Applied Sciences, 8(5), 658.

[10] Ericson L (2014). Swash plate oscillations due to piston forces in variable in-line pumps. In Proceedings of 9th International Fluid Power Conference, Aachen, Germany.

[11] Ericson L (2013). Movement of the swash plate in variable in-line pumps at decreased displacement setting angle. In Proceedings of the 22nd International Congress of Mechanical Engineering, Ribeirão Preto, SP, Brazil (pp. 3-7).

[12] SCHOEMACKER F, MURRENHOFF H (2019). Interaction Between Swash Plate Movement And Commutation In Axial Piston Machines. JFPS International Journal of Fluid Power System, 11(3), 49-54.

peer reviewed

INVESTIGATION OF THE WEAR BEHAVIOR OF THE SLIPPER IN AN AXIAL PISTON PUMP BY MEANS OF SIMULATION AND MEASUREMENT

Roman Ivantysyn*, Ahmed Shorbagy, Jürgen Weber

Institute for Fluid-mechatronic Systems, Technische Universität Dresden, Helmholtzstrasse 7a, 01069 Dresden
* Corresponding author: Tel.: +49 351 46333701; E-mail address: roman.ivantysyn@tu-dresden.de

ABSTRACT

Axial piston pumps are universal displacement machines that are used in a vast variety of applications. Their high pressure resistance and ease of operation make them very popular, especially in mobile applications. Some applications require more robust pumps with an extended lifetime, particularly those that operate in remote environments such as marine type or mining operations. Especially new applications like displacement control have high demands on pumps such as through shaft operation (many pumps on one shaft), high dynamics and multi-quadrant operation. These demands create challenges in terms of lifetime expectancy and robustness for pump manufacturers and machine OEMs. Currently most axial piston pumps go through a run-in process. During this process the softer bronze parts shave off and change their shape according to the necessary one for the pumps' proper operation. This process is highly dependent on the design of the parts and their manufacturing tolerances. In this paper the run-in process of the slippers of an axial piston pump was investigated by means of measurements of the gap height and wear profile as well as simulation. The measurements show a clear change of profile and gap heights for the first 120 h of the pumps operation. After that the gaps stabilize. The numerical simulations made with the program Caspar FSTI were coupled with contact wear models to output wear profiles. Different models will be introduced and compared with measurements. Both the amount of material removed and the performance of the pump before and after run-in will be discussed.

Keywords: Axial Piston Pumps, Wear, Gap Measurement, Simulation

1. MOTIVATION

Due to their high energy density, high efficiency and overall robustness, axial piston machines have been the primary choice for high pressure and mobile applications. The lifetime of such a machine can be very high, especially due to their hydrostatic bearings. However, todays pumps and motors go through a critical run-in process, where the nominal machined parts wear in. This wear can produce particles that influence other components downstream of the system. It is primarily the sealing lands that go through this crucial process, which are already machined within micron tolerances, changing their surface topology in order to withstand the required loads.

The moving parts of an axial piston pump and illustrations of the fluid films separating the parts, are shown in **Figure 1**. The slipper/swash plate interface, being the focus of this investigation, is shown on the right hand side.

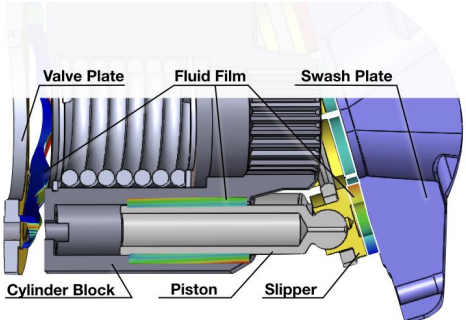

Figure 1: Tribological interfaces in axial piston pumps and their fluid films

The fluid film between the slipper and swash plate is a highly complex one, as it ranges from very small gap heights (<5 µm) on the high

pressure side, to rather large gap heights (around 100 µm) on the low pressure side, at typical fluid film behavior is shown in **Figure 2**. The simulation model was verified through very extensive measurements on two different pump designs, since the gap height ranges vary for each design [1, 2].

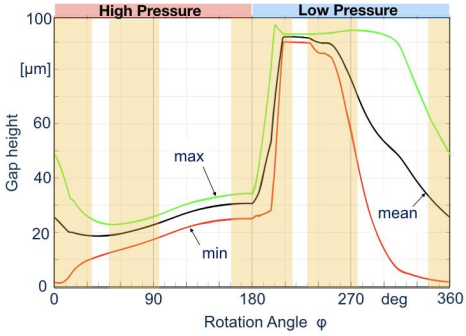

Figure 2: Typical Slipper Gap Heights of an Open Circuit Pump, simulated with Caspar FSTI and validated at the Highlighted Sections

Measurements published in a previous paper revealed that the slippers go through a run-in process, which can take up to 100 operating hours [1]. During this run-in the parts change their shape and have been shown to perform worse after the run-in was completed compared to before for this particular pump design. Other findings revealed that for specific operating conditions the simulated temperature field only matched the measurement, if the resulting material removal due to wear was considered in the simulation [3]. This wear process will be studied more in detail in this paper.

2. RESEARCH GOAL AND APPROACH

The aim of this paper is to present an approach to simulate the slipper run-in at various operating points using Caspar FSTI, which is a simulation tool that is capable of calculating the gap heights in axial piston pumps using numerical methods. The tool is explained in detail in [2,4,5], where the slipper calculations are described in full detail in Schenk [2].

The current version of Caspar FSTI does not incorporate the calculation of the wear of the parts. However, it is possible to input a measured wear profile, which enables indirect wear analysis. This is useful if a part design already exists.

The goal of the authors research is to develop a method that is capable of predicting the resulting wear based on simulation results only. Pump designers can then use this method to design parts with less, or possible even no wear. An example for this could be micro-surface shapes, which have shown to reduce the run-in of parts while also increasing efficiency [6]

3. GAP HEIGHT MEASUREMENTS

A 92 cc open circuit pump was analyzed for this research. A series of measurements were performed, including temperature and gap height measurements at both the valve plate and the swash plate of the pump. The methods, measurements and results can be seen in full detail in [1, 3, 6, 7, 8]. Both the valve plate as well as the slippers, each being the softer material than their counterpart glide partner, went through a run-in process, which could be observed in the measured signals.

The slipper gap height measurements were particularly interesting as they clearly illustrated the change in the fluid film thickness and the motion profile of the slipper throughout the run-in process. The fluid film thickness was measured using three eddy current sensors, carefully placed at four positions total, high and low pressure side, bottom dead center (BDC) as well as top dead center (TDC). The sensor placement at TDC is shown in **Figure 3**. The three sensors are positioned in a fashion, which enables an exact measurement at the TDC (phi $\varphi = 180°$).

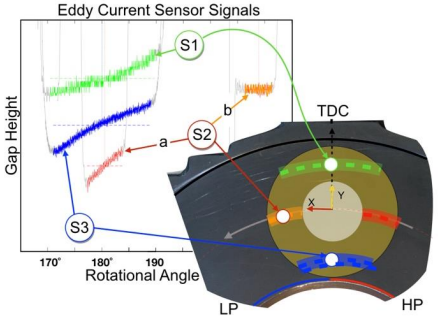

Figure 3: Measurement Location of the Eddy Current Sensors at the TDC

The graph in **Figure 3** illustrates the individual sensor outputs as the slipper slides over the TDC. It can be seen that sensors 1 (S1 in green) and 3 (S3 in blue) deliver a reading for the outer and

inner fluid film, respectively. Sensor 2 (S2a in red and S2b in orange) outputs two narrow bands as its reading is interrupted by the pocket. If S1 is higher than S3 the slipper is tilting towards the inside (around the x axis). If S2a is lower than S2b, then this indicates either that the slipper is lifting off after the TDC or that slipper is tilted forward (around the y-axis). The individual sensor signals also entail information about the current movement of the slipper at that instance in time. These individual slipper measurements (S1-3) were averaged over 50 revolutions for each slipper. The results for one operating point are shown in **Figure 4** and **5**. Since the pump consists of multiple individual slippers (nine in this case), it was observed that each slipper has a different initial gap height (**Figure 4**), and performs an individual run-in process. The measured fluid film thicknesses are shown for each slipper at the initial run (t=0 h in **Figure 4**) and after 120 h (**Figure 5**)

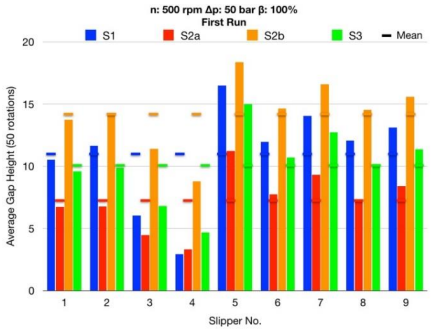

Figure 4: Measured Slipper Gap Height at t=0h

The horizontal lines that cross those bars are the mean of all slippers and act as a reference how uniform the slippers are to each other. For the initial run, it can be seen that many slippers deviate from the mean, some quite significantly. After the run-in the slippers are all very close to the mean.

In **Figure 4** each of the 9 slippers has a different gap height and position in space, as show in the relation between the sensors to each other. For example, in slipper 1 the S1 signal is higher than S3, indicating that the slipper is tilted slightly towards the inside. The mean gap height is 9 µm. However, slipper 3 shows an opposite tilt and an average gap height of 6 µm. Same analysis can be made for all 9 slippers.

After 120 operating hours (**Figure 5**) the gaps have all converged to a uniform fluid film. After the initial measurements slipper 5 was replaced with a different shape to act as a trigger, therefore it is missing, however all other 8 slippers are very close to the mean and show the same trends as well as positions in space.

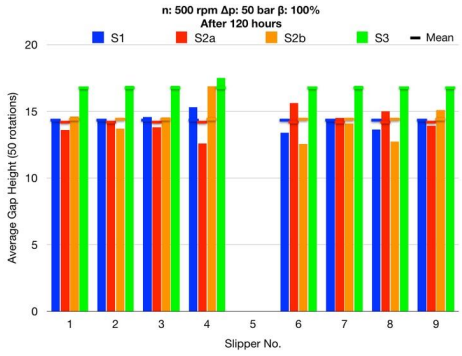

Figure 5: Measured Slipper Gap Height at t=120 h

It is important to note, that the pump was measured in a total of 78 different operating points from the initial measurement and the final after 120 hours. This means that the pump was run-in at various operating points and not just one single one. This would reflect a typical real-world application.

Interestingly the gap height of all slippers is higher after the run-in, than compared to the initial non-worn measurement. Higher gaps mean less viscous friction, but higher leakage. For each operating condition there is an optimal gap height, meaning the sum of the losses due to friction and leakage are at a minimum. The losses can be calculated as follows:

$$P_{leak} = Q_{SG} p_G = \frac{\pi h_G^3 p_G^2}{6\mu \ln\left(\frac{r_{out}}{r_{in}}\right)} \quad (1)$$

$$P_{friction} = F_{TG} \omega R_B = \pi \left(r_{out}^2 - r_{in}^2\right) \mu \frac{\omega^2 R_B^2}{h_G} \quad (2)$$

where h_G is the gap height, p_G is the pressure in the pocket, ω is the rotational speed, µ is the dynamic viscosity and r_{out} and r_{in} represent the inner and outer diameter of a single land slipper. The power loss is the sum of the P_{leak} and $P_{friction}$. The gap height is assumed to be constant and uniform for these analytical calculations [10].

The power losses for different slipper gap heights at 500 rpm, 50 bar and 100% displacement, the same operating condition as the measurement in **Figure 4-5**, is shown in **Figure 6**. Here the viscous and leakage losses are plotted with varying slipper gap height.

It can be observed that small changes in fluid film thickness can lead to rather large changes in power loss (10 W equal 2.6% efficiency drop).

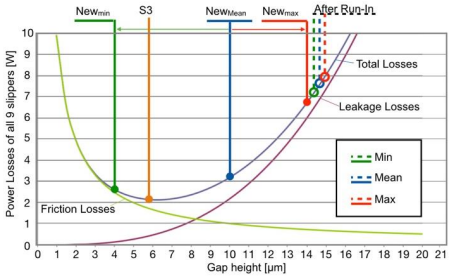

Figure 6: Predicted Power Losses with Changing Gap Heights at 500 rpm 50 bar 100% Disp.

In **Figure 6** the measured gap heights of the 9 slippers in their new shape (t=0 h in solid lines) and after the 120 h of operation (after run-in in broken lines) are plotted. The slippers in their new condition have a large spread in gap height, ranging from 4 to 14 µm resulting in power losses ranging from 2 – 6.5 W (0.5-1.7 % of the total power output) for all slippers. Slipper 3 had a rather perfect shape for this operating point, resulting in the lowest possible power loss at just 2 W.

After the run-in process the slippers all have converged to a tighter spread in gap heights, suggesting that they all have uniform surface shapes post run-in. However, the resulting fluid film height was higher than the worst of the slippers before the run-in (14.2-15.2 µm) and resulting in even worse power losses around 8 W which equals 2% efficiency drop of the pump.

This trend could be observed in a multitude of operating conditions, one other example can be seen in **Figure 7** for a higher speed and higher pressure. Here the power losses are an order of magnitude higher, resulting in a difference of 50 W, which results in a 2 % total efficiency drop at this operating point between the best new design and the worst worn in design for the entire pump.

These results clearly show that the run-in process must not result in an optimal shape of the parts, but rather serves the purpose to smoothen out manufacturing tolerances. The resulting shape can perform worse than before the run-in process. These findings cannot be taken as a general trend, as this was only measured on one pump series. However, they show that the run-in process needs to be considered during the design process, as it can influence the efficiency of the parts drastically.

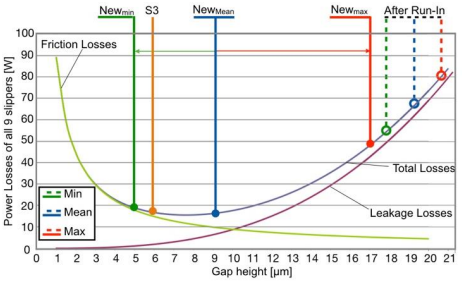

Figure 7: Predicted Power Losses with Changing Gap Heights at 1500 rpm 100 bar 100% Disp.

4. WEAR PREDICTION MODEL

Simulation tools are becoming more and more important in today's design process. CAD, CFD and FEM tools are one example how software tools have enabled new designs and developments by giving engineers a better insight into the products they are developing. The development of a capable tool to simulate the performance of axial piston pumps has been the goal of many researchers [12,12,13]. Such a tool would enable the use of new materials, shapes and most importantly optimization of the sealing lands of these machines. Caspar FSTI was developed by a series of researchers throughout many years and publications [2, 4, 5, 9]. This tool is already capable of simulating and analyzing the fluid film in axial piston pumps and has been validated in many different pumps and motors [1, 2, 3, 4, 5]. However, the wear-in process has not been fully captured by this tool yet. Therefore, the goal of this research is to develop a wear tool that uses Caspar FSTI to predict the wear-in process and more importantly the resulting performance of the parts after such wear.

The simulation solves a simplified version of the Navier-Stokes equation as shown in **Figure 8**. The simplifications are 1) no transient flow is considered in the gap 2) no fluid inertia is considered, 3) fluid forces are neglected. The resulting equation is further simplified assuming laminar flow, and no changes in velocity along x and y in the fluid grid (refer to **Figure 9** top left). The resulting equation is then solved along with the energy equation, Newtons equation of motion and considering deformation due to pressure and temperature. The thermal

temperature loop, which calculates the temperature of the parts and the fluid, is updated after each simulated revolution is completed, using the viscous losses as the heat source. The simulation is seen as completed when the temperature of the parts converged to a steady state value.

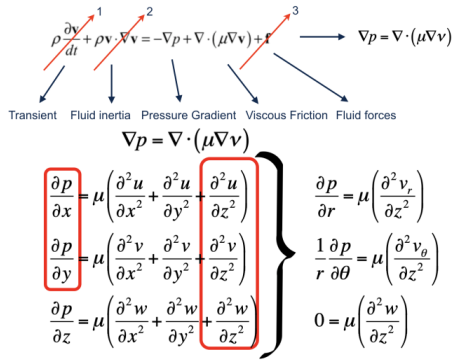

Figure 8: Simplifications of the Navier-Stokes Equation in Caspar FSTI

The primarily outputs of the simulation are the gap heights, temperature and pressure fields at each fluid grid point for each time step. They are illustrated in **Figure 9** for the slipper / swash plate interface.

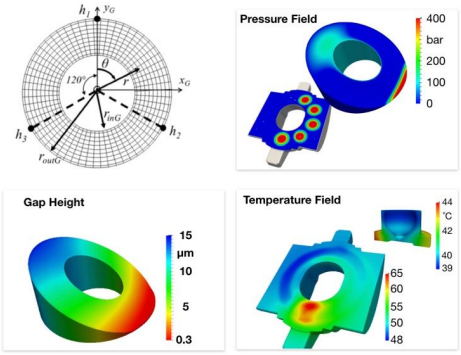

Figure 9: Fluid grid (top left), and important simulation outputs: gap height (bottom left), pressure and temperature field of the slipper during a wear process (right).

Other significant outputs of the simulations are the power losses, viscous friction, leakage, thermal load and contact pressure. The contact pressure is particularly interesting in this case, it is only outputted if the simulation is unable to balance the forces acting on the slipper with the pressure in the fluid film. Meaning that the fluid film alone is not sufficient to bear the loads and in reality it would come to metal to metal contact between the moving parts. The contact pressure is therefore the difference in the maximum pressure the fluid film is able to exert and the acting pressure from the external forces at one grid point. An example of a contact pressure is presented in **Figure 10**. Here the fluid film is shown as a function of rotation angle for a medium speed medium pressure operating point. The minimum gap height is plotted in blue. It can be observed, that the gap is very small around the TDC (ϕ = 180°, **Figure 10** top left). For this instance in time, TDC at this operating point, the resulting pressure field, gap height and temperature of the swash plate can be seen in **Figure 9**. The pressure is extremely high, 4x the pressure in the displacement chamber. The corresponding gap height is 0.3 µm at the leading edge of the slipper. This is the smallest possible gap height, as the surface roughness is larger than that. Therefore, the simulation will not decrease the gap further, but rather will counter the loading force with a contact pressure. The distribution of the corresponding contact pressure can be seen in **Figure 10** top right. The resulting normal force is the contact pressure multiplied with the area of the fluid cell - its distribution is visualized on the bottom left. Finally, the contact forces that occur at each grid point during one revolution are added, the result is plotted on the bottom of the figure. This force will now be used in the wear model.

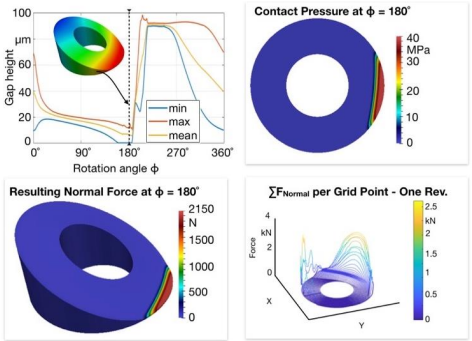

Figure 10: Contact Force Generation; min. Gap Height (top left), Resulting Contact Pressure at min. Gap Height (top right), Resulting Normal Force at min. Gap Height (bottom left), Summed Up Normal Force for one Revolution at each Grid Point (bottom right).

4.1. Archard's Wear Model

Archard developed a simple wear model, which is based on equation (3) below, where S is the contact length, N the normal force, H the hardness of the material and K is a wear coefficient.

$$W = K\frac{SN}{H} \tag{3}$$

The wear coefficient is therefore the only unknown in this approach. There are multiple publications that studied this coefficient, Romalho and Miranda for example have discovered that a linear correlation as suggested by Archard, can be confirmed by measurements [14]. Amiri used an energy-based approach, which seems very intuitive and most importantly physics based [15, 16]. In his work the coefficient K is based on the slope of the measured temperature rise vs. the heat transferred to the body during a wear process between two materials, an example is shown in **Figure 11**. For the material pairing of the slipper and the swash plate, the slope of the curve is K = $2x10^{-4}$ as can be found in his work [15]. This value was used for the later explained wear model implementation into the gap simulation.

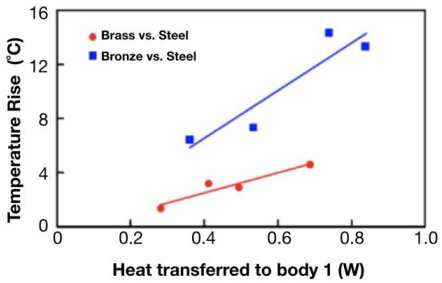

Figure 11: Experimental Determination of the Wear Coefficient [15]

Using an energy-based coefficient makes sense as the wear process must be explainable with energy conservation. Energy due to friction is converted into heat, however some energy must be lost when atoms are being broken out of their bonding. Archards's approach was first implemented into the wear model and it yielded good results as will be seen in the next chapter. However, Archard does not consider surface roughness, surface topology and other material properties that surely have an influence on the wear of the material. A more expansive approach, which considers many more factors than Archard, is discussed next.

4.2. Fleischer's Wear Model

Fleischer published a series of publications in German language, where he covered wear in great detail [17]. Without getting in too great of detail, his work can be summarized as follows: The wear volume V_V is a function of the wear work - w_R and the wear energy density – e^*_R as shown in equation 4.

$$V_V = \frac{w_R}{e^*_R} \tag{4}$$

To explain the wear work and energy density more information is necessary. Fleischer's work assumes that the process of wear is a series of discrete micro contacts, which are finite and mainly dependent on the surface topology. It can be described as a meshing of many tiny teeth that need form a small mechanical bond. Friction is the process that breaks this bond either by deformation in either plastic or elastic fashion, or shearing the teeth off. The smoother the surface the smaller the teeth and the less energy is required to "un-mesh" the teeth. Since the process occurs in a micro to nano scale, chemical reactions cannot be neglected, as heat and mechanical stress can lead to changes in the chemical bonds of the material, changing its material properties. This can be observed in brass materials that contain lead. They change their surface topology after the wear in process and become smoother. Chemical analyses of worn in surfaces have shown new types of alloys that were not present before the wear [18]. The wear work is the sum of all discrete miniature "un-meshing" processes and is a factor of surface roughness, material hardness, density, elasticity, chemical composition, thermal capacity, number of peaks and valleys in the surface and many more material properties of both surfaces. The wear energy density is a function of number of contacts ("teeth"), the shear rate, the shear energy, and the energy accumulation number, one of many factors that Fleischer introduced, can only be empirically determined through experimental surface analysis.

As can be seen Fleischer's approach is far more complicated and would require many more pages to explain in full detail, however it is explained in great extend in [17]. Due to the complexity of the model, especially with

parameterizing the correct inputs, the model has not yet been fully implemented, but will be so in future work.

5. SIMULATION RESULTS

The following simulation results are all based on Archard's approach. Its implementation into the simulation was done in a recursive loop until the wear-in process was completed, meaning no more contact was present.

The first step in the wear simulation, is to find out which operating conditions cause the most wear for a given pump design. This can be done by measurements using particle sensors, or by a validated simulation model. Particle measurements only deliver the total wear and cannot be separated into the individual components. The simulation model for the 92 cc pump was already verified using gap and temperature measurements in previous publications [3, 5, 6], hence it was used to determine the most critical conditions for the slipper.

Table 1: Simulated operating conditions with contact pressure for the 92 cc pump

OC	Speed [rpm]	Pressure [bar]	Displacement [%]
3	500	50	50
4			100
6		100	50
7			100
9		200	50
10			100
12		300	50
13			100
16	750	50	50
17			100
22		100	100
23		200	100
25		300	50
26			100
35	1000	200	50
36			100
38		300	50
39			100
51	1250	300	50
52			100

All 78 measured operating conditions were simulated, they ranged from 500 – 1800 rpm, 50 – 300 bar and 50 – 100% displacement. The operating conditions where the simulation predicted wear for the slipper are shown in Table 1 below. The yellow highlighted operating conditions (OC) were chosen for the wear in process, as the simulation predicted stronger wear. After the most critical operating conditions for the run-in were determined, a run-in procedure was performed for each operating point. This was done as explained in **Figure 12** and **13**.

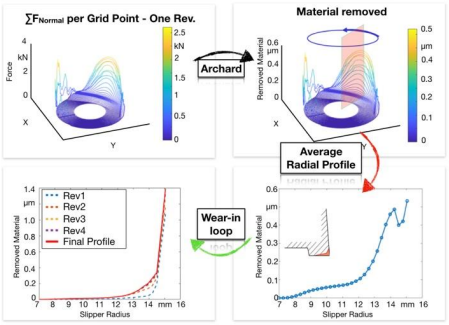

Figure 12: Wear-in profile calculation

First the non-worn surface was simulated. After the simulation converged (the part body temperature stabilized), the last simulated revolution would then be analyzed for wear. If there was contact pressure throughout the last revolution at any point, the wear was calculated using Archard's approach using the wear coefficient as described in section 4.1. The necessary normal force acting at each grid point in the gap was derived from the contact pressure. The resulting 3D wear (top right in **Figure 12**) was averaged around the perimeter, to yield a uniform wear profile. In reality this uniform wear takes many operating hours, as the slipper rotates around its own axis and would wear-in one small area at a time.

The averaged profile would be subtracted from the slipper material (bottom right in **Figure 12**) and would set the starting shape for the next simulation iteration. If the following simulation predicts contact pressure, the wear-in loop would be repeated and the resulting wear profile would be added to the previous one. This iteration was repeated until no more wear was predicted by the simulation. The wear profile would usually be quite strong in the first view iterations. For each operating point it was observed, that after the first 2 - 3 iterations, the predicted contact diminished, resulting in reduced wear as

illustrated in the bottom left in **Figure 12**. The described iterative procedure, as presented in **Figure 12**, was repeated for all 11 operating points, as highlighted in Table 1. The results can be seen in the next section.

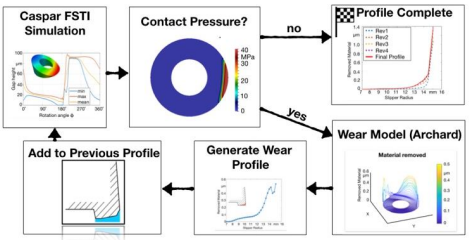

Figure 13: The Work Flow of the Wear-in loop

5.1. Isolated operating condition wear

In this section wear-in results are shown for various operating conditions, as predicted by the simulation using Archard's wear approach. **Figure 14** shows the final wear-in profile for all 11 simulated operating conditions. It can be seen that the OC 10 and OC 22, show the most wear. Both of these operating points are at medium pressure, 200 bar, and rather low speeds.

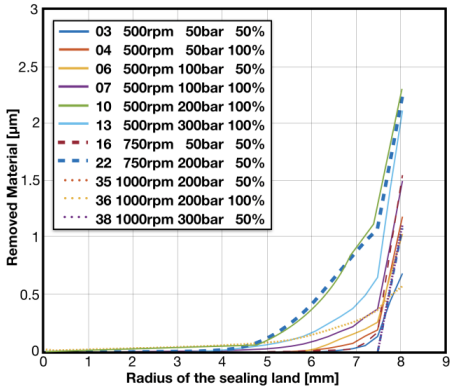

Figure 14: Final Wear Profile as Predicted by the Simulation for Various Operating Conditions.

It doesn't seem very intuitive, that the most wear occurs during a medium pressure level. One would expect it to either occur at low pressures, where the hydrodynamics of the slipper play a larger role, increasing tilt, or during high pressure, where pressure deformations tend to change the gap shape. However, it turns out that for this slipper design, the balance of the hydrostatics was quite low. This means that the hydrodynamics are needed to balance the forces, as the hydrostatics are not sufficient. At low speeds the hydrodynamics are insufficient, therefore the wear increases. As the speed increases there is barely any wear, and post 1500 rpm there is no wear on the slippers whatsoever at any pressure level.

The impact of speed on the wear amount is shown in **Figure 15**. Here 4 operating points are shown. Three speed level: 500, 750 and 1000 rpm, as well as two displacement level all at the same pressure. Comparable operating points are plotted in the same color, whereas the speed levels are shown in different line types: 500 rpm in dashed lines, 750 rpm in dotted lines and 1000 rpm in full lines.

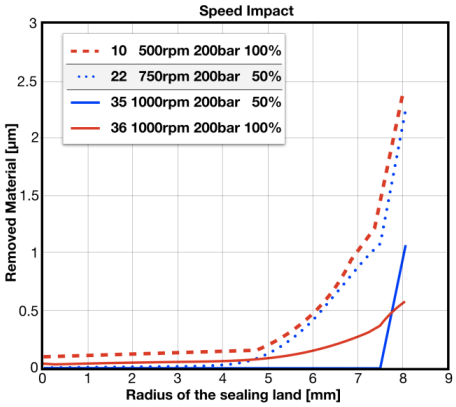

Figure 15: Speed Impact on the Wear Profile

It can be observed that lower operating speeds produce more wear than higher ones for the same pressure level. Whereas the higher the swash plate angle the higher the wear. This makes sense as the forces on the slipper increase with higher angle. This trend is displayed for more pressure levels in **Figure 16**. Similar to **Figure 15** each displacement level has its own line shape and comparable operating points are shown in the same color at the same speed 500 rpm. It can be seen that the same trend as in **Figure 15** for 1000 rpm and 200 bar can be observed for 50 and 100 bar at 500 rpm. The lower the displacement the lower the wear.

The impact the pressure has on the wear profile is introduced in **Figure 17**. Four pressure level are shown at the same speed and displacement. There is a trend visible that the higher the pressure the higher the wear. This

seems logical as the forces on the slipper increase with higher pressure, especially for underbalanced slippers. However, 200 bar is predicated to have a higher wear than 300 bar. This seems rather counter-intuitive at first, however it does make sense as the pressure and temperature deformation of the slipper increase with higher pressure and the deformation actually increases the gap heights at the outer diameter. This also explains why there are less 300 bar operating conditions with higher wear than ones at 200 bar.

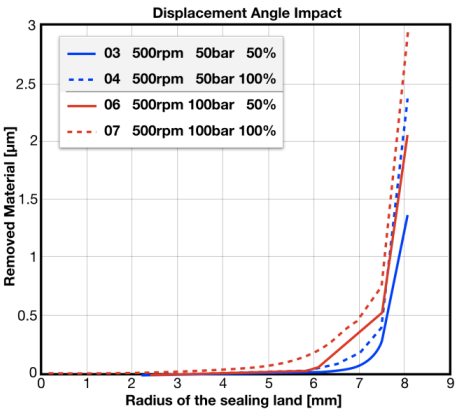

Figure 16: Impact of the Displacement Angle on the Wear Profile

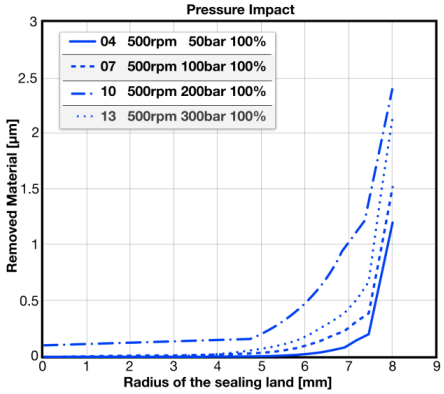

Figure 17: Impact of the Pressure on the Wear Profile

To summarize it can be said, that underbalanced slippers tend to have more wear at lower speeds, higher pressures and higher displacements. However, the deformation of the parts can inverse some of these trends.

5.2. Connected operating conditions

Section 5.1 analyzed the run-in for stationary points one at a time. In reality the pump will experience a series of operating conditions, which will lead to effects not considered in 5.1. In order to be able to compare the simulations to measurements, it is necessary to generate the wear profile as it was created in the measurements. The measurements always started in low operating speeds and then gradually increased pressure then speed. In **Figure 18** summarizes the resulting wear profile in exactly such a scenario. As expected combining operating conditions with each other results in different results.

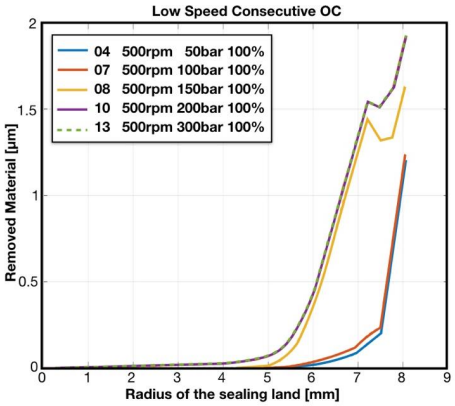

Figure 18: Low speed Wear Profile with Consecutive Operating Conditions

Figure 18 shows the resulting wear as it would occur after the first five operating conditions of the measurement series at 500 rpm and full displacement. The strongest wear would occur at OC 08, 500 rpm, 150 bar and 100%. The wear stopped after 200 bar as indicated by the overlying lines of OC10 and OC13. It should be mentioned at this point, that the numbering of the OC are not in the order they were measured, but rather in an systematic fashion increasing in speed, pressure and displacement.

By comparing **Figure 18** and 14 it becomes apparent that OC 08 does not show any wear by itself, however when the wear from OC07 and OC04 is given as an input, suddenly there is strong wear. In addition, OC13, which showed stronger wear by itself, does not show any sign of wear after all pressure levels until that point have run through the wear-in. This wear-in profile was simulated also with all pressure levels of

750 rpm, none removed more material. Therefore, it can be concluded that the order of which the run-in occurs does play a role and the resulting shape must not always be the same.

5.3. Comparison to Measurement

In order to validate the simulation findings, and to determine if Archard approach yields acceptable results, the simulation results are compared to measurements. Two approaches were taken to compare the results. The wear profile itself and gap height measurements. It should be noted, that the previously presented simulations were performed with the nominal slipper dimensions, taken from the drawings. However, in reality the dimensions vary with the manufacturing tolerances. Therefore, the slippers were measured with a profilometer and the simulations were repeated with the mean, max. and min. of the measured dimensions. Only the mean will be shown in the next section.

Wear profile

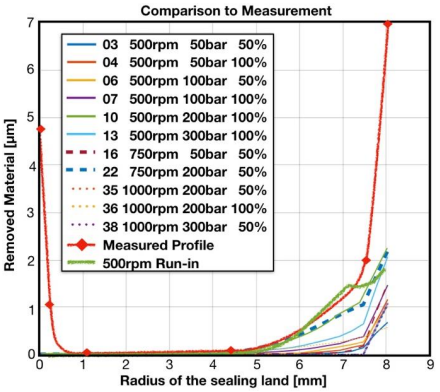

Figure 19: Measured Profile vs Simulated Ones.

The measured wear profile is plotted in **Figure 19**, it consists of a series of measured points that were averaged from all slippers. The profile on the outer edge seems to follow the overall trend very well. The outer edge maybe higher worn than in the simulation but one needs to consider that the simulation only considers steady state conditions. It is quite likely that during cold starts or highly dynamic conditions, such as rapid swashing, the slipper tilt increases and wears even more. This might also be the explanation for the wear on the inner edge of the slipper. Only a few simulations indicated wear at the inner radius of the sealing land, but they were on the maximum of the tolerance band and don't explain the wear for the mean dimensions. One explanation could be, that during a cold start, when all temperatures are equally low, the slipper starts to tilt and decrease its fluid film at the outer edge, increase friction and its local temperature. This thermal loading could lead to unusual deformation where the inner sealing land has a lower profile than the outer.

The thick green line represents the accumulated wear profile at low speeds with various pressures (see **Figure 18**). It suggests that a run-in at low speeds could be sufficient to achieve a working profile for all operating conditions. Overall one could say, that Archard's approach yielded reasonable results, especially for the high wear conditions such as OC10 and OC22.

Gap Height Measurement

In order to see if the simulation is capable of predicting the correct performance in terms of power loss and gap height before and after the run-in, the power loss chart will be used again. OC4, 500 rpm, 50 bar and 100 % displacement is shown in **Figure 20**.

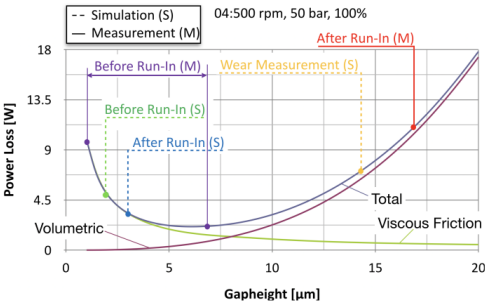

Figure 20: Gap Height Before and After Run-In for Simulation and Measurement at OC4

The measurement is shown in solid lines, and the simulation in dashed lines. The measured gap heights had a large spread before the run in, this is due to the tolerances of the manufacturing process. After the run-in the gap heights converged, but to a higher value with more losses. The simulation predicts the gap heights of the nominal slipper within the measured tolerance spread. Post run-in both the measured and simulated gap heights increased, however the simulated one does not increase as strongly as the

measured. This can be explained as follows. For this operating point the simulation predicted some wear, but not very significant. This means that the original shape of the slipper performs sufficiently well. Wear only occurs during low gap heights and therefore high friction. Once the slipper fluid film is sufficient to bear the loads, no more wear occurs. This means wear only occurs when the slipper is left of the optimum point. If the slipper wears off in a different operating point, let's say one with a higher pressure, then the shape changes and it can influence the performance at this lower pressure OC as well. The yellow dotted line shows the simulation output using the measured slipper profile. Using this profile, the simulation predicts a gap height, which is much closer to the measured one.

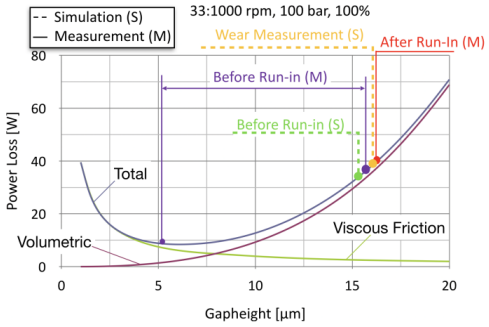

Figure 21: Gap Height Before and After Run-In for Simulation and Measurement at OC33

Figure 21 shows the power loss for OC33. 1000 rpm, 100 bar and 100% for the measurement (solid lines) and the simulation before and after run-in. The simulation actually did not predict any wear for this operating condition (before equals after). However, the simulation with the measured profile proves a clear change in gap heights towards higher gap heights and larger losses. These two examples show that the simulation is capable of predicting the resulting performance changes due to the shape change that occurs with wear, however more research is necessary to predict the final shape.

6. CONCLUSION

The run-in procedure plays a significant role in today's hydraulic pumps and motors. It allows for wider tolerances, as the incorrect shape of the slipper will be "corrected" by the wear process. However, it was shown that this final shape must not yield the best design, but rather a design that works in all operating conditions. The goal of this research is to improve the simulation tool Caspar FSTI, by adding a wear-in loop. This loop detects operating conditions that are insufficiently borne due to an insufficient fluid film and calculates the amount of material that needs to be removed. Currently the wear model is based on Archard's law, with an empirically determined wear coefficient. Future work aims to compare this approach with a more complex Fleischer model.

The simulation results are very promising, as it was capable of identifying operating conditions with wear and predicting realistic trends both in shape and magnitude of the wear. In addition, the slipper gap heights before and after run-in were correctly projected as confirmed by gap height measurements.

The wear-in process is not due to a single operating point, neither by extreme conditions at the border of the operating range, but rather consist of a mixture of operating points that occur after each other, each contributing a small part to the final profile shape.

In the next steps a tolerance analysis will be performed to determine the impact the manufacturing tolerances have on the wear process. Furthermore, the impact of the order of the operating points during the run-in will be studied, to answer the question if there is indeed an ideal run-in scenario. Finally, the difference between Archard's and Fleischer's wear model will be investigated.

NOMENCLATURE

TDC	Top Dead Center
FSTI	Fluid Structure Thermal Interaction
SX	Sensor X
cc	Cubic Centimeter per revolution
OC	Operating Condition
N	Normal Force
S	Wear length
H	Hardness
W	Work
k	Wear coefficient
p	Pressure
ρ	Density
μ	Dynamic viscosity
h_G	Gap height
HP	High pressure
LP	Low pressure
ω	Rotational speed
F_{TG}	Frictional force of the slippers

Q_{SG}	Leakage of the slippers
r	Radius of the slipper
V_V	Wear volume
e^*_R	Wear energy density
W_R	Wear work

REFERENCES

[1] Ivantysyn, Roman ; Shorbagy, Ahmed ; et. al.: Analysis of the Run-in Behavior of Axial Piston Pumps. In: IEEE GFPS 2018. Samara, Russia, 2018 — ISBN 9781538647851

[2] Schenk, Andrew: Predicting Lubrication Performance Between the Slipper and Swashplate in Axial Piston Hydraulic Machines, Dissertation, Purdue University, 2014

[3] Ivantysyn, Roman ; Weber, Jürgen: Investigation of the Thermal Behaviour in the Lubricating Gap of an Axial Piston Pump with Respect to Lifetime. In: 11. IFK 2018, 2018

[4] Pelosi, Matteo: An Investigation on the Fluid-Structure Interaction of Piston/Cylinder Interface, Dissertation, Purdue University, 2012

[5] Ivantysynova, Monika ; Baker, Jonathan: Power loss in the lubricating gap between cylinder block and valve plate of swash plate type axial piston machines. In: International Journal of Fluid Power Bd. 10 (2009), Nr. 2, S. 29–43

[6] Ivantysyn, Roman ; Shorbagy, Ahmed ; u. a.: An Approach to Visualize Lifetime Limiting Factors in the Cylinder block / Valve Plate Gap in Axial Piston Pumps. In: FPMC2017-4327, 2017, S. 1–12

[7] Ivantysyn, Roman ; Weber, Jürgen: “Transparent Pump” – An approach to visualize lifetime limiting factors in axial piston pumps. In: ASME 2016 9th FPNI Ph.D Symposium on Fluid Power. Florianapolis, Brazil, 2016

[8] Shorbagy, A., Ivantysyn, R., Weber, J. An experimental approach to simultaneously measure the temperature field and fluid film thickness in the cylinder block/valve plate gap of an axial piston pump. 9th International Symposium On Turbulence, Heat and Mass Transfer, Rio de Janeiro, Brazil, 2018

[9] Wieczorek, U. and Ivantysynova, M. 2002. Computer Aided Optimization of Bearing and Sealing Gaps in Hydrostatic Machines - The Simulation Tool CASPAR. International Journal of Fluid Power, Vol. 3 (2002), No.1

[10] Ivantysyn, J., and Ivantysynova, M. "Hydrostatic pumps and motors." Academia Book International, New Delhi, India (2001).

[11] Deeken, M. (2004). Simulation of the tribological contacts in an axial piston machine. In IMECE04 (pp. 1–5).

[12] Wegner, D. S., & Löschner, F. (2016). Validation of the physical effect implementation in a simulation model for the cylinder block / valve plate contact supported by experimental investigations. In IFK2016

[13] Dowd, J. R. and Barwell, F. T. 1974. Tribological interaction between piston and cylinder of a model high pressure pump. Transactions ASLE, 18, pp. 21–30.

[14] Ramalho, A.; Miranda, J.: The relationship between wear and dissipated energy in sliding systems. In: Wear (2006), 260., 361-367

[15] Amiri, M.; Khonsari, M.: On the Thermodynamics of Friction and Wear—A Review. In: Entropy (2010), 12.,1021-1049

[16] Amiri, M.; Khonsari, M. et al.: On the Relationship Between Wear and Thermal Response in Sliding Systems. In: Tribology Letters (2010),38., 147-154

[17] Fleischer, G. et al.: Verschleiß und Zuverlässigkeit, 1980

[18] Bushlya, Volodymyr, et al. "Wear mechanisms of uncoated and coated cemented carbide tools in machining lead-free silicon brass." Wear 376 (2017): 143-151.

peer reviewed

A FAST APPROACH FOR COUPLED FLUID-THERMAL MODELING OF THE LUBRICATING INTERFACES OF AXIAL PISTON MACHINES

Swarnava Mukherjee*, Lizhi Shang, Andrea Vacca

Maha Fluid Power Research Center, Purdue University, USA
* Corresponding author: Tel.: +1 (765) 496-1283; E-mail address: mukher25@purdue.edu

ABSTRACT

The temperature distribution of the lubricating interfaces is an important aspect of the functioning of positive displacement machines. It can determine the efficiency and the life time of the unit. In particular, it directly affects the fluid properties and the thermal induced deformations of the solid bodies. A simulation tool capable of predicting the fluid temperature in such gaps thus becomes very useful in the design process of these machines. The temperature distribution in a film comprises of many physical phenomena including convection and conduction along and across the film. Past numerical approaches solved this multi-directional conduction-convection problem using a three-dimensional(3D) grid, making the tool computationally expensive and unsuitable for fast simulations. This paper proposes a hybrid fluid temperature solver, based on, a low computational cost two-dimensional(2D) grid, to reduce the simulation time with reasonable accuracy. The piston/cylinder interface of an axial piston machine is selected as reference case to demonstrate the proposed approach. The hybrid approach was found to speedup the simulation times by 36%.

Keywords: Heat transfer, Lubrication, Piston/cylinder interface, Energy equation

1. INTRODUCTION

Lubricating interfaces form a very critical area when designing axial piston machines. They have a direct impact on critical performance parameters like energy efficiency and load carrying ability. The evaluation of the lubricating features of these interfaces is rather complicated due to several physical phenomena that occur through them. The pressure in these gaps can reach very high values owing to the loading these gaps balance. Due to the micron level thickness of these gaps, a considerable amount of viscous dissipation occurs, leading to high temperatures. Both pressure and temperature in the lubricating film directly affect the gap dimension of these films, owing to pressure as well as thermal induced deformations of the bounding solid bodies. The design of these interfaces through simplified numerical procedures and trial and error-based methods often is very expensive due to several design iterations. Thus, it becomes very important to develop simulation tools capable of accurately predict the performance of these interfaces.

Among all the different physical phenomena occurring in these interfaces, the thermal behavior is one of the most important ones to consider. The temperature in the interfaces directly affects the viscosity, the density and the thermal induced deformations of the bounding solids. Predicting the temperature of the film poses a challenge in terms of the problem size. The energy transport equation needs to be solved in the film to predict the temperature distribution in the film[1]. This equation is a 3D equation. The three-dimensions pose a numerically large problem to solve, which affects the simulation time. With the desirable goal of bringing simulation tools in within the design processes, the simulation time is a very important factor. At the same time, since the calculation of the gap fluid pressure distribution is in a 2D domain, the fluid viscosity and density field that is calculated using the 3D temperature distribution are always averaged into a 2D field. This will be further explained in the following paragraphs.

The goal of this paper is to propose a method to solve the energy equation in two dimensions, drastically reducing the size of the problem and

speed up the simulation time. The assumptions and simplifications are rationalized in the following sections.

Although the proposed approach is of general applicability to other lubricating interfaces, to demonstrate the proposed energy equation model, the piston/cylinder interface of an axial piston machine of swashplate type is chosen as reference. The piston/cylinder interface is one of the most important lubricating gaps in an axial piston machine owing to its tight clearances and its fundamental load carrying function. The first numerical simulation of pressure distribution in the piston/cylinder interface was conducted by Van der Kolk[2]. This was a simplified model considering a tilted journal bearing. The motion of the piston was firstly considered by Yamaguchi[3]. The first non-isothermal fluid model for the piston/cylinder interface was introduced by Ivantysynova[4] which addressed the non-constant fluid properties in the fluid film. Olems[5] first considered the piston micro-motion from the force balance between external loads and the pressure in the interface. Wieczorek et al.[6] introduced the simulation tool CASPAR, a computer aided optimization tool capable of predicting the pressure and temperature behavior in all the lubricating interfaces of an axial piston machine. Huang et al.[7] later introduced the effect of elasto-hydrodynamic lubrication in the piston/cylinder interface utilizing an offline influence matrix approach to evaluate the pressure deformations. Pelosi et al.[8] introduced the first coupled fluid-structure-thermal interaction model for the piston/cylinder interface accounting for the pressure and thermal deformations. Pelosi et al.[9] further updated this model for accurate prediction of pressure distribution in the film. Shang et al.[10] introduced a method to predict the port flow temperatures to make the previous models completely independent from requiring measurement data. Shang et al.[11] later introduced a coupled heat transfer model for the accurate evaluation of the solid body temperatures. The temperature distribution in the lubricating film of a plain journal bearing was studied by McCallion et al.[12]. A comparison between numerical and experimental thermodynamic behavior of a journal bearing was conducted by Ferron et al.[13]. A numerical study of the film temperature and its effect on the performance of the piston/cylinder interface of an axial piston machine was performed by Song et al.[14].

An overview of the state of the art fluid structure thermal interaction model developed by Pelosi et al.[8] is shown in **Figure 1**. In this model, the 2D pressure and 3D temperature distributions are solved for, in the fluid domain using the finite volume approach. The pressure and gap heights are solved accounting for the fluid-structure interaction through pressure deformations, followed by solving the energy equation. The heat flux from the fluid film is averaged over one shaft revolution to solve for the solid body temperature distribution followed by solid body thermal deformation. These temperatures and deformations are then used as updated boundary conditions for solving the fluid pressure and temperature in the following revolution.

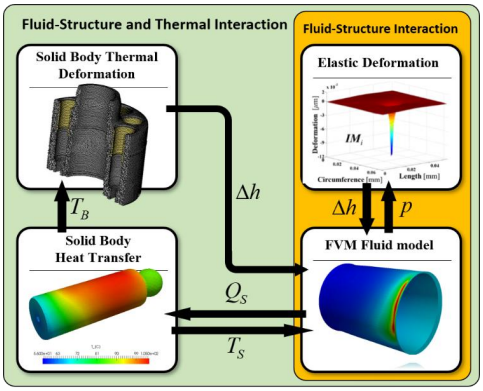

Figure 1 Fluid Structure Thermal interaction model

The current paper builds on the works of Wieczorek et al.[6] and Pelosi et al.[15] to introduce the mentioned 2D energy equation, for the simulation model to be more adoptable into iterative design and optimization processes.

2. 3D FLUID DOMAIN THERMAL MODEL

The energy equation is provided in Eq.(1). This equation is solved once the Reynolds equations is solved. The velocity in the first term of Eq.(1) is derived using a combination of the pressure field and the velocity of the piston running surface

contributing to both the Couette and the Poiseuille components.

$$\rho c_p \vec{V} \cdot \vec{\nabla}\mathrm{T} - \vec{\nabla} \cdot \left(\lambda \vec{\nabla} T\right) = \mu \Phi_D \qquad (1)$$

In the previous approach[6], Eq.(1) was discretized using the finite volume approach on a grid similar to that shown in **Figure 2**. The fluid domain between the bore and piston is discretized in the circumferential, axial as well as the radial direction. The grid shown in **Figure 2** is unwrapped circumferentially such that the circumference is along the x-axis, the axial direction is along the y-axis and the z-axis is aligned along the film thickness. **Figure 3** shows one finite volume cell from the unwrapped fluid domain. T_E, T_W, T_N, T_S, T_T and T_B represent the temperatures of the east, west, north, top and bottom neighbor temperatures of a given cell temperature T_P. The respective walls of the cell are represented by e, w, n, s, t and b. Δx, Δy and Δz represent the dimensions of the cell along the x, y and z axis.

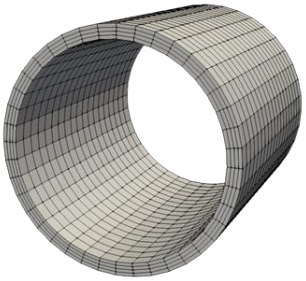

Figure 2 3D FVM grid

The discretized form of Eq.(1) for the cell shown in **Figure 3** is shown in Eq.(2). The coefficients are shown in Eq.(3) to Eq.(10).

$$\begin{aligned} a_E T_E + a_W T_W + a_N T_N + a_S T_S \\ + a_T T_T + a_B T_B \\ + b = a_P T_P \end{aligned} \qquad (2)$$

$$\begin{aligned} a_E = D_x \cdot \max\left(0, \left(1 - \frac{0.1|F_x|}{D_x}\right)^5\right) \\ + \max(0, -F_x) \end{aligned} \qquad (3)$$

$$\begin{aligned} a_W = D_x \cdot \max\left(0, \left(1 - \frac{0.1|F_x|}{D_x}\right)^5\right) \\ + \max(0, F_x) \end{aligned} \qquad (4)$$

$$\begin{aligned} a_N = D_y \cdot \max\left(0, \left(1 - \frac{0.1|F_y|}{D_y}\right)^5\right) \\ + \max(0, -F_y) \end{aligned} \qquad (5)$$

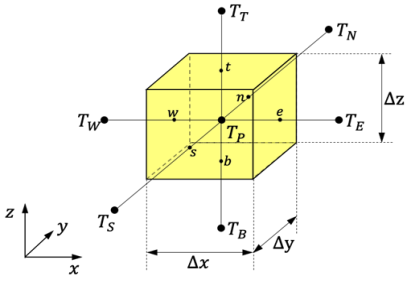

Figure 3 FVM cell from 3D grid

$$\begin{aligned} a_S = D_y \cdot \max\left(0, \left(1 - \frac{0.1|F_y|}{D_y}\right)^5\right) \\ + \max(0, F_y) \end{aligned} \qquad (6)$$

$$a_T = D_z \qquad (7)$$

$$a_B = D_z \qquad (8)$$

$$b = \mu \Phi_D \Delta x \Delta \mathrm{y} \Delta \mathrm{z} \qquad (9)$$

$$\begin{aligned} a_P = a_E + a_W + a_N + a_S + a_T \\ + a_S \end{aligned} \qquad (10)$$

D_x, D_y and F_x, F_y represent the diffusive and convective coefficients along the x and y axis respectively. D_z represents the diffusive coefficients along the z-axis. The expressions for these are shown in Eq.(11) to Eq.(13).

$$D_x = \frac{\lambda \Delta y \Delta \mathrm{z}}{\Delta \mathrm{x}}, D_y = \frac{\lambda \Delta \mathrm{x} \Delta \mathrm{z}}{\Delta \mathrm{y}} \qquad (11)$$

$$\begin{aligned} F_x = \rho \mathrm{c_p} u \Delta y \Delta z, \\ F_y = \rho \mathrm{c_p} \mathrm{v} \Delta \mathrm{x} \Delta z \end{aligned} \qquad (12)$$

$$D_z = \frac{\lambda \Delta \mathrm{x} \Delta \mathrm{y}}{\Delta \mathrm{z}} \qquad (13)$$

The system of equations formed by constructing equations resembling Eq.(2) for all the cells is then solved using a successively over relaxed Gauss-Seidel method.

3. HYBRID FLUID DOMAIN THERMAL MODEL

The current work focuses on eliminating the numerical discretization along the gap height, essentially transforming this 3D system to a 2D system. However, the error associated with the reduction of the grid size is unacceptable. In the proposed fast thermal solver, a hybrid scheme is used to capture the temperature distribution in the direction of film thickness analytically and in the rest two directions, numerically.

In order to capture the conduction on the solid boundaries considering the temperature distribution along the gap height, it is assumed that the temperature along the film thickness at a given x and y location varies quadratically. The rationale for this assumption is that the only mode of temperature transport along the film thickness is diffusion due to the absence of any kind of velocity along the same. This is also confirmed from Eq.(7) and Eq.(8), wherein the coefficients for the top and bottom neighbors (along the gap height) comprise only of diffusive factors.

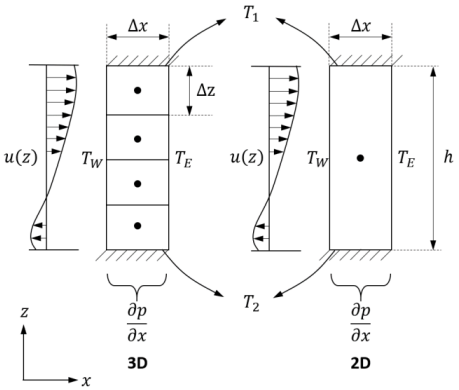

Figure 4 Simplified example

A simplified version of this idea is demonstrated by the example shown in **Figure 4**. The left part shows an analog of the 3D case discussed above and the right part shows a 2D analog to the proposed model. The 3D analog consists of finite volume cells along the z-axis which represents the film thickness. The dimension into the plane is taken to be infinite for the ease of demonstration. Each cell has dimensions Δz along the z-axis and Δx along the x-axis for the 3D analog and h along the z-axis and Δx along the x-axis for the 2D analog (h represents the film thickness). Both the analogs have their top most and bottom most surfaces at fixed temperatures of T_1 and T_2 as shown. Both the examples have the same pressure gradient of $\frac{\partial p}{\partial x}$ along the x-axis. The velocity profile along the z-axis, evaluated as a function of the pressure gradient and the velocities of the top and bottom most surface, are the same for both the analogs as shown. The temperatures on the right and left identical cells for both the analogs are represented by T_W and T_E respectively.

Equations similar to Eq.(2) to Eq. (13) are constructed for the 3D analog case and are shown from Eq.(14) to Eq. (21).

$$D_{x3D} = \frac{\lambda \Delta z}{\Delta x} \tag{14}$$

$$D_{z3D} = \frac{\lambda \Delta x}{\Delta z} \tag{15}$$

$$F_{x3D} = \rho c_p u \Delta z \tag{16}$$

$$a_{E3D} = D_{x3D} \cdot \max\left(0, \left(1 - \frac{0.1|F_{x3D}|}{D_{x3D}}\right)^5\right) + \max(0, -F_{x3D}) \tag{17}$$

$$a_{W3D} = D_{x3D} \cdot \max\left(0, \left(1 - \frac{0.1|F_{x3D}|}{D_{x3D}}\right)^5\right) + \max(0, F_{x3D}) \tag{18}$$

$$a_{T3D} = D_{z3D} \tag{19}$$

$$a_{B3D} = D_{z3D} \tag{20}$$

$$b_{3D} = \mu \Phi_D \Delta x \Delta z \tag{21}$$

A similar analysis is performed for the 2D analog and are shown from Eq.(27) to Eq. (32). The first obvious observation is that none of these equations have Δz term in them. This is attributed to the elimination of the discretization along the film thickness. It can also be observed that the diffusion coefficient along the z-axis shown in Eq.(28), has a factor of 6 multiplied to it when compared to Eq.(15). This can be explained using **Figure 5** and **Figure 6**. **Figure 5** represents a more traditional linear slope approach wherein the value of the temperature of a cell is taken to be at the center and the slope at the top and bottom wall are simply taken as a linear variation from the wall temperature to the cell center temperature. **Figure 6** represents a quadratic temperature profile where the temperature of a given cell, T_P, is taken to be the average of the quadratic temperature along the cell. The temperature profile is highlighted in blue. The temperature, as stated, is assumed to have a quadratic profile along the film thickness. This is represented by Eq.(22). The unknowns A, B and C are determined by the conditions shown in Eq.(23), Eq.(24) and Eq.(25). The resulting temperature profile is shown in Eq.(26). The factor 6 comes from the slope of this quadratic temperature profile at the top most and bottom most surface. The final change is that the coefficients for the top and bottom neighbors are eliminated. This is accounted for by having an extra term in the source term shown in Eq.(32). This extra term accounts for the diffusion along the z-axis.

$$T(z) = Az^2 + Bz + C \tag{22}$$

$$T(0) = T_2 \tag{23}$$

$$T(h) = T_1 \tag{24}$$

$$\frac{1}{h}\int_0^h T(z)dz = T_P \tag{25}$$

$$T(z) = \left[\frac{-3(2T_P - T_1 - T_2)}{h^2}\right]z^2 + \left[\frac{2(3T_P - T_1 - 2T_2)}{h}\right]z + T_2 \tag{26}$$

$$D_{x2D} = \frac{\lambda h}{\Delta x} \tag{27}$$

$$D_{z2D} = \frac{6\lambda\Delta x}{h} \tag{28}$$

$$F_{x2D} = \rho c_p u_{avg} h \tag{29}$$

$$a_{E2D} = D_{x2D} \cdot \max\left(0, \left(1 - \frac{0.1|F_{x2D}|}{D_{x2D}}\right)^5\right) + \max(0, -F_{x2D}) \tag{30}$$

$$a_{W2D} = D_{x2D} \cdot \max\left(0, \left(1 - \frac{0.1|F_{x2D}|}{D_{x2D}}\right)^5\right) + \max(0, F_{x2D}) \tag{31}$$

$$b_{2D} = \mu\Phi_D\Delta x h + D_{z2D} \cdot (T_1 + T_2) \tag{32}$$

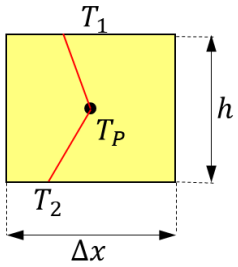

Figure 5 Traditional linear slope

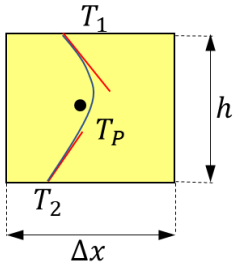

Figure 6 Quadratic slope

The 3D analog model solved for the temperature profile along the z-axis and the 2D analog model solves for the average temperature. In order to show a comparison of the results obtained using the two approaches, the difference of the average temperature solved using the 2D analog model and the average of the temperature profile obtained using the 3D analog model, for a range of gap heights and pressure gradients is shown in **Figure 7**. This case pertains to no velocity on both the top and bottom surfaces, the right and left neighbor temperatures as 50°C and 40°C, and the top and bottom surfaces are both at 50°C. It is observed that in general, both the analogs give similar average temperatures owing to the difference being around a null value everywhere. However, it is observed that for higher values of pressure gradients and gap heights, the 2D analog slightly overpredicts the temperature in comparison to the 3D analog. This is attributed to the fact that the velocity used for the determination of the convection coefficient in Eq.(29) is an average velocity. This underestimates the thermal energy convected out of the cell when the velocities are higher. It is noted here that similar trends were observed for different boundary temperatures and velocities.

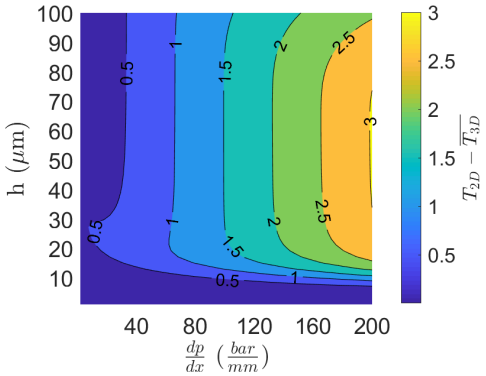

Figure 7 Difference of 2D and mean 3D temperatures

In order to account for the overprediction of temperatures at high velocities, the convection coefficient shown in Eq.(29), was multiplied with a correction factor f_c. To estimate the value of f_c, an optimization study was performed such that the difference of the temperatures as shown in **Figure 7** is close to zero. A plot of this coefficient f_c, as a function of the pressure gradient and gap height, for the same conditions as that of **Figure 7**, is shown in **Figure 8**.

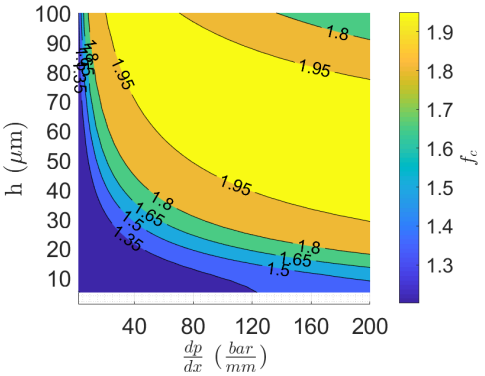

Figure 8 Convection coefficient correction factor

It is observed that the value of f_c for very small film thicknesses is not shown. This is attributed to the fact that at very low film thicknesses, where the velocity is low, the optimization fails to find a meaningful coefficient. For the rest of the space, a trend is observed with the correction coefficient, f_c. It is observed that as the amount of convective transport increases with either the pressure gradient or the film thickness, this coefficient rises from a value close to 1, to a value close to 2. At very high-pressure gradients and film thicknesses, the coefficient is seen to again drop but it is noted that pressure gradients of 200 bar/mm over gap heights of 100 microns is not physical in the lubrication regimes. Similar trends were obtained for different boundary temperatures and velocities as well.

A non-dimensional number that accounts for the combined effect of the film thickness and the pressure gradient is the Peclet number, shown in Eq.(33). Peclet number, Pe, is the ratio of the convective flux to the diffusive flux. It was observed that the variation of the correction factor, f_c, with the film thickness and the pressure gradient can be captured using the Peclet number, Pe.

$$Pe = \frac{F_{x2D}}{D_{x2D}} \tag{33}$$

Figure 8 can also be interpreted through Pe. A line of constant pressure gradient and a line of constant film thickness is taken from **Figure 8** and the variation of f_c is plotted along them as a function of Pe as shown in **Figure 9**. It is observed that both the lines represent the same values of f_c as a function of Pe along them. This confirms the fact that the correction factor depends on Pe. In order to have a generic expression of f_c as a function of Pe, the value of f_c is said to be 1 for very small Peclet numbers and 2 for very high Peclet numbers. The switch from 1 to 2 occurs smoothly across a correction value of 1.5 which was observed to occur at a Peclet number of 10^5. This is functionally obtained using a hyperbolic tangent function as shown in Eq.(34), where Pe_{lim} is the limiting Peclet number of 10^5 where f_c attains a value of 1.5.

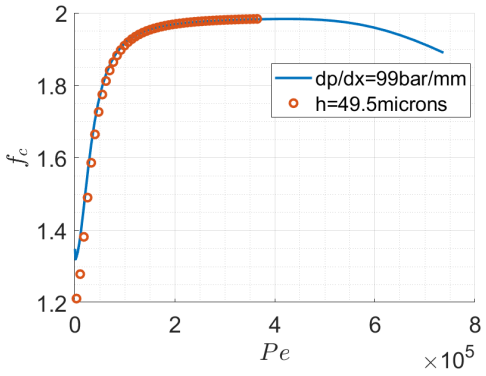

Figure 9 Correction factor as a function of Pe

$$f_c = 1.5 + \frac{\tanh\left(\frac{Pe - Pe_{lim}}{Pe_{lim}}\right)}{2} \qquad (34)$$

A comparison of the optimized correction factor and the correction factor derived in Eq.(34) is shown in **Figure 10**. It is observed that the derived f_c is slightly different from the optimized f_c. This is attributed to the fact that the optimized f_c was obtained using an optimization algorithm and the results need not be exactly perfect. The optimization algorithm tends to find the best possible coefficient to minimize the error between the 2D and 3D temperatures. It was observed that the optimized coefficient, although having a similar trend and bounding values, had slightly different slopes for different operating conditions. In order to make the derived coefficient, f_c, independent of operating parameters other than Pe, the hyperbolic tangent function was chosen such that it follows the same trend and bounding values as the optimized coefficient but differs slightly in terms of the slope of the function. **Figure 11** and **Figure 12** show the difference between the 2D temperatures and mean 3D temperatures, similar to **Figure 7**, using the optimized and derived convection correction factors. It is observed that although the differences in **Figure 12** are not as low as those in **Figure 11**, the differences are still very small. It is observed that the difference is relatively higher in regions of very high pressure gradients, it is noted that such high pressure gradients over a single cell is usually not seen.

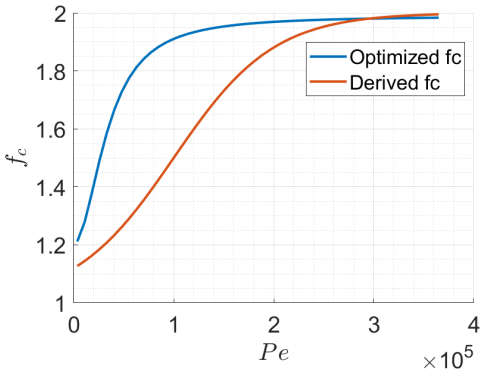

Figure 10 Derived correction factor

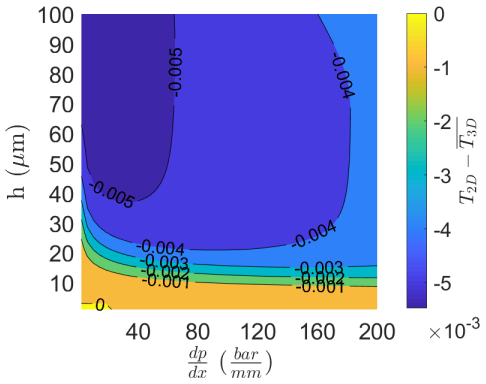

Figure 11 Difference of 2D and mean 3D temperatures using optimized fc

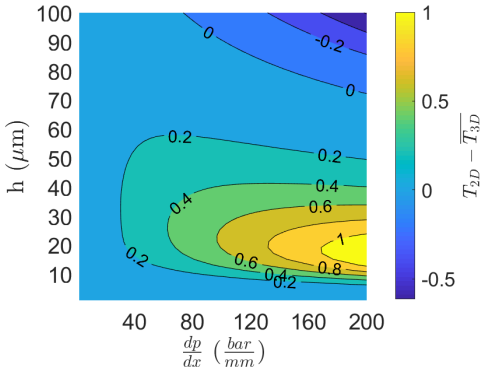

Figure 12 Difference of 2D and mean 3D temperatures using derived fc

This concept is applied to the energy equation solver in the interface between the piston and cylinder. The grid used for the new 2D solver is shown in **Figure 13**. It is to be noted that this grid is different from the one shown in **Figure 2** in the sense that there is no discretization along the film thickness. The modified finite volume cell for the unwrapped 2D grid is shown in **Figure 14**. It is observed that this cell has a dimension of h, the film thickness, along the z-axis. The top and bottom neighbors are absent due to the reduction in dimension. The top wall t and bottom wall b are at fixed temperatures corresponding to the bounding solids, piston and bushing running surfaces in this case. The parameters along the other two dimensions: x and y remain the same.

The modified coefficients for this cell are shown from Eq.(35) to Eq.(42). f_{cx} and f_{cy} represent the discussed correction factors in the x and y directions respectively.

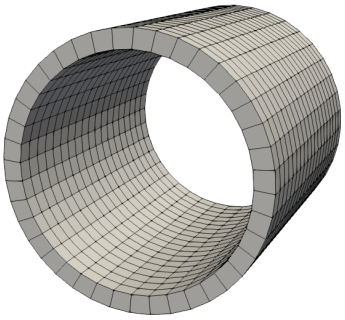

Figure 13 2D FVM grid

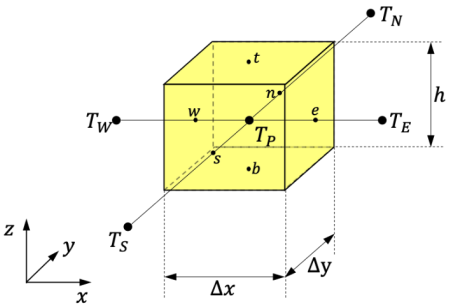

Figure 14 FVM cell from 2D grid

$$D_x = \frac{\lambda \Delta y}{\Delta x} h, D_y = \frac{\lambda \Delta x}{\Delta y} h \tag{35}$$

$$\begin{aligned} F_x &= f_{cx} \cdot \rho c_p u \Delta y h, \\ F_y &= f_{cy} \cdot \rho c_p v \Delta x h \end{aligned} \tag{36}$$

$$D_z = \frac{6 \lambda \Delta x \Delta y}{h} \tag{37}$$

$$a_E = D_x \cdot \max\left(0, \left(1 - \frac{0.1|F_x|}{D_x}\right)^5\right) + \max(0, -F_x) \quad (38)$$

$$a_W = D_x \cdot \max\left(0, \left(1 - \frac{0.1|F_x|}{D_x}\right)^5\right) + \max(0, F_x) \quad (39)$$

$$a_N = D_y \cdot \max\left(0, \left(1 - \frac{0.1|F_y|}{D_y}\right)^5\right) + \max(0, -F_y) \quad (40)$$

$$a_S = D_y \cdot \max\left(0, \left(1 - \frac{0.1|F_y|}{D_y}\right)^5\right) + \max(0, F_y) \quad (41)$$

$$b = \mu\Phi_D \Delta x \Delta y \Delta z + \mathrm{D_z} \cdot (T_t + T_b) \quad (42)$$

4. RESULTS

In order to show the potential of the proposed formulation, a corner operating condition of 3600 rpm, 450 bar and 100% displacement was chosen for a reference 75cc axial piston unit. The higher speeds lead to higher energy dissipation and the high pressure increases the convection of energy in the fluid. The high displacement ensures large fluctuations in the fluid temperatures. For the purposes of comparison, a fluid grid with 80 cells along the circumferential direction, 40 cells along the axial direction and 30 cells along the film thickness is chosen.

Figure 15 shows the average temperature along the film thickness, over an unwrapped film at a shaft angle of 90° obtained using the 3D energy equation. This profile will be used as a reference to compare the temperatures obtained using the 2D model.

In order to demonstrate a step by step evolution of the 2D model, the temperature field obtained using the 3D model, with 2 cells along the film thickness is shown in **Figure 16**. It is observed that this evaluation does not yield to a meaningful temperature field. The temperature in the lower portion of the film is underpredicted to a degree that does no longer represents the physics of the film properly. The temperature field obtained using the 2D energy equation, without the use of a quadratic slope, as described in Eq.(28), and without any convection correction, as described in Eq.(34), is shown in **Figure 17**. It is observed by comparing **Figure 15** and **Figure 17**, that the 2D model overpredicts the average temperature in the lower portion of the film and underpredicts the average temperature in the upper portion of the film. This mismatch is explained by referring to **Figure 5** and **Figure 6**. The temperature field in **Figure 17** corresponds to the linear slope. This formulation does not actually account for the physically correct diffusion through the top and bottom surfaces.

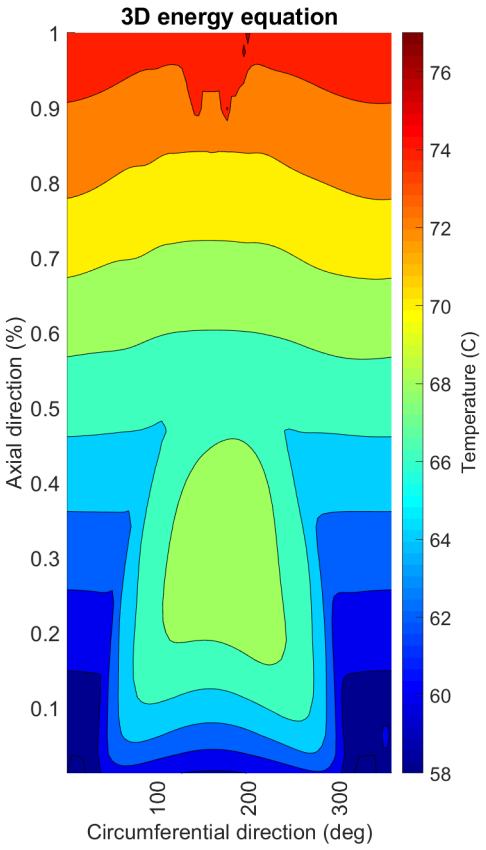

Figure 15 Unwrapped film temperature from 3D energy equation

The temperature profile over the unwrapped film thickness, obtained using the 2D energy equation with the modified quadratic slope and no convection correction is shown in **Figure 18**. A comparison of this profile with **Figure 15** shows that the underprediction in the upper portion of the film is not present. This is attributed to the modified slope which ensures that the right amount of energy is diffused through the bounding surfaces of the fluid film. It is observed that the overprediction in the lower portion of the film has reduced compared to **Figure 17**, although the temperature is still overpredicted. This is attributed to the film thickness and average axial velocity as shown in **Figure 19** and **Figure 20** respectively. The film thickness in the region of overprediction in the lower portion of the fluid film is relatively high. Combined with the fact that the axial velocity is high in this region, this leads to a higher Peclet number as discussed in the previous section. This leads to the underprediction of the convective flux of energy in this region leading to an overprediction of temperature. The correction factor, as shown in Eq.(34), is required to account for this phenomenon. It is also noted that the gap height is higher in other regions of the film, as the upper left and right sections. Although, the axial velocity in these regions is not as high as it is in the central portion and hence leading to a lower value of Peclet number resulting in reasonable prediction of temperature.

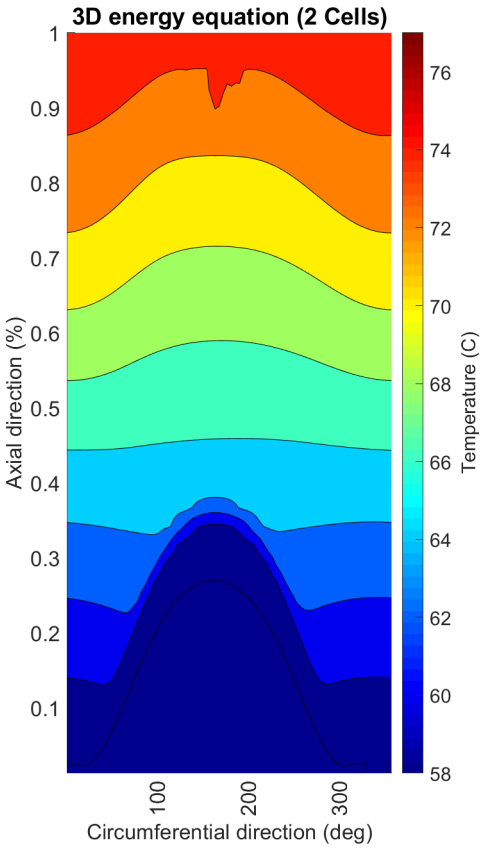

Figure 16 Film temperature from 3D energy equation using 2 cells

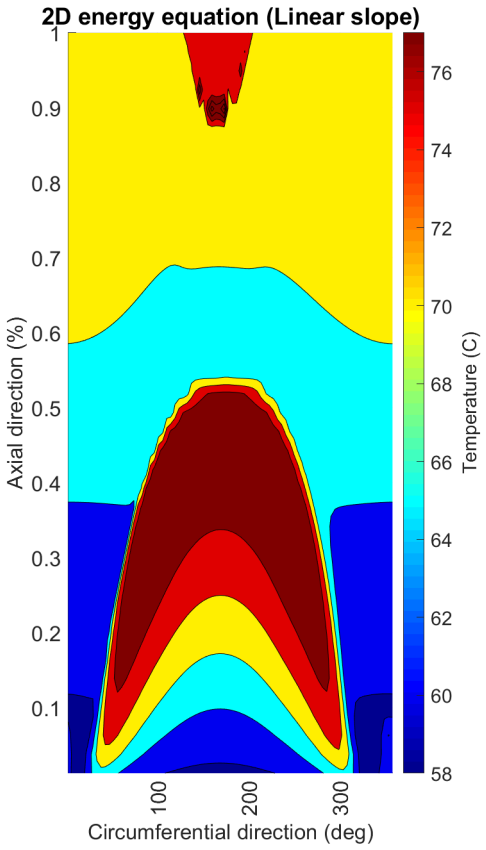

Figure 17 Film temperature from 2D energy equation with linear slope at the walls

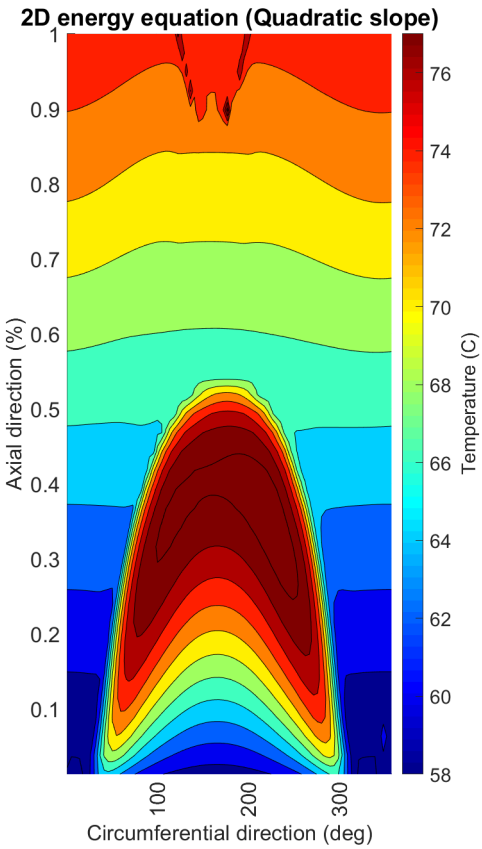

Figure 18 Film temperature from 2D energy equation with quadratic slope at the walls

The temperature profile obtained using the final 2D model accounting for the quadratic slope and the convective correction is shown in **Figure 21**. It is observed that the temperature profile is much closer to **Figure 15** than the ones shown in **Figure 17** and **Figure 18**. Although, there is a slight difference in the central portion of the film, the overall temperature in the film seems closely similar to **Figure 15**. The proposed model resulted in an average temperature difference of 2% throughout the film in comparison to the 3D model. The important factor here is that the time required to evaluate the 3D model till convergence was around 7.2 hours, whereas the 2D evaluation required around 4.6 hours. The 2D model is approximately 36% faster than the 3D model.

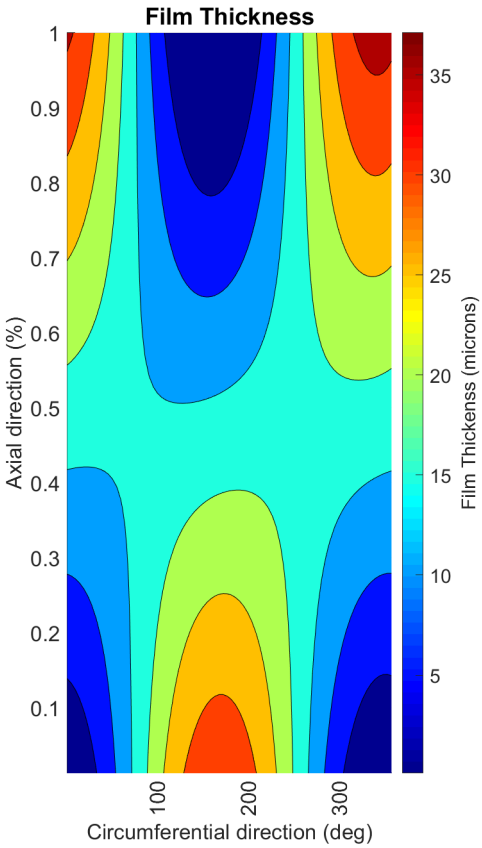

Figure 19 Film thickness over the unwrapped fluid film

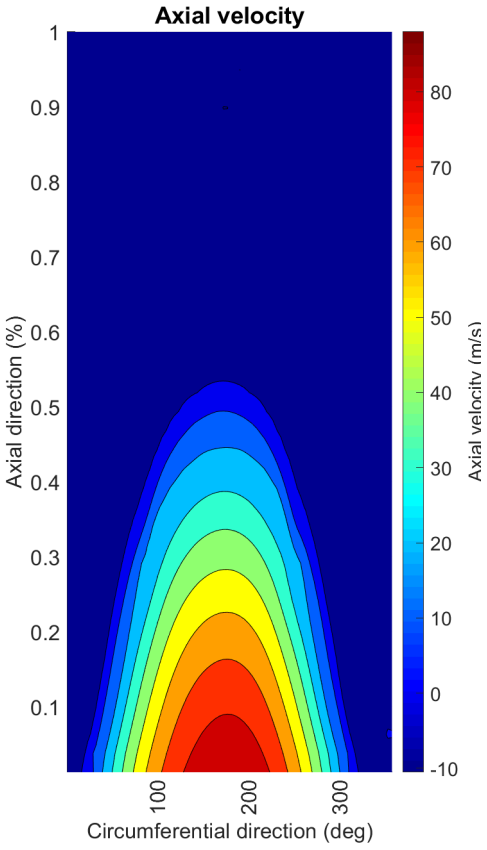

Figure 20 Average axial velocity over the unwrapped fluid film

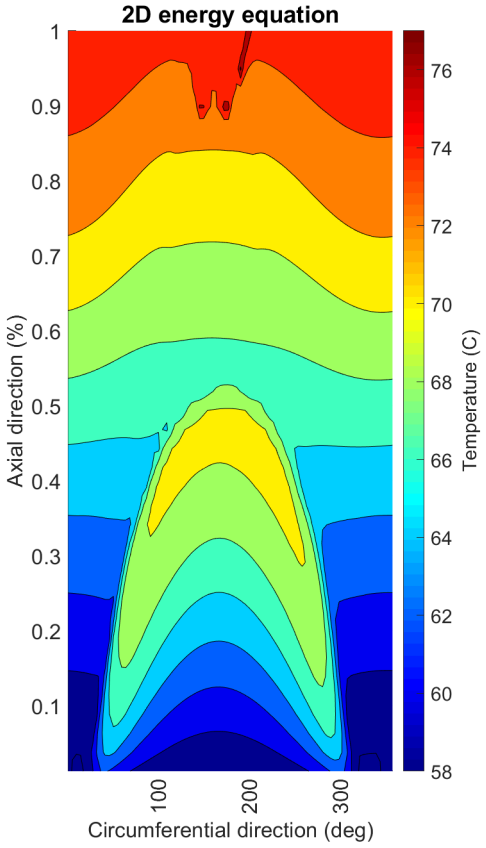

Figure 21 Unwrapped film temperature from 2D energy equation

5. CONCLUSION

A 2D energy equation model was proposed with the assumption of a parabolic temperature distribution along the gap height. New finite volume coefficients were derived for the proposed model along with a derived correction factor for the convective terms. The average difference between the 3D model and the proposed model was not observed to be more than 2%, but a speedup of 36% was observed in terms of simulation times. It is to be noted that although the model was demonstrated for the piston/cylinder interface of an axial piston machine, it can be applied to any lubricating interface simulation tool to reduce the simulation time taken to solve the energy equation.

NOMENCLATURE

ρ	Fluid density	Kg/m^3
c_p	Specific heat	J/kg K
u	x-velocity	m/s
v	y-velocity	m/s
T	Temperature	°C
λ	Fluid conductivity	W/m K
μ	Fluid viscosity	Pa s
ϕ	Viscous dissipation	W/kg
Pe	Peclet number	-

REFERENCES

[1] H. G. Elrod, D. E. Brewe, L. Rt, and H. G. Elrod, "Technical Memorandum 88845 Technical Report 86-C-33 Thermohydrodynamic Analysis for Laminar Lubricating Films," 1986.

[2] V. der Kolk, "Beitrag zur Bestimmung der Tragfähigkeit des stark verkanteten Gleitlagers Kolben – Zylinder an Axialkolbenpumpen der Schrägscheibenbauart," University of Karlsruhe, 1972.

[3] A. Yamaguchi, "Motion of Pistons in Piston-Type Hydraulic Machines," *Bull. JSME*, vol. 19, no. 130, pp. 402–419, 1976.

[4] M. Ivantysynova (at that time Berge), "An investigation of viscous flow in lubricating gaps. (In Slovak)," SVST Bratislava, Czechoslovakia, 1983.

[5] L. Olems, "Ein Beitrag zur Bestimmung des Temperaturverhaltens der Kolben-Zylinderbaugruppe von Axialkolbenmaschinen der Schrägscheibenbau-weise," *VDI Fortschrittsberichte*, vol. Reihe 1, no. 348, 2001.

[6] U. Wieczorek and M. Ivantysynova, "Computer aided optimization of bearing and sealing gaps in hydrostatic machines—the simulation tool caspar," *Int. J. Fluid Power*, vol. 3, no. 1, pp. 7–20, 2002.

[7] M. IVANTYSYNOVA and C. HUANG, "Investigation of the Gap Flow in Displacement Machines Considering Elastohydrodynamic Effect," *Proc. JFPS Int. Symp. Fluid Power*, vol. 2002, no. 5–1, pp. 219–229, 2002.

[8] M. Pelosi and M. Ivantysynova, "A novel fluid-structure interaction model for lubricating gaps of piston machines," *WIT Trans. Built Environ.*, vol. 105, pp. 13–24, 2009.

[9] M. Pelosi and M. Ivantysynova, “A Geometric Multigrid Solver for the Piston-Cylinder Interface of Axial Piston Machines,” *Tribol. Trans.*, vol. 55, no. 2, pp. 163–174, 2012.
[10] L. Shang and M. Ivantysynova, “Port and case flow temperature prediction for axial piston machines,” *Int. J. Fluid Power*, vol. 16, no. 1, pp. 35–51, 2015.
[11] L. Shang and M. Ivantysynova, “Advanced heat transfer model for piston/cylinder interface,” *11th IFK Int. Fluid Power Conf.*, vol. 1, no. 1972, pp. 587–595, 2018.
[12] H. McCallion, F. Yousif, and T. Lloyd, “The analysis of thermal effects in a full journal bearing,” *J. Tribol.*, vol. 92, no. 4, pp. 578–587, 1970.
[13] J. Ferron, J. Frene, and R. Boncompain, “A study of the thermohydrodynamic performance of a plain journal bearing comparison between theory and experiments,” *J. Tribol.*, vol. 105, no. 3, pp. 422–428, 1983.
[14] Y. Song, J. Ma, and S. Zeng, “A numerical study on influence of temperature on lubricant film characteristics of the piston/cylinder interface in axial piston pumps,” *Energies*, vol. 11, no. 7, 2018.
[15] M. Pelosi, “An investigation of the fluid-structure interaction of piston/cylinder interface,” 2012.

A CFD DESIGN OF ENGINEERED SURFACE FOR TRIBOLOGICAL PERFORMANCE IMPROVEMENTS IN HYDRAULIC PUMPS

Paolo Casoli[1]* , Fabio Scolari[1], Carlo Rossi[2], Manuel Rigosi[2]

[1]*University of Parma, Parco Area delle Scienze 181/A, 43124 Parma, Italy*
[2]*Casappa S.p.A., Via Balestrieri 1, 43044, Lemignano di Colecchio PR, Italy*
* Corresponding author: Tel.: +39 0521 905868; E-mail address: paolo.casoli@unipr.it

ABSTRACT

In the present paper the preliminary results of the potentialities that surface texturing has in improving the coupling of lubricated surfaces in relative motion is presented. This kind surface engineering requires careful design of the geometry to obtain relevant improvements; therefore, it is useful to study in detail the behavior of the fluid confined between the coupled surfaces by means of CFD analysis. The purpose of this research is to study the effect of dimples created on one of the two coupled surfaces and to observe the variation of tribological properties as their principal design parameters vary, such as dimple shape, size and spatial distribution. Furthermore, simulations have been carried out with different sliding velocities and fluid temperatures to analyze the effects that these variables have on the tribological performance of the textured surface. The simulations also consider the presence of cavitation and the influence of this phenomenon on the overall behavior of the textured surface is evaluated.

Keywords: laser surface texturing, CFD simulation

1. INTRODUCTION

Lubricated couplings between surfaces in relative motion are very common in hydraulic machines and new solutions able to improve their performance could lead to extend their working range.

The adoption of textured surfaces can lead to different benefits and improve the tribological properties of the surface coupling [1].

The geometric effects permit to obtain a greater hydrodynamic bearing capacity and a lower friction coefficient due also to a smaller contact area, which would allow to reduce the overall wear. Furthermore a “hollow” effect could occur with the function of collecting extraneous particles and contaminants as well as creating a reserve of oil is useful to avoid the breaking of lubricating film.

Accurate design of the surface geometry is a tough challenge because of the high number of variables that influence the final behavior of the coupling. Furthermore, the characteristics of the dimple profile strongly depend on the type of contact that occurs between the two facing surfaces, as well as the operating conditions [2].

Some researchers have studied these solutions applied to parallel thrust bearings, demonstrating that modifying the coupled surfaces in relative motion could lead to improved hydrodynamic lubrication [3, 4]. Other studies investigate the effect of surface texturing realized on circumferential seals proving that the dimples are able to generate a hydrodynamic force that could reduce the seal friction and wear [5, 6].

Many studies in this field have been carried out by means of finite difference method to numerically solve the Reynolds lubrication equation [6-8].

In this research in order to evaluate the influence of the geometrical characteristics of the dimples and the coupled surfaces, such as the gap and the relative sliding speed between the two coupled surfaces, in addition to the change in viscosity of the fluid, several three-dimensional CFD simulations were performed, the analysis were carried out using ANSYS® CFX to solve the Navier-Stokes equations and the energy equation.

The simulations were carried out considering cavitation phenomenon which could occur under some operating conditions and is able to modify

the coupling performance, even leading to negative effects.

This paper reports a preliminary study of the potentials of a textured surface. The final aim of this research is to apply textured surfaces on some components inside hydraulic pumps. Both in external gear pumps and in axial piston pumps there are numerous lubricated coupled surfaces that can become critical beyond certain operating conditions. The outlook is to extend the working range of these machines using the benefits offered by engineered surfaces.

2. CFD MODELLING OF TEXTURED SURFACES

2.1. Fluid model

The fluid has been modeled within the various CFD analysis performed is an ISO VG-46 hydraulic oil with the characteristics listed in the Table 1.

Table 1: Fluid parameters.

Density	850 kg/m^3
Viscosity (40 °C)	46 mm^2/s
Molar mass	240 kg/mol
Specific heat capacity	1950 J/ (kg K)
Relative saturation pressure	-0.7 bar

The analyses were performed considering the cavitation phenomenon, using the Rayleigh Plesset model [9]. In order to correctly model this phenomenon the definition of the physical and thermodynamic properties of the fluid is essential. Since the reference hydraulic oil is a complex mixture of heavy hydrocarbons, to simplify the properties definition the fluid has been assumed mono component considering the heptadecane $C_{17}H_{35}$. The vapor phase has been modelled as a real gas adopting a cubic equation of state, according to the Soave Redlich Kwong model [10]. All the simulations were carried out setting the fluid temperature equal to 40°C.

2.2. Single dimple

As reference geometry a square-shaped dimple has been adopted. In Figure 1 a schematic representation of the domain and the dimple position is shown, with the main geometric features indicated.

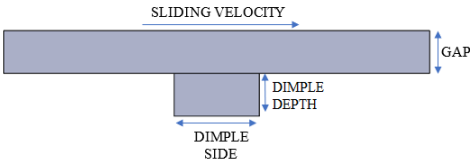

Figure 1: Graphic representation of the dimple with the main geometric features indicated.

The domain dimensions have been chosen in order to allow the pressure gradient due to the presence of the dimple to reach the zero value in both the x and y directions, as shown in the pressure contour in Figure 2. The reference domain is 500 µm long in the x direction and 300 µm along y. The reference value of the sliding velocity is assumed to be 5 m/s which is a typical value in many hydraulic applications.

The gap is in the order of micron, since it is a common value that characterize the lubricated couplings in hydraulic machines.

The boundary conditions are set as open boundary with a relative pressure of 0 bar.

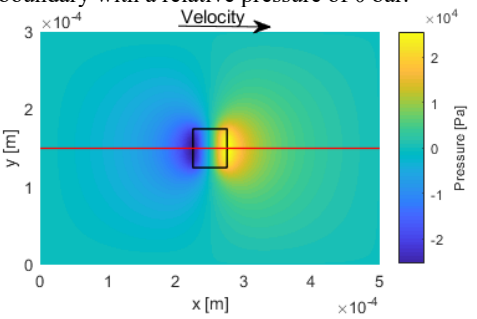

Figure 2: Pressure contour of a square dimple with side 50 µm and depth 10 µm. Gap 10 µm, sliding velocity 5 m/s

Several simulations have been performed varying the geometrical features of the dimple and of the gap as well as the viscosity of the fluid and the sliding velocity. Figure 3 reports the results concerning geometrical features, the pressure profile is calculated along the dimple median line on the moving plane (indicated by the red line in Figure 2) and it oscillates symmetrically around the mean value. The mean value is the reference relative pressure imposed as boundary condition.

It follows that the sustaining force generated is always equal to zero, regardless of the pressure conditions at the boundary, the working temperature (i.e. the viscosity of the fluid) and the relative sliding speed between the two surfaces.

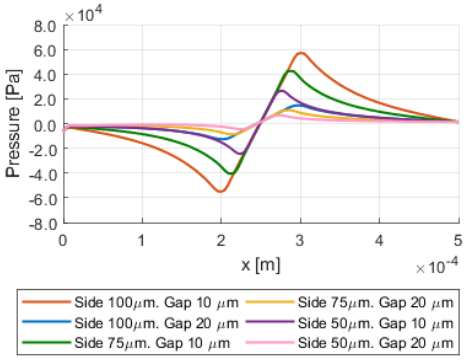

Figure 3: Pressure profile perturbation generated by a square dimple with different size and different value of the gap. Dimple depth 10 μm, sliding velocity 5 m/s

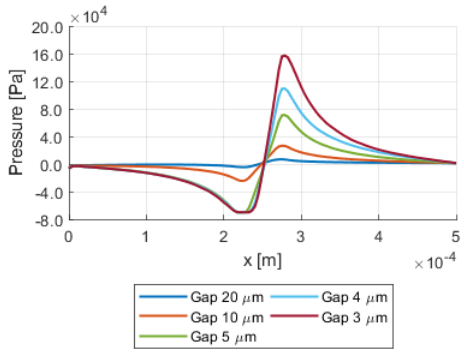

Figure 4: Pressure profile of a square dimple with side of 50 μm and depth 10 μm for different value of the gap. Sliding velocity 5 m/s

One aspect to be observed is the influence of the size of the dimple. Dimples characterized by large dimensions in the moving direction generate a pressure profile characterized by a bigger amplitude than smaller ones, but still symmetrical. Besides the reduction of the gap leads to similar effects, increasing the amplitude of the pressure oscillation.

These conclusions can also be extended to other dimple geometries that have a symmetrical structure, such as a rectangular or circular geometry; as a matter of fact in all these configurations the divergent zone is exactly the same as the convergent one, leading to a symmetrical pressure profile that do not create any bearing capacity.

However, there could be some operating conditions where, due to the onset of cavitation phenomenon, some sort of bearing action arises. As shown in **Figure 3**, both decreasing the gap and increasing the dimple size, bring to a higher amplitude of the pressure profile; as a consequence the minimum pressure value of the profile will be lower.

In the **Figure 4** it is possible to notice that the same square dimple produces a pressure profile of greater amplitude as the clearance decreases; for those cases where, in the depression area, the pressure drops down below the fluid saturation limit, cavitation arises. As a consequence, the pressure profile is not symmetric anymore and some sort of bearing effect is provided.

In **Figure 5** the load capacity generated by dimples of different dimensions is shown; the effect is amplified if the gap clearance is reduced. The values are divided by a reference value for confidential reasons. The force is the integral of the pressure calculated on the entire domain surface and the trend is more than linear as far as the gap thickness is decreased.

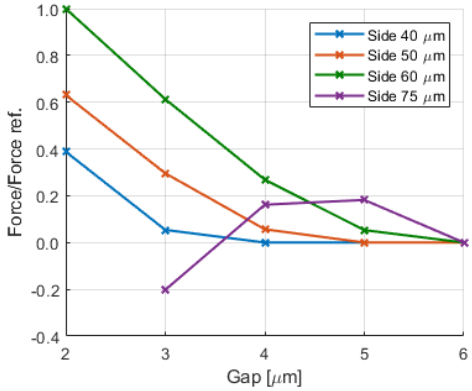

Figure 5: Bearing capacity. Influence of the gap for different size of the dimple. Dimple depth 10 μm, sliding velocity 5 m/s.

The increasing of the bearing capacity with the reduction of the gap could be a useful effect to compensate any approaching trend, hence preventing the condition of direct contact between the two surfaces.

From **Figure 5** emerges that larger dimples offer more benefits in term of load capacity; however a limit exists, beyond which the trend is opposite. Furthermore, the largest dimples are

characterized by greater cavitation phenomena with a wider area at saturation pressure. In **Figure 6** the pressure contour on the moving plane of a large square dimple is reported, while in **Figure 7** its own pressure profile, calculated along the central red line, is shown. The overall integral of the pressure on the surface is negative; in this case, worsening the bearing performance of the coupling.

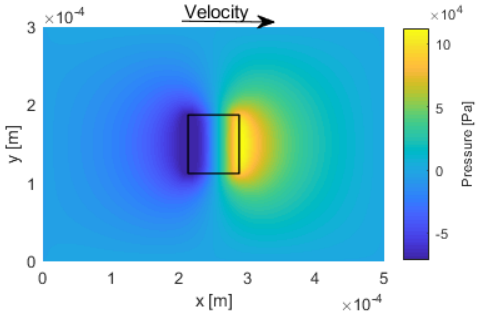

Figure 6: Pressure contour of a square dimple with side 75 µm and depth 10 µm. Gap 5 µm, sliding velocity 5 m/s

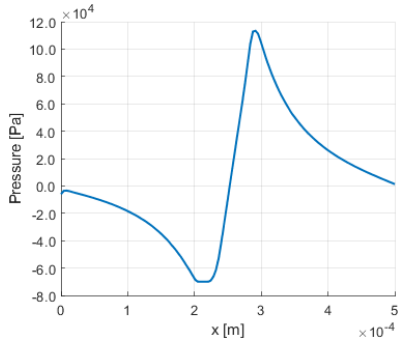

Figure 7: Pressure profile of a large square dimple with side 75 µm and depth 10 µm. Gap 5 µm, sliding velocity 5 m/s

In all the simulations presented the boundary conditions were set 0 bar, this value affect the minimum and maximum values of the pressure profile. Setting the pressure boundary at higher value the minimum pressure value can remain over the saturation pressure and cavitation is avoided. The generation of the bearing capacity is due exclusively to the onset of cavitation, therefore by modifying the pressure boundary condition, greater than 0 bar, cavitation does not occur and the pressure profile remains symmetrical without generating any force.

2.3. Influence of operating conditions and dimples depth

According to the lubrication equation and the Reynolds theory, Eq. 1, the dependence of the pressure on the fluid viscosity is linear. The viscosity of the fluid is related to the working temperature and decreases while it rises.

Therefore, the pressure profile near the dimple is amplified with lower fluid temperature (higher viscosity).

$$\frac{\partial}{\partial x}\left(h^3\frac{\partial p}{\partial x}\right) = 6U\eta\frac{dh}{dx} \qquad (1)$$

According to Eq. 1, the dependence of the pressure on the sliding speed between the two coupled surfaces is also linear; changing the fluid viscosity or the sliding velocity of a certain extent, the pressure profile will be scaled in the same proportion. In **Figure 8** it is possible to appreciate the variations in the pressure profile as a function of both the viscosity of the fluid and the sliding velocity, while in Table 2 the amplitude value of the pressure profile is reported as confirmation of the linear relation described above.

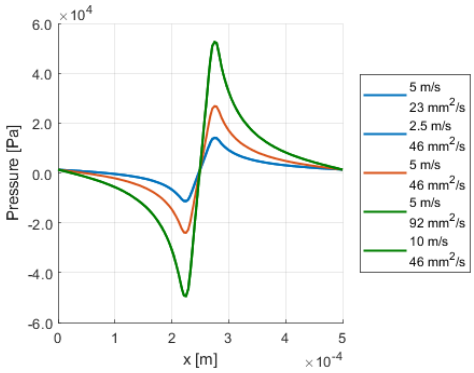

Figure 8: Effect of viscosity and velocity.

Table 2: Amplitude of the pressure profile.

Parameters	Amplitude [Pa]
5 m/s 23 mm²/s	1.27E+04
2.5 m/s 46 mm²/s	
5 m/s 46 mm²/s	2.55E+04
5 m/s 92 mm²/s	5.10E+04
10 m/s 46 mm²/s	

The increase of pressure amplitude obtained changing the sliding speed or the working temperature of the fluid, permits to reach the cavitation conditions for greater values of the gap, thus improving the bearing performance, with the limitations previously explained.

The influence of the depth of the dimple is rather marginal, because it does not change the pressure profile significantly, as shown in **Figure 9**.

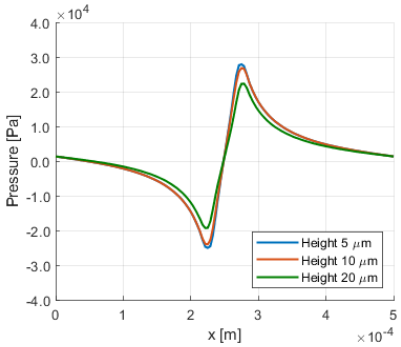

Figure 9: Influence of the dimple depth on the pressure profile. Square dimple with side 50 μm and gap 10 μm, sliding velocity 5 m/s.

2.4. Full texturing

The firsts simulations have demonstrated that with a single dimple it could be possible to obtain a positive load capacity, only for low pressure couplings and when localized cavitation phenomena take place. In order to overcome these limitations further analyses were carried out on a geometry characterized by a sequence of equally spaced dimples over the entire considered domain, **Figure 10**.

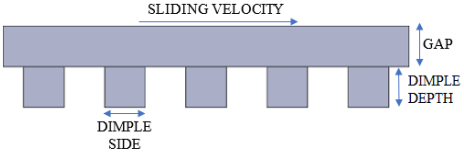

Figure 10: Graphic representation of a full texturing domain with the main geometric features indicated.

In case of the full textured surface the pressure profile trend near a dimple is similar at the single dimple case, already investigated. The pressure field has a periodic oscillation, as can be noted looking at the contour in **Figure 11**, also represented from the pressure profile calculated along the red line, **Figure 12**. The calculation of the average pressure value along the central pressure profile confirm that no bearing force is generated.

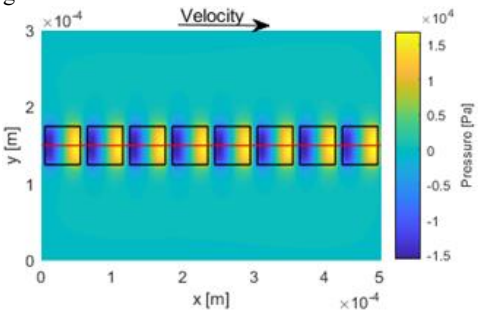

Figure 11: Pressure contour for the case of full texturing. Square dimple with side 50 μm and depth 10 μm. Gap 10 μm, sliding velocity 5 m/s.

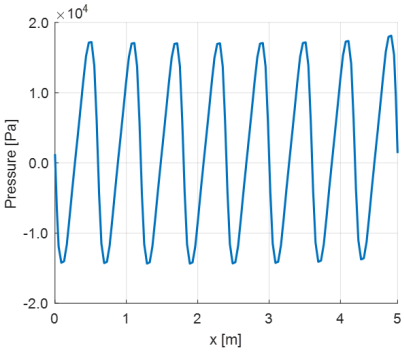

Figure 12: Pressure profile taken from red line of Figure 11. Square dimple with side 50 μm and depth 10 μm. Gap 10 μm, sliding velocity 5 m/s.

Therefore, it is clear that in presence of a fully textured domain, it is not possible to obtain any improvement in terms of load capacity, this result being valid regardless of the geometrical dimensions of the dimples.

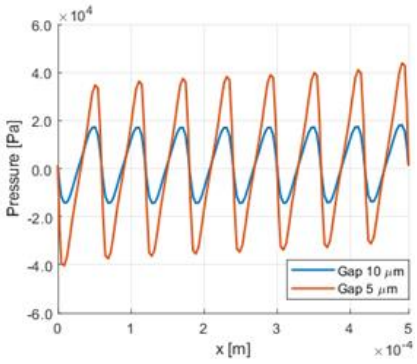

Figure 13: Pressure profile for full texturing, effect of the gap clearance. Square dimples with side 50 μm and depth 10 μm. Sliding velocity 5 m/s

As for the single dimple case, a reduction of the gap clearance leads to increase the amplitude of the pressure profile; the oscillatory trend remains unchanged not generating any bearing capacity, as shown in **Figure 13**.

In case of a full textured domain the onset of cavitation appears either when the gap is reduced (as for the single dimple) or also placing the first dimple far from the domain inlet, as shown in **Figure 14**, where the first dimple has been removed.

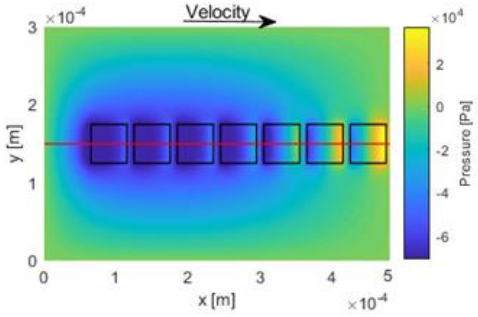

Figure 14: Pressure contour of a full texturing case without the first dimple. Square dimple with side 50 μm and depth 10 μm. Gap 5 μm, sliding velocity 5 m/s.

In this case, as can be seen from the pressure contour, the first dimples show considerable cavitating area, that progressively decreases until it completely ceases. As a consequence of the onset of cavitation the symmetry in the pressure is been distorted. After the firsts dimples the trend is an increasing of the pressure, since each dimple gives a contribution to raise the pressure, but the resulting force on the moving plane is still negative.

As reported in **Figure 15**, if the clearance is greater, 10 μm, and the dimples are arranged on the surface in the same way, there is not the formation of cavitation but it is still present an asymmetry of the pressure profile due to the marked depressurization of the first dimples, after that the pressure oscillates symmetrically. Increasing the domain length and the number of dimples the trend does not change and the consequence is an overall force on the moving plane negative.

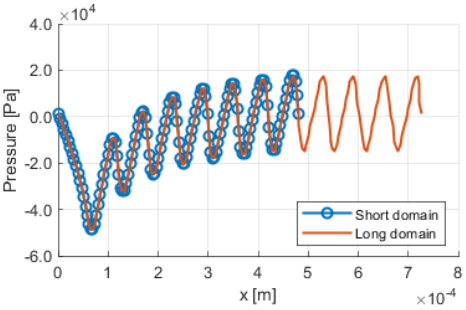

Figure 15: Pressure profile as varying the domain length and the number of dimples. Gap 10 μm, sliding velocity 5 m/s

The effects of the fluid viscosity or the sliding velocity of the moving plane are the same highlighted in the single dimple analysis. In the full textured domain the depth of the dimples affects the pressure profile in a negligible way.

The study of the entire considered domain was carried out considering a single row of dimples; moving to a multi-row configuration, taking care that all the dimples are the same and equally distributed, lead to a condition where all the pressure profiles (at the center of each row) are exactly the same. **Figure 16** shows the pressure contour on the moving plane in a generic two rows configuration with indicated two colored lines on each row of dimples. In **Figure 17** the pressure profiles along these lines are reported: the pressure perturbations are exactly the same.

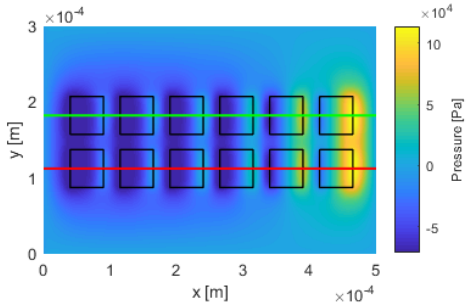

Figure 16: Pressure contour of two row of dimples. Square dimple with side 50 µm and depth 10 µm. Gap 5 µm, sliding velocity 5 m/s.

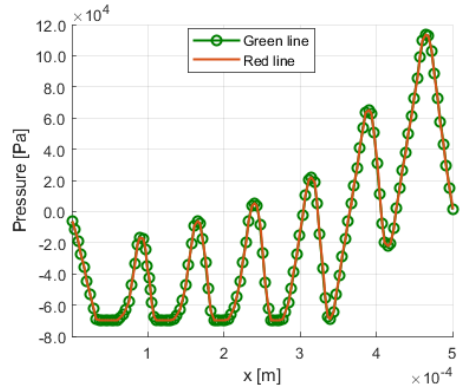

Figure 17: Pressure profiles calculated on the lines shown in the Figure 16.

From the simulations performed, texturing the entire domain does not appear a useful way to increasing the performance of lubricated surfaces coupled in relative motion since the pressure profile oscillates around a zero value and in case of cavitation onset the resulting force is negative.

A positive aspect due to the realization of a fully textured surface is the reduction of the friction coefficient. Since the average fluid film thickness is increased, a full textured surface allows to reduce the viscous friction coefficient: the greater the textured portion of the available surface, the greater the friction coefficient reduction; however, increasing the textured portion means also reduce the coupled surface.

2.5. Partial texturing

Starting from the results obtained on both the single dimple and the entire textured domain it is clear that only in a limited number of conditions it is possible to obtain a positive bearing capacity able to counteract against the approaching of the two surfaces in relative motion.

Further investigations are required to obtain a positive load capacity in any working configuration of a lubricated coupling. One possible option is to create a texture of dimples only in a part of the coupled domain. A partial texturing presents relevant improvements in this direction. Partial texturing means to position the dimples only on a portion of the available domain, as shown in **Figure 18**.

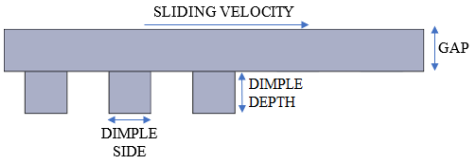

Figure 18: Graphic representation of a partial textured domain with the main geometric features indicated.

Figure 19 shows the pressure contour relating to the case of texturing the 47% of the entire domain. At the last dimple the pressure rises in a marked way and then gradually fades as can also be appreciated by analyzing the pressure profile.

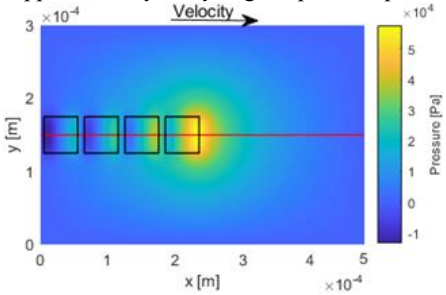

Figure 19: Pressure contour. Square dimple with side 50 µm and depth 10 µm. Gap 10 µm, sliding velocity 5 m/s.

In **Figure 20** the pressure profiles are shown as a function of textured portion, the pressure does not oscillate symmetrically like the previous cases, but each dimple provides a contribution that raises the pressure locally. The result is a pressure ramp capable of generating a relevant load capacity.

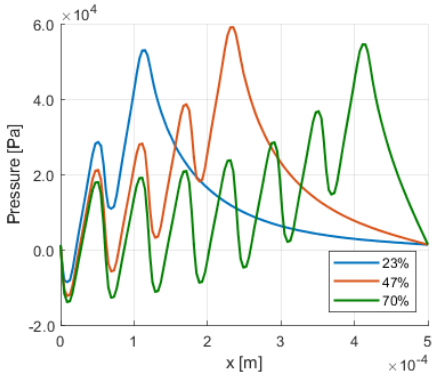

Figure 20: Pressure profile as a function of textured portion. Square dimple with side 50 µm and gap 10 µm, sliding velocity 5 m/s.

Since in the partial texturing each dimple gives a contribute on locally increase the pressure, it is preferable to have the dimples closest together as possible in order to insert a higher number of it on the same domain, improving the performance of the surface.

In **Figure 21** is reported the generated force as a function of the textured portion of the domain. The force values are divided by a reference value for confidential reasons. The best configuration is when the dimples are arranged in the initial 50-60% of the available domain.

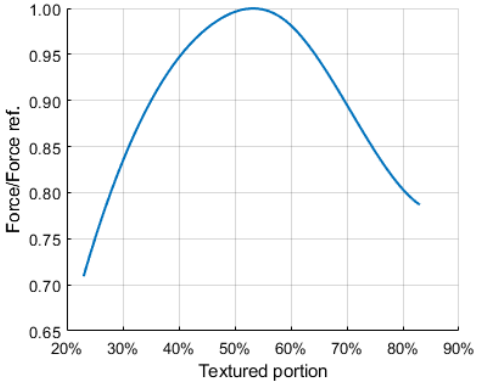

Figure 21: Force as a function of textured portion. Square dimple with side 50 µm and gap 10 µm, sliding velocity 5 m/s.

In the partial texturing the position of the first dimple is very important. Increasing the distance from the beginning of the domain means allowing the decrease of the pressure on the first dimples, **Figure 22**, reducing the peak of over pressure achievable. Moreover, in this configuration the problem of cavitation phenomenon is more pronounced, as the gap decrease. The first dimples are in strong depression, but the partial texturing allows to recover the pressure and guarantee, even in these conditions, a positive bearing capacity.

In order to completely avoid the onset of cavitation it is preferable to place the first dimple exactly at the beginning of the domain with the aim of not creating a divergent zone in the gap.

The reduction of the clearance value amplifies the pressure profile allowing to reach higher values of pressure, **Figure 22**; the negative aspect is that it also generates smaller values in the area in depression. For this reason it is fundamental to plan the position of the first dimple.

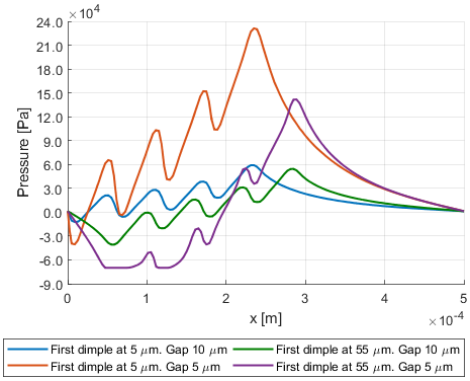

Figure 22: Effect of the disposition of the first dimple and of the gap depth. Textured portion 47%. Sliding velocity 5 m/s

In partial texturing, the effects of either the fluid viscosity or the sliding velocity of the moving plane are the same highlighted in the previous sections; the depth of the dimples affect the pressure profile in a negligible way also in this case.

A partial textured surface still allows to reduce the friction coefficient between the two moving planes but to a lesser extent than full textured surface since the fluid film thickness is increased only on a portion of the available domain.

Moreover, increasing the number of textured row (equal to each other) on the surface improve the results for a single row.

3. CONCLUSION AND OUTLOOK

In this work the preliminary study of a research activity concerning textured surfaces have been presented. The results have highlighted some of the tribological potentials that a textured surface

could express on a lubricated coupling between sliding surfaces.

The design phase, in terms of dimple geometric definition and spatial distribution, is a challenge due to the high number of variables involved, besides the achievable benefits depend on the operating conditions.

From the CFD simulations conducted it emerged that best solution is to texture only a portion of the available surface in the direction of sliding motion. CFD simulations were carried out considering the cavitation phenomenon, which can significantly influence the bearing performance of the textured surfaces.

Future developments should include a more accurate study of dimples geometry and distribution: the effects due to different dimple shape and orientation have to be analyzed.

Moreover a dynamic analysis of the cavitation phenomenon should be performed. It is worth to investigate how the vapor bubbles are generated and then reabsorbed into the fluid, correlating the characteristic times of the process with the pressure evolution through the dimples.

NOMENCLATURE

h	Gap
p	Relative pressure
U	Sliding velocity
η	Dynamic viscosity

ACKNOWLEDGMENTS

The authors would like to acknowledge the active support of this research by Casappa S.p.A., Parma, Italy.

REFERENCES

[1] Ibatan T, Uddin M S, Chowdhury M A K, (2015) Recent development on surface texturing in enhancing tribological performance of bearing sliders, Surface & Coatings Technology, Volume 272, pp 102–120

[2] Dobrica M B, Fillon M, Pascovici M D, Cicone T, (2010) Optimizing surface texture for hydrodynamic lubricated contacts using a mass-conserving numerical approach, Proceedings of the Institution of Mechanical Engineers Part J Journal of Engineering Tribology, Volume: 224 issue: 8, pp 737–750

[3] Yu H, Wang X, Zhou F, (2010) Geometric Shape Effects of Surface Texture on the Generation of Hydrodynamic Pressure Between Conformal Contacting Surfaces, Tribology Letters, Volume 37, Issue 2, pp 123–130

[4] Rahmani R, Shirvani A, Shirvani H, (2007) Optimization of Partially Textured Parallel Thrust Bearings with Square-Shaped Micro-Dimples, Tribology transactions, 50:3, 401-406, DOI: 10.1080/10402000701429261

[5] Kligerman Y, Etsion I, (2001) Analysis of the Hydrodynamic Effects in a Surface Textured Circumferential Gas Seal, Tribology Transactions, Volume 44, Issue 3, pp 472–478

[6] Razzaque M M, Faisal T R, (2008) Performance of Mechanical Face Seals with Surface Micropores, Journal of Mechanical Engineering, Volume 37, pp 77–80

[7] Brizmer V, Kligerman Y, Etsion I, (2003) A Laser Surface Textured Parallel Thrust Bearing, Tribology transactions, 46:3, 397-403, DOI: 10.1080/10402000308982643

[8] Etsion I, Halperin G, Brizmer V, Klingerman Y, (2003) Experimental investigation of laser surface textured parallel thrust bearings, Tribology Letters, Volume 17, pp 295–300

[9] Shah Y G, Vacca A, Dabiri S, (2018) Air Release and Cavitation Modeling with a Lumped Parameter Approach Based on the Rayleigh–Plesset Equation: The Case of an External Gear Pump, Energies, Volume 11, Issue 12, DOI: https://doi.org/10.3390/en11123472

[10] Reid R, Prausnitz J, Poling B, Properties of Gases and Liquids. McGraw-Hill Education, ISBN-13: 978-0070517998

A STUDY INTO FORCES AND MOMENTS ACTING ON THE SWASH PLATE OF AN AXIAL PISTON PUMP USING A NOVEL APPROACH TO REDUCE PRESSURE AND FLOW PULSATIONS.

Pratin J. Naik , Ganesh K. Seeniraj and Ram S. Chandran*

CNH Industrial, 6900 Veterns Blvd, Burr ridge, IL 60527
CNH Industrial-technology, 200 George C Delp Road, New Holland PA 17557
Mechanical Engineering Department, Kettering University, Flint, MI 48504 USA
* Corresponding author: Tel.: +1 810 762 7839; E-mail address: rchandra@kettering.edu

ABSTRACT

In hydraulic pumps, typically in axial piston pumps, reduction of pressure and flow ripples was attempted by providing relief grooves and pre-compression for noise reduction. Pre-compression is normally achieved by using the dead space between pump ports in the valve plate. Also valve plate profile modification is required, if system operating conditions such as pump output pressure and flowrate change, to maintain optimum operating conditions for reduced pressure/flow ripple. An earlier simulation study confirmed effectiveness of varying dead centre position to reduce pressure and flow ripples. A specifically designed mechanism, outlined in the earlier work, achieves this goal by varying the dead centre position of the pump swash plate. This study reports on the findings of the effect of varying dead centre position and groove configurations on forces and moments acting on the swash plate for various operating conditions. The simulation model cited in the earlier work was used in this study. This information is vital for the design of an actuating mechanism to vary dead centre position of a pump valve plate. These simulations were run using MATLAB/Simulink and S-functions. Results of this study are promising.

Keywords: Axial piston pump, simulation of an hydraulic pump, pressure and flow ripples and dead centers.

1. INTRODUCTION

For the past four decades, a large amount of work has been reported on modelling, design and control of axial piston hydraulic pumps. Most of the literature focuses mainly on mathematical modelling and design of pumps for performance improvement and control. An equal amount of material can also be found on noise generation in a hydraulic pump. The work presented in this paper is a continuation of an earlier work by Ganesh K Seeniraj and Ram Chandran [7]. This study presents results on forces and moments experienced by the swash plate when dead centre position and groove configurations are varied for various operating conditions. The same simulation model cited in the earlier work [7] was used in this study with some modifications. This information is vital for the design of an actuating mechanism to effect changes in dead centre position. The earlier paper [7] discusses a novel approach to minimize pressure and flow pulsations that may lead to reduction of noise generation in an axial piston swash plate pump.

Noise generation in an axial piston pump can be attributed to two main causes – "fluid causes and mechanical causes", according to Yamauchi and Yamamoto [8]. The mechanism of pumping action and the pressure variation inside piston volume are one of the main causes of noise generation. They relate to fluid causes through flow and pressure pulsations that propagate through the system and to mechanical causes by inducing cyclic strain causing pump components to vibrate.

The above said problem has been investigated by a number of other researchers in their unique way. Techniques adopted in noise reduction include providing relief grooves, pre-compression and ideal timing of the valve ports. These solutions introduce a major constraint on the controllability of a pump. i.e. the suggested

solution is suited only for a fixed operating condition. The performance of a pump is thus fixed and cannot be varied during operation. This is a drawback the valve plate has to be matched for a required operating point and cannot be used in systems requiring variable flow.

In the work presented by Seeniraj and Chandran [7] the authors attempt to minimize pressure and flow pulsations by combining two well-known strategies: providing relief grooves and varying port opening and associated pre-compression. Pre-compression is varied by shifting the dead centre location of the piston with respect to the valve plate. One of the main advantages of this approach is it can be applied to a variable displacement pump. Pump performance can be varied in real time as opposed to fixed performance offered by previous solutions. The aim is to vary the dead centre position (both top and bottom) of the pistons and find an optimum condition to keep the amplitude of the flow ripple and pressure pulsations to a minimum.

Becker [1] studied noise generation related to pressure transients in piston-cylinder chambers and suggested port modification and providing metering grooves to reduce pressure peaks. This addresses noise generation attributed to fluid compression and decompression. Metering grooves facilitated smooth transition.

Helgestad et al [2] investigated pressure transients in an axial piston pump through theoretical and experimental examination of pressure profile within each piston-cylinder chamber. Main focus of their work was noise generation due to pressure fluctuations. Two methods were tried to reduce noise generation: (1) 'Ideal Timing' (23 degrees from B.D.C) i.e., opening the valve port exactly when the pressure inside the piston had reached the required discharge pressure and (2) Providing 'relief grooves' at the start of both suction and discharge ports. The relief grooves had a problem of reverse flow into the piston chamber from the discharge at low speeds and induced cavitation at the suction port at high speeds.

Pettersson et al [4] proposed a simple mathematical model for flow ripple simulation. An important conclusion of their work was that a fairly simple model could be used for the study of effect of relief groove and pre-compression on pressure and flow pulsations. Pre-compression showed a remarkable impact on peak-to peak value of flow ripple.

Johansson [3] examined the effect of cross-angle on pump noise due to pressure and flow pulsations. Cross-angle is an additional incline to the traditional displacement direction. With cross-angle the piston dead-centres vary as a function of displacement, swash plate angle, enabling pre-compression and decompression.

2. PUMP MODEL, SIMULATION AND RESULTS

The pump model used in this work is an extension of the model used by Seeniraj and Chandran [7] in their research. Their model was an adaptation from the earlier work by Schoenau, Burton and Kavanagh [6]. Numerical values of parameters were taken from the work presented by Zhang, Cho, Nair and Manring [9]. Equations and the numerical values of the parameters are listed in the appendix. This model includes additional expressions to evaluate forces and moments acting on the swash plate and pump drive torque.

The model uses prime mover speed as the input and outputs are: pressure inside each piston, flow rates into and out of each piston, flow ripple and pressure pulsation at the pump outlet, moment and force on the swash plate and drive torque at the pump shaft. These outputs facilitate the visualization of the effect of noise reduction technique(s) on pump variables. Results obtained using this model agrees with earlier results presented by other authors.

The model has provision to vary the groove length. Groove length was varied in steps of 25% of the full length from zero to full groove length. Other parameters that were varied include dead centre position and buffer volume at the pump outlet.

The mathematical model of an axial piston pump was developed in MATLAB/SIMULINK® using S-functions. S-functions allow the user to include standard blocks in addition to MATLAB script code and custom defined blocks.

Figures 1 and 2 shows simulation plots of swash plate piston force and swash plate moment. The frequency of moment pulse is twice as compared to the pressure pulsation, this is due to the moment changing direction as it crosses the swash plate pivot axis.

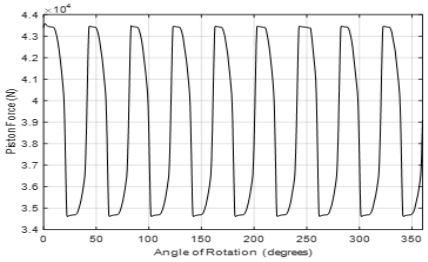

Figure 1: Swash plate Piston force plot

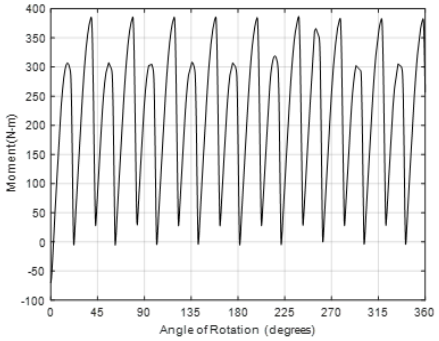

Figure 2: Swashplate moment plot

2.1. Effect of Groove Length

When a compressed fluid volume is connected to a discharge port suddenly via a full port area, there will be a large back flow into the piston chamber due to the pressure differential. On the other hand, if the piston chamber pressure is higher than the outlet pressure, a sharp pressure peak will result in output pressure. The optimum would be to exactly match piston pressure with the outlet pressure. This is difficult to achieve. Relief grooves facilitate smooth transition from suction to discharge and discharge to suction ports. **Figures 3 and 4** shows swashplate piston force and moment pulsation profiles for the five groove lengths. A reduction in amplitude of swash plate moment pulsation was observed when groove length was increased. Corresponding flow ripple and pressure pulsation plots for five groove lengths are provided in the earlier work by Seeniraj et. al [7].

Their work indicated that relief grooves reduced peak-to-peak value of the flow ripple. Pressure pulsations occur as a secondary effect due to the flow ripple. Variation in the flow ripple will affect the output pressure directly. The frequency of the pulsations is fixed by the prime mover speed. The effect of relief groove on pressure pulsation is far less compared to its effect on flow ripple. The model included a dead volume of one litre connected to the load side of the pump which is typical.

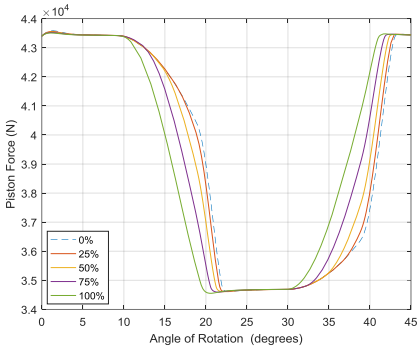

Figure 3: Swash plate piston force for different groove configurations

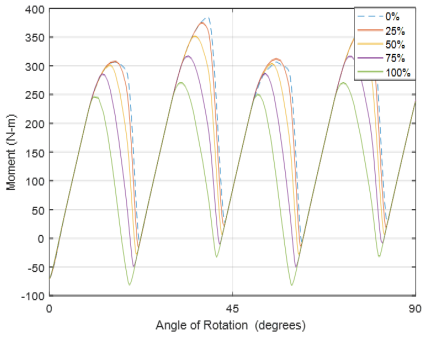

Figure 4: Swash plate moment for different groove configurations

2.2. Effect of dead centre location and TDC

In a normal swash plate pump, the pistons reach the end of their stroke(s) at the dead centres where the pistons come to a halt and the direction is reversed. At the dead centres, the displacement of the piston is nearly zero for a small change in the angular rotation. When the piston chamber is connected to the discharge port at this point there is likely to be a reverse flow in the beginning. One of the best solutions to reduce the reverse flow is to compress the fluid to the required outlet pressure before it reaches the discharge port. This is termed as pre-compression. This can be

accomplished through proper design of the valve plate such that the pistons do not open to the discharge until the fluid is compressed enough to the discharge pressure. The same effect can be achieved by varying the dead centre of the pistons without changing the valve plate profile. Changes in dead centre positions affect both the Top Dead Centre (TDC) and the Bottom Dead Centre (BDC). Typically changes in the TDC affect the suction flow and changes in BDC will change closure timing of the discharge port. A mechanism changing TDC is likely to affect the timing of BDC thus affecting suction port and its closure, and may cause cavitation. These issues are not addressed in this and also in the earlier referenced work.

TDC and BDC lie on the vertical axis of the swash plate. The pistons reach their maximum and minimum stroke position when they reach the TDC and BDC respectively. By advancing, the dead centres are shifted from the vertical axis. When the cylinders move to the actual dead centre position located on the vertical axis, the pistons would have already started moving in the reverse direction. This gives the required pre-compression.

Maximum reduction in flow ripple was achieved for a case with a full groove length and a five (5)-degree advance in TDC. Advancing the TDC beyond five (5) degrees to seven (7) and nine (9) degrees did not result in a reduction of the peak-to-peak value. Instead, the peak-to-peak value slowly starts to rise. These findings are reported in their work by Seeniraj et al [7]. They also reported that peak-to peak value of the pressure pulsations decreases as TDC was advanced. TDC delay increased the amplitude of pressure pulsations.

Amplitude of swash plate moment shows a decreasing trend when TDC is advanced and the opposite was observed when it is delayed. **Figure 6** shows this effect for 5 degree TDC advance compared to its no advance case. **Figure 8** shows the effect for 5 degree TDC delay**. Figures 5 and 7** shows swash plate force plots for two cases- TDC angle of advance (5 degrees) and an angle of delay (5 degrees) respectively. TDC angle of delay accentuates amplitude of pulsation for both swash plate force and moment.

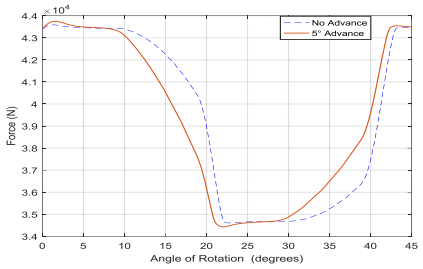

Figure 5: Effect of advancing TDC on swash plate force pulsation

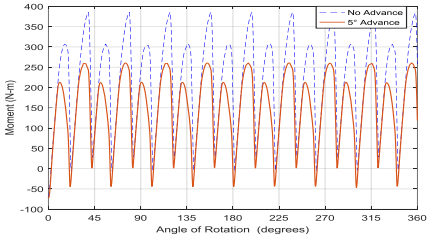

Figure 6: Effect of advancing TDC on swash plate moment pulsation

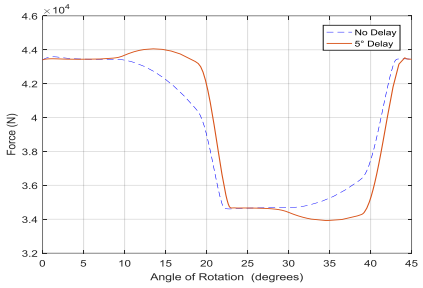

Figure 7: Effect of delaying TDC on swash plate force pulsation

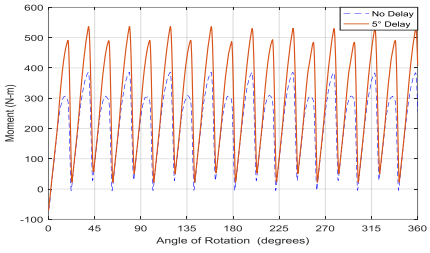

Figure 8: Effect of delaying TDC on swash plate moment pulsation

Figure 9 shows the effect of varying swash plate angle on swash plate moment. Swash plate moment shows an increasing tendency for a decrease in swash plate angle. This is a preferred

characteristic in terms of swash plate stability. In variable delivery pumps swash plate stroke will normally decrease in response to an increase in load pressure. **Figure 10** shows the effect of varying swashplate angle on the force acting on it. It can be noted that as the angle of swashplate increases, so does the force acting on it.

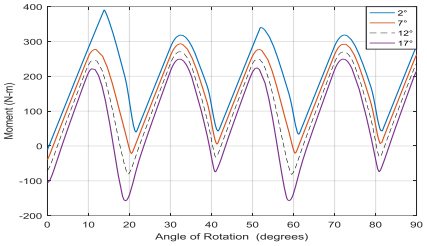

Figure 9: Effect of swash plate angle on swash plate moment

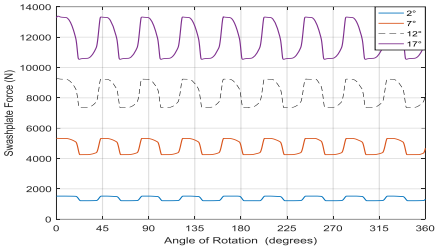

Figure 10: Effect of swash plate angle on swash plate force

Pressure pulsations, resulting effect of flow ripples, depends on the volume available for expansion inside and outside of the pump and in the immediate piping. This volume is referred to as the buffer volume. In the baseline model, a buffer volume of one litre was assumed. Pressure pulsations were simulated using the familiar bulk modulus relationship.

Seeniraj and Chandran [7] in their earlier referenced work examined effect on pressure pulsations due to different buffer volumes, for two cases of groove lengths (zero and full arc length). An increase in buffer volume reduces the amplitude of the pulsations proportionally.

This observation indicates that increasing the buffer volume is a viable option for reducing the amplitude of flow and pressure pulsations. But buffer volume available depends on the pump and the application. Increasing the buffer volume increases the compliance and can lead to an increase in system response time which may not be acceptable.

Figure 11 shows the effect of angle of advance on swashplate moment pulsation, a decrease in amplitude of pulsation was observed.

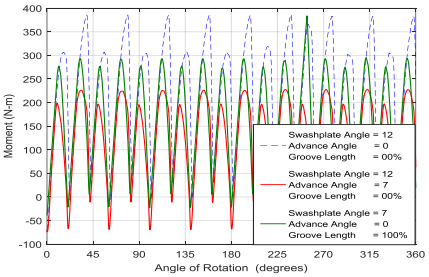

Figure 11: Swash plate moment amplitude reduction

Table 1 lists the effect of groove length and TDC advance angle on peak to peak moment values. It was observed that advancing the dead center position keeps the values low for no groove (0%) condition and when groove length is increased, advancing the angle does not help in reducing the peak to peak values.

Table 1: Moment Pulsation Peak-to-Peak Values in N-m for different groove lengths and TDC advance angles. Swash plate angle set at 12 degrees (Base line)

Groove Length	TDC Advance (degrees)				
	0	3	5	7	9
0	456	383	336	303	313
25	445	377	334	305	318
50	424	367	335	327	335
75	387	353	352	354	370
100	353	363	366	380	393

Figure 12 presents the same data for moment pulsation for changes in groove length and TDC advance angle.

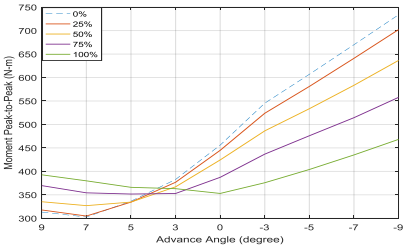

Figure 12: Moment pulsation for different groove lengths and TDC advance angles

Table 2: Moment Pulsation Peak-to-Peak Values in N-m for different groove lengths and swash plate angles

Groove Length	Swashplate Angle (degrees)			
	2	7	12	17
0	542	487	456	438
25	513	465	445	437
50	624	429	422	425
75	591	409	387	409
100	511	333	354	410

Table 2 lists the effect of groove length and swash plate angle on peak to peak moment values. It was observed that the peak to peak value increases with decreasing swashplate angle and when groove length increases, the peak to peak value decreases. A Minimum value was observed for a swash plate angle of 7 degrees.

Figure 13 presents the same data for moment pulsation for changes in groove length and swash plate angle.

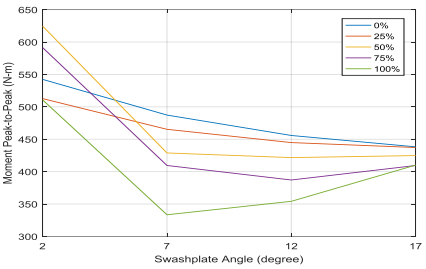

Figure 13: Moment pulsation for different groove lengths and swash plate angles

An examination of Tables 1 and 2 lead to following observations. A change in TDC angle of advancement is more effective compared to groove length change for reducing amplitude of pulsations for both swash plate moment and force. Change in groove length requires hardware modification-change of valve plate. Whereas, angle of TDC advance can be changed easily using the proposed swash plate design using a paired controller. This is the salient feature of this design.

3. CONCLUSIONS

A mathematical model of an axial piston pump was developed in MATLAB/SIMULINK® environment using S-functions. This model was exercised to study the effect of groove length and dead centre variations on swash plate moment and swash plate piston forces. Simulation results for pressure and flow pulsations correlated with the earlier work reported by Seeniraj and et al. Swash plate moments exhibited familiar pattern, not altered by introduction of dead centre position.

This study was started with an idea to explore the efficacy of a mechanism to vary dead centre position to minimize pressure and flow pulsations to minimize pump noise. An understanding of moments and forces acting on the swash plate is required to evaluate the proposed design. A simple sketch of the proposed mechanism is given in **Figure 14**. It employs two wedges separated by a bearing arrangement to minimize friction as a swash plate. When the wedges are rotated by equal amount (angular displacement) with respect to the Y-Y axis it provides the required swash plate angular displacement at the TDC and BDC. When the angular displacements of the wedges are unequal, it will provide the swash plate displacement whose TDC and BDC will be off-set from the Y-Y axis. This proposed design minimizes the effect of swash plate moments and forces on the actuating mechanism to change swash plate stroke. It is envisioned that this can be effected by a system of spring loaded electric drives acting on each wedge or by a combination spring loaded miniature hydraulic pistons regulated by pressure control valves. Load torque demand on the actuating system will be small due to the bearing arrangement separating two wedges. It is anticipated that this will be a stable system providing required speed of response. A future work will report details of this design and its development.

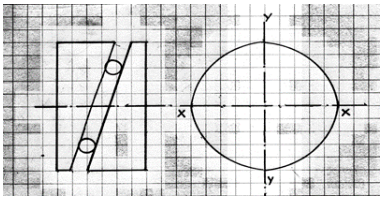

Figure 14: Sketch of a proposed two-wedge Mechanism

REFERENCES

[1] Becker R J, .1970. Quieting Hydraulic Systems and Components. Society of Automotive Engineers, 700711

[2] Helgestad B O, Foster K, Bannister F K. 1974. Pressure Transients in an Axial Piston Hydraulic

Pump. Proceedings of Institution of Mechanical Engineers, Vol. 188 17/74
[3] Johansson, A., 2005. Design Principles for Noise Reduction in Hydraulic Piston Pumps-Simulation, Optimisation and Experimental verification, Ph.D. Thesis Linkoping University, Sweden.
[4] Pettersson M E, Weddfelt K G and Palmberg J S. 1991. Methods of Reducing Flow Ripple from Fluid Power Pumps – a Theoretical Approach. Society of Automotive Engineers, 911762
[5] Pratin Naik, 2016. Modelling and Simulation of an axial piston pump-a feasibility study for an alternate design for pulsation reduction. M.S. Thesis, Kettering University, Flint, USA.
[6] Schoenau G J, Burton R T, Kavanagh G P. 1990. Dynamic Analysis of a Variable Displacement Pump. ASME Journal of Dynamic Systems, Measurement and Control, Vol. 112, pp. 122-132
[7] Seeniraj G K. and Ram S. Chandran, 2011. Study into effect of dead center position on pressure and flow ripples of a variable displacement axial piston swash plate hydraulic pump. The twelfth Scandinavian International conference on Fluid Power, May 18-20 2011,Tampere,Finland.
[8] Yamauchi K and Yamamoto T. 1976. Noises Generated by Hydraulic Pumps and their Control Method. Mitsubishi Technical Review, Vol. 13 #1, pp. 19-26
[9] Zhang X, Cho J, Nair S S, Manring N D. 2001. New Swash Plate Damping Model for Hydraulic Axial-Piston Pump. ASME Journal of Dynamic Systems, Measurement and Control, Vol. 123, pp. 463-470.

APPENDIX

The Model

Piston dynamics

The pump examined in this study has nine pistons spaced equally in a circular fashion in a cylindrical barrel. The swash plate angle and the pitch circle radius define the movement and the instantaneous position of a piston at any instance. The plane of piston reciprocation lies perpendicular to its plane of rotation. The equations adapted from the model proposed by Burton et al. (5) are used in this study and are given below.

The displacement of a n^{th} piston is described as

$$x_n = r.\tan(\alpha).\sin(\theta_n) \tag{1}$$

where r is the piston pitch radius and θ_n is the position of the piston with respect to the axis of the plane of rotation.

The velocity can be expressed as

$$\dot{x_n} = r.\tan(\alpha).\cos(\theta_n).\omega + r.\sin(\theta_n).\frac{1}{\cos^2(\alpha)}\dot{\alpha} \tag{2}$$

The swash plate angle is assumed to be a constant; the velocity of the piston can be simplified as

$$\dot{x_n} = r.\tan(\alpha).\cos(\theta_n).\omega \tag{3}$$

The instantaneous volume inside each piston chamber is given by

$$V_n = V_0 - A_p.x_n = V_0 - A_p.r.\tan(\alpha).\sin(\theta_n) \tag{4}$$

where V_0 is the initial volume of the cylinder.

$$\dot{V_n} = -A_p.\dot{x_n} \tag{5}$$

Piston pressure

The expression for pressure inside each piston chamber can be derived from the definition for bulk modulus.

$$\beta = -\frac{dP_n}{dV_n / V_n} \tag{6}$$

$$\frac{dP_n}{dt} = -\frac{\beta}{V_n}\frac{dV_n}{dt} \tag{7}$$

Figure 7 shows the schematic of a single piston, with a chamber volume C, flows into and out of the piston chamber (Q_{in} and Q_{dn}), leakage flow (Q_l) and flow due to the movement of the piston. Using the continuity equation for the control volume C, the change in volume can be expressed as

$$\frac{dV_n}{dt} = \left(Q_{dn} + Q_{in} + Q_l + \dot{V}\right) \tag{8}$$

The volume change in the piston chamber due to piston movement is

$$\dot{V} = -A_p.r.\omega.\tan(\alpha)\cos(\theta_n) \tag{9}$$

The flow rates Q_{in} and Q_{dn} can be calculated using the orifice flow rate relationship.

$$Q_{dn} = -A_{dn} C_d \sqrt{\frac{2}{\rho}} \sqrt{|P_d - P_n|}\, sign(P_d - P_n) \quad (10)$$

$$Q_{in} = -A_{in} C_d \sqrt{\frac{2}{\rho}} \sqrt{|P_i - P_n|}\, sign(P_i - P_n) \quad (11)$$

The leakage flow rate, Q_l, was approximated using the leakage coefficient C_l and is proportional to the pressure inside the piston chamber.

$$Q_l = P_n . C_l \quad (12)$$

Substituting equations 8 – 12 in equation 7, an expression for pressure, P_n, was obtained.

Valve plate profile was modeled using the data from an earlier work. Relief grooves are provided at the beginning of both suction and discharge ports. If there are no grooves, then the 9 degrees of valve land provides pre-compression. This configuration of valve plate accommodates the relief groove and pre-compression. The maximum groove length is fixed at the chosen value (9 degrees) because further increase in groove length might not offer any considerable reduction. The simulated groove profile is shown below in **Figure A-2**.

Table A- 1. System Parameters – Numerical Values

Fluid properties	β = 1.2e9 Pa ρ = 878 kg/m^3
Piston	A_p = 789.2e-6 m^3 C_d = 0.62 C_l = 4.6e-12 m^3/s/Pa N = 9 R = 0.06731 m V_o = 65.39e-6 m^3
wash plate angle	α = 12 degrees
Prime mover	ω = 210 rad/s

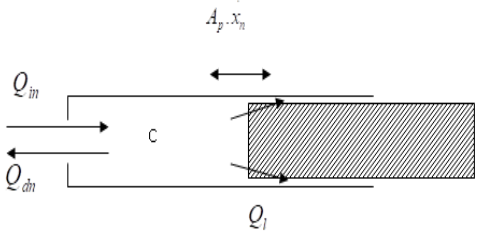

Figure A-1: Schematic of a single piston and its associated flows

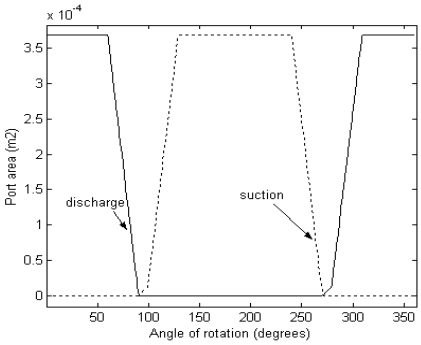

Figure A-2: Discharge/ suction port areas.

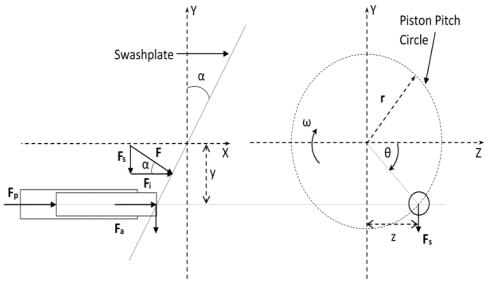

Figure A-3: Swash plate forces

$$F_i = F_P + F_a \quad (13)$$

$$F_a = m_P . \ddot{x}_i = -m_P . r . \tan(\alpha) . \sin(\theta_i) . \omega^2 \quad (14)$$

$$F_i = F_P + F_a \quad (15)$$

$$F_s = F_i . \tan(\alpha) \quad (16)$$

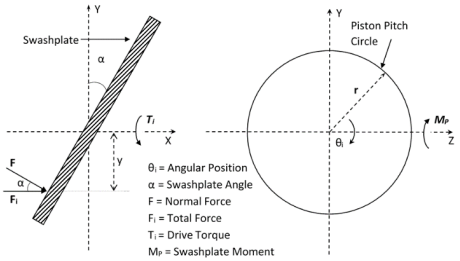

Figure A-4: Force, Torque and Moment in a Pump.

$$M_P = F . \frac{y}{\cos(\alpha)} = \frac{F_i}{\cos(\alpha)} . \frac{r . \sin(\theta_i)}{\cos(\alpha)} = F_i . r . \frac{\sin(\theta_i)}{\cos^2(\alpha)} \quad (17)$$

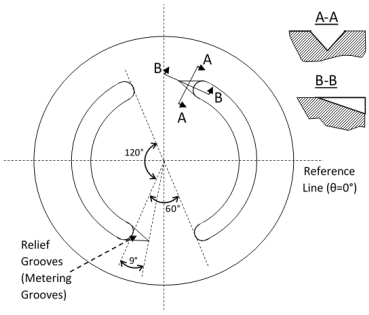

Figure A-5: Valve plate details

NOMENCLATURE

α	swash plate angle (degrees)
β	fluid bulk modulus (Pa)
ρ	fluid density (kg/m^3)
θ	angle of rotation (degrees)
ω	pump speed (rad/s)
A_d	discharge port area (m^2)
A_i	suction port area (m^2)
A_v	load orifice valve area (m^2)
C_d	coefficient of discharge
C_l	leakage coefficient (m^3/s/Pa)
P	pump outlet pressure(Pa)
P_d	discharge pressure (Pa)
P_i	suction pressure (Pa)
P_n	pressure inside piston chamber (Pa)
Q_{dn}	discharge flow rate (m^3/s)
Q_{in}	suction flow rate (m^3/s)
V_b	buffer volume (m^3)
V_o	piston initial volume (m^3)

WEAR PREDICTION OF PISTON/CYLINDER PAIR IN AXIAL PISTON PUMP

Fei Lyu, Junhui Zhang*, Bing Xu

State Key Laboratory of Fluid Power and Mechatronic Systems, Zhejiang University, No.38 Zheda Road, Hangzhou, China

* Corresponding author: Tel.: +86 153 81058508; E-mail address: benzjh@zju.edu.cn

ABSTRACT

The piston/cylinder pair is the key lubricating interface of axial piston pumps. It suffers from excessive wear due to the huge lateral force, especially under high output pressure. In order to achieve predictive maintenance, it is significant to detect the performance degradation of the piston/cylinder pair.

In this paper, a method to predict the wear of the piston/cylinder pair is proposed. The wear regions and corresponding wear depths under different conditions are investigated. The distributive characteristic parameters of the oil film are obtained, which can reflect the load-bearing and lubrication conditions at each region of the friction pair. Based on the oil film characteristic parameters, the most suitable wear model is chosen to calculate the wear depth, and then the entire wear profile of the piston/cylinder pair is obtained. The experimental investigation is carried out, and the results show that the accuracy of the wear regions and corresponding wear depth prediction is high. This method can be used to pump healthy management and choose the suitable working conditions of the axial piston pump.

Keywords: wear prediction, axial piston pump, validation

1. INTRODUCTION

The axial piston pump is the core component of a hydraulic system which provides the hydraulic power [1]. One of the most effective ways to enhance its power/weight ratio is to increase the pressure. The high working pressure leads to severer working conditions and a higher possibility of failure. In order to avoid the damage caused by sudden failure, performance degradation process and failure prevention have drawn the attention of more and more researchers. Statistical results show that the main failure in the axial piston pump is excessive wear of the friction pairs (piston/cylinder pair, cylinder/valve-plate pair, slipper/swash-plate pair). There are many methods for obtaining the wear condition [2]. It can be seen that most of the methods are related to the load-bearing and lubrication condition of the sliding surface. In the piston pump friction pair, the load-bearing and lubrication condition is directly reflected by oil film characteristic parameters. The oil film characteristic parameters will accordingly change after the surface wear occurs. Therefore, there is a strong interaction between the oil film characteristics and wear of the piston/cylinder pair.

Many researchers have contributed to the calculation of oil film characteristic parameters of the piston/cylinder pair. The pressure distribution of the oil film between friction pair was numerically solved by Kolk [3] firstly, but it was simplified to a sloping plain bearing with increased pressure on the laterally loaded side edge. The influence factors of the oil film thickness changing and the oil film extrusion effect were taken into account by Fang and Shirakashi [4] to calculate the thickness field of the oil film between the piston/cylinder pair. Ivantysynova [5] established the non-isothermal flow calculation model of the oil film in the friction pair clearance based on the Reynolds Equation and the energy equation. Based on these researches, there are several friction pair oil film calculation programs, like CASPAR [6], PUMA [7] and ViSPA [8]. The oil film parameters can be calculated by the above mentioned software.

As for wear mechanism of friction pair, Archard [9] put forward adhesive wear theory in 1953. It has been improved in the next few decades, and the Archard wear model was formed. Huang Ping,

et al [10] established an abrasive wear model for lubricated sliding contacts, which is suitable to analyze friction pairs in an axial piston pump. Hsu [11] summarized 32 parameters that influence the wear of the sliding pair, including fluid temperature, thermal capacity, velocity, contaminants, materials of contact surfaces, surface processing level, lubrication condition, load and so on. Meng [1] systematically elaborated 28 types of wear models, involving over 100 relevant parameters reflected in the wear process. Ma Jiming, et al [12] presented a method to analyze the wear behavior of slipper pair based on the EHL wear model, but the effects of surface wear on the oil film characteristics were not taken into account.

In this paper, a wear prediction method of piston/cylinder friction pair is put forward. The interaction between the distributed oil film characteristics and the surface wear is taken into account. In this way, the change of piston/cylinder pair load-bearing and lubrication condition and the wear profile with operating time can be analyzed. The accelerated lifetime test of an axial piston pump was carried out and the wear profile of piston/cylinder pair was measured for the purpose of validating the simulated results.

2. WEAR PREDICTION METHOD

2.1. Overview

Distributivity

There exists a micro-motion of the piston because of the clearance between the piston and the cylinder. Therefore, the wear conditions of the cylinder bore are variable in different regions. So it is necessary to analyze the different parts of the cylinder bore surface using a distributed approach. The most convenient and effective method is to divide the surface of the cylinder bore into several nodes and analyze the load-bearing and lubrication conditions of each node. The cylindrical surface of the cylinder bore can be spread out into a plane as shown in **Figure 1**.

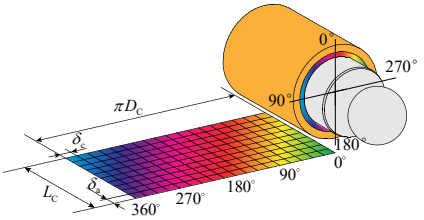

Figure 1: Divided cylinder bore surface

In this figure, D_C is the diameter of the cylinder bore, L_C is the effective length of the cylinder bore, δ_a and δ_c are the axial and circumferential lengths of the node, respectively.

For each node, the load-bearing and lubrication condition is described by the distributive oil film characteristics, and its wear volume is calculated separately. Finally, all the nodes are combined to fit the wear profile of the entire piston/cylinder pair.

Multiple sub-model

It is important to choose the most suitable wear calculation model under the corresponding load-bearing and lubrication condition. On the one hand, the adhesive node is considered to be formed when the hydrodynamic pressure or solid contact stress of this node is greater than a threshold value. The wear depth is suitable to be calculated by the adhesive wear model. On the other hand, the lubrication wear of cylinder bore occurred if the oil film thickness of this node is lower than the height of the rough peak. The Partial-EHL contacts sliding wear model is suitable to utilized to calculate the wear depth. The switch method of the wear calculation models is expressed as

$$\begin{cases} p_{\text{node}} \geq p_{\text{t}} & \text{adhesive wear model,} \\ h_{\text{node}} < h_{\text{t}} & \text{sliding wear model,} \end{cases} \tag{1}$$

where p_{node} is the hydrodynamic pressure of each node, h_{node} is the oil film thickness of each node, p_{t} is the pressure thresholds for using adhesive wear model and sliding wear model, h_{t} is the oil film thickness threshold to determine whether sliding wear occurs or not.

Update with operating time

With the pump operating, the profile of the cylinder bore surface will change when the wear occurs. The oil film thickness field will be affected by the wear as shown in

$$h_{\text{node}}^{T} = c_{\text{node}} + w_{\text{node}}^{T}, \quad (2)$$

where w_{node} is the wear depth of each node, c_{node} is the clearance between the piston and cylinder bore of each node without wear, T is the operating time of the pump.

The oil film thickness field is a key component for calculating the oil film characteristics. Therefore, the oil film characteristics should be updated after the wear occurs. The semi-steady solution is used to obtain the cumulative wear. The wear depth of each node w_{node} is calculated based on the oil film characteristic parameters, and then, the wear depth is utilized to recalculate the new oil film characteristic parameters.

This is a process that takes into account the interaction between wear and oil film.

2.2. Wear depth calculation

Adhesive wear

When the piston is working in the high-pressure area, the main external forces applied to the piston is shown in **Figure 2**. and the large lateral force F_{L} is bold. It should be noted that only main forces related to the piston lateral force including the pressure force F_{p}, the slipper friction force F_{SF}, the slipper supporting force F_{SS}, the axial component F_{SSz} and the lateral component F_{SSy} are presented. Other forces such as gravity and centrifugal force are relatively small, and they are not displayed for brevity. Due to the tiny clearance between the piston/cylinder pair and the large lateral force F_{L} which is bold in **Figure 2**, partial solid squeezing may appear between the piston and the cylinder bore as indicated in the red circle in **Figure 2**. The wear condition of the squeezed areas is suitable to be analyzed by the adhesive wear theory.

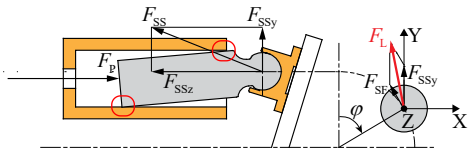

Figure 2: Main external forces applied to the piston

The adhesive nodes will be formed due to high pressure and contact stress of the contact areas when the friction pair surface slides relative to each other. It may lead to shearing fracture and surface abrasion. The wear volume V is related to the load on the sliding surface, and it can be calculated in

$$\frac{\mathrm{d}V}{\mathrm{d}s} = k_{\text{s}} \frac{p_{\text{node}} \delta_{\text{a}} \delta_{\text{c}}}{3\sigma_{\text{s}}}, \quad (3)$$

where s is the sliding distance, σ_{s} is the compressive yield limit which is related to the rigidity of the worn materiel, and k_{s} is the wear constant which represents the probability of shearing fracture in all adhesive nodes. It can be obtained from the existing literature.

Partial-EHL contacts sliding wear

As mentioned above, the adhesive wear model is suitable to calculate the wear when the pressure on the squeezed nodes is relatively high. However, the adhesive nodes will not form when the lateral force is relatively small. The external force still lets the tilt of the piston which will cause the contact of roughness peak. The sliding wear will occur when the height of the roughness peak after viscoelastic deformation is still higher than the oil film thickness. Therefore, the expression of h_{t} is shown in Equation 4:

$$h_{\text{t}} = \delta_0 / e^{\frac{\Delta}{2u\tau}}. \quad (4)$$

The wear depth of the cylinder bore can be calculated by the partial-EHL contacts sliding wear model which is shown in Equation 5:

$$\frac{\mathrm{d}V}{\mathrm{d}t} = u\left(\delta_0 e^{-\Delta/2u\tau} - h_{\text{node}}\right)^2 \Delta / \delta_0, \quad (5)$$

where t is the sliding time, u is the sliding velocity, δ_0 is the height of roughness peak, Δ is the wavelength of roughness peak, τ is the delay time of cylinder bore material.

The wear depth w can be obtained by

$$w = V / \delta_a \delta_c. \quad (6)$$

2.3. Oil film characteristics calculation

It can be seen from the wear models above that the oil film characteristics are the significant parameters of wear depth calculation. As for adhesive wear, the load on the worn surface, which is closely related to the hydrodynamic pressure or the solid contact stress, is one of the key parameters for calculating the wear depth. For partial-EHL contacts sliding wear, the comparison of oil film thickness and the roughness peak height is very important. For the reasons above, the requirement for solving the oil film characteristics is put forward. A numerical model is established to calculate the distributive oil film characteristics. The oil film

characteristics can be described by Reynold Equation as shown in Equation 7:

$$\frac{\partial}{\partial x}\left(\frac{\partial p}{\partial x}\frac{h^3}{\mu}\right)+\frac{\partial}{\partial z}\left(\frac{\partial p}{\partial z}\frac{h^3}{\mu}\right)=6\left(\omega_p\frac{D_C}{2}\frac{\partial h}{\partial x}+u\frac{\partial h}{\partial z}+2\frac{\partial h}{\partial t}\right) \quad (7)$$

where p is the hydrodynamic pressure, h is the oil film thickness, μ is the viscosity of the oil, and ω_P is the speed of piston spin.

The first two items on the right side of Equation 7 represent the dynamic pressure effects of the wedge-shaped oil film pair. The third item represents the squeezing effect of oil film caused by the micro-radial motion of the piston. As a partial differential equation with diffusion term and source term, it cannot be solved directly. Therefore, the finite volume method is used to discretize Equation 7.

The oil film of the entire piston/cylinder pair can be discretized into several nodes. At the beginning of the calculation, an initial oil film thickness field and corresponding thickness changing rates are assigned. In order to determine the action force of oil film on the piston at each node, the pressure distribution of piston/cylinder pair oil film is obtained by solving the discretized Reynolds Equation. After that, the dynamics of the piston and the hydrodynamic pressure distribution can be substituted into the force and moment balance equation. Then the Newton-Raphson method is used for the iterative solution. The oil film thickness and thickness changing rate will adjust automatically if the force and moment balance equations are not satisfied. The process above will repeat until the forces and moments are balanced. The calculation process of the numerical model is shown in **Figure 3**.

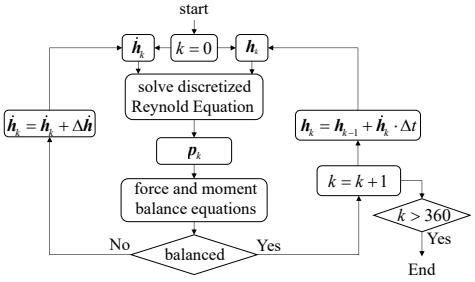

Figure 3: Calculation process of the numerical model

In **Figure 3**, k is the rotating angle of the cylinder with the resolution of 1 degree, $\boldsymbol{p}$ is the discretized hydrodynamic pressure, $\boldsymbol{h}$ is the discretized oil film thickness, $\dot{\boldsymbol{h}}$ is the discretized oil film thickness changing rates, $\Delta\dot{\boldsymbol{h}}$ is the variation of $\dot{\boldsymbol{h}}$ in each iteration.

2.4. Process of the wear prediction method

Here is the process of the wear prediction model.

1. Firstly, a set of initial oil film characteristic parameters is calculated by the numerical simulation model.
2. Then, the oil film characteristic parameters are fed to the wear model as key boundary conditions, and the wear depth at each node per cycle can be gained and superimposed to the previous cycle. Adhesive wear model and partial-EHL contacts sliding wear model are used to calculate the wear depth. They are switched according to the load-lubrication condition.
3. Since the wear influences the oil film thickness, the wear depth will be input to the numerical simulation model to recalculate the oil film characteristic parameters when the maximum wear depth exceeds a certain threshold.
4. The above steps repeat until the specified number of revolutions is reached.

The Schematic diagram of the model structure is shown in **Figure 4**.

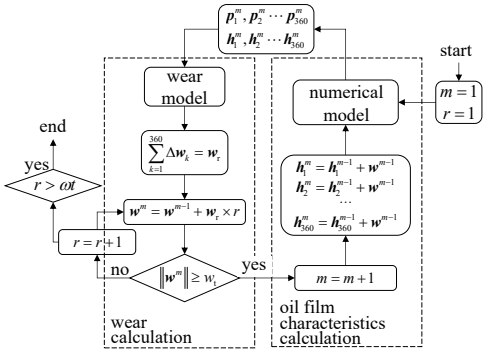

Figure 4: Schematic diagram of the model structure

In **Figure 4**, m is the number of oil film calculation, r is the revolution of the cylinder, $\Delta\boldsymbol{w}$ is the wear distribution during one degree, $\boldsymbol{w}_r$ is the wear distribution during one revolution, $\boldsymbol{w}$ is the wear distribution before the next oil film calculation, and $\boldsymbol{w}^0$ equals to zero, w_t is the is the wear threshold for calculating oil film.

The simulation was carried out in accordance with this method. The simulation condition is shown in **Table 1**.

Table 1: Simulation condition

Condition	Value	
Running time	240	[h]
Loading pressure	42	[MPa]
Rotating speed	1450	[rpm]

2.5. Simulated results

The simulated results can be displayed in the same way as the oil film parameters be displayed as shown in **Figure 5**. It can be seen that the wear of two ends of the cylinder bore is relatively serious in the specific ranges of circumferential angle.

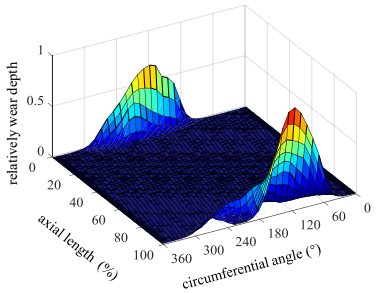

Figure 5: Simulated result of wear distribution

3. EXPERIMENTAL VALIDATION

3.1. Test of pump

In order to verify the wear regions and corresponding simulated wear depth, a real-machine experiment for an axial piston pump was carried out. A new KD-H180 axial piston pump was tested in an accelerated lifetime test bench, which lasted 240 hours. The test condition is consistent with the simulation condition as shown in **Table 1**.

The test bench is shown in **Figure 6**.

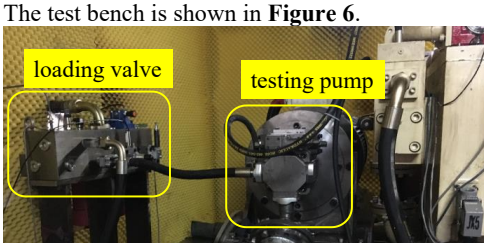

Figure 6: Test bench and test pump

3.2. Measurement of wear

The tested pump was disassembled and the cylinder was taken out to be measured before and after the durability test. In order to obtain the complete wear distribution of the cylinder bore, the cylinder bore was divided into several sections along the axis for measurement as shown in **Figure 7**. It can be seen from **Figure 5** that the axial wear gradient near the ends of the cylinder bore is much larger than that elsewhere, so the measurement section near the ends of the cylinder bore was more intensive than that elsewhere.

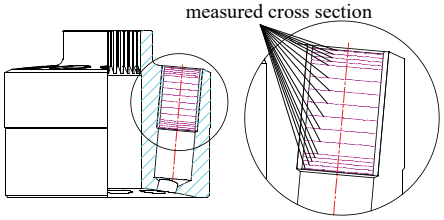

Figure 7: Site of the measured cross-section

The circumferential profile of each section was measured by a coordinate measuring machine (CMM), and these circumferential profiles can be fitted into a three-dimensional profile as shown in **Figure 8**.

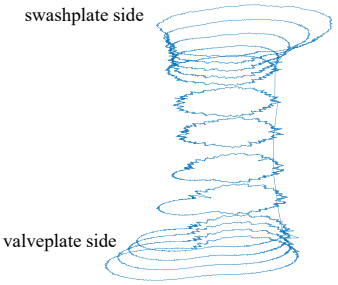

Figure 8: Three-dimensional profile of the cylinder bore

3.3. Support of measured results

The three-dimensional profile of the cylinder bore can be spread out into a plane for intuitively comparing the measured result with the simulated result more. The correspondence between the simulated result and the measured result can be shown in **Figure 9**. As shown in **Figure 9(a)**, both the circumferential angle coordinate and the axial length coordinate are the same as those of the simulated results. The wear regions and

corresponding wear depth in the simulated results are reflected in **Figure 9(b)**.

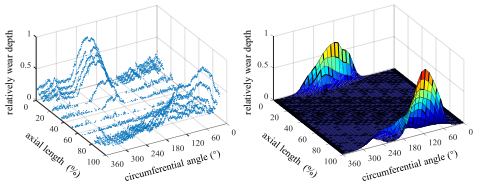

(a) measured result (b) simulated result

Figure 9: Entire profile of the cylinder bore

It can be seen from **Figure 9** that in the axial direction, the most serious wear regions are near the ends of the cylinder bore. The wear profile near the ends can be displayed in the circumferential direction for intuitive analysis. **Figure 10** shows the comparison of the simulated and measured profile of the cylinder bore.

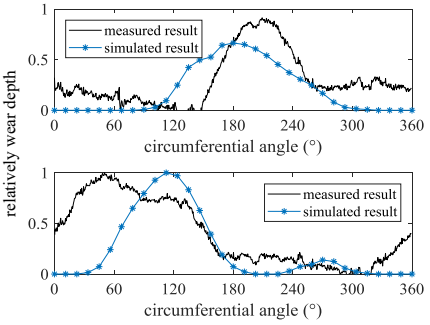

Figure 10: Circumferential profile of the cylinder bore

It can be seen that the measured profiles have a good correspondence with the simulated results. For the side of valve plate, the most severe wear regions are at the angle of 210 °. For the side of swash plate, the most severe wear regions are at the angle of 50 °. The cause of the above phenomena needs to be explored. When the piston is working in the high-pressure area, the piston inclines in the cylinder bore under the huge lateral force, and the oil film at the ends of the cylinder bore is thinner. The squeezing effect of oil film is strengthened in these regions, in other word, the load on these regions is enhanced. Solid contact is easy to occur at the ends of the cylinder bore because of the thinner oil film.

4. CONCLUSION AND OUTLOOK

In this paper, a wear prediction method of piston/cylinder friction pair is put forward. The wear regions and corresponding wear depth of piston/cylinder pair can be obtained by this method. The validity of the method is proved by the experiment, and the measured results show that the accuracy of the wear regions and corresponding wear depth prediction is high.
In the future, the effect of medium viscosity, swashplate angle, and other related structure parameters of the pump can be studied. The wear prediction method can be used to pump healthy management, and can help to choose the suitable working conditions and structural parameters of the axial piston pump.

5. ACKNOWLEDGEMENTS

The authors would like to thank Keda Hydraulic Co., Ltd for providing the testing pump and durability test, thank Liyuan Hydraulic (Suzhou) Co., Ltd. for providing coordinate measuring machine (CMM) and measuring technique. The research was supported by the National Key R&D Program of China (Grant Number 2018YFB2001101) and the National Natural Science Foundation of China (Grant Numbers 51835009 and 51890882).

NOMENCLATURE

D_C	Diameter of cylinder bore	[mm]
L_C	Effective length of cylinder bore	[mm]
δ_a	Axial lengths of node	[mm]
δ_c	Circumferential lengths of node	[mm]
p_{node}	Pressure of each node	[bar]
p_{ta}	Pressure thresholds for adhesive wear model	[bar]
p_{ts}	Pressure thresholds for sliding wear model	
h_{node}	Oil film thickness of each node	[µm]
h_t	Oil film thickness threshold for sliding wear model	[µm]
c_{node}	Clearance without wear of each node	[µm]
T	operating time of pump	[s]
F_p	Pressure force	[N]
F_{SS}	Slipper supporting force	[N]
F_{SSz}	Axial component of slipper supporting force	[N]
F_{SSy}	Lateral component of slipper supporting force	[N]
F_{SF}	Slipper friction force	[N]
F_L	Lateral force	[N]
V	Wear volume	[mm^3]
s	Sliding distance	[mm]
σ_s	Compressive yield limit	[MPa]
k_s	Wear constant	[-]

t	Sliding time	[s]
u	Sliding velocity	[mm/s]
δ_0	Height of roughness peak	[μm]
Δ	Wave length of roughness peak	[μm]
τ	Delay time of cylinder bore material	[s]
p	Hydrodynamic pressure	[bar]
h	Oil film thickness	[μm]
μ	Dynamic viscosity of oil	[Pa·s]
ω_P	Speed of piston spin	[rad/s]
k	Rotating angle of cylinder	[°]
$\boldsymbol{p}$	Discretized hydrodynamic pressure	[bar]
$\boldsymbol{h}$	Discretized oil film thickness	[μm]
$\dot{\boldsymbol{h}}$	Discretized oil film thickness changing rates	[μm/s]
$\Delta\dot{\boldsymbol{h}}$	Variation of $\dot{\boldsymbol{h}}$ in each iteration	[μm/s]
m	Number of oil film calculation	[-]
r	Revolution of cylinder	[-]
$\Delta\boldsymbol{w}$	Wear distribution during one degree	[μm]
$\boldsymbol{w}_r$	Wear distribution during one revolution	[μm]
$\boldsymbol{w}$	Wear distribution before next oil film calculation	[μm]
w_t	Wear threshold for calculating oil film	[μm]

REFERENCES

[1] Yang, H., Zhang, B., & Xu, B. (2008). Development of axial piston pump/motor technology. Chin. J. Mech. Eng, 44, 1-8.

[2] Meng, H. C., Ludema, K. C. (1995). Wear models and predictive equations: their form and content. Wear, 181, 443-457.

[3] van der Kolk, H. J. (1972). Beitrag zur Bestimmung der Tragfähigkeit des stark verkanteten Gleitlagers Kolben/Zylinder an Axialkolbenpumpen der Schrägscheibenbauart (Doctoral dissertation, Verlag nicht ermittelbar).

[4] Fang, Y., & Shirakashi, M. (1995). Mixed lubrication characteristics between the piston and cylinder in hydraulic piston pump-motor. Journal of tribology, 117(1), 80-85.

[5] IVANTYSNOVA, M. (1985). Temperaturfeld im schmierspalt zwischen kolben und zylinder einer axialkolbenmaschine. Maschinenbautechnik, 34(12), 532-535.

[6] Wieczorek, U., & Ivantysynova, M. (2002). Computer aided optimization of bearing and sealing gaps in hydrostatic machines—the simulation tool CASPAR. International Journal of Fluid Power, 3(1), 7-20.

[7] Fatemi, A., Wohlers, A., & Murrenhoff, H. (2008, March). Simulation of elastohydrodynamic contact between piston and cylinder in axial piston pumps. In Proceedings of the 6th International Fluid Power Conference (IFK), Dresden, Germany, March (pp. 539-552).

[8] Zhang, J., Xu, B., & Zhang, B. (2010, August). Analysis of the Piston/Cylinder Pair of Axial Piston Pump Based on Virtual Prototype (Fluid-Structure Interaction in MBS). In The Proceedings of the Asian Conference on Multibody Dynamics 2010.5 (pp. _58812-1_). The Japan Society of Mechanical Engineers.

[9] Archard, J. (1953). Contact and rubbing of flat surfaces. Journal of applied physics, 24(8), 981-988.

[10] Ping, H., & Shizhu, W. (1996). Visco-Elastohydrodynamic Lubricationand Lubricated Wear [J]. Chinese Journal of Mechanical Engineering, 3.

[11] Hsu, S. M., Shen, M. C., & Ruff, A. W. (1997). Wear prediction for metals. Tribology International, 30(5), 377-383.

[12] Ma, J., Chen, J., Li, J., Li, Q., & Ren, C. (2015). Wear analysis of swash plate/slipper pair of axis piston hydraulic pump. Tribology International, 90, 467-472.

peer reviewed

NUMERICAL CALCULATION OF DYNAMIC STIFFNESS AND DAMPING COEFFICIENTS OF OIL LUBRICATION FILM IN INTERNAL GEAR MOTORS AND PUMPS

Pham Trong Hoa, Nguyen Manh Hung

University of Transport and Communications (UTC), No.3, Cau Giay str., Lang Thuong ward, Dong Da district, Ha Noi, Vietnam.

ABSTRACT

Oil lubrication film plays an important role in analysis of dynamic behavior of the internal gear motors and pumps. During operation, the oil film is considered as the spring and damping system. Therefore, calculation of the dynamic stiffness and damping coefficients is necessary to build the mathematical model for studying of dynamic problem. In order to calculate these coefficients, the dynamic pressure and perturbing pressure distribution must be determined firstly. In this paper, the infinitesimal perturbation method (IFP) is used to calculate the dynamic pressure distribution. Based on that the dynamic stiffness and damping coefficients can be computed. The calculation results point out that the dynamic stiffness and damping coefficients are much dependent on the eccentricity ratio.

Keywords: Internal gear motors and pumps, dynamic pressure, stiffness and damping coefficients.

1. INTRODUCTION

The oil lubrication film is very important for rotating machines [1]. Dynamic behavior of the internal gear motor and pump is much dependent on the characteristics of the oil film between the outer ring gear and inner housing. A mathematical model for studying of dynamic behavior of internal gear motor and pump has not been introduced so far [2]. One reason is the difficulty of determination of dynamic stiffness and damping coefficients. Pham in study [3, 4] analyzed the dynamic problem of internal gear motor and pump by using the mobility method with some modifications. The stability problem of internal gear motors and pumps has been observed and introduced in study [5] through experimental results.

Unlikely to other rotating machines, for internal gear motor and pump, the oil lubrication is also the working oil. Among those parameters of oil film, the stiffness and damping coefficients are the most important. In the study [6] Pham et al., calculated the static stiffness and damping coefficients and analyze the effect of some geometric parameters on static stiffness and damping coefficients. These coefficients are found by linearizing the ring gear force at the steady state condition. In order to calculate the dynamic stiffness and damping factors, the dynamic pressure distribution must be determined. Lots of studies relating to the internal gear and pump so far, however, the study of dynamic stiffness and damping coefficients have been not performed. The calculation of the dynamic oil film stiffness and damping factors will be the fundamental issues to study dynamic problem of the internal gear motor and pump.

2. MATHEMATICAL MODEL

The cross section of the internal gear motor and pump is described in **Figure 1**. A motor/pump unit contains of three main elements, e.g., driving gear, ring gear and housing. It is widely used due to its simplification and economy. To avoid the metal - to - metal contact between the outer ring gear and inner housing, the oil thin film is required. Unlikely to other rotating machines, the oil lubrication of the internal gear motor and pump is also the working oil. During operation, the oil film is considered as the spring and damper system as shown in **Figure 2**. It contains both the direct coefficients (k_{xx}, k_{yy} and b_{xx}, b_{yy}) and the cross-coupling coefficients (k_{xy}, k_{yx} and b_{xy}, b_{yx}). These parameters are functions of the eccentricity ratio ε (e/c). The nominal gap between the outer ring gear and inner housing is called the radial clearance (c). e is the eccentricity of the ring gear. It is the distance from the ring

gear center to the housing center. The eccentricity is dependent on the working conditions. The oil lubrication film over the circumferential direction is not evenly as shown in **Figure 3**. The oil film thickness is a function of eccentricity (e) and position angle (θ) of the ring gear center which is presented in equation (1)

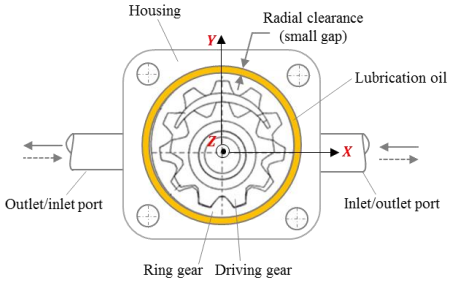

Figure 1: Internal gear motor and pump

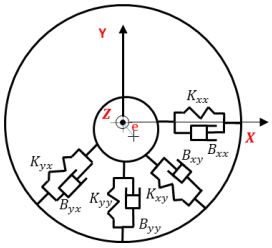

Figure 2: Mass-Spring-Damping model

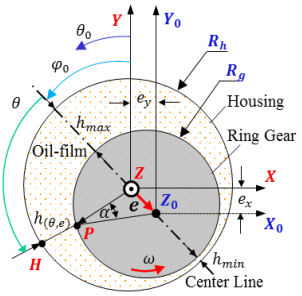

Figure 3: Oil film thickness

$$h_{(\theta,e)} = c(1 + \varepsilon\cos\theta) \tag{1}$$

2.1. The non-linear model

Oil film force is dependent on the ring gear position and velocities, i.e.,

$$\begin{cases} F_x = F_x(x, y, \dot{x}, \dot{y}) \\ F_y = F_y(x, y, \dot{x}, \dot{y}) \end{cases} \tag{2}$$

The oil film force can be calculated by integrating the oil film pressure in both horizontal and vertical directions [7]:

$$\begin{bmatrix} F_x \\ F_y \end{bmatrix} = -\int_{\theta_1}^{\theta_2}\int_{0}^{L} p \begin{bmatrix} \sin\theta \\ \cos\theta \end{bmatrix} (R\,d\theta)\,dz \tag{3}$$

The oil film force is determined as,

$$\begin{cases} F_x = K_{xx}x + K_{xy}y + B_{xx}\dot{x} + B_{xy}\dot{y} \\ F_y = K_{yx}x + K_{yy}y + B_{yx}\dot{x} + B_{yy}\dot{y} \end{cases} \tag{4}$$

In which, the stiffness and damping coefficients are defined as follows,

$$\begin{cases} K_{xx} = \dfrac{\partial F_x}{\partial x}, K_{xy} = \dfrac{\partial F_x}{\partial y}, K_{yx} = \dfrac{\partial F_y}{\partial x}, K_{yy} = \dfrac{\partial F_y}{\partial y} \\ B_{xx} = \dfrac{\partial F_x}{\partial \dot{x}}, B_{xy} = \dfrac{\partial F_x}{\partial \dot{y}}, B_{yx} = \dfrac{\partial F_y}{\partial \dot{x}}, B_{yy} = \dfrac{\partial F_y}{\partial \dot{y}} \end{cases} \tag{5}$$

These coefficients are called as nonlinear or dynamic oil-film stiffness and damping. Calculation of these coefficients is important in the dynamic analysis for internal gear motor and pump. Normally there are two theoretical model to calculate these linear factors, i.e., Infinitesimal perturbation method (IFP) and finite perturbation method (FP). In this study, the infinitesimal perturbation method (IFP) is used. The infinitesimal perturbation method uses the partial derivatives of the ring gear with respect to the displacements and velocities to calculate the force factors [8].

$$\begin{bmatrix} K_{xx} \\ K_{xy} \\ K_{yx} \\ K_{yy} \\ B_{xx} \\ B_{xy} \\ B_{yx} \\ B_{yy} \end{bmatrix} = \begin{bmatrix} \dfrac{\partial F_x}{\partial x} \\ \dfrac{\partial F_x}{\partial y} \\ \dfrac{\partial F_y}{\partial x} \\ \dfrac{\partial F_y}{\partial y} \\ \dfrac{\partial F_x}{\partial \dot{x}} \\ \dfrac{\partial F_x}{\partial \dot{y}} \\ \dfrac{\partial F_y}{\partial \dot{x}} \\ \dfrac{\partial F_y}{\partial \dot{y}} \end{bmatrix} = -R\int_{\theta_1}^{\theta_2}\int_{0}^{L} \begin{bmatrix} p_x \sin\theta \\ p_y \sin\theta \\ p_x \cos\theta \\ p_y \cos\theta \\ p_{\dot{x}} \sin\theta \\ p_{\dot{y}} \sin\theta \\ p_{\dot{x}} \cos\theta \\ p_{\dot{y}} \cos\theta \end{bmatrix} d\theta\,dz \tag{6}$$

These perturbing pressure component are computed as follows

$$\begin{cases} p_o = (p)_o \\ p_x = \left(\frac{\partial p}{\partial x}\right)_o \\ p_y = \left(\frac{\partial p}{\partial y}\right)_o \\ p_{\dot{x}} = \left(\frac{\partial p}{\partial \dot{x}}\right)_o \\ p_{\dot{y}} = \left(\frac{\partial p}{\partial \dot{y}}\right)_o \end{cases} \quad (7)$$

These pressure components are obtained by solving of the Reynold's equations:

$$\frac{\partial}{\partial\theta}\left(h^3\frac{\partial}{\partial\theta}\right)+\frac{\partial}{\partial z}\left(h^3\frac{\partial}{\partial z}\right)\begin{pmatrix} p_0 \\ p_x \\ p_y \\ p_{\dot{x}} \\ p_{\dot{y}} \end{pmatrix}$$

$$= \begin{pmatrix} \frac{\partial h}{\partial\theta} \\ cos\theta - 3\frac{\partial}{\partial\theta}\left(h^2 sin\theta \frac{\partial p_0}{\partial\theta}\right) - 3\frac{\partial}{\partial z}\left(h^2 sin\theta \frac{\partial p_0}{\partial z}\right) \\ sin\theta - 3\frac{\partial}{\partial\theta}\left(h^2 cos\theta \frac{\partial p_0}{\partial\theta}\right) - 3\frac{\partial}{\partial z}\left(h^2 cos\theta \frac{\partial p_0}{\partial z}\right) \\ 2sin\theta \\ 2cos\theta \end{pmatrix} \quad (8)$$

By solving the Reynolds equation for each pressure component, the dynamic forces components are defined. From equation (8), the static pressure po and four perturbing pressure px, py, p_x˙ and p_y˙ can be solved. Based on that, eight stiffness and damping coefficients can be calculated by integrating these perturbing pressure as in (6).

Definition of the solution domain and boundary conditions:

To increase the accuracy, perturbation is normally performed in both positive and negative directions. After governing the controlling equation for the pressure distribution Eq. (8), the boundary conditions for calculation of the pressure distribution must be defined. For the computation of the pressure distribution from the Reynolds equation, the pressure field at the edge is assumed to equal zero. For the m*n grid points of the pressure, m*n equations are established. However, the pressure at all the edge points (m+1)*(n+1) is equal to zero. Therefore it is needed to write the pressure equation for the other points inside the grid net. Numerical procedure is presented in **Figure 4**.

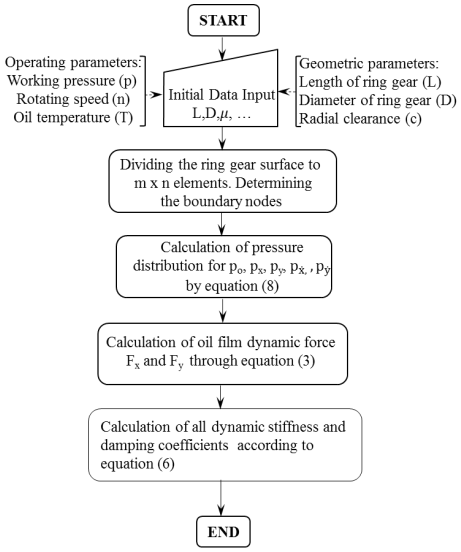

Figure 4: Calculation procedure

Table 1: Geometrics parameters of internal gear motor and pump

Parameter	Symbol	Value	Unit
Diameter of ring gear	D	0.11	m
Length of ring gear	L	0.017	m
Dynamic viscosity	μ (Oil HLP46)	0.04	Pa.s
Rotating speed	n	2000	rpm
Working pressure	Δp	200	bar
Radial clearance	c	50.10^{-6}	m
Temperature	T	40°	C

3. RESULTS AND DISCUSSION

3.1. Distribution of pressure components

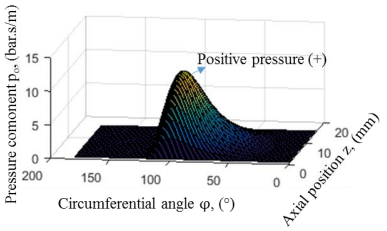

Figure 5: Hydrodynamic pressure distribution p_o

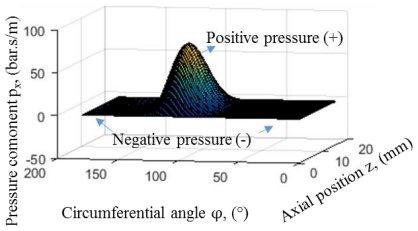

Figure 6: Distribution of pressure component p_x

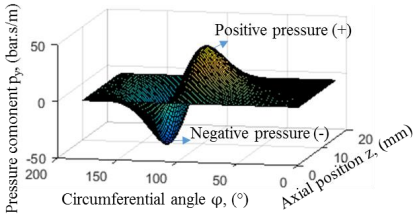

Figure 7: Distribution of pressure component p_y

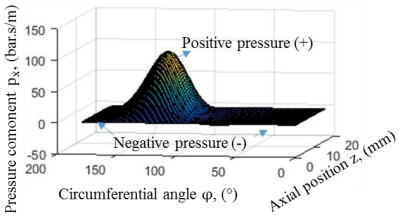

Figure 8: Distribution of pressure component p_x

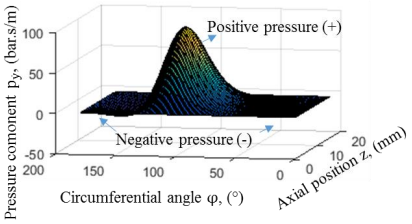

Figure 9: Distribution of pressure component p_y

Figure 5 shows 2D hydrodynamic pressure distribution at the eccentricity ratio of 0.5. The pressure mountain distributes from 30° to 125° in circumferential direction. The maximum value of hydrodynamic pressure stays around 110°. The perturbing pressure component are presented from **Figure 6** to **Figure 9**, respectively. One can see that for all perturbing pressure exists the both types of pressure, e.g., positive and negative pressure elements. The area of negative and positive pressure vary for different perturbing pressure component. The existence of the negative pressure component represents for the changing of velocities and acceleration of ring gear. It reduces the values of dynamic stiffness and damping coefficients. The dynamic stiffness coefficients are calculated through the perturbing pressure px and py. Meanwhile, the dynamic damping coefficients are dependent on the perturbing pressure component p_x and p_y.

3.2. Analysis of effect of eccentricity on pressure component

As mentioned above, the dynamic pressure is a function of the eccentricity. The effect of eccentricity on the hydrodynamic pressure distribution is shown in **Figure 10**. It is obviously to see that for low values of eccentricity ratio, the area of hydrodynamic pressure distribution is larger than that of high values of eccentricity ratio. However, the maximum hydrodynamic pressure at the high values of eccentricity is much larger than that of low values, for example the maximum pressure at eccentricity ratio of 0.2 is about 2.1 bar whereas the maximum pressure at eccentricity ratio of 0.8 reaches up to 105 bar.

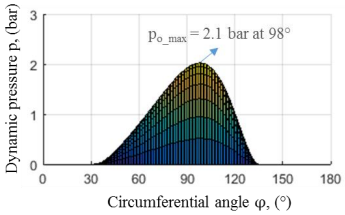

Figure a: Eccentricity ratio of 0.2

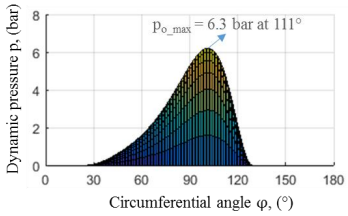

Figure b: Eccentricity ratio of 0.4

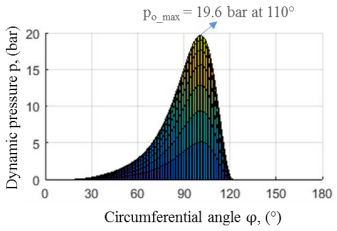

Figure c: Eccentricity ratio of 0.6

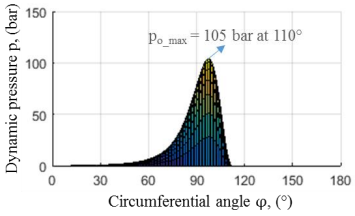

Figure d: Eccentricity ratio of 0.8

Figure 10: Effect of eccentricity on the hydrodynamic pressure distribution p_o at middle axial plane.

The effect of eccentricity on the perturbing pressure distribution p_x is shown in **Figure 11**. One can see that the perturbing pressure p_x changes according to the change of the eccentricity ratio. It always exists both negative and positive pressure elements. The area of positive pressure is reduced according to the increase of the eccentricity ratio, however, the maximum value of pressure is greatly increased, e.g., 1130 bar/m at 98° for eccentricity ratio value of 0.8 compared to 16.2 bar/m at 112° for eccentricity ratio value of 0.2.

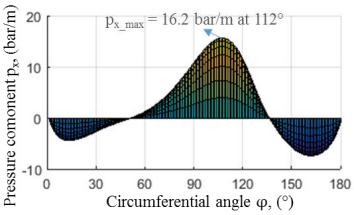

Figure a: Eccentricity ratio of 0.2

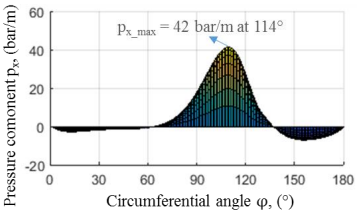

Figure b: Eccentricity ratio of 0.4

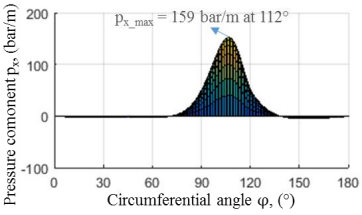

Figure c: Eccentricity ratio of 0.6

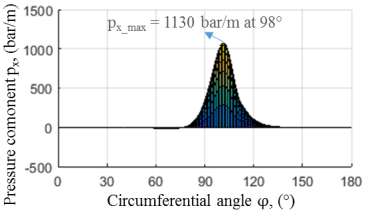

Figure d: Eccentricity ratio of 0.8

Figure 11: Effect of eccentricity on the 2D perturbing pressure distribution p_x at middle axial plane.

The effect of eccentricity on the perturbing pressure distribution p_y is shown in **Figure 12**. The pressure distribution is divided into two areas, e.g., the left area is the positive pressure and the negative pressure places at the right side.

As the increase of eccentricity ratio, the changing of both areas is not much, however, the maximum values and the position of the positive pressure is greatly changed, e.g., 8.3 bar.s/m at 78° for the eccentricity ratio value of 0.2 compared to 1190 bar.s/m at 96° for the eccentricity ratio value of 0.8.

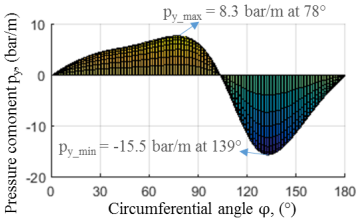

Figure a: Eccentricity ratio of 0.2

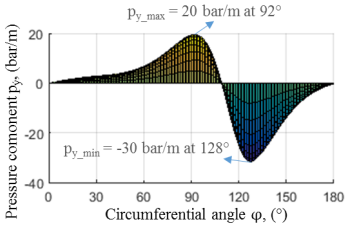

Figure b: Eccentricity ratio of 0.4

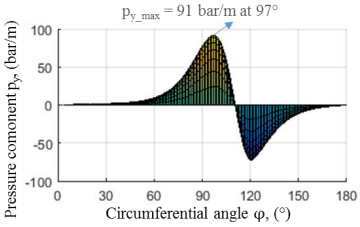

Figure c: Eccentricity ratio of 0.6

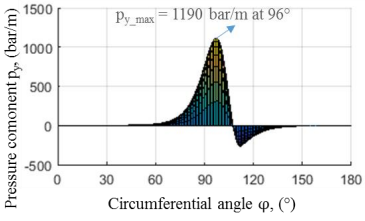

Figure d: Eccentricity ratio of 0.8

Figure 12: Effect of eccentricity on the 2D perturbing pressure distribution p_y at middle axial plane.

The effect of eccentricity on the perturbing pressure distribution p_x is shown in **Figure 13**. The pressure distribution is divided into two areas, e.g., the left area is the negative pressure and the positive pressure places at the right side. The area of positive and negative pressure is slightly changed regarding to the change of the eccentricity ratio. However, the maximum values as well as the position of the positive pressure are much dependent on eccentricity ratio, e.g., 34 bar.s/m at 132° for the eccentricity ratio of 0.2 compared to 680 bar.s/m at 105° for the eccentricity ratio of 0.8.

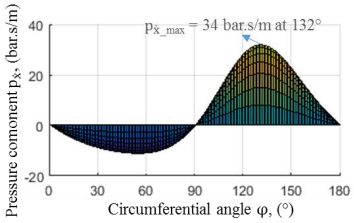

Figure a: Eccentricity ratio of 0.2

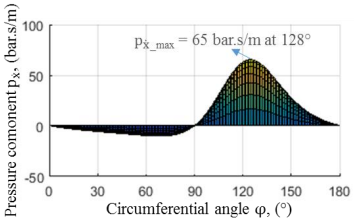

Figure b: Eccentricity ratio of 0.4

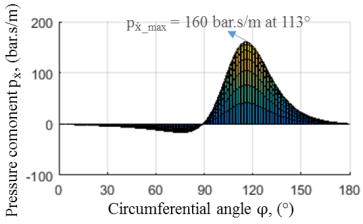

Figure c: Eccentricity ratio of 0.6

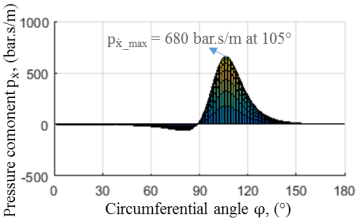

Figure d: Eccentricity ratio of 0.8

Figure 13: Effect of eccentricity on the 2D perturbing pressure distribution p_x˙ at middle axial plane.

Figure 14 shows the effect of eccentricity ratio on the perturbing pressure component $p_{\dot{y}}$.

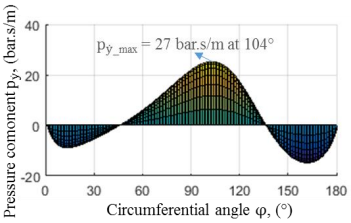

Figure a: Eccentricity ratio of 0.2

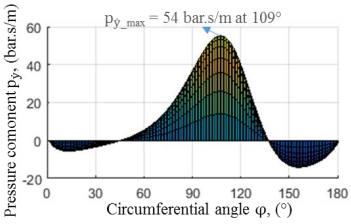

Figure b: Eccentricity ratio of 0.4

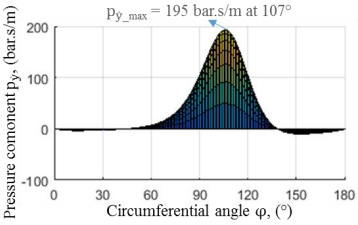

Figure c: Eccentricity ratio of 0.6

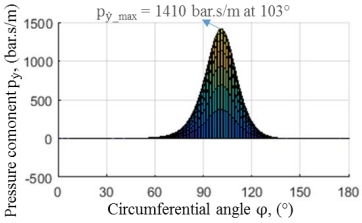

Figure d: Eccentricity ratio of 0.8

Figure 14: Effect of eccentricity on the 2D perturbing pressure distribution p_y˙ at middle axial plane.

3.3. Analysis of effect of eccentricity on dynamic force of oil film

The oil film produces the internal force or oil film force which against with the external force acting on the ring gear. In this study, the external or apply force is considered as a vertical force. The oil film force is dependent on the hydrodynamic pressure distribution and the eccentricity of the ring gear center. The oil film force contains two elements, i.e., the horizontal and vertical oil film force which are presented in **Figure 15** and **Figure 16**, respectively. The vertical oil film force increases with the increase of the eccentricity ratio. However, the changing of horizontal oil film force is nonlinear. The value of vertical force is much larger than the horizontal force. This means that the capacity of the oil film is mostly decided by the vertical force component. The details of calculation are presented in **Table 2**.

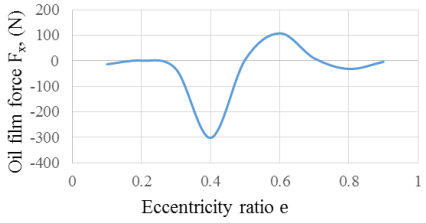

Figure 15: Effect of eccentricity on horizontal force F_x of oil film.

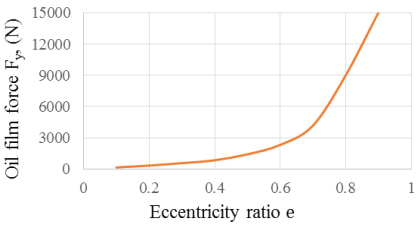

Figure 16: Effect of eccentricity on dynamic vertical force F_y of oil film.

Table 2: Dynamic oil film force, x102N

e	F_x	F_y	F
0.1	-0.013.6	1.60	1.60
0.2	0.0065	3.43	3.43
0.3	-0.33	5.75	5.76
0.4	-3.02	8.54	9.06
0.5	0.0049	142.12	142.12
0.6	1.07	232.78	232.78
0.7	9.50	418.76	418.87
0.8	-0.32	901.63	901.63
0.9	-0.04	1504.4	1504.40

3.4. Analysis of effect of geometric parameters on dynamic stiffness and damping coefficients

The direct and cross-coupling coefficients of the dynamic stiffness of oil lubrication film as functions of eccentricity ratio are presented in **Figure 17**. It shows that the dynamic oil film stiffness changes according to the change of the eccentricity ratio. These parameters are also called as dynamic oil-film force coefficients of the ring gear. Each dynamic stiffness coefficient have a wide range of values, dependent on the value of eccentricity ratio. For large value of eccentricity, these dynamic stiffness coefficients has large value, and vice versa. One can see from **Figure 17** that when the eccentricity ratio is larger than 0.7, two dynamic stiffness coefficients K_{yy} and K_{yx} reach to much larger values. Similarity, the direct and cross-coupling coefficients of the linearized oil film damping as functions of eccentricity ratio are also presented in **Figure 18**. Each dynamic damping coefficients have a wide range of values, dependent on the value of eccentricity ratio. For large values of eccentricity, these dynamic damping coefficients have large values, and vice versa. It is obviously to see from **Figure 18** that when the eccentricity ratio is larger than 0.7, the dynamic damping factor B_{yy} reaches to large value. The high values of stiffness coefficient component K_{yy} and damping coefficient component B_{yy} in the vertical direction will be better for stability of the ring gear at high value of eccentricity.

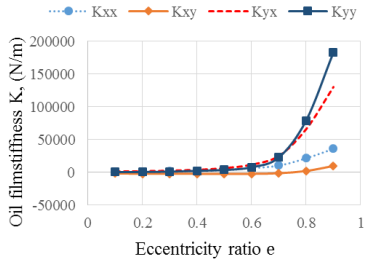

Figure 17: Dynamic stiffness coefficients as a function of eccentricity ratio.

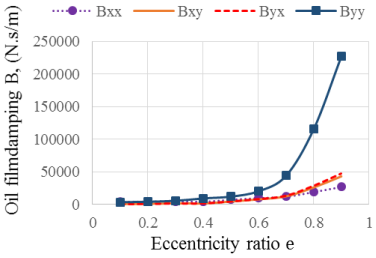

Figure 18: Dynamic damping coefficients as a function of eccentricity ratio.

The details of dynamic stiffness and damping coefficients are presented in Table 3 and Table 4, respectively.

Table 3: Dynamic stiffness coefficient, N/m

e	0.1	0.2	0.3	0.4	0.5	0.6	0.7	0.8	0.9
	$x10^3$				$x10^4$			$x10^5$	
Kxx	0.5	0.93	1.5	1.8	0.4	0.7	1.1	0.22	0.4
Kxy	-2	-2.2	- 2.2	- 2.4	-0.3	- 0.2	- 0.1	0.02	0.1
Kyx	1.8	2.1	2.9	4.3	0.7	1.2	2.5	0.67	1.3
Kyy	0.2	0.4	0.9	2.3	0.35	0.8	2.3	0.79	1.8

Table 4: Dynamic damping coefficient, N.s/m

e	0.1	0.2	0.3	0.4	0.5	0.6	0.7	0.8	0.9
	$x10^3$				$x10^4$			$x10^5$	
Bxx	4	4.5	4.8	4.2	0.7	0.98	1.2	0.19	0.23
Bxy	0.5	1.0	1.7	1.6	0.46	0.79	1.3	0.26	0.4
Byx	0.5	1.1	1.8	1.8	0.49	0.85	1.4	0.29	0.5
Byy	3.5	4.1	5.6	9.3	1.2	2.0	4.4	1.2	2.23

4. CONCLUSION AND OUTLOOK

Calculation of dynamic stiffness and damping coefficients is the background for analysis of dynamic behavior of internal gear motors and pumps. Based on the calculation results in this study, some following conclusions can be drawn

4.1 The dynamic pressure and perturbing pressure distribution can be calculated by the use of the infinitesimal perturbation method (IFP). These pressure component is much affected by the eccentricity ratio of the ring gear center.

4.2 Dynamic oil film force is changed according to the change of eccentricity. The capacity of the oil film is mostly dependent on the vertical force element.

4.3 Dynamic stiffness and damping coefficients of the oil lubrication film is much dependent on the values of eccentricity. For large values of eccentricity, the dynamic stiffness and damping factors has high values. Among these factors, the stiffness coefficient component Kyy and damping coefficient component Byy have largest values. It will be better for stability of the ring gear at high value of eccentricity in vertical direction.

ACKNOWLEDGEMENTS

This research is funded by Vietnam National Foundation for Science and Technology Development (NAFOSTED) under grant number 107.03-2019.17.

NOMENCLATURE

D, r	Diameter and radius of the ring gear (m)
Rh	Radius of inner housing (m)
L	The ring gear length (m)
e	Eccentricity of the ring gear center (μm)
c	Radial clearance (μm)
ε(e/c)	Relative eccentricity
ε_x,ε_y	Relative eccentricity in x and y axis
e_x,e_y	Eccentricity in axis x, y
h	Oil film thickness (μm)
K,B	Stiffness and damping coefficients
θ	Circumferential angle from the maximum-minimum film thickness line (°)
p	Hydrodynamic film pressure (Pa)
n	Rotating speed (rpm)
φ	Attitude angle (°)
μ	Dynamic viscosity of fluid (Pa.s)

REFERENCES

[1] B. J. Hamrock and S. R. Schmid, Fundamental of Fluid Film Lubrication Second Edition. 2004.

[2] Trong Hoa Pham, Analysis of the Ring Gear Orbit, Misalignment, and Stability Phenomenon of the Internal Gear Motors and Pumps, Shaker Verlag, 2018.

[3] Pham, T.H., Müller, L., Weber, J., Dynamically loaded the ring gear in the internal gear motor/pump: Mobility of solution, Journal of Mechanical Science and Technology, Vol. 32, No. 7, 2018.

[4] Trong Hoa Pham, Hybrid method to analysis the dynamic behavior of the ring gear for the internal gear motors and pumps, Journal of Mechanical Science and Technology, Vol. 33, No. 2, pp. 602-612 , 2019.

[5] Pham Hoa, Lutz Müller, Jürgen Weber, “Theoretical and Experimental Study of Whirl and Stability Phenomenon in Internal Gear Motor/Pump”, ASME/BATH FPMC Symposium on Fluid Power and Motion Control,Florida, USA, October 16-19, 2017 (doi: 10.1115/FPMC2017-4336).

[6] Trong Hoa Pham, Toan Thang Le, Wenming Cheng, Van Trung Vu, Anh Ngoc Nguyen, Thuy Chi Nguyen, “An approach to analyze the threshold stability of internal gear motors and pumps”, International Conference of Fluid Machinery and Automation Systems (ICFMAS2018), pp.622-629, October 27-28, Hanoi, Vietnam

[7] S. L. Qiu., “A Theoretical and Experimental on Dynamic Characteristics of Journal Bearings”, University of Wollongong, Dissertation 1995.

[8] A. . B. C. W. Stachowiak, Engineering Tribology fourth edition, vol. chapter 5. 2014.

peer reviewed

DAMPING STRATEGIES FOR ENERGY EFFICIENT PRESSURE CONTROLLERS OF VARIABLE DISPLACEMENT PUMPS

Florian Schoemacker*, Felix Fischer, Katharina Schmitz

Institute for Fluid Power Drives and Systems, RWTH Aachen University, Campus-Boulevard 30, 52074 Aachen
* Corresponding author: Tel.: +49 241 8047748; E-mail address: florian.schoemacker@ifas.rwth-aachen.de

ABSTRACT

In hydraulic-mechanically controlled variable displacement pumps, the actual pump controller produces additional power losses. Due to the low damping coefficients of all pump controller's components, hydraulic-mechanically pressure controlled pumps use to oscillate while adjusting the pressure level in the hydraulic system. In several state-of-the-art variable pump controllers, a damping orifice connects the control actuator's displacement chamber with the reservoir. This bypass dampens the movement of the control actuator but also leads to bypass losses during steady-state operation of the pump. A new concept for damping via feedback loops avoiding bypass losses is presented in this paper.

Keywords: Variable displacement pumps, Axial piston pumps, Pressure controller, Feedback loops

1. INTRODUCTION

The system "hydraulic variable displacement pump" consists of mainly two components. One is the pump itself with the cylinder block, pistons, valve plate and swash plate. The other part is the pump controller including the control valve and control actuators. The design of the pump controller depends on the function of the pump system, for example pressure compensation or flow control. In order to change the output flow rate, the pump controller acts on the swash plate via the control piston. This results in a change of the swash plate angle and the displacement volume, which determines the output flow.
During steady-state operation, the force of the control piston is in equilibrium with the torque load of the piston pressure forces and spring forces acting on the swash plate.
The scheme of a pressure controlled pump system is shown in **Figure 1**. For this study, the control piston is equipped with two pressurized areas. The smaller ring area is connected to the high pressure port of the pump. The opposing area is part of the control actuator's displacement chamber and applied with the control pressure, which is supplied by the pump controller.

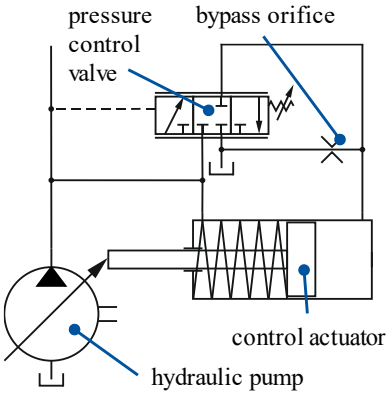

Figure 1: Pump system with hydraulic-mechanical pressure controller

In variable displacement pumps, the actual pump controller produces additional power losses. Due to the low damping coefficients of all the pump controller's components, pressure controlled pumps use to oscillate while adjusting the pressure level in the hydraulic system. In several state-of-the-art pump controllers, a damping orifice connects the control actuator's displacement chamber with the reservoir. This bypass dampens the movement of the control actuator, but also leads to bypass losses during steady-state operation of the pump.

The bypass-losses of the orifice have been measured in this study, see **Figure 2**. The typical control pressure yields to 70 bar. This value is valid for a control actuator with an area ratio of 1:4 and a system pressure level of 300 bar. At this operating point, a flow of 1.66 l/min occurs.

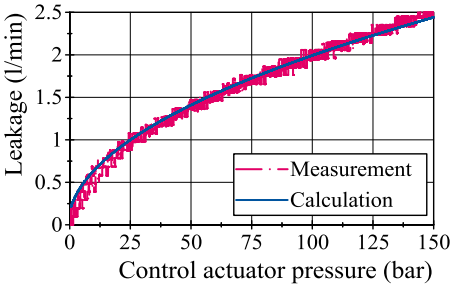

Figure 2: Characteristic curve of the flow via the bypass orifice

For controlling a pump pressure level of 300 bar, the power loss of the orifice results in 0.85 kW, see Eq. 1. The bypass losses are fed by the high pressure port of the pump.

$$P_{\mathrm{Loss}} = p_{\mathrm{HP}} \cdot Q_{\mathrm{Bypass}} = 0{,}85\ \mathrm{kW} \qquad (1)$$

These bypass losses occur continuously during the operation of the pump and are only influenced by the system pressure, which has an impact on the control actuator's pressure.

In addition to the loss of the bypass orifice, losses at the pressure control valve occur. The overall power consumption of the pump controller is shown in **Figure 3** as a percentage of the hydraulic output power, because the necessary volume flow is taken from the output flow rate of the pump. The pressure level is 300 bar and the maximum power output 35 kW.

The red line is the result of a measurement of a state-of-the-art pump controller [7]. The percentage is increased at lower swash plate angle, because the hydraulic output power is reduced but the power consumption of the pump controller do not vary.

Using an electro hydraulic pump controller the power consumption can be reduced by about 70 %. The goal of this research is to develop a pump controller without continuous bypass losses.

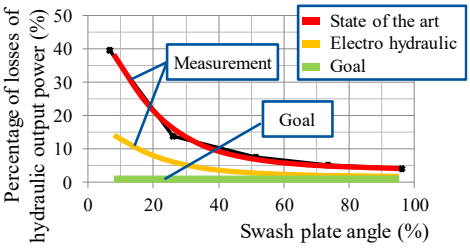

Figure 3: Power consumption of pump controllers as percentage of hydraulic output power

1.1. State of the art

Dreymüller [1] investigated the dynamic behaviour of hydraulic-mechanical pump controllers. The connection of the high pressure port to the ring area of the control actuator results in pressure pulsations. Dreymüller suggests that the pressure signal should be dampened before fed to the pressure control valve. Furthermore, Dreymüller shows the necessity of a system dampening of the pump controller, for example via the bypass orifice.

Murrenhoff [2] focused in his research on the control strategy for hydraulic motors. Motor controllers are able to control speed or torque output, but the architecture is similar to pump controllers. Murrenhoff showed that a controller can be dampened using a mechanical feedback loop.

Langen [3] compared hydraulic-mechanical to electrohydraulic pump controllers. For the electrohydraulic controller, the system pressure is measured electronically. The controller then forwards the control signal to an electrohydraulic valve, which determines the volume flow to the control actuator. Langen used this electronic system architecture to verify the function of the feedback controller described in this paper. Furthermore, Langen carried out a parameter study of the control actuator's geometry and found the optimum of the area ratio at 1:4.

For the simulation of the swash plate oscillations, a detailed model of the pressure built-up dynamics during commutation as well as a pump controller model is needed. Manring and Johnson [4] published a mathematical description of the model for a variable displacement pump. Manring [5] also studied the forces acting on the swash plate and their variation due to the odd number of pistons. For

the simulation of a controlled pump, Mandal et al. [6] developed a model of the pressure compensator for a variable displacement pump. The model was used for designing the pump controller according to the dynamics of the swash plate.

Lux [7] experimentally investigated the losses of pump controllers. He measured the flow rate needed for the pump controller during operation of the pump, showing an efficiency reduction of pumps in closed-loop control. The power loss is almost constant for all swash plate angles but differs with the pressure level.

The presented literature deals with the investigation of the dynamics and the power loss of pump controllers. As an improvement of state-of-the-art pump controllers, the authors propose an innovative pump controller, which uses its system architecture instead of the bypass orifice in order to dampen the control actuator.

2. NEW SYSTEM ARCHITECTURE FOR PUMP CONTROLLERS

The new concept is based on feedback loops within the pump controller. These feedbacks result in a systematic damping of the pump controller and avoid unnecessary bypass losses. The possible power saving is greater than it could be obtained with an optimization of pump's tribological contacts [7].

In order to dampen the pressure oscillation of a variable displacement pump, the pump's output flow rate needs to be fed back to the pressure controller, because the output flow is the rate of change for the pressure of the hydraulic system. This concept of damping is known from damped harmonic oscillators. The position of the control actuator is proportional to the pump's output flow rate. Therefore, feedback loops are used to signal the change of the actuator's position to the pressure control valve in order to create an additional closed loop control within the pressure control loop. The design of feedback loops, which use this intention, are shown in the following.

The current position of the actuator can be fed back mechanically to the valve using a spring. This concept has already been proposed by Murrenhoff [2] and experimentally validated.

However, this results in an error in steady-state operation. An additional damper, which moves relatively between the spring and the valve's spool, consumes the force with time and prevents an error in the closed-loop control. Therefore, the feedback loop acts as a derivative element with first-order lag.

A pump controller with this new system architecture is shown in **Figure 4**.

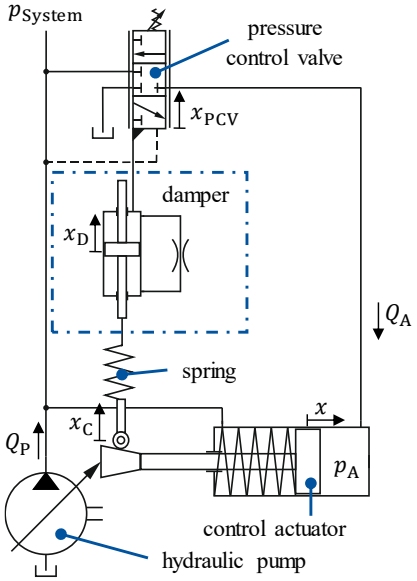

Figure 4: New concept with mechanical feedback of the control actuator's stroke

The function and the usability of systems built-up of derivative elements with first-order lag have been investigated by Luhmer [10] and Weingarten [11]. Their focus laid on the design of hydraulic circuits with this kind of function.

Applying their research, the same control scheme can be designed with hydraulic feedback in order to avoid a strict mechanical coupling between the control actuator and the valve's spool.

The hydraulic design of the concept is shown in **Figure 5**.

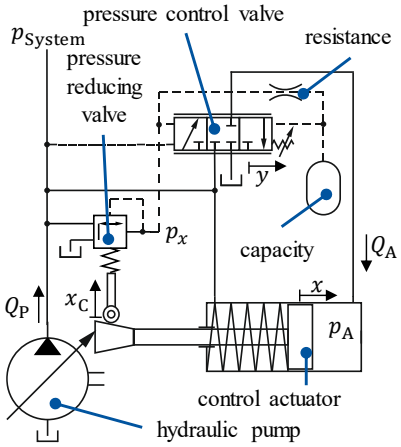

Figure 5: New concept with hydraulic feedback of the control actuator's stroke

The presented concepts are investigated via simulation. This simulation is made up of an already existing pump model, which provides the control forces by calculating the pressure build-up for all pistons and deriving the torque load of the swash plate, combined with the model of an actual pump controller. Furthermore, the feedback loops are included in the model. The simulation results state the dynamics of the control system and the power losses. These are compared to state of the art pump controllers.

3. GEOMETRY AND SIMULATION MODEL

In the following, the geometry of the pump and the controller are presented and the simulation model is described. For the analysis, a swash plate-type axial piston pump has been chosen as a variable displacement controlled pump. The pump controller type is a pressure compensator, which adjusts the output flow according to the hydraulic system's need in order to hold constant pressure. The pump's geometric data is derived from an axial piston pump with a power output of about 30 kW. **Figure 6** shows the assembly of the pump system and a sketch of the hydraulic system used for displacement control. Forces acting on the swash plate are displayed as well.

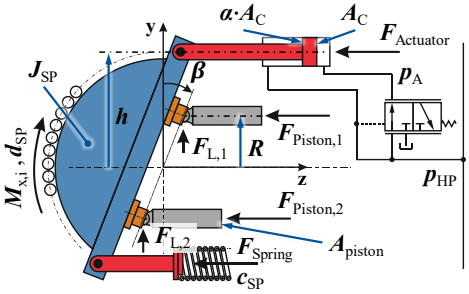

Figure 6: Pump system with pressure compensator [8]

The piston pressure forces act on the swash plate creating a periodically changing torque load. A spring provides the swash plate with an initial torque load for swiveling out, if the pump is in unpressurized condition. The torque load on the swash plate is balanced by the control actuator's force. The actuator is supplied by the pump controller, which changes the swash plate angle in control operation.

For the simulation of the pump controllers with additional feedback loops, a lumped parameter model is used within the simulation software DSHplus. The pump model consists of the piston assembly's mathematical description and its commutation to the high and low pressure kidney. The model is validated using the state of the art pressure controller.

The simulation model in DSHplus is shown in **Figure 7**.

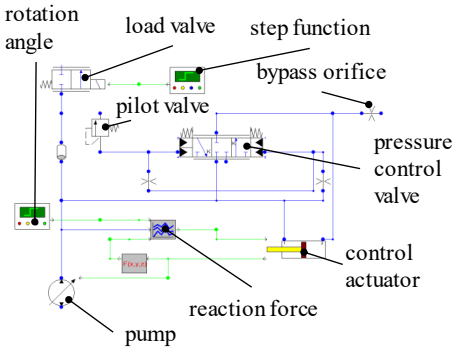

Figure 7: Model in DSHplus

The model contains the time behaviour of all components, which are necessary to simulate the dynamic response of the pump controller.

The control actuator is in equilibrium with the torque load on the swash plate. The torque load is

calculated using a complex model containing the pressure built up at each piston. The resulting forces are fed to the lumped parameter model using characteristic curves. The calculation is described in detail in chapter 3.1.

The characteristic curve of the valve within the pump controllers is obtained from the measurement of the volume flow via a real pump controller's valve.

Furthermore, the model needs to be completed with the new feedback loops. This description is presented in chapters 3.2 and 3.3.

3.1. Torque load

The simulation model is used as in [8]. In this model, the pressure built up of each piston of a nine piston pump according to its commutation with the valve plate is calculated. The commutation between piston chamber and valve plate opening is smoothed using silencing grooves. With the known pressure force of all pistons, the torque load of each piston and the resulting torque on the swash plate can be determined.

The mathematical calculation is based upon a Cartesian coordinate system, which is shown on **Figure 6**. The piston stroke of piston number i is given via Eq. 2.

$$s_i = R \cdot \tan(\beta) \cdot \sin(\varphi_i) \tag{2}$$

The torque load of each piston can be calculated using Eq. 3.

$$M_{x,i} = R \cdot (1 + \tan^2(\beta)) \cdot A_{\text{piston}} \cdot p_{i(\varphi_i)} \cdot \sin(\varphi_i) \tag{3}$$

The sum of all the piston's torque load is shown in **Figure 8** for one revolution of the pump.

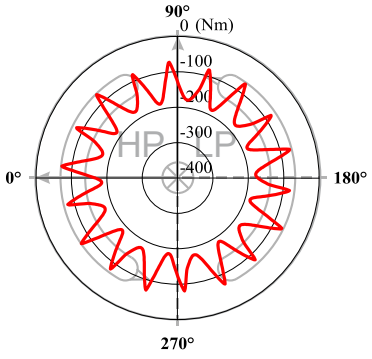

Figure 8: Torque load for one revolution [8]

In addition to the piston pressure forces, the spring and actuator forces act on the swash plate. Finally, the angle and angular velocity of the swash plate are determined using Euler's laws of motion (Eq. 4).

$$J_{SP} \cdot \ddot{\beta} + d_{SP} \cdot \dot{\beta} + c_{SP} \cdot \beta = \sum M_{x,i} + h \cdot A_C \cdot (\alpha \cdot p_{HP} - p_A) \tag{4}$$

The resulting force acting on the control actuator is calculated for different pressure, speeds and swash plate angles. The values are saved in characteristic curves and then fed to the lumped parameter model.

3.2. Mechanical feedback

For the mechanical feedback, a spring and a damper are installed between the control actuator and the pump controller. The components of the feedback loop are shown in **Figure 9**.

An additional spring c_{HD} assures that the pin is always in contact with the control actuator. The two springs c_{MF} allow the mechanical feedback to work in both directions.

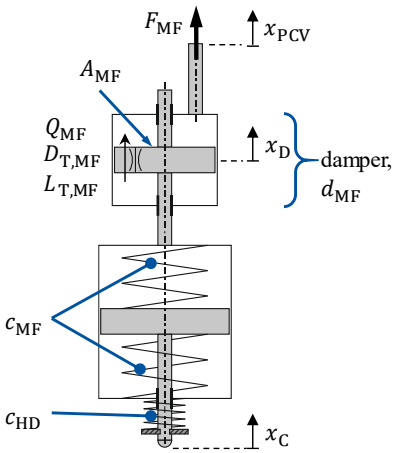

Figure 9: Mechanical feedback composed of spring and damper

The force feedback can be calculated using a mathematical description for the components. The equation of the spring damper with first order lag is given below. For the simulation, components with geometry parameters are implemented to show the impact of pressure built up in the damper. The variables x_C, x_D and x_{PCV} are absolute values.

$$F_{MF} = c_{MF} \cdot (x_C - x_D) \quad (5)$$

$$F_{MF} = d_{MF} \cdot (\dot{x}_D - \dot{x}_{PCV}) \quad (6)$$

Deriving Eq. 5 and combining the results with Eq. 6 leads to the differential equation for the spring-damper system in Eq. 7.

$$\frac{d_{MF}}{c_{MF}} \cdot \dot{F}_{MF} + F_{MF} = d_{MF} \cdot (\dot{x}_C - \dot{x}_{PCV}) \quad (7)$$

The damper coefficient determines the time behaviour, whereas the spring coefficient gives the value of the momentum. The damper coefficient can be calculated using the flow rate equilibrium of the throttle and the cylinder.

$$Q_{MF} = A_{MF} \cdot (\dot{x}_D - \dot{x}_{PCV}) = \frac{\pi \cdot D_{T,MF}^4}{128 \cdot \eta \cdot l_{T,MF}} \cdot \frac{F_{MF}}{A_{MF}}$$

$$\Rightarrow d_{MF} = \frac{F_{MF}}{\dot{x}_D - \dot{x}_{PCV}} = \frac{\pi \cdot D_{T,MF}^4}{128 \cdot \eta \cdot L_{T,MF} \cdot A_{MF}^2} \quad (8)$$

The damping coefficient is independent from the velocity. Previous simulations have shown that the flow rate of the damper cylinder is too small to use an orifice instead of a throttle for the resistance. The diameter of the orifice would need to be smaller than 0.2 mm, which is inconvenient for manufacturing.

3.3. Hydraulic feedback

The hydraulic feedback uses a pressure signal proportional to the control actuator's stroke.

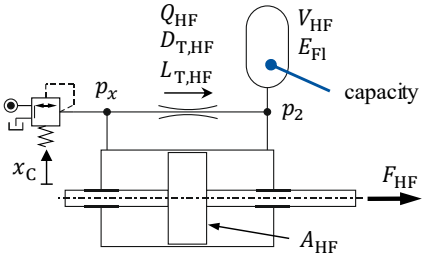

Figure 10: Hydraulic feedback composed of pressure valve

Pressure p_x is proportional to the control actuator's stroke. The time behaviour of the resulting force of the pressure difference due to the delayed pressure built up can be calculated using the following equation.

$$\dot{F}_{HF} = A_{HF} \cdot (\dot{p}_x - \dot{p}_2) = A_{HF} \cdot \left(K_{PRV} \cdot \dot{x}_C - \frac{E_{Fl}}{V_{HF}} \cdot \left(\frac{\pi \cdot D_{T,HF}^4}{128 \cdot \eta \cdot L_{T,HF}} \cdot \frac{F_{HF}}{A_{HF}} \right) \right) \quad (9)$$

This leads to the following equation.

$$\frac{V_{HF} \cdot 128 \cdot \eta \cdot L_{T,HF}}{E_{Fl} \cdot \pi \cdot D_{T,HF}^4} \cdot \dot{F}_{HF} + F_{HF} = A_{HF} \cdot K_{PRV} \cdot \frac{V_{HF} \cdot 128 \cdot \eta \cdot L_{T,HF}}{E_{Fl} \cdot \pi \cdot D_{T,HF}^4} \cdot \dot{x}_C \quad (10)$$

The time behaviour depends on the volume of the accumulator and the geometry of the throttle. As said for the mechanical feedback, an orifice cannot be used for the resistance, because of the marginal flow rate.

4. CRITERIA FOR COMPARISON

In order to compare the new pump controllers to the state of the art, criteria for the dynamics and the power loss are defined.

4.1. Dynamics

For the dynamic response, a rapid change in the volume flow demand is simulated using a step function. From the results, the time delay for reaching a certain pressure level can be compared. The dynamic response is shown in **Figure 11**.

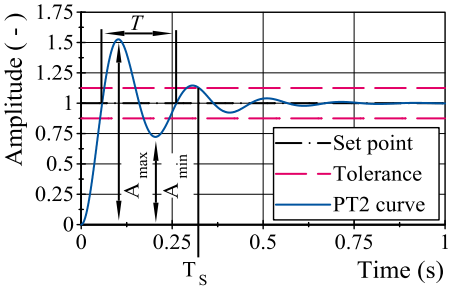

Figure 11: Dynamic response to a step function

Figure 11 displays several resulting values describing the dynamics of the oscillation. A_{max} and A_{min} are the maximum and minimum amplitude and T is the period of the oscillation.

The curve reaches a tolerance band, which is deliberately defined. The settling time T_S is the point, at which the curve does not leave the tolerance band again [12]. For the discussion of the simulation results, the value of T_S is used.

4.2. Power loss

The power loss for each pressure controller is calculated in the simulation. This is the entire

volume flow taken from the output flow and going into the pump controller.

The mechanical feedback loop increases the load of the control actuator due to force feedback and the friction within the damper. Therefore, the control pressure increases, which leads to lower volume flow into the actuator and slower response of the pump controller. Thus, by the chosen power loss definition, friction in the damper is not accounted as a power loss but a decrease in dynamics.

The hydraulic feedback loop requires additional hydraulic power, which is added to the power loss of the pump controller.

5. RESULTS

The two principles for the feedback are compared to the state of the art. In order to do so, the state of the art pump controller is validated at first.

5.1. Validation of the state of the art pressure controller

The response to a step from 0.5 to 0.75 of the maximum flow rate is shown in **Figure 12** for the simulation and the measurement.

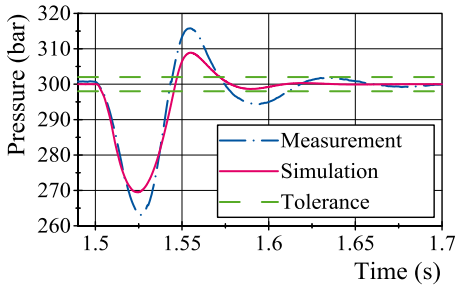

Figure 12: Dynamic response of the state of the art pump controller

The period of the two results match, but the amplitude of the measurement is higher than of the simulation results. This means, that the damping within the simulation model is higher than in reality. Concluding, the simulation model is sufficiently validated and can be used to calculate the pressure controller with additional feedback loops.

The continuous power loss is about 1.18 kW. This includes losses of the bypass orifice as well as the loss of the pressure control valve. For the comparison of the dynamics of the pump controller, the value of settling time T_S of the state-of –the-art controller is set to 100 %.

5.2. Mechanical feedback

The dynamic response of the mechanical feedback is shown in **Figure 13**. The curves allow a comparison between the mechanical feedback and the state of the art pump controller, and an ideal first order lag feedback. This shows the influence of disturbances, as e.g. inertia and friction in the mechanical parts.

The ideal DT1 curve represents the feedback via a DT1 element. The parameters have been obtained via an optimization towards the smallest error of the curve compared to the set point. These parameters do not necessarily represent the very ideal solution according the damping.

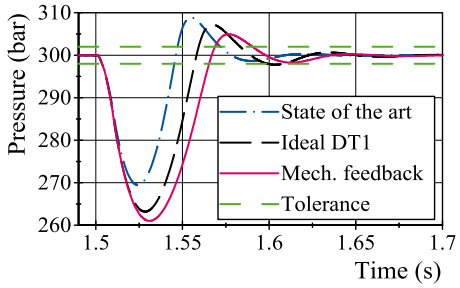

Figure 13: Dynamic response of the mechanical feedback loop

For the dynamics, the response of the mechanical feedback to the step function is a little bit slower and so the pressure drop of the system is larger. The delay is quantified by the settling time T_S, which is 25 % longer compared to the state-of-the-art pump controller.

The power loss of the pump controller with mechanical feedback is reduced to 0.64 kW. This is only 55 % of the power loss of the state-of-the-art pump controller. The reduction results from avoiding the losses of the bypass valve. But the volume loss of the pressure control valve rises due to an altered operation point. Within the state-of-the-art pump controller, the bypass leakage has to pass the valve first. Because this volume flow is avoided, the opening of the valve during steady-state operation is changed.

5.3. Hydraulic feedback

The dynamic response of the hydraulic feedback is shown in **Figure 14**. The hydraulic feedback can also be compared to the curve of the ideal DT1 feedback, which is the same as in **Figure 13**.

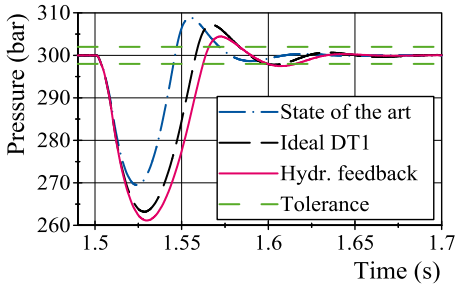

Figure 14: Dynamic response of the hydraulic feedback loop

The pump controller with hydraulic feedback is able to follow the curve of the DT1 feedback slightly better. The dynamic response is better than of the mechanical feedback with a value of the settling time T_S, which is only 15 % longer compared to the state-of-the-art pump controller.

For the hydraulic feedback, the necessary flow rate to pressurize the feedback loop is taken from the high-pressure port as well. Therefore, an additional power loss occurs. The power loss of the hydraulic feedback is reduced to 0.64 kW to the same value as of the mechanical feedback. Again, this is 55 % of the state-of-the-art pump controller's power loss.

6. CONCLUSION AND OUTLOOK

Several state-of-the-art hydraulic-mechanical pump pressure controllers are designed with a bypass orifice for the purpose of damping the pump controller. This leads to continuous bypass-losses, which are within the range of 1 kW and which are not ecological and economical reasonable anymore. Depending on the swash plate angle and the current hydraulic output power, the bypass losses are in the range of 3 to 40 % of the hydraulic output power.

Using a pump controller with an additional feedback loop as a damping strategy reduces the power loss of the entire system, consisting of pump and controller. For this purpose, concepts of pump controllers using mechanical and hydraulic feedback loops have been developed.

Simulation of the two concepts show that damping via this kind of systematic approach is possible. Compared to the state-of-the-art pump controller, the bypass leakage can be avoided. The dynamic response of the concepts is slightly decreased. Comparing the power loss and the dynamics, the pump controller with hydraulic feedback represents a reasonable compromise.

The benefit using this new system architecture is cost reduction for operating the pump. This is an advantage for both, the pump manufacturer and the costumer. Furthermore, the efficiency of the entire pump system is closer to the efficiency of the actual displacement part due to avoiding unnecessary bypass-losses.

6.1. Outlook

Within the scope of the research project, an experimental validation of the two concepts will also be performed. This will be done using a test bench, which allows to apply the same step function as a load upon the system. Furthermore, the pump controller will be investigated concerning the aspect of robustness against temperature change or particles.

ACKNOWLEDGEMENT

The IGF research project 19789 N / 1 of the research association Forschungskuratorium Maschinenbau e. V. – FKM, Lyoner Straße 18, 60528 Frankfurt am Main was supported from the budget of the Federal Ministry of Economic Affairs through the AiF within the scope of a program to support industrial community research and development (IGF) based on a decision of the German Bundestag.

NOMENCLATURE

A_{C}	Area of control actuator
A_{HF}	Area of cylinder in hydraulic feedback
A_{MF}	Area of damper cylinder
A_{piston}	Area of piston
c_{MF}	Spring coefficient of mechanical feedback
c_{SP}	Spring coefficient of swash plate
$D_{\mathrm{T,MF}}$	Diameter of throttle in mechanical feedback
$D_{\mathrm{T,HF}}$	Diameter of throttle in hydraulic feedback
d_{MF}	Damping coefficient of mechanical feedback
d_{SP}	Damping coefficient of swash plate
E_{Fl}	Bulk modulus
F_{HF}	Force of hydraulic feedback
F_{MF}	Force of mechanical feedback
h	Level arm
J_{SP}	Inertia of swash plate
K_{PCV}	Coefficient of pressure reducing valve
$L_{\mathrm{T,MF}}$	Length of throttle in mechanical feedback
$L_{\mathrm{T,HF}}$	Length of throttle in hydraulic feedback
$M_{x,i}$	Swash plate torque load of piston *i*
P_{Loss}	Power loss
p_{HP}	Pressure at high pressure port
p_A	Pressure of control actuator
p_i	Piston pressure of piston *i*
Q_{Bypass}	Flow rate of bypass orifice
Q_{MF}	Flow rate of damper cylinder
R	Pitch radius
s_i	Piston stroke of piston *i*
$\mathrm{T_S}$	Settling time
V_{HF}	Volume of cylinder in hydraulic feedback
x_{C}	Stroke of control actuator
x_{D}	Stroke of damper in mechanical feedback
x_{PCV}	Stroke of pressure control valve
α	Area ratio of control actuator
α_{D}	Flow rate coefficient
β	Swash plate angle
η	Dynamic viscosity of the oil
ρ	Density
φ_i	Rotational angle of piston *i*

REFERENCES

[1] Dreymüller J (1975) Hydraulisch-mechanische Druckregelung an verstellbaren Axialkolbenpumpen. Dissertation, RWTH Aachen University

[2] Murrenhoff H (1983) Regelung von Verdrängereinheiten am Konstant-Drucknetz. Dissertation, RWTH Aachen University

[3] Langen A (1986) Experimentelle und analytische Untersuchungen an vorgesteuerten hydraulisch-mechanischen und elektrohydraulischen Pumpenregelungen. Dissertation, RWTH Aachen University

[4] Manring ND, Johnson RE (1996) Modeling and Designing a Variable-Displacement Open-Loop Pump. Journal of Dynamic Systems, Measurement, and Control 118(2): 267-271

[5] Manring ND (1999) The Control and Containment Forces on the Swash Plate of an Axial Piston Pump. Journal of Dynamic Systems, Measurement, and Control 121(4): 599-605

[6] Mandal NP et al (2013) Pressure Compensator Design for a Swash Plate Axial Piston Pump. Journal of Dynamic Systems, Measurement, and Control 136(2)

[7] Lux J, Murrenhoff H (2016) Experimental loss analysis of displacement controlled pumps. In: 10th International Fluid Power Conference Proceedings, Dresden, 8-10 March 2016

[8] Schoemacker F, Murrenhoff H (2019) Interaction between Swash Plate Movement and Commutation in Axial Piston Machines. JFPS Journal of Fluid Power Systems 11(3): 49-54

[9] Murrenhoff H (2012) Servohydraulik- Geregelte hydraulische Antriebe. Shaker Verlag, Aachen

[10] Luhmer H (1981) Aufbau hydraulischer Netzwerke mit differenzierendem Verhalten und ihr Einsatz zur Dämpfung hydrostatischer Antriebe. Dissertation, RWTH Aachen University

[11] Weingarten F (1983) Aufbau hydraulischer Zeitglieder und ihr Einsatz im Signalzweig hydraulisch-mechanischer Regelungen. Dissertation, RWTH Aachen University

[12] Keviczky L et. al (2019) Control Engineering. Springer Nature Singapore Pte Ltd., Singapore

peer reviewed

OPTIMIZATION OF THE TRIBOLOGICAL CONTACT OF VALVE PLATE AND CYLINDER BLOCK WITHIN AXIAL PISTON MACHINES

Stefan Geffroy[1]*, Niklas Bauer[1], Tobias Mielke[1], Stephan Wegner[2] , Stefan Gels[3], Hubertus Murrenhoff[1], Katharina Schmitz[1]

[1]*Institut for Fluid Power Drives and Systems, RWTH Aachen University, Campus-Boulevard 30, 52074 Aachen*
[2]*Stackpole Powertrain International GmbH, Campus-Boulevard 30, 52074 Aachen*
[3]*P&G Hydraulische Antriebstechnik GmbH, Nettestraße 39, 58762 Altena*
* Corresponding author: Tel.: +49 241 80 47741; E-mail address: Stefan.Geffroy@ifas.rwth-aachen.de

ABSTRACT

In this paper, a simulation study is carried out for the development of concepts to optimize the tribological contact of valve plate and cylinder block in an axial piston machine in swash plate design. The valve plate/cylinder block contact is one of the three essential tribological contacts in axial piston machines. In a research project at the Institute for Fluid Power Drives and Systems (ifas), this contact is investigated by a specifically designed simulation tool. In addition, a test rig exists for the experimental investigation. With the results of simulation and experiment, it was shown before that the cylinder block is tilting to the high pressure side. Due to this movement, the gap height is not constant. In the area of minimum gap height, not only the fluid friction, but also the danger of solid body friction increases. Because of the higher friction losses in the area of minimum gap height, the temperature increase reduces the lifetime of the leaded coatings. In this paper, the results of the measurements as well as the simulation model are briefly summarized. It is followed by a simulation study of different possibilities to raise the gap height. Based on this pre-study, a first concept for the optimization of the tribological contact valve plate/cylinder block is presented and its applicability is discussed.

Keywords: Axial piston machine, simulation, unleaded coatings, temperatur hot-spot

1. INTRODUCTION

Axial piston machines are the most widely used type of hydraulic displacement machines and they are characterized by their high reliability and efficiency. **Figure 1** shows an axial piston machine in swash plate design and its three essential tribological contacts piston/slipper, piston/bushing and valve plate/cylinder block [1]. This paper focuses on the contact valve plate/cylinder block. To prevent leakage from the high to the low pressure side through the gap between valve plate and cylinder block, it is necessary to exert a force which presses the cylinder block against the valve plate. If this force is too low, the gap height between the components increases, causing additional leakage and thus a decrease in volumetric efficiency. If the force is too high, the gap height decreases which leads to unlubricated contact of the surface causing additional wear and decrease in mechanical/hydraulic efficiency. Therefore, it is important to design the components and parameters in such a manner that a thin and evenly distributed oil film over the whole contact area is ensured.

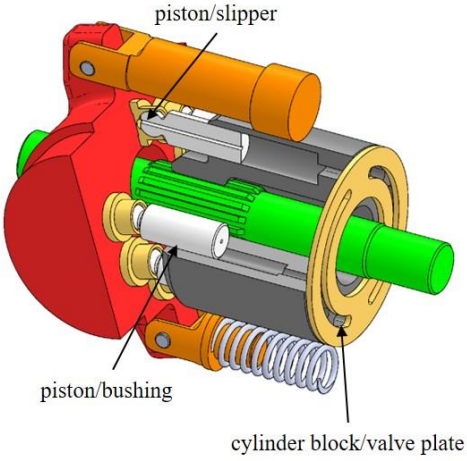

Figure 1: Three essential tribological contacts in axial piston machines [2]

Currently, a hard/soft pairing is used for the contact of cylinder block and valve plate. One option to realize such pairing is that the valve plate is made of steel while the surface of the cylinder block is coated with a brass alloy. A different option is that the valve plate is coated or made out of a brass alloy. This combination allows a bedding-in process, it is insensitive to manufacturing tolerances and generally leads to low wear and acceptable friction in case of direct contact of the surfaces. However, the use of leaded alloys causes disadvantages, including the occurrence of temperature-related cracks, fluid dependent wear and adhesion behaviour as well as material incompatibilities. In the EU, the use of the toxic heavy metal lead is strongly regulated [3].

Currently there are two approaches for the substitution of leaded alloys. First, an alternative unleaded material with similar properties can be developed, as shown in [4]. A second alternative is to realize a hard/hard pairing by the use of unleaded coatings or steel to steel. A simulation based pre-study as well as a first concept for the realization of these alternatives are presented in this paper.

2. SIMULATION MODEL

For a detailed investigation of the tribological contact valve plate/cylinder block a simulation model was built up at ifas. This simulation model is further development of a simulation model for the piston/bushing contact [5]. In [6], its development is described in detail and is only shortly presented in this paper.

The simulation tool was developed with the aim to compare several geometries at different operating points with acceptable computation time and sufficient result quality. To reach this goal, the simulation tool focuses on the following physical effects [5]:

- Hydrostatic and hydrodynamic pressure build up using the Reynolds equation
- Force and torque equilibrium on the cylinder block
- Squeeze film effect, viscous friction, microscopic part movement resulting from the first two points
- Macroscopic part movement calculated in an analytic way
- Simple contact and part deformation model

The finite volume method is used to solve the Reynolds equation. To calculate the gap height and the cylinder block movement, a linear system of equations coming from mass and momentum balances is set up and linked to the Reynolds equation. With the boundary conditions from the geometry and the known high and low pressure areas, the unknown variables and the number of equations are well balanced and the system can be solved numerically.

In the simulation model a simple method is used to calculate the solid friction. The gap height is compared to the reference gap height, which comes from the surface roughness. With it, the solid friction is calculated and takes place as a contact pressure in the Reynolds equation. **Figure 2** shows the schema of the simulation model.

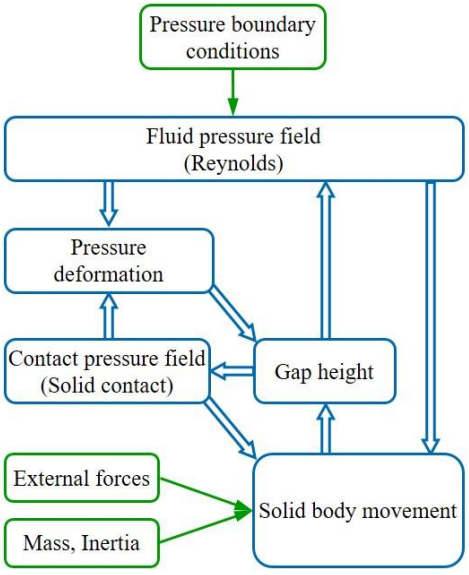

Figure 2: Schema of simulation model

3. MINIMAL GAP HEIGHT

For the validation of the simulation's results, a test rig was developed at ifas and is described in detail in [7]. The valve plate is installed to a hydrostatic measure of the friction torque with a force sensor. Radial displacement sensors measure the cylinder block movement while an axial sensor measures the gap height between valve plate and cylinder block. With these data, the movement of the cylinder block can be calculated. **Figure 3** side view of the test configuration.

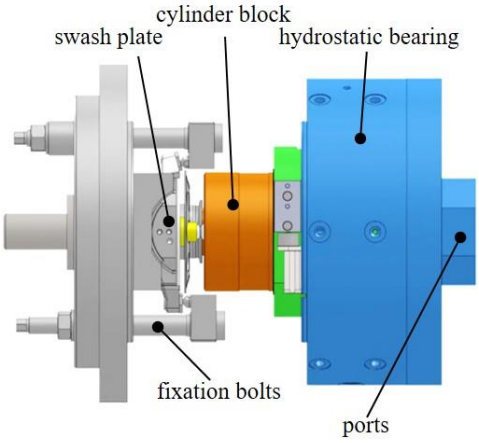

Figure 3: Test rig configuration

The test pump is a commercial pump with nine pistons and a displacement of 140 cm³. For the comparison of the experimental results with the simulated ones, the external forces and torques of the test pump were identified and implemented in the simulation tool.

In the simulation model Newton's law is used to calculate the cylinder block's movement. All external forces (mainly defined by the pressure within the cylinders), the fluid film forces (resulting from the pressure field calculated by the Reynolds equation) and the forces resulting from solid contact are summarized. Therefore, the gap height calculation represents the implementation of a fluid-structure interaction. [8]

To transfer the calculated movement of the cylinder block to the surface, two points are used. These two points lie on the main rotational axis of the cylinder block. The position of the two points are projected on a two dimensional coordinate system. **Figure 4** shows this method and the two points, which are used for the simulation. The cylinder block's sphere center (C) is given by the spherical surface. The spline shaft center (S) lies on the main rotational axis of the cylinder block.

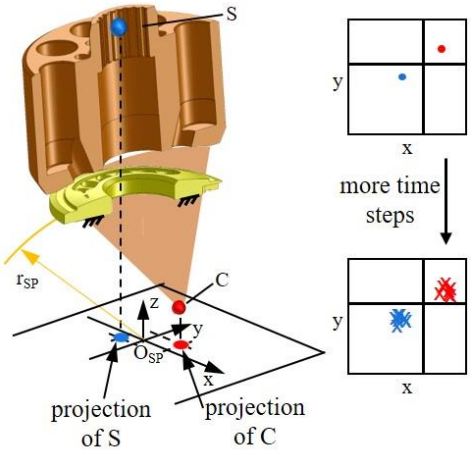

Figure 4: Projection of the cylinder block's movement

The gap height in axial piston machines is equal to the distance between the surfaces of the cylinder block and valve plate. The movement of the cylinder block defines the distance between the surfaces when assuming a stationary valve plate. For the investigation of the gap height distribution, the full movement in all degrees of freedom has to be considered. The location of the minimum and maximum gap height are of great importance for the understanding of friction, wear and contact pressure within the contact. Both, experimental results and those from the simulation show that the cylinder block performs a sliding movement over the valve plate's surface and tilts to the high pressure side. **Figure 5** shows the simulation of pressure and gap height distribution for the two most relevant scenarios, in which five or four pistons are pressurized with high pressure. Other studies also show this effect. [9] Due to the tilt angle, the minimum gap height lies on the high pressure side between 130° and 150°. The direction of rotation (DOR) of the cylinder block is clockwise.

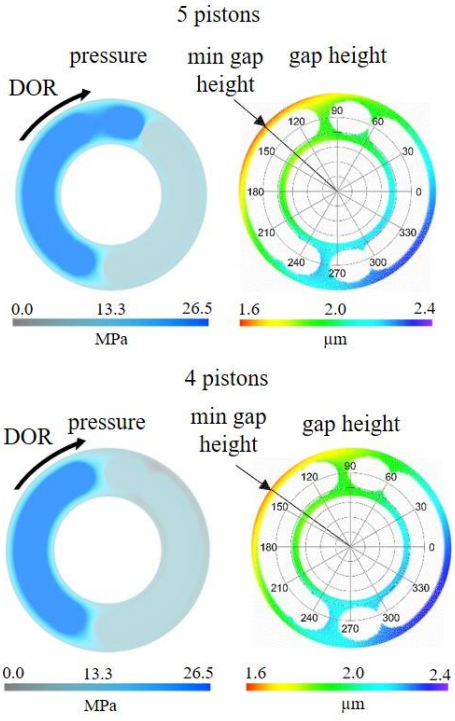

Figure 5: Minimum gap height position [8]

The measurement results of the experimental investigation are displayed in **Figure 6**. It shows the distribution frequency of the minimum gap height. The size of the red highlighted areas represents the occurrence frequency of the minimum gap height at the particular angular position for one revolution.

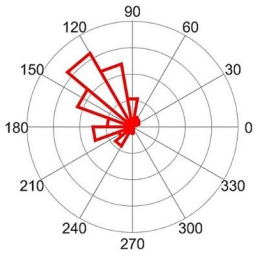

Figure 6: Frequency of minimum gap height [6]

The range 90° – 240° is much higher as those from the simulation, but on average the minimum gap height is located at 130°.

There are not only disadvantages coming from this preferred position of the cylinder block. The load situation is highly inconstant due to the changing number of pistons on the high and the low pressure side. For the same reason the number of cylinders filled with fluid is also changing. Due to this fact, the cylinder block is very imbalanced. The first advantage of the preferred position of the cylinder block and its rapid movement towards this position is that it probably improves the smooth running of the axial piston machine by reducing the imbalance. The second advantage of the tilted cylinder block is lower leakage on the high pressure side. With the gap width b, the gap height h, the gap length l, the dynamic viscosity η and the pressure difference Δp, the volume flow Q through a small gap results from Equation 1 [2].

$$Q = \frac{b \cdot h^3}{12 \cdot \eta \cdot l} \cdot \Delta p \qquad (1)$$

This equation shows the high influence of the gap height on the leakage and therefore on the volumetric efficiency of the machine. Because of the much higher pressure difference between the high pressure side and the housing pressure in comparison to the pressure difference on the low pressure side, there is a positive effect of the tilting.

These two advantages are countered by various disadvantages, which will be examined in further detail below. The tilting of the cylinder block reduces the already low gap height between valve plate and cylinder block. This increases the risk that the gap height becomes smaller than critical gap height and solid friction occurs. The resulting wear reduces the lifetime and efficiency of the axial piston machine or, in the worst case, can lead to immediate failure. In addition, the reduced gap height increases the fluid flow velocity as well as the shear rates. Due to this, the fluid load increases. The previously explained positive effect that the leakage decreases also includes a disadvantage. The reduced volume flow over the sealing gap reduces the heat dissipation. Therefore, in addition to the danger of solid friction a danger of local temperature hot-spots exists. This effect is also described in [10, 11]. Local high temperature ranges also limit the selection of possible alloys and coatings for the substitution of lead. Due to the risk of solid friction, it is not possible to use a hard/hard pairing in this tribological contact. Therefore, this paper presents a simulation study for the development of concepts to reduce the tilting of the cylinder block.

4. CONCEPT PRE-STUDY

For the reduction of the cylinder block's tilt angle the torque balance has to be influenced by additional created torques. Two basic concepts can be used for it. The first concept is to add one or more forces in z direction. The second is to add those forces in radial direction. These concepts can be extended by the possibility that these forces are stationary or synchronized with the movement of the cylinder block. This allows a static torque to be created to reduce the tilting more or less constantly. On the other hand, a dynamic torque can be created, which imposes an additional imbalance on the cylinder block. This could avoid or at least reduce a fixed temperature hotspot. In this simulation study, these four concepts are considered separately to investigate the influence on the main parameters. The parameter variation and the results of the study are presented and discussed below. The pump geometry used in this simulation is taken from the test pump. **Figure 7** shows the used cylinder block and valve plate. The geometrical data can be found in **Table 1**.

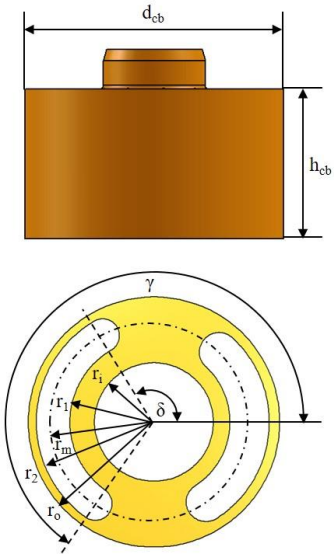

Figure 7: Cylinder block and valve plate

Table 1: Geometrical data

Parameter	Value
d_{cb}	97.2 mm
h_{cb}	80 mm
r_1	29.45 mm
r_2	44.55 mm
r_i	23 mm
r_m	37 mm
r_o	48.6 mm
γ	225°
δ	120°

4.1. Static force z-directional

The first option to create a counter torque against the tilting of the cylinder block is to add a force in positive z direction and to place this force around the area of minimum gap height. For the investigation of this concept, the three main parameters are the value of the force and the position described by the angle and radius. The force is variated in the range from 625 N to 2500 N. These values are equivalent to a pressurized surface from 25 mm² to 100 mm² at 25 MPa on high pressure side. The angle is varied around the area of the minimum gap height between 120° to 150° while radius is varied in the range from 29.45 mm to 44.55 mm due to the high pressure kidney's geometry of the valve plate. **Table 2** shows the parameter variation.

Table 2: Parameter variation

Fore [N]	Eq. surface (25 MPa) [mm²]	Angle [°]	Radius [mm]
625	25	120	29.45
1250	50	135	37
1875	75	150	44.55
2500	100		

24 configurations have been simulated. The relative angle change of the tilting is used here as a comparative value. The tilting can be calculated with the gap height difference and the cylinder block's diameter by the following equation.

$$\alpha = \sin^{-1} \frac{\Delta h}{d_{CB}/_2} \quad (2)$$

The relative angle change α_{rel} can be calculated with Equation 3. α_{new} is the tilting with the additional forces while $\alpha_{previous}$ is the tilting in the basic configuration.

$$\alpha_{rel}[\%] = \left(\frac{\alpha_{new}}{\alpha_{previous}} - 1\right) \cdot 100\% \quad (3)$$

Figure 8 shows the relative change of the tilt angle for the parameter variations. An additional force in negative z-direction with the same value was added, so only the torque works against tilting and the cylinder block is not lifted.

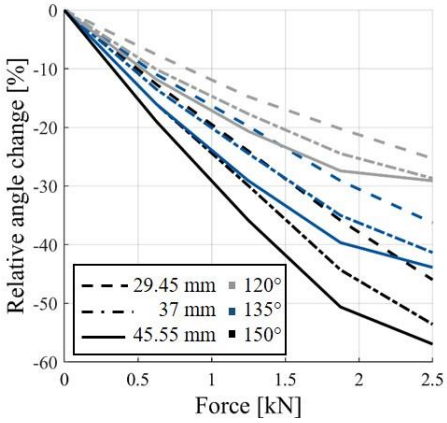

Figure 8: Relative angle change for static force in z direction

The simulation results show a major effect against the tilting for this concept. Even through the greatest effect is for the forces with an angle of 150°, the minimum gap height is at angle of 130°.

4.2. Dynamic force z-directional

By synchronising one or more additional added forces with the rotation of the cylinder block an additional imbalance results. The number of the added forces determines the frequency of this imbalance. These forces can be realized by pressurized surfaces on the cylinder block, which has an additional positive effect. The value of these forces depends on the rotational angle. The high pressure results in a high force and with it a high torque against the minimum gap height and tilt angle. The added surface has nearly no influence when it is not on the high pressure side. In this concept, the value of the added forces is varied as well as the radius. The parameter variation is concluded in **Table 3**.

Table 3: Parameter variation

Force [N]	Eq. surface (25 MPa) [mm²]	Radius [mm]
250	10	29.45
500	20	37
750	30	44.55
1000	40	
1250	50	

There are 15 configurations resulting from this parameter variation. The relative change of gap height is used here as a comparative value. Because the added force is not constant, no counterforce was implemented. Due to this, the force lifts up the cylinder block while the resulting moment works against the tilting. Both effects influence the gap height. The relative change of gap height h_{rel} results from Equation 4. h_{new} is the gap height with the additional forces while $h_{previous}$ is the gap height in the basic configuration.

$$h_{rel}[\%] = \left(\frac{h_{new}}{h_{previous}} - 1\right) \cdot 100\% \quad (4)$$

The simulation results are displayed in **Figure 9.**

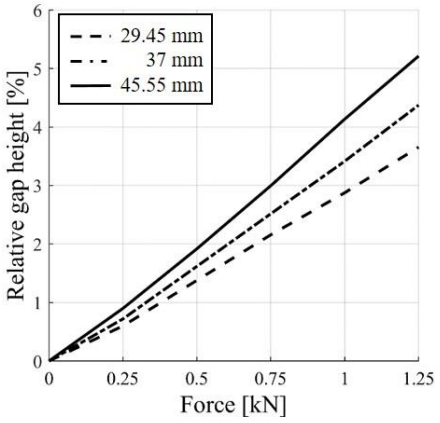

Figure 9: Relative change of gap height for dynamic force in z direction

4.3. Static force radial direction

Another possibility to create a torque against the tilting is to add forces in the radial direction which means the vector of the force lies in the x-y-plane. **Figure 10** illustrates this concept idea.

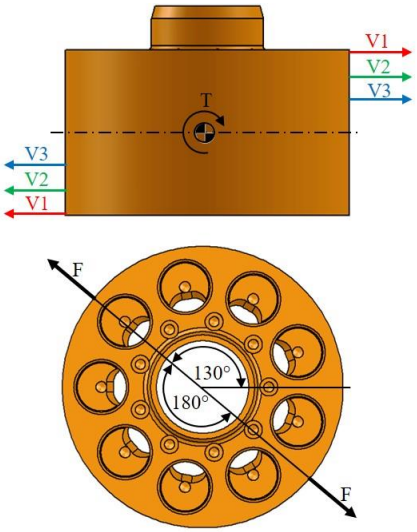

Figure 10: Concept illustration for additional forces in radial direction

A counter force with the same value is added to avoid eccentricity. The value of the force and three variations of the heights are varied. The relative angle change of the tilt angle is used here as a comparative value.
Figure 11 shows the simulation results for a simulation of the forces added at V1.

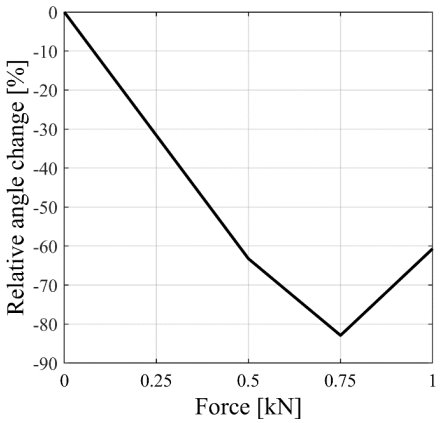

Figure 11: Relative angle change for static force in radial direction

The results show a reduction of more than 80 % for forces of 750 N. It is also evident that the cylinder block is tilting in another direction for forces of 1000 N.

4.4. Dynamic force radial direction

One or more forces in radial direction can be added and synchronised to the rotational angle. The parameters are varied as is it was done in the simulation of the static force in radial-direction. **Figure 12** shows the effect of this imbalance on the tilt angle.

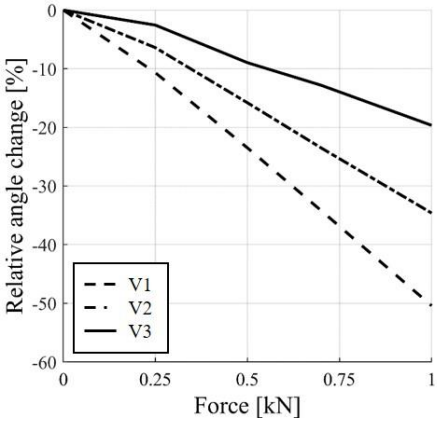

Figure 12: Relative angle change for dynamic force in radial direction

Due to the imbalance resulting from the additional forces, the relative angle change assumes positive and negative values. This concept even leads to a temporary reduction of the minimum gap height.

4.5. Comparison

Of the concepts presented against the tilting of the cylinder block, the static force in the z-direction in particular has great potential. The effect on the tilting angle is substantial even with relatively small forces. An additional pressure pocket in the high-pressure area of the valve plate makes this concept technically feasible. This concept and its potential have been investigated under consideration of the geometric limits. The investigation is described in the next chapter.

5. STATIC PRESSURE FORCE

From the previous explained concepts the realization of concept of the static force in

z-direction is presented and discussed in this chapter.

The realization of additional power in hydraulic machines can be achieved by additional pressurized surfaces. Haug [12], for example, added additional surfaces to control the degree of relief of tribological contacts. For the concept presented here, additional surfaces would have to be implemented in the sealing gaps of the valve plate's high pressure kidney. The position of these surfaces should be in the area of 150° which is the most effective area. **Figure 13** shows the geometry of the sealing gaps for the considered area.

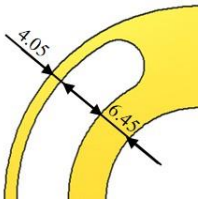

Figure 13: Sealing gap width

For the design of the sealing gap, it is recommended in [13] to choose the width depending on the length of cylinder block's kidney (t) in the interval of $0.125 \ldots 0.175 \cdot t$. In the geometry considered here, t corresponds to the diameter of the piston bore of 25 mm. The minimum width according to this guideline is therefore 3.125 mm. This results in a potential of 0.925 mm for the sealing gap to the housing and 3.325 mm for the one to the shaft. The maximum possible surface is 145.72 mm². This results in a maximum force of 3.64 kN by pressurizing it with the operating pressure of 250 bar. The surface 2 is 104.92 mm² and the surface 1 is 40.8 mm². The point of application of the resulting pressure force is at a radius of 33.67 mm. **Figure 14** shows the optimized geometry with maximum possible surface. It also shows a surface of 101.01 mm² with a resulting force of 2.5 kN. This was the maximum force of the pre-study. The surface 2 is 60.21 mm² and the surface 1 is 40.8 mm². The point of application of the resulting pressure force is at a radius of 35.44 mm. The sealing gap width is only reduced by 2 mm.

Both optimizations were implemented in the simulation model. In the first simulation runs, the value of the counter force, so that the cylinder block is not lifting, had to be found iteratively.

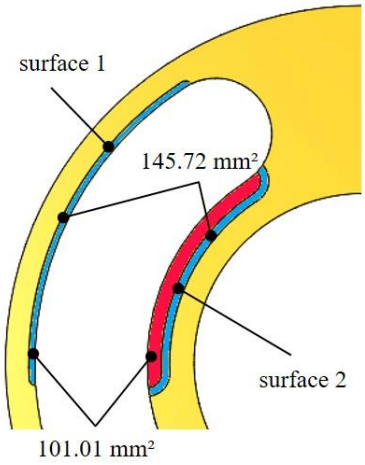

Figure 14: Additional pressure pockets

For the maximum surface, this additional force is 6 kN while for the surface of 101.01 mm² it is 5.5 kN. The simulation results show that the maximum possible surface reduces the tilt angle about 69.92 % and the contact pressure in the area of minimum gap height about 38.93 %. The surface of 101.01 mm² reduces the tilt angle about 56 %. In this case, the contact pressure is reduced about 37.69 %. These results show the high potential for the optimization of the tribological contact valve plate/cylinder block.

6. CONCLUSION AND OUTLOOK

The most widely used type of hydraulic displacement machines are axial piston machines. The tribological contact valve plate/cylinder block is one of three essential tribological contacts in such machines. Its optimization has a great influence on the efficiency of the whole unit. For the substitution of the commonly used leaded brass alloy to realize a hard/soft pairing in this contact the tilting of the cylinder block has to be reduced. In a research project at ifas a simulation model and a test ring has been built up. The results of simulation and experiments show that the cylinder block is tilting to the high pressure side. From this tilting a reduced gap height in the area of 130° occurs. There, wear and heat dissipation according to solid friction and higher fluid velocity increase.

This paper presents the pre-study of four concepts for the reduction of the cylinder block's

tilt angle. The reduction of the tilt angle was investigated by adding forces in z-direction and radial direction with various parameters. Dynamic forces in the same directions are added. The imbalance resulting from these forces reduces the tilting only for rotation angle range of high pressure kidney. All of these concepts have a good potential for the reduction of the cylinder block's tilting in a constant position. The realization of the static force in z-direction by additional pressure pocket at high pressure kidney of the valve plate has a very high potential. The simulation results show that a tilt angle reduction up to 69.92 % is possible by adding the maximum possible surface of 145.72 mm².

The next steps in the ongoing research project are to find the optimum geometry for this concept and its influence to leakage as well as power losses. Therefore, several simulation runs and prototype tests are needed for this iterative process. Possibilities for the realization of the other three concepts presented in this paper have to be developed.

7. ACKNOWLEGEMENT

This work was performed in the scope of the project "Increasing the efficiency of the cylinder block/valve plate contact in axial piston machines" (M41225/44-1), which is funded by the German Research Foundation (DFG). The authors would to thank the German Research Foundation for funding the project.

NOMENCLATURE

b	Gap width
C	Center point of cylinder blocks sphere
CB	Cylinder block
DOR	Direction of rotation
d_{CB}	Cylinder block's outer diameter
F	Force
h	Gap height
h_{CB}	Cylinder block's height
h_{min}	Minimum gap height
h_{new}	New minimum gap height
h_{rel}	Relative change of minimum gap height
$h_{previous}$	Previous minimum gap height
$ifas$	Institute for fluid power drives and systems
l	Gap length
Δp	Pressure difference
Q	Volume flow
r_1	Inner radius of high pressure kidney
r_2	Outer radius of high pressure kidney
r_i	Inner radius of valve plate
r_m	Medium radius of high pressure kidney
r_o	Outer radius of valve plate
t	Length of cylinder block's kidney
T	Torque
α	Tilt angle
α_{new}	New tilt angle
α_{rel}	Relative change of tilt angle
$\alpha_{previous}$	Previous tilt angle tilt angle
γ	Start angle of high pressure kidney
δ	End angle of high pressure kidney
η	Dyn. viscosity

REFERENCES

[1] Jang, D.-S. (1997) Verlustanalyse an Axialkolbeneinheiten, Aachen, Germany, 1997

[2] Schmitz K., Murrenhoff H. (2018), Grundlagen der Fluidtechnik Teil 1: Hydraulik, Shaker Verlag, Aachen, 2018

[3] Table of restrited substances under REACH, European Chemicals Agency

[4] Paulus A. (2016) Tribolayer Formation on Bronze Cu Sn12Ni2 in the Tribological Contact between Cylinder and Control Plate in an Axial Piston Pump with Swashplate Design, 10th International Fluid Power Conference, Dresden, Germany, 2016

[5] Gels S. (2011), Einsatz konturierter und beschichteter Kolben-Buchse-Paare in Axialkolbenmaschinen in Schrägscheibenbauweise, Aachen, 2011

[6] Wegner S, Gels S., Murrenhoff H. (2014), Simulation of the tribological contact cylinder block/valve plate and influence of geometry and operation points on the friction torque in axal piston machines, The 9th International Fluid Power Conference, Aachen, Germany, 2014

[7] Wegner S., Gels S., Jang D.-S., Murrenhoff H. (2015), Experimental investigation of the cylinder block movement in an axial piston machine, ASME Symposium on Fluid Power and Motion Control, Bath, Great Britain, 2015

[8] Wegner S, Gels S., Murrenhoff H. (2016), Validation of the physical effect implementation in a simulation model for the cylinder block/valve plate contact supported by experimental investigations, 10th International Fluid Power Conference, Dresden, Germany, 2016

[9] Achten P, Eggenkamp S. (2017), Barrel tipping in axial pumps and motors, 15th Scandinavian International Conference on Fluid Power, Linköping, Sweden, 2017

[10] Zecchi M., Mehdizadeh A., Ivantysynova M. (2013), A novel fluid structure interaction and thermal model to predict the cylinder block/valve plate interface performance in swash plate type axial piston machines, 13th Scandinavian International Conference on Fluid Power, Linköping, Sweden, 2013

[11] Ivantysyn R. (2017), An approach to visualize limiting factors in the cylinder block/valve plate gap in Axial Piston Pumps, ASME Symposium on Fluid Power and Motion Control, Bath, Great Britain, 2017

[12] Haug S., Geimer M. (2016), Optimierung von Axialkolbenmaschinen durch bedarfsangepasste Entlastung tribologischer Kontakte, 9. Kolloquium Mobilhydraulik, Karlsruhe, Germany, 2016

[13] Ivantysyn J., Ivantysynova M. (1993), Hydrostatische Pumpen und Motoren, 1. Auflage, Vogel, Würzburg, Germany, (1993)

peer reviewed

NUMERICAL AND EXPERIMENTAL STUDY ON NOVEL HYDRAULIC PUMP CONCEPT

Seong-Ryeol Lee*, Florian Schoemacker, Christian Stammen, Katharina Schmitz

Institut for Fluid Power Drives and Systems, RWTH Aachen University, Campus-Boulevard 30, 52074 Aachen
* Corresponding author: Tel.: +49 241 80-47747; E-mail address: seong.lee@ifas.rwth-aachen.de

ABSTRACT

This paper discusses an investigation on a novel hydraulic pump concept. The idea aims on a pump principle to be directly connected to high-speed electric motors to build compact high-pressure drives. The pump can theoretically work without solid contact and has no kinematic pulsation. The composition of the pump is basically similar to cylindrical journal bearings. In general, a journal bearing is used to support external loads on a rotating shaft. When the shaft rotates with the loads, hydrodynamic fluid force is generated in the fluid film, which compensates the external force and reduces an eccentricity of the shaft. The difference of the introduced pump concept from the bearing is that the eccentricity is fixed and it has an outlet port at the high pressure area, through which the fluid can be transferred. To examine the functionality of the pump, a test bench is constructed and experiments are performed to investigate the pressure build-up and discharging flow of the pump concept. The experimental results are numerically analyzed by using elasto-hydrodynamic lubrication (EHL) simulation, based on the 2D Reynold's equation. From these results, the functionality of the pump concept is confirmed. Moreover, several variables that influence the characteristic curve of the pump are studied. Based on these results, geometric parameters of the test pump are redesigned to discharge sufficient flow rate for usage as commercial pumps.

Keywords: Hydrodynamic Pump, High-Speed Drive, Journal Bearing, EHL Simulation

1. INTRODUCTION

Hydraulic pumps are widely used in many industry fields to supply hydraulic energy. The hydraulic energy is transformed from mechanical energy via the pumps, which is often connected to an electric motor for rotation. Thus, the pump can transform the energy with the permissible speed and torque of the connected motor, which determines the operating range of the configured hydraulic system. The further development of electric motor technology has increased operating speed limitations, as well as the miniaturization of the motor, even if it has the same power capacity [1].

The downsized electric motor is one of many ways to reduce weight and enhance compactness in the combined units. The combined unit has still leeway to be reduced by the weight of the pump. High-speed technology is the key to downsizing hydraulic pumps, which can significantly save weight and installation space [2]. This is because, even if the displacement volume is small, the same flow rate as that of the conventional pump can be discharged at high rotational speed.

Accordingly, studies on high-speed pump are in progress. In case of hydrostatic pumps, such as piston pumps, gear pumps and vane pumps, solid contacts are inevitably generated to form the displacement volume, which shortens the life of the components due to wear. Especially under the high-speed operating conditions, the components are prone to wear and deformation, which significantly reduces pump efficiency. One of ways to improve the tribological characteristic of the material, laser surface texturing is used [3]. In addition, high-speed piston pumps are experimentally proven to have large shear losses in the cylinder block due to the viscosity of the fluid and to increase leakage due to temperature rise [4]. Moreover, components, which create a displacement volume in the pump, result in dynamic unbalance and a slower response to a speed change due to moment of inertia [5].

Unlike the hydrostatic pumps, hydrodynamic pumps, such as impeller pumps, are more suitable

for high-speed drives because the pressure and flow pulsation are quite low and there is no contacting surfaces in the pump [6]. However, the maximum working pressure is normally lower compared to the hydrostatic pumps. Moreover, the impeller pump could generate oscillations with large dynamic pressures force at high operating speed, which could cause cracks in the impeller due to large stress [7].

In a previous research [8], two novel hydrodynamic pump concepts are introduced. The first concept is numerically studied, which is similar to radial journal bearings. The introduced pump concepts theoretically have no solid friction and no kinematic pulsation. It also has an advantage over the conventional hydrodynamic pumps in that it can reach a higher operating pressure. The research also describes a sophisticated concept that both walls are driven to avoid shear loss, based on methods developed with the first concept.

In this paper, the first pump concept is experimentally studied and analysed numerically. An elasto-hydrodynamic lubrication (EHL) simulation is used to analyse pressure distribution and discharging flow of the pump. Influence of several operating conditions on the discharging flow is examined. From experimental results, the functionality of the pump concept is confirmed, and the pump geometry is redesigned for larger volume flow by using the simulation.

2. WORKING PRINCIPLE OF THE NEW PUMP CONCEPT

Many mechanical elements inevitably generate friction during relative movement. To reduce the friction and wear, a lubricated fluid film is used on the conformal elements surface and it provides smooth motion and enhanced operating life for the machine elements. When the surface is moved, shear flow, so called Couette flow, is generated because of the viscosity of the fluid. A hydrodynamic pressure is developed, when the shear flow occurs on converged surfaces. This hydrodynamic pressure implies that it can support external forces and reduce the contact force between the surfaces. This phenomenon is called hydrodynamic lubrication [9].

The conformal surfaces can be shaped infinitely like a journal bearing (**Figure 1a**), and the flow and pressure are developed on the surfaces just by rotating the shaft. Standard journal bearings have one inlet port to supply fluid for the lubrication. However, installation variety is limited because the inlet port can be blocked, depending on the rotational direction of the shaft and the external load direction.

Unlike the standard bearings, two port journal bearings **(Figure 1b)** are used to supply fluid regardless of the operating condition [10]. However, when one port is located in the high pressure region, a negative flow occurs in which the fluid flows in the opposite direction due to the pressure difference from the port pressure [11]. This causes a pressure loss and reduces load carrying capacity of the journal bearing. To

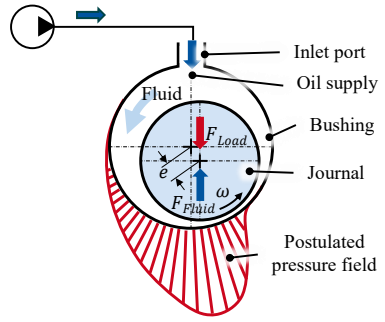

(a) Single inlet port

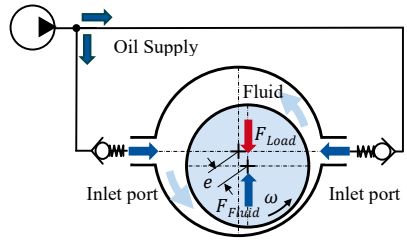

(b) Two outlet ports

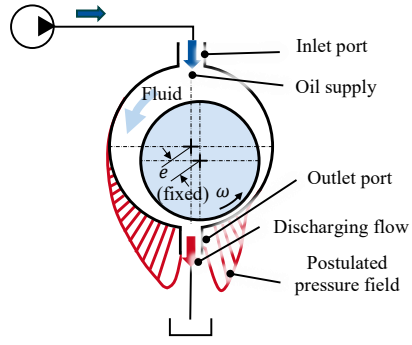

(c) Novel hydraulic pump concept

Figure 1: Two journal bearing types and a novel hydraulic pump concept

prevent the negative flow, check valves are used to restrict the flow direction of the fluid [12].

The idea of the novel pump concept originated from the lubrication theory and the two ports journal bearing points out the possibility of the idea. The negative flow in the two ports journal bearing can be a discharging flow as a hydraulic pump. As shown in the **Figure 1c**, the first pump concept is designed with the same shape as the two ports journal bearing. Differences are that the inlet port is used as an outlet port, through which the fluid can be delivered, and the eccentricity is fixed to allow pressure build-up without the external force creating an eccentricity. The functionality of the hydraulic pump was numerically examined in the previous study [8].

Discharging flow through the outlet port is composed of shear flow (Couette flow) and pressure flow (Poiseuille flow). **Figure 2** shows the postulated discharging flow in θ-direction. Under the assumption that there is a non-turbulent flow at the outlet, the discharging shear flow is calculated as the difference between inflow and outflow. The shear flow is proportional to the perpendicular length in flow direction (B in **Figure 2a**) and the difference of the gap height at the border of the outlet port. That is, the shear flow is significantly affected by the shape of the outlet port.

The pressure flow is generated by the difference between the outlet pressure and the fluid film pressure. The pressure flow is proportional to the pressure gradient at the outlet border. This flow becomes zero when the outlet pressure and pressure near the outlet port are equal, in other words, when the pressure gradient at the outlet boundary is zero. Due to the characteristic that the discharge flow is inversely proportional to the discharge pressure, this pump can be classified as a hydrodynamic pump.

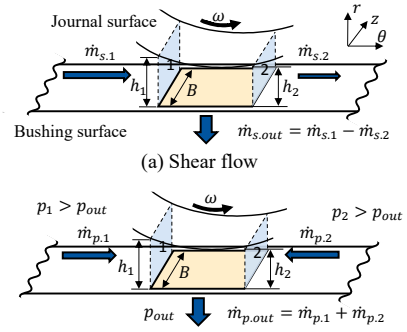

Figure 2: Composition of the discharging flow

3. TEST BENCH

The test bench, shown in **Figure 3**, is constructed for functionality examination of the pump concept. A rotating shaft, connected to the motor using an elastomer coupling, is supported with one ball bearing and two DIN 504 standard journal bearings [13]. The ball bearing is used to apply the external load to the rotating shaft to generate the eccentricity. The external force is applied by screwing and the load direction is adjustable. The first journal bearing has an outlet port and this works as the novel hydrodynamic pump. **Figure 4** represents the geometry of the pump and the parameters are given in **Table 1**. The second journal bearing is for force balance against the external force. The journal bearing used as the pump, has an outlet port, so it may have different pressure field from other journal bearings depending on the pressure of the outlet port even with the same eccentricity. However,

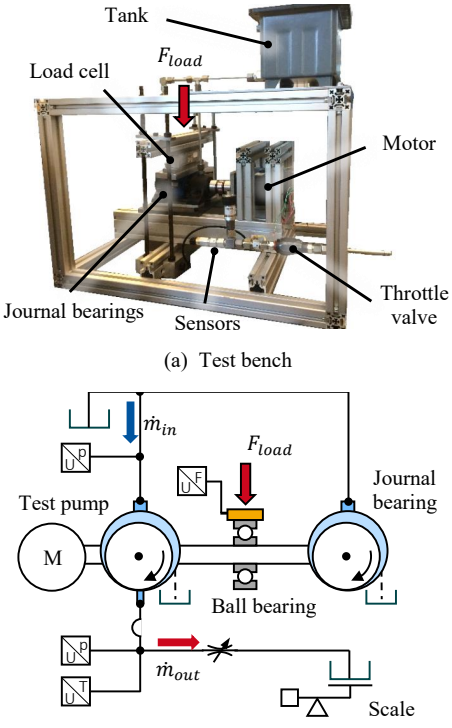

Figure 3: Test bench of the novel pump concept

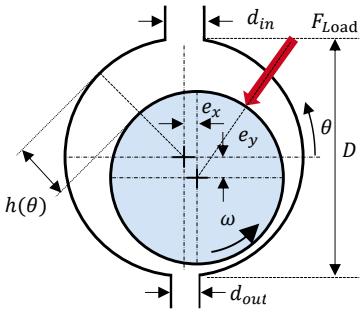

Figure 4: Geometry of the test pump

since the eccentricity of both journal bearings cannot be measured in this experimental setup, it is simply assumed that half of the external force is applied to the pump. HLP 46 mineral oil is used for the fluid, which is supplied from the tank at the top and the supply pressure is about 1bar tank pressure. A throttle valve is used to control the outlet port and the mass flow is measured with a platform scale. **Table 2** shows specifications of the test bench.

Table 1: Geometry parameter of the test pump

Parameter	Value [mm]
Journal diameter D	25
Journal width B	60
Nominal gap height h_G	15×10^{-3}
Inlet port diameter d_{in}	15
Outlet port diameter d_{out}	0.7

Table 2: Specification of the test bench

Parameter	Value	Unit
Max. Motor speed	1000	rpm
Max. External load	1000	N
Lubricant	HLP 46	-
Oil Temperature	25 ±1	℃

4. SIMULATION MODEL

In this paper, an elasto-hydrodynamic lubrication (EHL) simulation, set up using MATLAB, is used to interpret the pressure distribution and validate the discharging flow of the hydrodynamic pump concept in a steady state.

First, a fluid film mesh is generated from the geometry of the pump (shown in **Figure 4**) and journal bearing and the parameters (**Table 1**) are used. The gap height of the fluid film is calculated geometrically, as shown in Equation 1:

$$h(\theta) = h_G + e_x \cos\theta + e_y \sin\theta \qquad (1)$$

Then, the pressure boundary conditions, such as inlet pressure, outlet pressure and environment pressure, are defined. The pressure boundary conditions are constrained to the nodes where the geometry is located. For the unconstrained nodes, the pressure is calculated using the Reynolds' equation in two dimensions, which has been discretized for the mesh in the form of finite volumes. In addition, Jakobsson-Floberg-Olsson (JFO) cavitation model [14, 15] is used to avoid negative pressure for more accurate calculation. The Reynolds' equation with the JFO cavitation model is shown in Equation 2:

$$\nabla \cdot \left(\frac{\rho h(1-\xi)}{2} U\right) - \nabla \cdot \left(\frac{\rho h^3(1-\xi)}{12\eta} \nabla p\right) = 0 \qquad (2)$$

Fischer-Burmeister function is applied as a mathematical model to constrain the pressure (p) and the cavitation factor (ξ) [16].

The output flow of the pump can be simply calculated at the border of the outlet hole with the assumptions that the pressure at the objects is constant and that there is no turbulent flow in the outlet hole. Therefore, the output flow is calculated by summation of discretized volume flow at the nodes, which are defined as the border of the outlet hole. In the same way, the leakage to both sides of the journal can be calculated.

In this simulation, MATLAB PDE Tool is used to calculate the deformation of the solid structure [17]. Thereby, interfacing work between different programs is avoided and overall computation time is reduced. **Figure 5** shows a FEA model of the test bench. The FEA model is simplified to save calculation time. Material properties of steel (**Table 3**) are applied in each bushing and shaft. Then, as force

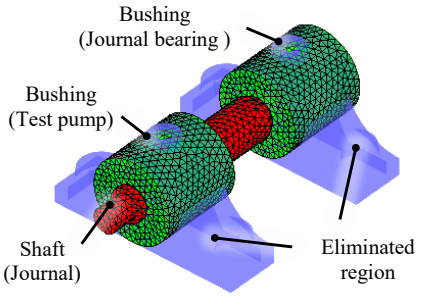

Figure 5: Simplified FEA model of the test bench

boundary conditions, the pressure fields, calculated from the Reynold's equation, are applied in the fluid area, and the distributed external load is applied to the center of the shaft.

Table 3: Material properties of the components

Parameter	Value	Unit
Young's modulus E	2×10^{11}	Pa
Poisson's ratio ν	0.3	-
Mass density ρ_{mass}	7850	kg/m³

The shaft in the bushing is set to be the eccentricity position where the total force is balanced, because the simulation is performed in a steady state. Since the stiffness of the elastomer coupling is sufficiently small compared to the shaft, it is assumed that the effect on the deformation of the shaft is negligible. Therefore, both sides of the shaft are constrained in an eccentric position where the total force is balanced. Under the FEA boundary conditions, the deformation of the shaft is calculated.

The deformation result is again applied to the fluid film simulation to calculate a new pressure field in the deformed surfaces. The iteration process is ended, when the results are converged. **Figure 6** shows the iteration process in the EHL simulation.

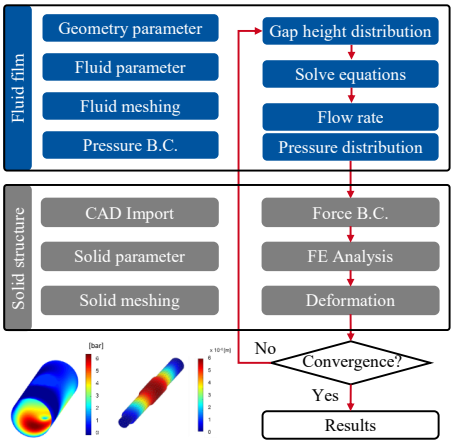

Figure 6: Iteration process of EHL simulation

5. RESULTS AND DISCUSSION

Several variables that could affect the discharging flow of the pump are classified into the cases in **Table 4**, and the discharging flow is measured by changing the outlet port pressure. The EHL simulation is used to analyze the measured results and validated under the same operating conditions.

Table 4: Cases of measurement and simulation

Case	Load [N]	Load angle [deg]	Rotational Speed [rpm]
1	500	90	500
2	500	90	1000
3	500	80	500
4	500	100	500
5	250	80	500

5.1. Deformation effects

In order to confirm the effect of deformation in the simulation, the experimental results for Case 1 are compared with the results with or without deformation. **Figure 7** represents the deformation of the shaft and test pump bushing under the same operating condition at 2 bar outlet pressure. In case of the shaft, the maximum deformation is 6.8 µm in the middle of the shaft, and the deformation appeared almost symmetrically through out the external load. In

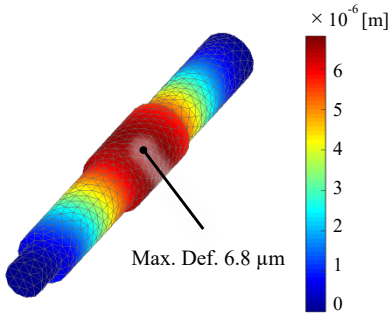

(a) Shaft

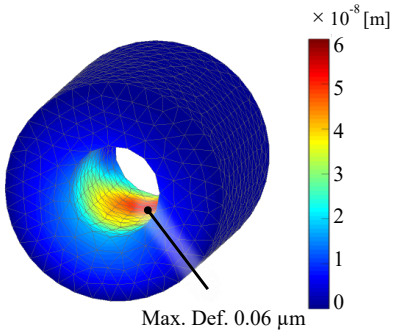

(b) Bushing (simplified)

Figure 7: Deformation of the pump components

the case of the pump bushing, the pressure distribution of the fluid film with a maximum pressure about 7 bar is applied to the surface. The maximum deformation is 0.06 µm, which is very small compared to the shaft, and the effect on the gap height is negligible.

Figure 8 shows the characteristic curve of the pump under the operating conditions of Case 1. The discharging mass flow is measured about 3.5 g/min at an outlet pressure of 0 bar (relative pressure) and it decreases with increasing outlet pressure, which is the characteristic of a hydrodynamic pump. The simulation results with deformation are shown to be more similar to the measured results and less error than the other simulation results, which do not consider the deformation.

From the results above, it can be seen that under the current operating conditions, the effect of the pressure on the shaft and bushing deformation is very small. However, it is shown that deformations, caused by external forces and fluid forces, influence the change in gap height and should be taken in to account. Therefore, this deformation is considered in subsequent simulations.

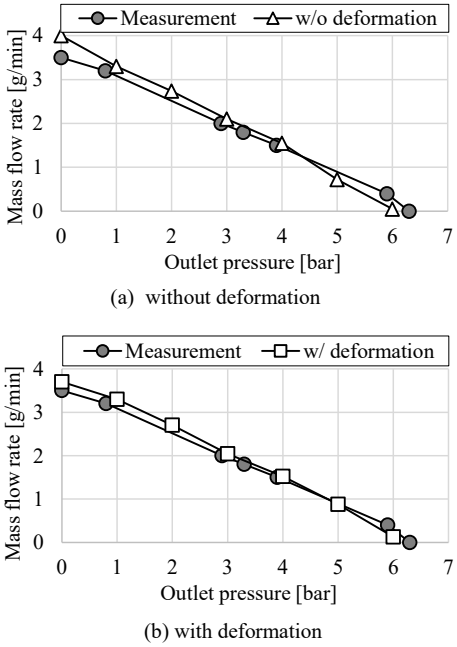

Figure 8: Comparison of measurement and simulation results in Case 1.1 operating condition

5.2. Influence of rotational speed

Figure 9 shows measured results under Case 1 and 2, which are under same load condition with different rotational speed. In addition, since the eccentricity cannot be measured in the test bench, the variation of the eccentricity is estimated through the simulation, as shown in **Figure 10**.

When the eccentricity is fixed, the pump has a wider pressure range because of the increased dynamic pressure at high rotational speeds. In this experiment, however, the eccentricity is not fixed. Therefore, the maximum pressure range of the pump is similar because a pressure against to the external force is formed in the fluid film.

In addition, the discharging flow is measured slightly higher at 1000 rpm in the overall range. Under current experimental conditions, the pressure field appears similar because pressure is generated in response to external forces. However, different eccentricities are created to form the same pressure field. Therefore, in case of 1000 rpm, there is a larger gap height at the outlet port position and has a slightly higher discharge flow. The shear flow is proportional to the rotational speed, but the outlet port is very small, so the portion of the total discharging flow is very small [12]. This explains the tendency that the discharging flow of the two cases becomes similar as the outlet pressure increases.

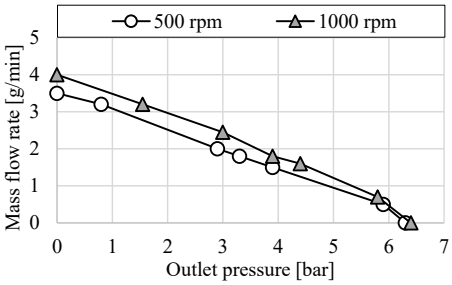

Figure 9: Measurements under Case 1 condition

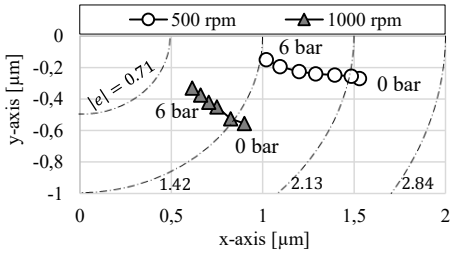

Figure 10: Simulation result of the eccentricity

5.3. Influence of load direction

Figure 11 shows measured results at the same rotational speed under the different load direction with 500 N (Case 1, 3 and 4). The graph represents almost the same characteristic curve when the load directions are 80 ° and 100 °. In the case of 90 °, the operating pressure range is until about 6.5 bar.

Figure 12 shows the simulated pressure field with each load direction at the 2 bar outlet pressure. When the external force is applied in 90 °, it can be seen that the pressure distribution is nearly symmetrical around the outlet port. However, when the direction of the external force changes, the pressure distribution centering on the outlet port is biased to one side, explaining that the maximum pressure of the outlet port is lowered.

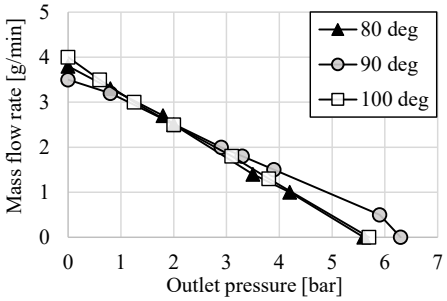

Figure 11: Measurements under Case 1, 3 and 4

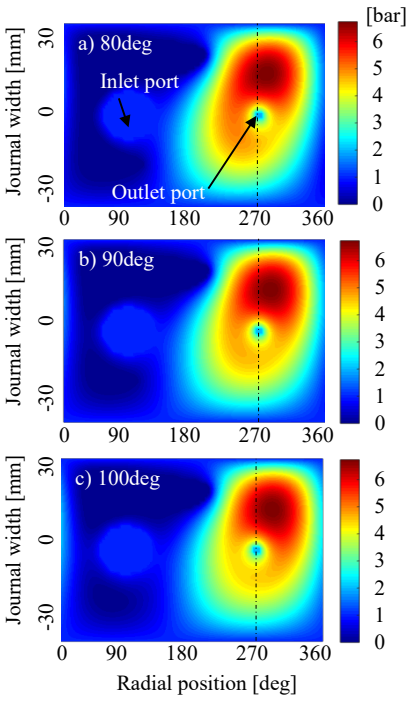

Figure 12: Simulation results for pressure distribution under different load directions

5.4. Influence of load magnitude

In order to confirm the effect of the eccentricity on the characteristic curve, the discharging flow is measured by varying the magnitude of the load force. **Figure 13** shows the experimental results under the test conditions of Case 3 and 5.

When 500 N force is applied on the pump side, the maximum outlet pressure is measured about 5.5 bar. In the other case, the maximum outlet pressure is about 3.5 bar.

Figure 14 shows the simulated results of changing the outlet pressure with 1 bar intervals under the same test conditions to confirm the change of eccentricity. The results represent that the eccentricity is increased when a larger external force is applied. In addition, as the outlet pressure is decreasing, the eccentricity is increased to compensate for the pressure loss in the pressure field, caused by the discharging flow through the outlet port.

Figure 15 shows the pressure distribution at the 2 bar outlet port pressure. Under the 250 N and 500 N load condition, the maximum pressure in the pressure field is calculated to be each around 4.5 bar and around 6.5 bar. Although the eccentricity is always large with the 500 N load, the mass flow varies, depending on the outlet pressure. This is because the gap height at the outlet port position is changed by the eccentricity variation. As mentioned previously, the discharging flow is also affected by the gap

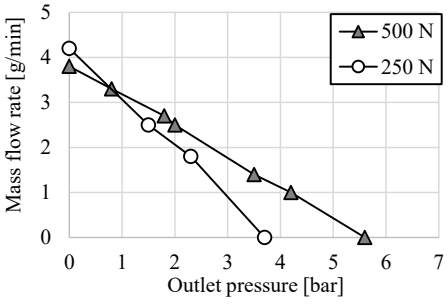

Figure 13: Measurements under Case 3 and 5

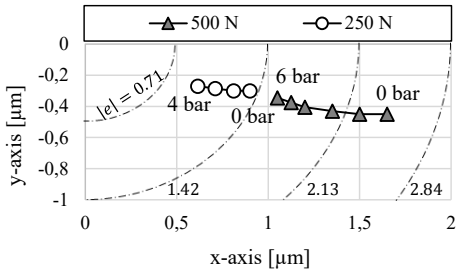

Figure 14: Simulation result of the eccentricity under different load

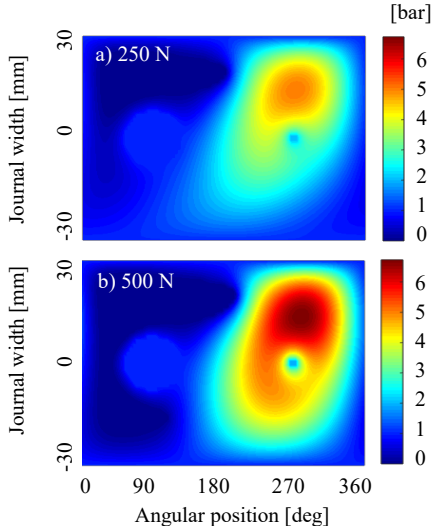

Figure 15: Simulation result for pressure distribution under different load

height. As the eccentricity increases, the gap height at the outlet port position is decreasing relatively. Therefore, although the pressure field has a sharp gradient, the discharging flow could be smaller, depending on the gap height at the outlet port location, like at 0 bar in **Figure 13**.

6. REDESIGN

In the previous experimental conditions, very small mass flows are measured. The reason is that it is difficult to apply a large load, generating eccentricity. In addition, the motor speed is not fast enough to generate a high hydrodynamic pressure. Moreover, it was numerically examined in the previous study that the pump can also generate more mass flow depending on the size of the outlet port [8]. Taken together, the factors affecting the magnitude of the discharging flow are as follows:

- Large gap height at outlet port position
- Large outlet port size
- High rotational speed

Therefore, to verify if it is possible to produce a discharge capacity suitable for use as a conventional pump, the pump is redesigned with different outlet shapes and larger eccentricity in the same journal size. The simulations are carried out under high-speed driving conditions, to the purpose of the pump concept.

Table 5 shows the redesigned geometry parameters. For the large gap height at the outlet port position, the eccentricity and nominal gap height are increased. The diameter of the outlet port is also increased to 15mm diameter. The inlet port shape is changed to rectangular. This is to reduce the cavitation area by widening the oil supply area, especially at high-speed area. These parameters are not yet numerically optimized, but are selected empirically for large outlet flow. In addition, FEA boundary conditions are symmetrically set up, as shown in **Figure 16**. The size of bushing and journal is the same as before.

Table 5: Redesigned geometry parameter

Parameter	Value	Unit
Journal diameter D	25	mm
Journal width B	60	mm
Eccentricity in x-direction e_x	25	µm
Eccentricity in y-direction e_y	-3	µm
Nominal gap height h_G	50	µm
Inlet port width a	30	mm
Inlet port angle b	68	deg
Outlet port diameter d_{out}	15	mm

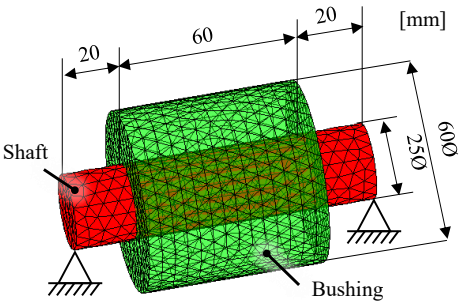

Figure 16: Redesigned pump model and FEA boundary conditions

Figure 17 represents the simulations results with the redesigned parameters. Not only the mass flow but also the pressure range is increased by increasing the rotational speed, due to the fixed eccentricity. These simulation results suggest that the magnitude of the mass flow can be significantly increased with optimized geometry parameter, compared to the experimental values.

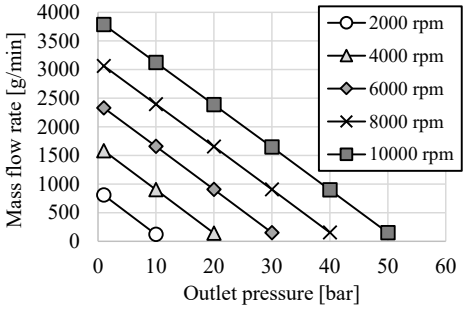

Figure 17: Simulation results of characteristic curve with the redesigned parameters

Figure 18 shows the pressure distribution at 10000 rpm and 1 bar outlet pressure, and **Figure 19** shows the deformation under the operating condition. Maximum pressure is about 50 bar, and the pressure is distributed symmetrically. In the high-pressure region, the gap height increased due to the deformation due to pressure, and it is confirmed that the gap height of the low-pressure side is decreased, as the journal is bent.

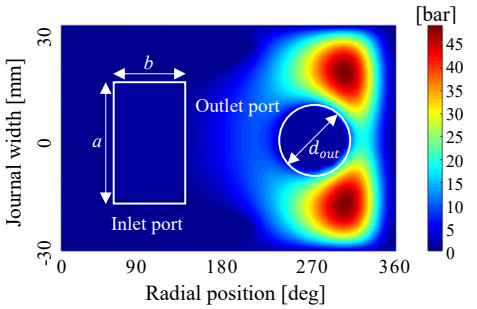

Figure 18: Simulation result of pressure distribution at 10000 rpm and 1bar outlet pressure

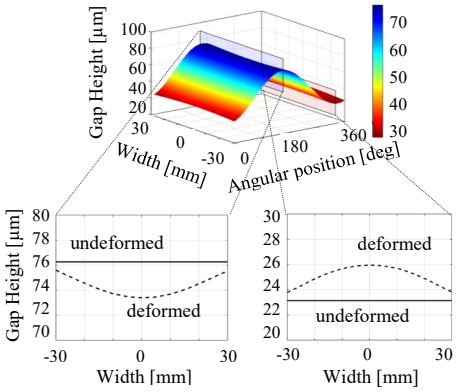

Figure 19: Deformed and undeformed gap height in low and high-pressure area

7. CONCLUSION AND OUTLOOK

In this paper, a novel hydrodynamic pump concept is introduced. The pump concept is inspired by hydrodynamic lubrication theory and has a design based on conventional journal bearings. The concept is studied experimentally to confirm its functionality as a hydrodynamic pump and analysed numerically using EHL simulation. The experiments and simulations have proven the feasibility of the pump concept. The following conclusions are obtained from the experiment and simulation results.

- The pump concept has the characteristic curve of a hydrodynamic pump, that the discharge flow is decreased with increasing the discharging pressure.
- The pressure of the fluid film is increased by increasing the eccentricity. This means that the pressure range of the pump can be controlled by adjusting the eccentricity.
- However, the discharge flow can be increased, when the gap height at the outlet port position is increased.
- The outlet port position on the pressure field affects to the pressure range and discharging flow, because it is related to the gap height.

Based on the conclusions from the results, the geometry parameters of the pump are designed for higher discharging flow and simulations are performed. From the simulation results, it is estimated that the discharge flow can reach the capacity of a conventional small pump with optimized pump geometry.

As a general observation, unlike conventional hydrodynamic pumps (e.g., impeller pumps), the introduced pump concept has a high maximum pressure range. The operating range of the pump (i.e., the maximum output flow and pressure) is influenced by many operating conditions and also pump geometry. However, the introduced pump

has a great advantage, which is that the components are very simple and easy to manufacture. Moreover, the pump can be operated without solid contact. This means that the pump has less friction and wear, which has long service times for higher durability. Therefore, it is expected to be a compact hydrodynamic pump with high reliability.

For future research work, the pump geometry will be optimized by using the EHL simulation. The optimized geometry is evaluated in a new test bench. The simulation will be updated to consider thermal effects under in unsteady state for calculating an efficiency. Also, an analytical equation for the output flow will be derived.

NOMENCLATURE

a	Redesigned inlet port width
B	Journal width
b	Redesigned inlet port angle
D	Journal diameter
d_{in}	Inlet port diameter
d_{out}	Outlet port diameter
E	Young's modulus
EHL	Elasto-hydrodynamic lubrication
$\|e\|$	Absolute value of eccentricity
e_x	Eccentricity in x-direction
e_y	Eccentricity in y-direction
F_{load}	Load force
F_{fluid}	Fluid force
h	Gap height
h_G	Nominal gap height
$\dot{m}$	Mass flow rate
p	Pressure
U	Relative velocity of surface
η	Dynamic viscosity
θ	Radial position
ν	Poisson's ratio
ξ	Cavitation factor
ρ	Fluid density
ρ_{mass}	Mass density

REFERENCES

[1] Roth D, Jacobs G, Pietrzyk T, Schmitz K (2019) Dezentrale kompakte Hydraulikversorgung durch High-Speed-Komponenten. ATZheavy duty 68-73.

[2] Brahmer B (2016) On Adaptive Electro Hydrostatic Actuators. 11th Int Fluid Power Conf 426–435

[3] Chen Y, Zhang J, Xu B, Wang F, Li H (2018) Investigation of Laser Surface Texturing for Integrated PV (Pressure×Velocity)-Value-Decreased Retainer in an EHA Pump. 11th Int Fluid Power Conf 408-418

[4] Zhang J, Li Y, Xu B, Chen X, Pan M (2018) Churning Losses Analysis on the Thermal-Hydraulic Model of a High-Speed Electro-hydrostatic Actuator Pump. Int J Heat Mass Transf 1023-1023

[5] Shi C, Wang S, Wang X, Zhang Y (2018) Variable Load Failure Mechanism for High-Speed Load Sensing Electro-Hydrostatic Actuator Pump of Aircraft. Int J Heat Mass Transf 1023-1023

[6] Schmitz K, Murrenhoff H (2018) Grundlagen der Fluidtechnik, Teil 1: Hydraulik. 172-173, Shaker Verlag

[7] Olimstad G, Thorvald P (2019) Failure and Redesign of a High-Speed Pump with Respect to Rotor-Stator Interaction. Engineering Failure Analysis 704-713

[8] Lee S.R, Schoemacker F, Stammen C, Schmitz K (2019) Numerical Study on Novel Hydraulic Pump Concept. German Tribology Conference

[9] Hamrock S, Schmid S, Jocobson B (2014) Fundamentals of Fluid Film Lubrication. 202-228

[10] Vogelpohl G (1958) Betriebssichere Gleitlager. Springer-Verlag.

[11] Brito F.P, Miranda A.S, Claro J.C.P, Fillon M (2012) Experimental Comparison of the Performance of a Journal Bearing with a Single and a Twin Axial Groove Configuration. Tribo Int 1-8

[12] Brito F.P, Miranda A.S, Fillon M (2016) Analysis of the Effect of Grooves in Single and Twin Axial Groove Journal Bearings under Varying Load Direction. Tribo Int 609-619

[13] DIN 504, Gleitlager-Augenlager, 2004.

[14] Jakobsson B, Floberg L (1957) The Finite Journal Bearing Considering Vaporization. Trans Chalmers Univ Tech 190 1–116

[15] Olsson K.O (1965) Cavitation in Dynamically Loaded Bearings. Trans Chalmers Univ Tech 308

[16] Woloszynski T, Podsiadlo P, Stachowiak G (2015) Efficient Solution to the Cavitation Problem in Hydrodynamic Lubrication. Tribol Lett 58:18

[17] MathWorks (2019) Partial Differential Equation Toolbox User's Guide.

peer reviewed

A NUMERICAL MODEL FOR THE EVALUATION OF GEROTOR TORQUE CONSIDERING MULTIPLE CONTACT POINTS AND FLUID-STRUCTURE INTERACTIONS

Zubin Mistry[1]*, Venkata Harish Babu Manne[1], Andrea Vacca[1], Etienne Dautry[2], Martin Petzold[2]

[1] *Maha Fluid Power Research Center, Purdue University, 1500 Kepner Drive, 47905 Lafayette, USA*
[2] *Thomas Magnete GmbH, Innomotion Park 3, 57562 Herdorf, Germany*
*Corresponding author: Tel.: +1 7656053090, email address: mistry7@purdue.edu

ABSTRACT

This paper presents a numerical model for the evaluation of the actual torque in Gerotor units. The model consists of two major modules: the pre-processor module and the HYGESim module. The pre-processor module consists of the geometric and the mechanical module. The geometric pre-processor module considers the CAD geometry of Gerotor with tolerances as input and it provides as output the geometric features needed to evaluate the rotor loading and the flow features. The mechanical pre-processor module evaluates the forces of interaction at the contact points between the rotors. The flow displaced by the unit is evaluated using a lumped parameter model whereas the lubricating gaps are evaluated by solving the Reynolds Equation. The main novel aspects consist of the evaluation of the frictional losses at various interfaces. An Elasto-Hydrodynamic Lubrication (EHL) approach is used to evaluate the frictional losses at the contact points between the rotors.

Tests on a prototype Gerotor unit are performed for the model validation, particularly as pertains to the features of the shaft torque. Additionally, the paper comments on the distribution of the different torque loss contributions associated with the operation of the unit taken as reference.

Keywords: Gerotor, Lumped Parameter Model, Multiple Contact Points

1. INTRODUCTION

Gerotor pumps are one of the popular types of hydrostatic units in low-pressure fluid-power and automotive applications. Low cost, compactness, robustness, and low noise are some of the factors behind the success of these units. **Fig. 1** illustrates a typical assembly of a Gerotor unit which consists of an inner rotor, outer rotor, body, suction, and delivery port.

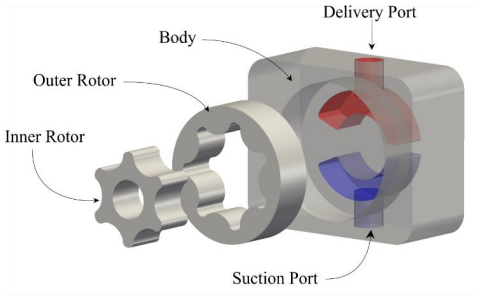

Figure 1: A typical Gerotor assembly

Fig. 2 illustrates the working of a Gerotor: the inner rotor and the outer rotor rotates about a fixed axis separated by a certain eccentricity. The figure shows the changes in pressures in different Tooth Space Volumes (TSVs) with time (where one of the TSV is labelled as TSV_i).

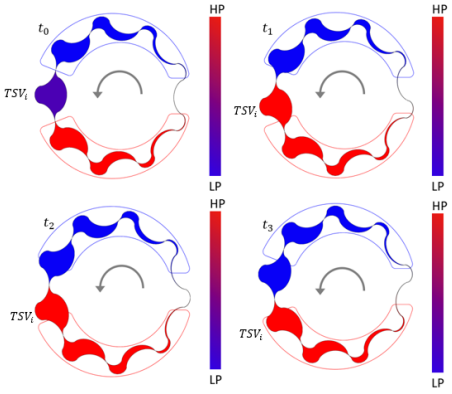

Figure 2: Principle of operation of a Gerotor

The unit has two primary lubricated interfaces which are shown in **Fig. 3**. One lubricated region is the radial gap which is a thin fluid film present between the outer rotor and the body. This lubricated interface also acts as a journal bearing. The second lubricated region is the lateral gap which is a thin fluid film present between the lateral surfaces of the gears and the body. This lateral gap is present on both the lateral surfaces of the gears. Fig. 3 shows one of the two lateral gaps.

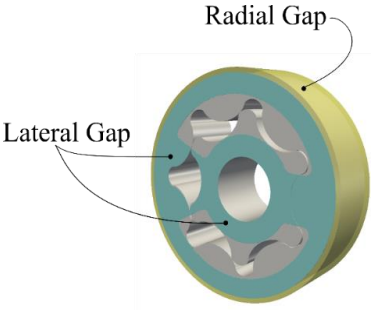

Figure 3: Lubricated interfaces in a Gerotor

Although a Gerotor was first conceived in the 1800s, recent advances in fluid power and automotive field pushes the limits of the working conditions of the Gerotor by demanding higher operating pressures and higher efficiency. This calls for accurate models that can aid the designers in predicting the behavior of different aspects of Gerotor under different operating conditions.

Various past efforts have taken up this challenging task of modeling the fluid-dynamic behavior of Gerotor units. The first analytical models were proposed by Bonandrini et al. [1, 2] where they presented analytical approaches to perform comparative evaluations between the flow parameters given by gears based on hypo trochoidal and epitrochoidal envelopes with different design parameters. Mentioned analytical approaches of study significantly contributed in advancing both the understanding and the modeling of Gerotors; however, they have limitations given by some simplistic assumptions, such as the absence of the clearance between the rotors, of fluid leakages or effects due to fluid compressibility.

Various numerical models have been introduced during the past few decades to describe these effects. Nervegna et al. [3, 4] formulated a control volume lumped parameter model, based on continuity and orifice equations, that can be used for basic studies on the flow displacing of the unit. A similar formulation was extended for a more generic case by Schweiger et al. [5], who included also a more detailed calculation for the internal leakages.

The rise in computational power saw a change in the modeling of a Gerotor unit. Studies of Gerotor units based on commercial CFD tools started to appear highlighting the possibility of showing more detailed flow features such as the work of Gamez-Montero et al. [6] and Altare and Rundo [7]. Simulation time can represent a limit for CFD simulation approaches for optimization studies involving numerous design parameters. Moreover, the need for a continuous fluid domain implies the impossibility of reproducing actual contacts between the rotors.

The recent study by Pellegri et al. [8] has shown a comparison between CFD, lumped parameter model and experimental results showing a close match between experimental, CFD and lumped parameter based model results for different operating conditions. In another research study, Pellegri et al. [9] illustrated the effect of rotor micro-motion on the prediction and experimental validation of flow pulsation and pressure ripple results with an advantage of having lower computational time when compared with traditional CFD based approaches. This study sets a very important base for the current research work as it shows that lumped parameter models are computationally inexpensive when compared to CFD based approaches and can be easily coupled with dynamic models to permit the study of micro-motions of the internal parts.

Much effort was also put by researchers into modeling the fluid dynamics of the Gerotor but less into the contact mechanics of the unit. In this regard, a significant work is the one published by Gamez-Montero et al. [10] where the authors studied the force transmission between the rotors assuming contact at multiple points, comparing an analytical approach for the evaluation of the contact stress between the teeth with a finite element approach under a quasi-static condition. This approach has its limitation that FEM method requires very high computational time and therefore limits its applicability to dynamics models.

However, there is still a gap in the numerical prediction of the torque loss that affects the hydromechanical efficiency of a Gerotor.

Moreover, the pulsation of the shaft torque, which can affect the sizing and functioning of the prime mover, is a parameter still challenging to determine. This paper tackles these challenges, building upon the model first presented by Pellegri et al. [9], by modeling the possibility of multiple contact points in a Gerotor unit and modeling frictional losses at those contact points using EHL formulation [11]. The model described in the present work includes online coupling of the lumped parameter model with lubricating interfaces with the capability of exchanging flows and imparting forces on the gears including the two-dimensional motion of the gears. Experimental results were also used to permit a fair validation of the simulation results and prove the potentials of the model for accurate studies of Gerotor units.

The following sections of the paper describe the different modules of the proposed model. Section 2 describes the simulation model developed by the authors elaborating on different sub-modules. Section 3 shows a comparison of the current model with experimental results for the torque ripple and overall torque for a simulated Gerotor unit with varying operating conditions.

2. GEROTOR SIMULATION MODEL

The model is primarily divided into two major groups i.e. Preprocessor Module and HYGESim: Hydraulic Gear Simulation Tool as shown in **Fig. 4.** The HYGESim tool will be discussed prior to the preprocessor modules as it would provide the necessary insight for understanding the preprocessor modules. The fluid-dynamic module and a portion of the force module were already published in the references [8, 9] but a brief explanation is provided here for completeness. Instead, the other modules represent the novel content of this paper.

The HYGESim tool consists of four major sub-modules. First, a fluid dynamics module is based on a lumped parameter approach that is used to evaluate the displacing action of the tooth space chamber and the main flow through the unit. The information of pressure evaluated by the fluid-dynamic module is passed to a forces module which evaluates the instantaneous forces acting on both rotors. The novel aspect of this model with respect to a first formulation published by the authors in [9] is that the module now relaxes the assumption of a single contact point that was previously made. Another novel aspect is the inclusion of Elasto-Hydrodynamic equations at the contact location. Accurate modeling of the radial and lateral surfaces is also important as they have an impact on torque losses

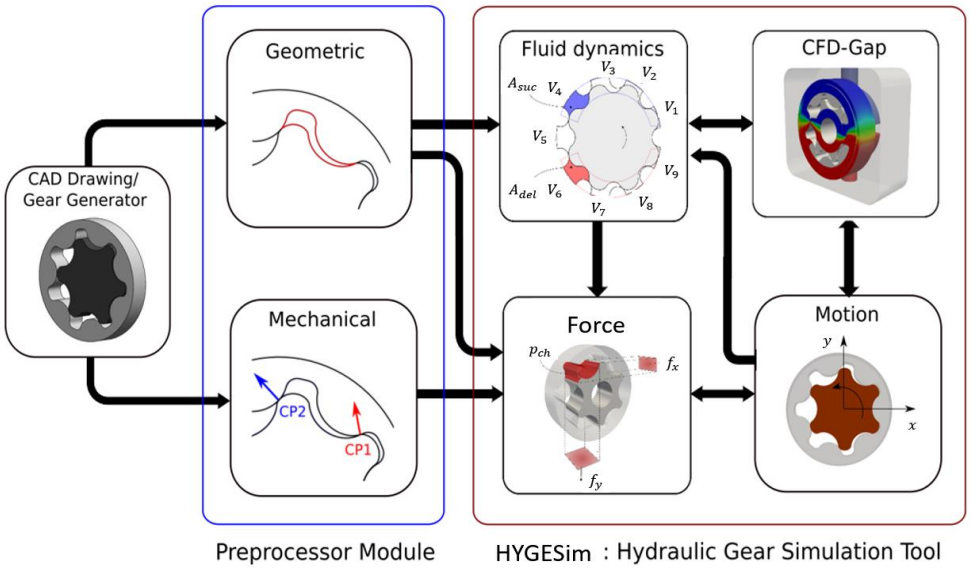

Figure 4: Structure of Gerotor simulation tool

and fluid leakages. The radial gap and lateral gaps are modeled using CFD-Gap module which solves the Reynolds equation in the film to apply forces to the gears and apply leakages to the connected chambers. All the forces and moments are applied to the gears and are integrated using Newton's laws of motion for a rigid body to generate the position and velocity for the next time step. The HYGESim tool requires a detailed calculation of several geometrical features based on both the rotors' position, a task performed by the geometric module and the mechanical preprocessor module. These modules can read the CAD file details of the unit and pass the information to the HYGESim tool.

2.1. Fluid Dynamics Module

The fluid dynamics module represents the core of the proposed simulation tool since all other modules rely on the correct prediction of the pressure distribution in the TSVs. The TSVs have the same properties such as density, pressure, etc. This is the essence of a Lumped Parameter Model. The choice of a lumped parameter approach for this module allows for fast computations and permits easy interfacing with the other sub-modules. The layout of the connections can also be represented with the schematic of **Fig 5**. The connections between the different Control Volumes (CVs) as well as between CVs and inlet/outlet ports are treated as variable orifices. The instantaneous values for the CV volumes, the flow area and the equivalent diameter for all the connections are evaluated as a function of the instantaneous shaft angle and the positions of the rotor, by the geometric pre-processor module as it will be clarified in Section 2.5.

Based on the flow between adjacent CVs, mass conservation and fluid state equations, the variation of the pressure p_i inside each CV with respect to time is determined through the pressure build-up equation:

$$\frac{dp_i}{dt} = \frac{1}{V_i}\frac{dp}{d\rho}\Big|_{p=p_i}\left[\sum \dot{m}_{in,i} - \sum \dot{m}_{out,i} - \rho|_{p=p_i}\frac{dV_i}{dt}\right] \quad (with\ i = 1, 2 \ldots . n) \tag{1}$$

In Eq. (1) V_i represents the instantaneous volume of the i^{th} CV. It can also be noted that the bulk modulus $\frac{dp}{d\rho}|_{p=p_i}$ depends on the fluid properties, particularly on the p_i the pressure of the i^{th} chamber.

The mass flow entering and leaving each CV ($\dot{m}_{\text{in}}$ and $\dot{m}_{out}$ terms in Eq. 1), is evaluated using

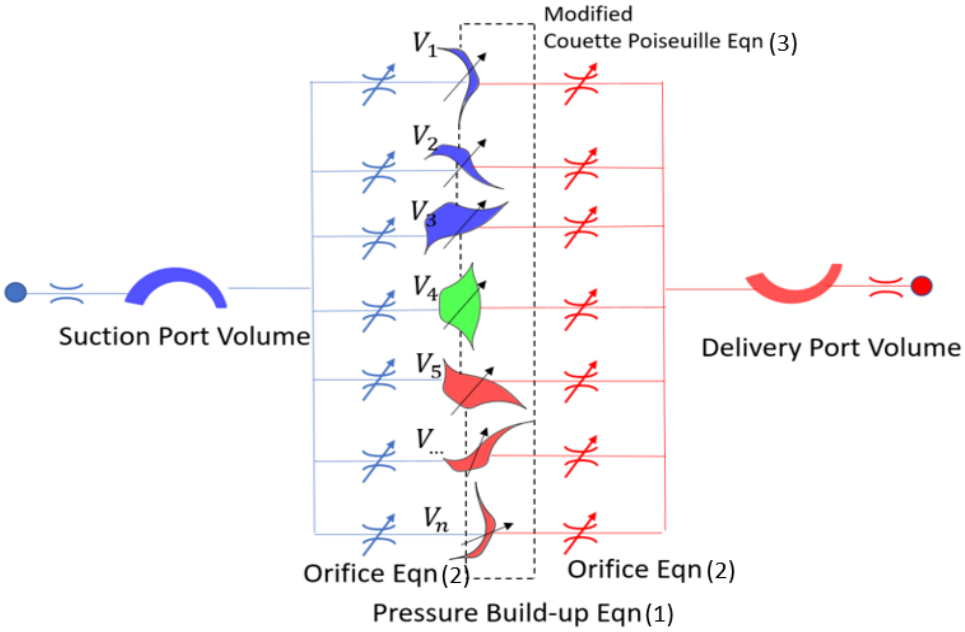

Figure 5: Representation of the control volumes and of the internal connections

two different approaches: for the connection between each CV and the inlet/outlet ports the orifice equation with a variable flow coefficient α [13] has been used, to account for both the laminar and turbulent regimes. The mass flow rate equation is as follows:

$$\dot{m} = \frac{p_i - p_P}{|p_i - p_P|} \cdot \rho|_{p=\overline{p_{i,P}}} \cdot \alpha \cdot A_{i,P} \cdot \sqrt{\frac{2.(p_i - p_P)}{\rho|_{p=\overline{p_{i,P}}}}} \quad (2)$$

Here, the orifice flow coefficient α is a function of Reynolds Number (Re), which is described in [13].

The inter-teeth connection between the different CVs, given by the radial clearance between the rotors (Fig 4.), is treated assuming laminar flow conditions. In the model, the modified Poiseuille equation derived by [14] based on the radius of curvature and gap height (evaluated in Section 2.6) that includes the Couette flow term is used,

$$\dot{m} = \rho \left[\frac{0.0456 b h_t^{2.4836} \Delta p}{\mu R_{eq}^{0.4836}} + \omega_{outer} \cdot 2\pi \cdot r_{outer} \cdot \frac{h_t}{2} - \omega_{inner} \cdot 2\pi \cdot r_{inner} \cdot \frac{h_t}{2} \right] \cdot b \quad (3)$$

2.2. Force Module

Force module evaluates all the forces and moments each gear is subjected to. This module is sub-divided into two sections: the forces due to fluid pressure (already described in the previous work [9]) and the forces due to contact, evaluated using contact mechanics relations including the effects of Elasto-Hydrodynamic Lubrication.

Fluid Pressure Force

The evaluation of the forces and moments acting on the rotors is based on the instantaneous pressure distribution, given by the pressures in the TSVs, calculated by the fluid dynamic module described in the previous section. The details of this sub-section have been published by Pellegri et. al [9] where for every displacement chamber, the areas of influence of the pressure with respect to the Cartesian coordinates are considered (**Fig. 6**). **Figure 6** illustrates that the forces F_x and F_y, can be evaluated using areas Ω_{zy} *and* Ω_{zx}, which assumes a constant pressure, $p_i(\theta)$ inside a TSV. The formulation with X_i and Y_i can be used to evaluate the moment contribution on each rotor. Based on this, the necessary forces and moments are calculated on each gear.

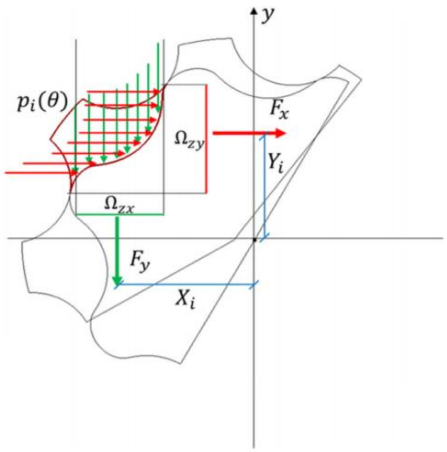

Figure 6: Evaluation of forces and torques [9]

Contact Force

The contact forces F_c, as well as the angle of action θ for each tooth is evaluated based on the look-up table supplied by the mechanical module which will be explained in detail in section 2.6. The contact forces and moment are added to both the gears as shown in **Fig. 7**. Therefore, the net force and moments on the inner gear can be evaluated as follows:

$$Net\ F_{x,C} = \sum_{i=1}^{n} \mathrm{F_{C_i}} \cos(\theta_i) \quad (4)$$

$$Net\ F_{y,C} = \sum_{i=1}^{n} \mathrm{F_{C_i}} \sin(\theta_i) \quad (5)$$

$$Net\ M_{z,C} = \sum_{i=1}^{n} -\mathrm{F_{C_i}} \cos(\theta_i) \cdot y_{C_i} + F_{C_i} \sin(\theta_i) \cdot x_{C_i} \quad (6)$$

Based on the above equations, all the forces and moments are summed vectorially, to get acceleration of the rotors which are integrated into the Motion module which will be discussed in Section 2.4.

Once the normal contact forces at each location are evaluated, the friction coefficient is evaluated assuming Elasto-Hydrodynamic Lubrication (EHL) at the contact points. The relation published by Hamrock [11] is used:

$$\overline{\mu_1} = 0.67 \cdot 10^{-6} \cdot (U^*)^{0.81} \cdot U^{0.26} \cdot (W \cdot G^2)^{3.32} \text{ when } \overline{\mu_1} \leq 0.8\gamma \quad (7)$$

$$\bar{\mu} = 0.8\gamma + 0.021 \cdot \tanh\left(\frac{\overline{\mu_1}}{\gamma} - 0.8\right) \text{ when } \overline{\mu_1} > 0.8\gamma \quad (8)$$

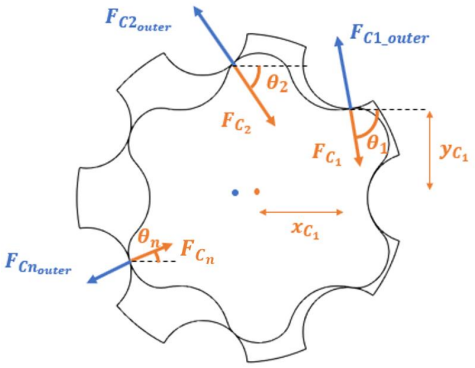

Figure 7: Illustration of forces acting on the gear

2.3. CFD-Gap Module

The CFD-Gap Module solves the Reynolds equation in the lubricating interfaces presented earlier (Fig. 3). The radial gap acts like a journal bearing generating resistive loads to support the outer rotor. The CFD-Gap module solves the Reynolds equation by defining a generic polar grid for the two surfaces. The general Reynolds equation where the fluid film is enclosed by a bottom surface "a" and a top surface "b" is written as follows [16]:

$$\frac{\partial}{\partial x}\left(\frac{\rho h^3}{12\mu}\frac{\partial p}{\partial x}\right)+\frac{\partial}{\partial y}\left(\frac{\rho h^3}{12\mu}\frac{\partial p}{\partial y}\right)=\frac{\partial}{\partial x}\left(\frac{\rho h(u_a+u_b)}{2}\right)+\frac{\partial}{\partial y}\left(\frac{\rho h(v_a+v_b)}{2}\right)+\rho(w_a+w_b)-\rho u_a\frac{\partial h}{\partial x}-\rho v_a\frac{\partial h}{\partial y}+h\frac{\partial \rho}{\partial t} \quad (9)$$

The Reynolds equation approximates the full Navier-Stokes equations when considering thin fluid films. The boundary conditions are pressures set by each tooth space volume for the lateral gap. And for the radial gap, wall boundary conditions are applied which is proved to be a good assumption as proved by Pellegri et al. [15]. Based on these boundary conditions, the CFD-Gap module applies forces and moments to the gears and outputs flows into and out of the different fluid domain.

2.4. Motion Module

The motion module evaluates the position of the gears based on the forces and moments acting on the gears from the force module, fluid-dynamic module and the gap module using Newton's six degree of motion dynamics equations, where the forces and moments acting on the gears gives acceleration of the gear and angular acceleration of each gear with respect to its center of mass. These accelerations are integrated to get velocities and angular velocities which are further integrated to get the position of the gears for the next time step.

2.5. Geometric Module

The geometric module is an essential pre-processor for all the modules of the simulation tool. This module evaluates features that are necessary for evaluating fluid-dynamic properties of a Gerotor i.e. DC volume, porting areas, etc. This module is entirely based on numerical calculation performed on the CAD files (in TXT or STL format) of rotors and of the inlet and outlet ports. Therefore, the model does not require a specific analytical definition of the rotor profiles. The output of the model is given in the form of TXT files that constitute the input for the HYGESim tool. This text file contains the geometrical features, as a function of the rotation angle of the rotors. All the essential features of the geometric preprocessor module are run for the varied position of the outer gear and features such as the tooth space volumes, porting areas are output into a text file.

2.6. Mechanical Module

The mechanical module is also one of the pre-processor modules used for accessing contact loads on the Gerotor. Due to radial clearances present between the outer rotor and the body, the outer gear has some degree of freedom in the planar direction which needs to be accounted for.

The mechanical module takes as input the profile of the inner and outer gear of a Gerotor and based on that evaluates the contact forces. It simulates various positions of the outer gear with varying planar displacement and angle micro-motion. In this simulation, there could be cases when at a certain position the outer gear profile (which is defined by points) can intersect the inner gear profile. At these locations, the module evaluates the penetration depth. Gap heights are evaluated if there aren't any intersections. This is illustrated by **Fig. 8**.

The contact forces are evaluated based on the research article published by Pereira C. [12], where the contact is modeled locally as an

intersection of two cylinders and depends on the local radius of curvature and the penetration depth. The following equation is used:

$$F_C = \frac{(a\Delta R+b)LE^*}{\Delta R}\delta^n\left[1+\frac{3(1-c_r^2)}{4}\frac{\dot{\delta}}{\dot{\delta}^{(-)}}\right] \quad (10)$$

Where a and b are constants described in the paper [12], c_r represents the coefficient of restitution. δ represents the depth of penetration, $\dot{\delta}$ represent the penetration velocity and $\dot{\delta}^{(-)}$ is the impact velocity.

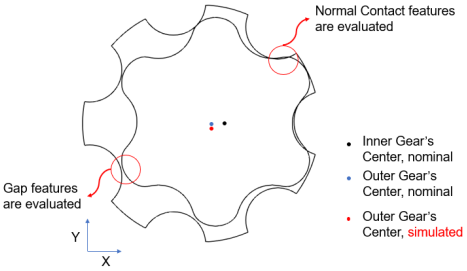

Figure 8: Gap height and Normal Contact feature evaluation

3. EXPERIMENTAL VALIDATION

In this section, results obtained by the proposed modelling scheme are compared with experimental measurements for the unit shown in **Fig. 7**. **Figure 9** shows the profile of the inner and the outer gear of a 6/7 tooth cycloidal gearset with suction and delivery ports shown in red and blue respectively which was used as a prototype unit for testing by Thomas Magnete GmbH. The schematic of the experimental setup is shown in **Fig. 10**. An orifice connected to a line was used in the experiment as a loading element. This helped to easily reproduce pressure pulsations for validation of the model. The measurements were taken for steady-state operating conditions. A comprehensive result showing the validation of pressure as well as torque ripple is shown in the following paragraphs. The units of all the results have been normalized for confidentiality reasons.

The model is simulated with a radial clearance between outer rotor and housing, to match the clearance in the experiments which allow for micro-motions of the outer gear. Experiments were performed at various shaft speeds and pressure differentials. The case with 19.18% of the maximum tested shaft speed (n_{max}) and the maximum tested pressure drop (Δp_{max}) is considered for illustration purposes.

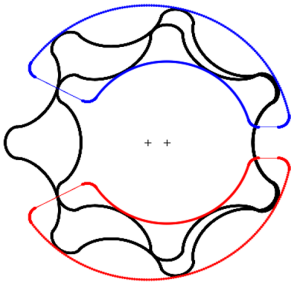

Figure 9: Cycloidal Gerotor Gear

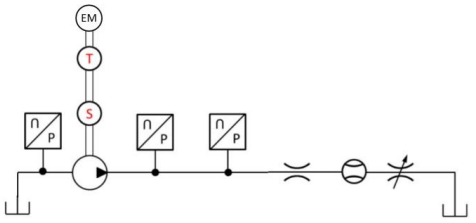

Figure 10: ISO schematic and Test Rig

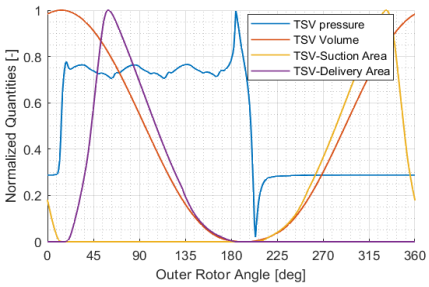

Figure 11: Normalized TSV pressure, volume and porting area with a rotational angle of the outer rotor

Figure 11 shows different normalized quantities for one of the TSV with respect to the angle of the outer rotor. The TSV expands when connected to the suction while it contracts when connected to delivery, thus displacing fluid. The figure also shows pressurization and depressurization of a TSV.

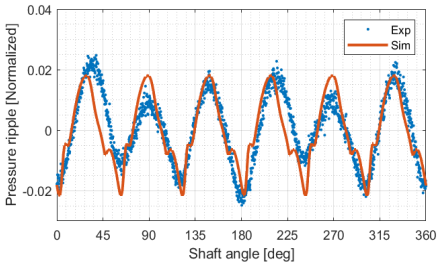

Figure 12: Comparison between experimental and simulated pressure ripple

Figure 12 shows the pressure ripple behavior of the pump at the chosen operating condition. Based on this, there is a very close match of the magnitude of the pressure ripple between the experimental results and the simulated.

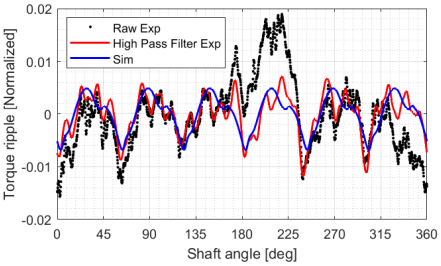

Figure 13: Comparison of torque ripple data of experiment vs simulated

Figure 13 shows a comparison of torque ripple between experimental data and simulated. The raw experimental data was filtered using a high pass filter to avoid any effects of shaft whirling or improper centering of the shaft. Once, the whirl frequency if removed, a very close match in the actual torque ripple magnitude is obtained. The source for the peak for raw experimental data in the range of 180° to 225° is due to the shaft misalignment.

Figure 14 shows a comparison of the torque obtained by simulation with ideal torque, and when the subsequent contribution of Gaps (radial and lateral) with contact friction following at the very end. These plots are also compared with the single contact point theory. It can be observed that in this operating condition the Gaps have a huge impact on the overall torque followed by the EHL effects at the contact location. The final torque is also compared with the single contact point assumption which ascertains that when evaluating torque ripple multiple contact points must be taken into consideration.

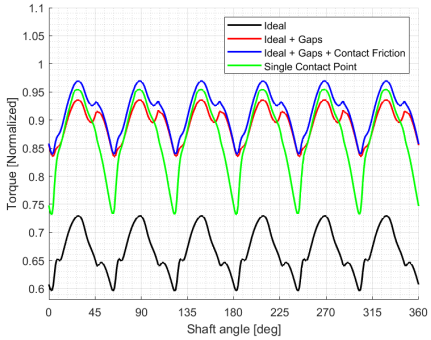

Figure 14: Distribution of torque, showing torque losses due to Gaps and Contact Friction and comparing with single contact point theory

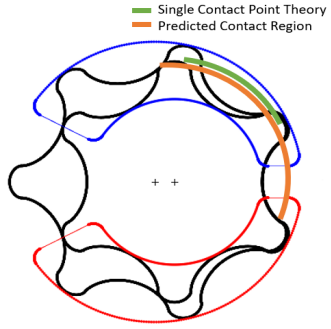

Figure 15: Angular span of predicted contact region versus single contact point theory

Figure 15 shows a comparison between the predicted angular region of contact by the current model versus single contact point theory. It can be observed that the predicted angular region of contact is nearly twice as that of the single contact point theory.

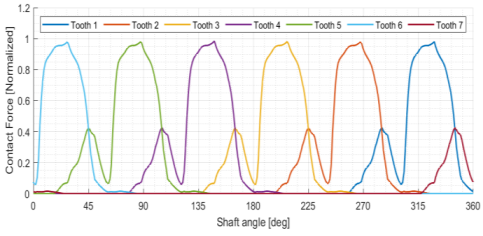

Figure 16: Contact forces by each tooth with respect to shaft angle

Figure 16 shows the variation of the contact force by each tooth. It is observed that at any shaft angle the contact force is applied by at least two different teeth and sometimes three. Therefore, this gearset has two contact points for the operating condition.

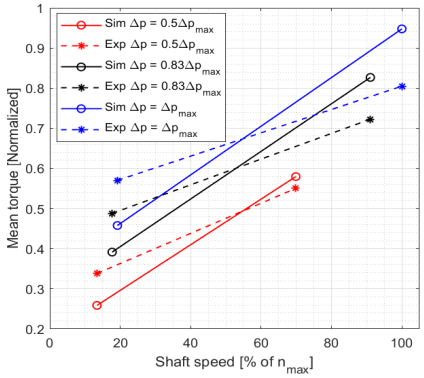

Figure 17: Comparison of mean torque with different operating conditions

Figure 17 compares the mean torque of experimental setup and simulated at different operating conditions. It can be observed that with an increase in rotational speed keeping the same pressure drop increases the mean torque. This general trend is matched by the simulation. But there are discrepancies which could have been caused by the asymmetric behavior of the lateral gaps which are on either side of the gears which is not accounted for in this study.

4. CONCLUSION

This paper presented a novel formulation of a Gerotor modeling tool. The Gerotor model is based on a fast lumped-parameter based approach which discretizes the Gerotor into a set of tooth space volumes that have the same properties inside a lumped volume. The model also considers the possibility of multiple contact points that drive the outer rotor with the presence of the radial gap that supports the outer rotor. The model solves for the Reynolds equation for the lubricating interfaces and Elasto-Hydrodynamic Lubrication (EHL) at the contact locations. It also solves for instantaneous micro-motion of the gears inside the body.

The results of the simulation are compared against that of the experiments. Within the research, experiments were performed for a 6/7 tooth Cycloidal prototype Gerotor unit. Steady-state tests performed with the experiments allowed a comparison of simulation and experiment.

The results show a good correlation between the simulations and experiments outlet pressure pulsations. With the inclusion of multiple contact points, friction at the contact points and radial gap for the outer rotor, a good correlation is obtained for the shaft torque ripple.

NOMENCLATURE

A	Area, m^2
E	Modulus of Elasticity, N/m^2
EHL	Elasto-Hydrodynamic Lubrication
E'	Effective elastic modulus, $\frac{2}{\left[\frac{1-\nu_a^2}{E_a}+\frac{1-\nu_b^2}{E_b}\right]}$, N/m^2
F	Force, N
F_C	Contact Force, N
G	Dimensionless Material Parameter, $\alpha E'$
R	The radius of Curvature, m
R_{eq}	Equivalent Radius of Curvature, $\frac{1}{\frac{1}{R_a}+\frac{1}{R_b}}$, m
TSV	Tooth Space Volume
U^*	Dimensionless sliding velocity, u_d/u_s
U	Dimensionless speed parameter, $\mu_0 u_s/E'R$
W	Dimensionless load parameter, $F_s/bE'R$
b	The face width of the Gears, m
h	Height, m
h_t	Height of the tooth tip gap, m
p	Pressure, Pa
u	Velocity in x-direction, m/s
u_d	Velocity difference, $u_a - u_b$, m/s
u_s	Velocity sum, $u_a + u_b$, m/s
v	Velocity in y-direction, m/s
w	Velocity in z-direction, m/s
μ	Friction Coefficient
μ_0	Absolute Viscosity
γ	Limiting-shear-strength proportionality constant
ν	Poisson's ratio
ρ	Density, kg/m^3
ω	Rotational Speed, rad/sec
θ	Angle, rad

REFERENCES

[1] Bonandrini G, Mimmi G, Rottenbacher C (2009) Theoretical analysis of internal epitrochoidal and hypotrochoidal machines. Proc Inst Mech Eng Part C J Mech Eng Sci 223(6):1469–1480

[2] Mimmi G, Bonandrini G, Rottenbacher C (2007) Theoretical analysis of internal lobe pumps. IFToMM World Congress
[3] Manco S, Nervegna N, Rundo M (2002) A contribution to the design of hydraulic lube pumps. Int J Fluid Power 3(1):21–32
[4] Manco S, Nervegna N, Rundo M, Torino P, Armenio G, Pachetti C, Trichilo R Gerotor lubricating oil pump for ic engines (1998) SAE Paper 982689, International fall fuels and lubricants meeting and exposition, San Francisco, USA and SAE Transactions
[5] Schweiger W, Schoefmann W, Vacca A (2011) Gerotor pumps for automotive drivetrain applications: a multi-domain simulation approach GRPs in AWD-powertrain systems. SAE Int J Passeng Cars Mech Syst 4(3):1358–1376. DOI:10.4271/ 2011-01-2272
[6] Gamez-Montero P-J, Castilla R, del Campo D, Erturk N, Raush G, Codina E (2012) Influence of the inner teeth clearances on the flow ripple in a gerotor pump for engine lubrication. Proc Inst Mech Eng Part D J Automob Eng 226(7):930–942
[7] Altare G, Rundo M (2015) CFD analysis of gerotor lubricating pumps at high speed: geometric features influencing the filling capability. ASME/BATH Conf 2015:1–10
[8] Pellegri M, Vacca A, Frosina E, Buono D, Senatore A (2017) Numerical analysis and experimental validation of Gerotor pumps: A comparison between a lumped parameter and a computational fluid dynamics-based approach. Proc IMechE Part C Vol. 231(23) 4413–4430
[9] Pelligri M, Vacca A (2017) Numerical simulation of Gerotor pumps considering rotor micro-motions. Meccanica (2017) 52:1851–1870
[10] Gamez-Montero PJ, Castilla R, Khamashta M, Codina E (2006) Contact problems of a trochoidal-gear pump. Int J Mech Sci 48:1471–1480
[11] Jacobson B O, Hamrock B J (1984) Non-Newtonian Fluid Model Incorporated Into Elastohydrodynamic Lubrication of Rectangular Contacts. J. Tribol. Apr 1984, 106(2): 275-282
[12] Pereira C., Ramalho A., Ambrosio J. (2015) An Enhanced Cylindrical Contact Force Model, J. Multibody Syst Dyn, 35: 277
[13] LMS Imagine SA (2015) Hydraulic library, User Manual, Rev 14
[14] Rituraj F, Vacca A. (2019) Modelling and Validation of Tooth Tip Leakages in Gerotor Pumps. Proceedings of the ASME-JSME-KSME 2019 Joint Fluids Engineering Conference AJKFLUIDS2019
[15] Pellegri M, Vacca A (2017) A Simulation Approach for the Evaluation of Power Losses in the Axial Gap of Gerotor Units. JFPS International Journal of Fluid Power System 11-3, 55/62, 2018
[16] Reynolds O (1886) On the Theory of Lubrication and Its Application to Mr. Beauchamp Tower's Experiments, Including an Experimental Determination of the Viscosity of Olive Oil. Philosophical Transactions of the Royal Society of London. Royal Society. 177: 157-234. doi:10.1098/rstl.1886.0005. JSTOR 109480

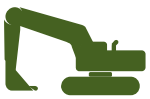

GROUP I | L

Mobile applications

peer reviewed

OPTIMIZATION OF HYDROSTATIC-MECHANICAL TRANSMISSION CONTROL STRATEGY BY MEANS OF TORQUE CONTROL

M. Sc. Yusheng Xiang*, Dr. Steffen Mutschler, Dipl.-Ing. Norman Brix, Dr. Christine Brach, Prof. Dr. Marcus Geimer

Department of system engineering, Bosch Rexroth AG, Glockeraustr. 2, 89275 Elchingen, Germany
* Corresponding author: Tel.: +49 17672361970; E-mail address: Yusheng.xiang@boschrexroth.de

ABSTRACT

The combination of hydrostatics and mechanical gearboxes cannot only improve system efficiency but also the usability of mobile machines. A possible solution could be a synchronized gearbox with two gears. Compared to the pure hydrostatic drivetrain, mobile machines with such a combination can have a larger drive torque with the first gear and higher efficiency at high speed. However, the calibration effort of this traditional drivetrain system is enormous; moreover, with a flow-based control, the degrees of freedom to achieve optimum shift performance in all conditions are limited. By adopting the primary torque control concept, we propose a novel hydrostatic-mechanical drivetrain control algorithm so that the holistic shift performance is better whilst the calibration effort is dramatically reduced by systematically adjusting only one hyper-parameter. Experienced engineers and machine operators validated the advantages mentioned here by a series of field experiments. Besides synchronized gearboxes, the controller proposed in this paper is also generalized to other kinds of mechanical transmissions.

Keywords: primary torque control, hydrostatic-mechanical transmission, control strategy, mobile machine

1. INTRODUCTION

The combination of hydrostatic and mechanical gearboxes cannot only improve system efficiency but also the usability of mobile machines. A possible choice could be a synchronized one with two gears. **Figure 1** illustrates the hydrostatic-mechanical drivetrain solution. Instead of directly connecting a hydraulic motor to the vehicle axle, a synchronized gearbox is installed between them. With such a drivetrain system, mobile machines can have two different drive ranges, such as a torque range and a speed range, with only one hydraulic motor. Due to favourable cost in comparison with multi-motor solutions, hydrostatics with synchronized gearbox dominates the market for medium-sized mobile machines with high speed capability up to 40 km/h. However, this successful drivetrain solution is rarely mentioned in academia. The main challenge is that current control solutions commonly adopt a flow-based approach resulting in complex control algorithms for the operation of the hydrostat and synchronizer actuators. Although a flow-based hydrostatic-mechanical transmission control strategy is well proven on the market, it still can be further optimized for simplicity resulting in better calibration effort, shift management, and shift process performance. In this paper, we are going to propose an alternative control concept for the drivetrain system shown in **Figure 1.**

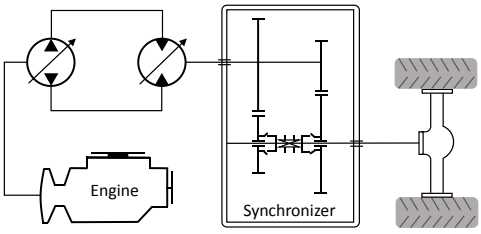

Figure 1: System layout of hydrostatics in combination with a synchronized gearbox

2. STATE OF THE ART

Currently, most of the mobile machines are equipped with hydrostatics or hydrodynamics transmissions [1]. Mobile machines with an

electric motor are typically only used in some special areas, such as a sealed working site.

The basic principle of a transmission with hydrodynamic torque converter on mobile machines is the same as the automatic transmission in passenger cars. Due to its smooth drive characteristic and thus relatively better drive comfort, hydrodynamics is still a preferable solution in North America and Asia [2].

By contrast, hydrostatics can decouple the engine rotational speed from vehicle velocity and torque so that the engine can theoretically work in its best efficient region resulting in a higher holistic efficiency up to 20% when combine with power split transmission [3, 4]. One major reason for this high consumption gap is the fact that, at low drive speed high engine speeds are needed for the implement hydraulics. If decoupling of both states is not given, excess drive torque from the engine is dissipated by the brake or in the torque converter.

As a consequence of that, torque control became one of the research trends for the hydrostatic drivetrain, which mainly aims at improving the drive comfort of hydrostatic mobile machines, reducing the application effort and introducing open, comprehensible software interfaces known from the automotive industry. At present, we can classify torque control into secondary control and primary control. **Figure 2** describes the definition of different control concepts, according to Murrenhoff [5, 6].

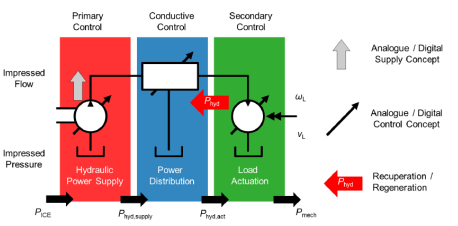

Figure 2: Fundamental structure of a mobile hydraulic system [6]

2.1. Secondary (torque) control

The concept of secondary control was brought forward in the 80's [7]. With more than 30 years of development, there are many variants of secondary control concept [8, 9]. However, the basic idea remains the same: the pressure is set to the desired level whilst the torque is controlled by the swivel angle of the motor.

A series of researchers have implemented secondary control in their applications. Among them, the most notable applications are STEAM for open circuit [10–12] and the concept proposed by Sprengel for closed circuit [13, 14]. Because the focus point of this paper is drivetrain, a more detailed description of STEAM is out of the scope.

Generally, a naive secondary controller uses the motor to control its drive direction and the torque outputted by hydraulic motor, resulting in a dilemma for mobile machine reversing. On the one hand, the swivel angle of hydraulic motor should be large so that the torque is large while approaching velocity zero. On the other hand, the hydraulic motor's swivel angle must go to zero to change its rotation direction. To solve this problem, Sprengel at Purdue University further developed the secondary drivetrain solution by adding a valve which allows the vehicle to smoothly change its drive direction. However, the system is complicated not only in hardware but also in software, compared to primary torque control.

We believe that secondary control is particularly useful for applications that make lots of reciprocating motion due to its excellent recuperation ability. However, in the case of mobile machines of which typical working process is reversing, secondary concept is still too expensive. As a light of that, we would like to go ahead with primary torque control.

2.2. Primary torque control

Primary torque control was first published in 2018 [2]. In contrast to secondary control, the primary torque controller controls the pressure instead of the motor swivel angle by adapting the pump swivel angle.

The advantages of this control algorithm are enormous. First and foremost, standard drivetrain components can be used and thus cost is lowered. Secondly, the swivel angle of the pump is always at a high level entailing a relatively lower energy loss. Thirdly, a constant motor can be used for this drivetrain. Fourthly, the pressure in the circuit is also adapted to the desired value and thus avoids system loss due to too high pressure. Last but not least, no accumulator is needed and therefore there is no risk of stored energy.

2.3. Synchronized gearbox for hydrostatic mobile machines and corresponding control algorithm

The success of this drivetrain mainly lies in the fact that it can shift without stopping the mobile machines [15]. The synchronized gearbox is slightly different from the standard manual gearbox on passenger cars: it does not have a neutral position. That is, either the first gear or the second is engaged. If there is still an active torque exerting on the input shaft during the shifting process, exactly in synchronization process, the destruction of the synchronizer is sure to ensue [16]. As a result of that, tractive effort is diminished to zero in order to shift the gear.

The-state-of-the-art hydrostatic-mechanical drivetrain solution uses a flow-based control concept. The first typical character is that the pressure inside of the closed-circuit is depended on the external load. The second is that the control variable is usually vehicle velocity or a rotational speed regard of vehicle velocity. For the sake of simplicity, we can summarize the control strategy as follows. The drive pedal controls the engine speed and the pump swivel angle resulting in the volume flow supplied by the hydraulic pump. In the meantime, the hydraulic motor is set to a certain angle depending on motor rotational speed. Consequently, the drive pedal determines the vehicle speed individually if the mechanical gear does not change. One disadvantage is that the desired velocity is set to different values with different gears which could cause a vehicle jerk during shifting with constant pedal position. The effect can be compensated with some additional software functionality; however, this leads to much higher calibration effort and more complicated control algorithms.

In the next section, we are going to describe a simple yet efficient control algorithm, which needs only little calibration effort while also has a better shift performance.

3. SHIFT CONTROL ALGORITHM

As mentioned above, during the synchronization process, the hydraulic motor should not produce an active torque. Formally, the torque can be calculated as

$$T_m = \frac{V_{g,max} \cdot \alpha_m \cdot \Delta p \cdot \eta_{me}}{2\pi} \quad 1$$

where T_m is the output torque of the hydraulic motor, α_m is the swivel angle of hydraulic motor, Δp is the actual pressure difference inside of the closed circuit, η_{me} is the mechanical loss coefficient. Here either the swivel angle or the pressure must be zero to enable the shifting process. Based on these two concepts, two control algorithms are proposed: swivel-angle based control algorithm (ABCA) and pressure-based control algorithm (PBCA). We firstly implemented both of them in Simulink. With a plant model in Amesim, the performance and feasibility of both algorithms are virtually validated based on basic requirements.

No matter which algorithm we use, the control scheme is the same, as shown in **Figure 3**. In order to simplify the complexity of the shift control system, we design the system, which uses 2-DoF-controller to reduce the calibration effort

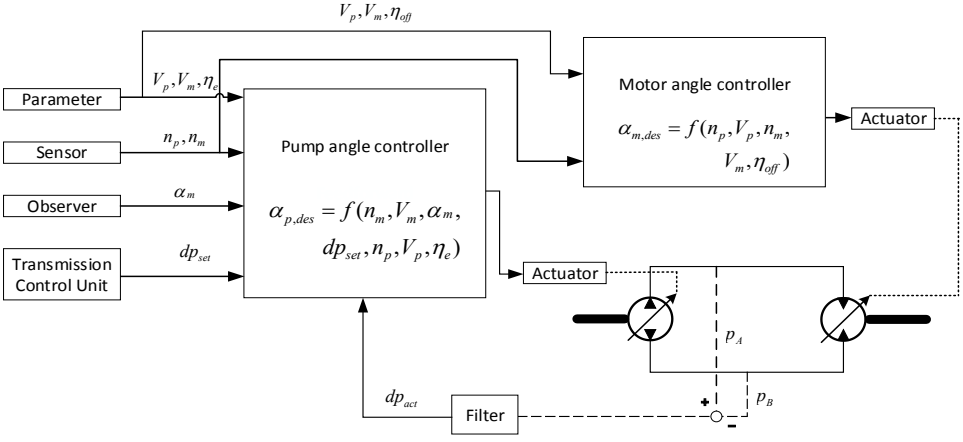

Figure 3: Novel control schema of the hydrostatic-mechanical drivetrain

having an interface so that engineers can systematically adjust the shifting performance with only one calibration parameter. Concretely, we adjust a time constant parameter in software sensor, which usually is used to estimate the motor angle. The time constant affects the output of observer and thus the compensation function of pump controller.

3.1. Pressure-based control algorithm

The basic idea of the pressure-based control algorithm is to adapt the pressure inside of the closed-circuit to zero so that the swivel angle of the motor can keep the same angle as before the shifting. Due to relatively higher dynamics, the shift duration is potentially shorter than the angle-based control algorithm if the pressure-based control algorithm is used.

Since the rotational speed of the hydraulic motor in the first gear is higher than that in the second gear at the same speed, the motor is accelerated during the synchronization process by downshifting. However, the swivel angle of the pump cannot always go up to compensate for the pressure change. Thus, for the downshifting process, a preparation step should be added to the entire shift process. Concretely, the swivel angle of the motor is reduced to a certain low level before synchronization process so that the swivel angle of the pump is also set to a lower level. The drive torque will not diminish since the pressure will correspondingly increase. **Figure 4** shows the control flow of shifting process with this algorithm.

Simulation result of PBCA

To study the feasibility of this concept, we built up a co-simulation environment in Simulink and Amesim. The parameters we used are chosen from the Bosch Rexroth A6 motor and A4 pump datasheet. The length of pipe plays no role in this simulation since we use torque control. We shift the gear at vehicle speed of 5km/h since it is the most common downshift speed. As visible in **Figure 5**, the pressure is reduced to zero and then the synchronization process occurs. In this way, the shift duration is even shorter than 1 second. However, the pressure is quite difficult to maintain at zero during the synchronization since this process is very quick. In this phase, the pump

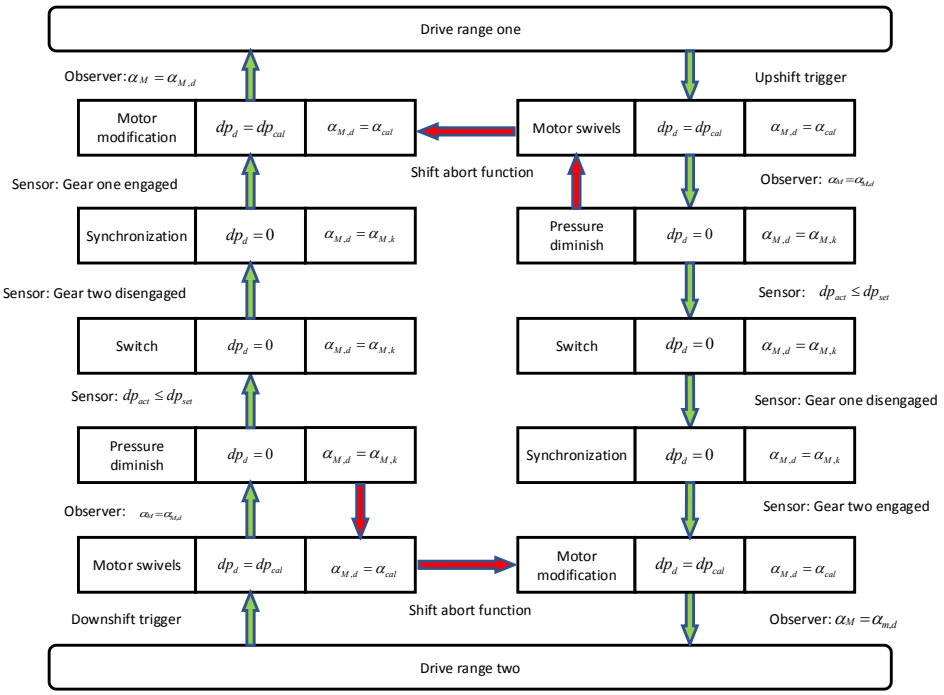

Figure 4: Control flow of Pressure based control algorithm

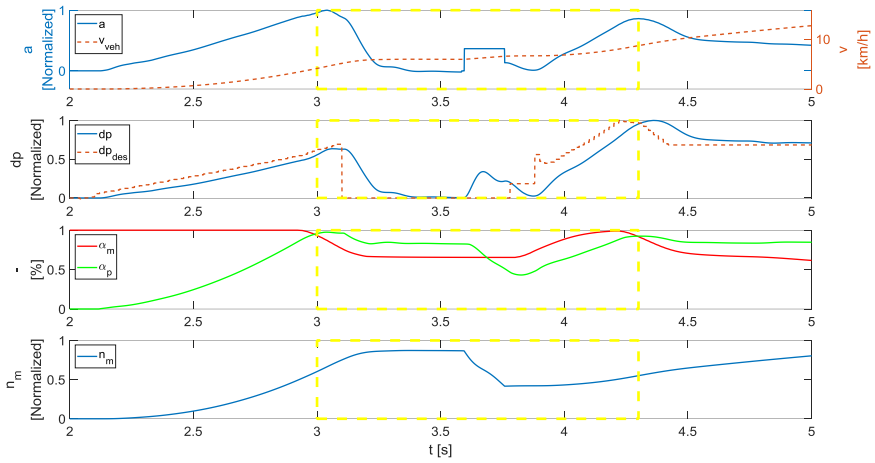

Figure 5: Simulation result of shifting with pressure based control algorithm

swivels back to compensate the effect due to the deceleration of the motor. Nevertheless, a pressure higher than 10 bar occurs, which will certainly damage the synchronizer. Moreover, we did the simulation at the vehicle speed of only 5km/h. Shifting at a higher speed with a larger rotational speed difference, the situation will exacerbate. Consequently, pressure-based concept might not be a viable solution or it needs further development. The shift process is demonstrated in the yellow rectangle.

3.2. Swivel-angle based control algorithm

By contrast, the swivel-angle-based control algorithm makes the motor swivels to its zero position. **Figure 6** demonstrates the flow of this control algorithm.

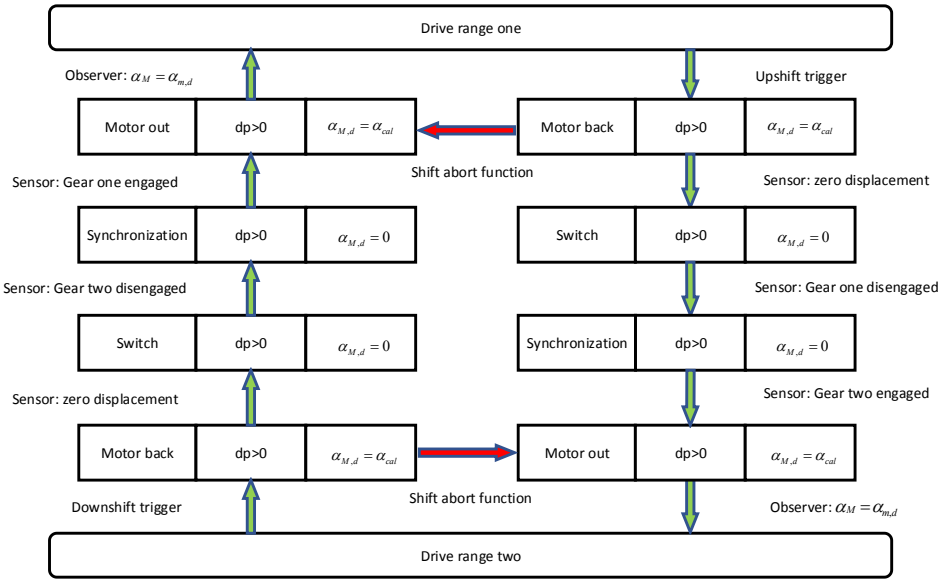

Figure 6: Control flow of angle based control algorithm

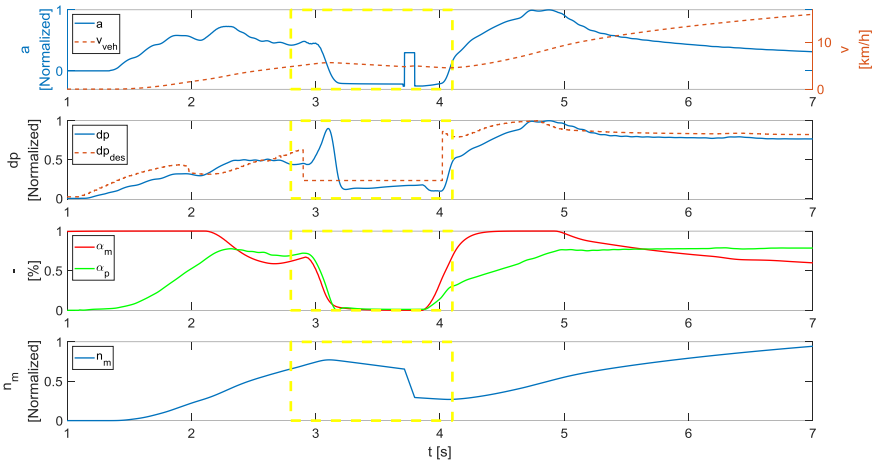

Figure 7: Simulation result of shifting with angle based control algorithm

Simulation result of ABCA

The simulation result in **Figure 7** shows that unlike pressure-based control, the pump has no burden within the synchronization phase. Thus, vehicle speed does not affect the shift performance except shift duration. A pressure peak occurs since the motor swivel back to zero position. Correspondingly, the pump also swivels back to an almost zero position. The desired pressure is set to a certain number in order to help the motor swivel faster. Based on the simulation results, we employed the ABCA concept.

4. SHIFT MANAGER

A complete shift function shall not only include a mature shift process but also a reasonable shift manager who determines when the machine shall change its gear.

The original purpose of designing hydrostatics with a synchronized gearbox was this: with the first gear, the machine can have higher torque whilst with the second gear, the machine can drive faster than pure hydrostatics. Furthermore, the energy loss can be considerably reduced. However, the additional synchronized gearbox makes the drivetrain no longer a continuous drivetrain. This may especially be critical with an automatic shifting function. If the vehicle shifts at an unwise situation, it may cause an unexpected accident due to the drive force interruption. For instance, if a machine drives uphill at a low speed, the machine may roll down because of the shifting. To avoid these hazardous events, a shift-prevent function and shift-protection function is designed, see **Figure 8**. The shift-prevent function rejects the unwise shift trigger based on the sensor signal, while the shift-protection function aborts the shifting process whenever the situation is no longer suitable for shifting. The difference of both functions is based on the fact that the shifting process needs about one second, and the situation may change within this one second.

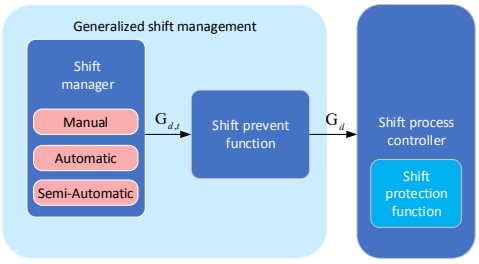

Figure 8: System architecture of shift function

For the novel-drivetrain control system, we suggest an automatic and a semi-automatic shift manager.

Shift manager: Efficiency based

The energy loss of the hydraulic system can be derived from some basic rules. Generally, swash plate pumps have a higher loss than bent axis motors. The principal factors to calculate loss of

hydraulic systems are rotation speed, pressure, and swivel angle [17]. From an efficiency perspective, a mechanical gearbox can undoubtedly give the system the potential to improve its efficiency by selecting the gear ratio appropriately. According to e.g. Ivantysyn and Ivantysynova, the loss model of hydraulic components can be mainly illustrated by the following equations [18].

$$Q_V = \sum_{i=0}^{f_1}\sum_{j=0}^{f_2}\sum_{k=0}^{f_3} K_{Q,kji} \cdot n^i \cdot V_i^j \cdot \Delta p^k \qquad 2$$

$$M_V = \sum_{i=0}^{f_1}\sum_{j=0}^{f_2}\sum_{k=0}^{f_3} K_{M,kji} \cdot n^i \cdot V_i^j \cdot \Delta p^k \qquad 3$$

Predominantly, the impact factors, such as the rotational speed of hydraulic motor and pressure, have a positive correlation with energy loss. In contrast, the swivel angle has a negative correlation with efficiency. In the first gear, the rotational speed of hydraulic motor and swivel angle of the pump are higher while the pressure inside of closed circuit and swivel angle of motor are lower compared to the second gear if we need to produce the same drive torque at the same vehicle speed. To optimize the efficiency by using appropriate gear selection, we calculate the loss with the different gears in advance and then choose the gear that has been considered as lower energy loss. The basic idea here is that we first measure the loss of hydraulic components and after that, we build an approximation model whose prediction of loss is similar to reality. Based on the estimation of energy loss by approximation model, a gear selector will output the appropriate gear.

Shift manager: Semi-automatic shift strategy

In contrast to the efficiency-based shifting manager, a semi-automatic shift strategy is recommended. One disadvantage of automatic shift function is the somehow unpredictable shift events leading to an unsafe feeling. With semi-automatic shift strategy, as shown in **Figure 9**, there are two regions where the shift manager will send the shift request.

Outside of these two regions, for example, at the place where the circle is, the machine will retain its current gear. By applying this strategy, the driver can easily operate between maximum drive torque with second gear or downshift to first gear since there is a large error space between them, providing a much better psychological safety. The dashed line shows the border to achieve a maximum drive torque with the second gear. Beyond this dashed line, for example, at place where pentagon is, the power manager limits the request from the drivetrain solution. Therefore, no additional energy loss occurs.

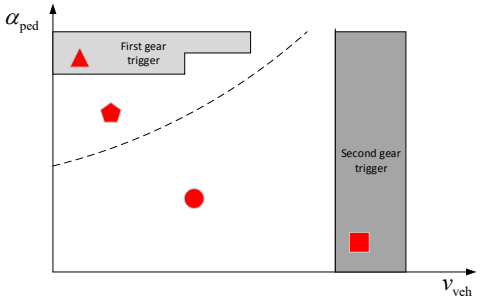

Figure 9: Semi-automatic shift algorithm

5. VEHICLE MEASUREMENT

The test machine is a 10t hydrostatic wheel loader with a synchronized gearbox. In this section, we will only experimentally validate the swivel-angle-based solution, which is considered as a more feasible solution based on the simulation, on our wheel loader.

Most of the "innovations" shows that they have a better performance than state-of-the-art solution, but they have an advantage only in some instances but lose the total competition compared to mass production. Certainly, a real innovation should always have a better performance, or at least in the most common cases. In this section, we consciously show the test results for the most common use case, shifting at speed of 5 and 14 km/h. Moreover, intensive tests are running in all use cases to ensure the robustness of the solution.

5.1. The criteria

The criteria can be summarized as follows:

- The shift duration must be as short as possible. Since mobile machines usually drive on the site, and the road is unsmooth, an extended drive force interruption may cause a roll down situation, and thus a shorter duration can avoid many problems.
- Usually, the driver triggers a downshift because they need more tractive effort, and the vehicle is at low speed. Therefore,

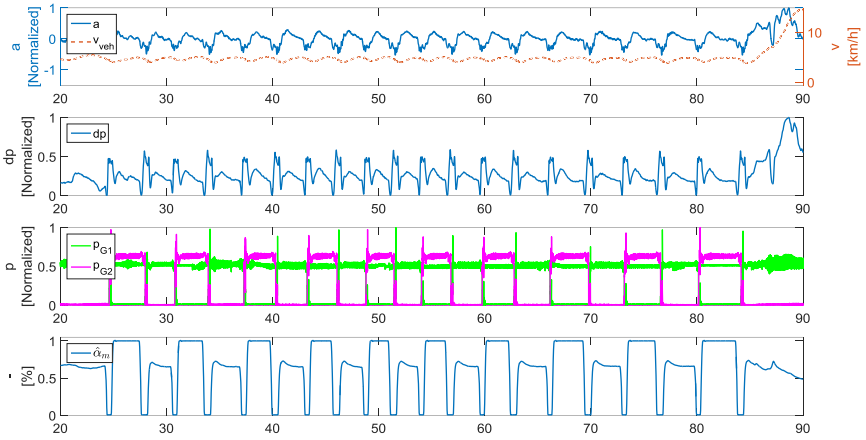

Figure 10: Measurement result of shifting at 5km/h

the shift duration of the downshifting process is more critical than the upshift.

- There should be no vehicle jerk due to the shifting process.
- The pressure peak during the shifting process should not be higher than 300 bar, which may harm the pipe lifetime.

5.2. Results

As **Figure 10** shows, the shifting performance is repeatable, which illustrates the robustness of our control system. The shift duration for upshifting and downshifting process are always about 1 second. The pressure peak is not more than 150 bar during the shifting process, and only a tiny proportion goes to 150 bar. The average pressure is roughly 100 bar. PG1 and PG2 denote the pressure exerts on the operation piston to let the synchronizer to engage with first gear and second gear, correspondingly. For instance, PG1=30bar shows that the first gear is engaged. For these measurements, we simply maintain the drive pedal position. The machine's velocity slightly

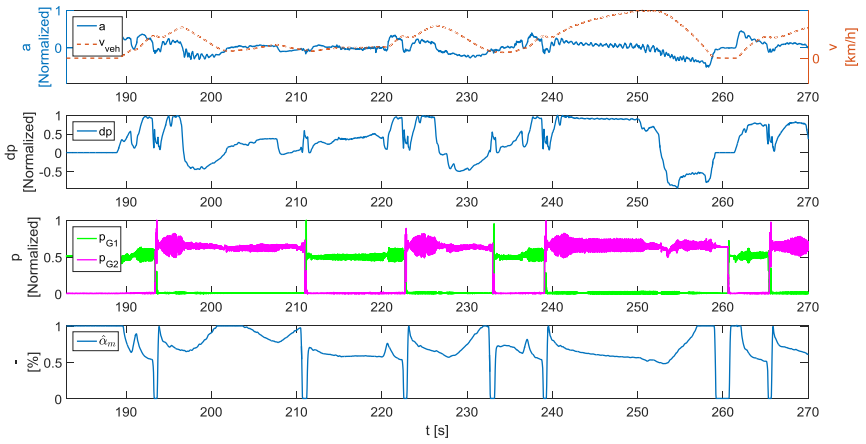

Figure 11: Measurement result of shifting at 14km/h

fluctuates at about 5 km/h, indicating that the drive torque on the wheels is almost the same before and after shifting.

From a system efficiency point of view, 14km/h is usually considered as the dividing point where first gear or second gear should be used. Thus, **Figure 11** illustrates the shifting process at 14km/h. The measurement results show that the most crucial criterion, shift duration, has almost no difference between at 5 and 14km/h. At relatively high speed, the speed different between ongoing and upcoming gear is larger than that at a lower speed causing a longer synchronization process whilst a higher pressure inside the closed-circuit accelerates the swivel speed of the hydraulic motor. The interactions compensate each other so that the shift duration in total is almost the same. The difference here is the pressure peak during shifting since the pressure in the closed circuit is already higher before shifting. Notice that at the time 260s, the shift duration is much longer than the other occurrences because the vehicle is stopped. In standstill, the pressure inside of the closed-circuit is set to zero so that the vehicle will not move in this case. Owing to lack of pressure in the actuator, hydraulic motor swivels back much more slowly, and the operation piston also needs more time to complete the engagement. Nevertheless, nothing can be harmed since the machine has already stopped. Obviously, the velocity and acceleration of the machine are smooth, and no jerk occurs. Notice that, the measurement result shows a better performance than simulation result since we adjust the calibration parameter.

6. GENERALIZED ARCHITECTURE

The control architecture proposed in this paper is initially for a synchronized gearbox drivetrain solution. However, mobile machines have a broad spectrum resulting in limited usage of the above-mentioned control algorithm. In order to make our control algorithm more useful, we designed a general controller architecture. With such an architecture, all kinds of commonly used drivetrain solutions can be controlled with the same architecture only with a little effort in adapting the software. Towards this goal, we consciously keep the interface of each module the same. **Figure 12** illustrates the basic idea.

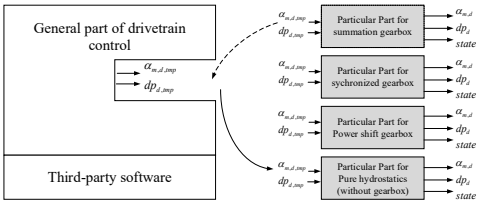

Figure 12: Purpose of the general control architecture

The controller is divided into a general part and particular parts. The particular part is the part that is designed only for a certain kind of gearbox.

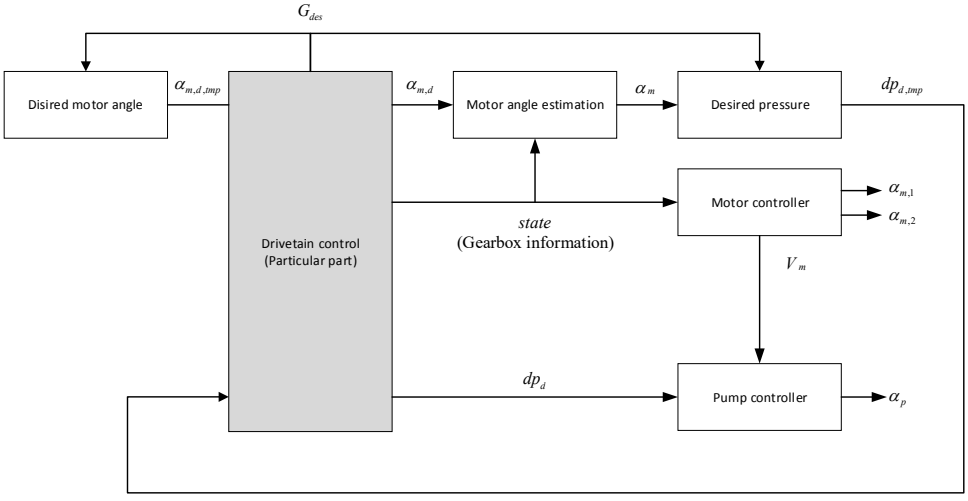

Figure 13: Control scheme with general architecture

Based on the control signal from general part, the particular part overwrites the control signals considering the requirement of the currently used gearbox. The third-party software can be connected to the general part to fulfill customers' individual requirements.

7. CONCLUSION AND OUTLOOK

In this paper, we introduced our novel hydrostatic-mechanical drivetrain solution that adopted the primary torque control concept. Starting with initial simulation studies, the potential shift strategies, such as pressure-based shift strategy and swivel-angle-based shift strategy, were compared and the swivel angle based control algorithm was finally selected. Vehicle tests validated the swivel-angle-based control algorithm approach. As the experimental results show, the novel hydrostatic-mechanical transmission control strategy can efficiently enhance the shift performance of a hydrostatic drivetrain with synchronized gearbox. The main contributions of this novel system can be summarized as follows. Firstly, due to the reduction of calibration parameters to one parameter, the calibration process can be decreased from hours to a few minutes in general. Secondly, a better shift quality in terms of drive comfort and system lifetime is reached thanks to pressure controller. Thirdly, no special experience is needed to achieve the best shift performance of this system, novice drivers can easily operate it. Lastly, a flexible system architecture was drawn so that not only the hydrostatics with a synchronized gearbox but also other commonly used drivetrain solutions, such as with a summation gearbox or with a power shift gearbox, can be controlled under this algorithm.

In addition, the system indicates that it is beneficial to improve the drivetrain efficiency by adopting an appropriate shift manager since it enables hydraulic components to have better working conditions.

OUTLOOK

Although we can reduce the duration of tractive effort interruption, we cannot eliminate it due to the principle of the synchronizer. A mature drivetrain solution to avoid drive torque interruption is hydrostatics with a summation gearbox. However, we need an additional hydraulic motor for this drivetrain solution and thus increase the system cost. Based on the above analysis, we believe it is a sensible idea to use a dual-clutch gearbox to achieve a continuous drivetrain torque during the shifting process even with only one hydraulic motor is a sensible idea. In the past, power shift hydrostatic drivetrain with a dual clutch transmission had a small market share. Thanks to its high dynamics, we believe primary torque control can strongly minimize the vehicle jerk during the shifting process as the dual clutch transmission is used. As the next step, we are going to extend our hydrostatic-mechanical drivetrain solution to power shift, in this case, dual-clutch gearbox.

Another research goal must be the improvement of the efficiency of our primary control algorithm during Y cycles. Unlike secondary control, primary torque concept does not have an accumulator to recuperate the kinetic energy of machines. Instead, it needs a competent solution to regenerate the energy.

NOMENCLATURE

V_p	Displacement of the pump
V_m	Displacement of the motor
η_e	Mechanical efficiency
n_p	Rotation speed of the pump
n_m	Rotation speed of the motor
α_m	Swivel angle of the motor
η_{off}	Offset of the swivel angle of the pump
$\alpha_{p,des}$	Desired pump angle
$\alpha_{m,des}$	Desired motor angle
dp_d	Desired pressure difference
$\alpha_{m,d,tmp}$	The temporarily desired motor swivel angle
$dp_{d,tmp}$	The temporarily desired pressure difference
G_{des}	Desired gear
$\alpha_{m,1}$	Swivel angle of the temporary motor
$\alpha_{m,2}$	Swivel angle of the permanent motor
α_p	Actual swivel angle of the pump

8. REFERENCES

[1] Geimer M, Pohlandt C (2014) Grundlagen mobiler Arbeitsmaschinen. Karlsruher Schriftenreihe Fahrzeugsystemtechnik, vol 22. KIT Scientific Publishing, Karlsruhe

[2] Mutschler S, Brix N, Xiang Y (2018) Torque Control for Mobile Machines. In: Murrenhoff H (ed) 11th International Fluid Power Conference. RWTH Publications, Aachen, pp 186–195

[3] Mercati S, Panizzolo F, Profumo G (2016) Power Split Hydro-mechanical Variable Transmission (HVT) for Off-highway Application. In: 10th International Fluid Power Conference. Technische Universität Dresden, Dresden, pp 69–80
[4] Legner J, Rebholz W., Morrison R. (2016) ZF cPower – Hydrostatic-Mechanical Powersplit Transmission for Construction and Forest Machinery. In: 10th International Fluid Power Conference. Technische Universität Dresden, Dresden, pp 45–52
[5] Murrenhoff H (1999) Systematic Approach to the Control of Hydrostatic Drives. Proceedings of the Institution of Mechanical Engineers, Part I: Journal of Systems and Control Engineering 5(213): 333–347
[6] Murrenhoff H (2008) Servohydraulik – Geregelte Hydraulische Antriebe, 3., neu überarbeitete Auflage. Shaker Verlag, Aachen
[7] Kordak R (1981) Neuartige Antriebskonzeption mit sekundärgeregelten hydrostatischen Maschinen. Ölhydraulik und Pneumatik 5(25): 387–392
[8] Bauer G (2016) Ölhydraulik: Grundlagen, Bauelemente, Anwendungen, 11. Auflage. Springer Fachmedien Wiesbaden, Wiesbaden
[9] Backé W (1994) Verlustarme hydrostatische Antriebe. Grundlagen und Anwendungen. VDI Berichte-Verein Deutscher Ingenieure, Düsseldorf 1132: 147–166
[10] Murrenhoff H, Sgro S, Milos Vukovic (2014) An Overview of Energy Saving Architectures for Mobile Applications. In: Murrenhoff H (ed) 9th International Fluid Power Conference. HP-Fördervereinigung Fluidtechnik, Aachen, pp 238–249
[11] Vukovic M, Leifeld R, Murrenhoff H (2016) STEAM – A Hydraulic Hybrid Architecture for Excavators. In: 10th International Fluid Power Conference. Technische Universität Dresden, Dresden, pp 151–162
[12] Vukovic M, Sgro S, Murrenhoff H (2013) STEAM - A Mobile Hydraulic System with Engine Integration. In: ASME/BATH 2013 Symposium on Fluid Power and Motion Control, Sarasota, V001T01A005-V001T01A005
[13] Sprengel M, Bleazard T, Haria H et al. (2015) Implementation of a Novel Hydraulic Hybrid Powertrain in a Sports Utility Vehicle. IFAC-PapersOnLine 15(48): 187–194
[14] Sprengel MW (2015) Influence of Architecture Design on the Performance and Fuel Efficiency of Hydraulic Hybrid Transmissions. Dissertations, Purdue University
[15] Hense H, Riggenmann F, Wille T (2008) Shift On Fly: Automatisierung des Schaltens während der Fahrt von Stillstandsschaltgetrieben. In: 5. Kolloquium Mobilhydraulik, Karlsruhe
[16] Fischer R, Küçükay F, Jürgens G et al. (2015) The Automotive Transmission Book. Powertrain. Springer International Publishing Switzerland, Cham
[17] Kohmäscher T (2008) Modellbildung, Analyse und Auslegung hydrosratischer Antriebsstrangkonzepte. Dissertation, RWTH Aachen
[18] Jaroslav I, Ivantysynova M (2003) Hydrostatic Pumps and Motors: Principles, Design, Performance, Modelling, Analysis, Control and Testing. Tech Books International

REINFORCEMENT LEARNING: A CONTROL APPROACH FOR REDUCING COMPONENT DAMAGE IN MOBILE MACHINES

Lars Brinkschulte*, Marina Graf, Marcus Geimer

Institute Mobile Machines, Karlsruhe Institute of Technology, Rintheimer Querallee, 76131 Karlsruhe
*Corresponding author: Tel.: +49 721 608 45382; E-mail address: lars.brinkschulte@kit.edu

ABSTRACT

This paper presents an active component damage reducing control approach for driving manoeuvres of a wheel loader. For this purpose, the front and rear axle loads will be manipulated by force pulses induced into the machine chassis via the lifting cylinders of the function drive. The associated control approach is based on the principles of Reinforcement Learning. The essential advantage of such methods against linear control approaches is that no descriptive system properties are required, but the algorithm automatically determines the system behaviour. Due to the high number of necessary training runs, the algorithm is designed and taught using a validated wheel loader simulation model. After over 850 training runs, an optimal strategy for damping the axle loads could not yet be determined. In spite of the unprecedented convergence, initial improvements of the damage values have already been achieved on tracks that deviate from the training track. Some of these results show a 4.9 % lower component damage compared to a machine setting with no damping system. The results and limits of this strategy are discussed due to a comparison with other scientific active vibration damping approaches. Currently, a linear control method (P-PI-controller) has a higher damage reduction potential, but it is expected that further training runs and another learning algorithm could make the reinforcement learning approach even more effective. Coupling the linear control method with the self-learning approach shows the highest potential for the axle damage reduction.

Keywords: Reinforcement Learning, Active Vibration Damping, Damage Reduction, Wheel Loader, Holistic Wheel Loader Simulation

1. INTRODUCTION

Wheel loaders are subjected to constantly changing motion sequences and load situations as the machine operators execute various tasks in the working process such as digging, loading and transporting a wide variety of bulk material. In addition to the working task and the operator, the operating environment of a machine significantly influences the loads acting on the machine. Uneven road conditions, obstacles, such as stones, and the ground surface on construction sites are the determining factors during a driving manoeuvre.

The wheel loader system is thereby an oscillatory system. Vibrations in the working kinematics and the vehicle chassis are therefore caused by any movement of the machine. The consequences are reduced productivity and driving comfort as well as a reduction in the lifetime of structural machine components, such as the machines axles and parts of the working kinematics. Today most of the wheel loaders are not equipped with suspensions at the wheel axles. The pneumatic tyres act as vibration damping elements and are often combined with passive vibration damping (PVD) systems. A standard PVD consists of a hydraulic accumulator and valves, which are connected to the cylinders of the working kinematics. The vibrations are reduced by dissipating kinetic energy, but are optimized for a specific frequency range and can therefore only dampen axle load vibrations to a certain degree [1].

In addition to the PVD methods, there are systems that actively counterbalance the vibrations. In the case of a wheel loader, this is achieved by controlling the function drive (FD). The hydraulic cylinder forces resulting from the working kinematic movements are induced into the front end of the machine, which in turn counteracts the vibrations themselves. If the

response and actuation time of the control system exceeds the frequency of the vibrations, active vibration damping (AVD) can be achieved for a broad speed and load range.

The damping can be achieved by valve-controlled [2–4] or displacement-controlled [5, 6] hydraulic systems. Depending on the driving manoeuvre, Madau shows in [4] a 45 % reduction in cabin acceleration vibration with a valve-controlled approach. The reduction is determined as the integral of the absolute cabin acceleration over the time. Williamson reduces the cabin vibration in [6] by up to 34 % using a displacement-controlled approach.

All control approaches, though, have in common that the control parameters must be determined and defined by technical expertise, often by carrying out test runs in simulation and reality. The analysis and interpretation of the results require a deep understanding of the interrelation-ships in the system. In contrast, artificial intelligence control systems can learn from their own experiences just as living creatures. These systems discover the optimum damping strategy by using for example the basic principles of reinforcement learning (RL).

The publication presents such a RL based AVD approach for driving processes of a wheel loader. The primary objective is to reduce the loads and therefore the damage of the machine axles. The application machine and the driving scenarios examined in the publication are presented in Section 2 of this paper. Section 3 deals with the description of RL approach. The training and testing of the control architecture takes place in a validated machine simulation, which is partly introduced in section 4. The presentation of the results from the training and testing as well as a comparison with other control approaches is given in section 5. The paper concludes with an outlook on possible improvements of the RL-AVD approach.

2. APPLICATION CASE: WHEEL LOADER

For wheel loaders of small power classes, the machine axles and parts of the working kinematics show the highest quantitative density of structural damage to components of these machines. This is the result of a scientific investigation in [7] that is based on maintenance and repair records. Since the vibrations in the axles lead to an increased component load and a loss of comfort for the machine operator, they constitute the component focus of this paper.
The considered machine is a wheel loader, which is mainly used for loading bulk material between two piles. In this publication, the passing over of obstacles on solid ground is investigated. Digging processes and their effect on the vibrations induction are not considered.

2.1. Application Machine L509 Speeder

The application machine is a wheel loader with a steering system combining articulated and rear wheel steering, an operating weight of 6.5 tonnes and a maximum payload of 1.8 tonnes. A hydrostatic drive with two speed levels is used for the traction drive. The working function is designed as a Z-kinematic system driven by a hydraulic pilot-controlled open-centre constant-flow system. To develop the RL-AVD approach a holistic machine simulation model has been developed for the L509 Speeder.

In order to validate the machine simulation, appropriate sensors were installed in a reference machine of the institute in order to record the relevant quantities to develop AVD approaches, see **Figure 1**.

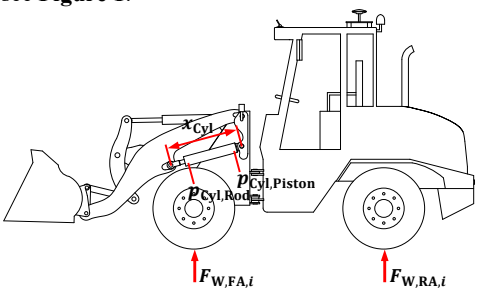

Measured quantity	Variable
Wheel-load-force	$F_{W,i}$ in N
Pressure in lifting cylinder	$p_{Cyl,i}$ in bar
Extension stroke of lifting cylinder	x_{Cyl} in %

Figure 1: Reference machine and measured quantities

The calculation method for the machine axle damage is based on knowledge of the wheel and axle loads. To measure the wheel-load-forces, a strain gauge full bridge was applied to the machine axle on each wheel side. These determine the material strain due to shear stresses in the neutral phase of the axles and can be converted into wheel-load-forces by a suitable calibration. The setup is based on the approaches

in [7–9]. Two wheel-load-forces are measured per axle, the sum provides the total axle load. Neglecting friction, the pressure in the rod and piston side of the lifting cylinders $p_{\mathrm{Cyl},i}$ are used to calculate the acting cylinder force F_{Cyl}. The cylinder extension stroke x_{Cyl} is measured by a laser sensor.

2.2. Driving Manoeuvres

Simple tracks were designed for developing, testing and validating the RL approach. They are characterized by a straight track with interchangeable obstacles. **Figure 2** shows the simplified setup of the tracks and configurations for the training and validation runs.

The training of the algorithm always takes place under constant conditions. The obstacles have the shape of a trapeze. The up and down gradients are equivalent, the length of the obstacle is smaller than the wheelbase. The lifting and tilting cylinders extension strokes are initially set in such a position that the lowest point of the bucket is 200 mm above the ground. For the validation process the number of obstacles and their positions are varied. For all test scenarios the mass of the bulk material in the bucket is $m_{\mathrm{PL}} = 1{,}500$ kg.

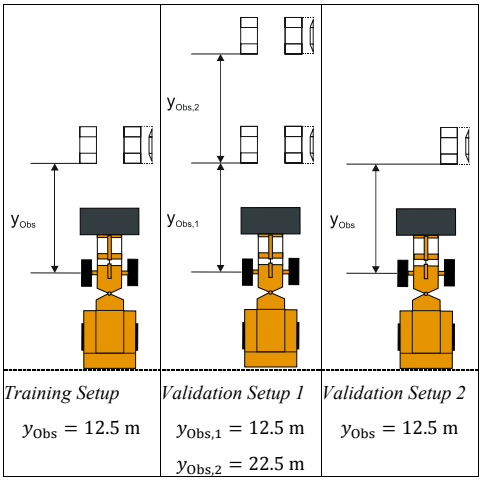

Figure 2: Training and validation setups

3. REINFORCEMENT LEARNING

3.1. General control approach

Reinforcement Learning is a machine learning method that learns through interaction with the environment. Trial and error are the basis on which the control-system (CS) learns an optimal behaviour for a given task; in case of the AVD for damping the axle load vibrations. The control-system consists of two main components:

- the environment, representing the evaluation part,
- and the agent, representing the learning part.

The system runs the same training track over and over again. Every run the agent can test different strategies for pressure pulses introduced into the lifting cylinder. At the end of every run, the vibration damping effectiveness is evaluated by the environment.

The whole problem is formalized as a Markov decision process. **Figure 3** shows the interaction between the agent and the environment, constituting the basic principle of reinforcement learning.

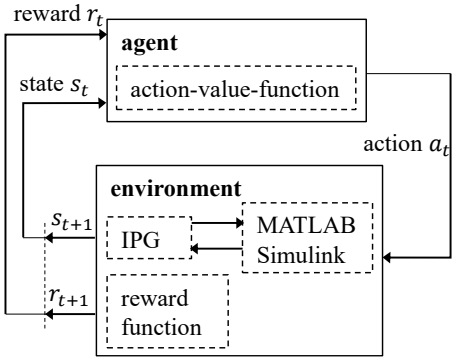

Figure 3: Reinforcement learning approach

For every time step $t = 0, 1, 2, \ldots, \mathrm{T}$ the system including the agent is in a state s_t out of a finite set of possible states $S(s_t \in S)$. According to the current state s_t the agent selects an action a_t. The action space $A(s_t)$ is also finite and it applies $a_t \in A(s_t)$. For the action a_t the agent receives a reward r_{t+1} from the environment at the next time $t + 1$. At time $t + 1$ the system has the state s_{t+1} as a consequence of the chosen action a_t.

The environment is composed of the simulation framework and the reward function. It is not practicable to evaluate every action, because it is not known, how good a single action

is. Therefore a delayed feedback is implemented after a completed training run.

The agent strives to maximize the sum of all received rewards. So the feedback of the environment leads the agent to actions, which are expected to be valued as positive. [10, 11]

3.2. State Space

The problem is described by a continuous state space. To simplify the matter, the space has been discretized. For the AVD-RL-CS, the state space is spanned of three different variables (s_1, s_2, s_3):

- s_1: the pilot pressure cylinder $p_{\mathrm{Cyl,Ctrl}}$ to control the lifting cylinder
- s_2: the force of the lifting cylinder F_{Cyl}
- s_3: the lifting cylinder extension x_{Cyl}

The objective of the learning process is to help the agent to learn how the control pressure can be used to actuate the lift cylinder so that the axle loads can be reduced. Therefore, the state s_1 provides partial information about the reaction of a chosen action. Of interest are the axle load vibrations. Typically, strain gages are not installed in series wheel loaders for measuring axle loads. However, the axle load vibrations behave similarly to the oscillations of the force at the lifting cylinder. This is due to the fact that the working kinematics and the vehicle chassis are connected without spring-damper elements. So the vibrations from the working hydraulics also affects the undamped attached axles. To describe the deviation of the cylinder force from its mean value $F_{\mathrm{Cyl,fil}}$, F_{Cyl} is filtered by a $\mathrm{PT_1}$ element (high pass filter).

The bucket should be prevented from touching the ground. This information is contained in the lifting cylinder extension.

The chosen discretisation is listed in **Table 1**. Nearest-neighbour interpolation was implemented for the assignment of the states s_1 and s_2, for state s_3 piecewise constant interpolation.

Table 1: Implemented state space

State	Discretization
s_1: $p_{\mathrm{Cyl,Ctrl}}$	[-57, -40, -27, 0, 27, 40, 57] %
s_2: $F_{\mathrm{Cyl,fil}}$	[-30 : 10 : 40] kN
s_3: x_{Cyl}	[0.03, 0.08, 0.15] mm

3.3. Action Space

The action space $A(s_t)$ is discretized like the state space. The delay between control signal and valve movement is modelled by a $\mathrm{PT_1T_t}$ element. These delays lead to the choice of an action space with five values $A(s_t)$ = [-40, -33, 0, 40 60] % of the pilot pressure for the lifting cylinder.

An action is selected with a defined frequency $f = 400$ Hz that is significantly higher than the frequency of the axle load vibrations, see **Figure 6**.

At the beginning of the training, the agent does not know which action leads to a big reward. Therefore, he has to do some trial and error.

For the AVD-RL-CS, the decreasing-ε-strategy is implemented. With this strategy the learning process starts with a high exploration rate, which is reduced over time. The value ε determines whether the agent chooses an explored action through choosing a random action or a profitable action he already knows. For ε = 0 the agents is greedy and takes profitable actions, for ε = 1 a random action $a_t \in A(s_t)$ is taken and so the agent explores the environment. [11]

As start value ε = 0.9 is set, the final value after 850 runs is close to 0. At this point, the agent only uses his knowledge and can maximize the sum of rewards. The knowledge will converge to an optimal strategy.

3.4. Reward

The reward indicates how positively or negatively the environment evaluates the chosen action by the agent.

For the AVD, the variant of a delayed feedback is implemented. The reward is defined by the results of the linear axle-damage-accumulation according to Miner elementary. The results are compared with those of a non-damped system. Four different cases are implemented:

- The agent will receive the maximum punishment, if a termination criterion is offended. These criteria are defined so that the agent does not leave the required bucket height.
- The second highest penalty is assigned for boosting the front and the rear axle load. If the agent only improves one axle load, whether

Initialize $Q(s,a)$, for all $s \in S$, $a \in A(s)$, arbitrarily, and Q (terminal-state, ·) = 0
Repeat (for each episode):
Initialize S
Repeat (for each step of episode)
Choose a from s using policy derived from Q (ε-greedy)
Take action a_t, observe r_t, s_t
$Q(s,a) \leftarrow Q(s_t,a_t) + \alpha\,[R + \gamma \max_a Q(s_{t+1},a_t) - Q(s_t,a_t)]$
$s_t \leftarrow s_{t+1}$
until S is terminal

Figure 4: Pseudocode Q-Learning

for the front or the rear axle, he receives a smaller penalty.

- The only positive reward the agent receives is when he improves both damage values for the axle load vibrations.
- Additionally to these huge rewards, a small positive one has been implemented for each action choice that does not infringe a termination criterion.

The rewards are saved using an action-value-function $Q(s,a)$.

3.5. Algorithm and Action-Value-Function

The agent is trained by a Q-Learning algorithm. This is an off-policy algorithm, which is based on Temporal-Difference-Learning. It is a model free algorithm. [10]

Figure 4 shows the pseudo code according to [11]. The agent observes his state s_t and uses it to select his next action a_t, which, according to the action-value-function $Q(s_t,a_t)$, is the most promising. The received reward r_t and the following state s_{t+1} is used to update the action-value-function $Q(s,a)$. For the update, two parameters are implemented:

- α: This parameter specifies how strongly the existing action-value-function is corrected by the new reward values.
- γ: The discount rate defines the actual value of the future rewards. For $\gamma = 0$ the agent is only interested in maximizing the immediate following reward. He is "myopic". For a higher value of γ, the agent is more farsighted and considers future rewards more strongly in the current action choice. If $\gamma < 1$, the sum of the return R has a finite value for non-episodic tasks. [11]

The agent with its learning algorithm is implemented as a Stateflow-diagram in MATLAB-Simulink [12].

4. HOLISTIC MACHINE MODEL

A holistic machine simulation model of the described wheel loader is set up to develop the AVD-RL-CS. The model considers the hydrostatic traction drive (HTD), the function and steering drives (FD and SD), the multi-body dynamics and the interaction with a 3D-environment. The hydraulics of the traction, function and steering drives are modelled in MATLAB-Simscape-Fluids, the multi-body simulation (MBS) models of the working and steering kinematics systems in MATLAB-Simscape-Multibody. The individual models were parameterized by manufacturer specifications and by measurements using the reference machine. **Figure 5** shows a schematic of the machine model and the coupled variables between the subsystems.

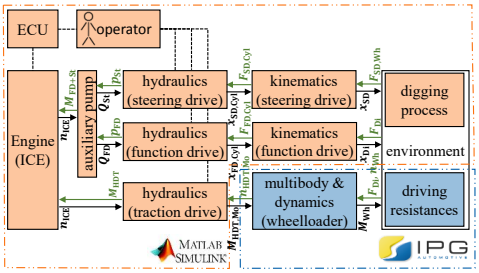

Figure 5: Holistic Machine Model

The IPG-TruckMaker 3D-environment is integrated into the coupling to consider the elastic and damping properties of the entire machine, which are largely defined by the tyres. The tyre-ground-contact is considered by the data interpolation based contact model IPG-Tire [13]. The model uses a single-point-contact between tyre and ground, but offers the advantage of short computing times and numerical stability. The forces transmitted from the lifting mechanism to the front carriage of the machine (connections of

the boom and the hydraulic cylinders) result in changing axle loads and tyre deformations. The resulting 3D-position-change of the kinematic linkages serves as an input to the MBS of the working kinematic. The virtual 3D-environment calculates the resulting driving dynamic variables, such as wheel speeds and steering forces, and transfers them to the simulation models of the HTD and the SD in Matlab-Simscape. This complex coupling of simulation models allows the testing of driving and working scenarios like they occur in reality as well as scenarios under load conditions that would otherwise be difficult to reproduce. A detailed description of the validation of axle load vibrations is provided hereafter. A validation of the traction and function drives are part of another contribution within the scope of this conference [14].

4.1. Validation of Axle Loads

For the validation of the holistic machine model, the front axle loads are analysed when passing an obstacle on the training course with $m_{\mathrm{PL}} = 1{,}510\,\mathrm{kg}$. The lifting cylinder extension is $x_{\mathrm{Cyl}} = 10\,\%$, the tilting cylinder is extended to its maximum stroke. This means that in a standstill position the lowest point of the bucket is approximately 240 mm above the ground in a fully tilted position and thus represents a realistic load case. The model has been compared and validated with respect to the real machine behaviour.

Figure 6 shows the exemplary results of the front-axle-forces in direction of gravity for crossing the obstacle. The upper graph shows the front axle (FA) loads, the middle graph the rear axle (RA) loads and the two lower graphs the results of discrete fast Fourier transformations of the FA and RA loads. The blue lines correspond to the experimental data and the dashed-dotted red lines to the simulation results.

In the measurement, the front axle load rises slightly as the machine drives onto the obstacle ($t = 12.2\,\mathrm{s}$). The force on the rear axle behaves in the opposite direction, as it is decreasing.

In simulation, the vibration initiation is much stronger than in reality. This is with high probability due to the simplified single-point-contact-model of the tyre. As a consequence, the resistance of the ground only has an influence when it is below the centre of the tyre. This leads to an abrupt change in the position of the tyre-ground-contact-point and thus to a sudden load build-up, as can be seen in the simulation in the period between $t = 12.5\,\mathrm{s}$ and $t = 12.7\,\mathrm{s}$. The maximum deviation during this period, defined as

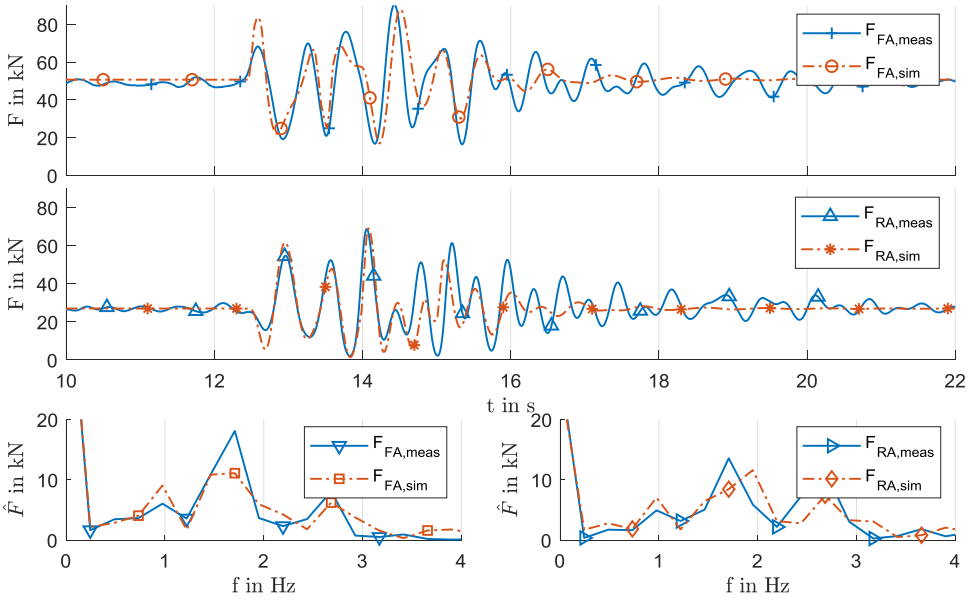

Figure 6: Axle loads for threshold crossing with all wheels

the difference between simulation and measurement divided by the measurement value, is 22 % for the front axle and 64 % for the rear axle.

In the following the mass shifts to the rear axle, whereupon the front axle forces decrease to a minimum and the rear axle force to a maximum ($t = 12.9$ s). When the front wheels have passed the obstacle ($t = 14$ s), the axle load of the rear axle rises to its maximum. The front axle reaches its global maximum at $t = 14.4$ s.

When the rear wheels have passed the obstacle completely, the axle load of the rear axle rises to its second highest amplitude ($t = 15.2$ s). With a slight deceleration, the front axle experiences its global minimum with a following maximum. After three seconds, the axle loads have settled in simulation. In the measurement, the decay of the vibration lasts five seconds.

The frequency of the occurring vibrations are similar in simulation and measurement. This can also be seen in the transformations of the vibrations into the frequency domain by a standardized, discrete fast Fourier transformation. The main frequencies in the measurement and simulation are between 0.7 and 2.7 Hz.

The deviations in the amplitudes are mainly caused by the simplified single-point-contact-model of the tyres. The parameters of this model have been determined on the basis of literature values and a similar scenario of an obstacle crossing with $m_{\mathrm{PL}} = 970$ kg.

However, the sequence of maxima and minima of the described events corresponds to the results of the measurement. In general, it can be concluded that the simulation represents the essential axles force vibration parameters such as amplitudes, frequency and decay time well.

4.2. Machine Axle Damage Model

The machine model is extended by damage models of different wheel loader components. To relate the wheel and axle forces to a damage value the bending beam theory is used. The axle is simplified as a construction of square tubes with different external and internal dimensions. The force is applied at the wheel mounting points. The centre of the axle is mounted to the machine frame, which counteracts with the force F, see **Figure 7**.

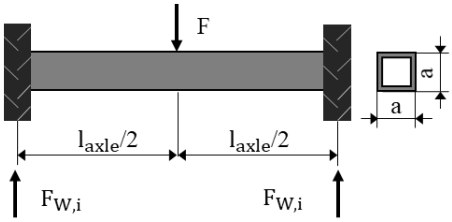

Figure 7: Damage model of the machine axles

For this load case, the maximum bending moment occurs at the fixed clamping to the machine frame and can be calculated as follows:

$$M_{\mathrm{B}} = F_{\mathrm{W},i} \cdot \frac{l_{\mathrm{Axle}}}{2} \tag{1}$$

The material stress due to the bending can be calculated by determining the resistance moment W_{Axle} from the second moment of inertia I_{Axle} of the square tubes:

$$\sigma_{\mathrm{B}} = \frac{M_{\mathrm{B}}}{W_{\mathrm{Axle}}} = \frac{F_{\mathrm{W},i} \cdot \frac{l_{\mathrm{Axle}}}{2}}{\frac{2 \cdot I_{\mathrm{Axle}}}{h}} = \frac{F_{\mathrm{W},i} \cdot l_{\mathrm{Axle}} \cdot h}{4 \cdot I_{\mathrm{Axle}}} \tag{2}$$

The loads occurring during a manoeuvre are separated into individual vibrations by the MATLAB rainflow counts according to the ASTM E 1049 standard [15]. The partial damage is calculated using the elementary form of the Miner rule [16]. The Woehler exponent k, which is directly related to the damage, is assumed to be $k = 5$ on the basis of the FKM guideline [17]. The sum of the partial damages results in the total damage of the respective axles D_i.

With this approach geometries and notch effects are simplified. Further the bending load case represents the main load case, but there are occurring others which are not taken into account. So the determined damage values represent the damage effects just to a limited extend and can therefore only be regarded as approximate values.

5. RESULTS

5.1. Training

In **Table 2** the results of the training are shown. The system was trained through 851 training runs (TR). In 19 TRs the training was stopped, because the actions of the agent lead to an abort criterion. 255 TRs have led to an increase in the damage values for the axle loads, in some TRs up to 160 %. In 392 TRs only one axle load has been optimized, see case 2. The training results show that often one axle load could be significantly

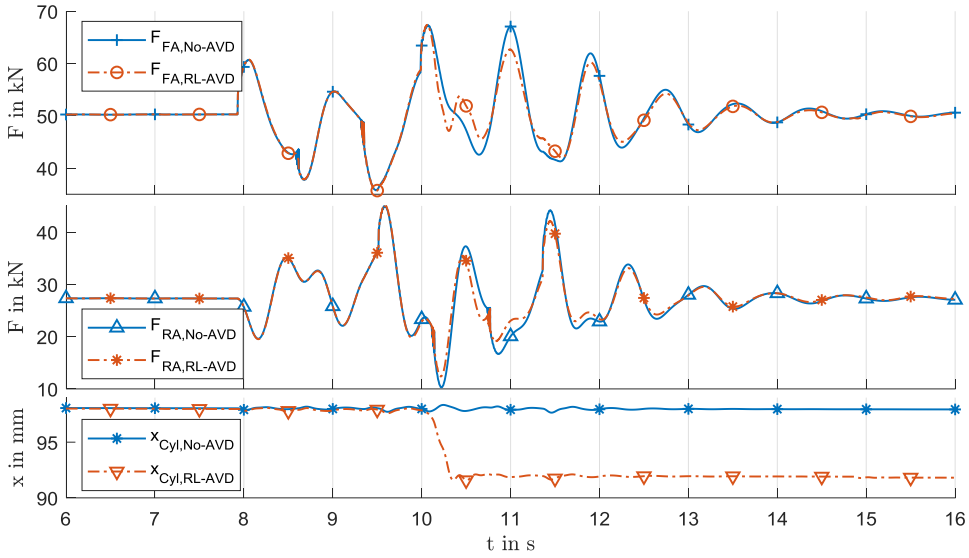

Figure 8: AVD using RL: Training Setup

reduced, while the second one was not necessarily worsened. The agent was able to reduce both axle loads in 185 TRs.

Table 2: Results TS

Case	Reward	Proportion of TRs [%]
1	Both axle loads optimized	21.7
2	One axle load optimized	46.1
3	No axle load optimized	30.0
4	Abortion	2.2

One exemplary training result is shown in **Figure 8**. The upper graph shows the axle loads on the front axle, the middle graph the rear axle loads and the lower graph the lifting cylinder extension. The blue lines correspond to the results of a non-damped system, the dotted red lines to the results of the damped system by the RL agent. For $t = 0\ s$ the wheel loader starts driving. The vehicle moves up the obstacle at $t = 8\,\mathrm{s}$. At $t = 12.5\ s$ the wheel loader has passed the obstacle.

The strategy, the agent is pursuing, is one of lowering the bucket. Therefore, the cylinder extension is reduced about $\Delta x_{\mathrm{Cyl}} = 6\,\mathrm{mm}$. This continuous lowering is leading to reduced force maximums of the front axle. The highest reduction is about $4.3\,\mathrm{kN}$ at $t = 11\,\mathrm{s}$. In conclusion the damage value for the front axle is about 15 % smaller compared with a non-damped system. Also the rear axle load could be reduced in several maximums. For the global maxima at $t = 11.5\,\mathrm{s}$ the reduction is about 2 kN. In sum, the damage value for the rear axle is reduced by 24 %.

The action selection by the agent is leading to additional pressure oscillations in the lifting cylinder chambers and in the pilot pressure for the lifting cylinder. For the pilot pressure the values vary between -35 % (lowering) and 30 % (lifting) of the maximum control pressure. The frequency with which the agent chooses the several actions is reflected here. For lower frequencies, the agility of the system decreases too much.

5.2. Validation

For the validation three different setups (One TS and two VSs) were used (cf. **Figure 2**).

The results are compared to a further AVD approach. Research well known approaches are AVD-CS using techniques from linear control engineering. An essential element of these approaches is the feedback of the current signal to the controller, which continuously counteracts any deviation from the setpoint [2–4]. In this publication, these approaches are transferred to the axle load vibrations in a proportional and proportional-integral (P-PI controller) form. The controller uses the wheel-load-forces of the front

axle F_{FA} and lifting cylinder extension as input variables. F_{FA} is cleared from the mean value by a high pass filter and thus provides the control deviation. The working kinematic system is actuated to counter-excitations, e.g. when F_{FA} increases by lowering the mechanics. In order to keep to the nominal extension of the lifting cylinder, the current lifting level is compared with the setpoint desired by the operator. The proportional and integral of the PI controller part is used to keep the piston position along the setpoint value over time. The output of the controller $(u(t))$ is the sum of the control-components and is therefore a combination of damping and position keeping. Mathematically, this can be considered as the sum of the proportional $(K_{\mathrm{P}}, K_{\mathrm{S}})$ and integral parts (K_{I}), cf. formula 3.

$$u(t) = K_{\mathrm{P}} \cdot F_{\mathrm{W}}(t) + K_{\mathrm{S}} \cdot x_{\mathrm{Cyl}}(t) + K_{\mathrm{I}} \int_0^t x_{\mathrm{Cyl}}(\tau) d\tau \quad (3)$$

The parameters K_{P}, K_{S} and K_{I} were determined by full factorial parameterization while passing the training course several times. Instead of the wheel-load-forces $F_{\mathrm{W},i}$, it would also be conceivable to use the cylinder forces F_{Cyl} as the controller input. However, using F_{Cyl} the authors' results for vibration damping and thus for damage reduction were significantly lower.

Another approach is the cumulative combination of the two approaches (P-PI and RL approach). The optimally working P-PI controller is used to reduce the fundamental vibration, the RL controller is used for fine adjustment and consideration of individual valve characteristics.
The results of all approaches for the driving manoeuvers listed in **Figure 2** are shown in **Table 3**. Compared to the undamped system, positive values describe a reduction of the damage, negative values describe an increase of the damage.

For the TS the RL agent can reduce the damage value about 4.9 % for the front axle. The damage of the rear axle remains unchanged. The agent uses a lowering strategy for the bucket. For the VS 1 (overrun two obstacles) and VS 2 (overrun one obstacle with only the left tyres) the damage values are reduced by a maximum of 1.9 %.
The linear control approach reduces the damage to individual axles by up to 77.7 % during the same manoeuvres. However, this factor is 15 times higher than the achieved results of the RL approach. The reason is the known fact in the controller design that the vibrations in the axles are compensated by counter-excitations. The RL approach must learn this knowledge on its own. The P-PI approach maintains the original lifting height, this behaviour is not known to the RF approach either and has to be learned as well.

The RL-P-PI-combination is able to reduce the damage to individual axles by up to 70.6 % (TS 1 Rear Axle) during the same manoeuvres. This is a further improvement of 31.2 % compared to the P-PI-approach. However, it also needs to be mentioned that compared to the P-PI approach, in the mentioned manoeuvre the reduced damage of the rear axle is accompanied by a small increase in front axle damage (-7.0 %).

It could be shown that a self-learning system is able to learn a damage-reducing behaviour. However, the chosen learning algorithm of Q-Learning reaches its limits due to the chosen number of training runs, the training manoeuvres itself and the discretization of the state space. An expansion of the state space and the use of advanced learning algorithms, such as SARSA, DQN and DDPG, could lead to further damage reduction of the machine axles. Nevertheless, it will be challenging to achieve the reduction potential of classical linear control techniques with self-learning systems. The coupling of the individual approaches shows the most promising results for the damage-reducing-application.

Table 3: Damage Reduction Results

	RL [%]	P-PI [%]	RL-P-PI [%]
TS			
Front Axle	4.9	65.6	58.6
Rear Axle	0.2	39.4	70.6
VS 1			
Front Axle	-20.5	77.7	55.9
Rear Axle	0.0	38.7	33.4
VS 2			
Front Left Axle	-0.8	2.7	-3.4
Front Right Axle	1.9	0.1	-45.5
Rear Left Axle	0.0	37.0	36.7
Rear Right Axle	0.0	-12.4	23.0

6. CONCLUSION

This contribution has presented a new and innovative reinforcement learning (RL) approach for an active vibration damping and damage reduction of wheel loader axles. It could be shown, that self-learning approaches are capable of learning a control behaviour that leads the machine to reduced-damage situations during operation. This approach has been developed using a holistic machine simulation model. A validation of the axle load vibrations using measurement data from a reference machine shows a good agreement between measurement and simulation.

Using reproducible training and validation scenarios, the self-learning system was trained, tested and validated. A maximum axle damage reduction of 4.9 % was achieved for the considered training and validation runs. The comparison between a linear control approach (P-PI-Controller) and the Reinforcement Learning system shows the potential of vibration damping to be achieved. Coupling of these two approaches shows the best damage reducing results, while the P-PI controller serves as the basic controller and the RL approach includes the properties of the valve characteristic behaviour.

In addition to the execution of further training runs, current work focuses on the implementation of the following optimization approaches.

An improvement of the algorithm could be achieved, if at the beginning of the learning process the RL approach would have information about an effective damping behaviour. For this the control signals and resulting axle loads from a linear control approach (P-PI-Controller) could be used.

In addition or instead of considering absolute cylinder forces, it could be more effective to consider the force gradients. Thus, the RL approach would not have to learn the relationship between these parameters independently, but would receive them directly as an input.

The transfer of the self-learning system from simulation to a real machine is still pending.

NOMENCLATURE

A	Action Space
AVD	Active Vibration Damping
CS	Control System
Cyl	Cylinder
D_i	Total Damage of Axle i
Di	Digging Process
F_{Cyl}	Lifting Cylinder Force
$F_{\mathrm{Cyl,fil}}$	Deviation of Lifting Cylinder Force from Mean Value
$F_{\mathrm{W},i}$	Wheel-Load-Force of Wheel i
FA	Front Axle
FD	Function Drive
HTD	Hydrostatic Traction Drive
I_{Axle}	Axle Second Moment of Inertia
ICE	Internal Combustion Engine
K_i	Factor i of P-PI-Controller
M	Torque
M_{B}	Bending Moment
MBS	Multi Body Simulation
P	Proportional
PI	Proportional-Integral
PVD	Passive Vibration Damping
Q	Action Value Function
RA	Rear Axle
RL	Reinforcement Learning
S	Set of Possible States
SD	Steering Drive
TS	Training Setup
TR	Training Run
VS	Validation Setup
W_{Axle}	Resistance Moment of Machine Axle
Wh	Wheel
a_t	Action at Time t
f	Frequency
fil	Filtered
k	Woehler Exponent
l_{Axle}	Machine Axle Width
m_{PL}	Payload in Bucket
$meas$	Measurement
n	Speed
$p_{\mathrm{Cyl},i}$	Pressure in Lifting Cylinder Chamber i
$p_{\mathrm{Cyl,Ctrl}}$	Pilot Pressure of Lifting Cylinder
r_t	Reward at Time t
s_t	State at Time t
sim	Simulation
t	Time
$u(t)$	Controller Output
x_{Cyl}	Lifting Cylinder Extension
$y_{\mathrm{Obs},i}$	Distance to Obstacle i
α	Learning Rate
ε	Greed Factor
γ	Discount Rate

ACKNOWLEDGEMENTS

The authors want to express special thanks to the IPG Automotive GmbH for providing the license for the IPG-TruckMaker program.

REFERENCES

[1] Latour C, Biener R (2003) Schwingungstilgung in Radladern - Vergleich von aktiven und passiven Systemen. Ölhydraulik und Pneumatik 47(3): 171–174

[2] Alexander A, Vacca A, Cristofori D (2017) Active Vibration Damping in Hydraulic Construction Machinery. Procedia Engineering 176: 514–528. doi: 10.1016/j.proeng.2017.02.351

[3] Bianchi R, Alexander A, Vacca A (2016) Active Vibration Damping for Construction Machines Based on Frequency Identification. In: SAE 2016 Commercial Vehicle Engineering Congress, SAE Technical Paper 2016-01-8121. SAE International400 Commonwealth Drive, Warrendale, PA, United States

[4] Madau R, Vacca A (2019) Active Ride Control for Construction Machines Based on Pressure Feedback. In: ASME/BATH 2019 Symposium on Fluid Power and Motion Control. American Society of Mechanical Engineers

[5] Rahmfeld R, Ivantysynova M, Eggers B (2004) Active Vibration Damping for Off-Road Vehicles Using Valveless Linear Actuators. In: SAE International400 Commonwealth Drive, Warrendale, PA, United States

[6] Williamson C, Lee S, Ivantysynova M (2009) Active Vibration Damping for an Off-Road Vehicle with Displacement Controlled Actuators. International Journal of Fluid Power 10(3): 5–16. doi: 10.1080/14399776.2009.10780984

[7] Bös M (2015) Untersuchung und Optimierung der Fahrkomfort- und Fahrdynamikeigenschaften von Radladern unter Berücksichtigung der prozessspezifischen Randbedingungen. KIT Scientific Publishing

[8] Küppers RT (2000) Untersuchungen zur Kippstabilität von Radladern. Dissertation, RWTH Aachen

[9] Hoffmann K (1987) Titel: Eine Einführung in die Technik des Messens mit Dehnungsmeßstreifen, 8th edn. Hottlinger Baldwin Messtechnik, Darmstadt

[10] Russell SJ, Norvig P (2016) Artificial intelligence: A modern approach, Third edition, Global edition. Always learning. Pearson, Boston, Columbus, Indianapolis

[11] Sutton RS, Barto A (2018) Reinforcement learning: An introduction, Second edition. Adaptive computation and machine learning. The MIT Press, Cambridge, MA, London

[12] MathWorks Maker Team (2018) Reinforcement learning with Self-balancing motorcycle. https://de.mathworks.com/matlabcentral/fileexchange/68396-reinforcement-learning-with-self-balancing-motorcycle. Accessed 13 Nov 2019

[13] Schieschke R, Wurster U (1988) IPG-TIRE Ein flexibles, umfassendes, Reifenmodell fuer den Einsatz in Simulationsumgebungen. Automobil-Industrie 33(5): 495–500

[14] Brinkschulte L, Pult F, Geimer M (2020) The Use of a Holistic Machine Simulation for the Development of Hydraulic Hybrid Modules to Reduce Transient Engine-Out Emissions (submitted, not yet published). In: Proceedings of 12th International Fluid Power Conference

[15] E08 Committee E1049 − 85: Practices for Cycle Counting in Fatigue Analysis

[16] Haibach E (2006) Betriebsfestigkeit: Verfahren und Daten zur Bauteilberechnung, 3., korrigierte und erg. Aufl. VDI-Buch. Springer, Berlin

[17] Rennert R, Kullig E, Vormwald M et al. (2012) Rechnerischer Festigkeitsnachweis für Maschinenbauteile aus Stahl, Eisenguss- und Aluminiumwerkstoffen, 6., überarb. Ausg. FKM-Richtlinie. VDMA-Verl., Frankfurt am Main

peer reviewed

INTELLIGENT TWIN STEERING SYSTEM

Eng. Biagio Borretti*[1], Eng. Nicola Musciagna[1], Eng. Luca Riccò Ph.D. [1], Eng. Andrea Fornaciari[2].

[1] *Dana Motion Systems Italia srl, Via Luciano Brevini 1/A, 42124 Reggio Emilia, Italy.*
[2] *Engineering department Enzo Ferrari, University of Modena e Reggio-Emilia, Via P. Allegri 10, 41124 Modena.*
*Corresponding author: Tel.: +39 0522 505 870, +39 338 94 30 298; E-mail address: biagio.borretti@dana.com

ABSTRACT

This article describes the Dana intelligent Twin Steering System designed for mobile vehicles with two steering axles (i.e. with four steering wheels).
Current vehicles with four-wheel steering function are typically equipped with a hydraulic configuration where the two steering cylinders are connected in series. This type of connection highlights some limitations on available power, steering comfort and enabling advanced working functions.

Dana evolved this type of hydraulic configuration introducing the possibility to disconnect the rear axle from the front one. In this way the rear axle, through the electronic control of its valve block, allows to improve the steering system performance and introduces advanced steering functions compared to the conventional steering systems.

Keywords: Steering, 4 Wheels Steer, Control Strategy, Fuel Efficiency, Tyre Consumption, Comfort.

1. INTRODUCTION

Mobile heavy-duty vehicles equipped with two steering axles allow to switch between two steering wheels (2WS) functioning and four steering wheels (4WS) functioning by connecting the front axle hydraulic steering cylinder in series with the rear axle (Figure 1.1).

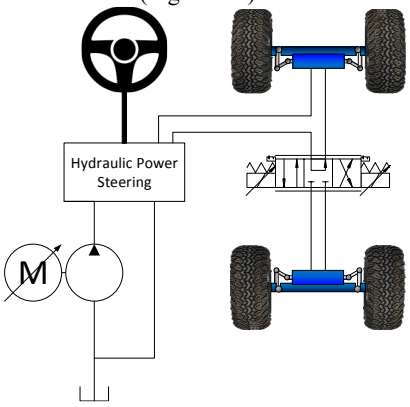

Figure 1.1: Typical hydraulic steering system layout

The series connection, where the front cylinder outlet port is connected to the rear cylinder inlet port, halves the total available force on the front axle cylinder during the steering maneuvers due to the rear cylinder force requirement. Consequently, the vehicle loses its steering full capability in terms of maximum achievable angle. Furthermore, switching from 2WS to 4WS mode, and vice versa, it is extremely uncomfortable and time consuming due to the manually alignment of all the wheels by the operator. In addition, this type of steering system forces at least one of the wheels to slip during the machine maneuvers due to the geometrical Ackermann error (being the kinematics typically not Ackermann) unless using complex kinematics [1] thus increasing fuel and tires consumption.

Steering systems have been studying with different objectives, including energy efficiency, safety, comfort and autonomous vehicles[2], [3], [4].

On the market some electro-hydraulic steering system are already available, among which the ones produced by Mobil Elektronik GmbH and HYDAC.

The first competitor provides an electronic hydraulic rear power steering systems (EHLA), Figure 1.2, [5].

In this solution the real axle steering system is of hydraulic-mechanical types and managed and controlled independently from the front axle.

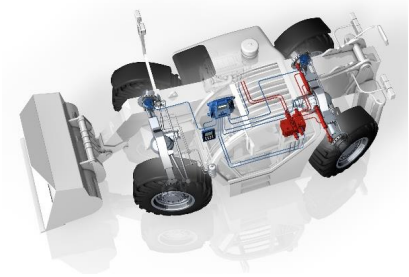

Figure 1.2: Mobil Elektronik EHLA Plus

Different steering modes are provided, such as 4-wheel steering, crab steering and manual steering of the rear axle. Moreover, is implemented a smart steering mode "automatic rear swing-out suppression" that prevents the swinging out of the rear part of the vehicle, during steering maneuvers, by turning the rear axle later than the front one.

The second competitor provides a steering system able to steer independently more than two axles [6], i.e. vehicles equipped with multiple axles. Figure 1.5 reports how any single steering axle could be controlled.

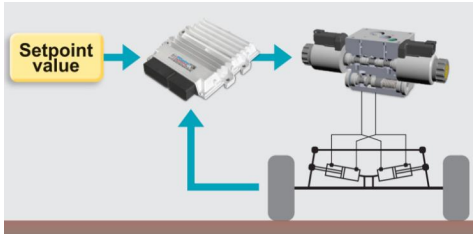

Figure 1.5: HYDAC Steering Architecture

As for the previous solution, there are no mechanical / hydraulic connections between the axles.

The available steering modes are on-road steering, all-wheel steering and crab steering. In the first a central axle is not steered and works as mid-point while the axles behind it are controlled in function of the front axles. In the second all the axles can be steered, while in the last all the axles are steered equally at the same steering angle resulting in the vehicle sideways movement.

Both the systems include a Fail-Safe Reaction. When an error is detected, the faulty axle is locked into a default position. In this condition the operator will be able to turn the vehicle, but the controllability results compromised.

2. DANA SOLUTION DESCRIPTION

The Dana "Intelligent Twin Steering System" (iTSS) is a novel steering system for mobile off-highway vehicles that introduces the possibility to switch from the series (Figure 1.3) to the parallel (Figure 1.4) connection of the hydraulic steering cylinders, advanced steering functions and application-based steering profiles.

The proposed solution adds to the actual steering system (Figure 1.1) a dedicated rear steering directional flow control valve and its controlling electronics.

The valve allows to switch from the series architecture (conventional one) to the parallel architecture, still maintaining the safety.

The iTSS system (Figure 2.1) is composed of:

- an intelligent valve, called iTSS valve;
- angle sensors, to detect front and rear axles steering angles;
- an electronic control unit (ECU) to manage the whole steering system.

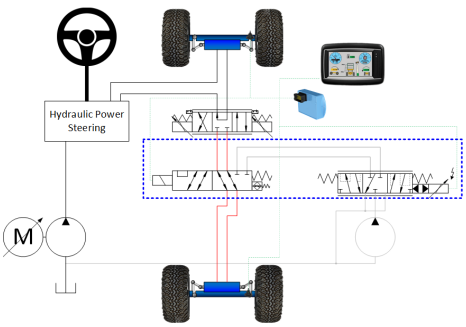

Figure 1.3: iTSS Off

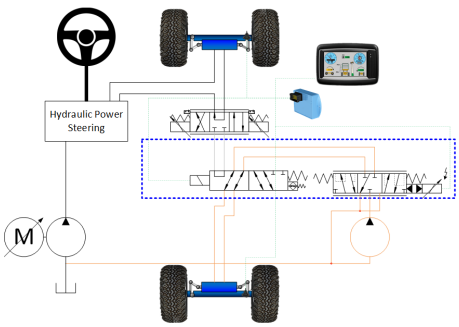

Figure 1.4: iTSS On

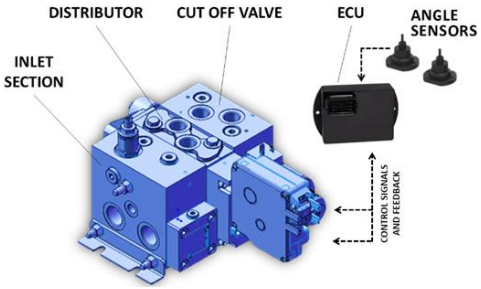

Figure 2.1: iTSS System

The main component of the proposed system is the iTSS valve. This valve is composed of three blocks: The Cut Off Valve, the Inlet Section and the Distributor. When the Cut Off Valve is energized the steering system switches from the traditional series hydraulic architecture to the parallel independent hydraulic architecture, i.e. the real axle is not anymore coupled to the front one but is managed by the electronics through the Distributor block according to the desired strategy. This configuration allows to double the steering force on both the axles (the hydraulic force is not split anymore between the front and rear axles), enable advanced steering functions (described in detail in section 4), and still maintain the safety of the system through dedicated Fail Operational Reaction. The Fail Operational reaction is one of the smartest features of this system. In fact, in case of any dangerous failure, if activated, the Cut Off Valve will be switched off in order to set the steering system from the parallel configuration back to the "conventional" series one. This allows to maintain the traditional steering modes and the control on all the wheels but with lower effectiveness and functionality. This feature is not actually provided by any competitor with similar steering system.

The distributor is the Dana Brevini HPV series 41, a proportional flow control valve acted by an electronic actuator (Sonceboz Sense 42). The Inlet Block regulates the inlet pressure according to the Load Sensing logic.

The iTSS requires angular (or position) sensors in order to measure the frontal steering angle and controls the rear axles steering angle according to the selected function. The sensors are based on contact-less Hall effect technology. Safety is provided by means of a doubled output signal, one redundant and opposite to the other.

The ECU, developed and programmed by DANA, reads the analog and digital inputs and manages the outputs in order to manage the steering system.

3. VEHICLE KINEMATICS ANALYSIS AND MATHEMATICAL MODEL

In this section are reported the kinematics analysis of the proposed steering system and its mathematical model. The aim of the model is that of calculates the wheels paths during arbitrary steering maneuvers and their slipping in order to evaluate and compare different solutions and control strategies.

The simplified scheme of the steering mechanism, installed on all the steering axles produced by Dana, is reported in Figure 3.1, where the neutral position (dashed lines) and a generical position assumed by the mechanism during a steering maneuvers (solid lines) are pointed out in order to identify the variables of interest. Solving the kinematic chain equations it is possible to define the correlation between the steering piston position and the wheels steering angles (Eq.s (3.1), (3.2)).

Knowing the wheels steering angles the position of the front and rear axles instantaneous rotational centers, OF and OR (Figure 3.2), can be calculated (Eq.s (3.3), (3.4)), under the hypothesis of null slip angles, due to the low vehicle speed.

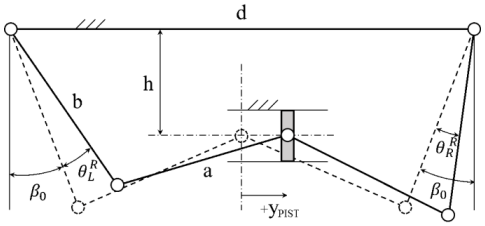

Figure 3.1: Axle simplified steering mechanism scheme

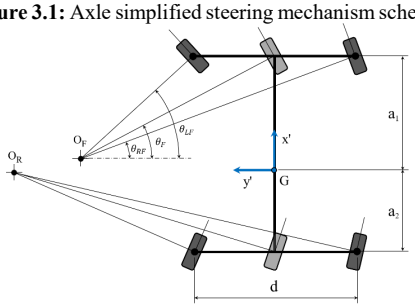

Figure 3.2: Axles rotational centres

$$\theta_L{}^R = \frac{\pi}{2} - 2\tan^{-1}\left(\frac{2hb + \sqrt{(2hb)^2 - \left(\left(\frac{d}{2}+y_{pist}\right)^2 + b^2 + h^2 - a^2\right)^2 + \left(2\left(\frac{d}{2}+y_{pist}\right)b\right)^2}}{\left(\frac{d}{2}+y_{pist}\right)^2 + b^2 + h^2 - a^2 + 2\left(\frac{d}{2}+y_{pist}\right)b}\right) - \beta_0 \tag{3.1}$$

$$\theta_R{}^R = 2\tan^{-1}\left(\frac{2hb + \sqrt{(2hb)^2 - \left(\left(\frac{d}{2}-y_{pist}\right)^2 + b^2 + h^2 - a^2\right)^2 + \left(2\left(\frac{d}{2}-y_{pist}\right)b\right)^2}}{\left(\frac{d}{2}-y_{pist}\right)^2 + b^2 + h^2 - a^2 + 2\left(\frac{d}{2}-y_{pist}\right)b}\right) + \beta_0 - \frac{\pi}{2} \tag{3.2}$$

$$\begin{cases} x_{O_F} = a_1 + \frac{d}{2}\tan\theta_{LF} + \frac{d}{2}\left(\frac{\tan\theta_{RF} + \tan\theta_{LF}}{\tan\theta_{RF} - \tan\theta_{LF}}\right)\tan\theta_{LF} \\ y_{O_F} = -\frac{d}{2}\left(\frac{\tan\theta_{RF} + \tan\theta_{LF}}{\tan\theta_{RF} - \tan\theta_{LF}}\right) \end{cases} \tag{3.3}$$

$$\begin{cases} x_{O_R} = -a_2 + \frac{d}{2}\tan\theta_{LR} - \frac{d}{2}\left(\frac{\tan\theta_{LR} + \tan\theta_{RR}}{\tan\theta_{LR} - \tan\theta_{RR}}\right)\tan\theta_{LR} \\ y_{O_R} = \frac{d}{2}\left(\frac{\tan\theta_{LR} + \tan\theta_{RR}}{\tan\theta_{LR}\tan\theta_{RR}}\right) \end{cases} \tag{3.4}$$

In order to define the vehicle instantaneous rotational center (O') the equivalent bicycle model has been considered (Figure 3.3).

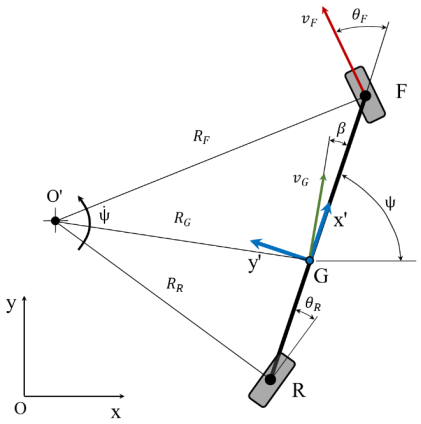

Figure 3.3: Equivalent bicycle model

Eq. (3.5) relates the wheels steering angles with the central axle equivalent wheel steering angle. This equation can be adopted for both front and rear axles.

$$\tan\theta_F = \frac{2\tan\theta_{LF}\tan\theta_{RF}}{\tan\theta_{LF} + \tan\theta_{RF}} \tag{3.5}$$

Following the approach reported in [7] the vehicle slip angle (Eq. (3.6)) and equations describing the equivalent bicycle model center of mass velocity in the plane (Eq.s (3.7)).

$$\beta = \tan^{-1}\left(\frac{a_1\tan\theta_R + a_2\tan\theta_F}{a_1 + a_2}\right) \tag{3.6}$$

$$\begin{cases} \dot{x_G} = v_G\cos(\psi + \beta) \\ \dot{y_G} = v_G\sin(\psi + \beta) \\ \dot{\psi} = \frac{v_G\cos\beta\,(\tan\theta_F - \tan\theta_R)}{L} \end{cases} \tag{3.7}$$

Once integrated in time the vehicle inclination and center of mass position can be found as reported in Eq.s (3.8).

$$\begin{aligned} \psi(t_i) &= \psi(t_{i-1}) + \dot{\psi}_i\Delta t \\ x_G(t_i) &= x_G(t_{i-1}) + v_{G_i}\cos(\psi(t_i) + \beta_i)\,\Delta t \\ y_G(t_i) &= y_G(t_{i-1}) + v_{G_i}\sin(\psi(t_i) + \beta_i)\,\Delta t \end{aligned} \tag{3.8}$$

Where

$$\dot{\psi}_i = \frac{v_G}{R_{G_i}} \tag{3.9}$$

and

$$R_{G_i} = \frac{a_1 + a_2}{\cos\beta_i\left(\tan\theta_{F_i} - \tan\theta_{R_i}\right)} \tag{3.10}$$

Defining a fixed reference system (Oxy) and knowing the vehicle center of mass position and inclination, referring to Figure 3.4, it is now possible to evaluate the position of the wheels (A, B, C, D). The calculation of the wheel A has been

$$(A-O)|_{Oxy} = \begin{pmatrix} x_G + (a_1 - e\sin\theta_{LF})\cos\psi - \left(\frac{w}{2} + e\cos\theta_{LF}\right)\sin\psi \\ y_G + (a_1 - e\sin\theta_{LF})\sin\psi + \left(\frac{w}{2} + e\cos\theta_{LF}\right)\cos\psi \\ 0 \end{pmatrix} \quad (3.13)$$

following reported (Eq.s (3.11), (3.13)). This approach can be adopted for all the wheels.

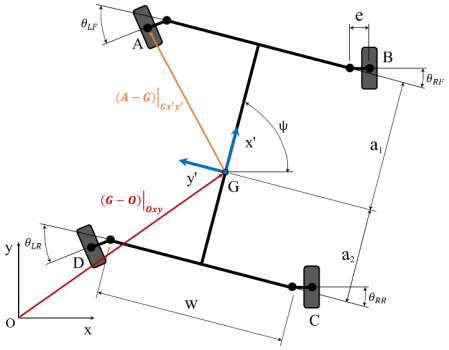

Figure 3.4: Wheels position calculation

$$(A-O)|_{Oxy} = (G-O)|_{Oxy} + \boldsymbol{R}(A-G)|_{Gx'y'} \quad (3.11)$$

Where **R** (Eq. (3.12)) represents the rotational matrix of the vehicle referring to the fixed reference system.

$$\mathbf{R} = \begin{bmatrix} \cos\psi & -\sin\psi & 0 \\ \sin\psi & \cos\psi & 0 \\ 0 & 0 & 1 \end{bmatrix} \quad (3.12)$$

4. ADVANCED FUNCTIONS

The reported steering functions take advantage of the independency of the front and rear axles in order to implement special steering manoeuvres.

4.1. Follow the path

This advanced steering function has been defined in order to overlap the rear wheels steering traces to the front wheel ones.
When the front axle starts steering, the action on the rear axle is then properly delayed.
The setpoint at "Regime" of the rear axle is calculated by Eq.(3.16).

$$\theta_R{}^{Regime} = -\theta_F \quad (3.16)$$

From the setpoint, the control system works as in **Figure 3.5**:

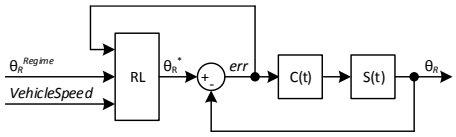

Figure 3.5: Follow the Path Control System

The setpoint of the rear axle $\theta_R{}^{Regime}$ is reached by a dynamic Rate Limiter (RL_{Dyn}), which delays the reaching of it.

$$RL_B = \frac{(VehicleSpeed)}{3{,}6 \times AxlesDistance} \times \Delta t \quad (3.17)$$

$$RL_{Dyn} = RL_B \times \max(|\theta_R - \theta_R{}^{Regime}| \times K_1;\ K_2) \quad (3.18)$$

Where K_1 and K_2 are parameters tuned for the specific vehicle / application.
Considering:

$$err = \theta_R{}^* - \theta_R \quad (3.19)$$

The value of RL_{Dyn} is the maximum quantity (in degrees) to be applied to increment / decrement the reference: $\theta_R{}^*$ in Δt time in order to reach the $\theta_R{}^{Reg}$. The Formula is detailed in Eq. (4.1).
This function is very useful in both on-road and on-field working conditions, because it allows to easily avoid obstacles and reducing the crop damaged by the wheels path during headland turning sequence.

4.2. Kinematronic Rotation Centre

During steering maneuvers due to the geometrical configuration of the axles is typically generated an Ackermann error (Figure 3.6). The effect of this error is that slippage occurs on the

$$\theta_R{}^*(t) = \begin{cases} \theta_R{}^{Reg} & |err| \le RL_{Dyn} \\ \theta_R(t-\Delta t) + sign(err) \times RL_{Dyn} & |err| > RL_{Dyn} \end{cases} \quad (3.14)$$

wheels during the steering maneuver. Thus, increasing tires and fuel consumption.

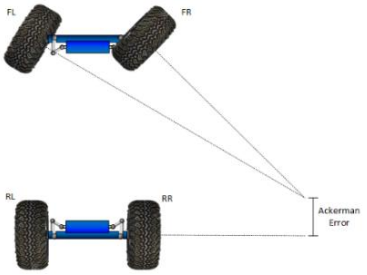

Figure 3.6: Ackermann Error

Ideal steering trajectories, i.e. with no Ackerman error, occur when all the wheels angle have a singular vehicle rotational center. Thanks to the capability of iTSS to independently control the rear axle steering angle from the front one, it is possible to minimize the Ackerman error for any front steering angle. The Kinematronic idea is to overlap the rear axle rotational center on the front axle one (Figure 3.7), thus the rear steering angle will be calculated by the ECU as a function of the front steering angle.

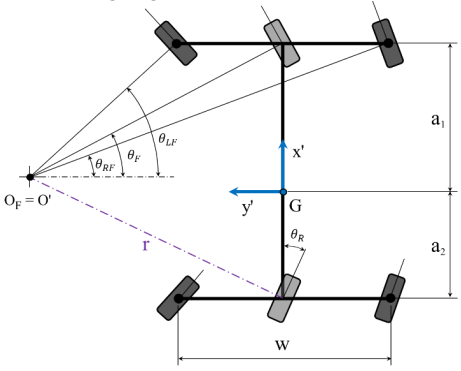

Figure 3.7: Kinematronic conceptual idea

5. RESULTS

In this section the wheels trajectories have been reported and compared between traditional steering configuration and the presented (Section 4) advance steering function during typical steering maneuvers. The calculation took count of the vehicle and axles geometrical dimensions, front and rear axle steering angles and vehicle speed.

The colour codes of the wheels paths on the plane is represented in Figure 5.1.

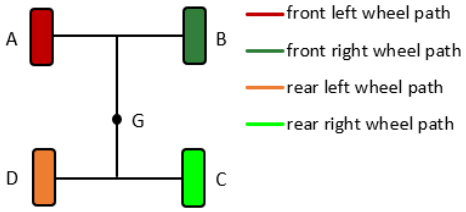

Figure 5.1: Wheels colour codes

5.1. Follow the path vs 2WS

Figure 5.2 reports the wheels path during a generic S steering maneuver of the considered vehicle in the 2WS mode, while Figure 5.3 depicts the same steering maneuver with the 4WS steering mode and the "Follow the path" enabled. Comparing the trajectories, it is possible to point out that by means of Follow the Path function the steering maneuvers results more effective in term of impacted area. Thus, it becomes easier and safer to avoid obstacles and turn with long vehicles and vehicles with trailer.

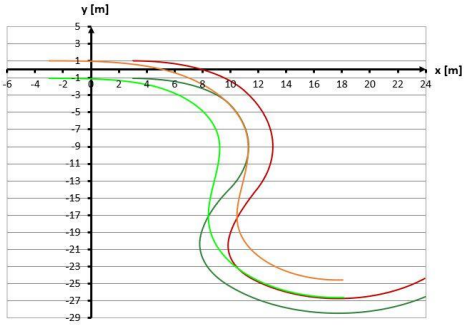

Figure 5.2: Wheels trajectory in 2WS steering configuration

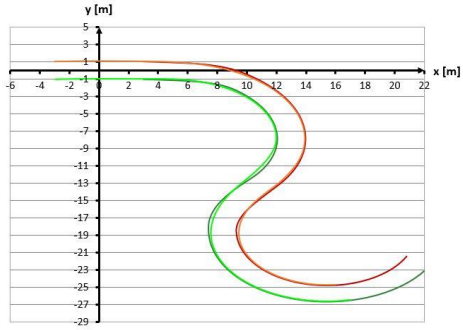

Figure 5.3: Wheels trajectory in 4WS and Follow the Path mode

5.2. Follow the path vs 4WS (Async)

Figure 5.4 reports the wheels path of sprayers, tractors or any other agricultural machine during a headland turning sequence of the considered vehicle in the 4WS asynchronous mode, while **Figure 5.5** depicts the same steering maneuver with the 4WS steering mode and the "Follow the path" enabled.

In the first steering mode this maneuver cause much more crop damaging due to the four different wheels path on the ground compared to the Follow the Path mode that left only two traces on the ground.

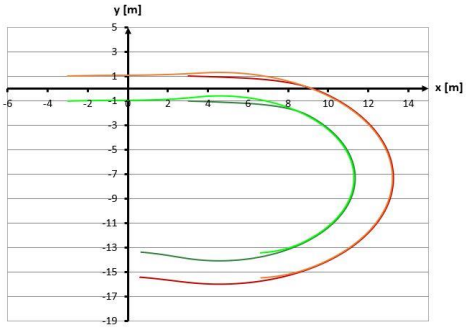

Figure 5.4: Vehicle Trajectory with Follow the Path NOT Active (4WS Async Active)

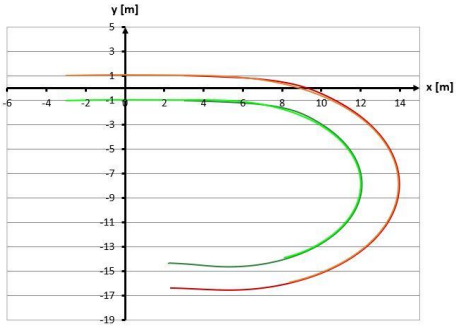

Figure 5.5: Vehicle Trajectory with Follow the Path Active

5.3. Kinematronic Rotation Centre vs 2WS

The generic S steering manoeuvre reported in Figure 5.2 has been performed with the conventional 2WS steering mode and the Kinematronic mode.

As reported in section 4, the Kinematronic algorithm works with the aim to reduce the Ackermann error controlling the rear axle steering angle (Figure 3.7). Due to the steering mechanism geometry the position of the real rear rotation centre is not the same of the calculated one (Figure 5.6). This introduces a slip velocity ($v_{LR,S}$), as depicted in Figure 5.7 for the rear left wheel only for simplicity, normal to the rolling velocity (v_{LR}).

The slippage on the front wheels has been neglected, while the total rear wheels slippage has been calculated integrating the slippage speed ($|v_{LR,S}|$) in time.

Nevertheless, thanks to the Kinematronic it is possible to reduce the wheels slippage up to 86% in the considered manoeuvre and similar improvements can be obtained for any other steering movement.

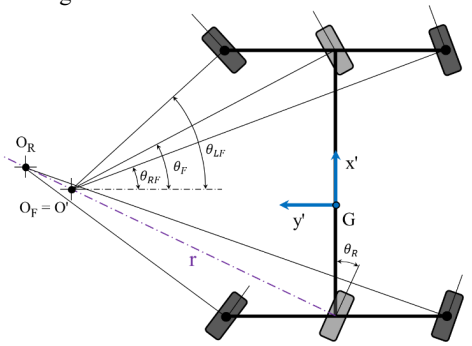

Figure 5.6: Vehicle rotation centre with kinematronic enabled

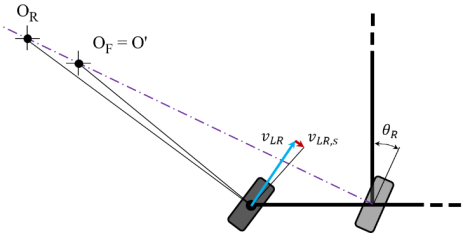

Figure 5.7: Left rear wheel velocities

6. CONCLUSION AND OUTLOOK

In this contribution, a novel electro-hydraulic steering system for mobile vehicles and dedicated advanced functions have been presented and described in detail. The proposed iTSS system introduces significant improvements in terms of functionality, comfort and performance compared to traditional steering configurations. Moreover, the DANA solution differs from other similar solutions already available on the market for the available steering functions and safety features.

NOMENCLATURE

a	Steering mechanism crank length [m]
a_1	Distance between centre of mass and front axle [m]
a_2	Distance between centre of mass and rear axle [m]
b	Steering mechanism outrigger length [m]
d	Distance between wheels rotational centres [m]
e	Wheels link length [m]
err	Error value in follow the path control [°]
G	Vehicle centre of mass
h	Distance between wheels axle and the steering hydraulic actuator [m]
O_F	Front axle rotational centre
O_R	Rear axle rotational centre
O'	Equivalent bicycle rotational centre
R_F	Front axle radius [m]
R_G	Centre of mass radius [m]
R_R	Rear axle radius [m]
RL_B	Rate Limiter Base Value for follow the path algorithm, it is used to calculate the RL_{Dyn} value
RL_{Dyn}	Rate Limiter Dynamic Value for follow the path algorithm [rad]
v_F	Front equivalent wheel velocity [m/s]
v_G	Centre of mass velocity [m/s]
x_G	Centre of mass x-coordinate [m]
$\dot{x}_G$	Centre of mass velocity x-coordinate [m/s]
y_G	Centre of mass y-coordinate [m]
$\dot{y}_G$	Centre of mass velocity y-coordinate [m/s]
y_{PIST}	Steering hydraulic cylinder stroke [m]
β	Vehicle slip angle [rad]
β_0	Initial axle steering angle [rad]
ψ	Vehicle inclination angle [rad]
$\dot{\psi}$	Vehicle rotational speed [rad/s]
θ_R^{Reg}	Value to be reached on rear axle at regime when follow the path algorithm is working [rad]
θ_F	Front wheel steering angle [rad]
θ_{LF}	Front axle left wheel steering angle [rad]
θ_{LR}	Rear axle left wheel steering angle [rad]
θ_R	Rear wheel steering angle [rad]
θ_{RF}	Front axle right wheel steering angle [rad]
θ_{RR}	Rear axle right wheel steering angle [rad]

REFERENCES

[1] Jing-Shan Zhao, Jian S Dai. Design of an Ackermann Type Steering Mechanism. Proceedings of the Institution of Mechanical Engineers Part C Journal of Mechanical Engineering Science 1989-1996 (vols 203-210), November 2013. DOI: 10.1177/0954406213475980

[2] Hiroyuki Miyazaki. Technical trends in steering systems. Proceedings of the 7th JFPS International Symposium on Fluid Power, TOYAMA 2008. September 15-18, 2008. ISBN 4-931070-07-X

[3] Keiichi Inoue. Steering control system for autonomous tractor. Proceedings of the 7th JFPS International Symposium on Fluid Power, TOYAMA 2008. September 15-18, 2008. ISBN 4-931070-07-X

[4] Arun Singh, Abhishek Kumar, Rajiv Chaudhary, R. C. Singh. Study of 4 Wheel Steering Systems to Reduce Turning Radius and Increase Stability. International Conference of Advance Research and Innovation (ICARI-2014). ISBN 978-93-5156-328-0

[5] http://www.mobil-elektronik.com/en/systems/ehla.html [access date: 01/10/2019]

[6] https://www.hydac.com/fileadmin/pdb/pdf/PRO00000000000000000000101169000011.pdf [access date: 01/10/2019]

[7] R. Rajamani, Vehicle Dynamics and Control, Springer Science & Business Media, 2011. ISBN 0-387-26396-9

AUTONOMOUS CONTROL OF HYDRAULIC MOBILE APPLICATIONS – A 21-TON EXCAVATOR CASE STUDY

Dr. Tim Opperwall*, Ben Holter, Simon Yardley

Husco International, 2239 Pewaukee Rd, Waukesha, WI 53188, USA
* Corresponding author: Tel.: +1 262 513-4266; E-mail address: timothy.opperwall@husco.com

ABSTRACT

Automation of mobile construction and agricultural equipment has gained wide acceptance based on increases in productivity, safety, and precision; while also helping upskill operators. On construction equipment, after-market automation of earthmoving crawler dozers and graders has driven a conversion of machines to electro-hydraulic (EH) implement control and integration into digital worksites. Unlike the aforementioned machines, conversion of the excavator into a semi or fully autonomous machine presents significant challenges due to kinematics, variable loads, non-linear multi-function of implements, safety, and robustness. The present work demonstrates the retrofit of a pilot-operated 21-ton excavator and development of automated controls to address these challenges. The operator pilot joysticks and existing hydraulic system were retained, while adding capability for autonomous functionality with integrated hardware, controls, and kinematic solvers within a production viable environment. Autonomous features for path planning, multi-function actuator velocity control, EH controls, and safety were developed to prove the value of precise and low latency control hardware for EH excavator operation.

Keywords: Hydraulic mobile applications, Electro-Hydraulics, Autonomous Excavator, Smart construction sites

1. INTRODUCTION

The present work describes a technically proven and commercially viable system to provide digital control and autonomous implement position control of a standard pilot operated machine. A 21-ton excavator was chosen as the applied research vehicle as it provided significant inherent challenges and is typically the first prime mover on construction sites globally. Some of the key challenges such as balancing the pressure, power, and flow of multiple functions in relation to command and desired function path are included in the research.

The majority of original equipment manufacturer (OEM) excavators in use today have hydraulic pilot joystick signals controlling the hydraulic main control valve (MCV). Although there are a small number of electro-hydraulic (EH) controlled machines emerging on the market as factory fit, few companies have been able to create a system that can easily be retrofitted into an existing circuit while providing precise digital control and enabling of autonomous functions such as auto-grade and geo-fencing. This gap in the market is due to the difficult transform of operator controls to precise kinematic motion. Excavators are different in control strategy than other precision equipment like bulldozers and motor graders in that excavators must coordinate many functions simultaneously at high velocity to control a precise implement position and path. Other types of machines such as crawler dozers and graders must only make small, single function positional adjustments as they move over the earth. This difference has made automated control very difficult from a hardware and software standpoint, which is why the market has lagged on adoption of autonomous excavator control.

Complex construction machines require skilled labour to operate them safely and productively to maximise the significant capital investment of the machine. Bringing in autonomous or augmented functions to support the operator brings several benefits. Automatic grade control can enable a machine to precisely follow a pre-set path or trajectory, minimising

wasteful under or over cutting of material, speeding up the digging process, and reducing the cognitive load of the operator allowing them to concentrate on other functions. Autonomous and augmented functions can also bring in advanced safety features such as object avoidance to automatically prevent collisions with dangerous, unseen items such as gas infrastructure and overhead powerlines. The only viable option to enable these features is a migration to EH control of the main control valve. The present work describes a system for converting any typical pilot-controlled machine into an EH controlled machine, while retaining the feel and controls of the original system. Layered on top of that work is demonstration of the EH capability of a retrofitted system through position and velocity control using the existing pumps and control valves on the excavator. The main work under consideration for this research was demonstrating the controls on the hydraulic excavator application on a rented Case CX210 excavator with 4000 operating hours. The pilot pressure control, function velocity control, and path planning controls were developed to work alongside the existing negative control hydraulic system on the machine.

2. ELECTROHYDRAULIC CONTROLS

There are three main styles of operator control of hydraulic systems on mobile applications. Namely, manual control, pilot pressure control, and electro-hydraulic (EH) control. Typically, manual controls are used on the smallest and/or most cost sensitive applications. Pilot pressure control is the industry standard and widely accepted for all working machines based on the balance of feel, control, and cost. Electro-hydraulic control is gaining acceptance on the market but has traditionally faced headwinds and scepticism with respect to cost, reliability, precision, and responsiveness on excavators.

In comparison to agriculture and other large industries, the construction industry has not achieved the same increases in productivity over the past decades as reported by McKinsey [1]. In part this is due to fragmentation of the market, the high customization and complexity of equipment and job sites, and underinvestment in innovation. One of the largest potential areas to boost productivity is electrification of equipment to enable automation [1]. Smart construction sites have accepted new technologies and increased demand for high precision work. This has driven a rapid transformation in the motor grader and dozer market towards full EH valves where the operator oversees steering and speed while global positioning systems replace and supplement traditional implement control and base surveying methods.

2.1. Challenges

A strong motivation for this paper is to demonstrate the effectiveness of EH control on excavators through a retrofit of an existing pilot operated system and development of coupled electrical, hydraulic, and kinematic controls. The goal of the research was to demonstrate the effectiveness of the Husco Exacto pilot pressure control system [2] by designing a generic and extensible control system for commanding an excavator in multi-function autonomous operation. Conversion of the excavator into a semi or fully autonomous machine presents significant challenges due to kinematics, variable loads, non-linear multi-function of implements, safety, and robustness. The main deliverables were enhanced performance of the existing hydraulic circuit, and a full speed automated flat grade at ±25mm tolerance using the full working range of the machine.

The requirement for the grade to be achieved at full machine speed is to prove that EH controls are not a limiting productivity or precision factor. Operating at the limit of machine performance increases the complexity of the control system when the pump pressure, flow, or power limit are reached as in **Figure 1** showing real machine data for a two pump excavator driven by an experienced operator. Flow and power are shared by all the moving functions which is a complexity an operator must compensate for, and must be replaced by sensors and algorithms.

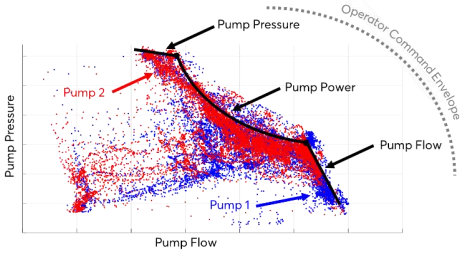

Figure 1: Working excavator power limits.

These challenges were evaluated with the Husco Exacto system in **Figure 2**. Exacto is an EH manifold valve with integrated controller, software, sensors and electrical harness. The system includes an advanced current servo with patented algorithms for dealing with changing environment and operating conditions, patent pending closed loop pilot pressure controls with two sets of pressure sensors per implement. The system is designed to interface with surveying/guidance systems and/or OEM instructions over CAN, and can be installed into existing pilot control systems without compromising any existing operator commanded performance or feel.

The Exacto system was also extended to include Husco developed path planning and function velocity control algorithms for this research. To supplement the EH controls, a human machine interface (HMI) was developed for triggering the system and selecting the commanded operation. String potentiometers and inertial measurement units (IMU) were added to facilitate the position and velocity control. This configuration is what was tested in the paper.

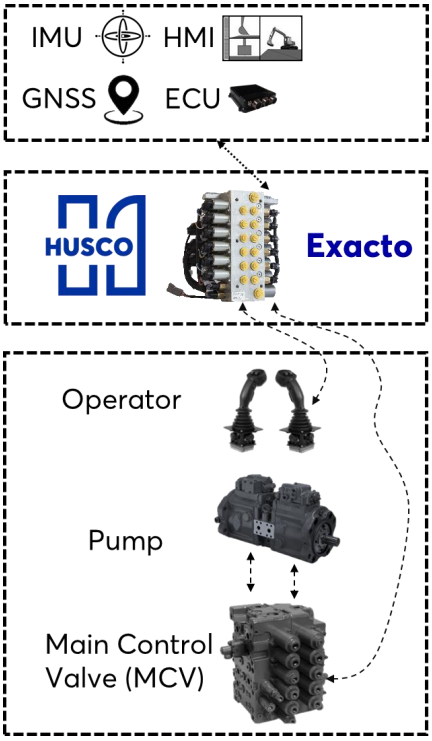

Figure 2: Exacto system implementation.

2.2. Pilot pressure control

Electrohydraulic control on the Exacto system is accomplished through the Firepower 2 family of Husco EH solenoid cartridge valves. The main working element is the electrohydraulic proportional relief valve (EPRV).

There are two main options for factory or retrofit using the Exacto system for EH pilot pressure control. The first version which was tested in the present work is a pilot interrupter system that sits between standard pilot joysticks and the spool end caps of the main control valve. When de-energized, the pilot interrupter system operates in pass-through mode where operator pilot joystick pressures reach the MCV unimpeded; retaining the machine in its original operating mode and operator HMI (the pilot joysticks). When the system is energized, the pilot joysticks can be blocked off to allow full EH operation or overriding/augmentation of operator commands. The second version allows for retrofit of the machine with digital or analog joysticks and removal of pilot hoses from the machine cab. Both options contain sensors to detect the hydraulic command generated to move the MCV spool and method for monitoring the operator joystick command.

The Firepower 2 EPRVs used by the system are fast, precise, and stable. Closed loop pressure controls leverage knowledge of the system to achieve the highest level of speed and repeatability. Safety and reliability is added to the EH system through monitoring of EPRV performance, detection of system fault or failure, and protection against change in EH performance over the life of the parts.

2.3. Velocity control

The development of the multi-function actuator velocity control system leveraged existing knowledge of hydraulic control systems and applied it to the reference machine. There is significant variation in excavator working function performance depending on the architecture of the hydraulic system, the loading of the individual functions, and machine to machine production variation. To establish multi-function harmony and control of the machine for coordinated high-speed movement, a plant model of the machine was developed with no prior knowledge of the valve design or flow

prioritization present on the existing negative control system on the CX210 excavator. No modifications were made to the existing hydraulic architecture other than installing the Exacto system in between the MCV and joystick pilot control valves. The multi-function system calculates the required feed-forward pilot pressures to achieve the commanded ratio of multi-function cylinder velocity commands. A closed loop velocity control system was wrapped around the system model to correct both instantaneous and long term errors.

2.4. Position control

The main focus of the research was development of the position control system included point inputs, path planning, cost functions, and coordination with the velocity control and feedbacks. There has been significant academic and industry work [3][4] on the topic of path planning and coordinated movement in multiple actuators. Hydraulic system instabilities, latencies, and load dependence increase the difficulty in creating a stable control system.

For reference, in a three-function excavator system (typically named boom, arm, and bucket), there are three degrees of freedom which combine to achieve the desired motion of the end effector. In the selected reference case, the controlled outputs included the position of the tip of the bucket in a cartesian x-y coordinate space, and an angle of attack of the bucket denoted by 'a'. For an example trajectory, the contributions from each function to the bucket tip position are shown in **Figure 3**. Each function pivot in a working arc centered on the respective pin. Each contribution can be calculated by solving the system of equations for the required function positions to achieve a specific location or the tip of the bucket and desired bucket angle over time.

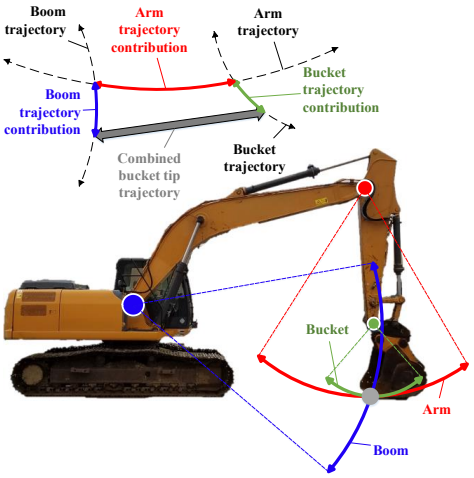

Figure 3: Excavator kinematics.

A set of path points was used to determine a path surface and bucket angle of attack. These points can be inserted into the controls via the HMI or computer connection.

The excavator contains many non-linear behaviors, so stable handling of induced errors and latencies is a key part of the control algorithm. An extrapolation of the trajectory was calculated from positional and velocity feedbacks as shown in **Figure 4**. Based on the proximity to the desired path, a blending of the perpendicular and following vectors was combined for both the current and projected positions.

The logic and flow of the algorithm can be seen in **Figure 5**. Positional and velocity feedbacks are combined with a kinematic model of the machine to understand the location of the bucket tip and angle of attack. The vector of travel is used to project a vector of travel for both the current moment in time and the future projected value as shown in **Figure 4**. Based on an input set of target coordinates, the projected

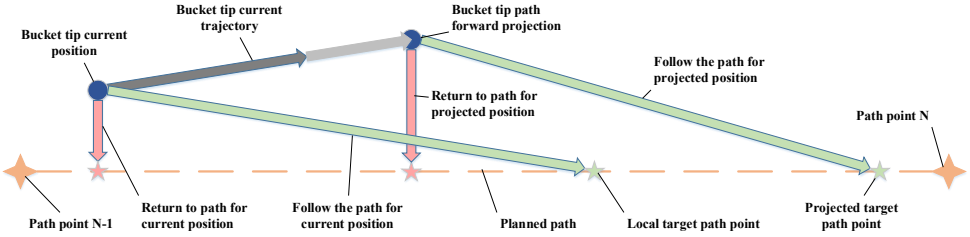

Figure 4: Path planning algorithm

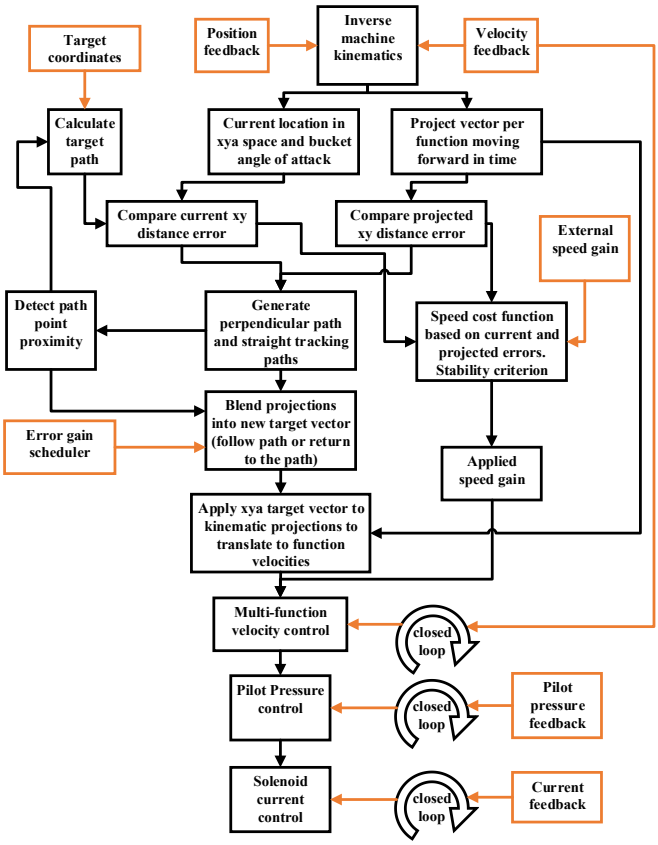

Figure 5: Path planning algorithm details and machine control architecture.

vector of travel is compared to the targeted path surface to generate a set of error terms. Additional error terms are generated based on system stability and acceleration. These error terms are combined into cost functions to govern the allowable speed of the system and change of states.

The cost functions and projected vectors of travel are blended to create a new target command vector, which can then be transformed into new function velocity commands. Closed loop velocity control of all function actuators is then completed iteratively. Each transient velocity control loop generates a set of pilot differential pressures for each control spool within the MCV in order to accomplish the desired velocity of the actuator. The core Exacto EH closed loop control then generates the desired pilot pressure differential using EPRVs.

3. VALIDATION AND RESULTS

The described system was designed, installed and tuned on the machine. With proper hardware, the hardware installation can be accomplished in less than one day with one technician. The installation is shown in **Figure 6**. The headline results demonstrate a system that successfully achieved a full automated grade using three functions (boom, arm, & bucket) at 95% of the flow capacity from the machine for the required motion and at a precision of ±25mm of the targeted grade. The maximum capacity of the machine was benchmarked by both time for cylinder stroke and pilot pressure commanded relative to maximum pilot pressure.

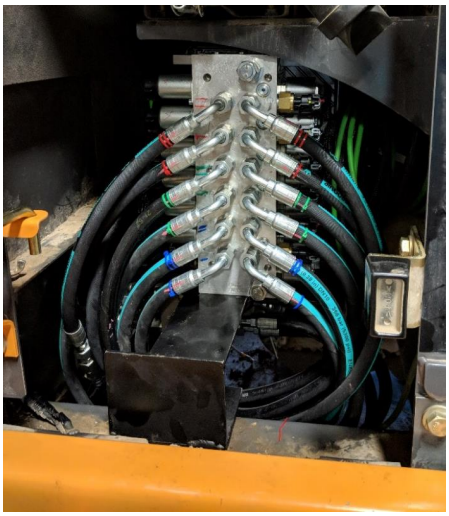

Figure 6: Installation of Exacto pilot interrupter

3.1. Pilot pressure results

The step response of the pilot pressure control system was benchmarked against the baseline machine. The EH system is used to replicate the operator command in a control-by-wire manner. The EH pilot control system has been proven to achieve response to >10 Hz before reaching a 3dB down value as installed on a machine. The spool response can be faster in EH mode than the original pilot controlled system since the EPRV with advanced algorithms can deliver a faster response and higher flow rate than the pilot joysticks, as well as shaping of commands to avoid overshoots. This response is shown in **Figure 7** comparing the Exacto pilot pressure response characteristic to a conventional mobile hydraulic solution and the machine response. As part of the study, the machine natural frequencies were also benchmarked.

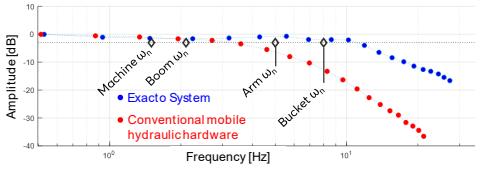

Figure 7: Pilot pressure step response.

The results demonstrated that the core Exacto EH system is not limiting the performance of the machine and can deliver the control efforts necessary to reach the full responsiveness of the function actuators.

3.2. Position and velocity control results

Establishing the full working range of the machine for a grading operation began with setting the bucket angle of attack to the desired angle and placing the bucket near the grading surface at maximum reach of the boom and arm. An example full range autonomous grade is shown in **Figure 8**. This includes the arm crossing beneath its pivot point while maintaining stable control as the load and boom motion switches directions. **Figure 8** shows the high speed grade at a precision of ±25mm of the targeted surface. The only operator input was the target path points for the start and end of the grade, and an enabling command.

Figure 8: Flat grade demonstration.

The pilot pressure, actuator velocity, and bucket tip position results for the example 7 meter grade over 7.2 seconds is shown in **Figure 9**. The velocity and position for high difficulty excavator working tasks demonstrates the effectiveness of the algorithms developed for the research vehicle and the EH controls.

An additional interesting test case for path planning and general excavator control algorithms, and one that is very difficult even for a proficient operator, is to draw a circle. The circle requires all functions to work in both extend and retract directions at varying speeds in different quadrants of the circle. A 14 second long exposure of a 2.5m diameter circle was taken of the fully automated machine with a light on the bucket tip shown in **Figure 10**.

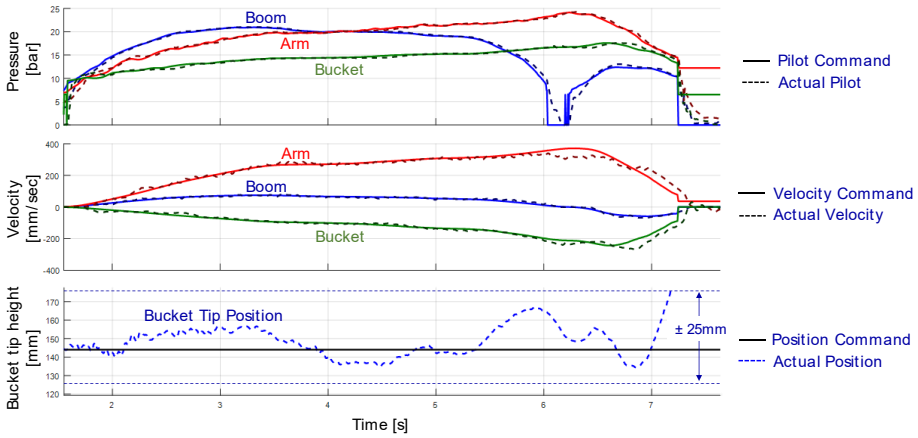

Figure 9: Flat grade results in automatic EH control

Figure 10: Position control demonstration

4. NEXT STEPS FOR MACHINE CONTROL

The present work demonstrated the ease of install of the Exacto pilot interrupter system and many of the benefits of EH control on excavator applications through a compact retrofit pilot manifold assembly.

After developing functional position and velocity control of all actuators, additional capabilities for safety and geo-fencing were explored and can be expanded in future work. With the command-by-wire methods, an expert operator can retain all the feel of a pilot control joystick system while also gaining computer override controls to stop function movement when reaching boundaries set by sensors or environmental hazards. Further development of the system and algorithms would be better integration with IMUs and GNSS systems, development of hardware HMI technology, and expansion of blended operator augmentation methods. Deployment of EH on excavators through both retrofit and factory-fit unlocks the potential for significant productivity improvements to help job sites keep up with global construction demand.

NOMENCLATURE

EPRV	Electrohydraulic proportional relief valve
EH	Electro-Hydraulic
MCV	Main control valve
CAN	Controller area network
HMI	Human-machine interface
IMU	Inertial measurement unit
ECU	Engine control unit
GNSS	Global navigational satellite system

REFERENCES

[1] McKinsey Global Institute (2017), Reinventing construction: a route to higher productivity, https://www.mckinsey.com/industries/capital-projects-and-infrastructure/our-insights/reinventing-construction-through-a-productivity-revolution

[2] https://www.husco.com/wp-content/uploads/2019/11/Exacto-article.-v2.pdf

[3] Gasparetto A, Boscariol P, Lanzutti A, and Vidoni R (2015) Path planning and trajectory planning algorithms: a general overview. Mechanisms and Machine Science, vol. 29

[4] Willms A, Yang S (2006) Real-Time Robot Path Planning via a Distance-Propagating Dynamic System with Obstacle Clearance. IEEE Trans. Syst. vol. 38

peer reviewed

ELECTRIFICATION OF HYDRAULIC SYSTEMS USING HIGH-EFFICIENCY PERMAMENT MAGNET MOTORS

Pablo Castro Palavicino [1]*, Bulent Sarlioglu [1], Dheeraj Bobba[1], Woongkul Lee[1], Tatiana Minav[2]

[1]*Wisconsin Electric Machines and Power Electronics Consortium (WEMPEC), University of Wisconsin-Madison, WI, USA*

[2]*Tampere University, Faculty of Engineering and Natural Sciences, IHA, Tampere, Finland*

* Corresponding author: Tel.: +1 608 262 2703; E-mail address: sarlioglu@wisc.edu

ABSTRACT

In this paper, electrification of hydraulic systems is proposed using high-efficiency permanent magnet (PM) motors and wide bandgap power electronic drives. Direct driven hydraulics (DDH) is selected because of its higher efficiency compared to other conventional technologies such as valve-controlled systems. The DDH is directly driven by a servomotor. The ratings and design guidelines for a servomotor used in DDH applications are provided in this paper. Specifically, a surface permanent magnet synchronous machine (SPMSM) is designed. Finally, a state-of-the-art inverter using silicon carbide wide bandgap devices are designed for high performance operation.

Keywords: Direct driven hydraulics, Electrification, Electric motors, Hydraulic actuator, High efficiency, Permanent magnet synchronous machines

1. INTRODUCTION

Hydraulic systems are known for their capability of applying large forces with a fast response. The further electrification of hydraulic systems is becoming popular, mainly for increasing the system efficiency. These additional features are attractive in a high-performance application such as heavy-duty mobile or stationary applications.

Electrification of powertrains in off-road mobile applications has been extensively studied [1]. The next step for further improvements consists of the electrification of working hydraulics or implements. Regarding drivetrain systems, electrification can be done by connecting an engine to an electric generator. Thus, a generator provides power to a combination of converters feeding electric motors to drive hydraulic pumps, which complete the electrification of the implements or actuators of hydraulic system.

Many examples of engine/electric generator type of electrification have been reported in the literature [1, 2], where authors demonstrated improvements in both force/position response and efficiency. Reduced energy consumption and higher efficiency are critical in electric and hybrid off-road mobile applications, such as construction equipment, forest, and mining machinery. The state-of-the-art research demonstrated that significant improvements to the system efficiency can be achieved by switching from valve-controlled to pump-controlled hydraulic systems. Moreover, using a variable speed electric drive with a fixed displacement pump allows further improvements in the hydraulics, making it more energy efficient [3–5].

To provide high-performance electrification to hydraulic systems, high torque-density electric machines are required. Surface permanent magnet synchronous machines (SPMSM), with fractional-slot concentric windings (FSCW) becomes a desirable candidate, due to their high efficiency and high-power density. The main goal of this paper is to design a high-performance and efficient electric drive for further electrification of working hydraulics in off-road machinery with pump-controlled systems such as direct-driven hydraulics (DDH).

2. HYDRAULICS ELECTRIFICATION

In a traditional diesel operated mobile machinery, the energy available in fuel is converted to hydraulic through an internal combustion engine (ICE). In [6], an accurate description of the sources of energy losses in a typical hydraulic system were described. The diagram of **Figure 1** depicts how losses are distributed in a conventional hydraulic system.

Based on **Figure 1**, it is possible to identify several opportunities for increasing the efficiency in hydraulic systems. Although several improvements have been made in the design of ICE and hydraulic components [6], many hydraulics based applications, such as excavators, offer opportunities to recover energy. Typically, in excavator applications there are plenty of possibilities for harvesting and storing the kinetic and potential energy, for example, when bringing down a heavy load on a bucket to the ground or during swing motion. A general diagram of how electrification can improve hydraulic systems is shown in **Figure 2**.

Several examples of energy savings by electrification have been reported in [1]. Most of the focus for energy saving was based on including electrical energy storage, such as batteries or super capacitors. Thus kinetic and potential energy can be recovered through electric drives. Companies have deployed commercial products with a combination of hydraulic and electric systems. Examples of these products can be found for Kobelco, Hitachi, Caterpillar, and Komatsu [1, 2]. Topologies combining hydraulic and electrical systems by several manufacturers are depicted in **Figure 3**.

In the academic side, in [7], energy recovery was proposed for electric hydraulic hybrid electric system by harvesting potential energy from the boom in an excavator. Other examples include the design of novel topologies as the one shown in [8], which combines closed-loop in a hydrostatic transmission circuit and a hydraulic accumulator for energy storage. Many of the efforts have been made in utilizing hydraulic accumulators to recover the potential and kinetic energy of the system. The hydraulic accumulator then drives an electric generator which store the energy in capacitors or batteries. Examples of hydraulic accumulators for energy saving are provided in [9–12].

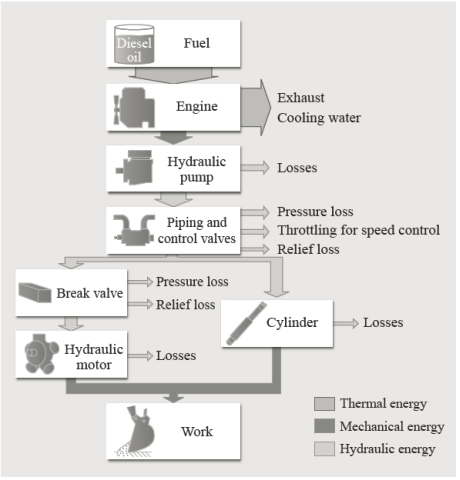

Figure 1: Power flow diagram for a hydraulic system depicting losses in the different stages of power conversion [6].

Industrial applications use open circuit hydraulic systems with large oil reservoirs with a valve to control flow, which is characterized by its low system efficiency. An alternative for valve-controlled hydraulic system is directly applying power in the hydraulic pump and omitting complex servo valves. Thus, a prime mover is connected to the pump, resulting in pump-controlled systems [4]. In pump-controlled systems, a variable displacement pump is controlled by a prime mover. Thus, by running the electric motor at a fixed speed, the control of flow is performed by modifying the displacement of the pump. Therefore, less energy consumption can be achieved.

Further improvements can be made by utilizing an electric drive with variable speed to drive a fixed displacement pump. Thus, directly controlling the flow by modifying the speed of the electric motor. Systems, where a variable speed electric drive is used for directly operate a pump, are referred to as direct-driven hydraulic (DDH) systems [3–5, 13, 14]. A figure of a typical hydraulic system and DDH system is demonstrated in **Figure 4** and **Figure 5**, respectively. By directly driving a pump, DDH systems become more efficient compared to their equivalent valve-controlled, thus improvements in efficiency up to 200 % can be achieved.

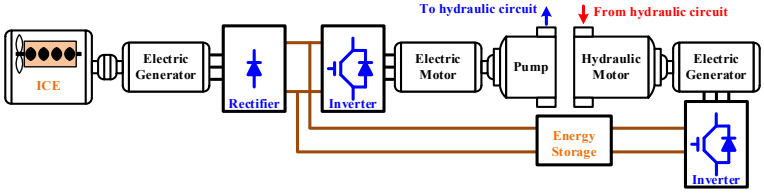

Figure 2: Generic scheme of how electrification allows to recover and store energy from hydraulic systems.

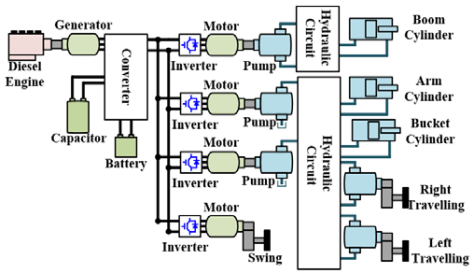

(a)

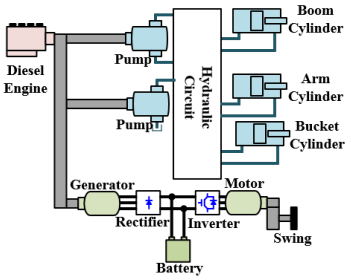

(b)

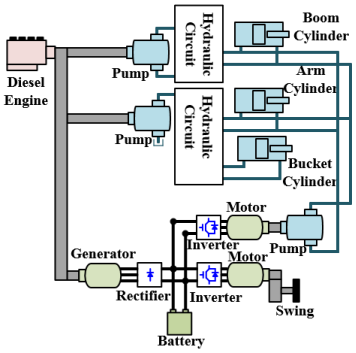

(c)

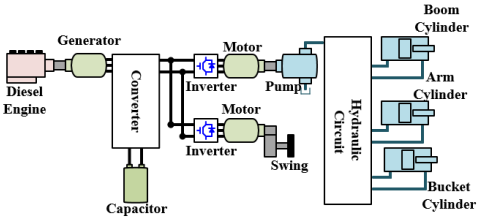

(d)

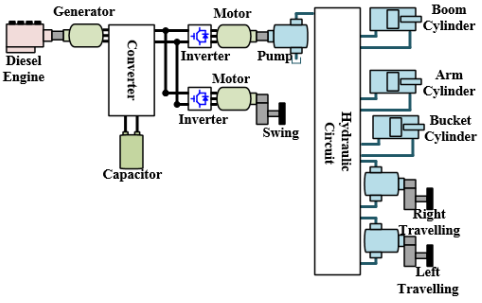

(e)

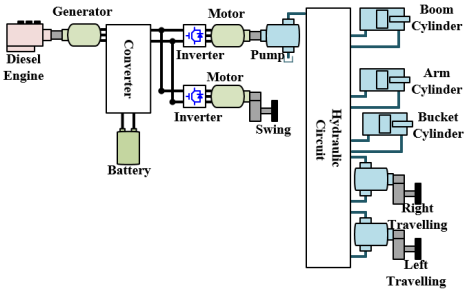

(f)

Figure 3: Examples of commercially available electrified excavators [1], (a) Kobe Steel series-parallel hybrid excavator, (b) Doosan series-parallel hybrid excavator, (c) Komatsu series-parallel hybrid excavator, (d) Hitachi parallel hybrid excavator, (e) New Holland parallel hybrid excavator, (f) Kobelco parallel hybrid excavator.

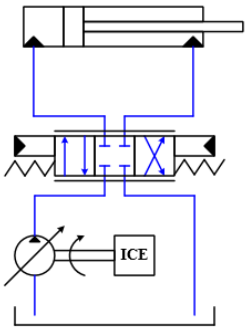

Figure 4: Simplified example of valve-controlled system.

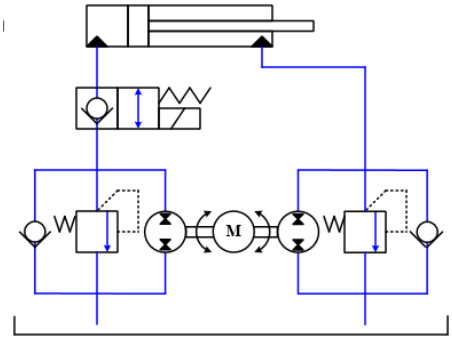

Figure 5: Direct driven hydraulic system.

Nowadays, electric drives can achieve a precise torque/speed/position control with minimal losses compared to hydraulic systems. One of the main objectives of this paper is to describe the design of a combination of an electric machine and an inverter for DDH systems. Based on the applications studied for DDH in [3, 5, 14], the ratings depicted in **Table 1** are used as a baseline for sizing and designing an electric machine. The details regarding the electric machine and drive are discussed in the following sections.

Table 1: Rating of Electric Machine

Rated values	Value
Rated speed, RPM	2000
Rated torque, Nm	25
Rated power, kW	5.2

3. PERMAMENT MAGNET ELECTRIC MACHINES

When selecting an electric motor for industrial and mobile applications, induction motors have been the standard choice due to their construction robustness and low cost. Nowadays, SPMSM are gaining a lot of attention for their superior efficiency and torque density compared to induction machines.

In this section, a SPMSM is proposed for high-performance electrification. The machine is designed to meet required frame size constraints and operate at the desired speed while maintaining high performance. The stator design must be carefully tuned to achieve high performance and fit reasonably small size, thus enabling to be used for electrifying hydraulic actuators.

3.1. Stator Design Considerations

A higher number of poles is desired to achieve higher torque density. However, machines with a higher number of poles typically use a higher number of stator slots to allocate the windings.

The function of the windings is to provide a sinusoidal magneto motive force (MMF) creating a rotating magnetic field. The magnets in the rotor will align with the stator rotating magnetic field, thus producing torque and making the rotor to spin. However, distributing the winding in a sinusoidal pattern in the stator is not practical. Alternatively, the winding can be distributed through the stator in such a way that a fundamental component of the rotating MMF is dominant compared to the rest of the harmonics.

In **Figure 6** a distributed winding (DW) for 10 poles is shown. The dots and crosses depict where the current is coming into or leaving the stator plane. Typically, for a 3-phase machine, generating necessary poles in the stator magnetic field involves the winding being distributed to create a repeating square wave whose fundamental component matches that of the rotor. Hence, a 10-pole design requires 30 slots, which in limited volume will result in small slots to accommodate the copper wires. A higher number of slots and small slot area result in lower overall copper fill and higher stator resistance which leads to a decrease in the efficiency. Also, this kind of distributed windings requires large end windings, which makes the machine bulkier.

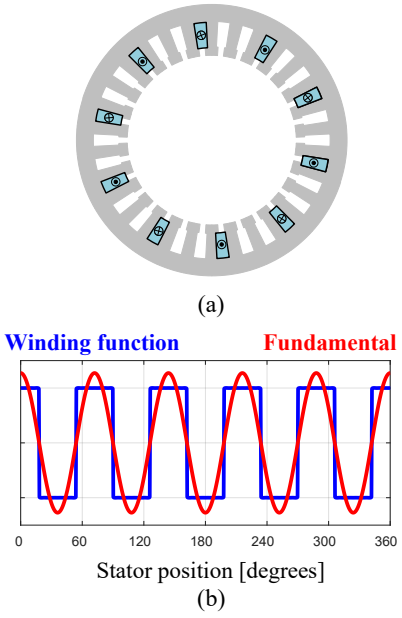

Figure 6: Distributed winding configuration, (a) Phase A windings, (b) winding function and fundamental

Alternatively, fractional slot concentrated windings (FSCW) [15–17], as shown in **Figure 7**, can be utilized in designs with a higher number of poles but limited stator volume. In this configuration the turns are distributed such that the dominant stator MMF harmonic matches the desired number of poles. It is to be noted that the dominant MMF harmonic is not necessarily the fundamental harmonic corresponding to the winding distribution.

The advantage of FSCW configuration is that rather than 30 slots, only 12 slots are needed, giving more room to allocate the coils in the stator teeth, thus decreasing the stator resistance. Also, as the coils are wrapped around each stator tooth, thus, the end windings are considerably shorter and require less volume compared to their distributed windings counterparts. The drawback of utilizing FSCW compared to DW is that for the same number of turns per phase the amplitude of the dominant harmonic component of the winding distribution is lower. Thus, more turns are needed to obtain a higher fundamental amplitude. **Figure 8** shows the difference regarding space in between DW and FSCW, showing that FSCW is more compact and easier to manufacture.

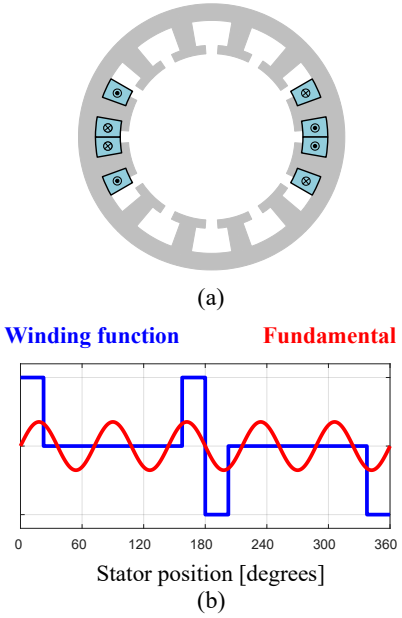

Figure 7: Fractional slot concentrated winding configuration, (a) Phase A windings, (b) winding function and dominant harmonic

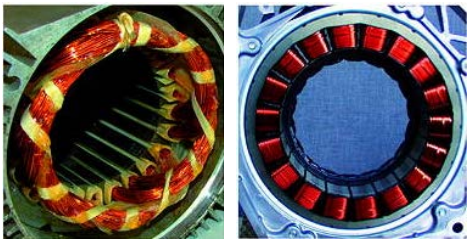

Figure 8: Comparison between stator winding configurations, (a) distributed winding, (b) fractional slot concentrated winding[18].

3.2. Rotor Design Considerations

Typically, for a surface PM rotor design, arc magnets are used in the rotor structure; however, in the proposed design, the magnets are shaped to decrease the ripple torque.

When a motor is designed for high-speed operation, then the rotor design becomes more challenging. However, this is not the case for hydraulic applications. As the machine is aimed to spin at 2000 RPM there are no additional structural requirements for the rotor design.

3.3. Proposed PM Electric Machine Design

The geometric constraints for this machine consider an outer diameter of 150 mm and a shaft diameter of 60 mm. 10 poles were chosen for the design to take advantage of the low-speed requirement and minimize the stator back iron thickness. The rated values obtained from the design are shown in **Table 2**. **Figure 9** shows the proposed design. Finite element analysis (FEA) was performed to obtain the torque waveform at rated conditions as shown in **Figure 10**. It can be seen that although the torque ripple increases slightly at overrated operation due to saturation effects, overall torque ripple is under 2% with a 0.5% ripple at rated operation (15 Arms).

An efficiency map is shown in **Figure 11**. In order to focus on the desired range of operation for this application, i.e. 300 to 3000 RPM and 5 to 25 Nm of torque, the efficiency bands are limited to a lower bound of 80% in **Figure 11**. All the data below 80% is represented by a single color band. From the results it can be confirmed that high efficiency and minimal torque ripple can be achieved within the desired operation range from the designed electric machine.

Table 2: Rating of SPMSM proposed design

Rated value	Value
Rated voltage, Vrms	380
Rated current, Arms	15
Number of poles	10

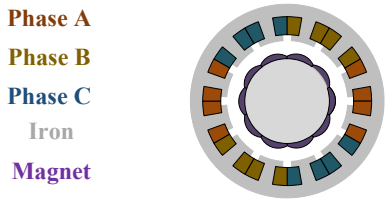

Figure 9: Proposed 12 slots/10 poles SPMSM design.

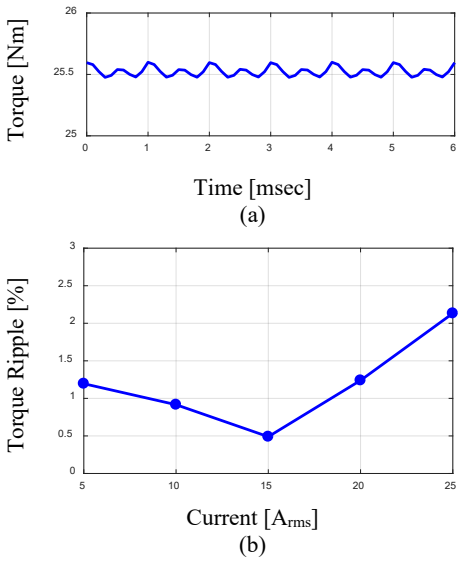

Figure 10: Shaft output (a) Torque at different current levels (b) Torque ripple percentage as a function of the stator current.

4. INVERTERS

An electric machine driven by variable speed drives (VSDs) provides higher efficiency and better dynamic performance than line-connected fixed speed electric machine. Depending on the types of the input power source, the VSDs can be classified into voltage-, current-, and impedance-source inverters, but the voltage-source inverter (VSI) has been playing a major role in industrial drive applications such as fan, blower, pump, and servo motors since the advent of insulated-gate bipolar transistors (IGBTs).

In this section, VSIs for electrified hydraulic actuators are introduced, and different switching device options are discussed in detail.

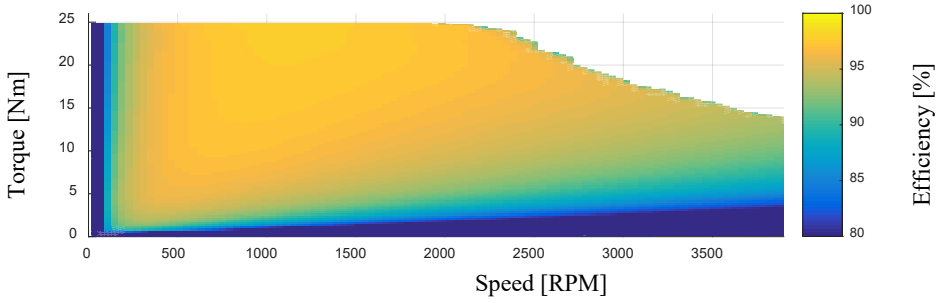

Figure 11: Efficiency map for proposed SPMSM machine with FSCW.

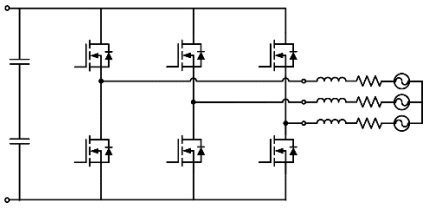

Figure 12: Schematic of 2-level voltage source inverter.

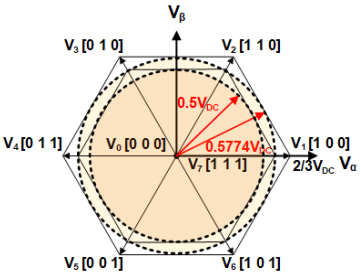

Figure 13: Vector diagram of space vector modulation and sine PWM.

4.1. Two-Level topology with IGBTs

A 2-level VSI has been dominantly used for VSD applications, and it requires a dc-link capacitor, six active switches, and six antiparallel diodes as shown in **Figure 12**. The voltage ratings of the power devices and capacitors need to meet the rated voltage of the electric machine designed in the previous section. Since the rated line-to-line rms voltage of the electric machine is 380 V, the peak phase voltage becomes 310.27 V. When space vector modulation (SVM) as shown in **Figure 13** is utilized the maximum peak inverter output voltage is 57.7% of the dc-link voltage indicating that the minimum required dc-link voltage is 537.7 V. For higher than 550 V dc-link voltage and 15 A rated current, 900 V silicon (Si) IGBT, SiC, and GaN devices are all applicable, and 1200 V Si IGBT and SiC are also available in the market.

Si IGBTs have been around more than three decades in power electronics industry [19], and their device characteristics and behavioral models are well understood. The price of the device is two to three times lower than the equivalent SiC or GaN devices as of 2019 [19], and there are large collections of device ratings and manufacturers. However, it is also well-known fact that IGBTs can only operate within limited switching frequency range (typically less than 20 kHz) due to excessive switching losses. It also generates high conduction loss, which significantly affects the motor drive system efficiency at light load conditions.

4.2. Two-Level topology with wide bandgap devices

The SiC and GaN devices are alternative options to Si IGBTs. These devices can operate over 50 kHz due to its 5 to 10 times faster switching speed and lower on-state resistance. The increased cost due to high device price can ultimately compensated by reduced passive component [20], minimized cooling component design such as heatsink and fan [21], and energy-saving from improved efficiency throughout the operating time [22].

A circuit simulation is conducted to validate the impact of switching frequency on the current waveform as shown in **Figure 14** and **Figure 15**. The dc-link voltage is set to be 600 V and SiC MOSFET C2M0080120D, which has a maximum blocking voltage of 1200 V and a current rating of 36 A is used for the simulation. The output current ripple is reduced by 60% in 50 kHz operation as compared to that of 20 kHz operation. The reduced output current ripple leads to low PWM-induced iron losses [23], low ripple torque [24], and low audible noise.

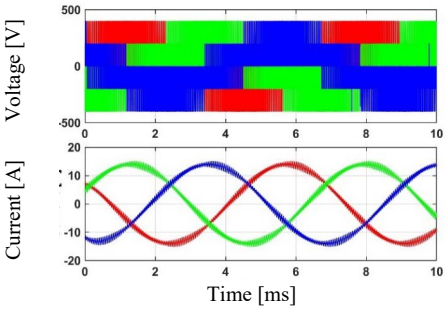

Figure 14: SiC inverter operating at 20 kHz with RL load at 150 Hz fundamental frequency.

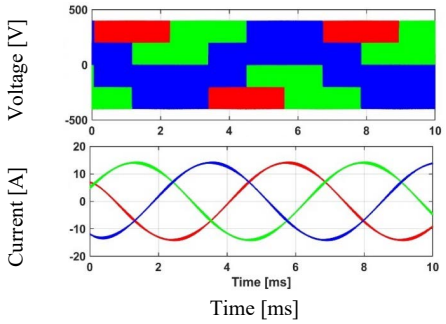

Figure 15: SiC inverter operating at 50 kHz with RL load at 150 Hz fundamental frequency.

5. DISCUSSION

The benefits of electric drives allow to improve efficiency of hydraulic systems by implementing DDH. Hydraulic pumps typically operate in a range between 300 to 3000 RPM [25]. In the DDH, the electric drive is directly connected to the pump where both the pump and the electric motor operate at the same speed. For a range where the operational speed varies between 300 through 3000 RPM the designed electric motor demonstrates a large efficiency, i.e. above 95 %. The efficiency only drops in low torque operation points that are unlikely to occur due to the pump operational characteristics [25].

Regarding controllability, the torque control in an electric drive is very high due to the capability of the inverter to inject current in the stator windings instantaneously. As the torque is mainly dependent in the injected current from the inverter, torque can be achieved extremely fast at any operational speed, thus making the electric drive suitable for deliver torque with good accuracy including the low speed or zero speed region. This last property makes inverter driven motors suitable for electrifying hydraulic systems where the low or zero speed operation can be a challenge otherwise.

Efficiency improvements were obtained when moving from valve-controlled to pump-controlled systems due to high performance servo drive. Moreover, direct-driven hydraulic systems are accepted as a promising technology for hydraulic hybridization which reduces the number of components and the size the overall system.

In terms of electric machines, SPMSM shows superior performance compared to induction machines. Thus, SPMSM was chosen for analysis for the electrification of a hydraulic system. For DDH applications, relatively low speeds, high torque, and limited size are the requirements while keeping the efficiency high. As machines with higher torque require typically more number of poles, a FSCW topology was chosen, thus being able to create the necessary number of poles, to match the torque needed in the limited volume constraint. The designed machine was analyzed with FEA showing efficiency above 95% in almost all the range of operation.

Finally, regarding the inverter, it was shown that higher switching frequencies can lead to small components and better performance in terms of torque and current ripple. However, high-switching frequencies are not achievable with IGBT switches. In this paper, it is proposed to use SiC switches that allow to increase the switching frequency and reduce the switching losses, thus, contributing to higher performance and efficiency.

6. CONCLUSIONS

In this paper, electrification of working hydraulics for off-road machinery application was discussed. The review in electrification of hydraulic system has demonstrated that significant improvements regarding efficiency were achieved by including electric drives.

Surface PM motor with FSCW and SiC-based power electronic inverter were designed and shown as a promising candidate for high-performance and high-power density pump-controlled systems as a way for further electrification of off-road machinery. Features of the propose system include high overall efficiency, compactness, and fast torque response.

ACKNOWLEDGEMENT

The authors would like to thank to the Wisconsin Electric Machines and Power Electronic Consortium for their support. Also, authors would like to acknowledge JSOL for providing the license for their software JMAG for finite element analysis.

REFERENCES

[1] Wang J, Yang Z, Liu S, et al (2016) A comprehensive overview of hybrid construction machinery. Adv Mech Eng 8:1–15. https://doi.org/10.1177/1687814016636809

[2] Casoli P, Riccò L, Campanini F, Bedotti A (2016) Hydraulic Hybrid Excavator—mathematical model validation and energy analysis. Energies 9:1002. https://doi.org/10.3390/en9121002

[3] Teemu K, Kauranne H, Calonius O, et al (2018) Experimental investigation of a directly hydraulic unit in an industrial application. 11 Int Fluid Konf. https://doi.org/10.18154/RWTH-2018-224644

[4] Koitto T, Calonius O, Kauranne H, et al (2018) Enhanced energy efficiency of industrial application by direct driven hydraulic unit. 2018 Glob Fluid Power Soc PhD Symp GFPS 2018 1–6. https://doi.org/10.1109/GFPS.2018.8472365

[5] Koitto T, Kauranne H, Calonius O, et al (2019) Experimental study on fast and energy-efficient direct driven hydraulic actuator unit. Energies 12:1–17. https://doi.org/10.3390/en12081538

[6] Edamura M, Ishida S, Imura S, Izumi S (2013) Adoption of electrification and hybrid drive for more energy-efficient construction machinery. Hitachi Rev 62:118–122

[7] Lin T, Wang Q, Hu B, Gong W (2010) Research on the energy regeneration systems for hybrid hydraulic excavators. Autom Constr 19:1016–1026.https://doi.org/10.1016/j.autcon.2010.08.002

[8] Ho TH, Ahn KK (2012) Design and control of a closed-loop hydraulic energy-regenerative system. Autom Constr 22:444–458. https://doi.org/10.1016/j.autcon.2011.11.004

[9] Wang T, Wang Q (2014) An energy-saving pressure-compensated hydraulic system with electrical approach. IEEE/ASME Trans Mechatronics 19:570–578. https://doi.org/10.1109/TMECH.2013.2250296

[10] Joo C, Stangl M (2016) Application of power regenerative boom system to excavator. 10th Int Fluid Power Conf 7–11

[11] Vukovic M, Sgro S, Murrenhoff H (2013) Steam - A mobile hydraulic system with engine integration. ASME/BATH 2013 Symp Fluid Power Motion Control FPMC 2013 1–11. https://doi.org/10.1115/FPMC2013-4408

[12] Kim YB, Kim PY, Murrenhoff H (2016) Boom potential energy regeneration scheme for hydraulic excavators. BATH/ASME 2016 Symp Fluid Power Motion Control FPMC 2016 1–7. https://doi.org/10.1115/FPMC2016-1740

[13] Niraula A, Zhang S, Minav T, Pietola M (2018) Effect of zonal hydraulics on energy consumption and boom structure of a micro-excavator. Energies 11:1–22. https://doi.org/10.3390/en11082088

[14] Hänninen H, Minav T, Pietola M (2016) Replacing a constant pressure valve controlled system with a Pump controlled system. BATH/ASME 2016 Symp Fluid Power Motion Control FPMC 2016 1–7. https://doi.org/10.1115/FPMC2016-1777

[15] Wang A, Wang C, Wang Y (2013) Performance analysis and comparison of interior permanent magnet machine with FSCW and distributed windings for a hybrid electric vehicle. In: International Conference on Electrical Machines and Systems, ICEMS. IEEE Computer Society, pp 1044–1047

[16] Cheng L, Wang M, Zheng P, et al (2018) Improvement of a Hybrid-PM Interior-PMSM with Six-Phase FSCW for EV Application. In: ICEMS 2018 - 2018 21st International Conference on Electrical Machines and Systems. Institute of Electrical and Electronics Engineers Inc., pp 425–429

[17] Li J, Zou J, Xu Y (2015) Analysis and design of FSCW SPM machines for a given constant power region. In: 2015 IEEE International Magnetics Conference, INTERMAG. Institute of Electrical and Electronics Engineers Inc.

[18] Single-tooth motors could bite into the EV market - Drives and Controls Magazine. https://drivesncontrols.com/news/fullstory.php/aid/4009/Single-tooth_motors_could_bite_into_the_EV_market.html. Accessed 14 Nov 2019

[19] Baliga BJ (2018) Fundamentals of power semiconductor devices, Second edition. SPRINGER-VERLAG NEW YORK

[20] Burkart RM, Kolar JW (2017) Comparative life cycle cost analysis of Si and SiC PV converter systems based on advanced η-ρ-σ multiobjective optimization Techniques. IEEE Trans Power Electron 32:4344–4358. https://doi.org/10.1109/TPEL.2016.2599818

[21] Murakami Y, Tajima Y, Tanimoto S (2013) Air-cooled full-SiC high power density inverter unit. World Electr Veh J 6:669–672. https://doi.org/10.1109/EVS.2013.6914864

[22] Power America _ Department of Energy

[23] Chang L, Jahns TM (2018) Prediction and evaluation of PWM-induced current ripple in IPM machines incorporating slotting, saturation, and cross-coupling effects. IEEE Trans Ind Appl 54:6015–6026. https://doi.org/10.1109/TIA.2018.2846718

[24] Shirabe K, Swamy M, Kang JK, et al (2012) Advantages of high frequency PWM in AC motor drive applications. In: 2012 IEEE Energy Conversion Congress and Exposition, ECCE 2012. pp 2977–2984

[25] Majumdar SR (2003) Oil hydraulic systems : principles and maintenance. McGraw-Hill, New York, pp. 98

peer reviewed

CHALLENGES AND POSSIBILITIES OF THE INTEGRATION OF ELECTRIC DRIVES IN MOBILE MACHINERY

Andreas Opgenoorth, Stefan Quabeck, Rik W. De Doncker, Katharina Schmitz

Institute for Fluid Power Drives and Systems, RWTH Aachen, Campus-Boulevard 30, 52072 Aachen;
* Corresponding author: Tel.: +49 241 80 47724; E-mail address: Andreas.Opgenoorth@ifas.rwth-aachen.de

ABSTRACT

This paper provides an overview of the challenges and possibilities of the integration of electric drives into diesel-hydraulic excavators. Due to the drivers of emission reduction, the use of renewable energies and more energy efficient systems, a global push leads to the integration of electric drives in excavators. In mobile machinery such as excavators, new possibilities and challenges of the adaptation of the drive train and energy storage arise.

Rotational actuators can be powered by direct electric drives to avoid losses of the hydraulic system. Adapted hydraulic system topologies enable recuperation and reduce throttling losses in hydraulic systems. Variable and overall higher electric motor speeds reduce the size of the electric and hydraulic components and enable operation in more efficient operating points.

To evaluate possible changes to the traditional hydraulic excavator systems, a simulation model is built and the proposed adaptations are implemented. The paper concludes with the evaluation of the proposed system changes and an outlook for further possibilities of hydraulic system adaptions in relation to the electric drive.

Keywords: Excavator, Electric, Mobile Machinery, Battery, Energy, Emissions

1. INTRODUCTION

1.1. Motivation

In order to counteract climate change and improve air quality, it is necessary to reduce relevant sources of greenhouse gases and air pollution. Considerable CO_2 emissions are caused by the construction industry. In the construction industry fossil fuels alone produce 300 million tons of CO_2 per year, representing 1 % of global CO_2 emissions [1]. Furthermore, research by Helms show in 2014, the emission rate of NO_x from mobile machinery was 20 % of the emissions from the transport sector and the particulate pollution from mobile machinery was on a par with the transport sector [2]. The environmental and health burdens caused by NO_x and particulate matter can only be reduced by complex exhaust gas after treatments. In particular, the avoidance of CO_2 emissions directly in combustion engines is not possible [3].

Restrictions are being imposed politically worldwide to reduce emissions. In the transport sector, for example, Norway will forbid the registration of new cars driven by combustion engines from 2025, the Netherlands and Germany from 2030 and France from 2040 [4]. Whilst currently effective bans are limited to passenger cars, there are already efforts to extend these developments to all machines with combustion engines, such as Japan‘s plans to integrate the use of hydrogen in all energy sectors from 2030 to 2050 [5].

In order to reduce emissions for mobile machinery, clean energy sources have to be used. Compared to the emissions of the Diesel engine, electric energy, especially from renewable sources, can lower the CO_2 emissions, as the CO_2 equivalents of the Diesel engine and electric energy sources imply and is in the diagram including the electric grid and charging losses in **Figure 1**.

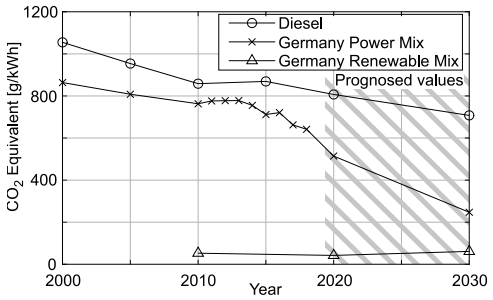

Figure 1: CO_2 Emissions of power sources based on mechanic output [6–8]

As it already has emerged in the transportation sector, electric drives can achieve this task by using electric energy from renewable energy sources. Therefore, the challenge arises to integrate electric drives into mobile machinery, for which the example of an excavator is used as a baseline in this paper.

1.2. Challenges

It has already proven possible and feasible to integrate electric drives with lithium-ion batteries into mini excavators, as there are models with a weight up to 4 t to be released from different manufacturers [9–11]. Nevertheless, for larger machines, challenges arise in the storage of the necessary electrical energy, as on the one hand the performance class of the machines increases and on the other hand the degree of utilization also rises. A 26-ton Caterpillar excavator prototype uses 300 kWh of batteries, with a battery weight of 3.4 tons [12]. Considering the large amount of required batteries in relation to global demand, not only the cost of batteries but also their availability is challenging [13].

In addition to the challenges of storing the energy, the electric drive induces a changed system behavior and additionally enables new possibilities of variable engine speeds, direct electric drives and recuperation. Traditional hydraulic systems however are built for a single direction power flow using variable displacement pumps running at constant speeds [14]. By adapting the hydraulic system, the advantages of the electric drive system can be utilized to improve the excavator system in terms of energy efficiency, thus reducing the necessary stored energy [15].

2. STATE OF THE ART

The current development in the electrification of excavators is driven by requests of energy-efficient and emission-free construction machinery [15]. Developments of battery technology and power electronics make it possible to build battery powered excavators, which can be operated for a working day without down time [9].

2.1. Batteries and Power Electronics

The first documented mobile application of electric was an electric car in 1827, even before the invention of the diesel engine in 1893 [16]. Nowadays, electric drives are used in a wide range of mobile applications, from small drives of only several watts for auxiliary drives to the 16.56 MW traction drive of a bucket-wheel excavator [17]. There are three types of electric machines which are used in most mobile drive applications: induction machines, synchronous machines and switched reluctance machines. The preferred machine type depends on the application. While switched reluctance machines are interesting for high-speed applications, synchronous machines achieve higher efficiency, and induction machines are cheaper and more reliable [18].

In most mobile drive applications, power-electronic inverters are applied to control the machine speed and torque, especially when variable speed is required or the machines are fed from a dc source. These inverters consist of semiconductor switches, a control unit, and several filter elements. They can reach efficiencies of up to 98% [19].

The electric power for the drive can be supplied from a battery (dc source) or directly from the grid (ac source). For mobile machinery, batteries are preferable, as they allow full freedom of movement. They offer an efficiency of up to 97 % from charging to discharging and energy densities of up to 240 Wh/kg [20]. For high-power applications and nearly uninterrupted operation, a direct connection to the grid is still the only feasible option.

2.2. Electric Excavators

There are three types of commercially available excavators using electric drives: Mining excavators, mini excavators and hybrid

excavators. The history of electric mining excavators reaches back over 100 years with electric rope excavators [21]. Today electric excavators are still widely used in surface mining, especially in large machines. Main reasons for electric mining excavators are reduced fuel costs, reduced emissions and a higher up-time [22]. Electric mining excavators are generally powered by cable as the large amounts of energy cannot be stored in batteries and, as the excavators move very little, the use of a cable is possible. An example for a cable-based mining excavator is the Liebherr R 9200 E [23]. The 850-kW engine power of the 210 t machine is made possible by a 6 kV cable. A limit for larger scales does not exist, as the largest machine in the world is an electric mining excavator, the Bagger 288. The machine weighs 12.840 t and the electric drives provide a sum of 16.56 MW of power with a voltage supply of 30 kV [17].

In contrary to mining excavators, mini excavators face different working environments and requirements. The installed engine power of available machines range from 7.5 kW in the Bobcat e10 excavator to 75 kW in the Suncar TB260E [10, 24]. In addition, the utilization of the machines is lower compared to large excavators. This results in an overall low energy consumption and it can be feasible to use batteries as an energy source. In the available electric mini excavators, no adaptations of the hydraulic systems besides the integrated electric drives are published by the manufacturers.

Hybrid excavators use electric drives to improve energy efficiency and reduce the fuel consumption of their combustion engines. Hybrid crawler excavators by Komatsu and Hitachi rely on electric swings to recuperate the kinematic energy from the heavy machines. The manufacturers state fuel savings from 20 % up to 40 % [25, 26].

2.3. Excavator drive train

The drive train of the excavator can be split up into the energy source, energy conversion and energy output. Traditionally, a diesel engine supplies the energy to the hydraulic system, which then directs it to the cylinders or engines. Topologies of the drive train of excavators are traditionally based on valve-controlled closed-center or open-center systems. The key drives of an excavator include the cylinders of the working equipment, the swing to turn the upper carriage and the travel drive to move the excavator, as it is displayed in a simple form in **Figure 2** [14, 27].

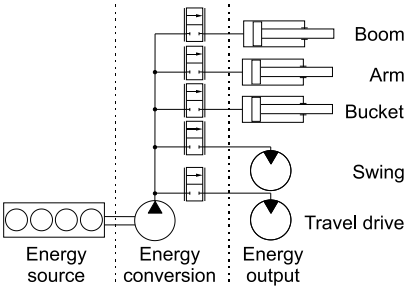

Figure 2: Traditional excavator system

3. POSSIBILITIES FOR ELECTRIC DRIVE INTEGRATION

In mobile applications, the diesel engine mostly runs at a fixed speed and it is physically impossible for the engine to recuperate energy. Based on those properties, the hydraulic systems are designed. The pumps run at a fixed speed and a possibility to recuperate negative loads is not included in the Load-Sensing or Open-Center systems [28]. With changing the energy transmitter to an electric machine, adaptations to the drive train are necessary to fully use the benefits of the electric drive.

3.1. Direct Electric Drives

In a hydraulic system, efficiency losses of the components cannot be avoided. Additionally, systematic losses due to throttling increase the required power of the system [29]. When using direct electric drives, the overall efficiency of the system can be improved. Rotational drives are directly powered by electric motors, while linear drives are powered by linear actuators or rotational motors with spindle drives. A major restriction for electric linear drives is the power density. Power densities of the hydraulic linear actuators are of magnitude 10 to 1000 higher compared to spindle drives with electric motors [30].

In contrast to electric linear drives, the power density of rotational high-speed drives is in the same order of magnitude as that of hydraulic drives. In 2009, Jacobs presents a comparison of the power densities of an electric high-speed drive with gearbox to an inclined axis and swashplate units with gearbox [31].The presented

power density of the electric unit is 0.11 kW/kg and that of the hydraulic units is 0.16 kW/kg. The application under consideration is a Baitrack BP 130/85 B mobile crusher. The benefit of a direct electric drive is the improved efficiency, especially in partial loads where the efficiency of the hydraulic units is sub-par [31].

In an excavator, the travel drive and the swing rotational movements can be powered by direct electric drives. To demonstrate a comparison of efficiency of the excavator, in chapter 4 the integration of an electric swing into the machine is evaluated based on a 90° digging cycle.

3.2. Dynamic Motor Speeds

The use of power electronic inverters enables variable motor speeds. When combing a variable speed electric drive with a constant displacement pump, the hydraulic volume flow can be controlled by the motor speed and the losses of the pump controllercan be avoided. Another possibility is to use variable drive speeds in combination with a variable displacement pump. This gives the option of a dynamic operating point to improve the efficiency of the components.

As the power density of the electric drive improves with increasing speed, high speed drives are an interesting option for mobile applications [32]. For traction drives, a gearbox is required to achieve a reasonable rotational speed of the wheels. But especially for the working hydraulics, high speed machines combined with high speed constant displacement pumps can offer a large increase in power density. In combined research by the Institute for Machine Elements and Systems Engineering and Institute for Fluid Power Drives and Systems of the RWTH Aachen, it is demonstrated that an increased speed by an electric drive can reduce the necessary installation space considerably. An increase of the maximum rotational speed from 2200 1/min to 3800 1/min reduces the required installation space by 68%, at 10000 1/min the installation space is reduced by 89% [33]. Using mechanic transmissions, high engine speeds can be integrated with moderate pump speeds.

3.3. Recuperation

As electric drives inherently allow bidirectional transformation of electrical and mechanical energy, they can be used to recuperate the breaking energy of the swing and the saved potential energy of the working hydraulics. Depending on the operating point, an efficiency of up to 95 % of the electric drive can be reached. Electric recuperation systems are traditionally used in swings of hybrid excavators, such as products from Hitachi and Komatsu [25, 26]. In an excavator with an electric swing, the recuperation system can be integrated without further adaptions. The recuperation of negative loads of the linear drives proves more challenging, as the movement must be transferred into a rotational movement for the electric drive.

4. DEMONSTRATION ON A COMPACT EXCAVATOR

In order to evaluate the proposed adaptions for the electric excavator, the integration into the machine is demonstrated with a simulation model. In this simulation model, the kinematic and hydraulic system of a 9 t compact excavator is modelled and used as a basis. In a 90 ° dig and dump cycle, the adapted system behavior of the machine is evaluated.

4.1. Modelling

The simulation model consists of three parts, power source, hydraulic system and kinematic structure. The kinematic structure represents the movement of the excavator and determines the cylinder and swing load. The engine, in this model a diesel engine is compared to an induction motor, provides the power for the system. The most common hydraulic system for compact excavators is an Open-Center system [14]. The Open-Center system distributes the power to the hydraulic drives and defines the system behavior. For the excavator model, a public layout by Hitachi is used as a basis [34]. The simulation is built in AMEsim as a 0D simulation model.

The modelled compact excavator uses a 40.5 kW diesel engine. The specific fuel consumption of the diesel engine is optimal in a small area of the engine map, as it is displayed in **Figure 3**.

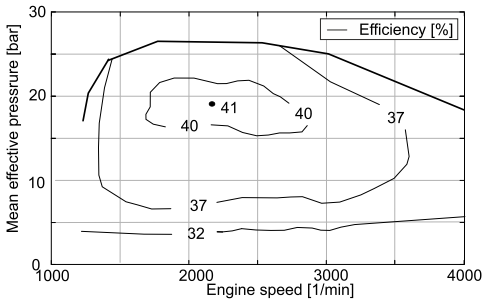

Figure 3: Diesel fuel consumption [35]

In contrast to the restricted work point of the diesel engine, the induction motor can be varied in a larger area without a major efficiency drop. In **Figure 5** the efficiency map of an asynchronous machine with inverter is displayed.

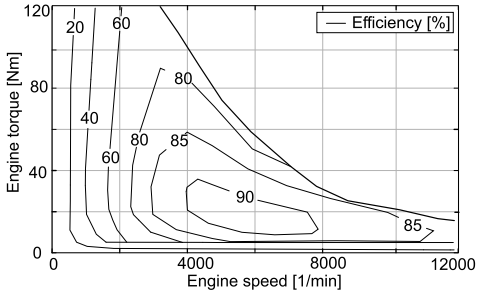

Figure 5: Efficiency induction motor with inverter [36]

Two variable displacement axial pump-motor-units size 36 are used in Open-Center system of the simulation model. The pump adjustment and valve actuation are modelled with a hydraulic pilot system but also with a direct electric actuation. A pilot system with a pilot pump volume flow of 20 L/min and a pilot pressure of 36 bar is used. To model the hydraulic losses of the pump controller, a bypass orifice is set according to measurements from Lux [37]. At a pump pressure of 200 bar, a volume flow of 2.8 L/min is used for the controller. The energy consumption of 28 W of the Parker RE06M*W is used for the electric pump controllers without a pilot pressure system [38]. For the electric swing break, the ROBAstop-M of the manufacturer Mayr is assumed [39]. For direct actuated valves, the energy consumption of the Parker D3FB, a proportional NG10 4/3 way valve is considered as data for the energy consumption of a direct controlled open-center valve of this size is not available [40].

In case of the electric engine, the engine speed can be set dynamically to run the pumps and the electric drives at more efficient operating points. In addition, the possibility of fixed displacement units with variable engine speeds arise. This method of flow control avoids using a pump controller and reduces by-pass losses [37].

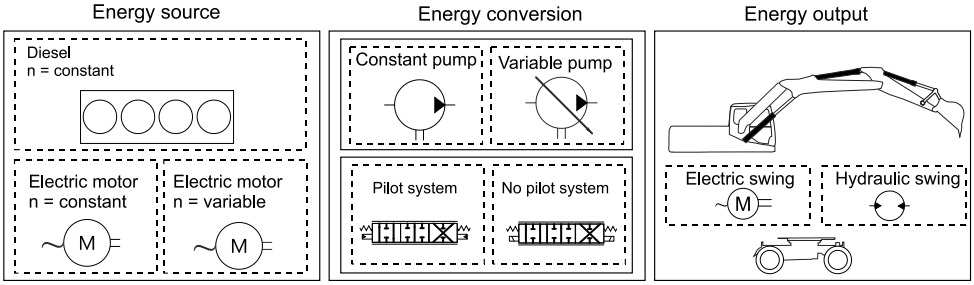

Figure 4: Excavator system layout and variants

An overview of the possible adaptions and the model layout presents **Figure 4** and as a list the explicit tested variants **Table 1**.

Table 1: Model combinations

#	Motor	Motor speed	Swing	Pump	Pilot system
1	Diesel	Constant	Hydr.	Variable	Yes
2	Electric	Constant	Hydr.	Variable	Yes
3	Electric	Constant	Electr.	Variable	Yes
4	Electric	Variable	Electr.	Constant	Yes
5	Electric	Variable	Electr.	Variable	Yes
6	Electric	Variable	Electr.	Constant	No

4.2. Test Cycle

In order to determine the forces impressed on the bucket, a model is used in which the digging forces are determined based on the current grave cross section, the grave movement and material parameters [41].

The movement of the test cycle is according to a 90° dig and dump cycle. The excavating movement of the excavator bucket is displayed in **Figure 6**.

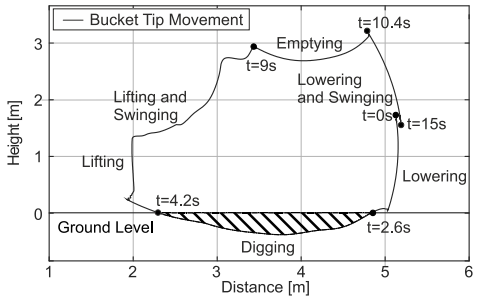

Figure 6: Excavating movement

The cycle starts with the empty bucket in the air. At first the boom is lowered, then in movement of all three cylinders the surface is dug out. It is followed by a lifting of the boom whilst turning the bucket to keep the dug ground material in it. With an upwards movement of the bucket by a movement of the boom and arm, the machine swings to the side. In a height of 2.8 m, the bucket is emptied and the excavator moves back to the initial position.

4.3. Evaluation

In the evaluation, the required power, operational costs and the impact on the carbon footprint are compared. Systematic losses appear in the hydraulic system due to throttling losses. Efficiencies of the pumps, the Diesel or electric engine further increase the required power. Considering a battery powered excavator, additional losses of charging and discharging the battery are considered. Research of Huss determined expected efficiencies of electric batteries in the year 2020 of $\eta_{\mathrm{Battery}} = 80.9\%$ [7]. An additional power loss is induced by losses in the power grid, which are elaborated by Mehlhorn with an average grid efficiency in Germany of $\eta_{\mathrm{Grid}} = 95.3\%$ [8]. This concludes in a required power for the electric machine P_{Grid} as shown in Equation 1.

$$P_{\mathrm{Grid}} = \frac{P_{\mathrm{Load}}}{\eta_{\mathrm{Grid}} \cdot \eta_{\mathrm{Battery}} \cdot \eta_{\mathrm{Drive}} \cdot \eta_{\mathrm{Pumps}} \cdot \eta_{\mathrm{Hydraulic}}} \quad (1)$$

For the Diesel engine, the required chemical power is determined as in Equation 2.

$$P_{\mathrm{Diesel}} = \frac{P_{\mathrm{Load}}}{\eta_{\mathrm{Diesel}} \cdot \eta_{\mathrm{Pumps}} \cdot \eta_{\mathrm{Hydraulic}}} \quad (2)$$

The energy consumption is defined as the use of diesel or electric power. The operational expenditure (OPEX) is the calculated cost based on the energy consumptions. Based on the lower calorific value of Diesel H_{u} with 43 MJ/kg and the density ρ_{Diesel} with 0.84 kg/L, the required Diesel consumption $\dot{V}_{\mathrm{Diesel}}$ is determined as in Equation 3 [28].

$$\dot{V}_{\mathrm{Diesel}} = \frac{P_{\mathrm{Diesel}}}{H_{\mathrm{u}} \cdot \rho_{\mathrm{Diesel}}} \quad (3)$$

With the relative costs of the Diesel C_{Diesel}, the OPEX are determined. As a basis, the Diesel costs of 2018 in Germany is used. The average price without value added taxes is 1,009 €/L and with value added taxes 1,289 €/L. The OPEX is determined as in Equation 4 [42, 43].

$$OPEX_{\mathrm{Diesel}} = \dot{V}_{\mathrm{Diesel}} \cdot C_{\mathrm{Diesel}} \quad (4)$$

For the electric excavator, the OPEX is based on the electricity costs for industry users with and without taxes. Without taxes, the price $C_{\mathrm{Electricity}}$ in 2018 is at 8.97 €cent/kWh and with taxes 18.44 €cent/kWh [44]. The determination of the OPEX excludes the grid losses, as the price calculations of the consumers is based on the delivered energy.

$$OPEX_{\mathrm{Electric}} = P_{\mathrm{Grid}} \cdot \eta_{\mathrm{Grid}} \cdot C_{\mathrm{Electricity}} \quad (5)$$

The CO_2 emissions of the electric excavator $E_{\mathrm{Electricity}}$ are determined based on the CO_2 equivalent of the German power mix and also based on the German electro mobile renewable mix. For the general German power mix, the

specific CO_2 equivalent $e_{\text{Electricity}}$ for 2019 is 445.7 gCO_2/kWh and for the renewable mix for electro mobile applications, the CO_2 equivalent is 43.3 gCO_2/kWh [6]. Included in the consideration of the CO_2 equivalent is the production and recycling of the lithium ion batteries. For this, a battery with a lifetime of 2000 h, a size to be able to run 4 hours under maximum load and a CO_2 equivalent of 175 $kgCO_2/kWh$ is considered [45].

$$E_{\text{Electricity}} = P_{\text{Grid}} \cdot e_{\text{Electricity}} + E_{\text{Battery}} \quad (6)$$

The CO_2 equivalent of the Diesel engine E_{Diesel} is specified by a [6] CO_2 equivalent e_{Diesel} of 819.5 $kgCO_2/kWh$. The value is based on the mechanic power output of an average Diesel engine in Germany in 2019 [6].

$$E_{\text{Diesel}} = P_{Diesel} \cdot \eta_{Diesel} \cdot e_{Diesel} \quad (7)$$

The required power and the losses in the drive train is displayed in **Figure 7**. The average power consumption is displayed at the top, the efficiency losses of the drive train relative to its required power next to the bars. The variants are detailed in Table 1.

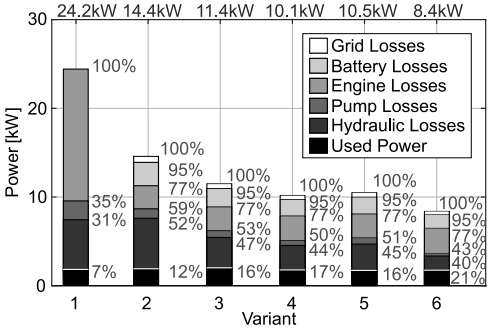

Figure 7: Power variants

Starting with the sole replacement of the diesel engine, first variant, by an electric motor, second variant, a significant change in the system behavior and efficiency cannot be noted. A 32 kW electric drive is able to power the system. In the third variant, in addition to the electric traction drive, the swing is electrically powered by an 8 kW electric drive. The electric drive allows negative energies to be recovered with corresponding efficiencies and additionally reduces throttle losses in the system. With the electric rotary actuator, a significant improvement of the drive system is possible, as the consumption of the electrical input power is reduced by 21% compared to the second variant.

In variants four and five, in addition to the electric swing, variable motor speeds are considered, on the one hand with a constant pump and on the other hand with a variable displacement pump. In both variants the power consumption of the machine is reduced even further. In case of the variant with constant pumps, the average efficiencies of the constant pumps are higher compared to the dynamic use of the variable displacement pumps and the hydraulic pump controller losses are avoided. In case of the variable displacement pumps at variable speeds, the relation of the pump rotation speeds and swivel angles is set for the most optimal work point based on the pressure and volume flow. Overall, the variable speed variants are able to reduce the power consumption further by 8-11% for a total 30% in variant four.

In the last adaption, an electric actuation system is considered and variant four is adapted with the electric actuation system. As the pilot system is not used, the power intake of the machine is lowered by another 17% and the total efficiency is improvement by 42%. The avoidance of the pilot system is displayed in more detail in **Figure 8**, as the power consumption of the electric actuation is compared to the required electric power to drive the pilot pump.

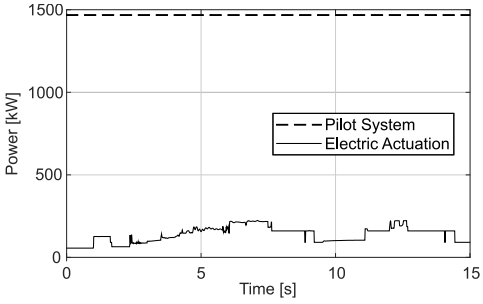

Figure 8: Electric valve actuation power consumption

With the required average power intake of the electric actuation of 138 W, 1329 W of electric power can be saved.

According to the power intake of the machine, the operational expenditure (OPEX) displayed in **Figure 9**.

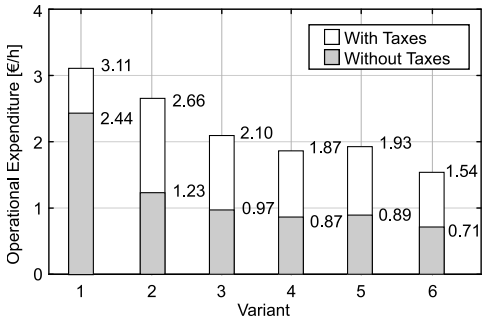

Figure 9: Operational expenditure

Even in the variant two without an electric swing, the operational costs are reduced by 15% while in the system with the lowest power intake, the costs to operate the machine are reduced by 50% compared to the Diesel engine. Further reductions are possible with tax breaks, which currently exist for electric cars.

The CO_2 equivalents of the different variants are displayed in **Figure 10**. The CO_2 production is elaborated for the Diesel engine, the use of the overall German power mix or the use of the renewable energy mix (RE) and under the use of a battery powered excavator or without the battery.

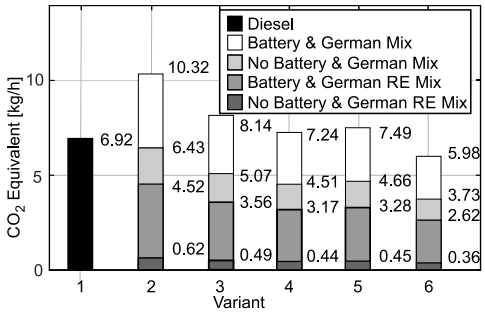

Figure 10: CO2 emissions

As it can be seen, the possible CO2 emissions of the excavator heavily depend of the system variant. Under the use of the German power mix and a battery, a CO_2 reduction is not possible. But under consideration of the use of renewable energy sources, even with a battery the CO_2 equivalent can be reduced by 68% in variant six. The largest contributor remains the battery production, as without the consideration of the battery, the CO_2 emissions are reduced from 6.92 kg/h of the Diesel engine to a 0.36 kg/h with renewable energy sources.

5. CONCLUSION AND OUTLOOK

Electrically powered excavators present a possibility to reduce CO_2 emissions and operational costs. In this paper system adaptations are elaborated and compared.

A major contribution to efficiency improvements are electric swings. Using a direct electric drive of the excavator rotation, hydraulic losses are reduced and parts of the kinetic energy can be recovered while breaking. In the simulated compact excavator, efficiency improvements of over 21% are possible.

Under the use of electric drives, variable motor speeds are able to further improve the system efficiencies. The use of constant displacement pumps with variable speeds improves the efficiencies of the components and avoids pump controller losses. Variable displacement pumps can be powered in more efficient operating points with variable motor speeds. With variable motor speeds, the efficiency of the system with electric swings is further improved by 8-11%.

Electric valve, pump and break control can be used to remove the losses of the pilot system. In the case of the electric excavator, the system losses are reduced by 17%.

With the proposed adaptations of the hydraulic system, a total efficiency improvement of 42% of the electric excavator is possible.

Further improvements can be focused on the adaptions of the layout of the hydraulic excavator, as the hydraulic losses are 74% of the total losses under the use of the hydraulic swing and 48% under the use of the electric swing.

NOMENCLATURE

Electr.	Electric
Hydr.	Hydraulic
OPEX	Operational Expenditure
RE	Renewable Energy

REFERENCES

[1] Huanga L, Krigsvolla G, Johansena F et al. (2017) Carbon emission of global construction sector. Renewable and Sustainable Energy Reviews

[2] Helms H, Heidt C (2014) Erarbeitung eines Konzepts zur Minderung der Umweltbelastung aus NRMM (non road mobile machinery) unter Berücksichtigung aktueller Emissionsfaktoren

und Emissionsverminderungsoptionen für den Bestand
[3] Umweltbundsamt (2009) Feinstaubbelastung in Deutschland. https://www.umweltbundesamt.de/sites/default/files/medien/publikation/long/3565.pdf. Accessed 22 Jul 2019
[4] Burch I, Gilchirst J (2018) Survey of Global Activity to Phase Out Internal Combustion Engine Vehicles. https://climateprotection.org/wp-content/uploads/2018/10/Survey-on-Global-Activities-to-Phase-Out-ICE-Vehicles-FINAL-Oct-3-2018.pdf. Accessed 23 Jul 2019
[5] Ministerial Council on Renewable Energy, Hydrogen and Related Issues (2017) Basic Hydrogen Strategy. https://www.meti.go.jp/english/press/2017/1226_003.html. Accessed 23 Jul 2019
[6] International Institute for Sustainability Analysis and Strategy (2019) Gemis 5.0
[7] Huss A, Maas H, Hass H (2013) Well-to-wheels analysis of future automotive fuels and powertrains in the European context. Tank-to-wheels report, version 4.0
[8] Mehlhorn K, Kliemt J (2004) Moderne Netzanalyse
[9] Wacker Neuson (2019) Emissionsfrei, leise und leistungsstark – Die elektro Minibagger EZ17e und EZ26e. https://www.wackerneuson.de/de/aktuelles/news/ez17e/. Accessed 23 Jul 2019
[10] Bobcat (2019) E10electric. https://www.bobcat.com/eu/de/company-info/news-media/e10-electric. Accessed 15 Oct 2019
[11] JCB (2019) Electric Mini Excavator 19C-IE. https://www.jcb.com/en-us/products/compact-excavators/19c-1e. Accessed 16 Oct 2019
[12] Lambert F (2019) Caterpillar unveils an all-electric 26-ton excavator with a giant 300 kWh battery pack. https://electrek.co/2019/01/29/caterpillar-electric-excavator-giant-battery-pack/. Accessed 15 Oct 2019
[13] Vikström H, Davidsson S, Höök M (2013) Lithium availability and future production outlooks. Applied Energy 110
[14] Murrenhoff H., Eckstein L (2011) Fluidtechnik für mobile Anwendungen
[15] Lajunen A, Sainio P, Laurila L et al. (2018) Overview of Powertrain Electrification and Future Scenarios for Non-Road Mobile Machinery. energies 11(5)
[16] Guarnieri M (2012) Looking back to electric cars. In: Staff I (ed) 2012 Third IEEE History of Electro-Technology Conference
[17] thyssenkrupp AG (2019) Bagger 288 – Ein Gigant unter den Schaufelradbaggern. https://www.thyssenkrupp-industrial-solutions.com/de/produkte-und-services/mining-systems/schaufelradbagger/bagger-288. Accessed 15 Oct 2019
[18] Finken T, Felden M, Hameyer K (2008) Comparison and design of different electrical machine types regarding their applicability in hybrid electrical vehicles. In: International Conference on Electrical Machines, 2008
[19] Maswood A, Vu P, Rahman M (2012) Silicon carbide based inverters for energy efficiency. In: IEEE Transportation Electrification Conference and Expo, Dearborn
[20] Becker J (2017) Flexible Dimensionierung und Optimierung hybrider Lithium-Ionenbatteriespeichersysteme mit verschiedenen Auslegungszielen. Dissertation, RWTH Aachen
[21] Komatsu History. Komatsu Germany GmbH. https://www.komatsu-mining.de/company/history/. Accessed 10 Sep 2019
[22] Andreev R (2015) Evaluation of Hydraulic Excavator and Rope Shovel Major Maintenance Costs in Operation, University of Alberta
[23] Liebherr (2019) R 9200 E. https://www.liebherr.com/de/int/bauma/exponate/mining/miningbagger/details/r9200e.html. Accessed 15 Oct 2019
[24] SUNCAR HK AG (2019) TB260E. Batteriebetriebener Elektrobagger. https://www.suncar-hk.com/files/datenblatt-TB260E.pdf. Accessed 15 Oct 2019
[25] Komatsu (2019) Wir sind Hybrid. https://www.komatsu.eu/de/komatsu-hybridsystem. Accessed 15 Oct 2019
[26] Hitachi (2019) Die logische Wahl. https://www.hitachicm.eu/de/hybrid/. Accessed 15 Oct 2019
[27] Schmitz K, Murrenhoff H (2018) Grundlagen der Fluidtechnik
[28] Baehr H D, Kabelac S (2016) Thermodynamik. Springer-Verlag Berlin Heidelberg

[29] Vukovic M, Leifeld R, Murrenhoff H (2017) Reducing Fuel Consumption in Hydraulic Excavators. energies
[30] Janocha H (2010) Unkonventionelle Aktoren. Oldenbourg Wissenschaftsverlag, München
[31] Schröter J, Jacobs G (2014) High speed electrical drives for mobile machinery – Drive concept and selected components. In: 13th CTI Symposium, Berlin
[32] Gerada D, Mebarki A, Brown N L. et al. (2014) High-Speed Electrical Machines: Technologies, Trends, and Developments. IEEE Trans. Ind. Electron. 61(6)
[33] Roth D, Jacobs G, Kramer A, Krech M, Pietrzyk T, Schmitz K (2019) Bauraumreduktion durch Drehzahlanhebung - Einsatz von High-Speed-Antrieben in elektrohydraulischen Linearaktuatoren für mobile Anwendungen. In: 7. Fachtagung Hybride und energieeffiziente Antriebe für mobile Arbeitsmaschinen, Karlsruhe
[34] Hanakawa K, Mutsuhashi M, Nakamura T (2011) Hydraulic circuit system for hydraulic excavator. Patent(US20110061755A1). https://patents.google.com/patent/US20110061755A1/en
[35] van Basshuysen R, Schäfer F (eds) (2012) Handbuch Verbrennungsmotor. Grundlagen, Komponenten, Systeme, Perspektiven, 6th edn. ATZ-MTZ-Fachbuch. Vieweg + Teubner, Wiesbaden
[36] Göhlich D, Fay T A, Jefferies D et al. (2018) Design of urban electric bus systems. Design Science 4
[37] Hartmann K, Frerichs L (2016) Development of innovative solutions for displacement variation in hydrostatic machines. In: 10th International Fluid Power Conference (10. IFK), Dresden
[38] Parker Hannifin Corporation (2018) Axialkolbenpumpen - Serie PVplus Verstellbare Ausführung. https://www.parker.com/Literature/PMDE/Catalogs/Piston_Pumps/PV+/MSG30-3245_DE.pdf. Accessed 15 Oct 2019
[39] Mayr GmbH (2018) ROBA-stop-M. https://www.mayr.com/synchronisation/documentations/k_891_v17_de_26_03_2018.pdf. Accessed 16 Oct 2019
[40] Parker Hannifin Corporation Proportional Directional Control Valves Series D3FB. Catalog HY14-2550/US. https://www.parker.com/Literature/Hydraulic%20Valve%20Division/hydraulicvalve/Catalog%20sections%20for%20websphere/Proportional%20Directional%20Control/Catalog%20-%20Static%20Files/D3FB.pdf. Accessed 16 Oct 2019
[41] Liu Y, Hasan M S, Yu H-N (2010) Modelling and remote control of an excavator. Int. J. Autom. Comput. 7(3)
[42] Mineralölwirtschaftsverband Deutschland e.V. (2019) Monatliche Verbraucherpreise für Mineralölprodukte 2005-2019. https://www.mwv.de/statistiken/verbraucherpreise/. Accessed 16 Oct 2019
[43] Bundesverband Güterkraftverkehr Logistik und Entsorgung (BGL) e.V. (2019) Dieselpreis-Information (Großverbraucher) – Vorabfassung für September 2019. https://www.bgl-ev.de/images/downloads/dieselpreisinformation.pdf. Accessed 16 Oct 2019
[44] BDEW Bundesverband der Energie- und Wasserwirtschaft e.V. (2019) BDEW-Strompreisanalyse Juli 2019. https://www.bdew.de/media/documents/190723_BDEW-Strompreisanalyse_Juli-2019.pdf. Accessed 16 Oct 2019
[45] Romare M, Dahllöf L (2017) The Life Cycle Energy Consumption and Greenhouse Gas Emissions from Lithium-Ion Batteries. https://www.ivl.se/download/18.5922281715bdaebede9559/. Accessed 25 Oct 2019

peer reviewed

RESEARCH ON EFFICIENT DRIVING METHOD OF HEAVY HYDRAULIC EXCAVATOR BOOM

Lianpeng Xia, Long Quan*, Lei Ge, Yunxiao Hao, Bin Zhao, Bin Li

Key Lab of Advanced Transducers and Intelligent Control System of Ministry of Education and Shanxi Province, Taiyuan University of Technology, Xikuang Street 53#, 030024 Taiyuan, China
* Corresponding author: Tel.: +86 0351 6014551; E-mail address: quanlong@tyut.edu.cn

ABSTRACT

There is a lot of gravitational potential energy waste when hydraulic excavators work, which seriously affects the efficiency of the whole machine and produces a large amount of emissions. In order to reduce the energy consumption and emissions of large hydraulic excavators which the boom is driven by two hydraulic cylinders, an integrated drive and potential energy recuperation principle is proposed. In the implementation, the original two-chamber hydraulic cylinders are replaced by three-chamber hydraulic cylinders with energy storage chambers, and the energy storage chambers are directly connected with the hydraulic accumulator. The dead weight of the working device is balanced by the initial hydraulic pressure of the hydraulic accumulator, and the gravitational potential energy is directly recuperated. A digital prototype is established for the simulation work to verify the energy-saving effect. Then a test prototype is constructed according to the simulation work. The standard 90° loading duty cycle tests show that compared with the standard hydraulic excavators of the same type, in the case of meeting the same digging force, the working efficiency of the excavator increases by 20.7% and the fuel consumption decreases by 17.1%. In terms of 8 hours of work per day, a single excavator can save fuel up to 47 L per day and reduce carbon dioxide emissions by 123.6 kg.

Keywords: Excavator, Boom, Energy saving and emission reduction, Three-chamber hydraulic cylinder, Hydraulic-gas energy storage drive

1. INTRODUCTION

The large hydraulic excavator working device will accumulate a large amount of gravitational potential energy in the lifting operation. However, the gravitational potential energy is converted into heat energy through the throttling action of the valve and wasted. Statistics show that the wasted potential energy of the medium-sized hydraulic excavator accounts for more than 15% of the whole energy consumption [1], which not only causes huge energy waste but also heats the fluid quickly, affects the continuous operation and causes failure. Therefore, recycling and utilizing the gravitational potential energy has always been an important research direction in the field of mobile hydraulic machines [2]. At present, the main methods include electric hybrid method, hydraulic hybrid method, recovery method based on constant pressure power source, closed pump control recovery method and hydraulic-gas energy storage drive method. The electric hybrid method is to convert the gravitational potential energy into electric energy by the hydraulic motor and the generator [3] then the energy is reused by an electric motor to drive the hydraulic pump [4-6] or the swing of the machine [7]. More than 7 conversions and multiple control links are needed in the whole process of energy recovery and reuse. Although the link of converting gravitational potential energy to electrical energy is omitted with the hydraulic hybrid method [8-10], there are still a lot of conversion and transmission links. In addition, the working device moves fast and the energy conversion time is short. Therefore, the hybrid power units tend to have large power and high cost, and the recovery and reuse efficiency of the gravity potential energy is limited by the number of energy conversion times and the conversion efficiency.

The constant pressure power source system uses a constant high-pressure accumulator as a power source and uses a hydraulic transformer to

control the hydraulic cylinder of the working device. When the working device is lowered, the gravitational potential energy is converted and stored in the high-pressure accumulator by the hydraulic transformer [11, 12]. The advantage is that the same components are used for driving and recycling, however the energy efficiency of hydraulic transformers needs to be improved. In Murrenhoff's research, a medium-pressure accumulator is added to the power source and a set of on-off valves are used to replace the hydraulic transformer. By controlling the on-off valve group, the potential energy of the working device can be directly recovered into the same pressure hydraulic accumulator [13, 14]. The system and control methods are more complex.

The closed pump control circuit recovery method is to add an energy recovery closed hydraulic pump connected with the hydraulic accumulator in the closed pump control circuit of the differential hydraulic cylinder. Storing and reusing gravitational potential energy of the working device by coupling with the torque of the main hydraulic pump [15, 16]. Quanlong innovatively integrates the two hydraulic pumps into one, and proposes an asymmetric hydraulic pump with three distribution windows [17]. Only using a single asymmetric hydraulic pump can realize the integrated drive of differential hydraulic cylinder [18] and energy recuperation [19-21]. The asymmetric hydraulic pump is still under further study.

With the hydraulic-gas energy storage drive method, a hydraulic-gas energy storage chamber connected with the hydraulic accumulator is added in the working device drive circuit, and directly recovering and reusing the gravitational potential energy by using the hydraulic accumulator oil pressure balance working device gravity. In the process of energy recovery and reuse, there is only one necessary conversion between mechanical energy and hydraulic energy. In addition, there is no energy-converting component, no limitation of installed power and no intermediate control link. At present, the hydraulic-gas energy storage drive method is the most efficient way to recycle energy, especially for large machines with heavy working devices and high recovery power. And this method is especially suitable for a variety of drive circuits and is easy to integrate into the existing control circuits of the machine. Early research used the method of adding the balance hydraulic cylinder in parallel with the position of the driving hydraulic cylinder to drive the working device [22-24]. The disadvantage is that the structure of the boom, which is the key structural member, needs to be changed. This will affect the service life. Limited by the installation space, this method is only applicable to large and medium-sized machines. Quanlong proposes a three-chamber hydraulic cylinder based on hydraulic-gas energy storage drive principle [25], which integrates energy storage and drive circuits. It can directly replace the original hydraulic cylinder without changing the boom structure. It is suitable for small machines driven by single hydraulic cylinder [26] and large and medium-sized machines driven by two hydraulic cylinders [27, 28]. At present, the team has applied the principles proposed in the boom drive systems of small hydraulic excavator [29] and medium hydraulic excavator [30]. Simulation and experimental research on the operation characteristics and energy consumption characteristics of the boom are conducted [31]. The existing experimental research is based on the small hydraulic excavator, which does not involve the energy consumption of the whole machine during the complete duty cycle. Compared with the small hydraulic excavator, the large hydraulic excavator has a large demand for digging force, and the influence of the hydraulic-gas energy storage unit on the digging force cannot be ignored. Therefore, this paper focuses on the efficient driving of large hydraulic excavator boom with the hydraulic-gas energy storage drive method.

A test prototype is built and the standard 90° loading duty cycle efficiency and fuel consumption are tested.

2. WORKING PRINCIPLE

Figure 1 shows the schematic diagram of a large hydraulic excavator boom hydraulic-gas energy storage drive system. The proposed hydraulic-gas energy storage drive principle integrates the energy storage chamber into the three-chamber hydraulic cylinder, and replaces the original double-chamber hydraulic cylinder by the three-chamber hydraulic cylinder directly. The chamber A and chamber B are the driving control chambers which are connected with the drive circuit. The chamber C is connected to the hydraulic accumulator through the control valve

group (valves 1-3) to form a hydraulic-gas energy storage unit for directly recovering and utilizing the gravitational potential energy of the working device.

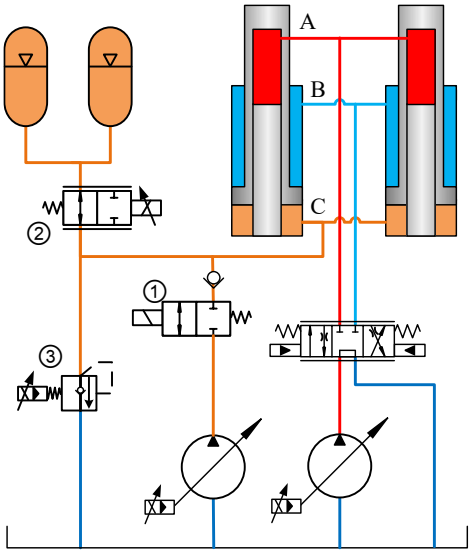

Figure 1: principle diagram of the hydraulic-gas energy storage drive system

The force balance equation of the three-chamber hydraulic cylinder is:

$$p_a A_a - p_b A_b + p_c A_c + \Delta p_c A_c = (m_1 + m_2)\ddot{x} + B\dot{x} + m_1 g + m_2 g \quad (1)$$

When the boom is lifted, Δp_c is a negative value, and when the boom is lowered, it is a positive value. In the equation(1), the gravity of the working device $m_1 g$ accounts for the largest proportion in the load force of the boom hydraulic cylinder. In the working process, the energy consumed by overcoming the gravity of the working device occupies a large proportion in the energy consumption of the whole machine. When the pressure of hydraulic accumulator is set appropriately, the accumulator can basically balance the gravity of the working device as shown in equation(2).

$$p_c A_c = m_1 g \quad (2)$$

$$p_a A_a - p_b A_b = (m_1 + m_2)\ddot{x} + B\dot{x} + m_2 g - \Delta p_c A_c \quad (3)$$

Equation (1) can be simplified according to equation (2). That is, while the hydraulic-gas energy storage driving system is adopted, the driving circuit only needs to overcome the inertial force of the working device, the material gravity in the bucket, and the compensation amount Δp_c of the accumulator pressure change. The energy consumed by the driving system can be greatly reduced. Under conditions of heavy load digging and support of the hydraulic excavator, the $(p_c A_c + \Delta p_c A_c)$ in equation (1) generates the force acting upward on the working device, hindering the digging and the supporting. Therefore, the hydraulic accumulator control valve group is designed to disconnect the hydraulic accumulator from the hydraulic cylinder and eliminate the influence of the hydraulic-gas energy storage unit on the digging force and the working condition of the supporting vehicle under the heavy load digging and supporting conditions. When it is necessary to disconnect the hydraulic accumulator from the hydraulic cylinder, the valve 2 is closed. Meanwhile, the valve 3 is opened to make the hydraulic cylinder chamber C have no force. When the boom is lifted, the valve 3 is closed and the valve 2 is opened. At this moment, the hydraulic accumulator is connected with the cylinder chamber C to provide the balance force and release the stored hydraulic energy.

3. SIMULATION RESEARCH

Based on the above theoretical analysis, a digital prototype of the 36-ton hydraulic excavator shown in Figure 2 is constructed. The main parameters of the system are shown in Table 1.

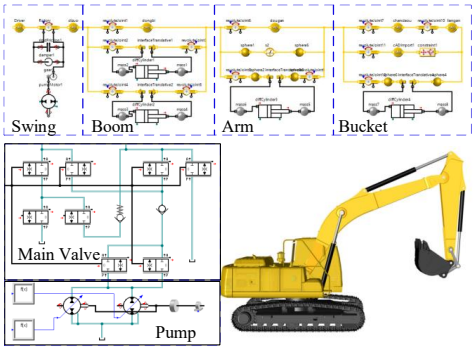

Figure 2: Digital prototype of the 36-ton hydraulic excavator

Table 1: Main parameters of the system

Parameter	Value
Chamber A area A_a	7084 [mm^2]
Chamber B area A_b	7300 [mm^2]
Chamber C area A_c	15601 [mm^2]
Hydraulic accumulator volume V	90 [L]
Hydraulic accumulator pressure p_{c0}	10 [MPa]

The boom operating characteristics simulation results of the hydraulic-gas energy storage drive system and the non-energy recovery system is carried out. Figure 3-4 shows the operating displacement characteristics curve, hydraulic pump output flow curve, and the power characteristics curve of the two systems. During the boom lowering process, the lowering time of the new system is slightly longer than that of the original system, but it has no effect on the actual operation. Since the hydraulic-gas energy storage unit of the new system basically balances the gravity of the working device, the boom could not fall completely rely on gravity. The flow regeneration function is cancelled in the new system so the output flow and power of the hydraulic pump are increased compared to the original system. However, this extra output energy and the gravity potential energy of the working device are both recovered to the hydraulic accumulator and reused when the boom is lifted. So, there is no energy waste. During the boom lifting process, under the condition that the lifting time of the hydraulic-gas energy storage driving system is the same as that of the non-energy recovery system, the output flow of the hydraulic pump is reduced from 500 L/min to 213 L/min, and the output power of the hydraulic pump is reduced from 150 kW to approximately 43 kW, 71% lower.

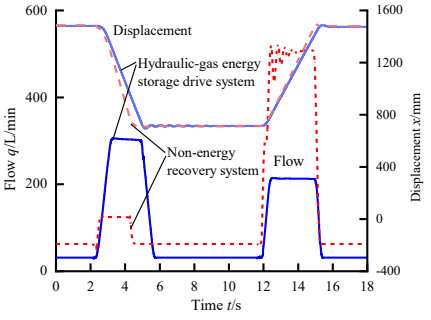

Figure 3: Simulation results of boom operating characteristics

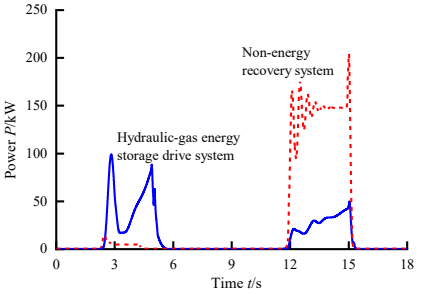

Figure 4: Power comparison between two systems

According to the whole working process, although the output power of the new system hydraulic pump increases compared with the original system, the lifting process has a significant drop. Through the comparison of the total energy consumption obtained from the power integration of the whole working cycle, it is found that the total energy consumption is significantly reduced.

4. TEST RESEARCH

4.1. Test system

A test prototype of hydraulic-gas energy storage driving system is built, as shown in Figure 5. Then the operation characteristics of the system and the energy consumption of the standard 90° loading duty cycle are tested.

Figure 5: Photos of test prototype and sensors

In the test prototype, the displacement of the two hydraulic pumps is 160 ml/r and the rated speed of the engine is 2000 rpm. The Parker SCP-400 pressure sensor is used to measure the pressure of hydraulic pump and the actuator. The HySense QT100 turbine flowmeter is used to measure the output flow of the two hydraulic pumps. The Micro-epsilon WDS-2500-P96 pull-wire displacement sensor is used to measure the displacement of the boom hydraulic cylinder and the arm hydraulic cylinder. The North Micro BW-AH200 gyroscope is used to measure the swing angle of hydraulic excavator. The above sensor data a collected through dSPACE MircoAutobox.

4.2. Boom operating characteristics

For the test prototype with hydraulic-gas energy storage drive system, the displacement of the cylinder and pressure of each chamber when the boom is lifted and lowered for one working cycle are shown in Figure 6.

When the boom is lifted in 3.2s-10.7s, the hydraulic pump and the accumulator supply oil to the chamber A and the chamber C, respectively. The piston rod is pushed to extend. The oil in chamber B flows back to the oil tank through the control valve, and the pressure is maintained at 2.3 MPa due to the action of the control valve. At this time, due to the decrease of oil in the hydraulic accumulator, the pressure in the chamber C is gradually lowered and the pressure in the chamber A is gradually increased to compensate for the decrease of the pressure in the hydraulic accumulator. When braking, due to the large inertia of the working device, after three fluctuations, the boom is stably parked.

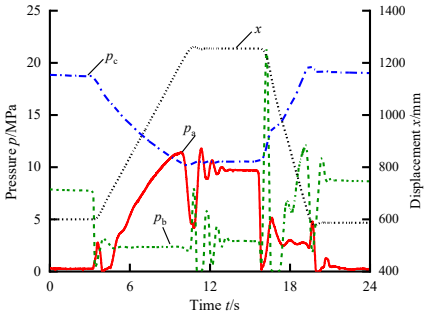

Figure 6: Characteristic curve of boom

When the boom is lowered in 15.7 s - 20.4 s, due to the dead weight of the working device and the pressure of chamber B, the piston rod is retracted. The oil in chamber C is pressed into the hydraulic

accumulator, and the oil in chamber A flows back to the tank through the control valve. When the boom starts to fall, the pressure in chamber B rises, pushing the working device to accelerate. As the boom gradually descends, the volume of oil charged into the hydraulic accumulator increases, causing the increase of pressure in chamber C and chamber B to compensate for the increase of the pressure in the hydraulic accumulator.

4.3. Energy consumption characteristics of complete 90° loading duty cycle

In order to further analyse the influence of the hydraulic-gas energy storage driving boom on the energy consumption of the whole duty cycle, a standard 90° loading duty cycle test is carried out on the test prototype. The digging work is carried out continuously. Although there is no clear time limit, it can be roughly divided into four stages: digging, lifting and swing, dumping and return. Figure 7-8 shows the characteristic curve of one duty cycle.

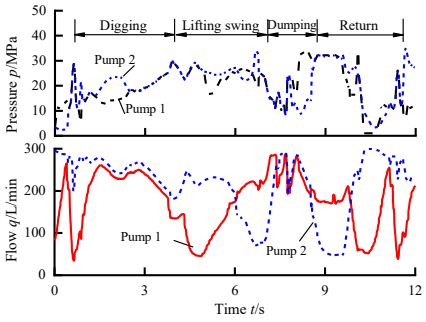

Figure 7: Pressure and flow of the pumps

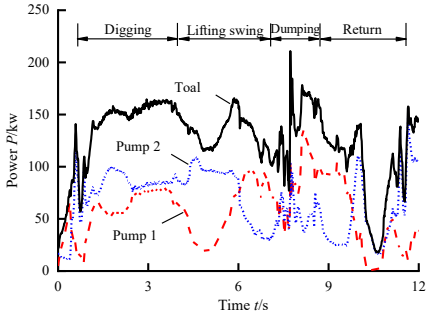

Figure 8: Power of the pumps

In the digging stage, the arm and the bucket are combined to dig, and the boom is assisted by a small range of motion. The combined action condition not only has a large load pressure, but also the output flow of the two hydraulic pumps is about 280 L/min, and the hydraulic power is 75 kW for each pump, reaching the full power working condition.

In the lifting and swing phases, non-energy-saving systems usually need two pumps combined to drive boom and swing, and it will reach full power operation. With the hydraulic-gas energy storage drive system, the flow required for the boom hydraulic cylinder is greatly reduced, which is only provided by the hydraulic pump 2, and the swing is separately driven by the hydraulic pump 1. In this way, the influence of other actuators on the rotary acceleration performance is avoided, and the loss of pressure difference between multiple actuators is also reduced. In this stage, the power of hydraulic-gas energy storage excavator is only 40% of that without energy saving system. Not only the work efficiency is improved, but also the energy consumption is greatly reduced.

In the dumping stage, not only the retraction action of the bucket hydraulic cylinder and the arm cylinder are combined, but also the swing action is present. This is the multi-action compound action so the flow demand is large. However, the load is light so that the total power is not high.

In the returning stage, it is mainly the combined action of boom lowering and swing. The hydraulic pump 1 supplies oil to the swing motor, and the hydraulic pump 2 supplies oil to the boom hydraulic cylinder. The main power consumption is the swinging action, and the power consumption of boom lowering is less.

As can be seen from the above process, when the hydraulic excavator performs a typical 90° loading duty cycle, there is often a compound action of multiple actuators. By adopting the principle of hydraulic-gas energy storage drive system, the output flow of the main hydraulic pump is lower when the boom is lifted because the accumulator basically balances its own gravity. In this way, the hydraulic pump output power is reduced, thus the engine output power is reduced, and the fuel consumption is saved.

In order to further study the working efficiency and fuel consumption of the test prototype, the same test is carried out using a standard excavator

with the same type. Two excavators are operated by the same operator. 45 times of 90° loading duty cycle is completed using each excavator. The time and fuel consumption to complete the same work is shown in Table 2.

Table 2: Fuel consumption of 90° loading duty cycle

	Time [s]	Fuel [kg]	Efficiency improvement [%]	Fuel reduction [%]
Standard excavator	577	4.74	-	-
Test prototype	478	3.93	20.7	17.1

Under the same working conditions, compared with the standard excavator, the fuel consumption of the test prototype with the principle of hydraulic-gas energy storage driving is reduced by 17.1%, and the working efficiency is increased by 20.7%. Suppose a machine works 8 hours a day, a single hydraulic excavator can save up to 47 L of fuel per day and reduce carbon dioxide emissions by 123.6 kg. The efficiency is significantly improved while the energy consumption of the whole machine is reduced. The carbon dioxide emission is effectively reduced.

5. CONCLUSION AND OUTLOOK

Based on the large hydraulic excavator driven by double hydraulic cylinders, the principle of hydraulic-gas energy storage drive is proposed. This principle can efficiently recycle the gravitational potential energy during the working process of the excavator boom, and significantly reduce the installed power of the main drive system.

By adopting the principle of hydraulic-gas energy storage drive, the 90° loading duty cycle test results show a 20.7% increase in efficiency and a 17.1% reduction in fuel consumption. The energy saving effect is remarkable.

NOMENCLATURE

p_a Pressure of chamber A
p_b Pressure of chamber B
p_c Pressure of chamber C
A_a Area of chamber A
A_b Area of chamber B
A_c Area of chamber C
m_1 Equivalent mass of the working device
m_2 Equivalent mass of the material in the bucket
x Displacement of the hydraulic cylinder
B Damping coefficient of the hydraulic cylinder
Δp_c Change value of the pressure of the hydraulic accumulator

REFERENCES

[1] Zhang S, Jiang J, Lian G: Research on Recoverable Energy Distribution of Hydraulic Excavator. Joumal of Zhengzhou University(Engineering Science), 2014, 35(2): 120-123.

[2] Quan L, Xia L, Zhao B: Innovation Progress in Research on Gravitational Potential Energy Recovery and Utilization of Hydraulic Driven Mechanical Arm. Journal of Mechanical Engineering, 2018, 54(20): 4-13.

[3] Zhang Y, Wang Q, Xiao Q: Simulation and test of energy recovery for hydraulic motor of hybrid hydraulic excavator. Journal of Mechanical Engineering, 2007, 43(8): 218-223.

[4] Wang T, Wang Q, Lin T: Improvement of boom control performance for hybrid hydraulic excavator with potential energy recovery. Automation in Construction, 2013, 30: 161-169.

[5] Lin T, Huang W, Ren H: New compound energy regeneration system and control strategy for hybrid hydraulic excavators. Automation in Construction, 2016, 68: 11-20.

[6] Zhao S, Zhao J, Li X: Design and simulation on boom energy recovery for hybrid hydraulic excavators. Chinese journal of Construction Machinery, 2016, 14(5): 445-448.

[7] Ochiai M, Ryu S: Hybrid in construction machinery. Proceedings of the 7th JFPS International Symposium on Fluid Power, September 15, 2008, TOYAMA, Japan, 2008: 41-44.

[8] Joo C, Stangl M: Application of Power Regenerative Boom system to excavator . 10th International Fluid Power Conference, March 8-10, 2016, Dresden, Germany, 2016: 175-184.

[9] Casoli P, Gambarotta A, Pompini N: Hybridization methodology based on DP algorithm for hydraulic mobile machinery — Application to a middle size excavator: Automation in Construction, 2016, 61: 42-57.

[10] Xiao Y, Guan C, Li P Y: Optimal design of a compound hybrid system consisting of torque coupling and energy regeneration for hydraulic

hybrid excavator. 2015 IEEE International Conference on Advanced Intelligent Mechatronics (AIM), July 7-11, 2015, Susan, Korea, 2015: 1525-1530.

[11] Martin I, Stephan L, Sebastian S: Energy efficient system layout for work hydraulics of excavators. The Twelfth Scandinavian International Conference on Fluid Power, May 18-20, 2011, Tampere, Finland, 2011:46-52.

[12] Shen W, Jiang J, Su X: Energy-saving analysis of hydraulic hybrid excavator based on common pressure rail. The Scientific World Journal, 2013, 2013: 1-12.

[13] Vukovic M, Sgro S, Murrenhoff H: STEAM : a holistic approach to designing excavator systems. 9th International Fluid Power Conference, March 24-26, 2014, Aachen， Germany, 2014: 250-261.

[14] Vukovic M, Leifeld R, Murrenhoff H: STEAM– a hydraulic hybrid architecture for excavators. 10th International Fluid Power Conference, March 8-10, 2016, Dresden, Germany, 2016:151-162.

[15] Chen M, Zhao D: The gravitational potential energy regeneration system with closed-circuit of boom of hydraulic excavator. Mechanical Systems and Signal Processing, 2017, 82: 178-192.

[16] Boehm D, Holländer C, Landman T: Hybrid drives for excavator concepts and solutions. 3th Hybrid drives for mobile machines, Karlsruhe， Germany, 2011: 117-124.

[17] Quan L, Li F: Closed electrohydraulic control system: China, 200610012476.2 [P]. 2006-8-16.

[18] Zhao H, Zhang H, Quan L: Characteristics of Asymmetrical Pump Controlled Differential Cylinder Speed Servo System. Journal of Mechanical Engineering, 2013, 49(22): 170-176.

[19] Ge L, Quan L, Li Y: A novel hydraulic excavator boom driving system with high efficiency and potential energy regeneration capability. Energy Conversion and Management, 2018, 166: 308-317.

[20] Ge L, Zhang X, Quan L: Experiment Study on the Characteristics of Speed-variable Asymmetric Pump Driven Excavator Arm. Journal of Mechanical Engineering, 2017, 53(16): 210-216.

[21] Jing J, Quan L, Huang J: Research on the Characteristics of Asymmetric Pump Directed Controlled Arm Cylinder of Excavator. Journal of Mechanical Engineering, 2016, 52(6): 188-196.

[22] Virvalo T, Sun W: Improving Energy Utilization in Hydraulic Booms - What It Is All about. 6th International Conference on Fluid Power Transmission and Control, March 20-22, 2005 Hangzhou, China, 2005: 55-65.

[23] Chen Q, Li B, Song C: Research on potential energy recycling system of a new hydraulic excavator boom. Journal of Guangxi University: Nat Sci Ed, 2013, 38(2): 292-299.

[24] Ren H, Lin T, Ye Y: Parameters Design and Experiment of Boom Potential Energy Recovery System Based on Balance Cylinder. China Journal of Highway and Transport, 2017, 30(2): 153-158.

[25] Ge L, Dong Z, Quan L: Potential energy regeneration method and its engineering applications in large-scale excavators. Energy Conversion and Management, 2019, 195: 1309-1318.

[26] Quan L, Liang T, Xia L: Control circuit for working device of engineering equipment: China, 201511003769.X [P]. 2015-12-29.

[27] Xia L, Quan L, Zhao B: Research on Hydraulic - Gas Combined Driving System for Hydraulic Excavator Boom. The 10th JFPS International Symposium on Fluid Power, October 25-27,2017, Fukuoka, Japan, 2017: 1-8.

[28] Zhao P, Chen Y, Zhou H: Control Strategy of Hybrid Excavator Based on Torque Prediction. Journal of Mechanical Engineering, 2018, 54(1): 99-106.

[29] Zhao P, Chen Y, Zhou H: Potential energy recovery and energy management strategy of hydraulic hybrid excavator. Journal of Zhejiang University (Engineering Science), 2016, 50(5): 893-901.

[30] Xia L, Quan L, Zhang X: Operating Characteristics and Energy Efficiency of Hydraulic-gas Combined Driving Hydraulic Excavator Boom. Journal of Mechanical Engineering, 2017, 53(20): 176-183.

[31] Xia L, Quan L, Yang J: Research on the Method of Hydraulic-gas Energy Storage Balancing Hydraulic Excavator Boom Weight. Journal of Mechanical Engineering, 2018, 54(20): 197-205.

[32] Hao Y, Quan L, Cheng H: Potential energy directly conversion and utilization methods used for heavy duty lifting machinery. Energy, 2018, 155: 242-251.

peer reviewed

OPTIMAL CONTROL OF THE HYDRAULIC ACTUATED BOOM SYSTEM BASED ON PORT-HAMILTONIAN FORMULATION

Lingchong Gao[1]*, Boyang Shi[1,2], Micheal Kleeberger[1], Johannes Fottner[1]

[1]*Chair of Materials Handling, Material Flow, Logistics, Technical University of Munich, Boltzmannstr. 15, 85748, Garching,Germany*
[2]*Department of Engineering Mechanics, Dalian University of Technology, Linggong Road No.2, 116085, Dalian V.R China*
* Corresponding author: Tel.: +49(89)351-15926; E-mail address: lingchong.gao@tum.de

ABSTRACT

The boom systems of mobile cranes and aerial platform vehicles are driven by hydraulic systems, to be specified, valve-controlled hydraulic cylinders. This hydraulic actuated boom system can accomplish the tasks such as lifting heavy loads or carrying personal to high position, by the design of a long boom structure. In practice, the boom structure is designed as light and slender as possible to control the structure self-weight. However, such structure is quite flexible and can be easily stimulated by the loads, including the driving force or torque from the hydraulic system. Our research focuses on trajectory planning for hydraulic actuated boom where both hydraulic driven system and boom structure deformation are considered. In this paper, the hydraulic actuated boom system is formulated as a port-Hamiltonian system which is a proper modelling method for multi-domain system. The problems of trajectory optimization and vibration control are formulated as optimal control problem based on port-Hamiltonian model and this procedure is tested on a model of hydraulic cylinder. A reasonable result is solved with the selected cost function and inputs.

Keywords: Hydraulic Actuated Boom, Optimal Contorl, Port-Hamiltonian

1. INTRODUCTION

The hydraulic actuated boom system is usually equipped by hydraulic mobile cranes and aerial platform vehicles to enable the ability of changing the configuration between operation status and mobile or transportation status. Besides, mounted with a complete hydraulic system which provides a stable and powerful energy source, the boom systems can handle heavy tasks such as lift and transport heavy payloads or personals to specified location or height.

The analysis of hydraulic actuated boom system including the elasticity of both system, hydraulic and boom structure, has drawn many attentions in the resent years. The researchers are interested to investigate the method to control the vibration respond of the hydraulic actuated boom system. Someone focuses on the active damper for the structure, some others pay attention on the fluctuation reduction of the hydraulic system. Sun combined mathematical formulations of hydraulic drive system with the finite element model of the boom structure, and formulated a complete model to describe the dynamic interaction between the boom structure and the drive system of mobile crane[1]. This method has been applied solve the dynamic calculation of slewing, lifting and luffing operations of lattice boom cranes[2][3]. Besides the mobile cranes and the aerial platform vehicles, fire-rescue turntable ladders also use such similar hydraulic actuated boom system. Prof. Sawodny and his team from Uni. Stuttgart has studied the active vibration control problem of this ladder system for more than ten years. They started with a discretion of the long fire-rescue turntable ladder as a flexible multi-body system[4] and the hydraulic drive system was included in the mathematical model as set of equations [5]. In the work of [6], the fire-rescue turntable ladder was built as a distributed- parameter model of Euler-Bernoulli beam and transferred into a low dimensional model space. In their recent work[7], a 3-dimensional model of ladder was derived to describe the coupled bending-torsional vibration

associated with the slewing operation and an active vibration damping control was developed with validation in real operation.

2. METHODOLOGY

2.1. Port-Hamiltonian system

The definition of port-Hamiltonian system is related with a space of power variables that are strictly connected with the geometry structure of the system. A series of geometric structures defined on this space are necessary to describe the different parts of the system in different domains separately and the internal or external interconnection of the whole system. These geometric structures are defined as Dirac structure which is the key mathematical concept to connect multi-domain system in a unified description. According to the definition given by Duindam[8], we give a linear space $\mathcal{F}$ (space of flow or velocity) and its dual denotes as $\mathcal{E} = \mathcal{F}^*$ (space of effort or force). And a Dirac structure on $\mathcal{F}$ is a linear subspace $\mathcal{D} \in \mathcal{F} \times \mathcal{E}$ with the property $\mathcal{D} = \mathcal{D}^{\mathrm{T}}$.

The Hamiltonian function, as the total energy function of the system, is used to illustrate the relation between the pair of flow and effort variables. We define the time derive of the state variables as the general flow variables as $f = \dot{x}$, and define the co-energy variables as the general effort variables as $e = \partial H/\partial x$. Then the port-Hamiltonian (PH) representation of state space model can be given in the I/O form of

$$\begin{aligned} \dot{\boldsymbol{x}} &= \big(\boldsymbol{J}(x) - \boldsymbol{R}(x)\big)\frac{\partial H}{\partial x} + \boldsymbol{G}(x)\boldsymbol{u} \\ \boldsymbol{y} &= \boldsymbol{G}(x)^{\mathrm{T}}\frac{\partial H}{\partial x} + \boldsymbol{D}\boldsymbol{u} \end{aligned} \tag{1}$$

with $\boldsymbol{J}(x)$, a skew-symmetic matrix, and the symmetric and positive semi-definite matrix $\boldsymbol{R}(x)$ which represents the passive part in the system.

For our tasks, at first, we have to consider the hydraulic actuated boom system separately, as boom part and hydraulic part. Many works have been accomplished related with the modelling and control of the flexible boom structure within the framework of port-Hamiltonian system. The pot-Hamiltonian model of Timoshenko beam was reformulated by Macchelli[9]. And the similar approach for multi-body system, including rigid body, flexible body and kinematic pairs, was also developed based on the idea of power conserving interconnection[10]. In order to transfer the model of distributed Timoshenko beam into a solvable discretized model, a discretization method which can preserve the geometric structure of the system is developed to preserve the property of (Stokes-) Dirac structure in the discretized finite-dimensional model[11][12]. Wang applied a geometric pseudo-spectral discretization to obtain the finite-dimensional Port-Hamiltonian framework of plana Timoshenko beam model, and solved the feed-forward motion control problem based on this lumped model [13]. For the hydraulic systems, Kugi designed a nonlinear controller for a system of hydraulic cylinder based on the Port-Hamiltonian model [14]. Grabmair designed an energy-based nonlinear controller for the hydraulic actuated wrapper assembly by using the port-Hamiltonian formulation of hydraulic cylinder[15]. Sakai developed passivity based control for a hydraulic robot arm system based on the port-Hamiltonian model of the hydraulic cylinder[16][17]. He also applied Casimir function to improve computation efficiency[18], and developed a nondimensionalization method which can preserve the parametric structure within the framework of port-Hamiltonian system to reduce the size of parameter space[19]. There is also some research related with the combination of hydraulic system and flexible boom system. Stadlmayr presented a port-Hamiltonian representation of flexible manipulator consisting with a long boom with a mass at the tip and hydraulic cylinder. Combined with feed-forward and feedback control system, a MIMO-control was designed to accomplish path tracking and vibration suppression for the flexible manipulator[20].

2.2. Problem formulation of optimal control

In this paper, the optimal control problem for the hydraulic system can be described as the following general optimal control problem:

$$\begin{aligned} \min J &= \textstyle\int_{t_0}^{t_\mathrm{f}} f_0(\boldsymbol{x}(t), \boldsymbol{u}(t), t)\mathrm{d}t \\ \text{s.t. } \dot{\boldsymbol{x}}(t) &= \boldsymbol{f}(\boldsymbol{x}(t), \boldsymbol{u}(t), t) \\ \boldsymbol{x}(t_0) &= \boldsymbol{x}_0, \boldsymbol{x}(t_\mathrm{f}) = \boldsymbol{x}_\mathrm{f} \\ \boldsymbol{h}(\boldsymbol{x}) &\le \boldsymbol{0} \\ \boldsymbol{g}(\dot{\boldsymbol{x}}) &\le \boldsymbol{0} \end{aligned} \tag{2}$$

where $\boldsymbol{x}(t) \in \mathbb{R}^{n_x}$ are state variables, $\boldsymbol{u}(t) \in \mathbb{R}^{n_u}$ are control inputs. J is a Lagrangian-type

cost functional where $f_0 \in \mathbb{R}^{n_x} \times \mathbb{R}^{n_u} \times \mathbb{R}^{n_u} \rightarrow \mathbb{R}$ is an integral term which is chosen to reflect the response of vibration or/and energy consumption. Differential equations $\dot{\boldsymbol{x}}(t) = \boldsymbol{f}(\boldsymbol{x}(t), \boldsymbol{u}(t), t)$ denote dynamics of the system. Boundary conditions $\boldsymbol{x}(t_0) = x_0,\ \boldsymbol{x}(t_\mathrm{f}) = x_\mathrm{f}$ are initial state variables and terminal variables, respectively. $\boldsymbol{h}(\boldsymbol{x}) \leq \boldsymbol{0}$ denotes inequality constraints with respect to state variables $\boldsymbol{x}$. $\boldsymbol{g}(\dot{\boldsymbol{x}}) \leq \boldsymbol{0}$ denotes inequality constraints with respect to rates of state variables $\dot{\boldsymbol{x}}$. The aim is to find optimal control inputs $\boldsymbol{u}^*(t)$ and state variables $\boldsymbol{x}^*(t)$ which minimize the cost functional and fulfil the differential equations, boundary conditions, and all inequality constraints.

To solve the optimal control problem Eq.(2) numerically, the software package ICLOCS 2.5 [21][22] is applied in this paper. In the ICLOCS 2.5, the direct collocation method is chosen to transform the optimal control problem (2). The main idea can be described as follows. First, the time domain $[t_0, t_\mathrm{f}]$ is divided into N intervals with N+1 time grids $\{t_0, t_1, \dots, t_1, \dots, t_N = t_\mathrm{f}\}$. The state variables and control inputs on grids $\{\boldsymbol{x}_0, \boldsymbol{x}_1, \dots, \boldsymbol{x}_k, \dots, \boldsymbol{x}_N; \boldsymbol{u}_0, \boldsymbol{u}_1, \dots, \boldsymbol{u}_k, \dots, \boldsymbol{u}_N\}$ are regarded as design variables which are rearranged as vector $\boldsymbol{z}$. Then, terms in Eq.(2) need to be transformed. For differential equations in Eq.(2), in each time interval $[t_{k-1}, t_k], k = 1,2, \dots, N$ they are discretized by the Hermite-Simpson method, which can be expressed as nonlinear equality constraints $\boldsymbol{x}_k = \tilde{f}(\boldsymbol{x}_{k-1}, \boldsymbol{u}_{k-1}, t)$. Thus, differential equations in the time domain $[t_0, t_\mathrm{f}]$ are transformed into a series of nonlinear equality constraints. Also considering boundary conditions at time t_0 and t_f, both differential equations and boundary conditions in Eq.(2) are transformed into a series of equality constraints $\bar{\boldsymbol{f}}(\boldsymbol{z}) = \boldsymbol{0}$. For inequality constraints in Eq.(2), assume they are fulfilled on all grids, all the inequality constraints can be transformed into inequality constraints $\bar{\boldsymbol{g}}(\boldsymbol{z}) \leq \boldsymbol{0}$ with respect to $\boldsymbol{z}$. For cost functional in Eq.(2), the Hermite-Simpson method is also applied to calculate the integral term, thus it is transformed into a function $y = \boldsymbol{c}(\boldsymbol{z})$ with respect to $\boldsymbol{z}$.

Combined all mentioned above, the optimal control problem is transformed into a standard nonlinear programming (NLP):

$$\begin{aligned} &\min\ y = \boldsymbol{c}(\boldsymbol{z}) \\ &\text{s.t. } \bar{\boldsymbol{f}}(\boldsymbol{z}) = \boldsymbol{0} \\ &\quad \bar{\boldsymbol{g}}(\boldsymbol{z}) \leq \boldsymbol{0} \end{aligned} \tag{3}$$

Next, a high effective solver IPOPT[23] is applied to solve the NLP (3) and obtain optimal design variables $\boldsymbol{z}^*$.Further, the optimal state variables and control inputs on each grid are obtained.

3. MODEL CONSTRUCTUON

3.1. Luffing mechanism of the hydraulic actuated boom system

The luffing mechanism is an essential mechanism for a hydraulic actuated boom system. It controls the boom to rotate around the end joint and transfer the linear motion of the cylinder to the rotation motion of the boom. By using luffing mechanism, the hydraulic boom system can be lifted from initial position (zero degree) to almost vertical position. For aerial platform vehicle with folded boom system, the luffing mechanism for the second boom can change the angel between booms to over 150 degree with additional links mechanism.

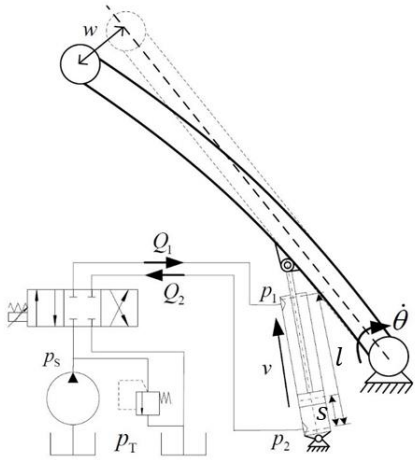

Figure 1: The luffing operation of the hydraulic actuated boom system

As shown in **Figure 1,** the luffing mechanism can be simplified as a valve-controlled hydraulic cylinder. With stable supply pressure p_s, the motion of the cylinder is governed by the in and out volume flow of the both chambers Q_1 and Q_2 which can be controlled by the direction valve. The angel velocity $\dot{\theta}$ and angel displacement θ of

the boom can be transferred from the piston's velocity of v and displacement s by a simple mechanism kinematic. If we consider the flexibility of the boom structure, an obvious deflection w will occur during the luffing operation if the input from the hydraulic cylinder is not smooth enough.

3.2. PH model of hydraulic system

Firstly, we start with the modelling of hydraulic system in port-Hamiltonian formulation. For our case, we consider the luffing operation and the luffing mechanism of the boom system. The main functional component of this hydraulic system is the hydraulic cylinder controlled by directional valve.

The continuity equations of the hydraulic cambers can be described as

$$\frac{\mathrm{d}}{\mathrm{d}t}(As) = Q_1, \frac{\mathrm{d}}{\mathrm{d}t}\big(\alpha A(l-s)\big) = Q_2. \tag{4}$$

where A is the area of the piston in the non-rod chamber, α is the area ratio between two chambers, s and l is the current displacement and the maximal displacement of the piston, Q_1 and Q_2 are the flow rate in and out through the chambers.

Applying the relation of bulk modulus β with the properties of oil

$$\beta = \rho\frac{\partial p}{\partial \rho} \tag{5}$$

the continuity equations can be rewritten as

$$\begin{aligned}\dot{p}_1 &= \frac{\beta}{V_{01}+As}\Big(-A\frac{P_\mathrm{m}}{m} + Q_1\Big)\\ \dot{p}_2 &= \frac{\beta}{V_{02}+\alpha A(l-s)}\Big(\alpha A\frac{P_\mathrm{m}}{m} - Q_2\Big)\end{aligned} \tag{6}$$

with the momentum of the piston P_m and its mass m. Combining the dynamic equation of the piston

$$\begin{aligned}\dot{s} &= P_\mathrm{m}/m\\ \dot{P}_\mathrm{m} &= p_1 A - p_2\alpha A - F\end{aligned} \tag{7}$$

we can construct a state model of hydraulic cylinder with the state variable vector as $\boldsymbol{\lambda} = [s, P_\mathrm{m}, p_1, p_2]^\mathrm{T}$.

The energy of the oil inside the both chambers of the cylinder can be described based on the assumption of isentropic fluid as following

$$\begin{aligned}U_\mathrm{Hydr} &= \textstyle\sum_{i=1,2} V_i\big(\beta e^{(p_i/\beta)} - \beta - p_i\big)\\ V_1 &= V_{01} + As, V_2 = V_{02} + \alpha A(l-s)\end{aligned} \tag{8}$$

the subscript number indicate the different chambers. If the kinetic energy of the fluid can be neglected compared to the kinetic energy of the piston, the total energy of the cylinder can be formed as

$$E_\mathrm{c} = U_\mathrm{Hydr} + P_\mathrm{m}^2/2m.$$

Using the total energy E_c as the Hamiltonian function of the cylinder H_c, the port-Hamiltonian model can be derived with the state vector $\boldsymbol{\lambda} = [s, P, p_1, p_2]^\mathrm{T}$ and the input vector $\boldsymbol{u} = [F, Q_1, Q_2]^\mathrm{T}$as

$$\begin{aligned}\boldsymbol{\lambda} &= \boldsymbol{J}(\lambda)\partial_\lambda H_\mathrm{c} + \boldsymbol{g}(\lambda)\boldsymbol{u}\\ \boldsymbol{y} &= \boldsymbol{g}(\lambda)^\mathrm{T}\partial_\lambda H_\mathrm{c}\end{aligned} \tag{9}$$

The matrices $\boldsymbol{J}(\lambda)$ and $\boldsymbol{g}(\lambda)$ are

$$\boldsymbol{J}(\lambda) = \begin{bmatrix} 0 & 1 & 0 & 0\\ -1 & 0 & \beta A/V_1 & -\beta\alpha A/V_2\\ 0 & -\beta A/V_1 & 0 & 0\\ 0 & \beta\alpha A/V_2 & 0 & 0\end{bmatrix}$$

$$\boldsymbol{g}(\lambda) = \begin{bmatrix} 0 & 0 & 0\\ -1 & 0 & 0\\ 0 & \beta/V_1 & 0\\ 0 & 0 & -\beta/V_2\end{bmatrix}$$

and the co-energy part is formulated as

$$\frac{\partial H_\mathrm{c}}{\partial \lambda} = \begin{bmatrix} A\Gamma_1 - \alpha A\Gamma_2\\ P_\mathrm{m}/m\\ V_1(\exp(p_1/\beta) - 1)\\ V_2(\exp(p_2/\beta) - 1)\end{bmatrix},$$

with $\Gamma_i = \beta\exp(p_i/\beta) - \beta - p_i, i = 1{,}2.$

The volume flow Q_1 and Q_2 can be controlled by the dominate equations of valves as following

$$\begin{aligned}Q_1 &= \begin{cases} k_v\sqrt{|p_\mathrm{s} - p_1|}|x_v|\mathrm{sgn}(p_\mathrm{s} - p_1), x_v \geq 0\\ k_v\sqrt{|p_1 - p_\mathrm{T}|}|x_v|\mathrm{sgn}(p_1 - p_\mathrm{T}), x_v < 0\end{cases}\\ Q_2 &= \begin{cases} k_v\sqrt{|p_2 - p_\mathrm{T}|}|x_v|\mathrm{sgn}(p_2 - p_\mathrm{T}), x_v \geq 0\\ k_v\sqrt{|p_\mathrm{s} - p_2|}|x_v|\mathrm{sgn}(p_\mathrm{s} - p_2), x_v < 0\end{cases}\end{aligned} \tag{10}$$

3.3. Discretized PH model of rotating Timoshenko beam

PH formulation

We simply consider the boom structure as an ideal rotating Timoshenko beam in a plana, when the axial loads can be neglected (due to the relatively small axial deformation). And we started with a rotating homogenous Timoshenko beam formulation to obtain the port-Hamiltonian representation to describe the dynamic behaviour of the boom structure.

In **Figure 2**, there is an illustration of a rotating Timoshenko beam with the translational deflection of the beam from the equilibrium position $w(z,t)$ and the rotation of the beam's cross section $\psi(z,t)$.

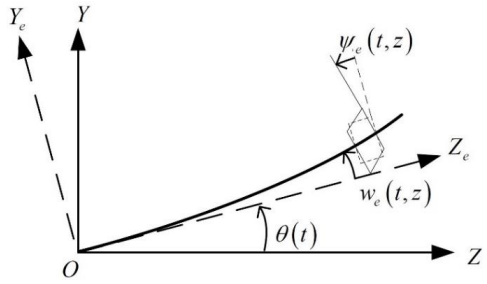

Figure 2: A rotating Timoshenko beam

The boundary condition of such rotating beam can be considered as a free tip with a fixed end, which rotates around an axis resulting an angel displacement $\theta(t)$. Then new definition of the system variables can be given as

$$\begin{aligned} w(z,t) &= w_e(z,t) + z\cdot\theta(t) \\ \psi(z,t) &= \psi_e(z,t) + \theta(t) \end{aligned} \tag{11}$$

which makes the formulation of the rotating Timoshenko beam still fits the original PDEs

$$\begin{aligned} &\rho\frac{\partial^2 w}{\partial t^2} - K\frac{\partial^2 w}{\partial z^2} + K\frac{\partial \psi}{\partial z} = 0 \\ &I_\rho\frac{\partial^2 \psi}{\partial t^2} - EI\frac{\partial^2 \psi}{\partial z^2} + K\left(\psi - \frac{\partial w}{\partial z}\right) = 0 \end{aligned} \tag{12}$$

In equation (12), ρ is the mass per length, I_ρ is the mass moment of inertia of the cross section, E is the Young's modulus and I is the moment of the inertia of the cross section. For K, there is $K = kGA$ and G is the modulus of elasticity in shear, A is the area of cross section and k is a constant depending on the shape of the cross section.

Combining the kinetic energy and elastic potential energy, we can give the Hamiltonian function of a Timoshenko beam as following:

$$H_{\mathrm{B}}(t) = \tfrac{1}{2}\int_0^L \big(\rho\dot{w}^2 + I_\rho\dot{\psi}^2 + K(\psi - \partial_z w)^2 + EI(\partial_z\psi)^2\big)\mathrm{d}z. \tag{13}$$

The kinetic energy is the function of the translational and rotational momenta which are given as

$$\begin{aligned} p_{\mathrm{t}}(z,t) &= \rho\dot{w}(z,t) \\ p_{\mathrm{r}}(z,t) &= I_\rho\dot{\psi}(z,t) \end{aligned} \tag{14}$$

and the co-energy variables are translational velocity and rotational velocity. The elastic potential energy is the function of the shear and bending deformation which are defined as

$$\begin{aligned} \varepsilon_{\mathrm{t}}(z,t) &= \partial_z w(z,t) - \psi(z,t) \\ \varepsilon_{\mathrm{r}}(z,t) &= \partial_z\psi(z,t) \end{aligned} \tag{15}$$

and the co-energy variables are shear force and bending momentum.

According to the definition of new state variables, the original PDEs of Timoshenko beam can be rewritten as

$$\dot{\boldsymbol{x}} = \begin{bmatrix} \dot{p}_{\mathrm{t}} \\ \dot{p}_{\mathrm{r}} \\ \dot{\varepsilon}_{\mathrm{t}} \\ \dot{\varepsilon}_{\mathrm{r}} \end{bmatrix} = \begin{bmatrix} 0 & 0 & \partial_z & 0 \\ 0 & 0 & 1 & \partial_z \\ \partial_z & -1 & 0 & 0 \\ 0 & \partial_z & 0 & 0 \end{bmatrix} \begin{bmatrix} \delta_{p_{\mathrm{t}}} H \\ \delta_{p_{\mathrm{r}}} H \\ \delta_{\varepsilon_{\mathrm{t}}} H \\ \delta_{\varepsilon_{\mathrm{r}}} H \end{bmatrix} \tag{16}$$

We denote $\boldsymbol{e} \in \mathcal{E}, \boldsymbol{f} \in \mathcal{F}$ as the effort and flow variables separately. They are related with the time derivative of state variables and the associated co-energy variables as

$$\boldsymbol{f} = \begin{bmatrix} f^{p_{\mathrm{t}}} \\ f^{p_{\mathrm{r}}} \\ f^{\varepsilon_{\mathrm{t}}} \\ f^{\varepsilon_{\mathrm{r}}} \end{bmatrix} = -\begin{bmatrix} \dot{p}_{\mathrm{t}} \\ \dot{p}_{\mathrm{r}} \\ \dot{\varepsilon}_{\mathrm{t}} \\ \dot{\varepsilon}_{\mathrm{r}} \end{bmatrix}, \boldsymbol{e} = \begin{bmatrix} e^{p_{\mathrm{t}}} \\ e^{p_{\mathrm{r}}} \\ e^{\varepsilon_{\mathrm{t}}} \\ e^{\varepsilon_{\mathrm{r}}} \end{bmatrix} = \begin{bmatrix} \delta_{p_{\mathrm{t}}} H \\ \delta_{p_{\mathrm{r}}} H \\ \delta_{\varepsilon_{\mathrm{t}}} H \\ \delta_{\varepsilon_{\mathrm{r}}} H \end{bmatrix} \tag{17}$$

The change of the total energy of the beam (quadratic energy only, ignore the gravity potential energy) is expressed as

$$\dot{H}_{\mathrm{B}} = \int_0^L (\partial_x H)^{\mathrm{T}}\,\dot{\boldsymbol{x}}\mathrm{d}z = -\int_0^L \boldsymbol{e}^{\mathrm{T}}\boldsymbol{f}\mathrm{d}z. \tag{18}$$

By applying integration by parts, the change of the total energy can also be illustrated as the variable pairs of power through the boundaries as

$$\dot{H}_{\mathrm{B}} = e^{p_{\mathrm{t}}}e^{\varepsilon_{\mathrm{t}}} + e^{p_{\mathrm{r}}}e^{\varepsilon_{\mathrm{r}}}|_0^L \tag{19}$$

and we define the boundary flow and effort as

$$\begin{bmatrix} f_\partial^{\mathrm{t}} \\ f_\partial^{\mathrm{r}} \\ e_\partial^{\mathrm{t}} \\ e_\partial^{\mathrm{r}} \end{bmatrix} = \begin{bmatrix} e^{p_{\mathrm{t}}}|_{\partial_z} \\ e^{p_{\mathrm{r}}}|_{\partial_z} \\ e^{\varepsilon_{\mathrm{t}}}|_{\partial_z} \\ e^{\varepsilon_{\mathrm{t}}}|_{\partial_z} \end{bmatrix} \tag{20}$$

where ∂_z denotes the boundary of the domain $Z = [0, L]$. And the power continuity and conservation equation are fulfilled as

$$\int_Z \boldsymbol{e}^{\mathrm{T}}\cdot\boldsymbol{f}\mathrm{d}z + (f_\partial^{\mathrm{t}}\cdot e_\partial^{\mathrm{t}} + f_\partial^{\mathrm{r}}\cdot e_\partial^{\mathrm{r}})|_{\partial Z} = 0 \tag{21}$$

Finally, the equation can be simplified as

$$-\boldsymbol{f} = \boldsymbol{J}(z)\partial_x H_{\mathrm{B}} = \boldsymbol{J}(z)\boldsymbol{e} \tag{22}$$

where $\boldsymbol{J}(z)$ is a skew-symmetric differential operator and further discretization method should be applied to solve the PDEs.

Structure-preserving discretization

The next step to solve the PDEs of Timoshenko beam is to transfer into a discretized model. And the skew-symmetric differential operator must be retained in the new model, which means that the certain geometric or structure property should be preserved after the discretization. In [10], Moulla applied a structure-preserving discretization method based on pseudo-spectral method to approximate the infinite-dimensional Timoshenko beam model.

The discretization of the differential operator $\boldsymbol{J}(z)$ has proven as a good approximation of the properties of the system in [13]. We list some essential steps of the discretization in this section.

In the formulation (22), the differential operator $\boldsymbol{J}(z)$ and the effort vector can be separated as two parts by the subject relation to differentiation. The new effort vectors are denoted as $\boldsymbol{e}$ and $\boldsymbol{e}_*$ and the new formulation is expressed as

$$-\boldsymbol{f} = \begin{bmatrix} & & 1 & 0 \\ & & 0 & 1 \\ 1 & 0 & & \\ 0 & 1 & & \end{bmatrix} \partial_z \boldsymbol{e} + \begin{bmatrix} & & 0 & 0 \\ & & 1 & 0 \\ 0 & -1 & & \\ 0 & 0 & & \end{bmatrix} \boldsymbol{e}_*. \quad (23)$$

According to the pseudo-spectral method proposed for canonical system of two conservation laws, we define different approximation bases for the flows $\boldsymbol{f}^v \in \{\boldsymbol{f}^{p_\mathrm{t}}, \boldsymbol{f}^{p_\mathrm{r}}, \boldsymbol{f}^{\varepsilon_\mathrm{t}}, \boldsymbol{f}^{\varepsilon_\mathrm{r}}\}$ and the efforts $\boldsymbol{e}^v \in \{\boldsymbol{e}^{p_\mathrm{t}}, \boldsymbol{e}^{p_\mathrm{r}}, \boldsymbol{e}^{\varepsilon_\mathrm{t}}, \boldsymbol{e}^{\varepsilon_\mathrm{r}}\}$.

$$\begin{aligned} \boldsymbol{f}^v(t,z) &\approx \textstyle\sum_{k=0}^{N-1} f_k^v \varphi_k(z), \\ \boldsymbol{e}_*^v(t,z) &\approx \textstyle\sum_{K=0}^{N-1} e_*^v \varphi_k(z), \\ \boldsymbol{e}^v(t,z) &\approx \textstyle\sum_{i=0}^{N} e^v \phi_i(z) \end{aligned} \quad (24)$$

$\varphi_k(z)$ and $\phi_i(z)$ are the basis functions for flows and efforts. We chose the interpolation Lagrange polynomials of degree N and $N-1$ as suitable basis functions:

$$\varphi_k(z) = \prod_{j=0, j\neq k}^{N-1} \frac{z - z_j}{z_k - z_j}, \phi_i(z) \prod_{j=0, j\neq i}^{N} \frac{z - \xi_j}{\xi_i - \xi_j} \quad (25)$$

with $z_k \in (0, L), k = 0, \dots, N-1$ and $\xi_i \in (0, L), i = 0, \dots, N$ are the collocation points for $\varphi_k(z)$ and $\phi_i(z)$ respectively.

We directly give the discretized formulation of a rotating Timoshenko beam as an input-output representation:

$$\bar{\boldsymbol{f}} = \begin{bmatrix} 0 & \boldsymbol{J}_{12} \\ \boldsymbol{J}_{21} & 0 \end{bmatrix} \cdot \bar{\boldsymbol{e}} \quad (26)$$

with

$$\bar{\boldsymbol{f}} = [\boldsymbol{f}^{p_\mathrm{t}}, -e_{\partial 0}^{\mathrm{t}}, \boldsymbol{f}^{p_\mathrm{r}}, -e_{\partial 0}^{\mathrm{r}}, \boldsymbol{f}^{\varepsilon_\mathrm{t}}, f_{\partial L}^{\mathrm{t}}, \boldsymbol{f}^{\varepsilon_\mathrm{r}}, f_{\partial L}^{\mathrm{r}}]^{\mathrm{T}}$$

$$\bar{\boldsymbol{e}} = [\tilde{\boldsymbol{e}}^{p_\mathrm{t}}, f_{\partial 0}^{\mathrm{t}}, \tilde{\boldsymbol{e}}^{p_\mathrm{r}}, f_{\partial 0}^{\mathrm{r}}, \tilde{\boldsymbol{e}}^{\varepsilon_\mathrm{t}}, e_{\partial L}^{\mathrm{t}}, \tilde{\boldsymbol{e}}^{\varepsilon_\mathrm{r}}, e_{\partial L}^{\mathrm{r}}]^{\mathrm{T}}$$

The details inside $\boldsymbol{J}_{12}$ and $\boldsymbol{J}_{21}$ are given in the previous work [24], and it can be proven that $\boldsymbol{J}_{12} = -\boldsymbol{J}_{21}^{\mathrm{T}}$, i.e. the interconnection matrix $\boldsymbol{J} \in \mathbb{R}^{(4N+4)\times(4N+4)}$ is skew-symetric.

$$\boldsymbol{\phi}_0 = [\phi_0(0), \dots, \phi_N(0)]^{\mathrm{T}}$$

$$\boldsymbol{\phi}_L = [\phi_0(L), \dots, \phi_N(L)]^{\mathrm{T}}$$

$$\boldsymbol{D} \in \mathbb{R}^{N\times(N+1)}, D_{k+1,i+1} = \partial_z \phi_i(z_k)$$

$$\boldsymbol{M} \in \mathbb{R}^{(N+1)\times N}, M_{i+1,k+1} = \textstyle\int_0^L \phi_i(z)\varphi_k(z)\mathrm{d}z$$

$$\boldsymbol{S} \in \mathbb{R}^{N\times N}, S_{i+1 j+1} = \textstyle\int_0^L \varphi_i(z)\varphi_j(z)\mathrm{d}z$$

Finally, we obtain an explicit linear port-Hamiltonian formulation with input and output as

$$\begin{aligned} \dot{\boldsymbol{X}} &= \boldsymbol{J}_{4N\times 4N}\boldsymbol{Q}_{4N\times 4N}\boldsymbol{X} + \boldsymbol{G}_{4N\times 4}\boldsymbol{U} \\ \boldsymbol{Y} &= \boldsymbol{G}_{4N\times 4}^{\mathrm{T}}\boldsymbol{Q}_{4N\times 4N}\boldsymbol{X} + \boldsymbol{D}_{4\times 4}\boldsymbol{U} \end{aligned} \quad (27)$$

The discretized flow vectors are remained as state variables $\boldsymbol{X} \in \mathbb{R}^{4N}$ .The properties of the cross section is reflected by the matrix $\boldsymbol{Q}_{4N\times 4N} = \mathrm{blockdiag}\{\boldsymbol{S}/\rho, \boldsymbol{S}/I_\rho, K_s\boldsymbol{S}, K_b\boldsymbol{S}\}$. The boundary flows efforts are relocated in the input and output vectors as

$$\boldsymbol{U}(\boldsymbol{t}) = \begin{bmatrix} f_{\partial 0}^{\mathrm{t}} \\ f_{\partial 0}^{\mathrm{r}} \\ e_{\partial L}^{\mathrm{t}} \\ e_{\partial L}^{\mathrm{r}} \end{bmatrix} = \begin{bmatrix} v(0) \\ \omega(0) \\ Q(L) \\ M(L) \end{bmatrix}, \boldsymbol{Y}(t) = \begin{bmatrix} -e_{\partial 0}^{\mathrm{t}} \\ -e_{\partial 0}^{\mathrm{r}} \\ f_{\partial L}^{\mathrm{t}} \\ f_{\partial L}^{\mathrm{r}} \end{bmatrix} = \begin{bmatrix} -Q(0) \\ -M(0) \\ v(L) \\ \omega(L) \end{bmatrix}$$

3.4. Model assembly

Between the hydraulic cylinder and the boom structure, there is the luffing mechanism to connect both sides and to transfer motion and load. We specify the relation between the displacement of cylinder s and the angel displacement of the boom θ as $\theta(s)$, the relation of load and velocity can be expressed as

$$\begin{aligned} F &= \partial_s\theta \cdot M(0) \\ \omega(0) &= \partial_s\theta \cdot \dot{s} \end{aligned} \quad (28)$$

Now we can connect the two system with the relation between the input and output. We found the matrix $\boldsymbol{G}_{4N\times 4}$ in the formulation of boom model can be written as

$$\boldsymbol{G}_{4N\times 4}=\begin{bmatrix}0 & 0 & \boldsymbol{G}_0 & 0\\ 0 & 0 & 0 & \boldsymbol{G}_0\\ \boldsymbol{G}_0 & 0 & 0 & 0\\ 0 & \boldsymbol{G}_0 & 0 & 0\end{bmatrix}$$

with $\boldsymbol{G}_0$ as $1\times N$ vector.

We can list the equations of both systems together with the details of interconnection terms as

$$\begin{bmatrix}\dot{\boldsymbol{\lambda}}\\ \dot{\boldsymbol{f}}^{p_t}\\ \dot{\boldsymbol{f}}^{p_r}\\ \dot{\boldsymbol{f}}^{\varepsilon_t}\\ \dot{\boldsymbol{f}}^{\varepsilon_r}\end{bmatrix}=\begin{bmatrix}\overbrace{\boldsymbol{J}(\lambda)}^{4\times 4} & 0\\ 0 & \underbrace{\boldsymbol{J}(X)}_{4N\times 4N}\end{bmatrix}\begin{bmatrix}\partial_\lambda H_c\\ \tilde{\boldsymbol{e}}^{p_t}\\ \tilde{\boldsymbol{e}}^{p_r}\\ \tilde{\boldsymbol{e}}^{\varepsilon_t}\\ \tilde{\boldsymbol{e}}^{\varepsilon_r}\end{bmatrix}+\begin{bmatrix}0\\ \partial_s\theta\boldsymbol{G}_0^{\mathrm{T}}\tilde{\boldsymbol{e}}^{\varepsilon_r}\\ \beta Q_1/V_1\\ -\beta Q_2/V_2\\ Q(L)\boldsymbol{G}_0\\ M(L)\boldsymbol{G}_0\\ v(0)\boldsymbol{G}_0\\ -\partial_s\theta\boldsymbol{G}_0\frac{P_m}{m}\end{bmatrix}$$

Then a complete model of the hydraulic actuated boom system can be formed with the new definition of the state variables as $\dot{\overline{\boldsymbol{X}}}=\left[\dot{s},\dot{P}_m,\dot{p}_1,\dot{p}_2,\boldsymbol{f}^{p_t},\boldsymbol{f}^{p_r},\boldsymbol{f}^{\varepsilon_t},\boldsymbol{f}^{\varepsilon_r}\right]^{\mathrm{T}}$, new definition of the input vector as $\overline{\boldsymbol{U}}=[Q_1,Q_2,Q(L),M(L),v(0)]^{\mathrm{T}}$ and the Hamiltonian function of the complete system as $H=H_c+H_B$.The equations for the complete system can be expressed as

$$\dot{\overline{\boldsymbol{X}}}=\bar{\boldsymbol{J}}(\overline{\boldsymbol{X}})\partial_{\overline{\boldsymbol{X}}}H+\overline{\boldsymbol{G}}\overline{\boldsymbol{U}}$$

with the detail of $\bar{\boldsymbol{J}}(\overline{\boldsymbol{X}})$ as following:

$$\begin{bmatrix}0 & 1 & 0 & 0 & 0 & 0 & 0 & 0\\ -1 & 0 & \mu_1 & -\mu_2 & 0 & 0 & 0 & \partial_s\theta\boldsymbol{G}_0^{\mathrm{T}}\\ 0 & -\mu_1 & 0 & 0 & 0 & 0 & 0 & 0\\ 0 & \mu_2 & 0 & 0 & 0 & 0 & 0 & 0\\ 0 & 0 & 0 & 0 & 0 & 0 & \boldsymbol{J}_{13} & 0\\ 0 & 0 & 0 & 0 & 0 & 0 & \boldsymbol{J}_{23} & \boldsymbol{J}_{24}\\ 0 & 0 & 0 & 0 & \boldsymbol{J}_{31} & \boldsymbol{J}_{32} & 0 & 0\\ 0 & -\partial_s\theta\boldsymbol{G}_0 & 0 & 0 & 0 & \boldsymbol{J}_{42} & 0 & 0\end{bmatrix}.$$

4. SOLUTION OF THE OPTIMAL CONTROL PROBLEM

In order to solve the optimal control problem related to the hydraulic cylinder, we firstly applied the nondimensionalization method proposed by Sakai[19].

With the definition of the new nondimensionalized state variables $s=s^*l$, $P=P^*\sqrt{ml\beta A}$, $t=t^*T=t^*\sqrt{ml\beta A}$, $p_1=\beta p_1^*$, $p_2=\beta p_2^*$, the original equations of the hydraulic cylinder (6) and can be reformed as

$$\begin{aligned}\frac{ds^*}{dt^*}&=P^*\\ \frac{dP^*}{dt^*}&=p_1^*-p_2^*-\frac{F}{\beta A}\\ \frac{dp_1^*}{dt^*}&=\frac{-P^*l+\frac{Q_1}{A}\sqrt{ml\beta A}}{V_{01}/A+ls^*}\\ \frac{dp_2^*}{dt^*}&=\frac{P^*l-\frac{Q_2}{A}\sqrt{ml\beta A}}{V_{02}/A+\alpha l(l-s^*)}\end{aligned}\tag{29}$$

In the optimal control problem, the state variables are nondimensionalized variables $\boldsymbol{\lambda}^*=[s^*,P^*,p_1^*,p_2^*]$. The differential equations are Eq.(29).

The cost functional is set as:

$$J=\int_0^{t_f}(Q_1^2+Q_2^2)\times 10^5+\left(p_1^{*2}+p_2^{*2}\right)\times 10^6\mathrm{d}t+P^{*2}\times 10^2\tag{30}$$

where simulation time is set as $t_f=0.76$s.

At initial instant, both the displacement and the velocity of cylinder are set as 0. Pressure p_1 and pressure p_2 are set as 5×10^5Pa and 0, respectively. At terminal instant, the position of cylinder is $l_{\max}=0.3935$m. The velocity of cylinder is 0. Pressure p_1 and pressure p_2 are set as 5×10^5Pa and 0, respectively.

Thus, the initial conditions and terminal conditions in optimal control problem are set as:

$$\begin{aligned}\boldsymbol{\lambda}_0^*&=\left[0\ 0\ \frac{5\times 10^5}{\beta}0\right]^{\mathrm{T}},\\ \boldsymbol{\lambda}_f^*&=[l_{\max}/l\ 0\ 5\times 10^5/\beta\ 0]^{\mathrm{T}}\end{aligned}\tag{31}$$

During the movement, pressure p_1 and pressure p_2 should be great than zeros. The rate of momentum also should be limited. One has the following inequality constraints:

$$\lambda_3^*\geq 0,\lambda_4^*\geq 0,-\lambda_{\max}^*\leq\dot{\lambda}_2^*\leq\lambda_{\max}^*\tag{32}$$

In this example, the threshold is set as $\lambda_{\max}^*=3\times 10^{-4}$.

Combining Eq.(29)-Eq.(32), an optimal control problem is defined properly. ICLOCS 2.5 is applied to solve the problem. The converged solution is obtained after 500 iterations which take 20.43s. The cost functional is 1.1897×10^4.

The cost function means the minimal input and the potential energy. All the parameters we use are listed in **Table 1**.

Table 1: Parameters of the cylinder

Cylinder parameter	Value
Cap end area A	1×10^{-4} m^2
Area ratio α	0.75
Bulk modulus β	1.29×10^9 Pa

Initial volume in chamber 1 V_{01}	1×10^{-7} m^3
Initial volume in chamber 2 V_{02}	1×10^{-7} m^3
Stroke of the cylinder l	0.5 m
Mass of the piston m	10 kg
Force on the piston F	50 N

We made a test simulation for a single hydraulic cylinder to be driven to a maximal displacement of 0.3m in a short time period of 0.765s (it comes from the nondimensionalized time variable). The results of state variables and inputs are shown in **Figure 3** to **Figure 6**.

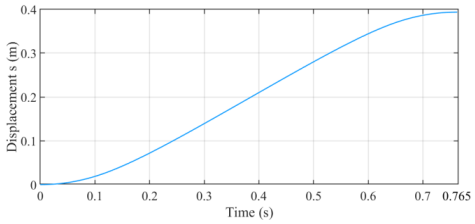

Figure 3: Optimal result of displacement s

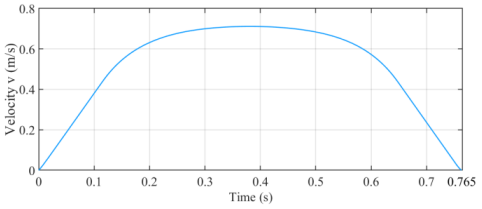

Figure 4: Optimal result of piston velocity v

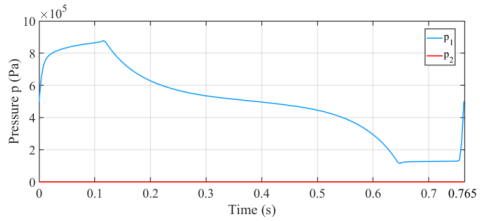

Figure 5: Optimal results of pressures p_1 and p_2

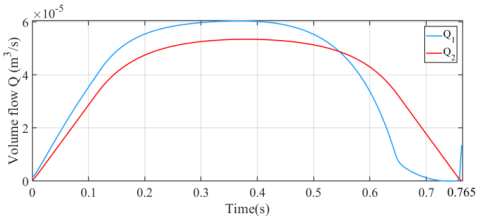

Figure 6: Optimal results of volume flows Q_1 and Q_2

The pressure p_2 in chamber 2 is calculated as 0 for the whole time period. It is reasonable because of the absent of the equation of control valve as Eq.(10), it means there is no throttling effect between chamber 2 and the tank. It reveals that only using volume flows as controlled inputs is not good enough for the solution of the optimal control problem of hydraulic cylinder. This also points out an improvement for us.

Next, we apply the piston velocity v combining with the Eq.(28) to calculate the corresponding input angel velocity for the input-output system of boom structure as (27). The parameters of the boom structure we designed are listed in **Table 2** which are modified from our previous model in [24].

Table 2: Parameters of the boom structure

Parameter	Beam 1	Beam 2	Beam 3
Length (m)		0.3	
Width (m)	0.2	0.15	0.1
Depth (m)	0.005	0.004	0.003
Density (kg/m^3)		7850	
Yong's modulus (GPa)		210	
Poisson's ratio		0.33	
Shear factor		5/6	

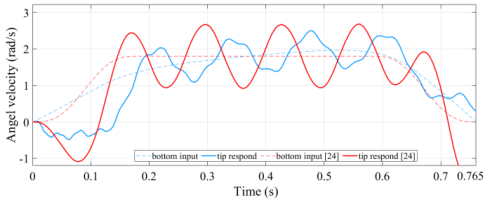

Figure 7: The angel velocity inputs, and the angel velocity outputs of two cases

The boom structure is modelled as a step beam with three different sections. The input is the angel velocity at the bottom of the boom and the output is the angel velocity at the tip of the boom. In **Figure 7**, the dot lines are the input curves of optimized angel velocity (blue) and the one (red) we applied in [24] generated by quadratic function. The solid lines are the corresponding outputs. The results present the improvement of less vibration amplitude between optimized input and the previous input. But the reduce of the vibration is not significant due to the lack of boom model in the optimization process.

5. CONCLUSION AND OUTLOOK

In this paper, we present a complete model of hydraulic actuated boom system in the formulation of port-Hamiltonian system. It is a foundation step to apply some dynamic control method to control the vibration of the flexible boom structure during the luffing operation. We also develop an offline trajectory generation method based on optimal control problem to generate the optimal motion of the hydraulic cylinder based on the energy related cost function.

There are still some parts of our work needed to be improved in the future, such as to include the dominate equations of control valve and the linear boom structure model in the formulation of the optimal control problem. An online model predictive control strategy will be investigated to solve the real-time vibration control problem in the next step.

NOMENCLATURE

PH Port-Hamiltonian
NLP Nonlinear programming

REFERENCES

[1]. Sun, G., & Kleeberger, M. (2003). Dynamic responses of hydraulic mobile crane with consideration of the drive system. Mechanism and Machine Theory, 38(12), 1489-1508.

[2]. Sun, G., Kleeberger, M., & Liu, J. (2005). Complete dynamic calculation of lattice mobile crane during hoisting motion. Mechanism and machine theory, 40(4), 447-466.

[3]. Sun, G., & Liu, J. (2006). Dynamic responses of hydraulic crane during luffing motion. Mechanism and Machine Theory, 41(11), 1273-1288.

[4]. Zuyev, A., & Sawodny, O. (2005). Stabilization of a flexible manipulator model with passive joints. IFAC Proceedings Volumes, 38(1), 784-789.

[5]. Sawodny, O., Aschemann, H., & Bulach, A. (2002). Mechatronical designed control of fire-rescue turntable-ladders as flexible link robots. IFAC Proceedings Volumes, 35(1), 509-514.

[6]. Pertsch, A., Zimmert, N., & Sawodny, O. (2009, December). Modeling a fire-rescue turntable ladder as piecewise Euler-Bernoulli beam with a tip mass. In Proceedings of the 48h IEEE Conference on Decision and Control (CDC) held jointly with 2009 28th Chinese Control Conference (pp. 7321-7326). IEEE.

[7]. Pertsch, A., & Sawodny, O. (2016). Modelling and control of coupled bending and torsional vibrations of an articulated aerial ladder. Mechatronics, 33, 34-48.

[8]. Duindam, V., Macchelli, A., Stramigioli, S., & Bruyninckx, H. (2009). Modeling and control of complex physical systems: The port-Hamiltonian approach. Springer Science & Business Media.

[9]. Macchelli, A. & Melchiorri, C. (2004). Modeling and control of the Timoshenko beam. the distributed port Hamiltonian approach. SIAM Journal on Control and Optimization, 43(2):743–767.

[10]. Macchelli, A., Melchiorri, C., & Stramigioli, S. (2009). Port-based modeling and simulation of mechanical systems with rigid and flexible links. IEEE transactions on robotics, 25(5):1016–1029.

[11]. Moulla, R., Lefevre, L., & Maschke, B. (2012). Pseudo- spectral methods for the spatial symplectic reduction of open systems of conservation laws. Journal of computational Physics, 231(4):1272–1292.

[12]. Vu, N. M. T., Lefevre, L., Nouailletas, R., & Bre´mond, S. (2013). Geometric discretization for a plasma control model. IFAC Proceedings Volumes, 46(2):755–760.

[13]. Wang, M., Bestler, A., & Kotyczka, P. (2017). Modeling, discretization and motion control of a flexible beam in the port-Hamiltonian framework. IFAC- Papers On Line, 50(1):6799–6806.

[14]. Kugi, A. & Kemmetmüller, W. (2004). New energy- based nonlinear controller for hydraulic piston actuators. European journal of control, 10(2):163–173.

[15]. Grabmair, G., & Schlacher, K. (2005) Energy-based nonlinear control of hydraulically actuated mechanical systems. In Proceedings of the 44th IEEE Conference on Decision and Control (pp. 7520-7525). IEEE.

[16]. Sakai, S., & Stramigioli, S. (2009). Passivity based force control of hydraulic robots. IFAC Proceedings Volumes, 42(16), 20-25.

[17]. Sakai, S. (2010). Passivity based control of hydraulic linear arms using natural Casimir functions. In Cutting Edge Robotics 2010. IntechOpen

[18]. Sakai, S. (2013). Casimir based fast computation for hydraulic robot optimizations. In 2013

IEEE/RSJ International Conference on Intelligent Robots and Systems (pp. 2874-2881). IEEE.

[19]. Sakai, S. (2017, May). A structure preserving nondimensionalization of hydraulic rotational joints. In 2017 IEEE International Conference on Robotics and Automation (ICRA) (pp. 26-32). IEEE.

[20]. Stadlmayr, R., & Schlacher, K. (2004). Modelling and Control of a Hydraulic Actuated Large Scale Manipulator. In PAMM: Proceedings in Applied Mathematics and Mechanics (Vol. 4, No. 1, pp. 141-142). Berlin: WILEY- VCH Verlag.

[21]. Nie, Y., Faqir, O., & Kerrigan, E. C. (2018, September). ICLOCS2: Try this Optimal Control Problem Solver Before you Try the Rest. In 2018 UKACC 12th International Conference on Control (CONTROL) (pp. 336-336). IEEE.

[22]. Nie, Y., Faqir, O., & Kerrigan, E. C. (2018). ICLOCS2: Solve your optimal control problems with less pain.

[23]. Waechter, A., Laird, C., Margot, F., & Kawajir, Y. (2009). Introduction to IPOPT: A tutorial for downloading, installing, and using IPOPT. Revision.

[24]. Gao, L., Mei, W., Kleeberger, M., Peng, H., & Fottner, J. (2019). Modeling and Discretization of Hydraulic Actuated Telescopic Boom System in Port-Hamiltonian Formulation. In Proceedings of the 9th International Conference on Simulation and Modeling Methodologies, Technologies and Applications (pp. 69-79). SCITEPRESS-Science and Technology Publications, Lda.

peer reviewed

THE USE OF A HOLISTIC MACHINE SIMULATION FOR THE DEVELOPMENT OF HYDRAULIC HYBRID MODULES TO REDUCE TRANSIENT ENGINE-OUT EMISSIONS

Lars Brinkschulte*, Felix Pult, Marcus Geimer

Institute Mobile Machines, Karlsruhe Institute of Technology, Rintheimer Querallee 2, 76131 Karlsruhe
* Corresponding author: Tel.: +49 721 608 45382; E-mail address: lars.brinkschulte@kit.edu

ABSTRACT

In contrast to constant operating states, particle and NOx emissions of internal combustion engines are significantly higher during transient operating states, which occur repeatedly at working cycles of mobile machines. This paper therefore deals with the conception, development and testing of hydraulic hybrid systems to reduce these emissions by phlegmatization of the engine. A wheel loader with its machine-typical working cycle serves as an example for the investigation of the benefits of such a system. Therefore, model based development techniques are used. In a holistic machine simulation, four different typical wheel loader cycles were carried out and the optimum size of the hydraulic accumulator for the hybrid system is identified by a parameter variation. The lowest emitted emissions and the smallest construction dimensions are the key elements for the accumulator selection. With an optimal hydraulic accumulator, a reduction in particle emissions of up to 29.4 % is achieved in one of the cycles investigated.

Keywords: Model Based Development, Holistic Machine Simulation, Hydraulic Hybrid System, Transient Engine-Out Emissions

1. INTRODUCTION

To meet climate change and air pollution targets, EU has tightened emission limits since Euro I in 1993. Since 2016, however, real driving emission (RDE) measurement have been mandatory for passenger cars and commercial vehicles. [1] [2] This means that exhaust aftertreatment systems (EAS) reducing emissions can no longer be designed for averaged emissions. Instead, RDE are now used for the design, which are mainly formed by transient engine-out emissions (TEE) [3]. Nitrogen oxides (NO_x), particulate emissions (PM), carbon monoxide and unburned hydrocarbons are the main constituents of TEE [4]. However, only NO_x and PM are considered in this paper as these are mainly produced in diesel internal combustion engines (ICE) [5].

For a better understanding of TEE, **Figure 1** shows the quantity of injected diesel and the resulting PM of a commercial vehicle ICE during a load step. The load step is performed from 10 to 40 % maximum load of 760 Nm at a constant engine speed of $n_{ICE} = 1{,}600\ 1/\text{min}$. Similar load steps occur frequently in typical cycles of mobile machines. The solid blue line demonstrates the classic operating strategy of an ICE. Diesel is injected immediately to deliver the required torque. The air path (AP) should react immediately to provide the necessary combustion air for a clean combustion. This requires a ramp-up time t_{AP} of almost $t_{AP} = 0$ s. Due to the delayed response of the turbocharger caused by its inertia, called turbocharger lag, such a fast supply of air to the combustion chamber is not possible. The lack of air in the combustion chamber leads to PM shown by the solid blue line in **Figure 1**, bottom. The behaviour of NO_x is comparable to that of PM. NO_x, however, is emitted, in contrast to PM, with partly sufficient amount of air and good mixing. [4]

Thus, the TEE are significantly higher than stationary emissions. By considering the RDE, the peaks are relevant for the reduction of TEE in the course of these EAS design. As a result, performance and size of the systems must increase by up to 50%, resulting in significantly higher costs and construction dimensions. [3]
In order to reduce the TEE and thus the costs for the exhaust aftertreatment, the ICE can be

operated with an increased t_{AP}. This delays the injection and gives the turbocharger more time to provide the required amount of air. The load step smoothing is called phlegmatization of the ICE and leads to significantly reduced TEE, as the dotted line in **Figure 1** bottom shows. Due to the phlegmatization, there is not enough power at the output, which must be supplied to the drive train via an additional hybrid module [6].

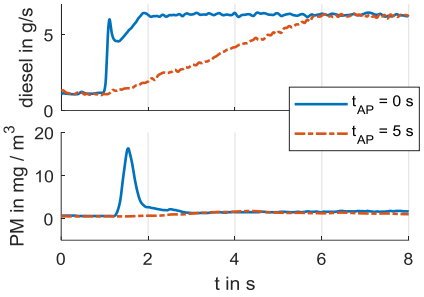

Figure 1: Phlegmatization potential according to [7]

Particularly in the construction industry, inner-city construction sites are placing greater demands on emissions of mobile machines. For this reason, in this paper a wheel loader as a very common machine on construction sides is used to present the development of a hybrid module.
To investigate and design such hybrid modules, holistic machine simulation models can be used. Therefore, the developed hybrid module and the simulation models for the wheel loader, the ICE and the hybrid module will be presented. Then follows the hydraulic accumulator design. The paper concludes with an outlook on possible system and modelling improvements.

2. APPLICATION CASE WHEEL LOADER

For parameterization and validation of the simulation model, a Liebherr L509 Speeder has been equipped with measurement technology. The transport of bulk material between two piles is investigated as the working cycle for this paper.

2.1. Machine Specifications

The considered wheel loader is characterized by a steering system combined of articulated and rear-wheel steering, an operating weight of 6.5 tons and a maximum payload of 1.8 tons. A hydrostatic traction drive (HTD) with two speed levels is used for the driving function. The function drive (FD) is designed as a Z-kinematics system with a hydraulic pilot-controlled open-centre constant flow system. A diesel five cylinder in-line engine serves as the primary energy converter.

2.2. Working Cycle

One typical task of a wheel loader is to transport bulk material between two piles, known as the Y-pattern loading cycle (see **Figure 2**). Due to recurring sequences of moving steps it is useful to separate the cycle into different states.
In the state ‘Empty Drive’ (ED) the wheel loader drives from a starting point to the loading pile. The ‘Loading’ (L) state starts with positioning the bucket close to the ground in advance of reaching the pile. In this position, the machine moves into the pile, whereby HTD and FD overcome the resistance of intrusion, digging and filling. At the end of a loading operation, the bucket is tilted and lifted to transport position. In state ‘Transport Drive’ (TD) the wheel loader sets back and moves to the unloading point. Unloading the bulk material can be assigned to the ‘Unloading’ (UL) state. After unloading, the machine reverses and repeats the entire loading cycle.

Figure 2: Y-pattern loading cycle [8]

3. HYDRAULIC HYBRID MODULE

This section describes the hybrid module’s operating principle and its developed structure.

3.1. Operating Principle

Figure 3 shows the hybrid module’s operating principle. In case of a positive load step (area 1) the ICE has to build up the required torque M_{req}. In order to reduce TEE it provides a lower torque $M_{ICE,phleg}$ within the ramp-up time t_{AP}. During

this time the difference torque M_{HHM} will be provided by the hybrid module. The charging can be done during the negative load step by recuperation (area 2) or by load point shift during partial load of the ICE. Through an additional operating strategy, the hybrid module can thus achieve lower TEE than with a conventional ICE. [9]

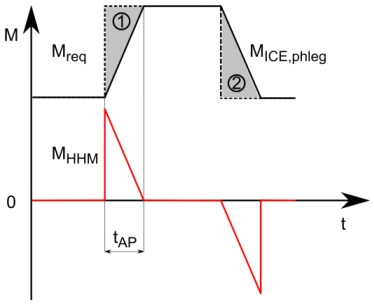

Figure 3: Hybrid module's operating principle [6]

3.2. Structure and Components

Application cases with load steps from more than 30 % of maximum load in a time interval of $t_{AP} = 0\,s$ to $t_{AP} = 5\,s$ shown in **Figure 1** are typical for mobile machines and thus high power density of the accumulator is required. Considering a ragone plot it becomes obvious that hydraulic accumulators (HA) are the best choice for those applications. In addition HAs are robust and machine operators and workshop staff are experienced with this technology [6].
In order to keep the required installation space of the hybrid module as small as possible, an HA of minimal size and capacity should be selected. This requires among other things an intelligent operating strategy. Furthermore the hybrid module should be located as close as possible to the ICE to influence its operating points as it is proposed by [10].

For those reasons, a hydraulic hybrid module (HHM) with a hydraulic unit and a bladder HA as shown in **Figure 4** will be used.

The hydraulic unit must be able to provide both the additional power to support the ICE during transient operating conditions and to charge the HA. It is therefore a hydraulic unit in swash plate design that can be used for both motor and pump operation. Due to sudden load steps, the hydraulic unit must be able to swivel fast. Swivel times from 40 to 100 ms are possible nowadays [11]. Bladder HAs are very robust, less expensive than comparable piston HAs and have been proved as best solution in terms of power density.

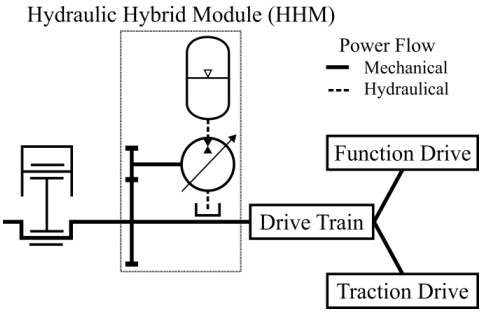

Figure 4: Structure of HHM [6]

The presented HHM-concept is adoptable to different ICEs and mobile machines. Only the component sizes have to be adapted according to the dynamics of load requirements and the various ICE performances.

4. HOLISTIC MACHINE SIMULATION

A holistic machine simulation model of the described wheel loader L509 is set up to develop the HHM. Using this simulation approach time-efficient tests of different architectures and operating strategies of the HHM are possible.

4.1. Simulation Structure

Domain-specific simulation programs are coupled with each other to achieve interaction between the individual subsystems of the wheel loader. A modular structure is used to reduce the complexity of individual systems and thus of the entire model, depending on the focus of the investigation. Matlab-Simulink serves as the master interface for the simulation. The simulation structure and essential system interactions are shown in **Figure 5**.

The hydraulic and mechanical systems involved in the power flow of the wheel loader are modelled in the 1-D simulation environment Matlab-Simscape-Fluids and Matlab-Simscape-Mechanics. These models interact with the machine-dynamics-model in IPG-TruckMaker. Depending on the movement of the machine and the environmental conditions, IPG-TruckMaker specifies the load requirements for the power dominant systems. For the HTD, these are the torque requirements of the hydraulic motor

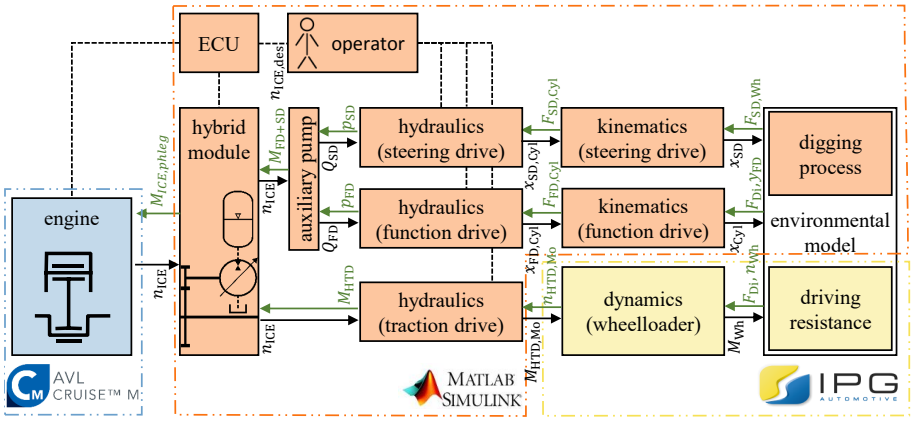

Figure 5: Structure of the holistic machine model

M_{HTD}. For the FD, the digging forces F_{Di} and the spatial displacement of the working kinematics mounting points y_{FD} and for the steering drive (SD) the steering forces F_{SD} are crucial. The quantities, which result from the physical interrelationships, are calculated in Matlab-Simscape and passed on to IPG-TruckMaker. These are the HTD motor speed $n_{\mathrm{HTD,Mo}}$, the displacements of the actuators of the function (x_{Cyl}) and the steering (x_{SD}) kinematics.

The digging forces F_{Di} are determined by an analytical approach. The cutting forces at the bucket tip, the friction forces between bucket and soil as well as the weight and inertia forces of the digged soil are taken into account. The soil material is assumed to be homogeneous and without internal friction processes. Friction effects at the side cutting edges are neglected.

After determining the required torque $\mathrm{M_{req}}$ from the sum of torques M_{FD}, M_{SD} and M_{HTD} of the wheel loader, it passes the torque on to the HHM. It then splits M_{req} between HHM and ICE in M_{HHM} and $M_{\mathrm{ICE,phleg}}$, to produce less TEE. $M_{\mathrm{ICE.phleg}}$ is finally transmitted to the ICE model within AVL's Cruise M software to simulate TEE and to return the engine speed n_{ICE} to the HHM and the wheel loader model. For that ICE simulation Cruise M uses a combination of 1D-air-path modelling and a black box model for the combustion process.

An operator model automatically calculates the path for FD and HTD for any machine position according to the coordinates of the loading and unloading piles. The characteristics of the control actions are based on scientific studies on operator behaviour with his individual characteristics.

A detailed description of the structure, parameterization and validation of the simulation environment for the FD and the HTD is given below, as these represent the largest power consuming systems in the wheel loader. Furthermore, the ICE and HHM models, their development and parameterization are further explained.

4.2. Function Drive (FD)

The SD and the FD hydraulics are supplied with hydraulic power by a fixed displacement auxiliary pump directly flanged to the shaft leading to the ICE. A priority valve divides the distributed volume flow between the SD and the FD, whereas the SD is always prioritised. 6-3 and 6-4 open-centre directional control valves enable a controlled movement of the cylinders. The excessive flow is directed to the tank via a neutral circulation.

The simulation considers the static and sliding friction for the sliding joints and the sliding friction for the rotary joints. The hydraulic line losses are modelled by series arranged throttle and orifice resistors. The valve flow rate characteristics, depending on the control signal and the pressure difference, are parameterized by extensive measurements of all individual valve sections. Additional actuators, supply circuits and filter units are not considered. While performing an exemplary short loading cycle, **Figure 6** illustrates the results of a measurement with the L509 (solid lines) and the simulation (dashed lines) for the parameters, which mainly describe the energy consumption. In addition, the states of the y-pattern loading cycle are illustrated. **Figure 6** top illustrates the cylinder forces F_i,

Figure 6 middle the pump outlet pressure p_{Pump} and **Figure 6** bottom the cylinder extension strokes x_{Cyl}. The only inputs to the simulation are the recorded operators control actions (i.e. Joystick movements, steering wheel speed, …) and the payload are used as the only inputs to the simulation. The mass of the bulk material is calculated to $m_{\mathrm{PL}} = 1{,}450\,\mathrm{kg}$, using the measurement data based method presented in [12]. The simulated mass increases over the temporary cutting depth during the digging process.

The main power consuming periods are the L and UL states. In state L, pressures above 200 bar are induced into the lifting cylinder by plunging into the pile ($t = 204.3$ s). This is occurs due to the high forces acting on the bucket and thus on the lifting cylinders exerted by the digging process when entering the pile. This force impact is well represented in measurement and simulation. Because of the force impact, a slight lowering of the bucket occurs in the simulation; in reality, the movement is restricted by the subsurface under the bucket. The forces associated with the tilting process ($t = 203.5 - 205$ s) are also mapped very well in the simulation compared to the measurement. The lifting and tilting cylinder extension stroke is simulated realistically.

In state TD, the measured and simulated forces in lifting and tilting cylinders overlap very well. The underground conditions during the measurements represent those of a construction site, soil ground with stone-diameters of up to 100 mm. In simulation, a plain underground is assumed, as a realistic representation of individual stones in position and size is not possible. Thereby the oscillations in the measurement are higher than the simulated ones. The valves are not controlled during the TD state, therefore the imposed volume flow passes through the neutral circulation. Thus the oscillating cylinder pressures have no effect on the power demand of the system. The lifting process of the bucket in the UL state results in an increase of the forces in the lifting cylinder due to the kinematics, the dynamics and the friction conditions. The lifting cylinder reaches its extension compared to the measurement after the same period of time ($t = 224$ s). The simulation results for the tilting cylinder movement, as the real bucket unloading sequence, show a good correlation as well. The reduction of the payload is assumed to be linear to the tilting cylinder movement. The

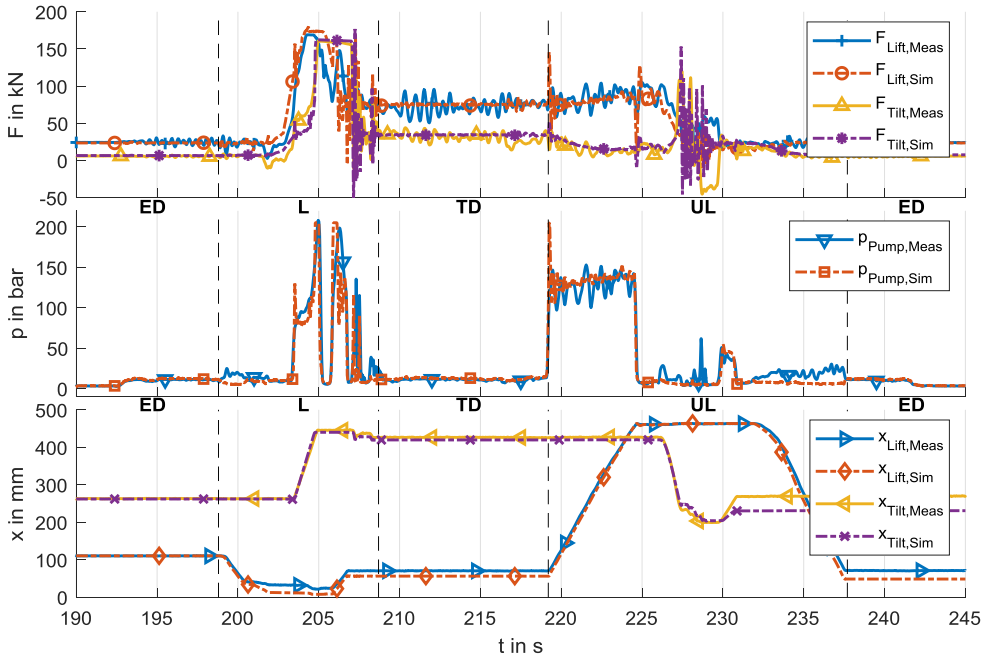

Figure 6: Comparison of results from measurement and simulation for the FD

subsequent lowering of the bucket to ground level by retracting the lift to ground level to repeat the loading process is very similar to the measurement.
The measured force oscillations in state ED are with a high certainty caused by the above-mentioned ground conditions, but have no influence on the required power.
For a statistical evaluation of the simulation results, the deviations of the power demand, defined as the product of the constant pump displacement, the pump speed n_{ICE} and the pressure at pump outlet p_{Pump}, are calculated. The deviation $s_{z,i}$ of a quantity z, here power demand of the FD P_{FD}, is defined as the difference between the simulation value and the measurement value at time i.

$$s_{z,i} = z_{\mathrm{Sim},i} - z_{\mathrm{Meas},i} \tag{1}$$

The sum of the absolute deviation $s_{z,i}$ divided by the average measured value is specified by Ranjitkar [13] as the mean relative deviation s_z.

$$s_z = \frac{\frac{1}{n}\sum_{i=1}^{n}|s_{z,i}|}{\frac{1}{n}\sum_{i=1}^{n}|z_{\mathrm{Meas},i}|} \cdot 100\,\% \tag{2}$$

Feature-based methods like this assume deviations of 20 to 30 % as acceptable [14]. Based on this literature and comparable simulation models, the authors define a deviation of less than 20 % as good and less than 10 % as very good.

In addition to the relative power deviation, the average power required for the FD is calculated for the measurement and simulation. **Table 1** shows the results of the statistic evaluation.

Table 1: Statistical evaluation of the simulation results for the FD

Sequence	s_{FD}	$\overline{P}_{\mathrm{FD,Meas}}$	$\overline{P}_{\mathrm{FD,Sim}}$
ED	10.8 %	1.0 kW	1.1 kW
L	17.0 %	5.9 kW	4.9 kW
TD	11.8 %	1.6 kW	1.8 kW
UL	3.7 %	6.9 kW	6.6 kW
Total	**5.0 %**	**4.0 kW**	**3.8 kW**

Considering all sequences, the deviation in the average power is 5 %. This means that the power demand is simulated very well. The largest deviation is while performing the loading process. Here, the simulated power (deviation of 17 %) is significantly lower due to the simplified digging model.

The pump pressure and therefore the power demand during the ED and TD states is defined by the steering processes. Results of the SD can't be shown in the paper due to the limited scope. However it has to be said, that the parameterization of the steering model is based on asphalt driving maneuvers where the steering forces are higher compared to loose surfaces like in the measurement.

Nevertheless, in general the power demand is very well represented by the simulation.

4.3. Hydrostatic Traction Drive (HTD)

A hydrostatic transmission is the central part of the HTD. The adjustable hydraulic displacement pump is flanged directly to the output shaft of the ICE. The pump displacement depends on ICE speed and the load pressure. The hydraulic motor is connected to the front and rear axle differentials via a spur gear stage and a cardan shaft. The torque is split between the individual wheels of the machine by the fixed transmission ratios, whereas the wheel speed result from the interaction with the machine dynamic model. During operation, the machine reaches driving speeds of up to 7 km/h in the first speed level and up to 30 km/h in the second speed level. The higher speeds in the second speed level are realised by the swivel process of the hydraulic motor.

The swivel characteristics of pump and motor have been determined by measurements of the entire machine on a chassis dynamometer.
Figure 7 shows the measurement and simulation results for the power-determining variables of the HTD: the difference of the forward and backward pressure levels of the HTD Δp_{HTD} (**Figure 7** top) and the volume flow of the hydraulic pump Q_{HTD} (**Figure 7** bottom).

The simulated volume flow correlates to the measured data in most of the time periods. In simulation, the acceleration processes at the starting point ($t = 193$ s), the piles ($t = 206$ s and $t = 232$ s) and the reversing point ($t = 217$ s) cause higher pressure gradients and a more dynamic acceleration behaviour. In reality, the acceleration, the pressure difference and therefore the power demand is lower due to a higher wheel slip on rough ground conditions.
When the bucket enters the pile in state L ($t = 203$ s), the machine is exposed to increased resistance which causes a pressure build-up in the

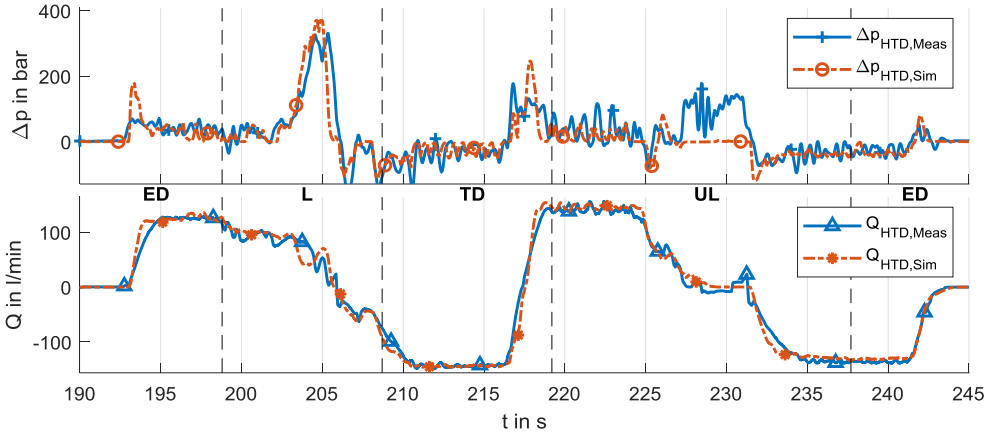

Figure 7: Comparison of results from measurement and simulation for the HTD

hydrostatic drive. This reduces the swivel angle in the hydraulic pump, resulting in a lower amount of pumped oil despite an almost constant pump speed. This effect can be seen in the simulation as well as in the measurement. The digging forces act in the measurement over a longer time period than in the simulation. This can be explained by the simplified assumed pile geometry and the analytical conditions of the digging force model.

During the UL state, the wheel loader drives with the front wheels into the extensions of the pile. The resistance against the direction of travel leads to an increased pressure level. This effect is not taken into account in the simulation, so that the increase in the pressure difference does not occur. Pressure oscillations in the ED and TD states occurring in the measurement are caused by uneven ground conditions.

Table 2 shows the results of the statistic evaluation for the average power demand and the relative deviation of the power demand in the HTD using equation 2.

Table 2: Statistical evaluation of the simulation results for the HTD

Sequence	s_{HTD}	$\overline{P}_{\mathrm{HTD,Meas}}$	$\overline{P}_{\mathrm{HTD,Sim}}$
ED	2.9 %	4.2 kW	4.4 kW
L	3.2 %	8.3 kW	8.0 kW
TD	21.3 %	9.7 kW	7.6 kW
UL	22.6 %	5.8 kW	4.5 kW
Total	**12.9 %**	**6.5 kW**	**5.7 kW**

The values show that the simulated performances match the measured performances at most sequences of the cycle with a good accuracy. The deviations occur due to the described phenomena above: the simplified digging model and the difference in ground conditions.

4.4. Internal Combustion Engine

Information to the ICE of the wheel loader L509 can be found in **Table 3.**

Combustion simulation using Cruise M is basically capable of simulating TEE. However, this requires a sufficiently large database in the form of a characteristic map measurement of the engine. As these data are not available, full load and no load measurements for different engine speeds were carried out with the wheel loader. Fuel quantities, engine speeds and torques were recorded. This data and a fully parameterized model of a larger ICE provided by AVL will be used. An interpolation based on this data basis made it possible to parameterize the model of the L509 ICE in the end.

Table 3: Investigated ICEs

	L509	$\mathrm{ICE_{ref}}$ in [15]
displacement	3,05 l	6,8 l
cylinders	5, in-line	6, in-line
max. power $P_{\max}$	54 kW	148 kW
at $n_{P,\max}$	2800 1/min	1900 1/min
max. torque $M_{\max}$	262 Nm	828 Nm
at $n_{M,\max}$	1680 1/min	1600 1/min

Measurements from [15] were used to qualitatively validate the simulation afterwards. Here, load steps were performed for various $\mathrm{t_{AP}}$ on an ICE with exhaust gas recirculation (EGR).

Information to this ICE can be found in **Table 3** as well. The load step took place from 24 to 85 % of M_{max} at constant $n_{\mathrm{M.max}}$. The results of this comparison can be taken from **Figure 8**.

The comparison of NO_x in the top of **Figure 8** shows quantitative differences. This can be attributed to the existing EGR in [15], whereby the ICE has lower combustion temperatures and produces correspondingly less NO_x. However, the qualitative progression and the decreasing NO_x values with increasing t_{AP} are roughly comparable. Due to the lack of EGR, the peak of the PM in the L509 ICE in the bottom of **Figure 8** is significantly lower than the PM of [15]. This is due to a significantly higher combustion temperature of the L509 ICE, which inhibits PM production. The PM peaks that decrease with increasing t_{AP} are comparable.

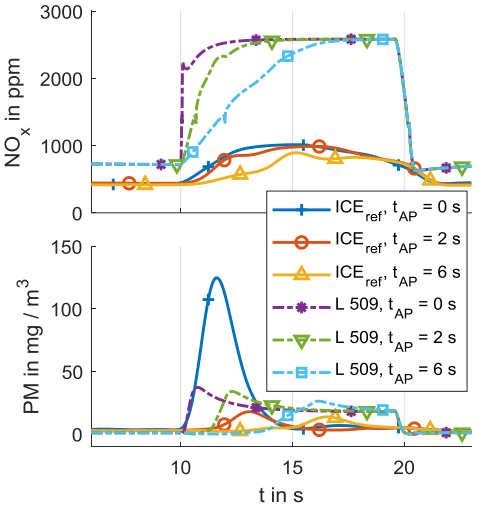

Figure 8: TEE of the investigated ICEs

Despite the different size of the ICE examined, it is nevertheless possible to show that the ICE simulation model is capable of reproducing TEE.

4.5. Hydraulic Hybrid Module

As shown in **Figure 4**, the hydraulic unit is mechanically connected to the ICE and the output of the wheel loader via spur gear and shaft.

To enable the HHM providing the torque M_{HHM} necessary for phlegmatized operation of the ICE, an operation strategy is required. This operating strategy uses the correlation in **Figure 1**: TTE decreases with an increasing t_{AP}. The higher t_{AP} is achieved by limiting the torque gradient. [16] shows that different limitations are required for several engine speed-torque combinations. Therefore, a map with so-called c-factors introduced in [16] was developed for different engine speed-torque combinations of the investigated ICE. Using this map, the torque required by the wheel loader is converted into the phlegmatized torque $M_{\mathrm{ICE,phleg}}$. This phlegmatizes both the positive and negative load steps. The negative load step is used to charge the HA as described in section 3.1.

The torque M_{HHM} to be applied by the HHM can now be calculated with equation 3. Due to the combination of M_{req} and M_{HHM} at the spur gear, only the phlegmatized torque $M_{\mathrm{ICE,phleg}}$ remains at ICE (see **Figure 3**). Thereby TEE are reduced.

$$M_{\mathrm{HHM}} = M_{\mathrm{req}} - M_{\mathrm{ICE,phleg}} \quad (3)$$

5. PARAMETER STUDY

The simulative development of the HHM is based on four various test scenarios (TS) according to the Y-pattern-loading cycle. The distances between the loading point (LP) and unloading point (UP) are varied, as is the unloading scenario itself: unloading onto a pile (TS 1 and TS 3) or unloading into a dumper truck (TS 2 and TS 4). For each of the four scenarios, one complete loading cycle is simulated. **Figure 9** shows the four defined scenarios.

TS 1 and TS 2 result in a very transient power demand for the HTD due to the short driving distances between the two piles. In TS 3 and TS 4, the driving distance is doubled, resulting in a less transient power demand in the HTD. TS 2 and TS 4 require higher hydraulic power in the FD due to larger extension strokes of the lifting cylinders. The loaded mass is 1,500 kg in all TSs.

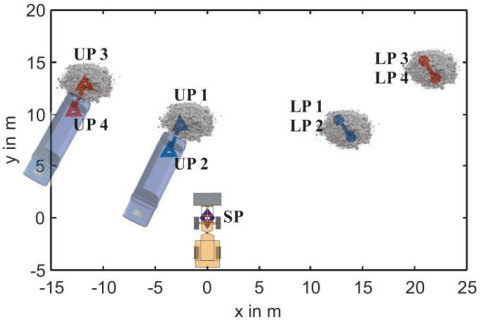

Figure 9: TS for the HHM development

5.1. System behaviour without HHM

To start with the design procedure, all four scenarios are simulated with the holistic machine simulation model, which initially contains the developed ICE model but not the HHM model. This means that n_{ICE}, M_{ICE}, PM and $\mathrm{NO_x}$ of the wheel loader with conventional (conv) ICE are known for each scenario. M_{ICE}, PM and $\mathrm{NO_x}$ can be found for the cycle of TS 1 in **Figure 10**.

In addition, the mean value of NO_x, the sum of PM and the cycle time t_{Cycle} is determined for all four cycles in **Table 4**. Both data sets are used as reference for the HA design.

The differences in TEE in **Table 4** can be explained as follows. The explanations for PM and $\mathrm{NO_x}$ are identical. First of all, the TSs with short loading cycles (TS 1 and TS 2) have a lower torque level and therefore lower TEE due to the lower driving speeds. The emissions relative to the cycle time are nevertheless higher compared to the longer driving distances, which is due to the high transient power requirement of the HTD. The differences in the differentiation by unloading point (truck or pile) can be attributed to the higher and earlier bucket lifting during the truck cycle. This means that higher torque is required from the ICE for a longer period, resulting in higher TEE.

Table 4: TEE without HHM

TS	NO_x	PM	t_{Cycle}
1	1002 ppm	60.2 mg	44.2 s
2	1082 ppm	96.6 mg	45.1 s
3	1120 ppm	87.5 mg	66.4 s
4	1168 ppm	118.9 mg	67.6 s

5.2. HHM design

The aim of the design is to keep the HA as small as possible. However, the HHM must be able to run M_{req} well with this HA and at the same time reduce the TEE to a minimum.

Due to the high computing time of the holistic machine simulation model, the HHM is dimensioned in a reduced simulation model which contains only the HHM and ICE (see Figure 5). M_{ICE} and n_{ICE} from the simulation in section 5.1 are applied to the simulation model as the approximated input of the wheel loader.

To perform a parameter study, the volume of the HA (V_{HA}) is then varied in simulation. Each simulation is started with a fully loaded HA. The variation was then performed from 2 to 18 litres with a step size of 4 litres at a maximum HA pressure of 300 bar. As a result of the parameter study, **Table 5** shows V_{HA} for which the TEE was lowest for each scenario investigated. In addition, the state of charge (SOC) of the HA at the end of each scenario is specified in **Table 5** as well.

Looking at **Table 5**, it can be seen that PM in particular is reduced, while NO_x is roughly constant. This is due to the c-factors, which are mainly optimized for PM. In addition, TS 1 shows the best reduction. Because of the short driving time and the short peak during unloading, this cycle also exhibits the most transient behaviour. TS 3 and TS 4 require a larger HA due to the higher driving speeds with higher torques. Moreover, in these scenarios the HA at the end of the cycle is not completely filled. This is because there is not enough time between the high and long torque peak during unloading until the end of the cycle. An optimized operating strategy could help here.

Table 5: TEE with HHM and optimal HA

TS	V_{HA}	NO_x	PM	SOC
1	6 l	1030 ppm	42.5 mg	99 %
2	6 l	1162 ppm	88.8 mg	100 %
3	10 l	1099 ppm	69.2 mg	62.8 %
4	10 l	1166 ppm	107.9 mg	74.3 %

5.3. HHM design verification

Due to the high calculation times of the holistic machine model, the verification was not performed using the whole couplings in the holistic machine model. Instead, it was checked how well the reduced model can follow the engine speed and torque input from the holistic machine model. For each scenario examined, the deviation for engine speed (s_{n}) and for torque (s_{M}) was determined according to equation 2. **Table 6** proves that the simulation accuracy is very good.

Table 6: Verification of pre-dimensioning

TS	s_{M}	s_{n}
1	2.5 %	0.4 %
2	2.5 %	0.5 %
3	1.2 %	0.3 %
4	1.5 %	0.3 %

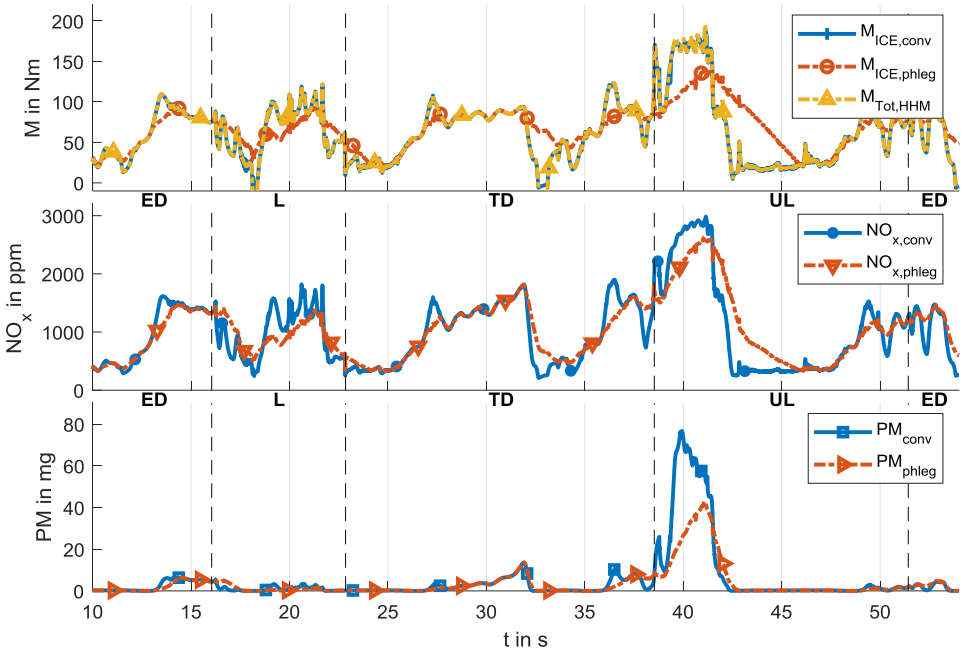

Figure 10: Comparison of results from TS 1

In addition, **Figure 10** shows that the combined output $M_{\mathrm{Tot,HHM}}$ of ICE and HHM of the reduced model corresponds very well with $M_{\mathrm{ICE,conv}}$ from the holistic machine model. This confirms the validity of the design procedure from section 5.2.

5.4. Results of the HHM design

By using the HHM the ICE can be phlegmatized without changing the system output $M_{\mathrm{Tot,HHM}}$ compared to conventional ICE $M_{\mathrm{ICE,conv}}$. This shows **Figure 10**. The investigated wheel loader behaves thus with the HHM in the same way as with its conventional ICE. The phlegmatization can be recognized by the significantly smoothed curve of $M_{\mathrm{ICE,phleg}}$ compared to $M_{\mathrm{ICE,conv}}$.
Due to the phlegmatization, the curves of PM and NO_x are also smoothed compared to conventional ICE. This leads to a maximum reduction in PM of 29.5 % in TS 1. However, due to the simple charging strategy of the HHA, the reduction of the TEE can be equalized again, especially for NO_x, as **Table 5** shows. However, the EGR used in modern ICE and an optimized operating strategy will reduce these NO_x-TEE.

6. CONCLUSIONS

This paper presents a hybrid system to phlegmatize the internal combustion engine of a mobile machine. With the aim of reducing transient engine-out emissions, the system was designed, parameterized and tested in a holistic machine simulation model. The simulation shows a very good correlation between measurements and reference machine.

Running 4 different cycles to design the hydraulic hybrid module, the transient engine-out emissions were determined. The design procedure of the hybrid module was carried out using a reduced modelling approach. This was validated by comparing the holistic machine model and the reduced model for all four cycles.

The optimally designed hybrid module resulted in a particulate emission saving of up to 29.5%. NO_x was hardly reduced. Nevertheless, it could be shown that transient engine-out emissions was effectively reduced by a relatively simple hydraulic hybrid module. This will enable a smaller exhaust after treatment system.

An optimization of the model structure could lead to the design of the hydraulic hybrid module on the holistic machine model with reasonable computing times. In addition, an improved

operating strategy could optimise the charging of the hydraulic accumulator. Knowledge of current and future driving and working states based on a state recognition [8] could determine and predict possible charging time periods in the future.

NOMENCLATURE

AP	Air Path
CO	Carbon Monoxide
Cyl	Hydraulic Cylinder
Di	Digging
EAS	Exhaust Aftertreatment System
ED	Empty Driving
F	Force
FD	Function Drive
HA	Hydraulic Accumulator
HC	Unburned Hydrocarbons
HTD	Hydrostatic Traction Drive
HHM	Hydraulic Hybrid Module
ICE	Internal Combustion Engine
L	Loading
LP	Loading Point
M	Torque
Meas	Measurement
Mo	Motor
NO_x	Nitrogen Oxids
NRTC	Nonroad Transient Cycle
P	Power
PM	Particulate Emissions
RDE	Real Driving Emission Measurements
SD	Steering Drive
Sim	Simulation
SOC	State of Charge
TD	Transport Driving
TEE	Transient Engine-Out Emissions
Tot	total
TS	Test Scenario
UL	Unloading
UP	Unloading Point
V	Volume
Wh	Wheel
Q	Volume Flow

conv	Conventional System
m_{PL}	Bulk Material in Bucket
max	Maximum
n	Speed
p	Pressure
phleg	Phlegmatized
req	Required
s_z	Mean Relative Deviation of Quantitie z
$s_{z,i}$	Absolute Deviation of Quantitie z at Timepoint i
t	Time
x	Hydraulic Cylinder Stroke
z	Evaluation Quantitie

ACKNOWLEDGEMENT

The study on the reduction of transient emissions using a hybrid system is funded by the Deutsche Forschungsgemeinschaft (DFG, German Research Foundation) – GE 2022/14-1. Without this support the shown investigations would not be possible to do. In addition the authors want to express special thanks to the Anstalt für Verbrennungskraftmaschinen List GmbH (AVL) for providing the license for simulation tool Cruise M, including MoBEO. We would also like to thank IPG Automotive GmbH for providing the license for the IPG-TruckMaker program.

7. REFERENCES

[1] Europäisches Parlament und europäischer Rat (2016) Verordnung (EU) 2016/1628. https://eur-lex.europa.eu/legal-content/DE/TXT/?uri=CELEX%3A32016R1628. Accessed 06 Sep 2018

[2] Tschöke H (2019) Real Driving Emissions (RDE). Springer Fachmedien, Wiesbaden

[3] Lox E (2019) Auslegung und Bepreisung von Abgasnachbehandlungs-Komponenten, interview

[4] Rakopoulos CD, Giakoumis EG (2009) Diesel engine transient operation: Principles of operation and simulation analysis, 1st edn. Springer, London

[5] Tschöke H, Mollenhauer K, Maier R (2018) Handbuch Dieselmotoren, 4. Aufl. 2018. Springer Reference Technik. Springer Vieweg, Wiesbaden

[6] Pult F, Engelmann D, Geimer M (2019) Hybridisierung einer Verbrennungskraftmaschine zur Emissionsreduktion. In: Geimer M, Synek P-M (eds) 7. Fachtagung Hybride und energieeffiziente Antriebe für mobile Arbeitsmaschinen. KIT Scientific Publishing, pp 95–115

[7] Hagena JR, Assanis DN, Filipi ZS (2011) Cycle-resolved measurements of in-cylinder constituents during diesel engine transients and insight into their impact on emissions. In: Proceedings of the Institution of Mechanical Engineers, vol 225, pp 1103–1117

[8] Brinkschulte L, Daiß K, Geimer M (2018) Der Nutzen einer Fahr- und Arbeitszustandserkennung am Beispiel eines Radladers. In: Land.Technik 2018: Conference of Agricultural Engineering: Leinfelden-Echterdingen, vol 2332. VDI Verlag GmbH, Düsseldorf, pp 41–50

[9] Pult F, Geimer M (2019) Phlegmatization of a Combustion Engine for Reduction of Transient Emissions. In: Huhtala K, Tikkanen S, Uusi-Heikkilä J (eds) The Sixteenth Scandinavian International Conference on Fluid Power, pp 28–38

[10] Nagel P (2016) Entwicklung einer Betriebsstrategie zur Energierückgewinnung in hybriden Mehrverbrauchersystemen. PhD-Thesis, Karlsruher Institut für Technologie

[11] Findeisen D, Helduser S (2015) Ölhydraulik: Handbuch der hydraulischen Antriebe und Steuerungen, 6th edn. VDI-Buch. Springer Vieweg, Berlin

[12] Brinkschulte L, Hafner J, Geimer M (2019) Real-Time Load Determination of Wheel Loader Components. ATZ heavyduty worldwide 12(4): 62–68

[13] Ranjitkar P, Nakatsuji T, Asano M (2004) Performance Evaluation of Microscopic Traffic Flow Models with Test Track Data. Transportation Research Record 1876(1): 90–100. doi: 10.3141/1876-10

[14] Beisbart C, Saam NJ (2019) Computer Simulation Validation. Springer International Publishing, Cham

[15] Engelsmann D, Wachtmeister G (2013) Untersuchung von Betriebsstrategien für einen elektrisch hybridisierten Traktor mittels einer multiphysikalischen Gesamtfahrzeugsimulation. In: Geimer M, Synek P-M (eds) 4. Fachtagung Hybridantriebe für mobile Arbeitsmaschinen. KIT Scientific Publishing, Karlsruhe, pp 1–11

[16] Nüesch T, Wang M, Isenegger P et al. (2014) Optimal energy management for a diesel hybrid electric vehicle considering transient PM and quasi-static NOx emissions. Control Engineering Practice 29: 266–276. doi: 10.1016/j.conengprac.2014.01.020

GROUP J

Fundamentals

IMPEDANCE MEASUREMENT IN A HYDROSTATIC DRIVE

Benedikt Müller[1]*, Heiko Baum[1]

[1]*FLUIDON Gesellschaft für Fluidtechnik mbH, Jülicher Straße 338a, 52070 Aachen*

* Corresponding author: Tel.: +49 241 96 09 260; E-mail address: benedikt.mueller@fluidon.com

ABSTRACT

Pressure oscillation in hydrostatic drive trains can cause noise and damage to components. They impair function and reliability. The visualization of the oscillation mode helps to clarify the causal relationships in the hydrostatic drive train and is a basis for the development of remedial measures.
Analysis of the pressure oscillation situation, however, can only be carried out in the complete system, since line branching and the impedance of the hydrostats have an influence on the resonance frequencies and the oscillation modes. If only the line length between the components is considered in the pressure oscillation analysis, neither the calculated frequencies nor the position of the pressure antinodes where possible remedial measures are to be placed are correct.
This paper presents the metrological determination of the impedance of a hydrostat on a functional test bench ("mobile impedance measurement") and the preparation of the measurement data for the subsequent simulative pressure oscillation analysis of a hydraulic drive train.

Keywords: Noise, Vibration, Pressure Oscillation, Pulsation, Impedance, Hydrostatic Drive

1. INTRODUCTION

In the case of commercial vehicles, the focus of development is on fulfilling the intended function. The hydrostatic drive train (**Figure 1**) as a subsystem of the vehicle concept is therefore subject to design restrictions regarding component positioning or line routing.

The required flexibility in the layout of the drive train repeatedly challenges the developers regarding the pressure oscillation behavior of the lines. The entire powertrain is excited by pressure pulsations in a wide frequency spectrum by the hydrostats' pulsations, and it must be ensured that no disturbing resonance oscillation occur. With modern fluidic 1D simulation tools [[2], it is now possible to predict under which operating conditions (steady-state pressure, dynamic pressure amplitude, frequency of pulsation) the drive train is subject to pressure oscillations. However, the acoustic behavior of all components installed in the drive train must be known, which is typically not the case for the hydrostatic displacement units in particular.

1.1. Pressure oscillation analysis

In principle, every hydraulic system, including a hydrostatic drive train, has several natural frequencies [3]. However, this does not necessarily

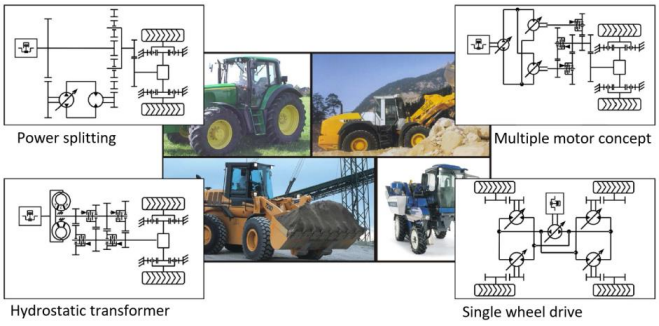

Figure 1: Schematics and application examples of different drive train concepts [1]

mean that resonance problems occur in the system. For this purpose, the natural frequencies must first be excited ("hit"). An excitation inevitably occurs in the drive train due to the reversal processes and kinematic irregularities of the hydrostats, which cause volume flow pulsations. Flow pulsations and resulting pressure pulsations travel as waves through the entire hydraulic system. Due to the variable speed of the hydrostats, the hydraulic system is excited by the pressure pulsations in a wide frequency spectrum, which increases the probability that a system resonance is "hit".

If a countermeasure is to be designed for a pressure oscillation problem in the drive train, it is not enough to identify the natural frequencies and the pressure pulsation amplitudes by means of measurements. As the following introduction to simulative pressure oscillation analysis shows, a deeper understanding of the interactions between the individual subsystems is essential. The example of a straight pipe of length L_P, closed on both sides, with constant diameter d_P (**Figure 2**) is the first step into pressure oscillation analysis.

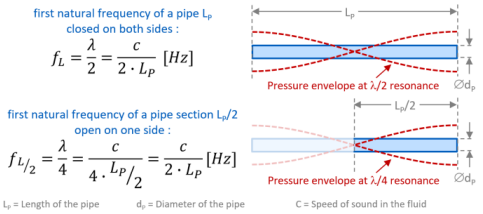

Figure 2: First natural frequency of a pipeline closed on both sides

Pressure and flow pulsations propagate as plane waves in the pipe and are reflected at the pipe ends. The dynamic behavior of the line terminating elements, the so-called terminating impedance, has a decisive influence on how the pressure waves are reflected. For additional information on sound processes in pipes, please refer to [4] and for technical acoustics in general to [5].

The closed end of a straight pipe represents the special case of an infinite terminating impedance, resulting in the reflection of a pressure wave with the reflection factor $R = 1$ (total reflection). The first natural frequency of the pipe is calculated using the formula shown on top of Figure 2, which shows that a pipe closed at both ends is subject to the $\lambda/2$ resonance condition.

Figure 2 also depicts the envelope of alternating pressure in the $\lambda/2$ resonance case. The envelope is symmetrical, and the pressure node is exactly in the middle of the pipe. If the pipe is cut exactly in the pressure node, then two subsystems with the length $L_P/2$ are created, which are now open on one side. The terminating impedance of an open line termination is zero, which is again a special case. A pressure wave is reflected at the open pipe end with the reflection factor $R = -1$. The first natural frequency of the unilaterally open pipe section is calculated using the formula shown in the lower part of Figure 2. The example shows that a unilaterally open pipe section is subject to the $\lambda/4$ resonance condition. The first natural frequency ($\lambda/2$-resonance) of the pipe L_P, which is closed on both ends, is thus composed of two subsystems which are subject to the $\lambda/4$-resonance condition and which abut with their open ends.

Figure 3 shows the effect that occurs in the pipe when the excitation frequency "hits" the natural frequency. The displayed "pressure vector plot" is a color scaled top view of the pressure values stored during the simulation. An explanation of the simulative procedure is given in [6].

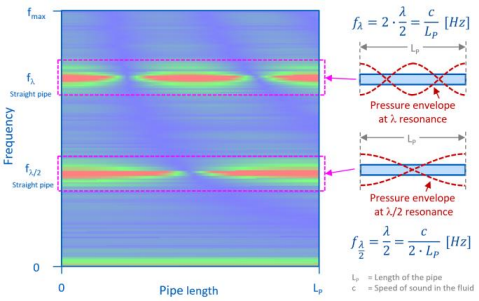

Figure 3: Pressure vector plot of the straight pipe closed on both sides

The x-axis starts at the pulsation source (e.g. the pump), which also defines the origin $x = 0$ of the pipe and ends at $x = L_P$ at a load. The y-axis does not show the simulation time, but the frequency of the excitation. The excitation frequency can also be converted into a hydrostatic speed depending on the number of displacers (number of pistons, blades or teeth). The horizontal lines indicate the first natural frequency ($\lambda/2$-resonance) and the second natural frequency (λ-resonance).

The pressure vector plot in Figure 3 clearly shows when the excitation frequency "hits" the natural frequencies of the pipe at $f_{\lambda/2}$ and at f_λ. If

the excitation frequency is continuously increased, the resonances initially build up slowly, reach their maxima and decay again. In top view, the shape of the visualized pressure pulsation resembles the envelope shown in Figure 2, making the resonances very easy to identify. A symmetrical distribution can also be seen at the second natural frequency of the pipe. Here the same decomposition approach (**Figure 4**) as for the first natural frequency in Figure 2 can be applied by cutting in the pressure nodes.

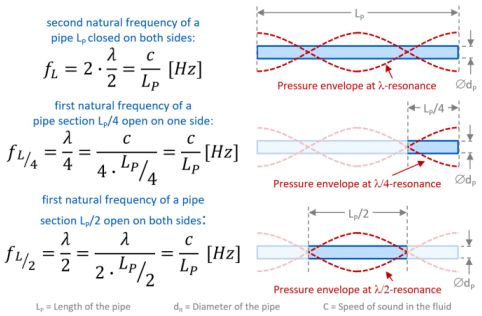

Figure 4: Second natural frequency of a pipe closed on both sides

Three subsystems are created, whose first natural frequency is equal to the frequency of the currently considered natural frequency order of the entire system. Figure 4 also shows that a pipe open on both ends is also subject to the $\lambda/2$ resonance condition, except that here the pressure antinode of the first natural frequency is situated at the center of the pipeline.

1.2. Consideration of hydrostats

A hydrostat acoustically represents a closed line termination. However, before the pressure waves are reflected inside the hydrostat, they must pass through a sequence of channels and volumes. The theoretical analysis of the pressure oscillations in a hydrostat is therefore difficult and can only be carried out with great effort using physical simulation models. Therefore, in pressure oscillation analysis the hydrostats are usually described by their so-called impedance.

For the pressure oscillation analysis, it is only relevant that a pressure wave coming from the pipe enters the hydrostat, somehow gets out of the hydrostat at some point and is superimposed on the pressure wave entering the hydrostat at that point. Depending on the phase difference between the two pressure waves, the pressure amplitude is then increased ($\Delta\varphi = 0$) or reduced ($\Delta\varphi = 180°$). The parameter that describes this behaviour is the impedance of the hydrostat.

The impedance is a complex frequency-dependent quantity that can be determined by measurement. In the next section, the standard measurement methods are explained with their advantages and disadvantages, and then the measurement method in the hydrostatic circuit presented in this article is discussed.

Once the impedance has been determined metrologically, the reproduction of the impedance curve by means of an analogous model is an elegant solution to incorporate it in the simulation. The hybrid pump model presented in [7] is available for the simulative pressure oscillation analysis.

One of the simplest replacement models of a hydrostat's impedance is based on the analogy between the measured impedance curve and the impedance curve of a Helmholtz resonator. **Figure 5** shows the principle schematic of the resonator and the most general formula for calculating its natural frequency, which is identical to the frequency of the attenuation point in the impedance curve of the resonator.

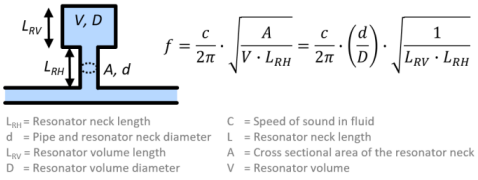

Figure 5: Schematic diagram and natural frequency of a Helmholtz resonator

The impedance curve of the Helmholtz resonator is adapted to the measured impedance of the hydrostat by selecting the parameters volume V, cross-sectional area of the resonator neck A and length of the resonator neck L_{RH} accordingly. This is done in the frequency domain and can be automated. Figure 5 does not show the calculation of the speed of sound c, considering the pressure-dependent compression modulus of the fluid and the friction in the resonator neck. The characteristic of the attenuation area of the analogous model is adapted to the measurement by the friction. The geometric values are then transferred to the hybrid pump model of the time domain simulation.

If the example pipe from Figure 2 is now extended by the analogous models of the impedances of two hydrostats, the resulting simulation model corresponds to a simple hydraulic drive train with one pump and one motor. As the pressure vector plot in **Figure 6** shows, this system also has its first oscillation mode at $\lambda/2$.

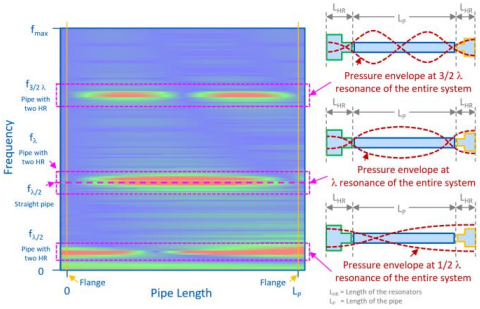

Figure 6: Schematic diagram of the oscillation modes in a hydrostatic transmission

As a result, the highest alternating pressure amplitudes occur at the hydrostats in the resonance case, which then lead to undesirable mechanical loads on sliding components subjected to pressure or on the seals, for example.

2. TEST PROCEDURE

Two methods for the experimental determination of the impedance of pumps are described in international standards: The secondary source method (ISO 10767-1:1996 [8]) and the 2 pressures / 2 systems method (2p2s, ISO 10767-1:2015 [9]). Several authors have proposed the use of a third pressure sensor in the measuring section and corresponding evaluation methods to improve the 2p2s method, e.g. [10]. Both methods are briefly presented in the following sections.

Theoretical approaches to determine the pump impedance via geometry and material properties have not yet been successfully applied.

2.1. Secondary source method

Figure 7 shows the basic measurement setup for the secondary source method: The test specimen is subjected to pressure pulsations which are generated by a second pulsation source, the "secondary source". These fluid-borne sound waves are reflected in the test specimen and superimpose themselves on the advancing waves.

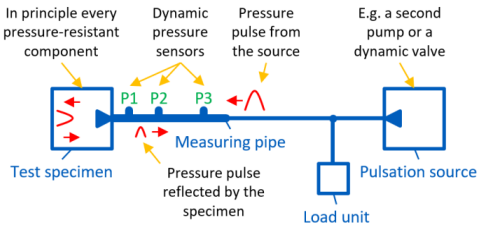

Figure 7: Principle setup of a secondary source test rig [8]

The waves travel through the measuring or reference pipe, which is connected to the pressure port of the test specimen with minimized diameter difference. Dynamic pressure sensors are mounted to this reference pipe to measure the superposition of the forward and backward travelling fluid-borne sound waves. If the transmission behaviour of the measuring pipe is known, the impedance of the test specimen can be calculated from the pressure signals. For details please refer to the standard. There you will also find further information on the design of the measuring pipe and recommendations on the sensor distances.

The transmission behaviour of the measuring pipe can be determined the more accurately the more precisely the speed of sound in the measuring pipe is known. It is therefore of decisive importance for the quality of the results. In principle, two pressure sensors in the measuring pipe provide sufficient information to calculate the impedance. However, the use of three sensors offers the essential advantage that the speed of sound can be determined from the same measurement data and thus a significant uncertainty factor in the evaluation can be excluded. The procedure is described in ISO 15086-2:2000 [11].

The test specimen is described as a positive displacement pump in ISO 10767-1:1996. However, the method can be applied to any pressure-resistant component. In a variation of the method, passive components (cf. ISO 15086-3:2008 [12]) or motors can also be tested if the pulsation source simultaneously provides the necessary pressure build-up.

2.2. 3p2s method

The 3p2s method (3 pressures / 2 systems) is an extension of the 2p2s method described in ISO 10767-1:2015. Figure 8 shows the measurement setup based on the standard. Here, the pulsation excitation is performed by the component under

test itself. The fluid-borne sound waves emitted by the test specimen are reflected at load valve 1 in a first system configuration and at load valve 2 in the second system configuration. The forward and backward travelling waves form a superposition state between the test specimen and the load valve, which is detected by the dynamic pressure sensors in the reference pipe. The impedance is then determined from the measured data of the two system states.

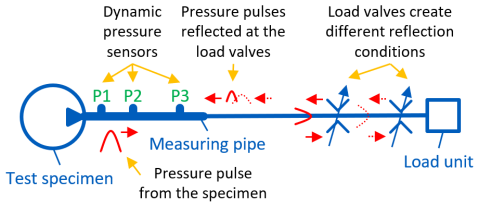

Figure 8: Principle setup of a 3p2s test rig [9, 10]

This method also requires precise knowledge of the transmission behaviour of the measuring section. The use of a third dynamic pressure sensor in the reference section is suggested, for example, in [12], which also allows the speed of sound in the reference pipe to be determined. Furthermore, the three sensors offer the advantage of a possible averaging or the selection of the "suitable" sensor pair (or sensor distance) for a frequency range.

2.3. Pros and cons

Both methods have the disadvantage that a special test setup is required, which is particularly costly for larger displacement units. In addition to the drive of the DUT, special attention must be paid to the load unit: This should not contain any components capable of vibrating, as these can lead to disturbance excitations and thus falsify the measurement results. The standards therefore recommend the use of needle valves. With the secondary source method, additional effort is required due to the required pulsation source (secondary source). This can be a servo valve, a second pump or a continuously rotating rotary valve, for example. The use of a pump has the great advantage that motors or passive components can also be tested.

The 2p2s or 3p2s method avoids the expense of an additional pulsation source, as the test object itself provides the excitation. However, this has the serious disadvantage that without an additional pressure source no motors and, due to the principle, no passive components can be measured. The impedance calculation requires measurement data of two different system states. Compared to the secondary source method, this results in twice the number of test runs and the risk of deviating measurement conditions. The measurement results of the speed of sound shown below indicate that, e.g. different test temperatures can already lead to significantly different measurement results. If the test constellation even requires a conversion from system 1 to system 2, the potential of deviating test conditions (e.g. air content) and the measuring effort will increase considerably.

The standard includes a stepwise frequency variable excitation by the secondary source. However, the excitation frequencies must not coincide with the pulsation frequencies of the DUT in order to ensure an interference-free measurement. It has proven to be a convenient method in practice to continuously adjust the excitation frequency of the pulsation source ("sweep") and thus cover the entire desired frequency range in one measurement run.

2.4. Method for impedance measurement in the hydrostatic circuit

The complex and dedicated test setup, as described in the previous sections, is one of the reasons why the described methods have so far not been widely used in practice for larger displacement units. FLUIDON has taken up the challenge to minimize this effort and to be able to measure pump and motor impedances with a single test setup.

The main requirement is to measure the impedances of the displacement units of a hydrostatic drive on an (existing) drive test bench or even in the machine. The measurement shall be performed in a run-up to continuously obtain data in the whole frequency range of interest.

Separation of desired signal components

The pressure at a measuring point in a hydrostatic circuit represents an initially uninterpretable mix of pump and motor pulsations that travel back and forth through the system and are partially reflected at various discontinuities. To extract evaluable signals from this "wave salad", the idea was developed to first extract the individual pump and motor orders from the overall signal.
Looking at the pressure signals in the frequency

range, it becomes obvious that the dominant pump and motor orders can be separated if they have sufficiently different frequencies. The respective frequencies result as a product of the speed, the number of displacers and the order. This relationship is shown in **Figure 9** for a run-up $n_{min} \rightarrow n_{max}$. The transmission ratio of the hydrostatic drive is approximately constant at constant displacements, i.e. there is a fixed speed ratio between pump and motor and the orders of different frequencies can be "separated" over the entire speed range.

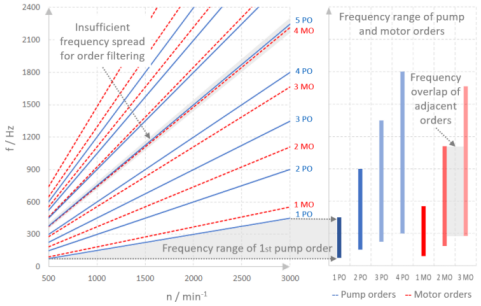

Figure 9: Frequency curves and ranges of the frequency orders of pump and motor during run-up

By varying the transmission ratio, i.e. by changing the pump and/or motor swivel, the speeds can be adjusted so that certain orders are "separable". In the example, the transmission ratio is selected so that the first to fourth pump order and the first to third motor order do not interfere. On the other hand, the frequencies of the 5th pump order and the 4th motor order, for example, are approximately congruent, so that no differentiation in the overall signal would be possible. Each order covers a certain frequency range, depending on the speed range. These are shown in the right diagram in Figure 9. The signals of several orders are available for further calculations in the overlapping ranges.

The extraction of the usable orders from the total signal is done in the time domain by a Butterworth bandpass filter of higher order, whose center frequency is guided by the speed signal.

Development of the method by virtual testing

The methodology of the "mobile impedance measurement" was developed in a virtual test using 1D simulation. This made it possible to prove the feasibility and test the method before the hardware was available. Expensive test bench time could be saved, and the subsequent measurement campaign could be carried out much more efficiently.

Figure 10 shows the simplified structure of the simulation model, which depicts the high-pressure part of the hydrostatic circuit. The displacement units are shown in the model as a combination of a volume flow source or sink and a branch resonator and describe the hybrid pump model presented in [7]. The branch resonator represents the impedance of a displacement unit in

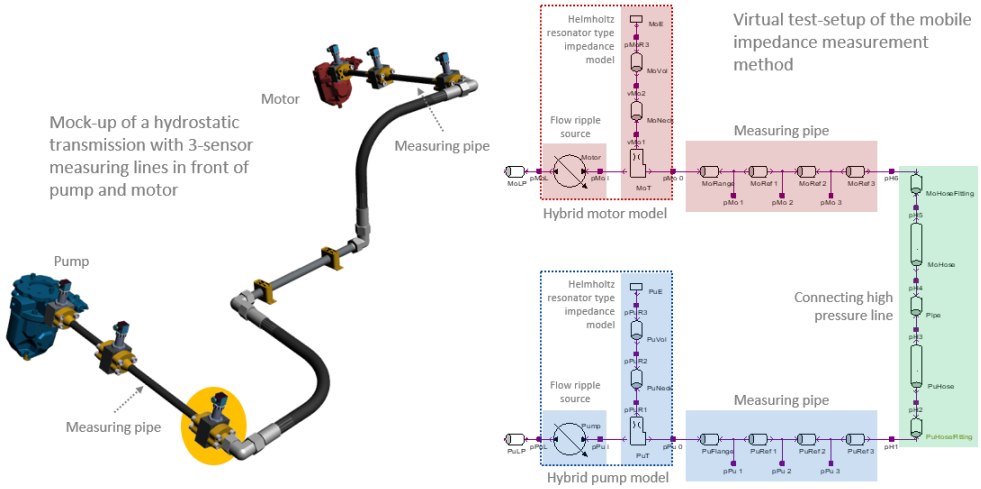

Figure 10: Hydrostatic drive with two reference pipes – simplified simulation model for the virtual development of the "mobile impedance measurement" method

good approximation, whose parameterization for the virtual test was first estimated.

The test setup developed for “mobile impedance measurement” could also be described as a dual secondary source and 3p2s test bench: A reference pipe with the three dynamic pressure sensors and a temperature sensor is installed in the existing piping on the high-pressure side of the pump and motor respectively (see Figure 7 or Figure 8). In a first evaluation, the pump serves as secondary source, and the motor’s impedance is calculated from the signals of its reference line. In the second evaluation the procedure is reversed, and the pump is the test specimen. However, both evaluations are based on a single run-up measurement. The analysis algorithms were developed and tested with “simulated measurement signals”. The calculated impedance curves were compared with the theoretical impedance curves.

3. RESULTS

In the following the step-by-step procedure of the evaluation and exemplary results are shown.

3.1. Measurement evaluation and results

First, the sound velocity in both reference pipes is determined from the measured data. The procedure according to ISO 15086-2:2000 can be applied to the unfiltered data from the run-up without modification. The measured speed of sound serves as input variable in later analysis steps.
Figure 11 shows the results of a total of 35 measurements. The speed of sound is determined for both the pump and the motor side, resulting in 70 data points which are plotted in the 3D diagram as a function of pressure and temperature and which scatter only slightly around the best-fit plane shown in the figure.

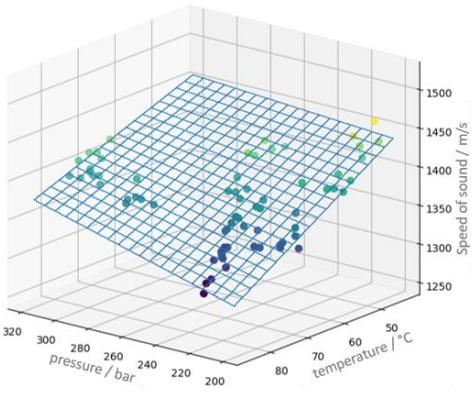

Figure 11: Speed of sound measurement results

The best-fit plane, which correlates well with published curves of pressure- and temperature-dependent speed of sound, makes it clear that large temperature and pressure changes should be avoided in one measurement. If the temperature varies over a series of measurements, further evaluation should take the temperature-dependent speed of sound into account.

In the further sequence (**Figure 12**), the impedance curve is determined. First, the raw signals are examined in the Campbell diagram, checking that the desired orders can be “separated”. If necessary, the transmission ratio of the hydrostatic transmission may be readjusted via the pump and/or motor swivel angle.

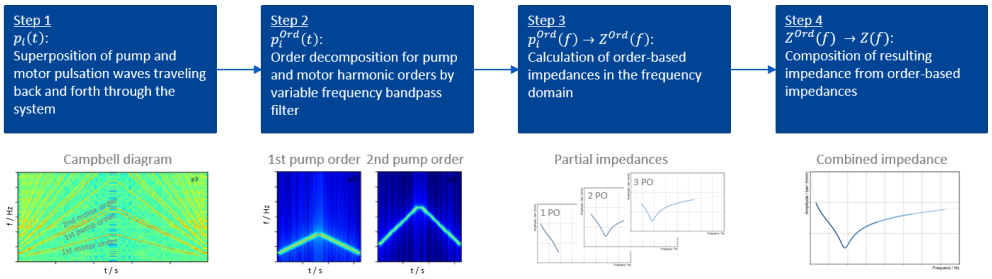

Figure 12: Sequence of the evaluation from the measurement data to the impedance curve

In the second step, the desired orders are filtered out of the time signals of the three specimen-side sensors using a bandpass filter: To determine the motor impedance, for example, the pump orders (pump = secondary source) are extracted from the sensor signals of the motor-side reference pipe. The center frequency of the bandpass filters is calculated using the measured and subsequently smoothed specimen's speed signal.

From the filtered pressure signals, the impedances belonging to each excitation order are determined in the third step. From each usable order an impedance curve results for the frequency range which this order has excited sufficiently (**Figure 13** left). This part of the evaluation procedure corresponds approximately to the calculation method proposed in ISO 10767-1:1996. The entire evaluation up to this point is performed semi-automatically via scripts.

Figure 13 on the right schematically visualizes how the "partial impedances" are combined to form the overall impedance, which covers the entire frequency range. Due to the run-up and the resulting continuously varying excitation frequency, not only single points of the impedance are present, but a continuous impedance curve.

An example of resulting impedance curves is shown in Figure 14: The three curves each represent the evaluation for one sensor pair. No excitation takes place in the frequency ranges highlighted in grey, so that no meaningful results are available. Between these ranges, both the amplitude and phase of the three measurement results are almost congruent and indicate upon an attenuation point. In the further course of the measurement, there are somewhat larger deviations in the evaluation of the sensor pair 1-3, whose distance is in the order of half the wavelength, so that the forward and backward travelling waves are partially extinguished, which means that a meaningful

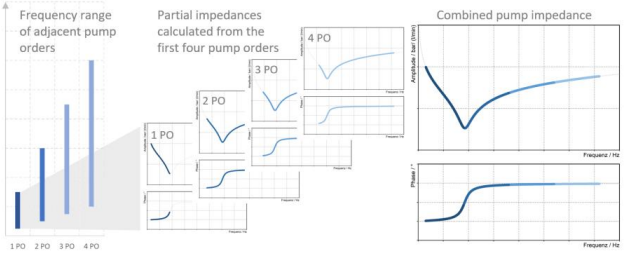

Figure 13: Order-based "partial impedances" and superposition to the overall impedance curve

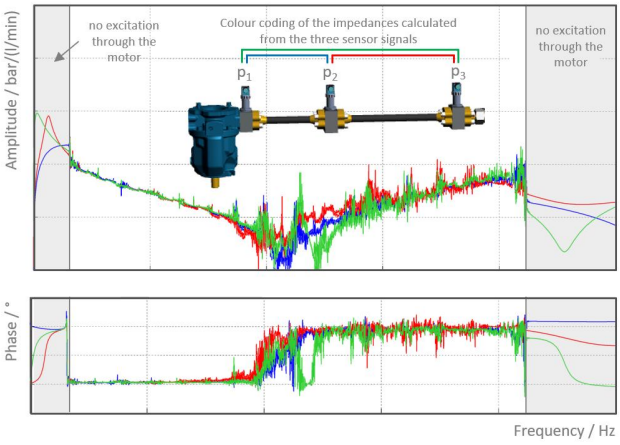

Figure 14: Measured overall impedance curves

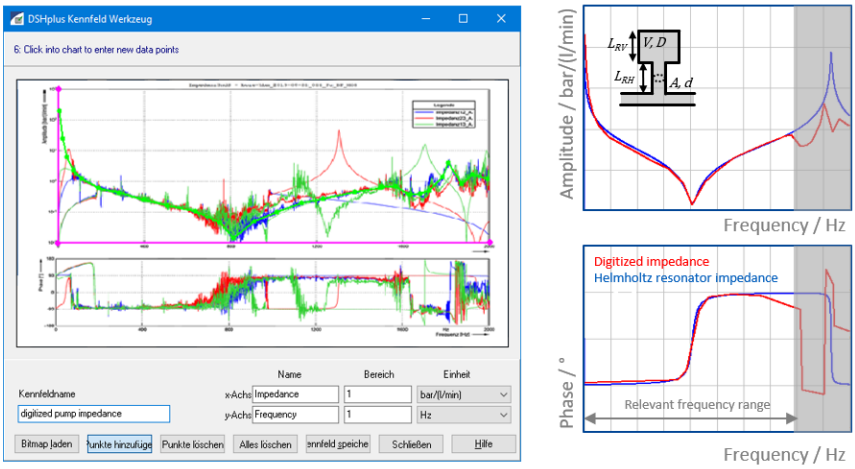

Figure 15: Approximation of measured impedance curves by the analogous model

evaluation is no longer possible. In higher frequency ranges, shorter sensor distances are therefore advantageous, while a larger distance in the low frequency range tends to produce better results. If the reference section is equipped with three sensors, the optimum distance for the frequency range can be selected.

3.2. Application in hybrid pump model

In order to make the measurement results usable for 1D simulation in the time domain, they are transferred to the analogous model presented in Figure 5.

First, the measured impedance curves are approximated by an averaged and smoothed curve. Up to now, this has been done visually with the aid of a digitization tool (**Figure 15** left). This step can also be automated in the future using suitable averaging methods.

The parameters of the Helmholtz resonator are then adjusted in an automated process with the aid of numerical optimization in such a way that the averaged impedance curves for the frequency range of interest are approximated as closely as possible (Figure 15 right). The correspondingly parameterized analogous model in the time domain then reproduces the impedance characteristics of the displacement unit in good quality with low computing effort.

4. CONCLUSION AND OUTLOOK

This paper presents a method for measuring the impedance of displacement units in the hydrostatic circuit. Based on the known methods “secondary source” and “2p2s” the method of “mobile impedance measurement” was derived, which considerably reduces the effort for measuring displacer impedances and is therefore easier to implement in practice. The method offers the following advantages:

- No special test bench is required.
- The impedances of pump and motor are determined in one setup and from one measurement run.
- The measurement data of one measurement run provides impedance curves over a wide frequency range.
- The current speed of sound is calculated from the same measured data.

The exact knowledge of the impedances of the displacers is a prerequisite for the pressure oscillation analysis of the hydrostatic circuit. The presented results were successfully applied for this purpose.

The future goal is to extend the evaluation of the measured data in such a way that the actual flow pulsations are also calculated from the measured data.

REFERENCES

[1] Kohmäscher T (2008) Modellbildung, Analyse und Auslegung hydrostatischer Antriebsstrangkonzepte. Dissertation, RWTH Aachen

[2] FLUIDON Gesellschaft für Fluidtechnik mbH (2017) DSHplus – Simulationsprogramm für fluidtechnisch mechatronische Systeme FLUIDON. Aachen

[3] Baum H (2019) Druckschwingungsanalyse hydostatischer Antriebsstränge. O+P Fluidtechnik 6/2019:36-41

[4] Veit I (2005) Technische Akustik: Grundlagen der physikalischen, physiologischen und Elektroakustik, Auflage: 6. (Juni 2005). Vogel Business Media, ISBN-13: 978-3834330130

[5] Möser M (2015) Technische Akustik, Auflage: 10 (30. Oktober 2015). Springer Vieweg, ISBN-13: 978-3662477038

[6] Baum H (2016) Druckschwingungsanalyse hydraulischer Leitungssysteme - Eine Alternative zu CFD. DIGITAL ENGINEERING Magazin 04-2016:30-32

[7] Baum H, Becker K, Faßbender, A (2014) Hybrid Pump Model for 1D Hydraulic System Simulation. The 9th International Fluid Power Conference, 24. - 26.3.2014, Aachen

[8] BS ISO 10767-1:1996: Hydraulic fluid power - Determination of pressure ripple levels generated in systems and components - Part 1: Precision method for pumps

[9] ISO 10767-1:2015(E): Hydraulic fluid power - Determination of pressure ripple levels generated in systems and components - Part 1: Method for determining source flow ripple and source impedance of pumps

[10] Liu, J, Suh, S, Butts, T (2018) Source Flow Ripple and Source Impedance Measurement for Different Hydraulic Pumps. INTER-NOISE 2018, Chicago

[11] ISO 15086-2:2000(E): Hydraulic fluid power - Determination of the fluid-borne noise characteristics of components and systems - Part 2: Measurement of the speed of sound in a fluid in a pipe

[12] ISO 15086-3:2008(E): Hydraulic fluid power - Determination of the fluid-borne noise characteristics of components and systems - Part 3: Measurement of hydraulic impedance

ON THE THERMODYNAMIC CONSISTENCY OF EXPERIMENTALLY DETERMINED FLUID PROPERTIES

Enrico Pasquini[1]*, Hubertus Murrenhoff[2] and Katharina Schmitz[2]

[1] *FLUIDON Gesellschaft für Fluidtechnik mbH, Jülicher Straße 338a, 52070 Aachen, Germany*
[2] *Institute for Fluid Power Drives and Systems, RWTH Aachen University, Campus-Boulevard 30, 52074 Aachen, Germany*
* Corresponding author: Tel.: +49 241-18298620; E-mail address: enrico.pasquini@fluidon.com

ABSTRACT

In the field of fluid power, accurate knowledge of fluid properties is vital for reasonable prediction of component behaviour and system performance. In general, these properties depend on the pressure and temperature levels that the respective medium is exposed to. The properties and their respective dependencies are not publicly accessible for many fluids commonly used in fluid power. If measured values – typically published in the form of mathematical fluid property models – are available at all, their quality is typically unknown. The paper aims to provide tools to objectively ascertain the quality of measured fluid properties. For this purpose, an equation is derived which establishes a relationship between the thermodynamic parameters of density, bulk modulus, heat capacity and thermal expansion coefficient. The presented equation is always satisfied by liquids as well as gases as long as they can be treated as a continuum. Based on this relationship, the degree of thermodynamic consistency of measured properties is evaluated: The less the equation is fulfilled by experimentally determined fluid properties, the more the measured values violate physical laws. The procedure of assessing the thermodynamic consistency is demonstrated by evaluating published fluid property models with the method outlined above. To aid engineers in judging which degree of thermodynamic inconsistency is acceptable, a cut-off value is suggested.

Keywords: Fluid properties, bulk modulus, thermodynamics, fluid property model

1. INTRODUCTION

For numerical analysis of fluid power systems, it is essential to know the properties of the pressure medium as accurately as possible. Inaccurate fluid properties may introduce considerable error in the calculation of leakage losses, natural frequencies, component heating or other individual effects. In the worst case, the function of the realised component or even system can even be impaired because of large differences between the actual fluid properties and the values used during design calculations.

1.1. Significance of fluid properties

The significance of the most relevant fluid properties viscosity, bulk modulus, density, speed of sound, thermal expansion coefficient and heat capacity for component or system performance is illustrated by some practical examples.

Example: Pressure drop and viscous heating

Consider the flow through a generic resistive element, e.g. a small throttle or an orifice. Depending on whether the flow within the resistive element is laminar or turbulent, the following relations between the pressure drop Δp across the resistor and the fluid properties hold true:

- For a given flow rate and laminar flow, the pressure drop is proportional to the absolute (dynamic) viscosity of the fluid, i.e. $\Delta p \propto \eta$.
- For a given flow rate and fully developed turbulent flow, the pressure drop is proportional to the density of the fluid, i.e. $\Delta p \propto \rho$.

As can be seen, the pressure drop depends linearly on the properties of the fluid.

For a system with imposed flow rate, this fact implies that the power requirement of the pump – approximately equal to the product of pressure drop and flow rate – is heavily influenced by the fluid's properties. Thus, wrong estimates for the

fluid's viscosity or density may lead to over- or undersized pumps.

For pressure-driven flows – e.g. a flow powered by the discharge of a pressure vessel – the strong dependence of the pressure drop on the fluid properties may lead to situations where the resulting flow rate is higher or lower than desired.

Depending on whether the dissipative heating within the resistor dominates over the generally cooling effect of expansion, the fluid's temperature will increase or decrease. If heat transfer between the fluid and the resistor can be neglected, the temperature change $\mathrm{d}T$ can be calculated as follows:

$$\mathrm{d}T = \mu_{JT}\,\mathrm{d}p = -\mu_{JT}\Delta p$$

In this equation, μ_{JT} denotes the so-called JOULE-THOMSON coefficient which only depends on fluid properties. It is calculated based on the fluid's thermal expansion coefficient, its density and its specific heat capacity at constant pressure. As can be seen from the equation above, the sign of the JOULE-THOMSON coefficient indicates whether a pressure drop across a resistor leads to an increase ($\mu_{JT} < 0$) or decrease ($\mu_{JT} > 0$) of the fluid's temperature. Depending on the temperature and pressure level, the sign of μ_{JT} can change. Thus, it is possible that calculations based on inaccurate fluid properties may indicate a cooling of the fluid when in fact its temperature increases.

Example: Natural frequencies

Through mathematical analysis, it can be shown that the natural frequency of any fluid-power element without moving parts (e.g. pipes, large volumes etc.) is proportional to the fluid's speed of sound a within the respective element:

- The natural frequencies of a fluid-filled pipe of length L depend on the kinematic and dynamic boundary conditions. If both pipe ends are open or both are closed, the natural frequencies for friction-free flow are given by the following expression:

  $$f = i\frac{a}{2L} \text{ with } i \in \mathbb{N}$$

  If one pipe end is closed and one pipe end is open, the natural frequencies are equal to:

  $$f = (2i-1)\frac{a}{4L} \text{ with } i \in \mathbb{N}$$

- A so-called *Helmholtz resonator* consists of a volume V and a neck of length L and cross-sectional area A. The combination of the neck's mass and the finite stiffness of the volume constitutes a simple oscillating system. By connecting the neck to a hydraulic or pneumatic system, the resonator can be used to absorb vibrations, e.g. within a pipeline. For negligible friction, the natural frequency f of the resonator is given by the following expression:

  $$f = \frac{a}{2\pi}\sqrt{\frac{V}{LA}}$$

The linear relationship between the fluid's speed of sound and the natural frequencies of the system delivers yet another example of how inaccurate fluid properties can have a strong impact on the calculated system behaviour. If the system is operated close to one of its natural frequencies, even small changes in the speed of sound lead to drastic changes in the system's response, e.g. pressure amplitudes.

1.2. Determination of fluid properties

Being aware of the significance of fluid properties for system performance, the fluid-power engineer is faced with the question how fluid properties can be obtained.

The properties of gases exposed to low pressures and high temperatures (as they are often encountered in pneumatic systems) can be calculated theoretically with satisfactory accuracy by using kinetic theory of gases [1].

Though useful for gases, statistical mechanics has failed to predict the properties of liquids with acceptable precision. Hence, for practical purposes, engineers and scientists must rely on experiments to determine the desired fluid properties. For many pure substances (e.g. water), an extensive body of literature regarding the results of such experiments is available. The data is typically presented in form of so-called *fluid property models*. A fluid property model is a collection of equations generated by curve fitting experimental data. These equations provide the desired physical properties (e.g. density) as functions of thermodynamic state variables, usually pressure and temperature. For the special case of water, the fluid property model developed by the *International Association for the Properties of Water and Steam* (IAPWS) has become an industrial quasi-standard [2].

Such broadly peer-reviewed and trustworthy fluid property models do not exist for many pressure media commonly used in fluid power (these are usually mixtures). In rare cases, fluid properties or even fluid property models for fluids relevant to hydraulic engineering can be taken from academic publications (e.g. the PhD theses of WITT or DRUMM) or commercially available software packages (e.g. *TILMedia Suite*) [3][4][5]. If the practising engineer finds such a source for fluid properties at all, he is often faced with the problem of assessing data of unknown quality with respect to its reliability. One necessary, although not sufficient, indicator for the quality of measured fluid properties or fluid property models is their *thermodynamic consistency*. Before this concept is discusses further, the thermodynamic fundamentals with respect to fluid properties are reviewed first. Additionally, the usual definition of the bulk modulus in fluid power is subjected to a critical review.

2. THERMODYNAMIC BACKGROUND

The only required assumption for the following derivations is that the fluid can be considered as a continuum. This is guaranteed if the mean free path of the fluid particles is significantly smaller than the smallest characteristic dimension of the problem to be analysed, e.g. the diameter of the pipe. This requirement is satisfied for virtually all fluids and geometries encountered in the field of fluid power.

2.1. Bulk modulus

One of the most important fluid properties is the *bulk modulus* K. The bulk modulus characterises the resistance of a substance against a volume-change induced by a change of the hydrostatic pressure. Most fluid power textbooks define the bulk modulus as follows [6][7][8]:

$$K = -V\frac{\Delta p}{\Delta V} \tag{1}$$

In this equation, ΔV refers to the volume change, V to the initial volume before the change took place and Δp to the causative pressure difference. Even though this approximation serves a good purpose for rough engineering estimations, in this paper preference is given to a more precise, differential definition based on the intensive quantities *specific volume* v or *density* ρ:

$$K = -v\frac{\mathrm{d}p}{\mathrm{d}v} = \rho\frac{\mathrm{d}p}{\mathrm{d}\rho} \tag{2}$$

Assuming ideal gas behaviour and a general polytropic process, the following relation holds true:

$$pv^n = \frac{p}{\rho^n} = \text{const.} \tag{3}$$

By differentiating the pressure with respect to density, one obtains an expression for the bulk modulus:

$$\frac{\mathrm{d}p}{\mathrm{d}\rho} = n\frac{p}{\rho} \rightarrow K = n \cdot p \tag{4}$$

Hence, the bulk modulus of an ideal gas undergoing a polytropic expansion or compression is directly proportional to the respective polytropic exponent n.

For an isothermal process, n assumes a value of unity such that the bulk modulus K corresponds to the static pressure p which the gas is subjected to. For isentropic processes, n equals the isentropic exponent k which – for ideal gases – is given by the ratio κ of specific heats at constant pressure and volume c_p/c_v [9]. It can therefore be concluded that the bulk modulus of an ideal gas is $k = c_p/c_v$ times larger when compressing the fluid isentropically rather than isothermally. For diatomic gases (e.g. O_2 or N_2), the isentropic exponent κ and hence the ratio of both bulk moduli equals $7/5 = 1.4$ which corresponds to a difference of 40 % in fluid stiffness. Since these two quite different values were both determined from equation (2), it is obvious that this relationship *does not* provide a unique definition of the bulk modulus of ideal gases.

A similar behaviour is to be expected for non-ideal gases and liquids as well. It is therefore evident that the bulk modulus of any substance must depend on the way in which the change of state, characterised by the pressure change per density change, is performed. In order to obtain a more hands-on formulation of this change of state, the thermal equation of state is resorted to.

2.2. Thermal equation of state

The thermal equation of state describes the relationship between density ρ, temperature T and pressure p of a certain medium. In general, any density change $\mathrm{d}\rho$ can be decomposed into contributions due to pressure change $\mathrm{d}p$ and due to temperature change $\mathrm{d}T$:

$$\mathrm{d}\rho = \left(\frac{\partial\rho}{\partial p}\right)_T \mathrm{d}p + \left(\frac{\partial\rho}{\partial T}\right)_p \mathrm{d}T \tag{5}$$

In the above equation, the partial derivative $(\partial\rho/\partial p)_T$ refers to the density change per pressure change at constant temperature; accordingly, the expression $(\partial\rho/\partial T)_p$ denotes the density change per temperature change at constant pressure. The latter differential quantity can be expressed through the (volumetric) *isobaric thermal expansion coefficient* γ_p [1]. This spatial counterpart of the linear thermal expansion coefficient known from the analysis of solids is defined as follows:

$$\gamma_p \coloneqq \frac{1}{v}\left(\frac{\partial v}{\partial T}\right)_p = -\frac{1}{\rho}\left(\frac{\partial\rho}{\partial T}\right)_p \tag{6}$$

Based on the above definition and the differential thermal equation of state, the ratio $\mathrm{d}p/\mathrm{d}\rho$ required to evaluate equation (2) is obtained:

$$K = \rho\frac{\mathrm{d}p}{\mathrm{d}\rho} = \rho\frac{1 - \left(\frac{\partial\rho}{\partial T}\right)_p \frac{\mathrm{d}T}{\mathrm{d}\rho}}{\left(\frac{\partial\rho}{\partial p}\right)_T} = \rho\left(\frac{\partial\rho}{\partial p}\right)_T^{-1}\left(1 + \rho\gamma_p\frac{\mathrm{d}T}{\mathrm{d}\rho}\right) \tag{7}$$

Other than the fluid properties ρ, $(\partial\rho/\partial p)_T$ and γ_p, the bulk modulus still depends on the yet undetermined ratio of temperature change per density change, i.e. the way how the compression or expansion is conducted. This implies that the bulk modulus defined by equations (1) or (2) cannot be a fluid property in the strict sense, since different bulk moduli could be observed for the same fluid if the thermodynamic boundary conditions were changed.

For arbitrary boundary conditions and fluid properties, the theoretical determination of the differential $\mathrm{d}T/\mathrm{d}\rho$ is very demanding and, in many cases, (currently) not possible. Most applications, however, require only knowledge of the bulk modulus for two particular changes of state where certain thermodynamic quantities are kept constant. For these two special cases, an exact relationship between the temperature and density change can be specified such that a theoretical determination of the respective bulk moduli is possible.

The lowest bulk modulus is to be expected if the density change occurs at constant temperature, i.e. the compression or expansion is isothermal ($\mathrm{d}T = 0$). Such an isothermal state of state can be assumed if the density change of a fluid element happens at such a low rate that all heat supplied can be dissipated to the environment of the element ("thermal reservoir"). The bulk modulus which can be observed during such a compression or expansion is therefore referred to as the *isothermal bulk modulus* K_T:

$$K_T \coloneqq \rho\left(\frac{\partial\rho}{\partial p}\right)_T^{-1} \tag{8}$$

If, on the other hand, the change of state occurs so rapidly that the compressed or expanded fluid element cannot exchange heat with its surroundings and, additionally, dissipative effects do not occur, the fluid resists compression as much as possible. Because the entropy s does not change during such a lossless change of state ($\mathrm{d}s = 0$), the respective bulk modulus is termed *isentropic bulk modulus* K_s:

$$K_s \coloneqq \rho\left(\frac{\partial\rho}{\partial p}\right)_s^{-1} = K_T\left[1 + \rho\gamma_p\left(\frac{\partial T}{\partial\rho}\right)_s\right] \tag{9}$$

Determining the relationship between temperature and density changes for isentropic processes requires additional relationships. These are provided by the *caloric equation of state* and the *fundamental thermodynamic equation*.

2.3. Caloric equation of state

The caloric equation of state establishes a relationship between the pressure, the temperature and the energy content of a substance. If the energy content is represented by the *specific enthalpy* h, the general form of the caloric equation of state reads:

$$\mathrm{d}h = \left(\frac{\partial h}{\partial T}\right)_p \mathrm{d}T + \left(\frac{\partial h}{\partial p}\right)_T \mathrm{d}p \tag{10}$$

The change of enthalpy with temperature at constant pressure is known as the *isobaric specific heat capacity* c_p:

$$c_p = \left(\frac{\partial h}{\partial T}\right)_p \tag{11}$$

Note that even though this property represents the enthalpy change per temperature change at constant pressure, the property itself is generally not constant with respect to pressure.

For the pressure-induced change in enthalpy, the following relationship can be derived using the second law of thermodynamics [9]:

$$\left(\frac{\partial h}{\partial p}\right)_T = v\left[1 - \frac{T}{v}\left(\frac{\partial v}{\partial T}\right)_p\right] = v\left(1 - T\gamma_p\right) \tag{12}$$

By incorporating the thermal equation of state in conjunction with the definition of the isothermal bulk modulus, the pressure differential in equation (13) can be replaced by a density change:

$$\mathrm{d}h = \left[c_p + v\gamma_p K_T\left(1 - T\gamma_p\right)\right]\mathrm{d}T + K_T\frac{1-T\gamma_p}{\rho^2}\mathrm{d}\rho \qquad (13)$$

If it is known how the enthalpy changes with respect to temperature and density for an isentropic process, the desired differential $(\partial T/\partial\rho)_s$ can be calculated from the previous equation. This information is obtained by incorporating the fundamental thermodynamic equation.

2.4. Fundamental thermodynamic equation

The fundamental thermodynamic equation combines the statements of the first and second law of thermodynamics and therefore introduces constraints which limit the possibilities how a thermodynamic process can happen. With the specific enthalpy h, its statement can be expressed as follows [1]:

$$T\mathrm{d}s = \mathrm{d}h - \frac{\mathrm{d}p}{\rho} \qquad (14)$$

Again, the pressure change dp can be substituted and the following expression is obtained:

$$T\mathrm{d}s = \left(c_p - \frac{T\gamma_p^2 K_T}{\rho}\right)\mathrm{d}T - \frac{T\gamma_p K_T}{\rho^2}\mathrm{d}\rho \qquad (15)$$

Since for an isentropic process $\mathrm{d}s$ equals zero, the temperature change per respect to density change is given by:

$$\lim_{\mathrm{d}s\to 0}\left(\frac{\mathrm{d}T}{\mathrm{d}\rho}\right) = \left(\frac{\partial T}{\partial\rho}\right)_s = \frac{T\gamma_p K_T}{\rho\left(\rho c_p - T\gamma_p^2 K_T\right)} \qquad (16)$$

Since the isobaric thermal expansion coefficient is virtually always positive (with a few exceptions such as liquid water in the temperature range $0\ °\mathrm{C} < T < 4\ °\mathrm{C}$ at standard pressure), an isentropic increase of density is invariably associated with an increase in temperature.

By substituting the above relation into equation (9), one arrives at the following identity [3]:

$$K_s = \frac{K_T}{1-\frac{T\gamma_p^2 K_T}{\rho c_p}} \qquad (17)$$

Though not new, this equation is not commonly encountered in mechanical engineering literature.

The isentropic bulk modulus K_s constitutes the upper limit of resistance that a fluid can offer to a change in density induced by a uniformly acting pressure change. Therefore, for real, frictional and lossy density changes, the following inequality applies:

$$K_T < K < K_s \qquad (18)$$

The equation above is an inequality since in reality, neither isentropic nor strictly isothermal processes are possible.

The reason why the isentropic bulk modulus of a given substance is always higher than the respective isothermal bulk modulus can be vividly explained by visualising how the fluid density depends on the pressure and temperature. A plot of the density of water versus temperature and pressure is provided in **Figure 1**.

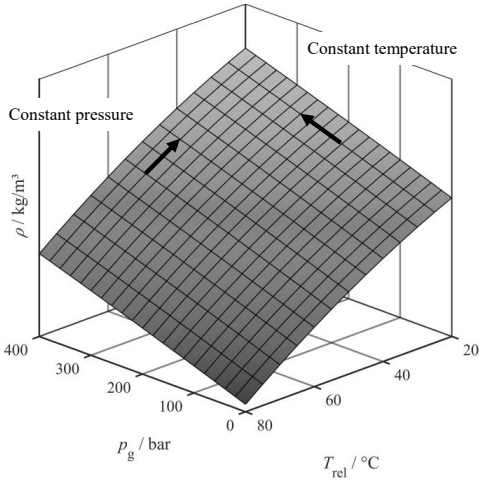

Figure 1: Density of water as a function of pressure and temperature.

As can be seen, a lower temperature (note the reversed orientation of the temperature axis) and a higher pressure generally correspond to a higher density. If the pressure is increased by $\mathrm{d}p$ at isothermal conditions, one moves along a line of constant temperature, i.e. $T = \text{const.}$ or $\mathrm{d}T = 0$. Clearly, the pressure increase is associated with a higher density, i.e. $\mathrm{d}\rho > 0$. If the same pressure increase $\mathrm{d}p$ were performed isentropically, the pressure rise would be associated with an increase of temperature $\mathrm{d}T > 0$. The temperature change can be calculated from the following identity which is derived by combining equations (16) and definition (9):

$$\left(\frac{\partial T}{\partial p}\right)_s = \left(\frac{\partial T}{\partial \rho}\right)_s \left(\frac{\partial \rho}{\partial p}\right)_s = \frac{T\gamma_p}{\rho c_p} \tag{19}$$

For water at standard pressure and a temperature of 20 °C, this expression assumes a value of approximately $1.5 \cdot 10^{-3}$ K/bar, i.e. a pressure increase of 1000 bar would increase the water's temperature by around 1.5 K. Due to the increase of temperature and the subsequent (small) expansion, the gross density increase gained through increasing the pressure dp is reduced. Hence, for the same pressure rise, the isentropic compression results in a smaller increase of density as compared to the isothermal case, i.e. the isentropically compressed fluid is stiffer than its isothermal counterpart.

Based on the isentropic bulk modulus, the speed of sound can be calculated.

2.5. Speed of sound

The speed of sound indicates the speed at which pressure and velocity disturbances propagate in a fluid at rest. The mathematical definition of the speed of sound in its present-day form dates back to LAPLACE [10]. As early as 1816, LAPLACE discovered that sound waves propagate almost without losses, so that the assumption of an isentropic change of state seems permissible. Therefore, the following identity can be derived [3]:

$$a_s := \sqrt{\left(\frac{\partial p}{\partial \rho}\right)_s} \tag{20}$$

By using definition (9), one can express the speed of sound through the isentropic bulk modulus and the density:

$$a_s = \sqrt{\frac{K_s}{\rho}} \tag{21}$$

If a bulk modulus other than the *isentropic* one is used for calculating the speed of sound, the propagation speed will be underestimated. When NEWTON tried to calculate the speed of sound of air in his famous *principia* published in 1687, he assumed an isothermal process and thus arrived at an expression which is wrong by a factor of $\sqrt{K_S/K_T} \approx 1.18$, i.e. by roughly 20 % [11].

3. THERMODYNAMIC CONSISTENCY

With the exception of viscosity, all essential thermophysical fluid properties are linked by relation (17). Since the equation is based on first principles and does not require the validity of any particular assumptions, the relationship applies to any fluid as long as it can be treated as a continuum.

Hence, any violation of this equation by measured fluid data or a fluid property model indicates a violation of fundamental physical laws. Here onwards, data which does not satisfy equation (17) is referred to as *thermodynamically inconsistent*. Due to limited accuracy of measuring devices, experimentally determined fluid properties will always be thermodynamically inconsistent to a certain degree. It is therefore important to define reasonable cut-off values above which one can *actually* speak of a thermodynamically inconsistent data set.

In order to obtain an indication of the degrees of consistency that can practically be achieved, published fluid property models are analysed.

3.1. Assessment of published fluid property models (I)

The analysis of thermodynamic consistency is demonstrated using the fluid property model presented by FLUCON GmbH [12]. The model provides equations for the calculation of all relevant thermophysical fluid properties as functions of pressure and temperature.

Model equations

Since the equations of the FLUCON model are numerical value equations, the temperature T has to be provided in K and the gauge pressure p_g (i.e. the difference between actual pressure and atmospheric pressure) must be inserted in bar. For the density, the following model equation is proposed:

$$\rho(p,T) = \frac{\rho(T)}{1 - m_1^\rho \cdot \ln\left(\frac{m_2^\rho + m_3^\rho \cdot T + m_4^\rho \cdot T^2 + m_5^\rho \cdot T^3 + p_\mathrm{g}}{m_2^\rho + m_3^\rho \cdot T + m_4^\rho \cdot T^2 + m_5^\rho \cdot T^3}\right)} \tag{22}$$

In this equation, the function $\rho(T)$ refers to the temperature-dependent density at a gauge pressure of $p_\mathrm{g} = 0$ bar and $m_1^\rho \ldots m_5^\rho$ are fluid-specific constants. The purely temperature-dependent density is given by:

$$\rho(T) = \rho_0(1 - T \cdot \gamma_0) \tag{23}$$

The equation above implies that the density at a gauge pressure $p_\mathrm{g} = 0$ bar (i.e. ambient pressure) varies linearly with temperature. Hence, the

fluid-specific constant γ_0 can be interpreted as a thermal expansion coefficient, whereas the constant ρ_0 can be thought of as the density at the virtual temperature $T = 0$ K.

The isentropic bulk modulus is calculated from the following equation:

$$K_s(p,T) = \frac{K_T(p,T)}{1-\frac{(\rho_0\gamma_0)^2 \cdot T}{\rho^3(p,T)\cdot c_p(p,T)} \cdot K_T(p,T)} \tag{24}$$

The isothermal bulk modulus is obtained by inserting the density equation (22) into definition (8). The specific heat capacity at constant pressure $c_p(p,T)$ is calculated as:

$$c_p(p,T) = c_p(T) - \frac{2\cdot T\cdot \gamma_0^2}{\rho_0(1-T\cdot\gamma_0)^3} \cdot p_\mathrm{g} \tag{25}$$

Analogous to the nomenclature used for the density, $c_p(T)$ denotes the purely temperature-dependent heat capacity at ambient pressure. This quantity is given by:

$$c_p(T) = \frac{(\rho_0\cdot\gamma_p)^2 \cdot T}{\rho^3(T)\cdot\left[\frac{1}{K_T(T)}-\frac{1}{K_S(T)}\right]} \tag{26}$$

The function $K_T(T)$ is calculated from $K_T(p,T)$ for $p_\mathrm{g} = 0$ bar. The temperature-dependent isentropic bulk modulus $K_s(T)$ is given by:

$$K_s(T) = \rho(T) \cdot a_s^2(T) \tag{27}$$

The speed of sound at ambient pressure $a_s(T)$ is modelled through a simple polynomial expression of second order:

$$a_s(T) = m_1^a + m_2^a \cdot T + m_3^a \cdot T^2 \tag{28}$$

The constants m_1^a, m_2^a and m_3^a are specific for each fluid. The general expression for the speed of sound is calculated based on the isentropic bulk modulus $K_s(p,T)$, the density $\rho(p,T)$ and the density $\rho(T)$ at zero gauge pressure:

$$a_s(p,T) = \sqrt{K_s(p,T)\frac{\rho(T)}{\rho^2(p,T)}} \tag{29}$$

Analysis of thermodynamic consistency

With knowledge of the equations presented in the previous section, all fluid properties required to analyse the thermodynamic consistency of the FLUCON model can be calculated. The examination is carried out for a transmission oil whose parameters were determined experimentally by FLUCON. In order to ensure that all equations and parameters were correctly transferred into the MATLAB evaluation routine, the computed values of the individual fluid properties were compared to a reference chart provided by FLUCON.

The thermodynamic inconsistency of the FLUCON model is quantified by rearranging equation (18) such that the left-hand side equals unity:

$$1 = \frac{K_S}{K_T}\left(1 - \frac{T\gamma_p^2}{\rho c_p} K_T\right) \tag{30}$$

Any deviation of the right-hand side from unity indicates thermodynamic inconsistency. The relative inconsistency ε can therefore be quantified by subtracting the deviant right-hand side from unity:

$$\varepsilon = 1 - \frac{K_S}{K_T}\left(1 - \frac{T\gamma_p^2}{\rho c_p} K_T\right) \tag{31}$$

A plot for the calculated relative inconsistency ε as a function of gauge pressure p_g and relative temperature T_rel is provided in **Figure 2**.

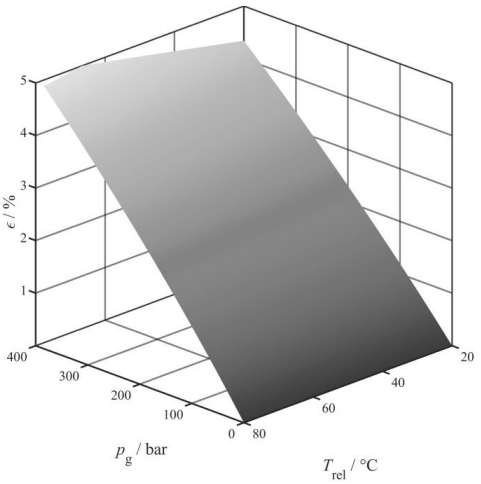

Figure 2: Thermodynamic inconsistency of the FLUCON model of a transmission oil as a function of gauge pressure and temperature.

As can be seen, the degree of inconsistency is below 5 % in the covered range of pressures and temperatures. Along the isobaric line corresponding to a gauge pressure of $p_\mathrm{g} = 0$ bar, the relative inconsistency is zero for all analysed temperatures. The inconsistency increases with the pressure level at a rate of $\Delta\varepsilon/\Delta p_g \approx 0.0125$ %/bar. This behaviour can be explained by examining the equations constituting the FLUCON model: Even though the equations relating different fluid properties with each other appear to be physically

sound, most of their statements are *not* true for pressures $p_\mathrm{g} \neq 0$ bar. An illustrative example of the described properties is given by equation (24). For zero gauge pressure, the statement of equation (24) is identical to the one of equation (17) since for $p_\mathrm{g} = 0$, $\rho(p,T) = \rho(T)$ and hence $\gamma_p = \gamma_0$. For all other pressures, this equation is invalid, since generally $\gamma_p = \gamma_p(p,T)$.

Despite these errors, the extent of thermodynamic inconsistency of the FLUCON model is more than acceptable, since the metrological limits caused by finite sensor resolutions are typically of the same order of magnitude.

3.2. Assessment of published fluid property models (II)

Another example is delivered by examining the fluid property model presented by DRUMM for consistency [4]. The model provides equations for the most important hydraulic fluid properties like density, viscosity, speed of sound and isentropic bulk modulus. An equation to estimate the mass-specific heat capacity is not provided. All fluid properties are modelled as functions of pressure and temperature.

Model equations

In order to model the dependency of the individual fluid properties on pressure and temperature, mostly polynomial expressions are used. Again, all model equations are numerical value equations, such that the relative temperature T_rel has to be provided in °C and the gauge pressure p_g must be given in bar. The model equation for the density reads:

$$\begin{aligned}\rho(p,T) = {} & m_1^\rho + m_2^\rho \cdot T_\mathrm{rel} + m_3^\rho \cdot p_\mathrm{g} \\ & + m_4^\rho \sqrt{p_\mathrm{g} + m_5^\rho} + m_6^\rho \cdot T_\mathrm{rel} \cdot p_\mathrm{g} \\ & + m_7^\rho \cdot T_\mathrm{rel}^2 \end{aligned} \tag{32}$$

The model equation for the sound speed is given by the following expression:

$$\begin{aligned}a_s(p,T) = {} & m_1^a + m_2^a \cdot T_\mathrm{rel} + m_3^a \cdot p_\mathrm{rel} \\ & + m_4^a \sqrt{p_\mathrm{g} + m_5^a} + m_6^a \cdot T_\mathrm{rel} \cdot p_\mathrm{g} \\ & + m_7^a \cdot T_\mathrm{rel}^2 \end{aligned} \tag{33}$$

Because the model presented by DRUMM does not provide a model equation for the specific heat capacity, a different approach is chosen in order to analyse its thermodynamic consistency. Since a thermal equation of state $\rho(p,T)$ as well as an equation for the speed of sound $a(p,T)$ are provided, the specific heat capacity can be calculated by rearranging equation (17):

$$c_p(p,T) = \frac{T\gamma_p^2}{\rho\left(\frac{1}{K_T} - \frac{1}{K_S}\right)} = \frac{T\left(\frac{\partial \rho}{\partial T}\right)_p^2}{\rho^2\left[\frac{1}{\left(\frac{\partial p}{\partial \rho}\right)_T} - \frac{1}{a_S^2}\right]} \tag{34}$$

This equation is actually used in scientific applications for determination of the specific heat capacity, particularly if direct calorimetric measurements are not possible because the pressure level of interest is too high [13].

If the coefficients m_i^ρ and m_i^a which DRUMM estimated for water are used to calculate values $c_p(p,T)$, the results can be compared to literature values for the specific heat capacity of water, taken e.g. from the commonly accepted IAPWS model [2]. Thus, even without knowledge of all quantities appearing in equation (17), the thermodynamic consistency of the DRUMM model can be assessed.

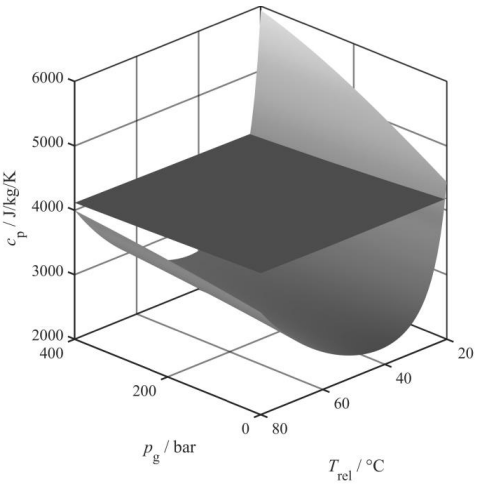

Figure 3: Calculated specific heat capacity of water as a function of pressure and temperature.

The specific heat capacity c_p which has been calculated from the model equations of DRUMM and the corresponding parameters for water is plotted as a function of the gauge pressure and relative temperature in **Figure 3** (curved surface). For comparison, the same quantity has been computed from the IAPWS model and is shown in the diagram, too (appearing as a plane) [2]. As can be seen, large differences between the DRUMM

model and the commonly accepted IAPWS dataset exist over a wide range of temperature and pressures. The maximum and minimum values of the specific heat capacities from the IAPWS model vary by less than 4 % in the analysed range, whereas the maximum c_p calculated from the DRUMM equations exceeds the minimal value by more than 150 %. The calculated values of the specific heat capacity obviously contradict published and accepted values. Clearly, even without calculating the degree of thermodynamic consistency ε, it can be concluded that the analysed fluid property model is thermodynamically inconsistent.

The main reason for the observed behaviour of the DRUMM model can be found in the structure of the model equations themselves: Since – according to equation (35) – the slope of the density function is vital for accurate determination of the specific heat capacity, the gradients $(\partial\rho/\partial T)_p$ and $(\partial\rho/\partial p)_T$ have to be known with high accuracy. Because of the polynomial approach used, the model equations of the DRUMM model cannot properly map the *curvature* of the density function, even if the values of the density function might be correct.

Thus, even if the measurements on which the published model parameters are based on were carried out with perfect accuracy, a thermodynamically fluid property model could not be created with the used model equations. Hence, it is important to choose model equations of sufficient mathematical complexity which are capable of correctly mapping the relevant features of the course of the desired property as a function of pressure and temperature.

4. SUMMARY AND OUTLOOK

The findings of the present paper can be summarised by the following statements:

- Accurate fluid properties are vital for accurate predictions of system and component performance in the field of fluid power.
- Practising engineers are faced with the problem of ascertaining the accuracy of experimentally determined fluid properties.
- An equation was derived which establishes a connection between the most important fluid properties density, bulk modulus, thermal expansion coefficient and specific heat at constant pressure.
- Based on this identity, the thermodynamic consistency of experimentally determined fluid properties presented in the form of a fluid property model can be assessed. The more the data violates the equation, the higher the degree of thermodynamic inconsistency.
- Thermodynamic inconsistency should be below 5 % to ensure accurate prediction of component or system behaviour.
- Thermodynamically inconsistent fluid properties should, if at all, be used very carefully because of the dangers outlined in the examples of chapter 1.
- The commonly encountered, purely *mechanical* definition of the bulk modulus – like equation (2) – does not suffice to uniquely explicate which quantity is referred to. Depending on the thermodynamic boundary conditions during compression or expansion, the observed bulk modulus may vary significantly.
- The highest bulk modulus is encountered for an isentropic process, whereas the lowest bulk modulus is observed if the fluid's density change happens at constant temperature, i.e. if the process is isothermal.

NOMENCLATURE

γ_p	Isobaric thermal expansion coefficient	K^{-1}
ε	Degree of thermodyn. inconsistency	%
η	Dynamic viscosity	Pa·s
κ	Ratio of specific heats	1
μ_{JT}	Joule-Thomson coefficient	1
ρ	Density	$kg·m^{-3}$
a_s	Speed of sound	$m·s^{-1}$
A	Cross-sectional area	m^2
c_p	Specific heat at constant pressure	$J·kg^{-1}·K^{-1}$
c_v	Specific heat at constant volume	$J·kg^{-1}·K^{-1}$
$f(x)$	Arbitrary function of x	
h	Specific enthalpy	$J·kg^{-1}$
i	Integer number	1
k	Isentropic exponent	1
K	Bulk modulus, not specified further	Pa
K_s	Isentropic bulk modulus	Pa
K_T	Isothermal bulk modulus	Pa
L	Length	m
$\ln(x)$	Natural logarithm of x	1
m_i^x	ith constant of the state equation for x	
n	Polytropic exponent	1
p	Pressure	Pa
p_g	Gauge pressure	bar
Δp	Pressure drop	Pa
s	Specific entropy	$J·kg^{-1}$

T	Temperature	K
T_{rel}	Relative temperature	°C
v	Specific volume	$m^3 \cdot kg^{-1}$
V	Volume	m^3
$\mathrm{d}f/\mathrm{d}x$	Total derivative of f with respect to x	
$\partial f/\partial x$	Partial derivative of f with respect to x	

REFERENCES

[1] BAEHR HD, KABELAC S (2016) Thermodynamik. 16th edn. Springer Vieweg, Berlin Heidelberg

[2] IAPWS (2020) Revised Release on the IAPWS Formulation 1995 for the Thermodynamic Properties of Ordinary Water Substance for General and Scientific Use – September 2018. http://www.iapws.org/relguide/IAPWS-95.html. Accessed 20th January 2020

[3] WITT K (1974) Die Berechnung physikalischer und thermodynamischer Kennwerte von Druckflüssigkeiten, sowie die Bestimmung des Gesamtwirkungsgrades an Pumpen unter Berücksichtigung der Thermodynamik für die Druckflüssigkeit. PhD thesis, TU Eindhoven, Netherlands

[4] DRUMM SB (2012) Entwicklung von Messmethoden hydraulischer Kraftstoffeigenschaften unter Hochdruck. PhD thesis, RWTH Aachen, Germany

[5] TLK-THERMO GmbH (2020) TILMedia Suite – Softwarepaket zur Bereitstellung thermophysikalischer Stoffeigenschaften. https://www.tlk-thermo.com/index.php/de/software/tilmedia-suite. Accessed 20th January 2020

[6] WILL D, GEBHARDT N (2014) Hydraulik – Grundlagen, Komponenten, Systeme. 6th edn. Springer Vieweg, Berlin Heidelberg

[7] BAUER G (2016) Ölhydraulik – Grundlagen, Bauelemente, Anwendungen. 11th edn. Springer Vieweg, Wiesbaden

[8] WATTER H (2017) Hydraulik und Pneumatik – Grundlagen und Übungen – Anwendungen und Simulation. 5th edn. Springer Vieweg, Wiesbaden

[9] BOŠNJAKOVIĆ F, KNOCHE KF (1998) Technische Thermodynamik Teil 1. 8th, corrected edn. Steinkopff-Verlag, Heidelberg

[10] LAPLACE PS (1816) Sur la vitesse du son dans l'air et dans l'eau. Annales de chimie et de physique, t. III:297–300

[11] NEWTON I (1687) Philosophiæ naturalis principia mathematica (Mathematical principles of natural philosophy). London

[12] FLUCON FLUID CONTROL GmbH (2020) Stoffanalyse von Fluiden. https://flucon.de/dienstleistungen/stoffanalyse-von-fluiden/. Accessed 20th January 2020

[13] GUILANO ALBO PA, LAGO S, WOLF H et al. (2017) Density, viscosity and specific heat capacity of diesel blends with rapeseed and soybean oil methyl ester. Biomass and Bioenergy, 96:87-95

peer reviewed

FLUID-THERMAL CO-SIMULATION FOR A HIGH PERFORMANCE CONCRETE MACHINE FRAME

Christoph Steiert[1]*, Juliane Weber[1], Alexander Galant[2], Janine Glänzel[3], Jürgen Weber[1]

1 Institute of Mechatronic Engineering, Chair of Fluid-Mechatronic Systems, Technische Universität Dresden, Helmholtzstrasse 7a, 01069 Dresden
2 Institute of Mechatronic Engineering, Chair of Machine Tools Development and Adaptive Controls, Technische Universität Dresden
3 Fraunhofer Institute for Machine Tools and Forming Technology IWU
* Corresponding author: Tel.: +49 351 46333989; E-mail address: christoph.steiert@tu-dresden.de

ABSTRACT

Thermo-elastic errors are one of the main drivers for reduced quality of workpieces in machining. Cooling systems can prevent these errors and improve quality. The paper describes a simulation method that takes into account both the temperature field of a machine tool frame and the fluid cooling system. Such simulations can help to improve the thermal stability of the machine tool frame.

Keywords: thermal simulation, model order reduction, cooling system, modeling

1. INTRODUCTION

The thermo-energetic behaviour of machine tools has recently become more and more important. A main driver for this development is to improve the workpiece quality and the energy efficiency of the machine. Power losses that occur during production induce heat in the machine tool and lead to temperature gradients within the structure. These temperature gradients are one reason for a tool centre point (TCP) displacement, which leads to a loss of quality in manufacturing. For this reason, power losses should be reduced and, if this is not affordable, the thermal state of the machine tool has to be stabilised. Fluidic cooling systems offer a good mechanism to do this by transporting heat from the critical workspace.

This paper presents a simulation method for investigating the thermal behaviour of a machine tool frame. The simulation consists of two parts. First, a fast calculating thermal finite element method (FEM) simulation of the machine tool frame and second, a network-based simulation of the fluid cooling system.

2. STATE OF THE ART

In recent years there were projects investigating the thermo-energetic behavior of machine tools [1–3]. The improvement of quality and productivity of machine tools and the reduction of energy consumption motivated these projects. For example, 75 % of the overall geometrical errors of workpieces are induced by the effects of varying temperatures in the machine tool [4]. Cooling mechanisms should transport heat from the machine tools. For this purpose, water or water-glycol mixtures are often used as cooling medium, as these have a higher relative heat capacity in comparison to air. The efficiency of fluid system components such as compressors, pumps, electric drives improved in the past as well as control strategies. Now the cooling unit often works in switching mode, so that no energy is needed in idle phases, but it was shown in [5] that this behavior, together with the use of constant drive pumps, has a negative influence on the temperature field in the machine tool. For better thermal stability in connection with an energetically better behavior, it is recommended to use variable speed drive pumps or control valves [6]. With these tools a demand-oriented cooling strategy is feasible.

Simulations are able to predict the thermal behavior of machine tools. For such simulations FEM is chosen. The models are quite complex and need computational effort if high accuracy is required. For analysis and controller design a long computing time is not acceptable. A solution for this problem are model order reduction

(MOR) methods based on Krylov subspace methods [7]. This method is used successfully in [8].

The research presented in this paper takes up the aspects described and applies them to the research object machine tool frame. In the view of the authors, the implementation of a coupled finite element (FE) model of a machine frame with a network-based model of a fluid system delivers new aspects to improve the thermal behavior of machine tool frames.

3. TEST RIG

The test rig consists of two subsystems: the solid machine tool frame and the fluidic cooling system. Hoses connect both subsystems.

3.1. Machine tool frame

The machine tool frame has a base area of 3.0 x 4.0 m and a height of 1.6 m. It is made of a high performance concrete (HPC) for better thermal properties and has a weight of 18.0 t. On top of the U-shaped machine frame, a parallel kinematic machine tool can be placed. The research presented in this paper is done without this parallel kinematic in order to focus specifically on the tempering of the HPC machine tool frame by means of the integrated six cooling channels. Their piping is made from steel. The cooling channels are located where the highest heat input from the process and the periphery is assumed. In **Figure 1** these locations are shown. They are under the linear guiding system on each side F1 and F2, the chip collectors S1 and S2 and in the mounting flanges of the two drives M1 and M2. The measuring of the temperature field inside of the HPC machine tool frame occurs with the help of 23 temperature sensors. **Figure 2** shows the position of the sensors and their labels. The sensors are mapped to different regions of the machine tool frame, according to **Table 1**.

Beside the temperature sensors inside the machine tool frame one has also temperature sensors on the edge of the machine tool frame and in the environment to get the temperature in different heights.

3.2. Fluidic tempering system

For tempering the machine tool frame a fluidic system is used, which consists of actors, sensors and connecting elements.

As actuators suit a fluid-air cooling system (FLKS), valves and a pool heater. The elements of the FLKS are a tank, a pump and a fluid-air heat exchanger. The tank is a reservoir for the cooling medium with a capacity of 31.0 - 41.0 l.

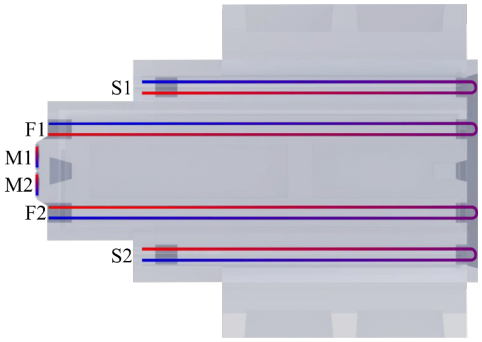

Figure 1: Machine tool frame with cooling channels, top view

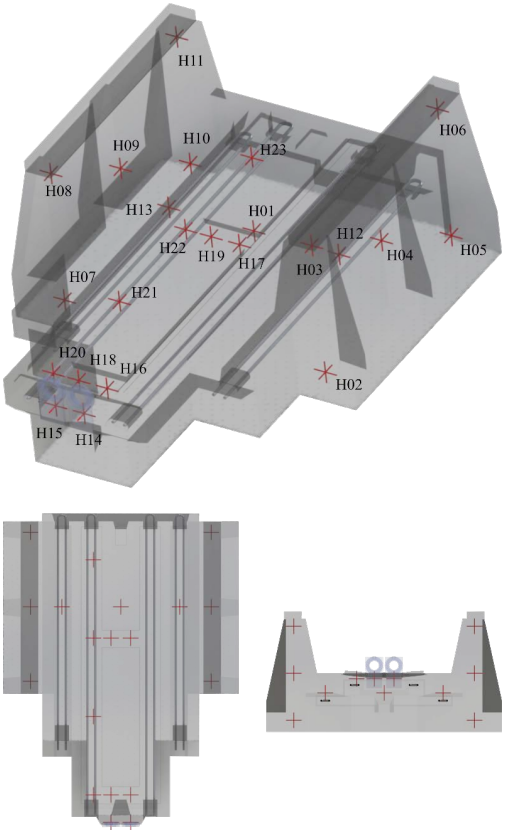

Figure 2: Machine frame with temperature sensors

Table 1: Sensor mapping

Region	Sensors
core	H01, H18, H19
left side	H02 – H06
right side	H07 – H11
left chip collector	H12
right chip collector	H13
left drive	H14
right drive	H15
left linear guidance	H16, H17
right linear guidance	H20 – H23

The pump is a centrifugal pump that delivers a volume flow rate $\dot{V}$ of 55.0 l/min at 2.8 bar. A constant speed drive unit powers the pump, so that there is no possibility to manipulate the amount of volume flow with the pump. The last component of the FLKS is the fluid/air heat exchanger with an integrated temperature control. With this control, one has the possibility to set the fan speed and to maintain a constant fluid temperature or the fluid temperature follows the ambient temperature with a desired offset ΔT of e. g. 5.0 K. In the use cases presented in section 5, the fan is not active.

The distribution of the correct amount of volume flow $\dot{V}$ is the task of six 3/2 proportional directional control valves. The valves themselves are controlled by a 0.0…10.0 V signal. A PI-controller sets the input signal for each valve. The volume flow not required is returned to the tank via a bypass pipe.

For tempering the volume flow a 3.0 kW pool heater is used. The pool heater enables the user to set a desired temperature. It operates as a switching two-point control with a peak-to-peak value of 3.0 K. The used cooling medium is water. The test cycles presented in section 5 are designed to heat the machine tool frame and not to cool it. This is done to bring more heat in the machine frame, by having larger temperature gradients between the fluid and the solid of the machine frame. This inverse procedure is sufficient in particular for the validation of the simulation model (from section 4) with regard to the temporal and local temperature behavior. In addition, the uncertainties when installing external heat sources and determining their heat input into the frame structure can be reduced.

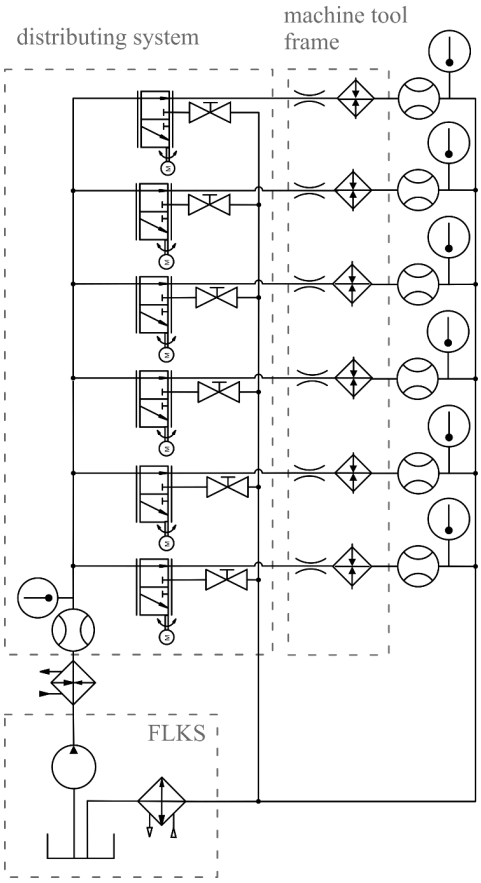

Figure 3: Schematic representation of the test rig

The sensors applied in the fluid system combine volume flow and temperature sensors. The volume flow sensors are based on the vortex principle [9]. One sensor is located in the common inlet and measures the total volume flow and additionally, each cooling circuit has one in the outlet for measuring the volume flow of each circuit. **Figure 3** shows a block diagram of the test rig including the cooling system and the machine tool frame.

4. SIMULATION MODEL

The simulation model consists of two subsystems. The first is a network-based model of the cooling system. This model is a fast computable model, which is able to consider the fluid domain as well as the thermal domain. The second subsystem is a thermal FE simulation of the machine tool frame. To get a fast computable

model one can use a MOR method. The MOR enables the user to obtain results within minutes instead of hours. The coupling between both systems is the wall temperature of the cooling channels inside the machine frame and the heat flux flowing through these walls. The cooling channels S1, S2, F1, and F2 are separated into 19 segments for spatial discretisation. The cooling channels M1 and M2 are so short that no discretisation is required. Overall, there are 78 segments for coupling.

4.1. Network-based model of the cooling system

The fluid circuit is simulated as a thermo-hydraulic network-based model with lumped parameters. The elements of the simulation model are e.g.:

- centrifugal pump for volume flow supply,
- volume elements with thermal and hydraulic ports,
- hydraulic resistances,
- variable throttle valves for setting the volume flow rate in each circuit and
- cooling pipes with heat exchange at the wall.

The centrifugal pump has a volume flow-pressure characteristic stored and operates at a constant speed. The volume flow depends only on the pressure drop of the system. After the pump, a volume is placed. On its thermal port, heat is introduced into the system. This volume represents the pool heater. The amount of heat is temperature dependent. The control element is a two point controller with a hysteresis of 3.0 K. The low level is 0 W and the high level is 3000 W. There are seven branches after the heat input, the six cooling channels S1, S2, F1, F2, M1, and M2 as well as a bypass branch. The bypass has a constant flow resistance and leads back to the tank. An independently controlled variable throttle valve is placed at the beginning of each cooling channel. These valves regulate the flow resistance and determine the volume flow through each branch. Some additional hydraulic resistances and volumes represent the connecting hoses and fittings in the system. The cooling channels inside the machine tool frame are the key elements for heat exchange. A combination of hydraulic resistances and volumes with thermal ports is suitable for this purpose. The heat flow density $\dot{q}$, which is transferred from the fluid system to the machine frame, is calculated from the heat transfer coefficient (HTC) α and the temperature difference between the fluid temperature T_F and the wall temperature T_W:

$$\dot{q} = \alpha \cdot (T_\mathrm{F} - T_\mathrm{W}). \tag{1}$$

The heat flow $\dot{Q}$ is calculated as follows:

$$\dot{Q} = \dot{q} \cdot A, \tag{2}$$

with the surface A of the pipe segment. The HTCs are calculated in an a priori simulation and are parameters for the network-based model [10]. The FE machine frame model calculates the wall temperatures and the network-based model of the fluid system calculates the fluid temperatures itself.

4.2. Modelling of the machine tool frame

There are two models with distributed parameters for simulating the machine frame. First, a CFD model (computational fluid dynamics), which numerically calculates the temperature field and the HTCs of forced convection in the cooling channel within a conjugate heat transfer (CHT) simulation. Secondly, in the FE model, the temperature field of the machine frame can be calculated in simplified form using the parameters determined in the CFD. Both models are based on the computer aided design (CAD) model including the HPC machine frame and the integrated cooling pipes made of steel. The HTCs from the CFD simulation are also used in the network-based model of the cooling system, e. g equation (1). They are calculated for a steady-state operating point. The authors know the dependency of the HTC on many variables, such as flow condition, temperature difference or the condition of the pipe surface. For the following investigations, they are initially assumed as constants. The reason for only using one steady state operating point is the high computational effort required by the CFD. To take the different workloads and environmental conditions into account, the surface of the machine tool, including the cooling pipes, is separated in different areas. Some of them perceive heat flows, the so-called Neumann boundary condition. For example, the 78 segments in which the cooling channels are separated and areas for working loads like power losses of drives and bearings. The second kind of boundary conditions are the Robin boundary conditions. For the environmental temperature load, three

zones are defined. One zone is on the ground, which is the coldest point in most cases. The next one covers the lower part of the machine tool and the third zone is the top part. This separation is used due to the different air layers covering the machine tool frame. In order to reduce the computational effort and the time needed for the simulation, a MOR is performed on the FE model. The MOR is based on Krylov subspace methods. A description of the method can be found in [11].

It is possible to represent the thermal FE model as a multiple input multiple output (MIMO) state space model:

$$\begin{aligned} \dot{T} + A \cdot T &= B \cdot u \\ y &= C^{\mathrm{T}} \cdot T. \end{aligned} \tag{3}$$

The state is the temperature T with its derivative $\dot{T}$. The input of the system is a vector u. This can be the ambient temperature or other loads on the machine frame. The system output y returns the temperature at specified points of interest. A, B and C are matrices that describe the system with its inner interrelation as well as the in- and output behavior of the system. Physically, A has elements describing conductivity and heat capacity. B selects the nodes affected by thermal loads. Similar to B, matrix C selects the output nodes. The dimension of A in particular is very high, which explains the computational effort of the FE simulation. In the presented case, the degree of freedom (DoF) is 90 854. The size of matrix A is 90 854 × 90 854. The reduced system looks structurally similar to the one in equation (3). It is given with

$$\begin{aligned} \hat{\dot{T}} + \hat{A} \cdot \hat{T} &= \hat{B} \cdot u \\ y &= \hat{C}^{\mathrm{T}} \cdot \hat{T}. \end{aligned} \tag{4}$$

The reduction is a projection into a Krylov subspace with a desired order. The projection rule is:

$$\begin{aligned} \hat{A} &= V^{\mathrm{T}} \cdot A \cdot V \\ \hat{B} &= V^{\mathrm{T}} \cdot B \\ \hat{C} &= V^{\mathrm{T}} \cdot C \\ T &= V \cdot \hat{T}. \end{aligned} \tag{5}$$

The projection matrix V is obtained with an Arnoldi algorithm [12, 13].

4.3. Coupling of subsystems

There are different types of software used. The meshing of the CFD and FE model is done in the ANSYS Workbench. An export of the mesh file

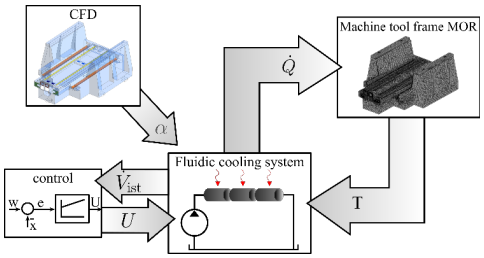

Figure 4: Coupling of the simulation subsystems

of the machine frame transfers data to MatLab, where one can perform the MOR. The software tool for implementing the network-based model of the cooling system is SimulationX. A C-code export gives offers the possibility to use the cooling system model in MatLab. With both subsystems, available in one software tool, the coupling is possible.

The coupling between the machine frame model and the model of the cooling system is done by exchanging thermal variables. The workflow is show in **Figure 4**. The heat flow density $\dot{q}$ is an output of the fluidic cooling system and input of the machine tool frame. In the other direction, the machine tool frames output is the pipe wall temperature T, which is an input for the fluid system. An external PI controller for each cooling channel enables the user to set a volume flow rate $\dot{V}$ for each channel.

5. RESULTS

To validate the coupled simulation model, five test cycles are used. The test cycles vary in the number of flooded cooling channels and the amount of volume flow through each circle. The settings for each test cycle are listed in **Table 2.** In test cases A and C, the machine tool frame is tempered symmetrically, whereas in the test cases B, D, and E an asymmetrical load is applied. Loads other than fluid and ambient temperature

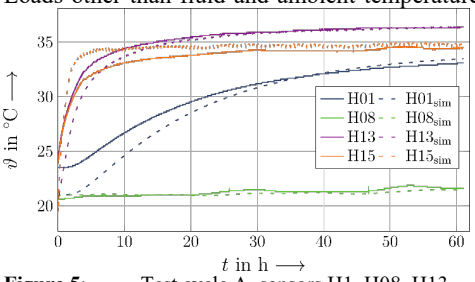

Figure 5: Test cycle A, sensors H1, H08, H13, H15, measurement and simulation

Table 2 Test cycles

Name	Fluid temperature ϑ in °C	Volume flow $\dot{V}$ in l · min^{-1}	Cooling channel					
			S1	F1	M1	M2	F2	S2
A	41.6 - 44.1	4	x	x	x	x	x	x
B	41.4 - 44.5	4	x	x	x			
C	40.5 - 42.9	8	x	x	x	x	x	x
D	41.4 - 44.0	8	x	x	x			
E	43.0 - 45.7	15	x	x				

are not applied. For this reason, the cooling system works as a heater instead of a cooler. There was no possibility for installing heating pads or the like to emulate thermal loads properly. This is sufficient for validating the simulation. Each test cycle lasts almost three days. During this time, the temperature sensors in the machine frame and the sensors of the fluid system are recorded. **Figure 5** shows the temperature chart for selected sensors for test cycle A. You can see that at sensor H08 that is located in the right side of the machine frame, far away from the fluid channels, only the ambient temperature has an influence. Here the temperature drift over three days is visible. A sensor near to the surface of the machine frame and near to a fluid channel is sensor H15. It is situated at channel M2, the motor cooling at the front of the machine frame. The ambient temperature and the fluid influence this sensor. It shows a rising of the temperature up to almost 35 °C with additional temperature fluctuations. Sensor H13 is close to the fluid pipe S2 and lies inside the machine frame. The ambient temperature has very little influence so the measured temperature rises more than the temperature at sensor H15. The last sensor shown in is sensor H01 located in the core of the machine frame. The heating through the fluid pipes only influences this sensor. Because of the distance between the sensor and the fluid channels the temperature rises not as strong as at sensors H13 and H15 that are nearer to the fluid pipes. After 62 hours you see that the machine frame is not in a thermal steady state. The temperature at sensor H01 rises slightly after this time. This shows the high thermal inertia of the machine frame.

At the beginning of the observed period, there is a difference between simulation and measurement. The simulation starts with a constant temperature for the entire solid frame. In Figure 5 you can see that the machine frame has different temperatures at the beginning of the measurement. Simulation and measurement get close at the end of the simulation.

Figure 6 shows the absolute error at the end of the simulation for the available sensors. A comparison of the different test cycles shows that the error behaviour of the five test cycles is similar. This discrepancy is due to different reasons. In the machine frame, reinforcing steel is installed from which the amount and position are not exactly known. The influence of the reinforcing steel is investigated in [14]. Therefore, there are unknown heat bridges in the machine frame that are not in the scope of the simulation. Another reason for the temperature

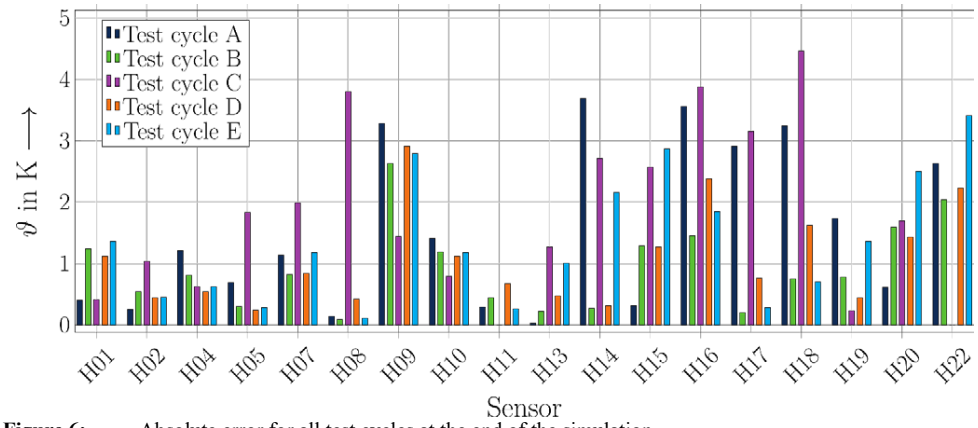

Figure 6: Absolute error for all test cycles at the end of the simulation

difference is the constant starting temperature of the simulation.

6. CONCLUSION AND OUTLOOK

This paper presented a method for modelling a fast calculating thermal fluid co-simulation of a machine tool frame. The cooling system is modelled with lumped parameter methods and the machine frame is simulated with FE methods improved by MOR. The validation with six test cycles showed a good consistency between the measurements on the test rig and the simulation results.

Further investigation concerns an optimised machine tool frame with seven cooling channels. Four of these channels are placed in the sides of the U-shaped frame, two for the chip conveyer and one spreads through the floor area. Furthermore, the cooling system has to be adapted. Small centrifugal pumps are used for each channel to improve the controllability of the volume flow. Additionally, the number of cooling circuits is fitted to the number of channels in the machine frame. These measures are intended to improve the thermal stability of the machine tool frame in terms of time and location.

NOMENCLATURE

A	Area	m^2
A	System matrix	div.
B	Input matrix	div.
C	Output matrix	div.
$\dot{Q}$	Heat flow	W
T	Temperature	K
V	Projection matrix	-
$\dot{V}$	Volume flow	$\mathrm{m}^3 \cdot \mathrm{s}^{-1}$
$\dot{q}$	Heat flow density	$\mathrm{W} \cdot \mathrm{m}^{-2}$
u	Input state space model	div.
y	Output state space model	div.
α	Heat transfer coefficient	$\mathrm{W} \cdot \mathrm{m}^{-2} \cdot \mathrm{K}^{-1}$
ϑ	Temperature	K, °C
CAD	Computer aided design	
CFD	Computational fluid dynamics	
CHT	Conjugate heat transfer	
DoF	Degree of Freedom	
FE	Finite element	
FEM	Finite element method	
FLKS	fluid/air cooling system	
HPC	High performance concrete	
HTC	Heat transfer coefficient	
MIMO	Multiple input multiple output	
MOR	model order reduction	
TCP	tool centre point	

ACKNOWLEDGEMENT

The presented research activities are part of the transfer project T02 “Robust and thermo-energetically optimal tempering of machine tool frames with fluidic tempering systems funded by the German Research Foundation – Project-ID 174223256 – TRR 96.

The authors would like to thank the German Research Foundation (DFG) and all project partners including HYDAC Cooling GmbH, FRAMAG Industrieanlagenbau GmbH and METROM Mechatronische Werkzeugmaschinen GmbH for the financial support.

DFG Deutsche Forschungsgemeinschaft
German Research Foundation

REFERENCES

[1] Brecher C (ed.) (2012) Effizienzsteigerung von Werkzeugmaschinen durch Optimierung der Technologien zum Komponentenbetrieb - EWOTeK, 1. Aufl. Apprimus, Aachen

[2] Denkena B (2015) Leanergie: Lebenszyklusorientierte Lösungen und Dienstleistungen für Gestaltung und Betrieb energieeffizienter Werkzeugmaschinen : Abschlussbericht Leibniz Universität Hannover, Institut für Fertigungstechnik und Werkzeugmaschinen

[3] Denkena B, Garber T (eds) (2013) NC Plus: Prozess- und wertschöpfungsorientiert gesteuerte Werkzeugmaschine ; Abschlussbericht. Berichte aus dem IFW. PZH-Verl., Garbsen

[4] Mayr J, Jedrzejewski J, Uhlmann E et al. (2012) Thermal issues in machine tools. CIRP Annals 61(2): 771–791.

[5] Shabi L, Weber J, Weber J (2018) Simulative Study of Different Control Concepts of Cooling System for Machine Tools. MATEC Web Conf.

[6] Shabi L, Weber J, Weber J (2016) Investigation of fluidic systems in machine tools. International Conference on Hydraulics and Pneumatics - HERVEX

[7] Lohmann B, Salimbahrami B (2004) Ordnungsreduktion mittels Krylov-Unterraummethoden (Order Reduction using Krylov Subspace Methods). at - Automatisierungstechnik 52(1-2004): 30–38.

[8] Beitelschmidt M, Galant A, Großmann K et al. (2015) Innovative Simulation Technology for Real-Time Calculation of the Thermo-Elastic Behaviour of Machine Tools in Motion. AMM 794: 363–370.

[9] Richardson DA, Robinson RJ (1974) Vortex flow meter transmitter including piezo-electric sensors (US3948098A)

[10] Weber J, Glänzel J, Popken J et al. (2019) Combined and fast computable thermal models for situationally optimal tempering of machine tool components. Procedia CIRP 79: 608–613.

[11] Galant A, Beitelschmidt M, Großmann K (2016) Fast High-Resolution FE-based Simulation of Thermo-Elastic Behaviour of Machine Tool Structures. Procedia CIRP 46: 627–630.

[12] Arnoldi WE (1951) The principle of minimized iterations in the solution of the matrix eigenvalue problem. Quart. Appl. Math. 9(1): 17–29.

[13] Salimbahrami B, Lohmann B (2002) Krylov subspace methods in linear model order reduchtion: Introduction and invariance properties

[14] Glänzel J, Geist A, Ihlenfeldt S (2019) Simulation-based investigation for heat transfer behavior of steel reinforcements in concrete machine frames and their thermal effects. Journal of Machine Engineering Vol. 19 No 3 17-30

THE APPLICABILITY OF THE MASS-FLOW-MODEL ACCORDING TO ISO 6358 WITH THE PARAMETER CRITICAL CONDUCTANCE C AND CRITICAL PRESSURE RATIO B FOR GASES IN HIGH-PRESSURE RANGE UP TO 300 BAR

Lucian Pasieka*

Eugen Seitz AG, Spitalstrasse 204, 8623 Wetzikon, Switzerland
*Corresponding author: Tel.: +41 44 931 81 18; E-mail address: lpasieka@seitz.ch

ABSTRACT

Mass flow models for gaseous media describe the relationship between gas flow through throttle elements depending on pressure, temperature and type of medium. These models are used to calculate pneumatic components, to simulate pneumatic systems or to plan facilities. The known flow models are verified for ideal gases, such those as according to ISO 6358-1 (International Standard ISO 6358-1: pneumatic fluid power – Determination of flow-rate characteristics of components using compressible fluids: General rules and test methods for steady-state flow, 2013). But they fail with real gases, especially at higher pressures. The objective of this contribution is to recommend a simple-to-use model for the mass flow calculation of real gases. The advantage of the C and b model is the use of only two parameters. A testbench for high pressure up to 300 bar was used for model verification with air and hydrogen. The Library for standard dry air and hydrogen up to 1000 bar was used for the state variables of the real gases. The parameters C and b are obtained, applied and verified in the state space of real gas. With the C and b parameter it is possible to simulate not only the single component (valve, throttle, nozzle and so on) but also the whole system with a complete system simulation, like such as hydrogen filling stations.

Keywords: mass flow model, real gas

1. INTRODUCTION

In the planning of facilities for gases the components such as valves and throttle valves must be considered as flow resistances. With a view to a system simulation, it is desirable to have the mass flow characteristics of all individual components to know the states and the operating behaviour of the entire system in a system simulation for the purpose of calculation. In the development of components, the goal is to identify the mass flow characteristic of the component concerned to make the selection easier for the user. In the 90s different methods of measurements have been compared in relation to their suitability for the simulation of pneumatic systems [2].

The proposed standard ISO 6358 "Pneumatic fluid power - Components using compressible fluids - Determination of flow-rate characteristics (1989)" [3] has become proved useful and a recognized standard in practice. This first edition of ISO 6358-1 (2013) [12], cancels and replaces ISO 6358:1989, which has been technically revised. This standard defines a method for measurement and the determination of fluid power parameters for components of pneumatics, such as valves. With the aid of the parameters, the mass flow in the stationary state for any pressure ratio under the assumption of the ideal gases are calculated. We use the alternative test method ISO 6358-1, Annex A, page 20. This method complies with ISO 6358 (1989) with the addition of using stagnation pressure instead of static pressure.

The advantage of the mass flow model according to ISO 6358-1 lies in the ease of handling, since only two parameters C and b are needed. Series and parallel circuits of components can be calculated, see [8]. All losses that occur as a pressure drop across a component are recorded using the two parameters. At this point, the question arises: what are the special features of mass flow in the high-pressure range?

For example, the design of safety valves in the high-pressure range based on models used up to 3000 bar according to [1] equations for ideal gases. Schmidt et al. [10] shows that there is no suitable mass flow model that can be used in the real gas range.

In ISO 6358-1 there are no application limits for the pressure range specified. The mass flow model is based on the assumptions of the ideal gas and, therefore, has been validated at low pressure applications up to 16 bar. The purpose of this study is to evaluate the proposed mass flow model of ISO 6358-1 in real gas applications and to verify the model based on measurements up to 300bar. Attention is focused on the non-linear flow characteristics in the subcritical flow range, due larger deviations in this range compared to the use of the model simplification.

2. BASICS OF THE MASS FLOW MODEL

The basis for the mass flow model is the stationary flow through a nozzle with the following assumptions:

- frictionless and adiabatic flow (= isentropic)
- nozzle with rounded contour
- no technical work is done and
- the potential energy of the gas can be neglected, see **Fig. 1**

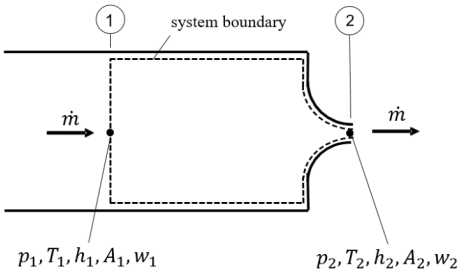

Figure 1: Schematic representation of the system boundary of a throttle element for the derivation of the mass flow equation as well as the specific heat capacities

With the help of the first law for stationary flow processes

$$h_1 + \frac{w_1^2}{2} = h_2 + \frac{w_2^2}{2} \qquad (1)$$

With the assumption of a large volume in front of the narrowest cross-section, it can be assumed that $w_1 \approx 0$. Consequently

$$\frac{w_2^2}{2} = h_1 - h_2 = c_p(T_1 - T_2) \qquad (2)$$

With the ideal gas law

$$T_1 = \frac{p_1}{R \cdot \rho_1} \qquad (3)$$

$$c_p - c_v = R \qquad (4)$$

$$\frac{c_p}{c_v} = \kappa \qquad (5)$$

$$\frac{c_p}{R} = \frac{\kappa}{\kappa - 1} \qquad (6)$$

and the equation for an isentropic state change

$$\frac{T_2}{T_1} = \left(\frac{p_2}{p_1}\right)^{\frac{\kappa-1}{\kappa}} \qquad (7)$$

follows

$$w_2 = \sqrt{2\frac{\kappa}{\kappa-1}\frac{p_1}{\rho_1}\left[1 - \left(\frac{p_2}{p_1}\right)^{\frac{\kappa-1}{\kappa}}\right]} \qquad (8)$$

By using the continuity equation

$$\dot{m} = w_2 A_2 \rho_2 \qquad (9)$$

$$\frac{\rho_2}{\rho_1} = \left(\frac{p_2}{p_1}\right)^{\frac{1}{\kappa}} \qquad (10)$$

one obtains (11) for the calculation of the mass flow [8]

$$\dot{m} = A_2\sqrt{2\,p_1\rho_1}\sqrt{\frac{\kappa}{\kappa-1}\left[\left(\frac{p_2}{p_1}\right)^{\frac{2}{\kappa}} - \left(\frac{p_2}{p_1}\right)^{\frac{\kappa+1}{\kappa}}\right]} \qquad (11)$$

The assumptions don't include flow-reducing effects, so it's necessary to introduce two geometry-dependent effects of beam constriction and fluid friction are introduced, see (12). The jet entanglement is the reason that due to the inertia and the nozzle contour not the entire geometric flow area is available for the flowing fluid. This is done with the beam constriction number α, which is always less than 1 (α < 1). The fluid friction leads to flow losses. The so-called speed digit φ is considered to be 0 <φ <1. This results in the following mass flow equation

$$\dot{m} = \alpha\,\varphi\,A_2\,\Psi\sqrt{2\,p_1\,\rho_1}\,. \qquad (12)$$

The right root expression in (11) describes the outflow function Ψ, see Fig. 2

$$\Psi = \sqrt{\frac{\kappa}{\kappa-1}\left[\left(\frac{p_2}{p_1}\right)^{\frac{2}{\kappa}} - \left(\frac{p_2}{p_1}\right)^{\frac{\kappa+1}{\kappa}}\right]} \qquad (13)$$

The flow function Ψ has a maximum that characterizes the transition between the supercritical and subcritical flow range. The pressure ratio at which the maximum occurs, is called critical pressure ratio b because there is speed of sound in the most-narrow cross-section. It results from building the 1st derivative of the outflow function with the respect to the pressure ratio.

$$\frac{d\Psi}{d\left(\frac{p_2}{p_1}\right)} = \Psi' = 0 \qquad (14)$$

$$\boldsymbol{\Psi' = \frac{0.5\kappa\left(\frac{2}{\varepsilon^{\frac{\kappa}{\kappa}}-1} - \frac{(\kappa+1)\varepsilon^{\frac{\kappa+1}{\kappa}-1}}{\kappa}\right)}{(\kappa-1)\left(\frac{\kappa\left(\frac{2}{\varepsilon^{\frac{\kappa}{\kappa}}-\varepsilon^{\frac{\kappa+1}{\kappa}}}\right)}{\kappa-1}\right)^{0.5}} = 0} \qquad (15)$$

with $\boldsymbol{\frac{p_2}{p_1} = \varepsilon}$

According to equation (15), the derivation can be reduced to the internal function. This means

$$0 = \frac{2}{\kappa}(\varepsilon)^{\frac{2-\kappa}{\kappa}} - \frac{\kappa+1}{\kappa}(\varepsilon)^{\frac{1}{\kappa}} \qquad (16)$$

$$\frac{2}{\kappa+1} = (\varepsilon)^{\frac{\kappa-1}{\kappa}} \qquad (17)$$

$$b = \left(\frac{p_2}{p_1}\right)_{crit} = \left(\frac{2}{\kappa+1}\right)^{\frac{\kappa}{\kappa-1}} \qquad (18)$$

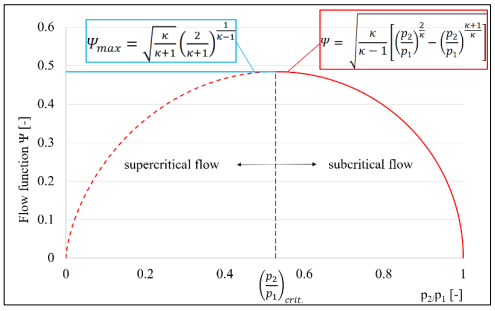

Figure 2: Flow function Ψ via the pressure ratio p_2/p_1

The maximum of the discharge function Ψ_{max} is obtained by using the critical pressure ratio b (18) in the discharge function (13).

$$\boldsymbol{\Psi_{max} = \sqrt{\frac{\kappa}{\kappa+1}}\left(\frac{2}{\kappa+1}\right)^{\frac{1}{\kappa-1}}} \qquad (19)$$

The fact that Ψ_{max} is a high point can be shown by forming the 2nd derivative starting from (15) and using the critical pressure ratio b from (18).

After evaluating it can be shown that $\kappa > 1$ applies to all: $\Psi'' < 0$ i.e. it is a maximum, see [11].

With the view to the mass flow model for ideal gases, (12), the outflow function Ψ is divided into two areas. In the subcritical area, the outflow function is (13), see Fig. 2. At the critical pressure ratio b the medium flows at the speed of sound through the nozzle. If the pressure ratio is reduced $p_2/p_1 < b$ (by reducing the outlet pressure p_2) the flow velocity does not increase any further, as this is limited by the speed of sound. As a result, the mass flow stagnates in the supercritical range at its maximum value, see blue line in Fig. 2. is used in the calculation of the mass flow through the maximum considered outflow Ψ_{max} (12).

With the generally valid mass flow equation (12) the mass flow thought throttle elements can be described analytically. The disadvantage of equation (12) is that the individual coefficients can be determined only with great effort. That's why there were different proposals, the generally valid mass flow equation with an approximation function that can be described by a few measurable parameters. Advantageous in this procedure is that the critical pressure ratio b is not a constant value (18) but assumes values as they occur in practice. The critical pressure ratio depends both on the medium and the flow-reducing effects and generally ranges between 0,2 … 0,54. According to a proposal by Sanville [9], the outflow function Ψ (13), can be described using an elliptical approximation (20).

$$\boldsymbol{\Psi = \sqrt{\frac{\kappa}{\kappa-1}\left[\left(\frac{p_2}{p_1}\right)^{\frac{2}{\kappa}} - \left(\frac{p_2}{p_1}\right)^{\frac{\kappa+1}{\kappa}}\right]} \approx \Psi_{max}\sqrt{1 - \left(\frac{\frac{p_2}{p_1} - b}{1-b}\right)^2}} \qquad (20)$$

Further approximations of the outflow function Ψ according to [9] are presented in [11] for comparison.

Because the approximation (20) has the smallest relative error of 0.30 % compared to (13), it was included as a basis in ISO 6358. This model contains two parameters: The critical pressure ratio b and the critical conductance C, see (21) and (22). The critical conductance C includes the maximum of flow function Ψ_{max}, as well as the cross-sectional area A_2 and the flow-reducing effects (fluid friction, wall friction, beam constriction, deflections, compaction surge losses), see (12). With the ratio $(T_0/T_1)^{0.5}$ the mass flow model was determined independently of the temperature at which C was measured. The mass flow model measured at temperature T_1, conductance C is related to temperature T_0, see (23), in order to be able to calculate the mass flow at any temperature T_1. Basically, this relationship is only valid for ideal gas.

$$\dot{m} = p_1 \cdot C \cdot \varrho_0 \cdot \sqrt{\frac{T_0}{T_1}} \sqrt{1 - \left(\frac{\frac{p_2}{p_1} - b}{1-b}\right)^2} \quad \text{for } \frac{p_2}{p_1} > b \quad (21)$$

$$\dot{m} = p_1 \cdot C \cdot \varrho_0 \cdot \sqrt{\frac{T_0}{T_1}} \quad \text{for } \frac{p_2}{p_1} \leq b \quad (22)$$

3. DETERMINATION OF THE MODEL PARAMETERS ACCORDING TO ISO 6358

The procedure for determining the model parameters C and b is described in detail in ISO 6358-1, Annex A [12]. This requires five individual measurements under steady-state conditions. The measured values which are shown in Table 1 as example. The critical conductance C_{LP} is determined at the supercritical measuring point marked with *. The influence of stagnation pressure (see [12] p22, A.1) has been checked and can be neglected because the diameter of the pressure measuring tube is large enough. Using the measuring points j = 1 ... 4 in the subcritical flow area, the critical pressure ratio b_{LP} is calculated as the arithmetic mean value. The parameters C_{LP} and b_{LP} are stored in the three right-hand columns of Table 1 the calculated and measured mass flow values are compared. The averaged relative deviation between mass flow model and measured values in this example is 3.2%.

In section 2 the basics of the mass flow model for ideal gases according to ISO 6358 were shown and illustrated with an example, Table 1. The following experimental investigations are aimed at examining the validity of the mass flow model in the real gas range. For this goal, experiments with air in the pressure range up to 300 bar and at a temperature of 20°C were carried out. Under these conditions, air has a real gas factor $Z_{Air} = 1.105$.

4. EXPERIMENTAL INVESTIGATION IN THE HIGH-PRESSURE RANGE

4.1. Determination of the model parameters in the high-pressure range

In the following tests the parameters C and b are determined at $p_1 = 300$ bar. These are referred to as high pressure C_{HP} and b_{HP}. The procedure is identical except for the pressure as in the example in section 3 in the low-pressure range. The pneumatic conductance C_{HP} was measured at supercritical flow identified by the following equation

$$C_{HP} = \frac{\dot{m}^*}{\varrho_0 p_1^*} \sqrt{\frac{T_1^*}{T_0}} \quad (23)$$

The measuring points for identifying the critical pressure ratio b, see j = 1...4 in Table 2, are in the subcritical flow range of the throttle at 80, 60, 40 and 20% of the supercritical mass flow ṁ*. At each measuring point a critical pressure ratio bj can be determined. The critical pressure ratio b of the nozzle element results from the arithmetic mean of these values, see (24), and

Table 1: Parameters ISO 6358-1

j [-]	p_1 Pa	p_2 Pa	p_2/p_1 [-]	T_1 [K]	b_j [-]	C_{LP} [s m^4/kg]	b_{LP} [-]	$\dot{m}_{calc}$ [g/s]	$\dot{m}_{meas}$ [g/s]	$\Delta\dot{m}/\dot{m} \cdot 10^2$ [%]
*	995216	102586	0,103	291,6		4,06E-10		0,481	0,481	0,00
1	995349	827861	0,832	291,7	0,539			0,358	0,372	-3,58
2	995825	892146	0,896	291,7	0,521		0,494	0,293	0,300	-2,41
3	996358	959180	0,963	291,7	0,488			0,181	0,180	0,57
4	997381	983959	0,987	291,7	0,428			0,110	0,104	6,23

indicates at which pressure ratio p_2/p_1 sound velocity in the narrowest cross-section prevails.

$$b_{HP} = \frac{1}{n}\sum_{j=1}^{n}\left(1 - \frac{\frac{p_{1,j}-p_{2,j}}{p_{1,i}}}{1-\sqrt{1-\left(\frac{\dot{m}_i}{C_{HP}\varrho_0 p_{1,j}}\sqrt{\frac{T_{1,j}}{T_0}}\right)^2}}\right) \quad (24)$$

4.2. Verification of the parameters C_{HP} and b_{HP} in High pressure range

To validate the parameters C_{HP} and b_{HP}, for 10 to 90% of the critical mass flow in 20% steps measurements are carried out, see j = 5...9 in Table 2. The investigation was made with two flow geometries. The "valve" geometry shown in Figure 3 in comparison to the "nozzle" nominal diameter (NW) 0.5 mm" has more cross-sectional changes and deflections. The mass flow function (25) and (26) with parameters C_{HP} and b_{HP} are measured in [11] and are valid for an inlet pressure p_1 = 300 bar.

$$\dot{m} = p_1 \cdot C_{HP} \cdot \varrho_0 \cdot \sqrt{\frac{T_0}{T_1}}\sqrt{1-\left(\frac{\frac{p_2}{p_1}-b_{HP}}{1-b_{HP}}\right)^2} \text{ for } \frac{p_2}{p_1} > b \quad (25)$$

$$\dot{m} = p_1 \cdot C_{HP} \cdot \varrho_0 \cdot \sqrt{\frac{T_0}{T_1}} \qquad \text{for } \frac{p_2}{p_1} \le b \quad (26)$$

A check of the model is only in the subcritical flow range $p_2/p_1 > b_{HP}$ necessary, since the flow in the supercritical range is only limited by the local speed of sound. At a further reduction of the pressure ratio p_2/p_1 the state variables determining the mass flow are constant, which also makes the conductance C_{HP} a constant variable.

The relative deviation between the calculated mass flow with the ellipse model and the measured mass flow is between - 1.2 and + 4.4 %. The maximum measuring error of the Coriolis mass flow sensor is according to the manufacturer's specifications (Endress and Hauser) 0.10% of the measured value.

The average of all 10 measuring points results in a relative mass flow deviation of 1.0%. In both measurements the maximum deviation is when the pressure ratio p_2/p_1 is close to 1. It is therefore to be expected that the relative deviation of the ellipse model continues to rise at $p_2/p_1 > 0.998$. In the remaining range of the pressure-mass flow characteristic a very good agreement can be established between model and reality.

For parameter determination at high pressure, the higher expenditure on pressure, temperature and flow measurement technology and an increased demand for media would be disadvantageous.

5. APPLICATIONS OF THE PARAMETERS C_{LP} AND B_{LP} IN THE HIGH-PRESSURE RANGE

The application of the C, b model in high pressure leads to the question of the validity range of the determined parameters. Since in the state region of real gases the gas properties are not linearly dependent on pressure and temperature, it can be assumed that the low-pressure parameters are not easily applicable in the high-pressure range.

Table 2: Measured values for identification of C_{HP}, b_{HP} at p_1 = 300 bar at the geometry "orifice NW 0,5 mm"

J [-]	p_1 bar	p_2 bar	p_2/p_1 [-]	$\dot{m}$ [g/s]	b_j [-]	C_{HP} [s m^4/kg]	b_{HP} [-]	j [-]	p_2/p_1 [-]	$\dot{m}_{calc}$ [g/s]	$\dot{m}_{meas}$ [g/s]	$\Delta\dot{m}/\dot{m} \cdot 10^2$ [%]
*	296,77	9,94	0,033	16,02		4,53E-10		5	0,695	14,44	14,49	-0,40
1	296,72	235,21	0,793	12,73	0,472			6	0.861	10,76	10,88	-1,17
2	296.48	265,70	0,896	9,58	0,478		0,463	7	0,930	7,91	7,90	0,14
3	297,21	282,41	0,950	6,70	0,456			8	0,978	4,57	4,52	1,05
4	297,22	293,72	0,988	3,30	0,448			9	0,998	1,44	1,38	4,40

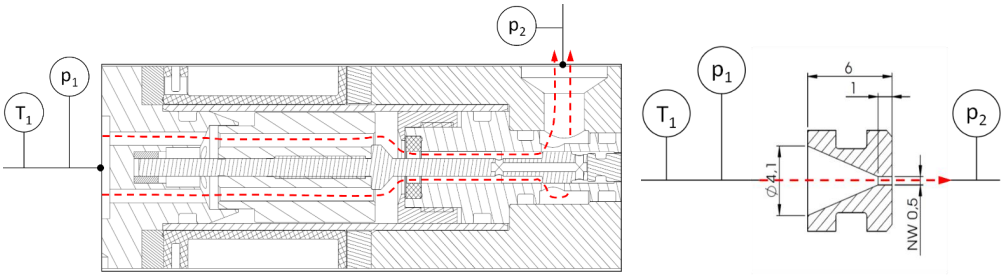

Figure 3: Illustration of the valve design (left) and the nozzle NW 0.5 mm (right).

The ellipse parameters C and b of the flow geometries "valve" and "nozzle NW 0.5 mm" were also determined in the ideal gas range according to ISO 6358. The comparison of the high- and low- pressure parameters in Fig. 4 shows that there is a "local validity" of the parameters in relation to the thermodynamic state. Strictly speaking, local validity means that the parameters C are only valid at the status point by which they were measured. The pneumatic conductance C_{HP}, which was determined at 300 bar, is at both geometries about 12% higher than at 10 bar, Fig. 4. The associated increase in mass flow through a geometrically identical throttle is on the one hand influenced by the real gas behavior of the air, as well as from the changed flow-reducing effects in the high-pressure range. The critical pressure ratio b_{HP} is reduced by about 9% versus the critical pressure ratio in the range of the ideal gas due to different thermodynamic state properties of the real gas.

The real gas properties lead to parameters that are only locally valid. Since the deviation of the pressure-flow characteristics is decisive for the user the parameters determined at high and low pressure were applied at 300 bar. The comparison of the two calculated mass flow functions is shown in Fig. 5 and 5. The deviation of the pneumatic conductivity leads to mass flow errors in the entire pressure range. As can be seen in equations (25) and (26), the pneumatic conductance C affects the overpressure and subcritical flow. The deviation of the critical pressure ratio b leads to comparatively lower mass flow errors than with the conductance, since the derivation of the ellipse function at critical pressure ratio becomes zero due to the definition.

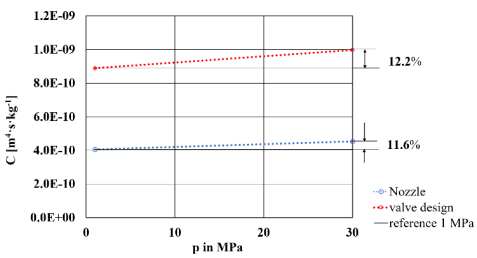

Figure 4: Comparison of measured conductance C of air in the ideal and real state range

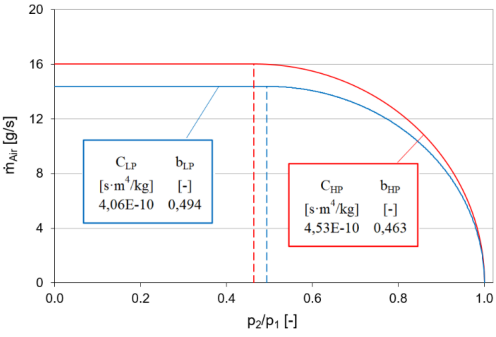

Figure 5: Comparison of the calculated mass flows with C_{LP}, b_{LP} and C_{HP}, b_{HP} at 300 bar. Geometry: "Nozzle" NW 0.5 mm

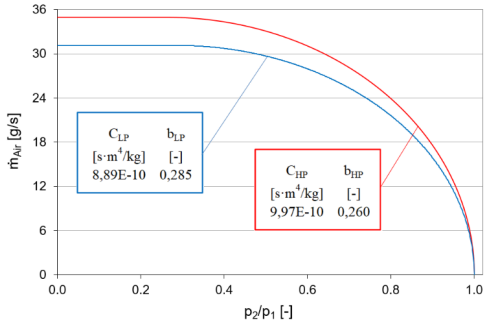

Figure 6: Comparison of the calculated mass flows with C_{LP}, b_{LP} and C_{HP}, b_{HP} at 300 bar. Geometry: "Valve"

6. APPLICATION OF THE PARAMETERS C_{LP} AND B_{LP} IN THE HIGH-PRESSURE RANGE UNDER CONSIDERATION OF THE REAL GAS BEHAVIOUR IN THE NARROWEST CROSS-SECTION

In the following, the influence of the real gas properties on the stationary mass flow through a throttle, considering pressure and temperature in the narrowest cross section is described. To calculate the change of state of a throttling of gaseous fluids, the system limit is chosen as shown in Fig. 1. The mass flow is limited by the thermodynamic state of the medium in the narrowest cross-section (state 2 in Fig. 1). The following assumptions were made to determine the condition of the medium in the narrowest cross-section:

- Real gas properties of dry air in the single-phase region according to Kretzschmar [5] based on the equation of state of Lemmon et al.
- The speed of sound prevails in the narrowest cross-section
- The media speed at the input is negligible
- $w_1 = 0$
- Height differences are neglected
- No technical work is performed
- No heat is exchanged across the system
- boundaries = > adiabatic
- No losses occur = > reversible
- Adiabatic and reversible = > isentropic

With the assumptions made, the thermodynamic state in the narrowest cross-section can be calculated iteratively and thus the influence of the real gas on the mass flow can be determined by the throttle. The schematic in Fig. 7 shows the sequence of calculation for the iterative calculation of the state variables.

The inlet pressure and the inlet temperature are constant in every iterative calculation. Exclusively for the starting point of the calculation it was assumed that ideal gas flows and an isentropic change of state is present. This results in the critical pressure ratio of the throttle ($b_{crit,\ ideal} = 0.528$), which means that the start pressure can be determined in the narrowest cross-section.

$$p_{2,real} = p_{1,real} \cdot b_{crit,ideal} \,. \tag{27}$$

Due to the pressure and temperature in the narrowest cross-section the thermodynamic initial state is defined. With the real isentropic exponent $\kappa_{2,real}$ and the real gas factor $Z_{2,real}$ the local isentropic sound velocity $w_{2,real}$ of the medium calculated

$$w_{2,real} = \sqrt{\kappa_{2,real} \cdot T_{2,real} \cdot R \cdot Z_{2,real}} \tag{28}$$

From the first law of thermodynamics follows for an adiabatic, stationary throttling without consideration of the height differences for the enthalpy in the narrowest cross-section

$$h_{2,real} = h_{1,real} - \frac{w_{2,real}^2}{2} \,. \tag{29}$$

The temperature of the first iteration step can be calculated from the enthalpy and the pressure at state 2. We use the backward function T=T(p, h), see [5]. With this temperature the next iteration loop starts, as shown in Fig. 7. The critical pressure ratio of the ideal gas is obtained from the derivative of the outflow function (13) according to the pressure ratio p_2/p_1.

In contrast to the critical pressure ratio of the nozzle under the conditions of the ideal gas in the starting step (18), in the further steps the critical pressure ratio is calculated as a function of the real isentropic exponent $\kappa_{2,real}$.

$$\left(\frac{p_{2,real}}{p_{1,real}}\right)_{crit,real} = \left(\frac{2}{\kappa_{2,real}+1}\right)^{\frac{\kappa_{2,real}}{\kappa_{2,real}-1}} \tag{30}$$

Since the real gas properties are strongly dependent on the medium, the iterative calculation for air and hydrogen is carried out. The real gas properties of Normal hydrogen in the single-phase region based on equation of state from Leachman et al. [7] is used, which were prepared by Kretzschmar et al. [4]. The convergence of the calculated quantities temperature and sound velocity at state 2 after 15 iteration steps was shown in [11]. The calculation of hydrogen or air was found at an inlet pressure

of 875 bar and an input temperature of 20 °C and was determined using of an appropriate convergence criterion.
Using the continuity equation and the calculated state data in the narrowest cross-section, the mass flow is calculated for critical flow conditions and the conductance C according to ISO 6358 is determined with (23).

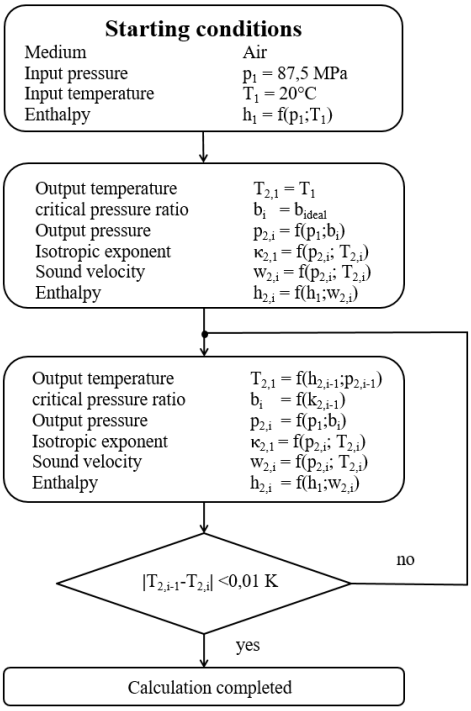

Figure 7: Flow chart for iterative state calculation in the narrowest cross section (all quantities were calculated with the equation of state of real gases; the index "real" was omitted for clarity)

The iteratively, with the equation of state of real gases, calculated parameter C is called C_{real} to distinguish it from the measured values. Using the same procedure, the parameters were determined at low pressure, i.e. with the equation of state of ideal gases, and is called the C_{ideal}.
The influence of the real gas properties on the conductance C, Fig. 8, can be described as follows (31).

$$100 \cdot \frac{C_{real} - C_{ideal}}{C_{real}} \qquad (31)$$

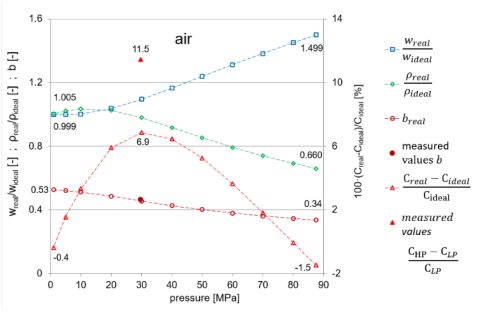

Figure 8: Iterative calculation of the state variables in the narrowest cross section. (assumptions: isentropic nozzle flow with real gas air)

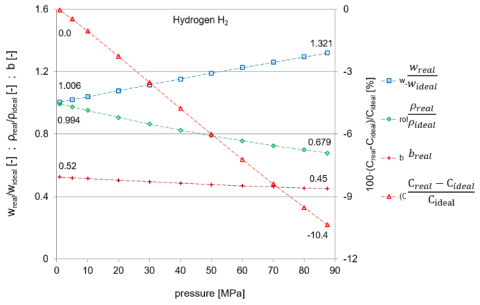

Figure 9: Iterative calculation of the state variables in the narrowest cross section. (assumptions: isentropic nozzle flow with real gas hydrogen)

An advantage of the iterative calculation of the thermodynamic state variables with the real gas data in the narrowest cross section is that the critical pressure ratio, the media density, the sound velocity and the pressure are calculated results. The process with increasing inlet pressure of the throttling shows, that the speed of sound increases significantly while the density decreases, see Fig. 8. These two properties have opposite effects on the mass flow, but they largely compensate each other. The critical pressure ratio measured with the geometry "nozzle" NW 0.5 mm is at b_{HP} = 0.463, Tab. 2, and deviates only 1.5% from the calculated value at p_1 = 300 bar. This agreement results from the fact that for this geometry the assumption of loss-free flow is close to reality. The coefficient from equation (31) shows that the conductance C_{real} increases about 7 % compared to C_{ideal} when flowing through a throttle at the pressure of

300 bar, thus the mass flow increases at the same rate. With a further pressure increase > 300 bar, the deviation between C_{ideal} and C_{real} decreases again, as the effects of density and sound velocity on the mass flow are increasingly compensated. At p_1 = 800 bar, the two coefficients are almost identical, but this does not mean that the gas behaves almost ideally. This is because the deviations in the speed of sound and density show that there is clearly real gas behavior in state 2. Figure 8 shows the difference between the measured and calculated conductance ratio according to (31). Differences exist is because the measured pneumatic conductance values contain the flow-reducing effects, in contrast to the calculated conductance values. The calculated coefficient according to (31) in Fig. 8 on the other hand only shows the change due to the real gas properties with increasing pressure. To enable conversion of LP parameters, the flow-reducing effects both at low pressure and at high pressure must be known. If this is not the case, at least the influence of the real gas properties with the help of iterative calculation can be compensated.

The real gas properties strongly depend on the medium and accordingly, the effects on the mass flow through a throttle. The iterative calculation for the hydrogen medium in Fig. 9 shows, that unlike air, no increase in mass flow can be expected from real gas. On the contrary the conductivity at an inlet pressure of p_1 = 875 bar and an input temperature of T_1 = 20°C is reduced by more than 10% in the comparison with the conductance of the ideal gas. The comparison between air and hydrogen under neglect of the flow-reducing effects also shows that the media properties have a significant influence on the critical pressure ratio. An isentropic change of the state starting at p_1 = 875 bar leads to different thermodynamic states for air and hydrogen in the narrowest cross section.

The proposed iterative calculation of the state data in the narrowest cross section confirms the local validity of the parameters. A significant proportion of the measured differences in the conductance can be explained by the changed gas properties in the real state range. It was neglected that the flow-reducing effects can change at high pressure, whereby an exact conversion of low-pressure parameters and their application in the high-pressure range is made more difficult.

7. SUMMARY

The model proposed in ISO 6358 for the description of a stationary mass flow through a throttle is very well suited for use in the real gas sector, since the losses in parameters C and b are completely included. A mathematical description of the mass flow in the supercritical and subcritical range is thus given. The procedure for determining the model parameters C and b can therefore be derived without restrictions from ISO 6358, whereby the appropriate high pressure must be used for inlet pressure. The existing model becomes the model for real gases by using the parameters C_{HP} and b_{HP}. The high-pressure parameters C_{HP} and b_{HP} of air at a pressure of 300 bar lead to low relative deviations of maximum 4.4% and average 1.0%. Because of the good agreement between calculated and measured mass flow using the model, this procedure is also suitable for the simulation of components where gases at high pressure and real gas properties are used.

NOMENCLATURE

A	[m^2] Area cross-section
b	[-] Critical compression ratio of pneumatic throttle valve [3]
C	[$s \cdot m^4/kg$] Sonic conductance of pneumatic throttle valve
c	[kJ/kg·K] Specific heat capacity
h	[J/kg] specific enthalpy
$\dot{m}$	[kg/s] mass flow
p	[Pa] pressure
R	[J/kg K] specific gas constant
T	[K] temperature
Ψ	[-] outflow function
w	[m/s] velocity
t. r.	From test result
Z	[-] Compressibility factor
α	[-] Flow contraction value
ε	[-] Pressure ratio p_2/p_1
κ	[-] Isentropic exponent
ρ	[kg/m^3] mass density
φ	[-] Speed characteristic number
$\frac{\Delta\dot{m}}{\dot{m}} \cdot 10^2$	[%] relative deviation between computed and measured mass flow

INDEX

0	Reference condition p = 10^5 Pa and T = 293.15 K (International Organization for Standardization, International Standard; ISO 6358: pneumatic fluid power – components using compressible fluids – determination of flow-rate characteristics, 1989)
1	State forward throttle valve
2	State in the flow area from the throttle valve
*	Supercritical flow condition (w = w_s velocity of sound an $p_2/p_1 \leq b$)
HP	High pressure - identification parameter values C and b in the high-pressure range of real gas state
I	Index for iterative calculation of the state in the flow area
ideal	Computed value based on ideal gas law
j	Index for the point of measurements for parameter identification
calc.	Calculated values
crit.	Critical flow condition (w = w_s velocity of sound an $p_2/p_1 = b$)
LP	Low pressure – parameter identification values C and b in the low-pressure range with ideal gas law
NW	Nominal diameter
max.	Maximum values
meas.	Measured values
real	Based on equation of state real gas
p	Isobaric
v	isochoric

REFERENCES

[1] Deutsches Institut für Normung e. V. (2004) Deutsche Norm DIN EN ISO 4126–1: Sicherheitseinrichtungen gegen unzulässigen Überdruck – Teil 1: Sicherheitsventile

[2] Haak S (1991) Theoretische und experimentelle Untersuchungen zur Aussagefähigkeit strömungstechnischer Kenngrößen an ausgewählten Strukturen pneumatischer Steuerventile. Dissertation, Hochschule Erfurt

[3] International Organization for Standardization (1989) International Standard ISO 6358: pneumatic fluid power – components using compressible fluids – determination of flow-rate characteristics

[4] Kretzschmar H-J, Stöcker I, Jähne I, Kunick M (2008) Stoffwertprogramm, Bibliothek für Wasserstoff – H2. Hochschule Zittau/ Görlitz – University of Applied Sciences, Fachbereich Maschinenwesen, Fachgebiet Technische Thermodynamik

[5] Kretzschmar H-J, Stöcker I, von Dolsperg GD, Kunick M (2009) Property library for standard dry air. Hochschule Zittau/Görlitz – University of Applied Sciences, Faculty of Mechanical Engineering, Department of Technical Thermodynamics

[6] Lemmon EW, Jacobsen RT, Penoncello SG, Friend DG (2000) Thermodynamic properties of air and mixtures of nitrogen, argon, and oxygen from 60 to 2000 K at pressures to 2000 MPa. J Phys Chem Ref Data 29(3):331–385

[7] Leachman JW, Jacobsen RT, Penoncello SG, Lemmon EW (2009) Fundamental equations of state for parahydrogen, normal hydrogen, and orthohydrogen. J Phys Chem Ref Data 38(3):721–748

[8] Murrenhoff H (2006) Grundlagen der Fluidtechnik, Teil 2: Pneumatik, 2 Aufl. Shaker Verlag, Aachen

[9] Sanville FE (1971) A new method of specifying the flow capacity of pneumatic fluid power valves. Second Fluid Power Symposium 4th–7th Jan. Guildford, S D3–37–D3–47

[10] Schmidt J, Peschel W, Beune A (2009) Experimentelle und theoretische Untersuchungen zu Hochdruck-Sicherheitsventilen – Auslegung und Design unterstützt durch numerische Rechenmethoden (CFD). Forschung im Ingenieurwesen 73:105–117

[11] Ramsperger M, Pasieka L (2014) Zur Anwendwendbarkeit des Massenstrom-Modells nach ISO 6358 mit den Kennwerten Leitwert C und kritisches Druckverhältnis b für Gase im Hochdruckbereich. Springer, Forsch Ingenieurwes DOI 10.1007/s10010-014-0177-7

[12] International Organization for Standardization (2013) International Standard ISO 6358-1: Determination of flow-rate characteristics of components using compressible fluids — Part 1: General rules and test methods for steady-state flow